Friction, Wear and Wear Protection

Edited by
Alfons Fischer and Kirsten Bobzin



DGM

WILEY-VCH GmbH & Co. KGaA

Related Titles

Mang, T., Bobzin, K., Bartels, T.
Industrial Tribology
Tribosystems, Wear and Surface Engineering, Lubrication
2010
ISBN: 978-3-527-32057-8

Stachowiak, G. (ed.)
Wear
Materials, Mechanisms and Practice
2005
Online Buch Wiley Interscience
ISBN: 978-0-470-01702-9

Kragelsky, I. V., Alisin, V. V. (eds.)
Tribology
Lubrication, Friction and Wear
2001
ISBN: 978-1-86058-288-2

Friction, Wear and Wear Protection

International Symposium on Friction, Wear and Wear Protection 2008 Aachen, Germany

Edited by
Alfons Fischer and Kirsten Bobzin

DGM
Deutsche Gesellschaft
für Materialkunde e.V.

WILEY-VCH

WILEY-VCH GmbH & Co. KGaA

The Editors

Prof. Dr.-Ing. Alfons Fischer
Institut Produkt Engineering
Werkstofftechnik
Lotharstr. 1
47057 Duisburg
Germany

Prof. Dr-Ing. Kirsten Bobzin
RWTH Aachen University
(IOT)
Intzestr. 10
52072 Aachen
Germany

All books published by Wiley-VCH are carefully produced. Nevertheless, authors, editors, and publisher do not warrant the information contained in these books, including this book, to be free of errors. Readers are advised to keep in mind that statements, data, illustrations, procedural details or other items may inadvertently be inaccurate.

Library of Congress Card No.:
applied for

British Library Cataloguing-in-Publication Data
A catalogue record for this book is available from the British Library.

Bibliographic information published by the Deutsche Nationalbibliothek
The Deutsche Nationalbibliothek lists this publication in the Deutsche Nationalbibliografie; detailed bibliographic data are available on the Internet at <http://dnb.d-nb.de>.

© 2009 WILEY-VCH Verlag GmbH & Co. KGaA, Weinheim

All rights reserved (including those of translation into other languages). No part of this book may be reproduced in any form - by photoprinting, microfilm, or any other means - nor transmitted or translated into a machine language without written permission from the publishers. Registered names, trademarks, etc. used in this book, even when not specifically marked as such, are not to be considered unprotected by law.

Typesetting WGV Verlagsdienstleistungen, Weinheim

Printing Strauss GmbH, Mörlenbach

Binding Litges & Dopf GmbH, Heppenheim

Cover Design Adam-Design, Weinheim

Printed in the Federal Republic of Germany
Printed on acid-free paper

ISBN: 978-3-527-32366-1

Preface

Friction, Wear, and Wear Protection 2008

Basics – Materials – Tools – Parts – Coatings – Processes

It is certainly one of the major challenges of material scientists and mechanical engineers to cope with the demands for long lasting and reliable systems in all markets and for all applications. The loss of energy by friction and the limits of endurance by wear should be countered by well selected materials and surfaces. The economical and ecological significance of this is undisputable and can sum up to 4 % of the gross national product of industrial countries. Although the basic understanding of the mechanisms of friction and wear has remarkably increased during the last five decades, many technical solutions are still carried out following "trial and error". But any well-aimed selection of the most suitable surface materials, the optimal topography, and the properly adjusted chemistry in combination with productional and structural properties require a systematic approach and a deep understanding of the acting mechanisms. Thus friction, wear, and wear protection are truly interdisciplinary fields that integrate scientists from basic and applied science as well as engineering.

This publication represents the contributions of many different aspects of tribology which have been presented at the International Symposium on Friction, Wear, and Wear Protection from April 9th to 11th, 2008, in Aachen, Germany.

Beside aspects of metals, ceramics, polymers and their composites as bulk materials or thick and thin coatings modelling and the emerging field of computer simulation were of certain interest. Thus new understanding could be gained by modern testing and surface analysis techniques supported by computer simulations on all length scales. This combination helps to correlate the macroscopic parameters with the micro- and nanoscopic alterations of topography, chemistry, physics and microstructure of near surface materials, the interfacial media, and the environment.

Today we can find wear resistant and low friction materials by means of a systemic analysis for any tribosystem e.g. under extreme environments or the demand of being environmentally friendly. Still these materials cannot be separated from appropriate production processes of whatever kind, which finally must result in a reliable and affordable product.

Besides the traditional areas like mining, plant construction, automotive, air- and spacecraft, tooling, and civil engineering modern tribomaterials have to be also available for micro- and nanosystems as well as for information and medical technologies. Thus members from all disciplines working in basic and applied research, development, and the application of tribomaterials took part and discussed the latest findings on the basic understanding of friction and wear and shared possible solutions for wear protection.

This publication would not have been possible without the authors and the reviewers of these papers. Thus we would like to thank all of them for their valuable contributions. In particular the editors would like to thank Prof. Dr.-Ing. Hubertus Murrenhoff and Dr.-Ing. Nazlim Bagcivan RWTH Aachen as well as Dipl.-Ing. Mareike Hahn and Dipl.-Ing. Robin Pourzal, Universitaet Duisburg-Essen, for their involvement and steady support during the reviewing process.

Prof. Dr.-Ing. Alfons Fischer — Universität Duisburg-Essen, Germany

Prof. Dr.-Ing. Kirsten Bobzin — RWTH Aachen, Germany

Inhalt

Part I: Plenary Lectures 1

Wear Simulation with a Focus on Mild Wear in Rolling and Sliding Contacts 3
S. Andersson, Royal Institute of Technology (KTH), Stockholm (S)

Polymer Composites in Tribology 20
K. Friedrich, Institute for Composite Materials (IVW GmbH), Technical University of Kaiserslautern, Kaiserslautern (D)

Part II: Lectures 31

Effect of Graphite and Silicon Carbide Addition on the Hardness and Wear Resistance of Al-4wt% Mg Alloys 33
A. M. Hassan, G. M. Tashtoush, J. A. Al-Khalil, Faculty of Engineering, Jordan University of Science and Technology, Irbid (JOR)

Aluminum Based Sliding Materials with Soft Phases – Intrinsic For-giving Overload Behavior? 45
F. Grün, CD-Laboratory for Fatigue Analysis, University of Leoben, Leoben (A); I. Gódor, W. Eichlseder, Chair of Mechanical Engineering, University of Leoben, Leoben (A)

Friction and Wear Behavior of the Magnesium Alloy AZ91D under Lubricated Sliding Conditions 52
C. Chen, H. Bosse, L. Deters, Otto von Guericke University Magdeburg (D)

Tribological Properties of Laser Interference Induced Microstructural Architectures in Metallic Systems 59
C. Gachot, P. Leibenguth, F. Mücklich, Saarland University, Department of Materials Science and Engineering, Saarbrücken (D)

Cu-graphite Composites: Composition Dependence of Friction Coefficient 67
J. Kovácik, Slovak Academy of Sciences, Bratislava (SK); J. Bielek, Å . Emmer, Slovak University of Technology, Bratislava (SK)

Laser Nitriding: A Promising Way to Improve the Cavitation Erosion Resistance of Components Made of Titanium Alloys 74
J. Kaspar, Jörg Bretschneider, Steffen Bonß, Bernd Winderlich, Berndt Brenner, Fraunhofer Institut für Werkstoff- und Strahltechnik, Dresden; J. Bretschneider, S. Bonß, B. Winderlich, B. Brenner, Fraunhofer Institut für Werkstoff- und Strahltechnik, Dresden (D)

Production of Coal Crushing Hammer Heads by Bi-metal Casting 81
T. Kirma, E. Selcuk, A. Kalkanli, A. Cetin, Department of Metallurgical and Materials Engineering, Middle East Technical University, Ankara (TR)

Characterization and Modeling of the Wear Behavior of Highly Wear-Resistant Special Structural Steels 93
A. Dietrich, TKS Profit Center Grobblech, Duisburg (D); P. Feinle, HS Mannheim, Mannheim (D); A. Kern, U. Schriever, TKS Profit Center Grobblech, Duisburg (D)

Effect of Die Material on Friction During Iron Powder Compaction..... 104
R. B. Wassenberg, M. Drygalov, P. Beiss, Institute for Materials Applications in Mechanical Engineering, RWTH Aachen (D)

Adhesion Resistance of Particle Reinforced Steel Matrix Composite During Sliding Against Aluminium 110
D. C. Lou, SINTEF Materials and Chemistry, Trondheim (N); L. O. Finnerud, J. K. Solberg , Norwegian University of Science and Technology, Trondheim (N); O. M. Akselsen, N. Dahl, SINTEF Materials and Chemistry, Trondheim (N)

Graded Layers for Wear and Corrosion Protection Produced by Laser Cladding..... 117
A. Weisheit, K. Wissenbach, Fraunhofer Institut Lasertechnik, Aachen (D)

The Influence of Induction Hardening on the Impact Wear Resistance of Compacted Graphite Iron..... 124
T. Slatter, The University of Sheffield, Sheffield (GB); M. Broda, Ford Forschungszentrum Aachen GmbH, Aachen (D); R. Lewis, The University of Sheffield, Sheffield (GB)

Thermally Sprayed Nanocrystalline Cylinder Running Surfaces in Modern Passenger Car Engines..... 130
K. Bobzin, F. Ernst, K. Richardt, T. Schläfer, Surface Engineering Institute, RWTH Aachen University, Aachen (D); C. Verpoort, Ford Research Center Aachen, Aachen (D)

Investigation of Wear Mechanisms and Microstructural Changes of Thermally Sprayed Coatings in Cylinder Bores after Motor Tests 140
M. Hahn, University of Duisburg-Essen, Institute of Product Engineering, Materials Science and Engineering, Duisburg (D); R. Theissmann, University of Duisburg-Essen, Faculty of Engineering and CeNIDE, Duisburg (D); B. Gleising, University of Duisburg-Essen, Institute of Product Engineering, Materials Science and Engineering, Duisburg (D); W. Dudzinski, Wroclaw University of Technology, Institute of Materials Science and Applied Mechanics, Wroclaw (PL); A. Fischer, University of Duisburg-Essen, Institute of Product Engineering, Materials Science and Engineering, Duisburg (D)

Hot Direct Extrusion of Abrasion Resistant Fe-Base Metal Matrix Composites – Microstructure and Wear Properties 152
M. Karlsohn, Köppern Entwicklungs-GmbH, Hattingen (D); A. Röttger, Ruhr-Universität Bochum, Bochum (D); P.A. Silva, S. Weber, A. R. Pyzalla, Max-Planck-Institut für Eisenforschung GmbH, Düsseldorf (D); W. Reimers, Technische Universität Berlin, Berlin (D); W. Theisen, Ruhr-Universität Bochum, Bochum (D)

Development of Wear-Resistant Composites Based on Heat-Resistant Fe-Cr-Al Alloys 159
O. Mikadze(Sp), E. Kutelia, D. Gventsadze, O. Tsurtsumia, B. Bulia, G. Mikadze, T. Dzigrashvili, Ferdinad Tavadze Institute of Metallurgy and Materials Science, Georgian Technical University, Tbilisi (GE)

Sliding Friction: Global Versus Local Analysis 165
A. Ramalho, M.C. Oliveira, L.F. Menezes, CEMUC; Dep. of Mechanical Engineering, University of Coimbra (P)

Deformation of WC-Co Hardmetals During Scratch Testing..... 171
S. N. Ndlovu, K. Durst, M. Göken, University of Erlangen-Nürnberg, Erlangen (D)

Nanotribology at Electrodes: Influence of Adsorbates and Potential on Friction Forces Studied with Atomic Force Microscopy 178
M. Nielinger, F. Hausen, N. Podghainiy, H. Baltruschat, Institute for Physical and Theoretical Chemistry, University of Bonn, Bonn (D)

Influence of Electrode Potential and Chelating Agents on Tribocorrosion Mechanisms of Tungsten 185
J. Stojadinovic, Ecole Polytechnique Fédérale de Lausanne EPFL, Laboratoire de métallurgie chimique, Lausanne (CH); D. Bouvet, M. Declercq, Ecole Polytechnique Fédérale de Lausanne EPFL, Laboratoire d'électronique générale 1, Lausanne (CH); S. Mischler, Ecole Polytechnique Fédérale de Lausanne EPFL, Laboratoire de métallurgie chimique, Lausanne (CH)

Corrosion Behavior of Silicon Carbide in Aqueous Media Lubricated Sliding Applications..... 191
O. Krummhauer, Fraunhofer-Institut für Werkstoffmechanik IWM, Freiburg (D); V. Presser, Eberhard-Karls-Universität, Institute for Geoscience, Applied Mineralogy, Tübingen (D); A. Kailer, Fraunhofer-Institut für Werkstoffmechanik IWM, Freiburg (D); K.G. Nickel, Eberhard-Karls-Universität, Institute for Geoscience, Applied Mineralogy, Tübingen (D); T. Hollstein, Fraunhofer-Institut für Werkstoffmechanik IWM, Freiburg (D)

On the P-T Conditions of Wet Silicon Carbide Tribo-corrosion 198
V. Presser, Institute for Geosciences, Eberhard-Karls-Universität, Tübingen (D); O. Krummhauer, Fraunhofer Institute for Mechanics of Materials, Freiburg (D); K. G. Nickel, Institute for Geosciences, Eberhard-Karls-Universität, Tübingen (D); A. Kailer, Fraunhofer Institute for Mechanics of Materials, Freiburg (D); R. Wirth, Geoforschungszentrum, Potsdam (D)

On the Tribological Characterization of Engineering Ceramics 207
Y. A-H. Mashal, University of Engineering & Technology, Taxila (PK); J. K. Lancaster, A. G. Atkins, School of Engineering, Reading University, Reading (GB)

Experimental Investigation on Wear of Ceramic Materials for Dental Restorations 216
H.G. Gräber, University Hospital, RWTH, Aachen (D); R. Wäsche, Federal Institute for Materials Research and Testing (BAM), Berlin (D)

Scratch Tests on Natural Nacre -- Reference for Implant Material 227
B. Denkena, L. de Leon, M. van der Meer, A. Moral, Leibniz Universität Hannover, Garbsen (D)

Influence of DLC Layer on the Wear Behavior of Unhardened Steel Moulds 234
W. Tillmann, E. Vogli, M. Gathen, S. Momeni (Sp), Dortmund University of Technology, Dortmund (D)

The Wettability of DLC Coatings with Ester and Polyalphaolefin 240
K. Bobzin, N. Bagcivan, N. Goebbels, K. Yilmaz, Surface Engineering Institute RWTH Aachen University, Aachen (D)

CVD-Diamond Coating as Wear Protection for Standard Heat-Treatable Steel 247
K. Kellermann, J. Fandrey, S. M. Rosiwal, R. F. Singer, Institute of Science and Technology of Metals, University of Erlangen-Nuremberg, Nuremberg (D)

Modeling and Simulation of Unlubricated Oscillating Sliding Wear of DLC-coatings 256
L. Steiner, V. Bouvier, S. Grosse, Robert Bosch GmbH, Stuttgart (D); N. Huber, Institut für Werkstoffphysik und Technologie, Technische Universität Hamburg-Harburg (D); V. Hegadekatte, Institut für Zuverlässigkeit von Bauteilen und Systemen, Universität Karlsruhe (TH), Karlsruhe (D); C.P.O. Treutler, Robert Bosch GmbH, Stuttgart (D)

A Study of Mechanical and Tribological Properties of Electroless Nickel-Boron Deposits after Heat and Thermochemical Treatments 264
V. Vitry, F. Delaunois, Faculté Polytechnique de Mons, Mons (B)

Multiple Asperity Dry Contacts -- Comparison of Experiments and Analytical Computer Simulation 271
Ch. Zietsch, A. Fischer, University of Duisburg-Essen, Duisburg (D)

Influence of the Surface Topography on the Transition between High and Low Wear Regimes under Multidirectional Reciprocating Sliding 278
I. Samerski, J. Schöfer, Robert Bosch GmbH, Stuttgart (D); D. J. Schipper, Laboratory for Surface Technology and Tribology, University of Twente (NL); A. Fischer, Universität Duisburg-Essen, Werkstofftechnik, Duisburg (D)

Various Influence Factors on the Development of Standstill Marks (False-Brinelling Effect) 290
M. Grebe, P. Feinle, W. Hunsicker, Tribology Competence Center – Hochschule Mannheim (D)

On Dynamic Friction Phenomena in Brake Systems 301
G.-P. Ostermeyer, K. Bode, Institute of Dynamics and Vibrations, Braunschweig University of Technology, Braunschweig (D)

Creep Behavior of an Asperity in Fully Plastic Contact 307
A. Goedecke, Institute of Technical Mechanics, Johannes Kepler University of Linz (A); Siemens AG Corporate Technology, Munich (D); R. Mock, Siemens AG Corporate Technology, Munich (D)

An Approach to Energy Based Fretting Wear Prediction at Low Frequency Loading 314
M. Becker, MTU Aero Engines GmbH, Munich (D); D. Nilsson, The Royal Institute of Technology, Stockholm (S); P. Wackers, A. Werner, V. Arrieta, MTU Aero Engines GmbH, Munich (D)

On Scratching of Elastic-Plastic Thin Films on Elastic Substrates 321
F. Wredenberg, P.-L. Larsson, KTH Solid Mechanics, Stockholm (S)

Tribological Approach of Forming Tool Performance Based on Finite Element Modelling (FEM) 327
R. Hernández, Department of Materials Technology, CTM-Technologial Center, Manresa (E); Department of Materials Science and Metallurgy Engineering, Universitat Politècnica de Catalunya, Manresa (E); M. R. Cruz, I. Picas, Department of Materials Technology, CTM-Technologial Center, Manresa (E); M.D. Riera, Department of Materials Technology, CTM-Technologial Center, Manresa (E); Department of Materials Science and Metallurgy Engineering, Universitat Politècnica de Catalunya, Manresa (E); D. Casellas, Department of Materials Technology, CTM-Technologial Center, Manresa (E)

Computation of Die Loads in Sheet Forming Using Dies of Tool Steel with Improved Anti-galling Properties 333
A. Thuvander, O. Sandberg, Uddeholm Tooling AB, Hagfors (S)

Wearing Effects in Cutting Processes - Development of a Combined Simulation Approach 339
U. Großmann, M. Rechberger, J. Blömer, J. Bertling, Fraunhofer UMSICHT, Oberhausen (D)

Modelling and Simulation of Wear in Micro-machines 347
V. Hegadekatte, Institut für Zuverlässigkeit von Bauteilen und Systemen, Universität Karlsruhe (TH), Karlsruhe (D); Institut für Werkstoffphysik und Technologie, Technische Universität Hamburg-Harburg (D); N. Huber, Institut für Werkstoffphysik

und Technologie, Technische Universität Hamburg-Harburg (D); Institute of Materials Research, GKSS-Research Centre, Geesthacht (D); O. Kraft, Institut für Zuverlässigkeit von Bauteilen und Systemen, Universität Karlsruhe (TH), Karlsruhe (D)

Development of Oil Lubricated Ceramic/Steel Friction Pairs at High Sliding Speeds 355
R. Wahl, K. Wauthier, K.-H. Zum Gahr, Universität Karlsruhe, Institute of Materials Science and Engineering II, and Forschungszentrum Karlsruhe, Institute for Materials Research I, Karlsruhe (D)

Surface Textured Steel/Ceramic and Ceramic/Ceramic Pairs Sliding in Isooctane 362
M. Wöppermann, K.-H. Zum Gahr, Universität Karlsruhe, Institute of Materials Science and Engineering II, and Forschungszentrum Karlsruhe, Institute for Materials Research I, Karlsruhe (D)

Influence of Surface Modification on Dry Friction Performance of Alumina Mated Against Steel 369
R. Wallstabe, J. Schneider, K.-H. Zum Gahr, Universität Karlsruhe, Institute of Materials Science and Engineering II, and Forschungszentrum Karlsruhe, Institute for Materials Research I, Karlsruhe (D)

Microtribological Characterization of Engineering Ceramic, Cemented Carbide and Steel under Rolling Conditions 376
S. Kurzenhäuser, J. Schneider, K.-H. Zum Gahr, Universität Karlsruhe, Institute of Materials Science and Engineering II, and Forschungszentrum Karlsruhe, Institute for Materials Research I, Karlsruhe (D)

The Behavior of Silicon Nitride Tools in Hot Rolling Copper Wire 383
I. Khader, Fraunhofer-Institut für Werkstoffmechanik IWM; Freiburg (D); Universität Karlsruhe (TH), Institut für Zuverlässigkeit von Bauteilen und Systemen (IZBS), Karlsruhe (D); S. Fünfschilling, Universität Karlsruhe (TH) – Institut für Keramik im Maschinenbau (IKM), Karlsruhe (D); A. Kailer, Fraunhofer-Institut für Werkstoffmechanik IWM; Freiburg (D); R. Oberacker, Universität Karlsruhe (TH) – Institut für Keramik im Maschinenbau (IKM), Karlsruhe (D)

Tribological Investigation of Si_3N_4 Composites 393
Z. Koncsik, M. Berkes Maros, L. Kuzsella, University of Miskolc, Department of Mechanical Engineering, Miskolc (H)

Wear Behavior of CMC and MMC under High-Speed Dry Sliding on Steel 402
S.N. Kulkov, N.L. Savchenko, S.F. Gnyusov, Institute of Strength Physics and Materials Science SB RAS, Tomsk (RUS)

Ultralow Friction and Wear of Reciprocating Systems Lubricated by Liquid Crystalline Fluids 409
A. Kailer, T. Amann, G. Konrath, Fraunhofer-Institut für Werkstoffmechanik IWM, Freiburg (D); D. Janietz, H. Sawade, Fraunhofer-Institut für Angewandte Polymerforschung IAP, Potsdam-Golm (D)

Study on the Wear and Friction of Short Carbon Fiber and/or Nano-TiO_2 417
L. A. Gyurova, Institut fuer Verbundwerkstoffe GmbH (Institute for Composite Materials), University of Kaiserslautern, Kaiserslautern (D); Z. Jiang, The Hong Kong Polytechnic University, Hong Kong (CN); A. K. Schlarb, K. Friedrich, Institut fuer Verbundwerkstoffe GmbH (Institute for Composite Materials), University of Kaiserslautern, Kaiserslautern (D); Z. Zhang, National Center for Nanoscience and Technology of China, Beijing (CN)

Dry Sliding Wear Properties of Thermal Spray Coatings in the TiO_2 423
L.-M. Berger, C. C. Stahr, S. Saaro, Fraunhofer Institute for Material and Beam Technology, Fh-IWS, Dresden (D); S. Thiele, Fraunhofer Institute for Ceramic Technologies and Systems, Fh-IKTS, Dresden (D); M. Woydt, Fraunhofer Institute for Ceramic Technologies and Systems, Federal Institute for Materials Research and Testing, BAM, Berlin (D)

Friction in Continuous Casting of Steel: Lubrication Experiments at 1200 °C 431
D. Senk, Department of Ferrous Metallurgy at RWTH Aachen University, Aachen (D); A. Münch, ThyssenKrupp Steel AG, Duisburg (D); K. Schulz, S & B Industrial Minerals GmbH, Business Unit, Stollberg (D)

Simulative Wear Testing of Tool Materials for Comminution of Hard Ore Material 439
D. D. Olsson, R&D Research Centre Dania, FLSmidth A/S (DK); N. Bay, Dept. of Mechanical Engineering, Technical University of Denmark (DK)

Online Wear Measurements in Advanced Lubricated Systems 446
C. Fehsenfeld, P. Fehsenfeld, A. Kleinrahm, ZAG Zyklotron AG, Eggenstein-Leopoldshafen (D); P. Berlet, Ph. Erhard, IAVF Antriebstechnik GmbH, Karlsruhe (D)

Friction and Wear of Highly Loaded Mixed Lubrication Contacts Influenced by Superposed Sliding Directions and Intermittent Surface Pressure Performed on a Novel Model Bench 453
A. Albers, M. Behrendt, S. Ott, IPEK - Institute of Product development at University of Karlsruhe (D)

Design and Evaluation of a Rolling Friction Apparatus for Micro Linear Bearings 460
R. Meeß, F. Löffler, Physikalisch-Technische Bundesanstalt, Braunschweig (D)

Advances in Thin Film Layer Sensors for Temperature Measurements in Highly Loaded Tribological Contacts under Mixed Lubrication 467
A. Albers, S. Beauvais, J. Bsul, W. Burger, IPEK, University of Karlsruhe (D)

Fatigue Life in Rolling Contacts with Rough Surfaces 473
M. Gleß, Robert Bosch GmbH, Stuttgart (D); V. Fafoutis, National Technical University of Athens (GR); G. Repphun, Robert Bosch GmbH, Stuttgart (D); C. G. Provatidis, National Technical University of Athens (GR); D. Bartel, L. Deters, Otto von Guericke University Magdeburg (D)

Reciprocating Sliding Wear of Surface Modified Austenitic High Nitrogen Stainless Steel and CoCrMo-alloy 479
R. Pourzal, A. Fischer, Material Science and Engineering, Institute of Product Engineering, University Duisburg-Essen (D)

Tribology of Human Skin: Effect of Epidermal Hydration on Textile Friction 487
L.-C. Gerhardt, Laboratory for Protection and Physiology, EMPA, Swiss Federal Laboratories for Materials Testing and Research St. Gallen (CH); Laboratory for Surface Science and Technology, Department of Materials, ETH Zürich, Zürich (CH); V. Strässle, Laboratory for Protection and Physiology, EMPA, Swiss Federal Laboratories for Materials Testing and Research St. Gallen (CH); N.D. Spencer, Laboratory for Surface Science and Technology, Department of Materials, ETH Zürich, Zürich (CH); S. Derler, Laboratory for Protection and Physiology, EMPA, Swiss Federal Laboratories for Materials Testing and Research St. Gallen (CH)

Introduction and Survey of the Research within the Collaborative Research Center 442 `Environmentally Friendly Tribosystems by Suitable Coatings and Fluids with Respect to the Machine Tool 494
H. Murrenhoff, RWTH Aachen University, Aachen (D)

Epoxidation of Oleic Esters for the Synthesis of Environmentally Friendly Lubricants 509
M.J.S. Küppers, D.H. Müller, F. Pontzen, D. Herzog, M.A. Liauw, L. Greiner, RWTH Aachen University, Aachen (D)

How Friction and Ageing Influence the Toxic and Ecotoxic Behaviour of Used, Bio-based Lubricants 515
J. Bressling, Institute of Hygiene and Environmental Medicine, RWTH Aachen (D); O.-C. Göhler, Fluidtronics GmbH, Krefeld (D); C. Bugiel, Vestas Nacelles Deutschland GmbH, Dortmund (D); W. Dott, Institute of Hygiene and Environmental Medicine, RWTH Aachen (D); B. Erlenkämper, Institute of Hygiene and Environmental Medicine, RWTH Aachen (D); EvonikDegussa GmbH, Hanau (Wolfgang) (D)

Characterization of Substantial Changes of Different Native Ester-based Lubricants Before and After Tribological Application 521
S. Michael, Institute of Hygiene and Environmental Medicine, RWTH Aachen (D); K. Bobzin, A. Krämer, Institute of Surface Engineering, RWTH Aachen (D); W. Dott, H. Maier, Institute of Hygiene and Environmental Medicine, RWTH Aachen (D)

High Performance PVD Tool Coatings 527
K. Bobzin, N. Bagcivan, P. Immich, M. Ewering, C. Warnke, Surface Engineering Institute (IOT), RWTH Aachen University, Achen (D)

Manufacturing Tool-Coating-Compatible Stamping and Fine Blanking Tool Surfaces 535
F. Klocke, C. Zeppenfeld, P. Mattfeld, M. Zimmermann, Laboratory for Machine Tools and Production Engineering, RWTH Aachen University, Aachen (D)

PVD Coating Systems for Environmentally Friendly Machining 541
F. Klocke, K. Gerschwiler, S. Cordes, R. Fritsch, Laboratory for Machine Tools and Production Engineering, Chair of Manufacturing Technology, RWTH Aachen University, Aachen (D)

Wear Resistant PVD-Coatings for Components 547
K. Bobzin, N. Bagcivan, N. Goebbels, A. Krämer, Surface Engineering Institute, RWTH Aachen University, Aachen (D)

Numerical Calculation of Failure Stresses of PVD Coatings Based on Test Data 554
P. W. Gold, J. Loos, H. Elgeti, Institut für Maschinenelemente und Maschinengestaltung (IME), RWTH Aachen (D)

Performance of DLC-coated Spindle Ball Bearings 560
C. Brecher, G. Gerlach, WZL Werkzeugmaschinenlabor, RWTH Aachen (D)

Effects of PVD-coatings on Fatigue of Roller Bearings 568
P.W. Gold, T. Wolf, M. Plogmann, Institute for Machine Elements and Machine Design (IME), RWTH Aachen University, Aachen (D)

Efficiency of Axial Piston Pumps With Coated Tribological Systems 575
C. Enekes, H. Murrenhoff, Institute for Fluid Power Drives and Controls of RWTH Aachen University, Aachen (D)

Influence of Friction on Ageing of Lubricants 582
J. Schumacher, O.-C. Göhler, H. Murrenhoff, IFAS, RWTH Aachen (D)

Improvement of the Efficiency of Parallel-Axis-Transmissions by Means of PVD-Coatings 588
C. Brecher, A. Bagh, C. Gorgels, RWTH Aachen University, Aachen (D)

Part III: Posters..... 595

Influence of Solidification Microstructure on the Wear Resistance of Al-Si and Al-Sn Alloys Directionally Solidified under Unsteady State Conditions..... 597
K. Sabat, N. Cheung, J. E. Spinelli, L. C. Casteletti, A. Garcia, State University of Campinas, Campinas (BR); State University of Sao Paulo, Sao Carlos (BR)

Study of Different Aspects of a Novel Method for Surface Carburizing of CP-Ti 604
M. Aliofkhazraei, A. Sabour Rouhaghdam, Faculty of Engineering, Materials Engineering Department, Tarbiat Modares University, Tehran (IR); H. Alimadadi, Department of Materials and Manufacturing Technology, Chalmers University of Technology, Göteborg (S)

Study on Hardfaced Wear Resistant Bronze Alloy..... 610
I. Voiculescu, V. Geanta, R. Stefanoiu, University "Politehnica" of Bucharest, Bucharest (H); H. Binchiciu, SC SUDOTIM AS SRL, Timisoara (RO); I. V. Simiti, N. Jumate, Technical University of Cluj Napoca, Cluj-Napoca (RO); R. Vasiu, SC TEHNOMAG SA, Cluj-Napoca (RO)

Study of the Abrasive Wear Behaviour of Electrified Railway Wires 618
A. Garcia, Escuela Politécnica Superior (UDC), Mendizábal s/n, Ferrol, A Coruña (E); V. Lorenzo, E.T.S.I.I. - U.P.M., Madrid (E); A. Varela, C. Camba, Escuela Politécnica Superior (UDC), Mendizábal s/n, Ferrol, A Coruña (E); V. Blazquez, E.T.S.I.I. - U.P.M., Madrid (E)

Surface Alloying of CP-Ti Using Tungsten Inert Gas Process With Pre-Placed BN..... 623
R. Yazdi, F. Kashani Bozorg, L. Moazzemi and K. Hazeli, The university of Tehran, Tehran; F. Kashani Bozorg, L. Moazzemi, K. Hazeli, The university of Tehran, Tehran (IR)

Influence of Surface Condition on Wear and Demoulding Behaviour of Mould Inserts for Micro Powder Injection Moulding 629
J. Schneider, Institute of Materials Science and Engineering II, University of Karlsruhe (TH), and Institute for Materials Research I, Forschungszentrum Karlsruhe (D); A. Kienzler, V. Schulze, Institute of Materials Science and Engineering I, University of Karlsruhe (TH), Karlsruhe (D); K.-H. Zum Gahr, Institute of Materials Science and Engineering II, University of Karlsruhe (TH), and Institute for Materials Research I, Forschungszentrum Karlsruhe (D)

Study of Pulsed Bipolar Nanocrystalline Plasma Electrolytic Carburizing on Nanostructure and Friction Coefficient of Compound Layer 637
M. Aliofkhazraei, A. Sabour Rouhaghdam, Faculty of Engineering, Materials Engineering Department, Tarbiat Modares University, Tehran, Iran (IR); H. Alimadadi, Department of Materials and Manufacturing Technology, Chalmers University of Technology, Göteborg (S)

Abrasive Wear Resistance of AISI 420 Stainless Steel After Laser Surface Treatment 645
M. A. Larosa, State University of Campinas, Campinas (BR); M. A. Pinto, Federal University of Ouro Preto, Ouro Preto (BR); M. C. F. Ierardi, State University of Campinas, Campinas (BR)

Enhanced Wear Resistance of Precipitation Hardening Steels by Laser Solution Annealing and Subsequent Aging Treatment 654
J. Kaspar, B. Brenner, A. Luft, F. Tietz, J. Bretschneider, Fraunhofer Institut für Werkstoff- und Strahltechnik, Dresden (D)

Smart Pastes for Improvement of Wear Resistance of Metals 660
N. Dahl, D. C. Lou, O. M. Akselsen, M. I. Onsøien, SINTEF Materials and Chemistry, Trondheim (N)

Tribological Properties of 316 LVM Austenitic Stainless Steel Processed by Mechanical Pulse Treatment and Hydrostatic Extrusion 667
J. Budniak, O. Kyryliv, M. Lewandowska, K.J. Kurzydlowski, Warsaw University of Technology, Faculty of Materials Science and Engineering, Warsaw (PL)

Trybological Properties of the Surface Layers, Rich in Nitrogen, Produced on Stainless Steel 316LVM 674
R. Slesinski, K. J. Kurzydlowski, Technical University of Warsaw, Faculty of Materials Science, Warsaw (PL)

Tribological Testing on the Steel Hardening with Laser 682
G. Demian, M. Demian, L. Grecu, V. Grecu, University of Craiova, Craiova (RO)

Hot Direct Extrusion of Abrasion Resistant Fe-base Metal Matrix Composites – Interface Characterization and Mechanical Properties of Co-Extruded Layered Structures 690
P.A. Silva, S. Weber, Max-Planck-Institut für Eisenforschung GmbH, Düsseldorf (D); M. Karlsohn, A. Röttger, W. Theisen, Institut für Werkstoffe, Ruhr-Universität Bochum, Bochum (D); W. Reimers, Institute of Material Sciences and Technologies, TU Berlin (D); A.R. Pyzalla, Max-Planck-Institut für Eisenforschung GmbH, Düsseldorf (D)

The Role of Admixed Solid Lubricants in Sintered Steels 696
A. Liersch, H. Danninger, University of Technology Vienna, Institute of Chemical Technologies and Analytics, Vienna (A); R. Ratzi, MIBA Sinter Austria GmbH, Vorchdorf (A)

Investigations of Wear Mechanisms in Diamond Tools with Fe-Based Matrices Reinforced with WC-Co Particles 703
J. Garcia, S. Weber, A. Kostka, A. Pyzalla, Max-Planck-Institut für Eisenforschung GmbH, Düsseldorf (D); L.F. Garcia, A. Lammer, Hilti Corporation, Schaan (FL)

Tribocorrosion Study of 316L Stainless Steel and TA6V4 Alloy in Various Electrolytes 708
P. Henry, J. Takadoum, P. Berçot, MINAMAS-MN2S-Institut FEMTO-ST-ENSMM, Besançon (F)

Wear Characteristics of Diamond Grain-Types in Steel-Ceramic-Compound Grinding 719
B. Denkena, N. Kramer, Institute of Production Engineering and Machine Tools (IFW), Leibniz Universität Hannover (D)

The Correlation of Thermo-Mechanical Stresses on Cutting Tool Wear 726
D. Biermann, J. F. Felderhoff, M. Heilmann, Institute of Machining Technology, Technische Universität Dortmund (D)

Influence of Microstructure and Coating on the Abrasive Edge Wear of WC-Co 732
P. Krakhmalev, Karlstad University, Karlstad (S)

Chromium Based PVD Coatings for Injection Moulding Tools 737
K. Bobzin, Surface Engineering Institute, RWTH Aachen University, Aachen (D); W. Michaeli, Institute of Plastics Processing, RWTH Aachen University, Aachen (D); N. Bagcivan, P. Immich, Surface Engineering Institute, RWTH Aachen University, Aachen (D); F. Klaiber, Institute of Plastics Processing, RWTH Aachen University, Aachen (D); S. Theiß, Surface Engineering Institute, RWTH Aachen University, Aachen (D)

Contact Stress Analysis of a Spherical Wear Particle between Seal and Steel Surface 744
T.-J. Park, H.-D. Cho, School of Mechanical and Aerospace Engineering, ReCAPT, Gyeongsang National University, Jinju (ROK)

Research Regarding Hot Wear Resistance of MARAGING Steels 750
D. F. Tarata, D.D. Cealicu, G. Vaduvoiu, University of Craiova (RO)

Author Index 757

Subject Index 761

Part I
Plenary Lectures

Wear Simulation with a Focus on Mild Wear in Rolling and Sliding Contacts

Sören Andersson
Professor in Machine Elements
Royal Institute of Technology (KTH)
Stockholm, Sweden

Abstract

The amount of wear occurring in high-performance rolling and sliding contacts is often quite small, and such contact surfaces often become glossy. To obtain good contact conditions, it is necessary that the form and the topography of the surfaces be good, that the materials and treatments be properly chosen, and that the lubrication be adequate for the contact. Such advantageous conditions – often referred to as 'mild' – are what engineers normally strive to attain. Sometimes severe conditions may arise, however, creating rough or scored surfaces; severe wear conditions are normally unacceptable in any modern high-performance machine.

Predicting the amount of mild wear is generally thought to be rather difficult and uncertain; this paper addresses this difficult task, outlining some possibilities for predicting mild wear in rolling and sliding contacts. Typical machine elements that include high-performance rolling and sliding contact surfaces are gears, cam mechanisms, and roller bearings. If the rolling and sliding contacts are moving under boundary or mixed lubricated conditions, the contact surfaces may be subject to mild wear. If the lubricants in the rolling and sliding contacts are contaminated with particles, wear may occur even if full-film conditions are predominant.

In a rolling and sliding contact, the two interacting surfaces characteristically move at different speeds in a tangential direction. The Tribology Group at KTH Machine Design has worked on simulating wear in rolling and sliding contacts for a fairly long time. The modelling principles the Group has successfully used are based on 1) the single-point observation method and 2) treating wear as an initial-value process. Two simple examples will be presented here, demonstrating how these principles can be used. As well, some of the Group's efforts at simulating mild wear in rolling and sliding contacts will be presented.

1 Introduction

Wear can be defined as the removal of material from solid surfaces by mechanical action. An acceptable amount of material removed is often quite small for rolling and sliding contact surfaces in high-performance machines. Wear can appear in many ways, depending on the materials of which the interacting contact surfaces are made, the operating environment, and the running conditions. In engineering terms, wear is often classified as either mild or severe. *Mild wear* is what engineers strive for by creating contact surfaces of appropriate form and topography. Choosing adequate materials and surface treatments is also necessary in order to obtain mild wear conditions. Often, however, the surface lubrication is the most important factor in ensuring

that mild wear conditions are obtained. Sometimes, *severe wear* may occur, producing rough or scored surfaces; severe wear is usually unacceptable in high-performance machines.

Wear may also be classified in terms of the fundamental wear mechanisms involved, the wear mechanisms described in the literature being adhesive wear, abrasive wear, corrosive wear, and surface fatigue wear. *Adhesive wear* is a type of wear that occurs due to adhesive interactions between rubbing surfaces. Such wear is also referred to as scuffing, scoring, seizure, and galling due to the appearance of the worn surfaces. Adhesive wear is often associated with severe wear, but is probably also a mechanism involved in mild wear. *Abrasive wear* occurs when a hard surface or hard particles plough a series of grooves in a softer surface. The wear particles generated by adhesive or corrosive mechanisms are often hard and will act as abrasive particles, wearing the contact surfaces as they move through the contact. *Corrosive wear* occurs when the contact surfaces chemically react with the environment and form reaction layers on their surfaces, layers that will be worn off by the mechanical action of the interacting contact surfaces. The mild wear of metals is often thought to be of the corrosive type. Another corrosive type of wear is fretting, which is due to small oscillating motions in contacts. Corrosive wear generates small sometimes flake-like wear particles, which may be hard and abrasive. *Surface fatigue wear*, which can be found in rolling contacts, appears as pits or flakes on the contact surfaces; in such wear, the surfaces become fatigued due to repeated high contact stresses.

The possibility of predicting the type and amount of wear is generally thought to be limited. Even so, many wear models are found in the literature [1]. These models are either simple ones describing a single wear mechanism from a fundamental point of view or simple empirical relationships fitted to particular test results. The wear models easily found in the literature are normally inconvenient or very difficult to apply in many practical cases.

2 Classic Wear Models

Surfaces in rolling and sliding contact may wear if they are not completely separated by a clean oil film; they may also wear if the oil film separating them contains abrasive particles. The amount of wear is dependent on the mechanical and chemical properties of the surfaces, surface topography, and lubrication and running conditions. The wear models that have been formulated often describe sliding contacts. The best-known such wear model is

$$\frac{V}{s} = K\frac{F_N}{H} \tag{1}$$

where V is the wear volume, s is the sliding distance, K is the dimensionless wear coefficient, H is the hardness of the softer contact surface, and F_N is the normal load. This model is often referred to as Archard's wear law [2], even though the basic form of the model was first described by Holm [3]. The wear coefficient, K, however, is interpreted differently by Holm and by Archard.

By dividing both sides of equation (1) by the apparent contact area, A, and by replacing K/H with a dimensional wear coefficient, k, we get the following, often used wear model:

$$\frac{h}{s} = k \cdot p \tag{2}$$

where h is the wear depth and p is the contact pressure. Some scientists have tried to analyze the validity of the wear model according to equations (1) and (2), and one result of this is the wear map presented in Figure 1. That figure depicts two wear mechanisms, namely, delamination wear and mild oxidational wear. Both these mechanisms can be considered mild wear mechanisms, in engineering terms, and both produce thin, plate-like wear debris. The intention of delamination wear theory, as developed by Suh [5], is to explain flake debris generation. He based his theory on the fact that there is a high density of dislocations beneath the contact surfaces. Under sliding interactions between the contact surfaces, these dislocations form cracks that propagate parallel to the surfaces. The total wear volume was assumed to equal the sum of the wear volume of each contact surface; the basic wear model, developed by Suh [5], is as follows:

$$V = N_1 \cdot (s/s_{01}) \cdot A_1 \cdot h_1 + N_2 \cdot (s/s_{02}) \cdot A_2 \cdot h_2 \tag{3}$$

where V is the wear volume, N_i is the number of wear sheets from surface i, A_i is the average area of each sheet, h_i is the thickness of the delaminated sheet, s_{Oi} is the necessary sliding distance to generate sheets and s is the actual sliding distance. It is noticeable that the wear volume from each contact surface is building up the total wear volume, which was not clearly formulated before. The other is that he stated that you need a certain sliding distance before a wear particle is formed. However, The sliding distance is set equal for both surfaces which indicate that he has not been aware of the single point observation method.

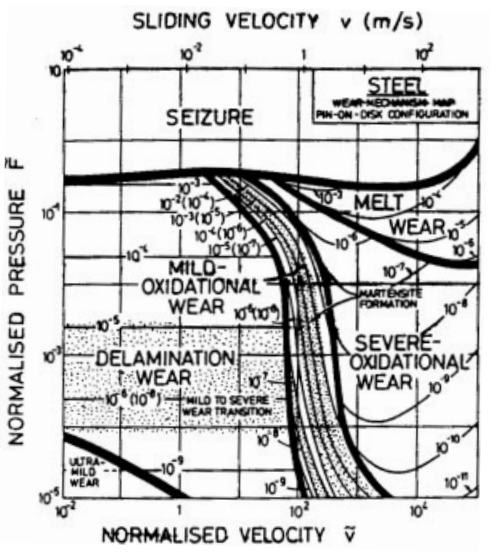


Figure 1: Wear map by Lim and Ashby [4].

Another interesting sliding wear mechanism is the oxidative wear mechanism proposed by Quinn [6]. Quinn stated that the interacting contact surfaces oxidize. The oxide layer will gradually grow until the thickness of the oxide film reaches a critical value, when it will separate from the surface as wear debris. Even in this case you need a certain sliding distance before

wear debris will be formed. Depending on if the oxide growth is linear or parabolic, the wear is direct proportional or proportional to the power of sliding distance. Experimental observations indicate that under steady-state mild conditions, the wear is nearly directly proportional to the sliding distance.

3 Wear Maps

Lim and Ashby [4] comprehensively classified wear mechanisms and corresponding wear models for dry sliding contacts. They studied the results of a large number of dry pin-on-disc experiments and came up with a wear map, presented in Figure 1. The parameters used by Lim and Ashby are $\tilde{Q} = \frac{V}{As}$, $\tilde{p} = \frac{F_N}{AH}$, and $\tilde{v} = \frac{vr_0}{a_0}$, where V is the wear volume, A is the apparent contact area, F_N is the normal load, H is the hardness of the softer material in the contact, v is the sliding velocity, r_0 is the radius of the pin, and a_0 is the thermal diffusivity of the material.

For lubricated contacts, the degree of surface separation by a lubricant very strongly influences the type and amount of wear. The degree of separation in a contact is often divided into boundary lubrication, mixed lubrication, and full-film lubrication.

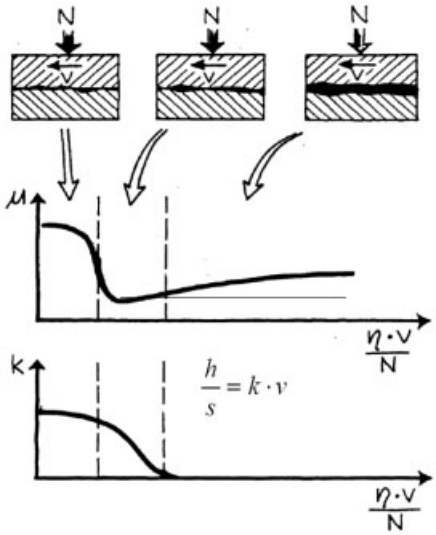


Figure 2: Friction and wear of a sliding contact as a function of the type of lubrication.

Boundary lubrication refers to lubrication in which the load is supported by the interacting surface asperities and the lubrication effect is mainly determined by the boundary properties of the lubricant between the interacting asperities. In *mixed lubrication*, the lubricant film itself supports some of the load in the contact, though the boundary properties of the lubricant are still important. In this case, the hydrodynamic and elastohydrodynamic effects are also important. Mixed lubrication is therefore sometimes referred to as partial lubrication or partial elastohydrodynamic lubrication (EHL). In *full-film lubrication*, the interacting contact surfaces are fully

separated by a fluid film. In the literature, full-film lubrication is sometimes referred to as elastohydrodynamic lubrication, since the film-formation mechanism of high-performance contacts and local asperity contacts is probably elastohydrodynamic.

Friction and wear under mild conditions vary depending on whether the surfaces are running under boundary, mixed, or full-film lubrication. Figure 2 shows how friction and wear normally vary in different sliding contacts as a function of the type of lubrication.

As mentioned in the introduction, the transition from the desired mild wear situation to a severe situation should be avoided. Research has been done to determine when and under what conditions transitions from one kind of wear to another may occur in lubricated contacts. In such studies a so-called IRG transition diagram [7] was developed. Using it, one can identify the different lubrication regimes: a mixed or partial elastohydrodynamic lubrication regime, a boundary lubrication regime, and a failure regime. The last regime is sometimes called the scuffed or unlubricated regime and is a severe condition. The other regimes are mild. The transition from a desired mild wear regime to a severe regime has also been studied by Andersson and Salas-Russo [8]. They found that for bearing steels, the surface topography has a stronger influence on the mild to severe transition level than does the viscosity of the lubricant.

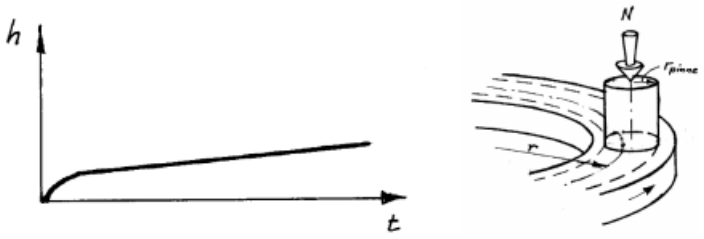


Figure 3: A schematic wear curve from a pin-on-disc test with a flat ended cylindrical pin.

4 Sliding and Wear in a Rolling and Sliding Contact

Wear in rolling and sliding contacts can be of different types, as mentioned above. If a surface is subject to high repeated dynamic loading, surface fatigue may occur, and pits of different forms may form on the surface. In this paper, however, we will not deal with surface fatigue or severe wear; instead, we will focus our attention on mild sliding wear. For lubricated surfaces, wear can occur if the lubrication is boundary or mixed and if the lubricant is contaminated with abrasive particles. To illustrate the wear process, a typical wear curve obtained in a pin-on-disc testing machine using a flat-ended cylindrical pin rubbing against a disc under mild conditions is shown in Figure 3. A typical wear process always starts with a short running-in period in which the highest asperities and the contact surfaces in general are probably plastically deformed and initially worn; this is followed by a steady-state period in which the wear depth is directly proportional to the sliding distance. The initial running-in period is rather brief but not very well understood. The general appearance of a wear curve seems to apply to dry as well as boundary and mixed lubricated contacts; it also applies to contacts lubricated with lubricants contaminated with abrasive particles. Aside from ease of testing, the pin-on-disc configuration is likely a popular

testing geometry because most of the wear is on the pin. The distance a point on the pin's contact surface slides against the disc is much longer than the corresponding distance a contact point on the disc slides against the pin during a single revolution of the disc.

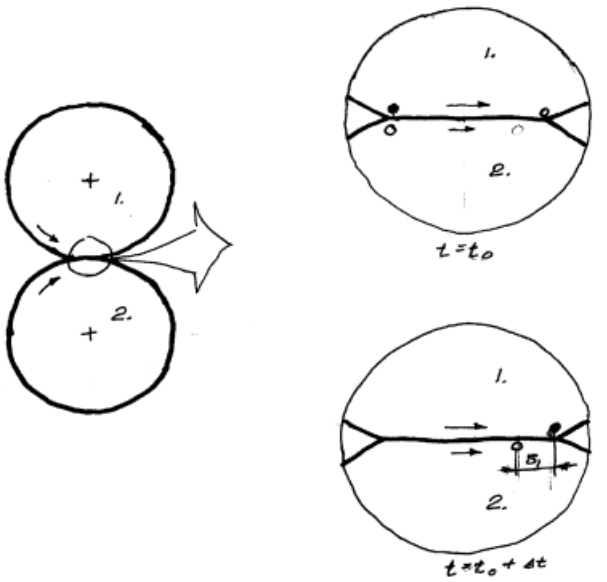


Figure 4: The basic principle for determining of the sliding distance in a rolling and sliding contact.

Simple pin-on-disc test results indicate that sliding distance is an important parameter determining sliding wear. For rolling and sliding contacts, the sliding part of the surface interactions, although not obvious, is therefore of interest. Some people maintain that the effect of sliding is negligible in most rolling and sliding contacts. Various investigations have demonstrated, however, that the distances the contacts slide against the opposite interacting surfaces during a mesh are sufficient to form wear debris in most rolling and sliding contacts. For this reason, I will show how much a point on a contact surface slides against an opposite contact surface during a mesh.

Consider two discs that are pressed together and run at different peripheral velocities (see Figure 4). This is a typical situation in tractive rolling contacts. The absolute value of the sliding distance, s_i, is for $i = 1$ a point on the contact surface of body 1 and for $i = 2$ a point on the contact surface of body 2. The sliding distance, s_i, during one mesh at a point on one of the contact surfaces sliding against the opposite interacting surface is equal to

$$s_i = 2a \cdot \left| \frac{v_1 - v_2}{v_i} \right| \tag{4}$$

where a is the half width of the contact, v_1 is the peripheral velocity of surface 1, and v_2 is the peripheral velocity of surface 2. The sliding distances in rolling and sliding contact according to equation (4) apply to rollers. For contacts between other bodies, such as gears, determining the sliding distances may be more complicated (see, e.g., Figure 5). The principle, however, is

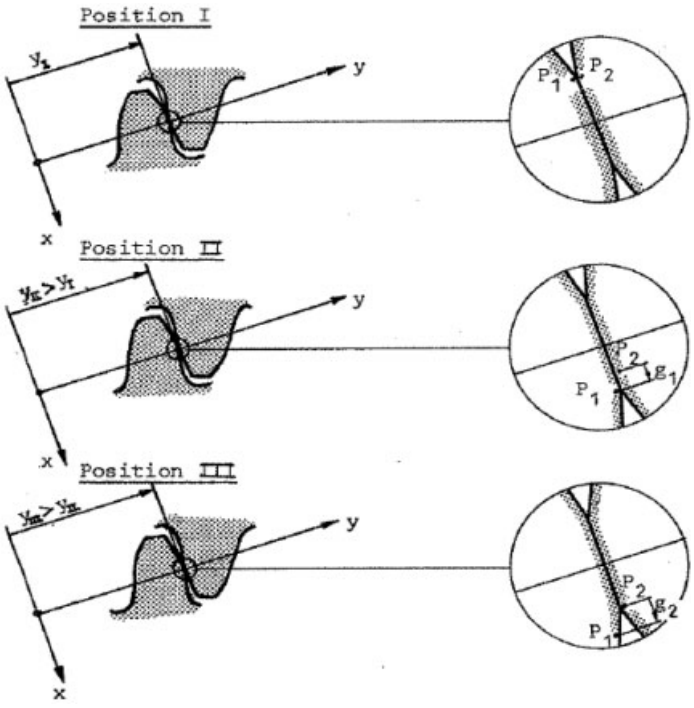


Figure 5: [9]

the same, namely, to study how great a distance a point on a contact surface slides against the opposite surface during a single mesh. In the examples shown, the elastic deformations of the contact surfaces in the tangential direction are ignored; those displacements would reduce the sliding distance a little, but micro-displacements normally have very little effect on the contact conditions.

5 Single-point Observation Method

The single-point observation method was found to be very useful during our work on simulating the mild wear of boundary-lubricated spur gears [10]. Long before those efforts, formulas for the sliding distances had been derived by the author in his PhD. thesis [9] (see Figure 5). The distances a point on a gear flank slides against an opposite flank during one mesh vary depending on the position on the flank, the gear ratio, the size of the gears, and the loads applied on the gear tooth flanks. The principle for determining these sliding distances and the corresponding equations are shown below. The sliding distance depicted in Figure 5 is referred to as g, but we will use s to refer to sliding distance elsewhere in this paper.

The distance, g_1, point P_1 on the pinion flank and the distance, g_2, point P_2 on the gear flank slide during one mesh; position I corresponds to the moment in time when P_1 and P_2 come into

contact with each other, while positions II and III correspond to the moments in time when P_1 and P_2 disengage, respectively.

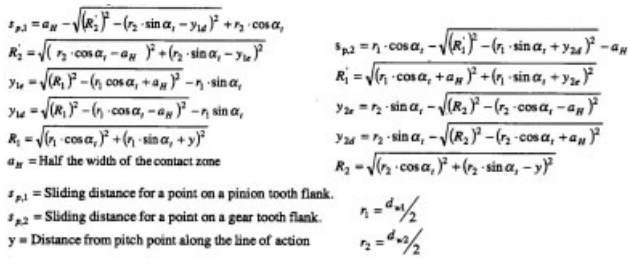


Figure 6: [11]

Obtained FZG test results indicate that the amount of wear on the gear flanks seems to be in line with the sliding distances recorded. That observation and many years of pin-on-disc tests (see Figure 3) have inspired me and others to try to simulate wear in rolling and sliding contacts. Our first such effort was a simulation of the mild wear of tooth flanks working under boundary-lubricated conditions [10]. The wear simulation was then based on the wear model, equation (2), i.e.,

$$\frac{h}{s} = k \cdot p$$

The simulation was simplified by assuming that the wear coefficient was constant throughout the process. The initial running-in period was not considered. The contact pressure between the flanks during one mesh was assumed to be constant, i.e., the mean contact pressure during a mesh was determined and used. By means of these simplifications and the sliding distance during one mesh as determined according to the above equations, it was possible to simulate the wear depth at a particular point on a gear flank (the wear simulation was run in Excel). The wear distribution and estimated wear coefficient were found to be in reasonably good agreement with the experimental observations from FZG tests conducted. Our awareness of the risk that the principle used and the simplifications made might only be relevant to the studied case, however, impelled us to continue our research into simulations of wear in rolling and sliding contacts. Further studies were therefore conducted to find out how generally applicable the principle and the simplifications are.

6 Wear as an Initial-value Process

A wear process is seldom a steady-state process, even if steady-state conditions are desirable and often comprise a dominant part of the wear process. Normally, the running-in wear is greater than the ensuing wear. The forms of the contact surfaces are often such that the wear depth will vary with time. Furthermore, it was found that in slow-running thrust roller bearings, mild wear of the contact surfaces caused geometrical changes that initiated other wear processes. Olofsson [12] found that mild wear of the contact surfaces of spherical thrust roller bearings caused an

increase of the contact pressure at the pure rolling points. Consequently, the increased contact pressure initiated surface fatigue wear at the pure rolling points much earlier than expected.

As a direct result of that finding and because wear simulations often contain many simplifications, we looked at wear simulations from a mathematical-numerical point of view. We found that simulations of wear processes can advantageously be regarded as initial-value problems [13]. We know the initial conditions and properties of the contacts fairly well, so if we can formulate how the surfaces change, it should also be possible to predict the states of the surfaces at any time during operation. The wear of contact surfaces can thus be treated as an initial-value problem. The wear rate may then be formulated according to the following model:

$$\frac{dh}{dt} = f\,(\text{material, topography, lubricant, load, velocity, temperature,.....}) \tag{5}$$

where h is the wear depth at a particular point on an interacting surface and t is time. This formulation is in agreement with that of the dynamic behaviour of mechanical systems and can easily be numerically integrated. A model often used in many wear simulations is

$$\frac{dh}{dt} = k \cdot p \cdot v_s \tag{6}$$

The wear model in equation (6) may be regarded as a generalization of Archard's wear law, i.e., equations (1) and (2) above.

Equation (6) is often reformulated thus:

$$\frac{dh}{ds} = k \cdot p \tag{7}$$

since

$$ds = v_s \cdot dt \tag{8}$$

where v_s is the sliding velocity.

7 Numerical Integration of a Wear Model in a Rolling and Sliding Contact

A commonly used wear model is equation (6). Numerically integrating a wear model entails making geometry and time discrete. The simplest numerical integration method is the Euler method. The wear depth at a chosen point on a gear flank or a roller, for example, is then determined by

$$h_{i,new} = h_{i,old} + n \cdot k \cdot p_i \cdot |v_1 - v_2| \cdot \Delta t$$

where $h_{i,new}$ is the obtained wear depth on surface i, $h_{i,old}$ is the wear depth on i in the simulation loop before the actual loop, n is the number of time steps, meshes, or revolutions before the geometry is changed, k is the dimensional wear coefficient, p_i is the local pressure at i when the actual time step starts, and Δt is the time step. The Euler integration method is the simplest numerical integration method. Other numerical integration methods can of course be used in the same way, as different schemes are used in behavioural simulations of technical systems. After

a simulation, one must always check the accuracy of the simulation. Common tests for doing so are the n and Δt checks, though if the values chosen for these are too great, the results may not be correct. A common way to handle this is to see whether the same results are obtained using half the values of n and Δt. One of the most difficult and time-consuming parts of a simulation is determining the pressure at a particular point in each simulation loop, pressure at any point being dependent on the pressure at all other points in the contact.

8 Determining the Wear of Interacting Rollers

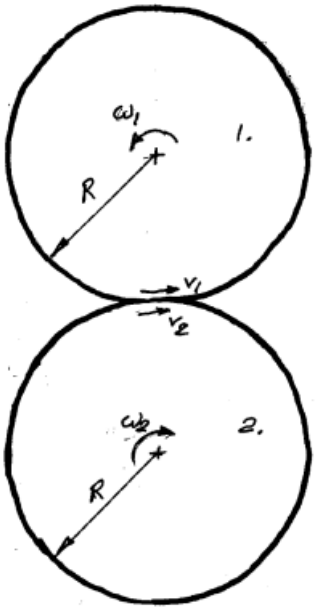


Figure 7: Interacting cylindrical rollers.

We consider two cylindrical rollers both of radius R. The rollers are pressed together with force F_N and rotated at angular velocities ω_1 and ω_2, respectively. The peripheral velocities of the contact surfaces are $v_1 = \omega_1 \cdot R$ and $v_2 = \omega_2 \cdot R$. The wear of the contact surfaces is assumed to be properly described by the following wear model:

$$\frac{dh_i}{dt} = k_i \cdot p \cdot v_{i,s}$$

where $i = 1$ for roller 1 and $i = 2$ for roller 2; h is the wear depth at a point on surface i when it rubs against the opposite contact surface, k_i is the wear coefficient for a point on surface i when it rubs against the opposite contact surface, p is the local contact pressure, and $v_{s,i}$ is the sliding velocity at a point on surface *i* sliding against the opposite interacting surface. The sliding

velocity, $v_{s,i}$, for points on both contact surfaces equals

$$v_{s,i} = |v_1 - v_2|$$

We assume that the rollers are subject to a constant load and that the angular velocities are constant. The wear model will then obtain the following form after integration:

$$\int_0^{h_i} dh_i = k_i \cdot |v_1 - v_2| \int_0^{\Delta t} p dt$$

$$h_i = k_i \cdot |v_1 - v_2| \cdot \int_0^{\Delta t} p dt$$

If we study complete meshes, the contact pressure, p, can be replaced by the mean contact pressure, p_m. The wear depth is small compared with the radius of the rollers; p_m can thus be determined once and used for all simulated revolutions. The integral equation can thus be reformulated according to the following:

$$h_{inew} - h_{iold} = k_i \cdot p_m \cdot |v_1 - v_2| \cdot \Delta t$$

If Δt is brief, so that only one point on each of the contact surfaces has passed the contact once, then the wear of each surface per mesh will be

$$h_{1/mesh} = k_1 \cdot p_m \cdot \frac{|v_1 - v_2|}{v_1} \cdot 2a$$

and

$$h_{2/mesh} = k_2 \cdot p_m \cdot \frac{|v_1 - v_2|}{v_2} \cdot 2a$$

respectively.

Surface 1, however, is moving faster than surface 2. In the long run, points on surface 1 will be in contact more often than points on surface 2. Consequently, the wear of the two surfaces will only differ in relation to the wear coefficients. This can be demonstrated by the following relationships: Assume that the mechanism has been running for a fairly long time and that roller 1 has rotated n_1 revolutions. Roller 2 has then rotated n_1 revolutions. The wear of the rollers will then be as follows:

$$\begin{aligned}
h_{1/longtime} &= k_1 \cdot p_m \cdot \frac{|v_1 - v_2|}{v_1} \cdot 2a \cdot n_1 \\
h_{2/longtime} &= k_2 \cdot p_m \cdot \frac{|v_1 - v_2|}{v_2} \cdot 2a \cdot n_2 \\
&= k_2 \cdot p_m \cdot \frac{|v_1 - v_2|}{v_2} \cdot 2a \cdot \frac{\omega_2}{\omega_1} \cdot n_1 \\
&= k_2 \cdot p_m \cdot \frac{|v_1 - v_2|}{v_1} \cdot 2a \cdot n_1
\end{aligned}$$

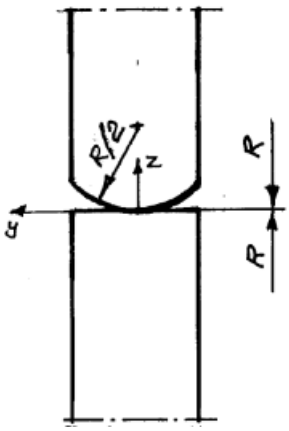


Figure 8: Interacting modified roller and cylindrical roller.

since $v_1 = \omega_1 \cdot R$ and $v_2 = \omega_2 \cdot R$.

From an experimental point of view, it is advantageous to change the form of roller 1 so that the contact surface will have a radius of R/2 perpendicular to the direction of motion of the contact surface (see Figure 8). The contact will then be a point contact instead of a line contact as in the previous example. This change will improve the experimental setup but unfortunately make the wear simulation more difficult (see Figure 9). The assumption that the wear coefficients for points on each surface are constant throughout the whole process, however, is relevant even in this case. The sliding velocity can also be assumed to be constant and the contact pressure variation during a mesh can, as in the previous example, be assumed to be replaced by a mean pressure. An important difference, however, is that the mean pressure does not remain constant throughout the wear process, since the wear of the contact surfaces will change the pressure distribution in the contact. We assume that the same wear model as in the previous example is valid in this case as well, and that the developed equation, after considering the simplifications, will be as follows:

$$h_{i,new} - h_{i,old} = k_i \cdot p_m \cdot |v_1 - v_2| \cdot (t_{new} - t_{old})$$

When the contact surfaces wear, the forms of the surfaces will change and thereby also the pressure distribution in the contact. This means that we cannot assume that the pressure is constant, so we cannot, as in the previous example, run a large number of revolutions in one simulation loop. The main problems in this case, therefore, are determining the local pressure at an observed point in every loop and deciding on the duration of each loop before a new local pressure determination must be made.

Determining the contact pressure at a particular point is often the trickiest and most time-consuming part of a wear simulation. The deformation at one point is dependent on the deformation at all other points around the observed point. This implies a rather complex process for accurately calculating the pressure distribution. Today, three different ways are used to determine the contact pressure. FE calculation is a method that is becoming increasingly popular as computer power increases and FE programs are improved. The main drawback of the FE method

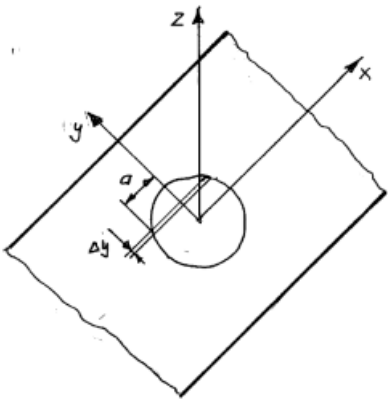


Figure 9: Contact point and coordinate system. Sliced contact.

is that determining the pressure distribution often entails considering a great many small elements on the surfaces. That is often difficult to do, since the combination with the body models often leads to a huge number of elements and a very long calculation time. The FE method will probably be used more in the future for interface-related problems than it is today. Some smart combinations of BE and FE methods are probably needed to speed up the calculations. To determine the micro topography in the contact zone, BE methods are commonly used. The BE programs used are often based on the same assumptions as Hertz used when he derived his equations. This means that most BE programs cannot be used in all applications. A common way to simplify the determination of local pressure is to use a third way, namely, the Winkler surface model. The surfaces are then replaced by a set of elastic bars; the shear between the bars can be neglected and the contact pressure at a point is then only dependent on the deformation at that point according to

$$p = K_N \cdot u_z$$

where u_z is the deformation of the elastic rod. The spring constant, K_N, can be determined by [14]:

$$K_N = C_w \cdot \frac{E'}{b}$$

where $C_w \sim 1$, E^* is the combined elastic modulus of the contact surfaces, and b is approximately the width of the elastic half axle according to Hertz. In this case, we do not have a standard Hertzian contact case, so we make b equal to the half axle of a sphere of radius $R/2$ against a plane. A Winkler surface model of rod stiffness K_N has been used to simulate the wear process of a modified roller interacting with a cylindrical roller (see Figure 8). The contact surfaces are then divided into a number of sliced surfaces of width $\Delta y = b/10$ perpendicular to the sliding direction (see Figure 9). We assume that we can simplify the wear simulation by determining the wear for each slice in the same way as above. The penetration, d, of the modified upper roller against the lower cylindrical roller is determined so that the sum of the load of each slice

support equals the applied force, F_N. The local wear is now determined and the geometry of the contact surfaces is modified. Thereafter, a new penetration, d, is determined, and so on. Figure 10 presents some simulation results for a modified upper roller interacting with a cylindrical roller. The rollers will wear during running, The wear of the discs will increase in both depth and width with time (see Figure 10).

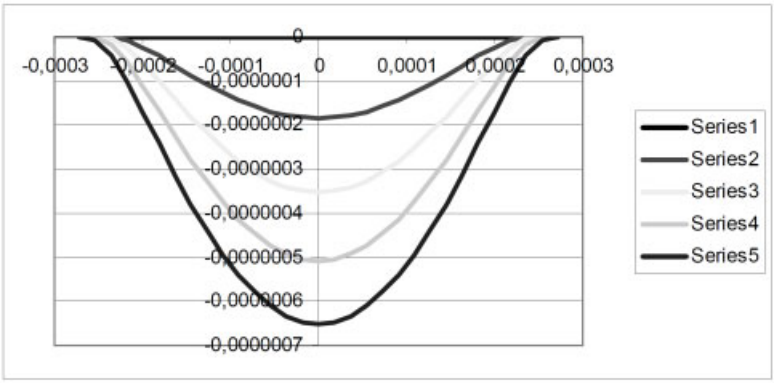


Figure 10: Simulated wear of an ellipsoidal roller 1 interacting with a cylindrical roller 2. R1x =25E-6 m, R1y = 12, 5E-3m, R2x =25E-3 m, FN=100 N, v1=1,25 m/s, v1-v2=6E-2 m/s. Series 1 is at t=0, Series 2 after n revolutions, Series 3 after 2n rev., Series 4 after 3n rev. and series 5 after 4n rev.. The figure show the form changes of the contact surface of the rollers during running.

9 Some Simulation Work of the Tribology Group at KTH

The wear modelling and simulation activities conducted by our Group began with the simplified simulation of the wear of gear tooth flanks mentioned previously in this paper [10], followed by the introduction of the principle of single-point observation. Then came several other wear simulation efforts, the main focus of which was to overcome some of the difficulties in determining various parameters, such as contact pressure and sliding speed, at each incremental step of the simulation process. The wear model, equation (8), or complemented versions of the model have mainly been used in the different simulation efforts of the Tribology Group.

A more accurate simulation of gear wear than the initial simulation was done by Flodin [15], whose simulation results were experimentally verified by FZG testing. He simplified the contact pressure simulations by using a Winkler surface model. Flodin considered the pressure variation during a mesh, the changed conditions, for example, when the load quickly changes in a gear contact, and the influence of the local displacements around the pitch point.

Another method to determine contact pressures in the contact between gear flanks was used by MackAldener [16], who combined an FE model with an analytical Hertzian solution to the contact problem. He developed an FE-based program and studied the noise of gears arising from manufacturing errors and wear.

A very complex simulation of a rolling and sliding contact was done by Hugnell et al. [17]. They simulated the wear between a cam and a follower. The main problem in that case, besides

determining the contact pressure distribution, was determining the motion of the interacting surfaces.

Oscillating sliding wear was simulated by Podra [18]. He used FEM to open up the possibility of simulating any contact, and also studied the applicability of the Winkler surface method in wear simulations.

Rolling and sliding mild wear in roller bearings was simulated by Olofsson et al. [19]. That simulation confirmed that the mild wear of the contact surfaces was the reason why surface fatigue occurred much earlier than expected. They used a slicing method similar to that in the above example.

You may find rolling and sliding contacts in many applications. Spiegelberg and Andersson [21] studied the friction and wear between a valve bridge and a rocker arm shoe of a cam mechanism in a diesel engine; that contact is a rolling and sliding contact. They used a brush model, which can be regarded as a modified or further developed Winkler surface model.

Nilsson [20] studied abrasive wear caused by particles in the oil lubricating a rolling and sliding contact. He derived an abrasive wear model.

Wear can be regarded as a random process, so wear models always represent mean values. Andersson et al. [22–24] have accordingly worked on developing a general wear model. They have so far based their work on a Greenwood and Wlliamson surface model, which has some similarities to the Winkler model.

An advanced wear simulation of a rolling and sliding contact was done by Brauer and Andersson [25] in working with gears with flank interference; FE technique was mainly used, but integrated with analytical contact determination.

10 Conclusions

The mild wear of rolling and sliding contacts can be simulated. The basic principles used by the Tribology Group at KTH Machine Design are 1) the single-point observation method and 2) treating the wear process as an initial-value problem. Using these principles, nearly any practical case can be simulated. The most common wear model is the so-called Archard's generalized wear model:

$$\frac{dh}{dt} = k \cdot p \cdot v_s$$

How well that model describes the wear process has yet to be investigated in detail. In many cases, however, the simulated wear distributions agree fairly well with experimental observations. During wear simulation, it is fairly common for the wear simulation to be done stepwise, with repeated determinations of pressure, sliding velocities, etc. Determining the pressure distribution in the contact is often considered the most difficult and time-consuming task. Most simulations are done numerically, and choosing the appropriate surface element size and time step is critical. Too long a time step may produce incorrect results or an unstable simulation, while too short a time step, on the other hand, may result in excessively time-consuming calculations.

11 References

[1] Meng, H.-C. (1994) Wear modeling: Evaluation and categorisation of wear. Dissertaion. University of Michigan. 1994.

[2] Archard, J.F. (1980) *Wear theory and mechanisms*. In the book: M.B. Peterson, W.O. Winer (eds.). Wear control handbook. ASME, 1980.

[3] Holm, R. (1946) Electric contacts. Almqvist&Wiksells Boktryckeri AB, Uppsala 1946

[4] Lim, S.C. and Ashby, M.F. (1987) Wear mechanism maps. Acta metal. Vol. 35, No. 1, pp. 1–24, 1987.

[5] Suh, N.P. (1973) The Delamination Theory of Wear, Wear 25 (1973) 111–124.

[6] Quinn, T.F.J. (1962) Role of oxidation in the mild wear of steel. Brit Journal of Applied Physics, 13 (1962) 33–37.

[7] Begelinger, A. and deGee, A.W.J. (1981) Failure of thin film lubrication. ASME J. Lubrication Techn., 103, 1981.

[8] Andersson, S. and Salas-Russo, E. (1994) The influence of surface roughness and oil viscosity on the transition in mixed lubricated sliding contacts. Wear 174 (1994) 71–79.

[9] Andersson, S. (1975) Partial EHD Theory and Initial Wear of Gears. Doctoral Thesis. Department of Machine Elements, KTH, Stockholm, Sweden, 1975.

[10] Andersson, S. and Eriksson, B. (1990) Prediction of the sliding wear of spur gears. Nordtrib'90, Hirtshals, Denmark.

[11] Flodin, A. and Andersson, S. (1997) Simulation of mild wear in gears. Wear 2007 (1997) 16–23.

[12] Olofsson, U. (1997) Characterisation of wear in boundary lubricated spherical roller thrust bearings, Wear vol. 208 (1997) 194–203.

[13] Strang, G. (1986) Introduction to applied mathematics. Wellesley-Cambridge Press. ISBN 0-9614088-0-4. 1986.

[14] Podra, P. and Andersson, S. (1997) Wear Simulation with the Winkler Surface Model. Wear 207 (1997) 70–85.

[15] Flodin, A. (2000) Wear of spur and helical gears. Doctoral thesis. KTH Machine Design, 2000.

[16] MackAldener, M. (2001) Tooth interior fatigue fracture and robustness of gears. Doctoral Thesis. KTH Machine Design, 2001.

[17] Hugnell, A., Björklund, S., and Andersson, S. (1996) Simulation of the mild wear in a cam-follower contact with follower rotation. Wear 199 (1996) 202–210.

[18] Podra, P. (1997) FE wear simulation of sliding contacts. Doctoral thesis, Machine Elements, Department of machine design, KTH, 1997.

[19] Olofsson, U., Andersson, S., and Björklund, S. (2000) Simulation of mild wear in boundary lubricated spherical roller thrust bearings. Wear 241 (2000) 180–185.

[20] Nilsson, R. (2005) On wear in rolling sliding contacts. Doctoral Thesis. KTH Machine Design, 2005.

[21] Spiegelberg, C. and Andersson, S. (2006) Simulation of friction and wear in the contact between the valve bridge and rocker arm pad in a cam mechanism. Wear 261(2006)58–67.

[22] Andersson, S and Olofsson, U. (2005) Towards a general wear model for wear simulation. IRG-OECD meeting, Uppsala, June 2005.

[23] Andersson, S., Söderberg, A., and Olofsson, U. (2008) A random wear model for the interaction between a rough and a smooth surface. Wear 264 (2008) 763–769.

[24] Andersson, S. and Olofsson, U. (2007) Simulation of plastic deformation and wear of a rough surface rubbing against a smooth wear resistant surface. Rotrib '07. 10th International conference on tribology, Bukarest, Nov 8–10, 2007.

[25] Brauer, J. and Andersson, S. (2003) Simulation of wear in gears with flank interference – a mixed FE and analytical approach. Wear 254 (2003).

Polymer Composites in Tribology

K. Friedrich
Institute for Composite Materials (IVW GmbH), Technical University of Kaiserslautern, D-67663 Kaiserslautern, Germany

1 Introduction

The use of polymer composites in many fields of application has become state of the art. High performance composites, consisting of a high volume fraction of continuous glass or carbon fibers (e.g. arranged in form of unidirectional layers) in a thermosetting or thermoplastic matrix, are building the basis for lightweight structural components in the aircraft and motor-sport industry. Discontinuous, short fiber or particulate reinforced systems have found their application in many automotive parts under the hood , often being loaded under additional friction and wear conditions. In all of these cases, the diameter of the individual reinforcing elements is in the µm-size range (glass fibers have a diameter of ca. 10 µm). Their length can vary between 200 µm (typical for injection moldable short glass fiber reinforced thermoplastics), several millimeters to centimeters (long fiber filled systems), and up to meters in case of continuous fiber composites. The principle composition of typical composite materials is demonstrated in Figure 1.

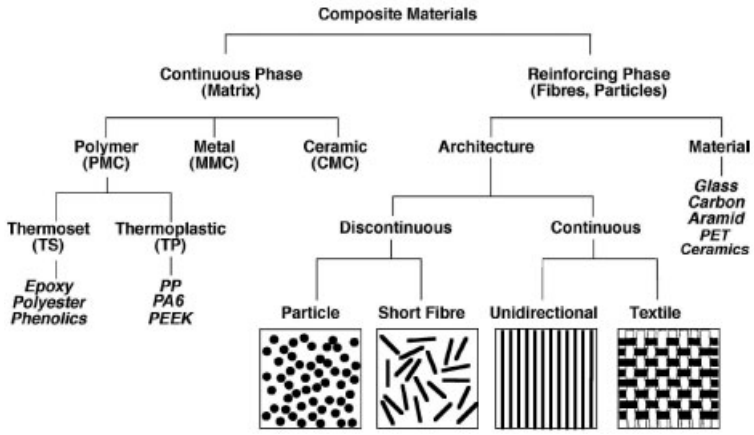


Figure 1: Systematic illustration of the structural components of composite materials

Polymer composites belong to the group of multiphase materials. They are characterized by a softer matrix containing harder and stronger particles or fibers. The latter act as the reinforcing phase, which sometimes also causes a certain degree of anisotropy. Under tribological loading conditions, the corresponding properties (coefficient of friction; specific wear rate) depend on the system in which these materials must function, including effects of the type and size of the counterpart asperities (e.g. abrasive particles; roughness of the mating steel partner). Quite often

sliding is the dominant wear mode, and the materials have to be designed for low friction and low wear against smooth metallic counterparts (e. g. as gears or bearings), but sometimes also a high coefficient of friction, coupled with low wear, is required (e. g. for brake pads or clutches) (Figure 2).



Figure 2: Machine elements made of polymer composites, and their different requirements, depending on the type of application

In the following part, different methods concerning the design of wear resistant polymer composites are discussed. In all cases it was of primary concern to develop polymeric composites that were supposed to have low friction and low wear under dry sliding conditions against smooth steel counterparts.

2 Rule of Mixtures for Short Fiber Reinforced Thermoplastics

From several studies in the past it is well known that the friction and wear behavior of polymer materials can be improved by a lower adhesion and a higher stiffness and strength [1–3]. This can be achieved quite successfully by using special fillers. To reduce the adhesion, e. g., internal lubricants, such as PTFE or graphite are frequently incorporated. Short aramid, carbon or glass fibers are used to increase the stiffness and strength of the polymer system (Figure 3).

As an example for the design of a polymer composites, used for injection moulded sliding shoes in textile drying machines, Figure 4 illustrates for room temperature testing that in three different high temperature resistant thermoplastics (PEN, PEEK, PEEKK) the fibers (GF = glass; CF = carbon) primarily reduce the wear rate, whereas the internal lubricants, such as polyetrafluoroethylene (TF) and graphite (Gr), result in an improvement of the coefficient of friction. Regarding both, the coefficient of friction and the specific wear rate, a system consisting of a PEEK-matrix with 10 % of each, CF, TF, Gr seems to be the best compromise, because in the temperature range considered (20 °C to 150 °C) a low coefficient of friction ($\mu < 0.2$) and a low wear rate ($W_S <$ 1.5 E-6mm^3/Nm) can be achieved for an applied pressure of p = 1MPa and a sliding velocity of v = 1 m/s.

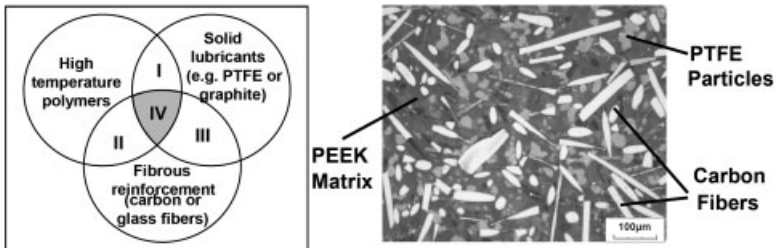


Figure 3: Classical design of polymer composites with low friction and low wear (region IV), and typical microstructure of a high temperature resistant polyetheretherketone (PEEK), filled with polyterafluoroethylene (PTFE) particles and short carbon fibers

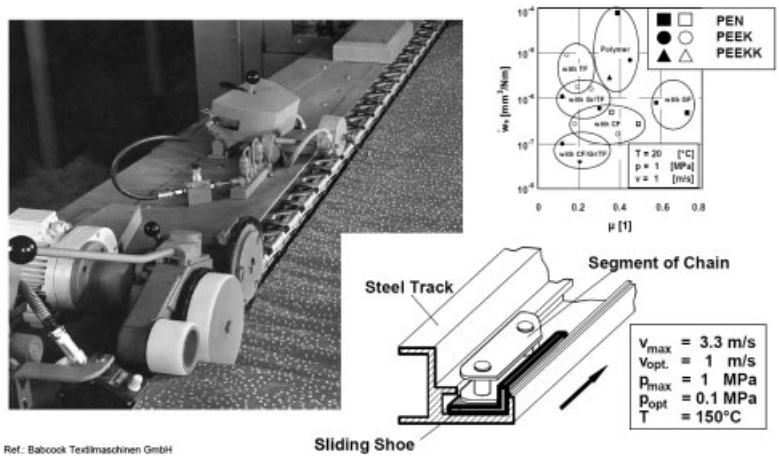


Figure 4: Design of a polymer composite for sliding shoes in textile drying machines

To illustrate the effects of various short fiber reinforcements on the sliding wear characteristics of various polymers in more detail, Figure 5 has summarized the result of many different fiber/matrix systems. One should look more at the general trends, rather then at the individual data. In those polymers that possess high specific wear rates in the unreinforced condition almost any type of reinforcing fibers results in both significant reductions in wear and further improvements of the mechanical properties. In addition, carbon fibers often improve the materials' wear resistance by a factor of five or more than the same volume fraction of glass fibers [4].

For predicting the general trend in these curves, a modified rule of mixtures was developed, based on the dominating wear mechanisms (matrix wear = plastic deformation, plowing, cutting, cracking; fiber wear = thinning, cracking, interfacial removal). The equation is given in Figure 6, and Figure 7 illustrates the tendency , if in a given matrix (here: PEN = polyethernitril) the fiber cracking and interfacial removal term is improved, e.g. by the use of more wear resistant fibers (here: Idemitsu Pitch-Based Carbon Fibers, in comparison to PAN-Based CF) and a better bonding between the fibers and the matrix [5].

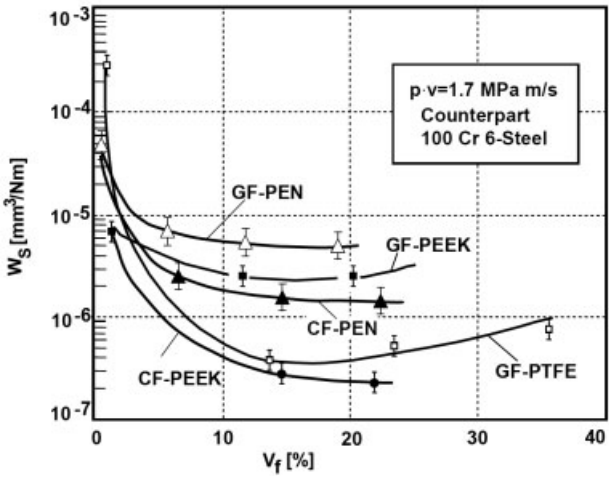


Figure 5: Influence of fiber volume fraction on the specific wear rate of various short fiber reinforced thermoplastics

$$\dot{w}_{S,C} = \frac{1}{(1-V_f)\cdot \dot{w}_{S,M}^{-1} + a\cdot V_f \cdot \dot{w}_{S,F}^{-1}} + b\cdot V_f \cdot \dot{w}_{S,F_{cl}}$$

$$a = 0.5\cdot(1+V_f^c) \qquad b = 0.5\cdot(1-V_f^c)$$

$\dot{w}_s$, C, M, F = Specific Wear Rates of Composite, Matrix and Fiber respectively

$\dot{w}_s$, F_{cl} = Specific Wear Rate due to Fiber Cracking and Interfacial Removal

V_f = Fiber Volume Fraction

c = Wear Exponent, which Accounts for Changes in Wear Mechanisms with V_f

Figure 6: Complex rule of mixtures equation for predicting the specific wear rate of the composite

3 Artificial Neural Networks for Wear Prediction

Relating wear to other mechanical properties is another way to estimate the tribological performance of materials in general. However, as wear processes are usually complex and depend on many mechanical and other parameters, simple functions cannot always describe in sufficient detail all the prevailing wear mechanisms. For predictive purposes, an artificial neural network approach has therefore been recently introduced into the field of wear of polymers and composites[6]. This is based on an empirical model which allows to analyze practical tribological situations in which many parameters (p) influence the wear behavior of a material. The model should be non-linear and have enough free parameters to model the "curved" dependence of a volume loss (ΔV) on $p_1,...,p_n$. To obtain optimized neural network constructions, a given dataset is divided into a training data set and a test data set. The training data set is used to obtain the

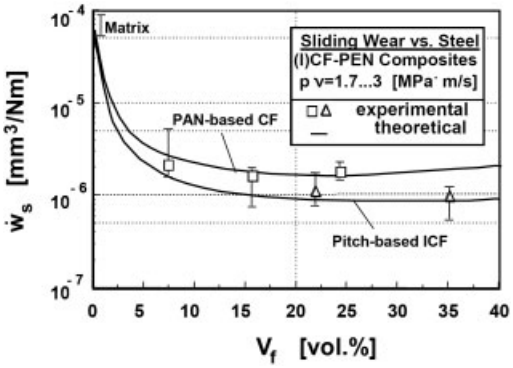


Figure 7: Use of the complex rule of mixtures equation for predicting theoretically the tendency in the specific wear rate as a function of fiber volume fraction (comparison between experimental data for two types of fibers and theory)

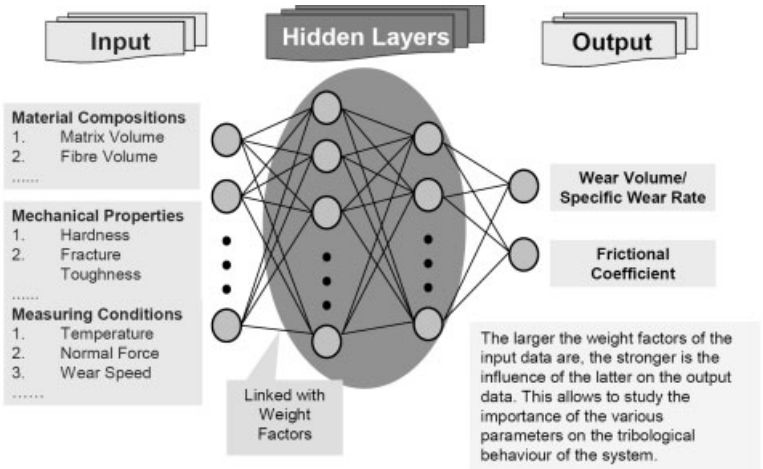


Figure 8: Schematic set-up of an artificial neural network, with input parameters (left), including mechanical properties of the materials, and output parameters, such as specific wear rate and coefficient of friction.

coefficients of the neural network equation (e.g., a_i, b_{ij}) such that the mean squared error of the predicted wear volume is minimized (Figure 8).

Figure 9 demonstrates for a polyamide 4.6 (PA4.6) composite the changes in the coefficient of friction and the specific wear rate as a function of PTFE particle- and carbon fiber- content. The grids refer to the predictions by the well trained artificial neural network, and the three error bars in each diagram represent experimental values for testing the predictions. The agreement between the two data sets is quite convincing.

The polyamide 4.6 (PA 4.6) composites developed in this study were used for friction torque limiters in damped flywheel clutches of modern automotives (Figure 10). They are important

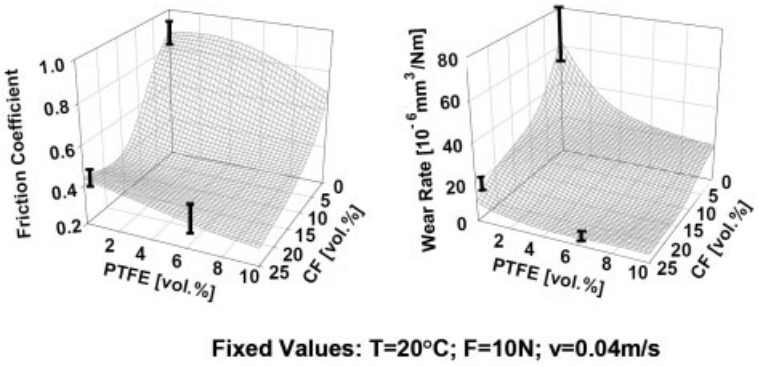


Figure 9: Proof of the prediction quality of an ANN approach

components, that have to limit the transmittable torque during engaging and disengaging, and in this way they protect both the engine and the transmission from torque peaks.



Figure 10: Use of PA 4.6 composites for friction torque limiters (left) in damped flywheel clutches (right)

The requirements for the tribological properties of the material are that (1) the coefficient of friction must not change during the entire lifetime, (2) there is no or only a very short running-in behaviour, and (3) the sliding wear resistance is very high.

4 Nanoparticles in Combination with Classical Tribofillers

More recently, new developments have shown that much smaller reinforcing dimensions can lead to special effects, which cannot be reached so easily with the traditional fillers. In this class of the so-called nanocomposites, at least one dimension of the reinforcing elements is in the range

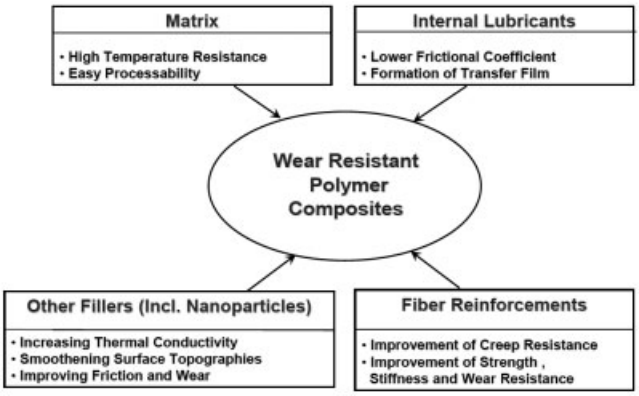


Figure 11: How to design polymer composites for high sliding wear resistance

of about 10 to 100 nm [7]. Under these conditions, the structure of the material is composed of a much larger interface between the fillers and the nanoparticles, being able to create a quite different mechanical performance of the material in comparison to a traditional composite with the same filler volume fraction [8-10]. In addition, the tribological properties of polymers and polymer composites can be changed by the use of nano-sized fillers. This has been demonstrated by many authors, of which only a few can be listed here (e.g. [11-13]). However, often the optimum effects for improving both, the coefficient of friction and the wear rate, can only be achieved if the nano-particles are used in combination with some of the traditional tribo-fillers (Figure 11) [14]. It is the objective here to demonstrate this on different examples of practical applications.

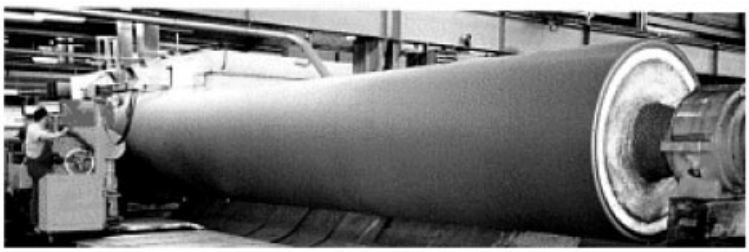


Figure 12: Calender roller covers for paper making industry. (Source: Stowe Woodward GmbH)

One example for wear resistant particulate filled epoxies is their use as thick covers for calender rollers, i.e. very important parts in paper making machines. Such rollers can be 10 m in length and 1 m in diameter, and the thickness of the covers can be a few centimeters, which requires ca. 500 kg of the polymer compound (Figure 12). The major position of such rollers is in the final part of the paper machine, where the paper is supposed to run through a final smoothening process. Additional requirements, besides a good resistance against abrasive/adhesive type wear, are a high impact toughness and elastic modulus. It is illustrated in Figure 13, that a combined

use of hard micrometer sized SiC-particles and nano-sized Al_2O_3-particles leads to remarkable improvements, when various properties are compared simultaneously to the values of the current standard material (9601 D 31, Stowe Woodward, Germany).

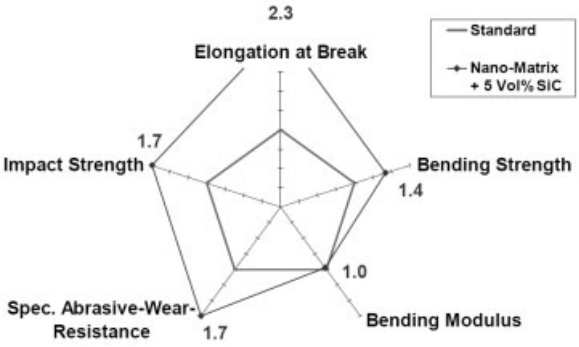


Figure 13: Illustration of property improvements by nanofillers.

Which additional effects can be achieved in epoxy resins by the use of nano-sized fillers, was the focus of recent investigations on their sliding wear resistance. Figure 14 illustrates the results of the specific wear rate of differently filled EP-compositions, as tested by the use of a block on ring-device (against ball bearing steel rings (100Cr6, German Standard)). Relative to the neat epoxy, the wear resistance (inverse of the wear rate) could be improved by almost a factor of 3 after the addition of 4 to 6 vol.% of 300 nm sized TiO_2-particles. Adding traditional fillers for wear and friction improvement, e.g. short carbon fibers (here: M-2007S, Kureha Chemicals, Japan) and graphite flakes (here: Superior 9039), the wear improvement was more effective than just in the case of the nanoparticles. However, a combination of both of them led to a synergistic effect, i.e. both advantageous mechanisms superimposed each other.

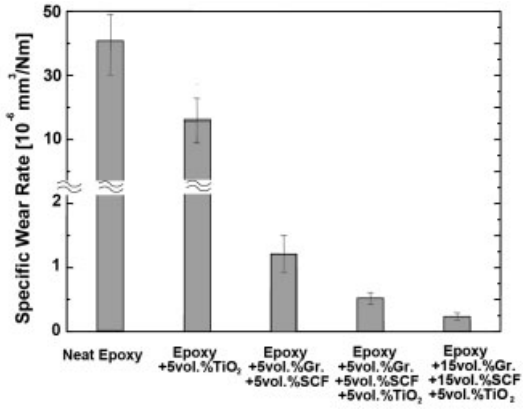


Figure 14: Specific wear rate of epoxy and selected composites with and without 300nm-TiO_2 particles.

Similar conclusions, which have been drawn for the epoxy resins with regard to the cooperative effects of nano- and micro-sized filler particles, can also be drawn in case of thermoplastic matrices. On the example of polyamide 4.6 (PA4.6), which was used in the above mentioned friction torque limiter, it is shown in Figure 15 that the use of traditional micro-fillers alone is not sufficient to reach the desired friction and wear characteristics. But the addition of nanoparticles resulted in a clear reduction of the running-in period, a lower scattering of the friction coefficient (therefore less vibration and noise development in the car), and a much better wear resistance [15].

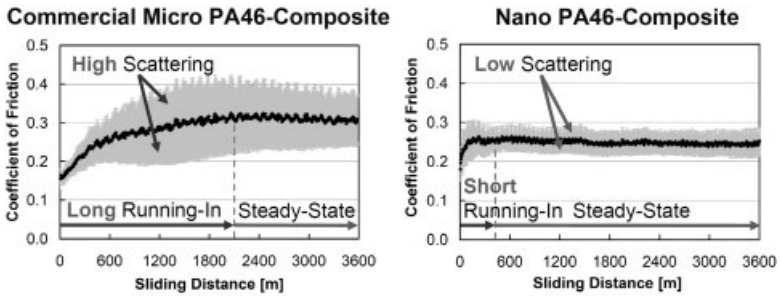


Figure 15: Coefficient of friction of PA4.6 composites without (left) and with (right) additional nanoparticles

From the SEM-figures of the worn surfaces of another polyamide system it can be concluded that the hard TiO_2-nano-particles possess a smoothening effect on the topography of the worn composite surface (Figure 16). In addition, it seems that simultaneously the thermal conductivity of the composite is improved, or at least the transport of heat out of the contact region through the steel counterpart is favorably changed due to the smoothening effect of the nano-fillers.

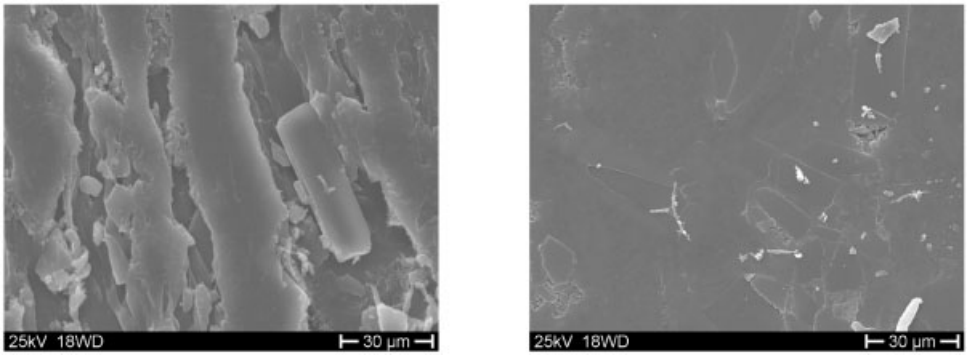


Figure 16: Comparisons of the worn surfaces of graphite+SCF/PA6,6 (left) with nano-TiO_2+ graphite+SCF/PA6,6 (right) under a wear condition of 2 MPa and 3 m/s.

It should be pointed out here, that similar tendencies have been found for a high temperature resistant thermoplastic, i.e. polyetheretherketone (PEEK). The addition of nano-particles led to an improved performance in wear and coefficient of friction at room temperature testing con-



Figure 17: Sliding bearings for automotive applications. (Source: KS-Gleitlager GmbH)

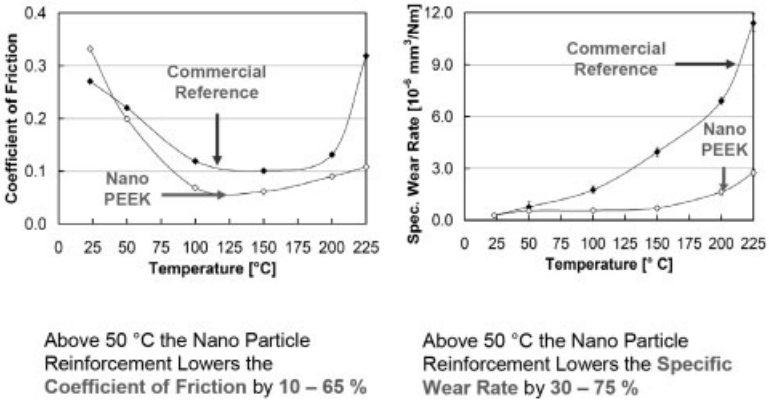


Figure 18: Variation in the coefficient of friction (left) and the specific wear rate (right) as a function of testing temperature

ditions, and this tendency could also be preserved when the materials were tested under sliding against smooth steel counterparts at elevated temperatures (150°C and 220°C). This has finally led to the use of these compounds as thin coatings on steel substrates, a material used for hybrid bushings in wear loaded components of automotive engine parts (Figure 17) [16]. The tribological performance of this material in comparison to another commercial product is illustrated in Figure 18. Especially at elevated temperatures (up to a testing temperature of 225°C) the new nanoparticle modified PEEK composites exhibited both a much lower coefficient of friction and specific wear rate.

5 References

[1] Häger, A. M., Davies, M., in Advances in Composite Tribology. (Ed. K. Friedrich), Elsevier Scientific Publishers, Amsterdam, The Netherlands, **1993,** Chapter 4, p. 107–157

[2] Friedrich, K., in Application of High Temperature Polymers. (Ed. R. R. Luise), CRC Press, Boca Raton, USA, **1997**, Chapter 12, p. 221–246

[3] Reinicke, R., Haupert, F., Friedrich, K., Composites Part A **1998**, 29, 763–771

[4] Friedrich, K., in Advances in Composite Tribology. (Ed. K. Friedrich), Elsevier Scientific Publishers, Amsterdam, The Netherlands, **1993**, Chapter 6, p. 209–273

[5] K. Friedrich, J. Karger-Kocsis, T. Sugioka and M. Yoshida, Wear **1992**, 158, 157-170.

[6] Zhang, Z., Friedrich, K. and Velten, K., Wear **2002**, 252, 668–675

[7] Nalwa, H. S. ,Handbook of Organic-Inorganic Hybrid Materials and Nanocomposites, Vol. 2, American Scientific Publ., Stevenson Ranch, California, USA , **2003**

[8] Wetzel, B., Haupert, F., Zhang, M. Q., Composites Science and Technology **2003**, 63, 2055–2067

[9] Wetzel, B.: Mechanische Eigenschaften von Nanokompositen aus Epoxydharz und keramischen Nanopartikeln, Dissertation Technische Universität Kaiserslautern, Germany, February **2006**.

[10] Zhang, M. Q., Rong, M. Z., Friedrich, K. in Handbook of Organic-Inorganic Hybrid Materials and Nanocomposites, Vol 2: Nanocomposites, (Ed. H.S. Nalwa), American Scientific Publ., Los Angeles, USA, **2003**, p.113–150.

[11] Schwartz, C. J., Bahadur, S., Wear, **2000**, 237 ,261–273.

[12] Xue, Q., Wang, Q.,Wear, **1997**, 213, 54–58.

[13] Haupert, F., Xian, G., Oster, F., Walter, R., Friedrich, K. Proc. 14th Int. Colloquium Tribology, Stuttgart, Germany, January 13–15, **2004**, p.5–11.

[14] Zhang, Z., Breidt, C., Chang, L., Haupert, F., Friedrich K., Composites Part A, **2004**, 35, 1385–1392

[15] Gebhard, A., Englert, M., Bittmann, B., Haupert, F., Schlarb, A.K., in Proc.2nd Vienna International Conference on Micro- and Nano-Technology, Vienna, Austria, March 14-16, **2007**, p. 41–48.

[16] Oster, F., Haupert, F., Friedrich, K., Bickle, W., Müller, M., Tribologie und Schmierungstechnik 51 (2004) 3, 17–24.

Part II
Lectures

Effect of Graphite and Silicon Carbide Addition on the Hardness and Wear Resistance of Al-4wt% Mg Alloys

Adel Mahmood Hassan, Ghassan Musa Tashtoush, and Ja'far Ahmad Al-Khalil
Faculty of Engineering, Jordan University of Science and Technology, P.O. Box: 3030, Irbid, 22110, Jordan

Abstract

Particulate metal matrix composite components (PMMC) consisting of Al-4wt% Mg alloys as a matrix and containing different mass fractions of graphite and silicon carbide particles as reinforcement were studied. The composite components were produced by compocasting technique. By this casting technique the graphite particles and silicon carbide particles were added into a stirred semi-solid melt of Al-4wt%Mg alloy. All the steps carried out in the production of these PMMC components were described. Then the effect of graphite and silicon carbide particles added on the hardness and wear resistance of the produced cast composite components were studied. The study showed that there was a decrease in hardness, but an increase in wear resistance by the addition of graphite and an increase in these two properties, if silicon carbide is added. These two properties are important for materials used in the manufacturing of bearings. Accordingly, it is thought, that there is a possibility of using these aluminum based cast composites as bearing materials especially in transport industry.

1 Introduction

In very early time, the problem of finding the most suitable material to satisfy the requirement of a specific job had been concentrated on the already existing materials. Later on it was found that the right combination of different materials may produce properties which were superior to those of the existing materials if each was considered separately. This had lead to carry out more intensive researches in order to develop new combination of different materials with specific desired properties. The new combination of materials, which are still under development, is known today as composite materials. Composite materials are multifunctional materials that provide characteristics not obtainable from any discrete material. They have cohesive structure made by physical combination of two or more compatible materials, differing in composition and characteristics and some times in form [1]. A Composite material generally consists of a matrix and reinforcements. At present several methods are used to classify composites, among these is a method, where the composites are classified as metal matrix, polymer matrix and ceramics matrix composites according to the material of the matrix [2]. Another method concerns with dividing composites according to the reinforcements, such as particle reinforced or fiber reinforced or structural composites [3].

Metal matrix composites (MMC) are making a remarkable success in different applications in industries, especially in automotive and aerospace industries, because of their high strength, high modulus of elasticity, high service temperature, high wear resistance, low weight and production cost [4]. Different conventional methods are available for the fabrication of MMCs such

as powder metallurgy, spray deposition and casting process. The most important and most difficult problem associated with fabrication of metallic composite materials is the production of good bonding between the reinforcement and the metal matrix. As the bonding strength is an important factor in the selection of matrix-reinforcement combination. Adequate bonding is essential to maximize the transition of stress from the matrix to the reinforcement [1]. There are several methods which can be used to enhance the magnitude of this bond, in order to improve the strength between the matrix and reinforcement. Rohatgi et al. [1] mentioned that the addition of Magnesium to an Aluminum melt improves the strength of this bond, because of the lower surface tension of Mg compared with the surface tension of Al.

Wettability can be defined as the ability of a liquid to spread on a solid surface, and represent the extent of intimate contact between a liquid and a solid. One of these methods to increase wettability is to add alloying elements to the matrix alloy. A mechanical force can also be used to overcome surface tension and improve the strength between the matrix and the reinforcements. One of the most important types of mechanical forces used is the stirring of the reinforcement within the melt, especially when the melt is in a semi- solid phase. This method is usually called compo-casting or stir-casting [5, 6, 7 and 8].

The most important advantages of compo-casting are: low processing temperature, high production cycle time, reduction of solidification shrinkage, close tolerance products and conventional foundry practices can be used to produce composites.

The disadvantages that may occur when process parameters are not adequately controlled are: the non homogenous particle distribution [4] and the possible existence of high level of porosities through out the casting [9 and 10].

In particulate metal matrix composites (PMMCs) relatively small size particles are dispersed throughout the matrix. These dispersed particles can be graphite, SiC, Al_2O_3, TiO_2, ZrO_2 and many other industrial ceramics. One of the promising fields in the application of such composites is the possible use of it as a bearing material [11]. Usually bearing material should possess sufficient hardness and wear resistance, but at the same time the hardness should not be very high relative to the hardness of the shaft or journal in order to avoid metal to metal contact particularly during the starting up process especially, when lubrication is used. Also the strength of the bearing material should be sufficient to sustain the load without, plastic deformation and to possess considerable toughness in order to resist shock loading [2]. It seems many of these apparently conflicting requirements can possibly be met by particulate metal matrix composites. These requirements were the motivation for the present work, where a soft metal matrix was reinforced by certain particles distributed throughout the matrix using a compo-casting process. The study is an attempt to examine the effect of graphite, SiC and the combination of graphite and SiC particles and the change in their amount percentages on the hardness and wear resistance.

2 Experimental Details

2.1 Test Materials

A high purity aluminum (99.85 %) as a matrix metal as shown in Table 1 with a density of 2.71 g/cm^3, fine graphite particles with average 300 μm in size and density of 1.7 g/cm^3, silicon carbide particles with 600 μm in size and 3.21 g/cm^3 density were used for the fabrication of the composite cast bars examined in the present study. Magnesium with a density of 1.7 g/cm^3

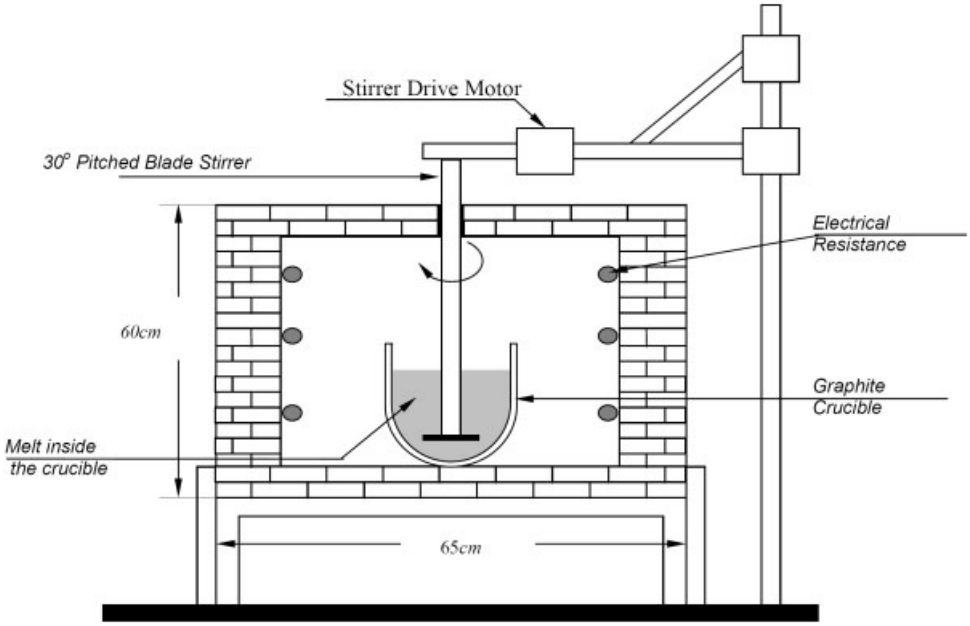


Figure 1: Schematic diagram representing the experimental set-up

was used in a bulk form in order to promote the wettability between aluminum and the reinforcement particles. The amount of Magnesium added was 4wt%, as it has been suggested by other researchers [12 and 13].

Table 1: Chemical compositions of aluminum.

Al	Fe	Zn	Mg	Si	Ti	Ni	Cu
99.85	0.08	0.0032	0.003	0.04	0.0043	0.0014	0.0005

2.2 Preparation the Test Specimens

2.2.1 Melting Furnace and Stirrer

The experiments were carried out using a relatively simple experiment set-up, which consists of an electrical furnace and stirring arrangement. The schematic diagram of the experimental set-up is shown in figure 1.

An electrical furnace, which was designed and constructed in previous work [14], was used to melt the charge inside a graphite crucible. The dimensions of the furnace were suitable to use different sizes of graphite crucibles and different types of stirrers. The inside dimensions of the furnace were 42 cm in length and 42 cm in width and 52 cm in height. At the center of the top surface of the furnace, there was a square hole of dimensions 10 cm $\times$ 10 cm, which can be

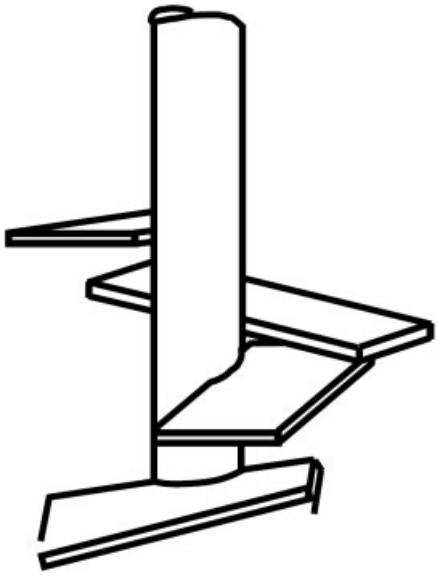


Figure 2: Schematic diagram of pitched-4 blades stirrer.

used to intrude the stirrer inside the furnace. The stainless steel stirring rod diameter was 1cm, which was fitted to an electrical motor having speed range from 150 to 1200 rpm. The motor of the stirrer was held rigidly over the furnace by a gripping steel structure arrangement shown in figure 1. A control unit with two indicators was used to control the temperature of the furnace and the stirring period. The two indicators could be set at the beginning of the stirring process.

A special type of a thermocouple was used to measure the temperature of the molten metal inside the crucible inside the furnace. The thermocouple was covered with stainless steel in order to protect it from the damage that may be caused by the high working temperature inside the furnace. This thermocouple was connected to a digital display in order to read the temperature of the melt.

A four stainless steel flat blade stirrer was used, figure 2. Each blade was inclined by a 30° from the horizontal axis and distributed along the vertical axis of the stirrer's shaft at different height and their center lines differ by 90° from each other [15].

2.2.2 Casting Procedure

Pure aluminum was placed in the graphite crucible and inserted inside the electrical furnace. The furnace was heated up to 850 °C until the aluminum inside the crucible was completely melted. After melting of the aluminum, the furnace was switched off to cool down the melt, which its temperature was monitored by the thermocouple, which was inserted inside the crucible to a depth of about 1 cm to 1.5 cm beneath the surface of the melt. Then a proper amount of magnesium was added to the molten aluminum taking into consideration an estimated weight loss of 20 % due to evaporating and burning. The added magnesium was wrapped in aluminum foil, and plugged

into the melt at temperature between 710–740 °C with the aid of holder. The magnesium lump was manually stirred inside the melt until it is completely melted. The surface of the melt was cleaned by skimming it with the aid of steel rule, prior to stirring stage. The stirrer was inserted inside the furnace for about 30 seconds in order to preheat it, then it was coated with aluminum oxide (alumina) powder in sodium silicate, and dried in air, in order to prevent dissolution of the stirrer blades in molten aluminum, when the temperature of the melt reached 640 °C, the stirrer is inserted into the melt and was vigorously agitated at speed of 600 rpm. The furnace was switched on again, when the temperature of the melt reached 635 °C, in order to have a constant holding temperature of 635 °C just below the melting temperature)660 °C of the aluminum. When the reinforcement particles were less than 4%vol. of the total volume of the charge inside the crucible, they were wrapped in aluminum foil and preheated to 400 °C for 1 hour, before immersing it in the melt, and stirred inside the melt for 4 minutes. But when the reinforcement particles were 4 % vol. or more, these particles were added in two stages, by divided the amount of the particles into two equal parts, then stirring each added part for about 2 minutes. At the end of the stirring period, the molten metal inside the crucible was taken outside the furnace and poured inside a metallic mould of size 3 cm diameter and 17 cm height, to be cooled in air, and solidified to cast metallic matrix composite bars. A small amount of all cast bars' surfaces were machined to remove possible oxide and contamination during the casting process and prepared for testing by cutting each bar into three portion (top, middle, and bottom) to be used for further study, as it will be seen later in the next paragraphs of the present work.

2.3 Hardness Test

In order to measure the hardness of the cast bars, three samples from top, middle and bottom of each cast bar were prepared for this test. Each sample were cut to a height of 4 cm and turn diameter of 2.5 cm. A lubricant was used during turning to reduce the affect of the increase in temperature, during turning, on the proceeding measurement of hardness. The hardness test was carried out using the Rockwell hardness testing machine with scale B.

2.4 Wear Test

The wear test specimens were studied under dry wear conditions using pin-on-disc wear testing machine, figure 3. The disc was made from hardened medium carbon steel with 50 mm in diameter, and 10 mm thickness, while the pin was made from the already cast bar with 0.4 cm in diameter, and height of 2.5 cm, figure 4. The tests were carried out under a constant load of 40 N and rotational speed of 150 rpm. The time of the test was constant and equal to 60 minutes. The mass of each test pin was measured, using a precision balance having 0.1 mg sensitivity, before and after the test to determine the amount of the mass-loss for each tested metallic matrix composite pin.

This mass-loss obtained from each test will give an indication of the wear resistance for the considered different type of composite materials.

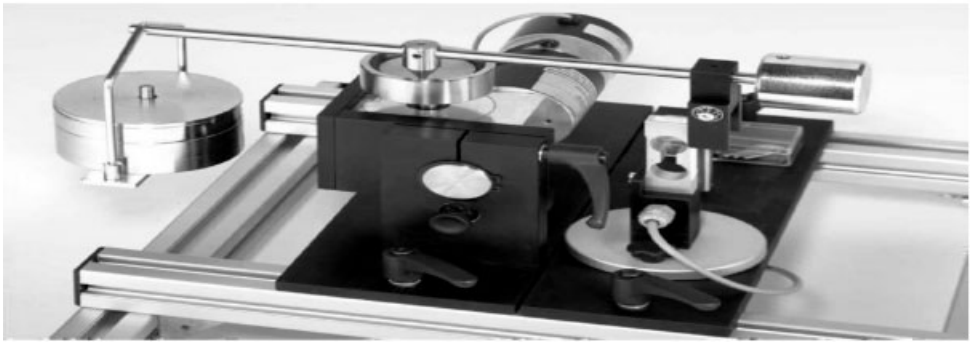


Figure 3: Wear test apparatus.

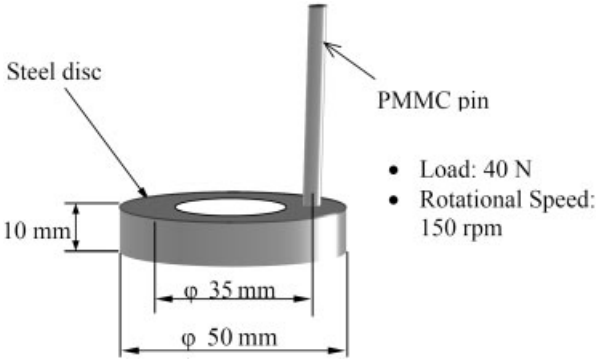


Figure 4: Wear test pin and rotating disc

3 Results and Discussion

3.1 Hardness

3.1.1 Effect of Graphite Addition on Rockwell Hardness Number

Figure 5 shows the effect of graphite addition on the Rockwell hardness numbers for the three parts taken from each cast composite bar (see section 2.2.2). The Rockwell hardness number is increased from bottom toward the top of each cast bar. It can be observed, also, from this figure that the Rockwell hardness number decreases with increasing graphite addition in each considered specimen. It was mentioned by Hassan et al. [10], that an increase in porosities in the structure of composites leads to a decrease in the total hardness. As the hardness testing machine's indenter will cause a plastic flow in the material being tested. Porosity is one of the disadvantages, as mentioned earlier, of the compcasting process. The pores in the indentation zone will cause a slight reduction in the resistance of the cast material to the intruding action of the indenter. Accordingly, it can be said, that the presence of pores results in lowering the resistance of the compocast material to deformation, and causing a decrease in the hardness measured

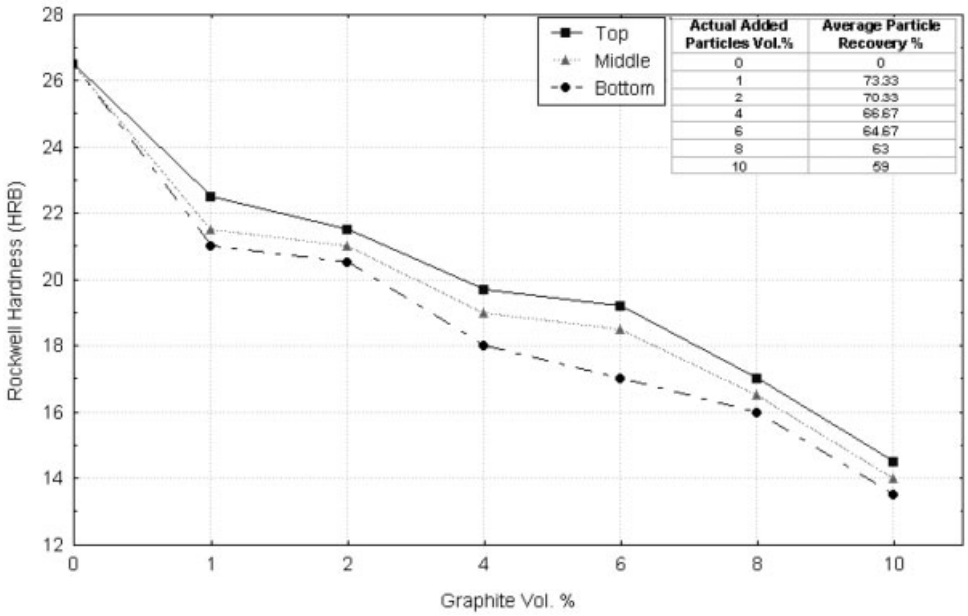


Figure 5: Effect of graphite addition on the Rockwell hardness number.

value. In addition, the presence of graphite, which acts as a lubricant, facilitates the slipping or sliding within the material during the deformation process caused by the penetration action of the hardness machine's indenter. This will lead even to more reduction in hardness.

The slight differences between the hardness along the cast composite bar is due to the low density of graphite, as mentioned earlier (see section 2.1), which causes the graphite particles to float upwards during the pouring and solidification processes of the molten metals. Not many of these particles can float, because of the fast rate of solidification and small cross-sectional area of the metallic mold. Still, the small amount of graphite particles, which can escape and float up, will cause the slight difference in hardness, as shown in figure 5.

3.1.2 Effect of Silicon Carbide Addition on Rockwell Hardness Number

The effect of silicon carbide particles addition on the Rockwell hardness number is shown in figure 6. The figure indicates that the hardness of the investigated composite is increased with the increasing in the amount of silicon carbide particles. Also, it seems from this figure, that, the Rockwell hardness number along the cast composite bar from the top to the bottom increases.

Silicon carbide, as an industrial ceramic, has a very high hardness. Its hardness (9 Mohs scale) is near that of diamond (10 Mohs scale) [11]. The presence of the hard particles in the tested composites will cause the observed increase in hardness. The density of SiC is higher than the density of the matrix (see section 2.1). Because of the difference in densities of the matrix and reinforcement, the SiC particles tend to descend to the bottom of the mould during pouring and solidification processes, but most of them will be trapped, due to the fast solidification rate of the

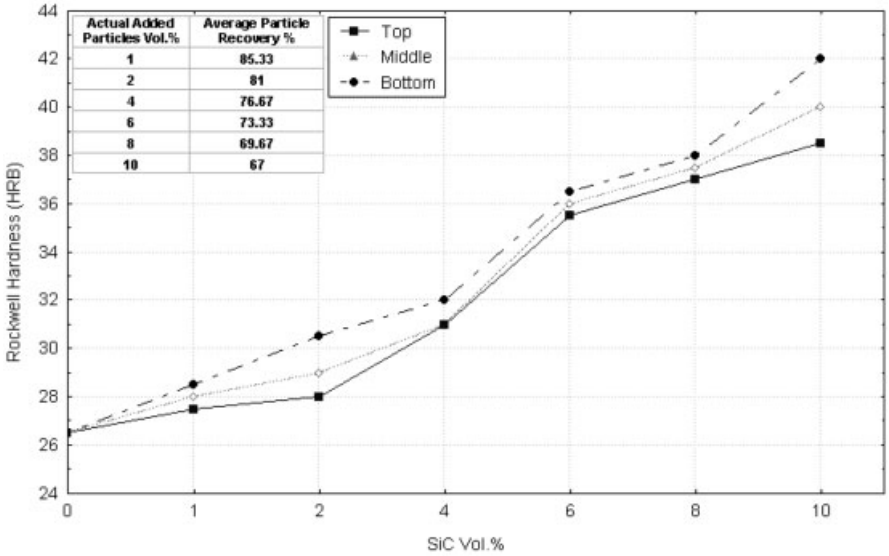


Figure 6: Effect of Silicon Carbide addition on the Rockwell hardness number.

matrix material. This can explain the slight differences between the hardness along the length of the cast composite bar.

3.1.3 Effect of Graphite and SiC Addition on the Rockwell Hardness Number

Figure 7 shows the effect of both the silicon carbide particles and the graphite particles addition on the Al-4%wt Mg alloy, the hardness of these composites is increased with the increasing in the amount of silicon carbide particles at a constant value of graphite particles in the alloy. When the percentage of graphite particles is increased in the composite at constant value of silicon carbide particles, the hardness of the composite is decreased.

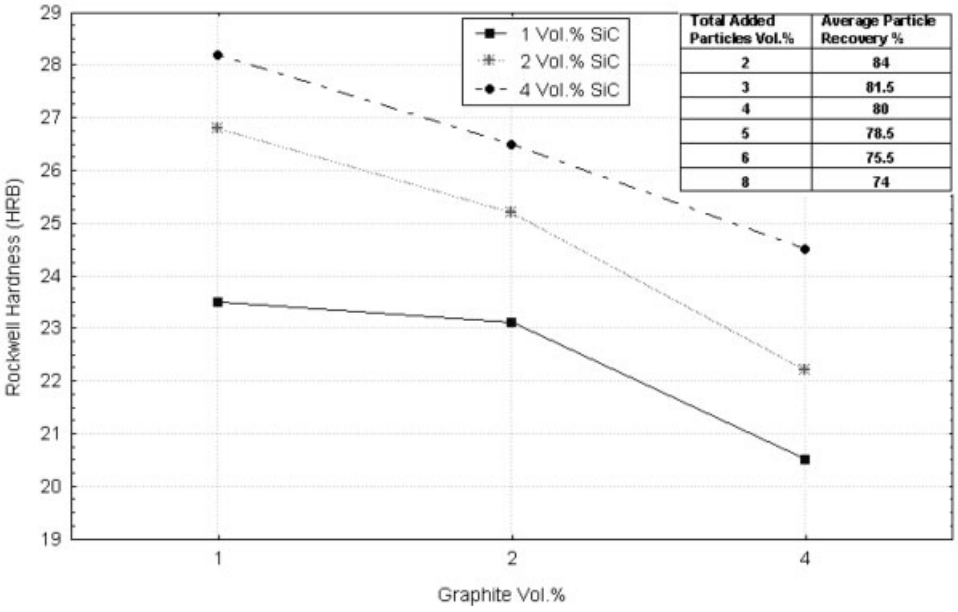
This can be explained by the difference between the properties of silicon carbide and graphite particles and their effects on the final properties of the metallic matrix. These results verify the results, which has been discussed in previous two sections.

3.2 Wear Resistance

3.2.1 Effect of Graphite Addition on the Wear Resistance of Al-4%wt Mg Alloy

Figure 8 illustrates the effect of graphite addition on the mass loss in wear of the considered aluminum alloy. It can be clearly seen that, mass-loss of the considered aluminum alloy is decreased with the increasing in the amount of graphite addition to the metallic matrix.

The main reason of the decrease in mass-loss is the presence of graphite particles, which acts as a solid lubricant causing a reduction in the temperature and the coefficient of friction between the mating interfaces. Also, the pin will always expose new layer, which is rich in graphite particles



Total Added Particles Vol.%	Average Particle Recovery %
2	84
3	81.5
4	80
5	78.5
6	75.5
8	74

Figure 7: Effect of graphite and SiC addition on the Rockwell hardness number.

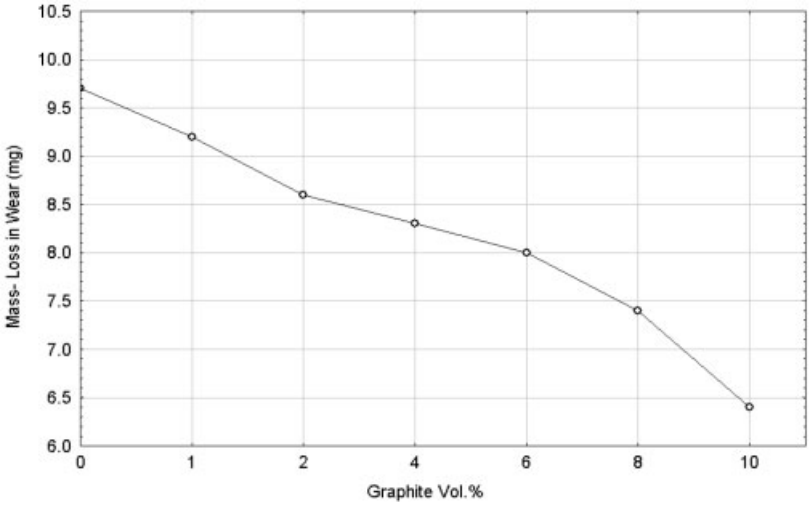


Figure 8: Mass-loss in wear of Al-4%wt Mg-Graphite composites

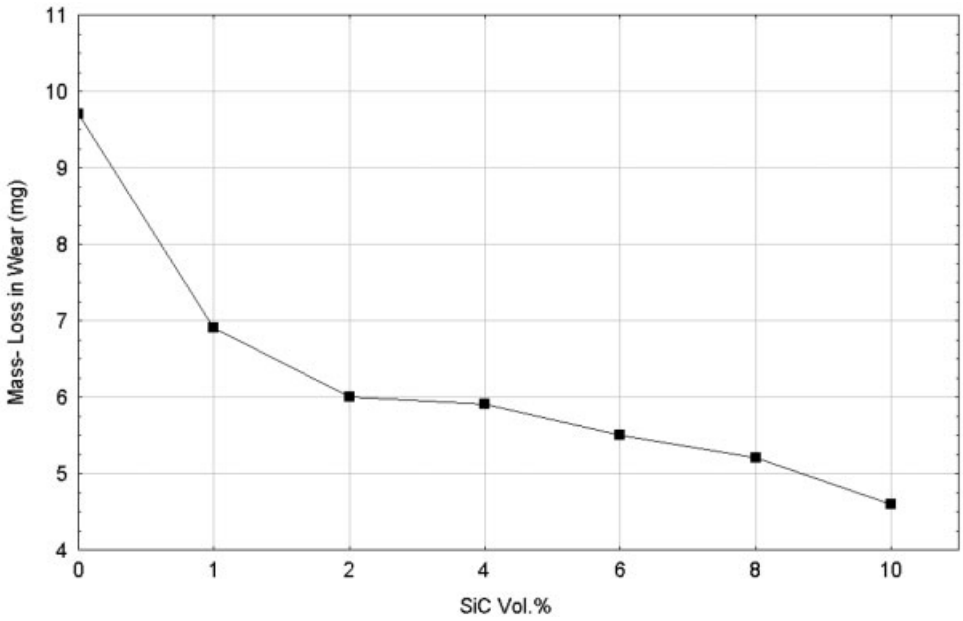


Figure 9: Mass-loss in wear of Al-4%wt Mg-SiC composites.

instead of the worn one. This action will provide a continuous film of graphite lubricant on the mating surfaces, which leads to a reduction in mass-loss of the composite material pin.

3.2.2 Effect of SiC Addition on the Wear Resistance of Al-4%wt Mg Alloy

Figure 9 indicates that the mass-loss of the considered composites decreases with the increase in the amount of added silicon carbide particles to the matrix. The addition of the abrasive hard particles of SiC to the Al-4%wt Mg matrix leads to an increase in the resistance of the composites to wear, providing, that the wettablity between the reinforced particles SiC and the Al-Mg matrix is sufficiently good. This statement can be held true for all hard particles or fibers added as reinforcements to produce composites.

3.2.3 Effect of Graphite and SiC Addition on the Wear Resistance of Al-4%wt Mg Alloy

Figure 10 shows the effect of graphite and SiC particles addition to the considered Al-4%wt Mg alloys on the mass-loss in wear. It can be observed from this figure that the increase in the added amount of graphite and SiC particles decreases the mass- loss in wear of the produced composite materials.

These results are expected due to the previous discussion carried out in section 3.2.1 and 3.2.2 above. The SiC particles will increase the hardness of the matrix, while the graphite particles act as solid lubricant between the mating parts in the wear test. Both actions of the different added particles will improve the resistance of the compocast composites to wear.

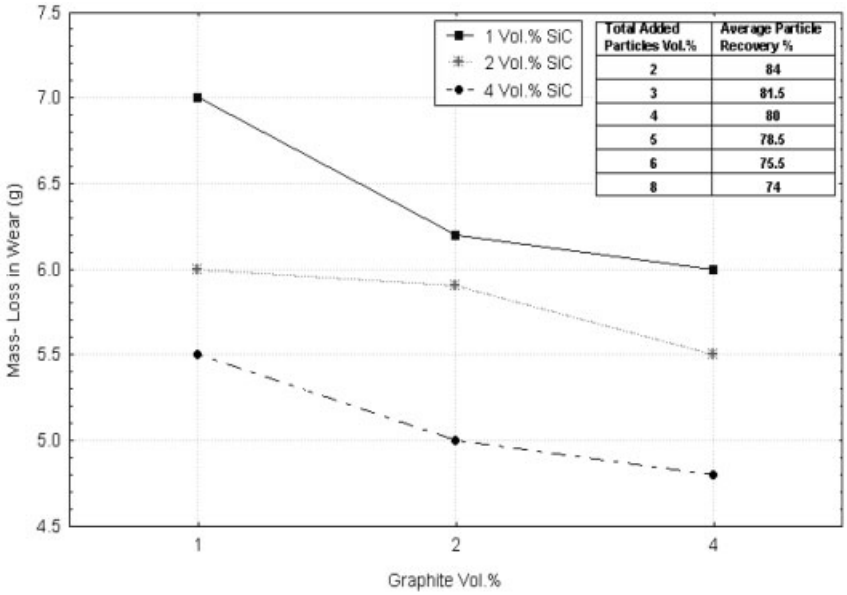


Figure 10: Mass-loss in wear of Al-4%wt Mg-Graphite-SiC composites.

4 Conclusions

The following conclusions can be withdrawn from the present study:

1. Metal matrix composite materials can be produced successfully by using compocasting method. As it has been shown, that this method together with the equipment needed for the production of cast composites are rather cheap and simple in design and operation.

2. The hardness of the produced composites decreases with the addition of graphite, due to the lubricating action of this material, while the addition of SiC increases the hardness, Because of the high hardness of this industrial ceramic material.

3. Both graphite and SiC particles, when added to the considered metallic matrix, will increase the wear resistance of the considered composites. This is due to the formation of a lubricating film between the mating materials' interfaces, when graphite is added and the resistance to wear property of the hard and abrasive SiC particles.

4. Wettability is a very important factor, which has to be considered, when composites are produced. In order to increase the wettability of the composites used in the present study, an amount of 4% wt. magnesium is added to aluminum to form the matrix, in order to improve the wettability between the considered matrix and the different used reinforcements.

5. Because of the smearing action of graphite, and the hardness of SiC, it can be suggested, that the light weight Al-4%wtMg-Graphite-SiC PMMC can be used as a bearing material, especially in transport industry, where weight is a decisive factor.

References

[1] Rohatgi P. K. and Asthana R.; Solidification; Structure; and Properties of Cast Metal- Ceramic Particles Composites, International Metals Review, **1992**, 31.

[2] John V. B.; Introduction to Engineering Materials, 4th Ed., Palgrave Macmillan Co. Ltd., **2003**, Chapter 19.

[3] Callister W. D. Jr.; Fundamental of Materials Science and Engineering, 2nd Ed., John Wiley, **2005**, Chapter 15.

[4] Naher S., Brabazon D.and Looney L.; Simulation of the Stir Casting Process, Journal of Materials Processing Technology, **2003**, 143-144.

[5] Hashim, J. and Looney, L.; The Wettability of SiC Particles by Molten Aluminum Alloy, Journal of Materials Processing Technology, **2001**,119.

[6] Hanumanth, G. S. and Irons, G. A.; Particle Incorporation by Melt stirring for the production of Metal Matrix Composites, Journal of Materials Science, **1993**, 28.

[7] Skolianos, M.; Mechanical Behavior of Cast Sic_p-Reinforced Al-4.5%Cu-1.5%Mg Alloy, Material Science and Engineering A, **1996**, 210.

[8] Kang C. G., Yoon J. H. and Seo, Y. H.; The Upsetting Behavior of Semi-Solid Aluminum Material Fabricated by Mechanical Stirring Process, Journal of Materials Processing Technology, **1997**, 66

[9] Hashim, J. and Looney, L.; Metal- Matrix Composites: Production by Stir- casting Method, Journal of Materials Processing Technology, **1999**, 92.

[10] Ghosh P. K. and Ray S.; Effect of porosity and alumina content on the high temperature mechanical properties of compocast aluminum alloy- alumina particle composite, Journal of Materials Science, **1987**, 22.

[11] Rohatagi P. K., Asthana R. and Das S.; Solidification, Structures and properties of cast metal-ceramic particle composites, International Metals Reviews, vol. **1986**, 31, No. 3.

[12] Zhou W. and Xu Z. M.; Casting of SiC Reinforced Metal Matrix Composites, Journal of Materials Processing Technology, **1997**, 63.

[13] Sahin Y.; Preparation and Some Properties of SiC Particle Reinforced Aluminum Alloy Composites, Materials and Design, **2003**, 24.

[14] Hassan, A. M., Hayajneh, M., T. and Al-Omari, M. A.; The Effect of the Increase in Graphite Volumetric Percentage on the Strength and Hardness of Al-4 weight percent Mg-Graphite Composites, Journal of Materials Engineering and Performance, **2002**,11.

[15] Al-Jarrah J., Ray S.and Gosh P.K.; Solidification Processing and Properties of Cast Al-Al_2O_3 Composites, Proc.of the 6th Asian Foundry Congress: Calcutta-India, **1999**, 271-283.

Aluminum Based Sliding Materials with Soft Phases – Intrinsic For-giving Overload Behavior?

F. Grün
CD-Laboratory for Fatigue Analysis, University of Leoben, Leoben
I. Gódor, W. Eichlseder,
Chair of Mechanical Engineering, University of Leoben, Leoben

1 Introduction to Sliding Materials

The demands posed on sliding materials are numerous: from a mechanical standpoint, high temperature stability and good sliding properties are critical to ensure a long-term reliability of journal bearings. Therefore several heterogonous layers of different materials plated on top of each other are used. Each of these layers is optimized for a specific function. Aluminum is a widely employed matrix due to its low density, its cost effectiveness and good heat conduc-tivity. Its tribological properties can be easily improved by the addition of soft phases such as tin. During casting tin and aluminum form a heterogeneous alloy, fine tin inclusions are inter-spersed in the aluminum matrix.

In technical applications up to 40 % tin is incoperated into the matrix. Fig. 1a shows a typical mixture composed of 20 % tin. The soft phase tin has a lower melting point than the aluminum matrix. When reaching a critical temperature, the tin melts and leaves the micro-structure. It now acts as a "liquid lubricant", thus greatly improving the dry-running proper-ties of the component.

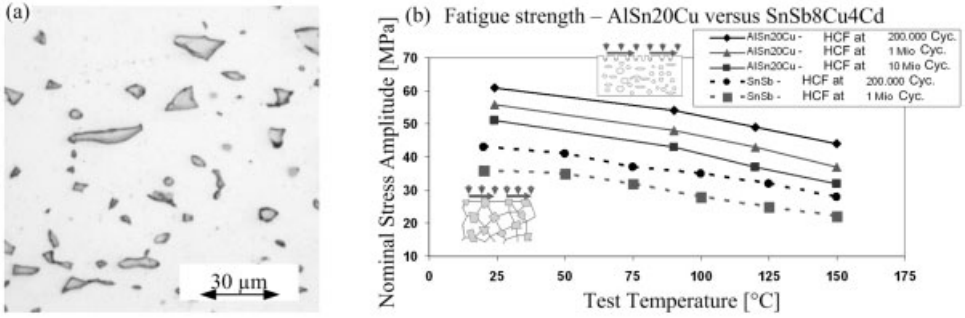


Figure 1: a) AlSn20Cu – Al-matrix with soft tin inclusions [1]; b) Strength of AlSn20Cu and SnSb8Cu4Cd [2, 3, 4]; notice the generally lower fatigue strength of the Babbitt metal.

One must consider the trade-off between structural stability and "forgiving overload or dry-running behavior" when determining the appropriate metal composition. Sn-basis materials, the so-called Babbitt alloys, possess the best sliding properties but the lowest ability to with-stand mechanical loading. Especially at elevated temperatures the breakdown of the mechani-cal strength of tin-based alloys becomes limiting. Fig. 1b shows that at 150 °C the fatigue strength at one million cycles of the Babbitt metal is just 22 *MPa*. In contrast, the fatigue strength of AlSn20Cu

is 37 *MPa*. Current oil sump temperatures reach 145 °C. The increasing loads on engines will further boost the temperatures.

One primary goal of materials design is the optimization of the soft-phase content and soft-phase distribution in the matrix material. It is therefore necessary to fully understand the tribological events taking place. As these events can not be elucidated using traditional compo-nent tests, tests on model scale are necessary. In this publication we want to demonstrate the influence of the soft phase on the tribological properties based on the examples Al99.6, AlSn20Cu, and AlSn40.

2 Test Method for Visualizing Tribological Properties

The method for testing the sliding properties is based on the test configuration ring-on-disc. The large contact surface is significant for journal bearing application and represents the primary advantage of this set up. The test configuration is depicted in Fig. 2a. A rotating disc of approximately 30 *mm* diameter is pressed against a fixed steel ring (34CrNiMo6), see Fig. 2b for details. The system is fully immersed in formulated engine oil. Sensors measure the temperatures T_1 and T_2, as well as mechanical wear and frictional torque.

One should not underestimate the importance of a carefully selected and fine-tuned test program to realistically represent the system properties and investigative goals. Fig. 2c shows schematically the applied seizure test program. The load is increased while the rotating speed is maintained at a constant level. The increase in temperature melts the Sn inclusions in the matrix and thus activates the dry-running properties. The energy input is substantially lower than in component tests that use, for example, full journal bearings. This way it is possible to extend the failure process to over several hours and sufficient time is available to perform damage analytical tests at different time intervals and damage levels.

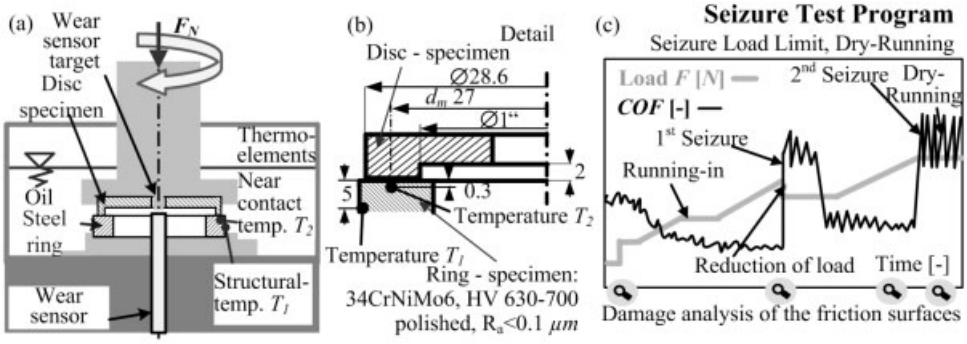


Figure 2: a) Test configuration ring-on-disc [5]; Detail [6]; Seizure test program [6].

3 Results – Tribometrics and Damage Analysis

In the following section we would like to present tribometric and damage analytical results for the materials Al99.6, AlSn20Cu, and AlSn40.

3.1 Pure Aluminium Without a Soft Phase – Al99.6

Fig. 3 shows the results of a characteristic test run employing pure aluminum. The sliding velocity is 0.7 *m/s*. The load is steadily increased after an initial running-in phase of approximately 10000 *m*. System stability starts to degrade from approximately 14 *MPa* onwards. The Coefficient of Friction (*COF)* before seizure is low, which is characteristic for comparatively hard frictional surfaces. It then increases sharply from 0.01 to 0.06. This increase in *COF* is accompanied with an increase in temperature. Mutations of the material relevant to dry-running processes could not be observed. Fig. 3b shows a characteristic surface shortly after the start of seizure. The observed friction is due to adhesion.

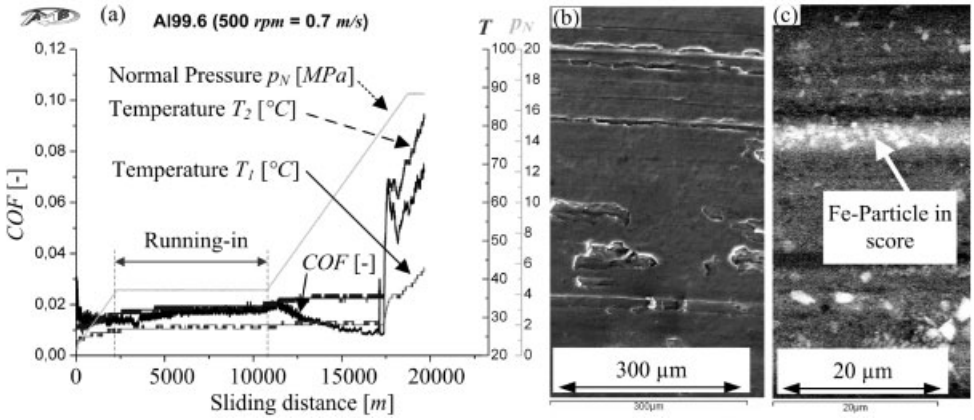


Figure 3: Al99.6: a) Results seizure test [4]; b) Adhesion marks [1]; c) Fe-particles structured surface [1].

Tribological loading over extended periods of time, such as during a long term test, results in incorporation of wear debris of the steel ring in the aluminium surface (see Fig. 3c). The steel counterpart also shows substantial wear. Fig. 4a depicts the associated topography of the aluminium disc and the steel ring. The wear for aluminium is 300 μm in average and up to 15 μm for steel. The surface topographies match each other perfectly.

Microscopic investigation of the boundary layer revealed a break down of delaminated Fe-particles. The paradox observation of the wearing down of the hard steel (hardness $HV \tilde{}$ 630–700) by the soft Al99.6 material (hardness $HV \tilde{}$ 60) can not be explained by traditional theory of solid mechanics. We postulate that mixing processes are responsible for modifying the properties of the surface material (see Fig. 4b). These mixed zones show unique properties in that they are substantially harder (measured values *HV* 167 and *HV* 208) than the Aluminum matrix (*HV* 57) (see Fig. 4c). This hardening of the boundary layer can be explained by two factors, first by the

formation of Al_2O_3, which is a factor of 60 times harder than metallic aluminum, and second, by the incorporation of iron particles from the steel matrix.

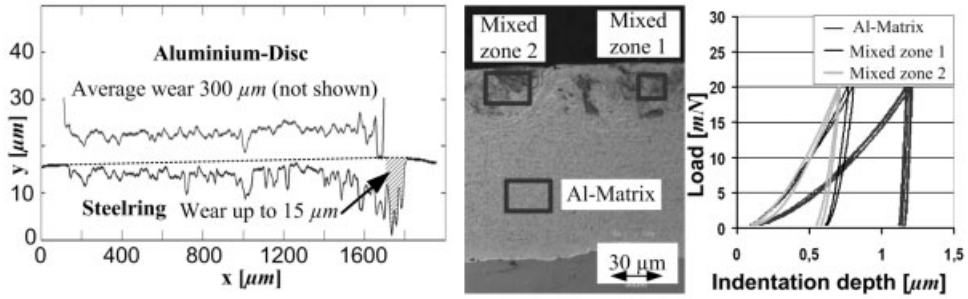


Figure 4: Al99.6: a) Surface topographies Al-Disc and Steelring; b) Cross-section of Al99.6 - formation of mixed zones; c) Indentation measurements [1].

3.2 Aluminium With 20 Percent Tin – AlSn20Cu

The addition of a soft phase alters the tribological behavior of the system. Fig. 5a illustrates a characteristic seizure test, in this case with an addition of 20 mass percent tin. The running-in phase is more pronounced than with pure Al99.6. A loss of stability occurs at approximately 11 *MPa*, typical values range from 10 to 14 *MPa*. At higher temperatures the soft phase Sn becomes tribologically active. Fig. 5b illustrates that Sn is capable of preventing adhesion events on the surface. As a consequence, the soft phase is gradually used up and the sliding properties are lost. This is manifested by an increase in COF. At the same time mixed zones start to form (Fig. 5c). Fig. 5d depicts, largely magnified, a scanning electron micrograph of such a mixed zone. It is clearly visible that the Sn is now distributed very finely inside the matrix. The following chemical composition of the fine grained mixed zones was detected, based on EDX-measurements: 6 % C, 28 % O, 51 % Al, 13 % Sn and 2 % Fe [5,7]. Indentation tests help to quantify the hardness of the material: Measurement of the soft phase resulted in a hardness value of 19 *HV* and 64 *HV* was determined for the Al-matrix. The mixed zone, in contrast, possesses more than 300 *HV*. This increase in hardness can be attributed mainly to the formation of Al_2O_3 [5,7].

3.3 Aluminium With 40 Percent Tin – AlSn40

The addition of 40 % (by mass) of a soft phase results in a superior sliding performance during operation, but also an increased wear. The plot depicted in Fig. 6a illustrates the events. The increase in *COF* before loss of stability at 18 *MPa* is characteristic, the typical range is from 16 to 18 *MPa*. The gradual increase in COF is an indicator for a degradation of the surface layer and a deformation of the matrix material. As a consequence, there is less lubricant in the area of contact. After loss of stability the system behavior is less erratic than with AlSn20Cu. In this particular test run, the COF gradually declines and a significant wear can be observed. Fig. 6b is a micrographic image depicting the surface at the end of the test. Sn-beads are visible, they are responsible for decreasing adhesion. Fig. 6c and 6d show that mixing processes do not

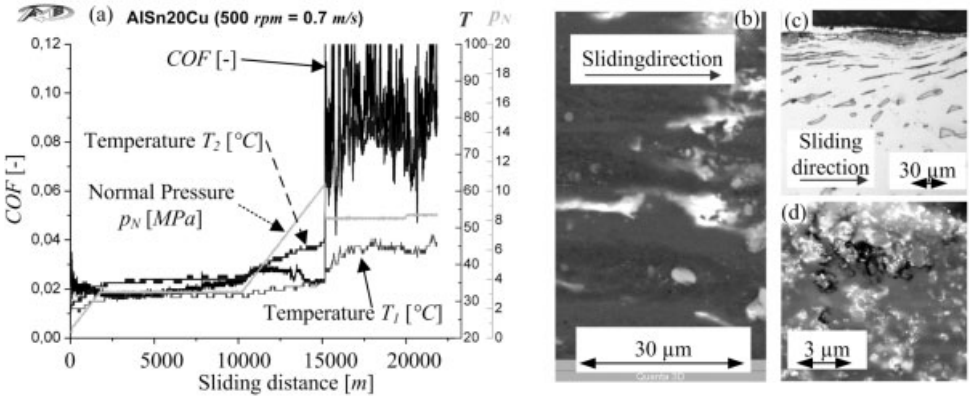


Figure 5: AlSn20Cu: a) Results seizure test [8]; b) Soft phase tin prevents adhesion; c) Mixed boundary layer; d) Detail – mixed zone (SEM).

occur in the matrix. These processes start to appear only at high speeds. The absence of mixing processes is an indication for lack of mechanical stability. Initially plastic deformation of the matrix material takes place, followed by a removal of the outermost layers. Mixing processes require a high degree of mechanical resistance. They can only occur if the matrix is hard enough to offer sufficient counterpressure.

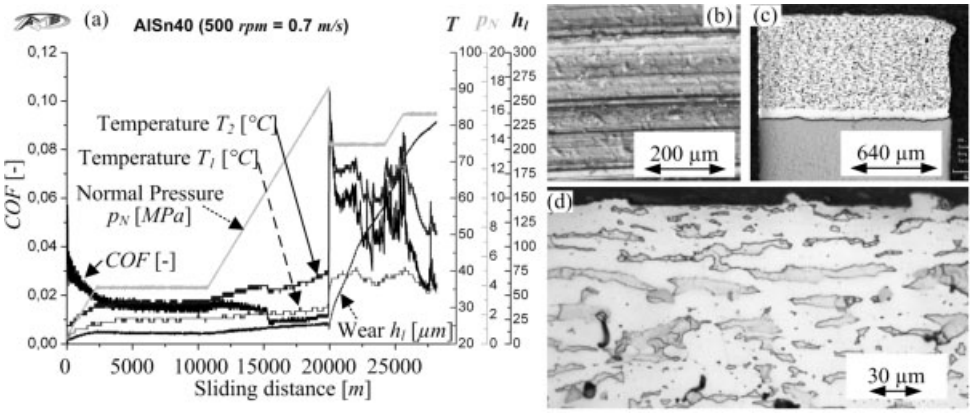


Figure 6: AlSn40: a) Results seizure test; b) Soft phase tin prevents adhesion; c) Cross section - mixed boundary layer; d) Detail - mixed boundary layer.

4 Tribological Functional Model of Aluminum With Soft Phase

The measured test results and results obtained from damage analysis were combined to formulate a functional model of the events taking place in the boundary layer (Fig. 7). Initially the soft

phases are still intact. This is before the runnung-in phase (state no. 1). With increasing tribological loading the soft phases become activated and melt. They are squeezed out of the matrix material and contribute to the dry-running properties. The soft phase is consumed (state no. 2). Additionally, the formation of hard aluminium oxide, which is pressed into the boundary layer, and mixing processes generate highly wear-resistant regions (states no. 3 and 4). In any case, these tribomutations are now responsible for carrying the tribological load. This „Double Effect Model“ is therefore capable of explaining both the dry-running properties and the load-bearing capacity of the system after consumption of the soft phase.

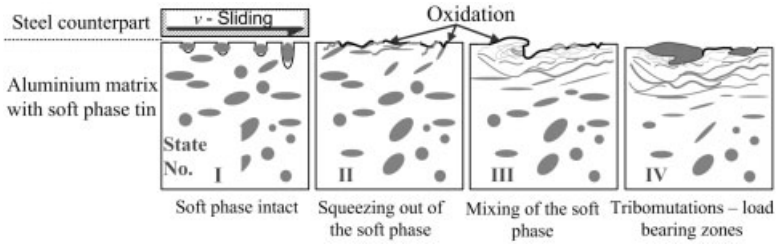


Figure 7: DE-Model, different states in AlSn20Cu [5, 7].

5 Conclusion and Outlook

The employed test method is capable of visualizing the differences of the tribological behavior of the materials. Systems composed of pure aluminium are able to withstand high loads under optimal conditions. They do, however, also show a tendency for spontaneous failure. The addition of a soft phase makes the system more failure tolerant, but significantly reduces the mechanical stability of the component. In the case of AlSn40, mixing processes do not occur anymore and the wear is high. The response is similar to the Sn-based Babbitt metal. The stability of AlSn20Cu is higher and after the consumption of the soft phase, the mixed zones are able to fulfill the load-bearing function. The authors described this behavior in a tribological functional model. Individual states were modeled on a micromechanical level. This model serves as the basis for a direct optimization of sliding materials. Our model can be expanded to include the effects of layer forming additives. In this context is should be emphasized that to this date almost no investigations concerning layer-forming effects of non-iron systems have been conducted. Unlike previously published methods, the presented methodology is suitable for such investigations, as it takes the load-bearing capacity into consideration.

Acknowledgements
The authors would like to thank the Christian Doppler Research Association for the financial support. We are also grateful to Miba Bearing Group for the declassification of the results.

6 References

[1] Grün, F. ; Gódor, I. ; Eichlseder, W., ÖTG Sym. **2007**, p. 93–103

[2] Gódor, I. ; Leitner, H., Abschlussbericht AMB01B22, AMB, **2001**

[3] Löhr, R. ; Eifler, D. ; Macherauch, E., Trib.+Schmierung. **1985**, 32, 278–285.

[4] Grün, F. ; Gódor, I. ; Gärtner, W. ; Eichlseder, W., Nordtrib **2008**, in submission

[5] Grün, F. ; Gódor, I. ; Eichlseder, W., Trib.+ Schmierung. **2007**, 54, 26–30.

[6] Grün, F. ; Gódor, I. ; Eichlseder, W., Tribotest **2008**, in print

[7] Grün, F. ; Gódor, I. ; Eichlseder, W. ; Gärtner, W., IJTC2007-44150

[8] Grün, F., Ph.D. Thesis, University of Leoben, **2007**

Friction and Wear Behavior of the Magnesium Alloy AZ91D under Lubricated Sliding Conditions

Canguang Chen, Hartmut Bosse, Ludger Deters
Otto von Guericke University Magdeburg, Germany

Abstract

The automotive industry has been increasingly utilizing magnesium alloys because of their high strength to weight ratio. Their inferior wear and corrosion properties are the chief constraints on further applications of magnesium alloys. This study investigates the friction and wear behavior of the magnesium alloy AZ91D sliding against the normalized steel 16MnCr5 under lubricated conditions with an Optimol SRV test system. Hydrocarbon-based fluids such as mineral oil or polyalphaolefin exhibited better tribological characteristics than polar base fluids such as esters and polyalkylene glycol. Conventional AW/EP additives displayed different antiwear effects in a magnesium-steel pair than expected. A scanning electron microscope (SEM) and an energy dispersive X-ray spectroscopy (EDS) were used to analyze the worn surfaces.

1 Introduction

With similar mechanical properties, magnesium is roughly one third lighter than aluminum and is characterized by excellent castability, processability and recyclability. Given the automotive industry's great demand for lightweight materials, it has again been increasingly utilizing magnesium as a structural material in recent years [1, 2]. The basic disadvantages of technically utilizing magnesium alloys are their inferior creep resistance, poor corrosion behavior and inferior wear resistance. The mechanical and corrosive properties of magnesium alloys have already been studied in depth [3–6]. The tribological properties of coated and uncoated magnesium samples in non-lubricated tribocontacts were set forth in [7–10].

To date, there have been few publications on the friction and wear behavior of lubricated magnesium contact pairs. Huang et al. [11, 12] determined that borate additives improve the antiwear effect of mineral oil, the borate additive with chlorine being more effective than that with sulfur or nitrogen. These authors are of the opinion that the reasons are to be found in the formation of magnesium chlorides on the magnesium surface. Nitrogenous additives also positively affected the wear behavior of the magnesium alloy AZ91D [13, 14]. The number of NH_2 groups and the length of the CH_2 chains played a crucial role in the nitrogenous additives. The reaction products on the tribologically stressed surfaces were assumed to be H_2NCH_2COOMg, $MgNH(CH_2)_2NH_2$ and friction polymers.

To reduce tool wear and prevent arcing and dusting, industry employs coolants and cutting fluids for the machining of magnesium alloys. When water immiscible cooling lubricants were applied, a mineral oil-based cutting oil proved very expedient [15]. Water-miscible cooling lubricants for the machining of magnesium alloys typically consist of water, mineral oil/ester oil,

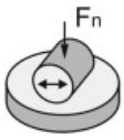
emulsifiers and other additives. Fatty alcohols and/or ester oils are used as the base fluid when magnesium is machined with lubricant starvation.

This study investigates the friction and wear behavior of the pressure die-cast magnesium alloy AZ91D in contact with a counterbody made of the normalized steel 16MnCr5 under mixed lubrication conditions. The antiwear performance of different base oils and additives as well as manufactured lubricants on steel and magnesium pairs was tested on an oscillating test bench under model conditions. Furthermore, a scanning electron microscope (REM) and energy dispersive X-ray spectroscopy (EDS) analyzed the surfaces of selected test pieces after they had been tribologically stressed.

2 Experimental Procedure

2.1 Test Pair and Conditions

The model tests with oscillating motion were performed on an Optimol SRV test system. Figure 1 presents the test pair selected and the test conditions applied. Each individual test was repeated at least twice.



Cylinder
- Diameter: 11 mm
- Length: 15 mm

Disc
- Diameter: 24 mm
- Thickness: 7 mm

Load: 300 N
Stroke: 1 mm
Frequency: 50 Hz
Temperature: 110 °C
Test time: 30 min
Sliding distance: 180 m

Figure 1: Test pair and conditions

2.2 Test Materials

The cylinders for the tests were made of the normalized steel 16MnCr5 (Martens hardness: approx. 2170 N/mm^2) and the discs of the magnesium alloy AZ91D (Martens hardness: approx. 610 N/mm^2). Table 1 specifies the chemical composition of the two test materials.

Table 1: Chemical composition of the test materials 16MnCr5 and AZ91D (in percent by weight)

	Si	Mn	Cr	C	Fe	Al	Zn	Mg
16MnCr5	< 0.4	1.1–1.3	0.8–1.1	0.14–0.19	Balance			
AZ91D	< 0.1	0.1			< 0.005	8.3–9.7	0.35–1.0	Balance

2.3 Test Lubricants

Altogether five different base oils (mineral oil, polyalphaolefin, monoester, polyol ester and polyglycol) were used. Their physical properties are specified in Table 2. At the selected test temperature of 110 °C, the kinematic viscosities of all five base oils are approximately equal.

Thus, any influence of oil viscosity on the friction and wear behavior of the test pairs can be ruled out.

In order to ascertain the different additives' effects on the friction and wear behavior of the steel-magnesium pairs, six additives were admixed to the mineral oil and all the thusly additized fluids were tested under the same test conditions (see Figure 1). Table 3 specifies the chemical composition and dosage of the individual additives admixed to the mineral oil.

In addition, three manufactured lubricants were tested, i.e. an engine oil SAE 5W30 (unconventional base stock + ZnDTP additive package), an automatic transmission fluid ATF (mineral oil + S/P additive package) and a hydraulic oil HEES (polyol ester + S/P additive package).

Table 2: Physical properties of the base oils

	Density [g/cm^3]	Kinematic Viscosity at 40 °C [mm^2/s]	Kinematic Viscosity at 100 °C [mm^2/s]	Viscosity Index	Pour Point [°C]
Mineral oil (MO)	0.87	32.0	5.4	97	-15
Polyalphaolefin (PAO)	0.83	31.0	5.9	135	-68
Monoester	0.86	24.8	5.4	157	-33
Polyol ester	0.94	20.0	4.4	140	-51
Polyglycol	1.05	21.0	5.3	169	-30

Table 3: Chemical composition and dosage of the additives (in percent by weight)

	S	P	Zn	Ca	B	dosage
Antioxidant (AO)						0.5
Corrosion inhibitor (CI)	36.1					0.3
Zinc dialkyldithiophosphate (ZnDTP)	10.5	4.7	4.5			1.0
Sulfur/phosphorus (S/P)	33.4	0.5				3.5
Detergent (DG)	1.8			10.3		3.0
Borate additive package (Borate)	10.8	0.5	0.3	0.4	2.4	8.5

2.4 Test Evaluation

The friction coefficient was continuously measured and evaluated during the SRV tests. The wear coefficient (wear volume / (normal force x sliding distance)) was applied as the wear index. REM images and EDS analyses were drawn on to establish the appearance and chemical composition of the magnesium surfaces.

3 Results and Discussion

3.1 Influence of Base Oils on Friction and Wear

Figure 2 plots the friction coefficients over the sliding distances and the wear coefficients from the tests of different base oils. Tests of polyol ester and polyglycol were broken off after a sliding

distance of approximately 105 m or a runtime of approximately 17 minutes because of high friction (friction coefficient > 0.4). The base oils clearly exert a significant influence on the friction and wear behavior of the steel-magnesium pairs. Wear principally occurred on the softer magnesium discs. The nonpolar hydrocarbon-based oils MO and PAO exhibited better friction and wear behavior than the polar base oils monoester, polyol ester and polyglycol, i.e. the base oil's polarity negatively influenced the friction and wear behavior of the lubricated steel-magnesium pairs. The polar groups (COOR and OH) of the base oils ester and polyglycol presumably react with the magnesium. This produces intense tribochemical wear. For the most part, the high friction is attributable to the high wear on the disc. A trough forms on the disc, which induces high friction at the reversal points.

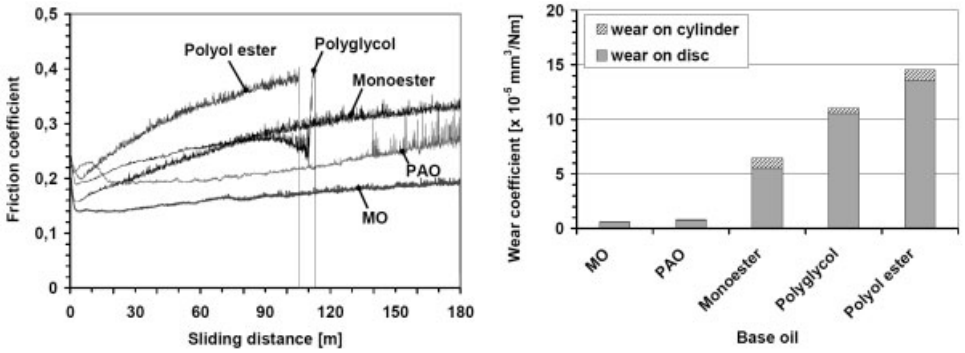


Figure 2: Friction and wear coefficients from SRV tests of different base oils

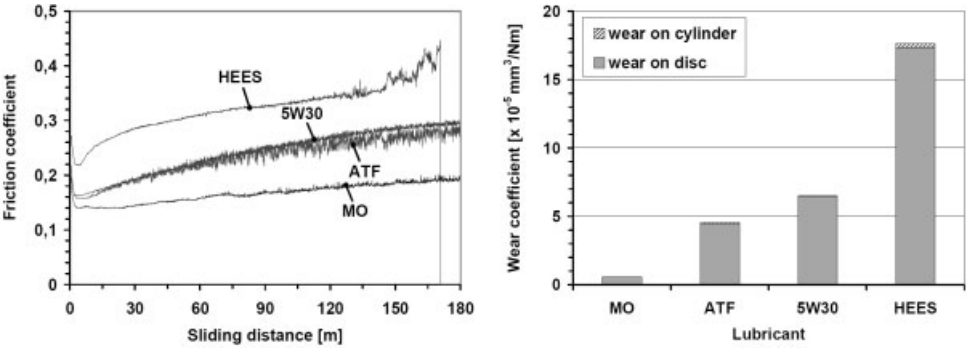


Figure 3: Friction and wear coefficients from SRV tests of different manufactured lubricants

The tested manufactured lubricants 5W30, ATF and HEES also exhibited poorer antifriction and antiwear performance than the pure mineral oil (Figure 3). The ester-based hydraulic oil HEES proved to be particularly unsuitable. This corroborates the base oil's great influence. The ATF's (mineral oil + S/P additive package) poorer tribological behavior than mineral oil indicates the S/P additive acts adversely. This is examined in more detail below.

3.2 Influence of Additives on Friction and Wear

Since the mineral oil exhibits good tribological behavior, it was used to test the effectiveness of different additives as base stock. The admixture of the borate additive package and the admixture of the antioxidant improved the mineral oil's tribological performance in the lubricated steel-magnesium pairs (Figure 4). Conversely, the admixture of the detergent, corrosion inhibitor, ZnDTP and S/P additive to the mineral oil degraded the base oil's friction and wear behavior, the additivation of S/P to the mineral oil producing the highest friction and wear values. The reasons for this can be identified with the aid of REM images and EDX analyses.

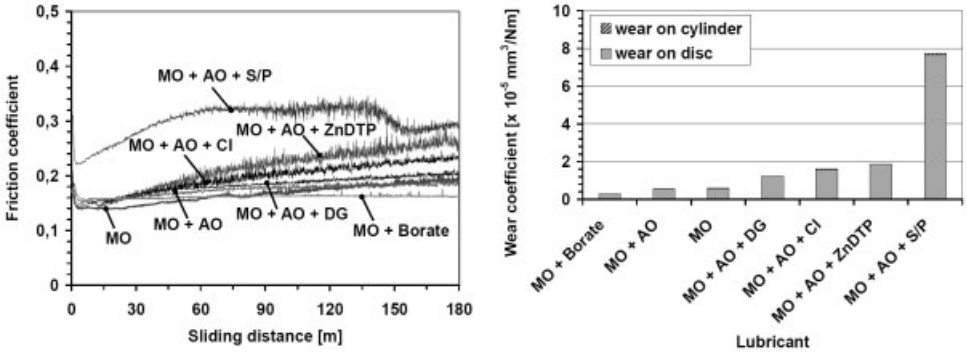


Figure 4: Friction and wear coefficients from SRV tests of different additized mineral oils

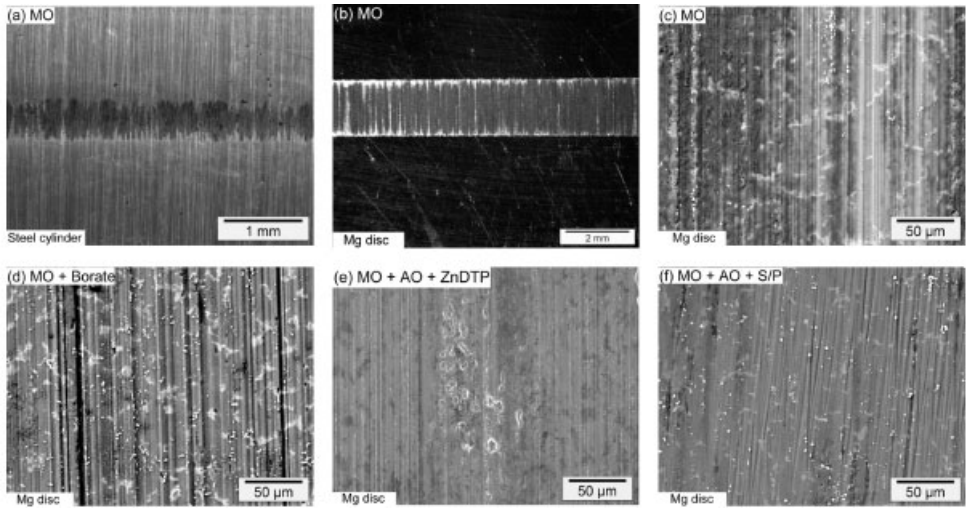


Figure 5: LM and REM images of test bodies after testing different lubricants

Figure 5a and Figure 5b show the cylinder and disc surfaces respectively after the test with pure mineral oil. EDX analyses verified that magnesium was transferred from the magnesium disc to the steel cylinder in all the tests. Use of the pure (Figure 5c) or borate-additized mineral oil (Figure 5d) scored the magnesium surface. This may well have been produced by the abrasive activity of wear particles. By comparison, the magnesium surfaces are noticeably smoother when the ZnDTP (Figure 5e) or S/P additized mineral oil (Figure 5f) is used.

The elemental compositions in the tribologically stressed region of the magnesium disc are compiled in Table 4. The high oxygen content in all four samples indicates an oxide layer on the magnesium surface. The additive elements S, Zn and B detected on the magnesium surface suggest that presumably an antiwear tribofilm developed on the magnesium surface when the borate additive package was used, which prevented direct metal-to-metal contact. The ZnDTP or S/P additive also reacted with the magnesium (the elements S and Zn being detectable on the magnesium surface), yet caused strong tribochemical wear.

Table 4: Elemental compositions in the tribologically stressed region of the magnesium disc after the tests with different additized mineral oils (EDS analyses with an accelerating potential of 5 kV, in atom percent)

	Mg	Al	C	O	S	Zn	B
MO	36.8	4.0	27.4	31.7			
MO + Borate	59.2	6.1	17.0	11.0	3.3	0.4	3.0
MO + AO + ZnDTP	52.0	4.9	19.8	19.8	2.1	1.4	
MO + AO + S/P	46.6	4.1	20.1	22.6	6.6		

4 Conclusion

The tribological tests yielded the following findings:

- The hydrocarbon-based base fluids mineral oil and PAO exhibited noticeably better friction and wear behavior in steel-magnesium pairs than the polar base fluids monoester, polyol ester and polyglycol. The base oil's polarity negatively influenced friction and wear behavior.
- The manufactured lubricants 5W30, ATF and HEES likewise exhibited poorer tribological properties than the pure mineral oil in steel-magnesium pairs.
- The conventional antiwear additives, i.e. ZnDTP and S/P, degraded the mineral oil's good tribological properties in steel-magnesium pairs. These additives caused strong tribochemical wear in a steel-magnesium pair.
- The admixture of a borate additive package increased the mineral oil's antiwear effect. In this case, a tribofilm protected the magnesium surface against wear even though the surface had been scored.

5 References

[1] C. Blawert, N. Hort, K.U. Kainer, Trans. Indian Inst. Met. 2004, Vol.57, No. 4, 397–408

[2] C. Kammer, Magnesium Taschenbuch, Aluminium-Verlag, Germany 2001, Chapter 1

[3] F. Renner, T. Troßmann, M. Gugau, FVA-Forschungsheft Nr. 676, 2001

[4] M. Gugau, C. Berger, J. Senf, FVV-Forschungsheft R 513, 2001

[5] J. Senf, Dissertation, Darmstadt, 2000

[6] J. Göllner, Abschlussbericht, AiF-Vorhaben Nr. 11582, 2000

[7] P.J. Blau, M. Walukas, Tribology International 2000, 33, 573–579

[8] H. Chen, A.T. Alpas, Wear 2000, 246, 106–116

[9] R. Galun, U. Kutschera, A. Weisheit, B.L. Mordike, Metall, 1999, Nr. 12, 672–675

[10] W. Huang, B. Hou, Y. Pang, Z. Zhou, Wear 2006, 260, 1173–1178

[11] W. Huang, Y. Fu, J. Wang, Z. Li, M. Liu, Tribology International 2005, 38, 775–780

[12] W. Huang, B. Hou, Z. Zheng, K. Xu, Y. Liang, Lubrication science 2006, 18, 77–86

[13] W. Huang, B. Hou, M. Liu, M. Liu, Z. Li, Tribology letters 2005, Vol. 18, 445–451

[14] W. Huang, C. Du, Z. Li, M. Liu, W. Liu, Wear 2006, 260, 140–148

[15] D. Hörner, Tribologie + Schmierungstechnik, 53. Jahrgang, 3/2006, 36–42

Tribological Properties of Laser Interference Induced Microstructural Architectures in Metallic Systems

C. Gachot, P. Leibenguth and F. Mücklich
Saarland University, 66123 Saarbrücken, Department of Materials Science and Engineering

1 Introduction

Laser-Interference-Metallurgy is a rather new surface processing technology, allowing a quick as well as direct structuring of geometrically precise periodic and long range ordered microstructures on macroscopic areas. In this technique, a high power nanosecond laser pulse is split into several coherent sub beams which interfere on the surface of the sample. This technique facilitates various metallurgical processes such as melting, recrystallization, recovery and the formation of intermetallic phases for example on the lateral scale of the microstructure but also topography effects in metals, ceramics or polymers. [1] With regard to topography effects, laser surface texturing is for many years an established method to reduce stiction in magnetic storage devices or to enhance the tribological properties by the production of micro dimples serving as lubricant reservoirs. [2, 3]

In this research work, we will focus on the microstructural tailoring of metallic thin films i.e. Au thin films and TiAl multilayer systems. The idea is to create lateral periodic grain size and intermetallic phase composites consisting of hard and soft regions and therefore providing an improved wear resistance. Many classical wear theories only emphasize the importance of hardness as the main factor influencing wear resistance. According to Archard´s equation, the volume loss per sliding distance is linearly proportional to the applied normal load F_N and reciprocal to hardness H. [4, 5] Recent studies revealed the relevance of the ratio of hardness to Young´s modulus (H/E), called the elastic strain to failure. Therefore, thin films being composed of hard nanocrystalline and soft microcrystalline grains or hard intermetallic phases laterally arranged in a ductile matrix could exhibit superior properties. By controlling the size and distribution of the corresponding phases, it could be possible to make a balance between hardness and elastic modulus which is decisive with respect to tribological applications.

2 Experimental Details

2.1 Materials

Two different samples were produced in order to study the effect of tailored microstructures on tribological properties. First, Ti/Au thin films were e-beam evaporated on double-sided polished, (100) - oriented p-type silicon wafers from pellets with a purity of 99.95% in standard equipment (*Balzers, PLS 570*). At a residual base pressure of less than $5 \cdot 10^{-7}$ mbar, the deposition process of both metal types is started and performed subsequently without breaking the vacuum to avoid oxidation effects. The titanium layers have a nominal thickness of 10 nm and serve as an adhesion promoter. The Au top layers have a thickness of 300 nm.

The second set of samples are TiAl multilayer thin films with an individual layer thickness of 17 nm for Ti and 5 nm for Al to achieve a certain stoichiometry of the intermetallic phases by the laser treatment. The total thickness of the TiAl multilayers is 300 nm. Here, a magnetron sputter facility (*von Ardenne, PPS – A200*) was used to deposit the multilayers at a sputter power of 100 W and a Argon gas pressure of 10^{-4} mbar on (100) oriented silicon wafers.

2.2 Laser Interference Experiments

A high power pulsed Nd: YAG laser (*Spectra Physics, Quanta Ray PRO 290*) with a fundamental wavelength of 1064 nm, a frequency of 10 Hz and pulse duration of 10 ns was employed for the laser interference experiments. Dependent on the particular pattern, the primary laser beam was split into two sub beams to interfere with each other on the sample surface resulting in a line-like interference pattern. The intensity of each individual beam can be controlled by using suitable beam splitters. The laser energy density was determined to be 476 mJ/cm^{-2} for Ti/Au as well as the TiAl layers. Due to the absorption characteristics of Au and Ti, the fourth harmonic of the Nd: YAG laser at 266 nm was selected. Moreover, because of the high reflectivity of Al, the final layer of the TiAl multilayer systems was chosen to be Ti. Details of the experimental setup have already been published elsewhere. [1]

Due to the ambient conditions of the laser-interference experiments, the lack of a native oxide layer in the case of gold is advantageous. Currently, a more flexible environmental chamber is build up to allow the laser interference experiments being conducted in vacuum or protective gases.

2.3 Sample Characterization

All samples were imaged with a high resolution scanning electron microscope equipped with a field emission gun (*FEI, Strata DB 235*) at 5 kV acceleration voltage. An Electron Backscatter Diffraction system with a TSL OIM analysis unit for micro-textural studies is integrated in the abovementioned FEI dual beam workstation. The Kikuchi patterns are generated at an acceleration voltage of 20 kV, and are recorded by means of a DigiView camera system, facilitating a maximum recording speed in the range of 0.05 s/pattern. [6] The analysis of the wear tracks is conducted by a white light interferometer (*Zygo, New View 200*).

For the evaluation of the mechanical and tribological properties a Tribo Indenter Nanomechanical Testing System (*Hysitron Inc.*) and a Nanotribometer (*CSM Instruments*) were used to perform the tests. The selected peak loads in indentation experiments were around 50 μN in the order to limit the indentation depth up to 10% of the total film thickness. Additional details about the nanoindentation experiments can be found in [7]. Regarding tribological tests, a normal load of 1 mN was applied to the samples. As a counter body, we have used polished Al_2O_3 balls with a diameter of 1.5 mm. The linear sliding velocity was 1 mm/s. All the experiments were performed at room temperature with a relative humidity of 30 % controlled by a dew point ruler. The amplitude in the linear mode was set to be 400 μm.

3 Results and Discussion

Figure 1 shows three different types of periodic patterns fabricated on 300 nm thick Au thin films. The line-like interference pattern in Figure 1 (a) results from two interfering sub beams. Hereby, different morphological regions can be identified. At first, elongated and needle shaped grains are visible in the so called laser intensity maximum positions. The formation of the large grains at the interference maxima positions with such a preferred growth direction is based on the local melting and posterior re-solidification of the film following the temperature gradient perpendicular to the interference fringes. This phenomenon is known as Super Lateral Growth (SLG). [8] This SLG-regime was identified to take place in a very narrow processing window, in which the films show a nearly complete melting. Within the SLG-regime large-grained polycrystalline microstructures with grain sizes many times larger than the film thickness can be achieved. The transformation scenario associated with this regime was modeled by Im and co-workers. [9] Above a given laser intensity, laterally growing grains appear originating from the non molten areas (interference minima) and propagating to the nearly completely molten regions (interference maxima). In Figure 1 (a) a centre-line at the interference maxima is observed, which results from the growth of the grains from both sides following the temperature gradient.

Cross-like pattern geometry can be obtained by a 90° sample rotation and a subsequent laser irradiation. The Au layers are molten twice at the intersection between the interference lines, and thus a different grain-morphology can be created. These grains are thus larger and are oriented following the temperature gradient of the second pulse.

Three interfering beams lead to a dot-like interference pattern. In this case, the grains are radially distributed also following the thermal gradient [6].

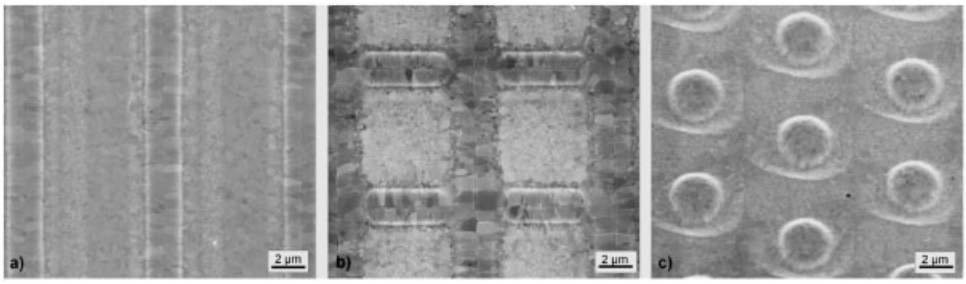


Figure 1: Laser induced crystallization of 300 nm thick Au layers. In (a) a line – like interference pattern resulting from the interference of two sub beams is visible. The needle shaped elongated grains correspond to the intensity maximum. The surrounding is the laser intensity minimum (pristine microstructure). (b) Cross – pattern after 90° sample rotation and subsequent laser irradiation. (c) Dot – like pattern geometry after interference of three individual laser beams.

The average length of the lateral grains is up to 1.5 µm and the width has a maximum value of approximately 0.4 µm. By a variation of the energy density, it is possible to adjust the extent of the recrystallized area and therefore to tailor the microstructure. Other factors, which strongly influence the width of the recrystallized area, are the periodicity, the laser pulse duration and the substrate temperature. Cross-sections of the patterned Au-films conducted by a focused ion beam (FIB) milling technique revealed that the laser induced recrystallization is not only located at the surface. Instead, the film was recrystallized throughout its entire thickness. [7]

In order to study the effect of film thickness and energy density on the microstructure, Au films with two different thicknesses were deposited on Si-wafers by e-beam evaporation. [8] Figure 2 displays a series of scanning electron micrographs for 300 and 690 nm thick Au films with increasing laser fluence. The center positions in each micrograph represent the laser intensity maximum and the adjacent areas the laser minima. For moderate laser fluences (476 mJ/cm^2) both films show a laser induced recrystallization area at the maxima positions with very different morphologies 2 (a) and 2(d). The 300 nm sample demonstrates the abovementioned SLG-regime (see fig. 2 (a)). The thickness dependent grain morphology and especially the grain orientation in the Au films were determined by electron backscatter diffraction. Figures 2 (c) and 2 (f) highlight the recorded inverse pole figure maps with the orientation triangle and the corresponding pole figures for the [001], [110] and [111] directions for both films. The microstructural morphology as well as the microtexture reveals the strong influence of film thickness. In the case of the 690 nm Au film, there is an increased pole density at $\psi = 0°$ which refers to a (111) - fiber texture. By decreasing the film thickness, the texture undergoes a change from the observed (111) - fiber texture to a distinct (001) - cube texture (see fig.2(c)).

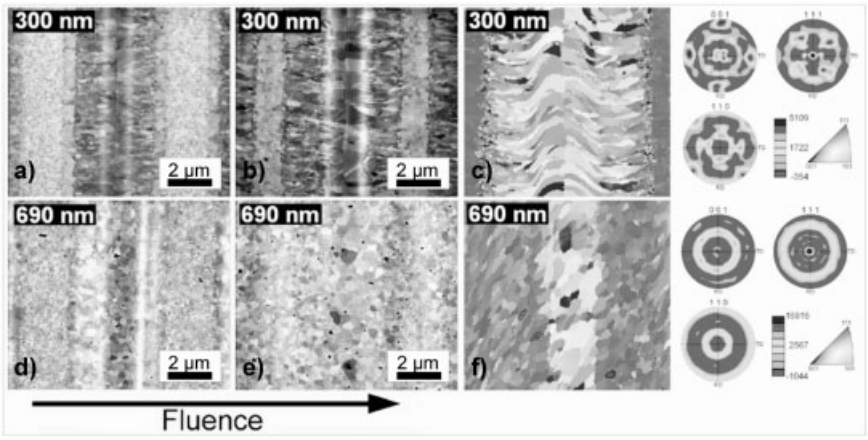


Figure 2: Thin film morphology dependent on laser fluence for a 300 (a-c) and 690 nm (d-f) thick gold films. Only one laser intensity maximum with the neighboring minima positions is depicted. (a, b, c, d) SEM images with corresponding (c, f) inverse pole figure maps and pole figures. The laser fluence was varied between 476 and 636 mJ/cm^2.

Besides the microstructure and the grain orientation, the mechanical properties for the as deposited Au and TiAl films were evaluated by nanoindentation.

For the Au-samples, a decrease in the hardness of the laser treated parts due to recrystallization and grain growth in the irradiated area could be observed. The average grain size in the nanocrystalline area is approximately 70 nm and in the irradiated region around 300 nm. Due to the Hall-Petch relationship, the hardness in the recrystallized area is reduced from 2.2 to 1.4 GPa for an indentation depth of 20 nm which is equal to a decrease of approximately 36 % in hardness.

For the TiAl multilayer samples, the change in hardness and Youngs modulus is even more pronounced due to the formation of the intermetallic phase $TiAl_2$. Figure 3 shows a SEM mi-

crograph of the laser irradiated TiAl thin film. The periodicity is around 4 µm. The left diagram represents the reduced Young´s modulus as a function of the lateral position. On the right side, the hardness depending on the lateral position is displayed. Evidently, the increase in hardness in the intensity maxima positions is up to 47 % compared to the neighbored minima positions. According to the effective heat of formation model by Pretorius et al., the $TiAl_3$ is the first intermetallic phase to nucleate at the aforementioned stoichiometry. The effective heat of formation model describes moreover the phase formation sequence in which an effective concentration moves in the direction of the remaining element and the next phase to form at the growth interface is the next phase richer in the unreacted element in that case the observed phase $TiAl_2$. [10]

The (H/E) ratio for the gold films varies between 0.02 and 0.03 which is in the same magnitude as the (H/E) ratio of hardened high speed steel. In case of TiAl, this ratio is even higher, reaching the typical values of some well known wear resistant materials such as TiN and Al_2O_3 with a (H/E) ratio of around 0.05. [11]

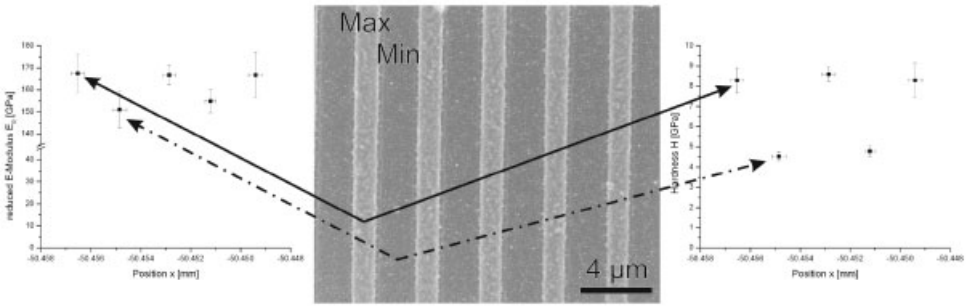


Figure 3: Laser irradiated TiAl sample with a fixed periodicity of 4 µm. Diagram on the left side shows the reduced elastic modulus for the maxima and the minima positions respectively and the right diagram the measured hardness in GPa.

In order to study the influence of the as tailored microstructures in Au and TiAl films, sliding tests with a nanotribometer at a normal load of 1 mN were performed. As a counterbody Al_2O_3 balls with a diameter of 1.5 mm were used. Before the sliding tests, the ball surface was imaged by a white light interferometer to measure the roughness of the ball and to compare the surface of the ball before and after the tribometer test. After every test, the ball was cleaned with ethanol. The sliding time for the Au films was limited to 250 s because at longer sliding times the wear scar depth was already larger than the film thickness of 300 nm. Figure 4 reveals the evolution of the wear scars dependent on the number of cycles.

The difference in the tribological behavior of the sliding motion parallel and perpendicular was however negligible. Therefore, we only focus on the results gained during the perpendicular motion of the cantilever. In consequence of a strong temperature and an associated surface tension gradient during the local laser heating of the films, there are Marangoni forces acting on the film surface moving material from the minima to the maxima regions in this case. [7] As a result, there is a slight topography with an average height of 100 nm related to a structure periodicity ranging from 2 to 12 µm for the Au layers. Concerning TiAl, the topography is less than 20 nm for a fixed periodicity of 4 µm. It is visible in figure 4 (b) that first the elevated maxima positions in the patterned Au films are worn which are softer than the nanocrystalline minima

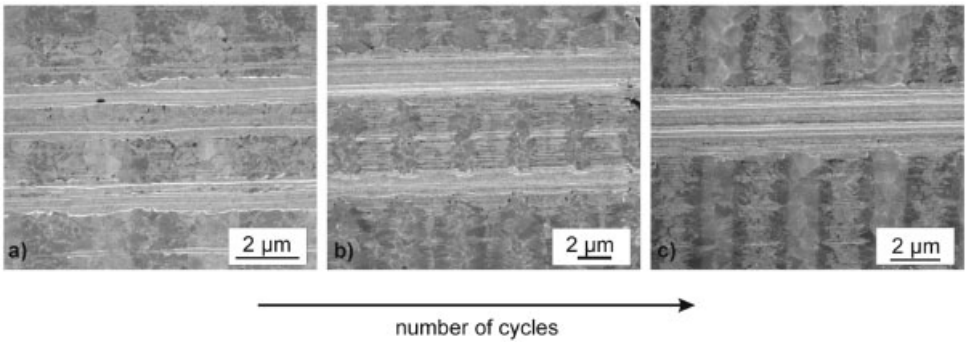


Figure 4: Evolution of wear scar in 300 nm thick Au layers as dependent on the number of cycles. (a) 1 cycle, (b) 5 cycles and (c) 10 cycles.

regions. After 10 cycles, a continuous wear track appears indicating a rapidly degrading surface by plastic deformation. Similar results were obtained for the TiAl multilayers. EDX analysis of the ball surface after the experiment showed no Au signal. Furthermore, no flattening of the ball could be detected.

With regard to a quantitative analysis of the worn volume, a representative set of wear tracks were studied by white light interferometry. The worn volume was determined by the measurement of the total length, the width and depth of the corresponding wear scars. In some cases, the use of the usual geometric formulae led to large error bars which can be attributed to the very irregular and asymmetric shape of the wear tracks. The results are plotted as a function of the structural periodicity. Due to the experimental setup and the thermal diffusivity of metallic samples, the periodicity is restricted to a minimum of 2 µm and a maximum of nearly 12 µm in our laser facility.

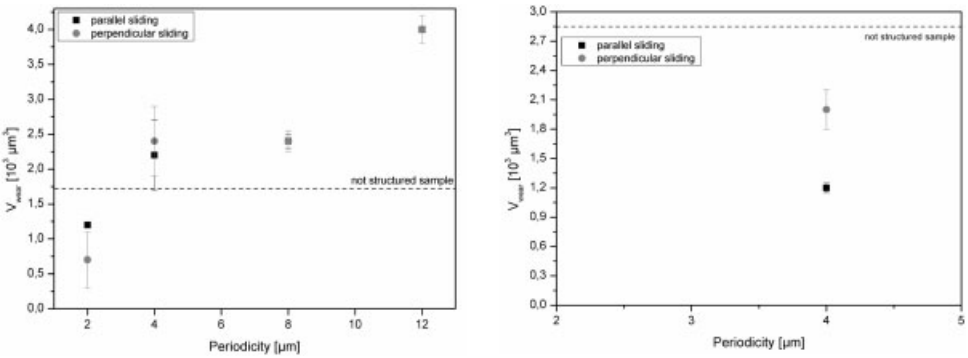


Figure 5: Wear volume determined by white light interferometry for Au films depending on the periodicity and sliding direction on the left side and for TiAl multilayer for a fixed periodicity at 4 µm.

Obviously, there is a dependence of the wear volume on the structural periodicity. For the 2 µm periodicity, the decrease in wear volume is approximately 31 % compared to the not structured

sample. TiAl multilayers also show for a constant periodicity of 4 µm a decrease in wear volume ranging from 31 % up to 58 %. A detailed investigation of the relationship between periodicity and worn volume for the TiAl samples is still in progress. Nevertheless, more sample sets are necessary to finally verify this scaling dependency.

In conclusion, the friction coefficient µ versus the sliding time was recorded for both samples. As can be seen in figure 6 (a), the friction coefficient µ exhibits strong fluctuations presumably arising from the sample topography or the fast degrading surface (see fig. 4).

There are no significant differences between the forward and backward motion for both sample types.

Considering figure 6 (b), it is evident that the friction coefficient is less fluctuating over sliding time, because the topography is only slightly pronounced (< 20 nm). However, it can be stated out that µ is generally less for the structured samples in comparison to the not structured film surfaces.

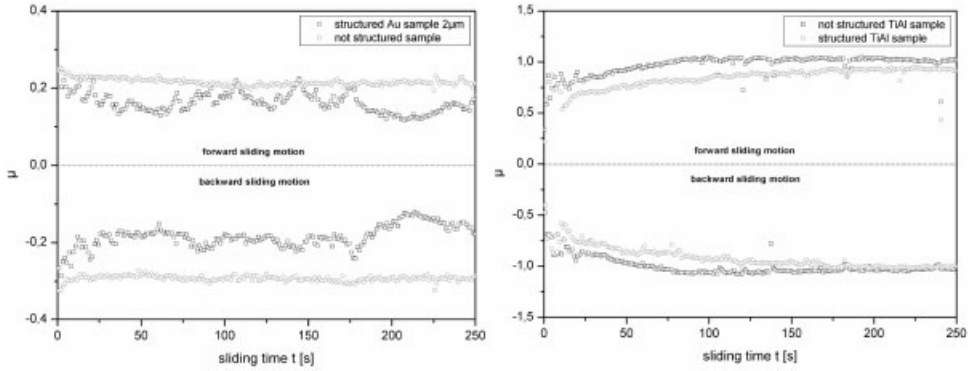


Figure 6: Friction coefficient as a function of sliding time in s for a structured Au sample with a periodicity of 2 µm recorded in forward and backward motion (left graph) and for TiAl with a periodicity of 4 µm compared to the not patterned sample.

4 Conclusions

It has been shown that Laser-Interference-Metallurgy is a powerful tool for the microstructural design of thin metallic films. Due to the precisely determined laser intensity distribution the microstructure in terms of controlled recrystallization and phase formation can be designed. Thus, texture, residual stresses and also topography may be controlled and various functional properties on macroscopic areas can be tailored in a unique way.

For micromechanical systems under dry friction, this method could be one promising approach to enhance tribological properties.

5 Acknowledgements

The research work is financially supported by the VW-Foundation in the framework of the project "Integration of Laser Interference Metallurgy and Micro Metal Forming to Functionalize Surfaces".

6 References

[1] Mücklich, F., Lasagni, A., Daniel, C., *Int. J. of Mat. Res.,* **2006**, 97, p. 1337.

[2] Tas, N., Sonnenberg, T., Jansen, H., Legtenberg, R., Elwenspoek, M., *J. Micromech. Microeng.*, **1996**, p. 385-397.

[3] Etsion, I., *Tribology Letters*, **2004**, 17, p. 733-737.

[4] Leyland, A., Matthews, A., *Wear*, **2000**, 246, p. 1-11.

[5] Dao, M., Lu, L., Asaro, R.J., De Hosson, J.T.M., Ma, E., *Acta Materialia*, **2007**, 55, p. 4041-4065.

[6] Catrin, R., Lasagni, A., Gachot, C., Schmid, U., Mücklich,, F., *Mat. Sci. & Eng. A* (accepted **2008**).

[7] Gachot, C., Lasagni, A., Leibenguth, P., Schmid, U., Barnoush, A., Mücklich, F., *Acta Materialia* (submitted **2007**).

[8] Bergmann, R.B., Köhler, J., Dassow, R., Zaczek, C., Werner, J.H., *Phys. Stat. Sol. (a),* **1998**, 166, p. 587-602.

[9] Im, J.S., Crowder, A., Sposili, R.S., Leonard, J.P., Kim, H.J., Yoon, J.H., Gupta, V.V., Jin Song, H., Cho, H.S., *Phys. Stat. Sol. (a),* **1998**, 166, p. 603-617.

[10] Pretorius, R., Vredenberg, A.M., Saris, F.W., De Reuss, R., J. Appl. Phys., 1991, 70, p. 3336-3346.

[11] Ni, W., Cheng, Y.T., Lukitsch, M.J., Weiner, A.M., Lev, L.C., Grummon, D.S., *Appl. Phys. Lett*., **2004**, 85, p. 4028-4030

Cu-graphite Composites: Composition Dependence of Friction Coefficient

J. Kováčik[+], J. Bielek, Š. Emmer
[+]Slovak Academy of Sciences, Bratislava, Slovak Republic
Slovak University of Technology, Bratislava, Slovak Republic

1 Introduction

Tin or lead copper matrix alloys or Cu-alloy/graphite composites are widely used in sliding bearings and brushes applications [1–2]. In the case of low voltage and high current densities, typically for sliding parts of welding machines, it is required to employ materials with a very high electrical conductivity, good thermal conductivity and low friction coefficient. Such conditions are well fulfilled by copper-graphite (Cu-graphite) composite material [3–6]. Various preparation methods can be used to prepare Cu-graphite systems [3, 7–9]. However, the proper preparation method is usually selected according to the required composition, manufacturing cost and desired industrial application.

Recently Moustafa et al. [10] and authors [11] studied the wear and coefficient of friction of Cu–graphite composites made by powder metallurgy from Cu-coated graphite particles or mixtures of copper and graphite powders in the composition range of 0–50 vol. % of graphite. Moustafa et al. [10] explained very precisely the wear mechanism in the investigated composites from the point of view of applied load. It was found that both coated and uncoated Cu-graphite composites exhibited the same wear mechanisms, namely, oxidation induced delamination, high strained delamination, and sub-surface delamination. Concerning composition dependence of sliding properties it was found that with increasing concentration of graphite the coefficient of friction and wear rate of coated and uncoated composites at first decreases. When a critical concentration threshold of graphite is reached, the coefficient of friction becomes independent on the composition while the wear rate decreases further. This threshold is not simply 20 vol. % of graphite as stated Rohatgi et al. [2] for metal matrix composites, but it significantly depends on the composite structure: For uncoated composites, it is 12 vol. % of graphite for fine graphite powder (16 μm), while for coarse powder (25–40μm, [10]) it is 23 vol. % of graphite. For coated composites the concentration threshold was found above 25 vol. % of graphite. The reason is that the increased number of fine copper debris within graphite rich tribolayer occurs homogeneously also at high graphite composition.

The main aim of this work is to model the observed composition dependence of the friction coefficient of copper-graphite composites at constant load for both uncoated and coated composite systems.

2 Experimental

At the beginning it is necessary to define the used preparation method and measurement conditions of friction tests for a better understanding of the observed results.

2.1 Preparation of Composites

Cu-graphite composites were prepared by HIP-ing using pure copper (particle size < 70 μm, average particle size 22 μm, purity 99.9 %) and graphite (average particle size 16 μm, purity 99.9 %) powders. The copper powder has dendritic shape while graphite powder is of the flake shape. The uncoated powders were used to prepare particulate Cu-graphite composites in the range of 0–50 vol. % of graphite [3, 4]. The same graphite powder was homogeneously copper coated using a conventional electroless coating process ([12] and references therein) at company Platingtech, Austria. The resulting volume fraction after coating is about 50 vol. % of graphite [6]. SEM investigations (see Figs. 1 and 2) of particles showed that the copper coating covers whole surface of each graphite particle and is approximately 2 μm thick. The amount of coated copper corresponds to 50 vol. % of graphite in the final composite. Cu-graphite coated composite with 30 vol. % of graphite was prepared by admixing of copper powder to copper coated graphite powder. The same powder metallurgical approach was used for the preparation: The starting powders were wet mixed (if necessary) and dried afterwards. Then the mixture was cold compacted to a pellet, which was put into a steel tube, evacuated and sealed. The sample was put into hot isostatic pressing equipment and was HIP-ed at 950 °C for 1.5 hour under the pressure of 150 MPa.

2.2 Friction Tests

Coefficient of friction of uncoated composites in the composition range of 0–40 vol. % of graphite was measured using pin-on-ring tribometer SaFM-3 at the Department of Materials and Technology. The samples of $10 \times \times 10 \times 35$ mm were tested. A steel ring (DIN ST 60-2) was used as a counterpart. Sliding was performed under ambient conditions (temperature 21 °C, humidity 60%) in air at a sliding velocity of 0.11 ms^{-1} and nominal load of 100 N for 20 minutes twice for each composition.

Coefficient of friction and wear rate of prepared coated and uncoated composites with 30 and 50 vol. % of graphite were measured using pin-on-disc tribometer at Austrian Research Centre, Seibersdorf, Austria. The sample of various lengths and diameter of 2.4 mm were tested. A steel disk (ASTM A295) of diameter 60 mm was used as a counterpart. Sliding was performed under ambient conditions (temperature 24 °C, humidity 50%) in air at a sliding velocity of 0.5 ms^{-1} and nominal load of 30 N. Track radius was 21 mm and total tested distance was 1200 m. The results of this measurement are further marked as pin-on-disc (30 N).

Measuring conditions from the work of Moustafa et al. [10] are as follows: Coefficient of friction and wear rate of prepared uncoated and coated composites in the composition range of 0–20 vol. % of graphite were measured using pin-on-ring tribometer. The samples with the diameter of 7.9 mm and length of 12 mm were tested. A steel ring (SAE 1045) was used as a counterpart. Sliding was performed in air at a sliding velocity of 0.2 ms^{-1} and nominal load varied between 50 – 500 N. For the data comparison the data at nominal load of 100 N are used. Total tested distance was 2160 m.

3 Model

During sliding of two pieces of material a tribolayer usually denoted as “mechanically mixed layer” (MML) [13] is created. The presence of the MML decreases the direct contact area between

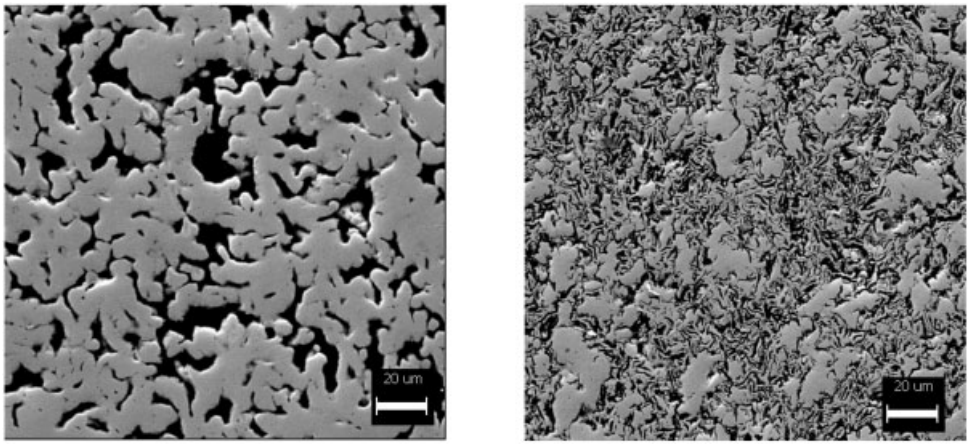


Figure 1: SEM photos of Cu- graphite composite structure at 30 vol. % of graphite prior to sliding: left – uncoated, right – coated graphite [11].

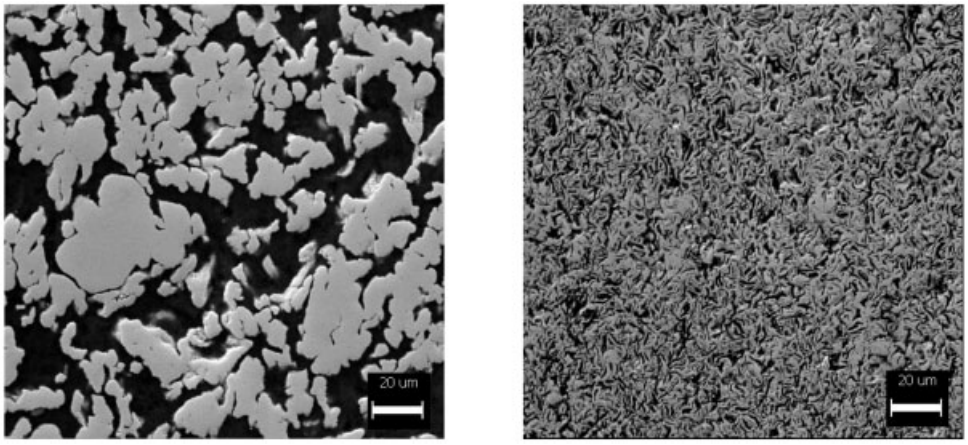


Figure 2: SEM photos of Cu- graphite composite structure at 50 vol. % of graphite prior to sliding: left – uncoated, right – coated graphite [11].

the composite and the counterpart, therefore improving the wear resistance of the composites. As graphite is a good lubricant material, almost small volume fraction of graphite in a copper matrix composite leads to the significant decrease of the coefficient of friction. It is the result of the mechanical properties of graphite and also of only mechanical bonding between copper and graphite (due to the low solubility of carbon in copper - solubility does not exceed 0.02 atom % up to high temperatures [14]).

This mechanical bonding between copper and graphite enables us to model the composition dependence of the friction coefficient in a simple way. Unfortunately, until now, there is no rigorous way how to model composition dependence of the friction coefficient for composites. From

the experimental results [11] it was suggested that composition dependence of the coefficient of friction of Cu-graphite composites is similar to S-shaped curve already used for the prediction of electrical and thermal conductivity, and modulus of elasticity of these composites. S-shaped curve is described in general effective medium theory [15, 16] in a following way

$$f\,\frac{\sigma_{lo}^{1/t}-\sigma_{eff}^{1/t}}{\sigma_{lo}^{1/t}+g\sigma_{eff}^{1/t}} \quad + \quad (1-f)\,\frac{\sigma_{hi}^{1/t}-\sigma_{eff}^{1/t}}{\sigma_{hi}^{1/t}+g\sigma_{eff}1/t} \quad = \quad 0 \tag{1}$$

where t is the characteristic exponent for the effective property – *eff*, f is volume fraction of the phase possessing low coefficient of friction – *lo*, g is a parameter connected to percolation threshold as $f_c = g/(1–g)$ and σ is considered here as coefficient of friction.

Table 1: General effective medium theory fitting results for Cu-graphite composite systems

	g [-]	f_c [vol.%]	t [-]	Coefficient of friction of graphite
Uncoated	0.03011 ± 0.00278	1.5	-8.98204 ± 2.07802	0.13656 ± 0.00779
Uncoated Moustafa et. al.	0.14631 ± 0.00087	12.8	–10.28794 ± 0.47692	0.14858 ± 0.00166
Coated	0.07999 ± 0.01376	7.4	–23.9584 ± 725.77939	0.15373 ± 0.32184
Coated MWCNTS Tu et. al.	0.03996 ± 0.01168	3.8	–23.48862 ± 639.23445	0.08918 ± 0.28576

As can be seen from Figs. 3-6 the model describes well the obtained experimental result. The values of the fitting parameters obtained by nonlinear curve fitting are listed in Table 1. The critical volume fraction of graphite in this case differs from the critical concentration threshold of graphite determined in previous work [11]. The second indicates the amount of graphite at/above which the properties MML are fully dominated by graphite content. On the contrary the first parameter, determined using proposed model, indicates the concentration of graphite at/above which the graphite phase placement within composite starts to influence significantly the properties of MML and also the coefficient of friction of composite. Therefore a significant decrease of the coefficient of friction can be observed in the vicinity of the critical volume fraction of graphite f_c.

Moreover, it is evident that the both parameters depend on the size of used graphite particles significantly. For example Figs. 3 and 4 indicate the critical volume fraction of graphite of 1.5 vol. % of graphite for fine uncoated composites and approximately 12.8 vol. % of graphite for coarse uncoated composites [10]. A small critical concentration of about 3.8 vol. % of multiwalled carbon nanotubes (CNTS) can be found for Cu – CNTS composites investigated by Tu et al. [17] (see Fig. 6). However it can be generally stated that the smaller the size of graphite phase prior preparation method the smaller are both studied parameters for the coefficient of friction – see the results for coated composite.

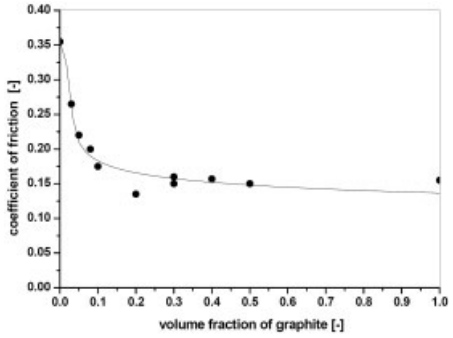


Figure 3: Composition dependence of friction coefficient on graphite phase content for uncoated composite system and GEM fitting function.

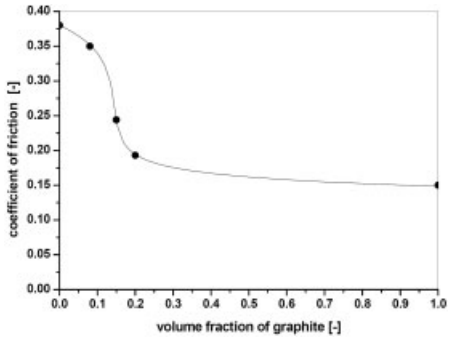


Figure 4: Composition dependence of friction coefficient on graphite phase content for uncoated composite system and GEM fitting function data from Moustafa et. al.[10]

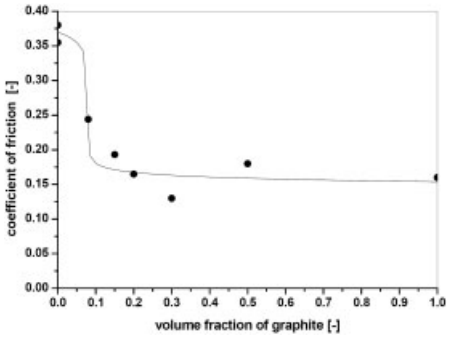


Figure 5: Composition dependence of friction coefficient on graphite phase content for coated composite system and GEM fitting function.

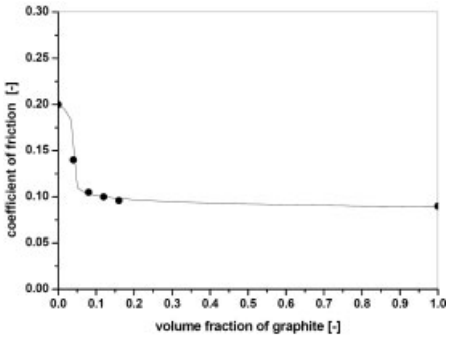


Figure 6: Composition dependence of friction coefficient on graphite phase content for coated composite system with MWCNTS and GEM fitting function – data Tu et. al. [17]

4 Conclusion

It can be concluded that the proposed empirical model seems to describe relatively well the composition dependence of Cu-graphite composite systems. However it must be checked and verified on other metal matrix composite systems to confirm its validity.

Authors would like to express their gratitude to Slovak Government for funding of this work within following projects: APVV-20-057805, VEGA 2/7167/27, VEGA 1/4102/07. One of them, Š. E. thanks to AMTT, Austrian Research Centers, Seibersdorf (LSF contract HPRI-1999-00024) for funding of pin-on-disk wear measurements.

5 References

[1] Feng Y.; Ying, M.; Wang, C. in: P. Ramakrishnan (Ed*.), Proceedings of Advances in composite materials*, ASM International, India Chapter, Bombay, India, **1990**, pp. 631–634,.

[2] Rohatgi, P.K.; Ray, S.; Liu, Y. Tribological properties of metal matrix graphite particle composites, Int. Mater. Rev. 37, **1992**, 129–149.

[3] Š. Emmer, A. Havalda, J. Bielek, Copper-graphite composite-material for application to sliding electrical contacts, J. Phys. IV 3 (1993) 1799

[4] Kováčik, J.; Bielek, J., Electrical conductivity of Cu/graphite composite material as a function of structural characteristics, Scripta Mater. 35,**1996**, 151

[5] Emmer, Š. ; Neubauer, E.; Korb, G. , in *Materials Week*, Munich, **2001**

[6] Kováčik, J.; Emmer, Š.; Bielek. J., Thermal properties of Cu-graphite composites, Kovove Mater. 42, **2004**, 365 - 374

[7] Whitehouse A.F.; Warwick, C.M.; Clyne, T.W., Electrical-resistivity of copper reinforced with short carbon-fibers, J. Mater. Sci. 26, **1991**, 6176

[8] Kúdela, S.; Schweighofer, A.; Kunkela, J., Compos. Manuf. 1,**1992**, 43

[9] Prakasan, K. ; Seshan, S.; Microstructure and properties of squeeze cast Cu-carbon fibre metal matrix composite, J. Mat. Sci. 34, **1999**, 5045

[10] Moustafa, S.F.; El-Badry, S.A.; Sanad, A.M.; Kieback, B., Friction and wear of copper–graphite composites made with Cu-coated and uncoated graphite powders, Wear 253, **2002**, 699 – 710

[11] Kováčik, J.; et al., Effect of composition on friction coefficient of Cu–graphite composites, Wear 265, **2008**, 411 - 416

[12] Shou, Y.Ch. ; Su, J.L., Fabrication of SiCw reinforced copper matrix composite by electroless copper plating, Scripta Mater. 35, **1996**, 225

[13] Zhan, Y.Z.; Zhang, G. ,Friction and wear behavior of copper matrix composites reinforced with SiC and graphite particles, Tribology Lett. 17, **2004**, 91 - 98

[14] Dorfman, S. ; Fuks, D., Diffusivity of carbon in the copper matrix. Influence of alloying, Composites A 27A, **1996**, 697

[15] McLachlan, D.S.; Blaszkiewicz M. ; Newnham, R.E., J. Am. Ceram. Soc. 73, **1990**, 2187

[16] McLachlan D.S. et al., J. Phys. : Condens. Matter 5, **1993**,4829

[17] Tu, J.P. ; Yang, Y.Z.; Wang, L.Y.; Ma, X.C.; Zhang, X.B., Tribological properties of carbon-nanotube-reinforced copper composites, Tribology Letters Vol. 10, **2001**, 4, 225

Laser Nitriding: A Promising Way to Improve the Cavitation Erosion Resistance of Components Made of Titanium Alloys

Jörg Kaspar, Jörg Bretschneider, Steffen Bonß, Bernd Winderlich, Berndt Brenner
Fraunhofer Institut für Werkstoff- und Strahltechnik, Dresden

1 Introduction

Among other techniques, laser nitriding has proven to be a promising way to enhance the poor tribological behavior of titanium alloys [1, 2]. In contrast to conventional gas or plasma nitriding, laser nitriding involves the melting of the metals surface in a nitrogen containing atmosphere. Due to the strong affinity of the molten titanium to nitrogen, nitrogen is very rapidly picked up and distributed within the melt by convection and diffusion, leading to the formation of titanium nitrides during solidification. Deep wear resistant layers of up to 1.5 mm thickness, exhibiting hardness in the range of 500–1500 HV could be achieved by laser nitriding of different titanium alloys [3–6].

In contrast to sliding and abrasive wear protection which requires a high surface hardness, a moderate hardness in the range from 400–800 HV has already shown suitable to improve the cavitation and water droplet erosion resistance of commercial pure (cp) Ti and (α+β)-Ti alloy Ti-6Al-4V [7–10]. To accomplish such moderate hardness, the laser nitriding has to be done under diluted gas atmospheres. However, up to now no systematic information exists about the correlation of processing parameters with microstructure, hardness and erosion behavior.

It is the aim of the present study to show that the cavitation erosion resistance of cp-Ti and Ti-6Al-4V can be significantly enhanced by laser nitriding under strongly diluted nitrogen atmospheres. For this reason the titanium alloys were laser nitrided using a CO_2 laser and mixtures of nitrogen to argon ratio below 1:3. The hardness and the microstructure of the laser nitrided layers were investigated by metallography and scanning electron microscopy (SEM). In addition the cavitation erosion behavior of the samples in deionized water was studied.

2 Experimental

2.1 Specimens and Laser Treatment

For the present work cp-Ti (grade 2) and the (α+β)-Ti alloy Ti-6Al-4V with the following composition: Al = 6.4, V = 4.1, Fe = 0.19, O = 0.156, C = 0.007, N = 0.007, Ti = balance (wt%) were used. Specimens SI60mm by SI40mm or SI110mm by SI40mm, each SI6mm thick, were laser nitrided utilizing a SI6kW cw CO_2 laser. Sets of 45 overlapping tracks were produced using mixtures of nitrogen to argon in the range from 0 : 100 to 25 : 75. To ensure a fine adjustable as well as oxygen free gas atmosphere with defined nitrogen concentrations a bell shaped inert gas device was used, which had been developed in our previous work [5]. The laser nitriding was done using 3.1 kW laser power, SI3.5mm beam spot diameter, 9 mm/s traverse speed, 2.75 mm track overlap and a constant gas flow of 100 l/min.

2.2 Characterization Methods

Metallographic cross sections of the laser nitrided samples were prepared by a sequence of cutting, grinding, polishing and etching and analyzed by optical microscopy. Further information about the structure and the spatial distribution of the phases formed during laser nitriding was obtained by SEM. The hardness of the samples was measured at the cross sections by means of a Vickers microhardness tester using a 100 g load.

An ultrasonic induced cavitation device was used to carry out the cavitation erosion tests in deionised water at 25 °C (ASTM G32-92). The specimens were set opposite to a vibrating tip of Ti-6Al-4V. Cavitation was induced by longitudinal oscillation at 20 kHz at an amplitude of 40 μm and a distance between tip and sample of 0.50 mm. The mass loss was determined at specific intervals during a total testing of 20 h exposure to cavitation with an accuracy of 0.1 mg. All samples to be tested were mechanically ground before the beginning of the test.

3 Results

3.1 Microstructure and Hardness

Laser nitriding of cp-Ti and Ti-6Al-4V under gas atmospheres containing 0–25 % nitrogen led to the formation of macrocrack free layers of about 0.5 mm thickness. Figures 1 and 2 exemplarily demonstrate how the nitrogen concentration of the gas atmosphere influences the structure of the laser nitrided layers. Although general structural features are similar for both laser nitrided cp-Ti and Ti-6Al-4V there are specific differences which result from the unequal chemical composition of the two alloys. The structure formed in laser nitrided cp-Ti for very low nitrogen concentrations is massive martensite, consisting of relatively coarse packets of α-plates (Fig. 1a and c). However, if the nitrogen concentration is above 7 %, the main structural feature is fine and homogenous arranged acicular martensite (α'-Ti), (Fig. 1b and d). The solidification of separate nitrogen rich phases does not start for nitrogen concentrations below 19 %. Hence, cp-Ti samples laser nitrided under gas atmosphere of 19 % and 25 % nitrogen concentration contained a few titanium nitrides, exhibiting a plate-like shape.

Remelting of Ti-6Al-4V under pure argon atmosphere resulted in a solidification structure consisting of large β-Ti grains. Upon rapid cooling to room temperature the bcc β-Ti crystal structure transformed martensitically forming α'-Ti [11]. The prevailing structure of laser nitrided Ti-6Al-4V is still α'-Ti if gas atmospheres containing less than 5 % nitrogen are used (Fig. 2a and c). However, the martensitic transformation is suppressed for nitrogen concentration above 5 %. The structure of Ti-6Al-4V laser nitrided under gas atmospheres containing 5-25 % nitrogen mainly consists of small α-Ti grains, which are surrounded by a thin film of β-Ti [11]. In contrast to cp-Ti the first titanium nitrides are already formed at nitrogen concentrations above 11 %. These titanium nitrides exhibit globular and plate-like shapes. From literature [12] and own TEM investigations [13] we know that the globular and plate-shaped titanium nitrides are hexagonal $TiN_{0.3}$. In Ti-6Al-4V already a considerable amount of $TiN_{0.3}$ is formed if laser nitrided under gas atmospheres containing 19 % and 25 % nitrogen (Figs. 2b and d). The dendritic crystallization of fcc TiN, a characteristic feature of cp-Ti and Ti-6Al-4V laser nitrided with nitrogen concentrations above 60 %, is only sparsely seen in Ti-6Al-4V laser nitrided under gas atmospheres containing 25 % nitrogen.

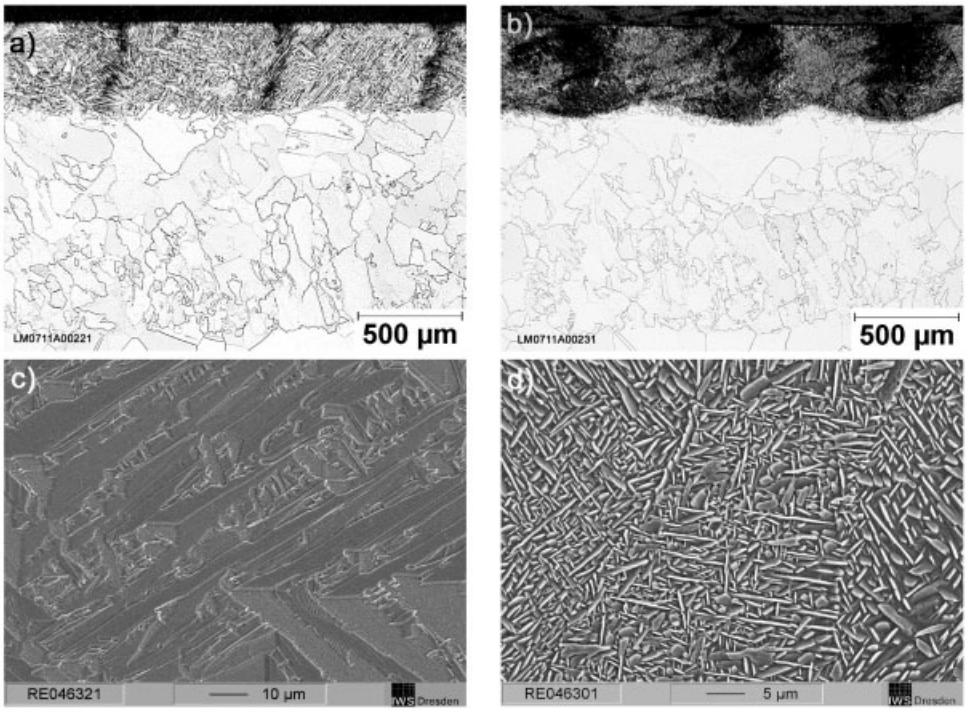


Figure 1: Micrographs of cross-sections through specimens of cp-Ti laser nitrided under different gas atmospheres. a) and c) $N_2/Ar = 5 : 95$, b) and d) $N_2/Ar = 20 : 80$
a) and b) Overview (optical micrograph), c) and d) Detail (SEM micrographs)

Figure 3 shows the measured hardness depth profiles and mean microhardness of laser nitrided cp-Ti and Ti-6Al-4V. It is evident, that the hardness of both Ti alloys can be considerably increased by laser nitriding. With respect to the as delivered state the hardness of Ti-6Al-4V considerably increases due to laser nitriding under gas atmospheres containing 2–13 % nitrogen but achieves a plateau at about 560 HV at nitrogen concentrations above 13 %. In contrast to Ti-6Al-4V, the hardness of laser nitrided cp-Ti continuously increases in the whole range of nitrogen concentration from 2-25 %. However, laser nitrided cp-Ti generally exhibits a lower hardness than laser nitrided Ti-6Al-4V over the whole range of nitrogen concentrations considered in the present study.

The increase in hardness observed in the laser nitrided cp-Ti and Ti-6Al-4V can be correlated with the structure formed in the laser nitrided layers. For both alloys the increase in hardness can be mainly attributed to solid solution hardening of nitrogen interstitially dissolved in the α- and α'-Ti lattice since hard fcc TiN phase is not formed if the nitrogen concentration of the gas atmosphere is set below 25 %. The observations that in laser nitrided cp-Ti the formation of titanium nitrides starts at higher nitrogen concentrations than in laser nitrided Ti-6Al-4V provides evidence that low alloyed cp-Ti can dissolve more nitrogen interstitially in the α- and α'-Ti lattice than the more alloyed Ti-6Al-4V.

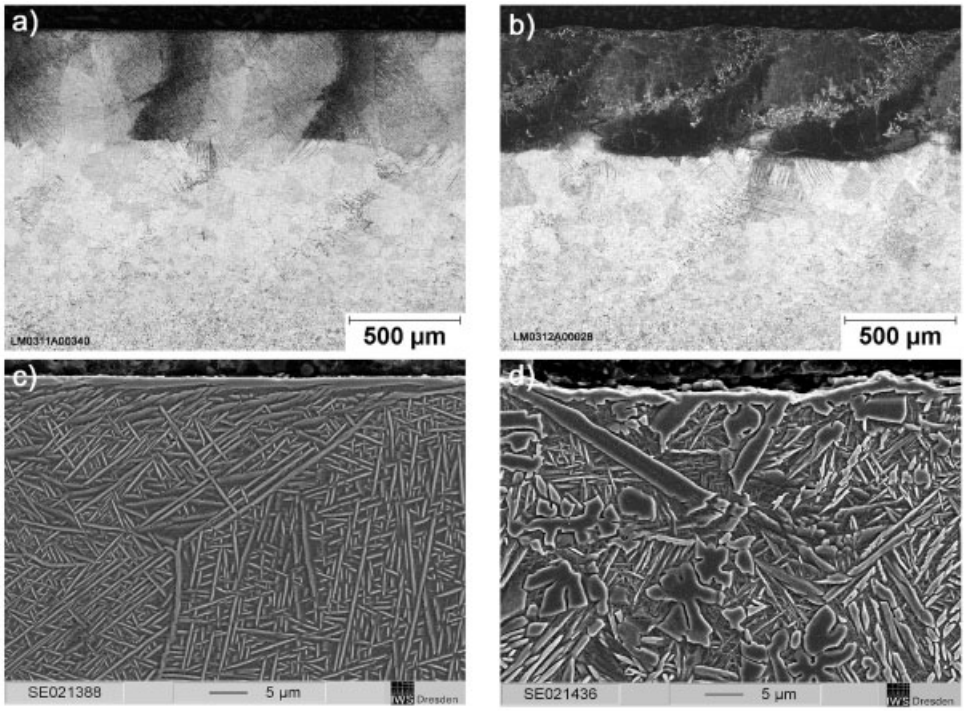


Figure 2: Micrographs of cross-sections through specimens of Ti-6Al-4V laser nitrided under different gas atmospheres. a) and c) N_2/Ar = 5:95, b) and d) N_2/Ar = 19:81
a) and b) Overview (optical micrograph), c) and d) Detail (SEM micrographs)

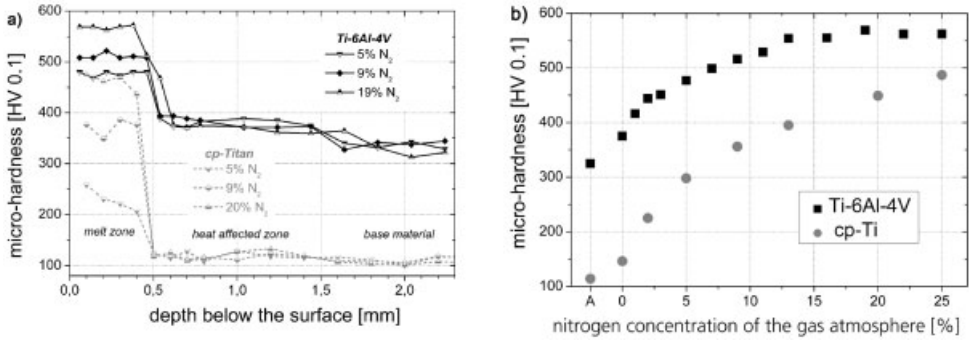


Figure 3: Microhardness measured at the cross section of laser nitrided cp-Ti and Ti-6Al-4V
a) Depth profile, b) Mean hardness in a depth of 200 µm

3.2 Cavitation Erosion Behavior

The cumulative volume loss during cavitation erosion of cp-Ti and Ti-6Al-4V in the as delivered and different laser nitrided states are plotted in the figures 4a and b, respectively. Usually, the erosion curves consist of an incubation period without any measurable volume loss, a transition period, where the rate of erosion increases towards a maximum and a steady state period, in which the material removal commences with constant erosion rate. Comparing the as delivered states of the both Ti alloys it is apparent that Ti-6Al-4V already exhibits an excellent resistance to cavitation erosion whereas the cavitation erosion resistance of cp-Ti is relatively poor. Independent of this different starting conditions the cavitation erosion resistance of both Ti alloys is considerably improved by laser nitriding with low nitrogen concentrations. Both, cumulative volume loss (Figs. 4a and b) and the erosion rate in the steady state period (Fig. 4c) distinctively reduce with increasing nitrogen concentration but reach a plateau at nitrogen concentrations of about 13 % for both Ti alloys. It is remarkable, that although the cavitation erosion resistance of Ti-6Al-4V is superior to cp-Ti in the as delivered state, the wear resistance of both materials becomes comparable if they are laser nitrided under gas atmospheres containing more than 9 % nitrogen. As a consequence, laser nitriding of cp-Ti and Ti-6Al-4V under gas atmospheres containing between 9-25 % nitrogen produce hard and wear resistant layers with excellent protection against cavitation erosion.

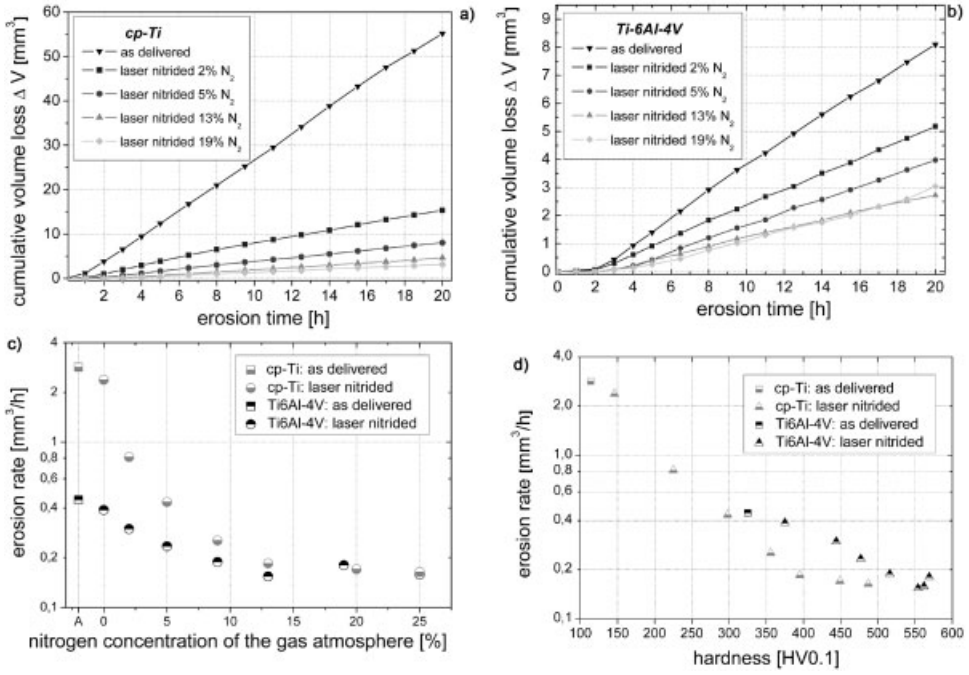


Figure 4: Cavitation erosion behavior of laser nitrided cp-Ti and Ti-6Al-4V a) Cumulative mass loss: cp-Ti, b) Cumulative mass loss: Ti-6Al-4V, c) Erosion rate in dependence of the nitrogen concentration of the gas atmosphere, d) Correlation of erosion rate and microhardness

In figure 4d the erosion rate in the steady state period is plotted against microhardness. Initially, for both laser nitrided Ti alloys the erosion rate continuously decreases with increasing layer hardness. However the erosion rate of laser nitrided cp-Ti and Ti-6Al-4V does not further reduce even though their hardness still increases if the nitrogen concentration of the gas atmosphere was set above 13 %. It is apparent from figures 4c and 4d that compared to laser nitrided Ti-6Al-4V the erosion rate of laser nitrided cp-Ti reduces more steeply. Thus in both laser nitrided alloys the same cavitation erosion resistance can be achieved even though laser nitrided cp-Ti exhibits lower hardness than laser nitrided Ti-6Al-4V. To clarify the microstructural mechanisms responsible for the slightly different cavitation erosion behavior of the both laser nitrided Ti alloys detailed investigations are currently in progress.

In the present work the influence of the nitrogen concentration of the gas atmosphere in the range of 0–25 % on the microstructure, hardness and cavitation erosion behavior of laser nitrided cp-Ti and Ti-6Al-4V has been investigated. The following conclusions are drawn.

1. The nature, volume fraction and distribution of the phases formed during laser nitriding are determined by the chemical composition of the alloy and by the nitrogen concentration of the gas atmosphere. Laser nitrided cp-Ti exhibits massive martensite structure and acicular martensite structure for nitrogen concentrations below and above 7 %, respectively. In contrast, the microstructure of laser nitrided Ti-6Al-4V changes from acicular martensite to a fine mixture of α-Ti and β-Ti grains if the nitrogen concentration exceeds 5 %. For higher nitrogen concentrations in both Ti alloys the formation of globular and plate-shaped $TiN_{0.3}$ phase is observed.

2. The increase in hardness in the laser nitrided layers of both Ti alloys is mainly attributed to solid solution hardening of nitrogen dissolved in the Ti lattice.

3. The cavitation erosion resistance of both Ti alloys can be distinctly improved by laser nitriding. Optimal cavitation erosion resistance is already achieved by laser nitriding under gas atmospheres containing relatively little nitrogen (9–13 %).

4 References

[1] T. Bell, H. W. Bergmann, J. Lanagan, P. Morton, A. M. Staines, Surf. Eng. 1986, 2, 133-143

[2] S. Mridha, T. N. Baker, Mater. Sci. Eng. A 1991, 115-124

[3] S. Yerramareddy, S. Bahadur, Wear 1992, 157, 245-262

[4] H. Xin, S. Mridha, T. N. Baker, J. Mater. Sci. 1996, 22-30

[5] S. Bonß, B. Brenner, E. Beyer, Mat.-wiss. und Werkstofftech. 2001, 32, 160-165

[6] M. Raaif, F. M. El-Hossary, N. Z. Negm, S. M. Khalil, A. Aolitsch, D. Höche, J. Kaspar, S. Mändl, P. Schaaf, J. Phys. D: Appl. Phys 2008, 41, in press

[7] J. M. Robinson, S. Anderson, R. D. Knutsen, R. C. Reed, Mater. Sci. Technol. 1995, 11, 611-618

[8] C. Gerdes, A. Karimi, H. W. Bieler, Wear 1995, 186-187, 368-374

[9] P. A. Coulon, J. Mater. Proc. Technol. 1993, 38, 247-263

[10] H. C. Man, Z. D. Cui, T. M. Yue, F. T. Cheng, Mater. Sci. Eng. A 2003, A355, 167-173

[11] J. Kaspar, J. Bretschneider, S. Jacob, S. Bonß, B. Winderlich, B. Brenner, Surf. Eng. 2007, 23, 99-106

[12] C. Hu, H. Xin, L. M. Watson, Acta Mater. 1997, 45, 4311-4322

[13] J. Kaspar, A. Luft, S. Bonß, B. Winderlich, B. Brenner, Proc. of the 10th World Conference on Titanium (Ed. G. Lütjering), 2003, 949-956

Production of Coal Crushing Hammer Heads by Bi-metal Casting

Turgut Kirma, Ekrem Selçuk, Ali Kalkanli, Arda Çetin
Department of Metallurgical and Materials Engineering, Middle East Technical University, 06531 Ankara, Turkey

Abstract

In this study, by considering different mechanical properties such as wear resistance and toughness of two different metal alloys in design and production stages, bi-metal casting technique was used for producing composite material which will be a solution for the wear and crack formation problem in coal crushing hammer heads and also impact bars. The failure analysis of the classical hammer heads and impact bars which are made from Hadfield steels (austenitic steel) showed that there are crack formations through austenitic grains, and SEM results showed that there are dimples which indicate ductile fracture, and also during the phase transformation from austenite to martensite, weight of the material decrease from 90 kg to 50 kg and it approximately corresponds 45 % weight loss.

The main aim of this study is trying to find an optimum conditions to produce bi-metal as an alternative wear resistant product. High chromium white cast iron (16 % Cr) was chosen for the wear resistant part and ductile iron was chosen as a tough part of the bi-metal. At first part of the study, unalloyed white cast iron and grey iron were investigated to form a bi-metal, than these results were applied to alloyed materials.

Thermal analysis is the basic technique in this study to determine the solidification conditions. By using thermocouples with a suitable set-up, the cooling curves of the materials were obtained. By using a Newtonian thermal analysis technique, the solid fractions of the materials during solidification were obtained by using cooling curves data. Different bi-metal producing experiments were done under different solid fractions and the specimens were analysed.
Keywords: Wear resistance, Bi-Metal composite casting, Hadfield Steels, Thermal Analysis,

1 Introduction

In coal-fired power generation stations the coal has normally to be crushed and milled before use. Wear has a great influence on the mill performance and maximization of the materials' life is important for the operators and manufacturers.

The crusher hammers are installed at the rotor and rotate at high speed. These hammers are subject to complex stresses following impact and thrust motions, abrasion and in the case of clinker mills frequent high temperatures. Under these conditions the plant operator expects high wearresistance as well as 100 % operational safety. As shown in Figure 1, the limits of wear resistance using mono-metallic components have been reached. Wear on plant components represents a considerable cost factor for the operators of excavating and processing machines. Degradation of power components is mainly due to abrasion by quartz and alumina-silicates that are in the

coal [1]. In addition to material composition, the service conditions also play a significant role in degradation of the components. Material properties such as hardness, fracture toughness and microstructure are also important factors in degradation of material and/or material removal due to interactions with abrading media [2]. One possible way of improving wear resistance lies in making components of composite castings. It is advantageous if different materials which selfcombine, and therefore can not be detached from one another, are combined in one cast component [3]. This means that one component can contain specific combinations of properties, such as impact resistance and wear resistance and these materials are called bi-materials.

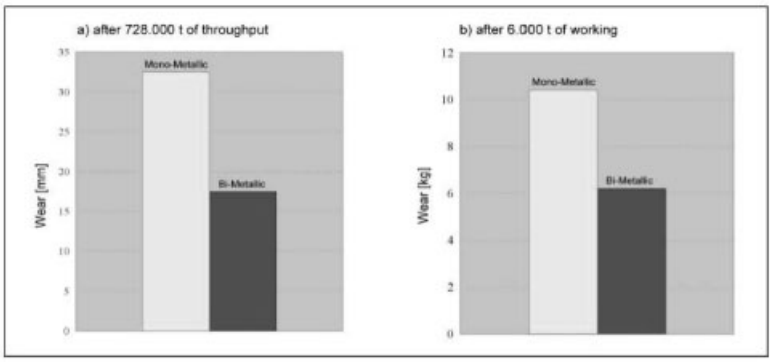


Figure 1: Wear of the Bi-Metallic hammer head compared with mono-metallic [3]

2 Experimental Procedure

2.1 Material Used

For the first part of the bi-metal production experiments; unalloyed white cast iron was used as a wear resistant material and grey iron was used as a tough material. Chemical composition of them are shown in Table 1. At the second part of the bi-metal production experiments, high chromium white cast iron was used as wear resistant material whereas ductile iron was used as a tough material, Table 2.

High-chromium white cast irons are in demand for the mining, mineral processing, metallurgical and cement industries. Very high abrasive wear resistance combined with relatively low production costs make these alloys particularly attractive for applications where grinding, milling and pumping equipment is used to process materials such as ore, coal, and gravel. Another important application of these iron alloys is the manufacture of working rolls for hot strip mills.

In abrasion-resistant cast irons, chromium content is in the range of 14–28 %; the chromium goes entirely into the carbide phase and serves to enhance the carbide stability [4,5]. For lower amounts of Cr in this range, the carbides are generally M3C. When the amount of Cr is higher, the as-cast structure consists of discontinuous (CrFe)7C3 carbides and the γ phase which may be completely or partially transformed to martensite during cooling.

In todays' technology, low carbon steel is used as a tough part of bi-metallic components. In this study, ductile iron was used instead of low carbon steel. Ductile iron, frequently referred to as

nodular or spheroidal graphite iron provides a wide spectrum of mechanical properties that can be obtained either by altering certain processing variables or through various heat treatments which present different and better combination of properties for application with special requirements.

Table 1: Chemical Composition of Unalloyed White Cast Iron and Grey Cast Iron.

	C %	Si %	P %	S%	Mn%	Cr %	Carbon Equivalent
White Cast Iron	3.2	1.18	0.006	0.003	0.033	0.02	3.6
Grey Cast Iron	3.5	2.4	0.01	0.003	0.31	0.015	4.3

Table 2: Chemical Composition of Alloyed White Cast Iron and Ductile Iron

	C %	Si %	P %	S %
16 % Cr White Cast Iron	2.66	0.76	0.03	0.01
Ductile Iron	3.5	2.5	0.01	0.01

2.2 Mold Design and Experimental Set-Up

A specially designed mould in bi-metal casting must be used as shown in Figure 2. Two different metals are poured and so two risers are used. The first metal is poured from the first riser up to 3 level(interface of the bi-metal) and when it solidifies up to a critical solid fraction, the second material is poured from the second riser.

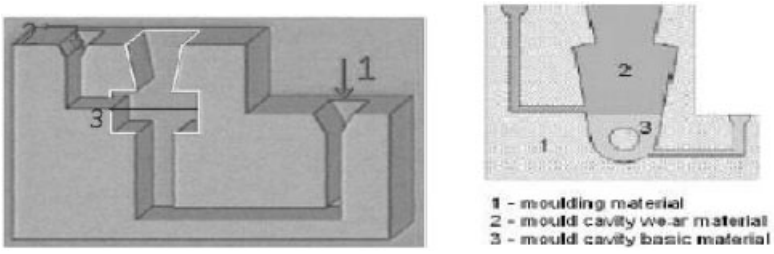


Figure 2: Mould design for bi-metal casting.

As shown in Figure 3, there is a thermocouple at the point 3 where is the interface of bi-metal. By using a K-type thermocouple and thermal analysis control system, the temperature of the interface are recorded by time. Then, these temperatures give the cooling curves of the materials.

2.3 Thermal Analysis

Solidification process parameters are identified and measured by thermal analysis may then be used to evaluate the effects of processing variables on solidification. When cast iron solidifies from the molten state, it passes through several phase changes.

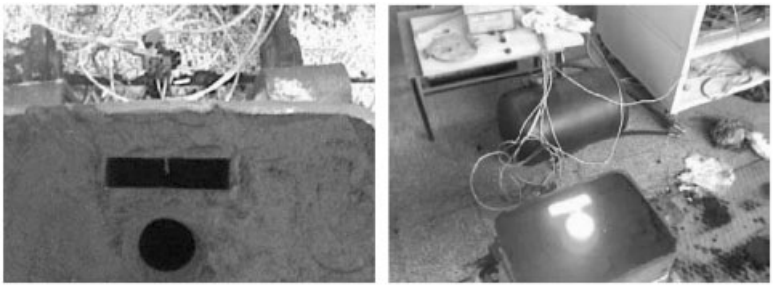


Figure 3: Experimental Set-Up.

The first phase change is the beginning of primary austenite formation; this is commonly called liquidus. The second phase change represents the end of austenite formation and the beginning of solid state transformation; this is commonly called solidus.

2.4 Newtonian Thermal Analysis of Cast Iron

Computer aided cooling curve analysis (CACCA), such as Fourier Thermal Analysis (FTA) and Newtonian Thermal Analysis (NTA) are valuable tools that give a deeper understanding of the solidification of cast alloys. The interest on these techniques relies on the successful identification of several cooling curve parameters by conventional cooling curve analysis. This allows the prediction of the microstructure of cast products. Another reason is the need to develop more elaborated cooling curve data processing methods in order to gain a better understanding of solidification and a closer control of the melt quality before pouring.

Newtonian Thermal Analysis (NTA) analyzes a cooling curve that is obtained with thermal analysis instruments, shown in Figure 4. NTA calculations are performed on the first derivative of that curve. In the classical version of this method , the times of start and end of solidification are located. The zero baseline curve is obtained from an exponential interpolation between these points. Integration of the area between the cooling curve and the zero baseline curve gives relevant information of the solidification kinetics [6].

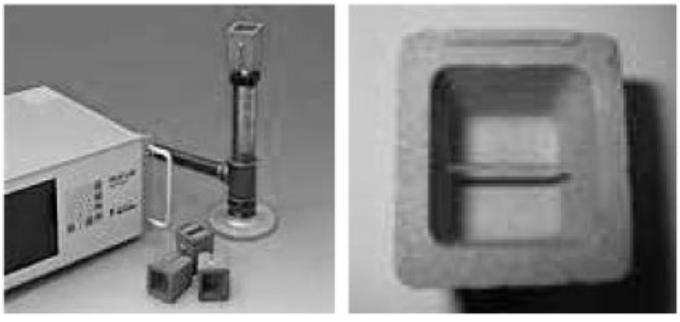


Figure 4: Thermal Analysis Instruments.

3 Results and Discussion

3.1 Metallographic Investigation of Hadfield Steel

As shown in Figure 5, the unused sample, which was taken from Çatalagzı Thermal Power Plant in Turkey, is fully austenite and there are no carbides. It is possible to say that, heat treatment of the steel is succesful.

Table 3: Chemical Composition of Hadfield Steel Hammer Head and Impact Bar Used in Coal Crushers and Grinders

	C %	Mn%	Cr %
GX 130 Mn Cr Hammer Head	1.20	17.0	1.5
GX 120 Mn 13 Impact Bar	1.20	13.0	0.5

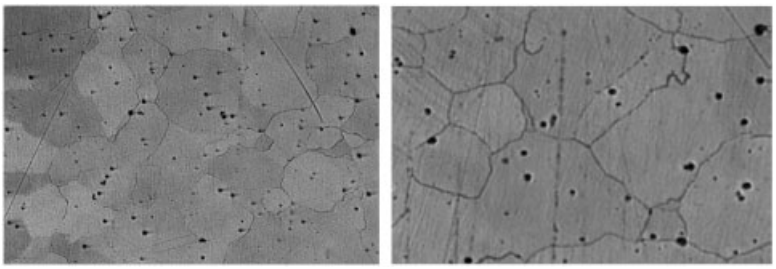


Figure 5: Optical micrograph showing unused Hadfield steel impact bar specimen at 50X and 100 X magnification.

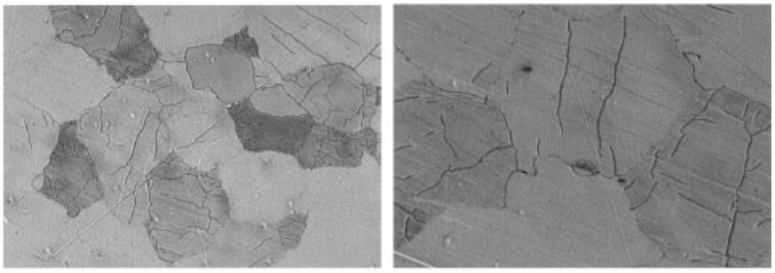
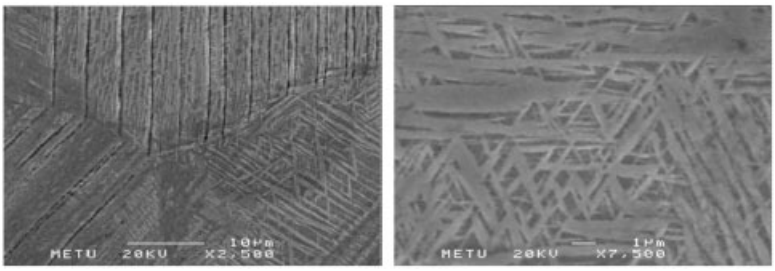


Figure 6: Optical micrograph showing used Hadfield steel impact bar specimen at 50X and 100 X magnification.

The specimens were taken from the surface of the component which were exposed the impact and abrasive wear. In Figure 6, the cracks are seen through the grains of the used Hadfield steel specimen. Also the matrix is still fully austenite. Addition to these microcracks there is an important degree of wear rate and it results 45 % weight lose.

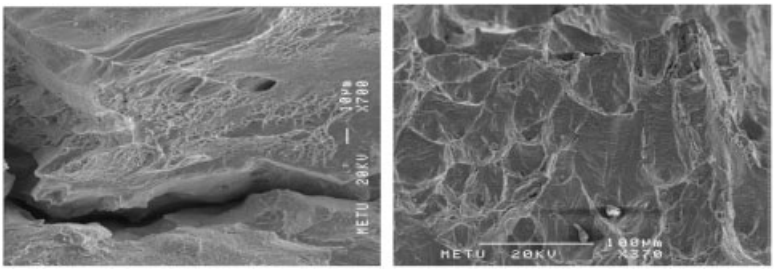
3.2 Scanning Electron Microscop Analysis

By deformation during the crushing and grinding processes, due to high work hardening capability of Hadfield steel, phase transformation from austenite to martensite starts. By the transformation, the hardness of the material increases and wear resistance also increases.



a) b)

Figure 7: SEM micrograph of used Hadfield steel impact bar specimen. a) Partial phase transformation, 2500X, b) Martensite phase, 7500X



a) b)

Figure 8: SEM micrograph of used Hadfield steel impact bar specimen. a) Austenite grain, 7000X, b) Dimples, 3700X

As shown in Figure 7, the ratio of martensite in the microstructure is low. It means that the hardness which is necessary for resistance to abrasive wear is still low. Also, as it can be seen in Figure 8, there are dimples in used/scrap components which indicates ductile fracture. Finally, the material is still tough and service conditions are not enough to provide high impact for an effective phase transformation.

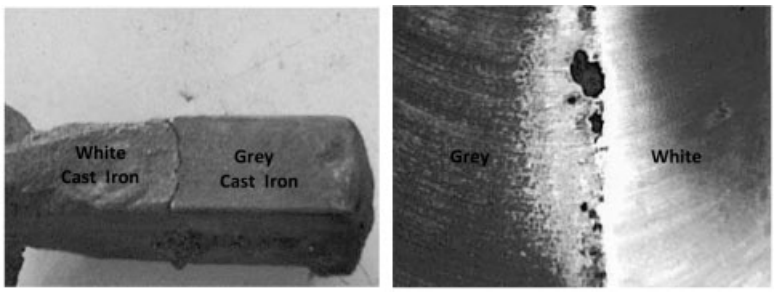
Hadfield steels are usually less resistant to abrasion than are martensitic white irons or martensitic high-carbon steels, but are often more resistant than pearlitic white irons or pearlitic steels [7]. Its some mechanical properties are ; 0.2 % offset yield strength 379 MPa, ultimate tensile strength 965 MPa, as quenched hardness 190 HB, hardness at fracture is 500 HB. The approximate ranges of tensile properties in other alloy steels by heat treatment are developed in manganese steel by work hardening. It is preferred choice where high shock resistance, toughness and absorption of energy are required. Excellent resistance to metal to metal wear, as in sheave

wheels, crane wheels and car wheels. An important use is in railway tracwork, such as frogs, switches and crossings, where the multiple impacts at intersections are especially severe [7].

3.3 Experiments of Bi-metal Production

3.3.1 Initial Experiment

The initial bi-metal production experiment showed that, there must be a critical time to pour the second material. At this experiment, white cast iron was firstly poured into the mold and 60 seconds later the second material, grey iron, was poured.



a) b)

Figure 9: a) Digital photograph of bi-metal specimen, b) Interface of initial bi-metal specimen.

As seen from Figure 8, there is not a good combination between two materials and there is a porous interface which is very brittle. According to this initial experiment results, it was determined that, starting point had to be thermal analysis of each material and then bi-metal would be produced.

3.3.2 Thermal Analysis

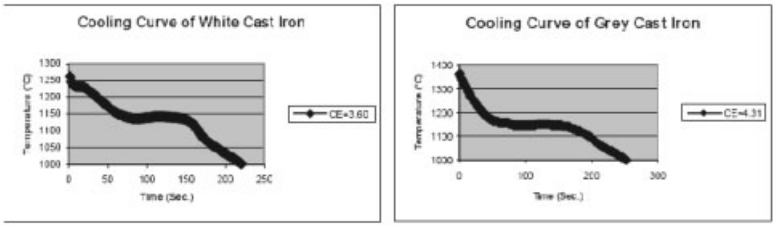


Figure 10: Cooling curves of white and grey cast iron.

Cooling curves, Figure 10, gave us the solid fraction values shown in Figure 11, by using Newtonian Thermal Analysis.

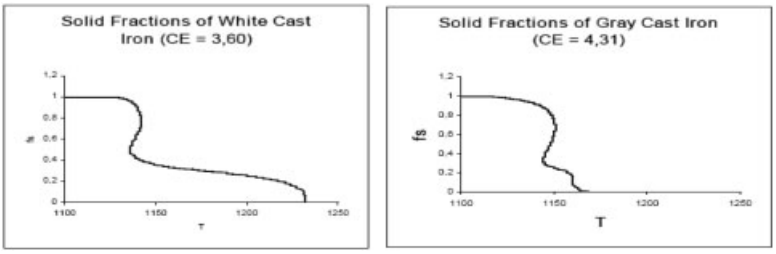
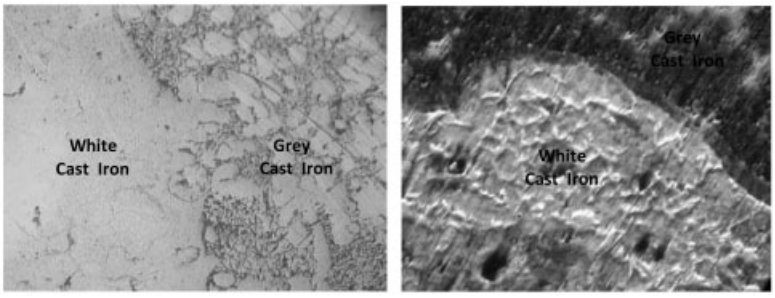


Figure 11: Solid Fractions by Temperature (°C).

3.3.3 Evaluation of Experiments

1. Firstly, white cast iron was poured and waited until the temperature decreased to 1150 °C. Then grey cast iron was poured at 1400 °C. 1150 °C corresponds 36.5 % solid fraction for white cast iron.
2. Secondly, the white cast iron was poured and waited until the temperature decrease to 1180 °C. Then the grey cast iron was poured at 1400 °C. 1180 °C corresponds 29.4 % solid fraction for white cast iron.
3. Grey cast iron was poured firstly and waited until the temperature decrease to 1150 °C. Then the white cast iron was poured at 1400 °C. 1150 °C corresponds 25 % solid fraction for grey cast iron.



a) b)

Figure 12: Optical micrograph, at 100X magnification, 36.5 % solid fraction, a) Polished, b) Etched with 2 % Nital.

Hardness transition is significant in bi-metals. The hardness transition must be gradually. The hardness of the interface should have the value between two materials. As shown in Figure 15, the hardness increases gradually. In addition, the interface must behave as a third phase between two different materials. There must be transitions between two different phases. As shown in Figure 16 there are transitions between two different materials while solidifying.

At the second part of the bi-metal production experiments, high chromium white cast iron as a wear resistant material and ductile iron as a tough material were examined.

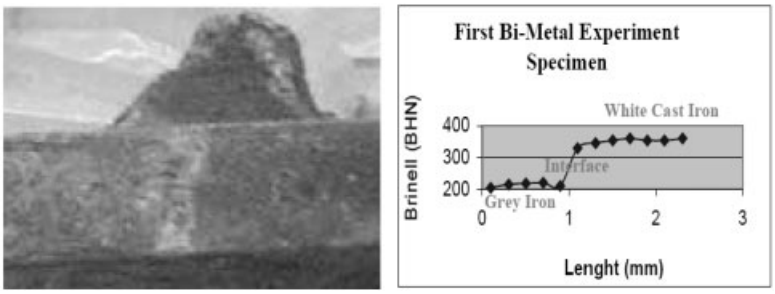
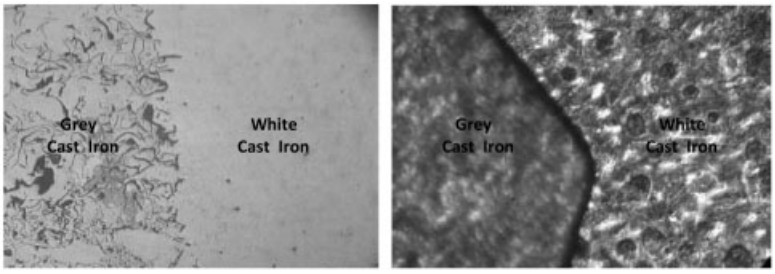


Figure 13: Digital photograph and hardness transition of first bi-metal specimen.



a) b)

Figure 14: Optical micrograph, at 100X magnification, 29.4 % solid fraction, a) Polished, b) Etched with 2 % Nital.

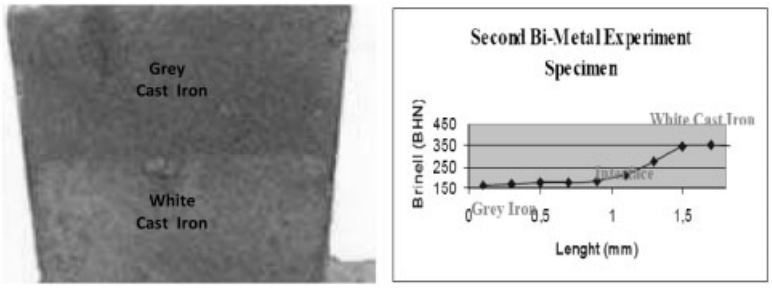


Figure 15: Digital photograph and hardness transition of second bi-metal specimen.

After investigating the high chromium cast iron and ductile iron, final bi-metal casting experiment had been done. The casting conditions, especially solid fraction value were decided according the results of first part of bi-metal experiments.

By using the solid fraction graphs of ductile iron, Figure 18, the necessary temperature and time for casting the second material, high chromium cast iron, was decided.

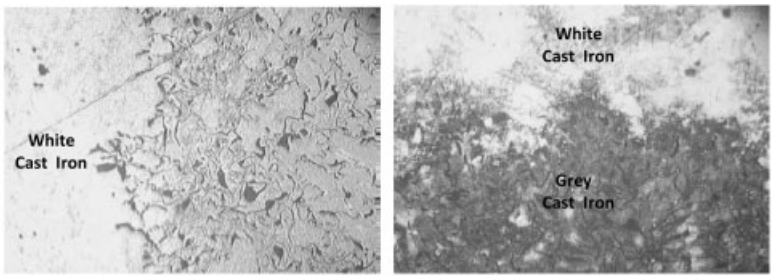


Figure 16: Optical micrograph, at 100X magnification, 25 % solid fraction.

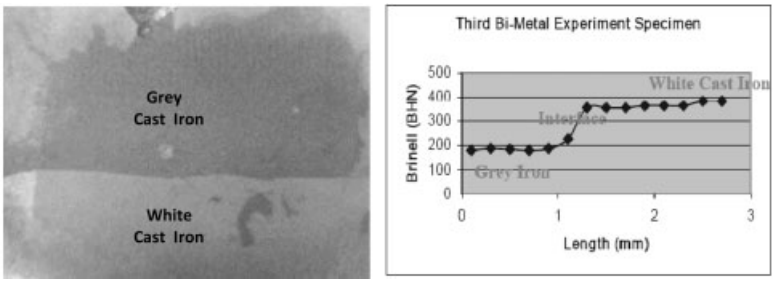
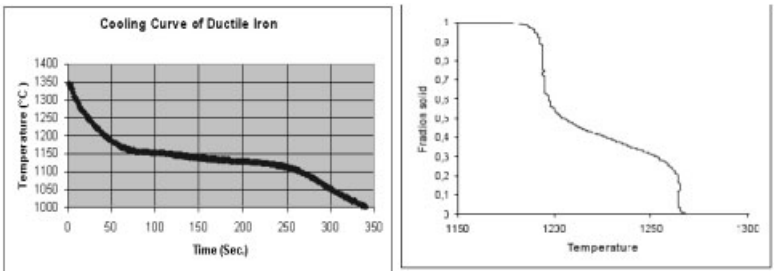


Figure 17: Digital photograph (macroetched with 10 % Nital) and hardness transition of third bi-metal specimen.



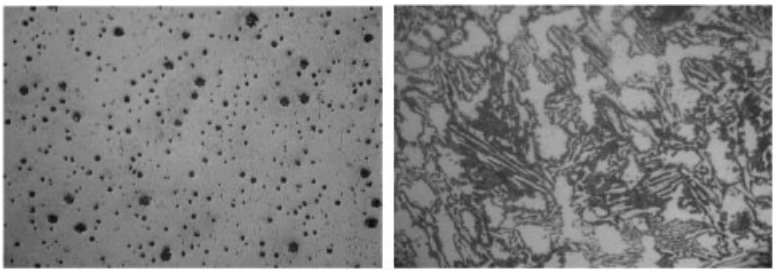
a) b)

Figure 18: a) Cooling Curve of Ductile Iron, b) Solid Fractions of Ductile Iron by Temperature (°C).

Finally, two alloys were prepared in two different induction furnaces at the same time. At first ductile iron was poured and waited until the solid fraction of it became approximately 30 %. Then, 16 % Cr white cast iron was poured at 1400 °C.

4 Conclusion

Hadfield steels are usually less resistant to abrasion than are martensitic white irons or martensitic high-carbon steels, but are often more resistant than pearlitic white irons or pearlitic steels. So



a) b)

Figure 19: Optical micrographs a) Ductile Iron, 200X, b) 16 % Cr White Cast Iron, 400X.

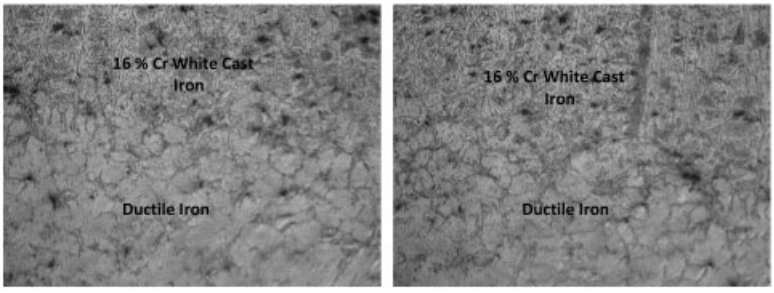


Figure 20: Optical micrograph of final bi-metal specimen, 200X magnification.

for example, if impact and shock are absent in the system, a martensitic cast iron is a much better choice. If light or moderate impact is involved, the specification of a hardened steel may be justified. But if heavy impact is expected Hadfield steel is the logical choice [7]. In coal crusher and grinder systems, abrasive wear is the main wear mechanism so abrasive wear resistance of material is more important than its impact resistance. Abrasive conditions results in the progressive removal of material and due to various phase transformations from austenite to martensite introduces surface volume changes and causes the generation of cracks and further lead the failure of the component [1]. One possible way of improving wear resistance lies in making components of composite castings. It is advantageous if different materials which self-combine, and therefore cannot be detached from one another, are combined in one cast component [3]. This means that one component can contain specific combinations of properties, such as impact resistance and wear resistance and these materials are called bi-materials.

The basic principle for producing bi-metals was to obtain the best solid fractions to make the interface behave as a third phase between two different materials. For this reason, different bimetal producing experiments had been done under different experimental conditions. The results of the experiments showed that, for white cast iron and gray iron duplex structure recommended temperature range for white cast iron is 1150–1180 °C. The grey cast iron is poured at 1400 °C on to this white cast iron. In this temperature range, solid fraction values are calculated as 40 % and 30 % for white cast iron. For high toughness the spheroidal graphite cast iron (ductile iron)

was choosen and produced instead of low carbon steel which is being used in todays' technology whereas 16 % chromium white cast iron was choosen as a wear resistant material.

References

[1] K. Venkateswarlu, S. G. Chowdhury, L. C. Pathak, A. K. Ray, "Microstructural Examination of Service Exposed Coal Mill Liner Material", Materials Characterization, Vol. 58 (2007), pp. 1029–1032.

[2] R. G. Wellman, C. Allen, "The Effects of Angle of Impact and Material Properties on the Erosion Rates of Ceramics", Wear (1995); 186–187 : 117-22.

[3] Hardtop Gießereitechnologie GmbH, Magdeburg Germany, "Experience with the use of composite cast hammers in the cement industry", ZKG International-No.2/2000 Vol. 53

[4] Jackson RS. Br Foundrym 1974; 67:34

[5] Dodd J, Parkes L. Int J Cast Met.Res. 1980; 5:47.

[6] M. R. Chavez, A. Amaro, C. Flores, A. Juarez, C. Gonzalez-Rivera, "Newton Thermal Analysis of Gray and Nodular Eutectic Cast Iron", Materials Science Forum Vol. 509 (2006), pp. 153–158

[7] S. Alyaz, "Effects of Heat Treatment and Chemical Composition on Microstructure and Mechanical Properties of Hadfield Steels", METU M.S. Thesis, December 2003

Characterization and Modeling of the Wear Behavior of Highly Wear-Resistant Special Structural Steels

A. Dietrich [1)], P. Feinle [2)], A. Kern [1)], U. Schriever [1)]
[1)] TKS Profit Center Grobblech, Duisburg, Germany [2)] HS Mannheim, Mannheim, Germany

1 Introduction

Steel plate designed with high wear resistance is used in industrial plants and machinery subject to wear. Typical applications of the wear-resistant structural steels are in plants for the extraction and processing of raw materials such as coal, ore, rocks, etc. These include excavator shovels, dumper truck bodies, crushers, shovel blades, side cutters, but also agricultural machinery and railway points elements (Fig. 1).

For a detailed evaluation of the reliability of these materials in such structures, knowledge of their wear behavior and expected durability in the effective operating conditions is particularly important. The wear behavior of the plates depends on their material properties, especially their hardness and strength, but also on the properties of the counter body and the ambient medium as well as the structural conditions. Any wear incurred is therefore not a material, but always a system property. These relationships can be described schematically by the tribological system configuration.



Figure 1: Shovel excavator.

In this paper, these relationships are studied in depth for the above-mentioned applications in order to create an appropriate basis for the selection of wear-resistant special structural steels to meet application requirements and accordingly to predict their durability in application.

Table 1: Chemical composition.

Steel number	TKS quality	Hardness [HB]	Delivery condition	Plate thickness [mm] max.	Chemical analysis [%]						typ. CET [%]	
					C max.	Si max.	Mn max.	Cr max.	Ni max.	Mo max.	8 mm	50 mm
1.8704	XAR® 300	270 - 340	N	60	0,21	0,65	1,50	1,20		0,30	0,39	0,39
1.8714	XAR® 400	360 - 440	Q	100	0,20	0,80	1,50	1,00		0,50	0,28	0,36
1.8734	XAR® 400 W	360 - 430	Q + T	40	0,26	0,80	1,30	1,20		0,60	0,40	
1.8722	XAR® 450	410 - 490	Q	100	0,22	0,80	1,50	1,30		0,50	0,29	0,39
1.8734	XAR® 500	450 - 530	Q	100	0,28	0,80	1,50	1,00	(1,50)	0,50	0,40	0,43
1.8735	XAR® 600	550 - 630	Q	40	0,40	0,80	1,50	1,50	1,50	0,50	0,53	0,53
1.8735	XAR® 650	> 600	Q	40	0,47	0,80	1,50	1,50	1,50	0,40	0,61	0,61

$$CET = C + {}^{Mn+Mo}/_{10} + {}^{Cr+Cu}/_{20} + {}^{Ni}/_{40}$$

2 Special Structural Steels

2.1 Chemical Composition

By way of introduction, the production and properties of the wear-resistant special structural steels are outlined below. Table 1 provides an overview of the chemical composition of plates made of wear-resistant special structural steels. In plate thicknesses up to 100 mm, the characteristic alloying elements of the steels are Mn, Cr, Mo and Ni at a C content up to 0.47 %. The steels exhibit hardness values from around 300 to 650 HB with acceptable toughness. The steels are produced mainly by water-quenching and -tempering. The steel plate is usually rolled and then re-austenitized and quickly quenched in water in order to ensure transformation into the martensitic or bainitic stage. The plate can be directly quenched from rolling heat. During cooling, the carbon content of the steel is important as this has a crucial influence on the hardness after quenching [1].

2.2 Microstructure

Important for the wear behavior of the special structural steels is their hardness, which is adjusted based on the production process and the selected chemical composition in conjunction with a tailored microstructure. With the hardness determined by the carbon content forced to remain dissolved in the martensitic matrix, the selectively defined very small packet size of the lath-like martensite of < 10 µm is the basic precondition for optimum wear resistance. Characteristic is also the arrangement of the individual laths at various angles to each other. Fig. 2 shows this lath structure in a SEM image. Precipitated within this structure are fine carbides, which are shown in the analysis as cementite (Fe, Mn, Cr, Mo)3 C or ultra fine NbC particles (Fig. 3).

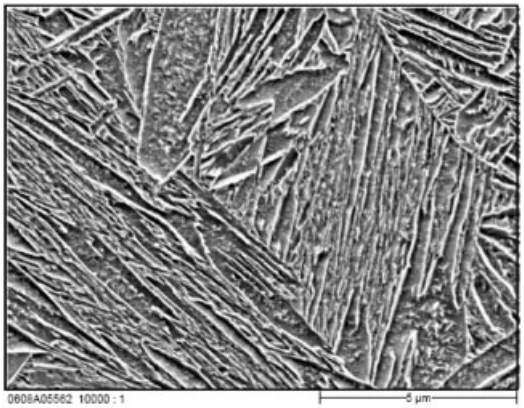


Figure 2: Lath structure.

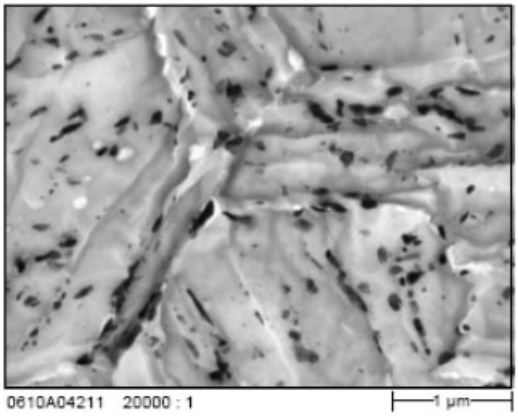


Figure 3: Carbide inclusions.

Contents of up to 5 % Mn, Cr and Mo are dissolved within these carbides. They show a high hardness of > 1000 HV. Owing to their vol. fraction and extremely fine distribution, they not only contribute to the high hardness of the martensitic basic matrix, but are also a significant factor ensuring high wear resistance, as they are responsible for an additional strengthening of the microstructure to prevent cold deformation and crack formation. The volume percentage of hard carbides and the package size of the martensite can be controlled based on the steel composition, the rolling process and the heat treatment. Corresponding microstructural investigations for a detailed insight in the microstructural processing of these steels during wear are in progress.

3 Wear Behavior

In the above-mentioned applications for the wear-resistant special structural steels, the characteristic wear mechanisms affecting the plates are abrasive or grooving wear. The plate surface is "scratched" by contact with an abrasive hard counter body (sand, rock, etc.) so that material is removed from the surface. A further important wear mechanism is impact wear. The impact of a counterbody leads to surface fatigue of the microstructure, which also results in the loss of material from the surface. The share of the effective wear type is essentially dependent on the angle of incidence of the wear material. Moreover, irrespective of the wear type, depending on the ambient medium, an additional corrosion attack and therefore tribochemical reactions ensue, which change the properties of the boundary layers and therefore increase the loss of material from the surface [7].

In the interaction between the wearing counter materials and the plate, the level of the wear stress depends essentially on the hardness relationship Hp. This is the key factor and defined by the quotient of the hardness of the counter materials and the hardness of the plate material:

$$H_p = \frac{H_{Counterbody}}{H_{Plate}}$$

This always results in the formation of upper- and lower shelf characteristics as shown in Fig. 4. If the hardness of the counter material is low relative to the hardness of the plate, this results in comparatively low wear. With a much higher hardness of the counter material compared to the plate, much higher wear is exhibited. The transition can usually be expected in the range of equal hardness. Corresponding limits for Hp can be specified for the upper and lower shelf.

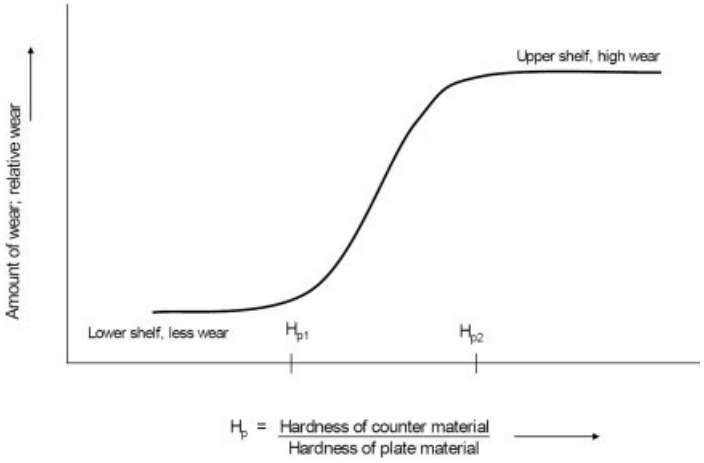


Figure 4: Characterization of the wear (schematic).

Working from this knowledge and preliminary considerations, tests on the wear behavior of wear-resistant special structural steels on grooving and impact wear were conducted at the Centre

of Expertise on Tribology at the University of Mannheim. Materials with different chemical compositions, microstructures and hardness values were tested.

4 Materials and Methods

4.1 Materials

To cover the largest possible range of composition properties, around 20 test materials with different chemical composition with graduated contents of C, Mn, Cr, Mo and Ni were tested in the test series. The plates were tested in a hardened or quenched and tempered state and had a martensitic or martensitic-bainitic microstructure. Depending on the composition of the steel, the plates exhibited hardness values from around 300 to 650 HB. As a reference material, a S355 with a ferritic-perlitic microstructure was used; this is available in the normalized state and has a hardness of around 170 HB.

4.2 Test Rigs (Abrasive Wear Pot, Solid Particle Erosion System)

The test plan included two different test rigs [12]. In the first step, an abrasive pot was used to exclusively test the grooving wear. Rounded silica gravel with a hardness of around 1150 HV10 was used as the abrasive material, so that here the behavior in the upper shelf region could be examined. In a second stage, tests on impact wear were performed on suitable specimens in a commercial solid particle erosion system. Besides quartz/corundum (1100–1600 HV10), here salt (around 200 HV10) and cast steel gravel (400–450 HV10) were also used so that the wear could be tested in the upper and lower shelf regions and in the transition region. All tests with different abrasive materials were performed at an impact angle of 30° (maximum wear, determined in preliminary tests [12]) and an impact pressure of 6 bars.

5 Test Results and Discussion

5.1 Test Results

The crucial characteristic for evaluation of the wear incurred by the specimens is the wear amount Wr. This is determined based on the difference in weight of the specimen before and after

the test and can be later converted, for example, into a plate thickness reduction rate per 1000 h. For determination of the wear, all specimens were processed over a constant test time. This was chosen so it lies in the range of the constant wear rate and no run-in effects can be expected. The wear behavior of the steels tested with pure grooving and impact wear can be evaluated with the help of Figs. 5 and 6. Precise details on the materials, test conditions and results are contained in [12].

The hardness or the hardness ratio H_p resulting from the steel composition and heat treatment conditions is shown to be an important wear parameter for the two types of wear. On every level of hardness, the achieved wear resistance is also dependent on the microstructure (e.g. carbide content, etc.).

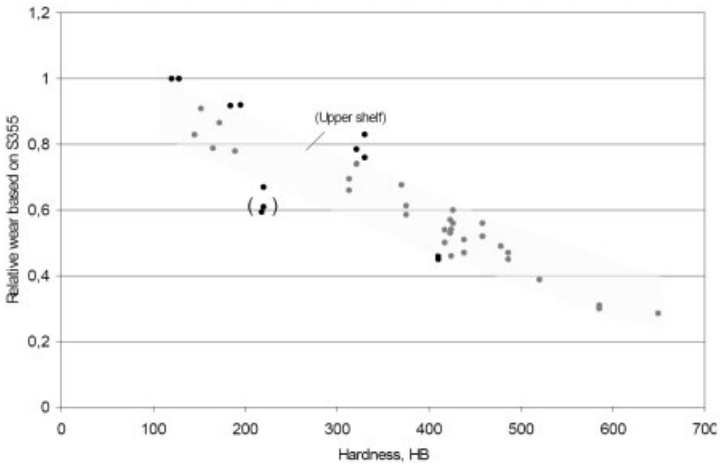


Figure 5: Influence of the hardness on the relative wear amount (pH value $\geq$ 7) with grooving wear.

5.2 Modeling of the Wear Behavior

In the modeling of the wear behavior, the mathematical description of the wear characteristics showed in Fig. 4 is important. Here the hardness ratio H_p is a key influencing parameter. Knowledge of the respective transition points H_{p1} and H_{p2} is also important. According to [7–10], the limit $H_{p1} \approx 0{,}9$ to 1,3 applies for the end of the lower shelf region while $H_{p2} \approx 1{,}3$ to 1,6 applies for the beginning of the upper shelf. The objective of the mathematical modeling of the wear behavior is the calculation of the wear amount Wr relative to S355 as a function of the hardness of the steel, the counter material and the steel composition and, if appropriate, the ambient conditions (pH value, temperature, etc.). The mathematical modeling is done in stages for the upper shelf, the lower shelf and the transitional regions.

It appears expedient to first to analyze the upper shelf behavior, i.e. $H_p > H_{p2}$. According to the relationships determined in the tests, the following model has proven suitable for the optimal description of the wear in the upper shelf region:

$$W_H = W_r / W_{r,S235} = A \cdot \exp(\lambda \cdot HB^*)$$

Here A is defined by the steel composition based on

$$A = \alpha + \sum \beta_i \cdot (C, Si, Mn....)$$

and HB^* as the hardness of the steel standardized to the range of ± 0.5 in the hardness ranges 120 to 600 HB based on

$$HB^* = \frac{HB - 120}{600 - 120} - 0,5$$

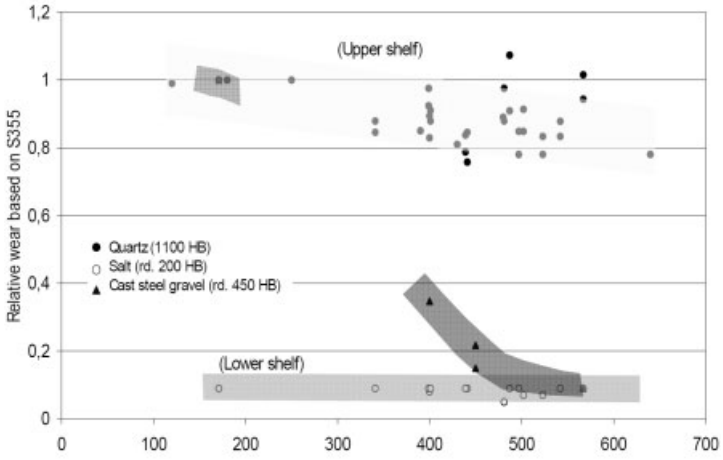


Figure 6: Influence of the hardness on the relative wear amount with impact wear.

α, β and λ are constants or coefficients; they can be calculated by multiple regression.

In the tested cases of grooving and impact wear, besides the hardness (C content), the Cr and Nb are shown to have a significant influence on the wear amount. The relative wear decreases with the addition of Cr and Nb. The Cr influence is comparatively stronger in the case of the grooving wear than with regard to impact wear. These effects can be explained metallurgically as the increase in Cr leads to a rise in the volume percentage of the carbides, with a positive effect on the reduction of the abrasive wear. Nb makes the microstructure finer so that the deformability of the wear-resistant special structural steel is increased. This leads to increased microploughing during grooving wear and increased crater formation in impact wear, i.e. to less material removal overall. In the case of the grooving wear, it can be seen that the positive Cr effect increases with decreasing pH value. With an additional corrosion-inhibiting effect [10], Cr should then have a particularly positive effect on abrasive wear resistance. Fig. 7 shows the good agreement of the measured results of the above empirical tests with the preliminary calculations for grooving and impact wear in the upper shelf region. The coefficient of determination for the relationships established is around 80 %. In the lower shelf region, i.e. $H_p < H_{p1}$, hardly any wear is incurred. Here it is expedient to use an almost constant value. Based on the empirical results, for the grooving wear, here the value

$$W_T = W_r / W_{r,S235} = 0,05$$

and for impact wear the value

$$W_T = W_r / W_{r,S235} = 0,08$$

are used.

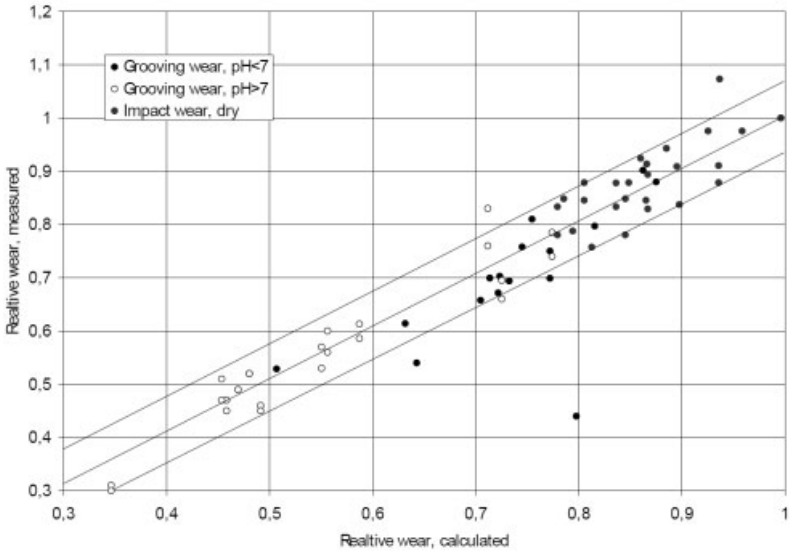


Figure 7: Comparison of measured and calculated wear (upper shelf).

In the transitional wear region, i.e. at $H_{p1} < H_p < H_{p2}$, a transitional function is defined; here mathematically the functional model

$$W = W_r/W_{r,S235} = C \cdot (1 + \tanh(D \cdot H_P))$$

can be chosen. The value of the constants C and D in this transitional equation can be determined from the conditions

$$W_H = W \quad \text{and} \quad \frac{dW_H}{dH_p} = \frac{dW}{dH_P}.$$

Depending on the formation of the upper and lower shelves and the position of the transitional points H_{p1} and H_{p2}, a corresponding transitional range with functionally smooth transitions between the lower and upper shelf regions is automatically modeled.

The equations obtained for the upper shelf region, transitional region and lower shelf region can describe in detail the wear behavior during grooving and impact wear. By combining this model with equations for calculating the mechanical properties of wear-resistant special structural steels [13], a universal integrative modeling program – ProWear – could be devised for wear-resistant special structural steels. This low-cost and time-saving software facilitates the selection and design of steels subject to an abrasive or impact wear load to meet application requirements. Fig. 8 shows the model system in a user-friendly interface on a computer.

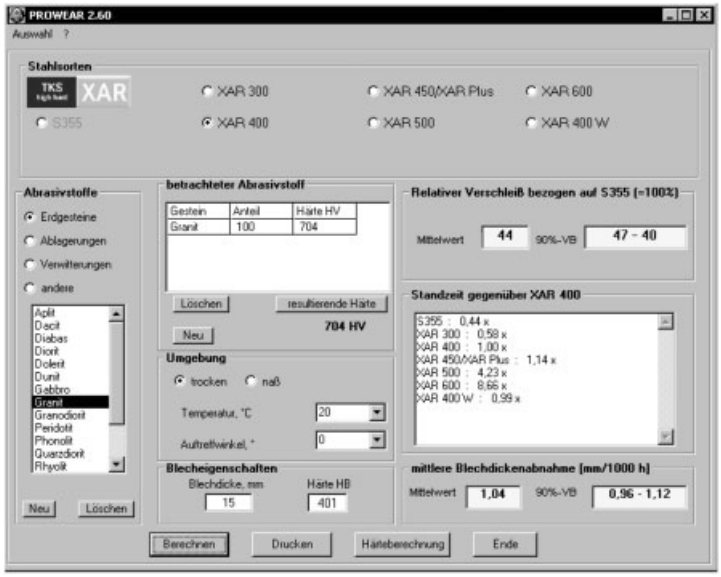


Figure 8: ProWear program interface.

5.3 Practical Modeling Applications

The system described is used as technical pilot plant both for steel production and the practical application of corresponding plates exposed to wear. It enables the determination of damage curves for the wear of different steels in the upper shelf regions.

As a result the wear of different steels relative to S355 can be determined and relative changes during service lifetimes based on material changes estimated. Influencing variables are the chemical composition of the steels, the hardness value of the counter material, the impact angle (only for impact wear) and the characterization of a wet environment based on the pH value. Fig. 9 shows model calculations for grooving wear as an example. Here the wear behavior of plates of varying hardness with a defined content of Cr and Nb is shown when exposed to wear from iron ore, feldspar and quartz in a neutral environment (pH = 7). According to this, steel with around 400 HB hardly suffers any wear (lower shelf) after attack with iron ore with around 450 HV10 (rd. 430 HB). For feldspar or quartz attack, however, an increase can be expected, which amounts to around 60 % of the wear of an S355. In addition, the model calculations enable the prediction of wear when the steels are exposed to the combined wear of more than one abrasive component with different hardness values as is often encountered in practical applications in industry.

To verify the usefulness of the modeling method in the field, data on the wear of the bodies in dump trucks used in extensive ore mines was collected, evaluated and compared with the calculations. The abrasive counter material comprised a mix of different minerals such as quartz, pyrite and feldspar. Its mean hardness is 6 on the Mohs scale (around 760 HV). Particularly interesting is wear at the hotspot of the dump body, which refers to the rear-centre section of a dumper body that is exposed to constant wear during loading and unloading of the bulk solids.

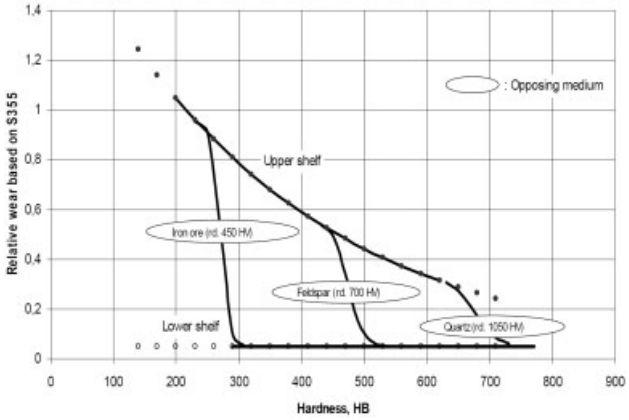


Figure 9: Wear behavior for different plate hardness values and abrasive materials (results of the pre-calculations).

Fig. 10 shows the result of a comparison between the empirically determined wear in the field test (internal TKS test results by ultrasonic measurement of the plate thickness at defined points after certain working hours) and the corresponding predictions. The wear rates calculated with ProWear largely correspond to the mean material removal rates of the dumper body in the critical hotspot (red circle). The calculation program enables a good integral analysis of the actual wear behavior of the dumper body and should therefore also prove suitable for field-oriented estimation of the behavior of real abrasive systems.

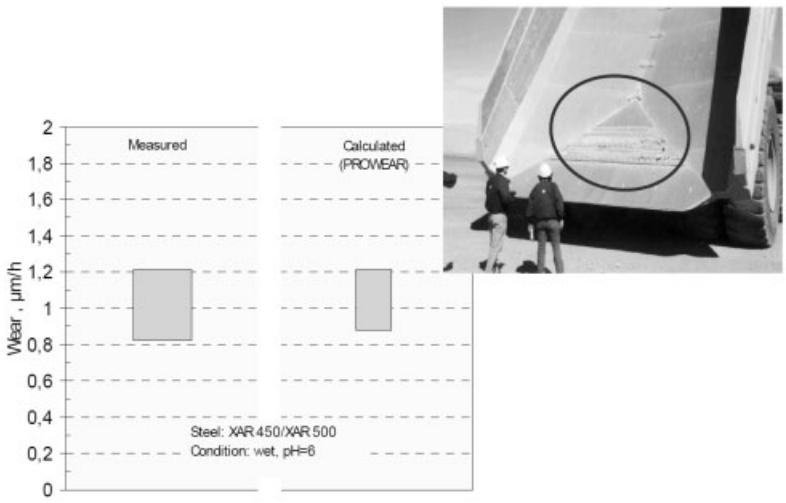


Figure 10: Comparison of measured and calculated (ProWear) values.

6 Conclusion

The present essay is about tests on the wear behaviour of wear-resistant special structural steels on grooving and impact wear. In addition, micro structural analyses provide information on the active relationship between micro structural compositions and wear resistance. The coherence between the hardness values of the plate and the abrasive counterbody is illustrated and test results are shown.

Models and methods for the mathematical simulation of the wear behavior of plates exposed to abrasion and solid-particle erosion are discussed and the ProWear simulation model for the prediction of the wear behavior developed from the results of the tests is outlined. Potential applications for the model as an aid to material selection are explained.

References

[1] Grobblech – Herstellung und Anwendung. Stahl-Informations-Zentrum, Dokumentation 570, 1. Auflage 2001

[2] Degenkolbe, J.: Thyssen Technische Berichte 25 (1993), S. 19/30.

[3] Hamme, U., Hauser, J., Kern, A. u. Schriever, U.: Stahlbau 67 (2000) Nr. 4, S. 295/305

[4] Kern, A.: Habilitationsschrift am Fachbereich 6 der TU Berlin (1997).

[5] Uwer, D. u. Höhne, H.: Schweißen und Schneiden 43 (1991) Nr. 4, S. 195/199

[6] Czichos, H.: Tribology: A systems approach to the science and technology of friction, lubrication and wear. Amsterdam: Elsevier (1978), S. 300 ff.

[7] Habig, K.-H.: Verschleiß und Härte von Werkstoffen. Hanser Verlag, München (1990)

[8] Zum Gahr, K.H.: Reibung und Verschleiß bei metallischen und nichtmetallischen Werkstoffen. DGM-Informationsgesellschaft, Oberursel (1987), S. 21/65

[9] Pigors, .O: Verschleißverhalten von Werkstoffen. VEB Deutscher Verlag für Grundstoffindustrie , Leipzig (1985), S. 92/105

[10] Pircher, H., Lendowski, H. u. Dißelmeyer, H.: Reibung und Verschleiß bei metallischen und nichtmetallischen Werkstoffen. Proc. DGM-Symposium Bad Nauheim 1986, S. 147/157

[11] Feinle, P., Kern, A. u. Schriever, U.: Heavy plate made of wear resistant special structural steels - manufacture, processing, application. Proc. Euromat ´01, München (2001)

[12] Feinle, P., Kern, A. u. Schriever, U.: Verschleißverhalten hochfester Sonderbaustähle XAR. GfT-Tagung 2006, Tagungsband II, S. 8/1–8/9; ISBN: 978-3-00-019670-6

[13] Just, E.: VDI-Berichte 256 (1976), S. 125–140

Effect of Die Material on Friction During Iron Powder Compaction

R. B. Wassenberg, M. Drygalov, P. Beiss
Institute for Materials Applications in Mechanical Engineering, RWTH Aachen

1 Introduction

During compaction of the base iron powder, which most sintered structural parts are made of, a fundamental impediment to higher densities and, thus, better mechanical properties is the friction between the powder and the tool walls. To reduce the friction, an organic solid state lubricant is mixed to the powder. The organics, however, occupy a certain volume fraction of the component which cannot be filled with metal. For this reason larger amounts of internal lubricants are prohibitive. The task during compaction is to balance the density reducing effects of tool wall friction and amount of solid state lubricant. Tool wall friction can be affected by the tool material itself. In this study dies of nominally identical dimensions and surface finish were manufactured from conventional HS12-1-4-5 steel and a powder metallurgical highly alloyed tool steel containing 1.8 % nitrogen. The nitrogen in this steel is supposed to effectively prevent or mitigate adhesive wear.

2 Background

If powder is pressed in one-sided die compaction, according to the so-called elementary theory, the pressure transmission from top to bottom is not hydrostatic because of the frictional shear stresses between powder and die wall. Fig. 1 illustrates schematically this situation for a die of cross-section Q, circumference U and total peripheral friction surface M. The equilibrium of forces for a volume element $QUdx$ is under these conditions

$$p_a Q = (p_a - dp_a)Q + \tau U dx \tag{1}$$

where p_a is the axial pressure and τ the frictional shear stress. Assuming a Coulomb friction mechanism, τ could formally be determined as the product of friction coefficient μ and radial pressure p_r. Two simple conceptual approximations can be thought of for a relationship between radial and axial pressure, firstly, with a constant pressure transmission coefficient q, the radial pressure is estimated as $p_r = qp_a$ and secondly, the radial pressure can be assumed as axial pressure diminished by the deformation resistance k of the powder mass $p_r = p_a – k$. In both cases q or k must not vary along the height of the die in order to integrate eq. 1, which is to say q and k must be pressure-independent. For the first case, $p_r = qp_a$, eq. 1 delivers with Fig. 1

$$p_{LP} = p_{UP} \exp(-q\mu M/Q) \tag{2}$$

and the second assumption leads to

$$p_{LP} = (p_{UP} - k) \exp(-\mu M/Q) + k \tag{3}$$

If powder compacts are pressed with different M/Q rations in a stationary die and the upper and lower punch forces are measured, the pressure ratio p_{LP}/p_{UP} plotted logarithmically versus M/Q should yield a straight line for the mechanism according to eq. 2 and a systematic curvature if the mechanism of eq. 3 prevails.

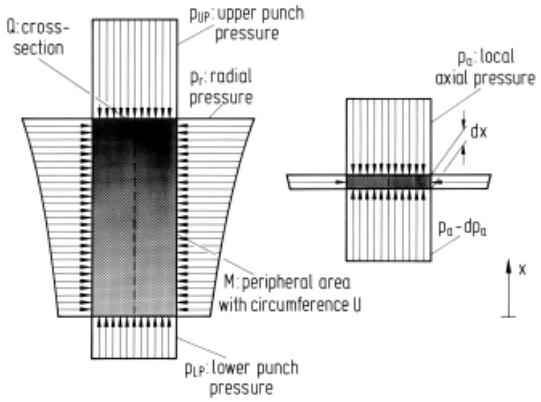


Figure 1: Pressure distribution assumed for the analysis by the elementary theory

From several investigations [1–3] it is, however, known that the radial pressure in die compaction of iron and steel powders is by no means a fixed fraction of the axial pressure and also the deformation resistance of a powder changes during compaction. For these reasons eq. 2 and 3 can at best be first approximations. In [1] radial pressures were extensively measured via radial pins through the die walls supported by load cells. For the same powder as in this investigation but with a different lubricant the radial pressures from this work are shown in Fig. 2 as depending on local axial pressure up to 800 N/mm^2. Neglecting the effect of the different type of lubricant, a relationship can easily be established between axial and radial pressures by a parabola:

$$p_r = a p_a^b \tag{4}$$

With $\tau = \mu p_r$, integrating eq. 1 yields then

$$p_{LP}^{1-b} - p_{UP}^{1-b} = (b-1) \cdot a \cdot \frac{M}{Q} \tag{5}$$

and finally

$$\mu = (p_{LP}^{1-b} - p_{UP}^{1-b})\, Q\, [Ma(b-1)]^{-1} \tag{6}$$

From Fig. 2, $a = 0.00514$ and $b = 1.7179$ up to 800 N/mm^2. As will be shown later, beyond about 800 N/mm^2 axial pressure, pure iron powder with 1 % solid state lubricant does virtually not increase further in density and, therefore, it is justified to assume a more or less constant deformation resistance for higher pressures. Beginning above 800 N/mm^2 the coefficient of friction is, thus, calculated from eq. 3 as

$$\mu = \frac{Q}{M} \ln \frac{p_{UP} - k}{P_{LP} - k} \tag{7}$$

where $k = 300\,\mathrm{N/mm^2}$ is taken from Fig. 2 as difference between axial and radial pressure.

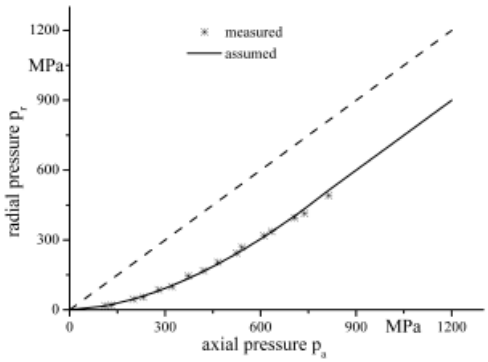


Figure 2: Relationship between radial and axial pressure during one-sided die compaction of iron powder with1 % lubricant [1]

3 Experimental procedure

The objective of this study was to see whether a steel with a very high nitrogen content has lower frictional shear stresses in powder compaction than a conventional tool steel. To this end two cylindrical compaction dies were built, one from the conventional high speed steel HS12-1-4-5 (1.3202) and the second one from the hot isostatically pressed powder metallurgical tool steel Vancron 40, which is alloyed with 3.7 % W, 3.2 % Mo, 8.5 % V and 4.5 % Cr. In addition to its carbon content of 1.1 % this steel contains 1.8 % N, making it an unusual alloy which should have the potential to counteract adhesive wear. Both steel cores were salt bath hardened and triple tempered to about 66 HRC, shrink fitted in a high carbon unalloyed steel case and ground to a cavity diameter of Ø 18 mm. Finally both dies were polished with diamond paste of grit size 3 µm to a surface finish of $R_z \approx 1$ µm.

Unalloyed water atomised pure iron powder ASC 100.29 from Höganäs AB was mixed for 20 min with the widely used solid state lubricant Kenolube P11 from the same supplier.

Compaction took place as depicted in Fig. 3: The upper punch was backed with a 50 to force transducer and connected to the stationary upper crosshead of the press. Lower punch and die were assembled to the moveable table of the press. The table was lifted against the stationary upper punch hydraulically via tie rods. A full bridge of strain gages was bonded to the cylindrical shaft of the lower punch and carefully calibrated. To vary the M/Q ratio in this arrangement, the die cavity height accepting the powder must be changeable. This was accomplished by a series of dead stops fixing the distance between lower punch foot and lower die face. For ejection the press table is lowered, the stops are removed and a slotted steel bush of sufficient length is placed around the upper punch. On lifting the die, the compact emerges from the cavity.

During the tests with five different filling heights and ten different upper punch pressures the upper and lower punch forces were registered versus the distance between die and upper punch. To each compaction ten nominally equal slugs were pressed to calculate average pressures. One

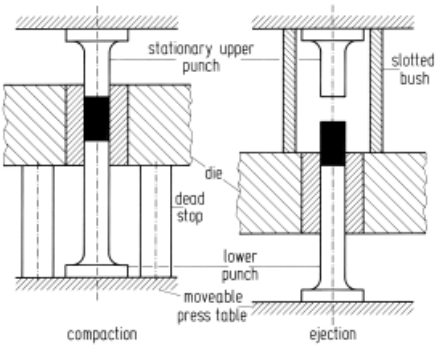


Figure 3: Experimental conditions for measurements with instrumented die

sample each was used for Archimedian density measurements according to DIN ISO 2738. The pressures ranged from 154 to 1156 N/mm^2 which covers the full industrially applied field.

4 Results

In Fig. 4 the compressibility of the powder-lubricant mixture processed here is shown for the two die materials as depending on the upper punch pressure and the M/Q ratio. Especially, below about 400 to 500 N/mm^2 the effect of the M/Q ratio is rather pronounced, short slugs having up to 0.25 g/cm^3 higher densities than longer ones. There is no clear difference between HS12-1-4-5 and Vancron 40. At pressures in excess of 600 N/mm^2 the density becomes more and more independent of the M/Q ratio. Details can be revealed from Fig. 5, where the as-compressed density is plotted versus the M/Q ratio with the pressure as parameter. The two die materials differ only negligibly with very minor advantages for Vancron 40 up to about 500 N/mm^2.

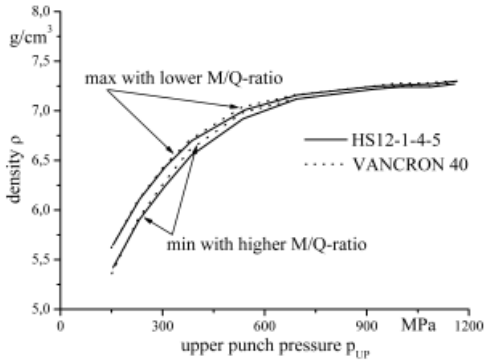


Figure 4: Compressibility of the investigated powder mix with different M/Q ratios and two different diematerials

Eq. 6 and 7 were used to calculate the coefficient of friction from the measured values of upper and lower punch pressure, M/Q ratio after compaction and radial pressure or deformation

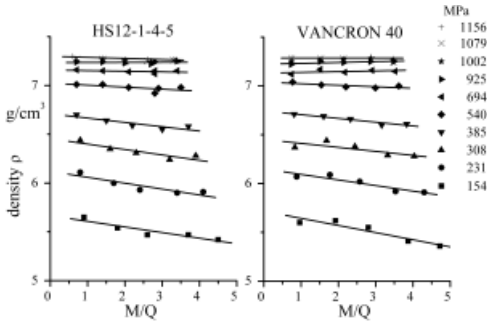


Figure 5: Density drop with increasing M/Q ratio as depicted by upper and lower limit in Fig. 4

resistance according to Fig. 2. These data are plotted as a function of upper punch pressure in Fig. 6. In order to show the strong pressure dependence, the values of the five M/Q ratios per pressure were averaged. At low pressures the coefficient of friction attains very high values, an observation which was also reported in [1]. In excess of 900 N/mm^2 a more or less constant friction coefficient below 0.1 seems to be asymptotically approached. The differences between HS12-1-4-5 and Vancron 40 are negligible. At 800 N/mm^2 upper punch pressure, where the evaluation is changed from eq. 6 to eq. 7, there is no discontinuity in Fig. 6. As mentioned before, Fig. 5 proves that the density increase and, thus, the deformation resistance growth is not of importance beyond 800 N/mm^2. Therefore the change from eq. 6 to eq. 7 at that pressure is well supported by the experimental evidence.

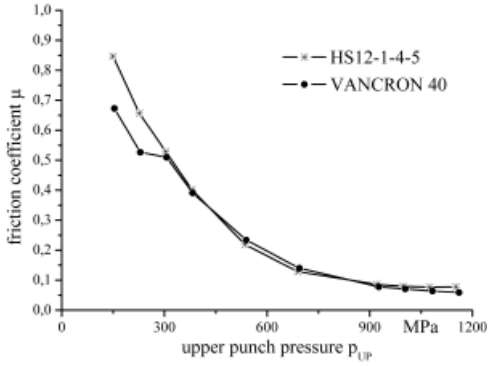


Figure 6: Dependence of friction coefficient on upper punch pressure as averages from the various M/Q ratios

In powder compaction simulations, the axial and radial pressure distribution is often approximated by eq. 2, presumably for reasons of simplicity [3]. If eq. 2 is a suitable approximation of the reality, a semilogarithmic plot of the lower punch pressure versus M/Q must give a straight line. Fig. 7 compares the results for the two dies with least square straight lines through the measured data. The slope of the lines is proportional to $-q$. Even though the deviations from

linearity are systematic for both dies up to about 700 N/mm^2 upper punch pressure, admittedly the curvature

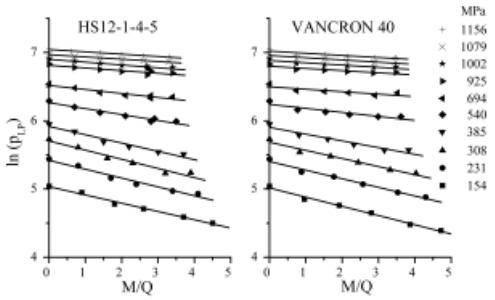


Figure 7: Semilogarithmic plot of the lower punch pressure versus M/Q

is not pronounced within the range of M/Q ratios investigated here. Therefore, as an approximation also eq. 2 may be useful, particularly at higher pressures above some 600 N/mm^2 where the difference between the coefficient of friction μ according to eq. 6 and 7 and the product qμ from eq. 2 is not very large. The drawback of eq. 2 is the fact that q and μ cannot be separated without a finite element analysis of the stress development during compaction [3].

5 Conclusions

Taking into account measured radial pressures from iron powder compaction, an elementary theory equation can be arrived at, which allows to determine coefficients of friction during the densification state only from measured data without further assumptions.

The results gave very high friction coefficients of $\mu \geq 0.5$ for an iron powder with 1 % lubricant at pressures below 300 N/mm^2 and a continuous transition to values of $\mu < 0.1$ for upper punch pressures exceeding 800 N/mm^2.

The two die steels which were compared in this investigation did not differ, within experimental error, in their friction behaviour, in spite of the extreme nitrogen content in one of the steels. Thus, the alloyed nitrogen of Vancron 40 does not reduce the coefficient of friction during compaction to any mentionable extent.

References

[1] E. Ernst: Axiale Pressvorgänge in der Pulvermetallurgie; VDI-Fortschritt-Berichte, Reihe 2, Nr. 259. VDI-Verlag, Düsseldorf, **1992**

[2] D. M. M. Guyoncourt, J. H. Tweed, A. Gough, J. Dawson, L. Pater: Constitutive data and friction measurements of powders using instrumented die. Powder Metallurgy 44 (**2001**), p. 25–33

[3] P. R. Brewin, O. Coube, P. Doremus, J. H. Tweed (Ed.): Modelling of Powder Die Compaction. Springer-Verlag London Ltd., **2008**

Adhesion Resistance of Particle Reinforced Steel Matrix Composite During Sliding Against Aluminium

D. C. Lou[a], L. O. Finnerud[b], J. K. Solberg [b], O. M. Akselsen[a], N. Dahl[a]
[a]SINTEF Materials and Chemistry, N-7465 Trondheim, Norway
[b]Norwegian University of Science and Technology, N-7491 Trondheim, Norway

1 Introduction

Abrasive wear and aluminium adhesion (sticking or galling) on tools are the common failure modes of tools in aluminium forming and machining processes [1, 2]. Abrasive wear of the bearing surface of the tools deteriorates the dimensional tolerance and surface quality of the profile [3]. Aluminium adhesion to the tool surface results in the necessity for heavy lubricants in aluminium cold forming, hot forging and machining processes [4]. Inadequate lubrication of the forming metal and tool will cause poor surface quality of the product [4]. This problem becomes severe when productivity related factors such as forming speed and thickness reduction are increased [4]. Nevertheless, lubricants are generally detrimental to the environment [5]. To improve abrasive wear and reduce aluminium adhesion on the tools, many new coating techniques, e.g. physical vapour deposition (PVD) and chemical vapour deposition (CVD) have been investigated [2–6]. Some coatings such as TiB_2 and DLC (diamond like carbon) gave promising results to reduce the aluminium adhesion, but they are often too thin (2–5μm) to withstand heavy abrasive wear during the forming process [3]. Consequently, untreated cold work tool steels or nitrided hot work tool steels are still by far the most common choice as aluminium forming tools [1, 2]. On the other hand, steel matrix composites bring new possibilities to produce extreme abrasive wear resistant materials owing to their good manufacturing properties combined with the possibility of heat treatment and low cost [7, 8]. However, so far very limited information is available on the aluminium adhesive resistance of reinforced steel composites.

In the present work, NbC, TiB_2 and WC/Co reinforced steel matrix composites were developed by a hot isostatic pressing (HIP) procedure, and the anti-adhesion properties of the composites during sliding against an aluminium alloy were investigated.

2 Experimental Procedures

2.1 Development of Materials

Hot work tool steel (H13) in powder form with particle size in the range 22–45 μm, high vanadium tool steel (CPM10V) powder with size less than 106 μm and high speed steel (HSS-ANVAL23) powder with particle size in the range 106-212 μm, all manufactured by Powdermet Sweden AB, were chosen as unreinforced steels and matrices of the composites. Their chemical compositions are shown in Table 1. NbC powder with particle size in the range 22–45 μm, TiB_2 powder with particle size less than 22.5 μm and Co-coated tungsten carbide with particle size between 22 and 45 μm, all supplied by H. C. Starck GmbH, were selected as reinforcements. The experimental unreinforced steels and composite materials were designed as shown in Table 2, and produced by

a typical hot isostatic pressing (HIP) procedure. The full mixing of the steel powders and ceramic powders were filled in capsules made of mild steel. The capsules were evacuated, sealed and put into the HIP equipment. The HIP parameters were 1180 °C and 100 MPa pressure for 3hrs.

Table 1: Compositions of unreinforced steel powders

Alloys	Elements, in wt%									
	C	Cr	Mo	V	P	Si	Mn	Ni	S	Fe
H13	0.42	5.04	1.33	1.06	<0.01	0.88	0.35	0.03	<0.01	Bal
CPM10V	2.43	5.24	1.39	9.6	<0.01	0.86	0.51		0.066	Bal
HSS	1.21	3.99	4.84	3.07	6.16W	0.25	0.27	0.9	0.017	Bal

After hipping, the materials were heat treated inside the capsules to avoid oxidation or decarburization. The heat treatment procedures were as follows: The H13 steel and its matrix composites were preheated at 850 °C for 1hr and then austenitized at 1025 °C for 1hr, followed by oil quenching. Afterwards, the materials were tempered: first at 560 °C for 2 hrs and then at 600 °C for 2 hrs. The heat treatment of steels CPM10V and HSS as well as their composites comprised preheating at 850 °C for 1hr, austenitizing at 1150 °C for 1hr prior to oil quenching. Steel CPM10V and its matrix composites were 2 + 2 + 2 hrs triple tempered at 520 °C, while steel HSS and its composites were 2 + 2 + 2hrs triple tempered at 560 °C.

Table 2: Experimental materials in this study

Material No.	Material composition	Material No.	Material composition
H13	Unreinforced H13	PM10V	Unreinforced CPM10V
H13-15NbC	H13+15vol% NbC	PM10V-15NbC	CPM10V+15vol%NbC
H13-30NbC	H13+30vol% NbC	PM10V-30NbC	CPM10V+30vol%NbC
H13-45NbC	H13+45vol% NbC	PM10V-45NbC	CPM10V+45vol%NbC
H13-15TiB_2	H13+15vol% TiB_2	HSS	Unreinforced HSS
H13-30TiB_2	H13+30vol% TiB_2	HSS-30NbC	HSS+30vol%NbC
H13-45TiB_2	H13+45vol% TiB_2	HSS-30WC/Co	HSS+30vol% (88WC+12Co in wt.%)

2.2 Materials Characterization

The unreinforced steels and the composites were characterized by optical microscopy, electron probe microanalyses (EPMA, JXA-8500F) and Rockwell hardness (HRC) testing. A total of 10 indentations were made to estimate the average hardness of each material. The bending strength and the fracture deflections of the materials were determined using a three-point bending tester with an applied load speed of 2 mm/min.

2.3 Aluminium Adhesive Test

The apparatus for the aluminium adhesive test, called pin-on-ring, has been developed at SINTEF. The pin is the test material specimen with a cross section of 14 mm × 14 mm and height of 8–12 mm. Prior to testing, the sample surface was polished to 1μm-grit. The test rings

(Ø100/135 mm × 12 mm high) were made of aluminium (AA6082), whose chemical compositions are given in Table 3. The pin was pressed against the ring with a normal force of 10 N or 30 N. The rotation speed of the ring was 200 rpm, giving a sliding speed of 1.2 m/s. No lubricant was employed in the sliding couple during the test. An attached computer recorded the friction coefficient and the real load. The time from the start of the test till the friction coefficient abruptly increased, is identified as the "*non-sticking time*", and then this time was converted to a "*non-sticking distance* (m)" to evaluate the aluminium adhesive resistance of a tool material. Three tests were normally repeated for each tool material to obtain an average result.

Table 3: Composition of aluminium ring

Alloy	Elements, in wt%									
	Fe	Si	Mg	Ca	Cu	Ti	Zn	Na	Mn	Al
AA6082	0.2	1.04	0.67	6 ppm	30 ppm	0.01	0.005	4 ppm	0.54	Bal

3 Results and Discussion

3.1 Microstructure Evaluation

Figures 1a through 1c show typical microstructures of the H13 matrix composites reinforced with 15, 30 and 45 vol % of NbC particles after hipping. Compared to the composite with 15 vol%NbC, the composite containing 30 vol%NbC particles appeared to have more uniformly distributed reinforcements, while local agglomeration of NbC particle was found around the steel matrix particles in the composite with 45 vol%, resulting in porosity or cracks (arrows in Figure 1c) due to contacts between hard, undeformable NbC, preventing densification. In Figures 1d through 1f, it is seen that the TiB_2 particles were uniformly distributed in the composite reinforced by 15 vol%TiB_2, while TiB_2 particles locally agglomerated around the matrix (H13) particles (arrows in Figure 1f) in the composites containing 30 and 45 vol%, giving rise to porosity. The 15 vol%TiB_2–reinforced composite has a relative uniform reinforcement distribution, but in the NbC-reinforced composites, the reinforcement must reach 30vol% to obtain a uniform distribution. The reason for this is that the NbC particle size (22–45 μm) was about twice that of the TiB_2 particle size (< 22 μm). The backscattered images revealed that the NbC particles were chemically stable in the steel H13 matrix composites, indicating that no new interface layer had formed. However, TiB_2 particles reacted with the H13 matrix and formed $(Fe,Cr,V)_2B$ laths and small TiC particles around the TiB_2 particle.

Figure 1g shows a typical microstructure of NbC-reinforced CPM10V matrix composite. Due to a larger size difference between the matrix and the reinforcement particles, i.e.<106 μm and 22–45 μm, the NbC particles distributed around the prior matrix particle boundaries. This was more obvious in the HSS matrix composite where the matrix particles were 106–212 μm, i.e. the continuous networks of the NbC particles and Co-covered WC particles are visible in Figures 1h and 1i, respectively. The backscattered images in previous work [9, 10] demonstrated that the NbC particles were chemically stable in the CPM10V matrix composites, and in the HSS matrix composites, but that the original carbides in the HSS matrix were dissolved in the vicinity of NbC

particles. The outer parts of the Co-covered WC reinforcements in the HSS matrix composite had dissolved significantly, and a new interface layer (M_6C, M=W, Co and Cr) had formed [9].

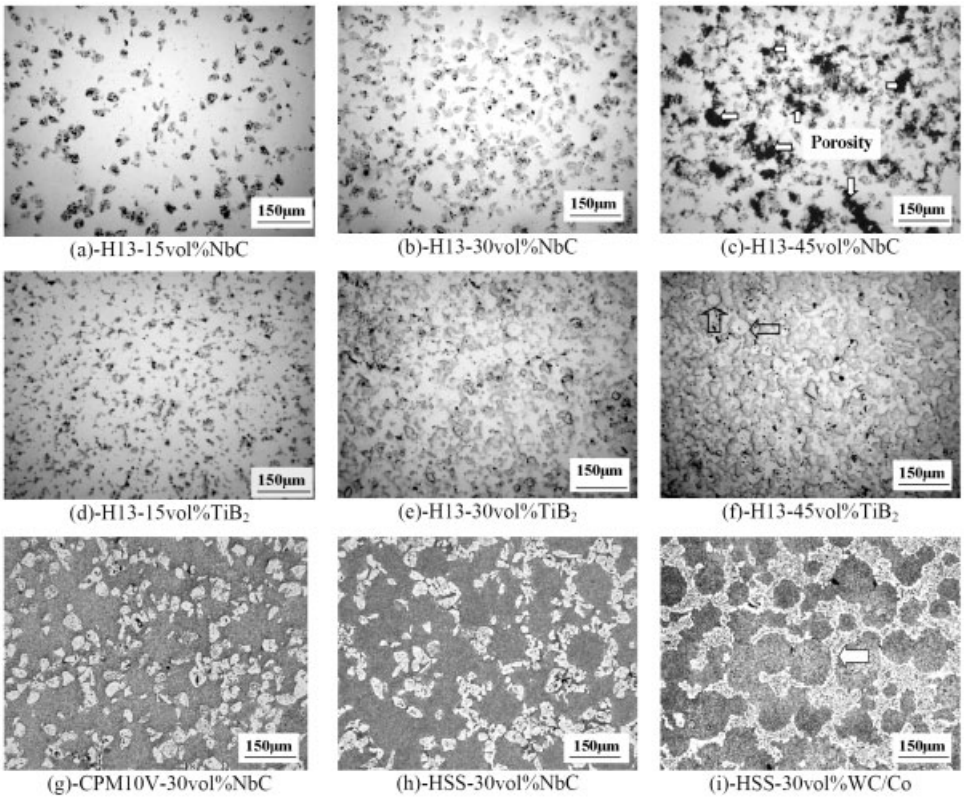


Figure 1: Optical microstructure showing the distribution of reinforcements in typical composites.

3.2 Mechanical Properties

It is seen from Table 4 that the hardness of NbC-reinforced H13 matrix composites increases with increasing reinforcement fraction from 15 to 30 vol%. However, the hardness of the composite dropped to the same value as that of the unreinforced steel H13 when the NbC reinforcements increased to 45 vol%. This is perhaps due to the presence of a larger amount of porosity or cracks in the 45 %NbC-reinforced composite (see Figure 1 c). The H13 matrix composites reinforced by 15 and 30 vol%TiB_2 exhibits abnormal behaviour, i.e. their hardness levels were lower than that of unreinforced steel H13. Nevertheless, the hardness of the composite containing 45 vol%TiB_2 reached the same hardness value as the composite reinforced by 30 vol%NbC. The lower hardness of the composites containing 15 and 30 vol%TiB_2 may be attributed to transformation into some amounts of non-martensitic constituents during quenching (further investigation is needed).

The NbC-reinforced CPM10V matrix composites exhibited a substantial increment when the amount of reinforcement was increased form 15 to 30 vol%, and a much smaller increment from 30 to 45 vol%. This may imply that the optimum reinforcement fraction is 30 vol%NbC. The hardness of the 30 vol%NbC-reinforced HSS and the 30 vol%WC/Co-reinforced HSS composites was higher than that of the unreinforced HSS steel.

Table 4 also shows that the bending strengths and fracture displacements of the composites were substantially decreased with an increased reinforcement fraction. In general, NbC-reinforced H13 matrix composites possess high bending strength and fracture displacements compared to the corresponding composites with the same volume fraction of TiB_2.

Table 4: Results of hardness measurement and three-point bend test

Material No.	Hardness (HRC)	Bending strength (MPa)	Bending displacement (mm)	Material No.	Hardness (HRC)	Bending strength (MPa)
H13	50.1	1678	3.889	CPM10V	62.5	2055
H13-15NbC	51.8	1107	0.574	CPM10V-15NbC	63.8	1209
H13-30NbC	56.5	611	0.270	CPM10V-30NbC	66.8	791
H13-45NbC	49.3	296	0.190	CPM10V-45NbC	68.0	526
H13-15TiB_2	25.5	494	0.276	HSS	62.9	
H13-30TiB_2	46.8	413	0.222	HSS-30NbC	67.5	
H13-45TiB_2	57.2	333	0.174	HSS-30WC/Co	69.0	

3.3 Resistance Against Aluminium Adhesion

Figure 2a shows that, among the NbC-reinforced H13 matrix composites, the longest sliding distance without the presence of aluminium adhesion was found in the composite containing 30vol%NbC for both test loads 10N and 30N. This might be attributed to the relatively uniform distribution of NbC particles, as shown in Figure 1b. However, an uneven NbC distribution in the 15vol%NbC-reinforced H13 matrix composite and a lot of pores or cracks existing in the H13 matrix composite containing 45vol%NbC are perhaps the main reasons for aluminium readily sticking to these materials, particularly at the higher test load. The effect of volume fraction of TiB_2 on the aluminium sticking resistance of TiB_2-reinforced H13 matrix composites is unambiguous. In addition, no evident improvement in the adhesion resistance was found by adding TiB_2 reinforcement to the H13 steel. This result does not conform to the result obtained on TiB_2 PVD coated H13 steel [6].

In the present work, it is generally demonstrated that NbC-reinforced H13 matrix composites have higher aluminium adhesion resistance than TiB_2-reinforced composites. In particular this is the case for 30vol%NbC-reinforced composite.

For NbC-reinforced CPM10V matrix composites (Figure 2b), the optimum added fraction of NbC particles proved to be 30vol% in order to obtain a high aluminium sticking resistance regardless of the test load. Among the HSS matrix composites, 30vol%NbC-reinforced HSS matrix

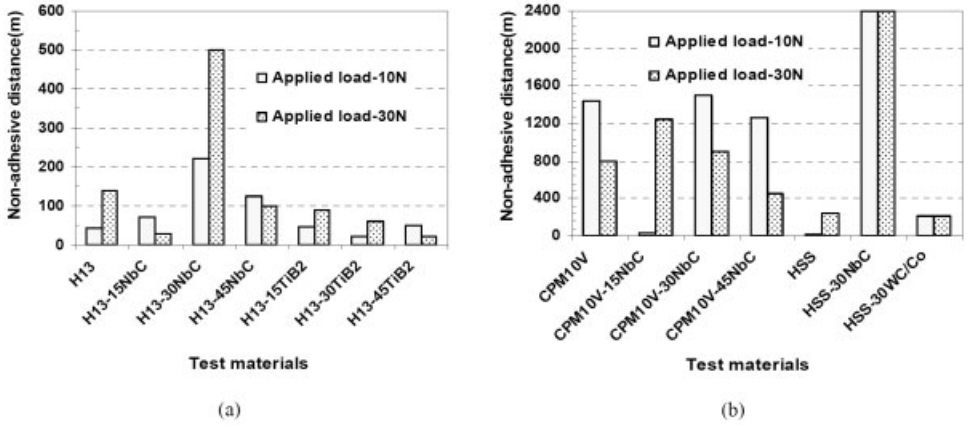


Figure 2: Aluminium sticking resistance of the different materials and applied loads.

composite showed the highest aluminium adhesion resistance. WC/Co-reinforcement of steel did not give any improvement, which correlates with the high aluminium adhesion on cemented carbides (92wt%WC+8wt%Co) [6]. In addition, although the reinforcement distribution was similar (Figures 1f and 1g), the NbC-reinforced HSS composite has much higher aluminium adhesion resistance than WC/Co-reinforced composite.

It is worth noting that there is no relationship between the aluminium sticking resistance and the hardness for neither the unreinforced steels nor their matrix composites.

4 Conclusions

The results of the present investigation can be summarized as follows:

- NbC particles were stable in the H13, CPM10V and HSS steel matrix composites. TiB_2 particles reacted with the H13 matrix and formed laths of $(Fe, Cr, V)_2B$ and small TiC particles. Co-covered WC particles were partly dissolved in the HSS matrix.
- The hardness of the composites increased with increasing the amount of reinforcement to a certain extent, depending on the size ratio of the reinforcement and the matrix powder.
- The bending strength and fracture deflections of the composites were substantially lower than those of the unreinforced steels. No relationship between the aluminium adhesion resistance and the hardness of the composites was found.
- 30vol%NbC reinforced H13 composite had a better aluminium adhesion resistance than TiB_2 reinforced H13 composites.
- 30vol% NbC-reinforced HSS matrix composite has the best aluminium adhesion resistance under the present test conditions.

5 References

[1] Saha P.K., Wear **1998**, *218*, 179–184.

[2] Konca E.; Cheng Y.-T.; Weiner A. M.; Dasch J. M.; Erdemin A.; Alpas A. T., Surf. Coat.Technol. **2005**, *200*, 2260–2270.

[3] Bjork T.; Bergstrom J.; Hogmark S., Wear **1999**, *224*, 216–225.

[4] Murakawa M.; Koga N.; Kumagai T., Surf. Coat. Technol. **1995**, *76–77*, 553–558.

[5] Nishimura T.; Sato T.; Tada Y., J. of Mat. Pro. Technol. **1996**, *62*, 235 –241.

[6] Gerge M.; Hogmark S., Hogmark, Surf. & Coat. Technol. **2002**, *149*, 14–20.

[7] Pagounis E.; Talvitie M.; Lindroos V. K., Metall. Mat. Trans. A **1996**, *27*, 4171–4181.

[8] Lou D.C.; Hellman J.; Akselsen O.M.; Lindroos V.K.; 44th Mechanical Working &Steel Processing Conference, Orlando Resort, Florida, USA, Sept.8-11, **2002**, *vol.XL* 1211–1220.

[9] Lou D.C; Hellman J.; Luhulima D.; Limatainen J.; Lindroos V. K., Mat. Sci. Eng. A **2003,***340*, 155–162.

[10] Lou D.C.; Solberg J.K.; O.M. Akselsen; Dahl N., Key Eng. Mat. **2007**, *334–335*, 21–24.

Graded Layers for Wear and Corrosion Protection Produced by Laser Cladding

A. Weisheit, K. Wissenbach
Fraunhofer Institut Lasertechnik, Aachen

1 Introduction

Graded materials offer the potential to combine various properties such as wear resistance, corrosion resistance, strength and ductility which are difficult to achieve in a bulk material. These materials are especially of interest for components which are exposed to complex operational conditions, e. g. die casting or injection moulding tools. Such tools are exposed to wear (due to friction), corrosion (due to reactions with the molten metal or polymer) and fatigue (due to thermal cycling) [1]. Layers of graded materials can help to improve the performance and life time of these tools which would be an important cost saving factor.

A method to produce graded layers is multi-layer cladding with powder additive materials. The graded materials are formed in-situ layer by layer with a continuous change of the composition in each layer. Some approaches for the production of graded layers or graded bulk volumes are documented in the literature [2-5]. This paper reviews the research on graded layers for injection moulding tools produced by laser cladding using powders as additive material. Graded layers on the basis of Fe and Ni were developed aiming at the improvement of wear and corrosion resistance as well as thermal shock resistance. Graded materials based on Fe were also cladded on a Cu substrate using a bonding layer based on Fe/Ni or Ni alloys. The layers were characterised by metallographic investigations and hardness measurements. Since laser cladding is a near-net-shape technology the layers have to be machined to the final dimensions. Typical methods used in the tool making industry like milling, grinding, electric discharge machining (EDM) and polishing were tested. The thermal shock resistance and the wear and corrosion properties of the layers were investigated in special test equipment.

2 Process Engineering for Laser Cladding of Graded Layers

During laser cladding [6] the additive material and a thin layer of the base material are melted by the laser beam. After solidification a dense layer with a metallurgical bonding to the substrate is produced. Larger areas are cladded with overlapping tracks. The additive material can be provided either as powder or wire. Using powder is more flexible regarding the process (especially 3D cladding) as well as the choice and combination of materials. The typical layer thickness is 0.1 to 2 mm. Thicker layers can be produced by multi-layer cladding. The deposition rate of laser cladding is smaller then for classic build-up welding techniques like PTA. However, laser cladding features a higher precision and a low heat input into the substrate. It is therefore sophisticated for a local treatment. Laser cladding is established in industry as a process for repair e. g. for injection tools [1] or aero engine components [7].

The experiments were carried out with a fibre coupled Nd:YAG laser (λ = 1063 nm). For powder feeding a coaxial powder feed nozzle was used. Cladding of steel substrates is done with a vertical incidence of the laser beam. In case of copper substrates the cladding head is tilted (20 °) to avoid back reflections into the beam path which might damage optical components [7]. The graded layers are produced in-situ by using two powder feed hoppers containing powder A and B. To produce a graded layer the feed rate of the hoppers is altered from layer to layer, e. g. starting with 100 % A in the bottom layer and ending with 100 % B in the top layer. Table 1 shows the main process parameters for laser cladding for two different beam diameters.

Table 1: Process parameters for laser cladding of the graded layers

Parameter	$d_{beam} \approx 2$ mm	$d_{beam} \approx 1$ mm
Laser power, P	1–1.3 kW substrate steel 1–3 kW substrate Cu	0.5–0.8 kW substrate steel 0.8–1.5 kW substrate Cu
Velocity, v	0.5 m/min	0.5 m/min
Track offset, Δy	1.1 mm	0.6 mm
Carrier gas flow, mPF (Argon)	5 l/min	5 l/min
Coaxial shielding gas flow, mSG	20–30 l/min	20–30 l/min
Layer offset for multi-layer cladding, Δz	0.3-0.5 mm	0.2–0.3 mm
Final layer thickness (5 single layers), d	approx. 2 mm	approx. 1 mm
Overall powder feed rate, mP	1–4 g/min	0.5–2 g/min

3 Materials

As substrate materials plates of the hot working steel X 38 CrMoV 5-1 and the copper alloy Cu2.5Ni0.7Si0.4Cr are used (thickness 10 -15 mm). Both alloys are commonly used for injection moulding tools. The additive materials used are listed in Table 2. The NiCrBSi-alloy Deloro 60, the aluminium bronze CuAl10 and Fe33Ni were only used for copper substrates.

4 Results and Discussion

4.1 Microstructure and Hardness of the Graded Layers

The developed graded layers are listed in Table 3. The alloy X 38 CrMoV 5-1 is the most important alloy for die casting tools and injection moulds. Improvement of wear resistance is expected when the precipitation of hard carbides (VC) is increased (graded material 1 and 4, Table 2). The alloy X 42 Cr 13 is also used in the tool industry. It features a higher corrosion resistance than X 38 CrMoV 5-1 but contains only Cr as carbide former. The addition of the alloy CPM 420 V should increase the wear resistance (graded material 2 and 3, Table 2). On steel substrates crack free layers can be produced up to a hardness around 60 HRC.

Copper alloys like Cu2.5Ni0.7Si0.4Cr are used in the injection moulding industry especially for mould cores where high heat conductivity is needed to reduce the cycle time. However, the wear and corrosion resistance of these alloys is inferior to that of hot working steels. Since cladding of steel onto copper substrates leads to an inhomogeneous transition zone due to incomplete mixing of molten Fe and Cu a bonding layer has to be cladded first. For these investigations

Table 2: Additive materials for the cladding of graded layers on steel and copper substrates

Alloy	C	Cu	B	Al	Si	Mn
X38 CrMoV5-1 (1.2343)	0.36-0.42	-	-	-	0.9-1.2	0.3-0.5
X42Cr13 (1.2083)	0.38-0.45	-	-	-	< 1	< 1
VC	9	-	-	-	-	-
CPM 420 V	2.3	-	-	-	-	-
Deloro 60 (NiCrBSi)	0.7	-	3.1-3.5	-	2-4.5	-
CuAl10	-	Bal.	-	10	-	-
Fe33Ni	-	-	-	-	-	-

Alloy	Cr	Mo	V	Ni	Fe
X38 CrMoV5-1 (1.2343) 4.8-5.5	1.2-1.4	0.25-0.5	1.2-1.4	Bal.	
X42Cr13 (1.2083)	12.5–13.5	-	-	-	Bal.
VC	-	-	Bal.	-	-
CPM 420 V 14	1	9	-	Bal.	
Deloro 60 (NiCrBSi)	14–15	-	-	Bal.	4
CuAl10	-	-	-	-	-
Fe33Ni -	-	-	-	33	Bal.

the alloy Fe33Ni was chosen. The graded layer of CuAl10 and Deloro 60 is intended to improve corrosion and wear resistance in combination with higher heat conductivity than for Fe-based alloys (graded material 5, Table 2). On Cu substrates crack free layers can be produced up to a hardness of only 50 HRC due to the difference in thermal expansion between Cu and Fe (Ni) which generates high thermal stresses during cooling.

As an example the graded layer X 42 Cr 13 + CPM 420 V is described in more detail. Figure 1 shows the cross section of the graded layer. The layer is free of pores and cracks. Three regions can be distinguished in the layer. In the upper region (layer 4 and 5) an equiaxed microstructure has formed (Figure 1). The concentration of Cr and V in the grain boundaries is significantly higher than in the grains which indicates that carbides have preferred precipitated in the grain boundaries. In deeper regions of the graded layer the content of Cr and V decreases which leads to less formation of carbides and some amount of martensite formation in the third layer. The first two layers have transformed almost completely into martensite. The martensite is tempered by the heat input during cladding of the subsequent layers. The decrease of Cr and V from top to bottom in the whole graded layer is verified in the EDX line scan shown in Figure 1. The hardness profile shown in Figure 1 is in good correlation with the above described microstructure. From bottom to top the hardness increases due to the increased formation of carbides.

Table 3: Graded layers; Substrate: A = X 38 CrMoV 5-1, B = Cu2.5Ni0.7Si0.4Cr

No.	Sub-strate	Bonding layer	Graded material		Average hardness on the surface	
			Comp. A	Comp. B	HV 0.3	HRC
1	A	none	X 38 CrMoV 5-1	X 38 CrMoV 5-1 + 5 wt.-% VC	830	65
2	A	none	X 42 Cr 13	CPM 420 V	780	63
3	B	Fe33Ni	X 42 Cr 13	CPM 420V	650	58
4	B	Fe33Ni	X 38 CrMoV 5-1	X 38 CrMoV 5-1 + 5 wt.-% VC	500	49
5	B	none	CuAl10	Deloro 60 (NiCrBSi alloy)	650	58

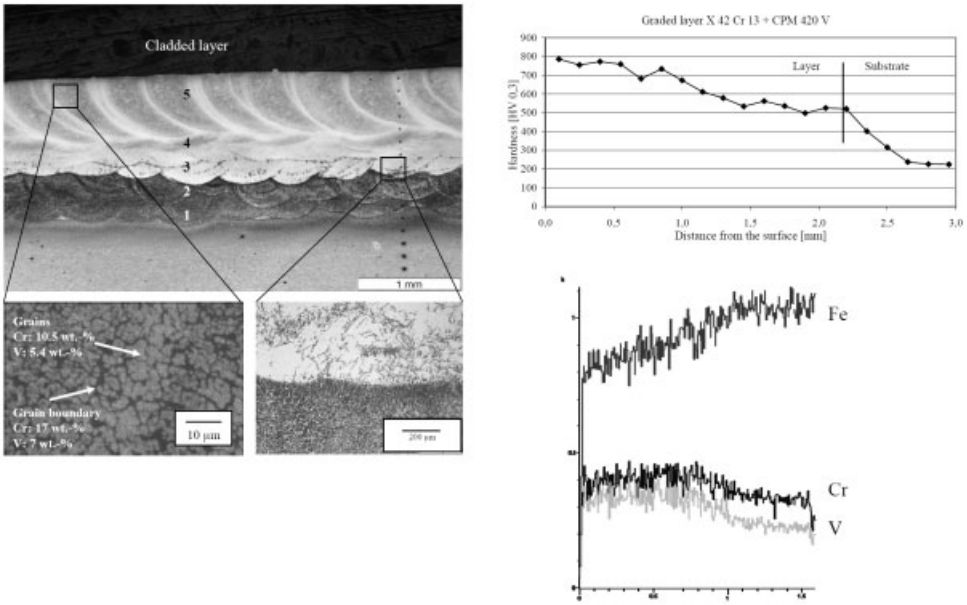


Figure 1: Left: Micrographs of the graded layer X 42 Cr 13 + CPM 420 V, substrate X 38 CrMoV 5-1 (annealed); Top left: overview; Down left: top layer with equiaxed grain structure; down right: transition zone between layer 2 and 3, dark phase martensite; Top right: Hardness profile across the graded layer; Down right: EDX Line scan across the layer top left

4.2 Machining of the Graded Layers

The machinability of the graded layer is an important criterion for the use of these layers for moulds and tools. The above described layers were tested with the following machining techniques which are commonly used in the tool industry: milling, grinding, EDM and polishing (Table 1). All graded layers can be machined without problems except the layer X 38 CrMoV 5-1 + (X 38 CrMoV 5-1 + 5 % VC) which shows some ripple formation after polishing. The ripples are due to local differences in hardness caused by annealing of the martensite in preceding tracks during cladding of the subsequent track.

Table 4: Evaluation of machining of various graded layers, composition see Table 3

Graded layer	1,4	2,3	5
Hardness (HRC)	58-60, 61-65	49-52, 62-64	60-62
hline EDM	good	good	good
Grinding	bad (ripple formation)	good	good
Milling	good	good	good
Polishing	bad (ripple formation)	good	good

4.3 Thermal Shock Resistance

Thermal shock resistance was tested in a special test rig simulating typical condition (Tmax = 500°C, duration per cycle 2 s) of the injection moulding process [7]. After 2000 cycles the samples were investigated regarding cracks (dye penetration test), microstructure and hardness. No cracks were found in the layers and none of the graded layers showed any change in microstructure or hardness compared to the as-clad condition.

4.4 Wear and Corrosion Resistance

Wear and corrosion were investigated in a test apparatus especially designed for the injection moulding process. Two test samples are placed opposite to each other leaving a small gap (0.2 mm) in between. The molten plastic is flowing through this gap (for details see [7]). Some test conditions are listed in Table 5.

Table 5: Selected conditions for the injection moulding test

Parameter	Value
Plastic	Ultramid A3WG7 (PA66 + 35% glass fibres)
Temperature range of moulding material	255-270 °C
Injection time	6 s
Cycle time for single shot	28 s
Volume for single shot	50 cm3
Flow rate	40 kg for each pair of test samples, approx. 1200 shots
Sample size	15x12x5 mm^3

As moulding material a plastic with additions of 35 % glass fibres is chosen. The glass fibres generate severe abrasive wear conditions. The wear measuring quantity is the weight loss of the test samples after 1200 shots. The tested layers are listed in Table 3.

The results of the wear tests of the layers cladded on the copper substrate are shown in Figure 2. For the Fe-based alloy similar results were obtained for the layers cladded on the steel substrate. The weight loss for the Fe-based layers is lower than for a nitrided steel 34 CrAlNi 7 which has a surface hardness of approx. 1000 HV. Only ceramic materials like Al2O3 are superior. The surface of the samples after the test show deeper grooves than the virgin layer (Figure 3). The grooves also indicate that the wear mechanism is mainly abrasion due to the glass fibres. No indications for corrosion could be found. The Ni-based graded layers show a higher weight loss probably due to less formation of hard precipitations and also corrosion.

5 Summary

Graded layers on the basis of Fe- and Ni-alloys were developed for applications in the tool making industry. The graded materials are formed layer by layer with a continuous change of the composition in each layer using the technology of laser beam cladding with powder feeding. The composition of the graded layers aims at the improvement of wear and corrosion resistance as well as thermal shock resistance. Depending on the composition a surface hardness up to 65 HRC can be achieved. The layers on steel substrates are crack free up to 60 HRC. The graded

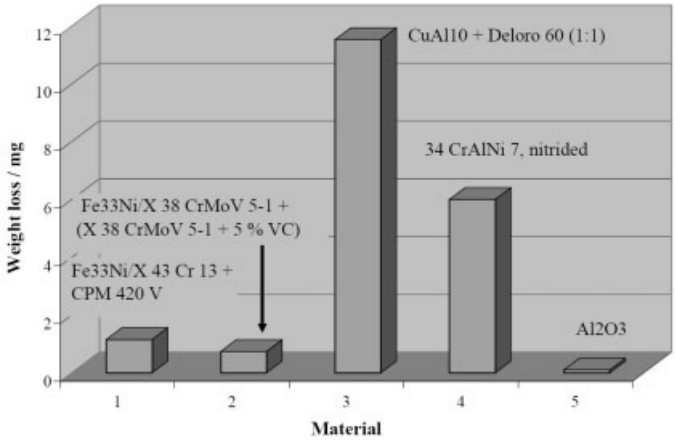


Figure 2: Weight loss of various coatings after testing in a special test apparatus for injection moulding; parameters see Table 5

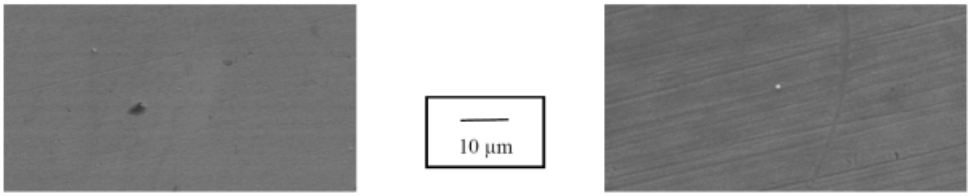


Figure 3: Surface of test samples of the graded layer X 38 CrMoV 5-1 + (X 38 CrMoV 5-1 + 5 wt.-% VC) before (left) and after the wear test (right)

materials can also be clad on a Cu substrate using the bonding layer Fe33Ni. The hardness should be limited to values around 50 HRC to ensure crack free cladding. Machining of the materials using milling, grinding, EDM and polishing was proved. A thermal shock test and a wear test process have shown promising results regarding the applicability of the various graded layers for the injection moulding process.

6 References

[1] Eimann, K. et al, Instandsetzung von Werkzeugen mit Laserstrahlung, in: Tagungsband Aachener Kolloquium Lasertechnik AKL 2000, 29–31 Mai 2000

[2] Ouyang, J.H.; Mei, H.; Kovacevic, R., Rapid prototyping and characterization of a WC-(NiSiB alloy) ceramet/tool steel functionally graded material (FGM) synthesized by laser cladding, Proc. Materials Solution Conference, TMS Fall Meeting, 2002, 77–93

[3] Theiler, C.; Sepold, G., Laser generation of functionally graded layers, Proc. Int. Conf. Metal Powder Deposition for Rapid Manufacturing, 2002, San Antonio, US, 216–224

[4] Abboud, J.H.; West, D.R.F.; Rawlings, R.D., Microstructure and Properties of Laser Produced Ti-Al Functionally Gradient Clad, Mat. Sc.Tech., Band 10 (1994) 10, 848–853

[5] Ditlhey,U.; Balachov, B.; Kabatnik, L., Processing and Characterization of Graded Aluminium Components with High Hardness and Improved Wear Behavior Using Plasma Transferred Arc Welding (PTA) Processes, Proc. Conf. Functionally Graded Materials 2000, American Ceramic Society, 151–158

[6] Poprawe, R., Oberflächentechnik, Beschichten, in: Lasertechnik für die Fertigung, Springer-Verlag, 2005, 191–197

[7] Weisheit, A., Bankowski, M., Fuchs, E., Freyer, C., Multifunktionale Gradientenwerkstoffe für den Werkzeugbau, Abschlussbericht, BMBF-Vorhaben 03N5045, 2006

Acknowledgement: The work presented in this paper was funded by the ministry for education and research BMBF of the German government. The authors also would like to thank the following project partners for their contributions: Braun, Gentner, Preh, ae group, Eifeler Lasertechnik, TLS and DKI.

The Influence of Induction Hardening on the Impact Wear Resistance of Compacted Graphite Iron

T. Slatter, R. Lewis
The University of Sheffield, Sheffield U.K.
M. Broda
Ford Forschungszentrum Aachen GmbH, Aachen, Germany

1 Introduction

Regardless of the continuing development and improvement of internal combustion engines, the wear of components still occurs. The current focus on new materials and processes as a mechanism for improvement also means that previously unseen or insignificant problems can appear. Of particular importance, and the driver for this work, is the wear of the valve, valve seat insert (VSI) and cylinder head contacts. The wear of these components promotes incomplete combustion and can cause exhaust gas emissions to rise and economy to fall. Even in situations where these components themselves have not changed significantly, the operating conditions may have altered, which can also promote wear. A particular example of this is the increase of in-cylinder peak combustion pressures in diesel engines. These elevated pressures are reaching the strength limits of aluminium cylinder heads prompting research into the use of different materials such as compacted graphite iron (CGI).

The use of newer, or just different, materials, in components opens up avenues of research to improve their performance. CGI has been used in relatively simple components, such as crank dampers, but it is only in recent years that it has been investigated for use in components that require subtle control of their microstructure. As a consequence, there is little literature on the influence of common treatment processes, such as induction hardening, on the mechanical properties of CGI.

2 Background

2.1 Compacted Graphite Iron (CGI)

In general the properties of CGI, also known as vermicular cast iron, lie somewhere between those of grey cast iron and ductile (or nodular) cast iron. It retains the castability of grey cast iron but has some of the ductility and strength of ductile cast iron. Historically, the predominant driver for the development of CGI has been that for weight reduction and up to a 10 % reduction can be typically achieved when compared to grey cast iron. Many components can be redesigned to use less material whilst maintaining, or improving, their mechanical performance. Even though CGI is 3.5 times denser than aluminium, the strength of CGI means components can be smaller and a complete engine can weigh a similar amount than one made from aluminium [1]. More recently, the focus has shifted towards using CGI to accommodate ever increasing combustion pressures whilst maintaining existing engine weights and packaging requirements. In modern direct injection turbo diesel designs the peak combustion pressure can reach over 200 bar, which

is towards the upper limit of the ability of grey cast iron and aluminium to withstand cylinder bore distortion.

Like ductile cast iron, the production of CGI relies on close control of the casting process and the careful addition of alloying elements to control the microstructure. The development of CGI components that require tight microstructural tolerances or require substantial machining has been difficult. For example, the successful and reliable formation of CGI is extremely dependent on the amount of magnesium in the material and can change the mechanical properties of the material by up to 40 %. The predominant characteristic is the presence of individual "graphite worms" that connect to their nearest neighbours to form a coral-like structure that gives CGI its superior mechanical properties. The combination of rounded edges and irregular surfaces create strong adhesion between the graphite and iron and restrict the initiation and growth of cracks.

2.2 Induction Hardening

Induction hardening is a widely used heat treatment process that involves using a large alternating electromagnetic field to rapidly heat the material into its transformation temperature range. This is followed by quenching and produces a hardened, but more brittle, outer layer surrounding an unchanged core of material. It can be controlled closely to produce locally hardened parts with a minimal amount of thermal distortion and works particularly well with ferrous metals with 0.4–0.45 % carbon. The properties of CGI lend themselves to induction hardening but there is little literature to suggest much work has been carried out in this field.

3 Experimental Details

Previous work [2] has developed a test rig designed to provide assessment of the ability of a particular material to resist wear due to impact and is shown in Figure 1. It is driven and controlled by a 1.1 kW electric motor and cam/spring system. The cam is from a production 2.4 litre D.O.H.C. diesel engine and acts directly onto a hardened flat present on the arm. Acting directly opposite the cam, on another hardened flat of the arm, is a stainless steel compression spring which recoils against the arm in hardened steel follower. The springs are easily interchangeable to vary the impact energy and closing speed of the striker. The closing velocity can also be varied by changing the clearance between the cam nose and the follower. Although the rig can operate at high speed the actual loads on the cam, spring and bearings are relatively low, so lubrication consists of light grease on the bearings and periodic applications of oil to the cam surface and spring/follower sliding contacts. The rig is predominately mild steel in construction; notable exceptions being the arm (silver steel for strength and hardness) and striker block (aluminium to reduce the mass at the end of the arm). The bearings that support the arm axle and the camshaft are of the steel single row radial ball type.

Throughout this work, a 15 mm diameter 400 series stainless steel ball bearing was used as the striker and nominally strikes the test specimen at 10 Hz. This can be altered by changing the pulley ratios or by using a speed controller. The specimen is retained in position by a two-part specimen holder and is nominally presented normal to the striker. Although not used in this work, different specimen holders have been developed to present an angle to the striker (to induce a small amount of sliding into the contact) and also to heat the specimen. The specimens are small discs, 50 mm in diameter and 10 mm thick, all of the same composition. A custom inductor was

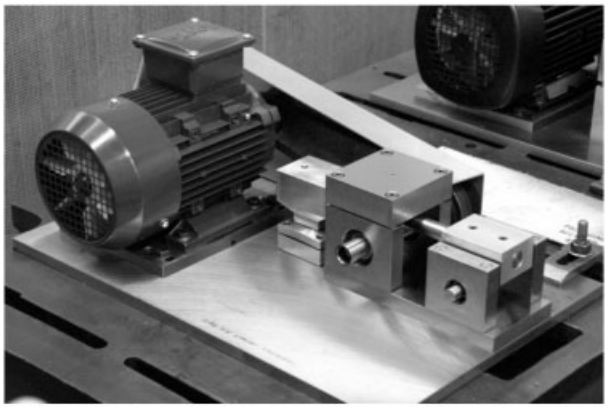


Figure 1: Impact wear test rig

manufactured to suit the specimens and all specimens were treated equally, the only difference being the nominal hardness depths of 2 mm and 3 mm.

4 Experimental Results

The typical properties of the specimens can be seen in Table 1.

Table 1: Specimen properties

Property	Value	Property	Value
Nodularity	5 %–15 %	Ultimate Tensile Strength	65 MPa
Pearlite	96 %	Yield Strength	57 MPa
Ferrite	3 %	Elongation	1 %–2 %
Carbide	Trace – 0.5 %		

Before any testing was performed, hardness measurements were taken of the specimens. The surface hardness of the untreated specimens was taken and assumed to be uniform throughout. For the induction hardened specimens, a sample was taken and the hardness was measured at 0.5mm depth intervals. The hardness of the untreated specimens was assumed to be uniform. The results can be seen in Figure 2.

All of the specimens were tested over a number of impacts ranging from 4500 to 72000 and a new specimen was used for each test. An example of a worn specimen is shown in Figure 3. The wear scar is the small light grey circle, typically 2mm in diameter, in the centre of the 50 mm disc. The coloured concentric rings are a product of the hardening process.

After each test, three the diameter of the wear scar was measured three times using an Engineer's microscope. Then three profiles across the diameter of the scar were recorded using a profilometer. The averages of these measurements were plotted against the total number of impacts and can be seen in Figure 4. Each data point is derived from an individual test on a unique specimen rather than a series of in-test measurements on the same specimen.

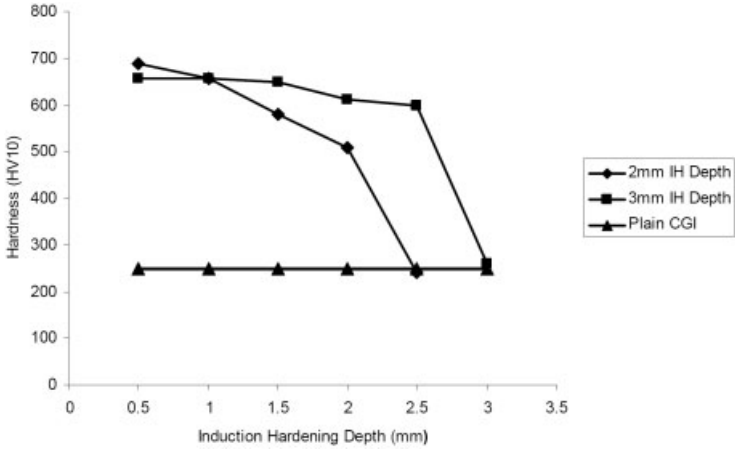


Figure 2: Measured hardness through the specimen

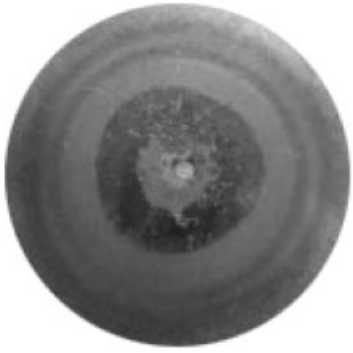


Figure 3: Example of a worn hardened specimen

As the total mass lost is very small when compared to the specimen mass it is difficult to measure. Also, some material may be displaced rather than removed. To calculate the wear volumes, the wear scars were modelled to be spherical caps using the data derived from the profiles. These volumes were plotted against the total number of impacts and can be seen in Figure 5.

5 Discussion & Conclusions

The results clearly show that induction hardening has a positive effect on the impact wear resistance of compacted graphite iron. It is interesting to note that the specimens that were hardened to a nominal depth of 2 mm performed better than those nominally hardened to 3 mm. This indicates that the depth of hardening should be optimized to obtain the desired hardening effect.

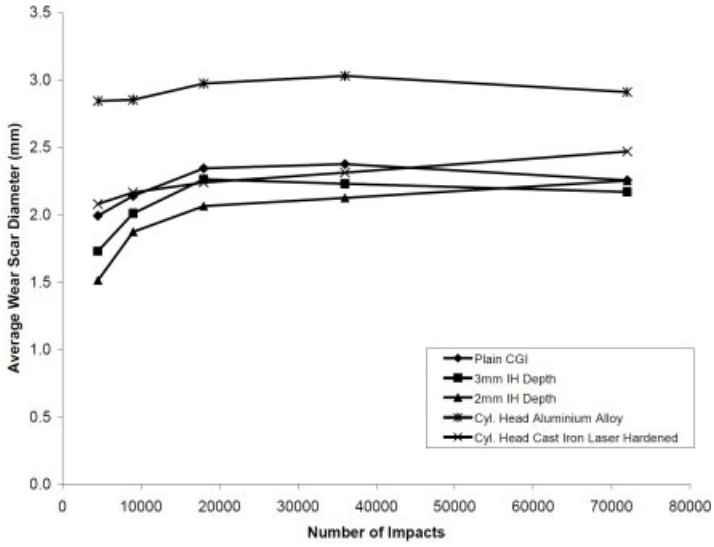


Figure 4: Average Wear Scar Diameter vs. Number of Impacts

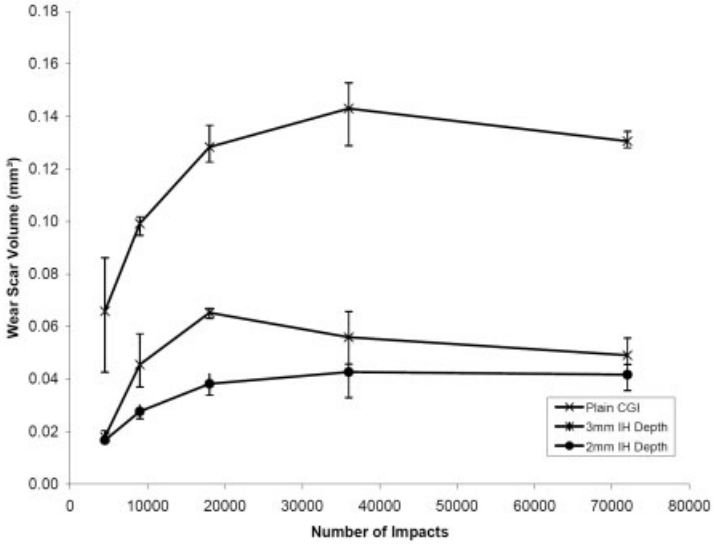


Figure 5: Average Wear Volume vs. Number of Impacts

As with other surface treatments, it appears that where the transitional zone between the treated and untreated sections of the specimen is in relation to the stress field imparted by the impact is

important. With respect to the initial curvature of both sets results, it appears that the hardening process has an effect on the rate of work hardening of the material.

It is instructive to compare the performance of the CGI against some other materials, both plain and treated, that have been subjected to identical tests. Figure 4 also shows the results of the CGI compared to an untreated cylinder head specification aluminium alloy and also cylinder head specification cast iron that has been laser hardened to achieve a similar effect to the induction hardened CGI. It should be noted that the performance of the induction hardened CGI is on a par with that of the laser treated cast iron.

Acknowledgements

The authors would like to acknowledge the Ford Motor Company and the Engineering & Physical Sciences Research Council for the sponsorship of this work and Ajax TOCCO for their technical support.

References

[1] Dawson, S., Indra, F., **2007**, "Compacted Graphite Iron – A New Material for Highly Stressed Cylinder Blocks and Cylinder Heads", *28th Internationales Wiener Motorsymposium*

[2] Slatter, T., Lewis, R., **2008**, *"Valve Recession – The Importance of Impact Wear"*, Journal of Engineering Tribology, Proceedings of the IMechE Part J. *In Press*

Thermally Sprayed Nanocrystalline Cylinder Running Surfaces in Modern Passenger Car Engines

K. Bobzin, F. Ernst, K. Richardt, T. Schläfer
Surface Engineering Institute, RWTH Aachen University, Aachen
C. Verpoort
Ford Research Center Aachen, Aachen

1 Introduction

One of the most important objectives of the automotive industry in the near future is to reduce emissions and fuel consumption. Both objectives depend on lowering the engine's weight along with the frictional resistance in the drive train. Especially the tribological system consisting of the piston rings and the cylinder running surface offers potential to reduce the fuel consumption since it is responsible for approximately 40 % of the friction losses within the engine. Decreasing the engine's weight is accomplished by using light-metal alloys, especially hypoeutectic aluminum-silicon (AlSi) alloys. Since these alloys do not show a sufficient wear resistance, the surface in the contact area between the piston rings and the cylinder bore wall has to be modified or replaced. Generally, the material on the surface is replaced by pressed in or cast in cylinder liners made of grey cast iron, which provides the required properties.

Besides high costs and an increase of the engines weight, the use of cylinder liners exhibits further problems. The different thermal expansion coefficients of grey cast iron and aluminum can cause a deformation of the liner and also local heat transfer problems if the liner disengages from the engine block. Particularly the deformation of the liner leads to an increased oil and fuel consumption and hence to increasing emissions.

A newer approach to produce iron based cylinder running surfaces on engine bore walls is to apply thermally sprayed coatings onto the bore walls.

The work presented was carried out within the framework of the joint project NaCoLab, funded by the German Ministry of Research and Education.

2 Thermal Spraying of Cylinder Bore Walls

Thermal Spraying comprises processes in which surfacing materials are heated to the plastic or molten state, inside or outside of the spraying gun, and then propelled onto a prepared surface. The substrate remains unfused. As surfacing materials, polymers, metals and their alloys but also ceramics can be used. The mechanism of bonding to the surface of thermally sprayed coatings is mostly mechanical interlocking. Thus, a roughened surface, characterized by numerous undercuts is essential to gain sufficient bond strength. For that purpose in general the surfaces to be coated are grit blasted prior to coating.

The process chain in the production of coated cylinder bores consists of four steps. First is machining the cylinder bore to a certain diameter and then roughening of the surfaces to be

coated. Next steps are the thermal spraying and the honing of the coated bore to receive a surface topography that meets the tribological requirements.

2.1 Substrate Pre-Treatment

The substrate pre-treatment in the production of engine blocks with thermally sprayed cylinder running surfaces can be carried out by grit blasting. Coatings applied onto grit blasted bore walls show bond strength values of more than 30 N/mm^2 which is considered to be the minimum required value. This procedure requires additional grit blasting equipment. Hence, the procedure is not considered to be the optimum solution for the production of engine blocks with thermally sprayed cylinder running surfaces. Besides grit blasting there are other processes which can be utilized to activate the bore surface, such as high pressure water jet blasting or the NiAl/Flux procedure [6].

The optimum surface roughening process on the one hand has to enable a high bond strength, on the other hand it should exhibit good integrability into the process chain. Ideally, the same machines, that are used to bore up the cylinder bores, can be employed to roughen the bore surfaces. Also, contamination of the cylinder block with lubricating oil or grit should be avoided, otherwise an additional costly cleaning process would be necessary.

These requirements have led to different mechanical roughening processes (MRP). One process was developed under the lead of the Institute of Machine Tools and Production Technology of Braunschweig University (IWF) within the framework of this project.

2.2 Thermal Spraying Equipment

The coating of cylinder bore walls requires specifically designed thermal spraying equipment. These systems in general are characterized by a gun head smaller than the bore diameter, which is being mounted to a rotating spindle. The overlay of the rotary motion of the gun head and its axial infeed thereby enables a 360° coating of the bore. At the moment there are at least 4 systems with this specification either under research or already in serial production. Out of the four systems one uses powdery feedstock while the three others process wire feedstock.

The coatings within the scope of this work were produced with the Plasma Tranferred Wire Arc (PTWA) process (Flame Spray Industries, Inc., Port Washington, USA).

The gun head of the PTWA system consists of a tungsten cathode, an air-cooled pilot nozzle made of copper and an electrically conductive consumable wire that is the anode, Figure 1.

The gun head is mounted to a spindle, which rotates with up to 600 rpm. The wire is fed perpendicularly to the center orifice of the nozzle. To start the process, a high voltage discharge is initiated, which ionizes and dissociates the gas mixture between the cathode and the nozzle. Due to a constricting orifice in the pilot nozzle, the plasma is forced to exit the nozzle at supersonic velocity. The elongated plasma is transferred to the consumable anode, the wire, completing the electrical circuit. A constant current power supply maintains the plasma from the cathode to the wire with an arc voltage of 100–120 V and a current of 60–100 A. This melts the tip of the wire and then the high-pressure plasma gas together with the atomizing gas strips the molten particles from the end of the wire. Thereby a jet of finely atomized particles is created, which is accelerated towards the substrate at high speed. The atomizing gas can be any non-combustible gas. In this work a mixture of argon and hydrogen is used as the plasma gas and compressed air is used to

atomize and accelerate the molten particles. With this system, cylinder bores with a diameter of 35 to 360 mm can be coated.

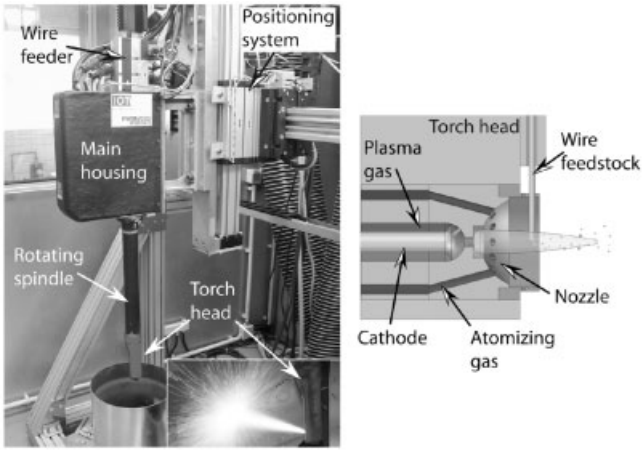


Figure 1: Picture of the Plasma Transferred Wire Arc system (left) and a schematic of the PTWA gun head (right)

2.3 Finishing of the Coatings

The finishing step in the process chain is the honing procedure. The honing procedure of thermally sprayed coatings varies from the honing of cast iron liners since the coatings show a higher roughness than the surfaces of cast iron liners. They also contain, depending on the coating material, embedded hard phases. Hence the honing of thermally sprayed cylinder running surfaces is a three step procedure. First, the roughness peaks have to be evened by using a coarse grained honing stone. In a second step the cylindrical shape of the bore is further improved by removing a large volume of material. The finishing is carried out by using a honing stone of fine graining to produce a run capable surface.

The surface is similar to cast iron liners in that it is characterized by the honing grooves which store a certain amount of oil to lower the friction between the piston rings and the bore wall. Since thermally sprayed coatings contain some porosity that is machined open by the honing process, the surface provides an additional oil storage capacity.

The thickness of the coating after the honing operation is typically 100–150 µm. Because of the as-sprayed roughness of the coating and the required machining allowance, the thickness as sprayed is typically 200–300 µm.

3 Experimentals

3.1 Surface Pre-Treatment

All substrates to be coated were roughened with a modified fine boring process, which was developed by the Institute of Machine Tools and Production Technology, Braunschweig, Germany.

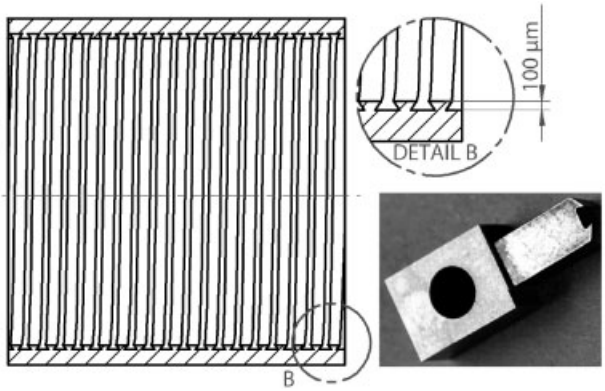


Figure 2: Schematic of the mechanical roughening process (dove tail like topography) and the cutting tool (source IWF, Braunschweig, Germany)

Different profiles were developed and evaluated. With this procedure the same machining centers which are used to bore up the cylinder bores of the engine blocks, can be employed to roughen the bore walls. Hence, the process provides, contrary to grit blasting, good integrability into the process chain. The cutting process was developed as a lube oil free process in order to avoid an additional cleaning operation.

The bond strengths of the coatings were determined with a PAThandy pull off adhesion tester (DFD-Instruments, Kristiansand, Norway). Compared to the established testing method following DIN EN 582, it is possible to measure the bond strength directly on coated parts such as the curved surface of a bore. Thereby, a cylindrical test element with the face side machined to the same curvature as the bore wall is glued onto the coating. In a second step all the coating has to be cut from the substrate surrounding the test element to define a specific area for the adhesion test which was done by laser cutting. The test element is then connected to the pulling head. With a hand-held hydraulic pump pressure is applied onto the four jack cylinders which tears the test element and the coating off the substrate. The pressure at which the coating separates from the substrate is measured and converted into the bond strength.

3.2 Surface Building Materials and their Processing

The low alloyed carbon steel feedstocks used as reference material contain 0.10–0.82 wt-% carbon. However, one of the aims of this project is to develop iron based wire feedstocks that, when processed by thermal spraying, form wear resistant, friction optimized coatings with embedded M_xB_y-precipitations. Therefore, besides other alloying elements such as Cr, Si, W, the wires contain between 1.9 wt.-% and 5 wt.-% of boron. Because of the high content of alloying elements (approx. 25 %), the wires, called SUNA, were produced as cored wires. The powder fillings were made of either crushed powders of coarse grain (-350 µm) or a mixture of crushed and gas atomized powders of a smaller grain size distribution (-180 µm, + 45 µm). Two different materials were used for the sheaths, Fe and FeCr.

All materials were sprayed with the Plasma Transferred Wire Arc (PTWA) process onto mechanically roughened liners made of aluminum EN AW 6060 (AlMgSi0.5) with an internal diameter of 83.3 mm and a height of 120 mm. Micrographs of the coatings were produced to evaluate the microstructure. To gain further information on the coating, especially on the size of the precipitations, transmission electron microscopy (TEM) investigations were carried out by the Institut fuer Produkt Engineering of Duisburg-Essen University, Germany.

The thickness of the coating after the honing operation is typically 100 – 150 µm. Because of the as-sprayed roughness of the coating and the required machining allowance, the thickness as sprayed is typically 200 –300 µm.

4 Results

4.1 Substrate Pre-Treatment

The investigations show, that bond strength values of more than 30 N/mm^2 can be reached for coatings applied onto mechanically roughened substrates. Early attempts at a mechanically roughened surface led to a bond strength of 40 N/mm^2. A micrograph of such a profile is given in Figure 3, left.

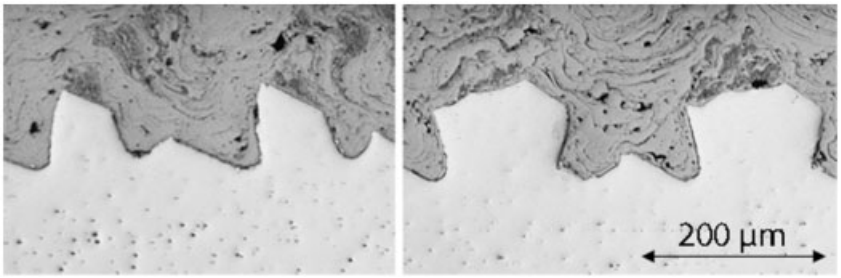


Figure 3: Micrographs of two investigated MRP topographies: early profile (left) and the "dove tail" like profile (right)

In order to produce a profile characterized by symmetrically arranged undercuts and thus increase the interlocking of substrate and coating the "dove tail" like profile was developed, Figure 3, right. For coatings applied onto liners, that were pre-treated with this process, an increase of the bond strength by 45 % was measured (58 N/mm^2).

4.2 Carbon Steel Coatings

When low carbon steel is used with the PTWA thermal spraying process and compressed air is used as the atomizing gas, the iron in the alloy reacts with the oxygen of the atomizing gas and forms FeO (wuestite), a high temperature oxide, which, due to the high cooling rates, is frozen at room temperature . Wuestite has a cubic closed packed structure. Due to its crystallographic shearplane it acts as a low shear strength, lubricous phase, that is responsible for the good tribological properties of Fe/FeO-coatings, especially in both top and bottom dead centers of the

cylinder running surface, where the relative speed between the piston ring and the cylinder running surface is near zero (mixed friction).

Typical spray parameters for producing steel coatings are given in Table 1 (parameter setting 1). To produce a coating with approximately 300 µm in thickness, 16 passes are required, whereas the material throughput is 4 kg/h.

Table 1: Typical parameters for processing C-steel with the PTWA system. slpm: standard liters per minute, WFR: wire feed rate, I: current. The axial infeed of the gun head is 1.75 m/min

Setting	Ar [slpm]	H_2 [slpm]	I [A]	WFR [m/min]	Air [slpm]	Revolution speed gun head [min^{-1}]
1	67	29	65	4.3	1100	400
2	70	10	65	4.3	1200	600

In order to lower the substrate temperature during the coating procedure, and thereby minimize the risk of overheating the substrate, the composition of the plasma gas was changed to 70 slpm Ar and 10 slpm H_2 (setting 2). With this parameter setting the temperature at the outside of the sample liners with a wall thickness of 6 mm drops from approximately 100 °C to max. 85 °C compared to setting 1. An increase in the revolution speed of the gun head from 400 min^{-1} to 600 min^{-1} leads to more finely distributed oxides within the coating.

Figure 4 shows a micrograph of a PTWA thermal spray coating made from 0.82 % C-steel. The coating was produced with parameters, which were optimized in order to increase the material throughput and thereby reduce the cycle time. Therefore, the current was increased to 80 A, the wire feed rate to 5.7 m/min (5.4 kg/h), the axial infeed to 2.0 m/min and the plasma gas flow to 105 slpm. The H_2-content of 30 % was retained. With this parameter setting the cycle time could be reduced by 12 %, compared to settings 1 and 2. The time required to spray one of the liners mentioned above was 59 sec. The coating contains very little porosity of less than 1 % and approx. 30 % of oxides. Both properties were determined by optical image analysis.

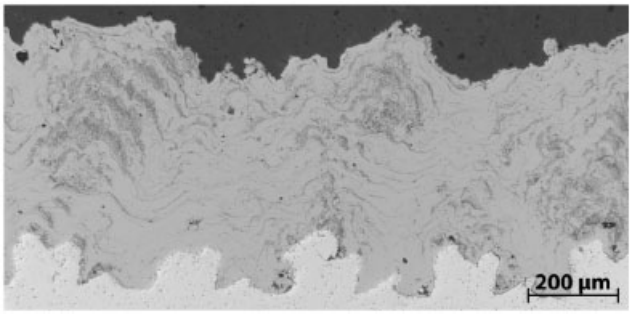


Figure 4: Micrograph of a 0.82 % C-steel coating applied with the PTWA system

For the 0.1 % C-steel coatings the hardness values range from 254 to 412 HV 0.1 with a mean value of 295 HV 0.1. The hardness of the 0.82 % C-steel coatings is significantly higher, the average ranges from 550 to 620 HV 0.1. For the coating which was produced with the optimized

parameters, the coating hardness was 590 HV 0.1. Because of the oxides the single values varied from 448 to 745 HV 0.1.

4.3 Nanostructured Coatings

The first developments of the SUNA feedstocks, called SUNA 2 and 3, were made from coarse (grain size –350 µm) crushed powders in an iron sheath with a high content of boron (5 wt.-%). The coatings made from this feedstock have a high hardness of 1200 HV 0.1. In the micrographs, numerous micro cracks and also disruptions were found.

This brittle behavior indicated, that this material is not suitable for the application in cylinder bores. Nevertheless, one coated liner was honed to determine the oil storage capacities caused by the honing grooves and the machined open pores. It was shown that due to the brittle behavior, many particles quarried out during the honing process and left behind a surface with the oil storage capacities of the machined open pores being too high (0.17 mm^3/cm^2) to meet the requirements of a cylinder running surface.

For the second batch (SUNA 6), the content of boron was lowered to 1.9 wt-%, which led to dense coatings free of micro cracks. A micrograph of such a coating is given in Figure 5.

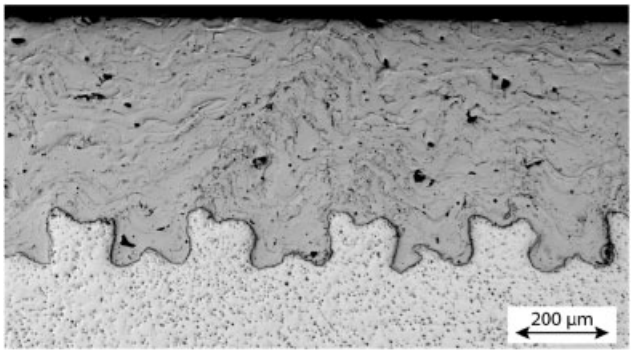


Figure 5: Micrograph of a honed coating made from SUNA 6 wire

The spray parameters are similar to those for processing C-steel (setting 2), only the current was increased to 85 A. Some un-melted particles of the powder filling and semi-melted pieces of the iron sheath were found within the coatings. Figure 6 shows two TEM bright field pictures of a SUNA 6 coating. The picture on the left hand side indicates a predominantly amorphous matrix, whereas the picture to the right shows nanoscale $(Fe, Cr)_{23}B_6$-precipitations in an amorphous matrix. The hardness of these coatings is 680–700 HV 0.1. the oil storage capacities of the machined open pores of these coatings lay within the recommended range.

In order to produce more homogeneous coatings, with the next batch (SUNA 6-3) the powder filler made of crushed material was replaced by a mixture of gas-atomized and crushed powders of a smaller grain size (–180 µm, +45 µm). Because of the smaller grain size, the wire feed rate could be increased by 30 %, which equals a material throughput of 4.3 kg/h. Contrary to the SUNA 6 coatings, only a small number of un-melted particles from the powder filling was found within the coatings, which was affiliated to the smaller grain size distribution of the powder

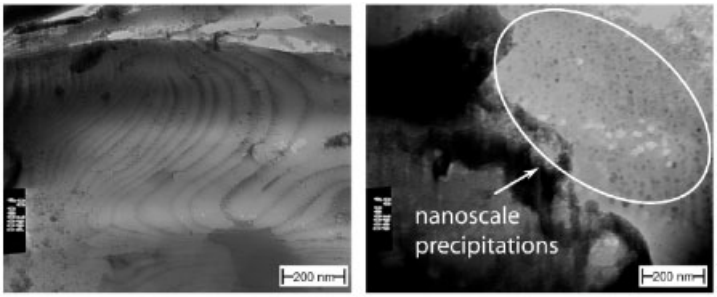


Figure 6: TEM bright field pictures of a PTWA sprayed SUNA 6 coating. In the picture to the left an amorphous structure is shown while the picture on the right hand side shows nanoscale precipitations (by courtesy of M. Hahn, Institut fuer Produkt Engineering, Duisburg-Essen University, Germany).

filling. Figure 7 gives a micrograph of such a coating with some semi-fused sheath material embedded (left). On the right hand side a SEM-image of a honed SUNA 6-3 coating is given. The image shows some machined open pores which serve as oil storage cavities.

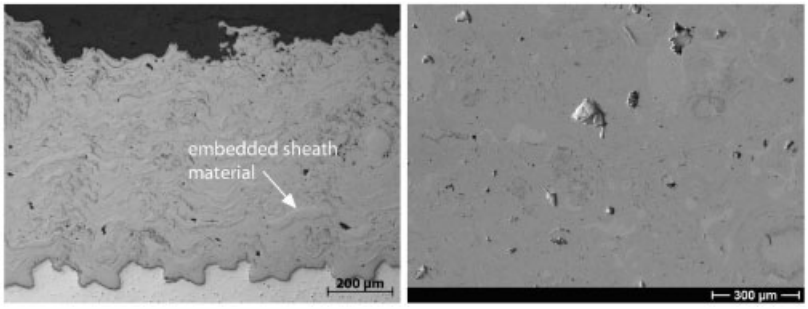


Figure 7: Left: Micrograph of a SUNA 6-3 coating with some sheath material embedded. Right: SEM image of a PTWA-sprayed and honed SUNA 6-3 coating.

The inclusion of semi-fused sheath material was affiliated to the malleable behavior of the wire, respectively the sheath. Due to the ductility of the wire, it could not be straightened as required. For the PTWA-process, a piece of wire of 300 mm in length has to fit in between two parallel planes with a distance of 5 mm in between them. With the three wires, this was difficult to achieve. With a wire, that is not well-straightened, the distance between the wire tip (the anode) and the cathode fluctuates, which causes an unsteady fusion of the feedstock and thus an inclusion of the sheath material. By carrying out TEM investigations, the presence of nanoscale M_xB_y- and M_3O_4-precipitations could be verified.

Finally, the iron sheath (SUNA 6-5) was substituted by a FeCr sheath to further improve the process stability and to avoid the inclusion of semi-fused sheath material. The hardness of these coatings lies within the same range as the SUNA 6 coatings. Compared to the coatings made of SUNA 6 and 6-3, the homogeneity of the coatings was further improved, as shown in Figure

8. From the latter three materials crack-free coatings could be produced, even if the coating thickness was 600 µm.

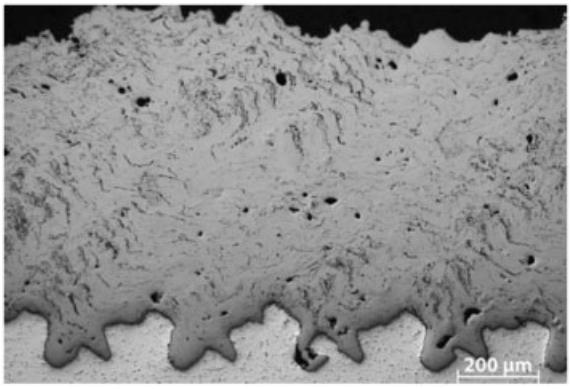


Figure 8: Micrograph of a SUNA 6-5 coating.

Besides test liners, so far, two Ford Zetec in-line 1.4 l engines were coated with the reference material 0.1 % C-steel and the SUNA 6-3 feedstock. Friction tests were carried out with a stripped down engine for the 0.1 % C steel coating.

Thereby the engine is driven by an electric motor. The torque required to rotate the crankshaft with the pistons is recorded. The test can be carried out with or without the cylinder head. For the engine including the cylinder head, the friction was determined to be 6.8 % below the values measured for the standard engine with liners made from grey cast iron. Without the cylinder head, the friction was 14.1 % lower compared to the standard engine. The SUNA 6-3 coated engine has not been tested yet. However, a decrease in friction of 10 % was calculated for the stripped-down engine with the mounted cylinder head, also compared to the standard engine .

5 Summary and Outlook

Within this study it could be shown, that substrate roughening by fine boring with a geometrically defined cutting edge provides a good alternative to the commonly used grit blasting process in the automotive industry. Bond strength values of nearly twice the required minimum value of 30 N/mm^2 could be proved.

Furthermore wire feedstocks were developed, that, when processed by Plasma Transferred Wire Arc spraying, lead to coatings with embedded, nano-scale boridic precipitations.

In order to evaluate the SUNA feedstocks with regard to their tribological behavior, at the moment honed coatings are being tested on a reciprocating and on a rotating sliding wear tester against nitrided and also against electroplated, alumina reinforced chromium coated (CKS) piston rings.

6 Acknowlegments

The presented investigations are part of the joint project “Nano-crystalline composite coatings for cylinder bores with nano-structured surface and wear forecast for highly loaded gasoline and diesel engines – NaCoLab”, promoted by the German Federal Ministry for Research and Education within the scope of the program “Nano-mobil” (grant ID 03X0003).

The Authors would like to thank the German Federal Ministry of Research and Education for funding the “NaCoLab” project.

7 References

[1] R. van Basshuysen, F. Schäfer [Editors], Handbuch Verbrennungsmotor, Friedrich Vieweg & Sohn Verlag, Wiesbaden, Germany, 2007 (in German)

[2] T. Kuhn, Messung der Zylinderverformung von Aluminiumkurbelgehäusen für Dieselmotoren (Measuring the Distortion of Cylinders in Aluminum Diesel Engine Blocks), PhD thesis, Hannover University, 2001 (in German)

[3] DIN EN 657:2005

[4] E. Lugscheider, Handbuch der thermischen Spritztechnik, DVS-Verlag, Duesseldorf, Germany, 2002

[5] G. Barbezat, S. Keller, G. Wuest, Internal Plasma Spray Process for Cylinder Bores in Automotive Industry, Proceedings of the 15th International Thermal Spray Conference, C. Coddet, May 25–29, 1998 (Nice), ASM International, Materials Park, Ohio, USA, 1998, p 963–979

[6] D. Cook, Processing, Structure, Property and Performance Relationships for the Thermal Spray of the Internal Surface of Aluminum Cylinders, PhD thesis, State University of New York at Stony Brook, USA, 2001.

[7] E. Lugscheider, R. Dicks, K. Kowalsky, D. Cook, K. Nassenstein, C. Verpoort, A materials system and method of its application for the wear protection of aluminium engine cylinder bore surfaces, Proceedings of the International Thermal Spray Conference 2004, ed E. Lugscheider, May 10–12, 2004 (Osaka), DVS-Verlag, Duesseldorf, Germany, 2004, p 334–340

[8] Q. Zhou, unpublished data, Jaguar Cars. Ltd., Whitley, United Kingdom, 2007

Investigation of Wear Mechanisms and Microstructural Changes of Thermally Sprayed Coatings in Cylinder Bores after Motor Tests

Mareike Hahn*, Ralf Theissmann**, Birgit Gleising*, W. Dudzinski***, Alfons Fischer*
*University of Duisburg-Essen, Institute of Product Engineering, Materials Science and Engineering, Duisburg, Germany
**University of Duisburg-Essen, Faculty of Engineering and CeNIDE, Duisburg, Germany
***Wroclaw University of Technology, Institute of Materials Science and Applied Mechanics, Wroclaw, Poland

1 Introduction

The future development of motor engine design and technology governs the increasingly demanding requirements on materials in terms of friction and wear properties. In order to reduce emissions and achieve economical and environmentally sound solutions thermal sprayed coatings are an option to manufacture wear resistant and low-friction cylinder running surfaces. Studies revealed that in automotive engineering versatile thermal spray processes and material combinations have been applied. Wear protection as well as reducing friction are of major concern and led to the development of powder and wire consumables adapted to the specific features of the different spraying processes for manufacturing and repair [1]. The structure and therefore the properties of metal sprayed coatings are governed by the thermal and kinetic energy introduced. Hitherto ferrous alloy powders, for example low alloyed carbon steels with 0.1 to 0.9 wt % C, have been successfully used for cylinder bore coatings [2].

Beside others two potential processes for coating cylinder bores are the Plasma Transferred Wire Arc (PTWA) and the High Velocity Oxygen Fuel (HVOF) spraying.

The energy to heat the feedstock and the kinetic energy to accelerate the molten particles to the substrate differ within these processes consequently resulting in differing lamellar microstructures of these coatings. Particle velocities vary from 100–130 ms^{-1} for the PTWA process up to 750 ms^{-1} for HVOF what makes the molten particles deform to splats when hitting the surface and leads to the characteristic lamellar structure including pores. Hard phases, which are either introduced by alloying (e.g. C for carbides) or by the atmosphere during spraying (e.g. O for oxides), are related to a sufficient strength of these coatings. Figure 1 shows the lamellar structures of an HVOF and a PTWA sprayed steel coating. The distribution of oxides can be perceived as dark phases within these cross sections. Depending on the spray processes and parameters the PTWA coatings (Figure 1 b)) exhibit coarser splat grains and contain inhomogeneous distributed oxide accumulations (oxide islands) where as the HVOF coatings (Figure 1 a)) have a fine lamellar structure with fine pores and might contain many oxide particles. Open machined pores in the layered microstructure function as oil storage capacity and, therefore, benefit lubrication.

Cylinder bores experience large variations in load concerning piston ring velocity, thermal and mechanical impact and lubrication regimes that can last from boundary to hydrodynamic lubrication. This results in different wear appearances along the cylinder wall [3, 4]. Within cylinder bores the coatings undergo high temperature corrosion in the combustion chamber (CC),

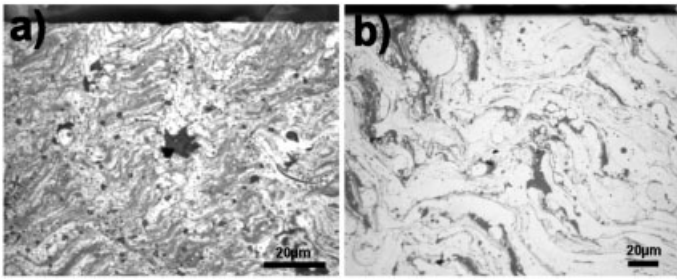


Figure 1: Light microscopy images of an HVOF (a) and a PTWA (b) steel coating (cross sections).

impact and sliding wear at the top dead center (TDC) and the bottom dead center (BDC) as well as sliding wear within the stroke. Ignition pressures allow for mechanical fatigue in the upper and lower region of a cylinder. Though piston ring – cylinder bore assemblies are lubricated and therefore assumed with mild wear conditions [5].

Local contacts in sliding systems of metal against metal cause large plastic strains which changes the near-surface areas in ways which makes the material unstable to local shear. Adhesion has a prominent influence on the development of transfer pieces, deformation and fracture of this material produces an ultrafine grained structure which is finally mixed with the environment by mechanical alloying [6]. The refinement of the microstructure to grains of tens of nanometer is determining the mechanical properties in the surface near zones. Lubrication additives reacting with the surface also have an influence on the chemistry of the surface zone. Chemical-mechanical mixing at surface near zones incorporates elements from lubrication into the surface. The properties in this surface layers would change significantly [5, 6, 7].

This contribution focuses on describing the wear mechanisms and microstructural changes under the different given thermal and mechanical load conditions in two different engines. Sample material was available from a PTWA spray coated cylinder of a grey cast iron 2.5 l diesel engine and an HVOF spray coated cylinder of a die-casted aluminium 2.0 l gasoline engine.

2 Materials and Experimental Method

2.1 Test Engines

Table 1 compares the different manufacturing and performance characteristics of the two motors examined in this investigation.

The grey cast iron engine block (2.5 l DI Transit Diesel, Ford) had been revised by PTWA spraying and was provided for investigations after a road test performance of 56.700 km. The coating had been applied onto the cylinder walls in three steps: The cylinder surfaces were not mechanically roughened but treated with a flux for a sufficient bonding of coating and substrate. Then a NiAl bond coat (approx. 50 µm) and finally the steel coating from a wire feedstock with 0.1 wt% C (SAE 1010, FeC0.1) was sprayed [8]. After honing the coating had a thickness of approx. 150 to 200 µm.

Table 1: Motor engine blocks

	Ford2.5 l DI Transit Diesel	GM2.0 l GDI L850 Gasoline
spraying process	PTWA	HVOF
feedstock	FeC0.1	FeC0.1
test mode	road test	engine test bench
performance	56,700 km	250 h in a motor test run

The cylinder bores of the aluminium die-cast engine block (2.0 l GDI L850 Gasoline, GM) have been surface treated by mechanical roughening with high pressure water jet blasting and afterwards coated by HVOF spraying with the same steel wire feedstock (FeC0.1) as the PTWA sprayed cylinder. Coating thickness after honing has been approx. 100 to 150 µm. This engine has been run in an engine test for 250 h whereas different load cycles had been applied.

2.2 Microscopy

Two different methods of sample preparation were used for each cylinder position. A special sample preparation of the surface cross section was necessary. Furthermore samples were made by using a focused ion beam (FIB). A detailed description about the preparation techniques for analysis with light-, scanning and transmission electron microscopy are published elsewhere [9]. Scanning electron microscope (SEM) examinations of the worn surfaces have been implemented in a field emitter SEM (LEO 1530 Gemini, Zeiss), for transmission electron microscopy (TEM) investigations were carried out in an EM 400 (Philips) with 120 kV acceleration voltage and for detailed investigation of the microstructure in the near surface zones a high resolution TEM (Tecnai G2 F20, FEI) with 200 kV was used.

To gain an overview about the wear depth in TDC the surface topography has been estimated by using a confocal white light microscope (µsurf, Nanofocus AG).

3 Results

3.1 Wear Appearances

3.1.1 PTWA Coated Road Test Motor

The SEM and depth estimation images in Figure 2 reveal the acting wear mechanisms tribochemical reaction, surface fatigue and abrasion. The impact of correlating mechanisms on the surface in the different positions of the cylinder is significantly different. Figure 2 a) is showing the area of CC and TDC, the stroke is shown in Figure 2 c) and BDC in Figure 2 d). The back scattered SEM images visualize the distribution of oxides as dark phases in the surface. Deformed material is visible in TDC where the piston ring stops which is found likewise in BDC. The depth estimation image in Figure 2 b) demonstrates the deformation and wear depth that the piston ring causes in TDC; in the area of CC one can perceive a tribofilm on the surface. EDX analyses at CC detected a high concentration of carbon and in TDC increased carbon as well as oxygen.

Surface fatigue turns out as delamination of individual fractures of splats (Figure 2 c)). The coating cohesion is provided by mainly interlocking of splat particles and adhesion strength.

Crack propagation will follow the splat boundaries where smooth surfaces hinder mechanical interlocking and finally a perpendicular microcracking can remove the splat particle from the surface. At a low rate this must not be detrimental because the open volume can store motor oil and benefit lubrication. But one has to notice that delamination of splats can already occur in the course of honing and a differentiation at what stage, manufacturing of the surface or engine operation, a splat particle is removed is unlikely possible when the piston ring slides over and modification of the surface is progressed.

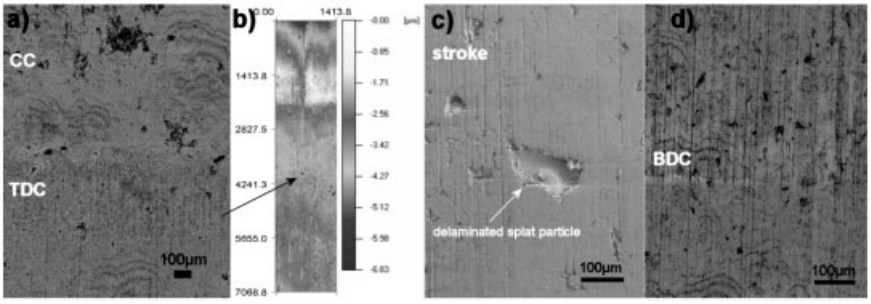


Figure 2: SEM and depth estimation images showing the wear appearances in different positions of the cylinder: a) back scattered SEM image of CC and TDC; b) depth estimation image of TDC; c) secondary electron SEM image of the stroke; d) back scattered SEM image of BDC

Another wear mechanism within the stroke is found to be abrasion. Grooves of different width can be seen in sliding direction of the piston all over the surface (Figure 2 c)). A three-body abrasion is revealed as a result of the piston carrying hard particles with it at every stroke which are ploughing the surface of the cylinder. The honing texture has been abraded completely.

3.1.2 HVOF Coated Bench Test Motor

Wear mechanisms found at the surface of the HVOF coated cylinder are similar as for the PTWA one but it seems less worn. Honing grooves are still visible in CC and the stroke (Figure 3 a) and c)), grooves from abrasion are smaller in width (Figure 3 c)) and the depth estimation image (Figure 3 b)) shows less deformation and wear depth in TDC. In Figure 3 d) the surface at BDC seems to be polished by the piston ring, it is less deformed than at TDC but the surface appears very smooth. With EDX analyses again a high carbon concentration was detected in CC just like in CC of the PTWA cylinder.

Delaminated splat particles are due to the fine lamellar structure of the HVOF coatings much smaller and will bring about fine grooves with abrasion. Honing has probably loosened some splats in the surface as we can find delamination of splat particles frequently at the edges of honing grooves.

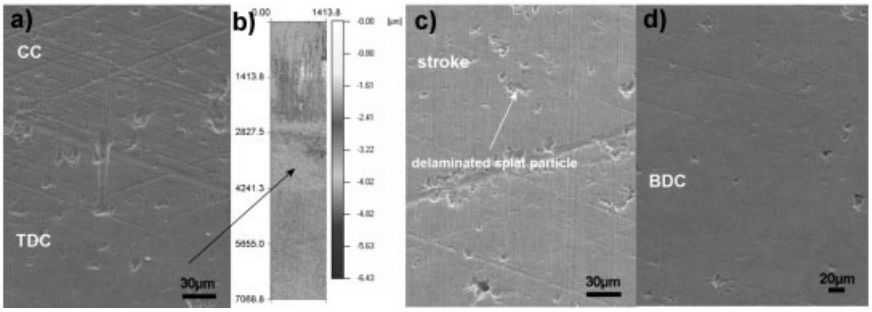


Figure 3: SEM and depth estimation images showing the wear appearances in different positions of the cylinder: a) secondary electron SEM image of CC and TDC; b) depth estimation image of TDC; c) secondary electron SEM image of the stroke; d) secondary electron SEM image of BDC

3.2 Initial Microstructure

3.2.1 PTWA Steel Coating

TEM investigations exhibit the underlying microcrystalline (µc) matrix of ferrite (α-Fe) and nanocrystalline (nc) precipitates of cementite (Fe_3C) and wuestite (FeO). Figure 4 shows the micrographs and diffraction patterns. The nc structure of cementite lamellas within the ferrite grains (Figure 4 b) and c)) indicates the formation of troostite. Due to the high cooling rates of the splats within the PTWA process (up to 10^6 C/s) mild steels solidify under second order supercooling and form these nc cementite lamellas [10]. Figure 4 c) presents very fine, round shaped oxides. This fine distribution of hard phases in the microstructure results in an effectual hardness and strength of the material.

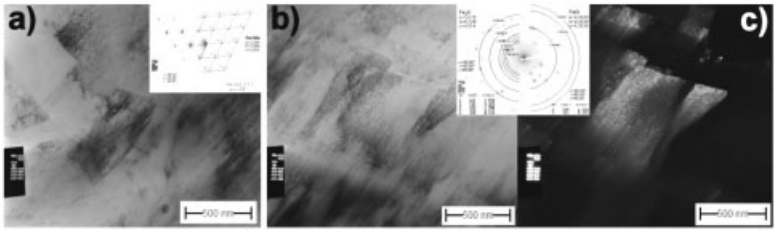


Figure 4: TEM micrographs of the initial microstructure showing the µc α-Fe matrix (a) and nc precipitates of Fe_3C and FeO in the bright field (b) and dark field image (c).

3.2.2 HVOF Steel Coating

The HVOF coating reveals a differing microstructure (Figure 5). The matrix consists of µc ferrite or wuestite (Figure 5 a)); nc precipitates were calculated from diffraction patterns as either wuestite or ferrite. Carbon could not be detected as cementite.

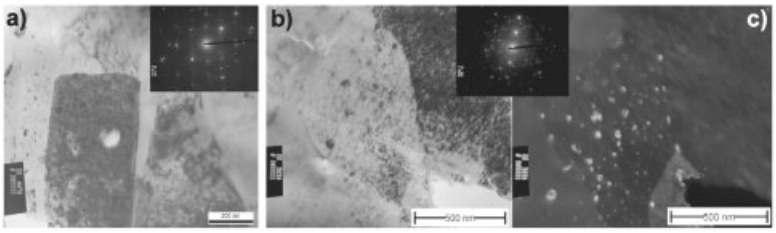


Figure 5: EM micrographs of the initial microstructure showing the μc matrix of α-Fe and FeO (a) and nc precipitates of FeO and α-Fe in the bright field (b) and dark field image (c).

The precipitates shown in the bright and dark field image in Figure 5 b) and c) are round shaped and consist of ferrite whereas the matrix is FeO. A high density of lattice imperfections is representative for the HVOF steel coatings.

Wuestite is a high temperature oxide but, due to the high cooling rates remains stable at room temperature. It is known as a lubricious oxide which can also occur naturally on the surface of Fe-based metals during tribological action. The lubricity of solid oxides is determined by the crystal chemistry and lattice structure [11]. Ionic potential and a cubic closed packed structure which has beneficial crystallographic shear planes originate a self-lubricating phase. Thus solid lubricants can backup lubricants in mixed and boundary lubrication regime [12].

3.3 Microstructural Alterations

3.3.1 Combustion Chamber (CC)

On the surface of the PTWA sample at CC an amorphous layer was detected containing nc wear particles. The micrographs in Figure 6 a) and b) are showing particles around 10 nm in size, the layer thickness is about 100 nm. The surface zone revealed a very fine nc layer of 50 to 100 nm thickness consisting of nc grains of 10 to 30 nm in size. Figure 6 c) and d) is showing the subsurface zone which appears as an ultrafine crystalline (ufc) structure. The grain size is about 100 to 150 nm and the depth of this subsurface zone outreaches approx. 0.5 to 1 μm.

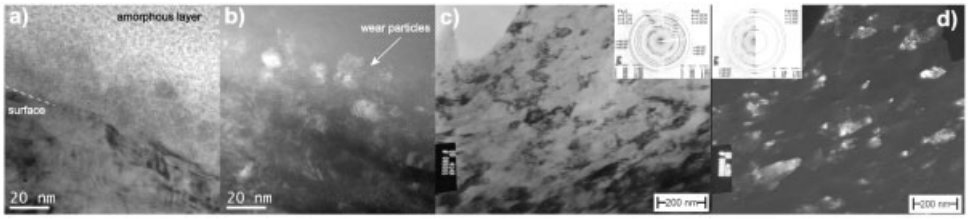


Figure 6: TWA coated cylinder: TEM micrographs of position CC: a) Bright and b)dark field micrographs showing an amorphous layer in CC with incorporated nc wear debris; c) Bright and d) dark field micrographs showing the subsurface zone with ufc-structure of α-Fe, Fe3C and FeO.

Figure 7 shows the microstructure of the HVOF coated cylinder in CC. An amorphous layer with incorporated wear particles can be found likewise as in CC of the PTWA coated cylinder.

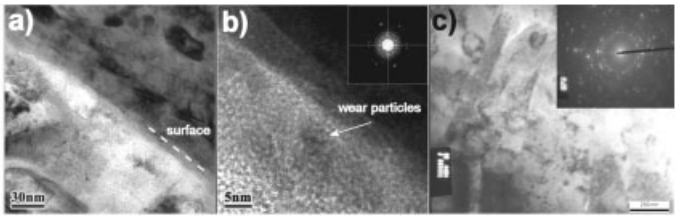


Figure 7: HVOF coated cylinder: TEM micrographs of position CC: a) Bright and b)dark field micrographs showing an amorphous layer in CC with incorporated nc wear debris; c) The subsurface zone shows ufc-structure of α-Fe and FeO.

Particle size is even smaller as for the PTWA coating, around 5 to 10 nm (Figure 7 b)). The layer thickness varies from 50 to 200 nm. The surface zone reveals a nc structure of 50 to 100 nm thickness consisting of nc grains of 10 to 50 nm in size. The subsurface zone in Figure 7 c) shows a ufc structure of ferrite and wuestite with nc precipitates.

3.3.2 Top Dead Center (TDC)

At position TDC of the PTWA coated cylinder a nc structured layer can be found with a grain size of 10 to 30 nm (Figure 8 a)). The thickness of this layer varies from 50 to 100 nm. A plastic deformation and refinement of grains according to the sliding direction of the piston ring can be seen in the subsurface zone (Figure 8 b)). The ufc structure has a grain size of 100 to 300 nm and the depth of this subsurface zone outreaches 0.5 to 1 µm.

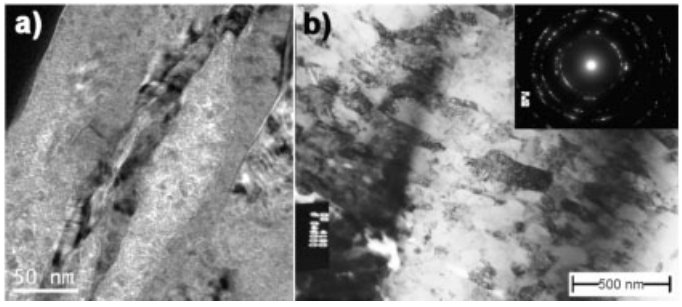


Figure 8: PTWA coated cylinder: TEM micrographs of position TDC; a) nc-structured surface zone; b) The subsurface zone has a ufc-structure.

Figure 9 shows the HVOF microstructure in TDC. The surface zone seems to be highly deformed as the grains appear to be flattened and are aligned tangential to the surface (Figure 9 a) and b)). The thickness of this layer is about 100 nm. The structure turns out to be rather ufc than nc. In some areas an amorphous layer as shown in Figure 9 a) is still visible. The subsurface zone reveals a ufc structure with a grain size from 100 to 400 nm (Figure 9 b)). Diffraction patterns depict a mixture of wuestite and ferrite structures.

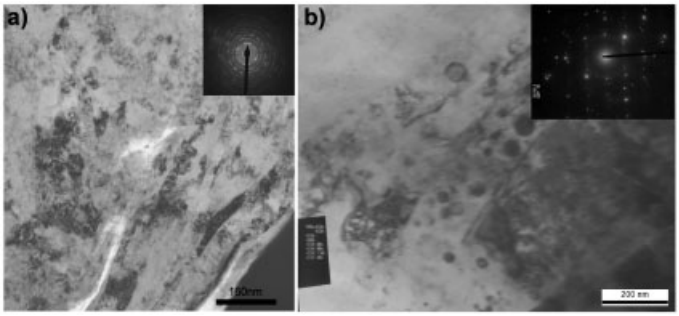


Figure 9: HVOF coated cylinder: TEM micrographs of position TDC; a) Highly deformed grains in the surface zone showing an ufc structure; b) The subsurface zone has a µc-structure.

3.3.3 Stroke

A microstructural alteration in the surface zone of the stroke is not verifiable within this investigation for both coatings. The samples were prepared as bulk samples, tangential to the surface, so that it should be possible to have a plane view in the contact zone. In Figure 10 a) the PTWA coatings shows ferrite grains with high amounts of dislocations. Diffraction evaluated the structure of a µc ferrite matrix and nc precipitates of cementite. The HVOF coating is shown in Figure 10 b). The microstructure here matches the one of the initial microstructure.

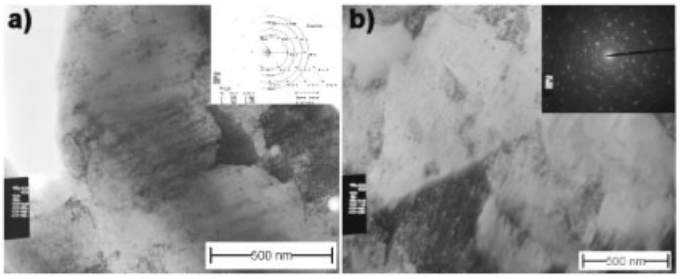


Figure 10: TEM micrographs of the surface zones in stroke for a) PTWA and b) HVOF coated cylinder

3.4 Bottom Dead Center (BDC)

For the PTWA coating the surface zone of BDC again shows a nc structure consisting of ferrite, cementite and wuestite (Figure 11 a) and b)). In this case the grain size is about 50 to 100 nm and a deformation of material in preferred orientation of the sliding direction of the piston ring can be perceived. The subsurface zone shows a µc structure with cell wall formation and subgrain structure (Figure 11 c)). The diffraction pattern verified the existence of wuestite.

Figure 12 shows the results for BDC of the HVOF coated cylinder. At the surface zone a ufc structure can be found where the grains again appear highly deformed according to the piston ring sliding direction (Figure 12 a) and b)). The subsurface zone has an µc structure.

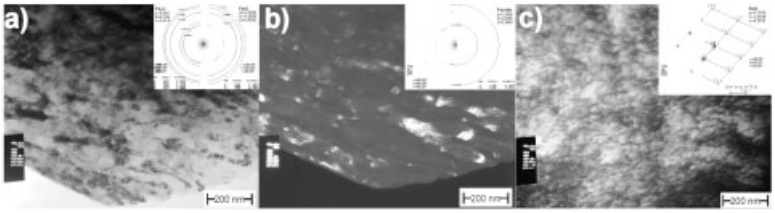


Figure 11: PTWA coated cylinder: TEM micrographs of position BDC; a) Bright and b) dark field micrographs showing a nc structure of α-Fe, Fe_3C and FeO; c) The Subsurface zone shows a µc structure with cell walls consisting of FeO.

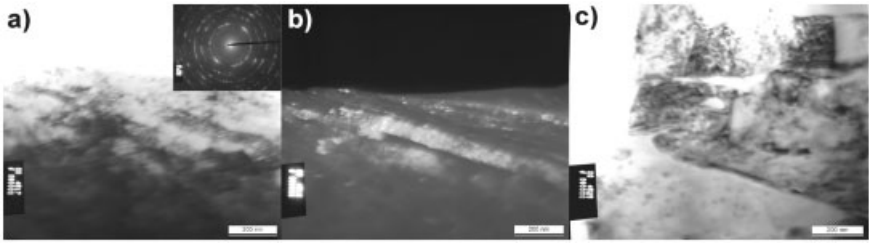


Figure 12: HVOF coated cylinder: TEM micrographs of position BDC; a) and b) Bright (left) and dark field (right) micrographs showing a highly deformed nc structure of α-Fe and FeO; c) Subsurface zone showing a µc structure.

4 Discussion

Both investigated cylinder running surfaces, PTWA and HVOF coated, showed similar wear appearances apart from the degree of wear. Different findings in terms of the microstructural alterations within both cylinders concerning the investigated positions CC, TDC, stroke and BDC have to be considered in relation with the different load situations in the cylinder and different affecting mechanisms. Comparing the two mild steel coatings, PTWA and HVOF sprayed, differing microstructural changes might be related to the different process dependent solidification, microstructures and mechanical properties. The amount of hard phases introduced during spraying, like oxides, and the amount of lattice imperfections differ a lot.

Samples from CC of both cylinders revealed amorphous layers with incorporated debris. The size of the wear particles found in the amorphous layer of CC matches the grain size that was pointed out in TDC. This leads to the conclusion that debris found in CC might have its origin in TDC and is moved with piston ring sliding. High gas pressures and ignition temperatures sintered residues from combustion and lubrication to an amorphous coating wherein wear particles are trapped.

PTWA and HVOF sprayed coatings from low alloyed carbon steels are known to form oxide layers under tribological stressing, especially in unlubricated metal on metal contacts when the oil film breaks down [13]. A formation of an oxide layer in TDC of the PTWA sprayed coating is likely as a higher amount of oxygen could be detected with EDX analyses. From diffraction patterns of the nc surface zone wuestite could be verified but was overlaid with diffraction patterns from ferrite and cementite. In literature a formation of various oxides like Fe_2O_3 and Fe_3O_4 is

described [13, 14]. Wuestite should not be stable under tribological stressing and additional oxides could be generated. Rainforth et al. showed that friction induced oxides in contact zones of ferrous alloys play a major role in wear of these materials. Oxides where identified by X-ray diffraction and TEM as nanocrystalline structured and mixed with the metal matrix [14]. Wear particles generated in TDC of both coatings therefore could be tribologically induced oxides. This should be analyzed in further investigations.

In TDC of the PTWA coating a tribofilm could not be found on the surface but one can recognize a distinct modification of the surface near volumes up to a several hundred nanometer. Dienwiebel et al. showed that anti-wear films do not necessarily remain on surfaces with increasing tribological stresses, they are also not replenished which is presumably related to unsatisfactory conditions in contact pressure or frictional energy needed for film formation [15]. The fine grain size (10 to 30 nm) stands for a prominent changing of the surface zone and therefore a changing of the mechanical properties. The nc material in the surface zone reacts differently to the initial microstructure. In this surface layer the size of grains causes grain boundary sliding and supports easy shearing of the material [5]. Shakhvorostov et al. described the effect of grain size on plastic deformation for grey cast iron. According to the Hall-Petch effect decreasing grain size causes grain boundary sliding and the material becomes viscous which results in low shear strength whereas the subsurface zone is work hardened due to suppressed dislocation motions [16]. This effect can be reflected in the deformed grains with high amount of lattice imperfections found in the subsurface zone of TDC of the PTWA coating. The HVOF coating showed heavy plastic deformation in the surface zones of TDC and BDC which seems to flatten the grains. In comparison to the PTWA coating in TDC one can not recognize a tribomaterial due to mechanical mixing. The surfaces near zones are deformed to a very fine lamellar structure where the grain size of the flattened grains is ufc or nc.

The investigation of the microstructure in the stroke showed no alterations in this investigation for both coatings. Lubrication regime has a great influence on wear mechanisms. Within boundary lubrication wear mechanisms and wear rates will change with friction. Tribomechanical alterations of the surface near volumes go along with a low wear rate; high wear rates will remove material in deeper layers and therefore inhibit microstructural alterations. A high friction level might cause grain removal without former grain refinement and therefore cause high wear rates [16]. Sample preparation in the stroke has been done as bulk preparation. However microstructural alterations in the surface near zones might occur only in a very thin layer of a few tens of nanometer. A cross section or FIB preparation might bring out more detailed information about the wear mechanisms in the stroke. The results shown in this investigation for wear appearances (Figure 2 c) and Figure 3 c)) depict that abrasion was presumably the predominant wear mechanism in the stroke of both cylinders. Material transfer from the piston ring could not be verified on the cylinder running surfaces, thus adhesion is unlikely.

The surface zone of the PTWA coating in BDC showed an nc microstructure. In the subsurface zone one can find a microstructure with cell walls and formation of subgrains. Rigney et al. characterized a nucleation-controlled mechanism by dislocations [6]. In different tribotests cell walls and subgrain structures occurred in surface near zones in analogy to the findings shown in Figure 11 c). These cell walls make it energetically favourable to remove subgrains from the surface during sliding. In case of rotation of the subgrains into a shear unstable orientation transfer of material occurs at sliding contact. Finally the material can be smeared, flattened, fractured and mixed with the environment to produce ufc or nc material [6]. The different acting mechanisms

found in TDC and BDC of the PTWA sprayed coating might be related to a temperature gradient along the cylinder length. Ignition heats the cylinder walls in TDC temporarily up whereas cooling and lubrication keep temperatures in the stroke and BDC lower. An effect related to temperature gradient could not be observed within the HVOF cylinder. Here deformation of grains to a very fine lamellar structure could be identified for both TDC and BDC.

5 Conclusion and Outlook

SEM and TEM investigations were carried out in four positions of two different thermal sprayed motor engine cylinders. Alterations in terms of microstructure and chemistry in the surface and subsurface zones of all investigated positions could be found for both coating systems, PTWA and HVOF. The different findings regarding the formation of a nc surface layer, layer thickness and character of the subsurface zone are closely related to variations in load along the cylinder. Piston ring velocity, the extent of thermal and mechanical impact as well as lubrication can be associated with differing surface modifications. Wear particles were found in CC incorporated in an amorphous layer that stems from combustion residues. Nc and ufc surface layers occurred in TDC and BDC, differing in grain size and layer thickness whereas subsurface zones showed differing microstructures like ufc structures with deformed grains or cell walls. The findings in stroke showed no microstructural changes within this investigation which is attributed to predominantly abrasion.

In further investigations chemical analyses of the surface near zones will be accomplished to backup the differing results in tribofilm and tribomaterial formation for the selected positions and within the different coating systems.

6 Acknowledgements

All results are part of the research project NaCoLab (financed by BMBF, code: 03X0003K), which is included in the supported programme “Nanomobil”. The authors would like to thank Ford Forschungszentrum Aachen GmbH and GM Powertrain Germany GmbH for sample material and all other partners for their steady willingness to support with information. We would also like to thank the DFG for the financial support of the residence of Prof. Dudzinski in Duisburg (code: WE 2671 / 2-1) and Prof. Farle (Experimentalphysik, University of Duisburg-Essen) for the opportunity to use the high resolution TEM.

7 References

[1] R. K. Betts, Surface Engineering – Coatings and Heat Treatments 2003, Proc. Conf., 716–721

[2] S. Uozato, K. Nakata, M. Ushio, Surface & Coatings Technology 2005, 200, 2580–258

[3] M. Priest, C.M. Taylor, Wear 2000, 241, 193–203

[4] P. Papadopoulos, M. Priest, W. M. Rainforth, JET 2007, Proc. IMechE 221, 333–343

[5] D. Shakhvorostov, K. Poehlmann, M. Scherge, Wear 2006, 260, 433–437

[6] D. A. Rigney, L. H. Chen, M. G. S. Naylor, A.R. Rosenfield, Wear 1984, 100, 195–219

[7] M. Scherge, A. Gerve, Mat.-wiss. u. Werkstofftech. 2003, 34, 934–937

[8] D. Cook, C. Verpoort, K. Kowalsky, R. Dicks, VDI Berichte 2003, 1764, 151–158

[9] M. Hahn, B. Gleising, W. Dudzinski, A. Fischer, in Prak. Metallographie Sonderband 39 (Ed.: H. Vetters, F. Mücklich), Springer, Germany, 2007, 137–146

[10] W. Domke, Werkstoffkunde und Werkstoffprüfung, 4th ed., W. Giradet, Düsseldorf, 1971

[11] A. Erdemir, S. Li, Y. Li, Int. J. Mol. Sci. 2005, 6, 203–218

[12] A. Neville, A. Morina, T. Haque, M. Voong, Tribology International 2007, 40, 1680–1695

[13] A. Edrisy, A. T. Alpas, Thin Solid Films 2002, 420–421, 338–344

[14] W. M. Rainforth, A. J. Leonard, C. Perrin, A. Bedolla-Jacuinde, Y. Wang, H. Jones, Q. Luo, Tribology International 2002, 35, 731–748

[15] M. Dienwiebel, K. Poehlmann, Tribol. Lett. 2007, 27, 255–260

[16] D. Shakhvorostov, B. Gleising, R. Büscher, W. Dudzinski, A. Fischer, M. Scherge, Wear 2007, 263, 1259–1265

Hot Direct Extrusion of Abrasion Resistant Fe-Base Metal Matrix Composites – Microstructure and Wear Properties

M. Karlsohn [1], A. Röttger[2], P.A. Silva[3], S. Weber[3], A. R. Pyzalla[3], W. Reimers[4], W. Theisen[2]

[1] Köppern Entwicklungs-GmbH, Hattingen (Germany)

[2] Ruhr-Universität Bochum, Bochum (Germany)

[3] Max-Planck-Institut für Eisenforschung GmbH, Düsseldorf (Germany)

[4] Technische Universität Berlin, Berlin (Germany)

1 Abstract

This paper discusses hot direct extrusion as a novel method to produce long cylindrical rods of a metal-matrix composite (MMC) and co-extruded rods of a low alloyed steel substrate cladded with a MMC layer. The excellent abrasive wear resistance of MMC is based on hard phase and iron powder mixtures, which can be tailored to the respective abrasive environment. This production process combines sintering of capsuled powder blends and subsequent pressing of the capsules through an extrusion die to produce an (almost) completely densified MMC. In contrast to HIP cladding (hot isostatic pressing), the standard method of producing powder metallurgical components (PM) and PM-layers, the simpler capsule technique is less expensive. The extruded MMC were investigated with respect to their microstructure, wear properties and the microstructural and mechanical properties of the interface of substrate and MMC layer.

2 Introduction

Increasing demands on technical surfaces, i.e. wear, corrosive or thermal load often prompt the development of tailored materials and coatings. In highly abrasive environments often MMC with an excellent wear resistance are put into application. Such materials are produced from a metal matrix (MM) based on Fe, Ni or Co and additional hard phases (HP), such as carbides, borides or oxides [1–2]. The use of powder metallurgical techniques offers a chance to adapt the particle size, the content and the distribution of the added HP to the tribological system in a large scale. HIP cladding is an established method of producing such MMC. A successful example of a wear resistant surface protection system produced by HIP-cladding is presented in [3]. The 5–30 mm iron based MMC-layer on a comminution roller surface extended the service life of these rollers by factor of 5–10 compared to a deposition welded surface. But due to its near net shape capsule technique HIP is quite expensive and prevents the acceptance of this technique in many areas of applications. In addition the limited dimensions of the equipment make the use of HIP inappropriate for long products. Because of these reasons hot direct extrusion of capsules filled with powder blends was researched in a DFG-Project as a method of producing long cylindrical products. Aiming at a high abrasive wear resistance in combination with moderate costs, powder blends of hardenable tool steels with additions of fused tungsten carbide (WSC) or titanium carbides (TiC) were used.

3 Material Selection and Experimental Method

3.1 Metal Matrix (MM)

The two standard tool steel powders X220CrVMo13-4 (1.2380, cold work tool steel) and X40CrMoV5-1 (1.2344, hot work tool steel) were chosen as the metal matrix on basis of the working temperature. The high wear resistance of the ledeburitic cold work steel 1.2380 permits its use for die cutting and extrusion tools in polymer processing industry. A carbon content of 0.6–0.8 wt% soluted in the metal matrix during austenitisation makes it hardenable to 54-62 HRC. In addition a content of approx. 19 vol% of chromium-rich M_7C_3 and 4 vol% vanadium-rich MC carbides precipitated in the metal matrix increases the hardness and the wear resistance of this steel [4]. In contrast to that, the carbide free metal matrix of 1.2344 reaches a typical hardness of 50–56 HRC. This causes a good wear and thermoshock resistance in a temperature range of 400–700 °C.

3.2 Hard Phases (HP)

The wear resistance of the two metal matrix powders was improved by the addition of coarse fused tungsten carbides (FTC) and titanium carbides (TiC) (+36 µm -125 µm). Monolithic FTC is an eutectic carbide with a high density of 16.53 g/cm³, which offers a good ratio of hardness (2200–2600 HV0.05) and fracture toughness (5–6 $MPa\sqrt{m}$). In contrast TiC with a density of 4.93 g/cm³ reaches a microhardness of approx. 2900–3100 HV0.05 and a lower fracture toughness (2–3 $MPa\sqrt{m}$). Because coarse monolithic TiC was not available agglomerated TiC had to be used. The influence of the volume fraction of coarse carbides in a MMC on the wear resistance was tested by the addition of 10 or 30 vol% of coarse hard phases. These limits were chosen, because lower and higher hard phase additions do not change the wear resistance significantly. All powder mixtures were blended in a shaker-mixer for 1 h. The compositions and the designations of the tested MMCs are given in Table 1.

Table 1: Designation and composition of MMC; C = cold-, H = Hot work tool steel, W = FTC, T = TiC, 1 = 10 vol%, 3 = 30 vol%

	Designation				
	CW1	CW3	CT1	CT3	HW1
vol% / MM-type	90 / 1.2380	70 / 1.2380	90 / 1.2380	70 / 1.2380	90 / 1.2344
vol% / HP-type	10 / FTC	30 / FTC	10 / TiC	30/ TiC	10 / FTC

3.3 Hot Direct Extrusion

Preheating of Fe-base extrudates (900–1200 °C) can reduce the pressing forces during the extrusion significantly but leads to sintering of the powder blends. The use of gas atomized tool steel powders reduces the densification so that the increase of the required pressing forces is limited. Sintering tests led to the conclusion that preheating of the powder blends at 1150 °C for 2 h gives an optimized sintered condition for the subsequent extrusion. All tests were performed at an 8 MN horizontal extrusion press at the Extrusion Research and Development Center of the Technical University of Berlin. The capsules ($d = 78$ mm, $l = 200$ mm) were filled with powder,

precompressed to tap density by vibration, evacuated and sealed by TIG welding. Figure 1 shows a scheme of the used capsules.

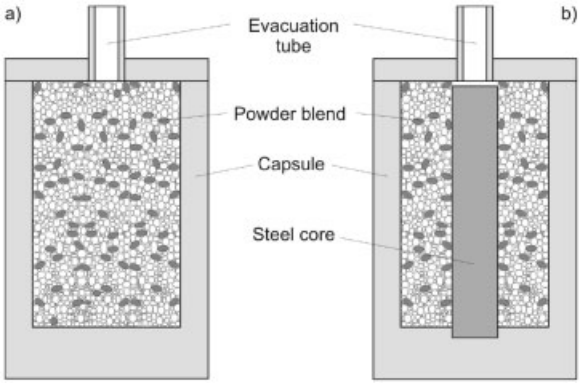


Figure 1: Cross sections of a capsule for : a) full MMC rods, b) co-extrusion of a steel core to be cladded with a wear resistant MMC-layer. Extrusion of sheet capsules protects the powder blends from oxidation [5].

To coat a cylindrical substrate a steel core (1.2714) of 30 mm diameter is placed in the capsule before filling it with powder (Figure 1b). Prior to heating the capsules were coated with anti-oxidant. The friction between die and capsule was reduced by rolling the hot capsule in glass powder (acts as a lubricant and solidifies during cooling down to room temperature). These coated capsules were put in the preheated extrusion container (480 °C, to minimise the heat loss) and subsequently extruded to rods of 35 mm in diameter (ram speed 36–38 mm/s, extrusion ratio 4.8–5.2 : 1).

3.4 Materials Testing

All samples were cut from rods by electrodischarge machining. The microstructure was characterised by grinding the samples on diamond discs, polishing with diamond suspension on buffs and etching with V2A or HNO_3 pickle if necessary.

In pin on disc tests against the three 80-mesh abrasives flint (1200 HV0.05), corundum (2100 HV0.05) and SiC (2700 HV0.05), the wear resistance was accessed by measuring the mass lost Δm at room temperature. The dimensionless wear rate $W = \Delta m/(\varrho \cdot l \cdot A)$ could be calculated by the density ϱ, the length of the wear path l, which is covered during the test, and the contact area A.

4 Results and Discussion

4.1 Hot Direct Extrusion

In the first step of the extrusion process the presintered powder blend is compacted in combination with the upsetting of the capsule to fit the diameter of the extrusion container. The required forming force increases steeply, because the friction between the rod and the die has to be overcome to pass the capsule through the die. After the capsule has begun to flow, the pressing forces

decrease continuously, because the decreasing length of the capsule reduces friction, which is generated between container and capsule. The die forces measured in these trials varied between 2.0 MN (CW1+1.2714) and 4.6 MN for the capsule filled with CW3. Recapitulatory the pressing forces tend to rise by increasing additions of HP. FTC additions have a strong effect on the required forces, while the deformation of capsules containing a steel core lead to a decrease of the forming forces.

The taken samples show that the adapted extrusion parameters result in rods with a high densification (> 97.5 %, decreasing with increasing HP-volume fractions) and in case of co-extrusion in perfectly dense coatings. Moreover tensile, bending and shear tests show a high interfacial strength and failure in the MMC-coating [6]. MMC with TiC additions show lower densities, because the agglomerated TiC particles are often porous and can't be filled with MM during the extrusion process.

In addition the extrusion ratio of ~ 5:1 causes an anisotropic microstructure, which is analysed in section 4.2. The deformation leads to diameter reduction in combination with a movement of the HP because of the material flow. The friction between rod and die creates a velocity gradient in the rod, so that the material in the outer diameter flows slower than in the core. These effects cause an alignment of the longitudinal axis of the HP parallel to the extrusion direction. Figure 2 illustrates the material flow during the extrusion.

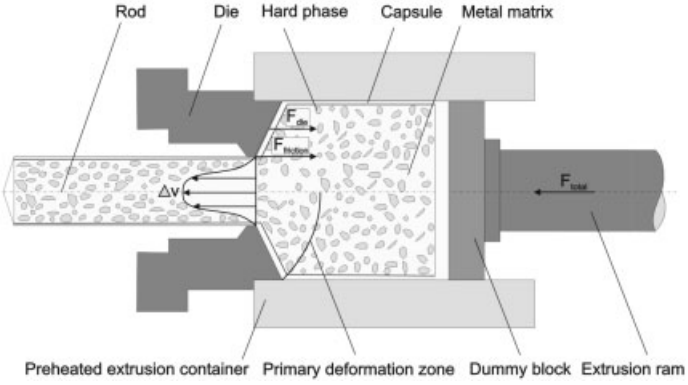


Figure 2: Scheme of hot direct extrusion

4.2 Microstructure

The deformation of the capsules during the extrusion process produces a microstructural anisotropy [7], which can be seen in Figure 3. Figure 3a shows an axial cross section (in extrusion direction) of the HW1 rod with a quite homogenous dispersion of the HP, while Figure 3b illustrates a radial cross section (perpendicular to the extrusion direction) in which the agglomerated TiC-particles are disrupted leading to a bead-like arrangement parallel to the extrusion direction, while FTC-particles were only aligned. It can be concluded, that the higher forming forces of the MMC with a FTC addition can be ascribed to the incompressibil-ity of the FTC. In contrast the brittle inner interfaces of the agglomerated TiC-particles failure under hydrostatic and shear load

while the capsule is passing the extrusion die. The disruption of the porous particles reduces the volume fraction, which has to be deformed and lowers the required pressing forces.

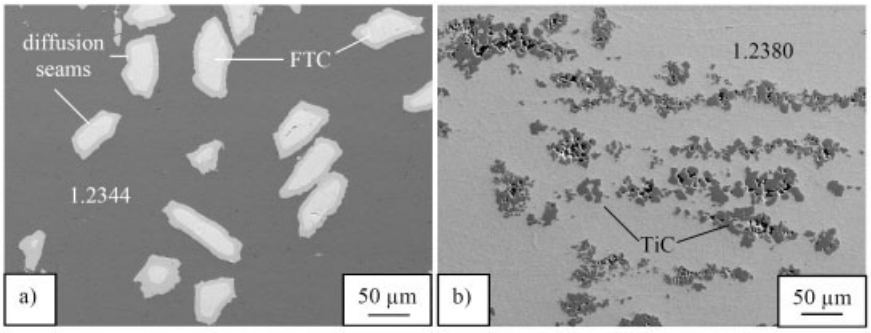


Figure 3: Cross sections of MMC rods : a) HW1 in axial direction b) CT1 in radial direction

Among the deformation, the properties of the materials are influenced by the microstructure of the atomised powders and by the sintering. The atomisation of 1.2344, leads to a marten-sitic microstructure without carbides. In contrast 1.2380 has a hypoeutectic structure, in which the primary solidified metal cells are surrounded by chromium rich M_7C_3- and vanadium rich MC eutectics. During the presintering of 1.2380 Oswald ripening of the lamellar eutectic car-bides starts which become spherical and grow to 3–5 µm. At the same time a formation of diffusion seams at the interfaces of MM and FTC is caused by interdiffusion. This results in the generation of the low carbon phases M_2C and M_6C while the released carbon is dissolved in the MM. EDX-measurements of these seams showed high W, Fe and C contents, so it can be concluded that they are of M_6C type (Figure 3a). While high resolution SEM investigation of the TiC / MM interface of TiC-reinforced MMC showed no diffusion, EDX-linescans veri-fied a diffusion of V-atoms into the TiC, which does not change the microstructure signi-ficantly. Recapitulatory a formation of diffusion seams is preferable, because the gradient of properties between the metallic bonding of the MM and the covalently bonded HP is reduced.

4.3 Wear Resistance

The pin on disc tests were executed with quenched and tempered samples. These samples were secondary hardened to produce a high wear resistance combined with a sufficient toughness. The tests can be used to evaluate the efficiency of the added HP against the different abrasives and to prove the influence of increasing volume fractions of HP on the wear resistance. The measured wear rates of all tests are summarised in Table 2.

It is obvious, that the increasing hardness of the abrasives increases the wear rates. These tests underline in addition the influence of the HP-particle size and the added volume fraction [8]. The disrupted TiC particles are too small to act as an obstacle against the grooving abrasives and were worn out of the contact surface. Furthermore the brittleness of the inner interfaces of the agglomerated TiC causes microfracturing and HP-particle break-out. Compared to the pure MM the addition of TiC does not influence the wear rate significantly.

In contrast to that increasing volume fractions of FTC are an effective wear protection against the softer abrasives SiO_2 and Al_2O_3. The addition of 30 vol% FTC in 1.2380-MM lowers the wear rate up to two orders of magnitude. This can be ascribed to the good bonding of the HP in the MM (diffusion seams) and the higher fracture toughness of FTC. The coarse FTC particles act as an obstacle against the grooving abrasives. Against the hard SiC, which is able to scratch all phases of the extruded material, the effect on the wear resistance is only minor. The dependence of the wear rates on the extrusion direction can be ascribed to the partial rotation of the HP during extrusion. The aspect ratio (length to width) of the FTC particles leads to a higher HP-fraction in the contact area in radial samples and therefore to a better wear protection. More detailed information on the wear resistance are summarised in [9].

Table 2: Wear rates of MM and MMC against different abrasives (80 mesh)

Denotation MMC	Wear rate against silicon carbide (SiC)	Corundum (Al_2O_3)	flint (SiO_2)
C_{radial}	4.08×10^{-5}	3.48×10^{-5}	2.26×10^{-5}
$CW1_{radial}$	3.19×10^{-5}	1.22×10^{-5}	5.40×10^{-6}
$CW1_{axial}$	3.59×10^{-5}	1.50×10^{-5}	7.48×10^{-6}
$CW3_{radial}$	2.33×10^{-5}	3.72×10^{-6}	3.92×10^{-7}
$CT1_{radial}$	4.52×10^{-5}	2.69×10^{-5}	2.01×10^{-5}
$CT3_{radial}$	4.75×10^{-5}	2.64×10^{-5}	1.40×10^{-5}
H_{radial}	4.06×10^{-5}	4.20×10^{-5}	3.04×10^{-5}
$HW1_{radial}$	4.70×10^{-5}	2.34×10^{-5}	1.58×10^{-5}

5 Conclusions

Hot direct extrusion of metal matrix composites based on tool steel matrices and reinforced by hard particles is introduced as a novel method to produce wear resistant rods. Optimized extrusion parameters lead to a high densification which qualifies the materials for service in abrasive environments. The alignment of the hard phases during the deformation process causes a dependency of the wear rates to the extrusion direction. The wear rates can only by decreased significantly by the addition fused tungsten carbides, while agglomerated TiC-particles have minor influence on the wear rate.

6 References

[1] Berns, H. ; Wewers, B. in Wear 251 (**2001**) p. 1386–1395

[2] Theisen, W. ; Packeisen, A. in Mat. Wiss. U. Werkstofftech. 35 (**2004**) No. 10-11, p.736–740

[3] Theisen W. in Wear 250 (**2001**) p. 54–58

[4] Packeisen, A. ; Theisen, W. ; Weber, S. in Proceedings of HIP 2005, Paris (**2005**)

[5] Roberts, P. ; Ferguson, B. in Int. Mater. Rev. No. 36, (**1991**), p. 62–79

[6] Karlsohn, H.M. Strangpressen von verschleißbeständigen Hartstoff-Metallmatrix- Verbunden auf Fe-Basis, PhD, Ruhr-Universität Bochum, Fortschr.-Ber. VDI Reihe 5, No. 733, VDI Verlag, Düsseldorf (**2008**)

[7] Dutta, B.; Samajdar, I.; Surappa, M. K. in: Materials Science and Technology 14, No. 1, (**1998**), p. 36–46

[8] Oliveira, M. M. ; Bolton, J. D. in: Journ. of Proces. Tech. 92–93 (1999), p.15–20

[9] Theisen, W. ; Karlsohn, M. in Wear 263 (**2007**) p.896–904

Development of Wear-Resistant Composites Based on Heat-Resistant Fe-Cr-Al Alloys

O. Mikadze,(Sp), E. Kutelia, D. Gventsadze, O. Tsurtsumia, B. Bulia, G. Mikadze, T. Dzigrashvili
Georgian Technical University, Tbilisi, Georgia
Ferdinad Tavadze Institute of Metallurgy and Materials Science

***Keywords*:** Alumina scale, modulated structure, friction, wear

Abstract

The heat-resistant Fe-Cr-Al alloys with high content of chromium (> 40 weight %), alloyed with rare-earth and carbide-forming elements, were undergone mechanical grinding and polishing up to formation of amorphous layer of 20 nm thickness. After the treatment, the initial samples were oxidized in atmospheric environment at 1200 °C for small periods of time, totally 10 hours. SEM and Auger-spectroscopic studies showed that microstructure of the oxidized surface with the precise contours of modulation is formed during the first hours of oxidation, and remains stabile for the whole cycle. The distinctive feature of the oxide film is that it is composed of mixture of oxide nanocrystallites ($\leq$ 500 nm). Heat resistance of the samples were assessed via periodic measurements of weight gain (W, mg/cm^2), which varied between 0.2 and 0.7 mg/cm^2, depending on oxidation duration. The latter indicates at improved heat resistance of the tested samples. The protective oxide layer, which mainly consists of α-Al_2O_3, is characterized by good tribological and mechanical parameters as well. Subsequent mechanical and chemico-thermal treatment of the alloys with the above oxide layer, including its saturation with iron phosphate, provides a drastic increase in wear resistance of the initial material. After lubrication the final product remains practically unchanged within the definite ranges of friction rate and loading.

1 Introduction

Resources saving and lifetime of metallic structures and machine components are strongly connected with their wear and corrosion. Currently, wear of machine components working in coarse and aggressive environment is most problematic. Therefore, design and development of the components which do not need major repairs during the whole performance period, and number of their minor repairs is considerably reduced, will practically double capacity of engineering plants [1].

The analysis of the existing experimental and theoretical data [1–6] leads to the conclusion that the processes of mechanical wear, corrosion and corrosion-mechanical fracture, actually represent a variety of one and the same phenomenon. Thus, the induced classical problems of wear and corrosion do not seem to be solved independently [1].

Such structural materials as stainless steels, not to mention conventional steels, are not able to ensure the required level of tribological behaviour of wearing parts working in severe conditions. The precondition of reliability and durability of wearing parts is a formation of special features of

their surfaces. The latter may be realized in two ways: 1. conventional alloying and 2. formation of coatings. The first way implies production of homogeneous bulk material, all the new surfaces of which have the same required properties. The second way assumes a formation of one or more layers with the required properties on the surface of conventional material.

The authors of this paper suggest a third way: the synthesis of the above two. Following this way, based on the classical principals of alloying, an extremely refractory and corrosion resistant homogeneous material is formed on the surface of which, subsequently, a barrier scale with stabile oxides is created in the optimal mode of its oxidation [2]. This scale, possessing good tribological property, and the main component of which is α-Al_2O_3, is acting as a protective coating during the performance period.

Preliminary research led to an assumption that mechanical and chemicothermal treatments (including impregnation with phosphate solutions), causing transformation of surface layer [7], will additionally increase its wear resistance.

2 Experimental

The stabile experimental zones of the corrosion-resistant Fe-Cr-Al alloys [8,9], in which a maximum heat resistance was ensured, were determined using a descriptive modeling and a correlation analysis of the obtained results. The nearly equiatomic Fe-Cr solid solutions, containing 43–48 wt% of Cr and 3–5 wt% of Al with small additions of La and carbide-forming elements, were melted using an arc melting in argon environment and studied after forging. The initial surfaces of disk-like samples were mechanically grinded and polished till obtaining a mirror-like appearance. Thereupon the samples were oxidized in quite air at 1200 °C over a period from 1 to 10 hours. The heat resistance of the samples, assessed by means of periodic weighting, varied from 0.2 to 0.7 mg/cm^2 depending on oxidation time. Some of the samples were also impregnated with the iron phosphate solution.

The morphology of the mechanically treated flat surfaces were studied by a scanning electron microscope (DSM-960, Zeiss, Germany). Auger spectra of the oxide films were taken using a LAS-2000 spectrometer (RIBER, France). The distribution of elements in the near-surface layers of the mechanically polished samples was determined within 1 μ depth via consecutive removal of the coats with the pace of 20–30 Å and 0.25 μ using ion-beam scattering and anodic dissolution respectively. The structure and phase composition of the subsurface layers situated deeper than one micron were controlled by X-ray diffractometry.

The tribological behaviour of the samples containing 45wt% of Cr and 4.0wt% of Al was investigated via sliding on a counterface made of tool steel Y8 (0.75–0.84C, 0.40Mn, 0.35Si, S$\leq$0.03, P$\leq$0.04). All tribological tests were conducted in ambient atmosphere using an IM-58 machine (typical device for torso friction, USSR) with overlapping coefficient equal to 1. The friction and wear properties were measured at room temperature in the mode of half-wet lubrication with the load of 0.2 MPa and sliding velocity varying from 0.125 to 1.25 m/s.

3 Results and Discussion

Since alumina scale is resistant to high-temperature gas corrosion and abrasive wear, an alumina-forming alloy based on nearly equiatomic Fe-Cr solid solution with small additions of rare-earth

and carbide-forming elements, was selected as an initial material. Formation of scale structure with the most distinct contours of modulation (see Fig.1a,b) has begun during oxidation of these alloys in the temperature range 1000–1400 °C. Its development began at 1200 °C during the first hours and remained without any appreciable changes for the whole oxidation cycle [3,5].

The surface morphology of scale formed at initial stages of high-temperature oxidation essentially depends on the structural condition of matrix. The scale formed due to the mechanical grinding and polishing of the metallic matrix generally represents a mixture of alumina and chromia nanocrystallites with the sizes 100÷500 nm (Fig.1), and has a modulated structure without oxide ridges in contrast to the widely investigated alumina- and chromia-forming alloys [10].

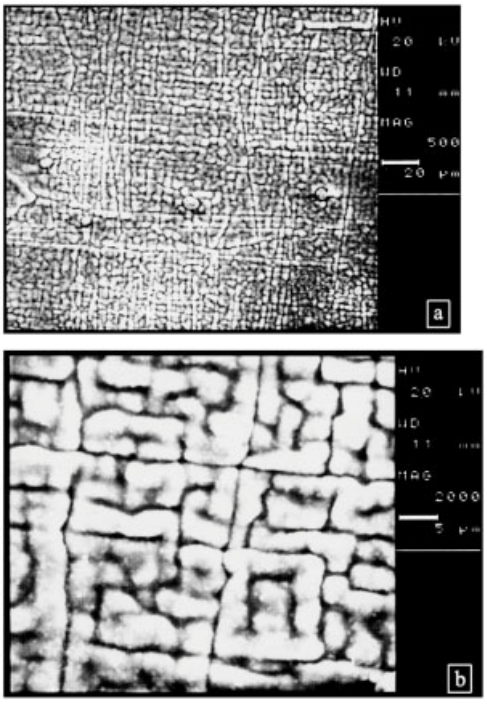


Figure 1: SEM image of the surface of mechanically treated sample after oxidation at 1200°C during 1 hour (a) and 5 hours (b).

The Auger-spectra taken from the samples oxidized under the above conditions at 1200 °C shows that all the main components of the metallic matrix are in chemical bonding with oxygen since the scale formation on the surface actually takes place in parallel with the nucleation of oxides of Fe, Cr and Al (Fig. 2). To the authors' opinion this is facilitated by an amorphized Beilbi layer on the mechanically treated (grinding, polishing) surface and the sublayer hardening caused by a plastically deformed, fine-grained, matrix layer. It is evident that such nonequilibrium surface layers are rapidly saturated with oxygen atoms causing simultaneous formation of scale.

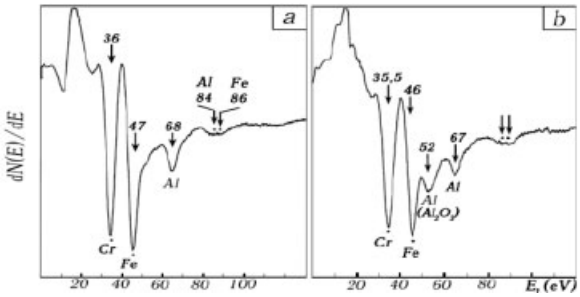


Figure 2: Auger-spectra of the sample oxidized at 1200 °C for 5 hours. a) metallic matrix, b) matrix/scale interface.

Electron diffraction patterns taken from the polished surface of grinded samples after removal of layers of different thickness are in accordance with the authors' assumption on structural changes with the thickness of scale.

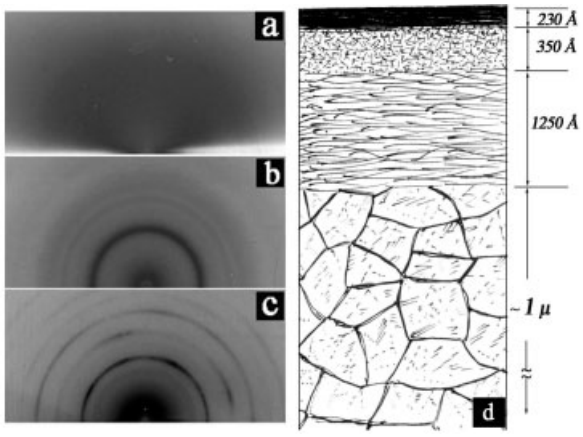


Figure 3: Electron diffraction patterns obtained via reflection from surface of the sample after removal of layers with the following thicknesses: a – 50 Å , b – 500 Å and c – 1300 Å.

The changes of structure with the thickness of the mechanically treated surface are schematically shown in Fig. 3d. The diffuse haloes (Fig. 3a), formed after removal of some ten-angstrom thickness layer, correspond to the absorbed atmospheric air elements. Under this layer a so-called Beilbi layer is situated.

Total thickness of both parts of Beilbi layer, truly amorphous and amorphous according to X-ray diffraction, is about 600 Å (Fig. 3). The specific structural features in the plastically deformed fine-grained layer of matrix, with the thickness of $\sim$ 1300 Å (Fig. 3d), were determined from the distribution of oxygen, carbon and the metallic components as well as from the analysis of the respective electron diffraction patterns (Fig. 3c).

The combination of the above-considered factors makes it possible to create suitable conditions for alumina formation which may well be protective against chemical and abrasive attack of an

aggressive environment. Such conditions are realized at 1200 °C during 1 ÷ 5 hours of oxidation. The tribological parameters for various states of Fe-45%Cr - 4%Al – 0.25%La alloy samples are shown in Table 1.

The results of preliminary study seem quite promising: mechanical grinding and polishing of the samples with optimal composition and subsequent purposeful oxidation results in considerable improvement of their tribological properties in comparison with the untreated ones. The impact of chemicothermal treatment on tribological behaviour is evident as well. Moreover, the material impregnated with the ion phosphate solution, after the above treatment and then lubricated with machine oil, does not practically wear within the definite range of friction velocity (Table 1). Starting from the most adopted point of view [7], this effect is conditioned by filling up of open porosity and reduction of gas-permeability in alumina scale.

Table 1: Tribological Properties of The Material Depending on Treatment (* wear is not fixed)

Material state	Sliding velocity V [m/s]	Friction temperature t [°C]	Friction coefficient f	Linear wear $\Delta h \times 10^{-3}$μ	Wear intensity $I \times 10^{-11}$
Untreated	0.125	22	0.05	0.37	80
	0.25	28	0.16	0.13	9
	0.38	28	0.16	0.17	5.5
	0.62	45	0.16	0.21	4.6
	1.25	55	0.18	0.42	9.3
Mechanically treated and oxidized	0.125	22	0.085	0.15	3.3
	0.25	28	0.080	0.07	1.4
	0.38	30	0.053	0.01	0.7
	0.62	40	0.085	0.01	0.44
	1.25	55	0.085	0.01	0.22
Impregnated with phosphate solution after mechanical treatment and oxidation	0.125	20	0.080	– *	–
	0.25	22	0.027	–	–
	0.38	24	0.035	–	–
	0.62	25	0.043	0.015	0.60
	1.25	25	0.020	0.009	0.21

4 Summary Remarks

Preoxidation of high-chromium-content Fe-Cr-Al-La corrosion-resistant alloys with the optimal mode of their oxidation (1–5 h, 1200 °C), after grinding and mechanical polishing, leads to the formation of scale with the most distinct contours of modulation (see Fig.1). Also, the distinguished feature of this scale is its fine-grained structure – a mixture of nanocrystallites ($\leq$ 500 nm), mainly of alumina and chromia. Such a structure is formed during the first hours of oxidation and remains practically unchanged for a long period of time, retaining its protective abilities against both corrosion and abrasion.

A deep structural changes taking place under geometrical surface layer during mechanical and chemicothermal treatments, can be used for the considerable improvement of tribological

behaviour of the initial material. The results of preliminary study in this direction appear to be forward-looking, and may be a good starting point for further research work.

References

[1] K.A. Yushenko, B.A. Movchan, Yu.S. Borisov, N.N. Borisova. Materials of All-Union Sesion on “Protective Coatings in Machine Building”. Kiev, Naukova Dumka (1987) 208.

[2] O. Mikadze, B. Bulia. Bulletin of Georgian AS, 163, N3 (2001) 495.

[3] E.R. Kutelia, O.O. Tsurtsumia, B.G. Eristavi, O.I. Mikadze, B.P. Bulia. GEN, N1(2005)19.

[4] O.I.Mikadze, M.N.Okrosashvili, D.D.Ebanoidze, B.P.Bulia, T.A.Dzigrashvili, N.I.Maisuradze. Metallofizika I Noveishie Technologii. 27, N10(2005)1297.

[5] O.Tsurtsumia, E.Kutelia, O.Mikadze, B.Bulia. The European Corrosion Congress. Lisbon, Portugal. Sept. 4–8 (2006).

[6] J.A.Laskowski, C.DellaCorte. Society of Tribologists and Lubrication Engineers. Cincinnati, Ohio. May 19–23 (1966).

[7] A.L.Borisova, A.A.Tkachenko. Powder Metallurgy. N11 (1987) 26.

[8] D.G. Garuchava, G.O.Mikadze, O.I.Mikadze, I.Z.Tsikhelashvili. Oil and Gas of Georgia. N15 (2005) 126.

[9] M.M.Nadareishvili, Z.A.Kvatadze, G.O.Mikadze, N.I.Maisuradze, O.I.Mikadze. Problems of Metallurgy, Welding And Materials Science. N2, (2006) 6.

[10] A.Rahmel, G.C.Wood, P.Kofstad, D.L.Duglas. Oxidation of Metals. 23 N5-7 (1985)251.

Sliding Friction: Global *Versus* Local Analysis

A. Ramalho, M.C. Oliveira and L.F. Menezes
CEMUC; Dep. of Mechanical Engineering, University of Coimbra (Portugal)

Abstract

Friction appears at the physical interface between two surfaces in contact and affects all mechanical systems. Friction is strongly influenced by the interfacial environment, either as lubricants or as dry films or contaminants between the surfaces. There is a wide range of physical phenomena that affect friction; this includes elastic and plastic deformations, fluid mechanics and wave phenomena. Friction was studied extensively in classical mechanical and there has lately been a strong resurgence driven by strong engineering needs and the availability of new material solutions and also high resolution measurement techniques. Despite the availability of several friction models as the Amontons-Coulomb, the Dahl model and bristle models like Haessig & Friedland's and the LuGre model, the experience shows that for most applications friction difficultly could be conveniently explained by any of the available models. The generality of models for contact with friction involve global analysis resulting on a friction coefficient, calculated based on the relationship between forces. Assuming that the friction coefficient value is independent of the stress distribution, a constant value is applied in local analysis, as for example Finite Element Analysis. The most elaborated models consider the effect of local sliding speed or local displacement. The present work aims to analyze and discuss the effect of stress distribution on friction in unlubricated sliding contacts. Based on a set of experiments carried out on load-scanning type equipment, the friction behavior of a 1045 AISI steel and the validity of the Coulomb model will be discussed for both elastic and elastic-plastic contacts.

1 Introduction

Friction is ever-present in all mechanical systems involving parts with relative motion. In most mechanical applications friction has a disadvantageous effect; but, in many other cases, friction is the key factor which assures the system main function. Considering the several aspect of the friction, in most cases friction operates as a force that resists to relative movement; however, in other applications friction acts as a dissipation mechanism or even as a mechanism of energy transfer. In different applications friction has different roles, thus any discussions about it should take into account the specific characteristics of the application.

In spite of the enormous development of tribology in the second half of the 20th century, very simple relations are considered in the mechanical design to take into account the effect of the friction. In fact the Amontons's friction laws [1, 2] support most of the design rules. Therefore, the mechanical design requires the knowledge of the friction coefficient value for the contact condition under study. This friction coefficient is calculated based on the relationship between forces. Assuming valid the 2nd Amontons's law, the friction can be assumed constant in any point of the contact area. However, in the substantiation of the Amontons's laws, which occurs only

after the 40's, especially with the work of Bowden and Tabor [3], the behavior of the contacting materials is usually considered as elastic-perfectly plastic.

Another important issue is the fact that the friction measurement involves global analysis of the total forces applied to the entire contact area, usually used to calculate a friction coefficient. Assuming that the friction coefficient value is independent of the stress distribution, a constant value is applied in local analysis, as for example Finite Element Analysis. The most elaborated models consider a correction factor based on local sliding speed or local displacement.

The present work aims to analyze and discuss the effect of the stress distribution on the friction in unlubricated sliding contacts. Based on a set of experiments carried out on load-scanning type equipment, the friction behavior of a 1045 AISI steel and the validity of the Coulomb's model will be discussed for both elastic and elastic-plastic contacts.

2 Materials and Experimental Details

The test equipment used in this study was developed to allow sliding contact under increasing normal loads [4]. The geometry of the specimens is cylindrical. If the specimens are placed in such a way that the sliding direction makes 45º relative to the axis of each cylinder, the sliding movement uses fresh contact points in both specimens, figure 1 a).

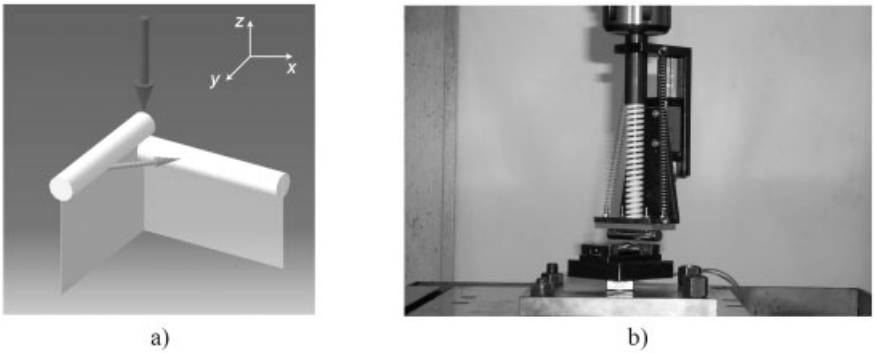


Figure 1: a) Outline of the contacting specimens. b) Picture of the experimental set-up.

The experimental equipment, figure 1 b), includes two high precision linear actuators placed in perpendicular directions; one to drive a spring normal load system and the other to produce the tangential relative displacement. The linear actuators are numerically controlled resulting in very accurate motion, allowing to follow different displacements or loading trajectories. A three components load cell supports the lower specimen; therefore both friction and normal forces are accurately measured during the test and their values are acquired using a suitable hardware and software.

In the present study the normal load was applied with a linear trend, increasing from 0 to 45 N (nominal values) with a loading rate of 4.5 N/s, while the specimen slides with a relative speed of 1 mm/s. In such conditions, the load increases 4.5 N for each mm of the wear track, in the direction of the cylinder axis. Figure 1b shows a picture of the specimens during the

test. The material used was the steel AISI 1045 sliding against itself. The tests were performed unlubricated in air with 20 ºC and 50 %RH. One of the advantages of this test is the fact that, for each specimen, a different and fresh contact point is used for each value of normal load. This fact allows the calculation of the contact stresses in each point, because both contact geometry and contact forces are absolutely well known.

In order to vary the contact stresses, keeping the contact loads, the diameter of the contact cylinders was changed. Seven different diameter values of: 4, 6, 8, 10, 12, 15 and 19 mm, have been tested. The cylindrical specimens were polished up to 1000-grit emery paper. The roughness of the specimens was measured in the axial direction obtaining: Ra = 0.47 μm and Rsk = –1.1. Prior testing the specimens was ultrasonically cleaned with acetone.

3 Results and Discussion

3.1 Theoretical Considerations

Considering only the effect of the normal load, therefore considering the Hertz's contact model [5], the contact stresses can be calculated as a function of the normal load and of the cylinders radius. Figure 2 shows the evolution of the contact stresses in the contact circle along the x axis (see the axis system in figure 1 a)) for a normal load of 14 N and considering cylinders with 10 mm of diameter. Figure 2 a) displays the evolution of normal stresses σ_r, σ_θ and σ_z, while figure 2 b) shows the evolution of the maximum tangential stress. Considering the mechanical properties of the AISI 1045, presented in table 1, and assuming the maximum tangential stress as yield criterion, it is possible to identify the part A_1 of the contact where plastic deformation occurs. In figure 2b) the plastic deformation occurs in the circle inside the points P_1 and P_2. Therefore the plastic deformation is predominant in the contact if $A_1 > A_2$, thus $r_1 > 0.707\ r_2$, being r_1 the radius of the plastic zone A_1 and r_2 the radius of the Hertz circle.

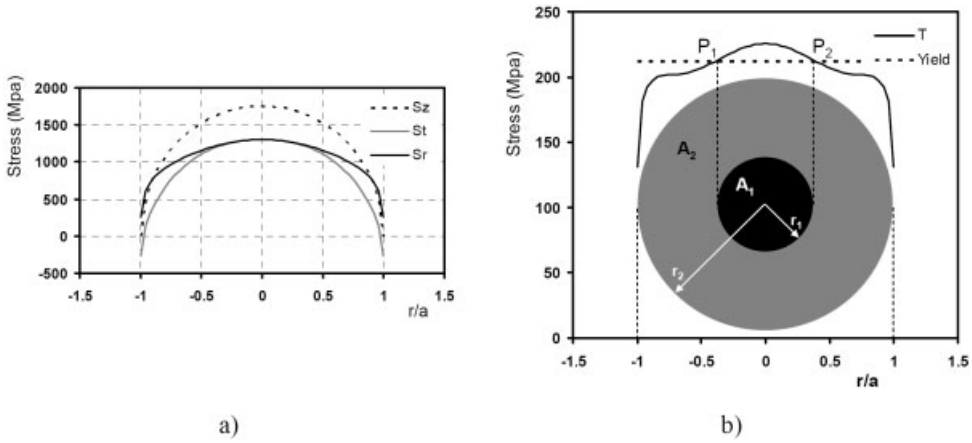


Figure 2: Graphic of the stresses on the contact plane considering the Hertz contact model and cylinders with $\phi =$ 10 mm and a normal load of 14 N. a) Normal stresses on the normal, tangential and radial directions. b) Tangential stress and identification of the contact area (A_2) and plastic deformed area (A_1).

Applying this criterion to all the cylinder diameters under study, it is possible to establish an equation to identify the threshold value of the force above which the contact is predominantly plastic, equation (1). In equation (1), r is the radius of the contacting cylinders in mm and F_n is the transition value of the force in N.

$$F_n > 0.65\, r^2 \tag{1}$$

As the nominal domain of the normal load range from 0 to 45 N, applying equation (1) to the medium value, 22.5 N, the value of 11.8 mm was obtained for the cylinders diameter. Therefore, from the former theoretical analysis, the diameter of the cylinders of around 12 mm establishes the limit between two distinct cases: for higher cylinder diameters the contact is predominantly elastic whereas for smaller cylinder diameters the contact is predominantly plastic.

Table 1: Mechanical properties of the AISI 1045 steel

Property	Value
Tensile strength (MPa)	707
Yield stress (MPa)	425
Elastic modulus (GPa)	207
Poisson ratio	0.28

3.2 Experimental Results

Both friction and normal forces were acquired during each entire test. Figure 3 shows the graphic of the friction force against the normal force for the test of the 4 mm diameter cylinders. Taking into account the Amontons-Coulomb friction model, the friction coefficient is the slope of the evolution of the friction force plotted against the normal force; therefore, the slope (0.16) of the trend-line presented in figure 3 is the friction coefficient. As along the test, the normal load range from 0 to 45 N, it is expected that the dimension of the contact increases continuously. Figure 3 displays also the evolution of the wear track width along the load trajectory.

The results obtained for all the tested specimens reveal a linear evolution similar to that showed in figure 3. Nevertheless, the values of the friction coefficient change with the increase of the cylinders diameter, as shown in table 2. In fact, the cylinders with diameters higher than 12 mm lead to an unchanged value of the friction of 0.129. However, for smaller cylinders, the friction coefficient ranged from 0.140 to 0.159.

Table 2: Measured friction coefficient for the different cylinder diameters.

Diameter (MM)	4	6	8	10	12	15	19
Frict. Coeff.	0.154	0.146	0.140	0.159	0.128	0.129	0.129

Considering the results obtained applying the Hertz contact model, the experimental tests leads to conclude that if the stresses in the contact plane are predominantly plastic the friction coefficient increases almost 20 %.

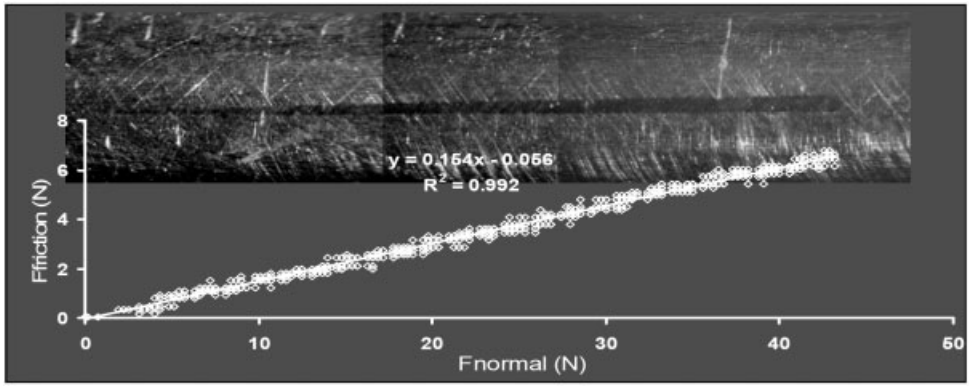


Figure 3: Friction force against normal force evolution for the test of the 4 mm diameter cylinders and evolution of the wear track width along the load trajectory.

In spite of the clear tendency displayed by the results, a deep study must be done to support a complete understanding of the influence of the plastic deformation on the friction. However, as the material used, the AISI1045 steel, presents a small strain-hardening effect, it is expected that materials with more ability to increase the mechanical resistance by strain could have a more marked change of the friction coefficient.

4 Concluding Remarks

Load scanner tests were applied to study the hypothetic interactions between contact stresses and friction coefficient.

Tests have been done using cross-cylinders contact submitted to normal loads increasing from 0 to 45 N under unidirectional sliding at a relative speed of 1 mm/s. The diameter of the cylindrical specimens has been increased from 4 to 19 mm to allow the change of the contact regime from predominantly plastic to elastic contact.

In spite of the cylinder diameters, all the tests reveal linear relations between the friction force and the applied normal load.

Applying the Hertz contact model, therefore considering only the normal load effect, and considering the Tresca's yield criterion, it was demonstrated that the contact is predominantly plastic or elastic when the cylinders diameter is lower or higher than 12 mm, respectively.

For contacts under predominantly elastic deformation, the measured friction coefficient was 0.129 while for contacts leading to predominantly plastic regime in the contact plan, the friction coefficient increases up to 0.159.

Acknowledgements

The authors are grateful to the Portuguese Foundation for Science and Technology (FCT) for the financial support for this work (project PTDC/EME-TME/74152/2006).

References

[1] G. Amontons. Sur les frottements des machines. Histoire de L'Academie Royale des Sciences, 1699.

[2] C.A. Coulomb. Theorie des machines simples. Mémoires de mathematique et physique, Academie des Sciences, Paris, 1785.

[3] F.P. Bowden, D. Tabor. The friction and lubrication of solids. The Calendron Press, Oxford, 1964.

[4] A. Ramalho, Study of the relationships friction – contact stresses using load scanner tests, Proc. 11th Nordic Symposium on Tribology – NORDTRIB 2004, (Ed. Kristian Tønder), Tromsø, Norway, June 2004.

[5] K.L. Johnson, Contact Mechanics, Cambridge University Press (1996).

Deformation of WC-Co Hardmetals During Scratch Testing

S. N. Ndlovu, K. Durst, M. Göken
University of Erlangen-Nürnberg, Erlangen

1 Introduction

WC-Co hard metals are well established powder metallurgy products. The unique composite structure of hard WC grains in a tough cobalt matrix results in excellent wear resistance. Recent developments have led to the production of nanostructured WC-Co hard metals which consist of nanoscale tungsten carbide grains in a cobalt matrix. These nanostructured hard metals are reported to have enhanced wear properties as a result of their increased hardness and the increased constraint of the WC grains in the binder phase which results from the reduced binder mean free path [1, 2]. Nanoindentation is a well established experimental technique to investigate the local mechanical properties of materials and a Nanoindenter can also be used for scratch testing of materials [3]. The local wear behaviour of WC-Co hard metals will thus be investigated using scratch testing. The mechanical and wear properties of WC-Co hard metals on the local scale will be investigated with emphasis on the WC grain size and the cobalt content.

2 Experiment

2.1 Materials

Seven commercial hard metal grades with varying cobalt content ranging from 6 to 15 % were tested in this study. The grades are classified as ultra fine (UFG), medium (MG) and coarse grained (CG) depending on the size of the WC grains. The characterisation data is given in Table1.

Table 1: Composition and properties of the investigated WC-Co cemented carbides

Sample	Average WC grain size (μm)	Description	Binder wt%	Vickers hardness H_v	Indentation hardness (GPa)	Young's Modulus (GPa)
J15	2.65	CG	15	1017	12.7	555
NY15	0.25	UFG	15	1486	19.7	561
T06M	1.21	CG	6	1380	18.4	530
T06MF	0.60	MG	6.5	1575	22.1	638
T06MG	0.48	UFG	6	1760	21.8	476
T06F[1]	0.66	MG	6	1710	22.0	615
T06SMG	0.25	UFG	6	1940	25.5	623

[1]Contains 0.5% VC and 0.2% Cr_3C_2

The specimens were prepared for scratch testing by polishing to a 1µm diamond finish. After each polishing step the samples were cleaned in ethanol in an ultrasonic bath. The microstructure of four of the samples is shown in figure1.

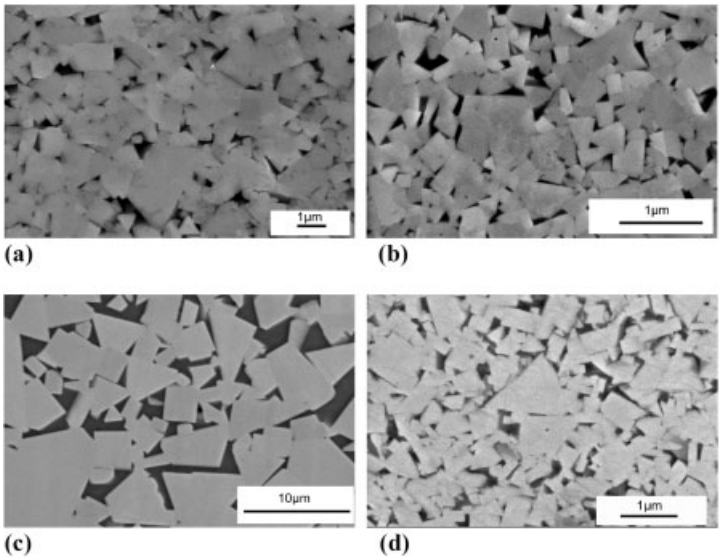


Figure 1: Micrographs of the samples (a) T06MG (b) T06SMG (c) J15 and (d) NY15

2.2 Instrumented Scratch Testing

Nanoscratch tests on the hard metals were performed using a Nano Indenter XP with a load controlled head. The maximum load capacity for the standard system is 500 mN with a precision of less than 1 mN. All the scratch tests were performed with one corner of a Berkovich indenter in the scratch direction since the tip orientation has been found to have an effect on the wear behaviour [4, 5]. The normal load ranged from 5 mN to 500 mN with a tip velocity of 10 µm/s. Two single scratches and one multiple scratch test were carried out for each load. The scratch depth and width were measured at 5 µm intervals along the length of the scratches. The average scratch depth for each load is reported. Tip calibration was performed using fused silica before each series of tests to monitor the tip function and no significant change in the tip shape was observed. The worn samples were examined using an atomic force microscope (AFM) and a scanning electron microscope (SEM).

3 Results

3.1 Low Cobalt Content

The scratch depth was determined using the section analysis mode of the AFM. Figure 2 shows the increase in scratch depth with increasing load for the samples containing 6 wt% cobalt binder.

A plot of the grain size versus the scratch depth was made at a load of 100 mN (figure 3) and shows that an increase in the WC grain size leads to an increase in the scratch depth i.e. a decrease in scratch resistance. A lower scratch depth was measured for the UFG sample (T06SMG) compared to the coarse grained hard metal (T06M). At a load of 100 mN the coarse grained sample exhibited a scratch depth of 297 nm compared to 227 nm for the UFG sample (T06SMG) for a single scratch.

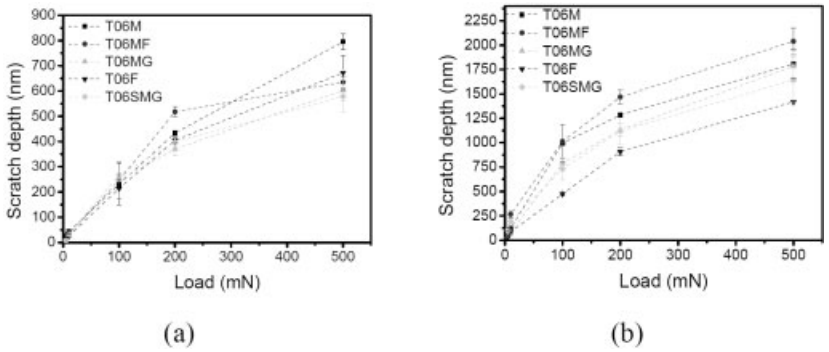


Figure 2: Plot of scratch depth against scratch load for the 6 wt% Co samples
(a) single scratch and (b) multiple scratch test (20 passes)

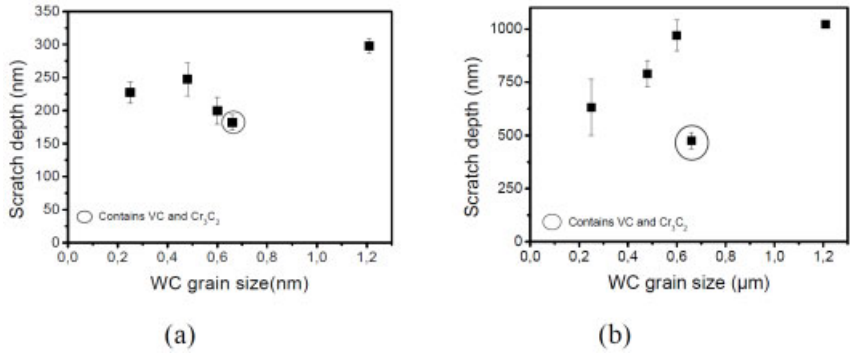


Figure 3: Plot of scratch depth against WC grain size at 100 mN(a) single scratch and (b) multiple scratch test

T06MF and T06F have similar WC grain sizes and therefore the difference in the scratch depth measured could be due to the chemical additions to the binder in T06F. This sample contains 0.5% VC und 0.2% Cr_3C_2 which resulted in a better wear performance of the material.

An increasing scratch depth was found for multiple scratch passes. The scratch depth increased from 298 nm to 1.022 µm and from 227 nm to 632 nm for T06M and T06SMG respectively, after 20 scratch passes. Scratch testing at low loads resulted in grooving of the WC grains and the formation of cracks in the WC grains as shown in figure 4. Multiple scratches at low loads led to the removal of material via WC grain fracture and fall out. In the UFG sample a film was observed on the surface of the damaged region as discussed in earlier work [6].

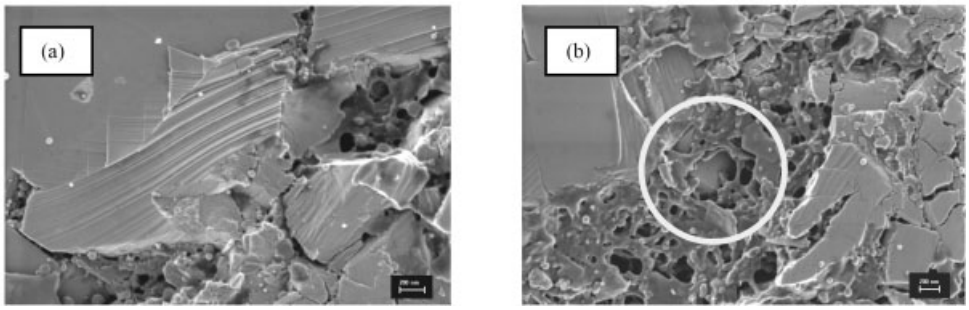


Figure 4: Micrographs of (a) T06F and (b) T06M after a single scratch test at 500 mN

At high loads single scratches resulted in more severe WC grain cracking and ductile deformation of the WC grains was also observed with extensive slip line formation as shown in figure 4a. The deformation of the cobalt binder was also observed, it attains a porous-like structure during scratching which makes it easier for WC grain fall out (figure 4b). Multiple scratches at high load led to the formation of a mechanically mixed layer composed of WC fragments and cobalt binder. There was also material loss as a result of grain fall out and fracture

3.2 High Cobalt Content

The UFG sample (NY15) displays a consistently higher scratch depth at all tested loads as shown in figure 5. Multiple scratch tests saw a significant increase in scratch depth for both samples with the UFG sample exhibiting a poorer behaviour. For example the change in depth from a single to a multiple scratch test at a load of 500 mN is 150 % for the coarse grained material and 84 % for the UFG sample.

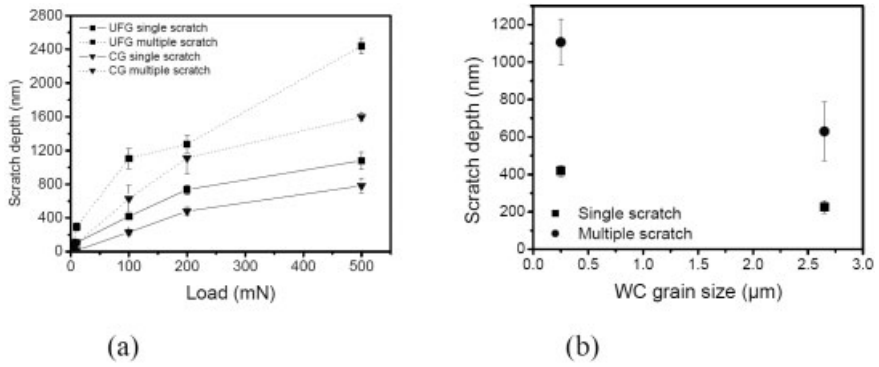


Figure 5: (a) The variation in scratch depth with load for the 15 wt% Co samples (b) scratch depth plotted against WC grain size at 100 mN

An examination of the sample with a SEM showed that the wear mechanisms in the UFG sample were much more severe. Grooving of the WC grains and pile-up of the binder phase was

observed in the CG sample after single scratch tests at low loads and multiple scratch testing resulted in chipping of the WC grains due to crack growth and intersection. Extrusion of the Co binder was also observed (figure 6a). The UFG sample exhibited cracking and chipping of the WC grains and fall out of the smaller WC grains as shown in figure 6b. Multiple pass tests led to increased material removal and the formation of a mechanically mixed layer on the material surface.

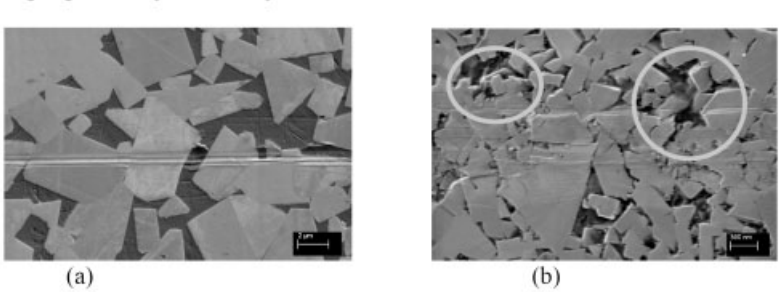


Figure 6: SEM micrograph of WC-15 wt% Co sample after single scratch test at 5 mN (a) CG sample and (b) UFG sample (please note the different scale bars)

The typical wear damage observed in the CG sample after single scratch tests at higher loads is shown in figure 7a. This shows the formation of slip lines in the larger WC grains and crack formation approximately normal to the slip line direction. Cutting and chipping of the WC grains was also found which led to the removal of material. Multiple scratch tests resulted in more material loss and the formation of a mechanically mixed layer. Single and multiple scratching in the UFG sample at high loads resulted in more extensive grain removal, fracture and the formation of the mechanically mixed layer which was also observed at multiple passes at low loads. The marked area in figure 7b shows a region on the edge of the scratch where WC grains have been removed from the bulk material after a single scratch with a 100 mN load.

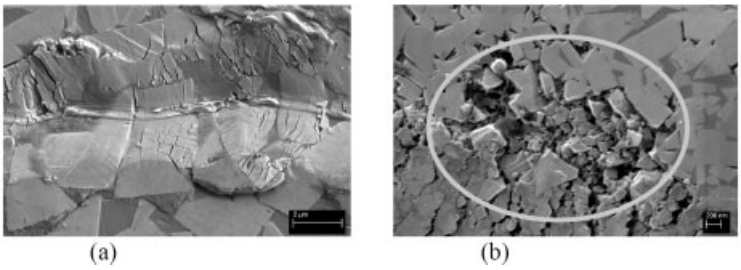


Figure 7: WC-15 wt% Co after a single at 100 mN (a) CG sample (b) UFG sample

T06SMG and NY15 have a WC grain size of 250 nm and were compared to determine the influence of binder content. The 6 wt% Co sample showed a lower scratch depth than the 15 wt % Co sample for both single and multiple scratch tests

4 Discussion

4.1 Low Cobalt Content

During a scratch test a load is first applied and the indenter penetrates the sample and then moves across the sample at the chosen velocity. At low loads the penetration depth of the indenter is very low and it only scratches the surface of the material which leads to cracks and grooves in the WC grains. Multiple scratching at low loads leads to fracture of the WC grains as a result of crack growth and intersection. The fractured grain segments may remain embedded in the material or be lost. Grain fall out occurs due to the movement of the sharp indenter tip which repeatedly pushes against grains which are loosely anchored as a result of binder extrusion. Grain fall out in the UFG samples was very limited, this is because these materials are harder and therefore the penetration depth of the indenter is lower and the damage mainly occurs on the surface of the material. At higher loads the penetration depth is increased and the damage occurs deeper in the material surface. A cross section of a scratch is shown in figure 8a and this shows that the cracks in the grains extend into the bulk material. The micrograph also shows that the material is not completely pore free and small pores can be seen in the material as marked. The presence of pores can be detrimental to the material during scratch testing as the pores compromise the material integrity.

The binder phase exhibits a porous like structure after scratch testing, which makes it much easier for the WC grains to be removed from the material (figure 4b). This explains the extensive grain fall out observed in the WC-6wt%Co samples during multiple scratch testing at high loads.

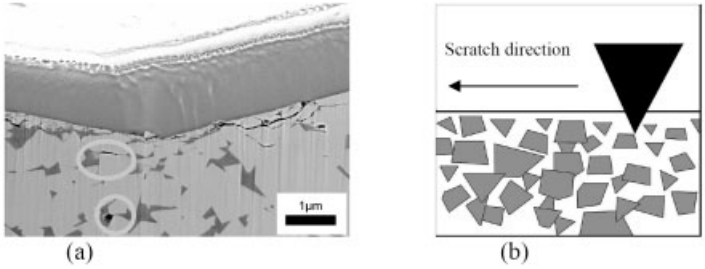


Figure 8: (a) Cross-section of multiple scratch on T06MF (b) Schematic of wear mechanism

4.2 High Cobalt Content

At low scratch loads the coarse grained material exhibits very low scratch depths and the damage is confined to grooving of the WC grains and extrusion of the cobalt binder. The UFG material on the other hand shows much more severe damage mechanisms. Single scratches resulted in grooving, cracking and chipping of the WC grains and also the fall out of WC particles in the UFG sample. A schematic of the proposed wear mechanism is shown in figure 8b. A low load results in a relatively low penetration depth, however due to the high content of the binder phase the penetration depth is higher than that in the WC-6Wt%Co samples. In the CG samples the grains are very large and even at the higher penetration depths only the surface of the WC grains

is damaged. In comparison the grain size in the UFG sample is comparable to the penetration depth and the movement of the indenter across the material can lead to the removal of the WC grains. At higher loads a similar mechanism would be expected. At a load of 500 mN a scratch depth of 614 nm was observed for the CG material after a single scratch test, this is very small in comparison to the average grain size of 2.65 µm. The scratch depth for the UFG sample at the same load was 1.024 µm which is more than four times the average grain size of the material.

Thus the material behaviour in the WC-15wt%Co samples during scratch testing is influenced by the local material properties and not the bulk material properties. It must however be noted that multiple scratch tests at high loads led to similar wear mechanisms in both the UFG and CG 15 wt% samples. In the case of the WC-6wt%Co samples the bulk material properties appear to play a bigger role in the material behaviour regardless of the WC grain size. This phenomena was reported for the erosive wear of WC-Co hard metals by Anand and Conrad [7]. They found that fine-grained materials responded in bulk to erosive attack when the damage zone was comparable to the microstructural dimensions. In coarser materials the microstructure was comparable to the damage zone and the constituent phases of the material responded individually to the erosive attack.

5 Conclusions

A finer WC grain size was found to result in a better wear performance for the 6 wt% Co samples. However a coarser grain size resulted in better wear performance in the 15 wt% samples. The UFG 15 wt% Co sample showed extensive WC grain fall out, not observed in the CG material. A lower binder content (for a given WC grain size) was found to improve the scratch resistance of the material. Therefore it could also be concluded that ideal microstructure for good scratch resistance would be a low binder content and ultra-fine WC grain size.

6 References

[1] K. Jia, T.E. Fischer, Wear **1997**, 203/204, 310–318.

[2] H. E. Exner, J. Gurland, Powder Metallurgy **1970**, 13, 13–21

[3] K. Durst, M.Göken, Materials Science and Engineering A **2004**, 387–389, 312–316.

[4] S. W. Youn, C. G. Kang, Wear **2006**, 261, 328–337.

[5] D. Mulliah, D. Christopher, S. D. Kenny, Roger Smith, Nuclear Instruments and Methods in Physics Research **2003**, B202, 294–299.

[6] S. Ndlovu, K. Durst, M. Göken, Wear **2007**, 263, 1602–1609.

[7] K. Anand and H. Conrad, Journal of Materials Science **1988**, 23, 2931-2942.

Nanotribology at Electrodes: Influence of Adsorbates and Potential on Friction Forces Studied with Atomic Force Microscopy

Michael Nielinger, Florian Hausen, Nikolay Podghainiy and Helmut Baltruschat
Institute for Physical and Theoretical Chemistry, University of Bonn
Römerstrasse 164, D-53117 Bonn, Germany
Email:baltruschat@uni-bonn.de

1 Introduction

The invention of the atomic force microscope [1] made it possible to study friction on atomic scale: The normal force acting on the cantilever, i.e. the interaction between the surface and the tip normal to the surface, leads to a bending of the cantilever. Lateral forces originating from friction during the movement of the tip lead to a tilt of the cantilever. Both are detected simultaneously by means of a reflected laser beam and a four quadrant detector. Although many insights have thus been gained on the atomic level, we still have to go a far way to obtain a true understanding of all the origins of friction.

One difficulty of the friction measurements on the atomic scale in ambient environment are capillary forces between tip and the surface due to humidity. Experiments under ultra high vacuum (UHV), however, require expensive instrumentation; another disadvantage is that adsorbates in most cases cannot be reversibly desorbed in short times – heating usually is necessary. The study of electrochemical interfaces offers the advantage that surfaces can nowadays not only be studied with a cleanliness and reproducibility as surfaces under UHV conditions, but that adsorbates can quickly and reversibly be formed and desorbed. Thus, effects due to the change of the tip structure will be immediately noticed. Moreover, electrochemical interfaces are extremely important: in a wet stage, each metallic surface is an electrode surface, the electrode potential being defined by the environment: the ambient atmosphere, the composition of the liquid or other metals contacting the material under consideration (and thus forming a galvanic cell).

Astonishingly, despite of this, importance of electrochemical measurements of friction, there are only two independent reports on friction measurements on the atomic scale, both on HOPG surfaces.[2–4] We recently presented first friction measurements performed on Au(111) single crystal electrodes modified by Cu. [5, 6] Here, we extend this to Pt(111) and give further results for a Au(111) electrode.

2 Experimental

The single crystals (obtained from Metal Crystals & Oxides) were orientated within an accuracy of 0.5°. The preparation of the single crystal was performed by flame annealing. The cooling was performed in a H-cell over Milli-Q water in a 5 N argon atmosphere. The electrolyte consisted of 0.05 M H_2SO_4 and 0.4 mM $CuSO_4$. In some experiments a pure 0.05 M H_2SO_4 solution was used. A gold wire was used as the counter electrode. As a reference electrode, a Cu wire

was immersed in a Cu containing solution, separated from the AFM cell by a glass frit. All potentials are quoted with respect to the Cu/Cu^{2+} redox couple. During the measurements the AFM cell was maintained under an argon atmosphere. The measurements were performed with a commercially available AFM scanner (Molecular Imaging) and a Nanoscope III E controller (Digital Instruments, Santa Barbara, CA) fitted with a liquid cell. Commercial Si cantilevers were used (Vecco MP31100).

The nominal spring constant was 0.9 N/m. The spring constant for this type of cantilever varies between 0.6 and 1.2 N/m (manufacture specifications). External load was calculated as the product of the z-displacement of the cantilever and the nominal force constant. Since the exact torsional force constant of the cantilever is unknown, the value for the friction force will be given in volts (output signal of the photo detector).

During the friction force measurements the lateral signal is recorded while the tip travels along a length of the surface in opposing directions (trace ↔ retrace). The forward and reverse direction components of the loop are subtracted. Because the direction of forces arising from topographical effects will be invariant with the direction of motion of the tip, while friction forces always oppose the tip motion, the resulting signal is proportional to twice the frictional force. In image acquisition, a friction image is obtained by subtracting images acquired with opposing scan directions.

3 Effect of Cu-deposits on Friction

The advantage of an electrochemical study of the effect of metal deposits is demonstrated in fig. 1 and 2. In the experiment shown in fig. 1, Cu was electrodeposited on an atomically smooth Au(111)electrode surface at a potential of –80 mV vs. Cu/Cu^{2+}. This leads to the formation of many 3-dimensional Cu Clusters of a triangular shape. (Fig 1a). The corresponding friction image shows that friction on top of the cluster is increased (Fig.1b). Fig. 1c and 1d were recorded during a potential sweep to more positive potentials (values as indicated in fig. 1c).The cluster starts to dissolve at 0 V. Interestingly, at those parts of the surface which before were covered by the Cu cluster, the brighter colour in the friction image shows that friction there is still increased, although no deposit is visible in the topographic image. Please note: in grayscale friction force images, brighter colors correspond to a higher friction force.

This effect, which is only observed after a lifetime of the cluster of about 30 min, is indicative of an alloy formation between Cu and Au.

The surface around the cluster is covered by a densely packed Cu monolayer at the potential of 20 mV , but at 180 mV only by 2/3 of a monolayer of Cu[7]. The dark stripe at 180 mV in Fig. 1d) shows that friction is then reduced. In fig. 1b and 1d, also an increase of friction at the edge of the Cu cluster is visible. This is not just a geometric effect – moving the tip “uphill” requires an additional lateral force – a friction increase also occurs when the tip is moving “downhill”, when for geometric reasons the energy win should lead to a reduced force.

Such effects are also visible on an atomic scale: In fig.2, a Cu monolayer was repeatedly deposited and dissolved; such a deposition occurs several hundred mV above the reversible Nernst potential of bulk Cu deposition (“underpotentical deposition”).The following is noteworthy: (1) When the load on the tip is low (90 nN, left image), friction on the bare Pt(111) surface and on the Cu covered areas is similar. However, at high loads friction on areas covered by a monolayer

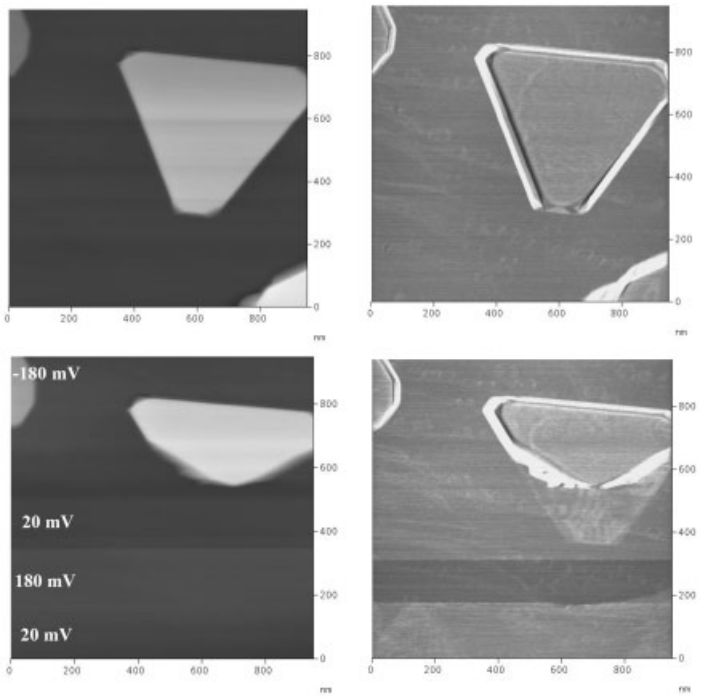


Figure 1: Copper cluster on (Au111) and dissolution of this cluster.
Left: Topographic images
Right: Friction images (bright colour corresponds to high friction)
Top: after deposition of Cu clusters at –80 mV vs. Cu/Cu^{2+}
Bottom: During a potential step to +20 mV, where Cu dissolves, a further step to 180 mV and back to 20 mV.

of Cu is clearly higher than on the bare substrate. (2) For both loads, friction is particularly large (dark horizontal stripes) during the transition from the bare surface to the Cu monolayer, i. e. when the surface is covered by single adatoms before the formation of a 2D lattice. (3) Even monoatomic steps lead to an increased friction (bent vertical dark stripes).

Fig. 3 shows the dependence of friction on load on the smooth parts of the surface. Classically, a linear dependence should be observed. However, a transition occurs around a load of 140 nN, above which the slope and thus the friction coefficient greatly increases. A similar effect was observed for Cu monolayers on Au(111) [5]. We assume that above a critical load the tip penetrates the adsorbed layer. Then, atoms or molecules have to desorb in front of the tip. The corresponding desorption energy represents the energy dissipation corresponding to friction. Since at the potential used here, the surface (both the bare Pt and the Cu monolayer) were also covered by a monolayer of anions, it may well be that the tip only penetrates the sulfate adlayer, not the Cu monolayer. The fact that such a transition also occurs for the Cu free surface suggests this latter interpretation. The drastic increase of friction during the onset of Cu deposition, however, is likely to be due to a hindrance of the tip movement by Cu adatoms. The increased

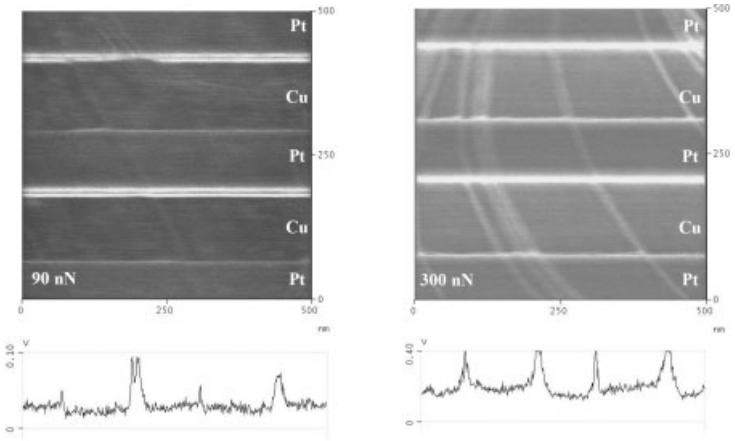


Figure 2: Change of friction forces during repetitive UPD of Cu on a Pt(111) electrode at two different normal loads. Below the images, a section analysis is shown; positive values and bright colours correspond to high friction.

friction at the step edges may, on the other hand, be ascribed to a non-elastic interaction of the tip with the atoms at the steps; it is well known that the mobility of atoms at steps is increased.

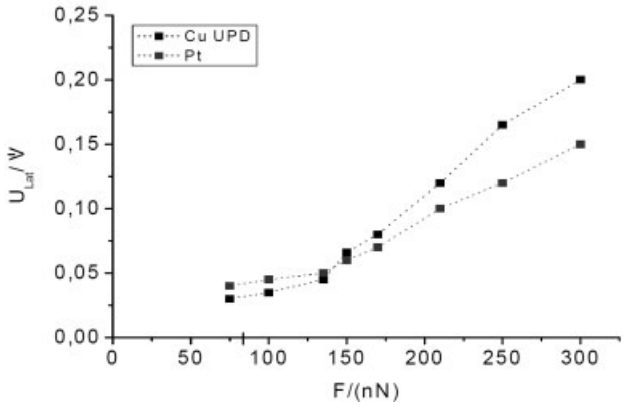


Figure 3: Dependence of friction (arbitrary units) on load for Cu – UPD on Pt(111).

4 Effect of Anions on Friction

The effect of anions was studied at a Au electrode. Fig. 4a shows the cyclic voltammogram – the capacitive charging current which flows to the electrode when the potential is linearly changed with time – during potential sweeps between 0.05 V (where no sulphate is adsorbed and the surface is reconstructed) and 1.2 V, where sulphate is adsorbed. The well known ($22 \times \sqrt{3}$) re-

construction is lifted around 0.6 V, the subsequent peak represents the capacitive charging due to adsorption of sulphate anions [8]. The small current peak close to 1.1 V is associated with the formation of an ordered sulphate overlayer. At this potential, also friction starts to increase (cf. fig. 4c), and reaches a maximum when sulfate adsorption is complete. The continuous, reversible increase between 0.6 and 1.0 V demonstrates that the increase of friction is not related to the lifting of the reconstruction, but rather due to sulphate adsorption. Fig. 4 b shows that the surface topography does not change with potential.

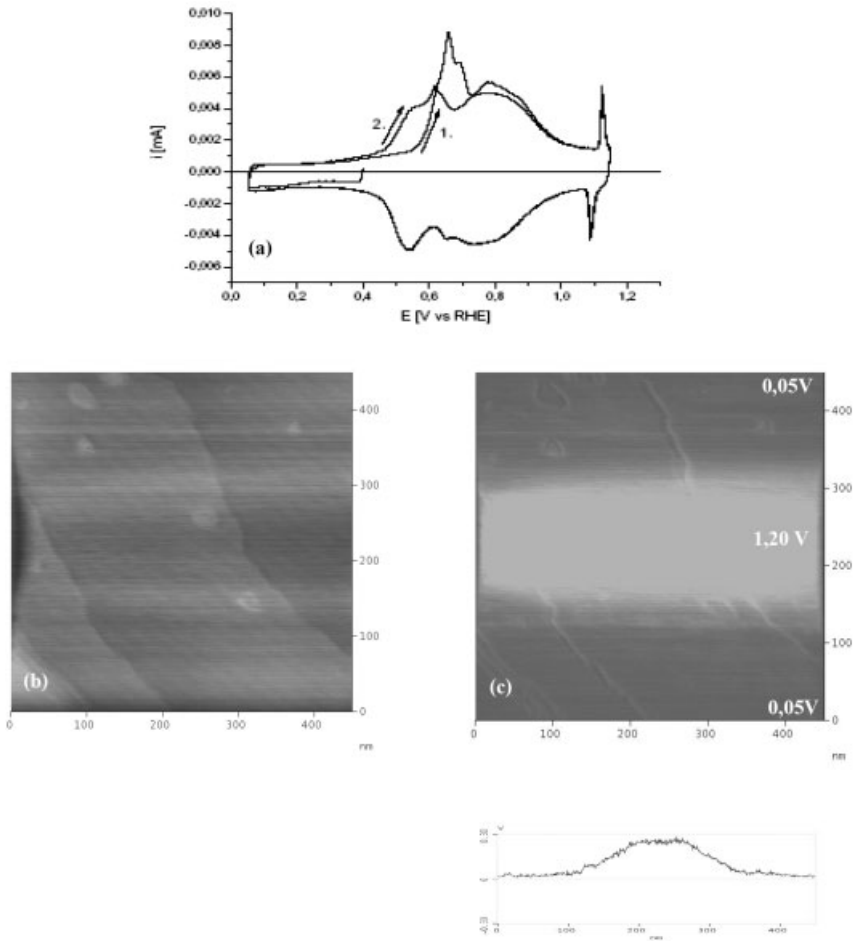


Figure 4: a) Cyclic voltammogram of Au(111) in the AFM cell
b) Topography
c) Friction image during the potential sweep

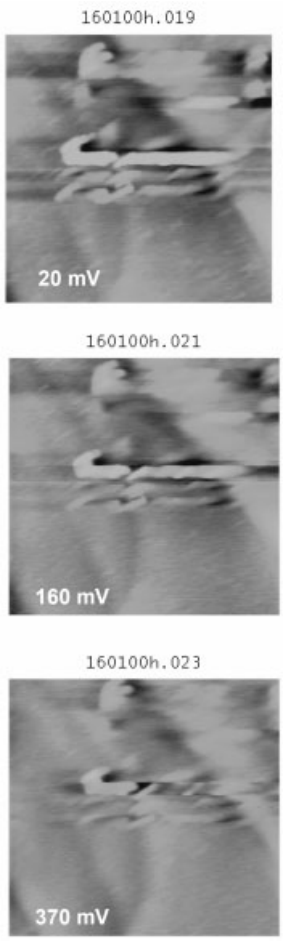


Figure 5: AFM-Tip induced Nanostructures on Au(111). (PtIr covered tips from Applied NanoStructures (TM Probes Model ANSCM-PT, force constant: 3 N/m) were used in this experiment)

5 Wear at Electrode Surfaces

The pressure exerted by the tip is quite appreciable: assuming a contact area of 10 nm², for a load of 100 nN a pressure of 10^{11} Pa (10^6 bar) is calculated. It is therefore astonishing, that under the above conditions we did not observe any defects or wear after the friction measurements. On the other hand, when scanning with an STM tip at large bias voltages, i.e. very close to the surface, we did observe a local nanostructuring, which we ascribed to a local alloy formation [9, 10]. Additional conditions for achieving such nanostructures were that the tip was made of PtIr and the solution contained a dissolved metal. To observe a similar effect by AFM, a Pt – covered AFM tip had to be used and the load had to be increased up to 1 μN (Fig.5). Here, first the tip was

scanning over a rectangular area of 800 nm$\times$100 nm at a potential of 10 mV vs. Cu/Cu^{2+} and a scan rate of 1.1 Hz. Afterwards, the larger area of fig. 5 was scanned for the images under normal conditions. A rectangular structure with a height of 1.4 nm is seen, which, after a potential change to more positive potentials is slowly dissolved, thus indicating the formation of a local alloy.

6 Conclusion

Measurements of friction at electrode surfaces are not only of great practical importance, but also provide a new insight in these phenomena. Monoatomic steps offer an additional channel for energy dissipation due to the higher mobility of atoms. An additional explanation is the Schwoebel-barrier [11]. Friction is also increased by both metallic and anionic adsorbates; the sudden increase of the friction coefficient at particular loads may be due a penetration of the tip into the adsorbate layer. The influence of the surface tension in the context of rolling friction still has to be elucidated.

7 References

[1] G. Binnig, C. F. Quate, C. Gerber, *Physical Review Letters* **1986**, *56*, 930.

[2] E. Weilandt, A. Menck, O. Marti, *Surface and Interface Analysis* **1995**, *23*, 428.

[3] M. Binggeli, R. Christoph, H.-E. Hintermann, J. Colchero, O. Marti, *Nanotechnology* **1993**, *4*, 59.

[4] B. Schnyder, D. Alliata, R. Kötz, H. Siegenthaler, *Applied Surface Science* **2001**, *173*, 221.

[5] M. Nielinger, H. Baltruschat, *Physical Chemistry Chemical Physics* **2007**, *9*, 3965.

[6] F. Hausen, M. Nielinger, S. Ernst, H. Baltruschat, *Electrochimica Acta* **2008**, *53*, 6058.

[7] M. H. Hölzle, U. Retter, D. M. Kolb, *Journal of Electroanalytical Chemistry* **1994**, *371*, 101.

[8] D. M. Kolb, *Progress in Surface Science* **1996**, *51*, 109.

[9] P. Berenz, X. Xiao, H. Baltruschat, *Journal of Physical Chemistry B* **2002**, *106*, 3673.

[10] M. Nielinger, P. Berenz, X. Y. Xiao, H. Baltruschat, *Surface Science* **2005**, *597*, 1.

[11] E. Meyer, R. Luthi, L. Howald, M. Bammerlin, M. Guggisberg, H. J. Guntherodt, *Journal of Vacuum Science & Technology B* **1996**, *14*, 1285.

Influence of Electrode Potential and Chelating Agents on Tribocorrosion Mechanisms of Tungsten

J. Stojadinović[1], D. Bouvet[2], M. Declercq[2], S. Mischler[1]
[1]Ecole Polytechnique Fédérale de Lausanne EPFL, Laboratoire de métallurgie chimique, CH – 1015 Lausanne
[2]Ecole Polytechnique Fédérale de Lausanne EPFL, Laboratoire d'électronique générale 1, CH - 1015 Lausanne

1 Introduction

Tribocorrosion is a material deterioration process which results from the interaction of wear and corrosion that takes place in tribological contact exposed to aggressive environment [1].

The lifetime and performance of many mechanical devices, such as orthopaedic implants, food processing equipment and pumps for chemicals, is limited by tribocorrosion. However, in some applications tribocorrosion can be conveniently used for manufacturing and finishing purposes. For example, chemical-mechanical polishing (CMP) process is widely used in production of integrated circuits.

In the CMP process suspended abrasive nano particles cause detachment of friable surface layers formed by reaction between the oxidizing aqueous suspension (slurry) and the material to be polished. Chemical additives such as chelating agents are added to the slurry in order to obtain better surface finish. Industrial improvement of the CMP process requires nowadays a better understanding of the involved tribocorrosion mechanisms and in particular of the role of the slurry components on material removal. This paper aims in particular at evaluating the effect of the oxidising conditions and of chelating agents on the tribocorrosion behaviour of tungsten as a typical microelectronic metal.

The tribocorrosion behaviour of metals was generally studied [2] by using sliding wear test rigs coupled with an electrochemical control of the samples.

Bielmann et al. [3] already showed that wear of tungsten under an electrochemically imposed potential was equivalent to wear under the same potential but established by adjusting the oxidizing power of the solution. Stojadinovic [4] studied the effect of electrochemically applied potential on the tribocorrosion behavior of a tungsten flat disk rubbed by an alumina ball in a 0.01 M H_2SO_4 solution and showed that for imposed electrode potentials up to 0.5 V MSE materials deterioration in the rubbed area proceeds by cyclic mechanical removal of the WO_3 passive film followed by repassivation of tungsten. Removal of tungsten metallic particles is only a negligible contribution to the overall deterioration. Above the electrode potential of 0.5 V wear was inhibited by the formation of a tribo layer that covers the wear track on tungsten and was probably formed by compaction of WO_3 particles previously detached from the metal surface.

Two types of solutions were used in this study, sulphuric acid and sulphuric acid with addition of chelating agent lactic acid, both with the same pH as technical CMP slurries. Electrochemical techniques (cyclic voltametry), and tribocorrosion techniques (tests on tribometer with electrochemical cell with reciprocating sliding motion) were used. Surface analysis techniques (SEM, XPS, AES) were used to assess surface chemistry.

2 Experimental Setup

Potentiodynamic polarization curves of tungsten were measured in a 0.01 M H_2SO_4 solution and in a 0.01 M H_2SO_4 + 0.1 M $C_3H_6O_3$ solution using an Autolab potentiostat PGSTAT 30 as described elsewhere [4]. Both solutions have a pH 1.5. The experiments were carried out at a room temperature. All potentials in this study are given in a respect to mercury sulphate reference electrode, which has a potential of +658 mV vs. SHE.

Tribocorrosion tests were performed on the tribometer, configuration ball on disk with reciprocating sliding motion, schematically shown in Figure 1.

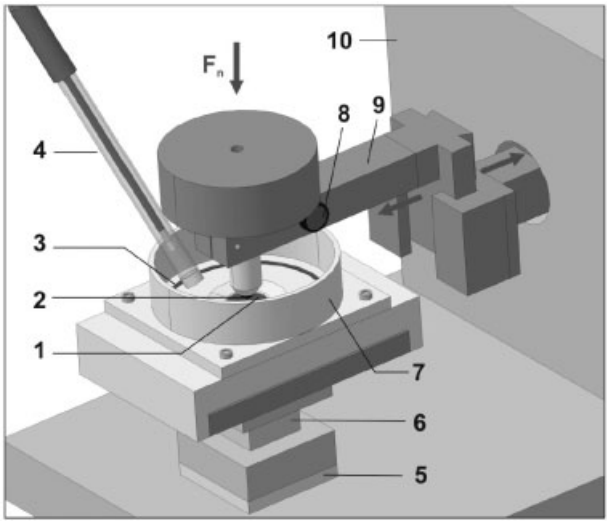


Figure 1: Schema of the tribometer KT – 01 for tribocorrosion experiments: (1) metal sample – working electrode, (2) alumina ball, (3) counter electrode, (4) reference electrode, (5) insulating block, (6) three – axes force transducer, (7) electrochemical cell, (8) laser, (9) drive arm, (10) linear motor.

Tungsten samples were fabricated by machining bars supplied by Good Fellow (purity 99.95 %) in form of 20 mm diameter disks, 6 mm in thickness. A platinum wire served as the counter electrode and a mercury sulphate electrode as the reference electrode.

The tungsten disk and the contacting alumina ball (6 mm diameter) were immersed in the solution and together with platinum and mercury sulphate electrodes connected to a Wenking LB 95 L potentiostat.

Tungsten disks were mirror polished and exposed to cathodic cleaning in the 0.01 M H_2SO_4 or 0.01 M H_2SO_4 + 0.1 M $C_3H_6O_3$ solution during 5 min at –1.7 V MSE. Afterwards, the electrode was stabilised at open circuit potential during 5 min, and passivated by applying the imposed potential during 5 min before starting rubbing at the same potential during 50 min. The rubbing was followed with static exposure of the sample surface at the imposed potential during 5 min.

Tribocorrosion tests in a 0.01 M H_2SO_4 solution were performed at imposed potentials of –1 V, –0.46 V, –0.2 V, –0.1 V, 0.2 V, 0.5 V, 1 V, and 1.5 V, selected on the polarisation curve (Figure

2). Tribocorrosion tests in a 0.01 M H_2SO_4 + 0.1 M $C_3H_6O_3$ were performed at two imposed electrode potentials, 0.2 V and 1 V.

The applied normal force was 6 N for all potentials. Frequency of rubbing cycle was 1 Hz. Tribocorrosion tests were carried out at a room temperature. Each measurement was performed twice with a new alumina ball to check for reproducibility.

The average width and depth of the wear track, extracted from cross section UBM profiles, were used to determine the wear track volume, V_{wt}, by multiplying it by wear track's length. Secondary electron microscopy SEM (JEOL 6300) was used to characterise wear patterns.

3 Results and Discussion

Figure 2 shows the polarization curve of tungsten in a 0.01 M H_2SO_4 solution and in a 0.01 M H_2SO_4 + 0.1 M $C_3H_6O_3$ solution. The presence of lactic acid yields higher anodic current densities but does not influence the corrosion potential (approximately –0.5 V for both solutions).

Higher anodic currents correspond to intensified dissolution caused by a thinning of the passive film [5]. By complexing the WO_4^{2-} ions released by the dissolution reaction of WO_3 passive film, lactic acid promotes passive film dissolution and thinning.

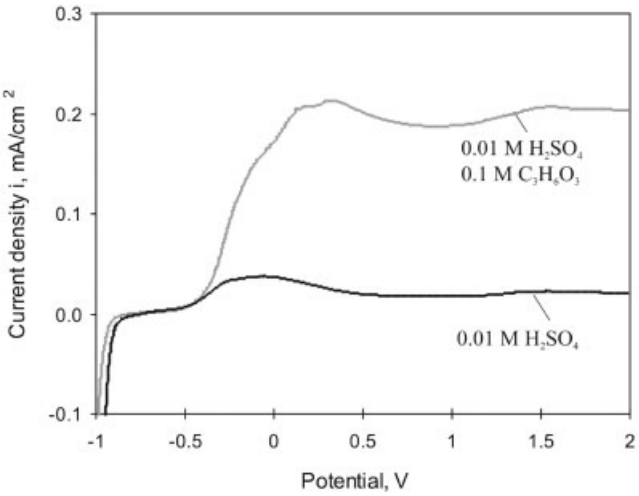


Figure 2: Typical tungsten polarization curves in a 0.01 M H_2SO_4 solution and in a 0.01 M H_2SO_4 with 0.1 M $C_3H_6O_3$ solution.

Except for the lowest value (–1 V), all selected tribocorrosion potentials lie within the passive domain, where a passive WO_3 film forms on the surface [4].

Figure 3 represents the coefficient of friction and current during rubbing at imposed electrode potential of 0.2 V in 0.01 M H_2SO_4. At the onset of rubbing the current increased sharply due to the abrasion of the passive WO_3 film covering the tungsten surface. The repassivation of the bare metal surface requires a certain time during which corrosion (and thus anodic current) is enhanced (wear accelerated corrosion). When rubbing ceased, the current decreased again to the

value observed before rubbing. The metal volume removed by oxidation (V_{wac}) was calculated from the wear accelerated corrosion current (I_{wac}) . The valence of a tungsten oxidation was assumed to have a value of 6.

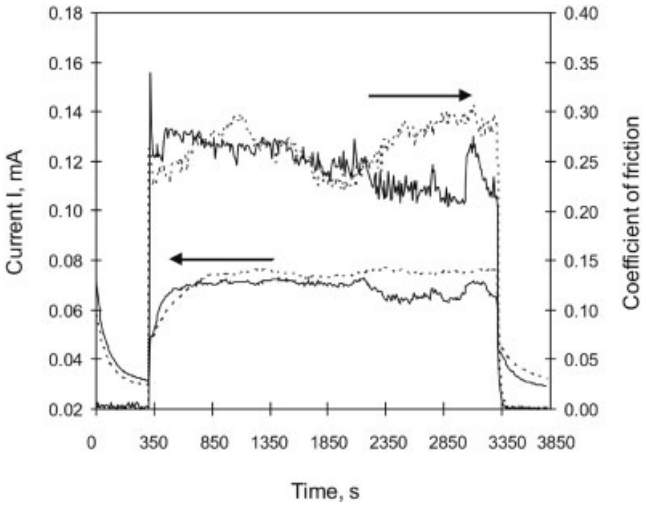


Figure 3: Evolution with time of the coefficient of friction and current during sliding of a smooth alumina ball against tungsten at imposed passive potential of 0.2 V. Results of two independent tests are plotted.

Figure 4 illustrates the variation of the wear track volume (V_{wt}) and of V_{wac} as a function of imposed potential. The values of V_{wt} and V_{wac} are very close for each potential. This indicates that most of tungsten is removed as oxidised metal (V_{wac}) through the abrasion of the WO_3 passive film.

In the 0.01 M H_2SO_4 solution two threshold potentials can be observed at –0.5 V and 0.5 V. Below –0.5 V wear is nearly independent of electrode potential because only negligible oxidation occurs in this potential region. In the region of potentials from –0.5 V up to 0.5 V wear increases with potential because WO_3 passive film thickness increases with potential [4]. Above 0.5 V wear volume decreases due to formation of a tribolayer (likely formed by compaction of WO_3 debris particles) in the wear track as shown by the SEM images (Figure 5 b). Figure 5 shows SEM images taken in the center of the tungsten wear tracks. The worn surfaces are generally smooth and featureless except at 1 V and 1.5 V in 0.01 M H_2SO_4 solution, where a tribolayer forms. No significant wear of the alumina ball was observed.

However, at the potential of 0.5 V wear is much higher in the presence of lactic acid. This is probably due to fast dissolution of WO_3 particles that prevents tribolayer formation. SEM images confirm the absence of a tribolayer on the sample rubbed at potential of 1 V in presence of lactic acid (Figure 5 c).

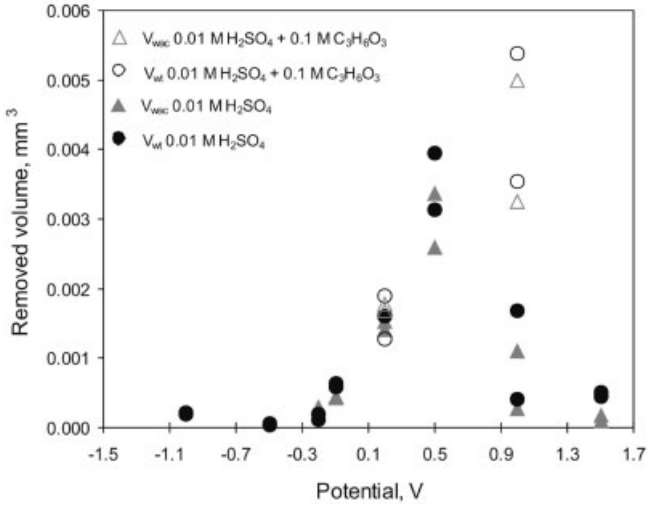


Figure 4: Influence of lactic acid and electrode potential on the wear of tungsten.

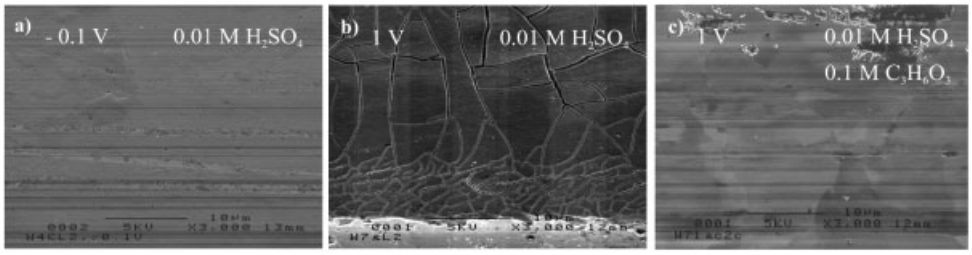


Figure 5: SEM images of the tungsten wear tracks obtained: a) at imposed electrode potential of -0.1 V in 0.01 M H_2SO_4, b) at imposed electrode potential of 1 V in 0.01 M H_2SO_4 and c) at imposed electrode potential of 1 V in 0.01 M H_2SO_4 + 0.1 M $C_3H_6O_3$.

4 Conclusions

The present tribocorrosion results show that wear of tungsten in 0.01 M H_2SO_4 depends critically on the prevailing electrode potential. Below 0.5 V material removal occurs trough the repetitive process of a WO_3 passive film formation and removal.

Above 0.5 V a thick tribolayer forms by agglomerated WO_3 particles, reduces wear and anodic oxidation.

By promoting WO_3 dissolution, chelating agent lactic acid impedes the tribolayer formation and enhances wear at high potentials.

5 References

[1] D. Landolt, S. Mischler, M. Stemp, Electrochim. Acta 46, **2001**, 3913–3929

[2] S. Mischler, Tribology International, In Press, **2007**

[3] M. Bielmann, U. Mahajan, R. Sigh, P. Agarwal, S. Mischler, E. Rosset, D. Landolt, Mat. Res. Soc. Symp. Proc. Vol. 566, **2000**, 97–101

[4] J. Stojadinovic, D. Bouvet, M. Declercq, S. Mischler, manuscript submitted to Tribology International Special Issue COST 532/Ecotrib **2007**

[5] C.-O. A. Olsson, M.-G. Vergé, D. Landolt, J. Electrochem. Soc., Vol. 151, No. 12, **2004**, B652–B660

Corrosion Behavior of Silicon Carbide in Aqueous Media Lubricated Sliding Applications

O. Krummhauer[1*], V. Presser[2], A. Kailer[1], K.G. Nickel[2], T. Hollstein[1]
[1] Fraunhofer-Institut für Werkstoffmechanik IWM, Woehlerstrasse 11, 79108 Freiburg
[2] Eberhard-Karls-Universität, Institute for Geoscience, Applied Mineralogy, Wilhelmstr. 56, 72074 Tübingen
*Correspondent author's email: oliver.krummhauer@iwm.fraunhofer.de

1 Introduction

Sintered silicon carbide (SSiC) is an advanced non-oxide ceramic material for applications in extreme chemical and high-temperature environments. The very high corrosion and wear resistance, the special mechanical properties and also the low friction coefficient in sliding applications in aqueous media explain why SiC is ideally suited as a material in face seals. The use of SiC for face seal applications in pumps is advantageous in many cases as the mechanical, chemical and economic properties of this material outreach any comparable material. Tribochemical reactions dominate the corrosion behavior of silicon carbide in aqueous media lubricated sliding applications. As described in literature, a reaction layer on the rubbing surfaces is formed due to a chemical reaction of silicon carbide and water. The reaction products are believed to improve the sliding characteristics of SiC and therefore the friction coefficient in medium lubricated sliding exposure is below 0.1. The formation of tribochemical layers depends on both thermodynamic and mechanical parameters. Environmental conditions, depending on load, sliding speed and friction type induce conditions of degradation and corrosion of self mated SiC face seals. It is well known that friction couples undergo tribochemical polishing of the surfaces in conditions of boundary lubrication in water. The following chemical equations describe possible reactions taking place on tribological exposed silicon carbide surfaces in aqueous media depending on temperature and pressure.

$$SiC + 2\ H_2O \Leftrightarrow SiO_2 + CH_4 \quad (1)$$

$$SiC + 2\ H_2O \Leftrightarrow SiO_2 + C + 2H_2 \quad (2)$$

The dissolution of the formed oxide layers depends on the solubility of the formed reaction products in the environmental media and of course on the concentration, already present in the solution. The dissolution of silica in aqueous media depends on the pH-value and is described in the following equation:

$$SiO_2 + 2\ H_2O \Leftrightarrow Si(OH)_4 \quad (3)$$

Due to very low wear rates in water lubricated sliding contacts of silicon carbide a semi-continuous-based model was performed to determine the wear characteristics in initial tribological exposure. Oxidation and degradation of silicon carbide may occur under very high loading and poor lubrication conditions. Elevated temperatures certainly increase the rate of oxidation,

the conditions of high pressure however is not clear. Calculating temperature and pressure based on micromechanical effects between contacting surfaces can be achieved using a micro-asperity-based model. Input data for the calculations are obtained via a stylus profilometry; thus having the advantage of real geometric surface data with a lateral resolution of two micrometers and the possibility to create localized temperature maps.

Wear models considering mechanical and chemical wear are primarily based on the work of T. F. J. Quinn in which he predominantly discussed tribooxidation of metals. These models basically comprise the heat development in rubbing rough surfaces and "hot spots" with temperature augmentation up to 1000 °C ("flash temperatures"). Oxidation occurs in these contact areas with high temperatures. In 2000, Xu et al. expanded this model for oxidative wear of ceramic materials.

Based on calculated temperature and pressure values, hydrothermal and tribological experiments were conducted and compared. This approach comprises static (hydrothermal) and dynamic (tribological) conditions of chemical degradation of silicon carbide in aqueous environments. The relations between tribological and hydrothermal corrosions of SiC are not well understood yet. A combined tribological – hydrothermal corrosion model should be beneficial for the improvement of lifetime prediction of ceramic face seals.

The scope of the present work is therefore the qualification of the tribological behavior in terms of the corrosion behavior under different loading cases. Parallel static corrosion experiments under high temperatures and pressures were conducted to determine the similarities in the tribochemical behavior to hydrothermal oxidation of silicon carbide. In the present paper, the first results of this project are presented: (1) Tribological experiments, (2) numerical interpretation of contact surfaces to estimate the local pressure and temperature conditions in the sliding surfaces. The results of hydrothermal corrosion are published in a companion paper.

2 Experimental Procedure

2.1 Characteristics of Used Material

Silicon carbide slide ring samples were supplied by ESK Ceramics GmbH Kempten, Germany. Two different materials were used in this work. The fine grained version EKasic ® F with a mono modal grain size distribution of about 5 microns and the coarse EKasic ® C characterized with a bimodal grain size distribution, where platelet like crystal aggregates in the range up to 2000 µm are embedded without preferred orientation in a fine grained matrix of about 10 µm averaged crystallites (Figure 1).

2.2 Tribometer

The experimental setup for the tribological tests is sketched in Figure 4a. A static slide ring is attached to a dynamometer and selfmated with a rotating slide ring. The applied load and the sliding velocity can be varied in wide ranges. Deionized water was used as a lubricant. Its salinity was monitored and kept below 0.09 µ-Siemens/cm. During the experiment, the lubricant was applied with a pressure of 0.1 MPa between the friction couple. The test apparatus provides the option for external cooling.

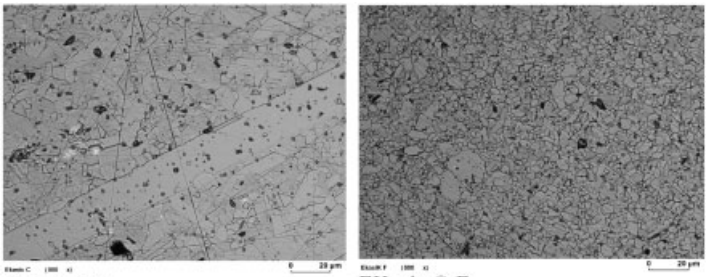


Figure 1: Microstructure of used materials

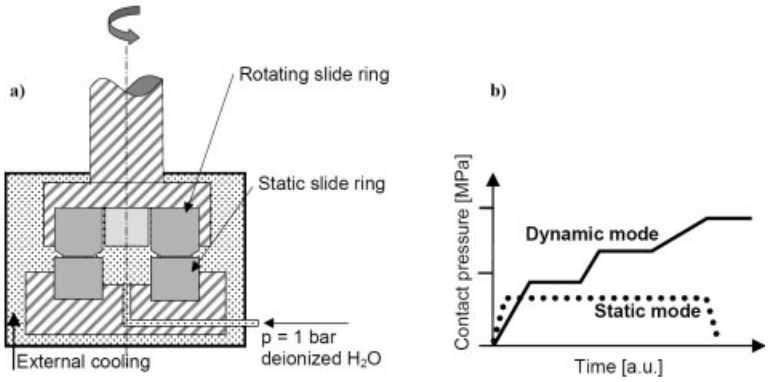


Figure 2: a) Experimental setup and b) used run modes

As displayed in Fig. 2b, two different test modes were chosen: (1) a static mode and (2) a dynamic mode. In order to determine the general running behavior, static pressure conditions at 0.5 MPa, external cooling and a sliding velocity of 6 m s^{-1} were chosen. In intervals of $\sim$ 2000 m sliding distance the sample surfaces were measured with the stylus profilometer and then numerically evaluated. Experiments in dynamic conditions were carried out without external cooling and with a sliding velocity of 6 m s^{-1}. To avoid excessive scuffing the experiment stopped automatically when the measured torque reached 2 N·m.

3 Results

3.1 Dynamic Friction Tests Without External Cooling

To determine the maximum tolerance in case of dry friction of both materials, experiments were conducted without external cooling in dynamic loading conditions. A blind hole (Ø 2 mm, depth 8 mm, 3 mm below the rubbing surface) was drilled in each specimen for thermocouples. This allowed recording the surface temperature during the experiment. The gap between the thermocouple and the material was filled with a heat conductive paste. After a short time period both

silicon carbide varieties reached a high level of friction and a strong increase of temperature (Fig 3). In particular the coarse silicon carbide material showed a higher resistance against poor lubricated friction conditions. The abort criterion of 2 N·m torque was reached with the fine-grained SiC after 10 minutes test duration, while the coarse type lasted 30 min until the experiment was automatically stopped. With the rise of friction coefficients a dramatic temperature gain up to 300 °C occurred simultaneously.

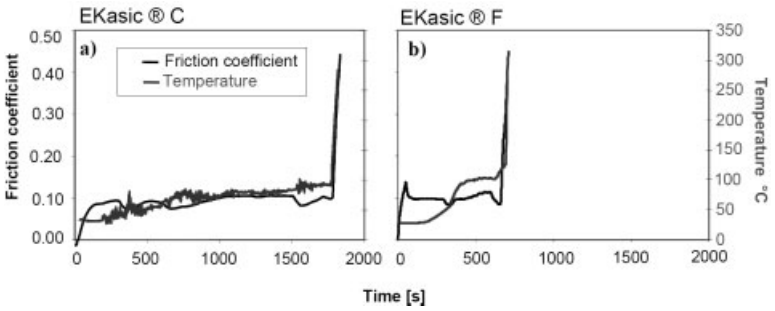


Figure 3: Monitored friction coefficient and temperature of a) EKasic ® C and b) EKasic ® F

SEM analyses showed the corresponding penetration depth in the cross sectional cuts of each material. In the case of the coarse grained material EKasic® C transgranular cracks were detected along the large needle-like microstructure down to a depth of > 10 µm (Fig. 4 left). The fine grained EKasic ® F material showed different wear characteristics (Fig. 4 right). The degradation of this material is limited to the topmost surface region. Plateau-like areas of debris were formed. The ratio of actual contact and geometrical contact surface is extremely enhanced.

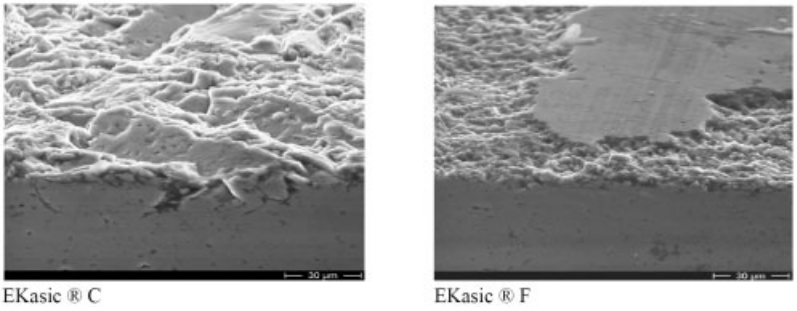


Figure 4: SEM cross sections of EKasic ® slide ring seal samples after dry friction experiment

EDX analysis showed gain in the oxygen content down to surface depths of ∼ 5 µm into the bulk material of the EKasic® C samples (Fig. 5). This value must carefully be evaluated because of the large exciting volume and the porous texture. In the topmost regions of the sliding surface up to 6 wt.% oxygen was observed.

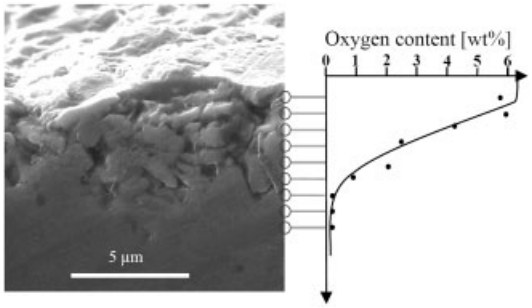


Figure 5: EDX Analysis of oxygen cross section EKasic®

3.2 Interval Experiments

To determine the tribological behavior during the initial lifetime of a slide ring seal, experiments in static conditions with intervals of applied static loads as shown in Figure 2b, were conducted. These experiments were performed with external cooling. Every 30 minutes the experiments were stopped ($\sim$ 2000 m wear distance) and the resulting tribologically influenced surfaces were examined. The development of friction coefficient vs. experiment time and the resulting surface morphologies are shown in Figure 6. Each morphology map has a size of 2 x 2 [mm] (Fig. 6b).

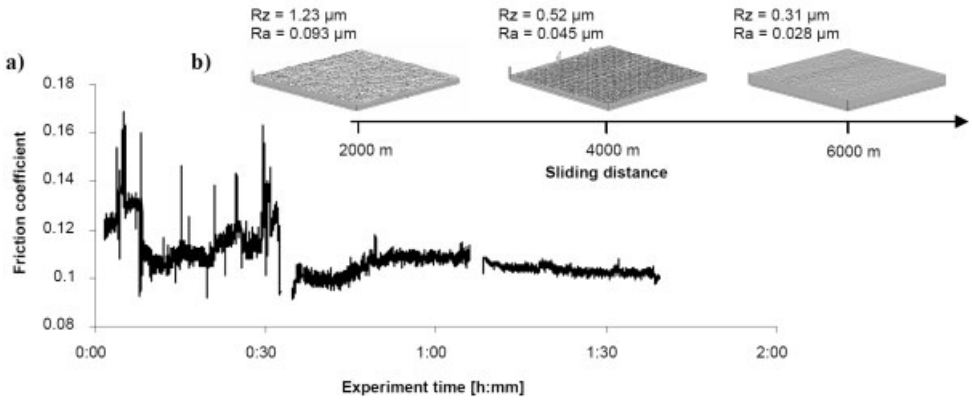


Figure 6: a) Tribological and b) morphological development of EKasic ® C during "running in"

After an initial phase with oscillating friction coefficients in the range about 0.08 ("runing-in", Fig. 6a), the tribologically exposed surface undergoes a smoothing process (Fig. 6b). The sliding behavior stabilizes after 2000 meters. The roughness value decreases from R_z 2.77 to 1.23 µm after 2000 m. In the further progress of the experiment the reduction of roughness values decreases. As a result of smoothing, the friction coefficient decreases to values of about 0.1.

3.3 Numerical simulation of tribological exposed surfaces

Both, the initial loading of ceramic slide rings and the first tribological exposure are accompanied with very complicated loading conditions. Thereby, the real contact area between pressed slide ring seals is several orders of dimensions smaller than the geometric contact area. On real surfaces, the pressure is applied on asperities and local forces easily exceed the yield stress of the material. Unstable running behavior is a direct result of the initial sliding characteristics of slide ring seals in self mating SiC pairs. The quantitative influence of topographic surface parameters on contact stress in mixed friction was calculated using numerical methods. To gain information about the topographic surface parameters, a stylus profilometer was used. Determination of the contact situation of actual surfaces was carried out approximating the asperities as ellipsoids. The mechanical material behavior was assumed to be linear elastic – ideal plastic so that the calculation of the solid body contact could be described using the Hertzian contact theorem. While one rough surface defined to have asperity peaks, the mating surface was assumed to be perfectly plain. Figure 7a depicts the preliminary assumption to the modeling showing a normally applied force (F_N) as a parameter for the sliding contact.

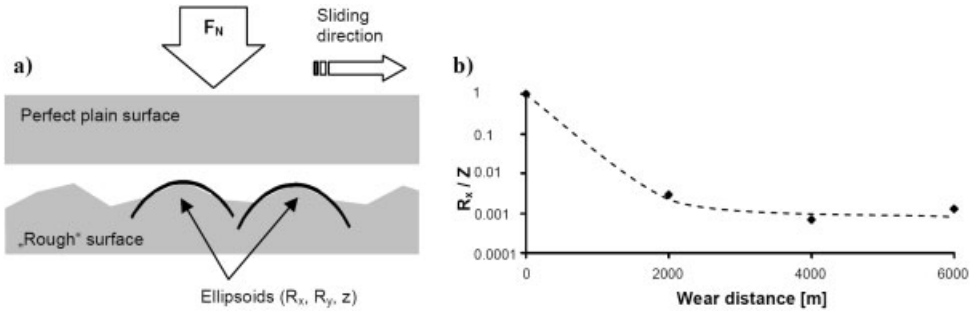


Figure 7: a) Idealized model of sliding contact, b) Ellipsoid radii-height ratio vs. wear distance

Quantitative evaluation of the wear can be achieved by monitoring the increase of the ellipsoids radii and the corresponding decrease of their height. The numerical approach includes a time scale resolution of the tribologically influenced surface. Due to the amount of received data, a statistical approach to describe the change of the surface geometry was possible. A median of the numerical results of surface parameters was calculated and the ratio of ellipsoids radii to ellipsoids height R_x/Z as a function of wear distance is shown in Figure 7b for an interval experiment described above. In the initial state of a non influenced surface of a slide ring seal the radius/height ratio is nearly 1 and the approximated ellipsoids are almost isotropic. The first tribological exposure has a major influence on the height of ellipsoids and the corresponding radii. In the further development of the wear experiment the ratio stabilizes as it drops down to a value approximately 0.001. This method of surface interpretation allows a very sensitive description of tribologically induced topographical surface changes.

4 Summary

Experiments in dynamic loading conditions in the absence of external cooling caused scuffing in both tested materials. SEM inspections showed the formation of plateaus composed of nanoscale debris and the development of lower rough regions. Cross sections showed mechanical deformation of the tribologically influenced surface. The EDX analysis showed an oxygen content in topmost regions of the samples. The coarse grained EKasic ® C showed improved dry sliding characteristics. The large grains in this material act in case of scuffing like ramps which reduce the formation of debris. The tribological results of the interval experiments showed significant smoothing of the sliding surfaces in the first 2000 m of wear distance. Afterwards the decrease of roughness values retards. The output of the numerical surface evaluation showed a similar effect: From the isometric ellipsoids of an unworn surface with a height to radius ratio of nearly 1 the value drops in the first 2000 m wear distance down to ~ 0.001 and remains almost static in the further progress of the experiment.

5 References

[1] Krummhauer, O.; Presser, V.; Kailer, A.; Nickel, K.G., in 48. Tribologie Fachtagung. Reibung, Schmierung und Verschleiß. Forschung und praktische Anwendungen. Band 1., Göttingen, 2007, 13/11–13/15.

[2] zum Gahr, K.-H.; Blattner, R.; Hwang, D.-H.; Pöhlmann, K., Wear, 2001, 250, 299–310

[3] Xu, J.; Kato, K., Wear, 2000, 245, 61–75.

[4] Kailer, A.; Hollstein, T.; Nosowicz, J.; Schiebel, H.; Meschke, F.; Schwetz, K.; Lesniak, C., Tribologie und Schmierungstechnik, 2003, 50, 10–13.

[5] Kitaoka, S.; Tsuji, T.; Yamaguchi, Y.; Kashiwagi, K., Wear, 1997, 205, 40–46.

[6] Zimmermann, M., Experimentelle Untersuchung und numerische Modellierung des Gleitkontaktverhaltens von gesintertem Siliciumcarbid (SSiC), Karlsruhe, 1998, VIII, 102S.:Ill. Karlsruhe, Univ., Diss., 1998

[7] Quinn, T.F.J., Wear, 1971, 18, 413–419.

[8] Quinn, T.F.J., Wear, 1992, 153, 179–200.

[9] Quinn, T.F.J., Wear, 1994, 175, 199–208.

On the P-T Conditions of Wet Silicon Carbide Tribo-corrosion

V. Presser[1], O. Krummhauer[2], K. G. Nickel[1], A. Kailer[2], R. Wirth[3]
[1]Institute for Geosciences, Eberhard-Karls-Universität, Tübingen, Germany
[2]Fraunhofer Institute for Mechanics of Materials, Freiburg, Germany
[3]Geoforschungszentrum, Potsdam, Germany

1 Introduction

Among non-oxide ceramics, silicon carbide (SiC) poses a special case because of its chemical inertness and high-temperature resistance explaining its widespread use in extreme environments. When exposed to sliding wear in aqueous media, silicon carbide shows a low friction coefficient after an initial run-in phase[1–4]. This is believed to be the result of bulk mechanical surface smoothening and chemical reactions – both parts combined yield a tribochemical wear process. As for the chemical reaction, an oxidation process with solid silica as product similar to the tribochemical wear of silicon nitride (Si_3N_4; Ref. [5]) was used to explain the low friction coefficient (≤ 0.1) observed under wet sliding conditions [4, 6, 7]. In particular, oxycarbides ($Si_4C_{4-x}O_2$, $Si_4C_4O_4$), adsorbates such as $C_xH_yO_z$ and finally silica and hydrated silica (i.e. $SiO_x \cdot n\ H_2O$) have been described so far as tribochemical reaction products for SiC [4, 6–8]

A major problem for the correct description of tribochemical processes is that the P-T conditions, in which those reactions actually occur can not be measured *in-situ* but only be simulated. The actual contact points during wear contact are usually the asperity peaks. The conditions calculated for their contacts come from static local stress calculations for round tips combined with energy input considerations. Such conditions are envisaged to affect a very superficial region and it is only there, that pressures typical for hardness values and flash temperatures up to or even exceeding 1000 °C were calculated but never measured [1, 5, 9–11].

Experimental evidence for high pressures and temperatures come from the mere fact of oxidation products such as hydrated silica or oxycarbides, because those phases are not expected to form at temperatures below 100 °C on pristine SiC surfaces. Schwetz and Hassler reported significant corrosive attack of sintered silicon carbide only at temperatures above 220 °C [12]. This is why we studied corrosion and tribochemical wear of silicon carbide and refer to it as hydrothermal.

Calculation of the contact temperatures take the real surface morphology of silicon carbide sliding parts into account by using the micro asperity based model approach [8, 13]. This means that both surfaces are not in direct contact with each other over the entire surface area but only with small asperity peaks. In-between those contact areas, water acts as both lubricant and cooling medium. Those parts in direct sliding contact are subjected to mechanical deformation and may experience the calculated locally increased P-T conditions. However, the areas away from the direct contact a local increased pressure may be induced by the flash temperature itself: water isochorically trapped, for example in closed cracks or pores, may mediate isostatic pressures to the surrounding ceramic body.

For an evaluation of these situations the consequences of static hydrothermal conditions to silicon carbide are of interest. There is an increased silica solubility in water at higher pressures

and temperatures [14, 15] and therefore not only silica formation, but graphitization and active corrosion are possible.

Recent studies indeed describe an active corrosion of SiC at temperatures up to 800 °C and several hundred MPa pressure, during which reaction products are either completely dissolved in the fluid or contain residual remains of carbon or silica [16–21]. Loose silica scales therefore were interpreted as a product of solution and reprecipitation. At lower pressures, Barringer et al. reported active corrosion of CVD-SiC for supercritical water (500°C, 25 MPa; [22]) and Kitaoka et al. [23, 24] reported an active oxidation mechanism for sintered SiC for lower temperatures (up to 300 °C) as well. The ratio of SiC:H_2O of the system should be an important parameter for the character of the process.

For our study, we performed tribological experiments for SiC sliding parts under water lubrication and for static hydrothermal conditions experiments using a hydrothermal diamond anvil cell (Bassett-type; Ref. [25, 26]).

2 Experimental Procedure

Undoped 6H-SiC single crystal plates (SiCrystal AG, Erlangen, Germany) ground to a thickness of 100 µm and polished with 1 µm diamond paste (of $R_z \approx 500$ nm and $R_a \approx 10$ nm) were cut into small cuboids of approximately $240 \cdot 240 \cdot 100\ \mu m^3$ to be used in hydrothermal runs. Each sample was carefully cleaned in tridestilled water and acetone for 30 minutes using an ultrasonic bath to remove remnants of the polishing paste.[1]

For tribological tests EKasic ® F from ESK Ceramics GmbH & Co. KG (Kempten, Germany) was used. This material has a fine grain size of about 5µm. It consists of app. 80 wt% 6H-SiC, 20 wt% 4H-SiC + 15R-SiC and additions of boron carbide as sintering aid. The sliding surfaces were lapped to values of R_z = 2.79 µm and R_a = 0.79 µm determined by a Hommel T 8000s profilometre (Hommel GmbH, Köln, Germany).

Hydrothermal experiments were performed with a hydrothermal diamond anvil apparatus (HDAC) after Basset et al. (Ref. [25, 26]). Pure tridestilled water was used as a medium and the pressure was calculated with the aid of the equations of state (EOS) of pure water substance and the determination of the homogenization temperature [27, 28]. Samples were heated with 20 $K \cdot min^{-1}$ up to 500 °C. This temperature, which corresponds to an isochoric pressure of 500–770 MPa, was maintained ±1 K for 5 h before cooling to room temperature with the same gradient.

Tribological tests were conducted in a sliding ring tribometer described elsewhere with deionized water as lubricant [1, 8]. During the experiment, the lubricant was applied with a pressure of 0.1 MPa between the friction couple.

Test runs in static and dynamic mode were executed at 1.5 MPa, external cooling and a sliding velocity of 6 $m \cdot s^{-1}$. In intervals of ∼ 2000 m sliding distance the sample surfaces were measured with the stylus profilometre and numerically evaluated. Experiments under dynamic conditions were carried out in absence of external cooling and with a sliding velocity of 6 $m \cdot s^{-1}$. The abort criterion in case of scuffing was a measured torque of 2 $N \cdot m$ [8].

Sampling of an EKasic ® F sample for TEM analysis was accomplished by using focused ion beam (FIB) milling. FIB preparation (cf. Ref. [29]) was conducted under ultra-high vacuum conditions in an oil-free vacuum system using a FEI FIB200 instrument (FEI Company, Eindhoven, The Netherlands) at the GeoForschungsZentrum Potsdam. As a result TEM-ready foils

of approximately $20 \cdot 10 \cdot 0.15$ µm were obtained. The FIB-cut foils then were placed on a highly perforated carbon grid on a copper mesh. TEM was carried out in a FEI F20 X-Twin instrument operated at 200 kV and equipped with a FEG electron source. Electron energy-loss spectroscopy (EELS) spectra were acquired with a Gatan imaging filter (GIF Tridiem; Gatan GmbH, München, Germany).

3 Results and Discussion

Hydrothermal treatment of single-crystal SiC yielded a bulk active oxidation mechanism as evidenced by higher surface roughness and pitting. In particular, the surface roughness increased from $R_z \approx 500$ nm and $R_a \approx 10$ nm to $R_z \approx 1900$ nm and $R_a \approx 22$ nm after HDAC experiments (500 °C, 5 h).

Chemical reaction(s) are also evidenced by higher dehomogenization temperatures, i.e. during cooling after the experiment the fluid separates into a liquid and a gaseous phase at much higher temperatures than observed during initial heating (e.g. at 310 °C instead of 80 °C). This process can be explained by the production of a gaseous reaction product (here: carbonaceous species). A graphitized surface layer was not found by Raman spectroscopy, which is sensitive to carbon layers even in the nm scale. Silica was observed, probably formed by precipitation. At least some of the found silica (partially containing aluminium and iron as remnants from sample machining) must be seen as a quench product when the water in the HDAC sample chamber is evaporated for sample extraction.

Tribological experiments conducted at 1.5 MPa under constant conditions show a thin tribolayer of ≈ 35 nm above a 500–800 nm thick region of heavily mechanically deformed silicon carbide (Fig. 1a), in which cracks are visible. Although the surface was locally smoothened, overall grooves are still dominant.

Contrasting, samples from a dynamic mode experiment, where the sample's surface was exposed to higher temperatures and mechanical stresses, are not only locally but generally smoothened under the wear track (Fig. 1b). In a transition zone boardering the main wear track we observe a mixture of smoothed elevated plateaus and rough, partly material filled areas (Fig. 1c).

From GDOES experiments [1] we know that the tribolayer contains significant amounts of hydrogen. EELS and EDX analysis (Fig. 2) of the tribolayer shows the presence of carbon, silicon and oxygen. Element mapping revealed that the tribolayer is not homogeneous. Oxygen in the tribolayer outlines nm-sized grains of SiC. We interpret this to come from a superficial oxidation and the gluing together of wear debris by silica. The presence of SiC nanoparticles makes it impossible to establish whether oxycarbides are part of the assemblage.

In Fig. 2b cracks well below the tribolayer are visible. These are often associated with oxygen-rich areas. Possible explanations are the direct oxidation of crack rims, a precipitation of silica within the cracks or the input of colloidal silica and oxidized wear particles.

In case of tribological exposure under dynamic conditions, we found crystalline silica (α-quartz) in some parts of the reaction layer as a result of the very high temperatures (> 350 °C). Reflections were attributed to α-quartz-(011) (d = 3.27 Å measured; literature: 3.34 Å, Ref. [30]) and α-quartz-($\bar{2}20$) (d = 2.06 Å measured; literature: 2.13 Å, Ref. [30]). The attribution

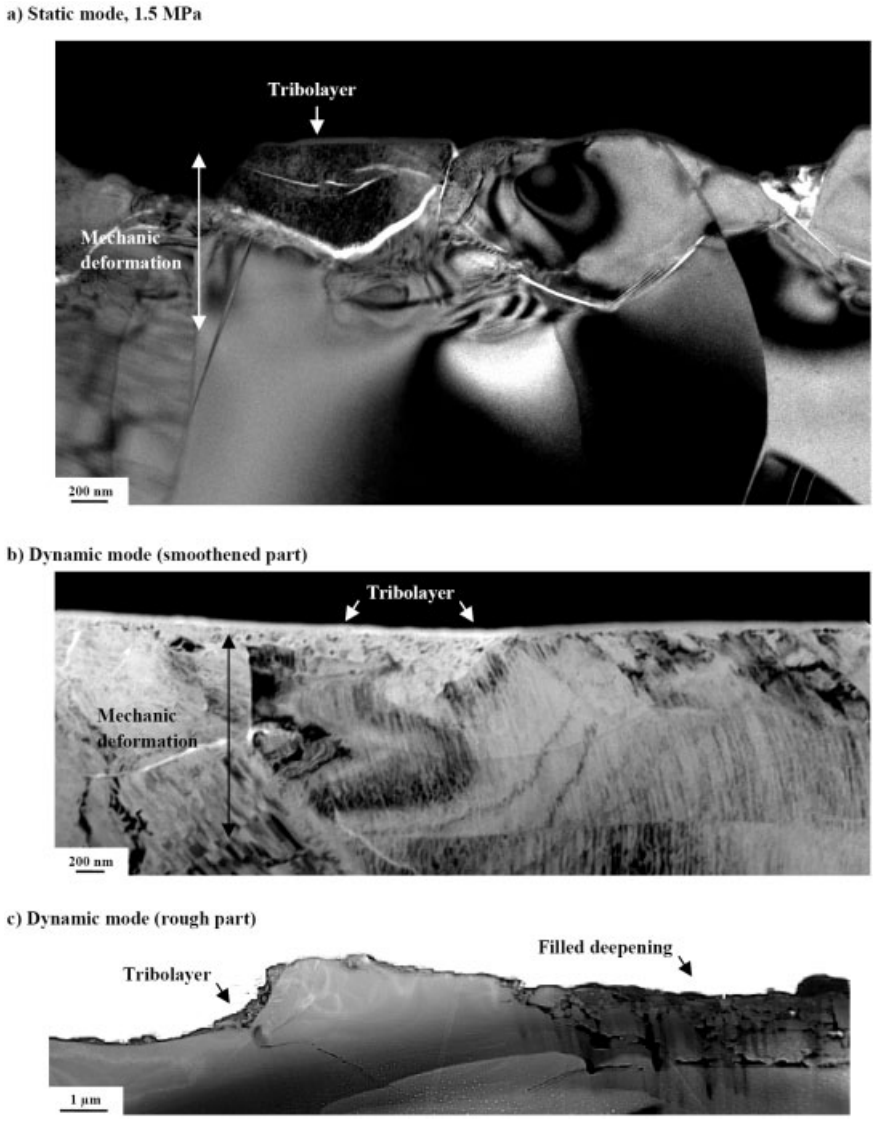


Figure 1: Electron microphotographs of the superficial area of EKasic ® F wear tracks under (a) constant and (b, c) dynamic mode. For the static mode and smoothened areas under dynamic mode, only a very thin tribochemically influenced layer is found (bright field TEM). In a rough part from a border region of the wear track from dynamic mode experiments thick, material filled deepenings are found (c). White spots in 1c are due to Ga-contamination.

to α-quartz is favourable compared to other silica polymorphs (like cristobalite or coesite etc.) [31].

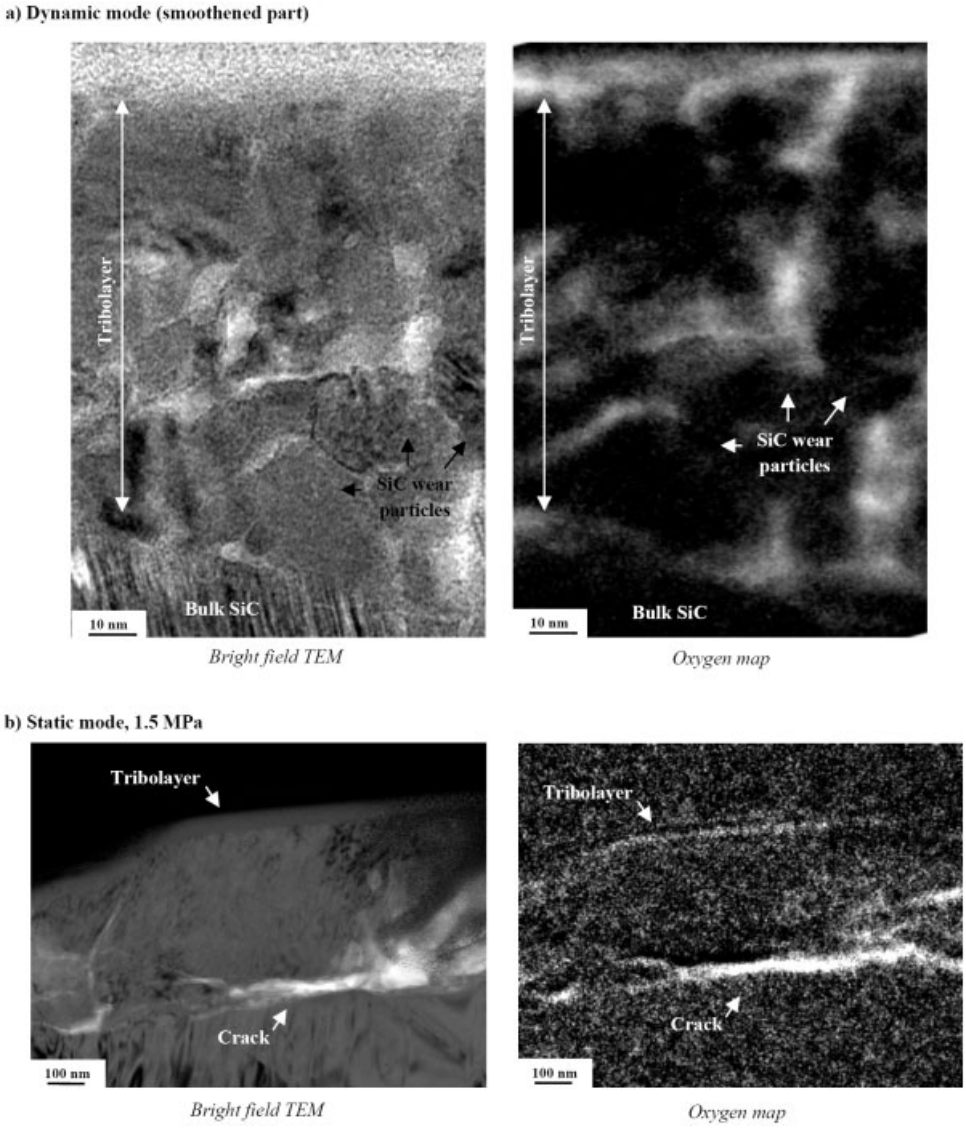


Figure 2: Electron microphotographs of the tribolayer formed on SiC. Oxygen-rich areas correspond to the tribolayer (in which SiC wear particles are rubbed in; 2a) and (partially redeposited) tears (2b).

It is well known (Ref. [32]) that the presence of quartz is a good indicator of a moderate hydrothermal regime, because at atmospheric pressures only cristobalite forms and does not transform into other modifications then the low-T-form of cristobalite. In fact amorphous silica transforms first to cristobalite and then to quartz under hydrothermal conditions [33] and the synthesis

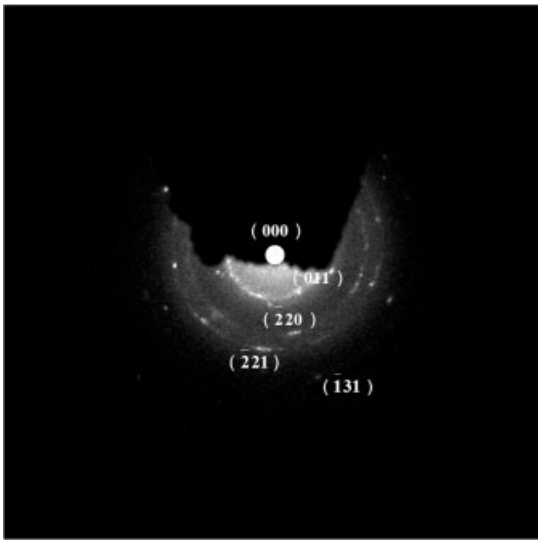


Figure 3: Selected-area diffraction (SAD) of crystalline silica (identified as α-quartz).

of silica powder in hydrothermal conditions gives cristobalite and /or quartz [34, 35]. This is also known from hydrothermal oxidation of SiC, where cristobalite was formed first and quartz appeared in longer runs at several hundred degrees °C. [20]. Under very high pressures other modifications of silica would form (coesite / stishovite), at high temperatures we would expect quartz to disappear. Hence the P-T-regime must have been limited to about 250–750 °C at the according pressures of several hundred MPa.

The results presented from HDAC and tribological experiments give evidence of a more complex tribochemical wear process than reported earlier. When SiC surfaces are in sliding contact, the contact areas are subjected to increased temperature and pressure regimes along with impact events that lead to crack formation and severe mechanical deformation of the grains in the first 1–2 μm of the polycrystalline body. The degree of mechanical deformation varies locally and ranges from simple dislocations, stress-induced twinning and basal-plane gliding.

Cracks may allow breaking small SiC particles from the surface and hydrothermal fluid to penetrate the ceramic body. The spalled SiC particles will be transported across the surface by the sliding counterpart and thus become both diminished in mean diameter and rounded in their form. This is seen as a contribution to the significant surface smoothening.

Any deepenings from grooves, spallation events or scratches in the original surface then will be filled with loose wear particles. The space between the particles is certainly containing water. Water may also penetrate further into the ceramic body along the cracks induced by the mechanical deformation of the surface. All in all we have then three regions with water present: (a) very superficial in the tribolayer, (b) the space between wear debris in deepenings and (c) in cracks, both shallow and deep.

Direct mechanical contact of asperity peaks induces not only temporarily high pressures, which, because of the dynamic nature of the event impacts, induce the observed cracks, but

also creates an energy input, which rises the asperity tip to high temperatures. The temperature will decrease rapidly because of energy lost to the lubricating water and into the material by heat conduction. Since contacts are often repeated a dynamic interface temperature gradient is established. Any measurement of the interface's temperature e.g. by introducing a thermocouple a few millimetres below the actual surface will thus record temperatures altered by this gradient and calculations of surface temperatures from this need to involve heat transfer models.

When the surface temperature has gained enough energy to exceed 100 °C at the interface the water will tend to evaporate or form a water vapour film, which could contribute to the observed low friction coefficient. The temperature alone will however be rarely exceeding conditions, which would allow effective oxidation reactions. But in all situations, where the water is entrapped we may enter hydrothermally enhanced pressure conditions. And only here significant tribochemical reactions can take place.

From HDAC experiments we know that active oxidation of SiC occurs in the hydrothermal P-T range of interest. This does not necessarily contradict the formation of an oxydic / oxycarbidic reaction layer, because silica will remain, if there is not enough water present to dissolve it and it may precipitate from the solution, when temperatures drop.

4 Conclusion

The wet tribo-corrosion of sintered SiC has been investigated by tribological tests in constant and dynamic mode. FIB/TEM investigations of the worn surface evidenced (1) tribochemical reactions and (2) mechanical deformation of the superficial region. In particular, we found a thin (app. 35 nm) tribolayer on the surface of the static mode sample consisting of nanosized SiC with an oxygen rich interphase. For the dynamic mode sample, this tribolayer at the wear track was app. 100 nm thick.

The mechanical deformed layer (1–2 µm) is much thicker than the chemically influnced region and contains cracks, which are partially also filled by an oxygen-rich phase. Wear debris is collected during the process in deepenings from grooves and spallation along with precipitated silica, acting as a glue for loose triboparticles.

The tribochemical model we concluded from the experimental results explains wet tribo-corrosion of polycrystalline, sintered SiC as follows. When in direct mechanical contact, asperity peaks will collide with each other giving drastic rise to temperature and pressure. This increase is just of local nature, but over time a dynamic equilibrium will be established.

Spalled SiC triboparticles then will be transported along the wear track, becoming smaller in diameter and more roundish in form. Critical P-T conditions cause oxidative reactions and finally the formation of a thin tribochemically influenced layer (app. 35–100 nm) can be observed. The SiC surface becomes smoothened at the same time by this lapping-like process. Deepenings will be filled with the loose debris, which are glued together by an oxygen-rich interphase.

Mechanic shattering of the ceramic matrix plays an important role as this effect applies to a much thicker surface layer (1–2 µm). Cracks within the solid body act as pathways and oxygen-rich areas (as a product of redeposition and / or local oxidation) were found accordingly.

Both the presence of α-quartz and the comparison to high-pressure-high-temperature experiments give evidence for P-T- conditions, which reflect the isochoric heating of entrapped water

to several hundred degrees °C and several hundred MPa pressure. Higher pressures (GPa-range) are only very superficially and temporarily present due to point contacts of asperities.

5 References

[1] Krummhauer, O.; Presser, V.; Kailer, A.; Nickel, K.G., in 48. Tribologie Fachtagung. Reibung, Schmierung und Verschleiß. Forschung und praktische Anwendungen. Band 1., Göttingen, 2007, 13/11–13/15.

[2] Andersson, P.; Nikkila, A.-P.; Lintula, P., Wear, 1994, 179, 57–62.

[3] Andersson, P.; Juhanko, J.; Nikkila, A.-P.; Lintula, P., Wear, 1995, 201, 1–9.

[4] zum Gahr, K.-H.; Blattner, R.; Hwang, D.-H.; Pöhlmann, K., Wear, 2001, 250, 299–310.

[5] Xu, J.; Kato, K., Wear, 2000, 245, 61–75.

[6] Kailer, A.; Hollstein, T.; Nosowicz, J.; Schiebel, H.; Meschke, F.; Schwetz, K.; Lesniak, C., Tribologie und Schmierungstechnik, 2003, 50, 10–13.

[7] Kitaoka, S.; Tsuji, T.; Yamaguchi, Y.; Kashiwagi, K., Wear, 1997, 205, 40–46.

[8] Zimmermann, M., Karlsruhe, 1998.

[9] Quinn, T.F.J., Wear, 1971, 18, 413–419.

[10] Quinn, T.F.J., Wear, 1992, 153, 179–200.

[11] Quinn, T.F.J., Wear, 1994, 175, 199–208.

[12] Schwetz, K.A.; Hassler, J., Ceramic Forum International, 2002, 79, D9–D19.

[13] Bowden, F.P.; Tabor, D., Oxford, 2001.

[14] Fournier, R.O.; Rowe, J.J., American Mineralogist, 1977, 62, 1052–1056.

[15] Iler, R.K., New York, 1979.

[16] Gogotsi, Y.G.; Yoshimura, M., Journal of Materials Science Letters, 1994, 13, 395–399.

[17] Gogotsi, Y.G.; Yoshimura, M., Nature, 1994, 367, 628–630.

[18] Gogotsi, Y.G.; Yoshimura, M., MRS Bulletin, 1994, 39–45.

[19] Gogotsi, Y.G.; Nickel, K.G.; Bahloul-Hourlier, D.; Merle-Mejean, T.; Khomenko, G.E.; Skjerlie, K., Journal of Materials Chemistry, 1996, 6, 595–604.

[20] Kraft, T.; Nickel, K.G.; Gogotsi, Y.G., Journal of Materials Science, 1998, 33, 4357–4364.

[21] Kraft, T.; Nickel, K.G.; Gogotsi, Y.G., Journal of Materials Science, 1998, 33, 4357–4364.

[22] Barringer, E.; Faiztompkins, Z.; Feinroth, H.; Allen, T.; Lance, M.; Meyer, H.; Walker, L.; Lara-Curzio, E., Journal of the American Ceramic Society, 2007, 90, 315–318.

[23] Kitaoka, S.; Tsuji, T.; Katoh, T., Journal of the American Ceramic Society, 1994, 77, 580–588.

[24] Kitaoka, S.; Tsuji, T.; Katoh, T.; Yamaguchi, Y.; Kashiwagi, K., Journal of the American Ceramic Society, 1994, 77, 1851–1856.

[25] Bassett, W.A.; Shen, A.H.; Bucknum, M.; Chou, I.-M., PAGEOPH, 1993, 141, 487–495.

[26] Bassett, W.A.; Shen, A.H.; Bucknum, M.; Chou, I.-M., Review of Scientific Instruments, 1993, 64, 2340–2345.

[27] Haselton, H.T.; Chou, I.-M., Jr.; Shen, A.H.; Bassett, W.A., American Mineralogist, 1995, 80, 1302–1306.

[28] Shen, A.H.; Bassett, W.A.; Chou, I.-M., in High-Pressure Research: Application to Earth and Planetary Sciences, Washington D.C., 1992, 61– 68.

[29] Wirth, R., European Journal of Mineralogy, 2004, 16, 863–876.

[30] Dušek, M.; Petříček, V.; Wunschel, M.; Dinnebier, R.E.; van Smaalen, S., Journal of Applied Crystallography, 2001, 34, 398–404.

[31] Keskar, N.R.; Chelikowsky, J.R., Physical Review B, 1992, 46, 1–13.

[32] Byrappa, K.; Yoshimura, I.; Yoshimura, M., Norwich, 2001.

[33] Campbell, A.S.; Fyfe, W.S., American Mineralogist, 1960, 45, 464–468.

[34] Zhu, Y.; Yanagisawa, K.; Onda, A.; Kajiyoshi, K., Journal of Materials Science, 2005, 40, 3829– 3831.

[35] Yanagisawa, K.; Zhu, Y.; Onda, A.; Kajiyoshi, K., Journal of Materials Science, 2004, 39, 2931– 2934.

On the Tribological Characterization of Engineering Ceramics

Y. A-H. Mashal*, J. K. Lancaster** & A. G. Atkins**
* University of Engineering & Technology, Taxila, Pakistan.
**School of Engineering, Reading University, Reading UK.

1 Introduction

Ceramic possess a number of physical and chemical properties which make them particularly attractive for applications in which wear resistance, chemical inertness and high temperature are important. Certain high strength ceramics are presently seen as promising materials for chemical applications such as ball bearings, cutting tools, mechanical seals, replacement of human hip joints, and variety of engineering parts where friction and wear are involved [1–3]. One of the important aspects of ceramic tribology, which is at first sight surprising in view of the general corrosion resistance of these materials is the large influence of environmental chemistry on their wear rates. From the previous work, it is very clear that there is considerable confusion about the way in which the environment, and particularly water, influence the magnitude and the mechanism of wear in different ceramics [4]. There are two probable reasons why the results of this previous work are so variable. First, most experiments have involved the sliding of ceramics against themselves (like-on-like) in apparatus of the pin-on-ring or pin-on-disc type [5–10]. In such experiment the counterface (ring or disc) plays an important role in determining the magnitude of the wear rate. When the counterface is of the same material as the pin, it will also be subject to wear, and so its topography will gradually change during sliding. These changes in topography are likely to depend significantly on the environment. Little or no attention appears to have been given in previous work to characterizing such changes in counterface topography. Secondly, in addition to any topographical changes resulting from wear, there may be also accumulation of wear debris within the contact zone. This sort of debris layer, commonly termed as “third” can greatly influence the wear rate [11], and its development will depend not only on the particular sliding arrangement but also on the environment. Debris aggregation is likely to be greater in dry sliding conditions and least in the presence of fluid lubricants. In principle it should be possible to minimize the effect of varying the counterface topography by sliding against a material which is harder and tougher than the ceramics of interest. In this work a very hard metal-bonded diamond disc “Syndite” (50 GPa hardness) was used as a counterface. The second aspect concerning wear debris, therefore, also needs to be taken into consideration when comparing the wear rates of ceramics in different environments.

2 Experimental Details

2.1 Selection of Specimens

In this work four different types of ceramics were chosen. These are: partially stabilized Zirconia (PSZ), alumina (Al_2O_3), silicon carbide (SiC) and ”Sialon” (silicon nitride sintered with yttria alumino-silicate glassy phase). All have reasonably good properties for engineering appli-

cations. PSZ has low thermal conductivity and a coefficient of linear thermal expansion near that of steel as well as excellent thermal shock resistance and toughness, Al_2O_3 is cheap and hard, Sialon has high fracture and high temperature strength whilst SiC has good high temperature creep characteristics and high hardness. Table 1 shows the properties of the ceramics used.

Table 1: Properties of the ceramics used supplied by the manufacturers.

	Density [g/cm^3]	Flex-ural-strength [MPa], at 20 °C	Hardness [kg/mm^2]	Elastic mod-ulus [GPa], 20 °C	Critical Stress-Inten-sity-Factor [MPam$^{0.5}$]	Thermal-conduc-tivity [W/m °K]	Grain size µ
Al_2O_3 (Sintered with SiO_2, CaO & Na_2O)	3.78	360	1930	330	3.4	23	5
SiC (Reaction bonded)	3.1	525	2500	410	3	180	10
Sialon (Silicon nitride sintered with yttria-alumino-silicate glassy phase)	3.3	945	1330	288	7.7	21.3	0.5
PSZ (Sintered)	6.05	1000	1400	200	9	1.9	0.5

2.2 Experimental Procedure

The experiments were performed on a pin-on-disc machine in which a stationary pin was loaded against a rotating cobalt-bonded diamond "Syndite" disc. This disc was chosen to minimize the effect of the counterface changes during sliding against ceramics. The disc was 50.8 mm thick and mounted on a rather thicker base of tungsten carbide. The average diamond particle size was 2 µm. To keep the initial surface roughness of the counterface constant, a new track was used for every experiment and the disc thus needed to be re-prepared after every few tests. A rotating cast iron disc, of radius 200 mm, charged with diamond paste (7 µm grain size) and lubricated with a proprietary alcohol-based fluid (DP lubricant-blue), was used for this purpose. The polishing operation was done on a conventional polishing machine (125-250 rpm) using 2 kg normal load. Consistent and reproducible values of Ra, (0.10 plus or minus 0.01 µm), could be obtained provided that the cast iron disc was kept adequately charged with diamond. All the ceramic specimens were supplied as cylinders 6.35 mm in diameter and 70 mm long and they were used in the as received condition from the manufacturers. The ceramic pins and the Syndite disc were cleaned before testing by washing in 1,1,1-Trichloroethane and then further degreased in 2-Propanol vapor bath for 20 minutes. The stationary ceramic pin is loaded to an angle of 45° by dead weights against the horizontally rotating disc. The frictional force was monitored continuously by strain gauge transducer mounted on the loading arm. The 45° angle loading arrangement was adopted as a simpler alternative to the more usual methods of using conical or hemispherical ended pins [8-10]. It was much more convenient to prepare a plane-ended cylinder than a cone or hemisphere. The wear volume v was computed from microscopic measurements of the wear scar dimension using the equation:

$$v = r_p^2 \left\{ \sqrt{2r_p b - b^2} - (r_p - b)\cos^{-1}\frac{r_p - b}{r_p} \right\} - \frac{1}{3}\sqrt{(2r_p - b - b^2)^3} \quad (1)$$

where r_p is the radius of the ceramic pin, b is the worn length and equal to $(l_w/\sqrt{2})$, where l_w is the wear scar length. A normal load of 9.81 N and a sliding speed of 22 mm/s were used in all experiments, unless otherwise stated. This particular combination of load and speed was chosen as a compromise to minimize possible hydrodynamic lubrication and to avoid significant frictional heating. The total sliding distance ranged from 5 to 210 m, and Talysurf profiles were taken to examine the wear tracks on the Syndite disc. X-ray diffraction was also used to determine the composition of the wear track. The worn surface of the ceramic pins were examined by scanning electron microscopy (SEM), to assess the wear mechanism. Wear tests were carried out in de-mineralized water, di-2 ethyl hexyl sebacate (diester, dried with a molecular sieve), water-saturated diester, and different proportions of dried and water saturated diester. (ranging from 25 % to 75 %). The amount of water in the diester was measured using a gas chromatography and a negligible amount of water (about 1 ppm) was found in the dry lubricant. The maximum solubility of water in diester at 22 °C was about 3000 ppm. Some experiments were also performed in the ordinary laboratory air (50% plus or minus 10% relative humidity at 22 °C). For the second set of experiments, the apparatus used was a modified Bowden-Leben Machine (Pin-on-diamond strip). The diamond strip used was 15 mm long by 2.5 mm wide and it was bonded by a double sided adhesive tape to a base-plate mounted on a table which also acted as a fluid container. The base plate was adjustable in a direction at right angle to the direction of motion in order to use a fresh part of the strip for each traverse. As in the previous experiments with Syndite disc, the ceramic pin was inclined at 45° angle. A normal load of 250 g was applied and the sliding speed was 0.35 mm/s. Before use the diamond strip and the holder were cleaned in 1,1,1-Trichloroethane and the pins were also further degreased in a vapor bath of 2-propanol for 20 minutes.

3 Results and Discussions

3.1 Wear Results for Sliding Ceramics Against Syndite Disc

Figure (1) shows that the wear rate (proportional to the slope of the graph) of alumina in the presence of water is higher than that in lab air, and is considerably higher still in the diester. Increasing the water content of the diester tends to reduce the wear rate towards the value found in pure water. As can be seen from figures (2 & 3), the results for silicon carbide and sialon show similar trends to that in alumina. However, neither Sialon nor SiC appeared to be very sensitive to the water content in diester, so intermediate contents between dry and water-saturated levels were not examined. For PSZ, Figure (4) shows that the wear rate in diester is much higher than that in water which is in turn, higher than the value in air. In contrast to the alumina results, however, increasing the water content of the diester increases the wear rate of PSZ. A talysurf charts for the Syndite disc after sliding against all ceramics showed no change in the surface topography.

3.2 Coefficient of Friction

The coefficient of friction as a function of sliding distance was measured during all the wear experiments. For the change in friction coefficient with the sliding distance for alumina in various environments. It was observed that the coefficient of friction increases during the early stages of sliding in all cases. It then appears to reach an approximately constant value in air and dried

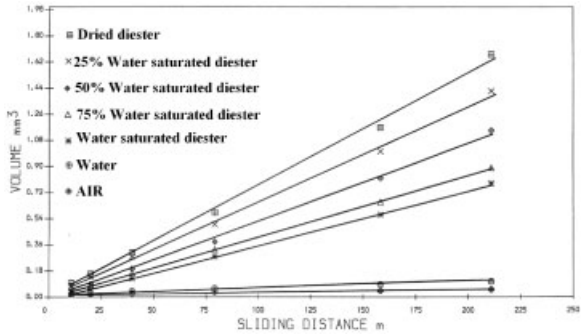


Figure 1: The worn volume-sliding distance relationship for alumina sliding against syndite disc.

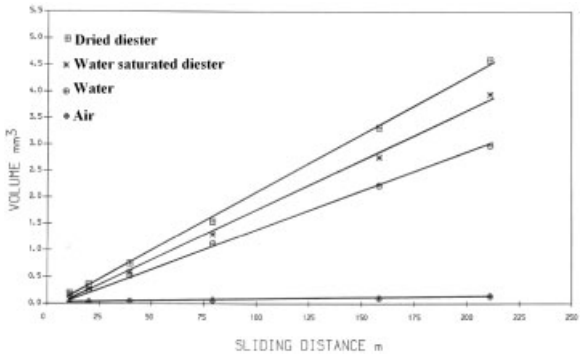


Figure 2: The worn volume-sliding distance relationship for SiC sliding against syndite disc.

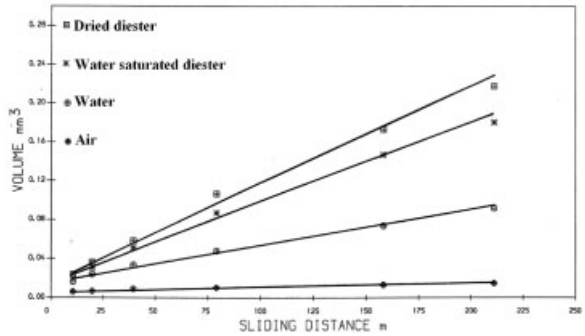


Figure 3: The worn volume-sliding distance relationship for Sialon sliding against syndite disc.

diester, but the coefficient of friction and silicon carbide and sialon, whose wear rates were not very sensitive to the water content of the diester, vary within a smaller range. For PSZ, the coefficient of friction is about the same in both dried and saturated diester, but increases continuously

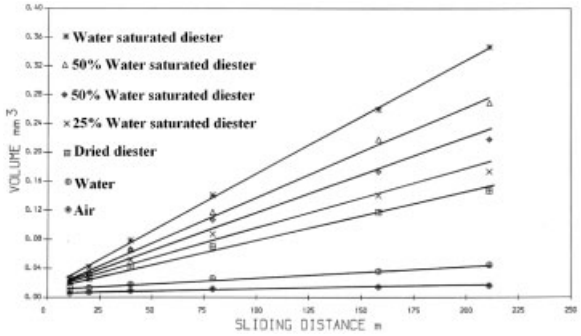


Figure 4: The worn volume-sliding distance relationship for PSZ sliding against syndite disc.

with sliding distance in water. It should be noted that despite the fact that the value of the friction coefficient will influence the magnitude of the localized contact stresses, there is not necessarily any direct relationship between the friction coefficient and the wear rates. In previous studies [12–15] it was noticed that for different ceramics, the wear rate is lowest in some environments whilst the friction was the highest. It has been also reported that the coefficient of friction increases with humidity, while the wear rate decreases with humidity [9]. In Air (50% rh), the wear was protected by an almost complete film of debris protecting the underlying substrate.

3.3 Results for Sliding Ceramics Against Diamond Strip

For sliding ceramics against diamond strip in diester water-saturated-diester and water , all the wear rates are very much greater than those obtained previously against the smoother Syndite disc, but it is the environmental trends of most interest. As before, SiC and Sialon showed wear rates decreasing in water saturated diester and in water. Sialon also exhibited low wear rates than SiC. No environmentally-accelerated crack growth has therefore been introduced as a consequence of using a rougher counterface and again the wear rates are decreasing in water as a consequence of tribochemical reactions. The trend for PSZ is also the same as before but with one additional aspect. Because the ceramic pin was always sliding against a fresh counterface surface, there is now no possibility that the reduced wear in water could have arisen from counterface smoothening. It would therefore seem that for PSZ, like SiC & silicon nitride, wear is reduced in the presence of large quantities of water by a tribochemical reaction. Finally it may be noted that the trend of alumina against the rougher surface is different from the previous one against Syndite and has become identical to that for PSZ where small amounts of water now increase wear as a consequence of accelerated crack growth and only in pure water tribochemical reactions occur.

3.4 SEM Analysis

The worn surfaces of the four types of ceramics were examined in a scanning electron (SEM) after 5 m of sliding distance, and at the end of an experiment (after about 210 m). In the lubricated experiments, the observations suggest that two different mechanisms control the wear process:

1- Microfracture of the surface. 2- Tribochemical reaction. For SiC sliding against Syndite, Figures 5 & 6 suggest that microfracture is the dominant wear mechanism in all environments. A few flake-like debris particles are present on the surface after sliding in water and water-saturated diester, which could indicate a tribochemical reaction of SiC in water. For alumina in dried diester, Figure 7 (A) suggests that microfracture is again the primary wear mechanism. In water saturated diester, however Figure 7 (B): suggests that wear is now a combination of microfracture and tribochemical reaction. For alumina sliding against Syndite in water, Figure 8 strongly indicates the presence of a layer on the worn surface and tribochemical reaction could thus be the dominant wear mechanism. A similar tribochemical layer was noticed on the surface of the worn Sialon after sliding in water (Figure: 9). Microfracture, however, also occurs in diester and water saturated diester (Figure:10) and this appears to be more significant in dried diester than in water saturated diester.

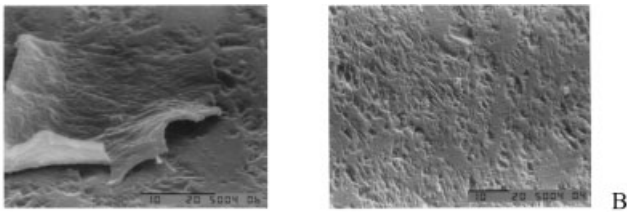


Figure 5: Scaning electron micrographs for SiC sliding against Syndite disc after 5 m in water (A: Formation of surface layer & B: Microfracture)

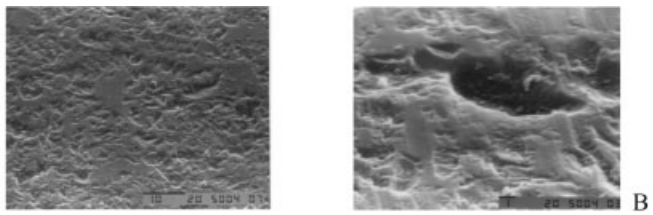


Figure 6: Scaning electron micrographs for SiC sliding against Syndite disc in dried diester (A: for 5 m & B: for 210 m)

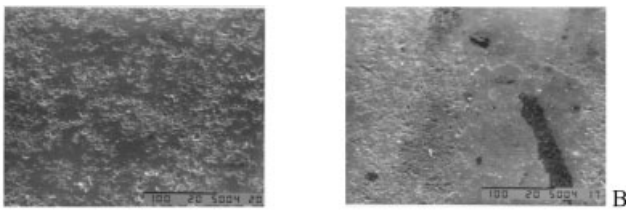


Figure 7: Scaning electron micrographs for Alumina sliding against Syndite disc for 210 m (A: in dried diester & B: in water saturated diester)

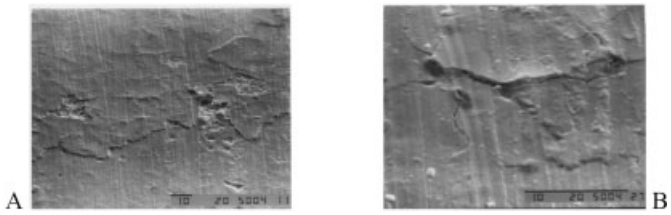


Figure 8: Scaning electron micrographs for Alumina sliding against Syndite disc in water (A: for 5 m & B: for 210 m

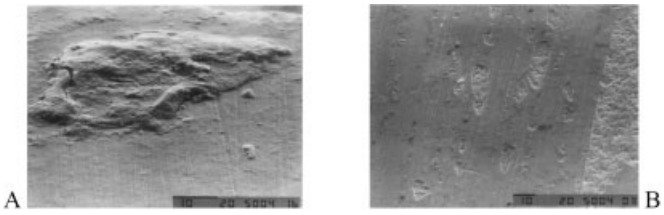


Figure 9: Scanning electron micrographs for Sialon sliding against Syndite disc in water (A: for 5 m & B: for 210 m)

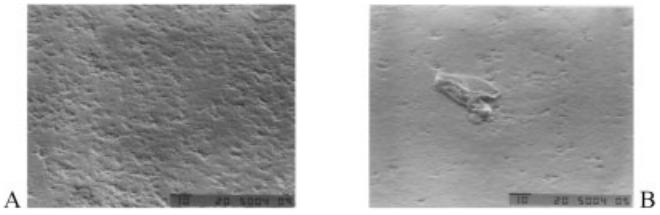


Figure 10: Scanning electron micrographs for Sialon sliding against Syndite disc for 210 m (A: in dried diester & B: in water saturated diester)

The worn surfaces of PSZ were rather different from these of the other ceramics. In diester Figure 11 (A): shows that a layer covering about half of the surface was found after only 5 m of sliding. This type of layer was not evident on any of the other ceramics. In water-saturated diester Figure 11 (B): shows that the worn surface seems to be affected by microfracture, but in water, Figure 12 shows that the worn surface is relatively smooth and the wear scar appears to be covered by some form of surface layer. When sliding the ceramics in air (= 50% rh), the wear process is significantly affected by the presence of debris in the contact between the two rubbing surfaces. In some instances the worn surfaces were covered by an almost complete film of debris. These debris films protect the underlying substrate material from direct contact and so tend to reduce the rate of wear [11]. When fluids, such as water or diester, are present they prevent the aggregation of debris into a protective layer and the wear rates are then higher than in air.

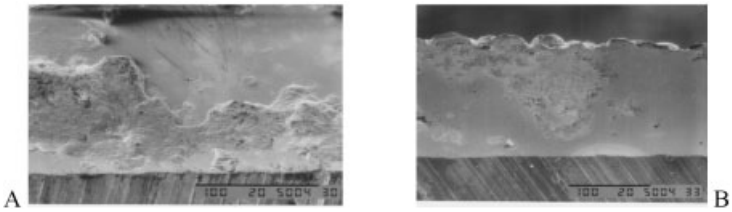


Figure 11: Scanning electron micrographs for PSZ sliding against Syndite disc for 5 m (A: in diester & B: in water-saturated diester)

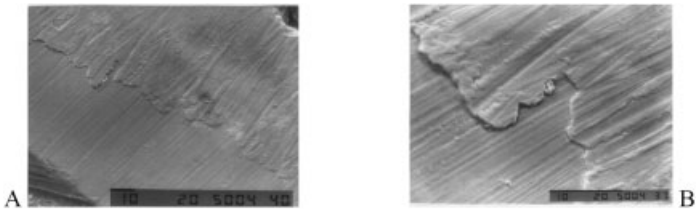


Figure 12: Scanning electron micrographs for PSZ sliding against Syndite disc in water (A: & B:)

4 Conclusion

1. The wear rates of all the ceramics are appreciably lower in air than in the fluids. In air the surfaces are protected by aggregated layers of debris but fluids prevent the formation of such layers.

2. Both microfracture and tribochemical reactions appear to be involved in the wear process for all the ceramics. However, the relative importance of these two mechanisms depends on the specific ceramic/environment combination.

3. The relatively high wear rate of SiC compared with Sialon in all environments is probably associated with its lower fracture toughness.

4. When sliding in water, the wear rates of all the ceramics are lower than in diester because of the wear reducing-effect of tribochemical reactions.

5. For Al2O3, SiC and PSZ, the presence of water in diester also reduces wear via tribochemical reactions. However, for PSZ, small amounts of water in diester increases wear and it is considered that this results from water-accelerated crack growth leading to enhanced microfracture.

   When sliding against diamond impregnated surface much rougher than the Syndite the following effects were observed :

6. The importance of microfracture in the wear processes increases, leading to an appreciable increase in the wear rate of all the ceramics in all environments.

7. The wear trends in the various environments remain similar to those found during sliding against Syndite except for Al_2O_3 in diester containing water. For this combination, the wear rate now increases as a consequence of water- accelerated crack growth.

5 References

[1] C. X. Li , J. Xia & H. Dong, Wear, 2006, 261, 693-701[2] Z. H. Xie, M. Hoffman, R. J. Moon, P. R. Munroe & Y. B. Cheng, Wear, 2006, 260, 1356–1360

[2] D. Klaffke, R. Wasche, N. Janakiraman & F. Aldinger, Wear, 2006, 260, 711–719

[3] Y. Mashal, Thesis, Reading University, 1990, Reading, UK.

[4] S. Guicciardi, D. Sciti, C. Melandri and G. Pezzotti, Wear, 2007, 262 , 529–535

[5] M. Hadad, G. Blugan, J. Kübler, E. Rosset, L. Rohr and J. Michler, Wear, 2006, 260, 634–641

[6] Y. Kimura, K. Okada and Y. Enomoto, Wear, 1988, 133, 147–161

[7] R.S. Gates, S.M. Hsu and E.E. Klaus, ASLE Transactions, 1989, 32, 357–363

[8] T. E. Fischer and H. Tomizawa, Wear , 1985, 105, 29–45

[9] S. Sasaki, Wear, 1989, 134, 185–200

[10] M. Godet, Wear, 1984, 100, 437–452

[11] O. O. Ajaya & K. C. Ludema, Wear, 1988, 124, 237–257

[12] P. Kapsa & Y. Enomoto, Wear, 1988, 127, 65–83

[13] H. Ishigaki, R. Nagata & M. Iwasa, Wear, 1985, 121, 107–116

[14] T. E. Fischer, M. P. Anderson, S. Jahanmir, & R. Sahler, Wear, 1988, 124, 133–148

Experimental Investigation on Wear of Ceramic Materials for Dental Restorations

H.G.Gräber[*], R.Wäsche[#]
[*] University Hospital, RWTH, 52074-Aachen, Germany [#] Federal Institute for Materials Research and Testing (BAM), 12205-Berlin, Germany

1 Introduction

Characterisation of the tribological response of tribosystems on certain conditions and the determination of wear is one of the main tasks of tribological testing activities. The difficulty encountered in tribometer testing is the challenge to meet the conditions under which the real systems are running. This is valid also for materials used for dental restorations and model testing makes sense if conditions can be met equivalent to those in the patient's mouth. This is, however, difficult since the variety of conditions with regard to contact pressure, multiaxial complex relative movements, pH and so on, is manifold. This is valid especially, when the relatively long periods of usage, typically more then 10 years, are taken into account.

For the tribological characterisation of dental materials several methods are available. In [1] the results obtained in round robin tests with different test machines are presented and discussed, whereas simulation problems are covered in [2] and [3]. An overview of different methods for wear simulation is presented in [4, 5]. Different factors influencing the wear behaviour of dental materials is discussed in [6].

With regard to the motion of the test bodies of the tribo couple, a forth and back movement relative to each other can be considered a simulation which makes sense. Therefore, candidate materials are often tested under reversal sliding [7] or fretting conditions [8, 9]. Besides a high wear resistance good machinability leading to smooth surfaces is often required.

Unfortunately, in wear tests time is a problematic factor: In the application of the materials the long term stability and high wear resistance if of interest and therefore the materials are optimized for low wear rates. In laboratory testing necessary for materials development it is necessary to obtain significant results in a relatively short time. The necessary time-acceleration in the test rig can lead to results deviating from real life behaviour.

2 Goal and Experimentals

For evaluation and comparison of the wear behaviour of dental restorative materials the ocilating sliding method with ball on disk arrangement was used. The ball being the countbody is pressed against the flat or disk like test body. A lubricating medium can be placed between ball and disk so that the tribological contact area is immersed in liquid.

The goal of this paper is the characterisation and quantification of the wear behaviour. Futhermore, characterisation of roughening of the sliding surfaces is also of importance since an increase in surface roughness during wear influences the comfort of the patient directly.

2.1 Materials

The investigated materials are commercial or near commercial materials used for dental restorations. From these materials crowns and inlets as well as other used shapes for dental restorative purposes are fabricated. Metal ceramic denotes a material which is used for a ceramic coating of metal bridges. The materials are all silicates containing a glass ceramic matrix and either feldspar or leucite microcrystalline phases. These materials have been used for preparing disk specimens by cutting plan parallel blocks and then polishing the surface. These blocks are glued to a metal substrate to fit into the tribometer sample holder. Figure 1 shows sample specimens as received and as prepared for the tribological testing.

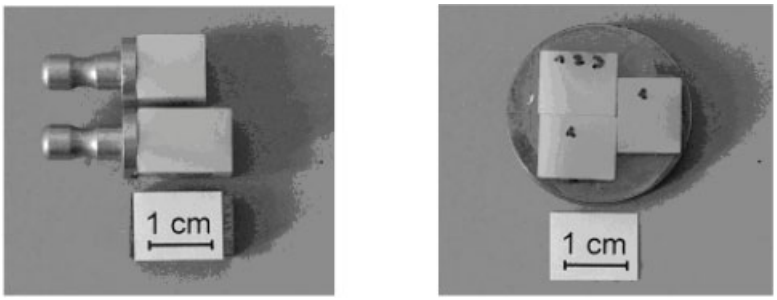


Figure 1: Specimens as received (left) and prepared specimens (disks) with parallel faces glued to a substrate ready for testing.

As spherical counter body material high purity α-alumina with 99.8% Al_2O_3 from Friatec AG, Mannheim, Germany, and 2 of the disk materials, Mark II and ProCAD, were used. Alumina was used in form of spheres with am diameter of 10 mm. The 2 other materials Mark II and ProCAD, a half sphere was prepared by machining to a diameter of 10 mm and subsequent polishing of the surface.

The different aqueous liquids were used for testing. Acetic acid was used to provide an environment with pH 2.2. For the neutral pH range, corresponding to physiological sodium chloride solution a 0.9% NaCl and distilled water was used. Sodium hydroxide solution with a pH of 10.2 was used to provide a basic environment. All liquids were pro analysis grade.

Table 1 shows the used materials, solids and liquids.

2.2 Tribological Testing

All tribological experiments were carried out with a gross slip fretting tribometer, described in [11] in more detail. This tribometer allows measuring the coefficient of friction (COF) and the linear wear W_l online. The linear wear is defined by the change of the distance between the ball and the disk. It detects possible changes of the wear rate during the tribological experiment. Quantitative determination of the wear is determined from a profilometric scan of the wear scar after the experiment has finished.

During the experiment COF and linear wear is measured, whereas after the experiment area and depth of the wear scar is determined; surface roughness inside the wear scar maybe evaluated

Table 1: Materials

Test materials (disk)	VITABLOCS® **Mark II** Feldspat (VITA Zahnfabrik)
	VITABLOCS® **TriLux** Feldspat (VITA Zahnfabrik)
	VITABLOCS® **Esthetic Line** Feldspat (VITA Zahnfa.)
	ProCAD Blocks Glaskeramik (Ivoclar Vivadent AG)
	Paradigm™C glass ceramic (3M ESPE), **ESPE-glass**
	Metal ceramic; manually prepared (3M ESPE), **ESPE-Met**
Counterbody (ball)	Al_2O_3
	Mark II
	ProCAD
Lubricating medium	none
	distilled Water
	physiological Sodium chloride solution (0.9 % NaCl)
	acetic acid (CH_3COOH; pH 2.2)
	sodium hydroxide solution (NaOH; pH 10.2)

from wear scar profiles. The measuring parameters were in all experiments the same and are compiled in Table 2.

Table 2: Test parameters

Tribological movement	Oscillating sliding (sinusoidal)
Stroke	200 µm
Frequency	20 Hz
Normal force	10 N
Number of cycles	100 000
Temperature	23 °C

3 Results With Alumina Ball as Counterbody – Friction and Wear

Figure 2 shows the coefficient of friction exemplified for one of the materials (Mark II) for tests both without a medium and with 4 different lubricating medias, according to table 1.

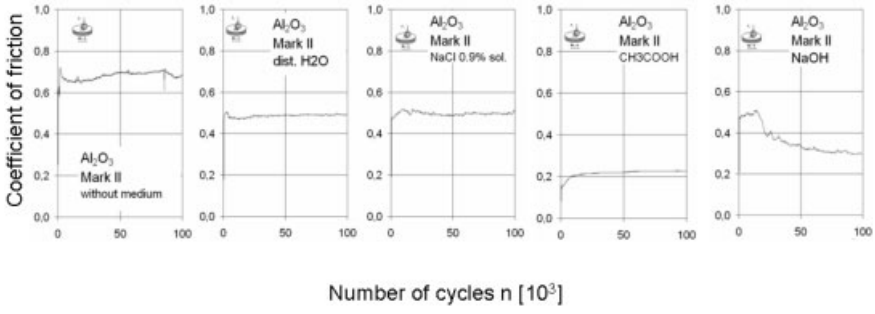


Figure 2: Cofficient of friction (COF) as a function of number of cycles (time) in tests of Mark II against alumina ball in different media.

COF is in all tests almost constant from beginning to the end , only for NaOH the COF drops from 0.5 at the beginning to 0.3 at the end of the test. COF is highest for the test without medium, and lowest with a COF of about 0.2 for acetic acid CH_3COOH with pH 2.2 .

The stationary COF, as the average value of the second half of one test period are shown for all materials and all lubrication conditions in Figure 3.

For a certain medium, all materials show very similar results, as i.e. already found for Figure 2. The differences between the materials are only marginal and lie within the normal deviation and can be considered practically equal.

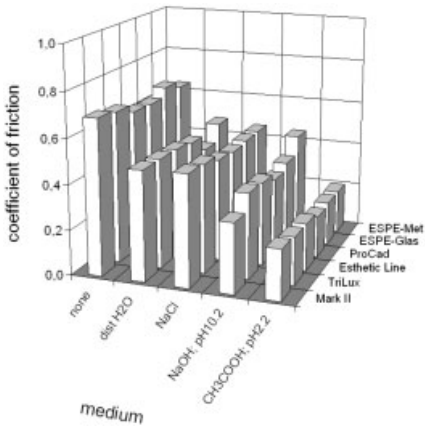


Figure 3: tationary COF for 6 different materials (see Table 1) and different lubrication conditions.

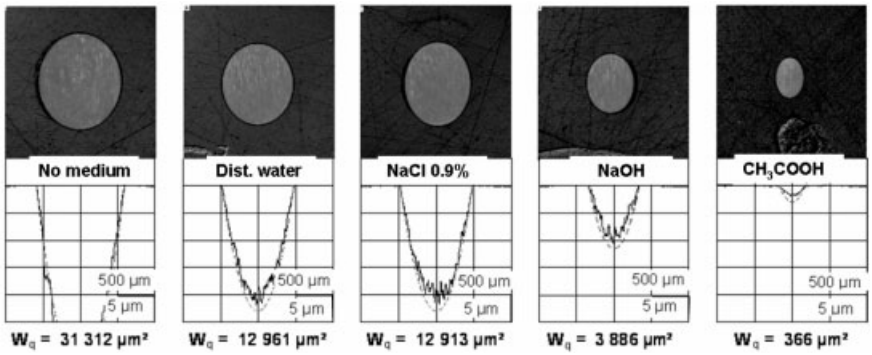


Figure 4: Wear scars and corresponding wear scar profiles for material Mark II and different media.

The profile of the wear scars together with the corresponding light micrograph as obtained after sliding in different lubricating media are shown exemplarily for one of the 6 materials (Mark II) in Figure 4. The other ones are very similar. The profiles shows 2 lines: a black profile line, corresponding to the scar on the disk, and a dashed line, corresponding to the contour of the ball.

In these profiles the dashed line is very close to the profile line, showing that the wear at the ball is rather low (but there is wear at the ball, because the dashed line happens to be beneath the profile line!), and consequently the wear takes place mainly at the disk. Below the profile the planimetric wear is given as a quantitative number. It is easily seen that the planimetric wear corresponds well with the profile and the wear scar on the photo micrograph.

Width and depth of the profile is greatest for the unlubricated tests, and decreasing with distilled water and salt water, and still lower for NaOH at pH 10.2 and lowest for acetic acid with pH 2.2. The planimetric wear amounts are shown for all materials in Figure 5.

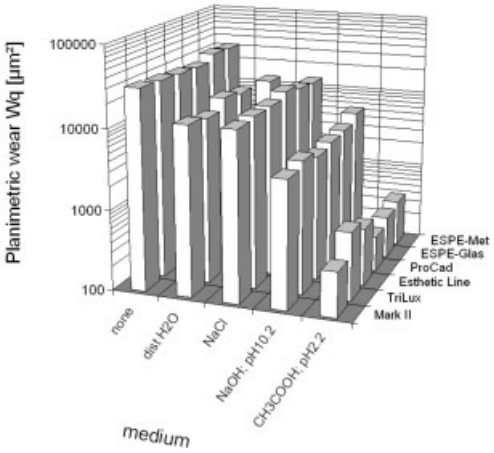


Figure 5: Planimetric wear for all materials and lubrication conditions

The planimetric wear is for all materials very similar, if the same lubrication condition is considered. Highest wear is observed in dry tests, smaller but similar tests in water and sodium chloride solution, significantly lower values in NaOH and the lowest values in acetic acid. However, it should be noted that the values have only a semi quantitative character. This is because they depend on ball radius, normal force and the testing time (number of cycles). A better quantity for comparison with other test results obtained in a different test series is the coefficient of system wear, in short wear coefficient k. It can be determined from the volumetric wear amounts, separately calculated for ball and disk according to the equations published in [12]. The wear coefficient corresponds to the volumetric system wear, normalized to sliding distance s and normal force F_n. However, one should bear in mind that the wear coefficient is depending on the wear mechanism and may change drastically when the mechanisms change, ie when passing from running in to steady state.

The wear coefficient over the entire test length is shown for all materials and the different lubricating conditions in Figure 6.

As already seen before in Figure 5, no significant differences between the materials can be noticed. However, wear is highest for the dry conditions with $k \sim 60 \cdot 10^{-6}$ mm^3/Nm, water and NaCl solution is lower with $k \sim 20 \ldots 30 \cdot 10^{-6}$ mm^3/Nm, NaOH at pH 10.2 with $k \sim 6 \ldots 9 \cdot 10^{-6}$ mm^3/Nm and acetic acid at pH 2.2 shows lowest values with $k \sim 0.6 \ldots 1.3 \cdot 10^{-6}$ mm^3/Nm.

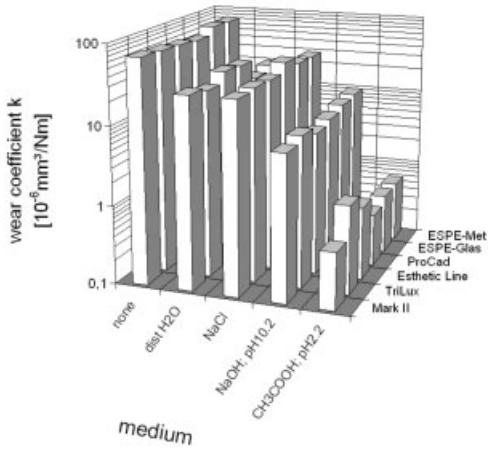


Figure 6: Coefficients of system wear for all materials in tests against alumina ball und different lubricating conditions.

4 Results of Self Mated Tests – Friction and Wear

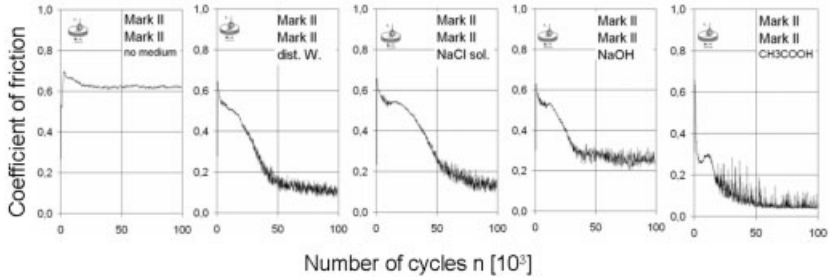


Figure 7: Development of coefficient of friction with number of cycles for self mated system Mark II under different lubrication conditions.

In comparison to Figure 2 the friction behaviour in the self mated couples is different for the lubricated tests. The unlubricated test, however, is similar with relatively high coefficient of friction, which starts at 0.7 and decreases during the test to somewhat lower values around 0.62. In the lubricated tests the friction in all cases starts at high values of 0.6, decreasing to significantly lower values of about 0.2 and below, and even lower than 0.1 in the case of acetic acid, during the first half of the test duration. This is represented in Figure 8, since it shows the differential friction coefficients, which is the average of COF of second half of the test period.

The drop to low friction in Figure 7 is also strongest for acetic acid. However, it can be noticed in all cases that in the low friction regime fluctuations between slightly higher and lower values do appear. Interestingly, these fluctuations are strongest for acetic acid.

Figure 9 shows the differential friction coefficients for self mated couples ProCAD/ProCAD, Mark II/Mark II as well as the corresponding cross combinations. In dry tests friction is very

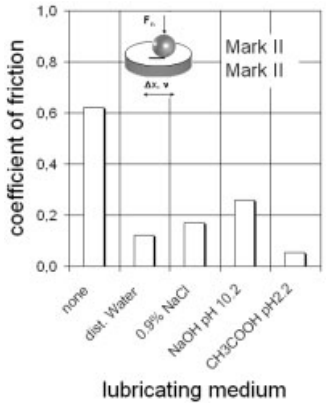


Figure 8: Differential friction coefficients for self mated couple Mark II/Mark II in different lubricating medias.

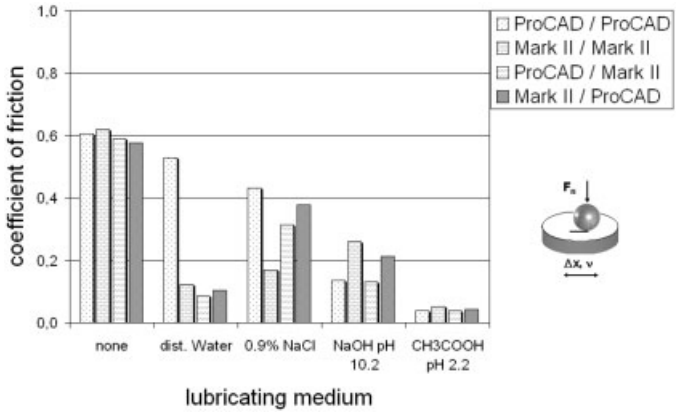


Figure 9: Differential friction coefficients for self mated couples ProCAD/ProCAD, Mark II/Mark II as well as the corresponding cross combinations in different lubricating environments.

similar and shows in all cases a COF of 0.6. In lubricated tests the results are a bit more differentiated and in distilled water and sodium chloride self mated proCAD couple has significantly higher friction than the other pairings. Nevertheless, the ranking found in the wear results (Figure 6) is valid here, too, finding lower friction in NaOH and the lowest and consistent values of 0.05 for the coefficient of friction for all 4 pairings in acetic acid with pH 2.2.

Wear The wear behaviour of the self mated couples does not follow the above stated findings directly. In all lubricating environment, except in acetic acid the wear is rather similar, even under unlubricated (dry) conditions. In these combinations, the wear differs only by a factor of 2–2.5. For acetic acid however, wear is for all combinations lowest again, and a factor of 2–3 lower than for the 4 other groups. Figure 10 shows the wear coefficient for these 4 combinations.

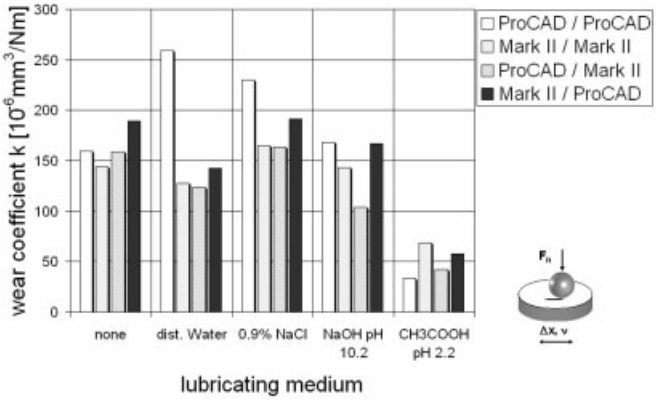


Figure 10: Wear coefficient for 2 self mated and the 2 related cross combined material pairings in different lubricating conditions.

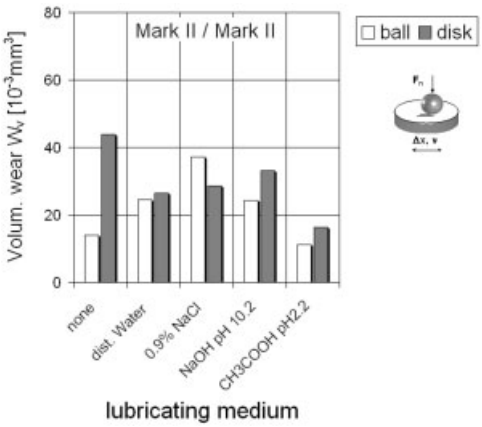


Figure 11: Volumetric wear for self mated material combination mark II.

Figure 11 shows the volumetric wear at ball and at disk exemplarily for self mated tribo couple Mark II/Mark II. Here is again a significant difference between lubricated and dry tests visible: in unlubricated tests wear is about 2-3 times higher at the disk, which is valid more or less for all material combinations. In lubricated tests this effect is much less pronounced.

Figure 12 shows the photo micrographs of the wear scars and the corresponding wear profiles, confirming these observations. The characteristic of the cross combined tribocouples Mark II/ProCAD and ProCAD/Mark II are very similar to that of self mated Mark II/Mark II.

Roughening of the surface due to wear is a common observation in sliding interfaces. However, in materials used for dental restorations this effect should be small, meaning that the surfaces in contact should stay smooth during use as long as possible, since roughening influences the comfort of the patient directly. In this regard the surface roughness of the sliding surfaces has

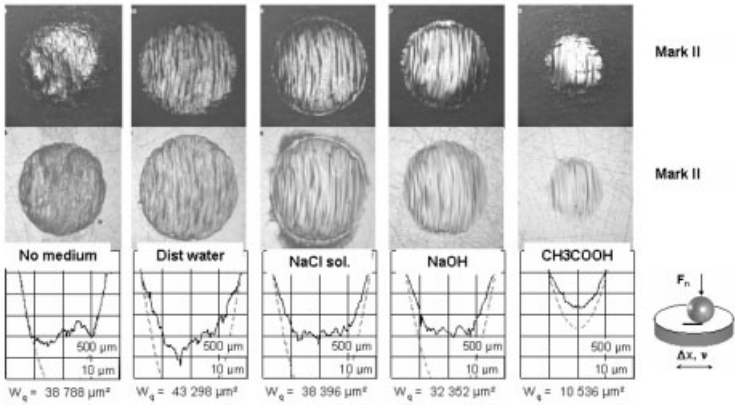


Figure 12: Photomicrographs of the wear scars and corresponding wear scar profiles of self mated pair Mark II/Mark II in different lubricating environments.

been analyzed by profilometry after the sliding experiments and compared with the roughness of the unloaded surface in each lubricating environment. The calculation of the roughness values was done by using data sets containing 4000 single data points across the wear scar profile, each as difference of the actual profile value and the average of 4 neighbour values. Thus the difference in roughness may be seen easily, however, one should bear in mind that this procedure will deliver only qualitative values.

Figure 13 shows the results of this calculation exemplarily for material Mark II run against alumina ball.

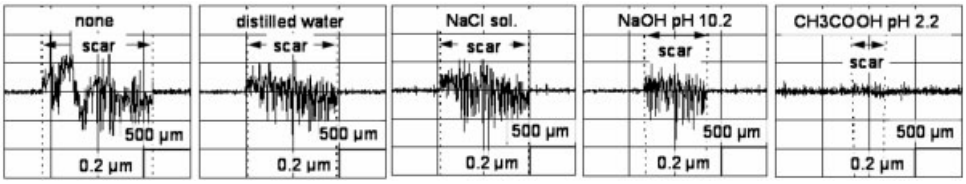


Figure 13: Roughness across wear scar as calculated from the roughness values measured by profilometry. Shown are the roughness profiles for material Mark II after testing against alumina in different lubricating environments.

As shown in Figure 13, unlubricated sliding produces the most rough surface, as in agreement with the highest friction and wear under these conditions (Figure 3 and 6). In media lubricated conditions distilled water and sodium chloride 9 % solution produce about the same surface roughness due to sliding. The roughness observed at the wear scar produced in NaOH is a little bit but not much less than the 2 former ones. However, acetic acid produces the less rough surface during sliding, in very good agreement with the friction and wear results. There is almost no difference to the roughness of the unloaded surface besides the wear scar.

Figure 14 shows the roughness values for all material combinations. This picture reveals that the results obtained for the combination alumina against Mark II is more or less valid for the

other combinations, too. However, there are slight differences up to a factor of 2 for the same lubricating regime.

Due to the more qualitative character of the roughness values according to the calculation procedure these differences should not be over interpreted.

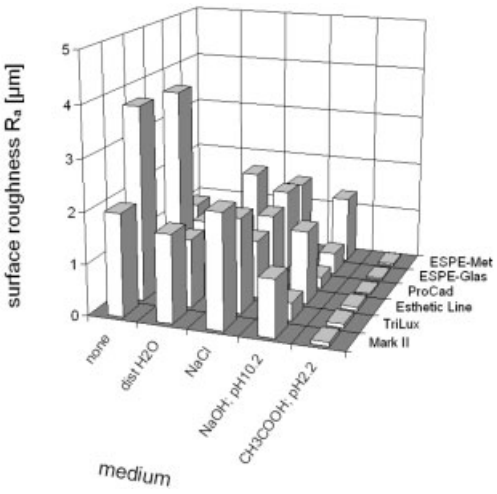


Figure 14: Surface roughness for all material combinations with alumina counterbody in different lubricating environments.

5 References

[1] S.D. Heintze, G. Zappini and V. Rousson: Wear of ten dental restorative materials in five wear simulators—Results of a round robin test, Dent. Mat. 2005, 21, 304–317.

[2] S.D. Heintze: How to qualify and validate wear simulation devices and methods. Dent. Mat. 2006 online 30 March.

[3] P. Lambrechts, E. Debels, K. Van Landuyt, M. Peumans and B. Van Meerbeek: How to simulate wear?: Overview of existing methods. Dent. Mat. 2006, online 18 May.

[4] S.D. Heintze, A. Cavalleri, M. Forjanic, G. Zellweger and V. Rousson: A comparison of three different methods for the quantification of the in vitro wear of dental materials. Dent. Mat.2005, online 28 Dec.

[5] E. C. Bianchi, E. J. da Silva, R. D. Monici, C. Antunes de Freitas and A. R. Rodrigues Bianchi: Development of new standard procedures for the evaluation of dental composite abrasive wear. Wear 2002,253, 533–540.

[6] Won-suck Oh, R. DeLong and K. J. Anusavice: Factors affecting enamel and ceramic wear: A literature review. The J. Prosth. Dent. 2002, 87, 451–459.

[7] A. Ramalho and P. Vale Antunes: Reciprocating wear test of dental composites: effect on the Wear, 2005, 259, 1005–1011.

[8] M.H. Zhu, H.Y. Yu, Z.B. Cai and Z.R. Zhou: Radial fretting behaviours of dental feldspathic ceramics against different counterbodies. Wear, 2005, 259, 996–1004.

[9] M.H. Zhu, H.Y. Yu and Z.R. Zhou: Radial fretting behaviours of dental ceramics. Tribology International, 2006, online 29 March.

[10] W.H. Mörmann, M. Brandestini: Die CEREC Computer Reconstruction. Inlays, Onlays und Veneers. Quintessenz 1989.

[11] D. Klaffke, On the Influence of Test Parameters on Friction and Wear of Ceramics in Oscillating Sliding Contacts. Tribotest J. 1995, 1–4, 311–320.

[12] D. Klaffke, Fretting wear of ceramics. Tribology international, 1989, 22, 89–101.

[13] A. C. Shortall, X. Q. Hu and P. M. Marquis: Potential countersample materials for in vitro simulation wear testing. Dent. Mat.2002 18, 246–254.

Scratch Tests on Natural Nacre – Reference for Implant Material

Berend Denkena, Luis de Leon, Marijke van der Meer, Analía Moral
Leibniz Universität Hannover, Garbsen (Germany)

1 Introduction

Endoprostheses must be able to resist the mechanical, thermical and chemical variations of their environment without being affected. Conventional implant materials, such as metal and ceramics, often fail to entirely fulfill this requirement. Ceramic implants, for example, tend to show surface disruptions due to their material brittleness and low fracture toughness. Nacre, as a composite implant material, is investigated not only in regard to its mechanical [1, 2] (i.e. high toughness and breaking resistance) and biological (i.e. biocompatible and biogenic) [3] properties but also to its composition and growth [4]. However, nacre machinability has not been fully researched until now. In this paper scratch tests on natural nacre are presented and their results are discussed. Scratch tests, as a simplification of the grinding process, are used to exemplify the mechanisms responsible for chip formation on the machined material. It has been observed that during the scratch tests on dry nacre an increase of the cutting speed or the tool tip radius results in a brittle behavior [5]. This paper focuses on the analysis of the forces engaged when scratching dry nacre. Particular attention is paid to the differently sized diamond tips of the scratch tool, the various cutting speeds and indentation depths used for the scratch tests and their influence on the forces involved in the scratch process. This work also intends to illustrate general directions for the machining process of artificial nacre by using natural nacre as reference.

2 Microstructure of Natural Nacre

Nacre is composed by aragonite (95 %) and a polymeric matrix (5 %) (Figure 1). The main component, aragonite, is a hard material made from $CaCO_3$ in form of pseudo-hexagonal platelets. The polymeric matrix can be divided into two different types, an intracrystalline and an intercrystalline matrix. The intracrystalline matrix is made from soluble proteins and its function is to join $CaCO_3$ subcrystals (20–180 nm in length) to form bigger aragonite platelets. The intercrystalline matrix is made of insoluble proteins which are placed between the aragonite platelets (1–5 µm width and 200-500 nm thick) and evolving them. These platelets form layers interconnected through mineral bridges and whose surfaces present small particles called nanoasperities. This hierarchical structure is responsible for the high toughness and high degree of strength of nacre [6], which makes it advantageous in comparison to conventional implant materials, like ceramics or metals. In figure 1 (bottom right) are also represented the natural and the polished surfaces of nacre. The surface of natural nacre has a curvature, which depends on genus and size of the shell.

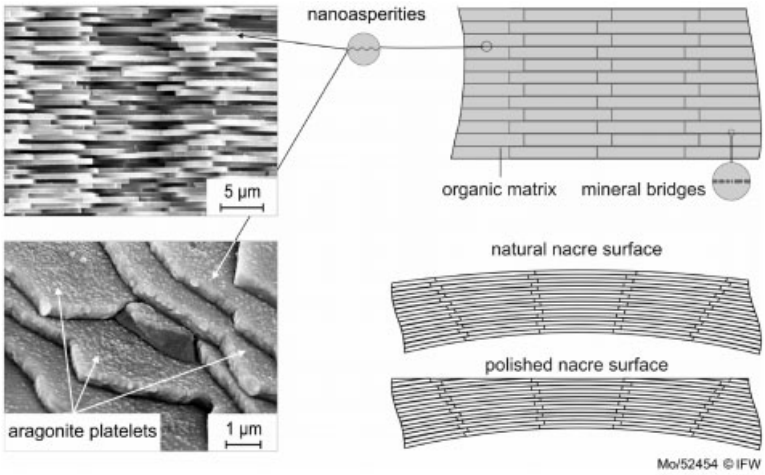


Figure 1: Microstructure of natural nacre.

3 Experimental Setup and Execution of the Tests

To study the interaction between tool and workpiece when machining nacre, scratch tests with single, geometrically defined diamonds were carried out. The experimental setup for the tests is shown in figure 2. The scratching tool is a conic diamond tip (figure 2, right) with a tip angle of 120°.

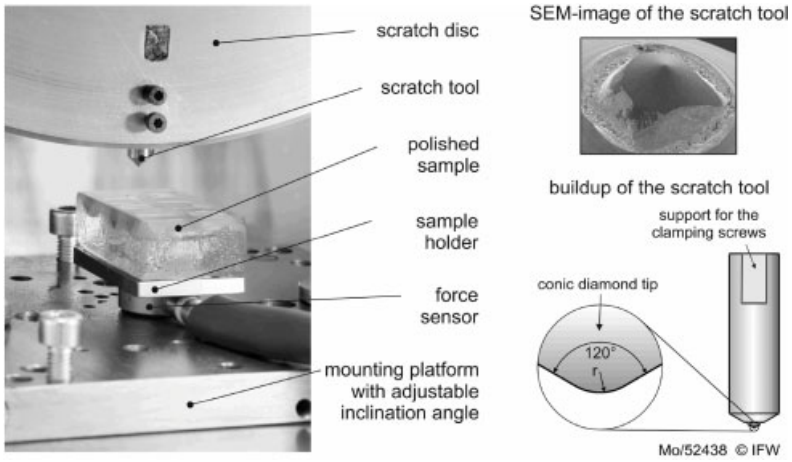


Figure 2: Experimental setup (left) and conic diamond tip geometry and its SEM image (right).

The samples for the tests were cut from a dry mollusk Haliotis rufescens (red abalone) shell in flat rectangles (11 mm × 11 mm) and embedded in group of six into glue mass. The surface of

each sample was then polished, so that sheets similar to that represented in figure 1 (bottom right) were obtained. The embedded samples were fixed on a mounting platform with an adjustable inclination angle. Between the samples and the mounting platform a force sensor was fixed to measure normal and tangential forces, F_n and F_t, involved in the scratch process. During the tests the mounting platform was oriented with an inclination angle of 0.27°, which resulted in a variation of the depth of cut h_c from 5 µm up to 50 µm. The cutting speed v_{cR} was varied from 2.5 m/s up to 10 m/s and the tool tip radius r_R from 50 µm up to 150 µm. A constant cutting speed v_{cR} = 10 m/s was selected for the variation of the tool tip radius. For each parameter variation the tests were repeated two times. The feed motion f_a = 1.05 mm was maintained constant for all the tests.

4 Investigation of Forces and Scratch Quality

During the scratch tests the forces occurring in normal and tangential direction for each scratch were measured and recorded. Maximal forces encountered in every scratch vs. the depth of cut h_c are shown in figures 3 and 4. The maximal depth of cut is obtained by the trajectory of the tool on the material, which is defined by the geometry of the scratch disc. In figures 3 and 4 it can be observed that when h_c increases, the forces increase too. This force increment is produced by bigger contact areas between material and tool when the tool is penetrating the material. The trend lines in both figures have been included only for guidance purposes. It is also worth to note that in every case the tangential forces remain below the normal forces, indicating an easier material removal in the tangential direction of the tool, parallel to the surface of the sample.

Regarding to the variation of the cutting speed v_{cR}, it can be seen in Figure 3, that its increase does not highly influence the normal or the tangential force. In all cases, when varying the cutting speed the normal and the tangential forces increase approximately up to 60 N and 30 N respectively.

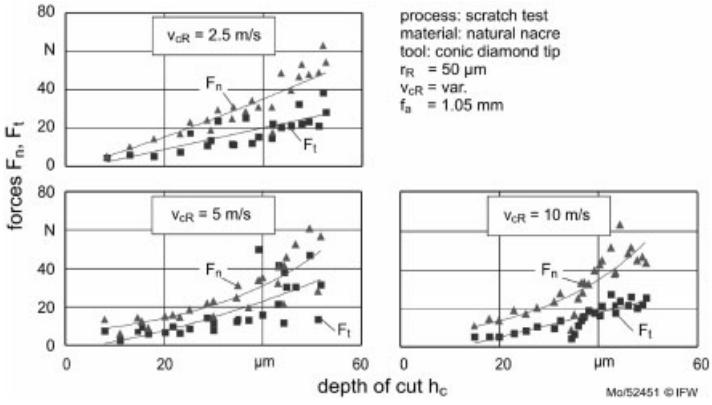


Figure 3: Influence of the cutting speed v_{cR} and the depth of cut h_c variation on the normal force F_n and the tangential force F_t.

On the other hand, the variation of the tool radius results in an increase of the normal and tangential forces. This can be observed in figure 4. When the tool radius is increased to 150 µm, the forces and the scatter increase. The reason for the increase of the scatter can be due to the curved form of the layers in nacre (Fig. 1, bottom right) and its natural defects like pores; this scatter is already known in nacre [8]. Furthermore, a higher radius results in a higher amount of removed material for the same depth of cut, which results in a rising tangential force. The main reason for the increase of the normal force is the decrease of the effective rake angle γ of the tool (Fig. 6, right).

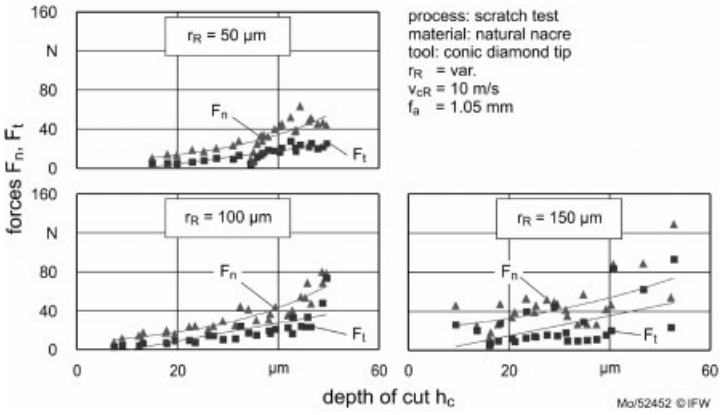


Figure 4: Influence of the tool radius r_R and the depth of cut h_c variation on the normal force F_n and the tangential force F_t.

The resulting surfaces are shown in figure 5. Larger lateral platelet detachments are observed when increasing the cutting speed (Fig. 5, left). At low cutting speeds only small detachments are observed; here chipping of the platelets seem to be the dominant material removal mechanism. At higher speeds, combinations of platelet chipping on the base of the scratch and lateral platelet detachments are observed.

When varying the tool radius (Fig. 5, right) the obtained surfaces show the opposite behavior. For small tool radius several lateral chips can be observed from the engagement to the exit zone of the scratch. As the tool radius increases these lateral chips decrease in size and number. For a tool radius of 150 µm almost no lateral chips are observed.

From figure 5 two principal material removal mechanisms can be identified in this work, which are in agreement with other studies [7]. While using a higher cutting speed (Figs. 6, left) a detachment of several platelets is observed. This detachment produces flat surfaces, which are probably the interfaces between different layers in nacre, where the polymeric matrix is placed and where the shear strength is lower than within the platelets.

When increasing the tool tip radius (Fig. 6, right) the rake angle of the tool γ becomes more negative and the tool orthogonal clearance angle α smaller. The first one produces greater compressive forces parallel to the platelets surface, leading to the layer chipping on the flanks and on the ground of the scratch. The second one, α, produces increasing friction forces between tool and material when it is smaller.

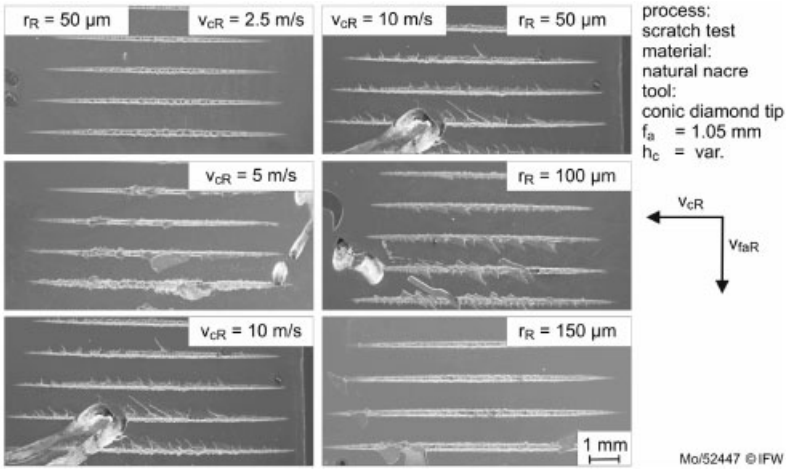


Figure 5: Influence of the cutting speed v_{cR} (left) and tool tip radius r_R (right) variation on the scratch quality.

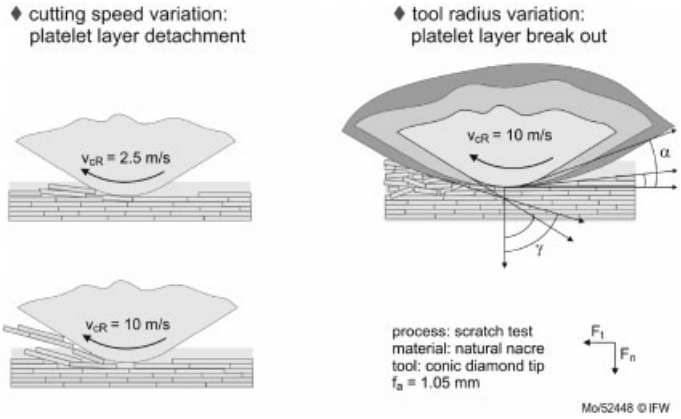


Figure 6: Material removal mechanisms on natural nacre observed during scratch tests.

By using small tool radius the material chips flow more easily over the cutting edge until the detachment of the chips is produced due to plastic deformation. A ductile material removal was observed only for small cutting speeds, depth of cuts and tool radius, this can be observed in figure 7 (top left). On the other hand, platelets layer detachment and chipping of the layers is mainly produced by using higher cutting speeds and tool tip radius (Figs. 7 bottom left and top right, respectively). A “step-like” surface produced by a bigger tool radius of 150 µm is shown in figure 7 (bottom right).

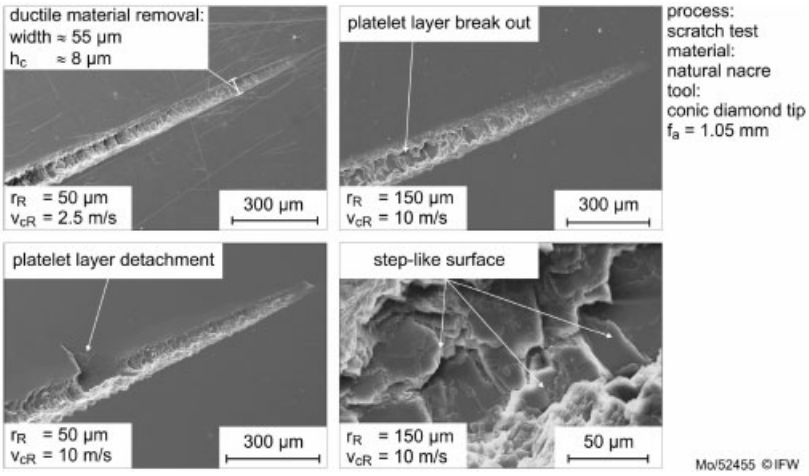


Figure 7: Scratch form most frequently observed during scratch tests on natural nacre.

5 Summary and Outlook

The material removal of nacre is highly dependent on its structure. The interlocked platelets embedded in the organic matrix give this material the possibility of distributing the shear forces in different directions. The chipping of the aragonite platelets is possible only when the loads are high enough, otherwise the organic matrix is sheared off and more platelets are cut off from the material. Only in a few cases when scratching with a diamond tip tool a ductile material removal was obtained. In future work, the machining process of nacre by using geometrically defined tools made of cemented carbide is going to be carried out. It is expected that varying the tool geometry a ductile instead of a brittle material removal of nacre will be reached, and therefore the quality of the surface could be improved.

6 References

[1] F. Barthelat, H.D. Espinosa, An experimental Investigation of Deformation and Fracture of Nacre - Mother of Pearl, Experimental Mechanics 2007, 47 (3), 311–324.

[2] R.Z. Wang, Z. Suo, A.G. Evans, N. Yao, I.A. Aksay, Deformation Mechanisms in Nacre, Journal of Materials Research 2001, 16 (9), 2485–2493.

[3] D. Oertel, A. Grunwald, Potenziale und Anwendungsperspektiven der Bionik, Forschungszentrum Karlsruhe in der Hemholtz-Gemeinschaft, TAB-Arbeitsbericht 2006, 108.

[4] G. Mayer, New Classes of Tough Composite Materials - Lessons from Natural Rigid Biological Systems, Materials Science and Engineering 2006, 26, 1261–1268.

[5] H. Menzel, O. Helmecke, S. Waraich, P. Behrens, B. Hering, B. Denkena, M. van der Meer, S. Ostermeier, C. Hurschler, Nacre as Model for Bio-inspired Implant Material, Biomaterialien 2007, 8 (3), 248.

[6] B.J.F. Bruet, H.J. Qi, M.C. Boyce, R. Panas, K. Tai, L. Fick, C. Ortiz, Nanoscale Morphology and Indentation of Individual Nacre Tablets from the Gastropod Mollusc Trochus niloticus. J. Mater. Res. 2005, 20 (9), 2240–2419.

[7] Stempfé, P., Brendlé, M., Tribological Behaviour of Nacre - Influence of the Environment on the Elementary Wear Processes, Tribology International 2006, 39, 1485–1496.

[8] Meyers, M.A., Lin, A.Y., Chen, P., Muyco, J., Mechanical strength of abalone nacre: Role of the soft organic layer, Journal of the Mechanical Behavior of Biomedical Materials 2008, 1(1), 76–85.

Influence of DLC Layer on the Wear Behavior of Unhardened Steel Moulds

W. Tillmann, E. Vogli, M. Gathen, S. Momeni (Sp)
Dortmund University of Technology, Dortmund, Germany

1 Introduction

One of the easiest and the most economic way for production of hard composite segments composed of metallic powder and diamond particles is cold pressing of the powder mixture in uniaxial direction in a pressing die. Although the pressing has been optimized over the years, further improvements on wear resistance of the dies are still necessary. The friction between the powder and the die during the pressing is one of the factors, which is responsible for the short life time of the die and is not fully understood [1]. During the pressing, diamonds come under high tangential and normal forces in contact with the die wall and result in damaging of the inner surface of the pressing mould. Hence, depending on the hardness of the die wall, pressing dies should be substituted after some pressings. Replacing these parts can be costly and time-consuming, and is related to slowing production.

WC-Co cemented carbides have been frequently employed in production of pressing moulds. However, manufacturing of the wear resistant pressing moulds using this material is costly and difficult to perform. Therefore, several works have been done to find suitable alternatives. For example, graded structures with cobalt content, ranging from 30 to 10 wt% from surface to the center of the die, have been employed to manufacture wear resistant parts [2]. In another work, it was shown that substituting carbides by diamonds result in increasing wear resistance of sintered cemented carbides tools [3]. Alumina reinforced with refractory carbides was also suggested as a suitable alternative for cemented carbides. Homogeneous distribution of WC grains was observed in an alumina matrix, which possesses large grains with very clean grain boundaries and thereby offer a high wear resistance [4].

Beside these techniques, some combined surface treatments have also shown positive results in increasing of the life time of mechanical tools. For example, Plasma over-carburizing and subsequent plasma nitriding of the forging dies, made of tool steel, increased the tool life by a factor of 1.5–3 [5].

Because of outstanding wear behavior, thin PVD films have been recently employed as an alternative to other surface treatments and material hardening techniques. For instance, Lousa et al. deposited Chromium / Chromium nitride multilayers on die-casting tools in order to increase the life time of the tools [8]. In our previous work [9], the positive effect of the PVD multilayers (Titanium/Titanium Aluminum nitride) on the wear resistance of the tools, used in electromagnetic sheet metal forming, was evidenced. In addition, several studies have shown outstanding mechanical and tribological properties of the DLC (amorphous diamond like carbon) PVD-coatings [6, 7]. Since this kind of PVD coating possesses very low friction coefficient, it has been also largely applied where very low friction is essential. For example, Reisel et al. have employed thin DLC coatings as an alternative for solid lubricant between tools used in warm massive forming [10].

These layers display some of the unique properties of the diamonds. They are usually applied as thin coating to the other materials and contain significant amount of sp^3 hybridization. The hardest DLC coating is known as tetrahedral amorphous carbon, ta-C. This coating contains only sp^3 hybridization. Additives such as hydrogen, graphitic sp^2 carbon, and metals are used in other forms of DLC layer to reduce the production expenses, but using additives results also in decreasing hardness and life-time of the coated parts. In other study [11], it was revealed that DLC coating with a hydrogen-free top layer presents higher wear resistance and lower friction coefficient under humid conditions in comparison to hydrogenated DLC layers.

The aim of this work is to develop very thin and hard PVD (physical vapor deposition) coating, made of diamond like carbon (DLC), for increasing the wear resistance and consequently, increasing the life-time of the pressing tools.

2 Experimental

Two different DLC coating systems were deposited, using an industrial magnetron device (Cemecon MLsinox800, Germany). These layers are hydrogen-free DLC (a-C), with a bias of 100 V, and hydrogenated DLC (a-C:H) with a bias of 130 V. The hydrogen-free (a-C) layer was deposited by sputtering of carbon targets in inert atmosphere, while the a-C:H layer was deposited by sputtering the carbon targets in acetylene gas. The targets have a dimension of 220 x 80 mm^2 and have a water-cooled plate at the back-side. In order to have a better adhesion between the DLC layer and the substrate, CrN-bonding layer was deposited directly on the substrate. To achieve this, two pulsed chromium targets were sputtered in nitrogen atmosphere.

DLC Coatings were deposited on samples made of steel C60 with an approximate hardness of 260 HV5. Coatings were deposited on the polished and unpolished samples. The samples used for pin-on-disc test have a diameter of 35mm and a thickness of 5mm, while rectangular samples, 10 x 20 x 30 mm, were employed for scratch test. These samples have been deposited with polished and unpolished surface. In order to investigate the effect of the PVD coating on increasing life-time of the pressing moulds, a-C:H 130 V and a-C 100 V coatings were deposited on two inner half-ring, forming pressing mould, which was pressed into an outer ring, figure 1.

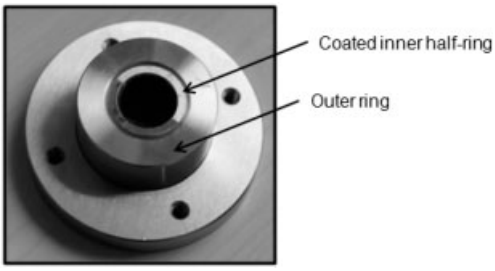


Figure 1: Coated pressing mould

To evaluate the adhesion of the coatings, the scratch test was employed. Before performing the test, samples were cleaned ultrasonically with ethanol for 10 minutes. During the test, the force was increased linearly up to 100N. Three measurements were performed on each sample,

and arithmetic median and standard deviation of the results was calculated. Simultaneously, the acoustic emission was recorded. After performing the scratch test, the samples were analyzed with Alicona 3D-analyzer (Infinite Focus) to investigate the failure modes of different coating systems.

In the pin-on-disc tests, a sphere, with a diameter of 6 mm, consisting of WC/Co, is pressed under 10 N on the coated samples. The linear velocity of the pins was set to 0.4 m/s. During the test, the tangential force was steadily measured. Afterwards, the friction coefficient was calculated as a fraction of the normal F_{n} and tangential force F_{t}, as follows:

$$\mu = \frac{F_{\mathrm{t}}}{F_{\mathrm{n}}} \tag{1}$$

The ambient temperature was around 25 °C with a relative humidity between 45%–60%. Before performing the test, the pin and the disc were cleaned ultrasonically for 10 minutes. In order to have a distance of 1000 m on the disc, the rotational speed and track radius were exactly set up.

The coated moulds were filled with 2.5 g powder mixture, composed of cobalt (Eckgranules, diameter ≤ 40 μm) as matrix and diamonds particles (Element Six, SDB1055, 40/50 US-mesh). The powder mixture was pressed uni-axial up to 50 kN. The force increased linearly from 0 to 50 kN. The morphology of the layers and the scratches on the pressing dies were characterized by using SEM (JEOL JXA-840).

3 Results and discussion

3.1 Adhesion characterization

The critical loads of two DLC coatings deposited on the steel C60 are shown in figure 2. As it can be seen, a-C:H 130 V deposited on the unpolished sample and a-C 100 V deposited on the polished sample have the highest and lowest average critical load respectively. Normally, it is expected that adhesion of coatings deposited on the unpolished samples is higher than adhesion of the coating on the polished samples. It relies on the higher mechanical bonding between the thin layer and the surface of the substrate.

The scratch traces of two coating systems under critical load are shown in figure 3. The tensile through-thickness cracking can be observed on both coated systems. These cracks are in angular form and are joined to both sides of the scratch rims. In addition to that, before reaching the critical load, spallation can be observed on samples. This kind of failure is a result of elastic recovery at the behind the stylus during the scratch test. Namely, after passing of the indenter and unloading the region, due to the plastic part of deformation, elastic strain of the coating cannot be fully relaxed. Consequently, it leads to generation of residual stress in the coating. Propagation of through-thickness cracks in this region can relax the residual strain. Afterwards, tensile stresses convert to shear stress at the interface between the coating and the substrate and close to these cracks. Finally, spallation occurs at one or both sides of the scratch trace as a result of the interfacial shear crack propagation.

Buckling is the major reason for the removal of the coatings under critical load, as shown in the figure 3. This failure occurs in regions ahead of indenter which are under compressive stresses. Pre-existing flaws at the coating interface are the most likely buckling beginning sites.

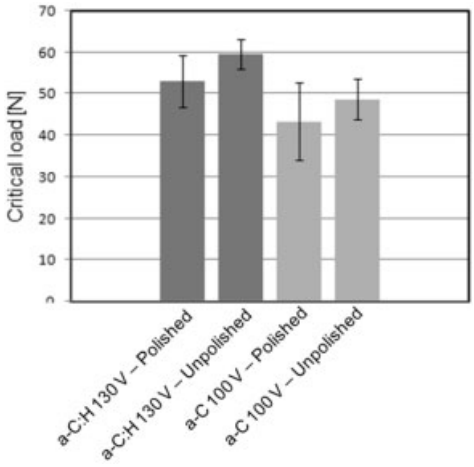


Figure 2: Critical loads of different DLC coating systems

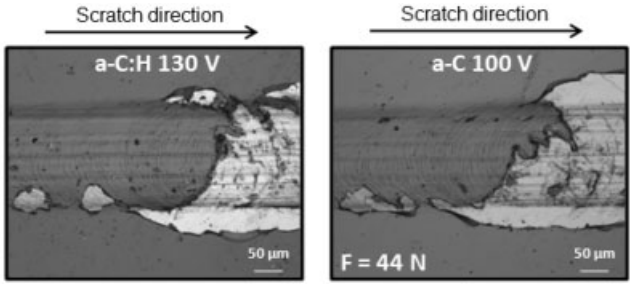


Figure 3: Failure modes of different coating systems under critical load

Friction coefficients of different DLC coating systems are shown in figure 4. Coating deposited on the polished samples have lower friction coefficient compared to coating deposited on the unpolished samples. Figure 4 shows also that a-C:H 130 V possess lower friction coefficient than a-C 100 V.

3.2 Coated Pressing Moulds

Macrographs of the inner surface of the coated and uncoated pressing moulds, shown in figure 5, evidence the effect of DLC coating systems on increasing life-time of pressing tools (thick lines at the middle of half-rings are just flash reflection). As it is shown, a-C:H 130 V coating systems on the unpolished sample possesses higher critical load and lower friction coefficient than a-C 100 V coating system. Consequently, on the inner surface of the half-ring coated with a-C:H 130 V, scratches can rarely be observed while on the inner surface of the half-rings coated with a-C 100 V, some scratches can be observed. Figure 5 shows also the SEM images of the scratches on the uncoated and coated mould with a-C 100 V. Obviously, in addition to reduction of the

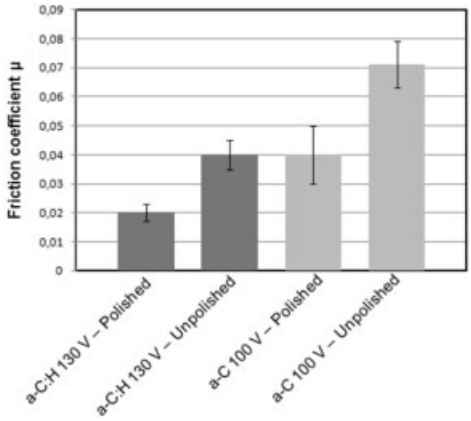


Figure 4: Friction coefficient of DLC coating systems

numbers of scratches, the depth and width of the scratches can also be reduced by employing DLC coating on the pressing mould. Moreover, on the deep scratches of the uncoated moulds, stick cobalt powders after pressing. This phenomenon was not observed on the coated moulds.

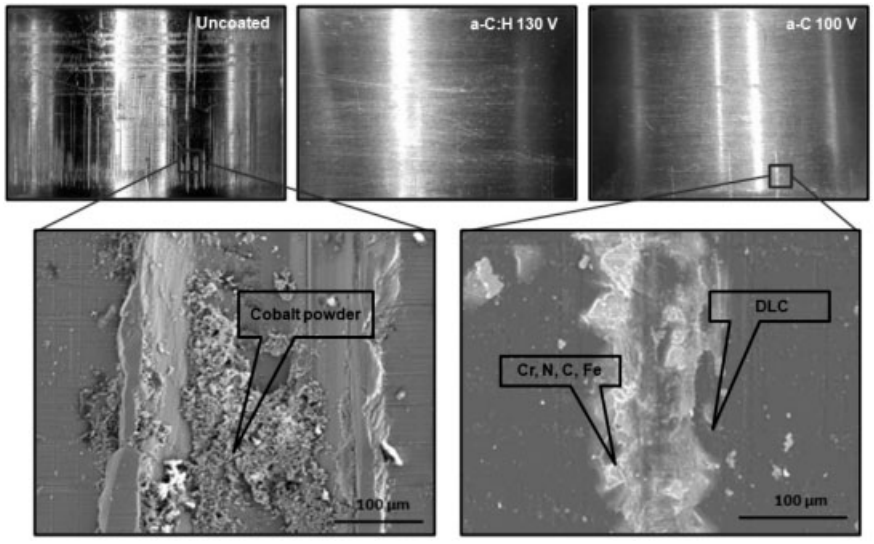


Figure 5: Inner surface of the coated and uncoated pressing moulds

4 Conclusion

Thin PVD coating deposited by sputtering magnetron device was employed as a novel solution to increase wear resistance of pressing moulds used in production of diamond composites. Two different DLC coating systems, a-C:H 130 V and a-C 100 V, were deposited on the unhardened steel C60. First, adhesion and tribological behavior of the coating were analyzed. Afterwards, wear resistance of the coated pressing moulds were compared with each other. It was shown that level of damaging on the coated moulds was lower than that of uncoated mould. In addition, depending on the sputtering process parameters, DLC coating systems showed different wear resistance on the pressing moulds.

5 References

[1] N. Solimanjad, R. Larsson, Mater. Sci. Technol. 19 (2003) 1777.

[2] C. Colin, L. Durant, N. Favrot, J. Besson, G. Barbier, F. Delannay, Intern. J. of Ref. Met. Hard Mater. 12 [3] (1993) 145.

[3] C. Cho, Y. Lee, Surf. Coat. Technol. 127 (2000) 59.

[4] W. Acchar, C. A. Cairo, M. Segãdes, Mat. Sci. Eng. 406 [1–2] (2005) 74.

[5] J.P. Souchard, P. Jacquot, M. Burvon, Mater. Sci. Eng. A140 (1991) 454–460.

[6] A. Erdemir, Surf. Coat. Technol. 146–147 (2001) 292.

[7] A. Erdemir, Tribol. Int. 37 (2004) 1005.

[8] A. Lousa, J. Romero, E. Martinez, J. Esteve, F. Montala, L. Carreras, 2001.. Surf. Coat. Technol. 146–147 (2001) 268–273.

[9] W. Tillmann, E. Vogli, J. Adv. Eng. Mat. 10, No.1–2 (2008) 79–84.

[10] G. Reisel, B. Wielage, S. Steinhäuser, H. Hartwig, Diamond and related materials 12 (2003) 1024–1029.

[11] W. Tillmann, E. Vogli, F. Hoffmann, Thin Solid Films 516, Issues 2–4 (2007) 262–266.

The Wettability of DLC Coatings with Ester and Polyalphaolefin

Kirsten Bobzin, Nazlim Bagcivan, Nico Goebbels, Koray Yilmaz
Surface Engineering Institute RWTH Aachen University

1 Introduction

Beginning from the mid 1990s the DLC (Diamond Like Carbon) coatings are playing major role against friction and wear in many industrial applications, among others the automobile industry [1]. The researches of the tribological behaviour of DLC coatings at the beginning were commonly focused on the non lubricated contacts for various environmental conditions. Due to the excellent tribological performance in boundary lubrication, the DLC coatings become important for the lubricated contacts in nowadays [6]. The right choice of the coating/lubricant pair enables not only a good performance in boundary lubrication, but also overall good wear resistance with very low coefficient of friction [2]. The type of the DLC coating is decisive, depending on the coating chemistry, whether hydrogenated, hydrogen free or metal doped, the DLC coatings can deliver different tribological characteristics with the lubricants [6]. E.g. M.I. de Borros'Bouchet et al. [4] found that Ti doped hydrogenated DLC coatings show a better tribological performance with Polyalphaolefin (PAO) with/without the additives molybdenum dithio carbamates (MoDTC) and zinc dithio phosphate (ZDDP) than hydrogenated DLC. Likewise Kano et.al. [2] found that hydrogen free tetrahedral amorphous carbon (ta-C) coatings can deliver friction coefficients as low as 0.006, if this DLC coating is used with ester additive containing PAO. Although the tribological results of DLC coatings can be influenced with additives [2, 6], it is well known that DLC coatings are chemically inert, which means that in contrast to ferrous surfaces any chemical reaction can not be responsible for the different tribological behaviour. The researches of Haque et al. [6] and Podgornik et al. [7] show that no additive derived tribological reaction could be found on DLC coated surfaces.

Due the chemical inertness, wettability of DLC coatings can be explained with the physical interactions. The physical interactions can be determined directly by means of contact angle measurements [8], only if the liquids don't spread over the surface. This requirement can be determined by means of spreading coefficient, such that if the spreading coefficient is positive, than contact angle measurement is not possible. In this case the amplitude of the spreading coefficient is decisive for the wettability [9]. Another factor which should also be considered for determining wettability of lubricants is adhesion energy. According to Robinowicz [17], the adhesion energy of the lubricants against a surface is an important criterion to asses its wettability, such that the higher adhesion energy, the more effective the lubricant.

2 Experimental Details

2.1 DLC Coatings

Two different types of DLC coatings were deposited on AISI 5115 steel substrates. DLC coatings can be classified as hydrogen containing (a-C:H) and hydrogen free amorphous carbon coatings

(a-C). The surface roughness (R_a) of the uncoated substrates prior to deposition amounts to 35 nm. The hydrogen containing and hydrogen free DLC coatings were deposited in an industrial coating facility by Magnetron Sputtering Ion Plating (MSIP) technology. The a-C type DLC coatings were deposited using a graphite target, with purity better than 99.5 %. Hydrogen containing DLC coatings were also deposited by MSIP technology in a reactive atmosphere consisting of acetylene and argon using a graphite target. The surface asperity of the with a-C and with a-C:H coated samples after deposition amount 37 nm and 44 nm respectively. Prior to deposition the substrates were cleaned with an etching process at –650 V at 250 kHz for 30 min. The DLC coatings are deposited on chromium based bond coatings for better adhesion. The characteristics of the DLC coatings are reported in Table 1. The mechanical properties, universal hardness and Young modulus, of the coatings were determined by nano indentation. Hydrogen content of DLC coatings was determined by Elastic Recoil Detection Analysis (ERDA).

Table 1: Properties of the DLC coatings

Coating	Thickness [µm]	Universal hardness [GPa]	Young modulus [GPa]	Surface roughness R_a [nm]	Hydrogen Content [% at.]
a-C	0.8	12.9±1.26	149.3 ± 11	37	0
a-C:H	2.4	12.6 ± 2.7	183.7 ± 22	44	25

2.2 Lubricants

The lubricants comprise two base oils, Polyalphaolefin (PAO) and Trimethylolpropan (TMP) Ester, with and without additives ZDDP and S-P. The ZDDP is a 2-Ethylhexyl-ZDDP. The concentration of ZDDP in base oils amounts 2 % and S-P (Sulphur-Phosphorus) additive amounts 4 %.

2.3 Determination of the wettability

The direct determination of wettability of DLC coated surfaces with lubricants is contact angle measurement. Due to spreading of the lubricants on DLC thin films, it is not possible to determine the wettability directly. This spreading phenomenon can be quantified by means of spreading coefficient (eq. 1). The spreading coefficient (S) describes the physical interactions between a lubricant and a solid, if directly determination is not possible.

$$S = W_A - W_K \tag{1}$$

S is the difference between the adhesion energy and cohesion energy. The adhesion energy (eq. 2) describes the reversible free energy change per unit area, if liquid brought on a solid surface. The cohesion energy defines the energy that keeps the lubricant together [10]. If S is positive, which means that adhesion energy is greater than cohesion energy, the lubricant doesn't form a drop on the surface, but spreads. This is the prerequisite for wettability. Otherwise a contact angle is measurable. For the determination of adhesion energy, the surface free energy of DLC coating and lubricant as well as the surface free energy at the boundary between DLC and

lubricant is necessary. The cohesion energy (eq. 3) can be calculated, if the surface free energy of the lubricants is known.

$$W_A = \sigma_s - \sigma_{sl} - \sigma_l \quad (2)$$

$$W_K = 2 \cdot \sigma_l \quad (3)$$

In general, the surface free energy of a solid surface can not be determined directly. The determination of the surface free energy of DLC coatings can only be carried out indirectly with reference liquids, whose surface energy is known (see Table 2). Measuring the contact angles of the reference liquids on the DLC coatings and using the equations from Young (eq. 4), Owens-Wendt-Rabel-Kealble (eq. 5) [14] and Fowkes (eq. 6) [15], the surface free energy of the DLC coating and the components of the surface energy σ^d and σ^p can be determined. The details of the methodic are explained in [9, 11, 13].

$$\sigma_s = \sigma_{sl} + \sigma_l \cdot \cos\theta \quad (4)$$

$$\sigma_{sl} = \sigma_s + \sigma_l - 2 \cdot \sqrt{\sigma_s^d \cdot \sigma_l^d} - 2 \cdot \sqrt{\sigma_s^p \cdot \sigma_l^p} \quad (5)$$

$$\sigma_s = \sigma_s^d + \sigma_s^p \quad (6)$$

Table 2: The surface free energy and the shares of the reference liquids

Test Liquids	Surface energy σ_l (mN/m)	Disperse share σ_l^d (mN/m)	
Dist. Water	72.1	19.9	52.2
Diiodmethan	50	47.4	2.6
Ethylenglycol	48	29	19
Glycerol	62.7	21.2	41.5

The free surface energy σ_1 of a lubricant can be measured directly by means of pendant drop method. The size and form of a drop is dependent on the liquid and using these characteristic magnitudes at hydro mechanical equilibrium (immediately before tear off), it is possible to determine the overall free surface energy by the Young-Laplace pressure equation (see eq. 7). Δp represents the pressure difference between inside and outside of the drop, the r_1 and r_2 are the main bending radiuses of a part of the drop surface. The detailed explanation of the pendant drop method can be found in [8, 9].

$$\Delta p = \sigma_l \cdot \left(\frac{1}{r_1} + \frac{1}{r_2} \right) \quad (7)$$

2.4 Tribological Tests

The tribological tests are carried out in a pin on disk tribometer at boundary lubrication. The DLC coated samples were put into a lubrication bath. As counter partner AISI 5210 steel spheres with a diameter of 6 mm are used. In order to prevent a chemical reaction, these spheres are coated with a-C type DLC. The parameters of the tribological tests are summarized in Table 4.

Table 3: Nomenclature of symbols used

W_A	Adhesion energy
W_K	Cohesion energy
S	Spreading coefficient
hline σ_l	Surface free energy of liquid (lubricant)
σ_s	Surface free energy of solid (DLC)
σ_{sl}	Surface free energy at the boundary between solid and liquid
σ^d	Disperse share of the surface free energy
σ^p	Polar share of the surface free energy
θ	Contact angle

Table 4: The Parameters of the measurements in pin-on-disk tribometer

Temperature [°C]	Linear speed [cm/s]	Wear track radius [mm]	Test distance [m]	Load [N]	Lubrication method
24 ± 5 %	10	2.5	750	5	Bath

3 Results and Discussion

The surface free energies of the lubricants as well as the DLC coatings are shown in Figure 1. According to these results, the surface free energy of TMP-Ester is higher than PAO. Mixing these lubricants with ZDDP additive doesn't change the surface energies remarkably but contrary the S-P additive decreases the surface energy with increasing the polar share.

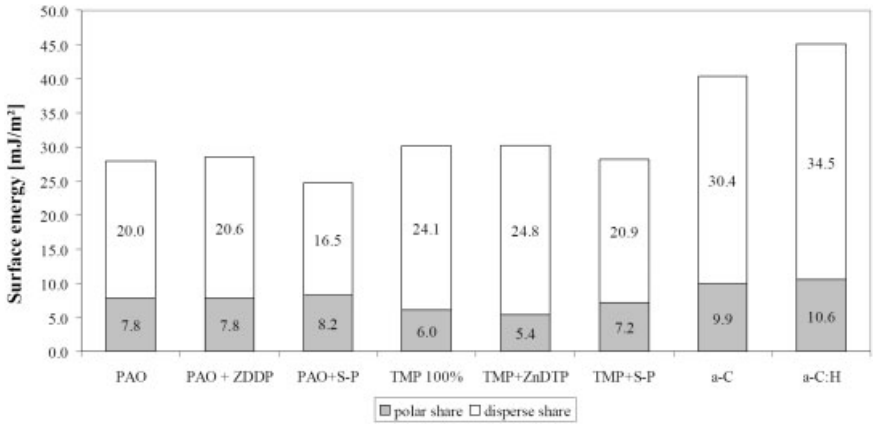


Figure 1: Surface free energy of the lubricants and the DLC coatings

The hydrogen free and hydrogen containing DLC show a disperse characteristic with approx. same polar share (see Figure 1). The surface free energy of a-C is 40 mJ/m^2 and the surface energy of the hydrogen containing DLC is approx. 5 mJ/m^2 higher than that of hydrogen free DLC, which is consistent with the result from Grischke et. al. [15]. Figure 2 shows the spreading coefficients of the lubricants on the DLC coatings. According to these results, TMP ester with

ZDDP additive delivers the smallest spreading coefficient on both of DLC coating, whereas the PAO with S-P additive shows the highest. The results also show that all of the spreading coefficients are positive; therefore the direct determination of the contact angles of the lubricants on the DLC thin films is not possible. If the spreading coefficients on one of the DLC thin films are considered, apart from PAO with S-P additive the spreading coefficients are very close to each other. Therefore a great difference in tribological performance e.g. between TMP with ZDDP and pure TMP is not expected.

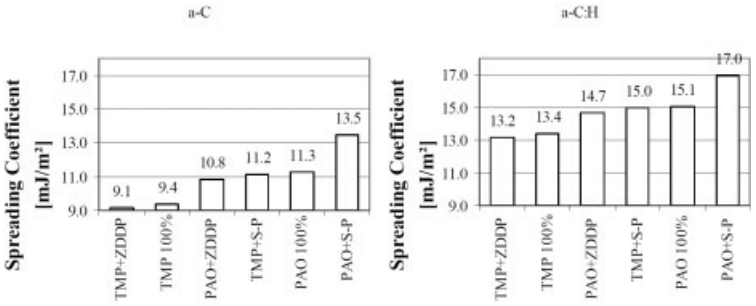


Figure 2: Spreading coefficients of the lubricants on the DLC coatings

Figure 3 shows adhesion energies of the lubricants on the DLC surfaces. If the adhesion energy is considered, the TMP ester with ZDDP additive as well as pure TMP ester should be the most effective lubricants on both a-C and a-C:H type DLC surfaces.

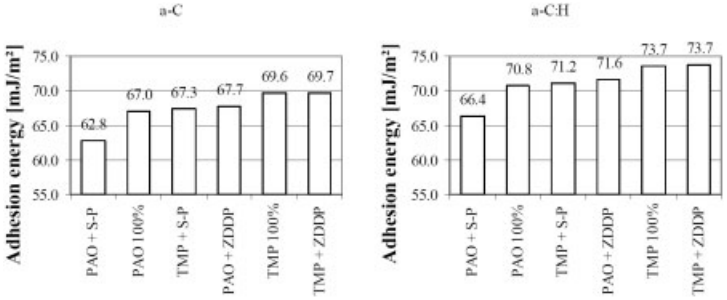


Figure 3: Adhesion energy between lubricants and DLC coatings

The results of the tribological experiments of DLC coatings in pin on disk tribometer against a-C coated AISI 5115 steel surfaces with lubricants are shown in Figure 4. Apart from the tribological results of the PAO with S-P additive, the average friction coefficients of the lubricants on a-C are close to each other and vary between 0.07 and 0.09. Commonly the progression of the friction coefficients tends to increase after the start up. But the PAO with S-P shows a different behaviour, such that the friction coefficient decreases rapidly, immediately after start up and reaches to an average friction value of 0.03. If we correlate the results from the pin-on-disk tribometer on a-C with the calculated physical interactions, spreading coefficients and adhesion

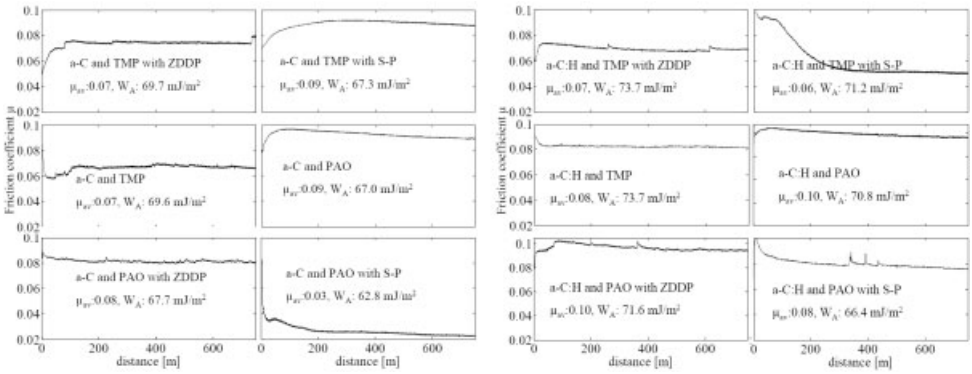


Figure 4: The progression of the friction coefficient of a-C coated AISI 5210 ball against a-C (left) and a-C:H (right) with lubricants

energy, apart from PAO with S-P additive the adhesion energy shows a direct relation. With increasing adhesion energy spreading coefficients decreases. This phenomenon can not be observed for PAO with S-P additive. Despite the lowest adhesion energy between a-C and PAO with S-P additive the friction coefficient was lowest. At the end of the experiments, it was detected that the coating on the sphere was worn out, which leaves the steel surface against chemical reactions unprotected. By means of energy dispersive X-Ray Spectroscopy (EDS) examination on the counterbodysurface, sulphur and phosphorus as well iron were detected, which can be an indication of a chemical reaction on steel counterbody surface, and hence reason for the deviance.

According to the tribological results of a-C:H in pin-on-disk tribometer (see Figure 4 right), the TMP with S-P additive delivers the lowest friction coefficient on a-C:H. There is no difference in average friction coefficient between pure PAO and PAO with ZDDP additive. An interesting result is between pure TMP ester and TMP ester with S-P additive. Although the friction coefficient progression of pure TMP ester with a-C:H is over the test constant, the friction coefficient progression of TMP ester with S-P additive decreases after app. 100 m. Same as on a-C surfaces the results of the tribological experiments can be correlated with the adhesion energy. The friction coefficient decrease with increasing adhesion energy. The two S-P additive containing lubricants, deviate from this presume. This result can also be correlated to a chemical reaction between the counter part and the lubricant, due to wear out of the DLC coating on the steel sphere. Although the adhesion energy of the lubricants on a-C:H is higher than a-C, the friction coefficients on a-C:H are higher than a-C. This phenomenon can be correlated to the easier disruption of the hydrogen containing DLC surface, which reacts with species present in the lubricants [3].

4 Conclusion

The results show that hydrogenating a DLC coating (25 % at.) can change the tribological behaviour noticeably. Generally hydrogen free DLC coatings show better compatibility with standard lubricants, which are developed for ferrous surfaces. The results also show that by means of determining adhesion energy, the compatibility of lubricants on DLC surfaces can be predicted,

such that the higher adhesion energy lowers the friction coefficient. The adhesion energy may be altered by means of matching the surface energy of the DLC coatings or the lubricants.

5 Acknowledgement

The authors gratetfully acknowledge the financial support of AIF. This publication based on the project (15418 N/1) of EFDS, supported by Bundesministerium für Wirtschaft and Technologie via AIF.

6 References

[1] R. Gåhlin, Mats Larsson, Per Hadenqvist, Wear 2001, 249, 302–309

[2] M. Kano, Trib. Int. 2006, 39, 1682–1685

[3] H. Ronkainen, S. Varjus, K. Holmberg, Wear 222 (1997), 120–128

[4] Barros' Bouchet , J.M. Martin, T. Le-Monge, B. Vacher, Trib.Int. 2005, 38, 257–264

[5] A. Neville, A. Morina, T. Haque, M. Voong, Trib.Int. 2007, 40, 1680–1695

[6] T.Haque, A.Morina, A.Neville, R.Kapadia, S.Arrowsmith, Trib.Int. 2007, 40, 1603–1612

[7] A. Erdemir, Trib. Int. 2005, 38, 249–256

[8] B. Podgornik, J. Vižintin, Surf. Coat. Tech. 2005, 200, 1982–1989

[9] K. Bobzin, Dissertation, RWTH Aachen, Shaker Verlag, Aachen, 2000

[10] E. Lugscheider, K. Bobzin, Surf. Coat. Tech. 2003, 165, 51–57

[11] Good, R.J. (1993) Contact Angle, Wettability and Adhesion, (Ed.:Mittal, K.L.), VSP BV, The Netherlands, 3–36

[12] E. Lugscheider, K. Bobzin, M. Möller, thin solid films 1999, 355-356, 367–373

[13] E. Lugscheider, K. Bobzin, Surf. Coat. Tech. 2001, 142-144, 755–760

[14] D.K. Owens, R.C. Wendt, J. App. Polym. Sci. 1969, 13, 1741–1747

[15] F. M. Fowkes, Ind. Eng. Chem. 1964, 56, 40–52

[16] M. Grischke, A.Hieke, F. Morgenweck, H. Dimigen; Diam. Rel. Mat. 1998, 7, 454–458

[17] E. Rabinowicz, J.App. Phy. 1961, 32, 1440–1444

CVD-Diamond Coating as Wear Protection for Standard Heat-Treatable Steel

K. Kellermann, J. Fandrey, S. M. Rosiwal, R. F. Singer
Institute of science and technology of metals, University of Erlangen-Nuremberg

1 Introduction

The coating of steel is a standard technique to adjust the steel surface properties to the requirements of technical applications. Diamond, due to its unique properties like highest hardness, high wear resistance and low friction would be an ideal coating material for several industrial applications. However for the diamond coating of steels several problems have to be solved. During the diamond deposition process, the steel is exposed to a carbon containing high temperature atmosphere. Due to the catalytic properties of iron for graphite formation the metastable iron carbide decomposes and a thick graphite layer is formed at the substrate surface at first. On this layer diamond growth occurs, but without adhesion to the steel and therefore useless for technical applications [1].

To solve this problem different interlayer or interlayer systems can be used. These layers have to fulfill a couple of requirements. The interlayer has to avoid the carbon diffusion from the gas phase to the steel substrate and the iron diffusion to the interlayer surface [2]. Furthermore the interlayer has to develop strong bonds to the steel as well as to the diamond layer [3, 4]. And last, to reduce the residual stresses in the diamond layer, the coefficient of thermal expansion (CTE) should be between the CTE's of diamond and steel.

During the last years different materials, like titanium or silicon were used as interlayers to achieve adherent diamond coatings on steel substrates [3–14]. At our institute high temperature diffusion chromizing interlayers were developed [4]. These layers show excellent bonding properties to steel due to the high chromizing temperature of 1150 °C [3, 4]. Also the problem of the great mismatch in thermal expansion between diamond (1.05 - $4.5 \cdot 10^{-6}$ K^{-1}, [15]) and steel (10.2 - $21.8 \cdot 10^{-6}$ K^{-1}, own measurements) has been solved by high temperature diamond deposition in austenite field [4, 14], using the steel volume expansion due to the γ -α-transformation during cooling down.

In this work we present the influence of the deposition temperature in a Hot-Filament Chemical Vapour Deposition (HF-CVD) process onto the adhesion of the diamond layer. For these experiments standard C35 heat treatable steel and a chromium carbide interlayer were used ($Cr_{23}C_6$) as mentioned by Bareiß et al. [4]. The influence of diamond deposition temperature onto the thermal residual stresses and the resulting steel microstructure was analyzed. The wear resistance of the diamond coating on steel was tested by erosion and compared to an uncoated and DLC coated steel.

2 Experimental

The steel samples were manufactured out of C35 (1.0501, ferritic-perlitic steel with 0.35 wt.-% carbon) steel with different geometries (i.e. rods: Ø 8 mm x 70 mm, discs: Ø 60 mm x 10 mm). The surface of the samples was ground up to 600 grit and sandblasted with SiC (30 µm). After that the specimens were diffusion chromized in a Cr-powder medium (99.8 %) added with activators in a vacuum ($p = 10^{-2}$ mbar) at a process temperature of 1150 °C for 5 h. Due to the diffusion of the carbon from the steel during chromizing, chromium carbides are formed at the surface. The formation of the chromium carbides is depending on time, temperature, activators and their concentration [3, 4]. After rinsing in ethanol, the substrates were pre-treated for 3 h in an ultrasonic bath using an alcoholic suspension with diamond and SiC particles. For CVD-diamond deposition a self-made HF-CVD (Hot-Filament Chemical Vapour Deposition) plant was used. The deposition parameters were: total gas pressure 10 mbar, methane 1.2 %, total gas flow 500 sccm and 5 h coating time. The substrate temperature was controlled by filament power varies between 685 °C and 885 °C.

Investigation methods: Dilatometer graphs for the steel C35 were realized in a NETZSCH DIL 402E. Residual stresses were calculated from Raman spectra using the relationship according to Ager et al. [16]. Cross sections of the samples were etched with an alcoholic 2 % HNO_3 solution to determine structural changes in the bulk material after deposition. With Glow Discharge Optical Emission Spectroscopy (GDOES) the diffusion of iron, chromium and carbon was analyzed. Erosion resistance was tested with Al_2O_3 EKF220 powder for 10 s, 35 mm distance to the sample and 2 bar pressure.

3 Results and Discussion

In this work the influence of diamond deposition temperature in a Hot-Filament Chemical Vapour Deposition (HF-CVD) process onto the thermal residual stresses in the diamond layer and the microstructure is presented. At first we show the characteristics of the chromium carbide interlayer and then the results of diamond coating for the different coating temperatures.

3.1 Barrier Properties of the Intermediate Chromium Carbide Layer

In these experiments diffusion chromized chromium carbide films were used as intermediate layer. One of the most important differences compared to other used interlayers (e.g. interlayers produced by electro deposition or PVD) [5–13] is the higher deposition temperature of 1150 °C. That leads to an improved chemical bonding of the layer to the substrate and to the formation of a thick diffusion zone.

After diamond deposition the multilayer compound shows the following composition: steel substrate, chromium carbide interlayer, diamond layer. The thickness of the diamond layer is approximately 2.5 µm and 10 µm for the chromium carbide interlayer. The concentration depth profiles of C, Cr and Fe measured by Glow Discharge Optical Emission Spectroscopy (GDOES), are shown in Figure 1. The iron concentration decreases rapidly at the Fe/CrC interface while carbon and chromium increase. At the interface between the diamond coating and the intermediate layer, iron is hardly detectable. In addition, Figure 1 shows that the chromium carbide intermediate layer is an effective barrier for both iron and carbon diffusion during the CVD diamond

process. The interdiffusion of carbon in the chromium layer and chromium in the iron substrate can clearly be seen. According to the atomic diameter the diffusion of chromium is small (up to 20 µm in 5 h, cp. Figure 1). Chromium diffusion into the substrate is desired and used for surface hardening of the steel substrate.

This gradient in composition with an outward increasing hardness (annealed steel sample → chromium enriched zone → chromium carbide layer →diamond film) may improve the mechanical properties of the whole compound, but has to be proven in further experiments.

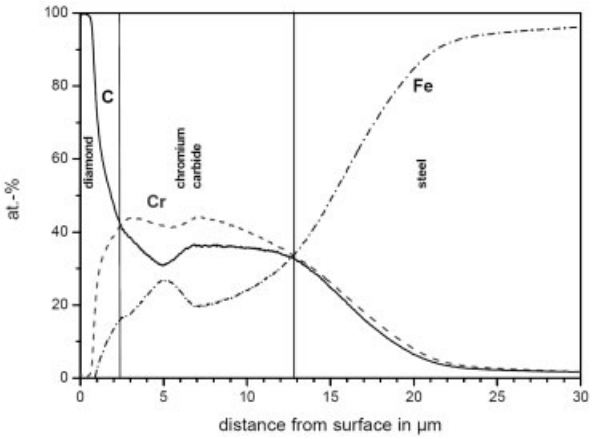


Figure 1: Carbon, chromium and iron concentration profiles for the diamond/chromium carbide/steel compound after diamond deposition.

3.2 Diamond Deposition and Properties of the Diamond Coating

Diamond deposition was carried out in a Hot-Filament CVD plant. The substrate temperature was varied between 685 °C and 885 °C and the deposition time was always 5 h. The multilayer compound adheres to the substrate without any delamination. The great mismatch in thermal expansion coefficient of diamond ($1.05–4.70 \cdot 10^{-6}$ K^{-1}, [15]) and C35 steel ($10.2–21.8 \cdot 10^{-6}$ K^{-1}, own measurements) results in high residual stresses in the diamond film after deposition. Sandblasting before diamond deposition of the intermediate layer ensures additional mechanical adhesion.

The residual stresses in the diamond layer depend on the phase and microstructure of the iron substrate during diamond deposition. In assistance with the time-temperature-austenitisation diagram of C35 in Figure 2 it is possible to determine the steel microstructure during diamond deposition. The deposition time is always over 1000 seconds so only the right frame (thermodynamic equilibrium) of the diagram is relevant. The digital photos on the right side of Figure 2 show the correlation between deposition temperature, the phases of the steel and the adhesion of the diamond coating. A substrate temperature (685 °C) below Ac_1 (first temperature of phase transformation α+Me_3C ↔ α+γ+Me_3C (metal carbide) in heating up of steels, 746 °C for C35) causes high residual stresses (-7.8 GPa, see Figure 3) and a slow diamond growth rate. Well adherent diamond coatings with admissible growth rate can be produced with deposition temperatures

between 760 °C and 825 °C. In this temperature regime the steel passes the phase transformation from γ (austenite) to α (ferrite) during cooling. Because of the elongation during this transformation (see Figure 4) a stress reduction in the diamond layer takes place. There is a minimum of the resulting residual stresses at a substrate temperature of 795 °C with –6.6 GPa. Above 885 °C substrate temperature the diamond layer chips of completely. At this temperature the steel passes the γ-α transformation, but the absolute temperature is too high, so the phase transformation is not sufficient for stress reduction. The wide temperature regime between 760 °C and 825 °C for well adherent diamond coatings and the stability of the chromium carbide interlayer demonstrates the high error tolerance of the deposition process.

The influence of the deposition temperature on the residual stresses of the diamond coating can be investigated by Raman spectroscopy (see Figure 3). The layers with low coating temperature 685 °C and 760 °C show no sharp diamond peaks in the spectra due to the fine grain size (< 1 µm) and low thickness (< 1 µm) of the diamond at this low deposition temperature. The residual stresses (calculated from peak shift in Raman spectra after Ager et al. [16]) of these specimens are –7.8 GPa and –8.5 GPa respectively. The minimum of the residual stresses has the specimen coated at 795 °C (–6.6 GPa). It passes the complete γ-α transformation during deposition. With increasing deposition temperature (825 °C and 885 °C) the peak shifts in Raman spectra and therefore the residual stresses increases (–7.9 GPa and –8.3 GPa). The specimen coated at 885 °C also shows flaking (cp. Figure 3) which is an indication that the residual stresses are higher than –9 to –10 GPa (limit of adhesion).

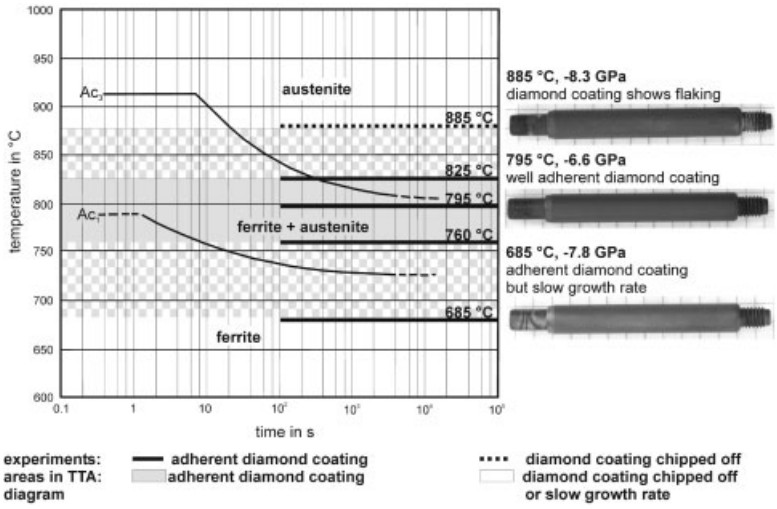


Figure 2: Isothermal time-temperature-austenitisation diagram for C35 [17] with regimes for ferrite, ferrite + austenite and austenite. On the right side you can see digital photos of diamond layers on C35 samples with different deposition temperatures. The grey shaded areas mark the temperatures where cracks and flaking or slow diamond growth rate is dominant. The graphic shows that only in ferrite + austenite and austenite area up to 825 °C well adherent diamond coatings on C35 are possible. (Ac_1: first temperature of phase transformation α+$Me_3C \leftrightarrow \alpha$+$\gamma$+$Me_3C$, Ac_3: third temperature of phase transformation α+γ+$Me_3C \leftrightarrow \gamma$ in heating up of steels, 805 °C for C35)

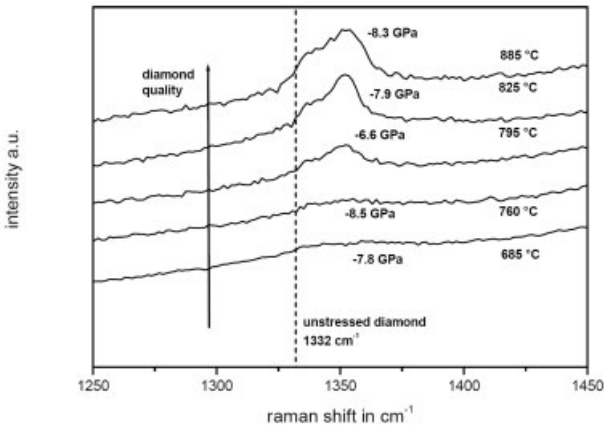


Figure 3: Raman spectra of diamond coated C35 series for investigations of adhesion and residual stresses depending on substrate temperature. Coating near to Ac_3-temperature (805 °C) leads to moderate residual stresses. The residual stresses for the coating at 885 °C can only be measured by adhesive coating fragments. With higher coating temperatures diamond quality increases.

It is also possible to calculate the residual stresses (Formula (1) [13]) from the difference of the thermal expansion coefficients (α_{C35}, α_{diamond} [15], see also Figure 4). This formula can only be used if the ratio of diamond thickness to substrate thickness is << 1. The calculated and measured residual stresses are displayed in Table 1. Please notice that α_{C35} (10.2-21.8·10^{-6} K^{-1}) and α_{diamond} (1.05–4.5·10^{-6} K^{-1}) depend on temperature. Young's modulus and Poisson's ratio for diamond were chosen 1000 GPa and 0.07 respectively.

$$\sigma_{calculated} = \frac{E_{diamond}}{1 - \nu_{diamond}} \int_{20°C}^{T_{coating}} (\alpha_{diamond} - \alpha_{C35})\, dT \tag{1}$$

Table 1: Residual stresses calculated after Ralchenko et al. [13] and measured for the C35 series compared to elongation.

temperature in °C	685	760	795	825	885
dL/L_0 in %	0.967	1.016	0.911	0.935	1.064
$\sigma_{\text{calculated}}$ in GPa	–8.2	–8.5	–7.0	–7.3	–8.4
σ_{measured} in GPa	–7.8	–8.5	–6.6	–7.9	–8.3

The calculated and measured values for the residual stresses correlate well what is an evidence for Formula 1. The calculated residual stresses are a little bit higher because of the roughness of the real surface, so stress relief can take place. To understand the good adhesion despite the higher substrate temperature (see 795 °C and 825 °C in Figure 2 and Figure 3) it is necessary to examine the shrinking of the steel with decreasing temperature. Figure 4 shows the thermal expansion for diamond (according to literature [15]) and C35 steel during cooling (according

to own measurements). As you can see in Figure 2 and Figure 4 the steel passes the austenite-ferrite transformation during cooling after diamond deposition. This transformation leads to a small elongation of the steel due to the lower density of the α-phase (bcc) compared to the γ-phase (fcc). This enlargement of the specimen acts against the formation of residual stresses when the coating temperature is above γ-α transition temperature. Please notice that higher cooling rates moves the phase transformation to deeper values (i.e. Ar_3 = 659 °C and Ar_1 = 569 °C for a cooling rate of 183 K/min measured in CVD plant).

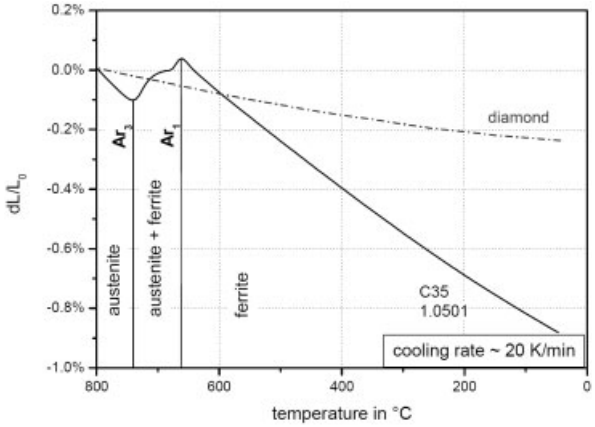


Figure 4: Thermal expansion versus temperature for diamond (according to literature [15] and own measurements) and for C35 (according to own measurements and cooling rate). Ar_3: third temperature of phase transformation $\gamma \leftrightarrow \alpha+\gamma+Me_3C$ in cooling down steels, that is 741 °C for C35 and a cooling rate of 20 K/min. Ar_1: first temperature of phase transformation $\alpha+\gamma+Me_3C \leftrightarrow \alpha+Me_3C$ in cooling down steels, that is 662 °C for C35 and a cooling rate of 20 K/min.

The change in microstructure of the steel can also be investigated by metallographic analysis. Coating above Ac_1-temperature leads to a change in microstructure. The high temperature of 1150 °C and the duration of 5 h of the diffusion chromizing process creates a coarse grained, ferritic-perlitic microstructure (154 HV5, cp. Figure 5 a) with coarse ferrite at former austenite grain boundaries and perlite between. If the Ac_1-temperature is not passed during diamond deposition ($T_{coating}$ = 685 °C) this microstructure does not really change and also shows a coarse grained ferritic-perlitic structure with an unchanging hardness (148 HV5, cp. Figure 5 b). The microstructure of the steel samples coated above Ac_1- or even Ac_3-temperature show a complete change in microstructure. The α-γ transformation during heating up to diamond deposition temperature and cooling down leads to a recrystallization and regeneration of grains and therefore to a fine grained microstructure. So a new fine grained ferritic-perlitic microstructure with an amount of 40 % ferrite and 60 % perlite results from coating above Ac_3-temperature (825 °C deposition temperature, cp. Figure 5 c). Due to the Hall-Petch relationship – the strength of the material is reciprocally proportional to grain size – the hardness increases to a value of 175 HV5.

In addition the microstructures of the coated steels (cp. Figure 5 b+c) show the diamond layer/interlayer/steel compound (cp. Chapter 3.1). Below the interlayer there is a small diffusion zone of chromium in the steel (about 10 µm). Thereupon is the decarbonized zone with a more ferritic microstructure due to the smaller amount of carbon in the steel (about 20 µm).

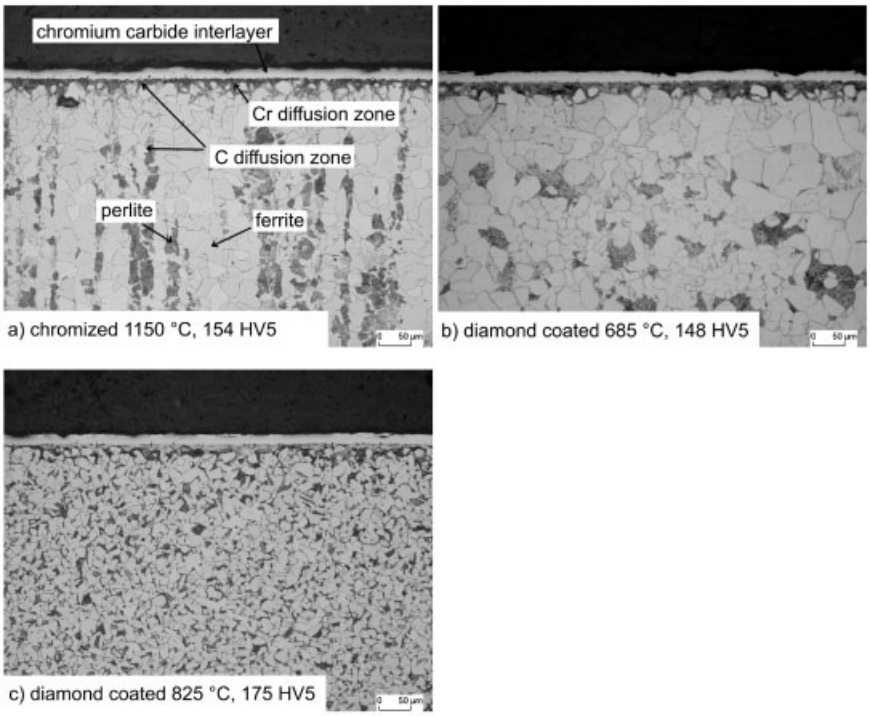


Figure 5: Microstructure and hardness (HV5) of the C35 series, a) after chromizing, b) and c) after diamond deposition with different substrate temperatures and cooling down to ambient temperature. A change in microstructure with an associated volume change is responsible for the adhesion of the diamond coating. In picture a) ferrite (white), perlite (grey), carbon diffusion zone (less perlite) and chromium diffusion zone (grey shaded band after chromium carbide interlayer) are indicated. The diamond layer is not visible because of small layer thickness of about 2 µm.

3.3 Erosion Resistance

Furthermore erosion tests were carried out. To compare the erosion resistance of the diamond coating the tests were done with an uncoated, DLC coated and diamond coated C35 steel (both coatings have a layer thickness of about 2 µm). After few seconds the uncoated and DLC coated specimens showed strong abrasion on the surface. The circles in Figure 6 demonstrate the region of erosion on the diamond coated specimen compared to the uncoated and DLC coated specimen. A small spot of delamination can be seen on the diamond coated specimen. The tests show the good erosion resistance of diamond coated steels compared to uncoated and DLC coated steel.

4 Conclusion and Outlook

Well adherent diamond coatings were deposited on C35 standard heat-treatable steel substrates using a diffusion chromium carbide interlayer. The interlayer demonstrated good barrier prop-

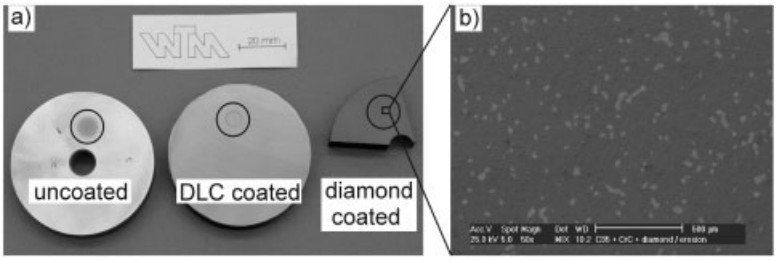


Figure 6: Encoated, DLC coated and diamond coated steel samples. Thickness of diamond layer is ˜2 µm. The black circles indicate the region of influence on the samples after 10 s of sandblasting. On the diamond coated specimen only small parts of the diamond layer are delaminated (right substrate and Figure 6 b).

erties for the diffusion of iron to the substrate surface. Deposition with substrate temperatures above Ac_1-temperature reduces the occurring thermal residual stresses in the diamond layer, because of the γ-α transformation in the steel substrate which results in a volume expansion during cooling down. Diamond coating narrow to the Ac_3-temperature in combination with chromium carbide interlayers enables adherent diamond coatings on steels for extreme wear and friction applications. A higher cooling rate after diamond deposition will generate a finer grained microstructure or even a hardened microstructure like bainite. These microstructures have a higher volume and hardness and so the supporting effect for the diamond layer will increase.

5 References

[1] Jentsch, H.-G., Rosenbauer, G., Rosiwal, S. M., Singer, R. F., Advanced Engineering Materials **2000**, *2*, 369–374.

[2] Spinnewyn, J., Nesladek, M., Asinari, C., Diamond and Related Materials **1993**, *2*, 361–364.

[3] Schwarz, S., Musayev, Y., Rosiwal, S. M., Schaufler, C., Singer, R. F., Meerkamm, H., Diamond and Related Materials **2002**, *11*, 757–762.

[4] Bareiß, C., Perle, M., Rosiwal, S. M., Singer, R. F., Diamond and Related Materials **2006**, *15*, 754–760.

[5] Buijnsters, J. G., Shankar, P., Gopalakrishnan, P., van Enckevort, W. J. P., Schermer, J. J., Ramakrishnan, S. S., ter Meulen, J. J., Thin Solid Films **2003**, *426*, 85–93.

[6] Silva, F. J. G., Fernandes, A. J. S., Costa, F. M., Baptista, A. P. M., Pereira, E., Surface and Coatings Technology **2005**, *191*, 102–107.

[7] Schäfer, L., Fryda, M., Stolley, T., Xiang, L., Klages, C.-P., Surface and Coatings Technology **1999**, *116–119*, 447-451.

[8] Polini, R., Mattei, G., Valle, R., Casadei, F., Thin Solid Films **2006**, *515*, 1011–1016.

[9] Fan, Q. H., Fernandes, A., Gracio, J., Diamond and Related Materials **1998**, *7*, 603–606.

[10] Buijnsters, J. G., Shankar, P., Fleischer, W., van Enckevort, W. J. P., Schermer, J. J., ter Meulen, J. J., Diamond and Related Materials **2002**, *11*, 536–544.

[11] Weiser, P. S., Prawer, S., Manory, R. R., Hoffman, A., Evans, P. J., Paterson, P. J. K., Surface and Coatings Technology **1995**, *71*, 167–174.

[12] Endler, I., Leonhardt, A., Scheibe, H.-J., Born, R., Diamond and Related Materials **1996**, *5*, 299–303.

[13] Ralchenko, V. G., Smolin, A. A., Pereverzev, V. G., Obraztsova, E. D., Korotoushenko, K. G., Konov, V. I., Lakhotkin, Y. V., Loubnin, E. N., Diamond and Related Materials **1995**, *4*, 754–758.

[14] Bareiß, C., Hackl, G., Popovska, N., Rosiwal, S. M., Singer, R. F., Surface and Coatings Technology **2006**, *201*, 718–723.

[15] Goldsmith, A., Waterman, T. E., Hirschhorn, H. J., Handbook of thermophysical properties of solid materials Volume I – Elements, Pergamon Press, Oxford, **1961**, 187.

[16] Ager, J. W., Drory, M. D., Physical Review B **1993**, *48*, 2601–2607.

[17] Orlich, J., Pietrzeniuk, H.-J., Atlas zur Wärmebehandlung der Stähle Band 4, Verlag Stahleisen m.b.H., Düsseldorf, **1976**, 31–35.

Modeling and Simulation of Unlubricated Oscillating Sliding Wear of DLC-coatings

L. Steiner[1*], V. Bouvier[1], S. Grosse[1], N. Huber[2], V. Hegadekatte[3], C.P.O. Treutler[1]
[1]Robert Bosch GmbH, Stuttgart, Germany
[2]Institut für Werkstoffphysik und Technologie, Technische Universität Hamburg-Harburg, Germany
[3]Institut für Zuverlässigkeit von Bauteilen und Systemen, Universität Karlsruhe (TH), Germany
*Corresponding Author E-Mail: leni.steiner@de.bosch.com

1 Abstract

In the present work, oscillating sliding wear tests of a diamond-like-carbon- (DLC-) coated 100Cr6 plate against a 100Cr6 steel ball have been performed to determine the relevant parameters contributing to wear and to better understand the tribological wear mechanisms under accelerated conditions (unlubricated, high contact pressures). Effects like stress peaks due to the surface topography or the formation of an oxidation layer in the contact area were examined. With a better understanding of wear and damage mechanisms, we developed a new wear model based on Archard's law. The extended model enables a realistic prediction of the coating's lifetime for different model-geometries. An important step was the enhancement of the numerical simulation tool Global Incremental Wear Model (GIWM) enabling a fast wear calculation and a rapid verification of the developed wear model.

2 Introduction

Industry has promoted the investigation of DLC-coatings due to their interesting tribological properties such as high wear resistance, high hardness, low friction coefficient, enhanced counterpart protection and chemical inertness [1, 2]. In modern fuel injection systems DLC-coatings are applied as a solid lubricant layer to protect sensitive mechanical parts from friction and wear [2]. A reliable prediction of lifetime represents a great challenge, as it would enable to reduce the number of endurance tests and lead consequently to cost reductions and faster development. Currently, the real lifetime is determined from expensive endurance tests, because no reliable wear models exist for the calculation of complex DLC-contacts. Therefore, in order to achieve a rapid classification of the coatings for a specific application, their lifetime is determined by means of simple oscillating ball-on-plate experiments under accelerated conditions (unlubricated, high loads). However the transfer of these results to the real application geometry is very difficult. We tackle this challenging problem through the combination of modelling/simulation and experimental results allowing the transfer of lifetime predictions from the model experiment to the application and thus validating the use of a coating for a specific application.

So far, several wear models for steel-steel-contacts have been developed to predict different types of sliding wear. The models are however restricted to the specific contact conditions and are therefore not suitable for different geometries or materials used in industrial applications. The important wear model is the empirical Archard's law, which is based on the assumption that the

contact pressure p and the sliding distance s are the major independent quantities for the wear depth h:

$$\frac{h}{s} = \frac{k}{H} \cdot p = k_D \cdot p \tag{1}$$

The material properties (including the hardness H of the softer material) as well as the other influencing parameters are supposed to be included in the wear coefficient k_D.

The wear of DLC-coatings has already been investigated by Jiaren Jiang [3], who developed a simplified wear model by neglecting the wear of the counterpart. He extended the Archard's law based on the assumption that the value of the wear parameter k_D modifies when the contact pressure p exceeds a critical pressure p_{crit}, where k_D and p_{crit} are determined from experiments for a given geometry.

To integrate the influence of roughness in the contact modeling, Greenwood and Tripp investigated rough spherical surfaces in contact without any tangential forces nor wear [4]. Their contact model includes the surface-height-distribution as well as several specific surface parameters of which the history-dependency is unknown. However it is already known from [6], that the elastic deformation is only relevant for the first few sliding millimeters where the geometries are not conform.

A further possibility of considering the surface topography in the wear model is to include the distribution of the roughness peaks described by the "Abbott-curve", and to consider thereby the so-called ratio of bearing contact area to total area. This approach has already been used by Põdra [5] for the calculation of wear in a steel-steel-contact by linearizing the Abbott-curve. His main assumption is that there is no elastic deformation, which leads to unrealistic results for non-conforming geometries, common in industrial applications.

To develop our new wear model and to achieve lifetime predictions we have used and essentially modified a numerical tool named Global Incremental Wear Model (GIWM) developed by Hegadekatte [6]. It consists of an incremental analytical implementation of Archard's model on the global scale. Hence it enables a rapid calculation of wear and thus a rapid verification of the developed wear models by comparing with experimental results. The improvement of the GIWM by the integration of the most relevant wear mechanisms is discussed in the following sections.

3 Experiments and Wear Modeling

3.1 Experimental Setup

For the experimental study of the wear resistance of two 2,5 µm-thick DLC-coatings deposited on 100Cr6 steel samples sliding against a 100Cr6 ball (radius 2 mm), a standard oscillating sliding wear tester has been used in unlubricated conditions. In order to study the effect of surface roughness on the wear behavior of the coated sample, substrates with different initial roughness (ranging from $R_z \approx 0{,}3$ µm (polished) to $R_z \approx 1{,}2$ µm (grinded)) have been investigated. The initial roughness of the ball is considered to be negligible. The two investigated DLC-coatings A and B differ in their hardness (B is harder than A) whereupon both coatings are hard in comparison to the hardness of the ball. With the aim of increasing the reproducibility of the initial contact conditions, a running-in phase has been performed at the beginning of each test. For each test, the

wear volume as well as the wear depth of the ball and of the coated sample have been measured. The continuation of a test after interruption is not possible.

3.2 Experimental Results

The experimental results (time-dependent progression of wear) for the coating and its counterbody are presented in figure 1 and 2 respectively. A linear relation between the wear-depth h of the coating, the sliding distance s and the contact pressure p could be observed (figure 1), which is in good accordance to the Archard's model. In figure 1 the linear wear coefficient k_D was derived from the wear calculation from the 40N experimental results and was used to predict the wear for 20 and 60 N. Therefore the red line fits the experimental results best. In this connection we calculate the pressure by means of the GIWM by the ratio of normal load and current area of contact. Other results concerning the coating's wear behavior showed no dependency of the sliding speed (for frequencies between 5 and 80 Hz). These results demonstrate that the Archard's model is an appropriate first approximation for modeling the wear behavior of the coatings.

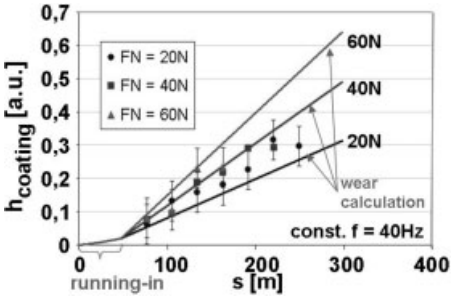


Figure 1: Variation of wear depth of the DLC-coating (layer A, R_z = 0,8 µm) as a function of sliding distance for 20, 40 and 60 N.

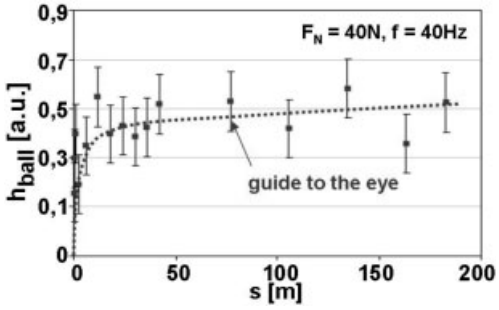


Figure 2: Variation of wear depth of the 100Cr6-ball in contact with a DLC-coating (layer A, R_z = 0,8 µm) as a function of sliding distance.

In contrast to the coating, the wear behavior of the ball is nonlinear. In the first seconds the wear depth of the ball increases dramatically and stabilizes on a high level, as shown in figure 2. The

curve progression cannot be explained alone by the widening of the nominal contact area caused by the wear on the ball. Although the experimental results for the ball exhibit a large scatter, the linear dependency between the wear depth described by Archard seems to be inadequate, unless two different wear rates are considered.

This decrease of the wear rate can be attributed to the formation of an oxide-containing film on the worn surface of the ball, leading to changes in the prevailed wear regimes from severe to mild wear [1]. Circumstantial investigations of the ball's worn scar (FIB-cut, SEM- and XPS-examinations) have evidenced the formation of an oxide layer having a thickness of about 300–600 nm and containing mainly Fe_2O_3 and eventually a small amount of FeO as shown in figure 3 and 4. Unfortunately no reliable measurement of the micro-hardness of this oxide layer was possible due to the surface roughness. Literature states that the hardness of Fe_2O_3 is around three times higher than the hardness of the steel substrate [7].

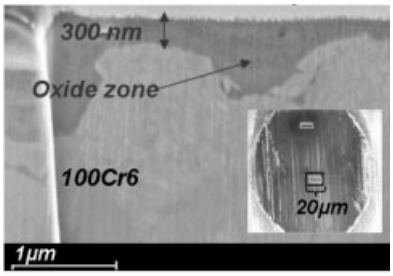


Figure 3: FIB-cut of the worn ball. The oxide layer has a thickness of 300–600 nm.

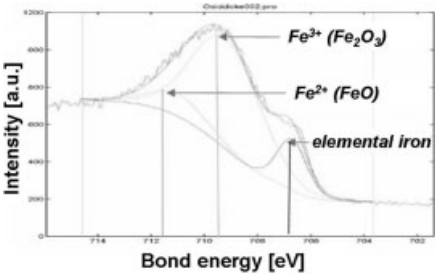


Figure 4: XPS-measurement of the oxide layer. The chemical composition is dominated by Fe_2O_3.

Further experimental investigations combined with contact simulations showed that the roughness of the DLC-coated sample leads to local stress peaks in the contact zone at the beginning of a test as shown in figure 5. The contact pressure can locally reach values which are five times higher than the maximum Hertzian stress, leading thus to plastic flow on the ball's surface. The distribution of the roughness peaks and the relative difference of hardness between coating and ball play a predominant role on the damage and wear on the softer contact partner. As evidenced in figure 6, the ball in contact with a grinded sample coated with layer B ($H_B \approx 42000$ MPa) wears significantly stronger than the ball in contact with a polished sample also coated with B. If

the relative hardness between coating and ball is reduced (coating A, $H_A \approx 24000$ MPa) the damage on the ball is diminished although the variation of the roughness is the same. It is remarkable to note that, contrarily to the ball, the wear kinetics of the coated sample is hardly influenced by the sample roughness and relative hardness.

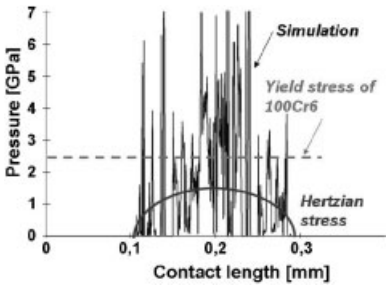


Figure 5: Contact simulation of a rough DLC-coating (layer A, R_z = 1,2µm) contacting a 100Cr6 ball. Local stress peaks due to roughness.

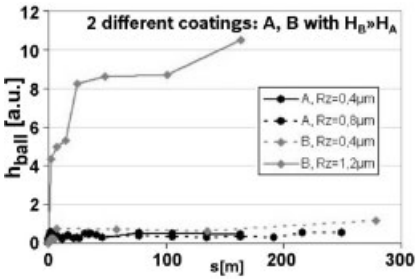


Figure 6: Variation of the wear depth of the ball as a function of sliding distance of two different layer A and B at different R_z-values.

Evidently the linear Archard's wear model is not sufficient to model the wear behavior of the entire system of DLC-coated sample sliding against a steel ball. For this reason we have improved the model by implementing the effect of surface asperities as well as the wear protective effect of the oxide layer in the wear calculation routine.

3.3 Wear Model Considering Surface Topography and Surface Oxidation

The GIWM-routine has been modified in order to implement the increase of pressure at the summits of the asperities. This is done by using the ratio of bearing contact area to total area similarly to Põdra's approach, with the following improvements: (i) consideration of the elastic deformations, (ii) no simplified linearization of the Abbott-curve. In the basic GIWM-routine the contact pressure p_i is approximated by the ratio of normal load F_N to nominal contact area $A_{i,0}$, leading to inaccuracy as the real area of contact $A_{i,real}$ is considerably smaller than $A_{i,0}$ in the first wear cycles i. By calculating p_i as the ratio of F_N to $A_{i,real}$ we obtain:

$$\Delta h = \frac{k}{H} \cdot \frac{F_N}{A_{i,real}} \cdot \Delta s = \frac{k}{H} \cdot \frac{F_N}{A_{i,0}} \cdot \frac{A_{i,0}}{A_{i,real}} \cdot \Delta s \tag{2}$$

The implementation of the real area of contact leads to an additional coefficient $A_{i,0} / A_{i,real}$ in the calculation of wear. This coefficient is the reciprocal value of the percentage contact area represented by the Abbott-curve which can be measured by means of confocal microscopy.

For non-conforming surfaces like our ball-on-plate geometry, the elastic deformation h^e has to be considered. In the first wear step, h^e is approximated using Hertz [8] and for the following wear steps using the elastic deformation according to Oliver and Pharr [9].

The normal approach $h^{approach}$ of two surfaces is the sum of h^e and the coating's wear h^c,

$$h^{approach} = h^e + h^c \,. \tag{3}$$

Since the Abbott-curve only takes into account the roughness of the coating, the wear depth of the ball is not considered in this equation. During the wear calculation we move iteratively along the bearing contact area curve. If q and x_c are fitting parameters, the curve is approximated by:

$$f(h^{approach}) = \frac{100}{1 + e^{-q(x - x_c)}}. \tag{4}$$

As shown in figure 7, the experimental results regarding the coating's wear are in good accordance with the wear simulation based on the Archard's law, especially for 40 N and 60 N.

For lower loads (F_N = 20 N) the contact temperature, after the running-in which depends on the normal force, is not high enough to support wear protection due to graphitization. Additionally the ratio of bearing contact area to the total area is smaller (more surface roughness), and thus the wear rate is increased. Together this leads to a systematic discrepancy between measurements and simulation.

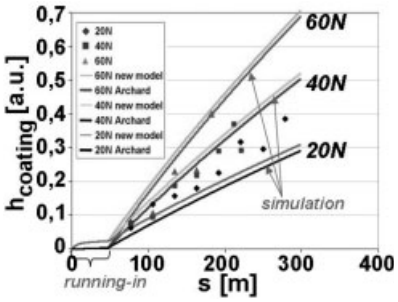


Figure 7: Variation of wear depth of the DLC-coating as a function sliding distance for 20, 40 and 60 N under consideration of $A_{i,real}$.

By implementing the effect of surface roughness by means of the Abbott-curve, a better agreement between simulated and measured wear for 20 N is obtained. But the major effect of considering the roughness in the model concerns the wear of the counterbody. The nonlinear progression of the ball's wear can thus be approached as demonstrated in figure 8. This is due to

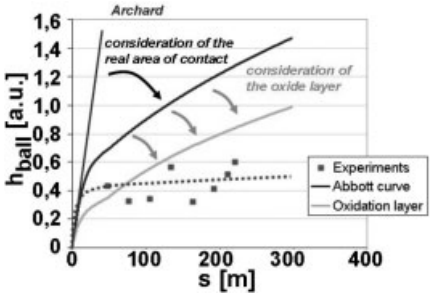


Figure 8: Variation of wear depth of the ball as a function of sliding distance considering $A_{i,real}$ und the oxide layer.

the reduction of the contact area at the beginning of wear described by the Abbott curve which is responsible for a severe wear regime. When wear progresses, the contact area and the ratio $A_{i,real}/A_{i,0}$ increase, leading to a change in the wear regime and to a reduction of the wear rate.

Nevertheless, the aforementioned improvement is not sufficient to describe realistically the wear behavior of the ball. A further enhancement of the wear model has been performed by considering the oxide layer and its wear protective properties. Within the wear routine of the GIWM, the formation of the oxide layer has been integrated by physical laws for steel-steel-contacts as described in [10] under the assumption that the oxidation of iron has parabolic kinetics. The increase of the temperature T^{flash} at the roughness peaks is implemented by:

$$T^{flash} = \frac{0.25 \cdot \mu \cdot F_N \cdot v}{(K_1 + K_2) \cdot a}, \tag{5}$$

with friction coefficient μ, normal load F_N, velocity v, thermal conductivity of the material K (= K_1+K_2) and the radius of the contact area a_i [11].

According to the experimental observations we assume that the oxide layer wears continuously with a wear coefficient k_D. As mentioned before the hardness of the oxide layer is three times higher than the hardness of 100Cr6. For this reason we chose a k_D-value reduced by a factor 3 for the wear calculation of the oxide layer. This gives rise to better agreement between modeling and the experimental results as shown in figure 8.

The implementation of wear influencing effects in the wear model (such as the effect of surface topography or the formation of a wear protective oxide layer), has enabled to develop a qualitatively good model for the description of the wear of the softer counterpart. The consideration of further wear mechanisms, like the graphitization of the DLC-coating which exhibits wear protective properties (lubrication effect), will lead to further improvements of the simulation and its implementation in the wear model is our next aim.

4 Conclusion

The wear behavior of DLC coatings sliding against 100Cr6 balls has been investigated with the aim of developing a reliable wear model for coating and counterpart which enables lifetime predictions for different geometries and loading conditions. It has been shown that the Archard's

law provides a good basis for the analytical calculation of the wear of a DLC-coating. By considering the surface roughness using the Abbott-curve and the formation of an oxide layer with wear protective properties, the wear model has been significantly improved.

5 References

[1] H. Ronkainen, *PhD Thesis*, Helsinki University of Technology, Helsinki, Finland **2001**

[2] C. P. O Treutler, Surface and Coating Technology **2005**, *200*, 1969–1975

[3] Jiaren Jiang, Wear **1998**, *217*, 190–199

[4] J. A. Greenwood, J.H. Tripp, Journal of Applied Mechanics **1967**, 153-159

[5] P. Põdra, *PhD Thesis*, University of Stockholm, Stockholm, Sweden **1997**

[6] V. Hegadekatte , Tribology Letters **2006**, *24*, 51–60

[7] Habig, Verschleiß und Härte von Werkstoffen, Carl Hanser Verlag München Wien **1980**

[8] K. L. Johnson, Contact Mechanics, 9th Edition, Cambridge University Press, **1985**

[9] W. C. Oliver, G. M. Pharr, J. Mat. Res., **1992**, *7*, 1564–1583

[10] S. C. Lim, M. F. Ashby, acta metal, **1987**, *35*, 1–24

[11] Z. F. Zhou, Wear **2004**, *258*, 1589–1599

A Study of Mechanical and Tribological Properties of Electroless Nickel-Boron Deposits after Heat and Thermochemical Treatments

Vitry Véronique, Delaunois Fabienne
Faculté Polytechnique de Mons,
Mons, Belgium

1 Introduction

Electroless deposition was discovered in 1946 by Brenner and Riddel [1]. This process leads to the deposition of continuous coatings having a constant thickness and can be used on conductive and isolating materials. There are three main classes of electroless nickel deposits: pure nickel, nickel-phosphorous and nickel-boron (which are the focus of this paper) [2]. Nickel-boron coatings show a high hardness (around 750 hv_{100}) in their as-deposited state and this hardness can be enhanced up to 1200 hv_{100} by the application of a well chosen heat treatment [3–7]. Beside their hardness, other features of electroless nickel-boron coatings are interesting: their typical cauliflower-like surface morphology which is well adapted to retain lubricating media, their good corrosion resistance [2, 8], and the thickness homogeneity which allows the use of those coatings for precision mechanics. The good adhesion and wear resistance of those coatings are also advantages for a lot of applications [4, 9–11].

Nanoindentation allows the hardness measurement of very small parts because it uses very small loads (typically a few mN). The loading and unloading curves are recorded and are used to obtain the hardness and Young's modulus of the material [12–14]. It is possible, using this method to follow the hardness evolution across a coating of no more than 20 microns [15].

Scratch testing is a very useful method to asses the adhesion and degradation mechanism of coatings. It is based on the application of an increasing load to a sliding sample [16–17].

Thermochemical treatments are a well know mean to enhance surface properties of materials such as hardness and wear resistance, however, their use on nickel-boron coatings is not yet documented.

2 Experimental Methods

2.1 Sample Preparation

Nickel-boron coatings were deposited on aluminum and steel substrates. Substrates were cylinder with a diameter of 25 mm and a thickness of 10 mm or 2 mm thick sheets. The 2 mm sheet substrates were cut into 100×100 mm square pieces or they were pre-cut for Taber abrasion tests.

Before plating, substrates were prepared by degreasing and etching in an acid solution (and nickel-phosphorous protective coating was deposited for aluminum alloys).

The plating bath contains nickel chloride, ethylene diamine, sodium borohydride and lead tungstate. It operates at 95 ± 1 °C, under constant agitation. The bath and the system used to plate small cylinders were described elsewhere [5]. Sheets were plated in a stabilized bath with a PTFE protective coating. Nickel boron coatings averaging 15 μm were deposited.

Heat treatments were carried out in a controlled atmosphere and vacuum furnace, under a flow of neutral (95 % Ar / 5 % H_2) gas. Treatment conditions were: 400 °C/1 hour and 180 °C/4 hours. The first set of conditions is reputed to maximize the hardness of nickel-boron deposits while the other one was proven by Delaunois et al. [5] to be a compromise for substrate and coating mechanical properties for aluminum alloys. Thermochemical treatments were carried out under ammonia and nitrogen-based atmospheres.

After heat treatments, the samples used for SEM observation and hardness measurements (except Vickers hardness) were cut with a Leco Microtom cutting machine with a diamond cutting disk then mounted in a non-retractable resin and polished to a mirror finish.

2.2 Sample Testing

Morphology and thickness of the coatings were studied using a Philips XL 20 Scanning Electron Microscope on the surface and polished cross sections of the samples. The microhardness of the samples was measured using a LECO M-400-A hardness tester. A Vickers indenter was used to determine the free surface hardness while a Knoop (lozenge shaped) indenter was used to measure the hardness on polished cross-sections. In both cases, the holding time was 20 s.

The nanohardness of the samples was investigated using a MTS nano-indenter XP with a Berkovitch (tetrahedron shaped) indenter, using depth-controlled indentation.

Roughness measurements were carried out using a Zeiss Surfcom 1400D-3DF apparatus. Scratch tests were performed on selected samples using the continuous load increase method up to 30 N with a Microphotonics Micro Scratch Tester (MST), with a load rate of 19.17 N/min and an advance rate of 9.58 mm/min, resulting in a scratch of 15mm. The tip was a diamond Rockwell C diamond stylus indenter with a radius of 200 μm. Taber testing was carried out with an Elcometer Taber 5155 apparatus, using CS-17 wheels, at 72 rpm with a 1 kg load.

3 Results and Discussion

3.1 Morphological Aspects

In the as-deposited state, the coatings present a columnar morphology and the characteristic cauliflower-like surface of nickel-boron coatings, as can be seen on figure 1. Neutral atmosphere heat treatments up to 400 °C do not modify those properties. However thermochemical treatments modify the coatings' morphology: after treatment under ammonia-based atmosphere, the coating presents a dual morphology with a porous outer layer and a dense inner layer near the substrate (see figure 2 b) while the coating looks completely dense after treatment under nitrogen-based atmosphere (see figure 2 a).

2D roughness measurements (see table 1) carried out on the samples showed that they are quite smooth in their as-deposited and heat treated states. However, thermochemical treatments are accompanied by an increase of roughness.

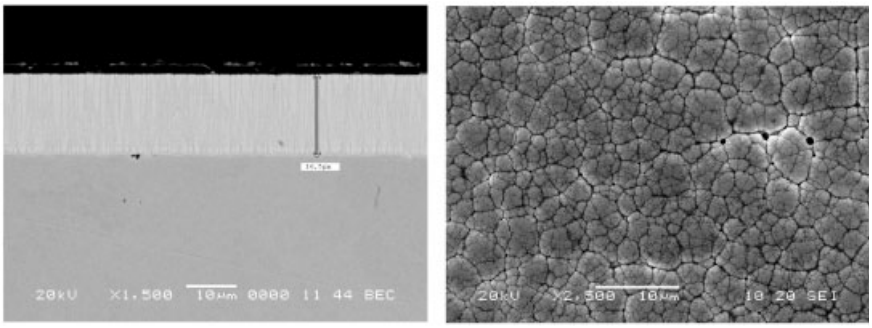


Figure 1: SEM micrograph of an untreated nickel-boron coating – left: cross section showing the columnar morphology – right: cauliflower-like surface.

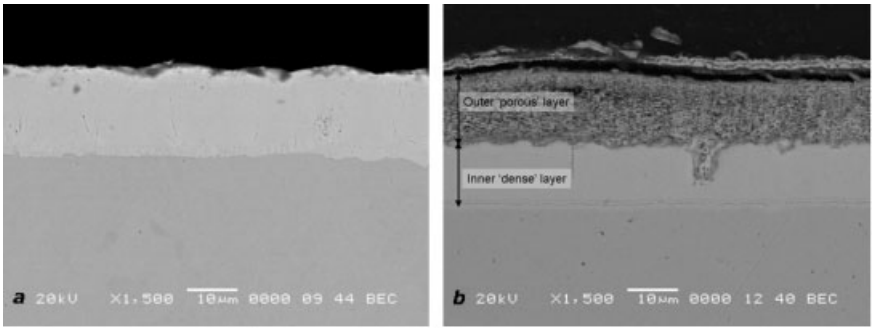


Figure 2: SEM micrograph of a "vacuum" treated (a) and an "ammonia" treated (b) nickel-boron deposit on steel substrate.

Table 1: Average roughness of nickel-boron samples

	Ra (µm)
Untreated	0,125 ± 0,016
400°C, 1h, neutral atmosphere	0,101 ± 0,021
Nitrogen-based treatment	0,297 ± 0,191
Ammonia-based treatment	1,361 ± 0,278

3.2 Hardness

Vickers hardness testing on the unprocessed free surface of nickel-boron samples is considered the standard hardness testing method. However we find it disputable for the following reasons: (i) The surface is unprepared and its smoothness is thus not warranted. (ii) The measurement may be influenced by the substrate's hardness if the applied load is too high (i.e.: when the indent depth reaches one tenth of the coating depth). In this view, Knoop indentation and Berkovitch nanoindentation were carried out on polished cross section to obtain values uninfluenced by the substrate. To ease comparison, nanoindentation values were converted from GPa into Berkovitch hardness points which are equivalent to Vickers points due to the indenter geometry.

Table 2: Vickers, Knoop and Berkovitch hardness values of nickel-boron coatings on aluminium alloys.

	Untreated	4h; 180 °C	1h; 400 °C
Knoop microhardness (hk_{50})	834 ± 20	927 ± 30	–
Vickers microhardness (hv_{100})	854 ± 40	1014 ± 40	1302 ± 40
Berkovitch nanoindentation (4000 μN)	823 ± 155	1140 ± 75	1584 ± 182

Table 2 presents hardness values for samples with and without neutral atmosphere heat treatment. Before treatment, all values are close to 825 points while they reach 1000 after low temperature heat treatment and at least 1300 after treatment at 400 °C.

The first hardness increase observed after heat treatment is caused by short order rearrangement in the coating [2, 18]. The increase observed after treatment at 400 °C is caused by crystallization of the initially amorphous coating [2, 5, 7, 9, and 18].

Knoop hardness measurement were also carried out on thermochemically treated samples leading to values of 1570 ± 100 hk_{25} after nitrogen-based treatment and 1630 ± 100 hk_{25} for ammonia-based treatment. It is thus possible by the way of those treatments to enhance the hardness of the coating to values higher than those reputed maximal.

3.3 Scratch Test Resistance and Taber Abrasion Test

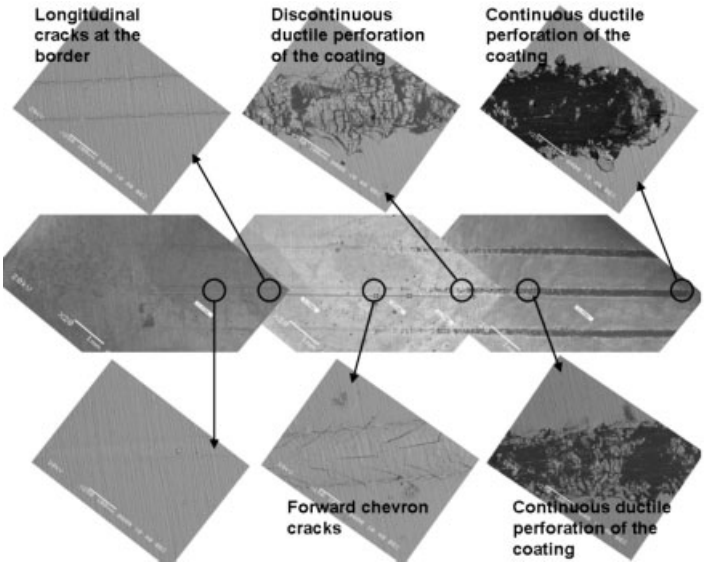


Figure 3: Micrograph of scratch tracks on 6 μm thick nickel-boron coatings (aluminium alloy substrate) after 4 hours at 180 °C under 95 % Ar + 5 % H2 atmosphere.

Samples with a typical thickness of 15 μm did not suffer from degradation after scratch test using a load up to 25 N. Further testing was thus carried out on thinner samples (6 μm). They

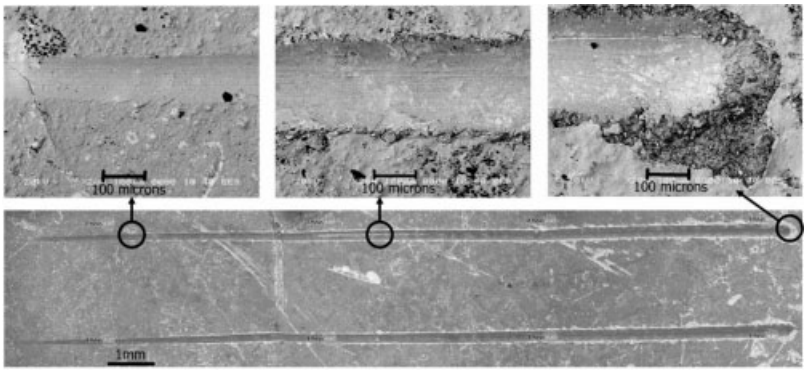


Figure 4: Micrograph of scratch tracks a nickel-boron coating after thermochemical treatment.

revealed that the failure of untreated and heat treated coatings is due to ductile perforation, preceded by forward chevron cracks on the edges of the scratch track (see figure 3). The critical loads were 21 N for untreated coatings and 13N after treatment at 180 °C, which is quite good keeping in mind the coating is only 6micron thick. This comportment is very encouraging for wear protection applications as there is no spalling nor delamination.

Scratch tests were also carried out on coatings submitted to the ammonia-based thermochemical treatment. The thickness of the coating was close to 15 μm and the adhesive failure was not achieved for loads up to 25 N (see figure 4).

Taber wear index (TWI) obtained with CS-17 wheels were 24.5 ± 1.3 for untreated coatings. Those values may appear to be high compared to other published results [2, 19, 20] but as we used CS-17 wheels which induce an harsher test it is not surprising to obtain higher TWI values. Moreover, when compared with results obtained on similar coatings with the CS-17 wheels, our coatings show good performances: Lee et al. [21] proposed TWI between 50 and 70 for electrodeposited nickel-boron coatings and Jeong et al [22] proposed values ranging from 20 to 40 for electroless nickel-phosphorous coatings.

Microscopic observation of the wear track showed that no major degradation occurs during wear test. The mass loss is due to polishing wear of the coating.

4 Conclusions

Electroless nickel boron coatings were deposited and submitted to various heat treating under neutral and reactive atmospheres including some that are not yet documented on this kind of coatings.

As-deposited coatings present a high hardness (around 825 hv_{100}) and a good scratch test resistance, even for thin coatings (critical load is 21 N for a 6 μm coating). Heat and thermochemical treatments enhance mechanical properties of those coatings: after heat treatment under neutral atmosphere, the hardness of the coatingsreaches 1300 hv_{100} and the scratch resista,ce stays good (critical load is 13 N for a 6 μm coating). Thermochemical treatments lead to an even higher hardness (up to 1500 hk_{25}) and those coatings resist to scratch tests up to 25 N. Taber abrasion

tests on untreated samples showed encouraging results with a TWI around 25. Taber testing of samples submitted to post treatment is in progress.

Aknowledgments

V. Vitry wishes to thank the FRIA for funding. The authors thank the BCRC (INISMA) for the SEM analysis and the scratch tests.

References

[1] A. Brenner, G. Riddel, J. Res. Nat. Bun. Stds. **1946** 37, 31

[2] Riedel A. Electroless nickel plating. London, United Kingdom, **1991** Finishing Publication LTD.

[3] F. Delaunois, J.P. Petitjean, P. Lienard, M. Jacob-Duliere, Surface and Coatings Technology **2000** 124, 201–209.

[4] K. Krishnaveni, T.S.N. Sankara Narayanan, and S.K. Seshadri, Surface and Coatings Technology, **2005** 190, 115–121

[5] F. Delaunois and P. Lienard, Surface and Coatings Technology, **2002** 160 139–148.

[6] Shi Ziyuan, Wang Deqing, and Ding Zhimin, Applied Surface Science, **2004** 221 32–68.

[7] V. Vitry, F. Delaunois and C. Dumortier, Surface and Coatings Technology, **2008** 202 3316–3324

[8] T.S.N. Sankara Narayanan and S.K. Seshadri, Journal of Alloys and Compounds, **2004** 365, 197–205

[9] Y.W. Riddle and T.O. Bailer JOM **2005** April 40–45

[10] Marie-Aline Clerc, PhD Thesis, Besançon, **1986**

[11] Eric W. Brooman, Metal Finishing, **2004** 9, 75–82

[12] K.-H. Lee, O. Takai, Diamond & Related Materials **2005** 14, 1444–1450

[13] P.-L. Larssont, A. E. Giannakopoulos, E. Soderlund, D. J. Rowcliffe, R. Vestergaard, International journal of Solids Structures **1996** Vol. 33, No. 2, 221–248.

[14] T. Miura, Y. Benino, R. Sato, T. Komatsu, Journal of the European Ceramic Society **2003** 23, 409–416.

[15] V. Fouquet, E. Le Bourhis, L. Pichon, M. Drouet, A. Straboni Scripta Materialia **2004** 51 899–903

[16] S.J. Bull, Tribology International **1997** Vol. 30, No. 7, 491–498.

[17] Advanced technical ceramics – methods of tests for ceramic coatings – part 3: Determination of adhesion and other mechanical failure modes by scratch test. european standard, european committee for standardization, **1999**.

[18] F. Delaunois, PhD Thesis, Faculté POlytechnique de Mons, Mons (Belgium), **2002**

[19] L. Lacourcelle, Nickelage chimique, Techniques de l'ingénieur, **1995**

[20] D.W. Baurand, in: Electroless Plating, ASM Handbook, Surface Engineering 5,ASM, **1994**

[21] K.H.Lee, D.Chang and S.C. Kwon **2005,** 50 (23), 4538–4543

[22] D.H. Jeong, F. Gonzalez, G. Palumbo, K.T. Aust and U. Erb, Scripta mater. **2001,** 44 493–499

Multiple Asperity Dry Contacts – Comparison of Experiments and Analytical Computer Simulation

Ch. Zietsch, A. Fischer
University of Duisburg-Essen, Duisburg

1 Introduction

The models of contact mechanics (CM) invented until now range from simple analytic models up to highly sophisticated ones. The best example for a simple model is the theory of Hertz [1]. It was introduced in the early 1880s and has been used since then. Based on the Hertzian theory Greenwood and Williamson (GW) developed an asperity based elastic contact model [2]. A simple model for purely plastic contacts was developed by Nayak [3]. The asperity definition used in this work comes from Majumdar und Bushan "an asperity is what" (could) "makes a contact" [4]. The initial asperity radius R and the asperity density D_{sum} can be calculated by the use of the spectral moments of the surface profile (see Nayak [5]). It is assumed that the asperities are spherical like with a constant radius but different heights.

For reality near results of the CM models (real area of contact, number of contact spots) reality near input data is required. Thus, one has to face certain problems. The calculation of R and D_{sum}, based on measured surface profile data, could lead to false results for certain reasons (e.g. see [6]). The GW and the Nayak model only regard "flat" surfaces. Therefore the estimation of the nominal contact area for non-conforming surfaces e.g. ball on flat could be required as well. The results of the CM models are the area of contact and the number of contact points. The area of contacts is the sum of all single contact areas of the elastic and/or plastic deformed asperities where the number of asperities in contact is an amount of the asperity density.

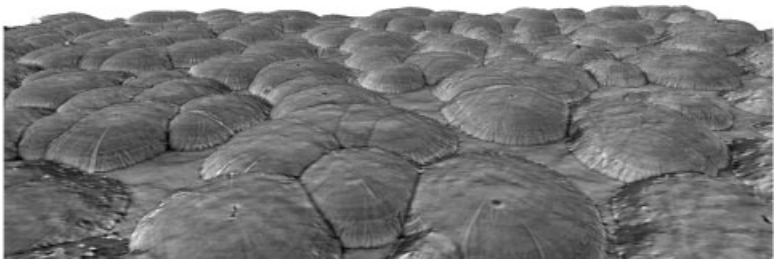


Figure 1: Electrochemically structured steel surface – 3D-SEM (here X13 CrMnMoN 18 14 3 after loading test)

The aim of this work is to find out a simple and easy to use procedure to estimate reality near input data for the use within analytical CM calculations. Those input data has to base on measured surface profile data, given macro geometries and the acting contact load in order to validate the analytical CM models as well.

2 Material and Methods

Dry loading and sliding tests were performed by means of model surfaces made of steel (Fig. 1) with spherical like surface structures. The surface structures were generated by electrochemical treatment in chromium sulphuric acid at elevated temperatures (see [7]). The tribological systems can be found in Tab. 1.

Table 1: Tribological systems

	Loading test	Sliding test
Flat steel body I (P2000, 1.4452)	X13 CrMnMoN 18 14 3 electrochemical structured	X13 CrMnMoN 18 14 3 electrochemical structured
Flat steel body II (Cronidur®30 1.4108)	X30 CrMoN 15 1 electrochemical structured	X30 CrMoN 15 1 electrochemical structured
Hemispherical shaped counter body	polycrystalline cubic boron nitride (pcBN) radius r_{pcBN} = 3.5 mm	hard metal (HM)radius r_{HM} = 6.0 mm
Interf., sur. medium	air	air
Ambient temp. T	room temperature	room temperature
Normal force F_{N}	5 N	1 N
Velocity v	0,57 µm/s (penetration)	2 µm/s (sliding)

2.1 Three Dimensional SEM Reconstruction, Tactile Profilometry

In order to generate surface profiles and to measure the nominal contact radius $a_{nom\text{-}m}$, the nominal contact area $A_{nom\text{-}m}$, the initial radii of asperities R_m, the asperity density $D_{sum\text{-}m}$, the plastic contact area $A_{pl\text{-}m}$ and the number of plastic contact points $n_{pl\text{-}m}$ three dimensional SEM reconstruction (3D-SEM) were used (MeX® 4.2, Alicona Imaging GmbH, Graz, Austria). For the purpose of comparison, additional surface profiles were measured with a stylus profiler with a stylus tip of 5 µm radius and a lateral resolution of 4000 data points / mm (0.25 µm).

2.2 Analytical Computer Simulation

The Hertzian contact values (contact radius a_{Hert}, contact area A_{Hertz} and contact deformation ω_{Hertz}) were calculated for the macro geometries of the performed tests.

The GW variation as described by McCool [8] and the Nayak model [3] have been used to calculate the real plastic contact area $A_{pl\text{-}c}$ and the number of (plastic) contacts $n_{pl\text{-}c}$. The degree of plasticity is indicated by the plasticity index Ψ [2]. The initial asperity radius R_c and the asperity density $D_{sum\text{-}c}$ were calculated by the use of the spectral moments (see Nayak [9]).

The used material properties of bodies I & II and the counter bodies can be found in Tab. 2.

3 Results

Table 3 gives an overview about the measured contact values for the performed tests.

Former unpublished studies have proven that the use of untreated surface profile data will lead to unrealistic results for R and D_{sum}, independent of the profile measurement method used. Thus, adequate mathematical treatment is required, achieved here by smoothening the profile data using

Table 2: Material properties

	1.4452 (austenite)	1.4108 (martensite)	pcBN	HM
Youngs modulus [GPa]	185	210	700	220
Poissons ratio	0.286	0.3	0.22	0.29
Hardness [HV10]	200	558	3500	1800
Yield strength [MPa]	615	2500	–	–

Table 3: Measured Contact Values

	Loading 1.4452	Loading 1.4108	Sliding 1.4452	Sliding 1.4108
$a_{nom\text{-}m}$ [µm]	91.9	92.6	90.0	100.0 µm
$A_{nom\text{-}m}$ [µm^2]	26558	26935	25447	31416
$D_{sum\text{-}m}$ [1/mm^2]	4669	2042	1217	2029
R_m [µm]	10.5 ± 7.7	13.1 ± 6.8	9.8 ± 5.6	2.6 ± 1.2
$A_{pl\text{-}m}$ [µm^2]	2452	830	851 ± 97.5	492 ± 120.5
$n_{pl\text{-}m}$ [1/mm^2]	2222	743	458 ± 116	917 ± 61

a 5-point moving average. The procedure was repeated until the calculated spectral moments lead to reality near results for R and D_{sum}, compared to the directly measured values. The calculated input data R_c and $D_{sum\text{-}c}$ as well as the measured nominal contact area $A_{nom\text{-}m}$ were used in order to calculate the CM values, given in table 4.

Table 4: Calculated contact mechanic values

	Loading 1.4452	Loading 1.4108	Sliding 1.4452	Sliding 1.4108
a_{Hertz} [µm]	43.6	42.1	34.5	33.4
		3D-SEM		
Ψ	28	17	40	15
$D_{sum\text{-}c}$[1/mm^2]	4670	2066	1212	2086
R_c [µm]	9.8	6.3	11.1	6.0
$A_{pl\text{-}c}$ Nayak [µm^2]	2323	885	499	182
$A_{pl\text{-}c}$ GW [µm^2]	270	133	43	35
$n_{pl\text{-}c}$ Nayak [1/mm^2]	1632	456	97	82
$n_{pl\text{-}c}$ GW [1/mm^2]	707	202	28	41
		Stylus		
Ψ	26	13	39	21
$D_{sum\text{-}c}$ [1/mm^2]	4694	2039	1211	2081
R_c [µm]	10.0	9.2	10.3	4.7

4 Discussion

The applied method of 3D-SEM reconstruction is appropriate to estimate surface profile data as well as specific information about the surface investigated. The values of surface parameters are

in a good agreement with the measured stylus data. An investigation on the traceability of the Alicona 3D-SEM reconstruction software has been given by Bariani [10].

The results of the measured nominal contact radius $a_{nom\text{-}m}$ and the calculated Hertzian contact radius a_{Hertz} can be used in order to estimate a correction factor φ with $a_{nom} = a_{Hertz} \cdot \varphi$. Barkan and Tuohy [11] have been given the value $\varphi \approx 1.7$ for normal engineering surface roughness. In the cases of the structured steel surfaces the correction factor can be given with $\varphi = 2.1 - 3.0$. In general φ is a function of the surface roughness and the macro geometries as well and will increase with the roughness. For very smooth surfaces $\varphi \approx 1$ and therefore the Hertzian contact area then can be used as nominal contact area.

The calculated plasticity index indicated predominantly plastic contacts (plastic for $\Psi > 1$). Therefore the Nayak model provides better results in both cases loading and sliding. As expected, the GW model delivers unsatisfying results. The determined and simulated plastic contact pressures (Nayak) for the loading tests are about 2039 MPa and 2152 MPa for the 1.4454 (see also fig. 2) and 6024 MPa and 5650 MPa for the 1.4108. This is, as expected, in the range of the measured hardness. Thus, the hardness based calculation the real contact area according to Nayak can be validated as well.

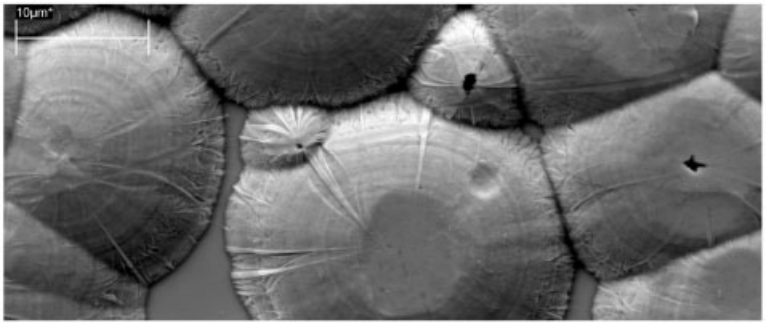


Figure 2: Plastically deformed asperities, SEM picture (here X13 CrMnMoN 18 14 3 after loading test)

The simulation results for the sliding tests differ from the measured values. The acting tangential force with the up and down movement of the counter body leads to material flow in the sliding direction. Consequently the visible size of the contact area is bigger than a static contact area would be. There are no remarkable differences for the accuracy of the results for the austenitic (1.4452) and the martensitic steel (1.4108), in both cases loading and sliding.

By the use of the model surfaces the assumption of spherical shaped asperities becomes nearly reality. Except form one case (cone shaped) the 3D-SEM investigations ensure the spherical shape of the surface structures. Consequently the calculated initial asperity radius and asperity density are useful as reality near input data. Therefore, the calculation procedure based on the spectral moments of the surface profile (see Nayak [9]) can be validated by measurement data. The reality near result for D_{sum} in the cone shaped case shows the robustness of that calculation method with respect to assumption unlike asperity shape. Unfortunately the use of that method could leads to unrealistic results for R and D_{sum}. The measured surface profile data is of discrete nature. If used as a "function" in order to calculate the deviations of the profile curve unrealistic high values occur due to the high slopes. The calculated results for R and D_{sum} show, ade-

quate signal processing is appropriate in order to overcome those difficulties. However, if this is achieved by smoothing the profile data (here 5-point moving average) the next problem will follow immediately. The right degree of the smoothening procedure must be determined. This is easy to do if valid values about the asperity density and/or the initial asperity radius are available, respectively.

The estimation of reality near values for R and D_{sum} is still a challenge. Greenwood himself apologised that the "assumption that peaks on a surface profile – points higher than their immediate neighbours at the sampling interval used – correspond to asperities is quite wrong and gives a false idea of both the number and the radius of curvature of the asperities." [6]. Archard's model of multiple roughness scales (1957!) is back again [12].

Therefore, the definition of the roughness scale which has to be taken into account is quite difficult with respect to the applied load. The surface peaks (micro asperities) are affecting only the first stages of the contact and then the (macro) asperities generate the acting surface.

An accurate surface profile based procedure for the estimation of load dependant values for *R* and D_{sum} can not be given easily. But, a simple and easy to perform way as described in figure 3 could be used. In a first step one has to ensure that the calculated Hertzian deformation as well as the roughness scale of interest is in an equal dimension or in the same order of magnitude, respectively. The main part involves a manual estimation of the asperity density per unit length D_{peak}, see figure 4. By the use of the D_{peak} equation (1) the ratio of the 4th and 2nd spectral moment can be determined. The smoothing procedure then has to be repeated until both ratios of the spectral moments match. In the last step the spectral moments based on smoothed profile must be used in order to calculate the initial asperity Radius *R* (2) as well as the asperity density D_{sum} (3).

$$D_{peak} = \frac{1}{2\pi}\sqrt{\frac{m_4}{m_2}} \tag{1}$$

$$R = \frac{3\sqrt{\pi}}{8\sqrt{m_4}} \tag{2}$$

$$D_{sum} = \frac{m_4/m_2}{6\pi\sqrt{3}} \tag{3}$$

If the range of interest of the surface profile is close to the vertical resolution of the used surface measurement system, a valid counting procedure is impossible. Thus, a higher resolution and/or more sensitive measurement system are required. The same attentiveness is needed in the case of very smooth or rough surfaces, respectively.

If one applies the method for a initial profile of the 1.4452, one counts 18 asperities on 293.6 µm (see fig. 4) and therefore the calculated D_{sum} is 4510 1/mm^2. This is in good agreement with the direct measured value of 4669 1/mm^2. But due to human influences and a limited profile length, the accuracy of the method is limited. If one would count 17 or 19 asperities in this particular case the values of D_{sum} are 3950 and 5025 1/mm^2, respectively. Consistently, the profile investigated should be as long as possible.

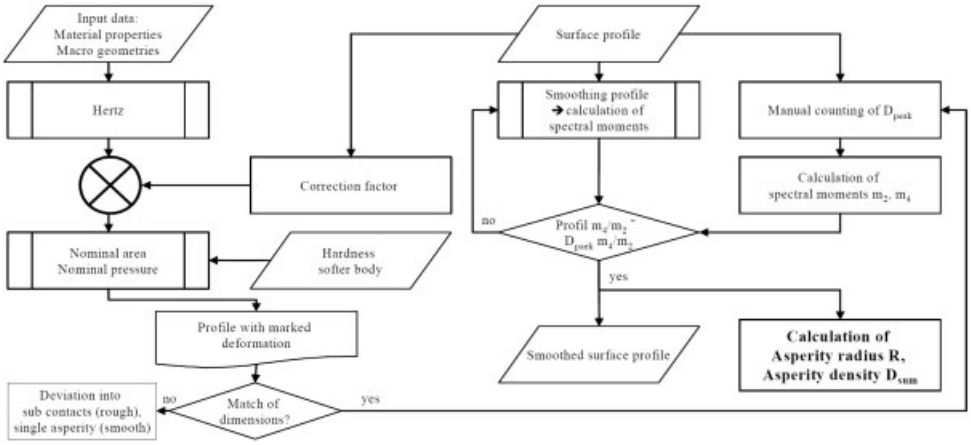


Figure 3: Flow chart for the load dependant estimation of asperity radius and asperity density

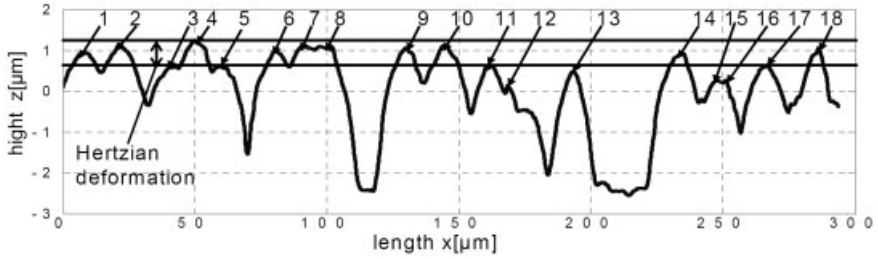


Figure 4: Surface profile with marked Hertzian deformation (here initial X13 CrMnMoN 18 14 3, structured)

For very rough or even wavy surfaces one has to deviates the contact into sub contacts until one fulfils the criteria of equal dimensions. In other words: one has to perform contact mechanic inside the contact mechanic, like Archard's protuberances on protuberances. On the other hand, if the surface is very smooth every valid theory on single asperity deformation, elastic, elastic-plastic or pure plastic, will do if the mode of deformation used is right.

In the case of two rough surfaces one has to perform the procedure for every profile separately. Given the calculated spectral moments for both profiles A and B, the corresponding values for the equivalent Profile are calculated as the sum of the two spectral moments ($m_0 = m_{0A} + m_{0B}$, $m_2 = m_{2A} + m_{2B}$, $m_4 = m_{4A} + m_{4B}$ see [8] & [9]).

5 Acknowledgment

The authors would like to thank Dipl.-Ing. K. Bambauer and U. Föckeler, Ruhr University of Bochum, Materials Technology for their support with the laboratory test.

6 References

[1] Hertz, H.R.; J. f.d. reine und angew. Math. **1881**, 92, p. 156–171

[2] Greenwood, J.A.; Williamson, J.B.P., Proc.R. Soc. London **1966**, A295, p. 300–319

[3] Nayak, P.; Wear 26, Pp. 300-333 (1973)

[4] Majumdar, A.; Bhushan, B., J. Tribol. **1991**, (ASME) 113, p. 1–11

[5] Pullen, J.; Williamson, J.B.P., Proc. R. Soc. London **1972**, A. 327, p. 159–173

[6] Greenwood, J.A., WU J.J., Meccanica **2001,** 36, p. 617–630

[7] Büscher, R.; Fischer A., Wear 254 **2003,** 12, p. 1318–1325

[8] McCool, J.I., Wear 107 **1986**, p. 37–60

[9] Nayak, P., J. Lubr. Technol. **1971**, 23, p. 398–407

[10] Bariani, P. et al.; Precision Engineering **2005**, 29, p. 219–228

[11] Barkan, P.; Tuohy, E.J., IEEE trans. o. pow. app. a. syst. PAS-84 **1965**, 12, p 1132–1143

[12] Archard, J.F., Proc. Roy. Soc. **1957**, A243, p. 190–205

Influence of the Surface Topography on the Transition between High and Low Wear Regimes under Multidirectional Reciprocating Sliding

I. Samerski[a], J. Schöfer[a], D. J. Schipper[b], A. Fischer[c]
[a]Robert Bosch GmbH, D-70049 Stuttgart, Germany
[b]Laboratory for Surface Technology and Tribology, University of Twente, The Netherlands
[c]Universität Duisburg-Essen, Werkstofftechnik, Lotharstr. 1, 47057 Duisburg, Germany

1 Introduction

In automotive engineering many mechanical fuel lubricated components like pistons or valves undergo a reciprocating sliding motion. Additional to that motion (primary oscillation), often an unwanted second oscillation is observed which can be caused, for example, by vibrations of surrounding parts or components. The direction of this oscillation usually is not parallel to the primary motion. It is of particular interest for engineers to know the influence of this additional secondary oscillation including the surface topography on the wear properties to define the maximum amplitude of this oscillation the system can tolerate.

Multidirectional wear has been investigated in connection with surface finishing processes like polishing and lapping [1–2]. Reciprocating sliding wear and fretting wear on the other hand has only been studied for unidirectional motion [3–5]. The influence of the surface topography on wear properties and life-time has been investigated so far for unidirectional oscillations [6–12]. For small amplitudes in the range of a few micrometers, significant differences in wear properties are expected if a second oscillation is superimposed.

The wear process that occurs during the polishing is called chemical-mechanical polishing. A wear model that describes the development of the surface roughness during the polishing process is based on the Greenwood-Williamson theory of contact and a Hamilton-Jacobi-like conservation equation [13–14]. Another model that describes the material removal during chemical-mechanical polishing originates from the deformation of hyper-elastic asperities attached to a linear-elastic pad [15]. The wear phenomena under chemical-mechanical polishing were investigated by Liang et al. [16]. Edge defects, pits and scratches were often detected and do possibly occur by chemical reactions in combination with asperity contacts under high pressure. Zhang et al. [17–18] investigated the polishing process with fixed abrasive particles. They assumed that the pressure distribution is Hertzian and the abrasion rate follows Archard's wear equation.

In contrast to these experiments, the present study focuses on influences on surface parameters on the wear properties during multidirectional oscillation. Therefore a wear model based on particle movement is developed [19].

2 Materials and Experimental Methods

The wear phenomena and wear characteristics of multidirectional oscillation were investigated by means of a ball-on-disc tribometer (Fig.1).

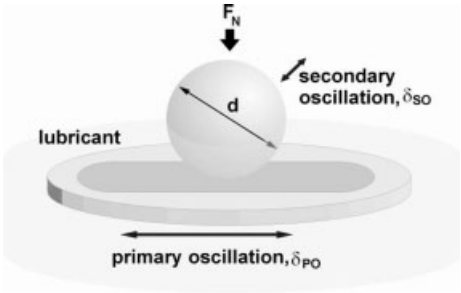


Figure 1: Scheme of the wear path between ball and disc. The relative velocity between ball and disc is generated by two oscillating sliding movements of different speed and stroke lengths. The primary and slower motion is connected to the longer amplitude δ_{PO}, which is normal to the secondary and shorter amplitude δ_{SO}.

Balls (hardness 7.2 GPa) were made of high quality AISI 52100 bearing steel with a martensitic microstructure. The diameter of the balls was d = 10 mm with a roughness of Ra = (0.018 ± 0.001) µm. Two different discs were used: One series were made of AISI 5115 case hardened with a roughness of Ra = (0.158 ± 0.009) µm and an average grinding mark distance of Rsm = (15.6 ± 1.1) µm. The other series of discs made of AISI 52100 bearing steel with a martensitic microstructure, an average roughness value of Ra = (0.056±0.005) µm and an average grinding mark distance of Rsm = (13.4 ± 0.9) µm. All discs were unidirectionally grinded and the roughness measured always orthogonally to the grinding marks. The ball-on-disc system was completely submerged in fuel lubricant, which was conventional additived diesel fuel (specifications acc. to DIN EN 590 [20]) with a density of 0.825 to 0.835 g/cm^3 (at 15 °C) and a kinematic viscosity of 2.5 to 3.0 mm^2/s (at 40 °C).

The primary oscillation was generated by a hydraulic pulsator with a frequency f_{PO} of 1 Hz and an amplitude δ_{PO} of 1 mm. The secondary oscillation was generated by a piezo-electric actuator and directed orthogonally to the primary motion with a frequency f_{SO} of 100 Hz and an amplitude δ_{SO} adjusted to a constant value between 0 and 20.2 µm during the test. The grinding marks were oriented parallel to the primary oscillation. Each experiment has been repeated two to three times. The normal load was 15 N and generated by dead weight. Each experiment was performed for 6 hours.

During all experiments δ_{PO} and δ_{SO} were monitored every hour by a laservibrometer (Polytec CLV 1000, Polytec GmbH, Waldbronn, Germany) with a sample rate of 50 kHz. The linear wear depth was measured with a temperature compensated displacement transducer and recorded every 46 s. The friction forces F_{PO} and F_{SO} and the normal force F_N were measured by means of a multiaxial piezo-electric force sensor (Kistler 9251, Kistler Instrumente AG, Winterthur, Switzerland) and monitored for one loop every hour with a sample rate of 50 kHz for F_{SO}, F_N and 500 Hz for F_{PO}, F_N respectively.

Ball and disc surfaces were cleaned before and after each experiment with a soft tissue and a solvent consisting of 50 % acetone and 50 % isopropanol. Afterwards the worn surfaces were visually inspected by means of an optical microscope (Leica DMR, Leica Mikroskopie und Systeme GmbH, Bensheim, Germany) and a scanning electron microscopy (LEO 1450 VP, Carl Zeiss AG, Oberkochen, Germany) with energy dispersive spectroscopy (EDS). The wear vol-

ume W_V of the ball and the disc was determined by measuring the surfaces with a confocal microscope (NanoFocus µsurf, NanoFocus AG, Oberhausen, Germany). The specific wear rate k_V was calculated from the measured linear wear depth and size of the worn areas of ball and disc. In order to measure the size of the wear particles, the fuel-lubricant including the particles was extracted by suction after the experiments. Afterwards the fuel-lubricant was evaporated and the diameter of the wear particles was determined with optical microscopy and image analysis software (Axio Vision 4.0, Carl Zeiss AG, Oberkochen, Germany). The height of the particles was studied by AFM (atomic force microscope) (Park Scientific Instruments CP Autoprobe, Veeco Instruments, Woodbury, USA) in the contact mode. In order to evaporate the fuel lubricant, the whole disc was heated on a hot plate at about 200 °C. Afterwards the topography including wear particles were determined.

The influence of wear particles on the wear properties was investigated with the tribometer (see Fig.1) including a lubrication flush. A pump (EKP 3D+, Robert Bosch GmbH, Stuttgart, Germany) pressed the lubricant trough a nozzle with a constant velocity direct in the ball-on-disc contact and flushed the generated wear particles out.

3 Results

3.1 Wear Volume and Specific Wear Rate

Fig.2 shows the wear volume W_V of ball and disc vs. the secondary amplitude δ_{SO} of the experiments with the smoother discs made of AISI 52100 (Fig. 2a) and with the rougher discs made of AISI 5115 (Fig.2b).

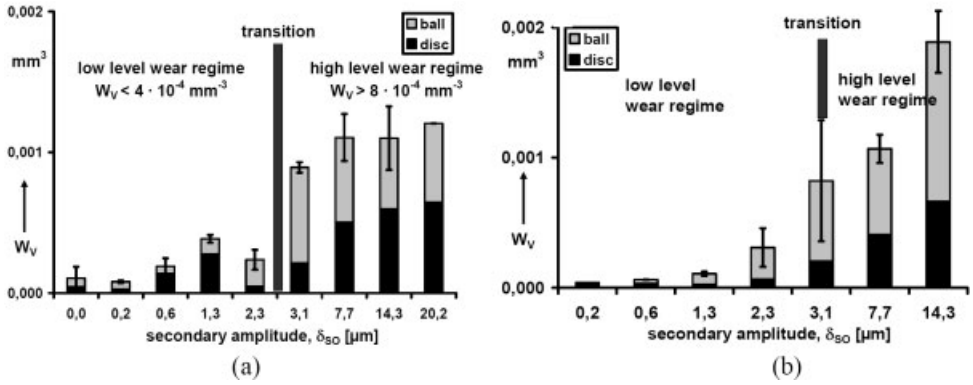


Figure 2: The wear volume W_V plotted vs. the secondary amplitude δ_{SO}. In Figure 2a there is between 2.3 and 3.1 µm a distinct transition from the low to the high level wear regime. In Fig. 2b the distinct transition is at $\delta_{SO} \approx$ 3.1 µm.

Fig. 2a shows for $\delta_{SO} \leq 2.3$ µm that the total wear volume is smaller than $0.4 \cdot 10^{-3}$ mm^3, which hereafter will be designated as low level wear regime. For $\delta_{SO} > 2.3$ µm the total wear volume is larger than $0.8 \cdot 10^{-3}$ mm^3 and therefore significantly higher. It increases with δ_{SO} up to $1.2 \cdot 10^{-3}$ mm^3. This regime is called high level wear regime. The rougher disc in Fig. 2b shows the transition between high and low level wear at $\delta_{SO} \approx 3.1$ µm. The wear volume at

this secondary amplitude varies between $0.3 \cdot 10^{-3}$ mm^3 and $1.4 \cdot 10^{-3}$ mm^3. Both figures show an increase of W_V with δ_{SO} which is attributed to the total sliding distance growing with δ_{SO}.

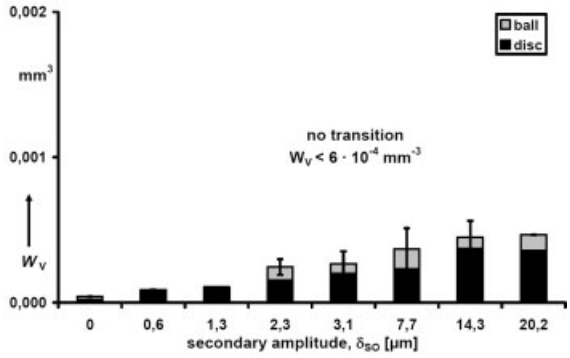


Figure 3: The total wear volume W_V plotted vs. the secondary amplitude δ_{SO} when wear particles flushed out.

Fig.3 shows that no transition between high and low level wear is visible when the generated wear particles are flushed out of the contact. The wear volume for $\delta_{SO} = 0.0$ µm until 20.2 µm is below $0.6 \cdot 10^{-3}$ mm^3 and therefore significantly lower than the wear volume at high level wear without particle flush.

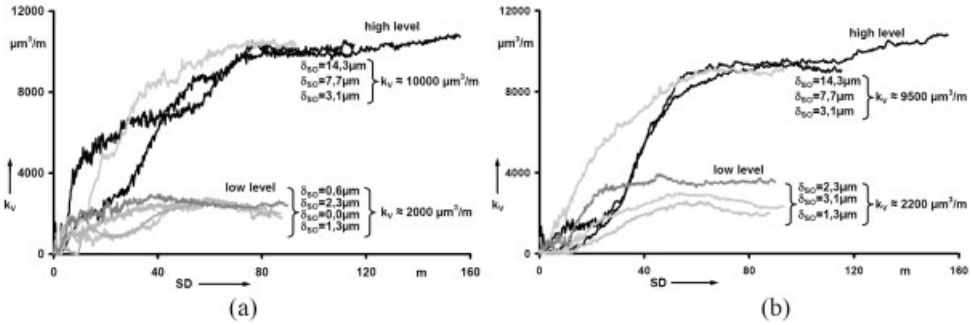


Figure 4: Specific wear rate k_V plotted vs. the total sliding distance (SD). After run-in both regimes are distinctly separated by their k_V-values.

In Fig.4 the specific wear rate k_V (wear volume per sliding distance) is plotted as a function of the total sliding distance SD for different δ_{SO}-values, when the wear particles are not flushed out. Obviously the specific wear rate can also be separated into two regimes. Fig.4a and 4b depict that the run-in periods are different, depending on δ_{SO}. This can be attributed to the fact that the gross surface area that has to be worn during run-in becomes larger with δ_{SO} as well. After a run-in period, k_V is nearly constant at about 2000 µm^3/m for $\delta_{SO} \leq 2.3$ µm and about 10000 µm^3/m for $\delta_{SO} \geq 3.1$ µm for the smoother surface in Fig.4a. For the rougher surface the constant value is 2200 µm^3/m for $\delta_{SO} \leq 3.1$ µm and at about 9500 µm^3/m for $\delta_{SO} \geq 3.1$ µm. In Fig. 4b is the variation of k_V at $\delta_{SO} = 3.1$ µm between high and low level visible.

3.2 Wear Appearance

Two examples of light microscopy pictures from worn ball and disc surfaces are shown in Fig.5. These pictures are typical for the two wear regimes of smooth and rough disc surfaces.

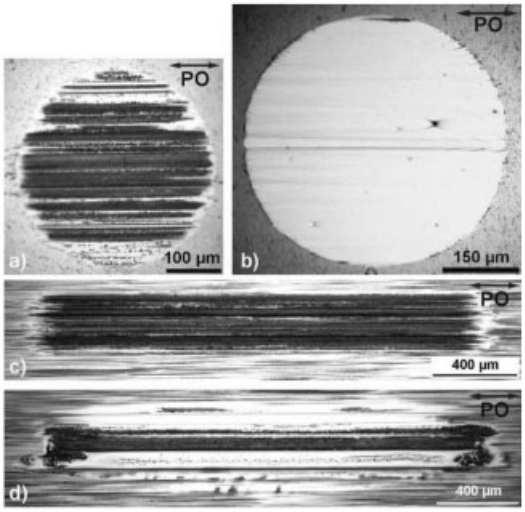


Figure 5: Optical microscope pictures of worn ball and disc surfaces at low level wear a) δ_{SO} = 2.3 µm, c) δ_{SO} = 1.3 µm and high level wear b) δ_{SO} = 3.1 µm, d) δ_{SO} = 14.3 µm. The arrows indicate the direction of the primary oscillation δ_{PO}.

The worn surface of the ball which oscillated with δ_{SO} = 2.3 µm in low level wear regime on the smooth disc surface shows the structure of the grinding marks of the disc and embedded wear particles (Fig.5a). In contrast the worn surface in high level wear regime is flat (Fig.5b). Figures 5c and 5d demonstrate the characteristic appearances of the tracks of the worn discs. At low level wear (Fig.5c, δ_{SO} = 1.3 µm) the topography does not change significantly. Within the high level wear regime smoothed tracks are visible on the worn surface (Fig.5d, δ_{SO} = 14.3 µm).

This illustrates that the transition is determined by different mechanisms. Detailed analysis revealed that the flat surface originated from a mechanical lapping process caused by wear particles. The tribochemical surface layer of the ball in low level wear also shows interruptions by lapped tracks that are parallel to the primary oscillation. The width of these lapped tracks varies from 2.5µm to 19.5 µm.

3.3 Wear Particles

Fig.6 depicts the cumulative frequency Σf of the average lateral diameter $\bar{d}$ of wear particles plotted versus $\bar{d}$ that is $\bar{d} = (d_{min} + d_{max})/2$, of every particle.

These particles originate from a high level wear experiment with a secondary amplitude of δ_{SO} = 14.3 µm and have been extracted after the experiment as described in section 2. Fig.6 shows that the particles of the rough surface experiments are larger than the particles of the smooth surface experiments.

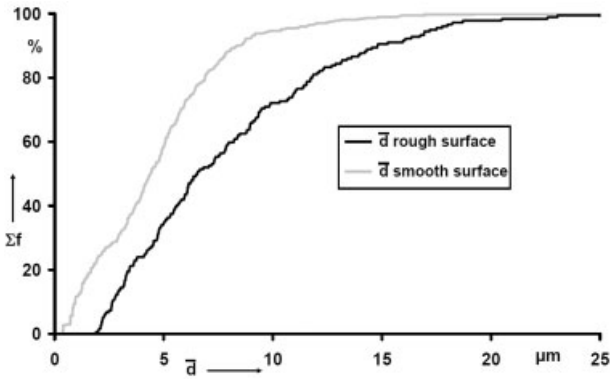


Figure 6: The cumulative relative frequency Σ f of the average diameter $\bar{d}$ of wear particles. The total number of measured particles is 369 for the smooth surface and 180 for the rough surface.

4 Discussion

In order to understand the reason for the existance of a certain secondary transition amplitude δ_{SO} that separates the two observed wear regimes, the contact situation has to be examinated.

4.1 Characterization of the Contact Situation

In order to illustrate the contact situation after running-in, a cross-sectional view parallel to the direction of the secondary oscillation is schematically shown in Fig.7.

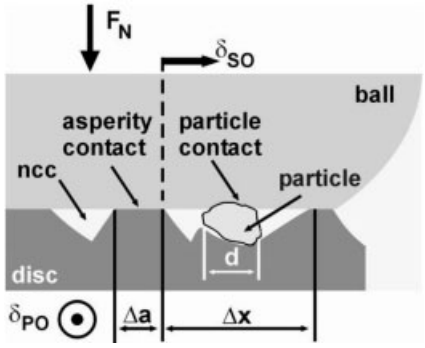


Figure 7: Scheme of the contact situation between ball and disc. The solid contacts are determined by particles with diameter d and asperity contact width Δa. Between the asperities, which stem from parallel grinding marks, are so-called non contact channels (ncc) with a width Δx.

It illustrates that the tips of the grinding marks are in contact with the ball surface (asperity contacts) leaving spaces in between which will be designated here as non-contact channels (ncc) to illustrate the channel-like character of their appearance. The width of the ncc is defined as Δx while the width of the asperity contact is Δa. It is important to note that a wear particle with

a thickness being smaller than the asperity height and a diameter d being smaller than Δx does not contribute to the real contact area. On the other hand particles with a thickness being larger than the asperity height do contribute to the real contact area which carries a part of the normal force by particle contact.

To determine depth and width of the ncc, a numerical simulation of the contact situation was performed. The surface topography of an unworn disk was measured with the confocal microscope and virtually pressed against a flattened, perfectly flat ball surface. The flattened part of the ball had a diameter (wear scar diameter) of 200 µm. The simulation of the contact was based on the Hertzian theory and extended for rough surfaces under the assumption that the surface segments do not interact laterally. Details of the numerical procedure can be found in [21, 22].

The simulation was performed with a ball diameter of 10 mm and a normal load of 15 N. The characterization of the contact situation clearly shows the asperity contact situation (Fig.8a and 8b, dark areas) and depicts the orientation of the ncc (bright areas) parallel to the primary oscillation.

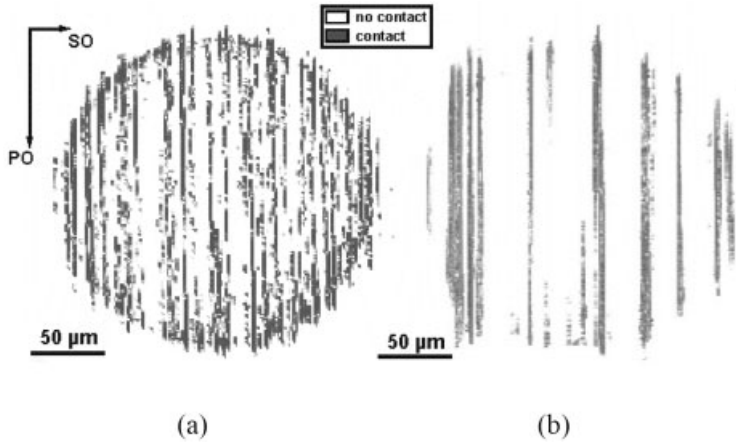


Figure 8: Simulation of a loaded contact a) smooth surface b) rough surface.

In Fig.8a the simulated contact with the smooth disc surface shows narrow and more ncc compared to the simulation in Fig. 8b of the rough surface. The largest ncc in Fig.8b has a width of Δx = 34–44 µm. The asperities along the primary oscillation are not continuously in contact with the ball.

AFM measurements of the particle height showed that the generated particles are about two to four times higher than the ncc depth. That means that the particles in the contact carry most of the load.

The geometrical distribution of Δx and Δa can be determined by means of simulation as well. From these the distribution of Δx and Δa were determined for both surfaces and plotted in Fig.10a and Fig.10b. The statistical distribution of Δa is quite narrow with 1.7 ± 0.34 µm for the smooth surface and 1.6 ± 0.35 µm for the rough surface. Further, the cumulative relative frequency of the particle diameter $\bar{d}$ (Fig.10a,b, dark line) can be compared with the width Δx of the ncc (Fig.10a,b, dashed line). The brightly drawn line of $\Delta x - \bar{d}$ represents the free space

of the particles located in the ncc. Whereas on the smooth surface the particles have always free space in the ncc, the particles on the rough surface start to move over the asperities at $\delta_{SO} > 0.0$ µm. Furthermore the free space $\Delta s - \bar{d}$ on the rough surface is up to 85 % not larger than 1 µm and turns to 14 µm at 90 %. The free space of the smooth surface increases between 85 % and 90 % just about 2 µm.

4.2 Simplified Wear Model

The wear model that is able to explain the transition amplitude of the secondary oscillation separating high and low level wear, is based on the motion of wear particles within the non-contact channels under steady-state conditions [19].

At the beginning of each experiment there are no wear particles present and the contact area is solely based on asperity contacts (Fig.8a).

The generated particles during running-in are deposited within the ncc and the contact situation changes from asperity contact to particle contact. Because of the ncc being oriented parallel to the primary oscillation, these particles can easily move within the ncc along with the direction of δ_{PO}. The possibility to move in the direction of the secondary oscillation is constricted by the asperities and therefore by the width Δx of the ncc.

Looking at one specific ncc with index i, a local transition amplitude δ_{Ti} can be defined. If the secondary amplitude δ_{SO} is smaller than δ_{Ti}, the particles would be basically able to follow this oscillation within the ncc. If they are e.g. sticking to the ball or to the disc surface, they will induce tribochemical reactions on both bodies and cause low wear (see Fig.5). If δ_{SO} is larger than δ_{Ti}, the particles start to move over the asperities resulting in high local contact stresses and bring about abrasion by scratches or surface fatigue by indentations. These mechanically dominated wear mechanisms, which act similar to polishing or lapping, lead to distinctly higher wear rates compared to tribochemical situation. If the particles are flushed out of the contact, the mechanically dominated wear mechanisms including the high wear volume will not occur which can be seen in Fig.3. Due to the fact that these particles might stick more pronounced onto the rough disc than on the smooth ball the latter will be worn more (Fig.2, high level wear regime).

The mathematical description for the local transition amplitude δ_{Ti} is [19]:

$$\delta_{Ti} = \frac{\Delta x_i - \bar{d}_i}{2} + \Delta a_i \,. \tag{1}$$

Equation (1) explains the correlation between *one* ncc, *one* particle and *one* asperity with the transition amplitude.

The wear model that predicts the experimental transition amplitude of 2.7 ± 0.4 µm for the smooth surface and about 3.1 µm for the rough surface (see Fig. 2) has to consider the interaction of many ncc and particles. Several ncc next to each other with different sizes and including different particles are schematically shown in Figure 9.

It is obvious that a specific asperity Δa_i can be worn by particles from both ncc in the direct neighbourhood. If the space for the particle movement $\Delta x_i - \bar{d}_i$ in the ncc differs significantly between the left-hand side and the right-hand side of the asperity, only the particles from the ncc with smaller space cause mechanical wear of the asperity.

As a consequence, not all values of $\Delta x_i - \bar{d}_i$ have to be taken into account for calculating the global transition amplitude.

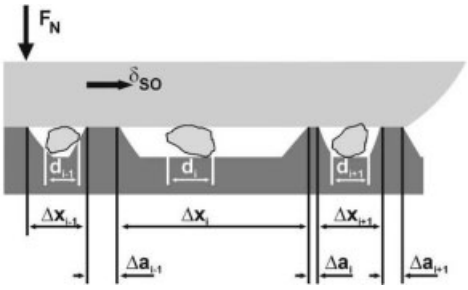


Figure 9: Schematically view of the contact situation between ball and disc. Three different ncc next to each other with different particles and different asperity widths. The particle with the diameter d_i does not contribute to the wear process of the asperities with Δa_{i-1} and Δa_i.

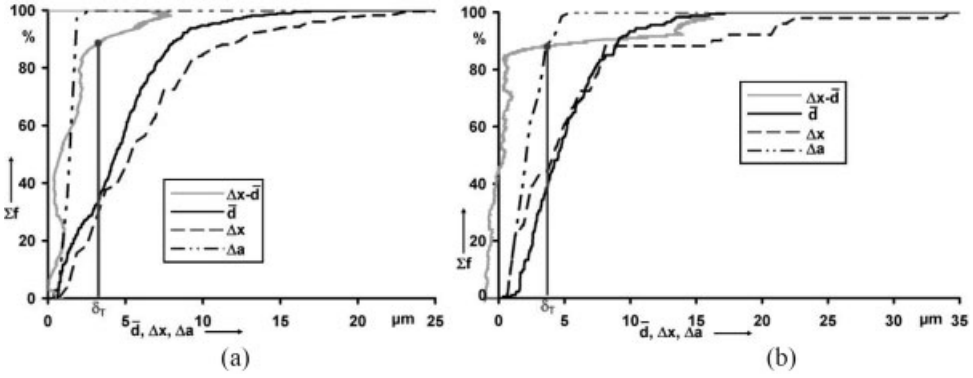


Figure 10: Statistical comparison of the distribution of non contact channel width Δx, the average particle diameter $\bar{d}$, the asperity contact width Δa and $\Delta x - \bar{d}$. In a) smooth surface and in b) rough surface results are given.

Therefore, a given asperity Δa_i is completely mechanically worn if the secondary amplitude passes the critical amplitude:

$$\delta'_{Ti} = \min\left(\frac{\Delta x_i - \bar{d}_i}{2} + \Delta a_i\ ,\ \frac{\Delta x_{i+1} - \bar{d}_{i+1}}{2} + \Delta a_i\right) \tag{2}$$

The global transition amplitude δ_{T}, for which all asperities are lapped or polished (see Fig. 5b), can now be defined as the maximum of δ'_{Ti}:

$$\delta_T = \max\ \left(\delta'_{Ti}\right) \tag{3}$$

As can be determined from Figure 10, the statistical distribution of asperity width $\Delta a_i$is comparatively small and can, therefore, assumed to be constant. Consequently, equation (2) can be written as:

$$\delta'_{Ti} = \min\left(\frac{\Delta x_i - \bar{d}_i}{2}\ ,\ \frac{\Delta x_{i+1} - \bar{d}_{i+1}}{2}\right) + \Delta a \tag{4}$$

Further it can be started that the size of the particles inside a given ncc increases with the ncc width. Therefore it seems to be reasonable to relate the distributions of $\bar{d}_i$ and Δx_i (see Fig. 10). Now each ncc width Δx_i is assigned to a particle diameter $\bar{d}_i$ that has the same cumulative added frequency Σf.

Equations (3) and (4) lead to a global transition amplitude δ_{T} of 3.3 ± 1.4 µm for the smooth surface, which is about 0.6 µm higher than the experimental determined transition amplitude. The transition amplitude δ_{T} for the rough surface is 3.6 ± 2.3 µm. The determination of the transition amplitudes is based on 9 line profiles in the direction of the secondary oscillation taken from each simulated contact (see Fig. 8). The profiles had a 10 µm distance from each other. From these 9 profiles the mean value of δ_{T} was obtained.

The reason for the high standard deviation of 2.3 µm of the rough surface is visible in Fig. 8b. From a line profile through the middle of the contact results a transition amplitude δ_{T} of 7.1 µm. This high value is caused by the two ncc with $\Delta x_1 \approx 34$ µm and $\Delta x_2 \approx 44$ µm located next to each other. Instead of a line profile in the middle of the simulated contact, a profile at the border of the contact could be taken, that result in a calculated transition amplitude δ_{T} of 2.1 µm. This low value is caused by the additional asperity contacts existing in one of the wide ncc. Because of equation (4) the other remaining wide ncc has no influence of the calculated transition amplitude δ_{T}. The variation in calculated values of transition amplitudes, depending on the position of the line profile in direction of the primary oscillation, is so caused by local differences of the asperity heights. In addition small asperities which are not visible in the simulation in Fig.8b, might also block particle motion in secondary direction. Especially in wide ncc, the surface is not perfectly flat like schematically shown in Fig. 9. There are quite a number of small asperities present in between the range of Δx and even in between the range of d. Certainly these smaller asperities would most effectively hinder the loaded particles from moving into the direction of δ_{SO} already at amplitudes being much smaller than δ_{T}. Thus the experimental value of the transition amplitude should be in some relation with the free space in between the smaller asperities in combination with the width of the ncc. Because the height of the smaller asperities play a significant role on their blocking capabilities a much more complex model is necessary.

So, a rough surface tends to change the number of asperity lines with the position on the contact surface in primary direction and may have small asperities within the ncc. These differences can cause at one distinct secondary amplitude a specific wear rate in low level wear regime or in high level wear regime (see Fig.4b). Using the presented wear model, the determination of the transition amplitude can be improved by taking more line profiles over the total contact on the disc.

5 Conclusions

The results of wear experiments with a ball-on-disc tribometer that simultaneously generates multidirectional reciprocating sliding have been shown and discussed. Smooth and rough disc surfaces have been used. The following conclusive statements can be made:

There are two wear regimes present in relation to the amplitude of the secondary oscillation. Below a transition amplitude of the secondary oscillation motion the wear volume is low, whereas above that value a high level wear regime prevails. Within these regimes the specific wear rate is independent of the sliding distance after running-in. While tribochemical reactions prevail within the low level wear regime, mechanically dominated wear mechanisms like abrasion and surface fatigue govern the high level wear regime. Using the smooth surface, the experimental determined transition amplitude was 2.7 ± 0.4 µm and at the rough surface about 3.1 µm.

A simplified wear model describes the transition amplitude on the basis of the particle contact situation. As long as the particles can move within the free space in between the asperities low level wear prevails. If the particles are forced to move over the asperities by an increasing secondary amplitude the specific wear rate increases by a factor of 5. A mathematical description of this phenomenon based on the concept of local transition amplitudes is derived which fits the experimental data fairly well. Remaining differences can be attributed to the over-estimation of the free space of motion of particles.

Further work will be to simulate a larger area of the ball-on-disc-contact with high resolution and to determine the transition amplitude automatically from *every* line profile.

Acknowledgements

The authors would like to thank Mr. Solovyev from the Robert Bosch GmbH, Gerlingen, Germany, for providing numerical gap simulations.

References

[1] Hird, J. R.; Field, J. E.; in: *A wear mechanism map for the diamond polishing process,* 258*,* Wear **2005**, 18–25.

[2] Su, Yaw-Terng; Hung, Tu-Chieh; Horng, Chuen-Chyi; in: *An experimental study on tool wear of hydrodynamic polishing process*, Wear **2000**, 246, 117–129.

[3] Fouvry, S.; Liskiewicz, T.; Kapsa, Ph.; Hannel, S.; Sauger, E.; in: *An energy description of wear mechanisms and its applications to oscillating sliding contacts*, Wear **2003**, 255, 287–298.

[4] Fouvry, S.; in: *Shakedown analysis and fretting wear response under gross slip condition*, Wear **2001**, 251, 1320-1331.

[5] Fouvry, Siegfried; Kapsa, Philippe; Zahouani, Hassan; Vincent, Leo; in: *Wear analysis in fretting of hard coatings through a dissipated energy concept*, Wear **1997**, 203–204, 393–403.

[6] Waterhouse, R. B.; in: *Fretting Corrosion,* Pergamon Press Ltd. **1972**.

[7] Volchok, A.; Halperin, G.; Etsion, I.; in: *The effect of surface regular microtopography on fretting fatigue life,* Wear **2002**, 253, 509–515.

[8] Menezes, L. Pradeep; Kishore in: *Effect of Roughness Parameter and Grinding Angle on Coefficient of Friction When Sliding Of Al-Mg Alloy Over En8 Steel* Journal of Tribology **2006**, 128, 697–704.

[9] Lakshmipathy, R..; Sagar, R.; in: *Effect of die surface topography on die-work interfacial friction in open die forging,* Journal of Machine Tools & Manufacturing **1992**, 32, 5, 685–693.

[10] Lovell, M.R.; Deng, Zhi; in: *Experimental investigation of sliding friction between hard and deformable surfaces with application to manufacturing processes,* Wear **1999**, 236, 117–127.

[11] Challen, J. M..; Oxley, P. L. B.; in: *An explanation of the different regimes of friction and wear using asperity deformation models,* Wear **1979**, 53, 229–243.

[12] Williams, J. A..; in: *Wear modelling: analytical, computational and mapping: a continuum mechanics approach,* Wear **1999**, 225–229, 1–17.

[13] Borucki, Leonard J.; Witelski, Thomas; Please, Colin; Kramer, Peter R.; Schwendeman, Donald; in: *A theory of pad conditioning for chemical-mechanical polishing*, Journal of Engeneering Mathematics **2004**, 50, 1–24.

[14] Borucki, L.; in: *Mathematical modeling of polish-rate decay in chemical-mechanical polishing*, Journal of Engeneering Mathematics **2002**, 43, 105–114.

[15] Seok, Jongwon; Sukam, Cyriaque P.; Kim, Andrew T.; Tichy, John A.; Cale, Timothy S.; in: *Multiscale material removal modeling of chemical mechanical polishing*, Wear **2003**, 254, 307–320.

[16] Liang, H.; Kaufman, F.; Sevilla, R.; Anjur, S.; in: *Wear phenomena in chemical mechanical polishing*, Wear **1997**, 211, 271–279.

[17] Zhang, L.; Tam, H. Y.; Yuan, C-M; Chen, Y-P; Zhou Z-D; Zheng, L.; in: *On the removal of material along a polishing path by fixed abrasives*, Journal of Engeneering Manufacture **2002** , Part B, 216, 9, 1217–1225.

[18] Zhang, L.; Tam, H. Y.; Yuan, C-M; Chen, Y-P; Zhou Z-D; in: *An investigation of material removal in polishing with fixed abrasives*, Journal of Engeneering Manufacture **2002**, Part B, 216, 1, 103–112.

[19] Samerski, I.; Vdovak, J.; Schoefer, J.; Fischer, A.; in: *The Transition between High and Low Wear Regimes under Multidirectional Reciprocating Sliding*, Wear **2008**. To be published

[20] DIN EN 590; *Dieselkraftstoff, Mindestanforderungen und Prüfverfahren,* Beuth Verlag **2004**, Berlin, Germany.

[21] Redlich, A.; in: *Simulation von Punktkontakten unter Mischreibungsbedingungen,* Ph.D.Thesis **2002**, University of Magdeburg.

[22] Solovyev, S.; in: *Reibungs- und Temperaturberechnung an Festkörper-und Mischreibungskontakten,* Ph.D.Thesis **2007**, University of Magdeburg.

Various Influence Factors on the Development of Standstill Marks (False-Brinelling Effect)

Grebe, M.; Feinle, P., Hunsicker, W.
Tribology Competence Center – Hochschule Mannheim (Germany)

1 Introduction

1.1 General Observations

On (seemingly) motionless bearings, minute movement through oscillation or vibration-induced elastic deformation can produce standstill marks on the runway. The subsequent overrolling of the marks in operation results in an uneven run and later to premature failure. (see figure 1 of an axial bearing with advanced damage). Such minute movement can be induced by machine or aggregate oscillation but also by the dynamic effects of road and rail transport.



Figure 1: Axial bearing with advanced damage. Typically there are marks in the distance of the rollers.

1.2 The State of Scientific Technology

The basics on the definition of the terms, the testing methods and fundamental correlations are outlined in paper 1.10.

A study of literature reveals that complex physical-mechanical processes occur in the contact zone of a false brinelling contact and that a single mechanism is unlikely to be responsible for the observed surface damages. The very extensive work of PITTROFF [2] contains a good summary of research and developments until 1961. Also the experimental results are very interesting and most of the relations found can be confirmed by the study presented. After Pittroffs project at SKF, the topic false brinelling was neglected for several years. Reseach concentrated on fretting conditions. Mathematic evaluations and solutions originate from the early work of MINDLIN et al [3]. Important publications of the last two decades are those of ÖDFALK and VINGSBO et al,

FOUVRY et al and SUNG-HOON et al. [4–8]. The results of this project will show that a part of the false brinelling contact is exposed to fretting conditions.

1.3 Objective of the Research Project at Hochschule Mannheim

The main objective of the current research project is to improve understanding of the processes caused by minute oscillation in the contact zone of roller and raceway and to use this new understanding to develop corrective measures. In contrast to fretting conditions, the test should also simulate the combined rolling / sliding movement in practice and not just linear sliding. For this purpose, a first project phase developed two standardizable testing procedures for systematic examination of standstill marks on bearings 1.10. These procedures are based on two different load situations:

1. Components exposed to dynamic axial load (without and with axial pretension) on servo-hydraulic testing equipment (with variation of the lubricants, frequency and load) (Figure 2)

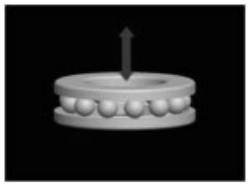


Figure 2

2. Components exposed to rotation oscillation on the existing false-brinelling test bench (with variation in lubricants, temperature, frequency, oscillation range and load) (Figure 3)

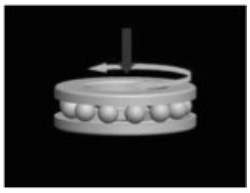


Figure 3

All tests are carried out with standardized axial ball bearings of the type 51206.

A subsequent project phase examines the influence of lubricant properties on the standstill marks by applying model and customary greases. The work focuses on variations of the thickener and oil base.

2 Test Results

2.1 Influence of the Type of Load: Axial – Pulsating or Rotating – Oscillating

One important feature is the damage symptoms revealed in the tests. The tests conducted so far show that some features clearly distinguish "real" standstill markers form other damage symptoms. The "wear symptoms" due to smaller oscillation (in this case +/- 0.2°) are the same as those of mere axial pulsation. This is revealed by the following figures of typical wear marks in figure 4. One outstanding feature is the clearly elliptic shape with an undamaged inner zone. A disadvantage of this testing parameter is that due to the undamaged inner circle there is only very slow damage progression and a clear differentiation between different lubricants thus becomes rather difficult. These results are very similar to that of SUNG-HOON et al [6] under high loaded fretting conditions. It shows partial slip in the outer zone of the Hertzian contact.

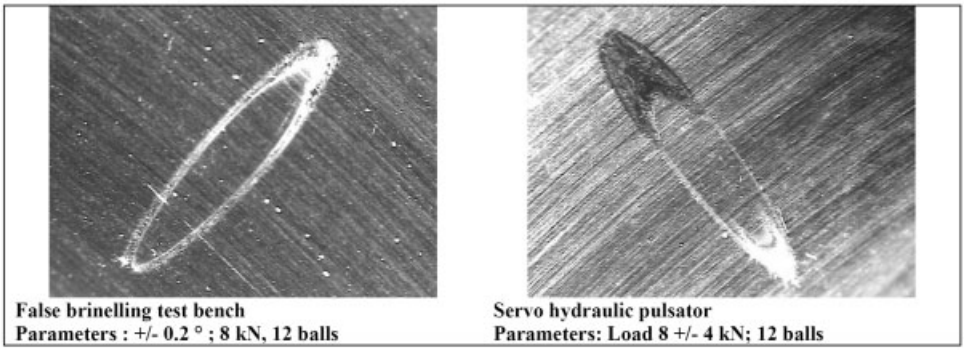


Figure 4: Comparison of standstill marks of the false Brinelling test bench (left) and the servo hydraulic pulsator (right)

The damage surface is bigger for axial pulse bearings exposed to constant maximal load and an increased proportion of pulsating load as this results in increased sliding within the outer zone. The influence of the oscillation frequency is relatively low and only relevant with certain lubricants.

Rotating oscillating tests on the false brinelling test rig achieve a clearer differentiation than axial pulse tests. Therefore the following sections only describe the results obtained on the false brinelling test bench.

2.2 Influence of the Testing Time

False brinelling tests performed so far, such as the SNR test, require testing times of several days and thus load cycle numbers of more than 4.5 million cycles. The false brinelling effect is therefore often associated with a life cycle problem. The current tests, though, show that with critical parameters there is severe damage on the contact zone after only a few minutes. In terms of strain cycling this comprises a time period of only a few thousand load cycles. This means that the standstill marks are not to be considered as an optical or fatigue problem that only occurs

towards the end of the estimated life cycle, but are critical early damage, which rapidly progresses from the first cracks and particles.

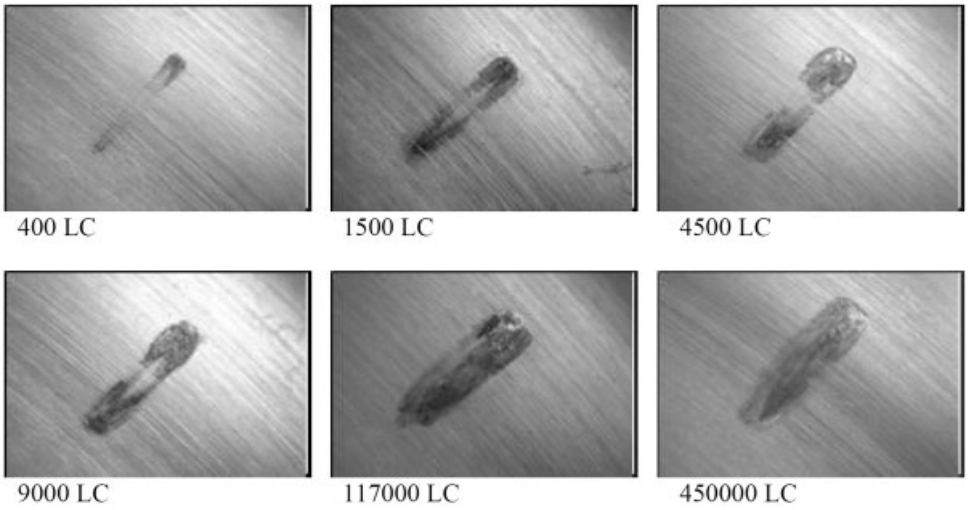


Figure 5: Influence of the load cycles (LC) – Parameters: 750 N/ ball; 25 Hz; +– 0.5°, 25°C; Low-Ref.-Grease

Compared to tests with lubrication, tests without lubrication show much higher oxide formation. Due to the high coefficient of friction in dry friction there is a clearly marked adhesive zone in the centre of the calotte. A test with 117,000 load cycles clearly reveals that parts of the adhesive zone remain entirely undamaged while there is extensive damage in the outer glide zone.

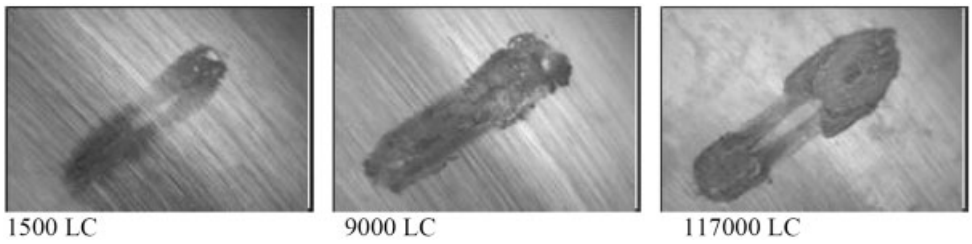


Figure 6: Influence of the load cycles (LC) at dry test conditions – Parameters: 750 N/ ball; 25 Hz; +– 0.5°, 25°C; Low-Ref.-Grease

2.3 Influence of Normal Force

The influence of normal force is considerably lower than one might assume. For the development of standstill marks it is, in principle, enough that the lubricant is pushed out of the contact zone and the surfaces are exposed to sufficient contact. It ought to be mentioned that this phenomenon

correlates with the development of friction induced corrosion. (e.g. tribo-oxidation). With increased normal force, however, damage progresses faster because the material tends to break off at the initial cracks under the influence of load and the particles produced add an abrasive damaging effect.

2.4 Influence of the Oscillation Frequency

Examinations on the influence of the oscillation frequency reveal increased damage with increasing frequency (see figure 7). This could be influenced by the fact that the oil given off by the grease needs some time to flow back into the friction point. Another influence factor could be the increased mass-changing forces.



Figure 7: Increased damage with increasing frequency (left 5 Hz, middle 12,5 Hz, right 25 Hz) – Parameter: Low-Ref.-Grease, 750 N/ Ball; +– 0.5°, 25°C, 117000 LC

2.5 Influence of Temperature

Examinations on the influence on the ambient temperature reveal totally different tendencies, which depend on the type of grease used. With most test greases, damage increases with decreasing ambient temperature. with increased oxide formation a frequent phenomenon. This can be easily explained with the clearly restricted oil emission and reduced flow properties. Some grease, however, shows hardly any reaction or even opposite properties when exposed to low temperatures.

One remarkable finding is that many greases which were tested positively at room temperature fail at low temperatures whereas greases tested negatively at room temperature show hardly any deterioration at minus temperatures. The reaction to temperature thus seems to depend mainly on the basic viscosity and the type of thickener (see figures 8 and 9).

2.6 Influence of the Oscillation Angle

Examinations on the influence of the oscillation angle reveal that the damage mechanism changes with a wider angle. While small oscillation angles predominantly cause damage from shattering, bigger oscillation angles produce more uniform wear and tear and sometimes even a flattening effect. A characteristic feature is that with higher oscillation angles there is no distinction between different wear mechanisms but that the angle affects the entire contact surface (see figure 10).

To date it is not clear why smaller oscillation angles produce such deep extensive damage in the form of cracks and loose material. From a general point of view the load and load changing

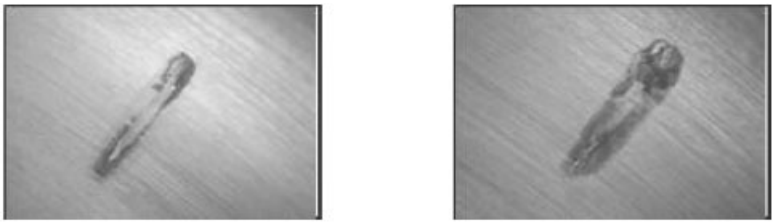


Figure 8: Comparison of the damages depending on the temperature (left 25°C; right –10°); Parameters: 750 N/ Ball; 25 Hz; +– 0.5°, 117000 LC; Ca-Complex-Grease

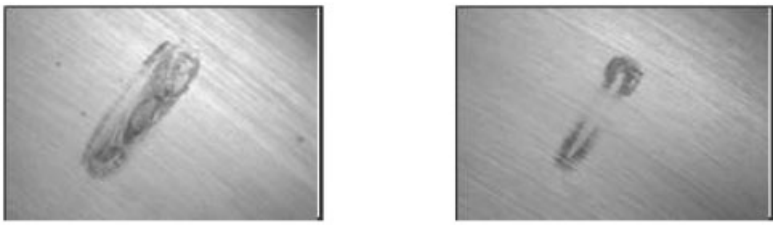


Figure 9: Comparison of the damages depending on the temperature (left 25°C; right –10°); Parameters: 750 N/ Ball; 25 Hz; +– 0.5°, 117000 LC; Li-Complex-Grease

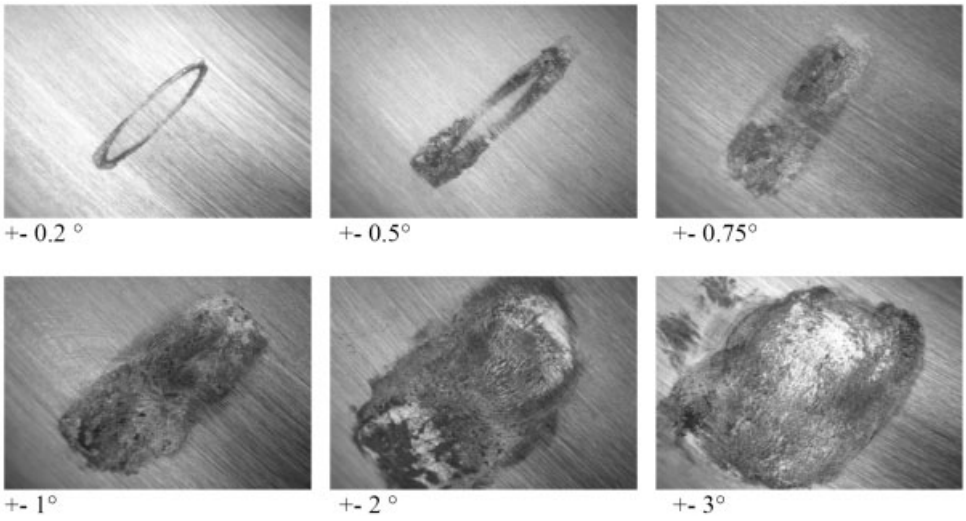


Figure 10: Influence of the oscillating angle; Parameters: 750 N/ Ball; 25 Hz; 25°C; 9000 LC

cycles are far too low to explain such extensive damage. For the standard conditions outlined in this paper, axial loading is approximately 36% of the dynamic load rating.

2.7 Influence of the Thickener

Examinations with different thickeners with the same basic oils and additive packages reveal that the type of thickener used has a clear influence. The following figure shows an exemplary comparison of the wear calotte of a complex calcium grease and that of a complex lithium grease (see figure 11).



Figure 11: Comparison of the damages of greases with the same base oil and additives but different thickener (left: calzium complex soap; right: Lithium complex soap); Parameters: 750 N/ Ball; 25 Hz; +- 0.5°, 25°C, 117000 LC

3 Discussion

The contact zone of a false brinelling mark can be divided into different zones, some of them optically discernible. Clearly visible are the undamaged adhesion zone in the centre of the marks (inner ellipse) and the damaged micro glide zone (between the inner and middle ellipse). This correlates with results under linear oscillated sliding (fretting test) of eg. SUNG-HOON and SEOK-JU [8]. But it should be considered, that the way of the movement is not the same because of the additional rolling part. At closer observation one can discern an outer zone, known as the affected zone. The size of this outer ellipse correlates with the calculated Hertz contact surface. In some cases this area shows color changes that could indicate chemical reactions between the lubricant and the material, but this was not investigated in this project. There is no relative movement in the centre of the elliptical mark (nonslip region or stick zone). Both the base body and counter body adhere well. On the edge, however, there are micro slip movements and local tension peaks which are caused by elastic deformation, bearing movements or shifting of the pressure centre, and these can cause extensive surface damage (see figure 12).

Although the elliptical marks produced in tests with small oscillation angles (+/– 0.2° to +/–0.5°) or with just elastic deformation (servo hydraulic pulser) might appear relatively harmless at first sight, there is already extreme local surface damage.

The following figures clearly reveal the correlation of several wear mechanisms. The outer end of the elliptical wear marks shows tribochemical reactions and surface disruption. The middle ellipse zone in the centre of the runway track only shows tribochemical reactions. There are no visible changes in the centre of the ellipse. The original grinding marks of the race are completely preserved. Even high resolution inspection methods can detect no topographic changes.

The deep indentations often observed in practical application are caused by the introduction of abrasive wear particles and reaction products or by a total lack of lubricant at the point of contact. Hence abrasion is a secondary wear mechanism that is not found at the beginning of the damage.

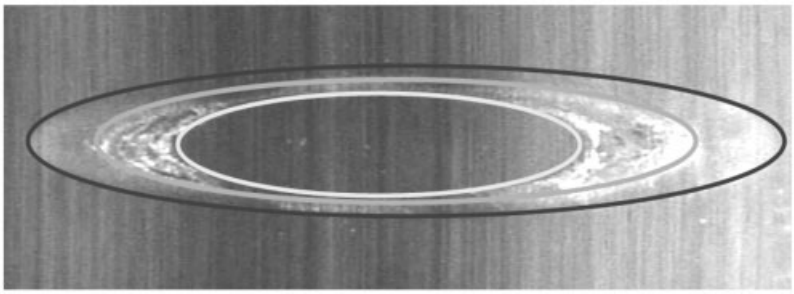


Figure 12: Division of the mark into different contact zones like stick zone, slip zone with microsliding and affected zone (from inside to outside)

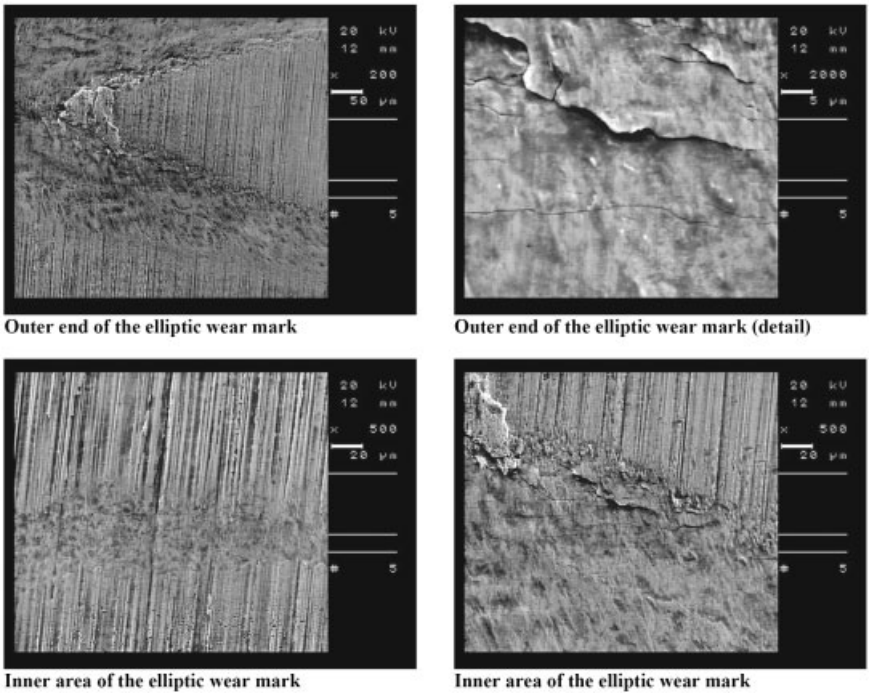


Figure 13: Areas of the elliptic wear mark (please consider the different resolutions)

In order to measure the depth of the visible cracks of the outer zone, the Robert Bosch GmbH company produced some focused ion beam cuts (FIB). The FIB cuts were taken from the outer glide zone. Four out of five examinations of different samples revealed cracks.

The FIB cut images clearly show in-depth crystalline cracks. Subsequent overrolling of the cracks in normal bearing operation will relatively quickly lead to particle break-off and bearing failure.

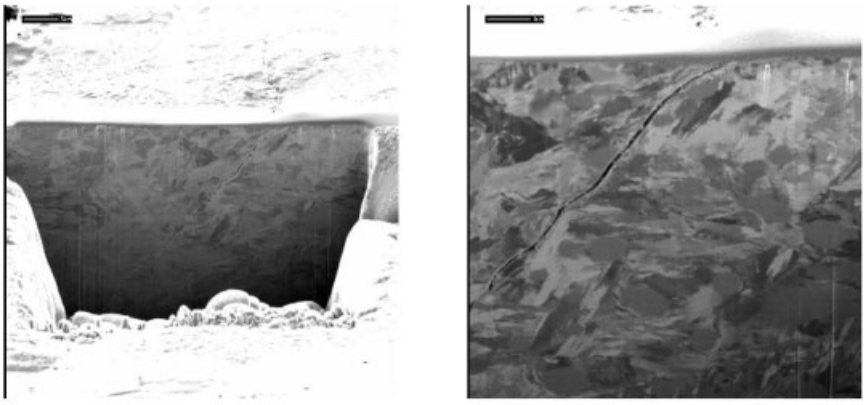


Figure 14: FIB/XB-Investigations at the outer end of the elliptic wear mark (width of the complete cut is about 20 µm, the visible depth is about 10 µm)

A fact which causes concern is that, at closer inspection, there is severe damage when using the grease which has so far achieved the best test results. This would indicate that such damage may never be fully avoided but can only be reduced. There is however still potential in the testing of other "lubricant-formula-variations".

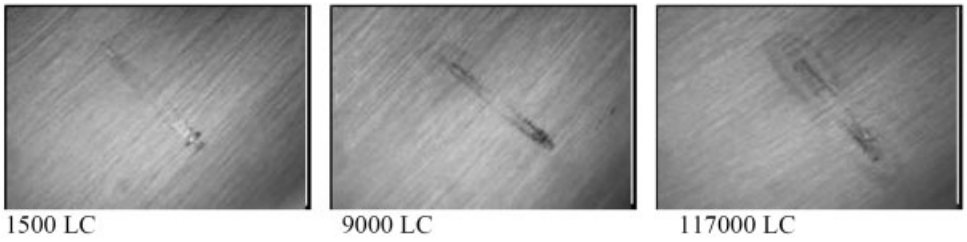


Figure 15: Influence of the load cycles on the damage with a high reference greaseParameters: 750 N/ Ball; 25 Hz; +– 0.5°, 25°C

4 Conclusion and Outlook

All tests conducted so far and the bibliography confirm the hypothesis that standstill marks develop due to various mechanisms:

- The lubricant is literally pushed out of the friction area by micro movement and high local pressure. This leads to a lack of lubricant and in the further process to typical wear mechanisms of abrasion and adhesion.

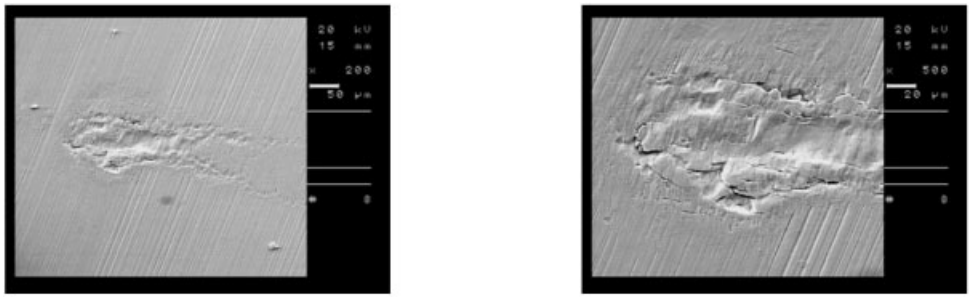


Figure 16: SEM pictures of the damaged area at the outer end of the elliptic wear mark of a test with a high reference greaseParameters: 750 N/ Ball; 25 Hz; +– 0.5°, 25°C

- The micro movement activate the surface energy (in particular the microcontacts on the surface roughness peaks). This leads to tricobchemical reactions down to a depth of several nanometres.
- Another important factor which is often not considered and can hardly be detected on superficial inspection are the microcracks caused by load changing on the surface. When exposed to further load, these cracks result in more extensive and deeper particle break-off.

The three damage mechanisms described above cause the production of wear particles and reaction products, which are not pushed out of the friction area due to a lack of "real" relative movement and thus have a strong abrasive effect. This phenomenon correlates with the formation of fretting corrosion (tribochemical reactions) and normally leads to damage progression and deep indentations which cover the traces of the original damage mechanism. In further damage progression and bearing rotation there are additional wear mechanisms (in particular abrasion and surface fatigue), which overlap and add to the covering of the real cause of damage. Depending on the predominance of one or several of the mechanisms described above, there are different types of standstill marks.

The predominance of one mechanism depends on the load conditions – and within those mainly from the oscillation angle. Another damage factor with strong influence is the lubricant used.

Due to their better flow properties, oils are in general more effective than greases in preventing damage due to lack of lubrication. Due to their better flow properties, oils may also be more suitable when it comes to preventing tribochemical corrosion, as oils achieve more reliable surface wetting and thus prevent the formation of dry friction oxides (Fe_2O_3), which, due to their abrasiveness, lead to quickly progressing damages.

One big problem is that the term "false brinelling" covers a wide variety of damage symptoms, which are partly caused by different mechanisms. The wear symptoms in tests with micro-oscillation differ significantly from the tests with relatively wide oscillation movements in the range of above 1°, as in the normal laboratory testing methods, such as the Fafnir or SNR test (Fafnir: +/–6°; SNR test: +/–3°). Such macroscopic oscillation movement leads to "real" bearing processes and not to the micro movements which occur and are particularly problematic with seemingly motionless bearings.

It is still unclear why only a few load changing cycles with loading far beyond the critical value can cause such massive damage. We will soon conduct computer simulations and FEM calculations. Future test bench setups will be designed to either confirm or disprove the existing hypotheses. Furthermore, the project members developing lubricant formula are working on concepts for improvement. But at this point of time we do not know yet if lubricants have an influence on the wear mechanism in surface disruption.

The examinations conducted so far show the complexity of wear damage due to the overlapping of all four main wear mechanisms. It is thus extremely difficult to find suitable lubricants for damage prevention.

5 Acknowledgements

The research project received financial support from the Karl-Völker-Stiftung at Hochschule Mannheim. We would also like to thank the following companies who contributed to this project for their outstanding cooperation, fruitful discussion and support: Fuchs Europe Schmierstoffe, Mannheim; Robert Bosch GmbH, Stuttgart; Fuchs Lubritech GmbH, Weilerbach; Dr. Tillwich – Werner Stehr GmbH, Horb.

We would also like to thank all students who participated in the project and conducted and analysed the many tests.

6 References

[1] M. Grebe; P. Feinle: Brinelling, False-Brinelling, “false” False-Brinelling; Tribologie-Fachtagung 2006: “Reibung, Schmierung und Verschleiß” in Göttingen; Tagungsband II, ISBN Nr. 3-00-003404-8, GfT, Moers, 2006, Band II S. 49-1-49-11

[2] H. Pittroff: Riffelbildung bei Wälzlagern infolge Stillstandserschütterungenpublished by SKF Kugellagerfabriken GmbH Schweinfurt, 1961

[3] R. D. Mindlin; G. HermannA Collection of Studies in the Development of Applied MechanicsPergamon Press, 1974; ISBN 0080177107, 9780080177106

[4] O. Vingsbo; S. Soederberg: On fretting mapsWear – An International Journal on the Science and Technology of Friction, Lubrication and Wear / 1988 / M8903 0393 671

[5] M. Ödfalk; O. Vingsbo: Influence of normal force and frequency in fretting. Tribology Transactions / 1990 / M9103 3691 582

[6] S. Fouvry ; P. Kapsa; L. Vincent: Description of fretting damage by contact mechanicsZAMM. Zeitschrift für angewandte Mathematik und Mechanik / 2000 / 200112 90799

[7] S. Munoz; H. Proudhon; J. Dominguez; S. Fouvry: Prediction of the crack extension under fretting wear loading conditionsInternational Journal of Fatigue / 2006 / 200610 07517J.

[8] Sung-Hoon; Y. Seok-Ju: Friction and Wear Characteristics Due to Stick-Slip under Fretting ConditionsTribology Transactions, 50, 564–572, 2007

On Dynamic Friction Phenomena in Brake Systems

G.-P. Ostermeyer, K. Bode
Institute of Dynamics and Vibrations, Braunschweig University of Technology (Germany)

1 Introduction

The implementation of friction into dynamic system models is generally accomplished by formulating the friction coefficient μ as a function of relative sliding velocity v_r of the contacting bodies.

In literature, such functions range from comparatively simple representations (e.g. piecewise linear definitions) to highly non-linear expressions, depending on the field of application and the accuracy required [1]. The most sophisticated friction laws of this type can generally be found in models of vibratory stick-slip systems, usually incorporating different equations for the stick phase, the slip phase and the transition from stick to slip [2].

What all the above mentioned algebraic functions assume a priori, is however no lag of time between a change in sliding velocity and a corresponding change in μ. From a control theoretic point of view, this is equivalent to the assumption that the tribological interface is always at steady state. This implies that all physical and chemical processes in the boundary layer, which determine the friction coefficient on the macro scale, respond to changes in external variables infinitely fast. That this in fact is not the case was discussed by Stelter [3].

In order to capture such transient effects, which is indispensable for the mathematical description of tribological systems with rapid changes in external variables (e.g. brakes and clutches), a general approach towards dynamic friction modeling will be suggested in chapter 2, leading to a system of differential equations. By a mathematical implementation of specific physical processes in the brake pad interface, this set of equations will be adapted to the tribology of disc brake systems in chapter 3. An application of the obtained friction law to selected case studies will follow in chapter 4.

2 General Approach Towards Dynamic Friction Modeling

An energetic interpretation of the friction coefficient μ at steady state, outlined in the following and first published in [4], will serve as a basis for the transient mathematical representation discussed in subsection 2.2.

2.1 Friction as a Sum of Power Fluxes

In 1993, Zum Gahr [5] published a mathematical formula, according to which the friction coefficient can be seen as a superposition of diverse tribological mechanisms. The respective equation, valid for steady state considerations only, is the following:

$$\mu = \frac{F_F}{F_N} = \mu_{thermal} + \mu_{elastic} + \mu_{plastic} + \dots \tag{1}$$

Tribological mechanisms are for instance elastic and plastic deformation on the micro scale, as well as heat generation, but also any other dissipative effects in the tribological interface contributing to μ. The linear shape of equation (1) might seem contradictive at first glance, since macroscopic friction phenomena are obviously non-linear. However, an energetic interpretation of μ, outlined in [4], gives new insights into the above cited formula.

If the classical definition of the friction coefficient, being the friction force F_F divided by the external normal force F_N, is expanded by the relative sliding velocity v_r, the friction coefficient appears as a normalized friction power in units of an external idle power $F_N\, v_r$:

$$\mu = \frac{F_F}{F_N} = \frac{F_F v_r}{F_N v_r} \tag{2}$$

This energetic interpretation is depicted in Figure 1, showing a classical μ vs. v_r graph, with additional indication of the different power fluxes that modulate the friction coefficient, in accordance with equation (1).

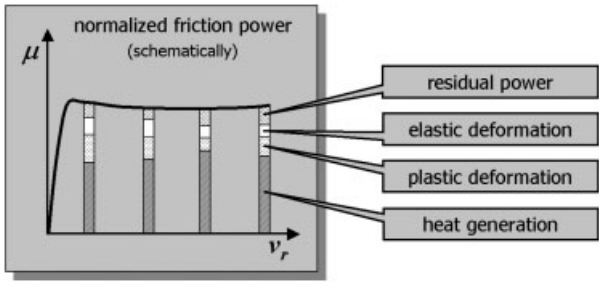


Figure 1: Coefficient of friction at steady state and interpretation in terms of power fluxes (schematically).

Worth to note is the fact that each power flux's contribution to μ may vary both in time and with external loading (e.g. with v_r), as also indicated by Figure 1. This is where the non-linearity and in particular the transient behavior of friction comes into the picture. The following subsection will show a general approach to capture these dynamics mathematically.

2.2 Friction as a Set of Differential Equations

Before going into detail, the following preliminary thoughts shall outline the principal approach towards dynamic friction modeling:

- In order to capture transient effects, the friction coefficient's first time derivative is the crucial variable that needs to be modeled, not the friction coefficient itself.
- The approach of modeling friction as a superposition of influencing factors (power fluxes), in correlation with equation (1), is also applicable to a dynamic representation.
- Each influencing factor will contribute differently to an increase or a decrease in μ, which needs to be covered by appropriate system (coupling) constants.

- The development of each influencing factor over time is determined by at least one external input variable to the tribological system and might be subject to a lag behavior. Different mechanisms in the contact zone might show a different lag characteristic, which needs to be considered by appropriate time constants.

According to the points stated above, the following principal layout of a dynamic friction model is suggested:

$$\dot{\mu} = -\alpha \left(\left(\sum_{i=1}^{n} a_i f_i \right) \mu - \sum_{i=n+1}^{m} a_i f_i \right) \tag{3}$$

α: time constant of friction coefficient
f_i: variable modulating the friction coefficient
a_i: coupling constant of influencing variable f_i

As equation (3) implies, some of the friction coefficient's influencing factors are mathematically coupled to μ itself. This is required in order to implement the lag behavior of friction, as discussed in section 1.

For each variable modulating μ, a representation as a first order lag element (PT1) with an individual time constant is suggested. Following the energetic approach discussed in the previous subsection, it is suitable to implement $F_N\, v_r$ as the input variable of all tribological mechanisms, since it unites the two macroscopic load parameters in units of a power. For the most general form of differential equation for f_i, the following expression is suggested:

$$\dot{f}_i = -\delta_i \left(f_i - f_{i,0} - \varepsilon_i \left(F_N v_r \right)^{k_i} \right) \tag{4}$$

δ_i: time constant of influencing variable
$f_{i,0}$: value at steady state for $F_N\, v_r = 0$
ε_i: coupling constant of external loading
k_i: system constant capturing non-linearity

Worth to note is the fact that not all variables f_i must necessarily depend on time, according to equation (4), but might also be constant values. In the following section, the set of differential equations outlined above will be adapted to actual physical effects in the boundary layer of disc brakes.

3 On the Physics of the Brake Pad Interface

The comprehensive work of Eriksson [6] discusses the properties of characteristic contact plateaus, which can be found on friction material surfaces after usual brake applications. They have properties that differ significantly from the surrounding matrix material (e.g. higher hardness and wear resistance) with a size usually ranging from 50 to 500 µm.

The fact that growth and destruction of contact plateaus over time is a key element for the understanding of transient friction phenomena was first discussed in [7]. This work developed

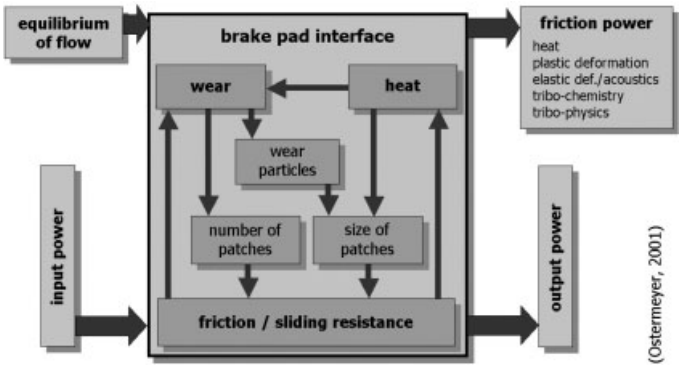


Figure 2: Equilibrium of flow in the brake pad interface.

detailed insights into a contact patch's life cycle and revealed the principal closed loop interaction between heat, wear and friction, which is illustrated in Figure 2.

Following the general approach outlined in chapter 2, the major influencing variables of the identified physics need to be modeled, in particular with their dependency on external loading $F_N\, v_r$. For the equilibrium of flow outlined in Figure 2, these are summarized in Table 1.

Table 1: Influencing variables and equations of the dynamic friction model.

Influencing variable	Dependence on external loading	Increase leads to
Patch temperature T_P	$\dot{T}_P = -\delta_1 \cdot (T_P - T_D - \varepsilon_1 \cdot F_N v_r)$	patch growth and μ-increase
Disc temperature T_D	$\dot{T}_D = -\delta_2 \cdot (T_D - T_\infty - \varepsilon_2 \cdot \mu F_N v_r)$	μ-decrease (fading effect)
Wear particle stream ψ	$\dot{\psi} = -\delta_3 \cdot \left(\psi - \varepsilon_3 \cdot \mu\,(F_N v_r)^2\right)$	patch growth and μ-increase
Patch area $A_p \sim \mu$	–	patch destruction and μ-decrease (due to stability limit of patches)
Friction power $F_F\, v_r$	$F_F\, v_r = \mu\, F_N\, v_r$	patch destruction and μ-decrease(due to mechanical loading)

Included in the above stated formulas is the assumption that patch area A_p and friction coefficient μ are proportional to each other. Worth to note is also that the temperature generation on disc and patches depends linearly on external loading $F_N\, v_r$. For the wear particle stream, this relation is quadratic, in accordance with measurement results by Trepte [8].

An implementation of all the influencing variables displayed in Table 1 into the general dynamic friction model of equation (3) finally yields the dynamic friction law for disc brakes:

$$\dot{\mu} = -\alpha\left((a_4 + a_2 T_D + F_N v_r)\,\mu - a_3\psi - a_1 T_P\right), \tag{5}$$

with the three additional first order equations, given in Table 1.

The following case studies will be based on a numerical integration of this set of equations.

4 Case Studies

This chapter is devoted to a simulation of real braking events. However, principal friction phenomena, such as time lag behavior, hysteresis and fading effect, are inherent in the model, as well. Previous papers [4], [7] discussed these phenomena with a similar set of equations.

As an example for the model's applicability to real braking situations, a series of six brake applications from 80 to 30 kph, with cooling in between, will be studied. This cycle is part of the AK-Master test, a standard industrial testing procedure for brake performance evaluation, consisting of several different braking events at various loads and temperatures.

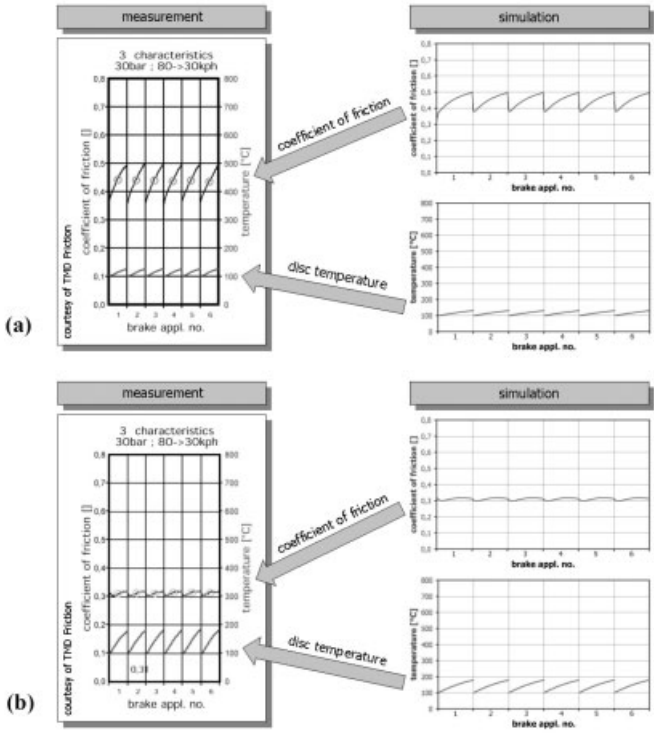


Figure 3: Friction coefficient and disc temperature for two different experimental pad materials.

In Figure 3(a), measurement results for a sample friction material, sliding against a grey cast iron disc, are compared with a numerical simulation. The observable dynamics of the friction coefficient is clearly inherent in the transient friction model, as it can directly reproduce the μ over time curve for an appropriate choice of parameters.

The same test cycle for a different experimental friction material is depicted in Figure 3(b). Obviously, this material shows only slight variations in μ throughout each braking event. However, with few changes in the parameters of the above introduced set of equations, this behavior can be obtained from simulation, as well.

5 Conclusion

The aim of this work was to sensitize the reader that friction is a dynamic process, showing transient characteristics, such as time lag and hysteresis, for changes in external parameters.

A modeling of these effects is essential for systems with rapid changes in external variables, which numerous technical systems are. This can only be accomplished by differential equations, with the friction coefficient's first time derivative as the crucial variable.

The physics of the boundary layer between brake disc and pad, being a closed loop interaction between heat, wear and friction, was implemented in chapter 3. With the obtained set of first order differential equations, it was possible to reproduce some principal transient effects in modern vehicle disc brakes. Moreover, real braking events could be simulated for different brake lining materials.

This confirms that the introduced model covers essential physical effects in the interface between brake pad and disc. Its parameters contain material specific information. Hence, their quantification in future work announces a material sensitive prediction of the tribological performance of various friction systems.

6 References

[1] Awrejcewicz, J.; Olejnik, P.: *Analysis of Dynamic Systems With Various Friction Laws*. Applied Mechanics Reviews, 58:389–411, 2005.

[2] Awrejcewicz, J.; Grzelczyk, D.; Pyryev, Y.: *On the Stick-Slip Vibrations Continuous Friction Model*. In: 9th Conference on Dynamical Systems Theory and Applications, 2007.

[3] Stelter, P.: *Nichtlineare Schwingungen reibungserregter Strukturen*. Diss., Fortschritt-Berichte VDI, Reihe 11, Nr. 137, 1990.

[4] Ostermeyer, G.-P.: *Thesen zur Modellierung von Reibung und Verschleiß*. Tribologie und Schmierungstechnik, 50:18-22, 2003.

[5] Zum Gahr, K.-H.: *Reibung und Verschleiß*. Deutsche Gesellschaft für Materialkunde e.V., 1993.

[6] Eriksson, M.: *Friction and Contact Phenomena of Disc Brakes Related to Squeal*. Comprehensive Summaries of Uppsala Dissertations from the Faculty of Science and Technology, Uppsala Universitet, 2000.

[7] Ostermeyer, G.-P.: *Friction and wear of brake systems*. Forschung im Ingenieurwesen, 66:267-272, 2001.

[8] Trepte, St.: *Tribology parameters for friction materials*. Materialwissenschaft und Werkstofftechnik, 33:142–154, 2002.

Creep Behavior of an Asperity in Fully Plastic Contact

A. Goedecke[1,2], R.Mock[2]
[1]Institute of Technical Mechanics, Johannes Kepler University of Linz, Austria
[2]Siemens AG Corporate Technology, Munich, Germany

Abstract

We present an FEM analysis of the transient creep behavior of a surface asperity.

Recently, numerical studies of surface asperities have received much interest. The existent studies mainly focus on the static behavior, omitting transient effects like creep. However, the transient creep of asperities has been suggested by Kragelskii, Rabinowicz, Scholz and others to be responsible for the time- and velocity-dependence of the friction coefficient.

We derive a simple one-dimensional transient asperity model from our FEM simulations. Moreover, we show how this model can be used as a building block for the *MIMEAC* fractal, transient friction model and how the time-dependent friction coefficient can be calculated.

1 Introduction

The behavior of elastic-perfectly plastic hemispheres in contact with rigid flats has been studied extensively in the last few years [1, 2]. Mostly, the interest was prompted by the development of asperity-based friction models, both of the statistical and fractal variety. In these models, the hemisphere is a model for a surface asperity, i.e. a microscopic contact patch.

In recent experimental [3] and theoretical [9] research, links have been established between the creep growth of the microscopic asperity contact areas and dynamic friction laws. Among the observed effects are the time-dependent increase of static friction and the velocity-dependent decrease of the dynamic friction coefficient.

However, the link between the asperity-based friction models and the idea of the creep-enhancement of asperity contact areas has until now not been fully understood. In addition, the existent theories, e.g. [9] are inherently inconsistent with the now more and more prevalent paradigm of fractal surface contact [8]. The present study tries to shed some light on these questions by presenting extensive FEM analyses of the creep behavior of asperities and suggests how the results can be used in the formulation of a transient, fractal friction model.

2 Modeling Approach

The asperity is modeled as a half-sphere with an undeformed radius of R. In accordance to previous work [1, 2], the contact geometry is assumed as a rigid punch displaced by an interference δ. The boundary conditions on the symmetry axis and the sphere base boundaries are assumed as sliding (roller) contacts, compare Figure 1.

The simulations were performed with the commercial Finite Element simulation code ANSYS 11. The mesh as displayed in Figure 1 consists of approximately 3300 predominantly rectangular

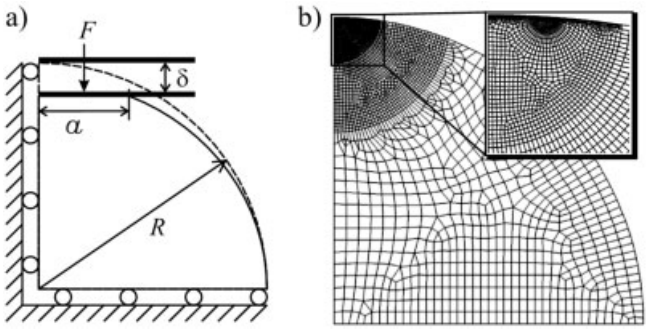


Figure 1: Basic geometry (a) and Finite Element mesh (b) used for the simulation.

elements with quadratic shape functions. The geometry is divided into regions with different meshing sizes, varying from fine to coarse based on proximity to the high-stress regions next to the contact line. This hierarchy of mesh sizes helped to produce accurate results with acceptable calculation times of about 1–2 hours on a 1.6 GHz Itanium 2 processing node.

The asperity material was assumed as isotropic and elastic-perfectly plastic, no hardening rule was applied. We used the von Mises formulation for the yield criterion and an associative flow rule. As standard material, we used a steel-like material with a Young Modulus of E = 200 GPa and a Poisson ratio of ν = 0.33. The yield stress was assumed at σ_{Y} = 400 MPa. Throughout the analysis, we used geometric nonlinear formulations.

The creep behavior of the material was modeled by separating the total strain tensor update into the creep, plastic and elastic strain tensors according to $\dot{a}_{tot} = \dot{a}_{cr} + \dot{a}_{pl} + \dot{a}_{el}$. The ANSYS formulation for the tensorial creep update $\dot{a}_{cr}$ is based on extending a uniaxial creep law $\dot{\varepsilon}_{cr}(\sigma)$ to a full tensorial creep law [4]. The uniaxial creep law therefore determines the simulated creep physics. For our simulations, we chose the Garofalo or hyperbolic sine creep law

$$\dot{\varepsilon}_{cr} = C_1 \sinh(C_2\sigma)^n \tag{1}$$

where C_1 and C_2 are material creep constants, $n = 1$. For high stress σ, the Garofalo creep law is asymptotically equivalent to the popular exponential creep law $\dot{\varepsilon}_{cr} = B' \exp(\beta\sigma)$ with $C_1 = B'2^n$ and $C_2 n = \beta$. For small stresses, it is equivalent to a power law $\dot{\varepsilon}_{cr} = B\sigma^n$. Note that this law can be shown to be a good approximation to the creep law predicted by the creep theory of Persson [5].

3 Analysis of Creep Behavior

As the most basic creep behavior of an asperity, we concentrated on the stress *relaxation* under constant interference δ. The experiments were conducted as follows: First, the asperities were quasistatically indented to an interference δ, no transient creep effects are simulated. This stage of elastic-perfectly plastic indentation is well understood [1, 2]. Second, we fixed the indentation at the specified value δ and observed the stress relaxation through creep.

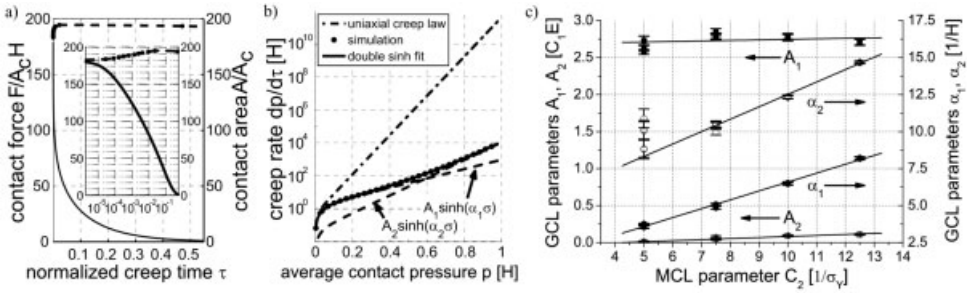


Figure 2: (a) Force (solid) and area evolution (dahed), the inset has a logarithmic time scaling. (b) creep law, derived from the experiment in a). (c) Dependence of the fit parameters $A_1, \alpha_1, A_2, \alpha_2$ of equation (2) on the parameter C_2.

The evolution of the normal contact force F and the contact area A during creep are shown in Figure 2. In this example, an initial interference of $\delta = 100\delta_c$ was assumed which is well in the fully plastic regime [1]. The contact force follows a characteristic creep curve with a steep initial decline that grows increasingly shallow. The contact area only shows a very modest increase of about 7%. As the area increase is only a secondary effect, we refer to [6] for a closer study and focus here on the force or pressure $p = F/A$ decrease instead.

For the description of the pressure decrease, it is advantageous to observe the average pressure decrease $\mathrm{d}p/\mathrm{d}\tau = \dot{p}(p)$. Here, we have used the normalized creep time $\tau = t/(H/C_1E)$ (see below) where H denotes the hardness of the asperity which is close to the hardness of the surface $H_S \approx 2.84\sigma_Y$ [2]. The $\dot{p}(p)$ law as depicted in Figure 2b is henceforth called geometric creep law (GCL) to distin-guish it from the material creep law (MCL) of equation (1). The GCL in essence reproduces the hyperbolic sine shape of the MCL with an exponential rise[2] for high pressures p and a linear rise for small pressures. Closer inspection, however, reveals that we have a transition between two different slopes at about $p \approx 0.6H$. As an analytical approximation, we propose the sum of two hyperbolic sine laws

$$\dot{p}(p) = A_1 \sinh(\alpha_1 p) + A_2 \sinh(\alpha_2 p) \quad \text{with} \quad \dot{p} = \partial p/\partial \tau. \tag{2}$$

The two summands are shown in Figure 2b as dashed curves and can be thought of as the high- and low-stress components of the creep law. The creep laws have the same structure as the MCL, while the parameters A_1, α_1, A_2 and α_2 are dependent on the input geometric and material parameters.

To understand the physical meaning of the transition between the two characteristic slopes, we take a closer look at the stress development during creep, depicted in Figure 3. Initially, the high stress and high pressure region directly underneath the contact line is contained by the surrounding material. While the semicircular center region is at yield stress and therefore easily deformable, the surrounding material has a lower von Mises stress and therefore stabilizes the center. The creep process starts a complex reordering of the stress states which is dominated by two processes: a) The center region expands, releasing hydrostatic pressure and elastic strain and thereby expanding its volume because creep strain – like plastic strain – is associated with

[2]Note that an exponential increase leads to a straight line in the logarithmic plot of Figure 2(b).

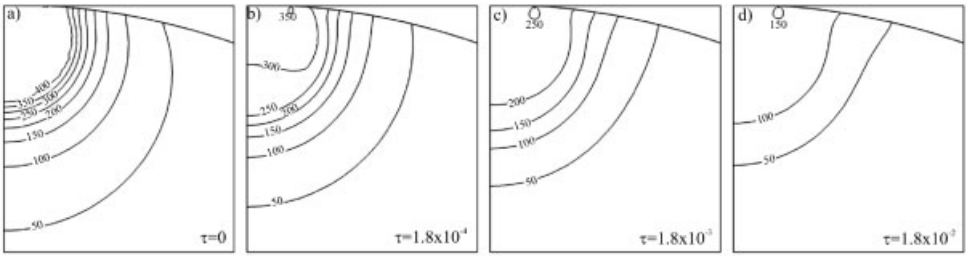


Figure 3: Stress evolution for a creeping asperity under constant displacement. Stress values indicated in MPa.

a Poisson ratio of $\nu_{pl} = 0.5 < \nu$. b) The containment region relaxes its elastic strain, thereby losing its stabilizing function and yielding to the contained pressure. All this causes the contact area to increase, as seen in Figure 2a and introduces new deviatoric strain components. This is evidenced by the stress plots in Figure 3b, c, d where an elliptical region at the outermost contact point shows elevated von Mises stress.

During the first part of the stress relaxation down to a pressure of about $p = 6H$, the relaxation is therefore accompanied by a stress reordering which the replenishes the deviatoric (von Mises) stress components and thereby leads to a high material creep rate. As soon as the reordering stops – evidenced by a constant contact area – the geometric creep rate decreases and leads over to the low pressure creep law.

In [6], we present a more detailed quantitative analysis of the creep evolution, including the area increase and the influence of the geometric and material parameters. One of the most important results is that the GCL shows universal behavior in terms of changes in the Young modulus E, creep parameter C_1 and yield stress σ_Y when introducing a normalized time $\tau = t/(H/C_1E)$. All plots in this paper therefore use this time scale definition. Other parameters like C_2 show a more complex influence on the fit paramaters $A_1, \alpha_1, A_2, \alpha_2$ of equation (2), as is exemplarily shown in Figure 2c. The dependence can be well fitted by a simple linear relationship in the form

$$\begin{pmatrix} A_1 \\ A_2 \end{pmatrix} = EC_1 \left\{ \begin{pmatrix} 2.67 & \pm & 0.06 \\ -0.06 & \pm & 0.01 \end{pmatrix} + C_2\sigma_Y \begin{pmatrix} 0.007 & \pm & 0.006 \\ 0.014 & \pm & 0.001 \end{pmatrix} \right\},$$
$$\begin{pmatrix} \alpha_1 \\ \alpha_2 \end{pmatrix} = \tfrac{1}{H} \left\{ \begin{pmatrix} 0.58 & \pm & 0.09 \\ 4.1 & \pm & 0.2 \end{pmatrix} + C_2\sigma_Y \begin{pmatrix} 0.60 & \pm & 0.01 \\ 0.84 & \pm & 0.02 \end{pmatrix} \right\}. \tag{3}$$

The errors given are error bounds at a 66% confidence interval, estimated by the nonlinear curve fitting algorithm. The resulting GCL law fits all creep rate simulations performed with a maximum error of about 6%. Equations (2) and (3) therefore present a simple 1D model for the transient creep behavior of an asperity.

4 Fractal Transient Friction Model

To showcase the practical importance of the presented results, we now paraphrase our *MIMEAC* [7] friction model which combines a) a fractal surface model and b) the above 1D transient asperity model to predict the time- and velocity dependent friction coefficient. To the authors'

knowledge, this is the first time a transient friction model is presented that is both based on asperity creep as a physical mechanism for a time- and velocity-dependent friction coefficient [9] and heeds the now more and more prevalent fractal surface paradigm [8].

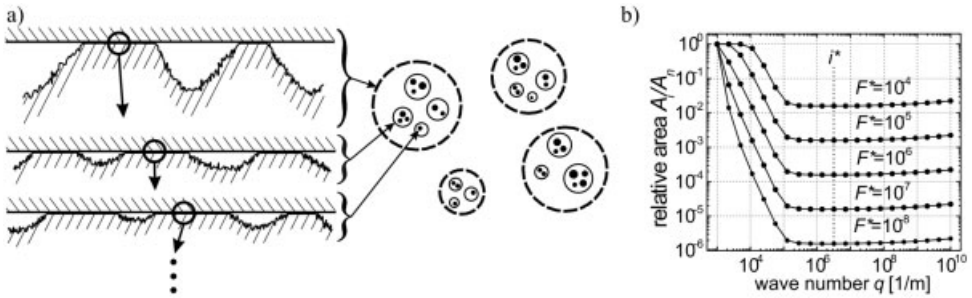


Figure 4: Illustration of the idea of fractal area iteration, (b) Examples for the area iteration of equation (3).

The underlying fractal surface contact model is a variant of Jackson's model [10], its basic idea is illustrated in Figure 4. According to the model, the observed real contact area A_r is dependent on the scale ("magnification") of the observation. Jackson's model uses discrete scales i with a corresponding apparent contact area A_i. By definition, $A_0 = A_n$ where A_n denotes the nominal or apparent contact area, defined by the contact geometry. When progressing to higher and higher magnifications of the surface, the observed contact patches are seen to break apart or fractalize due to the roughness at the specific scale

$$A_i(F) = \underbrace{A_{i-1}(F)\eta_i}_{\#\text{ofasperities}} \bar{A}(\bar{F}_i, R_i) \quad \text{with} \quad \bar{F}_i = \frac{F}{A_{i-1}(F)\eta_i} \tag{4}$$

where F denotes the total normal force, $\bar{A}(F\prime, R)$ the contact area of a single asperity of radius R under the force $F\prime$, η_i the density of contacting asperities and R_i a "typical" asperity radius at scale i. The latter two can be derived both from experiments [10] and theoretically from the power spectral density (PSD) of the surface [7].

An example for the resulting contact areas A_i is shown in Figure 4b for different loading forces $F^* = F/(A_n E')$. According to Jackson's model, the real contact area is calculated at the end of the fractali-zation process, i.e. $A_r = \min A_i = A_{i^*}$. Note that friction coefficient can be easi-ly calculated from the real contact area by invoking the standard adhesion friction theory: Assuming the shear strength s to be constant, the friction force is $F_r = sA_r$.

For the time dependent friction coefficient, we modify the area iteration of equation (4) by replacing the single asperity contact area $\bar{A}(F\prime, R)$ by the time-dependent, creep-enhanced contact area under constant load $\bar{A}(F\prime, R, \tau)$. Note that while Section 3 discusses the relaxation at constant interference, the area in-crease under constant load can easily be derived [7] from this using the results of Etsion et al. on unloading and reloading of an asperity [11].

Figure 5a shows the creep enhancement of the single asperity contact areas for a force of $F^* = 10^{-6}$. In Figure 5b, the resulting time-dependent real contact area $A_r(\tau)$ is shown. For comparison, the logarithmic increase calculated by Brechet [9] and well-verified by experiments

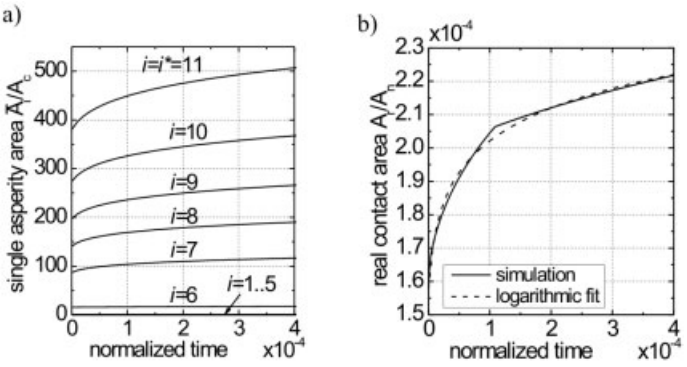


Figure 5: Creep evolution of the single asperity areas (a) and the real contact area (b) for a force $F^* = 10^{-6}$.

is shown with a dashed line. It is evident that our fractal, transient contact theory yields results that are in good agreement to the established theory.

5 Summary

Extensive Finite Element Analyses of the creep behavior of a hemisphere in contact with a rigid flat have been conducted and analyzed. The results were summarized in a simple, one-dimensional model for the transient behavior of a loaded asperity. The model is valid for a wide range of material and geometric parameters.

It was shown how the asperity model can be used to build the *MIMEAC* fractal, transient friction model. Exemplarily, the time-dependent real contact area has been calculated and was found to be in good agreement with experiments and older theories. This is to the authors' knowledge the first time a dynamic friction model based on creep has been formulated in the new paradigm of fractal surface models.

6 References

[1] L. Kogut, I. Etsion, J. Appl. Mech. 2002, 69, 657–662.

[2] R. L. Jackson, I. Green, ASME J. Tribol. 2005, 127, 343–354.

[3] B. Berthoud, T. Baumberger, Phys. Rev. B 1999, 59, 14313–14327.

[4] ANSYS Inc., ANSYS Theory Manual, Release 11, 2007.

[5] B.N.J. Persson, Phys. Rev. B. 2000, 61, 5949-5966.

[6] A. Goedecke, R. Mock, 2008, *under review.*

[7] A. Goedecke, R. Mock, in *Proceedings of ESDA 2008, 9th Biennial ASME Conference on Engineering Systems Design and Analysis*, ESDA2008-59366.

[8] J. Greenwood, J. Wu, Meccanica 2001, 36, 617–630.

[9] Y. Brechet, Y. Estrin, Scr. Metall. Mater. 1994, 30(11), 1449–1454.

[10] R. Jackson, J. Streator, Wear 2006, 261, 1337–1347.

[11] I. Etsion, Y. Kligerman, Y. Kadin, Int. J. Solids Struct. 2005, 42, 3716-3729

An Approach to Energy Based Fretting Wear Prediction at Low Frequency Loading

M. Becker[1], D. Nilsson[2], P. Wackers[1], A. Werner[1], V. Arrieta[1]
[1] MTU Aero Engines GmbH, 80995 Munich, Germany
[2] The Royal Institute of Technology, Stockholm, Sweden

1 Introduction

Fretting wear occurs at several locations in aircraft engines. For example in the contact surfaces between the blade shrouds, the blade and the disk or in the vane hooks. Thus with an advancing number of accumulated service cycles the components are increasingly worn out in the contacting surfaces resulting in mistuning, leakage or even failure. To prevent major damage to the modules or even the overall engine these components have to be repaired or replaced after certain service intervals. Thus it is of major importance to – on the one hand – a priori develop an engine design which implicates reduced wear and – on the other hand – to be able to reliably predict the amount of abrasion in order to specify the service intervals safely. To achieve this an effective model to predict fretting wear is essential. The development, validation and implementation of such a model within a finite element (FE) context is the key goal of the work presented in this paper. The major steps followed are: firstly a test rig is set up which allows to measure the abrasion in specimen tests for two selected aerospace alloys at certain temperatures and contact pressures at moderate sliding speeds. Secondly an energy based model for the prediction of wear is formulated and calibrated analytically to the test results. Finally this model is implemented into an ABAQUS-User Subroutine and the test results are modelled by means of a FE analysis of the test rig.

2 Fretting Wear Experiments

In order to experimentally quantify the amount of fretting wear in aero-space alloys at low frequency (LF) loading and at temperatures and contact pressures within the operating range a powerful test rig has been set up at MTU Aero Engines GmbH. Within the test rig two pads, see figure 1 a), are pressed against one another with a predefined normal Force P resulting in a contact pressure p. Therein the test rig allows for pressures up to 60 MPa and temperatures up to 1000 °C. Two materials are investigated in the following, Inconel 718 and Ti6Al-4V, thus resulting in three possible material pairings. Once the normal force is applied pad 2 is moved in vertical direction with a frequency of 0.1 Hz and a displacement amplitude of δ_{LF} = 1mm relative to pad 2 ("LF" denotes low frequency loading). Due to the normal force and the displacement amplitude a shear force Q is generated within the contact surface and depending on the loading conditions (normal force, frequency, temperature) and material pairing mild, strong or even severe wear is induced in the contact surfaces, see figures 1b) and 1c). The amount of wear occurring in each test is obtained via an optical image processing which provides for each pad the wear scar at any point within the contact surface, see figure 1 d), and the overall wear volume W lost during the test.

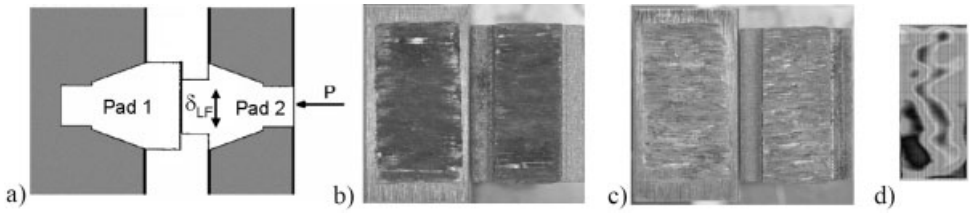


Figure 1: a) detail of the test rig showing the two pads in contact. Photographic image of the contact surface of pad 1 (left) and pad 2 (right) showing b) moderate and c) strong wear. d) typical output of the optical image processing quantifying the amount of wear throughout the contact surface.

During each test the shear force Q is recorded over time, such that at any time the friction coefficient μ can be computed via

$$\mu = \frac{Q}{P} \tag{1}$$

where the normal force P is prescribed and constant over time. The test results showed a strong dependence of the friction coefficient on temperature for both investigated materials. Furthermore a quite pronounced evolution of the friction coefficient was observed within the first 1000 loading cycles before a stabilized state was reached.

3 Selection of an Energy Based Model for Fretting Wear Prediction

Over the last 60 years a vast amount of models to describe wear has been published by many authors for all sorts of loading conditions such as sliding or fretting wear or lubricated or dry wear among many others, see [15] for an overview. As stated also by Meng and Ludema, most of these models are valid only for very specific cases. However two models have become widely accepted among researchers treating wear in a phenomenological manner as it is targeted in the present paper. This is on the one hand the model of Archard [1,2] and on the other hand an energy based wear model, proposed by [16,17,18] and by [8,9,11].

3.1 Model of Archard

The model of Archard was one of the first wear models, published in 1953. According to Archard the wear volume W [m^3] is directly proportional to the product of the normal force in the contact surface P [N] and the sliding distance δ [m] between both surfaces and inversely proportional to the hardness H [N/m^2] of the softer material [1,2]

$$W = K \cdot \frac{P \cdot \delta}{H} \tag{2}$$

here K [-] denotes Archard's wear constant. This rather simple phenomenological approach is quite successful in modelling various experiments. However, as also stated by [21], changes in the wear mechanism, as e.g. induced by changes in the surface condition, can not be captured

with Archard's model. With a modification of (2) regarding the introduction of a temperature dependence of H the model was recently applied successfully within a FE context by [19]. Another example of an application of Archard's model in a FE context are [5] and [6].

3.2 Energy Based Wear Model

The second model proposed by [16,17,18] and [8,9,11] correlates the wear volume W [m^3] with the accumulated energy $E_d{}^i$ [J] dissipated by the friction mechanism within one out of N fretting cycles through

$$W = \alpha \cdot \sum_{i=1}^{N} E_d^i \tag{3}$$

here α denotes the energy wear coefficient [m^3/J]. The accumulated energy $E_d{}^i$ dissipated in one fretting loop is given by the area enclosed by the hysteresis loop, i.e.

$$E_d^i = \int_0^{\delta_i} \hat{Q}(x) \cdot dx \tag{4}$$

see figure 2a) for a visualization. [3] verified the energy based wear model for different types of hard coatings. By [14] and [7] the energy based wear approach was confirmed under variable displacement amplitude conditions. [20] experienced that for elevated temperature the energy wear coefficient changes. [17] reported that the model holds for different normal loads, humidities and fretting frequencies. However as stated also by [13] the model holds only if the main wear mechanism does not change during the test.

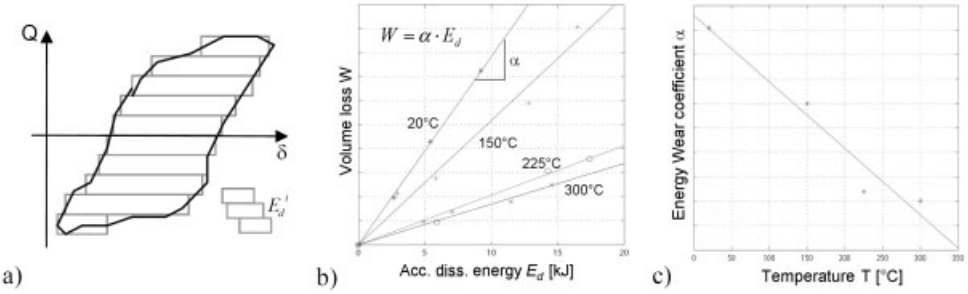


Figure 2: a) determination of the accumulated energy $E_d{}^i$ dissipated in one fretting loop. The green lines indicate the approximate determination for a real fretting loop based on the output of the test data.

3.3 Selection of a Wear Model

Like Archard's law the energy based model is a rather simple purely phenomenological model. Basically both models do not differ much (assuming a constant friction coefficient and contracting

all constants in each model into one, both models actually are identical in their local forms). Both models do not explicitly take into account the third body formation and can not capture changes in the wear mechanism from e.g. mild to severe wear. However the energy based model has a clear physical basis correlating the wear volume with a real energy (shear force and sliding distance being collinear) whereas Archard's model correlates the wear volume to a quantity with the units of an energy but without physical meaning since the normal force acts perpendicular to the sliding distance. Furthermore as stated by Fouvry [10] "[…] the energy approach can be considered as an extension of the Archard description, which better integrates the influence of the friction coefficient". Indeed the friction coefficient μ directly enters the energy based formulation. This can be seen after rewriting equation (3)

$$E_d^i = \int_0^{\delta_i} \mu(x) \cdot P(x) \cdot dx \tag{5}$$

hence changes in the friction mechanism (e.g. due to an evolution of the contact surface, temperature changes or even local variations of μ within the contact surface, etc.) can be accounted for within the energy based model. On the other hand, as stated also by [21] no direct correlation between the constants *K* and *H* entering Archard's model and the friction coefficient μ can be found. Consequently the energy based model is selected as the wear model to be used in the subsequent investigations. In view of an implementation of the energy based wear model within a standard local finite element formulation a local form of equation (3) is required relating the local wear depth at any point within the contact surface to the accumulated dissipated energy at this point. Assuming that at any position within the contact surface the local wear volume *dW* can be computed through (3) but with a local wear coefficient β the local wear depth observed in the infinitesimal surrounding *dA* of that point is obtained by

$$h = \frac{dW}{dA} = \beta \cdot \sum_{i=1}^{N} \frac{E_d^i}{dA} = \beta \cdot \sum_{i=1}^{N} \int_0^{\delta_i} \frac{Q}{dA} \cdot dx = \beta \cdot \sum_{i=1}^{N} \int_0^{\delta_i} \tau \cdot dx \tag{6}$$

Within a time discretized setting the incremental change in wear depth Δh associated with the incremental slip distance $\Delta\delta$ is obtained for $\delta_i \rightarrow \Delta\delta$ from (6), i.e.

$$\Delta h = \beta \cdot \tau \cdot \Delta\delta \tag{7}$$

where it has been assumed that the shear stress τ remains constant along the incremental slip distance $\Delta\delta$. Carefully note that in the subsequent investigations it is assumed that the global wear coefficient α and the local wear coefficient β are identical (i.e. $\alpha = \beta$) since the experimental setup discussed in chapter 2 does not allow for a determination of the local wear coefficient β. See [12] for a comparison between local and global wear coefficients.

3.4 Validation of the Energy Based Wear Model at Low Frequency Loading

In the following the energy based wear model is validated for the test results obtained with the test rig discussed in chapter 2 for a Ti6Al-4V versus Ti6Al-4V pairing subjected to isothermal

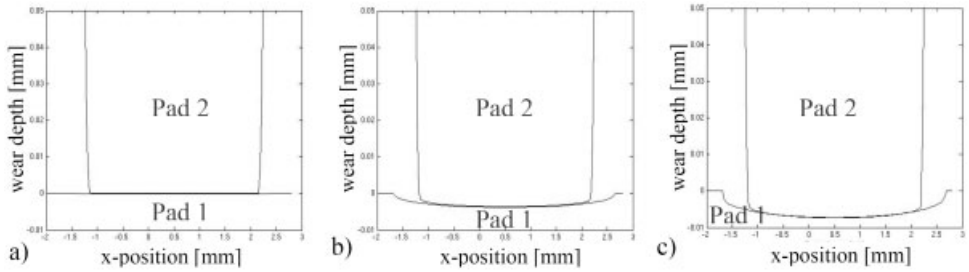


Figure 3: Wear depth evolution for a Ti6Al-4V pairing at 20°C. Wear scar after a) 10, b) 500, c) 1000 cycles.

low frequency loading between 20°C and 300°C. Figure 2b) visualizes the correlation of the energy based wear model with the test results. Therein clearly a linear correlation $W = \alpha E_d$ can be observed for each of the analyzed temperatures, thus proving the validity of the model for Ti6Al-4V. Similar observations have been made by the authors for Inconel 718 versus Inconel 718 pairings and for Inconel 718 versus Ti6Al-4V pairings. Note that the variation in the accumulated energy dissipated in each experiment reported in figure 2b) has been achieved by varying both, the contact pressure *and* the cycle number N, thus providing a validation of the model for both parameters. Finally a significant temperature dependence of the wear coefficient α has been observed, see figure 2c). Note: each dot in figure 2c) represents a value of α obtained from the test results as visualized in figure 2b).

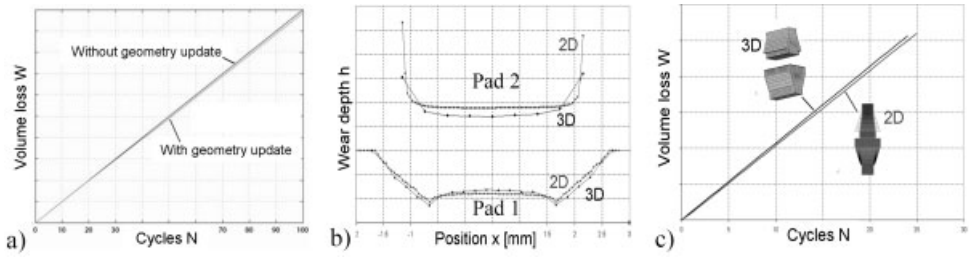


Figure 4: a) wear volume evolution W over first N=1000 cylces for a Ti6Al-4V pairing at 20°C, comparison between FE solution with and without geometry update. Comparison of 2D and 3D results for a) wear depth after first 25 cycles and b) wear volume evolution over first 25 cycles.

4 Implementation of the Wear Model into a Finite Element Solver

In order to employ the wear model within an analysis of real components the local form of the energy based wear law (7) has been implemented into the commercial FE package ABAQUS. Two alternative approaches have been implemented for 2 dimensional (2D) cases

1. Neglect the geometry change due to abrasion: The wear depth according to equation (7) is determined in a postprocessing step. Hence a standard contact analysis provides the required quantities τ_{node} and $\Delta\delta_{node}$. No changes of the FE solver are required.

2. Take the geometry change due to abrasion into account: For each iteration in the contact algorithm the nodal wear depth is determined through equation (7). Subsequently the nodes in the contact surface are moved accordingly (perpendicular to the surface by an amount Δh_{node}) employing the ABAQUS User Subroutine UMESHMOTION.

Apparently the second approach increases the computational costs but on the other hand gives more accurate results especially for curved contact surfaces. Furthermore the distribution of the normal stress in the contact surface shows pronounced stress peaks at the contact edges (see e.g. [4] for an analytical solution) which result in increased wear in these regions. With advancing abrasion the peaks decrease which can only be accounted for by the second approach. The result of a 2-dimensional FE analysis of the test setup discussed in chapter 2 employing the second approach is shown in figure 3. A comparison of both approaches for the "overall" result of the FE analysis in terms of the wear volume W is shown in figure 4a). Apparently both approaches give almost identical results for the present flat geometry. Finally both approaches have been implemented in 3 dimensions (3D) as well. Obviously the 3D setup dramatically increases the computational costs since the contact surface requires a rather fine discretization for the wear analysis. As can be seen in figure 4b) and figure 4c) the 2D and 3D results for the specimen centreline are in reasonable agreement. Clearly only a limited amount of fretting cycles can be modelled. However, looking at the linear evolution of the wear volume with the cycle number (see e.g. figure 4a)) a linear extrapolation of the stabilized state up to the cycle numbers investigated in the test rig (up to 20000) seems adequate. A FE analysis of all test results (ca. 40 tests) showed a reasonable deviation smaller than a factor of $2^{+/-1}$ between extrapolated FE results and the raw data from the tests. Carefully note that this deviation is mainly due to the scatter in the test raw data. The FE predictions without geometry update and analytical predictions based directly on equation (4) are almost identical.

5 Summary

In this paper an approach to the modelling of fretting wear at low frequency loading has been presented. An energy based model has been selected relating the wear volume (or the local wear depth) in the contact zone to the accumulated energy dissipated in the fretting cycles. The model has been validated for fretting wear tests at various temperatures, contact pressures and cycle numbers for low frequency loading and Ti6Al-4V as well as Inconel 718 pairings. The model has been implemented into the commercial finite element package ABAQUS for 2D and for 3D with and without consideration of wear induced geometry changes. Apparently the most efficient approach is a 2D-analysis without geometry update, whereas the most accurate approach is a 3D-analysis with geometry update. For the test setup with flat contact surfaces discussed in this paper all presented approaches are in good agreement *and* describe the measured test data with reasonable accuracy.

Acknowledgments: The authors gratefully acknowledge the support of the presented work by a LuFo-3 technology program funded partially by the BMWi.

6 References

[1] Archard, J.F., Appl phys **1953**, *24*, 981–988

[2] Archard, J.F.; Hirst, W., *Proc. R.Soc. A* **1956**, *236*, 397-410

[3] Celis, J.P.; Stals, L.; Vancoille, E.; Mohrbacher, H., Surface Engrg. **1998**, 14(3), 232–239

[4] Ciavarella, M.; Demelio, G., Intern. Journal of Mechanical Sciences **1999**, 41, 1533–1550

[5] Ding, J., Modelling of fretting wear, PhD thesis, Univ. of Nottingham, UK, January **2003**

[6] Ding, J.; Leen, S.B.; McColl, I.R., International Journal of Fatigue **2004**, *26*, 521–531

[7] Fouvry, S.; Wear **2003**, 255, 287–298

[8] Fouvry, S.; Kapsa, Ph.; Vincent, L., *Proc. Int. Tribology Conference* **1995***,* 277–282

[9] Fouvry, S.; Kapsa, Ph.; Vincent, L., Wear **1996**, *200*, 186–205

[10] Fouvry, S.; Kapsa, Ph.; Vincent, L., Wear **2001**, *247*, 41–54

[11] Fouvry, S.; Kapsa, Ph.; Zahouani, H.; Vincent, L., Wear **1997,** *203-204*, 393–403

[12] Fouvry, S.; Liskiewicz, T., Tribology International **2005**, 38, 69-79

[13] Huq, M.Z.; Celis, J.P., Wear **2002**, 252, 375–383

[14] Likiewicz,T.; Fouvry, S.; Wendler, B., Surf. and Coat. Technol. **2003**, 163–164, 465–471

[15] Meng, H.C.; Ludema, K.C., Wear **1995**, *181-183*, 443–457

[16] Mohrbacher, H.; Blanpain, B.; Celis, J.P.; Roos, J.R, Diam. Rel. Mater. **1993**, *2*, 879–884

[17] Mohrbacher, H.; Blanpain, B.; Celis, J.P.; Roos, J.R.; Stals, L.; Van Stappen, M., Wear **1995**, *188*, 130–137

[18] Mohrbacher, H.; Celis, J.P.; Roos, J.R., Tribology International **1995**, 28-*5*, 269–278

[19] Molinari, J.F.; Ortiz, M.; Radovitzky, R.; Repetto, E.A., Eng. Comp. **2001**, *18*, 592–609

[20] Ramalho, A.; Celis, J.P., Surface and Coatings Technology **2002**, 155, 169–175

[21] Williams, J.A., Wear **1999**, *225-229*, 1-17

On Scratching of Elastic-Plastic Thin Films on Elastic Substrates

F. Wredenberg, P.-L. Larsson
KTH Solid Mechanics, Stockholm, Sweden

1 Introduction

Thin films on substrates are a matter of considerable study because of its practical usefulness. There are numerous deposition techniques developed to improve their characteristics and to enlarge their field of application. The arrival of new, potentially interesting materials enhances the concern for understanding the mechanics of deformation, which allows for a better thin film design from a structural point of view and an increase of the surface durability. In practice, efforts have been directed towards improving the performance of specific parts or extending the life of components exposed to difficult environmental conditions. For example, the research dealing with quasi-crystalline coatings provided opportunities to increase the wear resistance of aluminium or steel parts in automotive systems while protective polymer coatings are an essential part in many electronic devices. From a practical standpoint, indentation has been successfully applied for a broad range of materials and is among the most widely used methods when performing the difficult task of determining the strength very near the surface. The commonly determined properties using microindentation are indentation hardness, the indentation load versus indentation depth curve and the actual area of contact. These quantities are used to determine the constitutive properties of the materials. The early theoretical works by Sneddon [1], Tabor [2] and Johnson [3], being the most notable for this purpose. Depending on the material properties and the type of indenter used, Johnson suggests that the outcome of a sharp indentation test on classical elastoplastic materials could be placed in one of three levels as specified by the parameter

$$\Lambda = \frac{E \tan \beta}{(1-\nu^2)\sigma_{\text{rep}}} \tag{1}$$

In eq. (1), E is the Young's modulus and ν is Poisson's ratio, β is the angle between the indenter and the undeformed surface (see Fig. 1) and σ_{rep} is the material flow stress at a representative value of the effective (accumulated) plastic strain. As for the three indentation levels, Level I ($\Lambda < 3$) corresponds to the occurrence of very little plastic deformation during indentation testing, meaning that all global properties can be derived from an elastic analysis. In level II ($3 < \Lambda < 40$), an increasing amount of plastic deformation is present and both the elastic and plastic properties of the material will influence the outcome of the test, and finally, in level III ($\Lambda > 40$) elastic deformation is present over the entire contact area. The last mentioned level is applicable to most engineering metals.

The fundamental knowledge about the mechanical behaviour at scratching, and in particular when it comes to scratching of thin films, is not nearly as developed as for indentation testing. Also such investigations have essentially without exception been devoted to severe scratching, i. e. fracture, delamination etc., cf. e. g. Holmberg *et al.* [4] , Subhash and Zhang [5], Malzbender and de With [6], Thouless [7] and Bull [8]. As far as a more general understanding

of the behaviour of different global (and also local) scratch variables at these types of problems is concerned, essentially only one investigation, Larsson and Wredenberg [9], has been presented. These authors studied the influence from strain-hardening and the Johnson parameter in eq. (1) on parameters such as normal and tangential hardness, apparent coefficient of friction, contact area and relevant local field variables. In doing so, the numerical strategy, based on the finite element method, developed by Wredenberg and Larsson [10, 11], was used while modified to also account for film/substrate boundary effects. The analysis was restricted to cone scratching, see Fig. 1, and the deformation of the substrate was neglected in all of the numerical simulations. However, in many situations of practical interest the deformation of the substrate severely influences the mechanical behaviour. Therefore, this feature is in the present study included in the analysis supplementing the previous results by Larsson and Wredenberg [9].

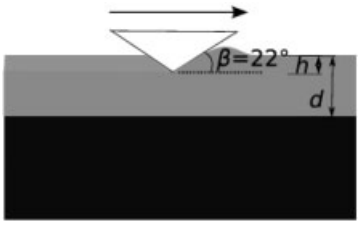


Figure 1: Scratching of a film/substrate system where the angle β defines the conical stylus/indenter. In the present study $\beta = 22°$.

2 Basic Considerations and Numerical Analysis

The present analysis concerns scratching of thin film/substrate systems using a sharp conical stylus assumed to be rigid. In order to simplify the interpretation of the results all calculations are performed for a constant scratch depth and consequently, steady-state conditions are aimed at. It is assumed that quasi-static conditions prevail and that far-field boundaries do not influence relevant global and field variables. In the presentation below F and A represent contact load and contact area respectively, indices n and t represent the normal and tangential components of these quantities and h is the scratch depth shown in Fig. 1. It should be emphasized that the contact area A is, if not stated otherwise, the true projected contact area given by the numerical simulations.

Assuming then that quasi-static and steady-state conditions prevail, the scratch problem is self-similar with no characteristic length present. Consequently, the normal hardness

$$H_{\mathrm{n}} = F_{\mathrm{n}}/A_{\mathrm{n}} \tag{2}$$

and the tangential hardness,

$$H_{\mathrm{t}} = F_{\mathrm{t}}/A_{\mathrm{t}} \tag{3}$$

as well as the ratio $h/\sqrt{A}$ are constant during the loading sequence of a scratch test on homogeneous materials and stresses and strains are functions of the dimensionless variables $x_i/\sqrt{A}$ (the Cartesian coordinate system is shown in Fig. 2 and material properties alone. At scratching (or

normal indentation) of thin film/substrate systems this is of course not the case, as at increasing load, the field variables also depend on the ratio h / d (d being the film thickness as shown in Fig. 1). However, when the indentation depth is held constant during the test steady-state conditions prevail and the global quantities defined above are constant facilitating a direct comparison with the corresponding homogeneous solution.

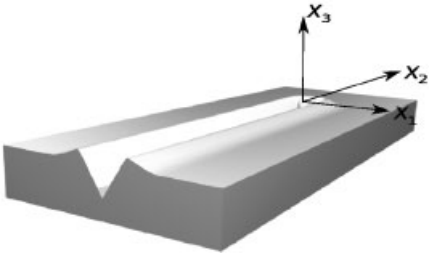


Figure 2: Cartesian coordinates x_i (following ht tip of the stylus). Scratching is performed in the x_2 direction

In the present analysis, as indicated above, it is assumed that the material behaviour of the film is adequately described by classical elastoplasticity and elasticity is accounted for as far as the substrate is concerned. The material strain-hardening is described by a standard power law relation according to

$$\sigma(\varepsilon_{\mathrm{p}}) = \sigma_{\mathrm{Y}} + \sigma_0 \varepsilon_{\mathrm{p}}^{n} \tag{4}$$

where $\sigma(\varepsilon_{\mathrm{p}})$ is the material flow stress, σ_{Y} is the initial yield stress, ε_{p} is the Mises effective strain and σ_0 and n are material constants.

The resulting boundary value problem becomes very involved (in particular so as a film/substrate boundary is introduced into the problem) and it is necessary to use the finite element method in order to arrive at results of acceptable accuracy. The basic numerical scheme and meshing for an analysis of the corresponding homogeneous problem is developed by Wredenberg and Larsson [10] and further developed for thin film problems by Larsson and Wredenberg [9]. This scheme was closely adhered to also in the present investigation. The numerical simulations were performed using finite element methods implemented in the commercial FEM package ABAQUS. As the material experienced very large strains, ALE adaptive meshing was used to maintain the element integrity. The mesh was composed of approximately 170000 linear eight node elements including both substrate and film elements. The number of elements would however vary slightly with the film thickness in the case with a rigid substrate.

3 Results and discussion

The results presented and discussed below concern the mechanical behaviour at scratching of thin film/substrate systems. The presentation is devoted to an analysis of the influence from the film/substrate interface on global scratch quantities. In all cases when the Johnson parameter in eq. (1) was used in order to evaluate the results, the representative stress level corresponded to

$$\sigma_{\text{rep}} = \sigma(\varepsilon_{\text{p}} = 0.08). \tag{5}$$

This choice is not of importance for the evaluation of the numerical results but was done based on the suggestion by Tabor [2] and is convenient to use when comparing different results. Explicit material constants (E, σ_0) were chosen so that σ_{rep} always takes on the value of 210 MPa for strain-hardening materials. In such a case the values $\sigma_{\text{Y}} = 105\,\text{MPa}$, ν = 0.3 were fixed. At perfect plasticity, however, the value $\sigma_{\text{Y}} = 210\,\text{MPa}$ was chosen.

It seems appropriate to start the present discussion with some previous results by Larsson and Wredenberg [9] concerning the case of scratching of elastoplastic thin films on hard (rigid) substrates. In [9], among other things, the behaviour of the indentation hardness and the contact area ratio,

$$c^2 = \frac{A}{A_{\text{nom}}},$$

where A is the actual (true) contact area and A_{nom} is the nominal contact area (given by purely geometric considerations for a cone indenter with $\beta = 22°$ and assuming no piling-up or sinking-in of material at the contact contour), was investigated for materials with the strain-hardening exponent in eq. (4) being $n = 3$ with the corresponding values for the Johnson parameter in eq. (1) being $\Lambda = 8$ and $\Lambda = 200$ respectively. The results for the hardness values are depicted in Fig. 3. Clearly at approximately $h / d < 0.2$ the presence of an interface does not influence the global properties. This being so not only for the normal and tangential hardness but also for all the scratch quantities considered, i. e. normal and tangential hardness and contact area ratio, even though boundary effects for the material pertinent to $\Lambda = 8$ are slightly more evident due to pronounced elastic effects. It should be mentioned in this context that the nominal contact area at scratching is calculated assuming that the contact boundary is a half-circle, this being a standard assumption at scratch test evaluations.

The present results for scratching in Fig. 3 are restricted to a single value on the material exponent n ($n = 3$). For the sake of generality, Larsson and Wredenberg investigated other types of hardening and in doing so, perfect plasticity ($n = \infty$) and linear strain-hardening ($n = 1$), with the value on the Johnson parameter being $\Lambda = 200$, were singled out for attention. Details are shown in Fig. 4. In short, scratching of perfectly plastic materials was less influenced, than the corresponding results shown in Fig. 3 for $n = 3$, by the presence of a film/substrate interface while the effect from the interface is most obvious for the linear hardening material. This is of course a direct consequence of the mechanical field behaviour at contact loading as large deformations and high stresses are more confined to the contact region at perfectly plastic material behaviour leading to a substantially larger plastic zone in case of a linear hardening material.

The main purpose of the present investigation concerns the influence from elastic deformation of the substrate. Representative results for this purpose is shown in Fig. 5 where the normal scratch hardness is depicted as a function of the ratio

$$\eta = \frac{E_{\text{substrate}}}{E_{\text{film}}},$$

between the two modulii of elasticity. The thin film is characterised constitutively by $n = 3$, $\Lambda = 8$ and $E_{\text{film}} \approx 3.8$ GPa (the substrate is as mentioned above assumed purely elastic). The

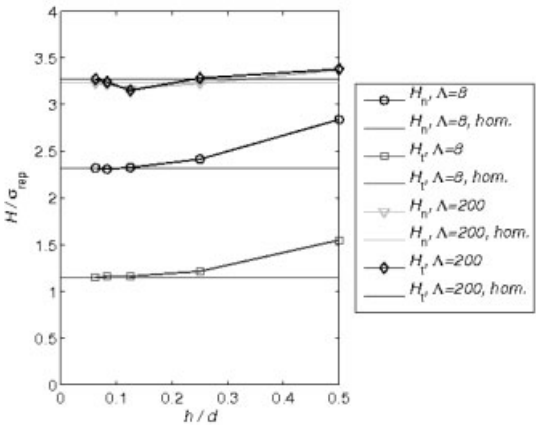


Figure 3: Normalized hardness results by Larsson and Wredenberg [9] for scratching of film/substrate systems. $\Lambda = 8$ and $\Lambda = 200$. Strain hardening material with exponent $n = 3$. The solid lines indicate the homogeneous results. The substrate is assumed rigid.

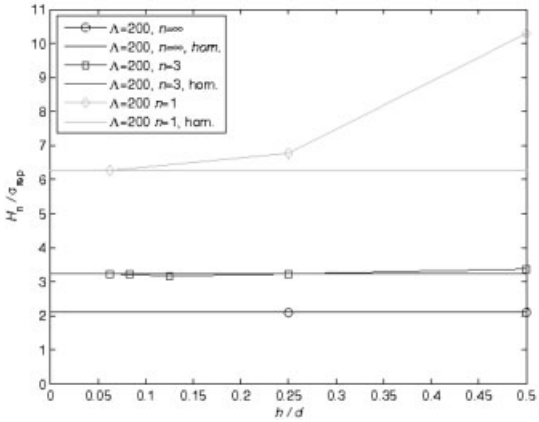


Figure 4: Results by Larsson and Wredenberg [9] for scratching of film/substrate systems with different hardening exponents n. The solid lines indicate the homogeneous results. The substrate is assumed rigid.

scratch thickness was chosen to be $h = d / 3$ in order to make sure that substantial influence from the interface was present. It is quite surprising that the influence from the deformation of the substrate is small. Indeed, the results in Fig. 5 show that even when $\eta = 1$ the deviation of hardness results (from the solution where the substrate is assumed rigid) is less than 10 % (which can also be deducted from Fig. 3). This indicates that the assumption of a rigid substrate, which is computationally favourable, gives results of sufficient accuracy in many situations of practical interest. It should of course be mentioned that the present study is restricted to the case when the substrate is stiffer, or equally stiff as, than the film i.e. $\eta \geq 1$, and that plastic deformation of the substrate is neglected.

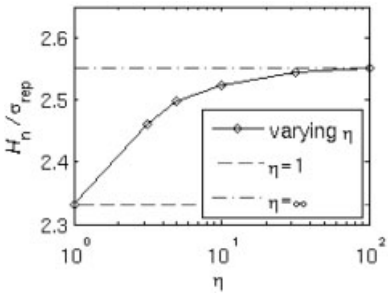


Figure 5: Present results for scratching of film/substrate systems with $n = 1/3$, $\Lambda = 8$ and $h/d = 1/3$. The substrate is assumed deformable.

4 Conclusions

In the present analysis, scratching of film/substrate systems was analysed numerically with particularly the influence from elastic deformation of the substrate in mind. The main conclusion from the present limited investigation is that as far as global properties are concerned, the influence is small at least when the substrate is stiffer (or equally stiff as) the film.

References

[1] Sneddon, I. N., Int. J. Eng. Sci. **1965**, 3, 47–57.

[2] Tabor, D., Hardness of Metals, Oxford University Press, Oxford , **1951**.

[3] Johnson K. L., J. Mech. Phys. Solids, **1970**, 18, 430–435.

[4] Holmberg, K., Laukkanen, A., Ronkainen H., Wallin K. and Varjus S.,Wear, **2003**, 254, 278–291.

[5] Subhash G and Zhang W., Wear, **2002**, 252, 123–134.

[6] Malzbender J. and de With G., Surf. Coat. Technol., **2001**, 135, 202–207.

[7] Thouless M. D., Eng. Fract. Mech., **1998**, 61, 75–81.

[8] Bull S. J., Surf. Coat. Technol., **1991,** 50, 25–32.

[9] Larsson P.-L. and Wredenberg F. J. Phys. D: Appl. Phys., **2008**, 41, 074022.

[10] Wredenberg F. and Larsson P.-L., J. Mech. Mater. Struct., **2007**, 2, 573–594.

[11] Wredenberg F. and Larsson P.-L., *Technical Report* 416, KTH Hållfasthetslära, 10044 Stockholm. **2006**

Tribological Approach of Forming Tool Performance Based on Finite Element Modelling (FEM)

Ricardo Hernández[1,2], Marlon R. Cruz[1], Ingrid Picas[1], Maria.Dolors Riera[1,2], Daniel Casellas[1]
[1]Department of Materials Technology, CTM-Technologial Center , Av. Bases de Manresa 1, 08242 Manresa (Spain)
http://www.ctm.com.es
[2]Department of Materials Science and Metallurgy Engineering, Universitat Politècnica de Catalunya, Avda Bases de Manresa 61, 08242 Manresa (Spain)

1 Introduction

The excellent combination of high mechanical strength, high elongation and strain hardening of Advanced High Strength Steels (AHSS) has permitted their increasing use in the automobile industry to reduce vehicle weight and thereby fuel consumption while improving crash performance. However, the implementation of AHSS has generated difficulties related to the mechanical performance of forming tools. Due to their high yield stress, forming AHSS implies high pressures that accelerate wear, even leading to their catastrophic and premature failure [1, 2]. Thus, a proper mechanical design of tooling is needed in order to optimize the process efficiency that must be conducted considering the acting damaging mechanisms: wear and fatigue

In this sense, a methodology that allows accurate wear prediction would be very helpful. Computer simulation by means of finite elements modelling (FEM) has been widely used in sheet metal forming for determining the sheet formability, evaluating the springback and calculating the press force. More recently it has been also used for evaluating mechanical solicitations on tools in AHSS drawing [2]. FEM could also give valuable information for wear prediction [3, 4].

Thus, the aim of this work is to simulate the wear behaviour of tools during AHSS sheet forming by FEM.

2 Experimental procedure

2.1 Computer simulation

The simplest approach to evaluate wear in tools is to simulate the forming process, obtaining the contact pressure distribution along the tool surface, as well as the relative sliding movements between the tool and the work-piece. Wear models are used to correlate the volume loss with the forces acting perpendicularly to the surface and the relative sliding movement between contacting surfaces. The Archard's model is one of the most accepted ones to evaluate wear behaviour [5]:

$$V = KFX/H \tag{1}$$

where V is the volume loss, F is the normal load, X is the relative sliding distance between the mating surfaces, H is the hardness and K is a wear coefficient, which depends on lubrication, materials interaction etc.

The values of F and X obtained by computer simulation of tools can be used to directly obtain the volume loss, the wear and thus the tool life. However, this approach leads to mistakes since such calculation is performed considering the original geometry of the tool and wear is localized in one region (where there is the highest pressure in the initial step). Considering that wear changes the surface tool geometry, the contact pressures are also modified and thus wear estimation must take into account such effects.

A better strategy is to perform cyclic updates of the surface tool geometry during tool life. Such approach has been used in the simulation of fretting wear [4]. In this way, wear estimation is associated to a number of discrete simulations, that are implemented on the surface tool geometry modified by the wear during the previous step. Such methodology has been implemented on ABAQUS/Standard software by adaptative meshing techniques and controlled by the UMESHMOTION subroutine. However, there is an important limitation, it can be only applied to processes where a steady state is reached from a geometrical point of view, and where geometrical changes are only due to wear. For example, drawing, rolling, extrusion and machining can be analysed with this procedure.

Aimed at studying wear on tools, such methodology has been implemented by programming a *script* by *Python*. Simulations are performed in this script modifying the geometry of the contacting surfaces following the previous simulation. The simulation strategy is summarized in figure 1.

With respect to simulation details, the size of the contact elements is 0.1 mm, and a penalty contact with a friction coefficient of 0.15 is used.

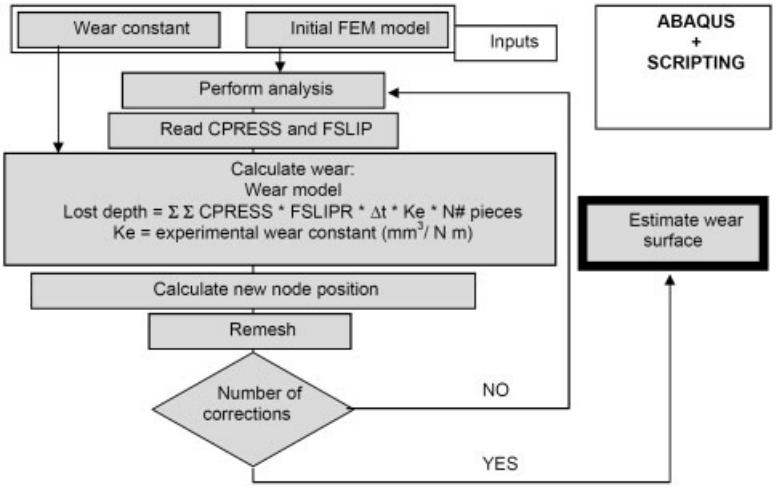


Figure 1: Simulation strategy

2.2 Forming Process and Materials

A drawing process of a 2 mm thick sheet of TRIP800 has been simulated (see figure 2). The metal sheet was considered as isotropic, with a Young modulus of 210 GPa and a Poisson's ratio

of 0.3. The elastoplastic behaviour has been evaluated in tensile specimens and incorporated in the simulation. The tool has been simulated as an elastoplastic material, with a yield stress of 1800 MPa. The chosen tool material is a cold work tool steel DIN 1.2379, due to their wide applicability in cold forming.

Wear resistance was evaluated by using the pin-on-disk tribometer (ASTM G99-95A). It should be emphasized that the real tribological pair has been characterized: the disk was made of a TRIP800 sheet, and the pin was the 1.2379 tool steel heat treated at 60-62 HRC (the usual hardness range when forming AHSS). The obtained experimental wear constant, Ke, is 1.06 10^{-6} $mm^3N^{-1}m^{-1}$. The friction coefficient measured between the tool steel (pin) and the sheet of TRIP800, with oil in the surface as it is usually formed, is 0.15.

Tools have been mounted in an experimental die and a total number of 3,500 strokes have been done. Tool wear was measured by a coordinate measuring machine.

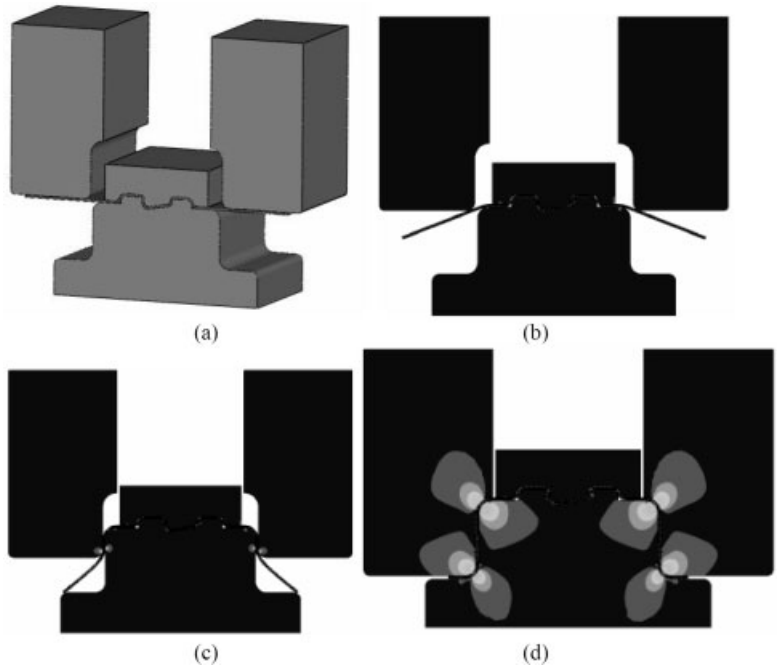


Figure 2: (a) Simulation of drawing a TRIP800. (b)–(c) After 10 % and 50 % of the total forming time respectively. (d) Final position of tools and stress distribution in the final step.

3 Experimental results

The stress distribution on tools is showed in figure 3. It shows that the higher contact stresses (about 450 MPa) together with the largest sliding distance, are located close to the corner of the forming tool (see figure 3(b)), is important to emphasize that the wear is controlled by the contact pressure, but in this case Von Mises stress peaks appears here close to the contact pressure peaks.

Simulation results show that wear damage is more pronounced in this region. In order to quantify wear, the actual radius of different positions along the tool surface in the analyzed punch radius has been obtained (figure 4). A decrease of the radius of about 0.05 mm is expected after 3,500 strokes in the most worn area.

Experimental measurements on tools are showed in figure 5. They fit reasonably well with the FEM results, but it should be noted that the measured values are within the machining tolerances. However, it is found that wear damage is located at the area predicted by FEM results.

Thus, it can be said that the proposed methodology can be used to understand the wear behaviour of tools, but currently, wear can not be quantified. More experimental results, after 10,000–20,000 strokes, are needed to validate the proposed methodology (bench tests are currently running).

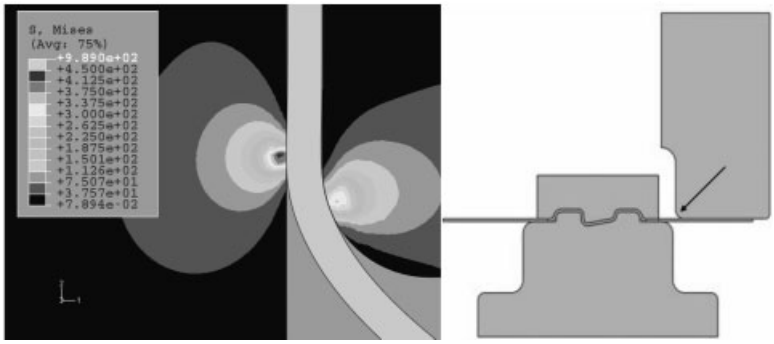


Figure 3: (a) Stress distribution on tools showing the location of the higher contact pressures. (b) The wear damage is concentrated near the corner indicated by the arrow.

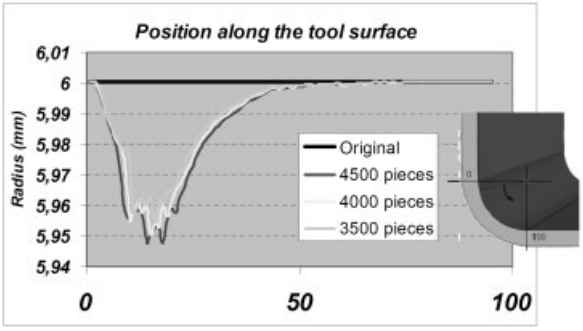


Figure 4: Evolution of the radius of the tool corner along the tool surface (from 0 to 100) obtained from FEM.

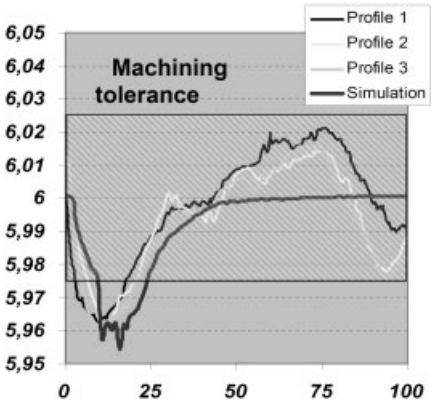


Figure 5: Experimentally measured profiles in the tool surface. The shaded area corresponds to the machining tolerance.

4 Conclusions

From the FEM results as well as the geometrical measurements of wear on tools the following conclusions can be drawn:

- A methodology for wear estimation based on FEM has been proposed.
- It is very important for obtaining correct wear estimation to select the appropriate wear model and to determine the wear constants by experimental tests.
- Currently only 3500 pieces have been produced in the bench tests that are not enough to give marked wear on tools. Changes in tool surface profile are within the machining tolerance
- However experimental measurements on tools are close to simulation. Bench tests are still running and future results will allow confirming the applicability of the proposed methodology

Acknowledgments

This work is part of the tasks held by the authors in the FORMA-0 project, supported by CDTI (Spanish National Board for Technological and Industrial Development) within the CENIT frame of National funds. The authors want to acknowledge the technical support of J. Blanch and J. Pedragosa of TROE S.L., and M. Villafranca of MOL-MATRIC S.C.C.L.

References

[1] H. Berns, C. Broeckmann, *Eng Frac Mec*. 1991, 58, 311–325

[2] R. Hernández, M.D. Riera, D. Casellas, I. Valls, B. Casas and J.M. Prado, in MS&T 2007: AUTOMOTIVE: Advanced High strength and other specialty steel products for the auto-

motive industry (Eds. J. Fekete, I. Garcia, J. Speer and M. Walp), Detroit, USA, 2007, pp. 235–243

[3] D. Hortig, D. Schmoeckel, Journal of Materials Processing Technology 2001, 115 153–158.

[4] I.R. McColl, J. Ding, S.B. Leen, Wear 2004, 256, 1114–1127.

[5] J.F. .Archard, J. Appl. Phys. 1953, 24, 981–988.

[6] D. Casellas, J. Caro, S. Molas, A. Beltran and J.M. Prado in 7th Tooling Conference, Tooling materials and their applications from research to market (Vol I) (Eds M. Rosso, M. Actis Grande, D. Ugues), Politecnico di Torino, Torino, Italy, 2006, pp 707–714

Computation of Die Loads in Sheet Forming Using Dies of Tool Steel with Improved Anti-galling Properties

A. Thuvander, O. Sandberg
Uddeholm Tooling AB, Hagfors, Sweden

1 Introduction

Sheet metal forming usually involves a sliding contact under high pressure between the sheet material and the die. Under these conditions it is common that galling occurs, which means that fragments of the sheet material is transferred to the active surface of the die. The pressure between the sheet and the die is one of the most important conditions that influence galling. High strength sheet materials can usually resist galling at higher pressure than softer sheet materials but the improvement in galling resistance is not enough to compensate for the increasing contact pressure and the temperature that result with increased strength. Accordingly the expanding use of high strength sheet materials in the automotive industry will increase the cost for tool maintenance due to galling damage.

The traditional method to improve the galling resistance for dies that are subjected to high contact pressure is surface treatment. The recent development of a nitrogen alloyed high performance PM tool steel has introduced an alternative to surface treatment. The steel has high galling resistance even without a coating and can in many cases replace a surface coated tool steel.

In order to predict in which applications the new type of tool steel can be recommended a method to determine the loads caused by the application is required as well as a model that gives a critical load for galling.

In the present paper FEM was used for prediction of the contact pressure between the sheet and the die and the galling limit was expressed by a simple criterion based on the contact pressure and the strength of the sheet. To calibrate the critical pressure a number of application tests were run and the same cases were simulated with FEM.

2 Tool material

All tests and simulations were performed with the cold work tool steel Uddeholm Vancron 40, which is a nitrogen alloyed PM steel. It was developed in order to create a tool material that can be used without coating but still have properties that are comparable with coated PM steels.

The material has the nominal composition shown in Table 1.

Table 1: Nominal composition of Uddeholm Vancron 40 in weight per cent.

C	N	Si	Mn	Cr	Mo	W	V
1.1	1.8	0.5	0.4	4.5	3.2	3.7	8.5

3 Modelling

The tendency for galling depends on several factors where one of the most important ones is the contact pressure in sliding contact. Other important factors are the friction, the strength of the sheet material and the surface roughness of the tool.

We here concentrate on the initiation and the early stages of material pick-up on the tool. The initiation is believed to take place on a surface defect or on an asperity from surface roughness on the die [1]. One can expect that with a high surface pressure even small surface defects can initiate galling. Pressure dependence of the growth of material pick-up has been reported by several authors [2, 3].

In our prediction we assume that the surface roughness on the tool is low and the lubrication as well as the sliding speed is similar in all cases. We then have the strongest influence from the contact pressure and the sheet material properties. The sheet material influences galling both by its adhesion to the tool material and by its strength. Increasing adhesion lowers the galling resistance, while increasing strength contributes to resist abrasive wear [2, 4] and as a consequence improves the galling resistance [3]. We thus assume that galling is initiated when the contact pressure p exceeds a value proportional to the ultimate tensile strength R_m of the sheet. The galling initiation criterion that we use here is

$$p > p_{crit} = C\,R_m \tag{1}$$

The constant C will depend on a number of factors but we here separate the fitting of C only for different types of sheet materials, on one hand carbon steel of the types high strength steel (HSS) and advanced high strength steels (AHSS) and on the other hand austenitic stainless steel. We also expect an influence of the tool material but the values used here were all evaluated from tests with Uddeholm Vancron 40.

The pressure was computed from FE simulation of each application using the FEM code ABAQUS [5]. In these simulations the sheet materials were assumed to be elastic-plastic and the tools were modelled as elastic parts. Solid elements were used. Most simulations were run in two dimensions, either with axi-symmetry or with plane strain.

4 Results from Application Tests

The calibration of the galling limit was performed by analyzing a number of application tests with the tool steel Uddeholm Vancron 40. One example of the tests is a U-bending operation performed in progressive dies shown in Figure 1. The sheet was a 2 mm Docol 800DP steel. The test was successful; i. e. galling was not a problem at the normal forming speed. Results from this test have been reported previously [6].

A second successful application involved a deep drawing application on 0.5 mm sheet of austenitic stainless steel AISI 304 Results from this test were published previously [7]. The progressive die set-up is shown in Figure 2.



Figure 1: Forming of a reinforcement part to the B-member in 2 mm thick Docol 800DP.

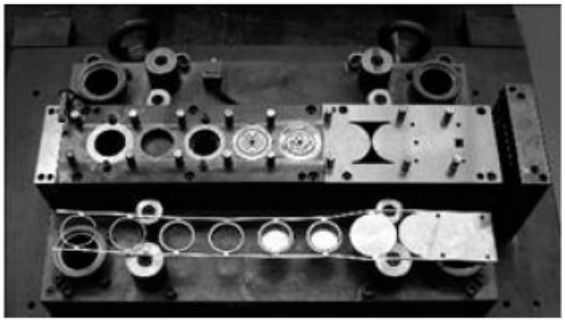


Figure 2: Deep drawing of a cup in 0.5 mm AISI 304.

5 Results of Simulations

In the application with U-bending of 2 mm 800 DP steel sheet, Figure 1, galling did not occur. The computed contact stress distribution is shown at the instance when the highest stress peak occurred in Figure 3. The maximum pressure was 1241 MPa.

The computed maximum pressure during the deep drawing operation of stainless steel sheet from Figure 2 is shown in Figure 4. The pressure distribution contains two peaks. The highest peak is about 600 MPa.

The resulting maximum pressure from the above simulations as well as other tests were plotted versus the tensile strength of the work material. The results for low alloyed high strength sheet steel are shown in Figure 5 with the symbol representing the case of Figure 1 encircled. Different symbols indicate successful application tests and tests where galling occurred.

A line corresponding to equation (1) was introduced to separate the two types of points. For the high strength sheet steels the parameter C was set to 2, indicating that a maximum die pressure up to twice the tensile strength of the sheet material can be accepted for Uddeholm Vancron 40. However, the number of data points is still too small to verify how well this result can be reproduced

occurred in Figure 3. The maximum pressure was 1241 MPa.

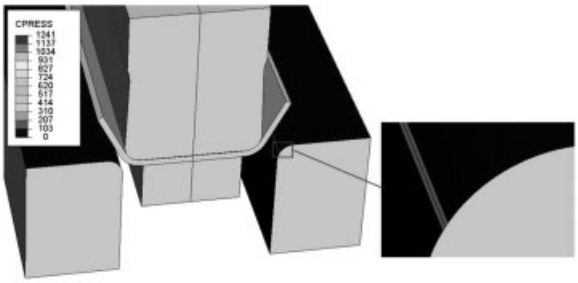


Figure 3: Computed distribution of contact pressure (MPa) on dies during U-bending operation.



Figure 4: Computed distribution of contact pressure (MPa) during deep drawing operation on 0.5 mm AISI 304.

During forming of austenitic stainless steel sheet galling generally occurred at lower contact pressure than for low-alloyed steel sheet. When the results of the application tests and computations were compared the galling limit was found to be approximately at $1.5R_m$ as shown in Figure 6. The symbol representing the case of Figure 2 is encircled.

6 Discussion

The intention with the above simulations was to create a method to decide in which applications the new uncoated nitrogen-alloyed tool steel is a suitable choice of die material. The analysis can presently be performed by running the simulation prior to the introduction of the material. If the computed contact stress is below the galling limit it should be possible to use the tool steel.

No comparison has been made to other tool steels in the present study. However, lab tests with D2-type tool steel have been published [4]. In the tests strips of cold rolled steel sheet of ultimate tensile strength in the range 295 to 464 MPa are sliding against the tool at various pressures. It was found that the galling pressure limit was approximately 1.2 times the yield strength, which

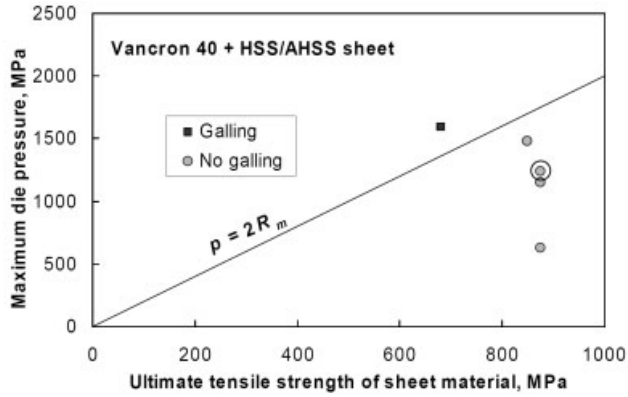


Figure 5: Computed maximum contact pressure on the die in different applications plotted versus the ultimate tensile strength of the formed low alloyed steel sheet. Different symbols indicate the outcome of the application test in terms of galling.

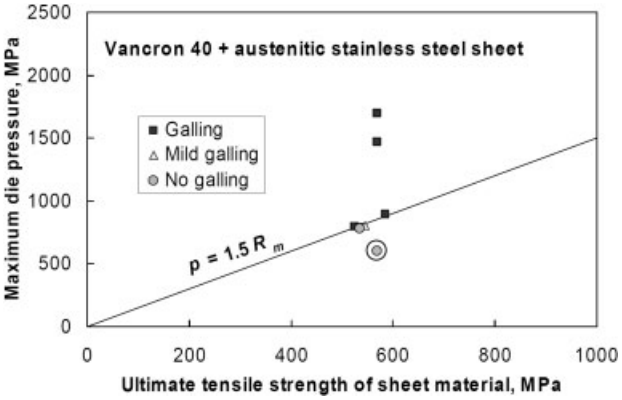


Figure 6: Computed maximum contact pressure on the die in different applications plotted versus the ultimate tensile strength of the formed stainless steel sheet. Different symbols indicate the outcome of the application test in terms of galling.

is less than the ultimate tensile strength. This could indicate that the new nitrogen alloyed steel has a galling limit, which is more than twice the galling limit of D2.

Even for a simple model as the one described here the number of data points to calibrate the model is too low. Furthermore, more data are necessary in order to construct a more advanced model which takes surface roughness and sliding speed into account.

The linear influence of the strength of the sheet on the galling limit that we assume in equation (1) was selected mainly because of simplicity. Other simple variants could be to assume a linear dependence of the yield strength . In any case, the relation between the galling limit and the strength is probably not linear through the whole pressure range since there should not only be an influence of the sheet strength but also an effect of lubrication and heat generation, which would

probably lower the slope of critical pressure versus sheet strength at high pressure. This would also be consistent with the apparently contradictory fact that increasing strength can both improve the galling limit and at the same time cause more severe galling. This would appear when the increase in galling limit is not enough to compensate for the increase in contact pressure from the higher forming load.

7 Conclusions

A measure of the galling limit of the tool steel Uddeholm Vancron 40 was estimated by a combination of application tests and numerical simulations by FEM.

- During forming of low alloyed steel galling occurred when the computed maximum contact pressure exceeded twice the ultimate tensile strength of the sheet material.
- For austenitic stainless steel sheet galling occurred if the computed maximum contact pressure exceeded 1.5 times the ultimate tensile strength of the sheet material.
- The calibrated criterions could separate all successful tests from those where galling occurred except a few test results that were very close to the limit.

8 References

[1] Schedin, E. and Lehtinen, B., Galling Mechanisms in Lubricated Systems: A Study of Sheet Metal Forming, Wear, *170*, **1993**, p. 119–130

[2] Archard, J.F. Contact and rubbing of flat surfaces. J. Appl. Phys. *24*, **1953**, p. 981–988

[3] de Rooij, M. B., Schipper, D. J., Analysis of Material Transfer From a Soft Workpiece to a Hard Tool: Part I – Lump Growth Model, J. Tribol. *123*, **2001,** p. 469–473

[4] Fujinaga, C., Kobayashi, T., IIzuka, E., Shimizu, T., Hira, T., Furukimu, O., Effect of Strength of Steel Sheet on Frictional Behavior, SAE Document 2000-01-0407, Presented at SAE 2000 World Congress, March **2000**, Detroit, MI, USA

[5] Manual to ABAQUS, Version 6.7, Dassault Systèmes, **2007**.

[6] Sandberg, O., Bustad, P-Å., Carlsson, B, Fjällström, M., Johansson, T., *International Conference on Recent Advances in Manufacture & Use of Tools & Dies and Stamping of Sheet Steels, 5-6 October 2004, Olofström, Sweden,* **2004**, p. 151–169

[7] Madsen, E., Scholer Sorensen, O., Heikkilä, I., *International Conference on Recent Advances in Manufacture & Use of Tools & Dies and Stamping of Sheet Steels, 5-6 October 2004, Olofström, Sweden,* **2004**, p. 215–229

Wearing Effects in Cutting Processes – Development of a Combined Simulation Approach

Uwe Großmann, Marcus Rechberger, Jan Blömer, Jürgen Bertling
Fraunhofer UMSICHT, Osterfelder Str. 3, 46047 Oberhausen, Germany

1 Motivation

Cutting is a frequently used process – not only in everyday life but also in many technical processes in the wood, plastics, food or textile industry. The performance of the cutting device is mainly determined by the first few microns of the knife forming the cutting edge (Fig. 1). Therefore, the cutting process is very sensitive to wear, while in the industrial production wear on tools causes immense expenses, mainly due to outage times, non-scheduled maintenance, overhaul and inventory costs for spare parts. To increase the wear resistance of the knife, different hardening and coating processes are commonly used.

To increase the understanding of the wear in dependence of material and geometrical parameters, the load on the blade has to be analysed with a high spatial and temporal resolution. These data are nearly not accessible experimentally and single simulation approaches can only provide specialised information. Therefore, here different simulation methods are combined to analyse the whole process. Finite-Element-Simulations (FEM) are used to calculate the cutting forces and the Discrete-Element-Method (DEM) is used to calculate the abrasion and change of shape.

2 Approach

The wear at the cutting edge is a very complex and multi-scale problem. The effect not only depends on the material properties of the blade, but also on the material properties of the cutting good – especially on the tribological interaction between these materials. Furthermore, hundreds of meters of cutting length are required to obtain only a few microns of wear on the edge. Therefore, just one single approach is not sufficient to model and understand the basic principles of the wear. In the combined approach, different simulation techniques, experimental data and empirical relations are combined (Fig. 2). Material tests are required to obtain the necessary data like Young's modulus, friction coefficient, and shore hardness for the simulations. Additionally, tribological examinations are made. FEM-Simulations are performed on the basis of these data to model the complete cutting process. Nevertheless, further calibration, especially of the tribological data, is required. Therefore, the simulations are compared to cutting experiments. During these calibrations, the material properties of the cutting good are varied while the material and the geometry of the blade and the friction coefficient between blade and cutting good are not altered. This is especially required because the material properties may be different from (quasi-static) literature data because of the high cutting velocity.

This device provides the normal force of the cutting procedure. It is assumed, that after fitting the normal force, the model is suitable to provide other data which are not accessible experimen-

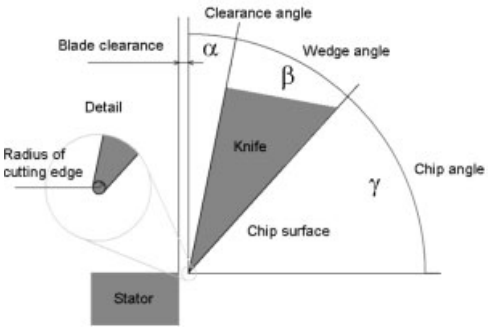


Figure 1: Technical terms of the cutting process

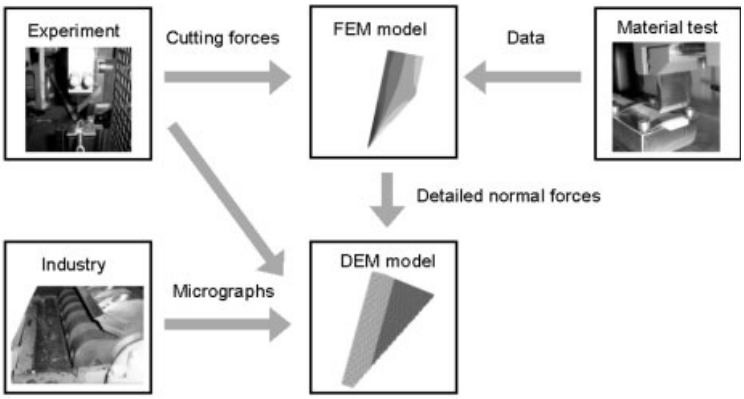


Figure 2: Different components of the approach

tally. The FEM simulations supply input data to the more detailed DEM simulations, such as the distribution of normal forces on the surface between chip and knife.

A laboratory device was constructed to perform cutting experiments under well defined conditions. In the stator, a piezo force sensor is integrated which measures the normal cutting force with a high frequency (60 kHz). Cutting speeds between 1 and 8 m/s can be used. The cutting material is an endless rod (diameter 8 mm) which is fed with a feeding speed automatically calculated in dependence of the desired chip length and cutting speed. Several sorts of TPE – varying in shore hardness and filled with chalk as additional abrasive to reduce measurement time - are applied as cutting material. Firstly, different blades of steel and aluminium are tested for the validation of the simulations.

The DEM was originally developed for the calculation of geotechnical tasks [1], and soon it was extended to process engineering problems [2, 3]. The advantage of DEM in comparison to FEM is the possibility to simulate abrasion and fractures in homogeneous and heterogeneous material with relatively little effort because the material is represented by single, discrete, free elements – usually spheres. Usually, springs, dashpots and friction are used to describe the interac-

tion between the elements (Fig. 3). To describe solid materials bonds are introduced additionally, which allow the description of bending and torsion moments (Fig. 4).

As usual in DEM the microscopic parameters have to be derived from the macroscopic, continuum mechanical properties of the material by calibration because of the lack of a closed transformation. Despite this handicap, tests show that essential effects of breaking and abrasion characteristics can be modelled by DEM correctly, although it is only a coarse model of the real material, if the parameters are sufficiently calibrated [4, 5].

The failure of the connections under defined conditions (max. force, max. elongation) makes it possible to model the breaking behaviour of different materials by DEM [6, 7]. Furthermore, DEM has already been used in wear simulations in the past [8].

Wear cannot be modelled directly, because of the high computational costs of DEM and the multi-scale character of wear. Hence, the simulation should yield a realistic picture of abrasion with a much smaller number of cuts. Therefore, the simulations have to be done with altered material properties, and reasonable care has to be taken in comparing simulation and experimental results.

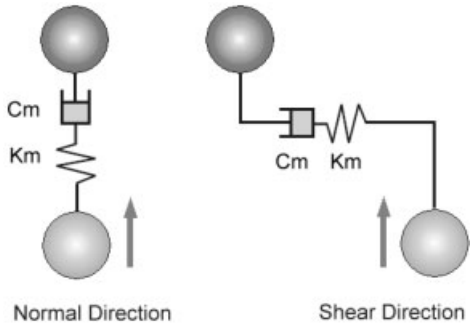


Figure 3: Maxwellmodel of the interaction of elements (granular matter

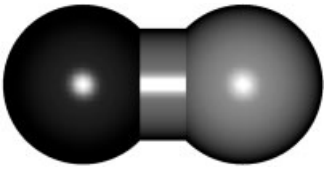


Figure 4: Model of two elements connected by a bond (solid material)

3 Results

Figure 5 shows the measurement of the normal force in a cutting experiment in relation to different cutting lengths (cutting speed 8 m/s, wedge angle 30°, clearance angle 20°, uncoated blade, cutting material TPE, 3 mm chip length). It can be seen, that the shape of the curve changes

dramatically with the first 40 m of cutting length, compared to its characteristics when a new knife (cutting length = 0 m) is used. The change from 40 m to 120 m and for the further steps, however, is much smaller. This indicates that there is a lot of wear during the run-in period, whereas later the change of the shape is much smaller. This effect is also known from literature [9]. Furthermore, it can be seen, the initial slope of the force is nearly constant, even after 600 m of cutting length. In this regard, it has to be noticed that the cutting good has a cylindrical shape which causes a variable cross section during the cut.

FEM simulations using the same conditions as in the experiments described above were performed (Fig. 6).

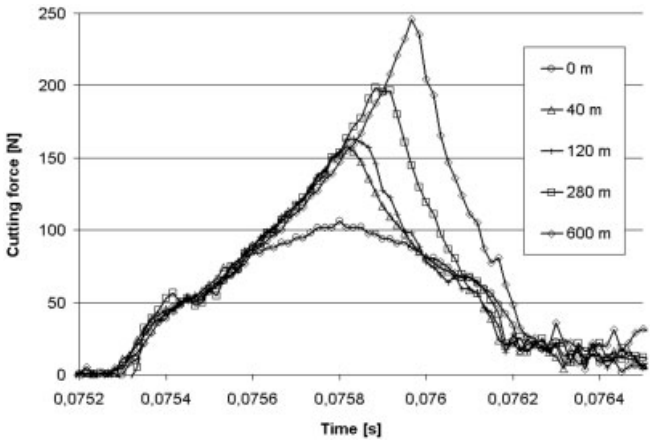


Figure 5: Normal cutting force depending on the cutting length.

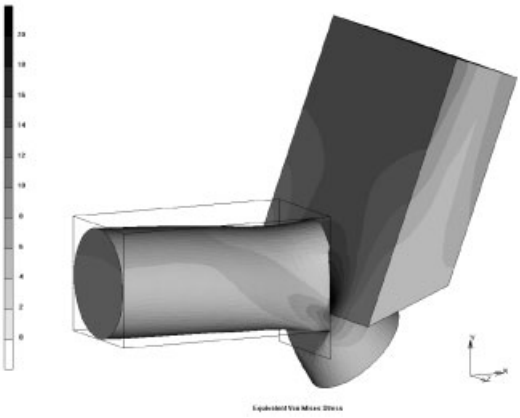


Figure 6: FEM-model

The Young's modulus of the cutting good is used to adapt the simulation results to the experimental values. Figure 7 shows the dependence of the cutting force on the Young's modulus. The FEM calculations were calibrated by data of the various laboratory tests. The properties of the cutting material in the FEM simulation were slightly ad apted, until the course of the normal cutting forces matched the experimental results as described above (Fig. 8). The Young's modulus for the cutting good is higher than the commonly used value because of the high loading velocity and the compression of the material in the cutting zone. Insights in the relative speed between chip and chip surface were provided. The normal forces could be determined with high resolution – depending on the model size.

Unlike the FEM model, the DEM model only represented the outermost tip of the knife (100 microns) to reduce the computational costs. This is reasonable because the important wear is located only near the tip of the knife. The material was represented by an irregular assembly of spheres. To prevent a regular assembly which would cause a preferred direction of breaking and wear, the radiuses of the single elements were varied between 100 % and 90 % of their maximum sizes by random distribution [10]. Parallel to the cutting edge, periodic boundary conditions were applied to virtually model an infinite blade.

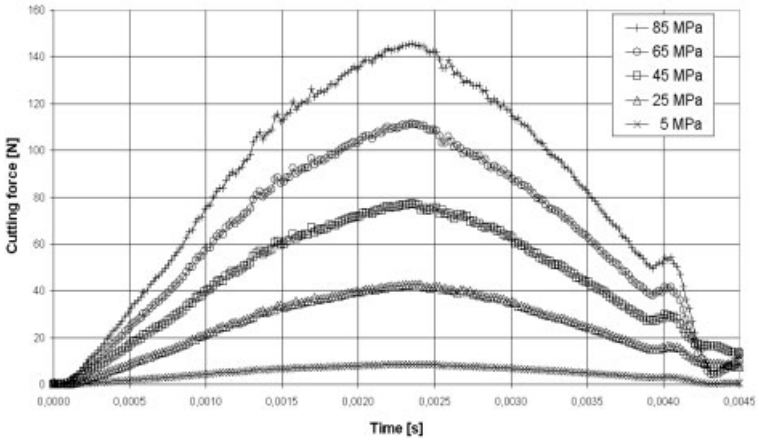


Figure 7: Simulated cutting forces depending on the Young's modulus.

The wedge angle, clearance angle and chip angle are freely eligible within a certain range. The properties of the elements and their interactions can be modified to simulate different coatings, gradients and diffusion zones.

To get appreciable wear in reasonable simulation times, it is necessary to alter the material properties of the blade and the cutting good: The blade was modelled with a high stiffness, but with a reduced breaking threshold of the interactions. This ensures loss of material without large deformations of the knife. In the cutting good the breaking threshold was increased to increase the cutting forces.

During the simulations, the knife was fixed, and the material was moved against the cutting edge. To reduce the amount of discrete elements, only the elements close to the wedge were simulated. For this, periodic boundaries in vertical direction were used. Elements leaving the

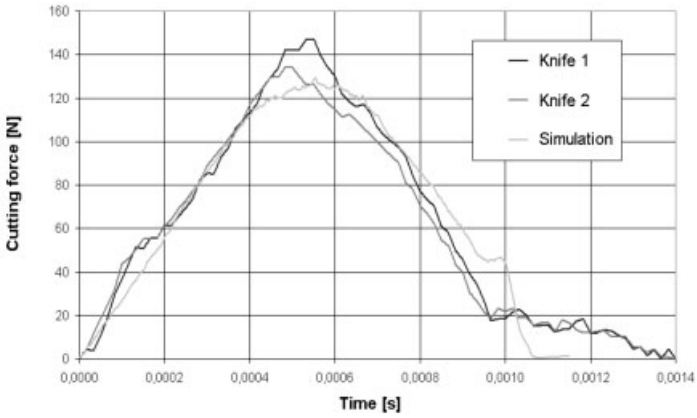


Figure 8: Comparison of cutting forces experiment/simulation

simulation zone at the top were fed back to the bottom while all other interactions were removed, i.e. the cutting material was supplied as single particles (granular material) which were newly "solidified" just before the blade. By this approach, the amount of elements used was constant, avoiding time consuming deleting and inserting procedures. Furthermore, it guarantees a continuously varying arrangement of the elements, preventing preferred directions of cutting characteristics (Fig. 9). To ensure a constant density and a continuous supply of cutting material, the elements had to be moved with speeds relative to the cutting speed *CS* in different areas of the model (Figs. 9, 10). In Figure 11 the change of the shape of the cutting edge due to wear can be seen. Figure 12 shows the comparison with experimental data. The major material loss occurred during the first cut. Later the wear stabilised, and further cuts did not alter the edge considerably. This was also observed experimentally (Fig. 5).

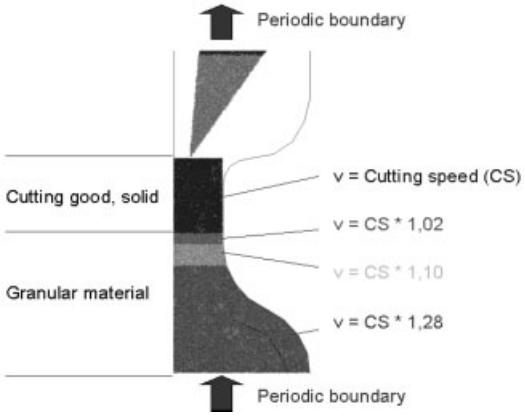


Figure 9: Model with knife and cutting good

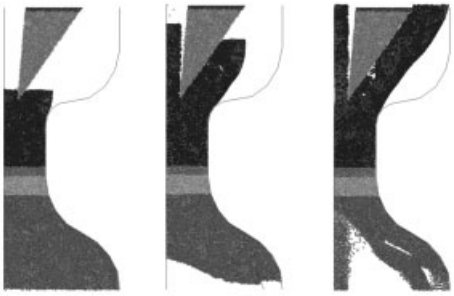


Figure 10: The simulation from beginning until steady state

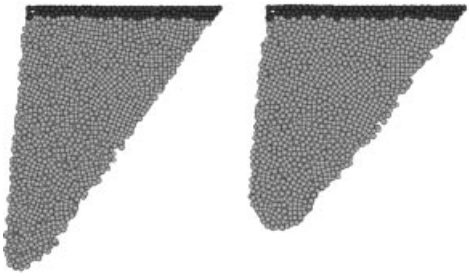


Figure 11: Wear at the cutting edge after first cut and after five cuts

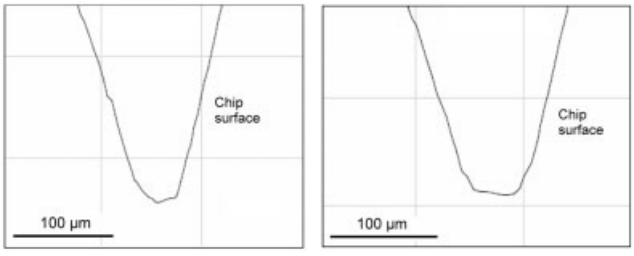


Figure 12: Shape of a cutting edge after 120 m and after 600 m cutting length. The shapes are not shown in cutting direction due to measurement limits.

4 Conclusion

It was shown that by the combined use of the simulation tools FEM and DEM, it is possible to model the wear at the cutting edge of knifes in principle. The biggest challenge that remains is the careful calibration of the material properties in the DEM simulations. Especially the influence of the modified parameters must be investigated. Additional tests with different blades and cutting materials have to be carried out to further improve the adaption of these parameters.

One further approach which will be tested to avoid the artificial altering of material properties is the introduction of fatigue mechanisms weakening the binding forces between the elements depending on the individual load history [11].

The procedure described will be used in the future to examine the influence of different geometries, material properties, and coatings. Especially, self-sharpening knifes, which are following biomimetic approaches by combining a hardened free surface with a weaker core material will be investigated [12].

5 References

[1] Cundall, P., Strack, O. D. L.: A discrete numerical model for granular assemblies; Geotechnica 29, 1979, 47–65.

[2] Lätzel, M., Besserer, H., Luding S.: Zur Modellierung von Schüttgut als Kontinuum und Diskontinuum; Schüttgut 7, 2001, 305–313.

[3] Theuerkauf, J., Dhodapkar, S., Manjunath, K., Jacob, K., Steinmetz, T.: Applying the Discrete Element Method in Process Engineering; Chem. Eng. Technol. 26(2), 2003, 157–161.

[4] Aström, J. A., Herrmann, H. J.: Fragmentation of grains in a two-dimensional packing; Eur. Phys. J. B 5, 1998, 551.

[5] Kun, F., Herrmann, H. J.: Fragmentation of colliding discs; Int. J. Mod. Phys. C 7, 1996, 837–855.

[6] Schubert, M., Khanal, M., Tomas, J.: Simulation der Aufschlusszerkleinerung eines Partikelverbundstoffs mittels Diskrete Elemente Methode. Chem. Ing. Tech 75, 2003.

[7] Thornthon, C., Yin, K. K., Adams, M. J.: Numerical simulation of the impact fracture and fragmentation of agglomerates, J. Phys. D: Appl. Phys. 29, 1996, 424–435.

[8] Popov, V. L., Psakhie, S. G., Gerve, A. et al.: Wear in combustion engines: Experiment and simulation by the Method of Movable Cellular Automata (MCA). - Physical Mesomechanics, 2001.

[9] Klemm, H.: Die Vorgänge beim Schneiden mit Messern, Akademie-Verlag Berlin, 1957

[10] Carmona, H. A., Wittel, F. K., Kun, F., Hermann, H. J.: Fragmentation processes in impact of spheres; Phys. Rev. E 77, 051302 2008

[11] Konietzki, H., Te Kamp, L., Bertrand, G.: Modeling of cyclic fatigue under tension with PFC; in Numercial Modeling in Micromechanics via Particle methods Konietzky Ed. Balkema, Lisse, 2003.

[12] Rechberger, M., Bertling, J.: Nagetierzähne als Vorbild für selbstschärfende, schnitthaltige Zerkleinerungswerkzeuge. Endbericht zum BMBF-Forschungsvorhaben 0311982. Fraunhofer UMSICHT, 2005.

Modelling and Simulation of Wear in Micro-machines

V. Hegadekatte[1,2], O. Kraft[1], N. Huber[2,3*]

[1]Institut für Zuverlässigkeit von Bauteilen und Systemen, Universität Karlsruhe (TH), Germany.

[2]Institut für Werkstoffphysik und Technologie, Technische Universität Hamburg-Harburg, Germany.

[3]Institute of Materials Research, GKSS-Research Centre, Geesthacht, Germany.

Abstract

Study of wear in complex micro-machines is often accomplished with experimental methods, like pin on disc, scratch test, atomic force microscopy or surface force apparatus. These experiments are often conducted within the parameter space of the micro-machine and at constant load and sliding velocity. In reality, the contact loadings are time dependent and, in particular in the case of micro-machines, fast moving and rapidly changing.

Using twin-wheel experiments, the wear law for the contacting materials is determined in form of the wear coefficient included in Archard's wear model. For the prediction of wear in more complex systems, a numerical simulation tool has been developed, which incorporates the identified wear model. This so-called Wear-Processor is capable of a fully transient wear integration scheme and is used to simulate wear in a micro gear, which is currently being developed within the collaborative research centre SFB 499. First results give an impression how fast the gear tooth geometry and the slip rates deviate from their original shape as a consequence of ongoing wear.

1 Introduction

Micro-machines promise to revolutionize our present environment by enabling the development of a wide variety of smart products. One of the main advantages of micro-machines is their quick response time due to their extremely low inertia. The Collaborative Research Centre SFB 499 establishes a complete process chain from design over materials processing to the testing of micromechanical demonstrator systems, of which one is the planetary gear train presented in Fig. 1 and 2 [1]. Part of this project is the clarification how far the advantages of micro mechanical systems affect negatively their reliability as they potentially fail due to excessive wear. Wear being a surface phenomenon is identified as a critical factor, which can limit the life span of micro-machines substantially.

A selection of promising materials have been carried out using miniaturizes pin-on-disc experiments [2, 3]. This type of unidirectional sliding wear is mainly relevant for the gear axes and bearings, as indicated in Fig. 1. To investigate the mixed type of sliding rolling wear, which is present in the gear teeth flank, a miniaturized twin-disc setup has been developed to carry out tribological model experiments at different load and slip conditions [4]. Different materials, such as Si_3N_4 and WC-Co have been tested in this setup in air and water.

To predict wear for different geometries and loading conditions, the experimentally observed wear behaviour is represented by a wear model, which is able to describe the relevant wear phe-

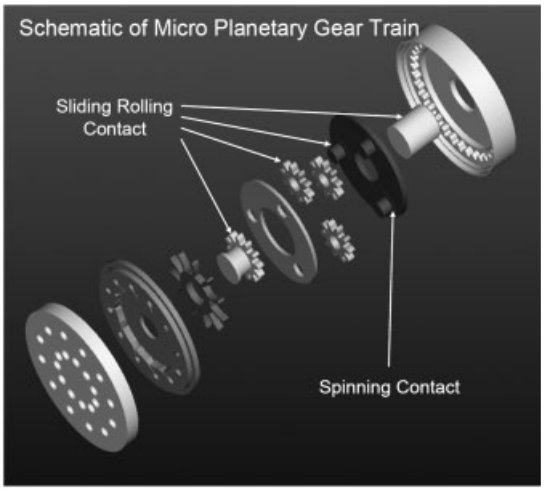


Figure 1: Schematic of the SFB 499 planetary gear train.



Figure 2: Photograph of the first micro planetary gear train (outer diameter ≈5mm) made of ceramics.

nomena. One of the most popular wear models is Archard's law [5], which is based on the assumption that the contact pressure p and the sliding distance s between the two contacting surfaces are the major influence factors for the wear h of the form:

$$\frac{dh}{ds} = k_D p \tag{1}$$

The material properties as well as the other influencing parameters, such as environmental conditions, are included in the wear coefficient k_D and have to be identified from experiments. The correct calculation of k_D from experimental data is however difficult, because contact pressure and also slip rate *ds/dt* are continuously changing. In pin-on-disc and twin-wheel experiments progressing wear changes the geometry of the contacting bodies causing a flattening of the pressure profile in the contact.

Concerning the iterative optimization procedure of a model identification, full numerical simulations [1,6] are too time consuming. Therefore a Global Incremental Wear Model (GIWM) has been developed specifically for the twin-wheel setup [7]. After identification of k_D and verification Archard's wear model for the mixed sliding/rolling contact, the model (1) is implemented in an advanced transient formulation of the Wear Processor [1,8], for which results are presented here for the first time.

2 Experiments and Model Identification

The experimental work has been carried out is described in detail in [9]. A sketch of the experimental setup is presented in Fig. 3, where the upper and lower wheel has a curved and a flat flank, respectively. Both wheels have the same initial diameter of 8 mm. Figure 4 depicts experimentally determined wear (markers) and wear predicted by the *GIWM* (lines) of self-mated Si_3N_4 in rolling contact as a function of the number of revolutions in air of 50% r.h. for $F_N = 250$ mN and $v_1 = 800$ mm/s.

In order to verify the applicability of the GIWM [7] for wear prediction under rolling conditions, unlubricated long time tests with self-mated Si_3N_4 were carried out. Fig. 4 shows the volumetric wear of driving and driven disc measured after the tests with 4% versus the number of revolutions together with the fitted curves from the numerical simulation GIWM. The volumetric wear calculated using a wear coefficient $k_{D,CD} = 3{,}3 \times 10^{-8}$ mm^3/Nmm for the driven (curved) disc and $k_{D,FD} = 1{,}5 \times 10^{-8}$ mm^3/Nmm for the driving (flat) disc showed a good agreement with the experimental data up to 5×10^6 revolutions whereas the wear measured after experiments over 7×10^6 revolutions was considerably higher than that calculated with the wear simulator GIWM. It should be noted, the driven disc has been produced with the identical manufacturing process within SFB 499 as the planetary gears while the driving disc was produced by an external manufacturer. Therefore only $k_{D,CD}$ for the driven gear is relevant for subsequent wear predictions.

The wear coefficients $k_{D,FD}$ and $k_{D,CD}$ determined from the fitted curves for 4% slip tests were then used for the calculation of the wear in tests with 4% and 10% slip over 10^6 revolutions. The calculated volumetric wear as a function of the number of revolutions N, together with the experimentally obtained data after 10^6 revolutions has also been verified for the different slips. For 10% and 4% slip, a good agreement between calculated and experimentally obtained wear volumes was found both for the driving and the driven disc [9].

For 1% slip the GIWM significantly underestimated the wear volume measured on the samples after the laboratory tests. In this case, contact fatigue seems to become the predominant effect. A similar effect can be observed for the largest numbers of rotations, for which the experimentally measured worn volume progressively exceeds that predicted by the GIWM. Again contact fatigue

seems to take a growing influence on the surface degradation of the wheels. This interpretation is supported by a significant increase of the number of surface cracks for these specimens.

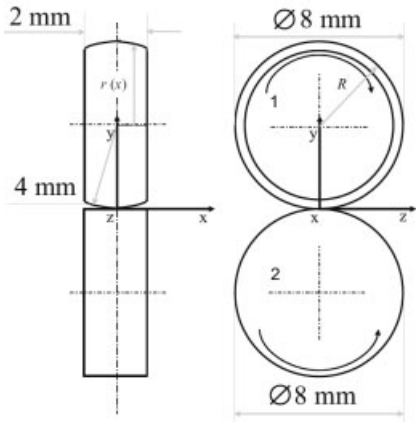


Figure 3: Wheel geometries used in the twin-disc tribometer.

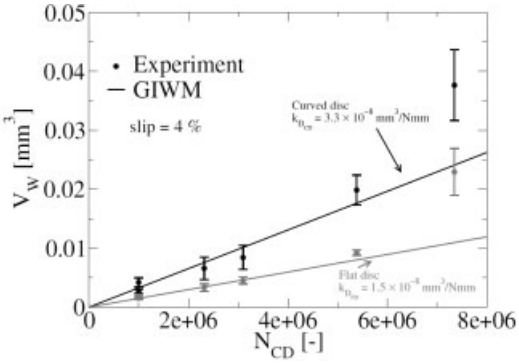


Figure 4: Volumetric wear measured and predicted with the GIWM at 4% slip.

3 Wear Prediction for Sliding/Rolling Wear in Gear Teeth

In contrast to pin-on-disc and twin-wheel experiments, the contact situation between the teeth of the planetary gear train is fully transient, i.e. location of contact, pressure and slip rate can rapidly change with time. A simulation of wear under such conditions requires the integration of wear depth with a generalized form of (1)

$$dh = k_D p(t) \frac{ds(t)}{dt} dt \tag{2}$$

which has been implemented in the Wear Processor [1] which includes an iterative pressure update by an FEM analysis after a significant amount of wear has been achieved. Similar approaches have been used by Andersson [6,10], where instead of a full FEM analysis an elastic foundation model or an analytical solution of the contact pressure has been used to accelerate the simulation. It should be noted, that clearly the FEM approach presented here is on the one hand time consuming. On the other hand it allows the prediction of geometry change due to wear without any assumptions on the development tooth profile.

Figure 5 depicts three representative situations for the contact between a tooth of the sun gear and a planetary gear. The torque of 5 Nmm has been kept constant for the driven planetary gear. While the sun gear tooth turns from left to right, slip decreases, becomes very small in the pitch point and then increases again. At the same time the pressure decreases continuously caused by the increasing lever of the sun tooth. Because the contact area is not limited to a point, there are situations, for which the product of pressure and slip are non-zero even in the pitch point.

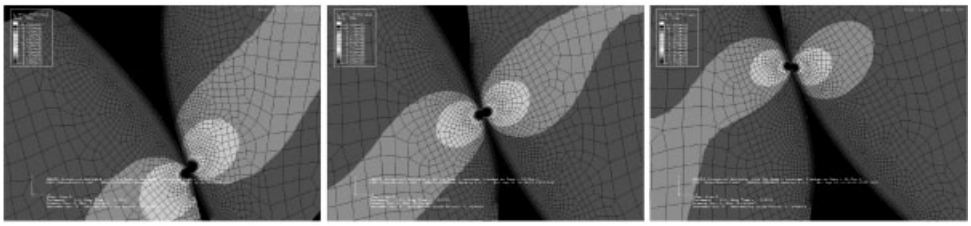


Figure 5: Moving contact and minimum principle stress field on the flanks of the rotating gear teeth.

The resulting variation of the slip rate *ds/dt* and the contact pressure *p* has been computed before and after wear at 3356 rotations of the sun gear assuming that both gears are made of Si_3N_4 ($k_{D,CD} = 3{,}3 \times 10^{-8}$ mm^3/Nmm). It can be seen from the results shown in Figs. 6 and 7, that wear has a significant effect on the evolving contact areas and pressures while the slip rate seems to be independent and simply a function of the current contact location.

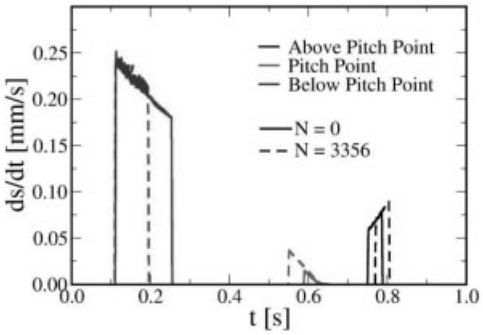


Figure 6: Variation of contact slip rate with time and wear.

The contact area and pressure is highly changed in particular below the pitch point, which results from the larger product of slip and pressure in this region. Surprisingly, the geometry

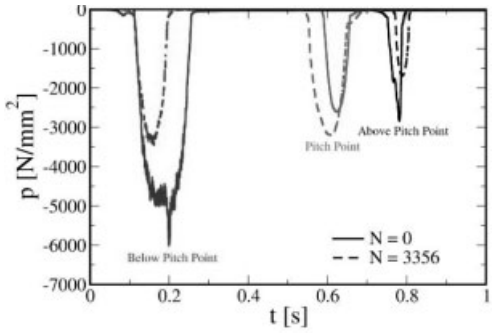


Figure 7: Variation of contact pressure and contact area with time and wear.

changing wear tends to equalize contact pressure and area for the three situations independent of the similarly increasing lever with time. Although the contact in the pitch point has in theory a zero slip rate (which should result in zero wear), it can be seen that the contact variables are still changing. The reason for this phenomenon is the extension of the contact area, which leads to a positive pressure in the pitch point shortly before and after the zero slip condition.

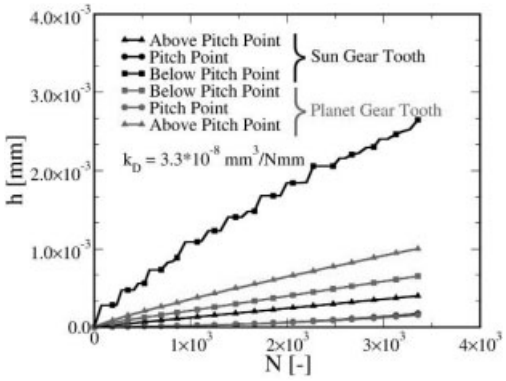


Figure 8: Wear depth over number of rotations of the sun gear at different locations on the sun gear tooth.

The resulting in the wear depths, are presented in Fig. 8. The highest amount of wear depth is about 3 µm and is reached below the pitch point while the lowest values are observed in the pitch point, as it can be expected from the previous discussion. For a sun gear tooth with a typical dimension of 100 µm in width, the amount of wear after about 3500 revolutions is 3%.

From this results a visible change in the kinematics of the gears, shown in Fig. 9. The green line represents the line given by the initial pressure angle of the gear, which is in excellent agreement with the contact co-ordinates from the simulation before wear (black line, N=0). After wear (N=3356), the contact trajectory $y(x)$ plotted in red has reached a nonlinear shape, which clearly deviates from the ideal slope.

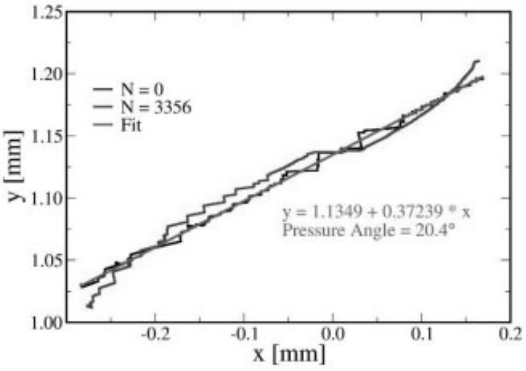


Figure 9: Contact trajectory $y(x)$ visualizes changing gear kinematics through wear.

4 Conclusions and Outlook

In this paper the complete chain has been presented consisting of tribo experiments, the wear model identification and its verification using the GIWM, and finally the transient wear simulation of a planetary gear train using the Wear Processor.

It can be concluded that the GIWM is a very efficient tool, that allows to determine the wear coefficient(s) of a given wear model. Further, it is very useful to identify phenomena, which obviously can not describe with e.g. Archard's wear model. This allows identifying limitations of the wear model potential for a model extension by e.g. fatigue wear. The deviation between experiments and prediction can be used as a quantitative basis for a further model development.

The implementation of a fully transient integration scheme in the Wear Processor allows for a very general wear simulation. The wear depth at a given point does automatically increase for time increments, where the product of contact slip rate and pressure is non-zero. This requires very time consuming simulations using very fine finite element meshes and time stepping. The outcome of this work is however very promising; large numbers of rotations have already been calculated resulting in significant amount of wear with consequences for the gear kinematics.

The goal of our further work is a full coupled two-scale simulation of the two-teeth with the full planetary gear train. It can be expected that the wear has a significant effect on the long-time behaviour of the planetary gear train.

5 References

[1] H. Baltes et al. (eds.), Microengineering of Metals and Ceramics – Design, Advanced Replication Techniques and Properties, Wiley-VCH Weinheim, Germany **2005**

[2] J. Herz et al, In Proc. MICRO.tec 2003, VDE Verlag GmbH, Berlin **2003**, 375–380

[3] J. Herz et al, In Proc. Tribologie Fachtagung 2004, GfT, Göttingen, **2004**, on CD

[4] S. Kurzenhäuser et al., In Proc. Minat Congress 2007, Stuttgart, **2007**, on CD

[5] J. F. Archard, J. Appl. Phys. **1953**, *24*, 981–988

[6] P. Podra, S. Andersson, Wear **1997**, *207*, 79–85

[7] V. Hegadekatte et al., Tribology International **2008**, in press

[8] V. Hegadekatte et al., Modelling Simul. Mater. Sci. Eng. **2004**, *12*, 1–19

[9] S. Kurzenhäuser et al., Microsystem Techn. **2008**, submitted

[10] J. Brauer, S. Andersson, WEAR **2003**, *254*, 1216–1232

Acknowledgment

The authors would like to thank the German Research Foundation (DFG) for funding this work under sub project D4 within the scope of the collaborative research center, SFB 499 – Design, production and quality assurance of molded microparts constructed from metals and ceramics. The authors would like to gratefully acknowledge Prof. K.–H. Zum Gahr, Dr. J. Schneider and Mr. S. Kurzenhaeuser for supplying the experimental data used in this work.

Development of Oil Lubricated Ceramic/Steel Friction Pairs at High Sliding Speeds

R. Wahl, K. Wauthier and K.-H. Zum Gahr
Universität Karlsruhe, Institute of Materials Science and Engineering II and
Forschungszentrum Karlsruhe, Institute for Materials Research I, 76021 Karlsruhe, Germany

Abstract

Friction behaviour of commercial Al_2O_3, Al_2O_3-ZrO_2 and SiC ceramics was characterized in paring with the steel 100Cr6 at oil lubricated unidirectional sliding up to 10 m/s. With respect to applications such as multiple disc clutches, effect of microtexturing of contact area on friction conditions was studied at a pellet-on-disc geometry by using laboratory tribometers. Results showed that oil film thickness was substantially changed by microtexturing depending on type of texture pattern used. Friction coefficient was reliant on the applied ceramic and was considerably greater at high sliding velocities at textured than untextured pairs at equal contact pressure.

1 Introduction

Oil lubricated multiple disc clutches represent an important part of modern gear boxes in automotive engineering but currently used friction materials such as paper, cork, sintered metal or polymer based materials encounter limits [1–4]. The demand of further increase in power transmission requires new solutions with higher values of friction coefficient, mechanical as well as thermal stability and wear resistance for long term reliability in service. Advanced ceramic materials as Al_2O_3, Al_2O_3-ZrO_2 or SiC offer a high potential as friction materials for components in such or similar applications due to their special properties, e.g. wear resistance and insensitivity against thermal or mechanical overloading.

Several theoretical and experimental studies [5–9] have shown important effects of surface roughness or texturing on friction and wear behaviour. Laser-assisted microtexturing allows inserting deterministic patterns with wide shape varieties in the functional areas of many materials and geometries of parts used for tribological applications. Studies [10–16] about the effect of microtexturing on tribological behaviour showed partly conflictive results. It is clear that texture pattern has to be adjusted to the tribosystem, operating conditions, materials and not least to the lubricant. Depending on the application a reduction or an increase of friction coefficient can be achieved by system oriented design of the texture pattern. Geometries such as microdimples as closed or microchannels as open elements of textures can promote micro-hydrodynamic or contribute to cooling of the contact areas, respectively, for example [16,17]. However, the present knowledge about texture effects is insufficient for proper design of functional areas with high reliability.

Friction-sliding velocity characteristic is an important factor in respect to the comfort behaviour of wet clutches. Vibrations or stick-slip effects can arise depending on the operating conditions, e.g. low velocity and high load, as well as degradation of the lubricating oil or wear

of the friction materials. In order to avoid vibrations, the friction-velocity relationship should be characterized by a low static friction coefficient and an increasing dynamic friction coefficient with increasing velocity [14].

Hence, the aim of the present study was the evaluation of different ceramics mated to the steel 100Cr6 using laboratory tribometers at lubricated unidirectional sliding contact and operating conditions related to those of wet clutches. Main interest was on the effect of microtexturing of the functional areas on friction-sliding velocity relationship as well as an improved understanding of the impact of texturing on film thickness and friction.

2 Experimental

2.1 Materials and Laser Texturing

Tribological behaviour of the commercial ceramics SSiC (EKasicF, ESK Ceramics), Al_2O_3 (HTC 99.9, hightech ceram) and Al_2O_3-15 vol. % ZrO_2 (SN80, CeramTec) was characterized using a pellet-on–disc geometry. In addition sapphire discs (GWI Sapphire) were applied for more fundamental studies. As counter body the steel 100Cr6 (SAE 52100) was used as delivered with hardened and tempered martensitic microstructure of 790 ± 10 HV30 for pellets and with normalized pearlitic microstructure of hardness of 300 ± 10 HV30 for discs. Microstructures of the tested materials are presented in Figure 1. Grain sizes and hardness values averaged out to 1.5 µm and 1610 HV_{500} for SN80, 1.9 µm and 2540 HV_{500} for EKasicF and 1 to 3 µm and 2084 HV_{500} for HTC ceramic, respectively. Before testing the functional area of the pellets was polished, lapped or additionally microtextured.

Laser-assisted microtexturing of the pellets was carried out by using a Ytterbium-laser (AC-SYS Lasertechnik). Additional details of the laser process are presented elsewhere [11]. Laser ablation process was used to generate circular microdimples or microchannels crossed to each other on the lapped or polished areas of the pellets (Fig. 2). The depth of both patterns was 10 ± 2 µm and the area coverage fractions were 35 and 75 %. After laser ablation the texture patterns showed debris, which was easily removed using gentle grinding and polishing.

2.2 Tribological Tests

The **simplified model test** and the **friction test rig** differed in the manner that hardened and tempered 100Cr6 steel pellets were mated to sapphire discs at the simplified model test while ceramic pellets were mated to normalized 100Cr6 steel discs at the friction test rig (Fig. 2).

Using the commercial **friction test rig** (Fig. 2c; UMT3, CETR), oil lubricated tests were carried out at unidirectional sliding up to relative velocities of 10 m/s and applied pressures of 2.12 MPa calculated for untextured circular contact area of Ø6 mm and normal force of 60 N. Textured or untextured ceramic pellets were mated with the directly in the tribometer lapped contact area to fine ground discs of the pearlitic 100Cr6 steel (R_a = 0.10 µm, 300 ± 10 HV30). Mineral oil (ISO-VG 100, FVA No. 3, $\eta_{40°C}$ = 85.2 mPas) without additives was fed into the contact area by drip lubrication. After loading the friction pair by the normal force, sliding velocity was continuously increased during 5 s up to the value wanted and it was hold constant for 120s before the velocity was shut down to zero (Fig. 2c). Each test at a given constant velocity (varied from 0.10 to 10 m/s), was followed by a cooling period down to room temperature before the run for

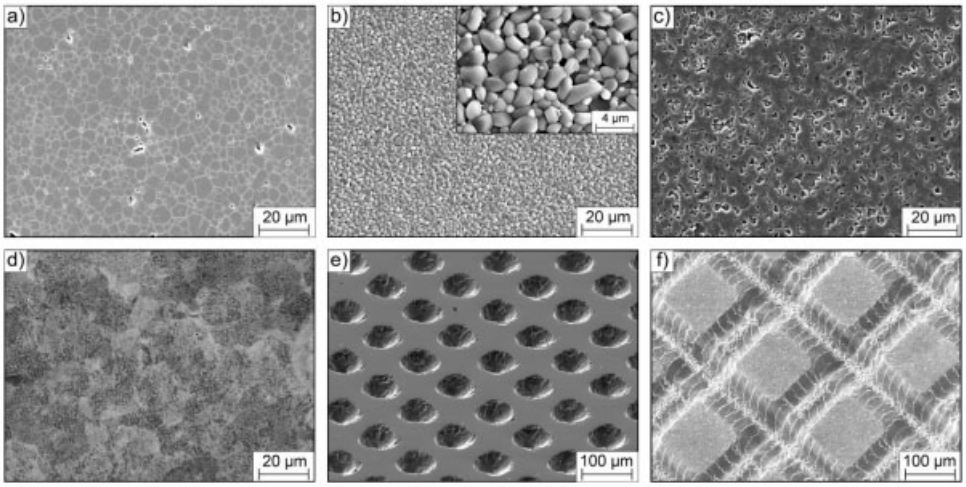


Figure 1: SEM micrographs of the polished and etched microstructures of the ceramics (a) Al_2O_3 (HTC 99.9), (b) Al_2O_3 -ZrO_2 (SN80), (c) SSiC (EKasicF) and (d) the pearlitic steel 100Cr6 as well as texture pattern used (e) circular microdimples on hardened steel 100Cr6 and (f) crossed microchannels on SSiC ceramic.

the next greater velocity was started. Tests were run in laboratory air at room temperature of 22 °C and 50 % relative humidity.

Studies using the **simplified model test** (Fig. 2a) were run at low velocities and low normal loads up to 0.3 m/s and 10 N, respectively. Martensitic 100Cr6 steel pellets (790 $\pm$ 10 HV30) with polished or microtextured contact areas of Ø 7.2 mm were mated at oil lubricated unidirectional sliding against polished sapphire discs. The same mineral oil as used in the friction test rig was fed at 2.0 mm^3/s by drip lubrication in front of contact area. Besides friction force, separation distances $h*$ between the contact areas of pellet and sapphire disc were continuously measured during each test by using a high accuracy distance transmitter with a resolution of $\pm$ 0.5 µm. Recorded values of separation distance "$h*$" represent a measure of the oil film thickness "h" but it has to be expected that these values can be greater than the real oil thickness "h" because waviness of the sapphire disc (< 1 µm after manufacturer data) or alignment variations will contribute to the measured data. In-situ observation of the contact area during sliding was possible using a special microscope with magnification up to 200 fold. It was preferentially applied for studying the development of the lubricant film and the oil flow at microtextured contact areas.

3 Results

3.1 Friction Coefficient and Thickness of Oil Film from Simplified Model Tests

3.1.1 Effect of Texture Pattern

Figure 3 shows friction coefficient and oil film thickness $h*$ as function of sliding velocity measured on polished or microtextured pellets of the martensitic steel 100Cr6 mated with polished

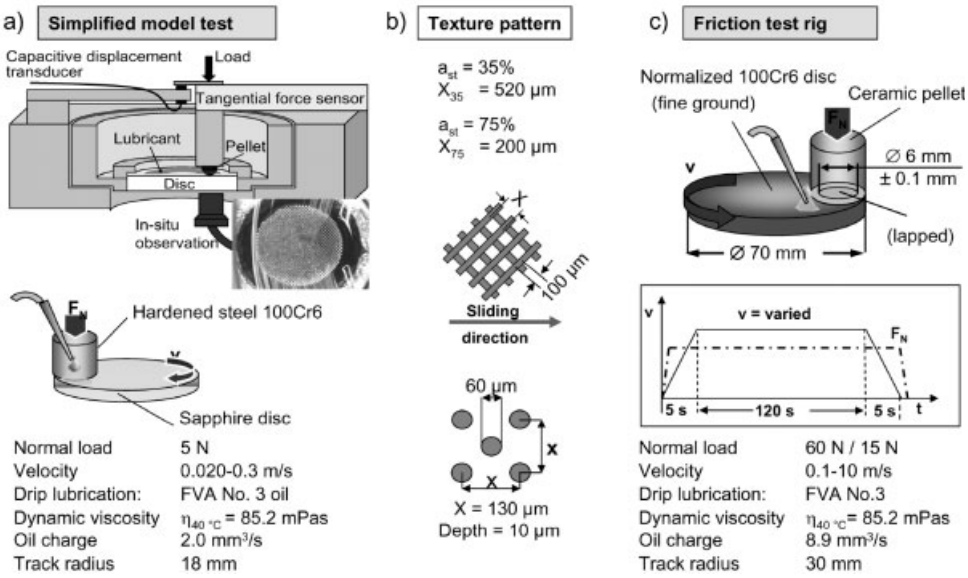


Figure 2: Schematic description of tribometers, materials, texture pattern, loading and lubrication parameters.

sapphire discs. In agreement with hydrodynamic lubrication theory, values of friction coefficient increased continuously with sliding velocity for both polished and with microdimples (area coverage fraction a_{st} = 35 %) textured contact areas of the pellets (Fig. 3a).

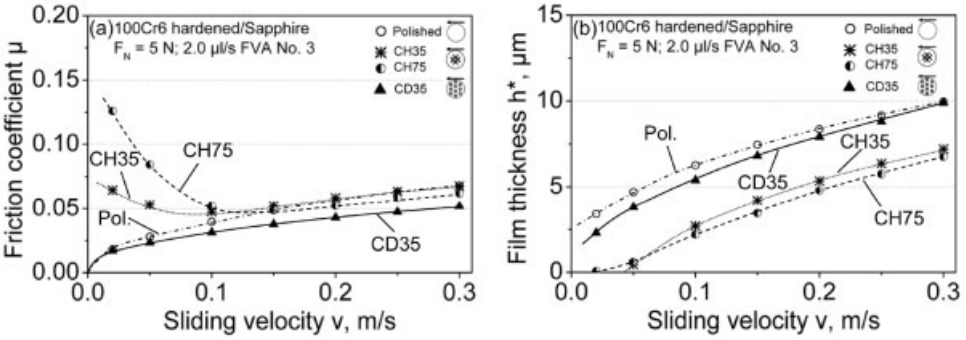


Figure 3: Polished or microtextured steel pellets mated to polished sapphire discs at the simplified model test (a) friction coefficient µ and (b) oil film thickness $h*$ versus sliding velocity at normal load of 5 N. CD35: circular dimples at a_{st} = 35 %, CH35 or CH75: crossed microchannels at a_{st} = 35 and 75 %, respectively.

However, crossed microchannels resulted in a far different behaviour at both a_{st} = 35 and 75 %. Similar to the "Stribeck curve", a minimum of friction occurred as function of sliding velocity. Measurements of oil film thickness $h*$ exhibited a great difference between the polished and with microdimples textured pellets on the one hand and with microchannels textured pellets on

the other hand (Fig. 3b). Film thickness increased in agreement with hydrodynamic lubrication theory at both polished and with microdimples textured pellets. Values of film thickness became zero, i.e. below the measurement resolution of <1 µm, at low sliding velocities of about 0.025 m/s in case of crossed microchannels. This means that boundary lubrication with solid-solid interactions on surface roughness level prevailed at film thicknesses on the nanometres' scale which led to high values of friction coefficient > 0.13 at a_{st} = 75 % (Fig. 3a). Independent of the absolute difference between measured values of film thickness $h*$ (separation distance) and true oil film thickness h, it is obvious that crossed channels reduced film thickness and promoted boundary lubrication at low sliding velocities under experimental conditions used. Texture pattern of microdimples reduced film thickness slightly which resulted in lower friction in the hydrodynamic region.

Normal load is an important factor with respect to friction condition in sliding pairs. Fig. 4 shows friction coefficient of polished and textured pellets mated with sapphire discs at constant sliding velocity of 0.3 m/s. Values of friction coefficient and film thickness $h*$ decreased continuously with increasing load whereas pellets with microdimples led to lower friction but to greater film thickness than pellets with microchannels. Increasing friction values with decreasing normal load were obviously connected with increasing film thickness $h*$. Greater area coverage fraction of CH75 yielded slightly lower film thickness and lower friction coefficient than CH35.

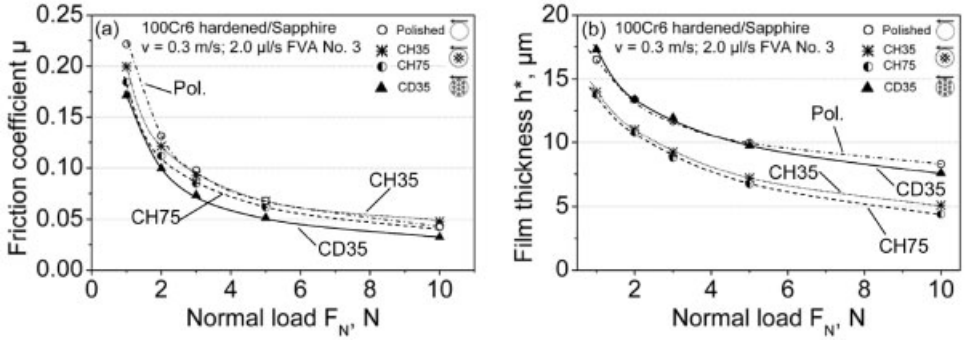


Figure 4: Polished or textured steel pellets mated to polished sapphire discs at the simplified model test (a) friction coefficient µ and (b) oil film thickness $h*$ versus normal load at sliding velocity of 0.3 m/s. CD35: circular dimples at a_{st} = 35 %, CH35 or CH75: crossed microchannels at a_{st} = 35 and 75 %, respectively.

3.2 Friction Behaviour Measured Using Friction Test Rig

3.2.1 Effect of Ceramic Material and Microtexturing

Figure 5 shows friction of ceramic pellets mated to pearlitic steel discs versus sliding velocity up to 10 m/s. Friction coefficient was calculated from loading cycle (Fig. 2c) at 125 s of testing at each velocity. Friction values increased with increasing sliding velocity up to maxima and then they decreased more or less slightly depending on the lapped ceramic pellets (Fig. 5a). Inserting microchannels CH75 on the contact areas of the pellets raised friction coefficient considerably compared with the only lapped pellets (Fig. 5b). Friction values decreased to minima at sliding

velocities below 1 m/s and increased at greater velocities. Depending on the ceramic, a more or less slight decrease of friction occurred at high velocities which was attributed to increasing oil temperature and hence to decreasing oil viscosity. Results from the model test indicated a reduced oil film thickness by microchannels. As consequence friction coefficient was raised with decreasing velocity below about 0.1 m/s due to boundary lubrication with partly solid-solid interactions between pellet and disc (Fig. 3a). Despite the differences between the simplified model test and the friction rig test quite similar friction behaviour was observed at low velocities (Fig. 3a, 5b). Increasing oil film thickness with sliding velocity led to high friction under hydrodynamic lubrication at high velocities. SSiC (EKasicF) has a substantially greater value of thermal conductivity than both oxide ceramics and hence removal of friction power from contact area and oil film is promoted, i.e. oil temperature should be lower at SSiC than at Al_2O_3 pellets which is indirectly supported by the measured greater friction of the SSiC pair (Fig. 5b). Lower temperatures were measured 0.15 mm below the contact area of the textured than the untextured ceramic pellets despite the greater friction power produced at textured pellets [17].

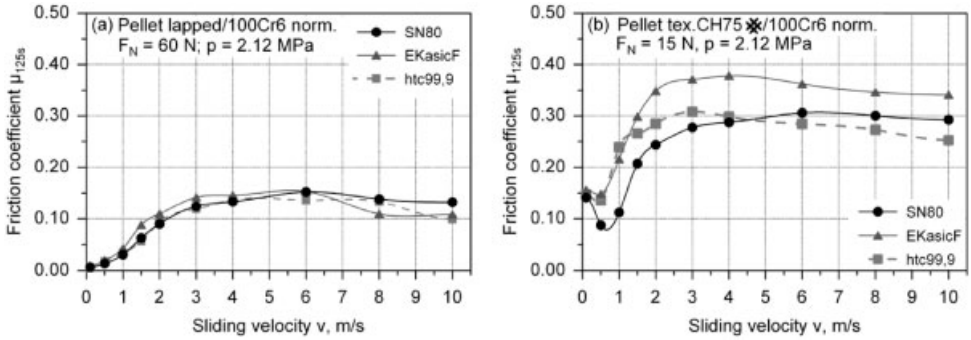


Figure 5: Friction coefficient of (a) lapped and (b) with microchannels CH75 (a_{st} = 75 %) textured ceramic pellets at 125s of sliding against pearlitic 100Cr6 steel discs at equal applied contact pressure of 2.12 MPa.

This "cooling effect" was attributed to increased contact area between pellet and oil as well as oil flow through the microchannels as observed by in-situ observation using the simplified model test (Fig. 2a).

4 Conclusions

Tribological evaluation of different ceramic materials and textured functional surfaces was carried out using model and practice-oriented operating conditions for applications such as oil lubricated multiple disc clutches. Results showed that a texture pattern of crossed microchannels reduced oil film thickness at low sliding velocities and increased friction by promoting boundary lubrication. At greater sliding velocities microchannels increased friction coefficient by a factor of two or even more depending on the ceramic used. SSiC with the greatest thermal conductivity led to the greatest friction values at high velocities which was attributed to lower oil temperature and higher oil viscosity, respectively, than at the oxide ceramics. Cooling effects due to oil flow through the channels and increased oil/pellet contact area can contribute together with flow

involving friction at thicker oil films at high velocities and low loads to the high friction values measured on microtextured pairs. Hence, high friction values can also occur at hydrodynamic lubrication due to oil flow induced friction losses.

Acknowledgments
The authors would like to thank the **Deutsche Forschungsgemeinschaft (DFG)** for financial support within the frame of the **Collaborative Research Centre 483** "*High performance sliding und friction systems based on advanced ceramics".* Laser-assisted microtexturing was carried out by Ms. Songül Yesilyurt.

5 References

[1] Ost, W.; et al., Wear **2001**, *249*, 361–371.

[2] Albers, A.; et al., *Tribologie-Fachtagung 2007 (GfT), Göttingen* **2007**, Bd. II, S. 51/1–10.

[3] Höhn, B.-R.; et al., *VDI-Ber. 1323,* Düsseldorf **1997**, 507–525.

[4] Becker, E. P., Tribology International **2004**, *37*, 569–575.

[5] Patier, N.; Cheng, H.S., Trans. ASME Ser. F., J. Lubrication Tech. **1979**, *101*, 220–230.

[6] Knoll, G.; et al., *Tribologie-Fachtagung 1997 (GfT),* Göttingen **1997**, Bd. II, 47/1–7.

[7] Illner, Th.; et al., *Tribologie-Fachtagung 2007 (GfT),* Göttingen **2007**, Bd. II, 53/1–14.

[8] Hwang, D.-H.; Zum Gahr, K.-H., Tribotest journal **2003**, *9*, 209–217.

[9] Nyman, P.; et al., Wear **2006**, *261*, 46-52.

[10] Etsion, I., Trans. ASME **2005**, *127*, 248–253.

[11] Schreck, S.; Zum Gahr, K.-H., Applied Surface Science **2005**, *247,* 616–622.

[12] Kovalchenko, A.; et al., Tribol. Intern. **2005**, *38,* 219–225.

[13] Mourier, L. ; et al, Tribol. Intern. **2006,** *39*, 1745–1756.

[14] Krupka, I.; Hartl, M., Trans. ASME **2007,** *129*, 502–508.

[15] Andersson, P.; et al, Wear **2007**, *262*, 369–379.

[16] Zum Gahr, K.-H.; Wauthier, K.; Wöppermann, M., *16th International Colloquium Tribology,* Esslingen **2008**, p. 26 and 5 pages on CD.

[17] Wauthier, K.; Zum Gahr, K.-H., *3. Statuskolloquium Sonderforschungsbereich 483*, Karlsruhe **2007**, 15–24.

Surface Textured Steel/Ceramic and Ceramic/Ceramic Pairs Sliding in Isooctane

M. Wöppermann and K.-H. Zum Gahr
Universität Karlsruhe, Institute of Materials Science and Engineering II and
Forschungszentrum Karlsruhe, Institute for Materials Research I, 76021 Karlsruhe, Germany

Abstract

Laser-assisted surface microtexturing was carried out on stainless steel/SSiC ceramic pairs for improving friction behaviour at high loaded reciprocating sliding in isooctane as a model substance for gasoline. Results show that running-in, values of friction coefficient, fluctuations in friction course versus sliding distance, abrasive grooving and degradation due to surface fatigue after long time of running could substantially be reduced by inserting circular microdimples into the ceramic functional surface.

1 Introduction

Reliability of sliding pairs can be deficient at lubricants or service conditions of low lubricity. An example are parts of hermetically sealed pumps with reciprocating sliding motion where the medium to be pumped replaces oil as lubricant. Reciprocating sliding represents an unfavourable motion with strongly varying velocities whereby at both dead centres the relative velocity goes to zero and shows its maximum value at the middle of the stroke. Gasoline injection pumps represent a system where low velocity, high applied load due to an injection pressure of more than 180 bar and gasoline's low lubricity impede the formation of a load bearing lubrication film [1]. Depending on the medium severe tribocorrosive problems can occur on metallic parts normally used at oil lubricated systems [2]. Hence, advanced ceramics are potential substitutes at such service conditions due to their chemical inertness in contact with many media such as acid or alkaline aqueous solutions or gasoline. Silicon carbide and alumina are already well established for water lubricated components such as bearings and seal rings in pumps. However, sliding pairs of monolithic ceramics can fail at severe working conditions, e.g. at temporary loss of lubrication and resulting thermal and mechanical overloading [3–7]. As consequence, problems can occur with the load carrying capacity, running-in, friction and wear behaviour of medium lubricated sliding systems.

Theoretical and experimental studies showed that the use of surface texturing of the functional areas can take effect in improving tribological performance of marginal lubricated systems [8–12]. Surface texturing on SiC is already applied for mechanical seals of hydraulic machines for years. However, the performance differs substantially and in some cases texturing showed no significant or even a detrimental effect on friction coefficient and load bearing capacity depending on the mated materials and experimental conditions used.

The objective of this research work is to study the effect of laser-assisted surface texturing on the tribological performance of SSiC ceramic in reciprocating sliding contact against stainless

steel under lubrication with isooctane as a model substance for gasoline. Stainless steels are widely used because of their favourable corrosion resistance in various aggressive environments.

2 Materials and Experimental Methods

2.1 Materials

In this study, tribological behaviour of a commercial non-oxide ceramic SSiC (EKasicF, ESK Ceramics) mated to the steels 100Cr6 and X105CrMo17 was tested. The steel 100Cr6 (SAE 52100) was used in a hardened and tempered condition (20 min at 860°C, oil quenched and tempered 2 h at 190 °C). The stainless steel X105CrMo17 (DIN EN 10088) was employed in an as delivered hardened and tempered condition. The martensitic stainless steel contained a relatively large volume fraction of carbides of 17% at a size of about 1 to 3 µm. Both steels showed comparable values of Vickers Hardness of 790 ± 10 HV30. In addition an as delivered spheroidized annealed microstructure of the steel X105CrMo17 with a hardness of 280 ±10 HV30 was used. Steel pellets of Ø16 mm and SSiC plates of 50 × 25 × 8 mm^3 with fine ground functional surfaces were produced for tribological testing.

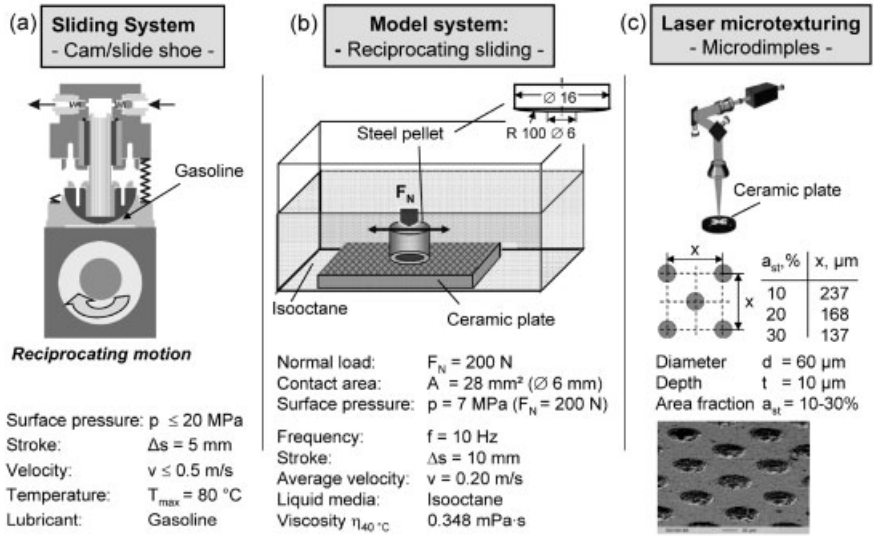


Figure 1: Schematic representation of (a) cam/slide shoe as example of a gasoline lubricated sliding system, (b) the model system used for evaluation of new material pairs and (c) texture pattern produced on the ceramic plates by laser-assisted ablation.

2.2 Surface Microtexturing

Laser-assisted microtexturing of the fine ground functional surfaces (R_a = 0.10 µm) of the silicon carbide plates was carried out by using a Ytterbium-laser (ACSYS Lasertechnik, Piranha II multi

F20 with laser source IPG YLP-1-100-20-20, wave length λ = 1.064 µm). Additional details of the laser process are presented in [11]. The laser ablation process was used to generate microdimples of a texture pattern as shown in Fig. 1c. The average depth of the microdimples was 10 ± 2 µm and the area fraction was varied between 10 and 30 %. After laser texturing the surfaces showed debris, which could easily be removed using gentle grinding by 1000 mesh SiC abrasive paper.

2.3 Tribological test

Tribological properties of the sliding pairs were measured using a pellet-on-plate tribometer (Fig. 1b) at lubricated reciprocating sliding contact in isooctane at room temperature. During all tests, the contact area was immersed at least 3 mm below the surface level of the isooctane bath. All tests were run at a normal load of 200 N, an oscillation frequency of 10 Hz and a stroke of 10 mm that resulted in an average sliding speed of 0.20 m/s. The pellet specimens sliding as counter bodies on the plates showed a circular flat contact area of Ø 6 mm which was fine ground to an average surface roughness of R_a = 0.10 µm. The ceramic plate specimens were fine ground to flatness using a diamond wheel (D25) of a grit size of 25 µm that resulted in an average surface roughness value of R_a (c.l.a) = 0.10 µm. Both textured and untextured ceramic plates were finally cleaned in an ultrasonic bath with isopropanol to remove residuals from the laser process and/or the machining. Friction force was continuously measured and recorded during each test. Reported values of friction coefficient are average values of at least two equal tests.

3 Results

3.1 Friction Behaviour of Fine Ground Ceramic/Ceramic and Steel/Ceramic Pairs

Fig. 2a shows that the tribological behaviour of self-mated SSiC was characterized by a very pronounced running-in connected with a strong decrease in friction coefficient. The two presented runs (R1, R2) at nominally equal conditions differed in the running-in distances. Very low values of friction coefficient less than 0.04 were measured beyond about 800 m of sliding in isooctane. Steel / SSiC pairs resulted at equal experimental conditions in friction values between about 0.20 and 0.25 (Fig. 2b). Running-in period and average friction coefficient of the martensitic stainless steel X105CrMo17 was greater than the values of the reference steel 100Cr6 at comparable hardness values of 790 HV30. This was ascribed to the larger average carbide size of the steel X105CrMo17 in which after loosening from the matrix the hard carbides can act abrasively on the steel pellets during sliding contact.

3.2 Friction Behaviour of Untextured and Textured Steel/Ceramic Pairs

3.2.1 Effect of Area Coverage Fraction

Figure 3a shows friction behaviour of the martensitic steel X105CrMo17 against fine ground untextured and textured SSiC plates, respectively. Initial values of friction coefficient of about 0.32 and final values of 0.25 at 4000 m were measured in case of the untextured ceramic plates. Microtexturing with an area coverage fraction a_{st} of 20% resulted in substantially lower friction values of less than 0.20 whereby the values decreased further on down to less than 0.10 with

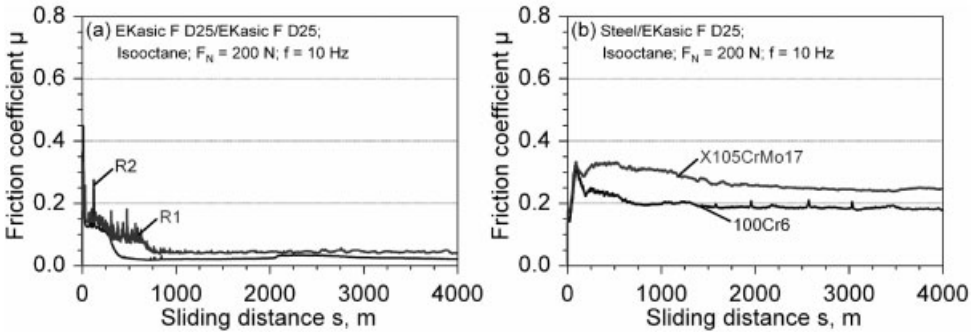


Figure 2: Friction coefficient of (a) self-mated SSiC and (b) X105CrMo17 or 100Cr6 steel pellets of 790 HV30 mated with fine ground SSiC plates versus sliding distance in isooctane at normal load of 200 N (p = 7 MPa).

prolonged sliding. The effect of a_{st} on friction course is presented in Fig.3b. Friction coefficient decreased continuously with sliding distance at a_{st} = 20% while it stayed almost constant at 10 and 30% whereby up to 1000 m higher values were measured at 10% than at 30% microdimples. Microtexturing resulted in reduced friction at all area coverage fractions studied. It has to be mentioned that which increasing a_{st} from untextured to 30% the nominal contact pressure increased from 7 MPa to 10 MPa because all tests were run at the equal normal load of 200 N.

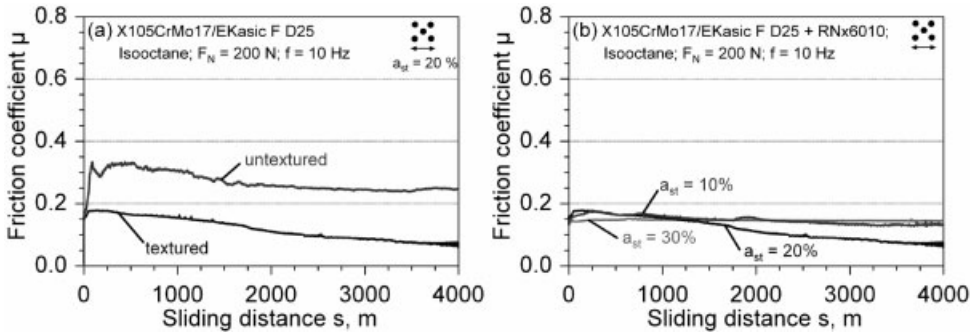


Figure 3: Friction coefficient versus sliding distance in isooctane at the normal load of 200 N of X105CrMo17 pellets (790 HV30) mated with (a) fine ground (untextured) and textured (microdimples of a_{st} = 20%) SSiC plates, respectively, and (b) for area coverage fractions a_{st} of 10, 20 or 30% microdimples.

Figure 4 shows SEM micrographs of worn surfaces of martensitic X105CrMo17 pellets (790 HV30) and the mated SSiC plates after 4000 m sliding in isooctane. The worn pellet surface exhibited grooves and cavities came locally along with them due to abrasion and loss of carbides from the steel matrix (Fig. 4a). A thin metallic layer was observed on the mated untextured ceramic plate (Fig. 4c) at which a grain like structure was visible. Obviously there was substantially less grooving on the pellet (Fig. 4b) mated with the textured ceramic plate (Fig. 4d). Small rolls on the plate surface indicated the presence of a friction reducing tribochemical film. The mechanism of collecting wear particles by microdimples is particularly important during running-in period and is clearly indicated by the microdimples partially filled with wear debris (Fig. 4d).

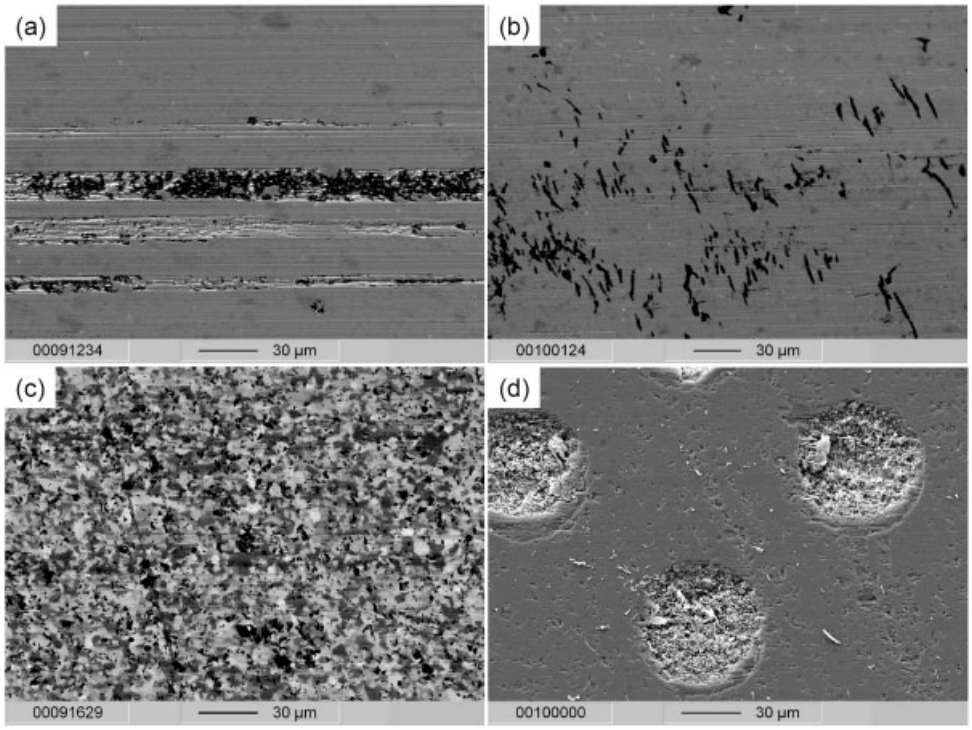


Figure 4: SEM micrographs of worn contact areas of the pairs (a) X105CrMo17 pellets (790 HV30) mated with (c) untextured SSiC plates as well as (b) X105CrMo17 pellets (790 HV 30) mated with (d) textured SSiC plates with area coverage fraction of 20% after 4000 m of sliding in isooctane at 200 N normal load.

Elongated cavities and cracks occurred also locally on the pellet surface (Fig. 4b) mated with the textured SSiC plate which were connected with loss of carbides from the steel matrix and were caused by fatigue effects owing to 2×10^5 double strokes of reciprocating sliding contact.

3.2.2 Effect of carbides of the steel matrix

An annealed microstructure of X105CrMo17 was used for studying the effect of hard carbides embedded in a soft steel matrix. Figure 5 shows friction behaviour of the spheroidized annealed steel pellets in sliding contact against untextured and textured SSiC plates, respectively. In both test runs (R1, R2) at nominally equal conditions, friction course of the annealed pellets mated to untextured SSiC plates was characterized by distinct fluctuations (Fig. 5a). After a distinct running-in distance, average values of friction coefficient were substantially lower than those of the pair with hardened pellet (Fig. 3a). Microstructure of the annealed pellet is presented in figure 5c. As expected the spheroidized annealed microstructure featured a considerably greater amount of carbides then the hardened one. During the reciprocating sliding the carbides were pulled out of the steel matrix and caused a high density of grooves on the contact area of the pellet (Fig. 5d). Additionally cracks and spalling (Fig.5d) appeared with increasing sliding distance due to

surface fatigue which led to the pronounced fluctuation in the friction course (Fig. 5a). In the case of the mated textured SSiC plate, wear particles produced could be removed from the contact area by the microdimples (see also Fig. 4d) and after the running-in a smooth friction course was measured (Fig. 5b). Worn pellets exhibited substantially less features of surface fatigue such as cracks or spalling along grooves on the pairs with textured SSiC plates (Fig. 5e). This means that microtexturing improved resistance of the sliding pairs against failure by surface fatigue, i.e. it can extend service life at the high loads used.

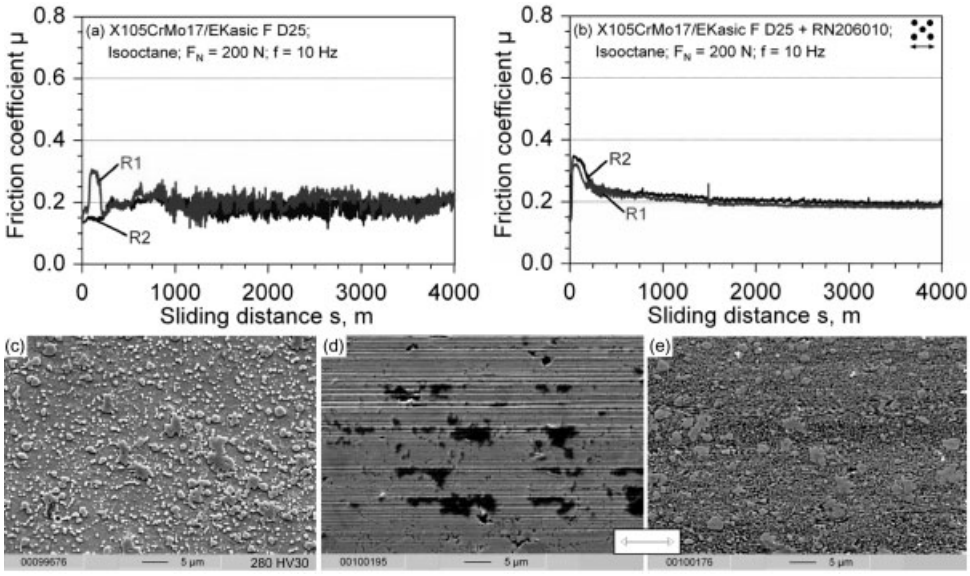


Figure 5: (a,b) Friction coefficient of pellets with annealed (280 HV30) microstructure of the steel X105CrMo17 in sliding contact against (a) untextured and (b) textured SSiC plates with a_{st} = 20% microdimples versus sliding distance in isooctane at normal load of 200 N. SEM micrographs of (c) the steel microstructure and (d,e) worn surfaces of steel pellets after sliding along 4000 m against (d) untextured and (e) textured SSiC plates, respectively. Arrow indicates sliding direction.

4 Conclusions

Self-mated SSiC ceramic achieved lower friction values after a certain running-in period than steel/SSiC pairs at the test conditions used. Steel/ceramic pairs may however become particularly interesting for components of high loaded gasoline injection pumps as one example due to advantages in manufacturing and damage tolerance if friction coefficient can be reduced below about 0.10. Hence, the objective of this work is to study new approaches for an optimized design of high loaded contacts of components at reciprocating sliding under lubrication with media of low lubricity. The results show that laser-assisted microtexturing can be very effective in improving the tribological performance of steel/SSiC pairs at reciprocating sliding in isooctane. In case of the hardened stainless steel X105CrMo17 friction coefficient was reduced from values

of about 0.25 or even greater to less than 0.10 by texturing the mated SSiC plate with an area coverage fraction of 20% of circular microdimples at a diameter to depth ratio of about 6. It was also shown that fluctuations in the friction course as function of sliding distance can be caused by pull out of carbides from the steel matrix or wear particles trapped in the contact area. As consequence friction and wear were increased due to abrasive grooving on the mated surfaces. This problem was very effective reduced by texturing because carbides or wear particles could be removed from the contact by the microdimples. Besides gathering wear particles or carbides (Fig. 4d), the texture pattern can also serve as lubricant reservoir or promote formation of a hydrodynamic lubricant film. Depending on microstructures of the mated materials and operating conditions, surface fatigue can be promoted under reciprocating sliding at a lubricant of low lubricity and as result local cracks and/or loss of grains or carbides can occur on the steel or ceramic surfaces. Results showed that microtexturing improved resistance of the sliding pairs against failure by surface fatigue at the high applied loads and can prolong service life. SiC grain pull-out can lead to abrasive grooving on both the steel pellets and the ceramic plates while loosening of hard carbides from the softer steel matrix acts abrasively on the steel pellets, particularly.

Acknowledgments

The authors would like to thank the **Deutsche Forschungsgemeinschaft (DFG)** for financial support within the frame of the **Collaborative Research Centre 483** "*High performance sliding und friction systems based on advanced ceramics"*. Laser-assisted microtexturing was carried out by Ms. Songül Yesilyurt.

5 References

[1] Häntsche, J. P.; et al., SAE Technical Paper Series No **2005-** 01-2103, p. 1–10.

[2] Mischler, S.; Spiegel, A.; Landolt, D., Wear **1999**, *225-229,* 1078–1087.

[3] Löffelbein B.; Woydt, M.; Habig, K.-H., Wear **1993**, *162-164*, 220–228.

[4] Chen, M.; Kato, K.; Adachi, K., Wear **2001**, *250*, 246–255.

[5] Takadoum, J.; et al., Journal of Materials Science Letters **1994**, *13*, 474–476.

[6] Hsu, S; M. Shen, M., Wear **1996**, *200,* 154–175.

[7] Peter, E.; Zum Gahr, K.-H., Mat.-wiss. u. Werkstofftech. **2005**, *36* 129–135.

[8] Etsion, I., Tribol. Lett. **2004**, *17*, 733–737.

[9] Wang, X.; Kato, K.; Adachi, K.; Aizawa, K., Tribology International **2003**, *36*, 189–197.

[10] Wakuda, M.; Yamauchi, Y.; Kanzaki, S.; Yasuda, Y., Wear **2003,** *254*, 356–363.

[11] Schreck, S.; Zum Gahr, K.-H., Applied Surface Science **2005**, *24,* 616–622.

[12] Zum Gahr, K:-H.; Mathieu, M.; Brylka, B., Wear **2007**, *263,* 920-929.

Influence of Surface Modification on Dry Friction Performance of Alumina Mated Against Steel

R. Wallstabe, J. Schneider, K.-H. Zum Gahr
Universität Karlsruhe (TH), Institute of Materials Science and Engineering II and
Forschungszentrum Karlsruhe, Institute for Materials Research I
Postfach 3640, 76021 Karlsruhe

1 Introduction

High performance friction systems such as dry clutches have rising demands regarding loading capacities. Organic friction materials have reached their limitations [1–4] but engineering ceramics like Al_2O_3 and SiC have great potential since they can withstand higher thermal and mechanical stresses. However their tribological performance is still unsatisfactory [5,6].

Previous work has shown that the tribological behavior of alumina can be influenced by co-sintering with e.g. tungsten carbide and titanium nitride [7]. Laser surface modification of the present study has a slightly different approach. Since the contact surface is most important for tribological behavior only a thin surface zone is modified. Powders of carbides, nitrides or oxides are injected directly into the laser-induced molten pool. Previous publications [5,6,8] showed that the tribological behavior of alumina could be substantially improved. It was shown that under dry sliding conditions higher stability of friction coefficient could be achieved compared with monolithic alumina. Therefore in the frame of this research work the laser process was further developed using powders as additives.

2 Materials and Experimental Procedure

2.1 Materials

Reference materials were the commercial Al_2O_3 ceramic (F99.7, Friatec) and the SSiC ceramic (EKasicF, ESK Ceramics). The ceramics were used as cylindrical pellets (Ø16 mm, h = 7 mm) with spherical end faces (r = 100 mm). The counterbody for tribological testing was a disc (Ø60 mm, h = 8 mm) of the normalized steel C45E (DIN EN 10083) with a Vickers hardness of 206 ± 6 HV30. Microstructures of the different materials are shown in figure 1.

The substrate material used for the laser surface modification was the Al_2O_3-ceramic Al24 (Friatec) with an open porosity of < 5 vol% and an average grain size of 30 µm. The geometry of the pellets was the same as for the reference ceramics. The added powders were titanium nitride (TiN), titanium carbide (TiC), tungsten carbide (WC), boron carbide (B_4C), zirconium boride (ZrB_2) and a commercially available mixture of chromium (Cr) and nickel (Ni) with a volume ratio of 1:5. The average particle size is shown in Table 1.

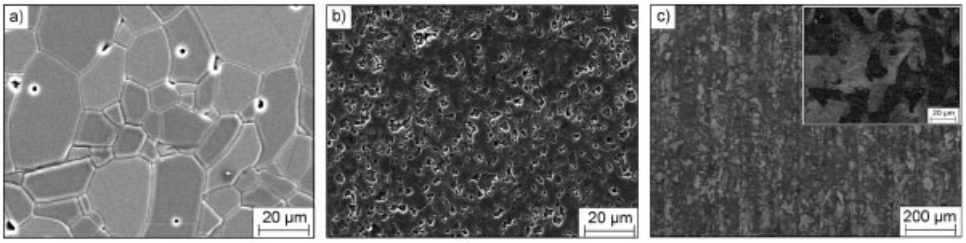


Figure 1: Microstructure of (a) Al_2O_3 (F99.7), (b) SSiC (EKasicF) and (c) the normalized steel C45E.

2.2 Laser Surface Modification

Since the alumina substrate offers only limited thermal shock resistance controlled preheating was carried out by a laser-induced process (Fig. 2a) that was superior to conventional furnace preheating. Advantages are that only the desired surface zone is heated and higher heating rates are possible avoiding the problem of grain growth within the substrate material (Al24). Laser-induced heating resulted in shorter process times and better mechanical properties of the surface-modified specimens. A CO_2-laser combined with a scanner system was used. Scanning velocity was 10.5 m/s and laser power was increased continuously from about 50 W to a maximum of about 600 W. Substrate temperatures of 1100 °C and 1400 °C could be achieved within 10 and 15 minutes.

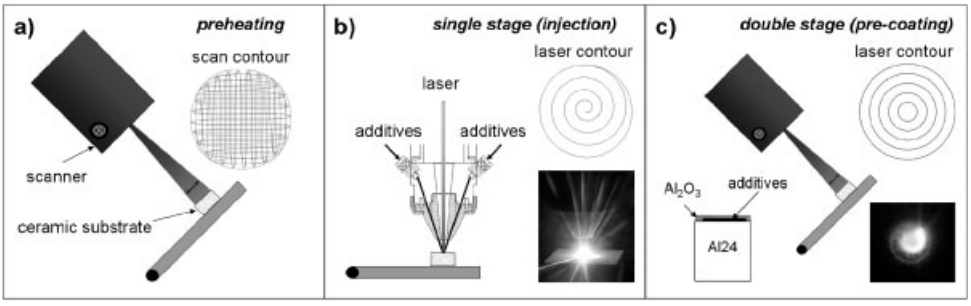


Figure 2: Schematic representation of laser-assisted surface modification process.

There were basically two methods used for laser surface modification: a single stage and a double stage process. At the single stage process (Fig. 2b) powders were injected directly into the laser-induced molten pool of the ceramic substrate after preheating it to 1400 °C. The main advantage of the single stage process is reducing the thermal load of the powders to a minimum. One disadvantage was that the particle size of the additives should not be smaller than about 5 µm due to conveying limitations.

At the double stage process (Fig. 2c) the ceramic substrate (Al24) was pre-coated using a sedimentation process. For this a suspension of powders and an organic solvent was prepared and applied on the surface. In order to reduce oxidation processes during heating an additional layer of alumina was applied on top and was also slowly dried. The pre-coated substrate was preheated

to 1200°C with additional argon-flushing. For melting the surface and consequent dispersing or alloying with the added powders the scan velocity was decreased and simultaneously the laser power was adjusted. The advantages of this process were smaller thermal shock loading due to immediate modification after preheating and the possibility to use powders with a particle size much smaller than 5 µm.

2.3 Tribological Tests

Tribological investigations were performed at unidirectional sliding motion using a pin-on-disc tribometer (Plint, TE92HS) in air at a relative humidity of 50 %. The surface-modified ceramics as well as the reference ceramics (F99.7, EKasicF) were tested against the steel C45E discs. The ceramic pellets were fine ground on the spherical side to an area of 8 mm in diameter by using a diamond disc (D25). The metallic discs were fine ground using a corundum grinding wheel (EK200). A schematic view of the tribological test setup is given in Fig. 3. The normal load of 100 N resulted in a nominal contact pressure of 2 MPa. Five velocity ramp cycles (ramp time t_R = 5 s, v_{max} = 12.6 m/s) were performed at different starting temperatures of the disc (55 °C, 70 °C, 85 °C). To ensure that running-in processes were finished, the block (15 ramp cycles) was repeated and only the second one was used for further data analysis. The mean sliding distance for one test comprising 30 ramp-cycles was 5760 m. Normal load, friction moment, disc temperature at the circumference (start criteria) and temperature within the wear track were recorded continuously during the test. Before and after testing the specimens were examined by optical 3d-profilometry (confocal white light profilometer, Fries Research Technology) and linear wear of the steel disc was determined at eight lines. Reported values are the mean of at least two identical tests.

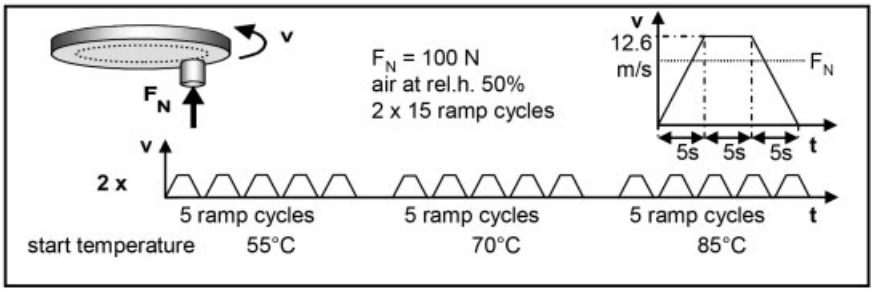


Figure 3: Schematic of the tribological setup.

3 Results and Discussion

3.1 Laser Surface Modification

Resulting microstructures of the differently surface-modified alumina (Tab. 2) are shown in figure 4. The single stage modification of Al24-WT showed a microstructure where the additives

were still mainly in particle form and partly melted at the surface (Fig. 4c). The modified surface consisted of the alumina matrix and embedded WC-particles (15 ± 4 vol%) and TiN-particles (7 ± 2 vol%). Chemical analysis (WDX-microprobe) revealed that tungsten carbide particles had a titanium rich edge which may explain the smaller volume content of TiN-particles. The other ceramic Al24-ZCN produced by single stage modification showed a reaction phase along the grain boundaries that was not evenly distributed (Fig. 4a). Furthermore there were some conglomerations of nickel and chromium (< 200 µm). The bonding between the metallic conglomerations and the alumina matrix has to be further improved and the size of conglomerations should be smaller than 100 µm because of the better connection. During the double stage modification of the ceramic Al24-TTB the added powder particles were melted and a reaction phase (17 ± 7 vol%) was formed along the grain boundaries of the alumina matrix (Fig. 4b). This reaction phase was titanium rich.

Table 1: Powder used at laser-assisted surface modification and resulting phases (reaction phase – RP).

	Al24	Al24-WT	Al24-ZCN	Al24-TTB
added powders, vol% (particle size, µm)	–	50 WC (5.1) 50 TiN (7.5)	50 ZrB_2 (3.8) 50 CrNi (16.3)	33 TiN (1.7) 33 TiC (2.0) 33 B_4C (9.0)
resulting microstructural phases, vol%	Al_2O_3	WC 15 ± 4 TiN 7 ± 2 Al_2O_3 balance	RP 17 ± 3 CrNi 7 ± 7 Al_2O_3 balance	RP 17 ± 7 Al_2O_3 balance
Vickers hardness HV_{100}	1153 ± 429	1988 ± 259	2061 ± 354	1928 ± 212

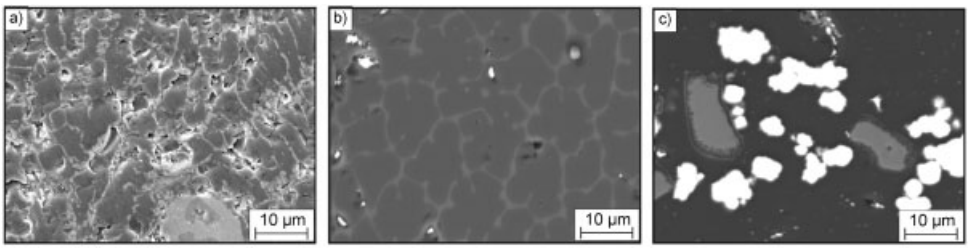


Figure 4: Microstructure of the surface-modified alumina (a) Al24-ZCN, (b) Al24-TTB and (c) A24-WT.

3.2 Tribological Behaviour

Figure 5 shows the averaged values of friction coefficient and the corresponding disc temperature of the reference ceramics F99.7 and EKasicF as well as for one surface modified ceramic (Al24-ZCN) against the steel C45E exemplarily for the start temperature of 70°C. Arrows indicate the upward (increasing velocity) and downward ramp (decreasing velocity). All couples showed a velocity dependence of the friction coefficient and also a temperature dependence. Friction coefficient decreased with increasing sliding velocity and increasing temperatures. EKasicF/C45E showed the greatest temperature hysteresis which means that it showed a greater difference in friction coefficient between upward and downward ramp. However it also had lower sliding

velocity dependence than the other couples. The sliding pair of modified alumina Al24-ZCN showed friction values that were remarkably higher than the one of F99.7/C45E and they were comparable to those of EKasicF/C45E. While the characteristics (slope) of the friction coefficient were comparable for F99.7 and Al24-ZCN, EKasicF showed a different behavior. There were several relatively sharp increases and decreases of the friction coefficient especially at lower velocities of the upward ramp. Considering also the non-averaged data there were more oscillations of the friction coefficient than for the modified ceramic Al24-ZCN or the alumina reference F99.7.

A statistical analysis of the recorded data (ramp cycles 16-30) was performed. The values of the friction coefficient were regressed (n = 5) and the friction coefficient stability which was defined as dμ/dv was calculated for each point of the regression. The given values were calculated from at least two identical test runs.

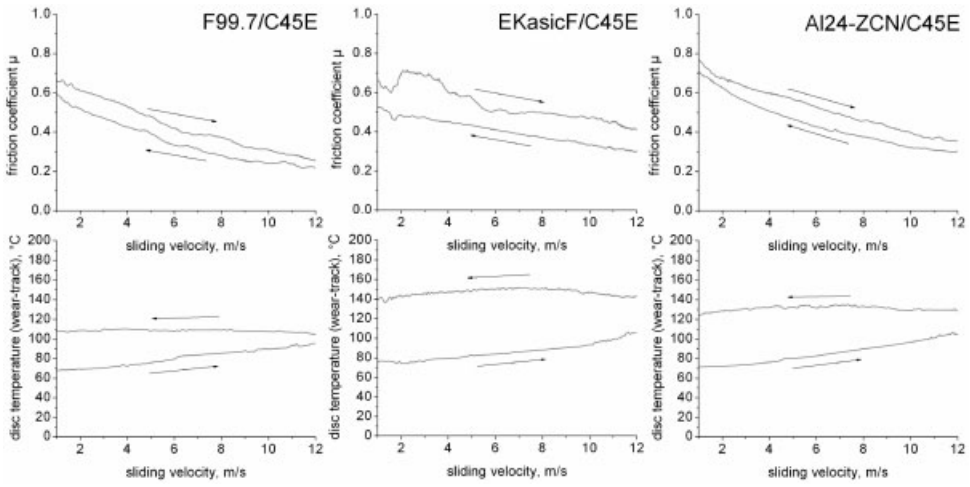


Figure 5: Tribological performance of the reference and laser surface modified ceramics (70°C start temp.).

In order to have a measure of the static friction the values of friction coefficient at the lowest measurable speed (v = 0.001 m/s) were determined. Another important issue for high-performance friction systems is the friction coefficient stability dμ/dv. Negative friction coefficient stability value results in excitement of oscillations and a positive one in damping behaviour of the friction system. The latter is wanted for good comfort behaviour of dry clutches for example. A further important issue is the wear behaviour.

Figure 6 shows the minimum values of friction coefficient from statistical analysis versus the volumetric wear coefficient k_v (Fig. 6a) and the mean friction coefficient stability vs. quasi-static friction coefficient (Fig. 6b) for the downward ramp. It can be seen that the disc wear of the EKasicF couple was greater than that of Al24-WT, Al24-ZCN and Al24-TTB. Lowest wear coefficient of the disc was measured for the monolithic F99.7. Friction level indicated by the minimum friction coefficient was greater for EKasicF and Al24-ZCN than for Al24-WT, Al24-TTB and F99.7.

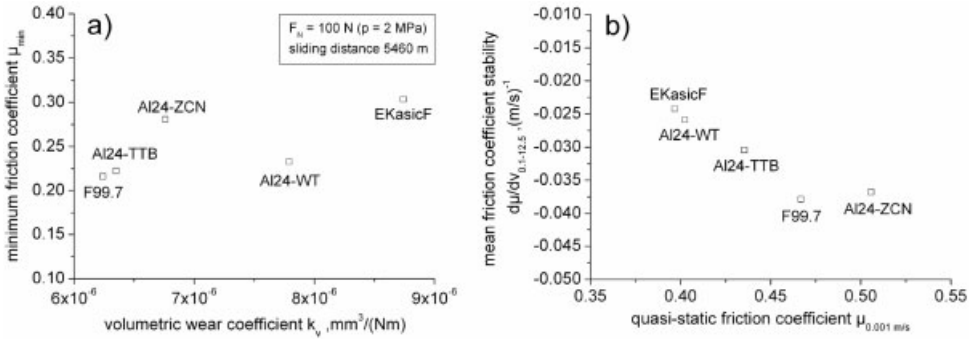


Figure 6: (a) minimum friction coefficient between (downward-ramp) 0.1 and 12.5 m/s vs. volumetric wear coefficient (steel disc) and (b) mean friction coefficient stability (downward ramp) between 0.1 and 12.5 m/s vs. quasi-static friction coefficient (downward-ramp).

Stability of friction coefficient vs. quasi-static friction coefficient is shown in Fig. 6b. The higher the quasi-static friction the lower was the friction coefficient stability. The modified ceramic Al24-ZCN showed the highest quasi-static friction coefficient of slightly above 0.5 followed by F99.7 and Al24-TTB. EKasicF and Al24-WT showed lower values of quasi-static friction coefficient of about 0.4 but better friction coefficient stability. Thus there has to be a compromise of comfort (friction coefficient stability), torque transmission capacity (quasi-static friction coefficient) and wear resistance (volumetric wear coefficient k_V). A good compromise for all requirements could be the modified ceramic Al24-TTB. If comfort aspects (friction coefficient stability) are less important and torque transmission capacity is in focus Al24-ZCN would be the material of choice offering remarkably higher transmission capacities.

Friction layers play an important role for tribological behaviour [9–11]. Investigation of the formed layers on the contact surface of the ceramics was carried out by preparing cross-sections and SEM- and EDX-analysis. The layer formed on the EKasicF was the thinnest (ca. 5 µm) and consisted mainly of iron and ferrous oxides as well as SiC-particles. The F99.7 friction layer was thicker (ca. 10 µm) and consisted of iron and ferrous oxides. The Al24-WT layer was the thickest (ca. 15–20 µm) and consisted besides iron and ferrous oxides of TiN- and WC-particles which were removed from the modified surface.

4 Conclusions

It was shown that surface modification of alumina has a strong influence on its tribological behaviour. By alloying alumina with various added powders it was possible to improve the friction coefficient stability (Al24-WT, Al24-TTB), raise the friction level and quasi-static friction coefficient (Al24-ZCN) for transmission of higher torques in applications such as dry clutches.

Acknowledgements
The authors would like to thank the German Research Foundation (DFG) for financial support

within the Collaborative Research Centre 483 *"High performance sliding and friction systems based on advanced ceramics"*.

5 References

[1] Bergheim, M. ,VDI-Berichte 1323, VDI-Verlag **1997**, 527–548.

[2] Diemer, M.; Kühner, M. ,VDI-Berichte 1827 VDI-Verlag **2004**, 531–547.

[3] Kato, T.; Magario A. ,Tribo. Trans., 37, **1994**, 559–565.

[4] Severin, D. ,VDI- Berichte 1323, VDI-Verlag, **1997**, 43–62.

[5] Poser, K.; Rohde, M.; Schneider, J.; Zum Gahr, K.-H. ,Mat. u. Werkst., **2005**, 122–128.

[6] Poser, K; Schneider, J.; Zum Gahr, K.-H. , Wear, 259, **2005**, 529–536.

[7] Jianxin, D. et al. , Ceramics International, 32, **2006**, 499–507.

[8] Schaupp,D.; Schneider, J.; Zum Gahr, K.-H. ,Tribology Letters 9, **2000**, 125–131.

[9] Österle, W.; Urban, I. ,Tribology International, 39, **2006**, 401–408.

[10] Cho, M.et al. ,Tribology Letters, 20, **2005**, 101–108.

[11] Gee, M. G.; Jennett, N. M. ,Wear, 193, **1995**, 133-145.

Microtribological Characterization of Engineering Ceramic, Cemented Carbide and Steel under Rolling Conditions

S. Kurzenhäuser, J. Schneider, K.-H. Zum Gahr
Universität Karlsruhe (TH), Institute of Materials Science and Engineering II and
Forschungszentrum Karlsruhe, Institute for Materials Research I
P.O. Box 3640, 76021 Karlsruhe, Germany

1 Introduction

Performance and reliability of micro-mechanical systems with movable components are strongly affected by the tribological behavior, which depends on the manufacturing process and alignment of the components as well as the operating conditions and the materials mated in the sliding or rolling contact. High friction forces reduce the usable output torque and even very small amounts of wear resulting in loose wear debris can cause the loss of function of micro-mechanical devices. Several studies on friction and wear of tribologically loaded micro components clarified, that results from tests on the macro scale cannot be simply transferred to the micro scale, especially due to the much higher surface area to volume ratio in micro-mechanical systems [1–4]. Therefore friction and wear behavior of any material pair which is considered for utilization in microtribological systems have to be systematically characterized on the micro scale [5–13]. The aim of the present research work was the tribological characterization of self-mated Si_3N_4-ceramic, WC-12Co cemented carbide and precipation-hardened steel 17-4PH under unlubricated slip-rolling conditions at different normal loads and slip ratios. The tribological tests were accompanied by analysis of the worn surfaces using scanning electron microscopy and optical profilometry.

2 Materials and Experimental Methods

2.1 Materials

A commercially available sintered reaction-bonded Si_3N_4 (SRBSN) ceramic (SL200BG, Fa. Ceramtec) with columnar microstructure and an average grain size of 1.2 µm, a fine grained (0.4 µm) cemented carbide WC-12Co (TSF44, Fa. Ceratizit) and a precipitation hardened steel 17-4PH (solution annealed at 1350°C and age hardened at 560°C for 4h, Fa. Remystahl) were employed in the rolling tests. SEM micrographs of the materials microstructures are shown in Fig. 1. The Si_3N_4 discs were used as-delivered with polished circumferential surface whereas the WC-12Co and 17-4PH samples had to be ground and polished. All functional surfaces had a comparable arithmetic surface roughness value R_a below 0.02 µm.

2.2 Tribological Model System and Loading Conditions

A specially designed twin-disc laboratory microtribometer developed at the Institute of Materials Science and Engineering II of the Universität Karlsruhe (TH) was used for the tribological tests under rolling conditions. Tests were run in ambient air with an adjusted relative humidity of 50%.

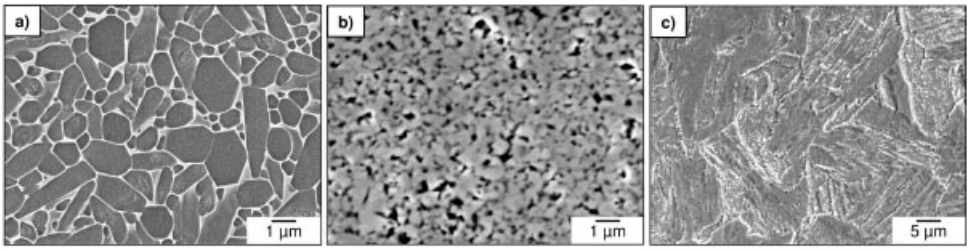


Figure 1: SEM micrographs of the etched microstructures of (a) Si_3N_4, (b) WC-12Co and (c) steel 17-4PH discs used for the rolling tests.

A normal load of F_N = 250 mN, a rolling speed of the driven disc of v_1 = 800 mm/s and slips of 1, 4 and 10% were chosen (**Fig. 2**) based on a system analysis of an exemplary mechanical microsystem containing of a turbine and a planetary gear box [14]. The duration of the rolling tests was 10^6 revolutions. The driver disc (Ø 8 mm) had a flat and the driven disc (Ø 8 mm) a curved rolling surface (radius 4 mm) which ensured a reproducible contact pattern.

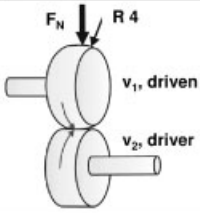
a) **Laboratory tribosystem** for rolling contact	b) **Loading conditions**
	F_N = 250 mN (*1000 mN, 2000 mN*) v_1 = 800 mm/s ($v_2 > v_1$) S = 10% (*1%, 4%*) N = 10^6 Environment: air of 50% r.h. at RT Disc: Ø 8 x 2 mm^2

Figure 2: (a) Schematic description of the twin-disc laboratory tribosystem and (b) the test conditions.

Applied normal force F_N and resulting friction force F_R were measured by strain gauges and recorded continously. Rolling speed of both rollers was computer controlled, while the normal force F_N was kept constant by a software-PID controlled piezostage. Amount of wear was determined after 10^6 revolutions by integrating the profile differences before and after the test runs, which were measured by optical surface profilometry and averaged out at eight different positions at the circumference of the disc. Furthermore the worn surfaces were examined using scanning electron microscopy.

3 Results

3.1 Influence of Slip

Influence of slip values of 1%, 4% and 10% on friction coefficient for the self-mated pairs is illustrated in Fig. 3.

For a slip of 1%, the silicon nitride rolling pair (**Fig. 3a)** showed a friction coefficient of 0.12 at the beginning of the test run which increased to a quasi-stationary value of μ = 0.4 at about

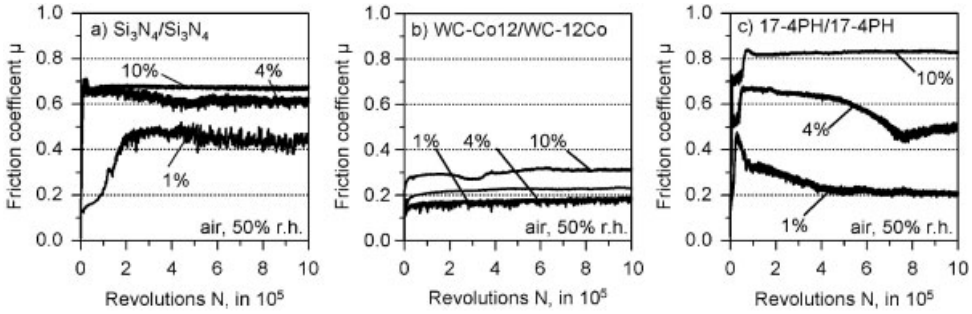


Figure 3: (a) Friction coefficient of self-mated (a) Si_3N_4, (b) WC-12Co and (c) 17-4PH rolling pairs versus the number of revolutions (F_N = 250 mN, v_1 = 800 mm/s)

200000 revolutions. Increasing the slip to 4% and 10% resulted in a shorter running in period of 5000 and 3000 revolutions respectively with a friction coefficient of about 0.3 followed by a steep increase in the friction coefficient exceeding values of 0.7. With increasing number of revolutions the friction coefficient showed a slight decrease to quasi-stationary values of 0.67 at 10% while a more pronounced reduction at 4% slip was observed, resulting in a quasi-stationary friction coefficient of 0.62 at 4×10^5 revolutions. Self-mated WC-12Co pairs running at a normal load of 250 mN with 1% slip (**Fig. 3 b)** showed a quasi-stationary value of $\mu = 0.19$. At 4% and 10% slip the quasi-stationary friction coefficient increased to values of 0.23 and 0.30 respectively, but was significantly lower than that of the Si_3N_4 pair. Friction coefficient of the steel 17-4PH pair showed an increase from low values of 0.12 at the very beginning of the tests at 1% slip (**Fig. 3c)** to peak values of 0.48 after around 0.3×10^5 revolutions, while at prolonged running an exponential decay to quasi-stationary values of 0.20 was observed. An increase of the slip to 4% resulted in a friction coefficient of 0.53 until 0.4×10^5 revolutions, followed by a steep increase to values of 0.67. With prolonged time of testing, the friction coefficient decreased to a quasi-stationary value of 0.5. At 10% slip, the self-mated steel 17-4PH showed a friction coefficient of 0.73 until 0.5×10^5 revolutions, followed by an increase to the quasi-stationary value of 0,83 at the end of the test. **Fig. 4** shows surface profiles of the driven and driver discs recorded after test runs over 10^6 revolutions at the normal load of 250 mN at 10% slip in air of 50% r.h. Under these loading conditions, the Si_3N_4 pair showed an amount of linear wear measured in the center of the rolling surface of 2.0 μm for the driven disc and 0.75 μm for the driver disc.

The linear wear for both discs of self-mated WC-12Co was below the resolution of the employed profilometer, which is below 100 nm. Linear wear of the driven and driver disc for the 17-4PH pairs was 6.1 μm and 6.0 μm, respectively.

SEM micrographs from the middle of the wear tracks after 10^6 revolutions at a normal load of 250 mN and 10% slip are shown in **Fig 5.** The worn Si_3N_4 driven disc showed formation of a third body layer of compacted wear particles (**Fig. 5a**) and, locally, cracks perpendicular to the rolling direction. On the surface of the Si_3N_4 driver disc, no visible cracks but loose wear debris were partially found (**Fig. 5d**). Under the same operating conditions, the SEM micrographs of WC-12Co showed small amounts of fine lose wear debris at the edges of the driven disc's wear track (**Fig. 5b**). The worn surface of the WC-12Co driver disc (**Fig. 5e**) was covered by a layer of compacted wear debris, which was partially delaminating due to cracks. EDX analysis revealed

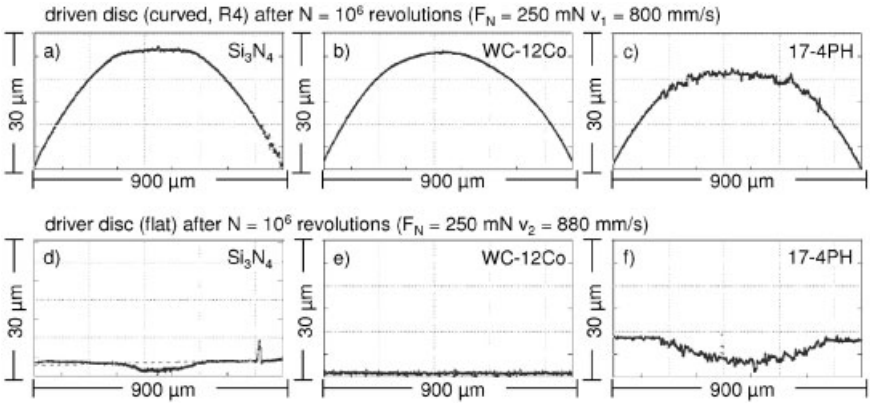


Figure 4: Optical profilometry scans recorded perpendicular to the rolling direction of the worn (a, b, c) driven and (d, e, f) driver discs after 10^6 revolutions at 10% slip of self-mated (a, d) Si_3N_4, (b, e) WC-12Co and (c, f) steel 17-4PH rolling pairs (F_N = 250 mN, v_1 = 800 mm/s).

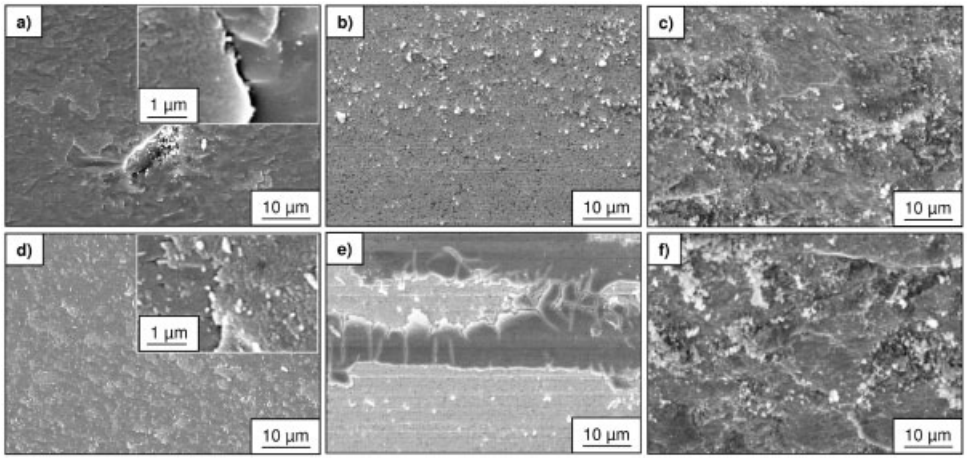


Figure 5: SEM micrographs of the worn surfaces of (a, b, c) driven and (d, e, f) driver discs after 10^6 revolutions at 10% slip of self-mated (a, d) Si_3N_4, (b, e) WC-12Co and (c, f) steel 17-4PH (F_N = 250 mN, v_1 = 800 mm/s).

an oxygen content of the layer which was by at least a factor of 5 higher in comparison to the unworn surface, indicating the formation of WO_3 and $CoWO_4$ [15, 16]. Both 17-4PH (**Fig. 5c, f**) discs have been covered with loose or partially densified wear particles in the form of layers which were locally spalled of. Additionally, fine lose wear particles could be found.

3.2 Influence of Normal Load

The influence of normal load on the friction coefficient for tests at 10% slip is shown in **Fig.6**. For the self-mated Si_3N_4 pairs, the quasi-stationary friction coefficient was 0.67 for 250 mN normal

load, 0.73 for 1000 mN and only slightly increased to values of 0.76 at 2000 mN. The quasi-stationary values for the unlubricated WC-12Co pairs (**Fig.6 b**) was 0.30 and 0.29 for normal loads of 250 mN and 1000 mN respectively, but increased to 0.34 at 2000 mN normal load. In contrast to the 250 mN test runs of the 17-4PH pairs (**Fig.6 c**), the normal load of 1000 mN resulted in temporary drops of the friction coefficient from high values of about 0.8 as seen at the 250 mN test runs to 0.7 until about 4×10^5 revolutions. Thereafter the friction coefficient decreased to values between 0.41 and 0.48. After about 7.5×10^5 revolutions, the experiment had to be stopped because linear wear increased strongly between about 5×10^5 and 7×10^5 revolutions, excessing 500 µm per disc.

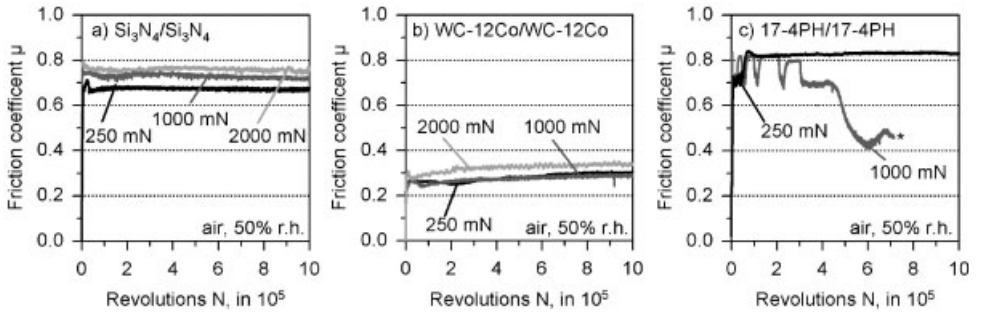


Figure 6: Influence of normal load on the friction coefficient
of self-mated (a) Si_3N_4, (b) WC-12Co and (c) 17-4PH rolling pairs versus the number of revolutions (F_N = 250 mN, v_1 = 800 mm/s, slip S = 10%) (*: experiment abandoned as disc wear exceeded 500 µm)

4 Discussion and Conclusions

The influence of slip and normal load on the microtribological performance under rolling conditions was examined for self-mated Si_3N_4, cemented carbide WC-12Co and steel 17-4PH in air at a relative humidity of 50%.

The results of this research work showed that cemented carbide WC-12Co is a suitable material for tribologically high-loaded micromechanical components, showing a high wear resistance even under severe unlubricated slip-rolling conditions. Under the most severe test condition (F_N = 2000 mN, S = 10%), wear on WC-12Co was still not measurable (<100 nm per disc) and the friction coefficient was on an acceptable level below 0.34. Corresponding to other results [15, 16] this could be attributed to the smoothing of the surfaces and the formation of thin WO_3 films.

The same test conditions resulted in a cumulative linear wear of about 7 µm after 10^6 revolutions for the self-mated Si_3N_4 and a high friction coefficient of about 0.76. The steel 17-4PH completely failed due to high wear and friction coefficient, indicating that adhesion was the dominant wear mechanism. Under mild test conditions (F_N = 250 mN, S = 1%) the Si_3N_4 rolling pairs showed moderate wear, originated in microfracture and tribochemical reactions, but the in-

creased roughness of the worn surface and the formation of SiO_2 [17, 18] resulted in a relatively high friction coefficient above 0.3 compared to that of the WC-12Co pair ($\mu = 0.19$).

Further tests should be employed with lubricants suitable for applications in microsystems in order to achieve suitable friction coefficients below 0.1 in addition to the already convincing high wear resistance.

5 Acknowledgment

The authors would like to thank the **Deutsche Forschungsgemeinschaft (DFG)** for financial support within the frame of the **Center of Excellence in Research 499 (SFB 499)** *"Construction, production and quality assurance of molded micro components made from metallic and ceramic materials"*.

Literature

[1] Zum Gahr, K.-H., *Micro Mechanical Systems – Principles and Technology*, Fukuda T.; W. Menz, W., Elsevier, Amsterdam 1998, 83–113.

[2] Scherge, M., *Proc. World Tribology Conference 2001*, Vienna, 2001, 489/1–489/7.

[3] Zum Gahr K.-H.; Blattner, R.; Hwang, D.-H.; Pöhlmann, K., *Wear* 2001, 250, 299–310.

[4] Tambe, N. S.; Bhushan, B., *Nanotechnology,* 2004, 15, 1561-1570.

[5] Kaneko, R., *Tribology Letters*, 2000, 9, 89–96.

[6] Maboudian, R.; Ashurst, W.; Carraro, C., *Tribology Letter*s, 2002, 12, 95–100.

[7] Hegadekatte, V.; Kurzenhäuser, S.; Huber, N.; Kraft, O., *Tribology Letters*, 2008, accepted.

[8] Kurzenhäuser, S.; Schneider, J.; Zum Gahr, K.-H., *Proc. Tribologie Fachtagung 2006*, Gesellschaft für Tribologie, Göttingen, 2006, S. 12/1–12/9.

[9] Kato, K., *Tribotest*, 2006, 12, 201–210.

[10] Berg, S.; Johannsmann, D., *Physical Review Letters*, 2003, 91, 145505.

[11] Kim, S.; Asay, D.; Dugger, M.T., *nanotoday*, 2003, 5, 22–28.

[12] Williams, J.; Lee, H.; *J. Physics D - Appl. Phys.*, 2006, 39, R201–R214.

[13] Filippov, A.E.; Dienwiebel, M.; Frenken, J.W.M.; Klafter, J.; Urbakh, M., Phys. Rev. Let., 2008, 100, 046102.

[14] Schneider, J.; Zum Gahr, K.-H.; Herz, J., *Advanced Micro and Nano Systems*, 2005, 3, 579–604.

[15] Enqvist, H.; Högberg, H.; Botton, G.A.; Ederyd, S.; Axén N., *Wear*, 2000, 239, 219–228.

[16] Murray S.F.; Lewis, P., *General Electric*, Feb. 7, 1958.

[17] Kato, K.; Adachi, K., *Wear*, 2002, 253, 1097–1104.

[18] Kalin, M.; Vizinitin, J., *J. Eur. Cer.am. Soc.*, 2004, 24, 11–15.

The Behavior of Silicon Nitride Tools in Hot Rolling Copper Wire

I. Khader[1,2], S. Fünfschilling[3], A. Kailer[1], R. Oberacker[3]

[1] Fraunhofer- Institut für Werkstoffmechanik IWM; Freiburg

[2] Universität Karlsruhe (TH)- Institut für Zuverlässigkeit von Bauteilen und Systemen (IZBS), Karlsruhe

[3] Universität Karlsruhe (TH)- Institut für Keramik im Maschinenbau (IKM), Karlsruhe

Keywords: ceramics, silicon nitride, copper, rolling, FEM, reaction

Abstract

The aim of this study is to investigate the behavior of silicon nitride rolls in rolling copper wire. Experimental tests and FE-based simulations were conducted for this purpose. After running the experiments, several inspections were carried out to examine the surfaces of the used specimens. In order to furnish the final conclusions, experimental findings were compared to the outcomes of the simulations. The FE simulations predicted very low thermo-mechanical stresses. Hot rolling experiments showed considerable metallic adhesion on the surface of the ceramic rolls, which was significantly reduced by applying cooling lubricants. Rolling-contact experiments showed moderate wear rates when the proper lubrication was applied. Due to severe selective corrosion of silicon nitride, the same experiments showed high wear rates when carried out in distilled water. The nature of adhesion between copper and silicon nitride was investigated through reaction experiments. Bulk ceramic materials with different sintering additives as well as synthesized pure secondary phase compositions were tested. Non-wetting behavior was observed between silicon nitride bulk ceramics and copper. The secondary phase samples also showed no significant reaction with copper.

1 Introduction

The application of non-oxide ceramics in wire rolling exhibits a prospective innovative improvement to this metal forming process. Recent advances in the manufacturing of silicon-nitride-based ceramics enabled the production of materials of high potential to be utilized as rolling tools. Its chemical stability, high strength and high fracture toughness at elevated temperatures, combined with a moderate elastic modulus, remarkable resistance to wear and good thermal shock resistance, enables silicon nitride to be a plausible alternative to steel and cemented carbide rolling tools.

The behavior of silicon nitride, in contact with various metal alloys, was investigated by several researchers [1–3]. Akdogan et al. [2] pointed out the formation of metallic tribofilms and debris on the surface of silicon nitride, when brought in sliding contact with bronze. Very high wear rates were also recorded, even at low speeds and small loads. The adherent layer was described as being “not easily detachable” and was attributed to a possible chemical interaction with the surface of silicon nitride; this chemical interaction was presumed to be augmented by the high interface temperature during sliding.

A non-wetting behavior between molten copper and hot-pressed silicon nitride (HP-Si_3N_4) was separately recorded by Klein et al. and Sangiorgi et al. in [4,5]. Nonetheless, corrosion of HP-Si_3N_4 by molten copper was previously investigated by Sangiorgi et al. in [6] and was argued to be a function of the chemical composition, type and amount of the secondary phase of the silicon-nitride-based ceramic. Corrosion and surface pitting in the HP-Si_3N_4 samples was attributed to chemical attack on the secondary phase and the decomposition of the grain boundary phase. This corrosion took the form of surface pitting.

Wötting et al. [7,8] presented a case in which silicon nitride rolls were used to hot-roll copper wire. Significant copper adhesion, formation of pits, and an increased caliber surface roughness were observed. The authors accounted this to grain boundary phase damage occurring in silicon nitride due to its interaction with copper.

To acquire a clear understanding of the applicability of silicon-nitride-based ceramics in wire-rolling high purity copper, this study was carried out as a part of the German Research Foundation (DFG) Center of Excellence in Research-483 (SFB-483 High Performance Sliding and Frictions Systems based on Advanced Ceramics) program; wherein, the main objective of the research group [9] is to establish a system-oriented model for the failure mechanisms of ceramic materials used in wire-rolling processes.

2 Materials

Experimental ceramic rolls were prepared from a commercial silicon nitride powder (Si_3N_4, CeramTec) and sintered through a gas-pressure sintering process. This variation of hot isostatically-pressed silicon nitride (HIP-Si_3N_4) contains 3 wt.% Al_2O_3 and 3 wt.% percent Y_2O_3 as sintering additives. After sintering, the microstructure of the system Si_3N_4-Al_2O_3-Y_2O_3 comprised β-Si_3N_4 grains and an intergranular glassy phase of approximately 12%. More details about the material and sintering processes are given by Fünfschilling et al. in [10]. High purity copper (Cu-OF1) was used in the hot rolling and rolling-contact experiments. Yield stress and elastic modulus values of copper were acquired by conducting room- and high-temperature tensile tests.

Reaction tests were carried out on three silicon-nitride-based bulk ceramics. These were prepared through a gas-pressure sintering process at 10 MPa reaching densities >99% td. The secondary phase in silicon nitride was assumed to be the critical reaction partner in contact with copper compared with the β-grains; thus, bulk samples of two secondary phase were also included in the tests: an amorphous oxynitride glass (Si_3N_4-MgO-Y_2O_3-SiO_2) and a crystalline disilicate (SiO_2-Y_2O_3). The production of the oxynitride glass samples is described in detail in Satet et al. [11]. To synthesize the disilicate samples, green bodies were pressed from a starting powder of 65.3 wt.% Y_2O_3 and 34.7 wt.% SiO_2 and sintered in air for 8 hours at 1450 °C. The disilicate samples reached densities up to 73.3% td. The chemical composition and description of the tested materials are shown in Table 1. The tested bulk ceramic material (Si_3N_4-Al_2O_3-Y_2O_3) is identical to the commercial powder used to prepare the experimental rolls. High purity oxygen free copper (Cu-OFHC) was used for these experiments.

Table 1: Materials tested in the reaction experiments with high purity copper

Sample	Composition	Description
1	Si_3N_4-SiO_2-Y_2O_3	Bulk ceramic
2	Si_3N_4-Al_2O_3-Y_2O_3	Bulk ceramic
3	Si_3N_4-SiO_2-Lu_2O_3	Bulk ceramic
4	Si_3N_4-MgO-Y_2O_3-SiO_2	Amorphous oxynitride glass
5	SiO_2-Y_2O_3	Crystalline disilicate

3 Experimental Procedure

Three sets of experiments were conducted to study the behavior of silicon nitride when brought into contact with copper.

3.1 Wire Hot Rolling Experiments

Lubricated and unlubricated hot rolling experiments were carried out using high purity copper wire. The wire was heated to 650 °C in an inert gas atmosphere (argon), to reduce oxidation. Friction between the work rolls and the wire pulls the latter into the roll gap. The diameter of the wire is then reduced by 30% into an oval cross section. The corresponding force applied to the work rolls is in the range of 2.7 kN. All parameters (i.e. temperature, feed rate and reduction) were fixed for both lubricated and unlubricated tests. In the lubricated tests, a special-purpose mineral oil-based cooling lubricant (UNOPOL G 600, Bechem) was applied to the caliber surface at the exit zone side of the roll gap. This reduces the influence of the lubricant on the rolling temperature of the wire. In each test, approximately 2000 meters of copper wire were rolled. A detailed description of the test rig is found in Khader et al. [12].

3.2 Rolling-Contact Experiments

In rolling-contact experiments ceramic rolls are loaded under cyclic mechanical loading conditions. This can be compared to the loading situation in wire rolling. The tests were conducted under emulsion-lubricated, water-lubricated and unlubricated (dry) conditions at room temperature. Copper discs ($Ø_o$ 60 mm) were brought into rolling-contact with silicon nitride rolls ($Ø_o$ 55 mm). The Cu-Si_3N_4 mating pairs were forcibly driven with different rotational speeds. The copper disk was driven at a speed of 200 rpm and the ceramic roll at 175 rpm; thus, creating a slip ratio of 22% between the mating surfaces. The slip ratio is calculated according to the equation $\Delta U/U$; where U represents the average surface velocity of the two bodies in contact, and ΔU is the differential surface velocity. An ascending pressing force, starting at 175 N and reaching 260 N, was applied to the mating pairs for the test duration of 230 hours. The lubricant was filled in a retainer, pumped on the surface of the roll, and its level was checked regularly. The emulsion lubricant used in rolling-contact experiments is identical to that used in hot rolling.

3.3 Reaction Experiments

The nature of adhesion between copper and silicon nitride was investigated by conducting reaction experiments. The ceramic and secondary phase specimens were cut using a diamond blade

into dimensions of 10 × 10 × 3 [mm]. Their surfaces were polished by using a slurry comprising diamond particles up to 1 μm in size to ensure good contact with the copper plates (dimensions 10x10x2 [mm]). The specimens were assembled in a sandwich configuration, shown in Fig.1, then placed in a Gero tube furnace, pressed together imposing a contact pressure of 0.06 MPa and held for 24 hours at 1000 °C in an argon atmosphere, Table 2.

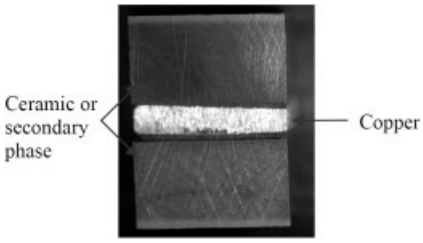


Figure 1: Sandwich assembly of the reaction couples

Table 2: Reaction experiments' parameters

Experimental parameters	
Temperature	1000°C
Holding time	24 hours
Atmosphere	Argon
Contact pressure	0.06 MPa

4 Numerical Simulations Results and Discussion

A finite element (FE) analysis was carried out to predict the thermo-mechanical stresses developed in copper wire rolling at elevated temperatures. Minimum principal stresses (compressive stresses) give a rough estimation of contact stresses, while maximum principal stresses (tensile stresses) are commonly considered to predict failure in brittle materials such as ceramics. The simulations were adapted to the model designed for hot rolling experiments. A detailed description of the FE-model is found in [12].

The ceramic roll's initial temperature was 50 °C. The first analyzed case used copper wire with an initial temperature of 600 °C; accordingly the yield stress of copper, obtained from tensile tests, is approximately 14 MPa. The analysis reveals maximum tensile stresses in the range of 40 MPa, compressive stresses in the range of 230 MPa, and maximum surface contact temperature of 470 °C. The tensile stress field distribution shows maximum stresses appear in the depth of the roll, below the caliber surface. Raising the wire temperature to 825 °C reduces the yield stress of copper to approximately 6 MPa. However, this results in an increase in the maximum tensile stress up to 45 MPa, in the compressive stress up to 320 MPa and the maximum contact temperature on the surface of the roll reaches 640 °C as shown in Fig. 2. The fact that the highest tensile stress appears in the depth of the roll and that increasing the wire temperature increases the developed stresses, despite a reduction in the strength of copper, indicates that

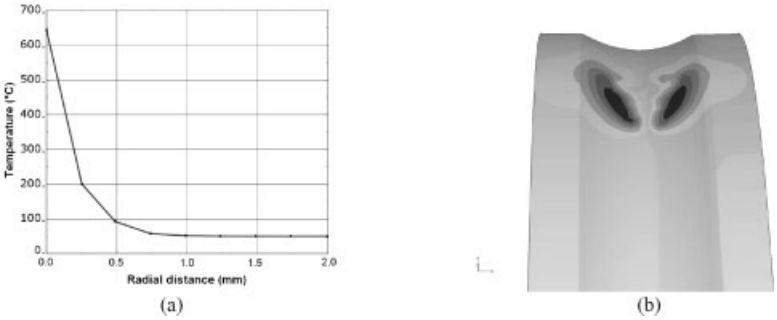


Figure 2: FE simulations' results of hot rolling copper wire with an initial wire temperature of 840°C, (a) temperature distribution in the depth of the roll, showing maximum temperature of approximately 640 °C on the caliber surface, (b) lateral shear stress distribution (maximum in red) on the surface of the caliber

the greater proportion of the developed stresses are thermal stresses. The acquired temperature distribution shows steep gradients developed in the depth of the roll. In any case the associated thermal stresses were too low to induce thermal shock in silicon nitride. In accordance with the experimental observations, no failure of the silicon nitride rolls was expected to take place. The simulations showed that the thermo-mechanical stresses developed throughout the rolls were too low to induce damage. Fig. 2 also shows the lateral shear stress distribution on the surface of the caliber. This distribution coincides with the locations of maximum copper adhesion on the surface of the caliber as will be shown in the next section.

5 Experimental Results and Discussion

5.1 Hot Rolling Experiments

After running both lubricated and unlubricated hot rolling experiments, tribofilms appeared on the calibers' surfaces. A significant reduction of metallic adhesion was noticed when applying the lubricant. Fig. 3 shows the calibers before and after running the experiments. It was previously noticed in [12] that copper oxidation plays a significant role in reducing metallic adhesion on the surface of silicon nitride. This was attributed to the fact that the oxide layer acted as an anti-scuffing layer.

Examining the calibers under the scanning electron microscope (SEM) after rolling indicated a slight change in the surface texture of the calibers. SEM images of the three cases presented in Fig. 3 are shown in Fig. 4.

Unlubricated rolling left a metallic adhesive layer on the surface of silicon nitride in the form of agglomerates of small particles. Under lubricated conditions the adhesion formed sparse adhesive micro-particles on the ceramic surface. These micro-particles are the reason behind the coloration observed on the surface of the caliber. EDX analyses indicated that the major constituents of the metallic adhesive layer are copper and oxygen. In order to inspect silicon nitride surface under this layer, copper was etched using a solution of 53% HNO_3 for 8 minutes. This acidic solution does not react with the surface of the ceramic. SEM inspection of the etched specimen showed less grinding micro-spalls on the caliber surface compared to what was observed in the unused

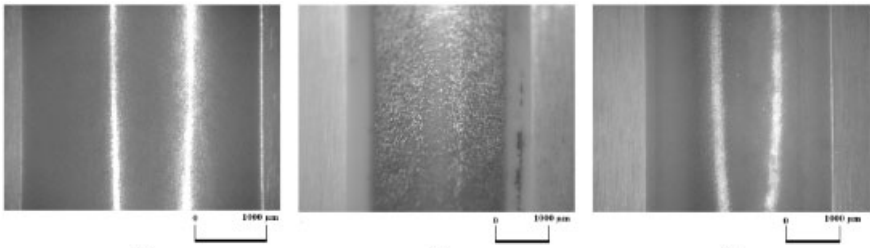


Figure 3: Hot rolling experiments showing (a) the caliber status before running the tests, (b) after rolling ˜2000 meters of copper wire without lubrication, (c) after rolling ˜2000 meters of copper wire with lubrication

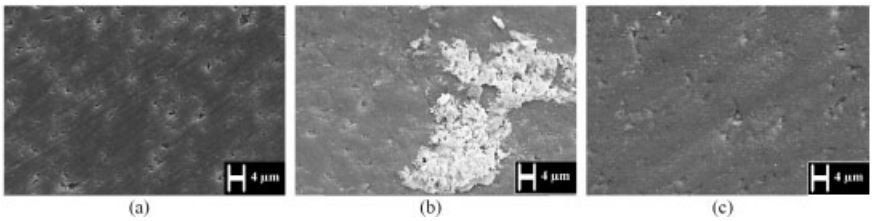


Figure 4: SEM images showing (a) the caliber surface of an unused specimen, (b) after rolling $\sim$ 2000 meters of copper wire without lubrication, (c) after rolling $\sim$ 2000 meters of copper wire with lubrication

specimen. No chemical pitting was observed on the surface of silicon nitride in lubricated and unlubricated experiments. In both cases, grinding undulations and grooves, which were obvious on the surface of the unused specimen, were removed and the surface of silicon nitride was smoothed. Additionally, the remaining micro-spalls on the caliber surface were blunted.

Table 3: Summary of roughness measurements before and after hot rolling

Description	R_a [µm]	R_z [µm]
Before rolling	0.36	1.08
Unlubricated hot rolling	0.36	0.51
Lubricated hot rolling	0.35	0.42

A slight decrease in roughness was noticed after conducting the experiments. Average caliber roughness values measured before and after rolling are shown in Table 3. The decrease in roughness indicates an insignificant amount of wear.

5.2 Rolling-contact Experiments

The dry sliding tests were stopped shortly after running due to a rise in temperature of the mating pairs.

This temperature raise caused the formation of an oxide layer on the copper disk that prevented direct Cu-Si_3N_4 contact. Emulsion-lubricated tests showed a reduction in roughness and slight abrasion on both the ceramic roll and copper disk, Fig. 5. No pitting, damage or chemical reaction

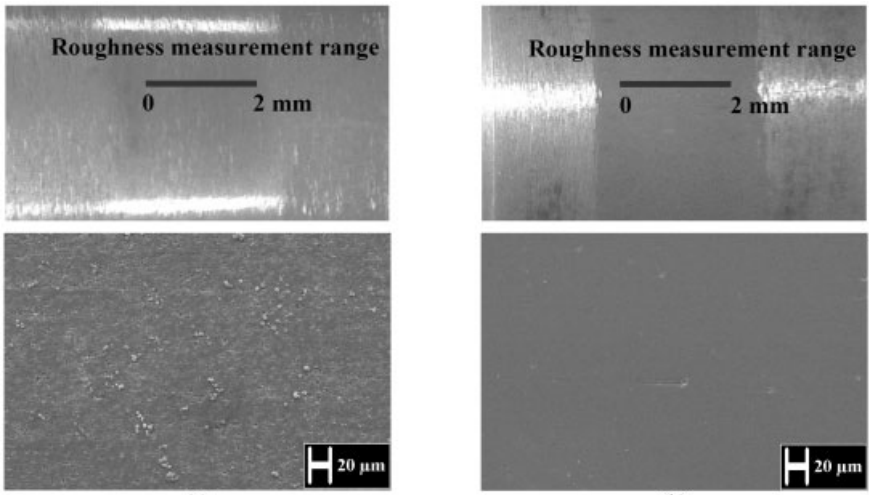


Figure 5: Rolling-contact experiments, showing the wear track on the ceramic surface after 230 hours (a) with emulsion lubrication, (b) with distilled water lubrication.

between copper and silicon nitride was observed. Water-lubricated tests showed considerable silicon nitride wear and less abrasion on the copper disk than that measured after the emulsion-lubricated tests. The surface of silicon nitride was polished and roughness decreased sharply as shown in Fig. 5 and Table 4. No damage or chemical reaction between copper and silicon nitride was detected. The polished ceramic surface explains the low wear rate of the copper disk. Friction between the two mating surfaces was significantly reduced after a short running time. The SEM analysis on the rolls showed that the glassy phase of silicon nitride was attacked by distilled water causing high wear rates.

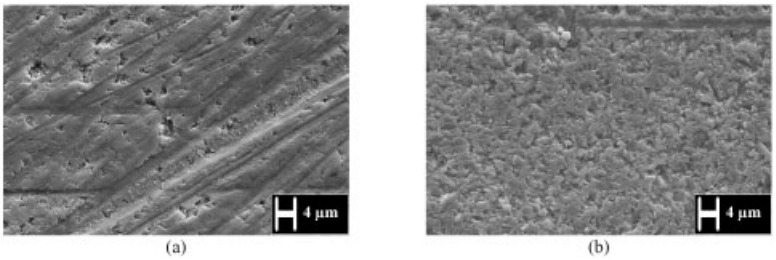
Table 4: Summary of roughness and wear measurements before and after running the experiments

Description	Copper cut[µm]	Si_3N_4 cut[µm]	Si_3N_4 wear volume[mm^3]	R_a[µm]	R_z[µm]
Before	0	0	0	0.45	3.40
Emulsion-lubricated	300	1-2	0.86	0.10	0.98
Water-lubricated	250	25	10.79	0.02	0.18

Corrosion of silicon nitride in aqueous media at low temperatures was previously investigated and attributed to the solution of the glassy phase (selective corrosion). Fig. 6 shows the surface of the rolls before and after being exposed to distilled water during the experiments. Selective corrosion of the glassy phase can be clearly depicted from the SEM images.

5.3 Reaction Experiments

After running the reaction experiments, the contact surface of each specimen was inspected. SEM, EDX and X-ray diffraction (XRD) analyses were carried out. The results are summarized



(a) (b)

Figure 6: SEM images showing (a) the surface of an unused HIP-Si_3N_4 roll, (b) the same surface outside the wear track after being chemically attacked by distilled water during rolling-contact experiments, some of the grinding grooves are still visible in the photo.

in Table 5. In the XRD column, only new phases are listed. Fig. 7 shows the XRD-patterns of the three ceramic bulk materials and an SEM image of the surface of an examined Si_3N_4-SiO_2-Y_2O_3 specimen.

Experiments conducted on bulk ceramics showed no influence of the additives on the reaction of HIP-Si_3N_4 with copper under these experimental parameters. These results are in accordance with the observations of Sangiorigi et al. [5] and Leroux et al. [13]. Additionally, no traces of damage were found on the contact surface of the ceramics. The SEM images showed small (2µm) spherical copper particles on the surface of the ceramic, Fig. 7, which indicates a non-wetting behavior with copper.

The oxynitride glass bulk samples showed no Cu- containing reaction products after running the tests. The detected $YMgSi_2O_5N$ and $Y_4MgSi_3O_{13}$ phases are crystallisation products of the glass. This was also the case for the disilicate bulk samples; where no new crystalline phases were detected. It is clearly obvious from the results obtained in these experiments that no significant chemical reaction takes place, either between copper and silicon nitride, or between copper and pure silicon-nitride secondary phase. Moreover, no damage or significant surface changes could be detected on the surface of the samples.

Table 5: Summary of the outcomes of the reaction experiments

Sample	Description	XRD (new phases)	SEM/EDX
Si_3N_4-SiO_2-Y_2O_3	Ceramic bulk	Cu	Spherical copper particles
Si_3N_4-Al_2O_2-Y_2O_3	Ceramic bulk	Cu	Spherical copper particles
Si_3N_4-SiO_2-Lu_2O_3	Ceramic bulk	Cu	Spherical copper particles
Y_2O_3-SiO_2	Disilicate	Cu	Spherical copper particles
Si_3N_4-MgO-Y_2O_3-SiO_2	Oxynitride glass	$YMgSi_2O_5N$, $Y_4MgSi_3O_{13}$, Cu	Copper deposits

6 Summary and Conclusions

The FE simulations of hot copper wire rolling using silicon nitride rolls predicted very low stresses in general. The maximum developed tensile stresses in silicon nitride were lower than

10% of the material's bending strength. Steep temperature gradients were developed within the roll material but the associated thermal stresses were too low to cause damage. In hot rolling copper wires, where the material exhibits low yield stress and high thermal conductivity, the dominant proportion of the developed stresses within the roll material is due to thermally induced expansions. It was also noticed that the locations of maximum lateral shear stresses on the caliber surface coincide with the locations of maximum copper adhesion.

Hot rolling experiments showed considerable metallic adhesion on the surface of the tested silicon nitride (Si_3N_4-Al_2O_2-Y_2O_3). The adhesive metallic layer consisted mainly of copper and oxygen. In dry rolling, it took the form of agglomerates of small particles which distorted the profile of the caliber. Adhesion was significantly reduced by applying cooling lubricant to the rolls. In both lubricated and unlubricated tests, the surface roughness of the calibers slightly decreased. Micro-spalls and grinding grooves were removed, but neither cracks nor a chemical reaction with copper was detected. Along with the results obtained from the simulations, this highlights the role of friction as a crucial factor in the adhesions of copper.

Rolling-contact experiments showed a reduction in roughness of the ceramic rolls. Experiments carried out with cooling emulsion lubrication showed smooth wear tracks with no traces of cracks, pitting or chemical reaction with copper. Water lubricated tests formed polished wear tracks and metal cuts in copper disks were lower than expected. No traces of cracks, pitting or chemical reaction between copper and silicon nitride were observed. It was noticed distilled water reacted with the surface of silicon nitride causing selective corrosion of the glassy phase.

Reaction experiments carried out on the three bulk ceramics showed a non-wetting behavior with copper and neither chemical pitting nor chemical reaction could be detected. Sintering additives had little or no effect on the behavior of HIP-Si_3N_4 when brought in contact with high purity copper. The crystalline disilicate (SiO_2-Y_2O_3) showed no significant reaction with copper and no new crystalline phases were formed. This was also the case for the amorphous oxynitride glass (Si_3N_4-MgO-Y_2O_3-SiO_2), which showed no evident reaction with copper as no Cu-containing reaction products were detected. Based on these experiments it can be concluded that the reaction of copper with silicon nitride or its pure secondary phase is highly improbable.

Based on the results obtained in this study, the wear of HIP-Si_3N_4 when brought in contact with pure copper can be described as minimal. Hot rolling and rolling-contact experiments showed no chemical damage on the surface of silicon nitride caused by copper. Reaction experiments showed a non-wetting behavior and almost no chemical reaction between the tested silicon nitride materials and copper. In conclusion, rolling tools made of silicon nitride could be successfully applied in rolling high purity copper wire, provided the suitable lubricant was used. Nevertheless, HIP-Si_3N_4 shows high wear rates when running under sliding contact loading in aqueous media due to selective corrosion. This corrosion can be significantly reduced by applying suitable lubrication. A continuation to this study will consider the suitability and limitations of silicon nitride rolling tools in rolling high strength steel alloys under various conditions.

Acknowledgments

The authors acknowledge the financial support of the German Research Foundation (DFG) under grants SFB-483/TP-A7 and SFB-483/TP-B5. Thanks are also due to the staff at Fraunhofer IWM in Freiburg and at Universität Karlsruhe (TH) for their help and extended support.

7 References

[1] P. Andersson, M. Wild, J. Levén, B. Hemming, Transfer of surface texture from silicon nitride rolls to stainless steel wire in cold-rolling. *Journal of Materials Processing Technology*, 173, Issue 3, 2006, 394–400.

[2] G. Akdogan, T.A. Stolarski, Wear in metal/silicon nitride sliding pairs. *Ceramics International*, 29, Issue 4, 2003, 435–446.

[3] P. Montmitonnet, F. Delamare, B. Rizoulieres, Transfer layer and friction in cold metal strip rolling processes. *Wear*, 245, Issue 1-2, October 2000, 125–135.

[4] R. Klein, M. Desmaison-Brut, P. Ginet, A. Bellosi, J. Desmaison, Wettability of silicon nitride ceramic composites by silver, copper and silver copper titanium alloys, *Journal of the European Ceramic Society,* 25, Issue 10, 2005, 1757–1763.

[5] R. Sangiorgi, M. Muolo, A. Bellosi, Wettability of hot-pressed silicon nitride materials by liquid copper. *Materials Science and Engineering*, 103, Issue 2, 1988, 277–283.

[6] R. Sangiorgi, A. Bellosi, M.L. Muolo, G.N. Babini, Corrosion of hot pressed silicon nitride-based materials by molten copper. *Journal of Materials Science*, 24, 1989. 4080–4087.

[7] A. Kailer, T. Hollstein (Ed.), Walzen mit Keramik. Fraunhofer IRB Verlag, Stuttgart, ISBN 3-8167-6462-2, 2004.

[8] G. Wötting, H. Drachsler, H.-J. Pohlmann, Werkstoffqualifizierung und Bauteilherstellung, in [7], 2004, 23–35.

[9] K.-H. Zum Gahr, J. Schneider (Ed.), Hochbeanspruchte Gleit- und Friktionssysteme auf Basis ingenieurkeramischer Werkstoffe: In the proceedings of the 3rd colloquium of the DFG-SFB 483, Keramische Walzensysteme, ISBN 978-3-933733-00-9, 2007, 89–136.

[10] S. Fünfschilling, R. Oberacker, M.J. Hoffmann, Verhalten von Siliciumnitrid-Keramiken mit unterschiedlichen Korngrezphasen im Kontakt mit Kupfer, in [9], 2007, 105–112.

[11] R. Satet, M. Hoffmann, Grain growth anisotropy of β-silicon nitride in rare-earth doped oxynitride glasses. *Journal of the European Ceramic Society*, 24, Issue 12, 2004, 3437–3445.

[12] I. Khader, P. Gumbsch, A. Kailer, Damage Mechanisms of Silicon Nitride Rolls in Hot Rolling of Copper Wire. In the proceedings of the Tribologie-Fachtagung, Göttingen, ISBN 978-3-00-022603-8, 2007, 73/1–14.

[13] V. Leroux, J. Labbe, T. Nguyen, M. Shanahan, Wettability of non-reactive Cu/Si-Al-O-N systems I. Experimental results. *Journal of the European Ceramic Society*, 21, Issue 6, 2001, 825–831.

Tribological Investigation of Si_3N_4 Composites

Zsuzsanna Koncsik[1, a], Mária Berkes Maros[2, b], László Kuzsella[3, c]
[1] PhD. Candidate, University of Miskolc, Department of Mechanical Engineering
[2] Associate Professor University of Miskolc, Department of Mechanical Engineering
[3] Assistant Lecturer, University of Miskolc, Department of Polymer Engineering
[a] metkzs@uni-miskolc.hu, [b] metmar@uni-miskolc.hu, [c] femkuzsy@uni-miskolc.hu

1. Introduction

Nowadays one of the most up-to-date directions of material development is represented by the particle reinforcement. In case of structural ceramics, e.g. silicon nitride based composites, the most often used reinforcing phase is SiC, that can be introduced or created in the ceramic composite in several ways [1-5].

The main topic of the current work consists in analysing the tribological behaviour of graphite reinforced Si_3N_4 composites. The basic aim was to investigate the influence of microstructural features, i.e. amount and grain size of the added reinforcing graphite, as well as the effect of loading force on the wearing characteristics like wearing profile, wear rate, friction coefficient or mechanism of the wear damage process. Tribological tests were performed on a pin-on-disc tribometer with on-line measurement of friction coefficient and wear profile. Wear tests were completed with traditional micro-hardness and instrumented hardness tests, furthermore morphological analyses of the wear tracks by SEM were executed.

2. Experimental procedure

2.1. Preparation of test specimens

Wear tests were executed on five specimens made of Si_3N_4 ceramic matrix composites reinforced by graphite particles. The test specimens were produced by the Institute of Inorganic Chemistry of the Slovak Academy of Sciences in Bratislava. The initial disc shape samples (of ϕ 47 mm diameter and 3 mm height) and one of the test pieces are illustrated in Fig. 1.

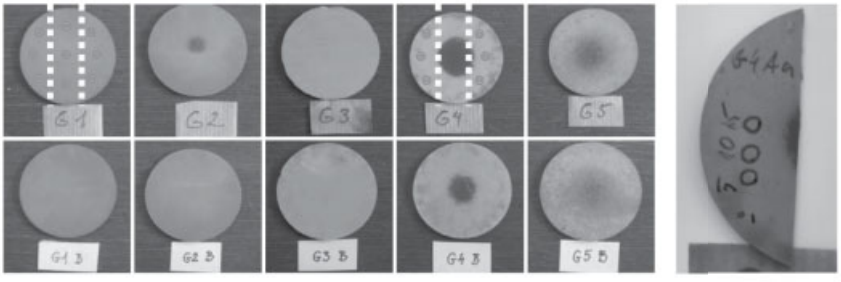


Figure 1. The two faces of the initial Si_3N_4 – C composite discs and G4 test piece with wear traces (circles on the G1 and G4 samples represent the planned location of the wear traces on the certain test pieces separated along the dotted line; Dark inner regions in G2, G4, G5 specimens show graphite rich zones)

Due to the limited fixture dimensions of the tribo-tester the discs were cut along the dotted lines into smaller test pieces (see Fig.1). During manufacturing Si_3N_4 powder of class E10 as base material was used, with Y_2O_3 as sintering additive. Chemical composition of the starting mixtures, prepared in two steps is listed in Table 1.

Table 1. Chemical composition and density of the initial mixture

Specimen	Si_3N_4*	Y_2O_3	Graphite		Density
	[wt%]	[wt%]	Content [wt%]	Grain size [μm]	[g/cm^3]
G1	93,1	4,9	2	< 25	3,246
G2	90,3	4,7	5	< 25	3,239
G3	85,5	4,5	10	< 25	2,494
G4	85,5	4,5	10	< 71	2,822
G5	85,5	4,5	10	< 125	3,141
G6**	85,5	4,5	10	>125	3,090

* UBE Industries, Ltd., Japan, SN-E10

** Tribological tests on G6 specimen — due to technical problems — are not completed yet, therefore only test results of G6 from the other tests are presented in this work.

The dried mixed powders were hot-pressed in a carbon die at 1750 °C by pressure of 30 MPa and 0.2 bar over-pressure of nitrogen [6]. During sintering the mutual reaction of the graphite particles, the sintering additive and the silicon nitride may lead to formation of various new phases. Among the others SiC grains (intra- and intergranular), various complex new phases e.g. oxides, oxi-nitrides, carbo-nitrides, etc. can be developed. Thus an in-situ reinforced Si_3N_4 based composite can be produced.

2.2. Material characterisation

The *microstructure* of the specimens was studied on the fracture surface of samples in the vicinity of the wear trace. Fig. 2. illustrates the microstructure of the G1, G2 and G3 test pieces, containing different amount of graphite additives (2; 5 and 10 wt% respectively), and the same grain size (ϕ<25 μm). In the microstructures of the G1 and G3 test pieces the β-Si_3N_4 grains can be clearly recognized. They are larger in case of the G1 specimen, while G3 sample has a finer grained microstructure. In the G2 specimens the β-Si_3N_4 needles are embedded into a high amount of second phase (that seems to have been plastically deformed during breaking).

After sintering some of the specimens showed differently coloured regions along the diameter, as well as through the thickness (see Fig. 1). It is assumed, that inhomogeneous temperature distribution during the heat treatment resulted in compositional inhomogeneity, and non-reactive graphite agglomerates were left in the specimens, as shown in Fig. 2. d). The graphite content of the different regions (i.e. along the diameter) was characterized by image analysis during the SEM investigations determining the area of the graphite phase. Considering the most inhomogeneous, i.e. the G4 specimen, the graphite area was ~3,7 % in the inner region. Here the length of the particles varied between 1 μm and 5 μm, while in the outer region, where the wear tests have been performed, these values were ~0,5% and 1 μm and 2 μm, respectively. In case of the G5 specimens the characteristic graphite content and length of particles were ~9,4% and 40 μm and 100 μm, while for the G6 piece ~12,9% and 100 μm and 200 μm, independently of the location. From Fig. 2. d) it is also seen, that increasing the initial grain size of the graphite additives, the graphite agglomerates become larger. XRD results are available at the moment only for two specimens, i.e. for G3 and G5

specimens. They proved presence of SiC in both cases, while in case of G5 probe free graphite was also found.

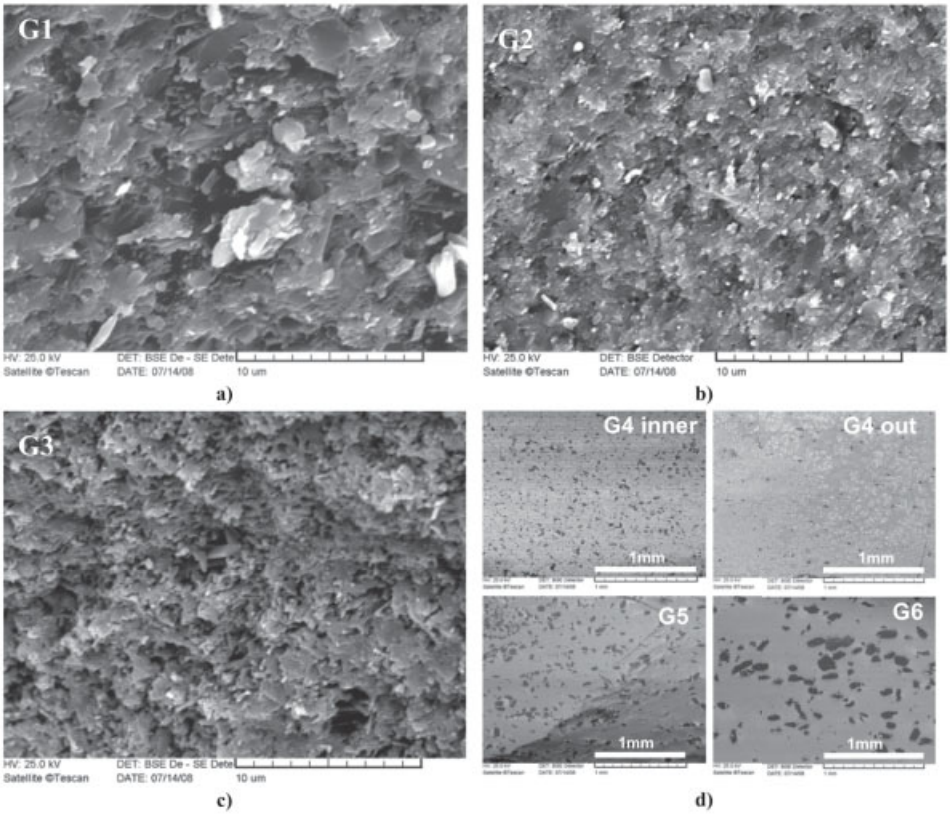


Figure 2. a), b) and c) Microstructure of the G1, G2 and G3 samples (by SEM); **d)**. Graphite agglomerates in the G4, G5 and G6 samples, having an initial graphite grain size of $\phi_{G4} < 71$; $\phi_{G5} < 125$; and $\phi_{G6} > 125$ μm.

Specimens were polished to 1 μm finish with diamond paste. The usual roughness data are shown in Table 2. (*P* is depth of the certain bearing ratio, t_p from the highest peak.)

Table 2. Characteristics of roughness and the Abbott Firestone curve

Sample	R_z, μm		R_a, μm		P, μm [at t_p=50%]		P, μm [at t_p=95%]	
	average	St. dev.	average	St. dev.	average	St. dev.	average	St. dev.
G1	0,863	0,069	0,125	0,010	0,538	0,101	1,033	0,172
G2	0,836	0,070	0,121	0,005	2,337	1,122	3,438	1,624
G3	1,383	0,124	0,190	0,041	1,643	0,256	2,628	0,326
G4	1,182	0,225	0,155	0,019	0,908	0,440	1,622	0,446
G5	1,722	0,327	0,193	0,045	1,848	0,461	3,347	1,189
G6	2,717	0,457	0,439	0,070	1,583	0,567	3,907	0,691

The Vickers hardness [7] has been determined at 5 N and 10 N loads along the straight edge of specimens, as well as inside the wear traces. The average hardness values felt into the

range of HVM 600-700 (G3), HVM1100-1300 (G4), HVM1500-1800 (G1, G2, G5). Large scattering of the measured values reflected the inhomogeneity of the materials. In order to distinguish between the various regions containing the supposed in-situ created new phases *instrumented hardness tests* [8] with 1 N have also been accomplished. By this latter method two hardness ranges could be distinguished, i.e. regions of HVM=3-5 GPa and HVM=25-40 GPa hardness.

2.3. Test methods

Tribological tests were executed on a high temperature CSM Type THT-S-AX-0000 pin-on-disc tribometer [9, 10], at the Department of Polymer Engineering, at the University of Miskolc. During tests a SiC ball of ϕ 6mm diameter (supplier CSM) as a counterpart was applied, and tests were executed at room temperature with applied normal load of 5, 10 and 15 N, at 50% relative humidity in dry conditions. The number of the planned tests were 3 measurements for each test regime, however due to technical problems, only the first test series relating to 1 measurement for each test regime have been executed till now.

The total sliding distance was 100 m, the radius of the wear track 1,2 mm, the circumferential velocity 0,01 m/s. Tests were performed according to DIN 50324 standard [10]. The wear rate, k was determined based on the following equation [9, 10]:

$$k = \frac{W}{L \cdot F_N} \left[\frac{mm^3}{Nm} \right], \tag{1}$$

where W is the worn volume [mm^3], L is the total sliding distance [m], F_N is the applied normal load [N].

2.4. Experimental results

Tribological characteristics gained from 2D profilometry are summarized in Table 3.

Table 3. Characteristics derived from the tribological tests

Speci-men	Load, F [N]	Worn volume, W [μm^3]	Specific wear rate k [mm^3/(Nm)]	Average friction coefficient μ	Onset of steady state [No. of cycles]	Friction coefficient at the steady state μ
G1 Ac	5	0,0034	6,7048E-06	0,369	no	no
	10	0,0045	4,5484E-06	0,433	no	no
	15	0,0165	1,1028E-05	0,526	no	no
G2 Ac	5	0,0138	2,7677E-05	0,585	6000	0,65
	10	0,0142	1,4214E-05	0,518	4000	0,6
	15	0,0206	1,3747E-05	0,539	6000	0,6
G3 Ac	5	0,0019	3,8502E-06	not evaluated	not evaluated	not evaluated
	10	0,0034	3,3920E-06	0,264	no	no
	15	0,0149	9,9117E-06	0,348	no	no
G4 Aa	5	0,0073	1,4648E-05	0,372	3000	0,4
	10	0,0063	6,3127E-06	0,334	8000	0,35
	15	0,0082	5,4789E-06	0,326	9000	0,35
G5 Aa	5	0,0037	7,3909E-06	0,263	2000	0,26
	10	0,0088	8,7990E-06	0,294	5000	0,3
	15	0,0186	1,2430E-05	0,407	5000	0,45

Wear volume: The increase of the applied load was generally less expressed for loads ranged from 5 to 10 N, while a drastic growth of the cross sectional area of the wear traces,

consequently the worn volume was measured for normal loads ranging from 10 to 15 N, as seen in Fig 3. As an exception of this trend specimen G4 showed closely constant wear rate independently of the loading force. This behaviour will be analysed further on.

The effect of the *graphite content:* We observed a decreasing wear volume with the increase of the initial graphite content in case of the 5N and 10N tests, however an opposite trend could be seen for the 15N measurements (based on data of G1, G2 and G3 specimens having the same grain size). Reliable estimation of the effect of the graphite content requires repeated measurements on the certain specimens. It should be taken into account that on the one hand the inhomogeneity of the test pieces after heat treatment is an important factor that could significantly modify the actual graphite content on the given tested area, on the other hand the observed microstructural differences of specimens may mask the effect of one certain parameter.

The effect of the *grain size of graphite additives* on the wear volume can be approximated from test data of G3, G4 and G5 specimens having the same graphite content. In Fig. 4. an increasing tendency of the wear volume with increasing grain size is assumed and taken as a first approximation. The distinctions are represented by the results of the G4 test piece (see data at ϕ71 μm max. diameter of graphite) that had a very inhomogeneous microstructure. The aforementioned more than 7x lower carbon content in the outer regions, i.e. at the location of the wear traces and the its local variation can not be neglected, since the free graphite can significantly modify the friction conditions, consequently the wear performance. This aspect is discussed and illustrated for G4 specimen further on.

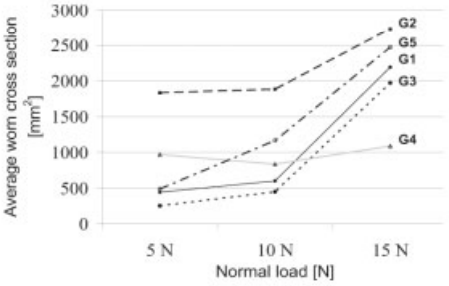


Figure 3. Worn cross section vs. normal load

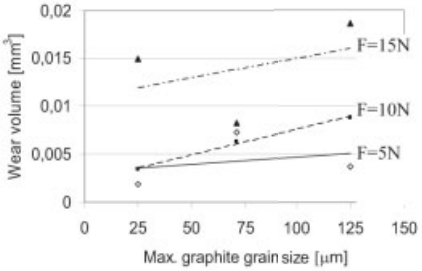


Figure 4. Effect of graphite grain size on wear volume

Friction coefficient generally increased with the sliding distance, but in some cases (G2, G4, G5) a characteristic onset of a steady state appeared, as shown in Fig. 5. In Table 3. both the average friction coefficients, and the steady state values are given. Generally lower friction coefficients were accompanied by a lower wear rate. Increasing the applied load the average and steady state friction coefficients (or if it is missing the last measured value) increased for the G1, G3, and G5 samples.

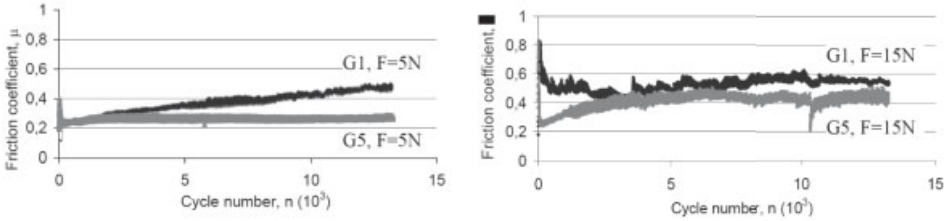


Figure 5. Friction coefficient vs. cycle number for the G1 and G5 specimens at F=5N and F=15N

The effect of the graphite content on the friction coefficient can be evaluated based on the specimens with the same grain size (G1, G2, G3). It can be stated that both the average and the steady state friction coefficients show a decreasing tendency at higher graphite content. In case of the G3 specimen with 10 wt% of initial graphite content both friction coefficients was significantly (by 25-45%) lower as compared to those of the G1 specimen having 2 wt% of initial graphite content. The result of the G2 specimens do not fit absolutely this trend, however it should be noted, that the overall extremely poor wearing behaviour of this probe at each loading force (illustrated in Fig. 3.) can not be explained by the initial composition. Therefore further detailed microstructural and compositional analyses at the location of the wear traces will be necessary, e.g. the local graphite content, the possible SiC and other phases, as well as morphological features should be determined that may be responsible for the extremely poor wearing performance.

The effect of the initial graphite grain size on the friction coefficient could be evaluated similarly for specimens having the same graphite content, (i.e. G3, G4, G5 probes). Comparing the G3 and G5 test pieces the higher initial graphite grain size was accompanied with higher friction coefficient.

The unique behaviour of the G4 specimen due to local variation of the graphite content should be considered separately. On the one hand graphite agglomerates of different dimension and amount in samples G4 and G5 (see Fig. 2.d) should influence the wear behaviour. Furthermore the very low graphite content at the location of the wear traces in G4 sample can be the reason of the special wear behaviour shown in Fig. 3. The wear volume seems to be independent of the applied load, as well as the average friction coefficient changes weakly (between 0,3-0,4) with increasing load. The investigation of the wear tracks provides an explanation as shown by the SEM pictures of the wear traces for G4 in Fig. 6.

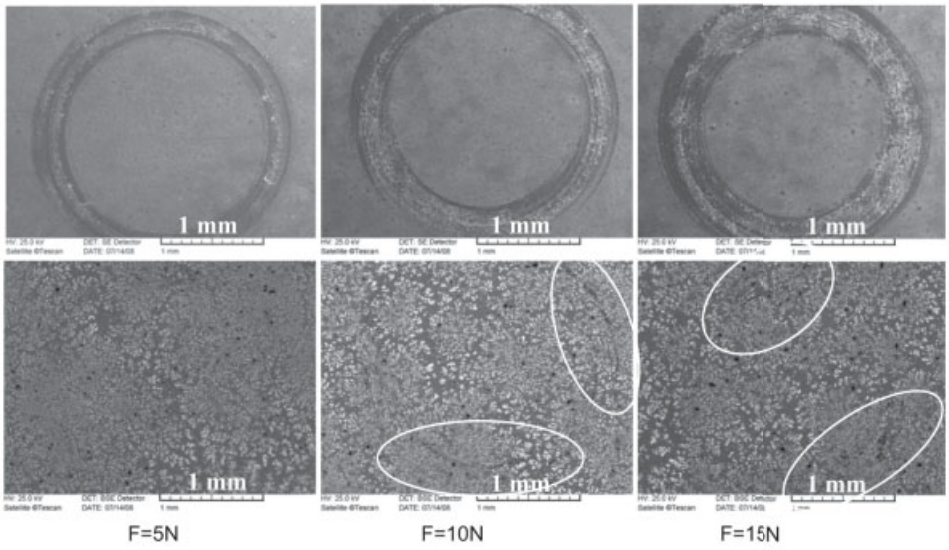


Figure 6. SEM pictures of the wear tracks on the G4 specimen taken in SE (above) and BSE (below) mode

Photos above were taken in SE mode to visualize the track morphology, while pictures below were produced in BSE regime to reveal the location of the greased graphite particles (photos below). It is well seen that in case of the F=10 N and F=15 N loads clear traces of the

The effect of the graphite content on the friction coefficient can be evaluated based on the specimens with the same grain size (G1, G2, G3). It can be stated that both the average and the steady state friction coefficients show a decreasing tendency at higher graphite content. In case of the G3 specimen with 10 wt% of initial graphite content both friction coefficients was significantly (by 25-45%) lower as compared to those of the G1 specimen having 2 wt% of initial graphite content. The result of the G2 specimens do not fit absolutely this trend, however it should be noted, that the overall extremely poor wearing behaviour of this probe at each loading force (illustrated in Fig. 3.) can not be explained by the initial composition. Therefore further detailed microstructural and compositional analyses at the location of the wear traces will be necessary, e.g. the local graphite content, the possible SiC and other phases, as well as morphological features should be determined that may be responsible for the extremely poor wearing performance.

The effect of the initial graphite grain size on the friction coefficient could be evaluated similarly for specimens having the same graphite content, (i.e. G3, G4, G5 probes). Comparing the G3 and G5 test pieces the higher initial graphite grain size was accompanied with higher friction coefficient.

The unique behaviour of the G4 specimen due to local variation of the graphite content should be considered separately. On the one hand graphite agglomerates of different dimension and amount in samples G4 and G5 (see Fig. 2.d) should influence the wear behaviour. Furthermore the very low graphite content at the location of the wear traces in G4 sample can be the reason of the special wear behaviour shown in Fig. 3. The wear volume seems to be independent of the applied load, as well as the average friction coefficient changes weakly (between 0,3-0,4) with increasing load. The investigation of the wear tracks provides an explanation as shown by the SEM pictures of the wear traces for G4 in Fig. 6.

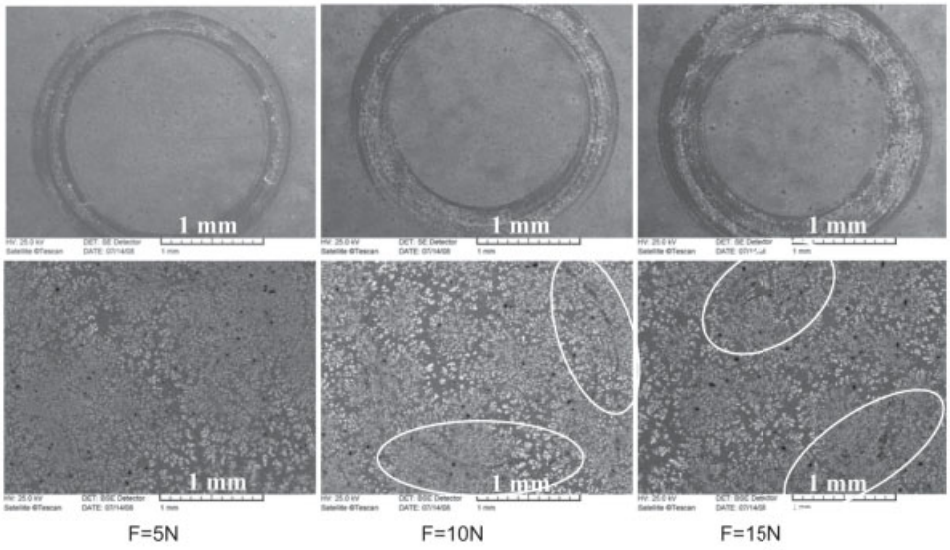


Figure 6. SEM pictures of the wear tracks on the G4 specimen taken in SE (above) and BSE (below) mode

Photos above were taken in SE mode to visualize the track morphology, while pictures below were produced in BSE regime to reveal the location of the greased graphite particles (photos below). It is well seen that in case of the F=10 N and F=15 N loads clear traces of the

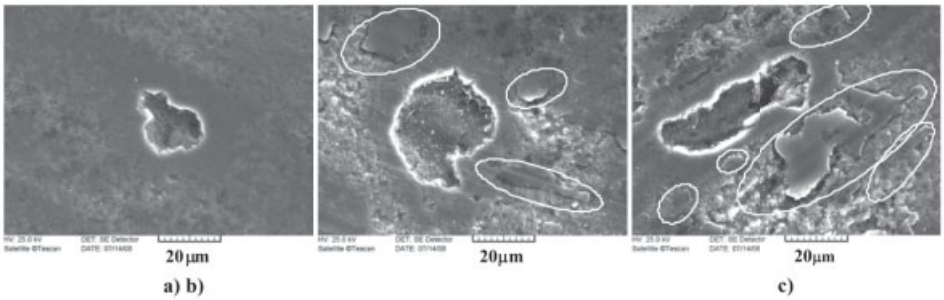


Figure 8. Holes due to graphite break-out in the wear track of specimen G4: a) F=5N; b) F=10N c) F=15N. In photos b) and c) supposed SiO_2 layer, and the yielded glassy phase is seen in the white circles

The plastically deformed layer, shown in Fig. 8. b) and c) may consist of the sintering additive Y_2O_3, as well as of the SiO_2 layer, that formed during the wear process. In the white circles presence of O and Si was confirmed by SEM investigations. It is assumed, that Si_3N_4 in the base material reacted with the oxygen content of the air producing SiO_2 on the wear surface. The plastic deformation of the glassy phases is enhanced by the high temperatures and high local pressures, as concomitant the friction process. This assumption is supported by Ref. [15], as well.

3. Summary and Conclusions

Pin-on-disc tests of in–situ reinforced Si_3N_4 composites have been performed to investigate the effect of the amount and grain size of the graphite additives on the wear performance at different normal loads (F=5, 10 and 15N). Graphite content of the test pieces varied between 2 and 10%, the initial graphite grain size varied from ϕ_{max}= 25 µm to 125 µm.

Three of the tested materials, i.e. G1, G3 and G5, having the most homogeneous microstructure showed similar wear behaviour in the function of the applied load, while for the other two specimens (G2 and G4) different tendencies could be observed, that is mostly ascribed to the compositional and microstructural inhomogeneities of these samples.

The most important establishment, that the currently available test data are not sufficient for the overall tribological characterization of the test materials, hence for evaluating the certain influencing factors with acceptable reliability. However based on the observed trends and results, some important conclusions can be made, as follows:

1) The wear rate generally increased with the increasing applied load. This effect was generally less expressed for loads ranging from 5 to 10 N, while a drastic growth of the wear rate, was experienced for normal loads ranging from 10 to 15 N. As an exception of this trend specimen G4 showed closely constant wear rate and friction coefficient, almost independent of the loading force.
2) Graphite additives may improve the wear rate of Si_3N_4 ceramics in different ways:
   - It can serve as a solid lubricant, lowering the friction coefficient.
   - During sintering SiC grains (intra- and intergranular), and various other complex phases can be developed.
   - The presence of the free graphite and SiC has been certified by SEM and XRD in certain test pieces. In order to evaluate their real influence on the wear behaviour an overall microstructural and compositional analyses involving each sample

should be completed. Due to the observed local inhomogeneities of the test pieces these investigations should be accomplished carefully with special attention to the local material characteristics in the vicinity of the wear traces.

3) Generally lower friction coefficients were accompanied by a lower wear rate. This was realized through the combined effect of the varying amount and size of the added graphite particles:
   - It is assumed, that finer initial graphite grain size leads to decreasing wear volume of the investigated silicon nitride-graphite composites, however the observed tendency should be strengthened by further investigations.
   - It was shown, that both the average and the steady state friction coefficients can be lowered by increasing the graphite content, however the optimal amount should be determined by further experiments.
4) The usual roughness data, i.e. R_a and R_z could not be correlated with the wear rate, while the features of the Abott-Firestone curve showed that higher bearing ratio results in lower wear volume. This effect was especially strong for the F=15N cases.
5) Hardness is not a controlling factor of the wear behaviour of the tested composite ceramics. Nevertheless it can be stated, that higher hardness is not advantageous from the point of view of the wear rate
6) For the applied test conditions the dominant wear mechanism at low loading forces (F=5 N) was a brittle fracture dominated wear, while at higher normal loads (10 N, 15 N) plasticity dominated wear and tribo-oxidation was confirmed to occur.

Due to the system character of the wear damage process and the several influencing factor, furthermore their possible interaction further investigations are required first of all in order to reveal the qualitative and quantitative characteristics of the existing phases, based on which the measured pin-on-disc test results can be interpreted with higher reliability.

Authors express their thanks to the Slovak Academy of Sciences, Dept. of Structural Ceramics, Bratislava for the test materials; to the Slovak Academy of Sciences, Institute of Materials Sciences, Dept. of Ceramics, Kosice and to Á.. Kovács at the University of Miskolc for the SEM investigation. Thanks to Dept.of Solid State Physics, ELTE, Hungary for the professional and technical aid. The research work has been supported by the T046467 and NI 61724 OTKA projects, and by Apponyi Albert Mecenatura, and Peregrinatio IV. foundations.

References

[1] P. Šajgalík, M. Hnatko, F. Lofaj, P. Hvizdoš, J. Dusza, P. Warbichler, F. Hofer, R. Riedel, E. Lecomte, M. J. Hoffmann: SiC/Si_3N_4 nano/micro-composite — processing, RT and HT mechanical properties, Journal of the European Ceramic Society, Volume 20, Issue 4, April 2000, Pages 453-462.

[2] M. Hnatko, D. Galusek, P. Šajgalík: Low-cost preparation of Si_3N_4–SiC micro/nano composites by in-situ carbothermal reduction of silica in silicon nitride matrix, Journal of the European Ceramic Society , Volume 24, Issue 2, 2004, Pages 189-195. 8th International Conference on Ceramic Processing

[3] A. Jalowiecki, J. Bill, M. Friess, J. Mayer, F. Aldinger, R. Riedel: Designing of Si_3N_4/SiC composite materials, Nanostructured Materials,Volume 6, Issues 1-4,1995, Pages 279-282.

[4] Kinemuchi, T. Yanai, K. Ishizaki: In-situ formation of Si_3N_4-nano SiC composite, Nanostructured Materials, Volume 9, Issues 1-8, 1997, pp 23-32.

[5] W. Dreßler, A. Greiner, M. Seher, R. Riedel: Fabrication of nanostructured ceramics by hybrid processing. Nanostructured Materials, Volume 6, Issues 1-4, 1995, Pages 481-484.

[6] M. Kašiarová, E. Rudnayová, J. Dusza, M. Hnatko, P. Šajgalík, A. Merstallinger, L. Kuzsella: Some tribological properties of a carbon-derived Si_3N_4/SiC nanocomposite, Journal of the European Ceramic Society, 24 (2004) 3431-3435

[7] Standard test method for microindentation hardness of materials ASTM E 384, 1999.

[8] DIN 50359-1: Universalhärteprüfung, Teil 1: Prüfverfahren, 1997.

[9] I. M. Hutchings: Tribology: Friction and Wear of Engineering Materials, Edward Arnold (Hodder Headline PLC), 1992. ISBN 0-340-56184-X

[10] Tribologie, Prüfung von Reibung und Verschleiß, DIN 50 324, 1992.

[11] Bohn, Lothar, Hornbogen, Erhard: Hochfeste Werkstoffe, Verlag Stahleisen, 1974. ISBN 3514001480.

[12] Verschleiss; Begriffe, Systemanalyse von Verschleissvorgängen; Gliederung des Verschleiss-gebietes, DIN 50320, 1979.

[13] Bharat Bhushan: Modern tribology handbook, Volume One, 2001, CRC Press, ISBN 0849384036, pp. 276-300.

[14] Gwidon W. Stachowiak, Andrew W. Batchelor: Engineering tribology, Second edition, ISBN 0-7506-7304-4, 2001. Butterworth-Heinemann

[15] S. M. Hsu, M. C. Shen, T. N. Ying, Y. S. Wang, S. W. Lee: Tribology of silicon-based ceramics; in Silicon-Based Structural Ceramics, eds: B. W. Sheldon, S. C. Danforth, The American Ceramic Society; 1994, ISBN 0-944904-76-9

Wear Behavior of CMC and MMC under High-Speed Dry Sliding on Steel

S.N.Kulkov, N.L.Savchenko and S.F.Gnyusov
Institute of Strength Physics and Materials Science SB RAS, Tomsk, 634021, Russia

Abstract

We study the wear behavior of zirconia-based ceramic composites and WC-based hard alloys under high-speed dry sliding on steel. A pin-on-disk technique is used at a sliding speed of up to 45 m/s.

It is shown that during wear tests an interlayer of very complex composition is formed, which governs non-monotonous wear and friction behavior of CMC – steel and MMC – steel couples. On the first stage the wear rate is normal and wear increases to catastrophic one. On the second stage for MMC the wear rate stabilizes together with a decrease of the friction coefficient. For CMC the wear rate reduces to its almost initial value (like for low speed 0.1 m/s). In this speed interval the CMC material exhibits wearless behavior.

1 Introduction

Transformation-toughened CMC and MMC materials show much promise for being applied in heavily loaded friction units [1, 2]. Of special note among them are ceramics on the basis of yttria-stabilized tetragonal zirconia polycrystals (Y-TZP [1]) and metal matrix WC – Hadfield steel composites [2]. The major toughening mechanism for Y-TZP ceramics is the phase transformation from the tetragonal ZrO_2 phase to monoclinic, which occurs under applied stresses [1]. For WC – Hadfield steel composite it is the relaxation of contact loads at the cost of $\gamma \rightarrow \alpha$ and $\gamma \rightarrow \varepsilon$ phase transformations [2] in its structurally unstable binding phase.

It should be noted that there are currently no sufficient data on the behavior of such CMC and MMC materials at high sliding speeds (above 10 m/s). The main emphasis is now put on studying the material behavior at low speeds (up to 1 m/s) under abrasive wear [3], at cutting and polishing [4].

At the same time, in order to choose an optimal structure of composites and to widen their possible application areas, it is necessary to gain data on friction and wear and to study structural changes in composites in speed intervals characterized by high temperatures in the tribocontact zone.

Particularly, if sliding speed increase above 10 m/s temperature in the tribocontact grows, which can significantly change the structural phase state of the composite material and its tribotechnical properties. As shown in [5], under high-speed friction of SiC-Al_2O_3-Al composite on steel the coefficient of friction and wear decreases due to the formation of a layer containing various oxide mixtures on the friction surface. At elevated contact temperatures this layer has low shear stability, playing the role of a lubricant [4]. Similar cases of preserving high tribological characteristics and protective function of transfer layers formed in high-speed friction on

steel have been discussed in papers [6–8], which consider zirconia- and alumina-based ceramic materials. According to [8], at high sliding speeds up to 34 m/s ZrO_2-Y_2O_3 ceramic specimens demonstrate high wear resistance despite high temperatures in the tribocontact zone and related high-temperature phase transitions.

The present paper is aimed on studying tribological characteristics and structural phase state of the friction surface of Y-TZP ceramics and WC – Hadfield steel composite after dry sliding on steel in a wide speed interval.

2 Material and Investigation Techniques

Friction tests were carried out on a friction machine UMT-1 using a pin-on-disk technique with a stepwise speed increase under dry friction. The disk was made of cast high-speed steel (HS6-5-2, DIN EN 10027-1, HRC60) and rotated in the vertical plane. The test ceramic specimens (3 psc) were of rectangular or cylindrical shape with a total area of 60 mm^2. The test pressure made up 5 MPa, and the sliding speed varied up to 50 m/s. The test time was chosen so that the sliding distance at all speeds amounted to 2 000 meters. Prior to each test the specimens were grinded at speed 0.2 m/s and pressure 5 MPa to get friction surfaces of planar geometry. In every experiment the friction force moment was recorded by the computer at 1 sec intervals and later it was recalculated into the friction coefficient. The measure of wear intensity was the ratio between the volume of the material removed from a specimen during test and sliding distance. The structure and phase composition of friction surfaces were examined with X-ray structural analysis, optical and scanning electron microscopy. The objects of investigation were Y-TZP ceramic specimens of composition 97 mole % ZrO_2 + 3 mole % Y_2O_3 and specimens of hard alloy WC – 30 wt % Hadfield steel.

3 Results and Discussion

3.1 Ceramics

The performed tests have shown that with increasing sliding speed the wear intensity and friction coefficient of ceramics first increase and then decrease with further speed growth, Fig. 1a,b. The friction coefficient at speed 34 m/s reduces down to ~ 0.1.

By the electron scanning and optical microscopy data, friction in the speed interval up to 1 m/s results in the formation of grooved surface typical of abrasive wear. Above sliding speeds of 3 m/s the worn surfaces have large areas with traces of pitting, and at speeds above 6 m/s they appear smoother. Of special note is that there is a network of cracks on friction surfaces which divides the surface into separate fragments. We have measured crack spacings along the sliding direction and found that their size distributions are nearly normal with a clear peak, with the average crack spacing changing with sliding speed variation: the increasing crack spacing at low speeds decreases almost twice with increasing sliding speed growth and remains constant at speeds of 15 m/s, Fig. 1c.

After low-speed tests the X-ray images of ceramic friction surfaces demonstrated traces of the monoclinic phase that was not observed after testing with speeds up to 10 m/s. At high sliding speeds up to 34 m/s we revealed, along with tetragonal, the cubic phase on the friction surface

whose content increased with increasing speed. The appearance of the cubic phase on the specimen surface after maximum sliding speeds is evidently due to that part of the tetragonal phase transforms to cubic by the diffusion mechanism. This transition is favored by high temperatures in the tribocontact zone, e.g., in [6] temperature in the tribocontact zone at speed 10 m/s is estimated to be $\sim 2000\,^{\circ}C$.

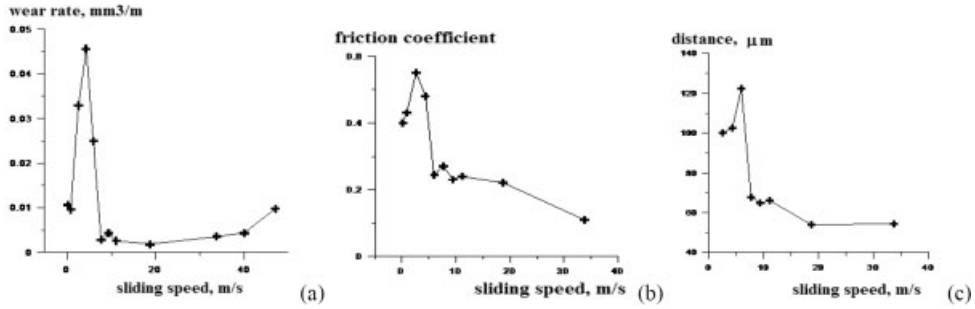


Figure 1: The sliding speed dependence of the wear rate (a), the friction coefficient (b) and the mean intercrack distance on wear surface. The contact pressure 5 MPa.

Optical and scanning electron microscopy revealed that above high speeds (higher than 6 m/s) friction surfaces were uniformly covered with a transfer layer. After low- and medium- speed sliding friction the transfer layer distribution on the surfaces was extremely inhomogeneous, which appeared as large friction surface areas with absolutely no transfer layer.

We have also examined near-surface regions of the ceramics and found that this surface layer (evidently having submicrocrystalline structure) is rather thin, about 1–2 μm. In the speed interval from 0.2 to 6 m/s where the wear rate rapidly increases, there is a material region beneath the layer in which the grain shape is significantly changed in the sliding direction. The thickness of this region is maximum ($\sim$ 10 μm) at medium sliding speeds ($\sim$ 3 m/s), i.e. at the speeds when the wear rate is maximum, Fig. 1a.

The wear processes occurring at speeds 2–6 m/s correspond to high-temperature adhesive interaction between ceramic and steel. This wear regime is characterized by high wear intensity and friction coefficient, which is illustrated in Fig. 1a,b. Subsequent decrease in wear intensity at sliding speeds higher than 6 m/s is a result of contact stress reduction owing to the formation of the transfer layer and its transition from the ductile to quasi-liquid state, which is also favored by high tribocontact temperature. The formed quasi-liquid film uniformly covers the ceramic friction surface and acts as "soft" coating. The latter facilitates contact stress decrease on the surface by reducing the true contact area between the specimen and disk. In case when the quasi-liquid "soft" film covers the ceramic surface, the friction coefficient is minimum and approaches values typical of boundary lubrication friction.

3.2 Hard Alloy

The tests have shown that at sliding speed growth three regions can be distinguished in which wear intensity changes considerably: a smooth increase in the wear intensity of WC – Hadfield steel composite is followed by its sharp growth in the sliding speed interval 23–30 m/s, and then the

wear value remains almost constant up to 37 m/s, Fig. 2a. The friction coefficient first decreases with increasing speed from 0.5 to 0.05 and then increases again to 0.2, Fig. 2b. Notice that in the domain of minimum friction coefficient values depend on test time: the initially high friction coefficient equal to 0.15–0.2 is reduced to 0.05 for about the first twenty seconds of sliding and then its value did not almost change until the end of testing. At sliding speeds up to 10 m/s and above 26 m/s the friction coefficient value is nearly independent of test time.

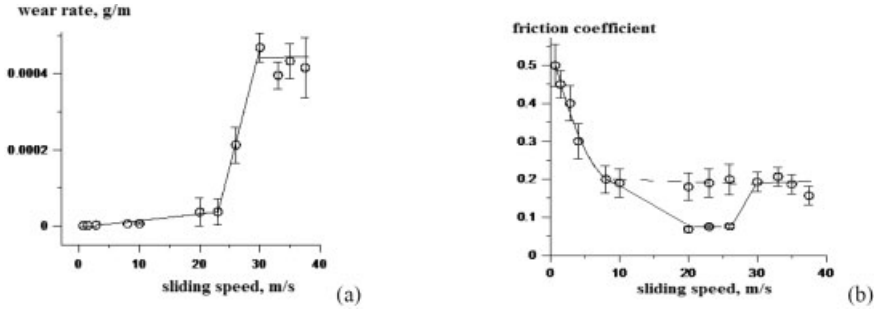


Figure 2: The dependence of wear rate and friction coefficient of WC – Hadfield steel composite on the sliding speed. The contact pressure 2 MPa.

In the low speed interval 0.65–4 m/s the friction surface exhibits a regular grooved relief with sparse inclusions of white-colored particles which corresponds to normal wear by microcutting. Abrasive particles here are wear debris of friction couples which present complex $Me_{12}C$ carbide [2]. The number of the particles tends to decrease with increasing sliding speed. The X-ray structural analysis of the friction surface after the sliding speed interval 0.65–8 m/s revealed, apart from phases referring to the WC – Hadfield steel composite, $M_{23}C_6$, $Me_{12}C$, Fe_3O_4 and Fe_2O_3 phases.

Starting from sliding speeds 10 m/s and higher the friction surface of all specimens independently of the sliding speed is represented as white and dark-gray regions or their mixture. The performed X-ray fluorescent analysis of the specimens prior to and after tests has shown that there are elements on their surface which enter into the composition of the steel disk. By the X-ray structural analysis data, the dark-gray layer is $FeWO_4$ oxide whose content, judging from diffraction peak intensity, increases with sliding speed growth. It is actually the transfer layer that has formed as a result of mixing and subsequent oxidation of chemical elements of the steel disk on the composite friction surface.

Above sliding speeds 10 and 20 m/s this layer is distributed extremely nonuniformly over the friction surface, which is manifested as large areas having absolutely no transfer layer. With increasing sliding speed the area occupied by the layer increases and by 37 m/s almost completely covers the friction surface.

The crack network that divides the friction surface into separate fragments like in ceramics is observed only in the speed interval 10–20 m/s, and their propagation depth does not exceed 10–20 μm.

According to X-ray structural analysis, in the speed interval 0.65–20 m/s the near-surface volume of the binding phase undergoes partial martensitic $\gamma \rightarrow \alpha$ transformation, which is manifested in a reduction of the γ-phase volume fraction. The presence of martensite is evidenced by the

splitting of the (110) and (200) lines referred to the bcc iron lattice and by its needled morphology revealed at metallographic examination of the specimen structure. With further increasing sliding speed above 20 m/s only the γ-phase is found on the friction surface.

The strengthening phase of the composite after all tests, independently of sliding speed, is represented only by tungsten monocarbide. A feature of the X-ray peak profiles of tungsten carbide for specimens after friction is that they can be divided into a "narrow" and a "broad" component, which were used to calculate the crystallite size, Fig. 3. An opposite form of the sliding speed dependence of crystallite sizes for the broad and narrow components of the (100) tungsten carbide peak, Fig. 3, points to an interrelation between these sizes. In fact, the data given in Fig. 4 are testimony to this: crystallite size increase for the broad component of the (100) peak causes a decrease in the size of crystallites corresponding to the "narrow" component. This means that the finer is the structure of the "white" layer, the less fragmented is the underlying composite layer.

Thus, a feature of the friction surface structure of the composite material is the presence of three layers differing from each other in structure and properties. The first layer (2–3 μm thick) is the dark-gray transfer layer consisting of oxides of mixed composite and disk components and containing $FeWO_4$ phase. Below is the "white" layer that presents fine WC – Hadfield steel composite fragmented during friction. Beneath the "white" layer there is a composite layer with increased volume content of WC particles as compared to the initial material.

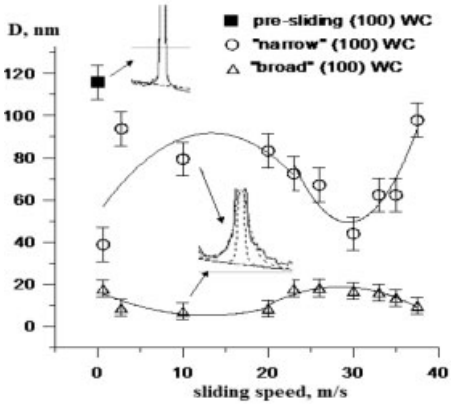


Figure 3: The dependence of the crystallite sizes for the "broad" and "narrow" components of the (100) tungsten carbide peak on the sliding speed.

The broad component in the diffraction peak pattern of tungsten carbide, Fig. 4, is directly related with the presence of the "white" layer on the friction surface, whose thickness amounts to 2–3 μm. This is demonstrated by the fact that after the removal of this layer the broad component of the tungsten carbide peaks also disappears. According to [2], the "white" layer structure presents a fine mixture of carbides and binder compared to the initial composite structure. The narrow component of the diffraction peaks of tungsten carbide is in turn related to the composite layer underlying the "white" layer. Probably, in the conditions of transfer layer deficiency at sliding speeds 10 and 20 m/s the "white" layer plays the role of protective coating, easily undergoing deformation and covering the entire friction surface.

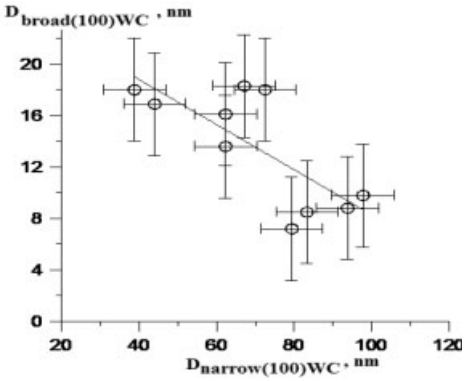


Figure 4: The dependence of the crystallite sizes for the "broad" components of the (100) tungsten carbide peak on the crystallite sizes for the "narrow" components of the (100) tungsten carbide peak.

Based on the obtained results, we may formulate the following sequence of changing wear mechanisms in the "hard alloy – steel" couple. At sliding speeds up to 4 m/s normal abrasive-oxidation wear takes place. Low-rate wear is characterized by the maximum friction coefficient value that reaches 0.5. In this case, the disk metal is cut by the specimen. Phase composition variation consists in martensitic $\gamma \rightarrow \alpha$ transformation. Further, the wear processes occurring at speeds 10–20 m/s can be related to high-temperature adhesive interaction between the composite and steel. Typical of the given wear regime are the rough wear surface, pits and cracks, which is observed experimentally. In the speed interval where wear intensity sharply increases (23–30 m/s) the minimum friction coefficient values do not rise above 0.07. They are characteristic of friction regimes with the formation of quasi-liquid films, because in all friction regimes at sliding speeds higher than 10 m/s a large amount of heat was released in the tribocontact zone and the composite specimens were strongly heated throughout the volume. The estimate obtained in accordance with [9] shows that local temperature at high sliding speeds can attain 1500 ^{0}C, i.e. it is comparable to the melting temperature of the binder. This causes binder softening, then, possibly, melting in near-surface regions of the composite and its extrusion on the surface to the tribocontact zone between the composite and steel disk. Nevertheless it is a region of catastrophic wear, where wear rate increases by almost an order of magnitude. Finally, at sliding speeds above 30 m/s the stage of steady-state wear begins which can be related to the action of the oxidation wear mechanism.

4 Conclusions

The performed experiments have revealed that at high sliding speeds up to 34 m/s ZrO_2-Y_2O_3 ceramic specimens have high wear resistance, despite high temperatures in the tribocontact zone and related high-temperature transitions. In this case, there is a wide interval of speeds where the process is nearly "wearless".

In the “hard alloy – steel” couple the smooth growth of wear rate is followed by its sharp (four times) increase, after which steady-state wear begins. The found changes in tribotechnical characteristics can be interpreted from the viewpoint of the changing wear mechanisms.

The structural phase state of the composite binder plays different roles depending on sliding speed. At low speeds (up to 4 m/s) the martensitic $\gamma \leftrightarrow \alpha$ transition assists in preserving the high wear resistance of the composite without visible traces of deformation and failure. In the speed interval 20–30 m/s the high-temperature diffusion $\gamma \leftrightarrow \alpha$ phase transformation, along with binder melting and its extrusion to the tribocontact zone, favors friction coefficient decrease to 0.05 and abrupt wear intensity increase.

We have found a relation between crystallite sizes in carbide layers formed near the friction surface. In this case, the refinement of the uppermost surface layers occurs together with the coarsening of fragments in the underlying layer. If the upper layers contain ˜ 10–20 nm crystallites, the underlying composite layer remains almost unfragmented and differs slightly by the crystallite size from its initial state prior to testing.

5 References

[1] I.M. Fedorchenko. Powder Metallurgy and Metal Ceramics. 2002, **41**, No. 9–10, 489–497.

[2] L. Nettleship, R. Stevens. Int.J. High Technology Ceramics.1987. No. 3, 1-32.

[3] S.N. Kulkov, S.F. Gnyusov. NTL (Ed.: E.F.Dudarev), Tomsk, 2006, p. 240. (in Russian).

[4] A.J. Gant, M.G. Gee. Wear, 2001, **251**, 908–915.

[5] J.W. Hegeman, J.Th.M. De Hosson, G. de With. Wear, 2001, **248**, 187–196.

[6] A. Ravikiran, V. Jayaram, and S.K. Biswas. J.Am.Ceram.Soc, 1997, **80**, No. 12, 19–24.

[7] A. Ravikiran, V. S. Nagarajan et al. J. Am. Ceram. Soc, 1995, **78**, No. 2, 356–364.

[8] N.L. Savchenko, K.M. Pyatova, S.N. Kulkov. Vestnik of Tomsk State University : Scientific periodicals. 2008, No.32, 84–89 (in Russian).

[9] S.C. Lim, M.F. Ashby, Acta Metallurgica, 1987, **35**, 1–24.

Ultralow Friction and Wear of Reciprocating Systems Lubricated by Liquid Crystalline Fluids

Andreas Kailer, Tobias Amann, Georg Konrath
Fraunhofer-Institut für Werkstoffmechanik IWM, Freiburg
Dietmar Janietz, Hans Sawade
Fraunhofer-Institut für Angewandte Polymerforschung IAP, Potsdam-Golm

Abstract

Tribological systems that are lubricated with liquid crystals exhibit ultralow friction coefficients and wear. This effect, which has not yet been well examined and which is even less understood, has been reproducibly observed in reciprocating friction after a certain running-in period and at temperatures around 90° C.

Aim of the present work is to study the tribological behaviour of different liquid crystals in more detail. Special focus was on the influence of tribological loading (load, velocity and temperature) on the friction and wear coefficients. Additional surface analysis was performed to correlate the tribological characteristics with surface features. Some attempts were also made to influence the friction coefficients by electrical fields.

A better understanding of the tribological behaviour is essential for the development of efficient production routes and for the qualification of liquid crystalline lubricants for possible future applications.

1 Introduction

Liquid crystals (LCs) – also denoted as mesogens or mesophases – have been so far developed for electronic devices such as displays because of their anisotropic electronical and optical properties. Today a huge number of LCs have been developed for this applications [1]. Multi-component mixtures in such displays also contain compounds that in pure form do not attain liquid crystalline structures at normal conditions. Their transition temperatures to LC phases often lie far below room temperature.

The use of liquid crystals for tribological applications has been studied under different conditions that demonstrated the feasibility of this class of compounds as lubricants [2-6]. Due to their ability to form liquid crystalline structures that reorient themselves under frictional loading, extremely low friction coefficients may be realised. In addition, if electrically active liquid crystals are used these orientation processes can be influenced by electric fields [7,8].

In a collaboration of Nematel GmbH and the Fraunhofer-IWM, extreme low friction coefficients were detected with fluids that under normal conditions are isotropic and are supposed to form a molecular order in a shear field of a slide bearing. These observations gave further reason to improve and optimise new thermotropic liquid crystals.

Although first results showed the positive effect of several specific liquid crystals in tribological applications, essential questions on the relation between molecular structures and tribological effects of liquid crystalline compounds aroused:

- Under which conditions do liquid crystals or isotropic mesogenic fluids induce ultralow friction (depending on chemical structure of the LC, temperature, load, sliding velocity, material combinations)?
- Are they miscible with conventional base oils?
- Do they respond to external electric fields?
- What are the fundamental effects of ultralow friction?

Furthermore, the exact mechanisms of the mesogenic lubricants, which lead to the extreme low friction, are poorly understood, however this unprecedented behaviour has recently been discussed under the aspect of other ordering phenomena in fluids [6]. The knowledge and modelling of fundamental mechanisms leading to ultralow friction values is indispensible of the tailored design of new liquid crystals with a broadened range of practical applicability.

In a cooperation of Nematel GmbH, Mainz and Fraunhofer-Institut für Angewandte Polymerforschung, Potsdam, a tribological investigation of several mesogenic compounds has been started to create empirical results as a basis for a better theoretical understanding of the prevailing tribological mechanisms. In this paper, the results of these investigations are summarised.

2 Experimental Setup and Materials

The tribological tests were performed using a reciprocating cylinder-on-disc geometry (RCD, fig. 2) using a SRV-III test rig (Optimol Instruments). The temperature was controlled by heating up the test assembly. Specimen materials and geometry, typical test parameters used for the test series and LC compounds and lubricants used as reference compounds are given in tables 1 to 3. In each test, only one droplet (0.025 ml) of lubricant was placed on the disc before applying the contact and starting the experiment. It should be pointed out that a number of different LC compounds were tested, however, not all LCs led to ultralow friction. Because of the limited space we summarize just on the results of LCs leading to ultralow friction.

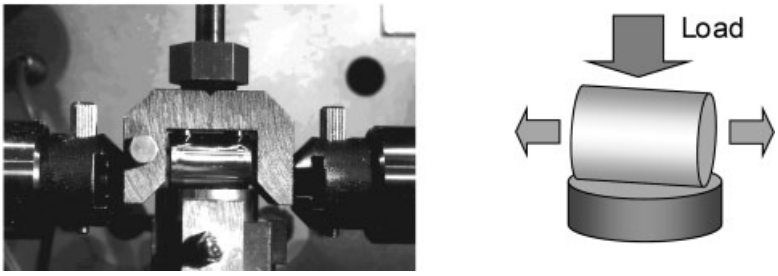


Figure 2: Picture of test setup and sketch of loading geometry of reciprocating cylinder on disc (RCD)

Table 1: Characteristics of the test specimens

	Cylinder	Disk
Material	Steel 100Cr6	Steel 100Cr6
Diameter	15.0 mm	24.0 mm
Length, Height	22.0 mm	7.9 mm
Surface roughness		
R_a	0.15 µm	0.13 µm
R_z	0.18 µm	0.28 µm

Table 2: Test parameters of tribological experiments

Temperature	90 °C
Normal load	50 N
Frequency	50 Hz
Stroke	1 mm
Duration	20 hours

Table 3: LC compounds and materials

Name	description of molecular structure	kin. viskosity ν mm²/s at 40 °C	Transition temperatures*
D1	Hexakis[octylthio]-benzene	53.0	Cr -6.0 Col_{ho} -10.0 I
KI-07/10	1-(4-Ethylphenyl)-nonan-1,3-dion	6.5	*(Cr 0 Sm_B 10 I)*
KI-887	1-(4-Methylphenyl)-decan-1,3-dion	7.6	*(Cr 21 Sm_B 34 I)*
KI-904	1-(3-4-Dimethylphenyl)-nonan-1,3-dion	10.4	*(Cr 10 Sm_B 17 I)*
CCN-47**	4'-Butyl-4-heptyl-bicyclohexyl-4-carbonitrile	-	Cr 28.0 Sm_A 33.0 N 61.0 I
10W40 (Dura Blend)	(standard motor oil, used as reference compound)	93.0	–
n-Hexadecane	n-$C_{16}H_{34}$	2.9	–

** Cr: Crystalline (solid), Col_{ho}: Columnar (hexagonal ordered), Sm: Smectic, N: Nematic, I: Isotropic; data put in parentheses are estimations based on DSC-results*

***Anisotropy of the dielectric permittivity $\Delta\varepsilon$: -7.0*

3 Results

3.1 Tribological Behaviour of Different Compounds

The results of the RCD-test of several LC compounds are compared in fig. 3. In contrast to the reference compounds 10W40, the LC compounds showed extremely low friction coefficients. The low-friction regime usually was observed after a running-in period of 5 to 10 hours, depending on the type of mesogen. It is worth mention that during these (rather long) running-in periods friction-spikes occurred that may be ascribed to solid-solid contacts, i.e. temporary breakdown of the lubrication film.

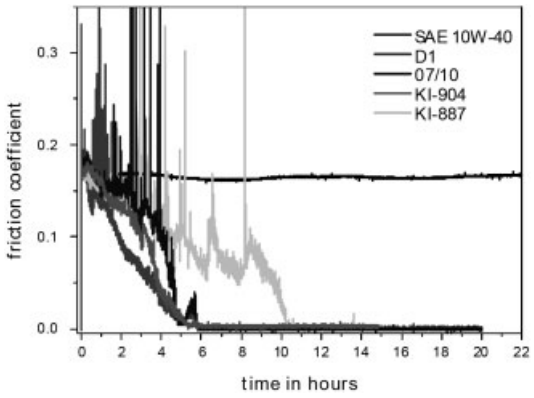


Figure 3: Friction coefficients as a function of testing time of LCs and reference lubricant

3.2 Variation of Test Parameters

To study the temperature dependence of the tribological behaviour of LCs, tests were performed at temperatures between 60 °C and 120 °C (fig. 4). While the course of the friction coefficients of D1 is hardly changing within this temperature range (fig. 4a), the KI-7/10 shows a decrease of friction coefficients only at relatively higher temperatures and also a shorter running-in period at higher temperatures (fig. 4b). The temperature dependence has not yet been studied for all LCs, but it is supposed that the temperature range for ultralow friction conditions will be different for each compound and may depend on many factors, e.g. transition temperature, liquid crystalline structure that is formed in shear fields, chemical structure, viscosity, chemical interaction with the surface.

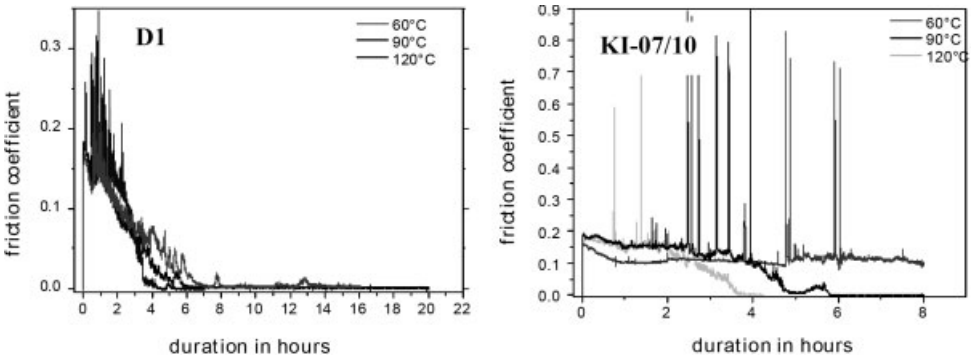


Figure 4: Friction coefficients as a function of testing time of D1 and KI-7/10

The variation of the frequency of the reciprocating motion between 10 Hz and 60 Hz (20 mm/s and 120 mm/s) resulted in a extension of the running-in period that was not proportional to the

number of cycles, indicating that the running-in distance is significantly longer at lower sliding speed for the mesogenic fluids D1 and 07/10.

The variation of normal load showed only small changes of the duration of running-in period. However, the course of the friction coefficient was different, since at higher loads, friction remained at ca. 0.15 for a longer time and the decrease of friction was more abrupt.

3.3 Variation of Material Combinations

Several material combinations were studied, including steel/ceramic and steel/polymer combinations. As shown in fig. 5, ultralow friction coefficients were not obtained in all cases. The combination of steel cylinder and silicon nitride ceramic yielded low friction, when D1 was used as a lubricant (fig. 5a). Steel cylinder in combination with polymers and D1 lubricant yielded low friction only with PMMA (fig. 5b) after a very short running-in period.

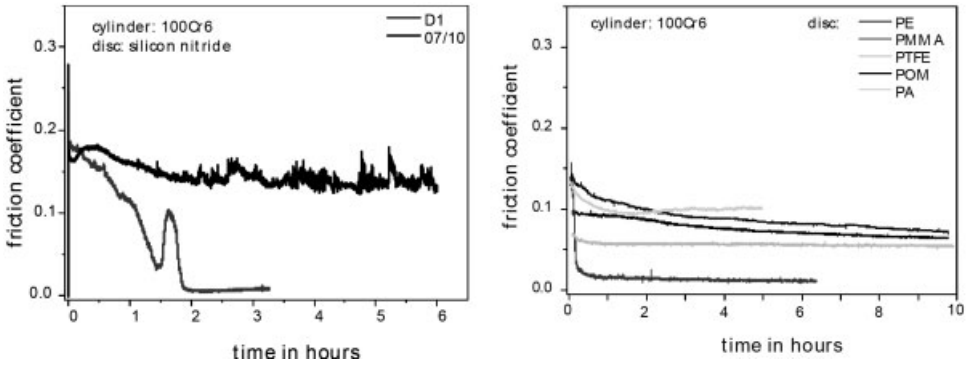


Figure 5: Dependence of friction coefficients on the material combination for a: steel/silicon nitride; b: steel/polymer combination. Lubricant: D1

3.4 Mixtures of LCs with Paraffin Oil

Different weight ratios of paraffin and D1 were tested under standard conditions. The paraffin oil was used because of a similar viscosity compared to D1. The results in fig. 6 indicate that in the case of D1 already 10% to 25% of LC decrease the friction coefficient significantly. At least 40% of D1 are necessary to realize ultralow friction conditions. Similar tests, made with other LCs and standard lubricants indicated that between 40% and 60% of LC lead to ultralow friction regimes.

3.5 Influence of External Electrical Fields

To study the influence of electric fields on the friction behaviour, a LC compound with high anisotropy of electric permittivity was used (CCN-47), although this LC did not show ultralow friction coefficients. To electrically insulate the disc surface, a diamond-like coating was applied with a coating thickness of 5 µm. During the test the temperature was varied to form different

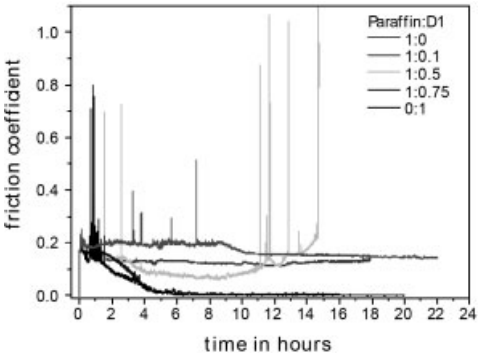


Figure 6: Dependence of friction coefficients on mixtures of D1 with paraffin oil

LC modifications. At each temperature the electric voltage was turned off and on twice (once at 25 N load and once at 50 N load).

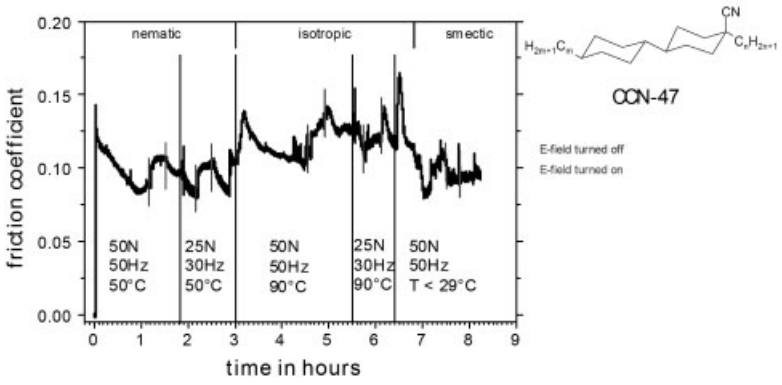


Figure 7: Friction coefficient of CCN-47 as a function of test parameters and electric fields (30V DC)

The largest effect of the electric field on the friction coefficient was observed at 50°C where the LC has a nematic phase. As soon as electric field was turned off, the friction coefficient increased by more than 20%. After turning on the electric field, the friction coefficient slowly decreased to former values. At 90°C (isotropic phase) this effect is also clearly visible. At temperatures below 30°C (smectic phase) the electric field had no significant influence on friction.

3.6 Surface Analysis

For surface analysis, different methods were used. In fig. 8, the typical surface features of wear scars on steel samples are visible. At higher magnification (fig. 8b) surface pits and tribofilms were detected. On samples lubricated with D1, traces of sulphur were detected by energy dispersive x-ray analysis (EDX).

Considering the course of the friction coefficients (see fig. 3) and the observation that most of the wear was formed during the running-in period, it can be concluded that adhesive wear and surface pitting must have been caused by occasionally solid-solid-contact during the running-in period. The tribofilms may have been formed and stabilised under the mixed lubrication conditions during the running-in period and the subsequent ultralow-friction regime.

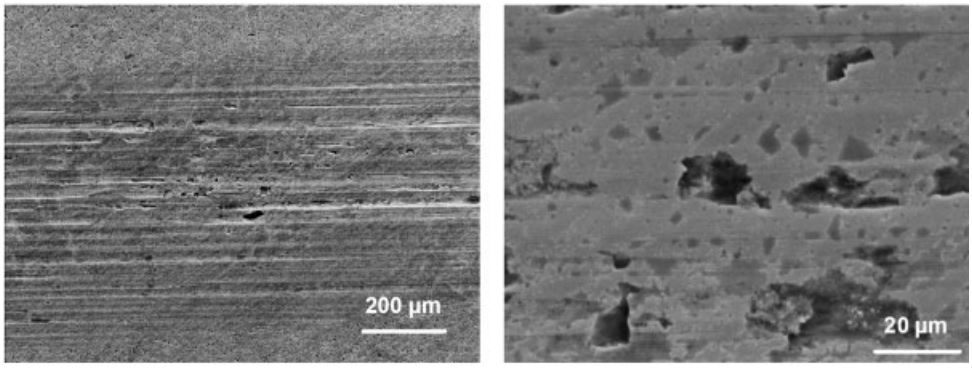


Figure 8: SEM-image of wear scar on steels disc (lubricant: KI-07/10)

Further surface analysis is being conducted including surface topography (atomic force microscopy, interferometry), wettability and vibrational spectroscopy (micro-Raman) and will be published in the near future.

4 Discussion

Although there are many results that show ultralow friction coefficients under various conditions with different LC compounds and materials used, the mechanisms that are responsible for this tribological behaviour are not completely clear. It is remarkable that ultralow friction was observed (without exception) at temperatures, at which the isotropic phases of the LCs are stable. On the basis of the tribological analysis presented in this paper, the following frictional mechanism is suggested:

To realize ultralow friction, LCs with a rod-shaped molecular structure may be favourable (but D1 having disc-shaped molecules is an example that also different orders are possible). Although they are normally isotropic at test temperature, there must be orientation effects between the sliding surfaces probably leading to liquid crystalline order. These near-surface liquid crystalline structures cause highly anisotropic viscosity, the direction of lowest viscosity according to the sliding direction. The formation of this structure will also take a certain time and will only take place under moderate contact pressures (in the order of 100 MPa and lower) of flat surface contacts (under high and inhomogenous contact stresses of rolling contacts, ultralow friction was not observed). During the running-in period, there is considerable wear of the sliding parts. In addition, wear-induced changes of the contact geometry from Hertzian line contact (130 MPa) to more flat contact geometry with lower contact pressure (ca. 15 MPa) as well as changes of the surface roughness during the running-in period will influence the tribological behaviour significantly.

In addition, the physico-chemical interaction of the LC with sliding surfaces must also be crucial. Low friction conditions were not observed with all material combinations, but only partly in steel/ceramic contacts as well as steel/polymer contacts. The measurement of surface energies by the determination of wetting angles has indicated that higher surface energies and/or polarity may be beneficial.

5 Summary and Outlook

In the presented study extensive analysis was carried out on the tribological behaviour of liquid crystals in reciprocating line contacts. For several fluids, ultralow friction coefficients were observed under a variety of test conditions and material combination. These results allowed first indications about a correlation between molecular structures and their ability to induce ultralow friction. Moreover, a model of the prevailing friction mechanisms is proposed. However, there are many open questions and more work is clearly needed to understand this effect. This work is in progress and further results will be published in the near future.

6 Acknowledgment

We gratefully acknowledge Dr. Rudolf Eidenschink (Nematel GmbH, Mainz) for very helpful discussions and supply of LC compounds.

References

[1] Chandrasekhar, S.: *Liquid Crystals*, 2nd edition, Cambridge: Cambridge University Press (1992)

[2] G. Biresow, Tribology and the liquid crystalline state, ACS Symposium Series 441 (1990)

[3] S. Mori, H. Iwata, Tribology International 29 (1996) 35–39

[4] B.I. Kupchinov, V.G. Rodnenkov, S.F. Ermakov, V.P. Parkalov, Tribology International 24 (1991) 25–28

[5] R. Eidenschink, G. Konrath, H. Kretzschmann, M. Rombach, Molecular Crystals and Liquid Crystals 330 (1999) 327

[6] R. Eidenschink, Molecular Crystals and. Liquid Crystals 461 (2006) 71–81

[7] Y. Kimura, K. Nakano, T. Kato, S. Morishita, Wear 175 (1994) 143–149

[8] A. Korenaga, S. Sasaki, Y. Ando, K. Ono, Japanese Journal of Tribology 50 (2005) 119–130

Study on the Wear and Friction of Short Carbon Fiber and/or Nano-TiO_2 Reinforced Polyphenylene Sulfide Composites Using Artificial Neural Networks

L. A. Gyurova[1], Z. Jiang[2], A. K. Schlarb[1], K. Friedrich[1], Z. Zhang[3]

[1]Institut fuer Verbundwerkstoffe GmbH (Institute for Composite Materials), University of Kaiserslautern, 67663 Kaiserslautern, Germany

[2]The Hong Kong Polytechnic University, Hong Kong, China [3]National Center for Nanoscience and Technology of China, 100080 Beijing, China

1 Introduction

In recent years a great interest was raised in scientific and industrial communities to apply polymer composites in sliding components, where their self-lubricating properties can be exploited to avoid the need for oil or grease lubrication accompanied with the problems of contamination [1]. The choice of an appropriate matrix is of huge importance in design of wear resistant polymer composites. The required property profile of such a tribo-matrix includes high service temperature, good chemical resistance and outstanding mechanical performance [2]. Within the frame of the aforesaid, polyphenylene sulfide (PPS) is regarded as a proper tribo-matrix material [3]. Neat PPS, however, is a brittle material with relatively low impact strength [4]. Therefore, various fillers have been incorporated in order to enhance the property profile of PPS. Short carbon fibers (SCFs), which are widely advocated as a decisive reinforcement component, show a remarkable capability to increase the wear resistance of PPS as well [5]. As for the incorporation of particulate fillers, the problem becomes more sophisticated. Some micro-particles such as Ag_2S, CuS, NiS, SiC and Cr_3C_2 have been reported to reduce the wear rate of PPS, but others like PbTe, PbSe, ZnF_2, SnS and Al_2O_3 have been found to exercise an opposite effect [6–11]. The concept of adding nano-particles into polymers has already called for a big furor in the field of material science in the last decades. On the one hand, the influence of the particle angularity, which is unfavorable to the wear resistance, is significantly diminished in the nano-range. On the other hand, appropriate particulate nano-fillers contribute positively towards the development of a thin and uniform transfer film and better adhesion of the transfer film to the counterpart during sliding [12, 13], which play a crucial role in the enhancement of wear resistance [14]. Still, to our best knowledge, except our own studies there are only few papers that investigated the influence of the hybrid reinforcement of nano-particles and short carbon fibers on the tribological behavior of polymer composites [15–18].

Motivated by the recent enthusiasm in the field of nano-science and technology, we present an investigation on the tribological behavior of PPS composites filled with short carbon fibers (14.5 μm in diameter and 90 μm in length) and/or nano-TiO_2 (300 nm in diameter) particles. An artificial neural network (ANN) technology, which is a powerful analytical tool in diverse fields, is introduced to model the functional relationship between the wear properties of PPS composites and the chosen parameters including material compositions and testing conditions.

2 Experimental

Polyphenylene-sulfide (Fortron 214 C, Ticona GmbH) was used as a matrix material. Pitch-based short carbon fibers (Kureha M-2007S, Kureha Chemicals GmbH), and nano-TiO_2 (Kronos 2310, Kronos Titan GmbH) were selected as fillers. For the purpose of testing, samples were cut into pins with a contact surface of 4×4 mm^2. In order to ensure identical flow conditions, only the middle section of the injection molded plates (80×80×4 mm^3) was chosen for machining the samples. Sliding wear tests were completed on a pin-on-disc test rig under different pv-conditions at room temperature (see below Table 1). The surface roughness of the counterpart (LS 2542, INA Scheffler KG) was measured as average roughness R_a = 0.19 μm by a Mahr Perthometer (Perthen, Mahr-Perthen). The testing time was fixed at 20 hours. For some of the materials, e.g. pristine PPS, the test was stopped after 1 hour due to the severe wear. In the course of the experiments both the normal and frictional forces were recorded to determine the friction coefficient. The specific wear rate, w_s, was evaluated by:

$$w_s = \frac{\Delta m}{\rho \cdot v \cdot t \cdot F_N} \left[\frac{mm^3}{Nm}\right] \tag{1}$$

where Δm is the mass loss, ρ is the density of the material, v is the sliding speed, and t is the duration of test. F_N represents the normal force imposed on the specimen during sliding.

3 Artificial Neural Network Analysis

3.1 Principle

The ANN is an information processing model inspired by the way the biological neural system (the human brain) process information and has been used to solve a wide variety of problems in diverse fields (see ref. [19–21] for the reviews about its application in material science). As illustrated in figure 1, a neural network commonly consists of three parts connected in series: input layer, hidden layer and output layer [22]. The raw information is accepted by the input layer, and processed in the hidden layer. Finally, the results are exported via the output layer. The neurons in the neighboring layers are cross-linked by the weighted inter-connections, which is similar to the bioelectricity passing through the real axons. Besides the weight, the neurons also possess a bias value, which refers to their initial states. During the training process, the generalized knowledge is memorized in terms of the combination of weights and biases. In the hidden layers and the output layer, the individual neuron gets the information from the neurons in the previous layer, and modulates the information with a transfer function, weight as well as bias, and then outputs the result.

In order to facilitate the evaluation of the network performance a mean relative error is introduced, which provides the comparisons between predicted values for different network parameters and desired values. The mean relative error (MRE) is computed by:

$$MRE = \frac{1}{n}\sum_{i=1}^{n}\frac{|d_i - o_i|}{d_i} \tag{2}$$

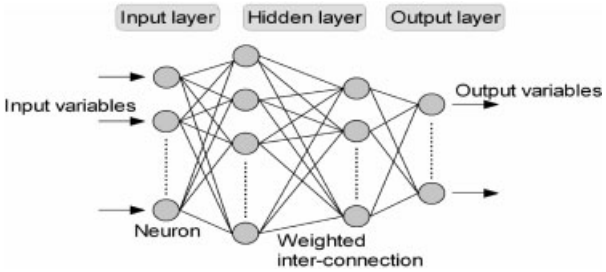


Figure 1: A schematic illustration of artificial neural network.

where d_i is desired value, o_i the predicted output value and n the number of data. The lower the MRE, the better the network performance is.

3.2 Procedure

Table 1 lists the chosen input variables (material compositions and testing conditions), the output variables (specific wear rate and friction coefficient) as well as the range of the experimental values.

Table 1: Measured parameters for input and output of ANN

Input	PPS [vol.%] 65÷100 Sliding speed [m/s] 1÷3	Short carbon fiber [vol.%] 0÷15 Applied pressure [MPa] 1÷3	Nano-TiO_2 [vol.%] 0÷7	PTFE [vol.%] 0÷10	Graphite [vol.%] 0÷10
Output		Specific wear rate	Friction coefficient		

The prediction quality of ANN has been proved to be susceptible to the size of the database for network-training. Thus in the present study a larger experimental database including 66 groups of independent tests, in which compositions that contain lubricant fillers (graphite and PTFE) in addition to short carbon fibers and nano-TiO_2, were used to train the network. Based on our earlier methodology research [23, 24], two networks with the structures of 7-$[9\text{-}3]_2$-1 and 7-$[3\text{-}1]_2$-1 were selected by training and testing process in this study. The former is employed to model the relationship between the specific wear rate and the chosen input variables. The latter is used for the friction coefficient. A Powell-Beale conjugate gradient algorithm [25] was chosen as the learning algorithm.

4 Results and Discussion

Figure 2 shows both the measured (data points with error bars) and the predicted (3D profiles) results of the specific wear rate and friction coefficient. These plots demonstrate how well the ANN models capture the wear and friction behavior of PPS composites.

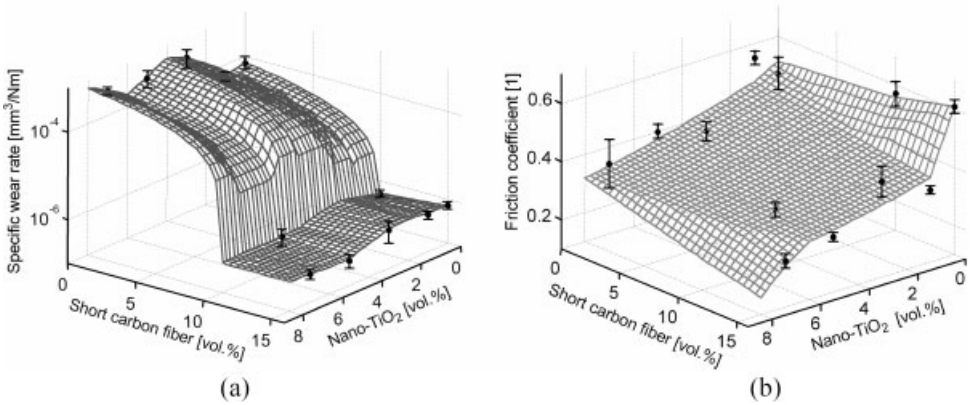


Figure 2: 3D plots generated from an ANN of (a) the specific wear rate, (b) the friction coefficient as a function of the content of short carbon fibers and nano-TiO_2 particles (pv=1 MPa*m/s)

It can be seen that the sole incorporation of nano-particles exerts a detrimental effect on the wear resistance of the PPS matrix (figure 2a). As a consequence, an upward trend in the specific wear rate originated when the content of nano-TiO_2 increases. A significant improvement in the wear resistance (approximately two orders of magnitude) was obtained by adding short carbon fibers, both as a single or a second reinforcement phase. Moreover, the hybrid reinforcement of short carbon fibers and nano-particles began to reduce the wear rate even more when compared to the single reinforcement with short carbon fibers. According to the experimental results the composition of PPS with 15 vol.% SCF and 5 vol.% nano-TiO_2 gives the highest wear resistance. Still, it can be estimated from the predicted trends that the lowest specific wear rate might be obtained for PPS with 15 vol.% SCF and 6 vol.% nano-TiO_2.

In contrast to the specific wear rate, short carbon fibers when acting alone did not decrease, but increased the friction coefficient of the PPS matrix (figure 2b). However, the addition of nano-particles as second phase did not only neutralize this effect, but even diminished the friction coefficient approximately 6-fold as compared to SCF-reinforced PPS.

A prudent question arose at this point, namely how this hybrid reinforcement of nano-particles and SCFs led to such a great improvement in the wear resistance of a pristine polymer matrix. Zhang et al. [15–17, 26, 27] presumed that the nano-particles roll rather than slide between the two mating surfaces and reduce the shear stress, friction coefficient and contact temperature. Such ball-bearing concept has also been reported with fullerene-like WS_2 nano-particles as additives for lubrication fluids [28]. Still, this rolling mechanism is until now only hypothetical. Additional investigations are warranted to verify it or reject it experimentally. We believe that the elucidation of this mechanism will advance to a great extent the understanding of tribological behavior of nano-compounds, and may promote a new promising approach in designing polymer-based tribo-materials.

5 Conclusions

The results of this study illustrated the feasibility of using ANN for characterizing given tribo-system over broad range of operating conditions. The ANN prediction and the experimental observation showed a good agreement. The lowest specific wear rate of approximately 4.0×10^{-7} mm^3/Nm was found for PPS with 15 vol.% SCF and 5 vol.% nano-TiO_2. A more optimal composition of PPS with 15 vol.% SCF and 6 vol.% nano-TiO_2 was estimated by the ANN. A synergistic effect of short carbon fibers and nano-TiO_2 particles on the wear resistance was reported both experimentally and by ANN prediction. The latter might be interpreted in terms of the rolling action of the particulate filler in the boundary layer, which helps keeping the fibers in the matrix and reduces significantly the frictional coefficient. Still, the rolling mechanism is so far only hypothetical. It is the objective of the future works to prove it experimentally.

References

[1] A. I. Sviridyonok, Tribol. Int. 1991, 24, 37-43.

[2] U. S. Tewari, J. Bijwe in Advances in Composite Technology (Ed.: K. Friedrich), Elsevier, Amsterdam, 1993, Chapter 5.

[3] J. Bucher, Polyphenylene Sulfide, Plast. World 1997, 5–53.

[4] J. R. Fred, Polymer Science and Technology, Pearson Education, New York, 2003.

[5] C. Lhymn, J. Bozolla, Adv. Polym. Tech. 1987, 7, 451–461.

[6] L. Yu, S. Bahadur, Q. Xue, Wear 1998, 214, 54-63.

[7] L. Yu, S. Yang, W. Liu, Q. Xue, Polym. Eng. Sci. 2000, 40, 1825–1832.

[8] Q. Zhao, S. Bahadur, Wear 1998, 217, 62–72.

[9] Q. Zhao, S. Bahadur, Wear 1999, 225–229, 660–668.

[10] C. J. Schwartz, S. Bahadur, Wear 2001, 251, 1532–1540.

[11] M. H. Cho, S. Bahadur, A. K. Pogosian, Wear 2005, 258, 1825-1835.

[12] C. J. Schwartz, S. Bahadur, Wear 2000, 237, 61–273.

[13] S. Bahadur, C. Sunkara, Wear 2005, 258, 1411–1421.

[14] S. Bahadur, Wear 2000, 245, 92-99.

[15] Z. Zhang, K. Friedrich in Polymer Composites: From Nano- to Micro- Scale (Ed.: K. Friedrich, S. Fakirov, Z. Zhang), Springer, New York, 2005, Chapter 10

[16] L. Chang, Z. Zhang, H. Zhang, K. Friedrich, Tribol. Int. 2005, 38, 966–973.

[17] L. Chang, Z. Zhang, C. Breidt, K. Friedrich, Wear 2006, 260, 869–878.

[18] M. H. Cho, S. Bahadur, Wear 2005, 258, 835-845.

[19] P. Zeng, Ap. M. Rev. 1998, 51, 173-197.

[20] Z. Zhang, K. Friedrich, Compos. Sci. Technol. 2003, 63, 2029–2044.

[21] H. E. Kadi, Compos. Struct. 2006, 73, 1–23.

[22] S. Haykin, Neural Networks: A Comprehensive Foundation, Prentice Hall, Upper Saddle River, 1999

[23] Z. Jiang, Z. Zhang, K. Friedrich, Compos. Sci. Technol. 2007, 67, 168–176.

[24] Z. Jiang, L. Gyurova, Z. Zhang, K. Friedrich, A. K. Schlarb, Mater. Design. 2008, 29, 628–637

[25] H. Demuth, M. Beale Neural network toolbox: for use with MATLAB (Version 4.0). The MathWorks, Inc., 2004.

[26] K. Friedrich, Z. Zhang, A. K. Schlarb, Compos. Sci. Technol. 2005, 65, 2329–2343.

[27] Z. Jiang, L. A. Gyurova, A. K. Schlarb, K. Friedrich, Z. Zhang, Compos. Sci. Technol. 2008, 68, 734–742

[28] L. Rapoport, M. Lvovsky, I. Lapsker, V. Leshinsky, Y. Volovik, Y. Feldman, A. Zak, R. Tenne, Adv. Eng. Mater. 2001, 3, 71–75.

Acknowledgement
The authors gratefully acknowledge the financial support of the German Research Foundation (DFG FR 675/45-1: Wear prediction of polymers and composites using an artificial neural network approach).

Dry Sliding Wear Properties of Thermal Spray Coatings in the TiO_2-Cr_2O_3 System

L.-M. Berger, C. C. Stahr, S. Saaro
Fraunhofer Institute for Material and Beam Technology, Fh-IWS, Dresden, Germany
S. Thiele
Fraunhofer Institute for Ceramic Technologies and Systems, Fh-IKTS, Dresden, Germany
M. Woydt
Federal Institute for Materials Research and Testing, BAM, Berlin, Germany

1 Introduction

Since Gardos [1] used the term "lubricious oxides" in 1988 to describe expected low coefficients of friction (COF) and wear rates in unlubricated dry sliding conditions for titanium suboxide materials, numerous tribological studies have been carried out on materials such as bulk (Ti,Mo)(C,N)-NiMo hardmetals (e.g. [2,3]) or TiC-based thermally sprayed hardmetal coatings (e.g. [3,4]) which form titanium suboxides as a result of tribo-oxidative and/or high-temperature reactions. Other extensive investigations have been carried out on bulk titanium suboxides (e.g. [5,6]) and coatings prepared by different spray processes (e.g. [7,8]). The predictions of Gardos [1] were based on the ability of the defects in the oxygen sublattice of titanium suboxide TiO_x to form the so-called crystallographic shear planes. These ordered planar defect structures are called Magnéli phases and are better described by the formula Ti_nO_{2n-1} with $4 \leq n \leq 9$ than by TiO_x [9].

As a rule, commercially available titania feedstock powders for the preparation of thermal spray coatings are substoichiometric. In the spray process the Ti/O ratio is changed, but the coatings are characterised by substoichiometry and defect structures as well. Application of the coatings at high temperatures in air will lead to reoxidation and to changes in the coating properties. Thus, the application of Magnéli phases with higher (oxidative) stability during the spray process and during service in air would be advantageous. Such phases are found in the TiO_2-Cr_2O_3 system.

The phase diagram of the TiO_2-Cr_2O_3 system is very complex. Figure 1 shows the latest proposed phase diagram, published in 1978 by Somiya et al. [10]. This phase diagram and that of Werner [11] are limited to temperature ranges that do not provide information about the solidus and liquidus lines. Both phase diagrams show the existence of different, distinct low-temperature Magnéli phases with a phase transition to a so-called high-temperature phase (designated by 'n', see Fig. 1) with a wide homogeneity range [10,11].

Initial studies on coating microstructures with systematically varied compositions in the TiO_2-Cr_2O_3 system sprayed by high velocity oxy-fuel (HVOF) spraying and by APS were recently published [13,14]. Coatings sprayed by atmospheric plasma spraying (APS) from the powder composition of 27/73 (in mass%) were studied in dry and lubricated sliding conditions [7,12]. In this paper the dry sliding wear resistance up to 800°C of two other selected coating compositions sprayed by APS was studied. The results are compared with those of the composition of 27/73 [7] and those of Cr_2O_3 coatings [4].

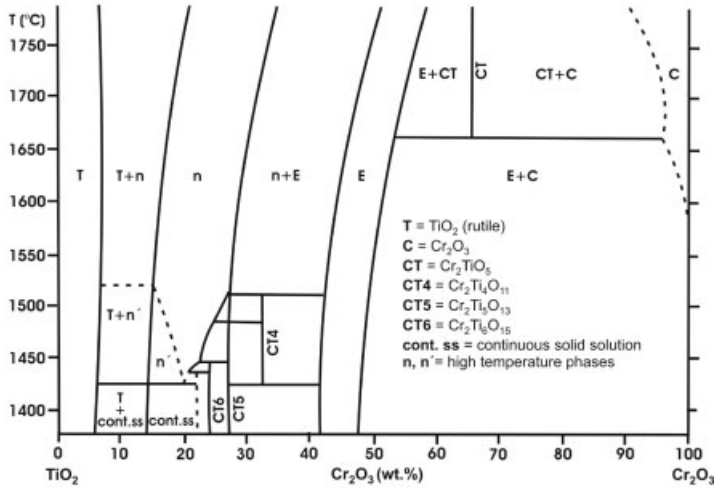


Figure 1: TiO_2-Cr_2O_3 phase diagram according to Somiya et al. [10]

2 Experimental Procedure

2.1 Starting Materials and Coating Preparation

Each of the powder and coating compositions is given in this paper in mass% as a Cr_2O_3/TiO_2 ratio. The coatings studied in this work were sprayed from feedstock powders of composition 75/25 and 23.5/76.5. The nominal and phase compositions, trade names, preparation methods and feedstock particle sizes of the feedstock powders are given in Table 1. For comparison purposes, the characteristics of the experimental powder with the composition of 27/73 [7] and the chromia powder [4] are also included in Table 1.

Table 1: Nominal and phase compositions, trade names, preparation methods and particle sizes of the feedstock powders used for coatings for studying the dry sliding wear resistance. * corresponds to shifted lattice parameters compared to the standard; $^+$ for this composition (phase E in the phase diagram) several standard cards exist; $^\#$ a&s correponds to 'agglomerated and sintered'.

Composition	Supplier	Trade name	Preparation method$^\#$	Particle size [μm]	Phase composition
100/0	Ceram GmbH	Cr_2O_3 99.7	sintered	10-40	Cr_2O_3
75/25	HC Starck GmbH	Amperit 712.066	a&s	15-53	Cr_2O_3*, Cr_2TiO_5*
27/73	HC Starck GmbH	experimental	a&s	10-45	$Ti_6Cr_2O_{15}$, $Ti_2Cr_2O_7^+$
23.5/76.5	Fh-IKTS	experimental	a&s	15-45	$Ti_7Cr_2O_{17}$, $Ti_6Cr_2O_{15}$

The phase compositions of the feedstock powders and the coatings were analysed by XRD using CuKα radiation and a D8 Advance diffractometer (Bruker AXS). The XRD patterns were measured in the range of 2θ from 15° to 90° with a step size of 0.05°.

Coatings were prepared by APS with optimised spray parameter sets using the F6 Plasma Gun (GTV mbH, Germany) and an Ar/H_2 plasma gas mixture. The tribological substrates are described together with the tribometer below. For microstructural studies and hardness measurements coatings of the compositions 75/25, 27/73 and 23.5/76.5 were deposited on mild steel substrates using the same spray parameter sets. All substrates were degreased and grit-blasted as usual before spraying. The microstructures of the coatings were investigated by optical microscopy of metallographically prepared cross sections. Hardness HV0.3 was measured on the cross sections.

2.2 Sliding Wear Test

For the unlubricated sliding wear tests performed according to DIN 50324 (ASTM G-99), a BAM-designed high-temperature tribometer, described in detail elsewhere [15], was used. This tribometer is shown in Figure 2.

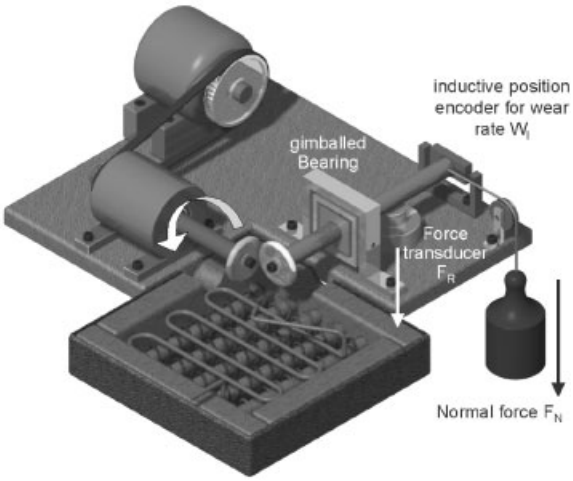


Figure 2: BAM-designed high-temperature tribometer

Coatings were deposited on to one planar surface of the rotating specimen made of steel Ni36 (Invar, 1.3910). Coatings from the previous study [7] were deposited on to grey cast iron GG20HCN. The deposited coating thickness was about 250 µm. Before testing the coatings were finished by lapping to a surface roughness as indicated in Figures 5–7 below. Sintered alumina (99.7%) bodies were used as stationary spherical (R_1 = 15 mm and R_2 = 21 mm) specimens with polished surfaces (R_a = 0.033 µm and R_{pk} = 0.019 µm) which were pressed against the coated planar surfaces of the rotating specimens during the tests. A normal force of 10 N was applied, resulting in an initial Hertz pressure P_H of ˜ 1,000 MPa. The sliding distance was 5,000 m. Experiments were performed at 23°C, 400°C and 800°C in air with sliding speeds of 0.1, 0.3, 1, 3

and 7.5 m/s. Continuous measurements of frictional force, total linear wear and specimen temperature were made. The wear volume was calculated from the dimensions of the wear scar and the results of profilometry of the wear tracks. The resolution limit of the wear rate for the rotating specimen corresponds to about 10^{-8} mm^3/Nm. One test per parameter was performed in this study.

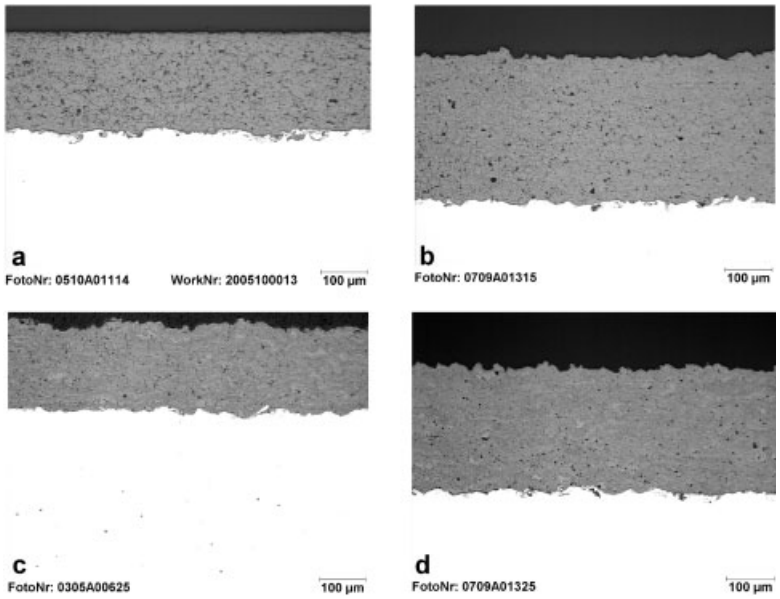


Figure 3: Optical micrographs and hardness (in parentheses) of the coatings; compositions: a) 100/0 (HV0.3: 1054) [4], b) 75/25 (HV0.3: 980), c) 27/73 (HV0.2: 851 [7]), d) 23.5/76.5 (HV0.3: 799)

3 Results and Discussion

The optical micrographs of the coating cross sections and the hardness values are compiled in Figure 3. For all compositions typical structures for APS-sprayed coatings with porosities below 5% (as estimated from the optical micrographs) were obtained. However, measurement of the true porosities of oxide coatings requires more detailed SEM studies [16] which are the subject of continuing work. The hardness values of the coatings are included in the caption of Fig. 3. There is a systematic change in hardness with coating composition for the TiO_2-Cr_2O_3 system; this has been described in detail elsewhere [14].

Although the 100/0 feedstock powder consisted solely of Cr_2O_3, metallic chromium was detected in the coatings by XRD. However, the metallic chromium oxidises during high-temperature sliding testing [4]. Figures 4a and 4b compare the x-ray diffraction patterns of the feedstock powders and the coatings of composition 75/25 and 27/73, respectively. As shown in Fig. 4a, for the composition 75/25 the phase $CrTi_2O_5$ which was contained in the feedstock powder was not found in the coating. The coating contained only a Cr_2O_3 crystal lattice with

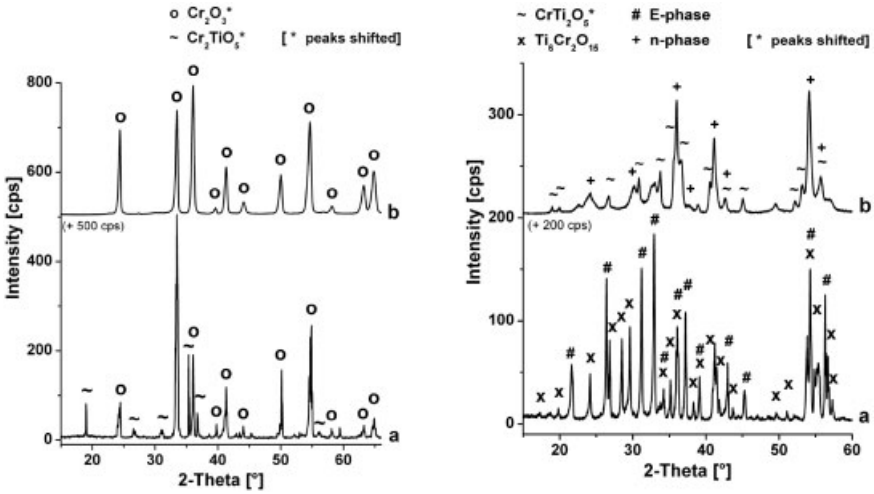


Figure 4: a) XRD patterns of the 75/25 powder (line a) and the APS-sprayed coating (line b)
b) XRD patterns of the 27/73 powder (line a) and the APS-sprayed coating (line b)

shifted lattice parameters. The phase compositions of the 27/73 (see Fig. 4b) and the 23.5/76.5 feedstock powders corresponded to the chemical compositions given in the phase diagram (see Fig. 1). For both coatings the diffraction pattern showed the presence of the high-temperature Magnéli phase ('n' phase). In addition, $CrTi_2O_5$ was present in the coating of composition 27/73. This phase is not shown in the phase diagrams, but has been described in the literature [17]. Due to the complexity of the diffraction patterns in the TiO_2-Cr_2O_3 system other phases could not yet be clearly identified.

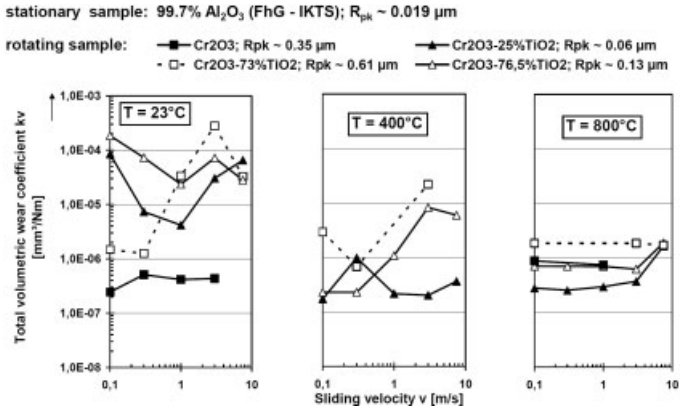


Figure 5: Dependence of total wear rate on sliding speed and temperature for the coatings

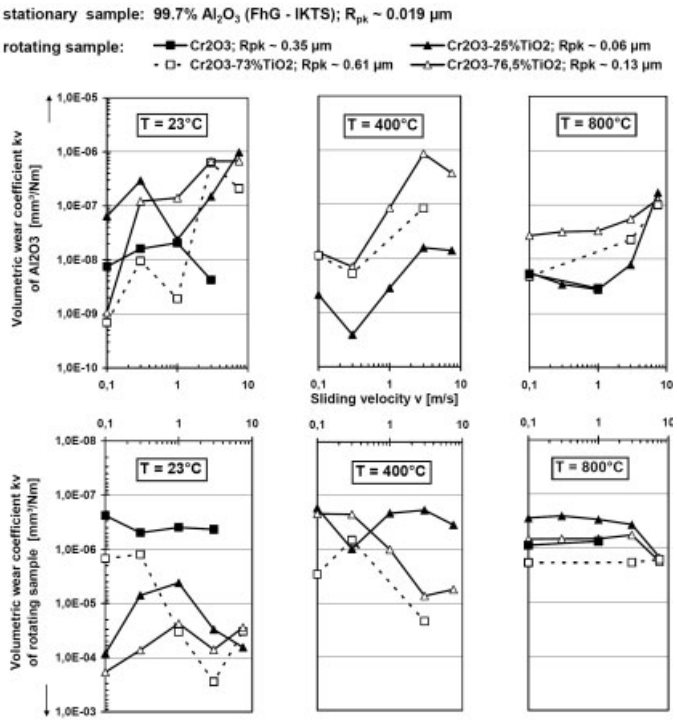


Figure 6: Dependence of wear rate on sliding speed for the stationary (top) and rotating (bottom) samples

The total wear rates for the unlubricated sliding wear tests are compiled in Figure 5. The wear rates for the rotating and stationary samples are given separately in Figure 6. Figure 7 shows the coefficients of friction (COF) of all couples. Analysis of the results indicated that wear of the coating was the main component of the total wear rate, with wear of the sintered alumina conterpart being at least one order of magnitude lower. At room temperature, with the exception of the results for the Cr_2O_3 coating, the total wear rates were high. For most test conditions at 800°C the wear rates were below 10^{-6} mm^3/Nm and less sensitive to sliding velocity. This value characterises the borderline between dry friction and mixed/boundary lubrication and underlines the potential of these coatings for use in dry high-temperature sliding wear applications. Differences in the coating surface roughness might have been responsible for some differences in the total wear rate and COF between different compositions, as they ranged from R_{pk} = 0.06 – 0.61 µm. At 800°C with increasing sliding speed the COF decreased to nearly 0.2 (see Fig. 6).

4 Conclusions

Application of APS-sprayed coatings of the TiO_2-Cr_2O_3 system in high-temperature sliding conditions has been studied in this work. Changes in the phase composition from the feedstock

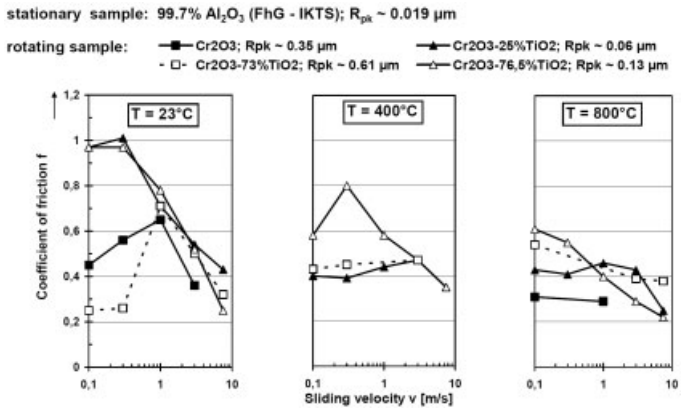


Figure 7: Dependence of the coefficient of friction on sliding speed against sintered alumina

powder to the coating occurred as a result of the spray process. The diffraction patterns of the 27/73 and the 23.5/76.5 coatings showed the presence of the high-temperature Magnéli phase ('n' phase), while only a Cr_2O_3 crystal lattice with shifted lattice parameters existed in the 75/25 coating. Inconsistencies in the roughness values obtained for the tested specimen prevented clear conclusions on the influence of the coatings' phase compositions on their dry sliding wear properties from being able to be made. However, all coatings showed very low total wear rates and low COF values at the test temperature of 800°C.

5 Acknowledgments

The authors would like to thank all coworkers as well as B. Wolf for metallographic work.

The results presented here are part of the DVS research project 'Development of multifunctional ceramic coatings of the system TiO_2-Cr_2O_3 (Entwicklung multifunktionaler Schichten im System TiO_2–Cr_2O_3)' (AiF No. 14.926 B) which is funded via AiF by the Federal Ministry of Economics and Technology within the framework of the program for promotion of 'Industrial joint research (Industrielle Gemeinschaftsforschung (IGF)'. The authors gratefully acknowledge this funding.

6 References

[1] M.N. Gardos, Tribol. Trans. **31** (1988) 4, 427–436.

[2] A. Chavanes, E. Pauty, M. Woydt, Wear **256** (2004) 7–8, 647–656.

[3] L.-M. Berger, M. Woydt, S. Saaro, Wear (2008) doi:10.1016/j.wear.2008.04.13.

[4] L.-M. Berger, S. Saaro, M. Woydt, in *Jahrbuch Oberflächentechnik 2007 (Ed.: R. Suchentrunk)*, Eugen G. Leuze Verlag, Bad Saulgau, 242–267. ISBN 978-3-87480-234-5

[5] M. Woydt, A. Skopp, I. Dörfel, K. Witke, Wear **218** (1998) 1, 84–95.

[6] M. Woydt, Tribol. Lett. **8** (2000) 2-3, 117–130.

[7] M. Woydt, Tribologie & Schmierungstechnik **52** (2005) 4, 5–12.

[8] A. Skopp, N. Kelling, M. Woydt, L.-M. Berger, Wear **262** (2007) 9–10, 1061–1070.

[9] L.-M. Berger, Thermal Spray 2004, Adv. in Technol. and Application, *Proc. Int. Thermal Spray Conf., Osaka, May 10–12, 2004,* ASM International, Materials Park, 934–945. ISBN 0-87170-809-4

[10] S. Somiya, S. Hirano, S. Kamiya, J. Solid State Chem. **25** (1978) 3, 273–284

[11] H.-D. Werner, Neues Jahrbuch Mineralogische Monatshefte (1974) 5, 218–234

[12] M. Woydt, B. Criqui, G. Desplanches, T. Linnemann, Ind. Lubrication Tribol., **60** (2008) 2, 14-23, also: *Proc. 15th Int. Coll. Tribol., TAE Esslingen, Jan 17-19, 2006,* 10 p.

[13] C.C. Stahr, L.-M. Berger, S. Thiele, Materialwiss. Werkstofftech. **39** (2008) 1, 24–28.

[14] C.C. Stahr, L.-M. Berger, S. Saaro, S. Thiele, *Proc. Int. Thermal Spray Conf., Maastricht, June 2–4, 2008,* DVS-Verlag, Düsseldorf, 1114–1119. ISBN 978-3-87155-979-2

[15] M. Woydt, K.-H. Habig, Tribol. Int. **22** (1989) 2, 75–88.

[16] C.C. Stahr, L.-M. Berger, M. Herrmann, D. Deska, Proc. Werkstofftechnisches Kolloquium Chemnitz (WTK) 2008, in press.

[17] H. Müller-Buschbaum, K. Bluhm, Z. anorg. allg. Chem. **558** (1988), 28–34.

Friction in Continuous Casting of Steel: Lubrication Experiments at 1200°C

Dieter Senk[1], Andreas Münch [2], Klaus Schulz[3]
[1] Department of Ferrous Metallurgy at RWTH Aachen University
[2] like[1], now with: ThyssenKrupp Steel AG, Duisburg
[3] S & B Industrial Minerals GmbH, Business Unit STOLLBERG Germany

1 Abstract

During continuous casting of steel the main goal of applied mould slags is the lubrication of the solidifying strand surface in the mould because steady state and oscillating movement are causing unwanted friction. Shear stresses have to be minimized to prevent of surface hot cracks. Considering the facts that the viscosity of slag changes from Newtonian viscosity based friction by crystallization to Coulomb´s friction, the prediction of lubrication effects is a complex task.

Thus the friction cannot be calculated but it has to be determined experimentally. Therefore a friction force simulator has been developed at the Department of Ferrous Metallurgy of RWTH Aachen University. By this method measurement of friction forces in hot condition under almost continuous casting conditions is possible in a wide temperature range. In laboratory trials values of friction forces and lubrication effects of liquid and crystallising mould fluxes for different types of fluxes are given. Surface temperatures of the steel are between 1,250°C and 1,000°C.

2 Introduction

Liquid steel is continuously cast at temperatures of about 1,500 °C in casters consisting of a water cooled copper mould and a strand guiding system with secondary cooling equipment. The steel solidifies in contact to the mould walls which have a length of about 1 m. The tube-like solidifying shell of the strand contains liquid steel which solidifies finally after 10 to 40 m. The mould oscillates vertically while casting velocity of the strand is adjusted constantly. In combination with an applied lubricant this measure diminishes the friction between the withdrawn strand and the mould to prevent of surface cracks in the hot and sensible solidified steel shell. In worst conditions an un-sufficient lubrication leads to sticking of the steel to the mould wall and subsequently a breakout. In cases of casting small billets special oils are applied as lubricant which cracks to carbon and burning hydrogen and carbon-oxide, but in the most cases of casting so called casting fluxes consisting mainly of different oxides in well tuned mixtures are used. Worldwide about 1 Mio tons of steel is produced annually by this method.

Mould fluxes have to fulfill several tasks besides the most important task, the lubrication of the strand in the mould. The flux is added directly onto the liquid metal surface (so called meniscus level), melts and forms a mould slag which is continuously drawn into a forming gap between strand and mould walls [1]. Hydro-dynamical conditions are created at the triple point of mould, liquid steel and liquid/solidifying flux in combination with the oscillating movement to transport liquid flux between strand and mould. The rate of flux entrapment is depending on both, the

pressure conditions and the fluidity of the flux expressed as viscosity and temperature of crystallization start. The fractions of liquid and solid parts of the flux in the gap of less than 1 mm thickness control the friction forces and so the shear stress to the hot strand surface. The temperature gradient within that flux layer is more than 1,000 K/mm. The perpendicular force to the friction area is caused by internal ferrostatic pressure of the liquid steel and the geometrical conditions of shrinking steel shell and tapered mould walls.

While the flux is completely in liquid state the viscosity as a measure for inner friction can be determined by calculation, several models have been released throughout the recent years [2,3,4], also with respect to a crystalline part. By passing the meniscus level of the mould the flux starts to solidify as crystals, i.e. from that point on the flux is not completely liquid but heterogeneous. The solidification process continues during the descent of the flux in the gap between mould and strand, the result is a rising content of crystallized slag in the flux [5,6]. From the point when first crystals appear in the slag the former Newtonian viscosity is transferred into an apparent viscosity. That apparent viscosity is not calculable with sufficient accuracy to predict the friction forces. A measurement of friction forces during operation at a running caster is difficult because only overall forces or accelerations of the driven mould can be recorded. Therefore a friction force simulator was developed and approved at the Department of Ferrous Metallurgy. With this new facility friction forces and friction coefficients of mould fluxes can be determined in the laboratory under hot conditions similar to continuous casting.

3 Basics

Friction is the resistance that occurs when two materials in contact are shifted against each other. The amount of force can be determined after (Eq. 1). Coulomb's coefficient μ determines the amount of force to shift a materials pair. This approach is chosen because the lubricant is not completely liquid, but mainly solid/ liquid.

$$F_r = \mu \cdot F_n \tag{1}$$

F_r = Friction force, F_n = perpendicular force, μ = friction coefficient.

The determination of a temperature depending friction coefficient μ of mould fluxes is important in order to give validated statements on possible development of stickers in the mould or breakouts related to this phenomenon [7,8].

4 Testing Equipment and Trials

At the Department of Ferrous Metallurgy several studies were carried-out before to create a thin solidified shell like an as-cast strand under controlled conditions in the lab [9]. In order to simulate continuous casting conditions properly the friction is to be measured in the system steel strand – mould flux – copper mould. To form the hot surface of a fresh solidified steel shell on which the flux can be applied is the most important problem to overcome in an experiment. A special mould was developed in which steel melt solidifies and offers a free surface for experiments like the application of the also developed measurement system (**Figure 1**).

The testing equipment consists of two units: A) Casting box (mould) relined with 40 mm of chamotte lining in which an ingot is cast which provides sufficient heat to hold the flux in a liquid state for several minutes, even when the water cooled copper tester comes in contact. The ingot´s dimensions are 170 mm by 150 mm by 520 mm. Three thermocouples were installed in order to measure the temperature close to the surface and to calculate the recent surface temperatures. B) The friction measurement system which consists of a motor with constant speed, a torque sensor and a mould simulator made of a revolving water cooled copper plate. By shifting the copper mould simulator over the steel surface a torque is induced by friction which is measured by the torque sensor and recorded on a computer. To determine the friction forces from the torque, the following equations (**eq. 2…6**) are taken into account in addition to eq. 1:

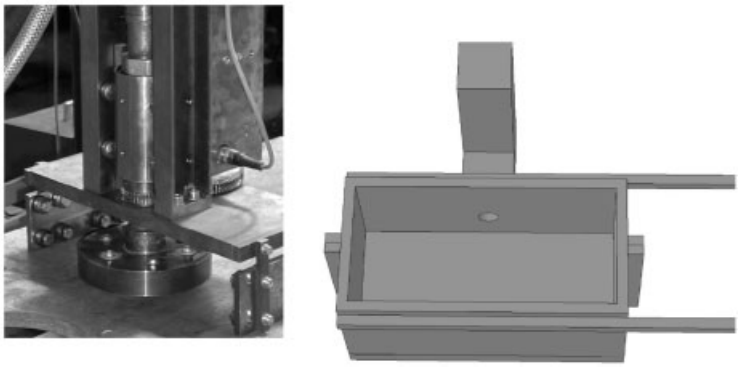


Figure 1: Measurement facility and casting box (mould)

$$F_n = p \cdot A \tag{2}$$

$$dA = 2 \cdot \pi \cdot r \cdot dr \tag{3}$$

$$M = \int r \cdot dF_r \Rightarrow M = \frac{2}{3}\pi \cdot p \cdot \mu_r \cdot r^3 = \frac{2}{3} F_n \cdot \mu_r \cdot r \tag{4}$$

$$\Rightarrow F_r = \frac{3}{2}\frac{M}{r} \tag{5}$$

$$\Rightarrow \mu_r = \frac{3}{2}\frac{M}{F_n \cdot r} \tag{6}$$

p = pressure in Pa, A = Area in m², r = radius in m, M = torque in Nm,F_γ = friction force, μ_γ = friction coefficient

Before any hot measurement the friction force tester has to be calibrated. The calibration was carried-out at room temperature with the pair copper and polished steel. The friction coefficient for this pairing is well known and gives a friction coefficient of $\mu = 0.3$ [10] used as reference for the following hot tests. Within the calibration an apparatus factor is determined in order to correct the inner friction of the testing rig. Calibration curves with (*'raw data'*) and without (*'real'*) inner friction of the facility are oscillating because both planes are not in parallel but with a small angle to capture flux later-on.

All trials were carried-out in the following pattern: The steel was cast into the casting box. To ensure a smooth solidified shell the box was covered with a steel plate of 40 mm thickness. The steel plate was removed after a defined time to make sure that the shell thickness is 15 mm minimum, and the mould flux was applied as powder onto the hot steel surface at about 1,500 °C. Then, the measurement system was moved into position. During that time the mould flux melted to a liquid slag. The rotating water cooled mould simulator was lowered onto the slag layer. During the measurement, the values of time, surface temperature of the shell and the torque in the motor drive were recorded. Each trial with rotating copper plate lasted about 1 minute.

5 Experimental Results

Several mould fluxes - bounded for casting of different steel grades - were tested by this method. **Figure 2** is given as an example of such a measured curve. The torque is changed to friction coefficients by comparison with the reference values as explained above. Due to the rotation of the sampler and the fact, that it was impossible to ensure that the surface and the mould simulator are completely parallel during the trials. In order to determine the friction coefficient itself, the data were treated to find an average for the μ-value. At the end of each trial the rotating plate was elevated to measure the apparatus constant again; in the given curves that factor is already taken into account and removed from the results mathematically.

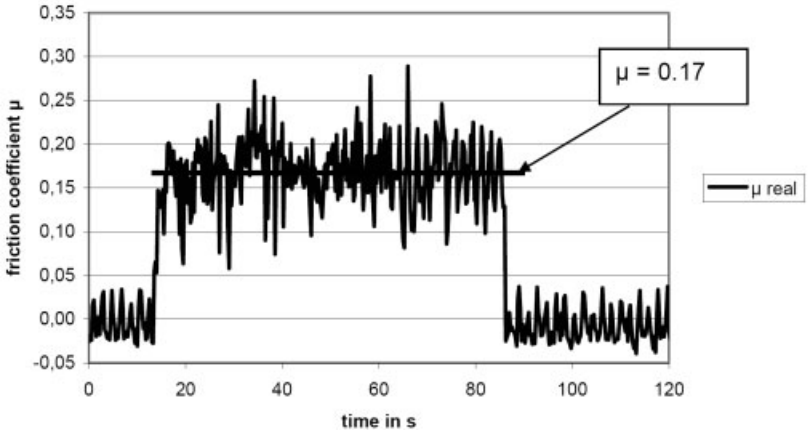


Figure 2: Friction force coefficient of the mould flux grade ST-C39/26 Al4D

The flux (grade Accutherm St-C39/26-AL4D) in the test of figure 2 is used for TRIP-steels with high alumina content. This first test was carried out with the initial chemical composition of this flux which consists of a low alumina fraction and a high SiO_2 content (low basicity).

In its initial state this flux has a calculated viscosity (after Riboud [2]) of 0.049 Pa· s at 1,500 °C.

The friction coefficient by lubrication of flux in this case is lowered to $\mu = 0.17$ compared to dry friction of the material pair copper / steel, respectively –44 %.

During real casting processes the casting flux can react chemically with the elements dissolved within the liquid steel, mainly the redox-reaction (**eq. 7**) with aluminium

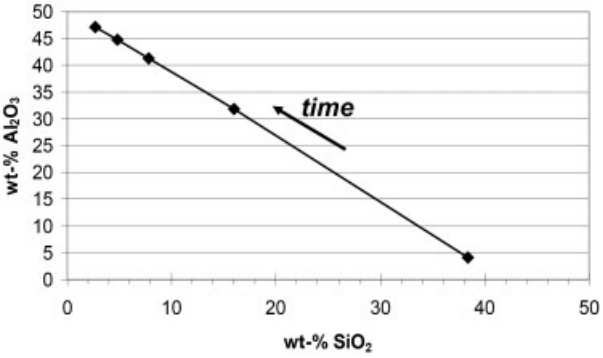


Figure 3: Change of concentrations by redox-reaction during 50 min

$$4[\mathrm{Al}] + 3(\mathrm{SiO_2}) \Leftrightarrow 2(\mathrm{Al_2O_3}) + 3[\mathrm{Si}] \tag{7}$$

is active; reactions between aluminium and manganese have been also observed. The brackets mean that [ ] is dissolved in steel and ( ) is a component of the slag. The result is an increasing viscosity of the slag when alumina is picked-up and silica is diminished. The influence of the chemical composition of real slags was also tested in laboratory: Therefore specimens of this flux were taken from the running casting process at ThyssenKrupp Steel AG in Duisburg-Beeckerwerth steel plant. The change of silica and alumina concentrations during the time period of about 1 hour (**Figure 3**) took place in respect to equation 7.

In the second trial run the specimens were taken after 10 and 50 min of the continuously running cast also directly from the mould. The samples were chemically analysed and the viscosity was calculated on the basis of Riboud´s formula. Though the calculated viscosity rises from 0.049 Pa s to 0.079 Pa s (+61 %) after 50 min. Figure **4** shows a summary of 3 lubrication trials, carried-out with the origin flux (like already shown above), with the re-molted flux after 10 min of residence time on the mould, and the re-molted flux after 50 min. The friction force raised and the friction coefficient μ increased from 0.18 to 0.22 (+22 %).

The influence of the strand surface temperature on the friction was measured, too. Therefore the testing facility was equipped with a thermocouples type B which were located in the solidifying shell in distances below 15 mm to the surface. The friction coefficient was measured 4 times during one trial of 25 min of duration while the temperature decreased continuously; 3 times the friction coefficient was at the same level but when than the friction increased clearly. That phenomenon is to be understood with respect to the partly crystallization of the slag as well as the roughening of the surface of the steel ingot to a R_z of about 25 µm.

6 Conclusions

In order to validate this result on influence of the chemical composition several mould fluxes with different chemical compositions have been tested, subsequently. **Table 1** shows a comparison of

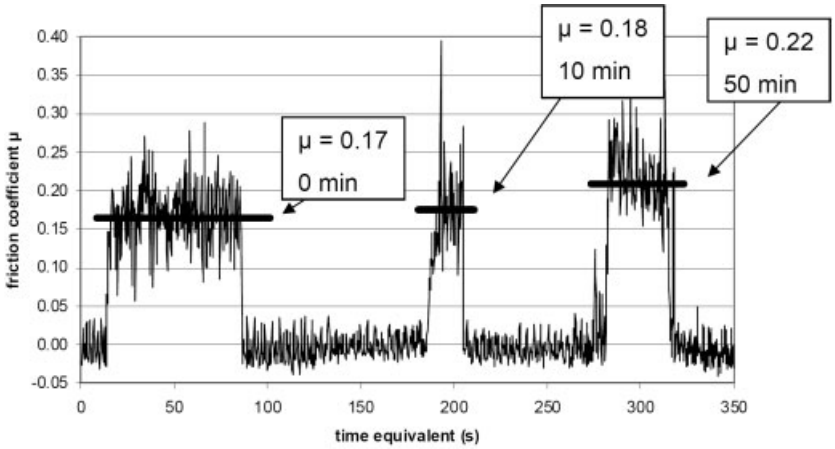


Figure 4: Determined friction coefficients μ of the mould flux Accutherm St-C39/26-Al4D

the friction coefficients of several mould powders with different chemical compositions to the calculated viscosity. It is obvious that the friction is not influenced only by the viscosity in that complex system.

Table 1: Comparison of friction coefficients μ and viscosity η

Flux (Accutherm St-C39/26-…)	H 12-1	26-6 KS	Al 4D	616 W4	220 DR
viscosity (after Riboud)	0.032 Pa s	0.036 Pa s	0.049 Pa s	0.022 Pa s	0.059 Pa s
friction coefficient	0.2	0.22	0.17	0.16	0.14

But taking into account the fraction of crystalline phases in the liquid-solid-mixture in that temperature gradient of more than 1000 K/mm the friction must be explained as complex process of Newton´s and Coulomb´s approaches. Particularly, in the Newton´s part of liquid friction an apparent viscosity helps to explain the influence of chemical and mineralogical composition of the flux on the lubrication behavior.

There are empirical formulas to determine the following values:

1. *Break temperature:* The temperature where the liquid and solid fraction are approximately equal. S. Sridhar et al. [3] give proposals to apply chemical composition in wt-% to that special temperature.

2. *Dynamical viscosity:* Chemical composition in mole-% is applied to predict the viscosity by the approach $\eta = A \cdot T \cdot \exp(B/T)$ where A and B are function of chemical composition and T is the temperature [2]

3. *Ratio NBO/T:* Gives a relation to the fraction of crystalline phase in the slag as a function of chemical composition in mole-%. It is similar to basicity, but the formula takes into account rather all components of the slag parted in network formers (like SiO_2) and network destroyers (like CaO) [11].

It can be assumed that, the crystalline portion (expressed by break temperature and NBO/T), and the liquid fraction (expressed by dynamic viscosity in the Newton´s law of shear stress $\tau = \eta \cdot dv/dx$) are influencing the friction coefficient. But in those first experiments direct dependence couldn´t be found by statistical correlation.

The change of chemical composition of the lubricant during casting leads to less viscosity and by that purpose to a thinner film in the gap combined with the danger of increasing friction.

In spite of suppressing in the experiments the oscillating effect of the mould which is changing the direction of the friction force in each period, the unidirectional laboratory test of measurement of friction and lubrication behavior leads to reasonable values of both, influence of surface temperature and chemical composition of the flux. The application of solidifying steel and a water cooled copper tester are able to simulate industrial continuous casting in the process step of initial solidification. The increasing pressure of the strand to the mould by rising ferrostatic pressure can be simulated by change of the load of the copper plate.

7 Summary

In continuous casting there is a relatively movement between oscillating mould and withdrawn solidifying steel strand. Using liquid slag as lubricant the knowledge of a friction coefficient helps to predict critical shear stress situations and to provide surface cracks. At RWTH Aachen University a hot testing rig was designed and operated to measure the friction at surface temperature between 1,000 °C and 1,400 °C. At conditions similar to industrial casting, measurements leaded to friction coefficients of μ = 0.17 and 0.22 between the solidified hot steel surface and a water cooled rotating copper plate. Also effects of chemical compositions of the fluxes on lubrication could be observed taking into account that in the thin gap the lubricant is partly in solid, heterogeneous and liquid states.

8 References

[1] Macias, E.A.; Castillejos, H.E.; Acosta, A.G; Herrera, M.G.; Neumann, F.: Modelling molten flux layer thickness profiles in compact strip process moulds for continuous strip casting, Ironmaking and Steelmaking, Vol. 29, (2002) 5, pp. 347-359

[2] Riboud, P., Eigenschaften und Aufgaben von Stranggießschlacken, Metallurgie des Stranggiessens, Verlag Stahleisen, Düsseldorf 1992, Kap. 3.2, pp. 233-256

[3] Sridhar, S.; Mills. K.C.; Afrange, O.D.C; Lörz, H.P.; Carli, R.: Break temperature of mould fluxes and their relevance to continuous casting; Ironmaking and Steelmaking 27 (2000) 3; pp. 468–473

[4] Koyama, K.; Nagano, Y.; Nagano, K.; Nakano, T.: Nippon steel tech. Rep., (1987) 34, pp. 41–47

[5] Heller, H.-P.; Fenzke, H.-W., Zur Schmierwirkung von Gießpulverschlacken beim Stranggießen, Neue Hütte, Heft 1/1988, pp. 9–14

[6] Hering, L.; Seher, B.; Fenzke, H.-W., Zur Wirkung des Gießpulvers beim Brammenstranggießen, Neue Hütte, 37. Jahrgang, Heft 9/92, S. 339–343

[7] Yao, M.; Fang, D.C.; On line measuring method for mould friction in continuous casting, Ironmaking and Steelmaking Vol. 23., (1996) 6, pp. 522–527

[8] Royzman, S.E., Coefficient of friction between strand and mould during continuous casting: mathematical model, Ironmaking and Steelmaking Vol. 24., (1997) 6, pp. 484–488

[9] Hamadou, H.: Makro- und Mikromodellierung der Strukturentwicklung beim Stranggießen von Stahl, Dissertation RWTH 2006

[10] Tipler, P.A. Physik. Für Wissenschaftler und Ingenieure, Spektrum Akademischer Verlag, 2. Auflage, 2004

[11] Mills, K.C; Fox, A.B.; Thackray, R.P., Li, Z.; The Performance and Properties of Mould Fluxes; Ironmaking and Steelmaking 32(2005)1, pp. 26–34

Simulative Wear Testing of Tool Materials for Comminution of Hard Ore Material

D. D. Olsson[1)], N. Bay[2)]
[1)] R&D Research Centre Dania, FLSmidth A/S, Denmark,
[2)] Dept. of Mechanical Engineering, Technical University of Denmark

1 Introduction

Wear is a general problem in many industries and much effort is done to impede premature wear out of often costly equipment. Unexpected high wear rates imply high economic losses due to production stops, unscheduled maintenance or in rare cases catastrophic breakdown of critical wear parts. This is especially the case for mining and cement industries where the vast majority of production equipment suffers from severe wear due to processing of often very hard and abrasive minerals and ores. Hence, careful selection of wear resistant materials based upon dedicated wear tests is vital to ensure sound production. Furthermore, such tests may be applied to study abrasiveness of the treated ores, [1].

Wear is complex and should be regarded as a system, covering numerous parameters as illustrated in Figure 1, showing a bed of mineral particles of varying size and shape compressed and crushed between two tool surfaces of wear resistant material sliding relative to each other. The interaction between the tool surfaces, mineral particles and surroundings during comminution causes a severe and complex wear situation.

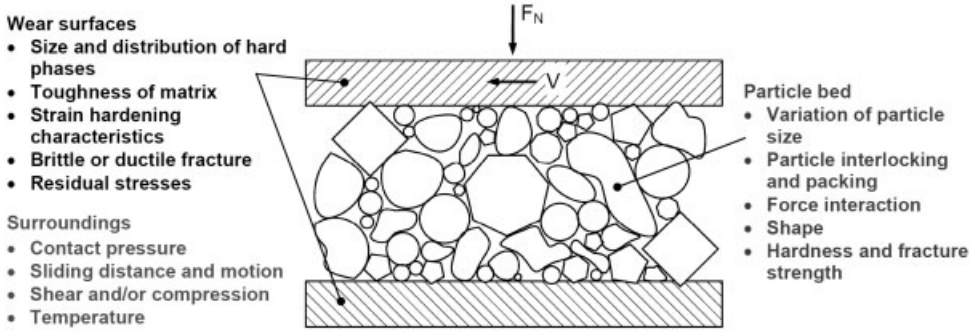


Figure 1: Illustration of factors influencing wear during comminution of mineral particles.

Successful studies of this kind of wear are heavily depending on selection of appropriate test methods. In principle, two different approaches may be considered for evaluation or predicting wear appearing on industrial size equipment: 1) Field testing and 2) Laboratory testing, each having their advantages and disadvantages.

Field testing possess the major advantage that candidate wear samples are subjected to the exact conditions under which they are later to be applied and as such it may be able to disclose

unforeseen events influencing wear. However, such field-tests are very costly and time consuming, since replacement and evaluation of in-situ wear samples in production lines may be limited to time intervals already planned for maintenance. Moreover, depending on the application, it may be difficult to access the wear parts during the test, and the insertion of test tool parts in existing equipment for production, which turns out to be inappropriate causing unexpected downtime or even catastrophic breakdown may imply significant costs. Parametric studies of the numerous parameters which may influence wear are impractical or impossible implying that the results are limited by the rather limited conditions tested and often poorly documented due to the poor control of fundamental process parameters such as normal pressure and sliding length, and variations in abrasive media composition, temperature, moisture etc.

Laboratory testing implies that wear is measured under more controlled conditions using simplified test setups compared to the industrial equipment. Downscaling and off-line testing implies much larger flexibility to test different tool and ore materials under varying process parameters like normal pressure, sliding length, temperature and moisture, [2, 3]. In order to succeed in such simulations of the real production it is vital to select/develop proper laboratory tests modelling the production conditions appropriately, [4, 5].

2 The Proposed Test

A fundamental objective of the present wear test has been to include particle breakage thus simulate wear mechanisms, which appears when comminuting especially hard and brittle minerals. This rarely the case for existing wear tests such as the dry sand rubber wheel wear test (ASTM G36). In praxis, comminution processes involve both compressive and shear forces implying a multidirectional stress field between mineral particle and wear surface. The proposed test includes shear forces as well as compressive forces between tool surface and mineral bed.

Page et al. [6] have found that a compressive force superimposed with a shear force acting on a bed of quartz minerals generates a thin layer of fines at the boundary layer between the tool surface and the mineral bed due to comminution. The generation of fines is likely to have large influence on the resulting wear since particle size and shape has been found to be important for abrasive wear [7, 8]. Establishing of this so-called autogenous wear protection layer is important in many comminution applications since it effectively impede wear by retention of fines. The fines are captured in voids or pockets on the active wear surface, hence acting as a buffer layer against fresh abrasives to be crushed. Excessive moisture may disturb an autogenous layer and direct washing out of the fines must of course be avoided. Thus the primary purpose of the proposed test has been to establish a method by which wear can be evaluated for various candidates for tool material under conditions similar to typical comminution conditions in which generation of fines comes into play.

The test principle is shown in Figure 2 and is hereafter denoted ‘compression-twist test’ or ‘CT-test’ in short. The abrasive mineral is enclosed in a container and compressed between identical upper and lower wear discs. Precision-machined grooves in the wear discs ensure a tight connection and torque transfer between punch and upper disc as well as between lower disc and container assembly. Contact pressure is build up between the wear discs and the bed of abrasive particles by applying an adjustable axial force on the upper punch, which is not able to rotate. By subsequent rotation of the lower disc and container assembly sliding wear occurs on the stationary

upper disc. Friction between the inner wall of the container and the particle bed implies that pure indentation, with no relative sliding of the abrasive particles against the lower disc, occurs. This means that actually two different mechanisms appear during testing, representing two important test conditions, namely resistance towards 1) indentation and 2) abrasive wear. Both mechanisms may cause significant wear in case that the abrasive mineral particles are capable of indenting the tool surface either by contacting regions of the matrix structure more prone to wear or by directly damaging hard phases such as carbides, [4].

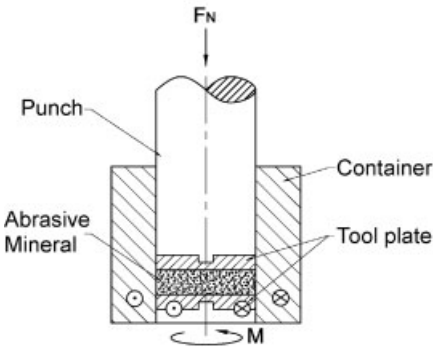


Figure 2: The CT-test schematically shown

3 Test Equipment

The presented test principle requires combined axial loading and rotation, which calls for special equipment. Such equipment for performing the CT-test is placed at Department of Manufacturing Engineering, Technical University of Denmark, see Figure 3, where it was originally developed for cold welding with superimposed sliding, [9] and later applied for testing of friction and lubrication in cold forging, [10].

A hydraulic cylinder provides the axial load of maximum $F_{N,max}$ = 175 kN. A hydraulic motor below the press table connected to a worm gear drives the vertical spindle axle on which the container and the lower tool disc is mounted. Maximum torque on the spindle is T_{max} = 140 Nm. A custom-built strain gauge transducer, which measures load as well as torque, is placed between the upper tool plate and the hydraulic cylinder. Corresponding values of axial load, torque, angular displacement and punch travel are collected during testing by a data acquisition computer and software. Data are collected at 100 Hz sampling rate, stored on hard drive and extracted for subsequent data treatment. The container bore diameter is 40 mm and the upper and lower tool plate has a slide fit with the bore. These are both 6.0 mm in height. The above mentioned load capacity allows a maximum contact pressure of p_{max} = 140MPa. This is however not feasible in the test since the torque capacity limits the maximum allowable pressure to ensure rotation of the lower tool parts and the mineral particles towards the upper tool due to excessive friction. The torque capacity corresponds to a maximum in average friction stress on the upper tool plate of τ_{max} = 8.35 MPa. Appropriate levels of contact pressure have been selected ensuring proper relative sliding between mineral particles and upper tool plate.

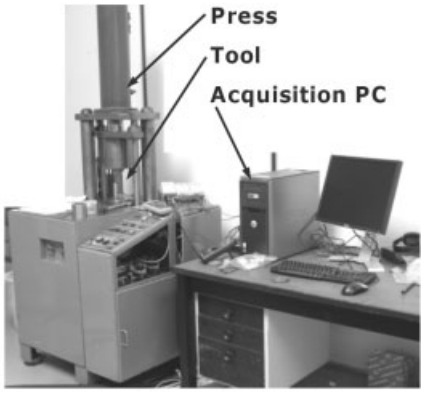


Figure 3: Equipment for wear testing

The wear resistance of four different tool materials has been studied using the CT-test, see Table 1 for properties. Mild steel C45 would never be used as a tool material in practice, but it represents a material with no hard phases. Cromin 15 is commonly used as tool material for roller and grinding tables in vertical roller mills for cement industry. It is a white cast iron having a structure of large chromium carbides distributed in an martensitic matrix.

Table 1: Properties of tool materials included in study

Description of steel	Standard	Hardness
Mild steel	Wn. 1.0503 (C45)	266 HV30
White cast iron	EN 12513-2000, JN3029 (Cromin 15)	630 HV30
Hardened tool steel	AISI D2 (Sverker 21, Uddeholm)	764 HV30
Hardened PM tool steel	AISI M3:2 (Vanadis 23, Uddeholm)	796 HV30

AISI D2 is widely used cold work tool steel with high contents carbon and chromium and furthermore alloyed with molybdenum and vanadium. The structure is dominated by chromium carbides 7μm to 10μm in diameter and hardness between 1200HV and 1400HV. It should be noted that this steel is not common for cement nor mining industry, but usually applied as a tool-steel for metalforming applications.

The fourth tool material included in the present investigation is a powder metallurgical (PM) steel, AISI M3:2, which is manufactured by Hot Isostatic Pressing (HIP). The HIP-process allows a complex composition of several alloying elements, which is also the case of the AISI M3:2 steel having contents of: chromium, molybdenum, tungsten and vanadium. The HIP-process implies that a very homogenous structure is obtained in terms of very small (< 3μm) and evenly dispersed Cr, W, Mo and V and Mo carbides.

Two types of silica sand of different particle size (coarse and fine) have been applied as abrasive media in the present investigation. The particle of the coarse sand is in average 2000 μm, whereas the fine sand is 300 μm. Both types contain mineral particles with a average hardness of approximately 1200 HV and with rounded grains.

Testing was performed at a contact pressure of 7MPa and 20 MPa for coarse and fine sand respectively. The number of rotations of the lower tools was different depending on the silica sand used; five rotations in case of coarse sand and one rotation in case of fine sand. The resulting wear was quantified by measuring weight loss and by roughness testing of worn surfaces. The weight loss, Δm was measured using a precision scale with a resolution of 0.1 mg.

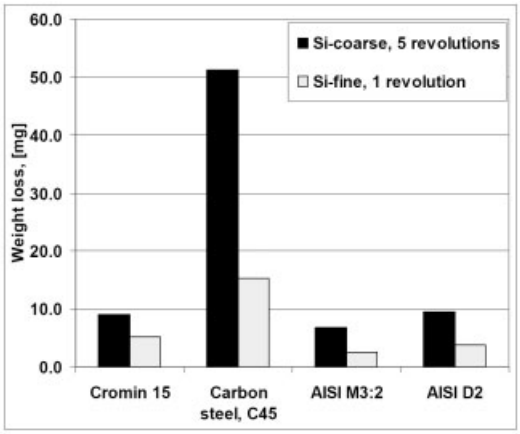


Figure 4: Weight loss of the tested tool materials and the two different of abrasive silica sand

Roughness measurements were carried out for each of the tested discs on the active surface before and after wear testing. Each surface was measured along two perpendicular diameter lines tracing from the outer circumference towards centre implying four perpendicular roughness profiles. Each roughness profile was 16mm in length. However, according to existing standards, only 4mm of this distance was applied for actual roughness parameter calculations, refer to Figure 5. The roughness test equipment was from Taylor–Hobson having a stylus tip radii of 5 µm with a resolution of 0.01 µm

The measured weight loss, Δm is shown for all of the investigated tool materials in Figure 4. The weight loss is generally found to be higher when worn against coarse silica sand using five rotations compared to the fine sand and using only one rotation.

Table 2: Average roughness values measured on the different tool materials.

Type of tool material	Fine sand Ra [µm]	Coarse sand Ra [µm]
C45	1.13	1.11
Cromin 15	0.50	1.33
AISI D2	0.38	0.63
AISI M3:2	0.29	0.70

The same ranking of wear resistance is found for the two types of silica sands. It is obvious that significant weight loss occurs of mild steel C45 than the other three tool materials. Cromin 15 and AISI D2 are very similar as regards the wear, but both are less wear resistant than the powder metallurgical steel AISI M3:2 showing the best performance.

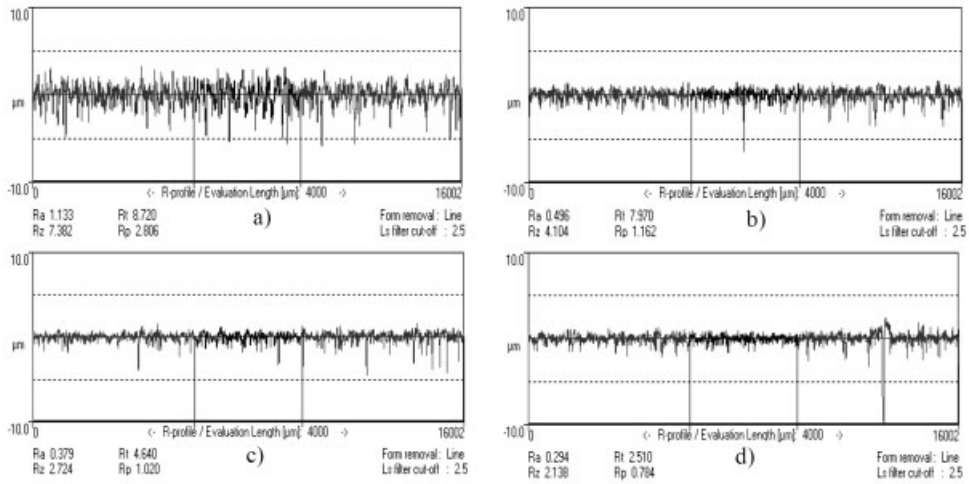


Figure 5: Representative roughness profiles from worn surfaces by fine silica sand by a single rotation; a) mild steel C45, b) Cromin 15, c) AISI D2 and d) AISI M3:2. Blue markings on each profiles indicate the areas where roughness parameters have been calculated.

A comparison of the roughness profiles of the worn surfaces confirms the weight loss measurements. Figure 5 shows the profiles measured on the different tool materials subjected to wear by the fine silica sand and a single rotation. A significant change in roughness is noted for the mild steel due to severe scoring by abrasive wear of the surface. The wear tests have also changed the topography of the other tool surfaces, but a clear difference from the mild steel is observed. Next after the mild steel, highest roughness is measured on the Cromin 15 alloy followed by AISI D2 and lowest roughness is found for AISI M3:2 indicating lowest wear rate. Similar results were obtained by coarse silica sand. A smaller difference in roughness between C45 and Cromin 15 as well as between AISI D2 and AISI M3:2 were however observed. Table 2 summarizes average values of the arithmetical mean roughness value, Ra, for all of the tool materials and both types of silica sand.

4 Conclusions

A new test method called the Compression-Twist test for evaluation of tool wear due to abrasion by hard minerals has been proposed. The test enables large contact pressure and controlled relative sliding between tool material samples and mineral particles thus ensuring breakage of mineral particles and generation of fines which influence the resulting wear. This implies, that the proposed test simulates the production conditions in processing of hard minerals, where autogenous wear protection is present.

The test furthermore allows fracture of mineral particles to be studied under varying loading conditions, since shear stress and well as compressive stresses can be separately applied. This has, however, not been a topic of this work.

The investigation of four different tool materials demonstrates the ability to rank wear resistance by the proposed CT-test. Roughness profilometry as well as weight loss measurements have been found to be useful methods for quantifying wear resistance. Results confirm that larger particle size increase wear, but only until fines starts to form, [7]. The test is fast and allows reconditioning of wear samples, which may thus be used several times.

5 References

[1] T. S. Eyre, Tribology Int. 1976, 203–212.

[2] L. Xu, C. Vose, D. StJohn, Wear. 1993, 162–164, 820–832.

[3] Spero, D. J. Hargreaves, R. K. Kirkcaldie, H.J. Flitt, Wear. 1991, 146, 389–408.

[4] J. H. Tylczak, J. A. Hawk, R. D. Wilson, Wear. 1999, 225–229, 1059–1069.

[5] Misra, I. Finnie, Transactions of the ASME. 1982, 104, 94–101.

[6] N. W. Page, M. Yao, S. Keys, W. McMillan, A. Cenna, Wear. 2000, 241, 186–192.

[7] M. Lindqvist, M. Evertsson, T. Chenje, P. Radziszewski, Minerals Engineering. 2006, 19, 1328–1335.

[8] M. G. Hamblin, G. W. Stachowiak, Wear. 1997, 206, 69–75.

[9] P. Andreasen, N. Bay, T. Wanheim, Proc. 4th Int. Conf. Prod. Engn., Tokyo (1980) 793–797.

[10] B. G. Hansen, N. Bay, J. of Mech. Work. Techn. 13 (1986) 189–204.

Online Wear Measurements in Advanced Lubricated Systems

C. Fehsenfeld, P. Fehsenfeld, A. Kleinrahm
ZAG Zyklotron AG, Eggenstein-Leopoldshafen P. Berlet, Ph. Erhard
IAVF Antriebstechnik GmbH, Karlsruhe

1 Introduction

The RTM - Radionuclide Technique in Mechanical engineering – developed continuously and systematically in Karlsruhe is a high precision technique [1–5] for wear and corrosion diagnostics in mechanical and process engineering. This nondestructive online measurement technique is widely used for research and development work of the industries in Europe, North America and Japan [6,7]. The application of new industrial materials (synthetic materials, ceramics, hard coatings etc.) and the worldwide problems in medicine technique (prosthetics) demand further development of RTM, especially the labelling of critical surfaces with radionuclides.

2 RTM – the Radionuclide Technique for Online Wear Diagnosis

The irradiation at the cyclotron accelerator with Thin Layer Activation Technique, TLA, produces an accurate, thin radioactive layer on the surface of the critical machine component. The activation parameter must be selected in such a way that the generated activity versus material depth has a linear dependence, and that the physical and chemical properties of the components are not affected. TLA technique has been developed at Karlsruhe Cyclotron for all industrial iron and steel grades (low-alloy steels up to high-alloy steels), non-ferrous metals and alloys: Al, Co, Cr, Cu, Mo, Ni, Pb, Sn, Ti, V, W, Zn, sintered and hard metals, special ceramics.

As an example of irradiation, Figure 1 demonstrates the adjusting of a large piston ring of a marine diesel engine in front of the beam line of the Karlsruhe cyclotron. The surface over the full circumference has been activated.

The labelled part is remounted in the machine under investigation on a test bench. Two measuring methods are available: TLM and CMM. With TLM, Thin Layer difference Method, the decrease of the radioactive layer during the wear process is measured using a gamma ray detector outside the machine. The wear diagnostics device determines the wear value online on the basis of the calibration ratio of measured activity versus material depth. Precondition of correct function is the transport of the wear particles away from its place of origin.

CMM, Concentration Measuring Method, is usually the more sensitive measurement of wear than TLM. But the resolution depends on the volume of the lubricant and on the level of the specific activity of the labelling. The radioactive wear particles in the lubricant are measured with a gamma ray detector in the flow chamber of the closed measuring circuit. The wear of the machine part is proportional to the measured activity of the wear particle concentration in the lubricant. Required is a constant specific activity in the activated volume of the component for the reliable allocation of the measured activity value to wear mass. The required levels of radioactivity are considerably lower for CMM than for TLM. Precondition is that the wear par-

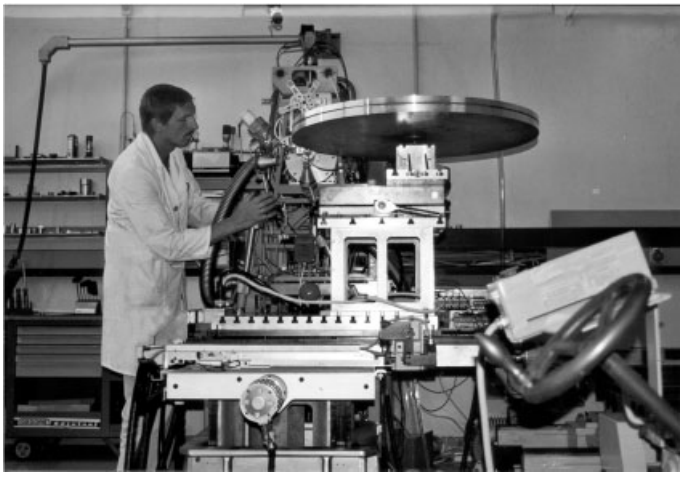


Figure 1: Adjusting of a piston ring of a marine diesel engine in front of the ion beam line in the RTM facility of Karlsruhe cyclotron.

ticles enter the lubricant circuit and are suspended homogeneously in the lubricant. The method is described in detail in [1,2,5,10].

3 Application

RTM is a widely used tool for wear analysis of engine components such as bearings, gears, camshafts, valves, tappets, piston rings, cylinder walls etc. This is the main field of RTM application. But the technique is also used to evaluate corrosion, cavitation and erosion phenomena in pipes, steam and gas turbines, offshore platforms and sea bed pipe work, Chemical and Textile Industry.

RTM has been applied to the development of the first non-C-F-C (Chlorofluorocarbon) refrigerant compressor of production stage. For this purpose a special test bench was developed which has been applied furthermore to larger compressors for air conditioning [4].

Figure 2 demonstrates the result of a wear test with a small piston of a refrigeration compressor labelled in its critical circumference area. The wear of the run-in phase during first hour could be clearly demonstrated because of the high resolution power of 0.2 μg.

RTM has been applied to biomechanical engineering [8]. The number of surgeries for total replacement of bone joints by prostheses increases continuously. One reason is the limited life time of the actual hip joint prostheses which requires a considerable number of revision surgeries. Wear particles are the main reason for the late aseptic slackening of the implants. So a sensitive and reliable measurement of wear is required for the improvement of the life time of prostheses.

A ceramic prosthesis is for a wear measurement technique the most sophisticated friction couple due to the very low wear rates. The conventional standardized simulator test demands long testing periods. Of significant disadvantage is the interruption of the test run, the dismantling of the joint for measuring the weight. Each new start produces a new run-in effect. Moreover the

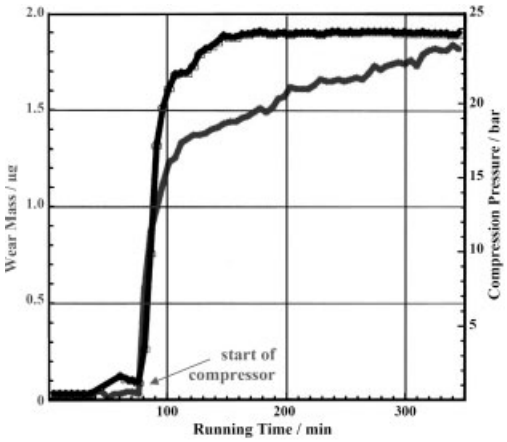


Figure 2: Typical run-in wear of the piston skirt (red curve) of a C-F-C free refrigeration compressor together with its increasing pressure (blue). Activation depth: 15 µm. Detection limit: 0.2 µg, Refrigerant: propane.

usual weight loss measurement is inaccurate because of the hygroscopic properties of the used ceramic material.

We labeled three heads of a ceramic – ceramic hip joint (Al_2O_3). An on-line wear diagnostic system for artificial hip and knee joints was established using the know how of the RTM method (cf. Figure 3). The real time wear measurements of the ceramic prosthesis were performed at a hip joint simulator.

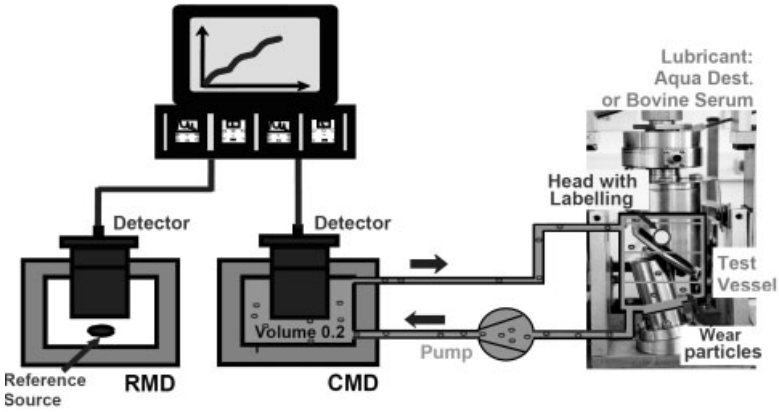


Figure 3: Schematic sketch of the RTM measuring system for prosthetics with Concentration Measuring Device CMD for measuring the activity of the wear particles in the lubricant (calibrated wear mass is displayed online), with Reference Measuring Device RMD for accurate correction of half life and control of correct functioning of the measuring system, and with the hip joint simulator (right) containing the labelled head under investigation. As lubricant were used Aqua dest. as well as Bovine Serum.

The test results in figure 4 demonstrates the strong run-in wear with an integral wear rate of 40 µg per hour followed by a steady state phase with only 0.3 µg/h. With a higher difference between the lower and the upper load the wear rate increases to 0.5 µg/h.

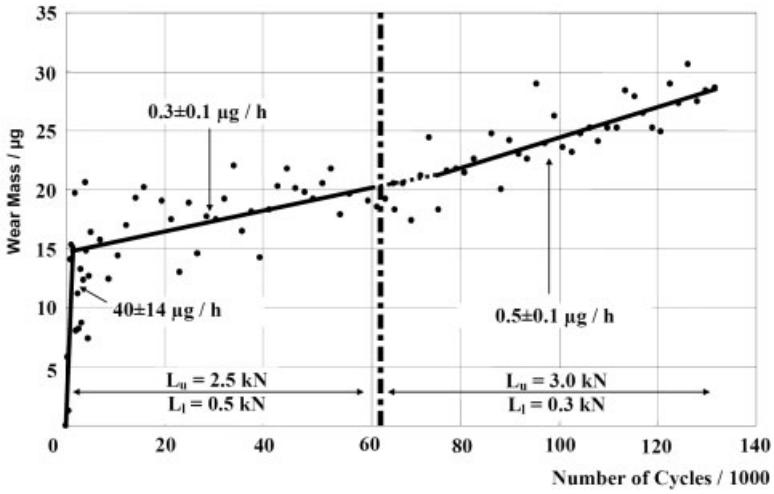


Figure 4: Real time wear measurement of a hip joint prosthesis in a simulator. Material of labelled head and acetabular cup: Al_2O_3; frequency: 1 Hz; 3600 cycles correspond to 1 hour; upper and lower load L_u/L_l in two steps. Raising the load from 2.5/0.5 kN to 3/0.3 kN results an increase of wear rate by 66 %. Remarkable is the high run-in wear rate of 40 µg/h.

4 Developments of RTM

RTM has been developing in Karlsruhe since 50 years. Regarding logistics and radiation protection the beginning in the year 1958 with neutron activation at a nuclear reactor was complicated. The development of RTM measurement and Thin Layer Activation technique, TLA, at Karlsruhe cyclotron in cooperation with RTM customers strongly improved the sensitivity of the method, and the handling of radioactive parts. At this time the application was usually limited to metal components.

The actually running development of Ultra Thin Layer Activation UTLA will allow the labeling of nearly all synthetic and ceramic materials in a depth of some µm [2,3,9]. So the application fields of RTM will become larger. The accuracy will increase and the handling of the radioactive parts will become uncomplicated.

The labeling of DLC coatings has already been established as routine method. The labeling of plastic materials like PTFE and PEEK is in development to a routine method within a cooperation project of ZAG Zyklotron AG and IAVF Antriebstechnik GmbH supported by AiF.

The effect of material damage by radiation was investigated in several activation tests with DLC and PTFE coated engine parts. Microscopic tests, adhesion tests, Raman spectroscopy, X-ray spectroscopy and pin-on-disc tribometer tests have proved that no material damage is generated by the special UTLA.

For test and demonstration purposes a PTFE coated journal bearing (25×30 $^{\varnothing i}$) mm, was radioactive labeled by 7Be implantation to a depth of approx. 5 µm. The applied total activity of 7Be was 10 kBq: that is one thousandth of the free handling limit (10MBq) for this radioactive material. The wear measurements with this labeled bearing were performed on a bearing test bench with the concentration measuring method (CMM). The results are illustrated in figure 5 and demonstrate the high sensitivity in the region of 30 nm or 0.01 nm/h. Even in the case of such small wear rates as 0.2 nm/h, the wear step after increasing the surface pressure by 100 % is clearly detectable. At the step of increase of surface pressure a strong decrease of the friction coefficient by 50 % occurs. That is a distinctive feature of this PTFE material.

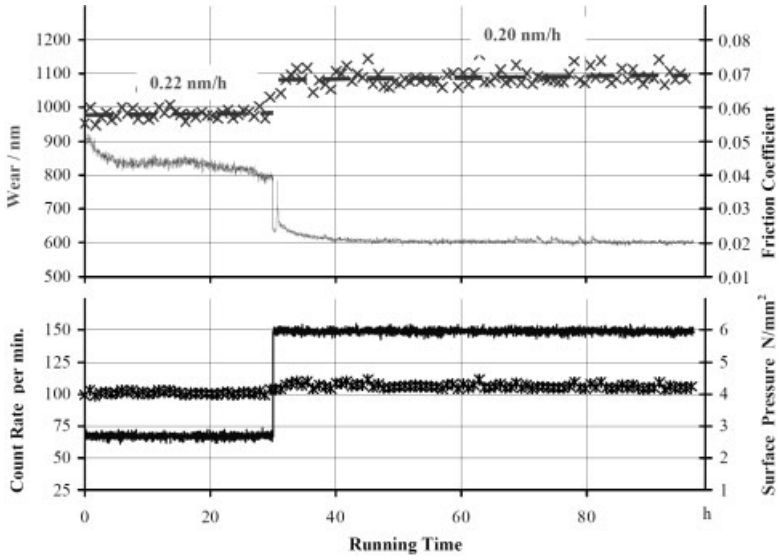


Figure 5: Online measurement of the wear after run-in of a PTFE coated journal bearing on a bearing test bench. The PTFE coating (in the range of 7 µm) was labelled with 10 kBq of 7Be to a depth of 5 µm. The count rate in the lower part of the diagram determines the pure output of the radiation detector without calibration, the upper part shows the calibrated result as wear depth. Lubricant: diesel. Sliding speed: 0.5 m/s. The relative standard deviation of wear results is 1.5 %.

The results of a tribometer test (pin-on-disc) with a radioactive labelled DLC coated tappet are presented in figure 6. The test run shows clearly the increase of wear with the stepwise increased surface pressure. At a pressure of 110 N/mm2 a dramatic increase of wear rate from 1 nm/h to 3.3 nm/h was observed in this example of application.

5 Acknowledgements

We are grateful to the RTM team, especially to our colleagues Richard Mayl and Jürgen Daul for solving engineering problems and analysing the irradiated material samples, as well as to the CEO of ZAG Hermann Schweickert and the CEO of IAVF Bernhard Kehrwald who created this UTLA project and the financial support from AiF.

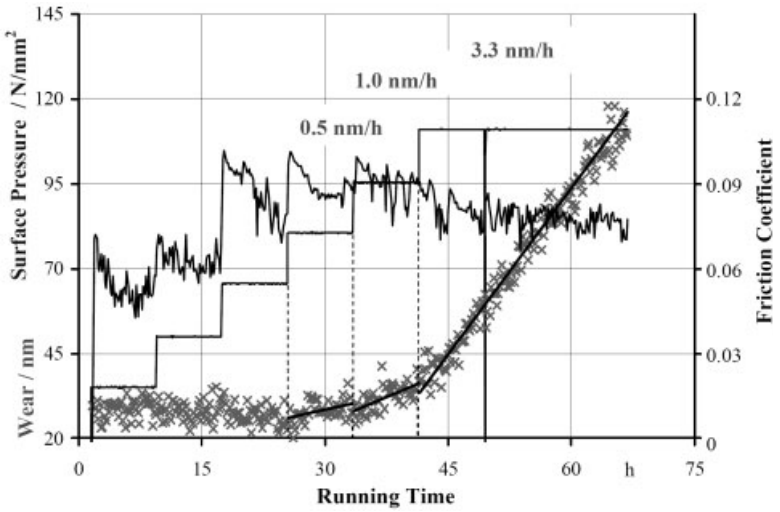


Figure 6: Online measurement of a DLC coated tappet with a pin-on-disc test bench. The test results show clearly the increase of wear with the stepwise increased surface pressure. At a pressure of 110 N/mm
[2] a dramatic increase of wear rate from 1 nm/h to 3.3 nm/h was observed. Lubricant: engine oil. Temperature of oil: 125 °C. Sliding speed: 3 m/s (high load test). The relative standard deviation of the wear results is 1.3 %.

Great thanks to Lucio Gialanella of INFN, Naples, for his support in radioactive ion implantation technique.

We are grateful to Dr. U. Kremling of the company IMA, Dresden, and her team for cooperation in the wear measurements of the three ceramic prosthesis at the IMA hip joint simulator with our RTM measurement system.

We gratefully acknowledge the AiF sponsoring this UTLA development project.

6 References

[1] Essig, G.; Fehsenfeld, P., in Nuclear Physics Methods in Materials Research (Ed.: K. Bethge), Friedr. Vieweg & Sohn, Wiesbaden, 1980, p.70–81.

[2] Fehsenfeld, P.; Kleinrahm, A., in XII Int. Conf. on Cyclotrons and their Applications, Berlin, Germany, 8-12 May 1989, Proceedings (Eds.: B. Martin, K. Ziegler), World Scientific, London, 1991, p.577–581.

[3] Fehsenfeld, P.; Kleinrahm, A.; Novikov, V., in: XIII Int. Conf. on Cyclotrons and Their Applications, Vancouver, Canada, 6-11 July 1992, Proceedings (Eds:.G. Dutto, M. K. Craddock), World Scientific, London, 1992, p.171–174.

[4] Eifrig,C.; Fehsenfeld, P., Deutscher Kälte- und Klimatechnische Verein, DKV-Tagungsbericht, 21. Jahrgang, Bonn, 16.-18.11.1994, Arbeitsabteilung II.2, Band II/2, p.25–34.

[5] Fehsenfeld, P.; Kleinrahm, A.; Kubat, R., Werkstoffprüfung, in: Werkstoffwoche 98 (Eds.: W. Muster, R. Link, J. Ziebs) Vol 10, Wiley-VCH, Weinheim, 1999, p.313.

[6] Balnaves, M.A.; Schneider, E.W., SAE-Paper 880672, 1988.

[7] Shaub, H.; Pandosh, J.; Searle, A.; Sprague, S.; Treuhaft, M., SAE-Paper 941983, 1994.

[8] Fehsenfeld, P.; Kremling, U.; Eifrig, C., Biomaterialien 2001, 2, 2/3, p.100.

[9] Fehsenfeld, P.; Eifrig, C.; Kubat, R., Nuclear Physics**,** 2002, A 701, p.235c–239c.

[10] Ditroi, F.; Takács, S.; Tárkányi, F.; Reichel, M.; Scherge, M.; Gervé, A., Wear, 2006, 261, p.1397–1400.

Friction and Wear of Highly Loaded Mixed Lubrication Contacts Influenced by Superposed Sliding Directions and Intermittent Surface Pressure Performed on a Novel Model Bench

A. Albers, M. Behrendt, S. Ott
IPEK – Institute of Product development at University of Karlsruhe, Germany

1 Introduction

Actual market requirements aim increasing power density and economics ideally for all operating conditions as for example by increasing efficiency. Technical systems as for example continuously variable transmissions (CVT), multiple-disk clutches or synchronizations are based on friction contacts operated under mixed lubrication conditions. Improvement of the tribological system regarding wear and coefficient of friction has to consider economical production processes (e.g. surface treatment and finishing) and efficiency requirements influencing the tribological performance. In order to investigate the influences of parameter changes on friction and wear a relation and a correlation to a technical system is promising since the technical system defines relevant load collectives. Taking recent research and development into account, there is an exerted knowledge and data base for lubricated tribological contacts that is mainly based on experimental investigations. The yet available model descriptions for the mixed lubrication are increasingly supported by advanced simulation approaches. In order to validate simulation models adequately or to optimize the related technical system (e.g. CVT) all influence parameters have to be regarded and varied independently. Therefore IPEK has invented and validated an experimental method - a novel system-related model test bench - which provides independent variation of all expected influence parameters, particularly multiple (three-dimensional) slip directions, contact pressure and operating temperature in order gain qualitative and quantitative information on friction and wear behavior of the friction contact. A main feature is the intermittent tribological contact that enables the investigation on “squeeze-effects”. First results emphasise major influence of superposed sliding speeds (sliding vectors) and contact intermittent frequency on the friction coefficient and the wear quality and quantity. This paper will cover extending investigations in order to validate the test bench capabilities for identification of minor tribological changes such as directional properties.

2 State-of-the-Art

Considering a friction system based on steel vs. steel under mixed lubrication the coefficient of friction is mainly influenced by the boundary condition of the contact element as well as the shear stability of the lubricants. Especially in mixed lubrication regime the pressure flow factors become very sensitive to the directional properties of the surface roughness [1]. Regarding the selected technical reference system (CVT) the local contact conditions become even more complex since intermittent contact conditions occur and surface pressure as well as sliding speed are varying during operation. Getting pin and disk into contact the lubricant has to be rearranged

(squeeze-effect). Focusing a high coefficient of friction a pure steel-steel-contact is ideal but since sliding is occurring in the friction contact at least a minimum of lubrication has to be kept active. Assuming occurring fully-lubricated areas during mixed lubrication lower viscosity results in a higher coefficient of friction, because the above mentioned squeeze effect and oil film thickness decreases. During operation with mixed lubrication a special focus is set on additives. On the one hand the type and quantity of extreme-pressure additives heavily influences the frictional behaviour in addition to the type and viscosity of the base lubricant [2]. On the other hand anti-wear additives are effective regarding wear and fretting. IPEK's recent research carried out on the novel test bench matches with common sense for influence of the surface topography and surface pressure on friction and wear [2, 4]. Furthermore, the influence of sliding speed, sliding directions (tangential, radial and drilling) – the sliding vector – and the contact time in relation to surface pressure and temperature bas been identified and quantified. Hereby, it is important to mention the excellent correlation to a system test bench using an original variator as well as the occurring difference in relation to a elementary single-dimension pin-on-disk model test bench. This emphasizes the importance for future investigations on the mixed lubrication using the new model test bench.

3 Objectives

The methodological objective is to enable a knowledge transfer with material sciences. As well, the set-up of a holistic chain of tribological testing aiming a relation of elementary physical mechanisms and system specific influence parameters is aimed. In addition the objective is to deepen and to extend the knowledge of the mixed lubrication conditions focusing on frictional and wear behavior as well as to extend the understanding for transferring model test bench results to system behavior predictions. The objective also includes extending and establishing the given development tool that offers the differentiation and characterization of measures on friction contact's based on objective results using single parameter variations. This offers an investigation method which enables to save time, cost and resources.

A mid-term objective is to improve steel-based tribological contacts by including the influence of viscosity, surface topology (micro- and macroscopic), material and hardness based on common results and technical realizations. High values of the coefficient of friction are important but not the single research objective. Generally spoken, it is important to realize a high but additionally constant coefficient of friction which does not change or at least is predictable regarding lifetime, varying loads due to surface pressure, sliding vector, contact time and temperature.

By the use of the novel model test bench detailed system-related investigations are to be performed. Exemplary, the investigations will be related to the tribological contact conditions as they occur in chain-based CVTs since they are characterized by a complex and highly loaded intermittent contact with high surface pressure and low but superposed sliding speeds. By establishing a detailed tribological data base, simulation models and modeling approaches can be validated. They can even be extended by skipping the global coefficient of friction approach in order to enable a multi-dimensional look-up table for gaining local values for each contact element. These gained results are expected to be transferable to other technical systems that operate under mixed lubrication.

4 Proceeding – Methodological Approach

Based on the methodological approach [3] the system-related model test bench was developed, validated and harmonized with a variator test bench (on system level) [4] of the cooperating research institute IMKT (Hannover University). Based on simulations of the local sliding speeds und surface pressures – the local contact losses – the operating conditions of the model test bench were defined. The validation results regarding the coefficient of friction and wear - qualitatively and quantitatively - prove an accurate friction level as well as accuracy for wear prediction above ninety percent [4]. It has to be considered that the validation was based on seven friction pairings which differ extremely regarding the properties as for example hardness and surface topology. Thus, it can be assumed that the tribological contact is correctly simulated on the model test bench and therefore the tribological properties are comparable. Regarding this, basic investigations were performed with the focus on the influence of the tangential slip, tangential slip with superposed radial slip as well as tangential slip with superposed drilling regarding wear and damage of steel-based tribological systems [5]. Thus, the coefficient of friction was determined using 256 operating points depending on contact time, surface pressure, sliding speeds and their superposition as well as the lubricant temperature. Furthermore, the time-dependent wear behavior was determined using constant operating points. As a result several “Friction Maps” [4, 5, 6] are available for every friction pairing. Recent research was focused on evaluation of model test bench capabilities regarding surface directional property changes.

5 System-Related Model Test Bench

The novel system-related model test bench displayed in Figure 1 enables tribological investigations of 5th and 6th category using multi-dimensional pin-on-disk tryouts under intermittent cyclic contact pressure [4]. It offers an independent adjustment of multiple slip directions (sliding vectors), the contact pressure and the operating temperature in order to detect the related influences. By superposing the three independently adjustable sliding directions (tangential, radial, drilling) a multi-dimensional load collective is effective that results in geometrically forced sliding conditions. Here, always three pins are transmitting torque to the disk and the other three are disengaged for relaxation. Constant torque transmission is guaranteed due to a short overlapping phase of the pins during state shift. This intermittent contact realizes the pin lift-off from and pin approach toward the disk in order to disable quasi-static lubrication conditions and to enable periodic loading and relaxation of the contact areas.

The investigations are performed for six contact element pins at once interacting with one planar disk (see Figure 2) in order to enable a statistical consideration of wear and failure. The pins displayed in Figure 2 with diameter of 8 mm and length of 12 mm have a spherical surface in the contact area. In addition to auxiliary hydraulic pressure variation the Herzian pressure can be adjusted without changing the test bench operating parameters by varying the sphere radius. Thus, recent investigations were performed with sphere radius between 20 to 2000 mm in order to determine this influence. To increase test bench accuracy a method has been developed which determines online the test bench losses dependent on temperature, load and speed, generally spoken for every possible operating point.

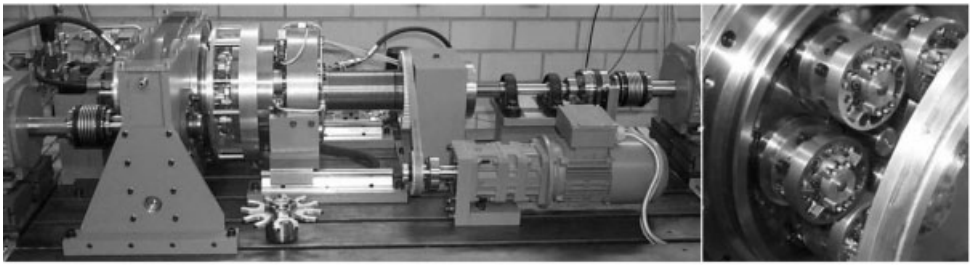


Figure 1: System related model test bench

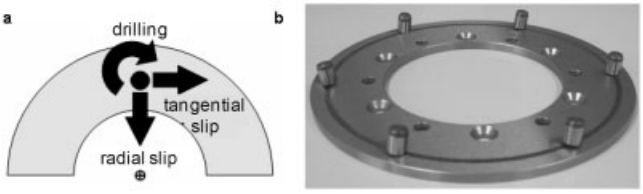


Figure 2: Multiple sliding speeds (a) and specimen (b)

6 Results

Figure 3 shows several specimens with deterministic (directional) as well as stochastic (isotropic) patterns (surface roughness about Ra 0.3) that have been investigated in order to quantify the topology influence regarding sliding vectors and intermittent surface pressure. Therefore, only disks have been varied without changing test bench parameters or counter part steel pins. The investigations are performed using varying superposed tangential and radial slip (sliding vectors) at 64 operating points. In order to determine the influence on friction's distribution and wear behavior single parameter variations are used [2].

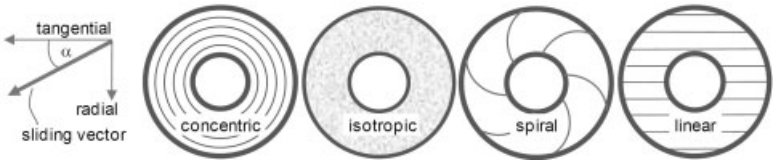


Figure 3: Specimen with applied directional and isotropic patterns (schematic)

The following results due to surface change (directional properties) are considered relatively to results of a friction pairing based on steel vs. steel [5] shown in Figure 4. Thus, the coefficient of friction vs. the increasing argument of nominal sliding vector α (relative to tangential direction) is displayed for several surface pressures and viscosity regimes. The operating parameters of vector α and surface pressure are in technical relevant ranges of the reference system (CVT). It has to be mentioned that the absolute coefficient of friction is displayed; sliding vectors argument's influence on measured tangential force is already compensated by sophisticated

data interpretation. The first issue was to point out the influence by switching from directional concentric ground steel disk to isotropic pattern by the use of coating since this is expected to increase the pressure flow factor σ_x in sliding direction [1] by providing $\gamma = 1$ (ratio of correlation length; can be visualized the length-to-width ratio of representative asperity [1]). Apparantly, the test bench is capable to identify this measure (s. Figure 5a,b) especially for higher viscosities about 40 mm²/s. In regards of sliding vector dependency there is still a decreasing coefficient of friction. This is expected to be reasoned by constantly changing contact conditions. Especially the intermittent contact avoids quasi-static lubrication and the superposed radial slip results in continuously changing sliding track radii. Due to statistic consideration a pin approaching the disk hardly will interact with a track of another pin.

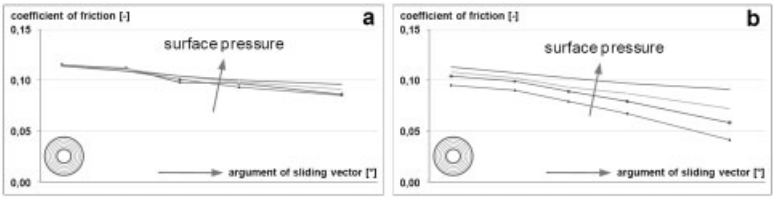


Figure 4: Coefficient of friction for directional concentric pattern – low viscosity (a) and high viscosity (b)

The Second issue was to change the directional properties by using a directional spiral ground steel disk in order to change the interacting angle without changing the test bench operating parameters. Figure 5c shows no significant influence of lower viscosities about 8 mm²/s since the sliding vector partially compensates the directional patterns. However, spiral pattern additionally increases the lubricant flow along the surface pattern and increases the flow in radial direction due to centrifugal forces towards the pin movement and therefore can hinder the oil-squeezing that is observable in Figure 5d.

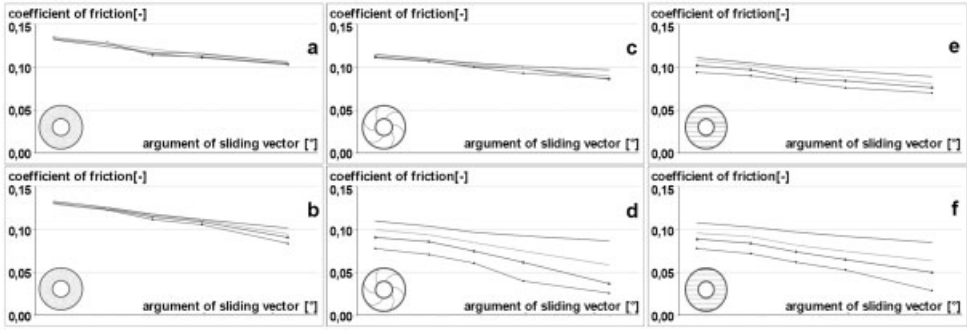


Figure 5: Coefficient of friction for varying patterns - low viscosity (a,c,e) and high viscosity (b,d,f)

The third issue was to use a directional linear ground steel disk that partially will lead to interacting surface patterns perpendicular to sliding direction and therefore to $\gamma << 1$. Regarding higher viscosities (s. Figure 5f) there is marginal influence compared to spiral pattern since the pattern as well changes oil flow in radial direction. But applying low viscosity the influence becomes

obvious (s. Figure 5e) due to heavily decreased pressure factor σ_x. Additional investigations applying tangential slip only ($\alpha = 0$) provide increasing coefficient of friction that merges with the theory of $\gamma > 1$ influence.

7 Conclusion and Outlook

Using IPEK's novel system-related model test bench it has been proven that the complex load collectives of a belt-supplied CVT can be experimentally simulated by significantly decreased testing time and specimen quantity. It has been identified that the level of the coefficient of friction can heavily decrease by switching from tangential operating condition to superposed tangential and radial operating or drilling conditions. Furthermore the model test bench capability for identification of optimization measures on surfaces is shown. These results of course differ from elementary pin-on-disc tests using tangential slip without intermittent contact but this especially emphasizes the importance of this novel approach. The test bench now offers a test procedure to differentiate and characterize the friction contact's optimization measures based on objective results by using single parameter variations. Actual research is focused on influences of decreased viscosity as it is increasingly required due to efficiency issues considering low temperature usage. Future investigations will cover extended investigations on surface topology (micro- and macroscopic), material and hardness based on common results and technical realizations will be performed in order to extend the yet existing "Friction Maps" by adding these influence parameters. This data base will support the improvement and validation of existing simulation models. A mid-term objective is to correlate investigations with elementary pin-on-disk test benches by disabling the intermittent operation. Since the parameters are independently adjustable a long-term objective is to correlate the model test bench with other referring technical systems as for example multiple-disk clutches or synchronizations. Special interest will be the practical result transfer since the contact conditions change from high pressure and low sliding speed to low pressure and high sliding speed.

8 References

[1] Patir, N.; Cheng, H. S.: An Average Flow Model for Determing Effects of Three-Dimensional Roughness on Partial Hydrodynamic Lubrication. Journal of Tribology VOL 100, **1978**, p. 12-17

[2] Knauss, C.: Der Werkstoffeinfluss auf die Reibung im elastohydrodynamischen Schmierfilm, Proceeding of „GfT Tribologie-Fachtagung 1995", Göttingen, Germany, **1995**, p. 11/1–11/4.

[3] Albers, A.; Behrendt, M.; Stuffer, A.: Holistic optimisation of lubricated friction contacts with 4-dimensional load collectives by multi-stage engineering. Proceedings of the TMCE 2004, April 13-17, Lausanne, Switzerland, **2004**, article No.1026.

[4] Albers, A; Behrendt, M.; Ott, S.: Systemtribometer zur Untersuchung hochbelasteter nasslaufender Friktionskontakte unter mehrachsigen Gleitbewegungen, Proceeding of „GfT Tribologie-Fachtagung 2006", Göttingen, Germany, **2006**, p. 50/1 – 50/14.

[5] Albers, A; Behrendt, M.; Ott, S.: Investigations on highly and complex loaded friction contacts under mixed conditions based on a novel model bench. 16th International Colloquium Tribology – Automotive and Industrial Lubrication, Esslingen, Germany, **2008**, p. 9.

[6] Zum Gahr, K.-H.; Dulias, U.; Poser, K.: Modelluntersuchungen zum Einsatz von Ingenieurkeramik in Gleit- und Friktionssystemen. Proceeding of „GfT Tribologie-Fachtagung 1995“, Göttingen, Germany, **2005**, p. 56/1-59/12.

Design and Evaluation of a Rolling Friction Apparatus for Micro Linear Bearings

Rudolf Meeß, Frank Löffler
Physikalisch-Technische Bundesanstalt, Braunschweig, Germany

1 Introduction

In technical systems, the breakaway forces of rolling element bearings can be comparatively large due to the preload or to external loads. Friction force and displacement show nonlinear interrelationships. Therefore, macroscopical rolling element bearings for precision positioning are the topic of widespread research [1, 2, 3, 4]. However, linear ball bearings with radii of curvature smaller than 500 µm and frictional forces less than 100 mN are investigated only infrequently. Such bearings are interesting for medical devices, e.g. minimal invasive surgery or endoscopy, for analysis equipment, e.g. dispensing or probing tasks, and for metrology, e.g. miniaturized precision stages for displacements over several mm with sub-µm increment of motion.

The friction behavior of miniaturized linear bearings has been studied by Tan et al. [5], using an inertial set-up with displacement detection by means of a vision system. Phataralaoha and Büttgenbach utilized a microtactile 3-D sensor for force measurement and application [6]. An inclined plane was used for the determination of the coefficient of friction in [7]. The apparatus in the present study minimizes the influence of the coupled mechanism on the friction force measurements further and realizes arbitrary force- and displacement-loops with high resolution measurements. Particular attention is paid to visibility and ease of handling and assembly of the sensitive microparts in the device.

2 Design

The rolling friction apparatus has four main tasks: Firstly, to determine the axial displacement of the carriage. Secondly, a normal force and thirdly, an axial force have to be applied. Fourthly, this axial force has to be measured.

In this study, the axial force is induced by a Lorentz actuator. The straining line, the axis of movement of the center of mass of the carriage and the displacement measurement are collinear, see Figure 1. The voice-coil design allows a high dynamic range of the driving unit. The additional moving mass is less than 1 g. The coil is coupled by means of a glued or screwed carbon rod. The magnetic unit of the voice-coil drive is designed to maintain a constant magnetic flux in the gap, see Figure 2. The coil can move with a stroke of approx. 3 mm, even with a radial deviation of up to 0.5 mm. The maximum deviation from the linearity of the current and the force is then less than one percent, predominantly due to nonlinearities of electrical amplification, see Figure 2 right. Likewise, the resolution is restricted in terms of the noise of the amplifier. To avoid parasitic forces and to reduce the influence of force measurement, the applied force is also determined with the Lorentz actuator, by means of the coil-current. The active current in the coil

is measured directly, including the fraction of self-induction. The linear relationship between force and current is beneficial for designing the driving unit, see Figure 2 right.

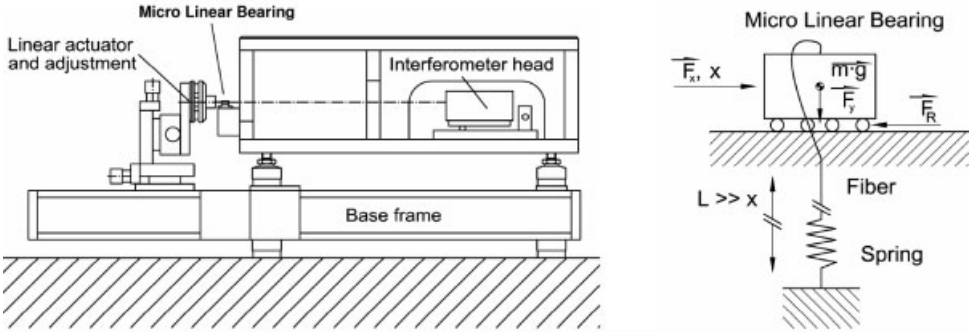


Figure 1: A: Sketch of experimental set-up; B: Force diagram

Displacements are measured optically by means of interferometry. The maximum measurable velocity is 1.5 m/s, the maximum resolution 0.3 nm. 5 mm of displacement can be detected. The minimum frequency used here of the moving object is 0.5 Hz, the maximum detectable frequency is 500 kHz. The laser spot of 100 µm in diameter is focused onto the center of the front face of the carriage, taking Abbe's principle into account. No additional mirrors or retroflectors are required.

Relative cosine errors due to misalignment are less than 4×10^{-3} for both the force and displacement measurements.

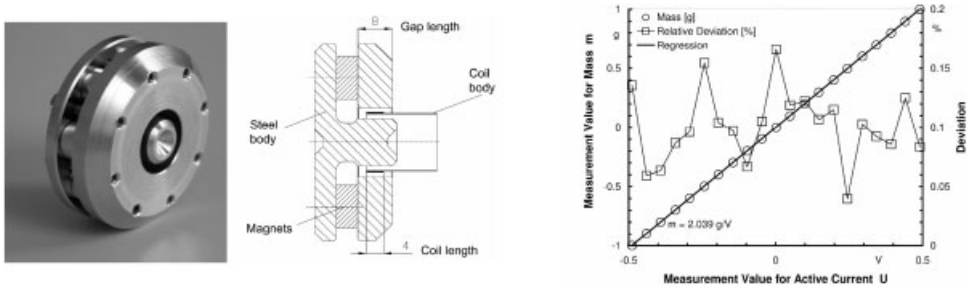


Figure 2: Magnetic drive unit.Left: Photograph; Mid: Cross-sectional view with coil; Right: Characterisitic

For the experiments, the apparatus is driven both in force mode, with a preset developing coil current, and in positioning mode, by means of a controller. An analog positioning loop is then used for controlling the driving force with the displacement signal as feedback. Arbitrary force and displacement loops can be passed through in the pre-rolling regime. The stability of the PID-controller is limited by the non-linear frictional behavior of the contacting bodies, highly affected by their topography.

The first and second derivative of the displacement x are needed to determine the inertial forces of the moving mass, affected by the friction force F_R and driving force F_x

$$m\ddot{x} = F_x - F_R\,, \tag{1}$$

see figure 1 B. These are obtained from curves, fitted to the noisy primary data by averaging. The difference quotient is used to differentiate with respect to time t:

$$dx/dt = (x_{i+1} - x_{i-1})/2\ \Delta t\,. \tag{2}$$

For averaging approx. 10 values, sampling frequencies are in the range of 50 kHz to 500 kHz. All friction forces F_R displayed below are determined with respect to inertial forces.

An additional normal load is applied onto the center of the top face of the carriage by means of an elongated spring with a low spring constant, which is extended by a fiber of a length of up to 1 m, see figure 1 B. Thus, the additional moving mass is very small. Prior to an experiment, the spring is preloaded by a known mass and then fixed at the bottom. The resulting ratio of parasitic and measured axial force is kept in the order of 10^{-4}.

In future, separate calibration procedures for force- and displacement measurement are possible, similar to the guidelines for tensile testing machines. The characteristic of the voice-coil, figure 2 right, is determined statically by means of a calibrated balance. To calibrate dynamically, the coil can be coupled with a calibrated load cell. The displacement measurement can be calibrated using an traceable interferometer simultaneously.

3 Evaluation

The apparatus is capable of running experiments with frequencies of displacements up to 10 kHz in positioning mode. In this study, the maximum velocities are approx. 2 mm/s, which leads to frequencies of approx. 20 Hz. For the evaluation, dry-running and lubricated bearings are tested, in the brittle and ductile contact, respectively. Selected results are discussed. The main focus is on small displacements in the pre-rolling regime and the transition into the regime of complete rolling. All plots are steady state.

First, a non recirculating, retainerless micro linear bearing (MB) with 2 x 2 spheres is tested. Each sphere is 200 µm in diameter and contacts two raceways, each formed by a pair of cylindrical rods, 250 µm in diameter. The bearing is dry-running and run in before measurement. The overall dimensions are $6 \cdot 4 \cdot 8$ mm³. Carriage and body are made of stainless steel. As material for the spheres, ruby (99 % Al_2O_3 monocrystalline, 1 % Cr_2O_3) is used, for the raceways, carbide (6 % Co, mixed carbides <0.5 %, WC rest). The kinematics of rolling motion under external load is complex due to the spin motion of the spheres.

For sinusoidal displacements over several microns in positioning mode, a wavy characteristic of the friction-force can be observed, see Figure 3. No additional normal load is applied here. The spheres are in rolling motion and contact the raceways at different points of their surfaces. These runs are highly repeatable and so the shape can be attributed to surface topography. When the displacement is reduced to very small amplitudes, almost smooth hysteresis loops appear, see Figure 4 B. The spheres no longer execute a rolling motion.

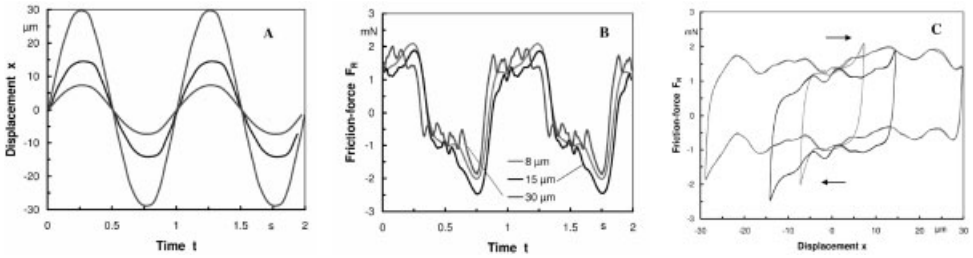


Figure 3: Measurement results for MB in positioning mode. A: Displacement vs. time plot. B: Corresponding force vs. time plot. C: Resulting force vs. displacement plot.

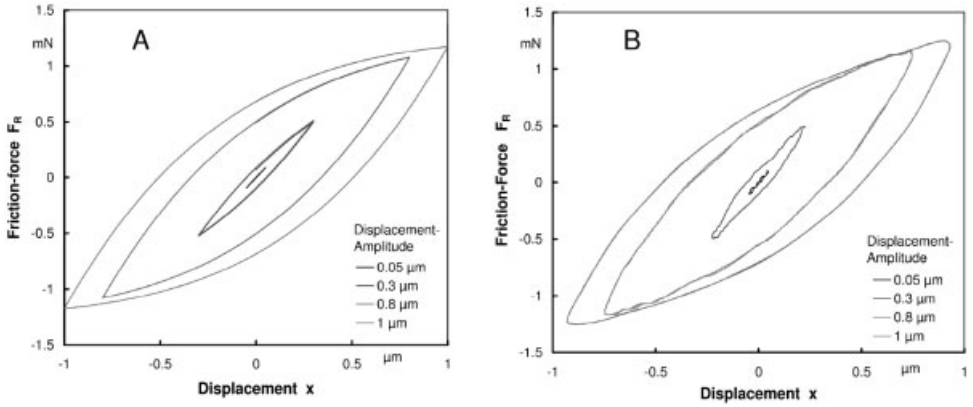


Figure 4: Force-displacement plots for MB in positioning mode. A: Results of the simulation; σ = 1.8 mN/µm, α = 0.8, F_C=1.25 mN in equation 1. B: Measurements

The Dahl model captures dissipation in the pre-rolling regime [8]. The friction force F_R is a function of the velocity v, the maximum friction force in the steady state F_C, the slope σ and the state variable z.

$$F_R = \sigma \cdot z \tag{3}$$

$$\frac{dz}{dt} = v\left(1 - z\frac{\sigma}{F_C}\mathrm{sgn}(v)\right)^{\alpha} \tag{4}$$

The exponent α is a shape element. Figure 4 shows the simulation results (A) in comparison to the measurement results (B) for a sinusoidal displacement with a frequency of 1 Hz. In the simulation, σ was set to 1.8 mN/µm, F_C = 1.25 mN and α = 0.8. A good agreement of this model can be seen in the case of small amplitudes up to 1 µm over a wide range of displacements and velocities. The model is dissipative in the pre-rolling regime, with a fixed characteristic shape.

For comparison and further investigation, commercially available, non-recirculating, two-row linear bearings (CB) are tested. They have 10 spheres of 1 mm in diameter, running in V-grooves.

The stroke is 5 mm. The bearings are oil-lubricated for life and run in. The materials for both the raceways and the spheres are non-corrosive steel. The retainer is made of brass.

The onset of rolling motion can be detected in terms of drifting, non-closed force-displacement loops of the force-mode experiments. Remarkably – not shown here – the required axial force for the transition to pure rolling decreases with increasing normal load. Figure 5, left, shows steady state force-displacement loops in force mode for amplitudes in the range of 0.092 mN up to 0.957 mN and a normal load of 0.66 mN at 1 Hz. The loops are centered for symmetry. For 200 µN of force amplitude, an intermediate spring-like correlation can be observed. The shapes of the loops differ from the characteristic shape of Dahl´s model.

In positioning mode under increasing normal load, the dissipative tendency becomes more obvious, see Figure 5, right. A linear correlation no longer exists in the x-F_R-plot for 2.11 N of normal load. The steep reversals remain with a decreasing amplitude.

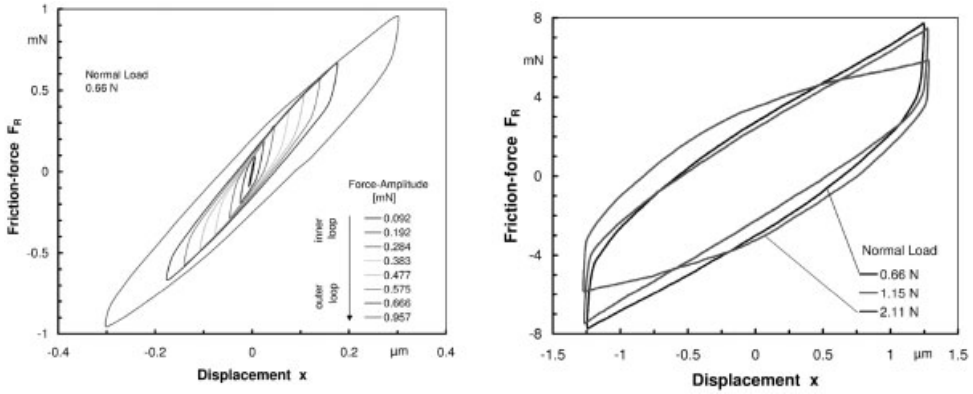


Figure 5: Force-displacement plots for CB (1Hz). Left: Force mode with a normal load of 0.66 N, Right: Positioning mode with different normal loads.

For displacements in the transition regime, the friction force depends in an unexpected way on the velocity in the lubricated contact. Figure 6 shows force-displacement loops for different velocities and the resulting force-velocity plots under preload. For increasing velocity the wavy local force alterations flatten, which leads to a remarkable vertical force increase in the v-F plot. The envelope of maxima is similar to a Stribeck-curve.

In the macroscopic displacement range, with increasing normal load, the frictional force amplitudes increase slightly, see Figure 7, with triangular trajectories. This can be due to the level of the outer load, which does not compensate for the bearing's preload. In the range of normal forces up to 2 N, no significant change of the typical run of the curves can be observed. Rather than defining an integrated value for a coefficient of friction, it seems reasonable to investigate the run of friction force for both types of miniaturized bearings. The variations of the amplitude and the slope are relative large.

Compared to the ruby carbide bearing, the steel bearing shows a ten times higher axial stiffness and maximum friction force under preload. However, the breakaway forces are comparable, defined as maximum cyclic axial force without residual carriage displacement.

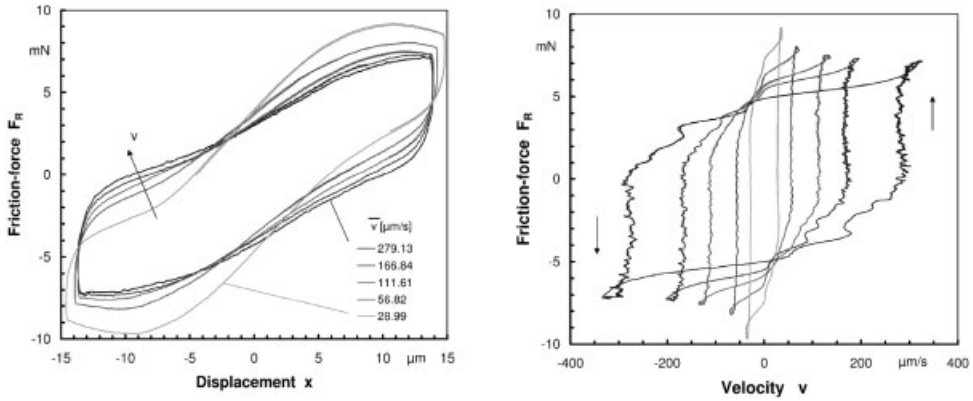


Figure 6: Variation of velocity for CB in positioning mode. The driven trajectories are of triangular shape.

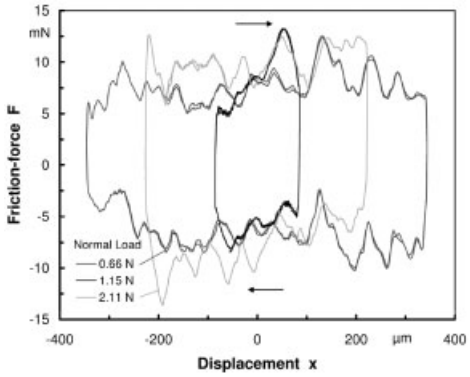


Figure 7: Force-displacement plots for CB in positioning mode.

4 Conclusion and Outlook

A new apparatus for determining the friction forces of miniaturized linear ball bearings is presented. The compact, highly dynamic design enables comprehensive studies in positioning and force mode. The measurements under different normal loads of both the miniaturized lubricated steel contact and the dry-running brittle contact reveal different complex behavior in the pre-rolling regime, the transition mode and the rolling motion. In the macroscopic displacement range, force amplitudes are relatively large, but highly repeatable. The measurements in the pre-rolling regime of the brittle contact are in good agreement with simulations of Dahl's model [8]. In a next step, the design of the apparatus will be upgraded for low velocity studies.

5 References

[1] M. Kosinskiy, Y. Liu, S. I. U. Ahmed, M. Scherge, J. A. Schäfer, VDI Berichte **2006**, 1950, 215–224.

[2] S. S. Futami, A. Furutani, S. Yoshida, Nanotechnology **1990**, 1, 31–37.

[3] J. Otsuka, T. Masuda, Nanotechnology **1998**, 9 (2), pp. 85–92.

[4] B. Armstrong-Hélouvry, P. Dupont, C. Canudas de Wit, Automatica **1994**, 30 (7), 1083–1138.

[5] X. Tan, A. Modafe, R. Ghodssi, Journal of Dynamic Systems, Measurement, and Control **2006**, 128 (4), 891–898.

[6] A. Phataralaoha, S. Büttgenbach, Proc. 4th Euspen Conference, Glasgow **2004**, 310–-311.

[7] R. Meeß, F. Löffler, Proc. 7th Euspen Conference, Bremen **2007**, 192–195.

[8] P. Dahl, The Aerospace Corporation, El-Segundo, California, TOR-158(3107-18), **1968**.

Advances in Thin Film Layer Sensors for Temperature Measurements in Highly Loaded Tribological Contacts under Mixed Lubrication

A. Albers, S. Beauvais, J. Bsul, W. Burger,
IPEK, University of Karlsruhe, Germany

1 Introduction

In tribological contacts and particularly in sliding bearings a failure of lubrication quickly leads to damage which usually implies expensive repairs and standstill periods. Nowadays the mechanisms of hydrodynamics (HD) and elastohydrodynamics (EHD) are well studied, as well from a theoretical as from an experimental point of view. Measurement of temperature and pressure directly in the contact could be reached in these domains thank to the use of resistive thin film sensors.

Actual tribological applications have to fulfill high requirements on power density and on environmental compliance. The second is often reached by the use of medium lubrication (e.g. diesel oil), and the combination of the different boundary conditions of the systems often lead to the occurrence of mixed lubrication. Studies concerning the theoretical explanation and simulation of mixed friction states are available [1, 2]. Nevertheless, the results of experimental studies are still incomplete due to a lack of suitable measuring methods to confirm the developed models.

Therefore, the aim of the studies presented in this article is to provide advances in thin-film-sensors-technology, which allow measurements even under friction involving contacting solid bodies. Furthermore, a new test bench for examining diesel-lubricated sliding bearings under conditions of mixed friction is developed as an example of application for the sensors.

2 State of the Art

In the past years thin film sensors were successfully used to investigate hydrodynamic and particularly elastohydrodynamic contacts [3, 5]. Depending on the properties of the studied tribological contact, the sensors consist of an insulating film (Figure 1), which separates the (electrically working) sensor from the surface of the machine element – if the mechanical part is electrically conductive. In the case of insulating substrates (cf. studies on ceramic parts [4], this layer is not necessary. The real sensor layer is located on top of this insulation layer. For mechanical protection of the sensor as well as for electrical insulation towards the opposite part in the tribocontact, a third film is deposited. The insulating and protection layers usually have a thickness of 0,5…2 µm. Contrary to these films, the sensor layer is not covering the complete friction surface. Therefore, its thickness is reduced to 100 to 200 nm in order not to change the geometry of the tribocontact.

During the recent years ceramic materials have commonly been used for insulating and as top films (e.g. Al_2O_3). These films were resistant against the strains under hydrodynamic and

elastohydrodynamic conditions, however, they always failed at the first occurrence of solid body friction.

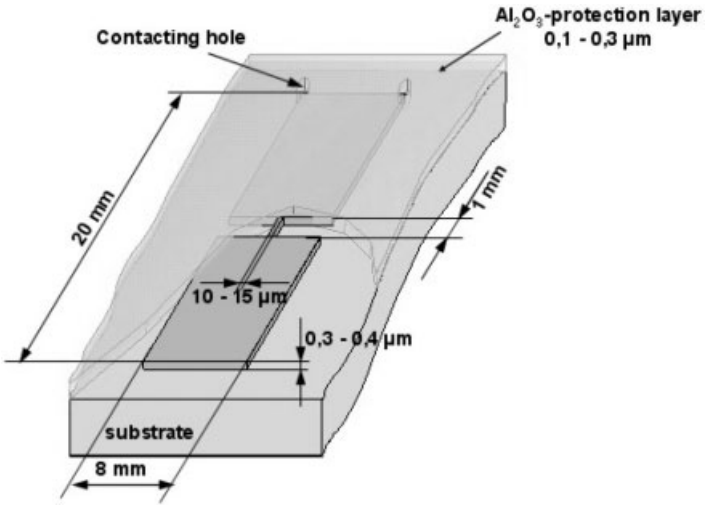


Figure 1: Schematic illustration of a thin film sensor.

Sensors based on a resistive principle permit the measurement of pressure or temperature distributions: The sensors consist of a very thin wire of a metal, which changes its electrical resistance depending on temperature and pressure. Most of the metals respond more on temperature than on pressure, but some alloys like manganin show sufficient pressure dependant characteristics, which allow the measurement of pressure repartitions in the contact.

The sensor filament usually has a width of 10…20 µm, which is sufficient for resolving the phenomena in the EHD-contact.

3 Objectives

In order to use the described thin film sensors in future also under conditions of dry and mixed friction, wear resistance and adhesive strength of the films have to be improved significantly. Due to their enormous hardness and adhesive strength this target can be reached with electrically non-conducting carbon-based coatings [6]. Earlier theoretical estimations [7] predicted the effect of the coating system on the studied parameters to be in acceptable limits for correct measurements.

At the same time, the theoretical studies on mixed lubrication, as well as experimental work on simplified systems have shown that a higher resolution of measurement is needed for the description of the repartitions of temperature and pressure in the mixed lubrication. Therefore, new sensor-designs are developed in the form of a micro thermocouple [7, 8].

For the application of the sensors, many test benches are available at the IPEK, allowing the study of different contact geometries (two-disc-machine, cam-follower-test-bench, sliding-bearing-test-bench). However for the study of diesel-oil lubricated contacts, a new test-bench is

developed, considering the actual boundary conditions in fuel injection systems and the special aspects of safety induced by these working conditions.

4 Coating Systems – Production and Characteristics

4.1 Coating Deposition

The coating systems used for the production of the sensors are described in earlier publications [7, 9].

For coating, different substrate geometries have been used: square parts ($10 \times 8 \times 3$ mm) for first developments. These small parts allow to coat many parts at the same time and herewith to get statistical information about the coatings properties. In a second step of the coating development, some tests have been made on rings used in a two-disk-machine (100 mm outer diameter, 80mm inner diameter and 20 mm width). These systems allow testing of the complete sensor system for the function verification in the test rig. Due to the very long coating times necessary for the production of such rings, further sensor development has been made on smaller planar substrates (40 mm diameter and 5 mm thickness). Like the rings, these substrates can be used for testing the functionality of the sensors, being placed in another test bench available at IPEK: the EDH-test-bench. In all three cases the sample material was 100Cr6-steel.

4.2 Current Coating Properties

Earlier coatings systems with lower thickness used to delaminate due to the high internal stresses in the coating. On the new substrates, the thickness of the DLC-coating could be enhanced by a large amount (from 2 µm up to 8 µm), using multilayer concept through graded variation of Methane proportion by r.f. magnetron sputtering of a graphite target in an argon discharge.

The increase of the thickness of the DLC-films is promising for the electrical insulation properties of the sensor systems. The coating operations for the deposition of the sensor layer are strongly modifying the properties of the insulation layer: sputtering of titanium for the sensor layer integrates metal atoms in the insulating layer, reducing its electrical resistance.

Figure 2 shows the enhancement of the insulation properties of the developed coatings with the increasing thickness. The resistance of the films is hereby measured between the substrate and the sensor layer after its deposition. The bad correlation of the resistance measured for the 6µm-thick film is due to variations in the profile of the methane-flow supplied to the process for this experiment.

Other experiments showed actual limits of the coating systems under full sliding conditions at 600 MPa of Hertzian pressure.

.

5 Present State of the Sensor Development

Before setting up the thin film sensor in tribocontact its characteristics were identified. Figure 3 (left) illustrates a linear calibration curve of this sensor. The first application of the ring with sensors in the two-disk-rig has shown first reactions (Figure 3, right). These are signal peaks with a frequency corresponding to the rotational speed of the disks, and a width corresponding to the

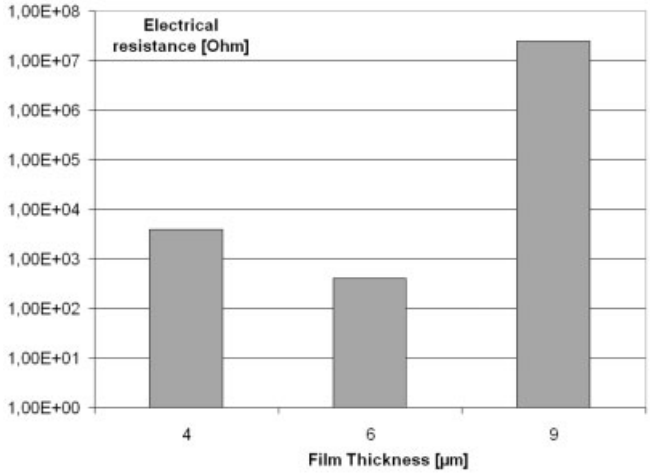


Figure 2: Insulation properties (logarithmic scale) of the developed coatings.

one of the Hertzian pressure zone. Due to some electronic problems (saturation of the amplifiers, sampling rate), the measured signal could not be evaluated regarding their physical significance.

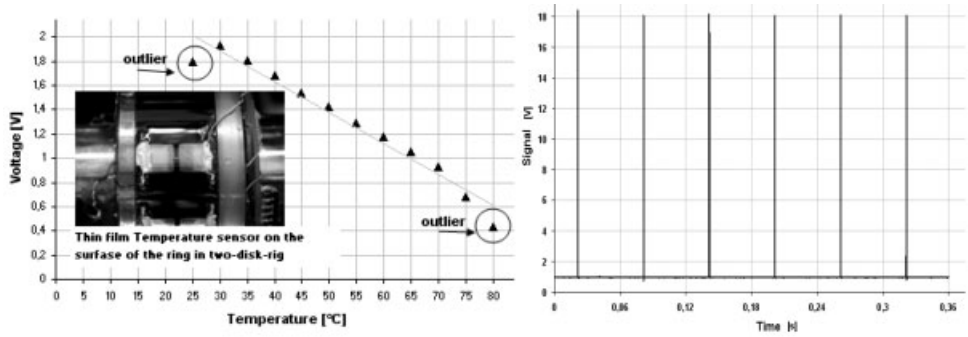


Figure 3: Left: Sensor characteristics; Right: Signal delivered by sensors in a two disc rig

For reasons of efficiency in the development of the coatings and sensor systems, new substrate geometry is used for current work. The planar parts allow a better control over the coating process and over the structuring of the sensor layer. At the same time, these parts allow the verification of the function on the sensors using the EHD-test bench available at IPEK. For further applications of the sensors in the two disk machine, a scaling of the production process of the coating systems will be needed in the future.

6 Sliding Bearings-test-bench as an Application for the Sensors

Due to the propagation of medium lubrication in praxis with liquids of low viscosity, an adjustment of the boundary conditions for testing machines is necessary. In some cases increased safety measures (e.g. for the application of diesel oil under high pressure and high temperature) are necessary as well. In order to meet these requirements a new type of test bench is currently being developed [7].

At the actual state of development, the function of the test-bench (max. load, rotation speed, torque measurement) is being verified by the use of dry sliding bearings. By the use of air bearings as support bearings, an exact measurement of the friction torque of the tested bearing is allowed. Figure 4 shows first friction coefficients measurements in these bearings at two different specific loads for the bearing. Further studies with variations of the specific load for the bearing, sliding speed as well as the use of lubricants will permit to build very exact friction maps for different working conditions, until the achievement of the development of the thin film sensors.

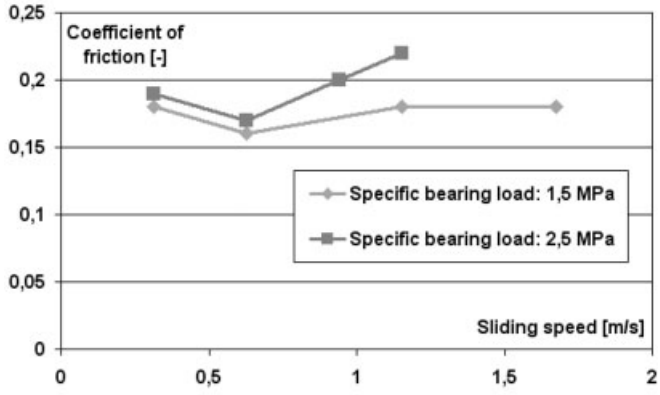


Figure 4: Coefficients of friction of a dry sliding bearing.

7 Summary and Outlook

In this paper, the current advances in the development of thin film sensors on the basis of insulating DLC-coatings are presented. In the future, such sensors will allow measuring of pressure and temperature distributions in lubricating films with high local and temporal resolution under conditions of mixed friction. These sensors will provide a better understanding of the phenomena of mixed lubrication. They will help to align theoretical models with reality. Maybe they can serve for controlling tribological contacts not only in the laboratory and on test benches but also in serial products.

The test benches with which the sensors will be tested and applied during the upcoming project steps are presented, permitting the precise examination mixed lubrication and of medium-lubricated sliding bearings.

Nevertheless, still much remains to be done. The mechanic characteristics of the developed electric non-conducting DLC-coatings are considerably worse than those of other known wear protection films. In this context further development work is required. Combining the concept of the micro thermocouple with the DLC-coatings is also an important step in the direction of the final system.

8 References

[1] Bartel, D.: Berechnung von Festkörper- und Mischreibung bei Metallpaarungen, Diss. Magdeburg, 2001

[2] Knoll, G.: Lastübertragungsverhalten elastischer Körper mit Festkörper- und Fluidkontakt, Habilitationsschrift, G.H. Kassel, 1986

[3] Baumann, H.: Druck- und Temperaturmessungen mittels aufgedampfter Dünnschichtaufnehmer in einem elastohydrodynamischen Linienkontakt, Diss. Universität Karlsruhe (TH), 1985

[4] Dauber, O.: Elastohydrodynamische Rollreibung in Stahl-Keramik-Kontakten. Diss. Universität Karlsruhe (TH), 2001

[5] Holland, J.; Schwarze, H.; Buchheister, C.: Kontaktauflösende Messung von Druck-, Temperatur- und Spaltweitenverlauf in EHD-Kontakten. In Tribologie + Schmierungstechnik 48. Jahrgang, 5/2001, Seite 33–38

[6] Stüber M.; Ulrich S.; Leiste H.; Kratzsch A.; Holleck H.: Graded layer design for stress-reduced and strongly adherent superhard amorphous carbon films. Surf. Coat. Technol. 116–119 (1999) 591–598

[7] Albers, A.; Beauvais, S.; Bsul, J.; Burger, W. : Advancement of thin film layer sensors for pressure and temperature measurements in highly loaded tribological contacts under mixed lubrication. 16th International Colloquium Tribology, TAE Esslingen, 2008

[8] NASA: Development of thin film ceramic thermo-couples for high temperature environments; NASA Center for Aerospace Information, TM-2004-213211, AIAA-2004-3549

[9] Albers, A.; Bsul, J.; Beauvais, S. ; Burger, W. : Weiterentwicklung von Dünnschichtsensoren zur Messung von Drücken und Temperaturen in hoch belasteten tribologischen Kontakten unter Mischreibungsbedingungen. 48. Tribologie-Fachtagung, GFT, 2007

Acknowledgments:
The IPEK would like to thank the IMF1 at the Research Institute in Karlsruhe (FZK) for their help in the coating development methods.

Fatigue Life in Rolling Contacts with Rough Surfaces

M. Gleß[3], V. Fafoutis[2], G. Repphun[3], C. G. Provatidis[2], D. Bartel[1], L. Deters[1]
[1] Otto von Guericke University Magdeburg, Germany
[2] National Technical University of Athens, Greece
[3] Robert Bosch GmbH, Stuttgart, Germany

Abstract

Experimental investigation of highly loaded rolling contacts with rough surfaces and low film thicknesses under boundary or mixed lubrication conditions showed various locations of crack origin, as well as competitive modes of contact fatigue damage. Endurance tests for rolling contact fatigue with different mechanically-induced residual stress states and various surface topographies were obtained using a newly developed two-disc test rig.

For the prediction of fatigue life, a damage accumulation model for rolling bearings based on Weibull statistics according to Ioannides and Harris is introduced. Comparing the obtained fatigue life of experiments with theoretically data of Ioannides/Harris model and FEM simulations indicate that it is possible to estimate crack initiation time quite correctly.

Keywords
Rolling element fatigue model, rolling contact fatigue, boundary/mixed lubrication, residual stresses, surface roughness, crack initiation

1 Introduction

Due to low frictional losses, rolling contacts are often used in varying applications, as for instance in bearings, gears, rail wheel contacts and in cam-roller contacts of high-pressure pumps, which will be the particular focus of this paper. Apart from the technological demand of high reliability under high loads, the lubrication with low viscosity lubricants, e.g. Diesel fuels, is a great challenge. Under such lubrication the film thickness is only marginal and insufficient. Despite good surface finishing, a complete separation of the contacting bodies is not possible. While operating under mixed lubrication, micro-contacts between asperities of the contacting surfaces are responsible for high local stresses and friction forces [1], [2]. Consequently, a reduction of the lifetime is expected.

In highly loaded rolling contacts, surface fatigue is an unavoidable failure mechanism to limit lifetime. For lifetime calculations many approaches are found in literature. Comparing stresses with material strength, local concepts and integral concepts that consider the whole stressed volume are available [3], [4], [5]. This work investigates the applicability of the rolling bearing fatigue life model based on Weibull statistics according to Ioannides and Harris to highly loaded rolling contacts.

2 Fatigue Model (Weakest Link Model)

Lundberg and Palmgren [6] introduced Weibull's weakest link model for the life prediction of rolling bearings [7]. Ioannides and Harris [8] extended Lundberg and Palmgren's model by considering the effects of surface roughness, and introducing a fatigue limit depending on the material. This experimentally based model has been widely used in bearing manufacturers' catalogues and was standardized in ISO 281 [9]. Requirements for its application are that subsurface fatigue is the main failure mechanism and crack initiation is the by far longest period of the lifetime of the examined specimen.

$$\ln\left(\frac{1}{S}\right) \propto N^e \int_V \frac{(\tau - \tau_u)^c}{{z'}^h} dV \tag{1}$$

S: probability of survival; N: number of cycles; e: Weibull-Exponent, e = 10/9; τ: stress-related fatigue criterion (see section 4: Results and Discussion); τ_{u}: fatigue limit (see section 4: Results and Discussion); c: stress criterion exponent, c = 31/3; V: volume; z': stress weighted average depth; h: depth exponent, $h = 7/3$ or $h = 0$ for real roughness profiles

3 Experiment and Simulation

3.1 Two-Disc Test Rig

Experimental investigations and determination of lifetime data were carried out on a newly developed two-disc test rig [12]. The test rig consists of two independently driven disks. The twin disc machine simulates the operating conditions of a high-pressure pump cam-roller contact. Rolling and sliding speed, contact pressure, lubrication and temperature were measured and controlled. Investigations were carried out for three surface topographies and three different residual stress states. Residual stress profiles were measured by X-Ray diffraction. The main tests were executed under the following conditions: bearing steel SAE 52100 in bainitic condition for both specimens, contacting surface shot peened and finished (Rq = 0.3µm), mean pressure p_{mean} = 3100 MPa, elliptical contact, rotating speeds v_1 = 7.1 m/s and v_2 = 7.027 m/s, lubricant diesel fuel (DIN EN 590), inlet temperature of lubricant ϑ_{in} = 20°C.

3.2 FEM-Simulation

Two simulation approaches were made with ANSYS: **1**. 3D FE model for the investigation of the effect of different mechanically induced residual stresses in the Hertzian sub-surface stress distribution under constant load; and **2**. 2D FE model for the description of the effects of different surface roughness profiles under the same surface treatment (shot-peening) and loading. The lubricant film thickness is extremely small (boundary/mixed lubrication) and was considered to be constant. The friction coefficient was set to μ = 0.1 based on experimental results. Bainitic SAE 52100 steel was modelled as an elastic-plastic material, with no hardening effects included and its properties were retrieved from compression testing (DIN 50106). The measured material data of the bainitic SAE 52100 steel are: compression modulus of elasticity E = 136 GPa, Poisson's ratio ν = 0.26, elastic limit σ_{e} = 2460 MPa.

3D FEA: In order to reduce model complexity and thus computational time, geometry and loading symmetry, was taken into consideration, whenever applicable, as well as submodelling technique. Coarse and sub model were meshed with $\sim$ 20k and $\sim$ 300k hexahedral elements respectively (high density of mesh needed for the application of residual stresses). External load was applied as a multi point constraint. Augmented Lagrangian contact algorithm with the basic Coulomb friction model was used for an ideally smooth point contact area consisting of approximately 2.5k elements. Mechanically induced residual stresses were implemented as initial stress condition of every element below the surface ($\sigma_{\text{in}} = f(\text{depth})$). The model was validated with theoretical solutions of the simple Hertzian loading without residual stresses.

2D FEA: Due to high requirements in mesh density in order to calculate the stress distribution of a rough surface in contact, the 3D model was reduced: The cross section of the two specimens, perpendicular to the rolling direction, was simplified to a 2D plane strain model. The sub model was meshed with $\sim$ 50k plane quad elements. The geometry and loading conditions were altered, so that the new mean pressure and contact width are equal to the initial ones. The roughness profile is produced by spline interpolation of points created by a Gaussian random number generator. The amplitude and the wavelength of the produced roughness depend on the deviation of the Gaussian distribution and the number of points created respectively. Consequently, real roughness profiles, that are measured by ISO standards (Rq, Rz etc.) are recreated in the FEM environment. Residual stress distribution is constant - shot peened - for all experiments.

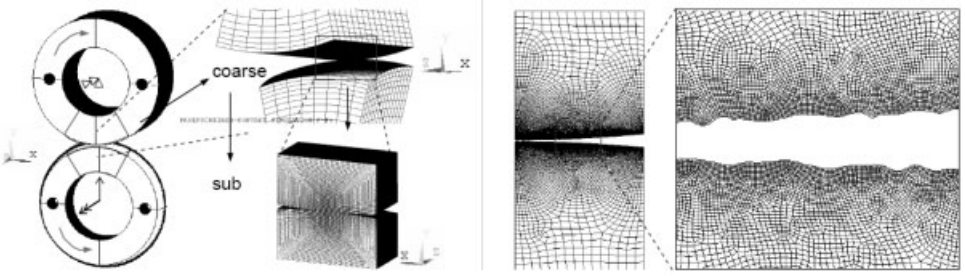


Figure 1: 3D and 2D models respectively

4 Results and Discussion

The Ioannides/Harris model is applied as a post processing routine to the simulation results. All constants, c, h, τ_{u} are retrieved from Ioannides et al. original paper [8]. Attention needs to be given to the exponent 'h' of the stress-weighted depth. For all cases, 'h' is considered to be equal to zero. This is justified by literature [8], [10]. In the 3D model, roughness effects are excluded; and rough surface profile is created in the 2D model. Dang Van fatigue criterion is applied, as proposed in [3], and in all examined cases showed better agreement than other classic fatigue criteria as von Mises and Tresca. The behaviour of the fatigue limit τ_{u} must also be emphasised. In the elastic region τ_{u} has a constant value, but τ_{u} decreases linearly in the region between the elastic limit σ_{e} and the fracture strength σ_{f} of the material. Finally, as suggested in [8], results of this model are calibrated to the experimental data set with the minimum dispersion. Thus, by

altering the investigated parameters (residual stresses and roughness profiles) and calculating the stress integral for the 3D or 2D model respectively, the tendency of lifetime can be predicted.

In the following figures, the stress distribution produced by the effects of various mechanically induced residual stresses and roughness profiles as well as the lifetime calculated by the Ioannides/Harris model in comparison to the experimental values are demonstrated. Lifetime of rough profiles is presented in dependence of the film parameter Λ [4] with:

$$\Lambda = \frac{h_0}{\sqrt{(R_{q1}^2 + R_{q2}^2)}} \tag{2}$$

Λ: film-parameter; h_0: film thickness according to Hamrock and Dowson [11]; $R_{q1,2}$: RMS-heights of surfaces 1 and 2 of contact partners

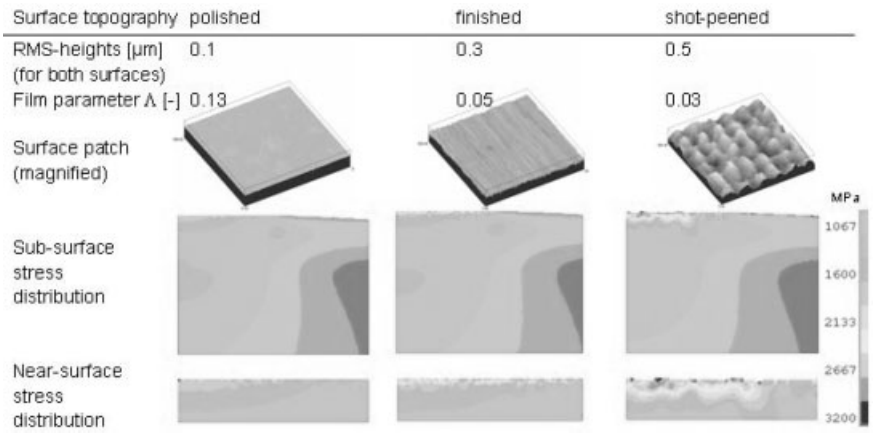


Figure 2: Influence of surface roughness on stress distribution

In highly loaded contacts it is apparent that the surface roughness has a graver impact on the lifetime of specimens, due to high local stresses emerging from local micro Hertzian contacts between asperities. As observed by the experimental results, the Ioannides/Harris model appears to be able to describe the positive influence of residual stresses as well as of smoother roughness profiles. However, the limitations of the model and the simplifications made in this paper should be taken into consideration. On the experimental side, long term phenomena (tribochemical and material effects) could not be investigated, because of the high loading conditions and the thus shortened lifetimes. Furthermore, a proper statistical basis of the results is lacking. Concerning the simulation, the roughness wavelength in rolling direction is considered to remain constant, because of the approximation method used. Further, residual stress changes as well as different micro-structural modifications that appear in real endurance tests after many load cycles are excluded. Finally, Ioannides/Harris model was developed for sub-surface fatigue as main failure mechanism and for calculating the time until a crack initiates in the examined volume. Here the predicted lifetimes correspond with the experimental ones, since the duration from crack initiation to complete failure of the component (crack propagation) is extremely small under high

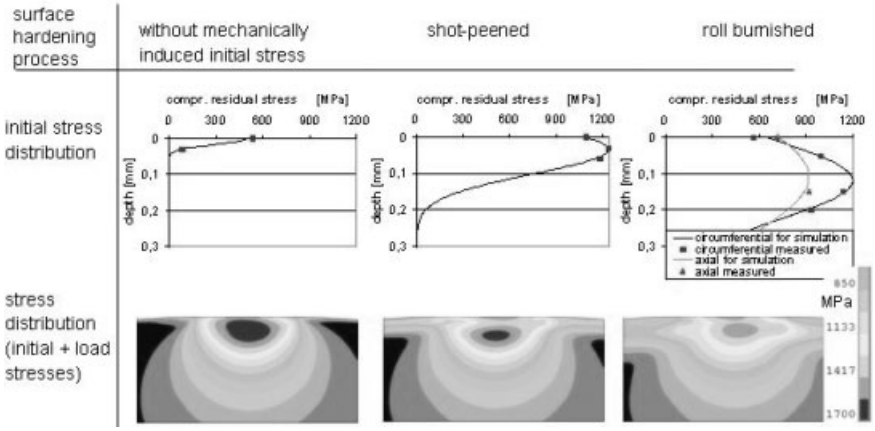


Figure 3: Influence of mechanically induced residual stresses

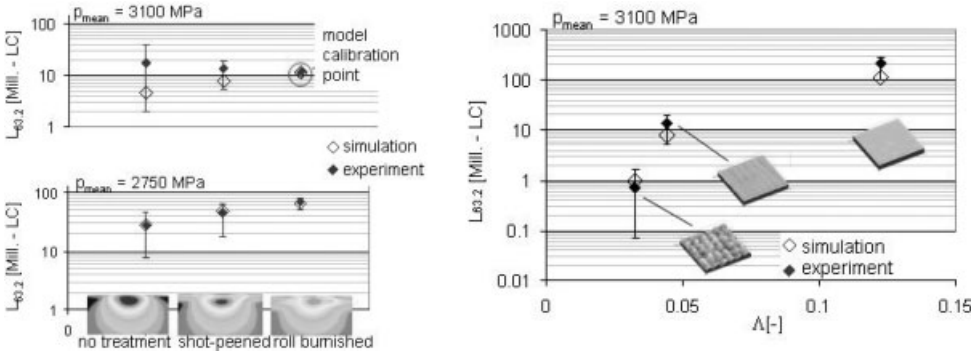


Figure 4: Comparison of experimentally and theoretically predicted lifetimes in logarithmic scale (left side: lifetime at different cases of compression residual stress, right side: lifetime at different cases of surface roughness characterized by the film parameter Λ)
– distribution range corresponds to lifetimes between L_{10} and L_{90}
– least number of experiments per loading level = 3

loads compared to the complete life. It is apparent to conclude from the above mentioned that the applicability of this model requires further evaluating.

5 Conclusion

Rolling fatigue is a complex phenomenon of high interest for the industry. In this paper, the damage accumulation model proposed by Ioannides and Harris (ISO 281) for the prediction of lifetime of rolling bearings has been applied to predict rolling contact fatigue. Fatigue endurance tests performed in a newly created two-disk test rig showed the positive influence of mechanically introduced residual stresses and smoother surfaces. Comparisons between experiment and sim-

ulation show the ability of the model to describe the influence of residual stresses and roughness profiles on the lifetime of highly loaded rolling contacts.

6 References

[1] Ioannides, E., Kuijpers, J. C., Journal of Tribology, Trans ASME, 1986

[2] Paulin, C., Ville, F., Sainsot, P., Coulon, S., Lubrecht, T., Transient processes in tribology, 2004, pp. 611–617

[3] Ioannides, E.; Bergling, G.; Gabelli, A., Acta Polytechnica, Mechanical Engineering Serie, 1999, No. 137

[4] Harris, T. A., Rolling bearing analysis, 2001, Ch. 12

[5] Zhou, R.S., Cheng, H.S., Mura, T., ASME J. Trib., 1989, 111, pp 605–613

[6] Lundberg, G., Palmgren, A., Acta Polytech., Mechanical Engineering Series 2, 1952, No. 4

[7] Weibull, W., A Statistical Theory of the Strength of Materials, Proceedings of the Royal Swedish Institute for Engineering Research, No. 151, Stockholm, 1939, 45 pp.

[8] Ioannides, E., Harris, T. A., Journal of Tribology, 1985, 107, pp. 367–378

[9] ISO 281: Rolling bearings — Dynamic load ratings and rating life, second edition, 2007

[10] Tripp, J. H., Ioannides,E., Proceedings of the Japan international tribology conference, Nagoya pp. 797–802, 1990

[11] Hamrock, B.J.; Dowson, D., Trans ASME J. Lubr. Eng. 99 Ser. F (1977

[12] Gleß, M., Repphun, G., Bartel, D., Deters, L., Wälzkontaktermüdung im Mischreibungsgebiet, GfT Tribologie Fachtagung, 2007

Reciprocating Sliding Wear of Surface Modified Austenitic High Nitrogen Stainless Steel and CoCrMo-alloy

R. Pourzal, A. Fischer
Material Science and Engineering, Institute of Product Engineering, University Duisburg-Essen

1 Introduction

For years surface texturing is known to be an effective method to improve the properties of certain tribological systems [1,2]. One approach is to create lubricant reservoirs by non-corresponding dimples in the surface of one of the articulating surfaces. In MEMS devices, surface texturing is used to reduce the contact area in order to overcome adhesion and friction. Another interesting beneficial effect of a textured micro-topography is its function as a wear particle trap. By eliminating particles from the tribological system, third-body-wear is prevented [1,3,4]. The metal-on-metal (MOM) artificial hip joint is a system which does not suffer third body wear by means of abrasion. Nevertheless, wear particles are suspected to be responsible for implant failure due to osteolysis, a bone degrading disease that causes implant loosening. A major improvement would be the elimination of wear particles, in particular, during the run-in of the artificial joint.

In order to apply a micro-topography different techniques can be performed like machining, ion beam texturing, laser texturing, and etching [2,5]. For this study an electrochemical etching process was used. The advantage of this process is the homogeneity of the material. Furthermore, this process is a less expensive application than, for example, laser texturing.

In order to observe whether an electrochemically textured surface is beneficial for wear performance in a first step, a reciprocating sliding wear test rig has been established. This paper shows and discusses the results, which were achieved with two austenitic materials.

2 Materials and Methods

2.1 Sample Material

For this study two different alloys were tested: a CoCrMo-alloy (Protasul, Zimmer Inc.; Warsaw, USA) which is used by default for the manufacturing of total joint replacements in orthopaedics and the austenitic high nitrogen stainless steel 1.4452 (P2000, VSG Energie- und Schmiedetechnik GmbH, Essen, Germany) which has proven similar wear performance as CoCrMo in an earlier study [6].

2.2 Reciprocating Sliding Wear Test

For the sliding wear testing a cylinder-on-bar apparatus was established (fig.1). Two cylinders (ø 10 $\times$ 15 mm) applied a normal force to a bar (80 $\times$ 10 $\times$ 10 mm) which conducted a reciprocating movement on a vertical axis. The test was performed in new born calf serum at 37°C isolated from the laboratory environment. Even though the unidirectional reciprocating sliding motion

does not represent the circumstances in a hip joint it allows for a similar nominal contact mechanical and comparable tribomechanical loading situation in a first and rough approach..During testing the normal and friction force were recorded. Furthermore, the cylinders and the bar were isolated from the sample holders in order to prevent the formation of a galvanic element in the testing fluid. The bar was electrically contacted in order to measure the open corrosion potential during the wear test against a kalomel electrode placed in the testing chamber. The tests were conducted on bars of CoCrMo and HNS steel as well as a polished (R_a = 0.04) bar surface. The topographies on cylinder and bar exhibited large differences. The cylinders had machining marks in order to produce more wear during testing. Each sample coupling was tested with 10^3, 10^4 and 10^5 cycles. The operating variables are given in table 1. The measurement of the open corrosion potential began one hour prior to test start and ended one hour after each test.

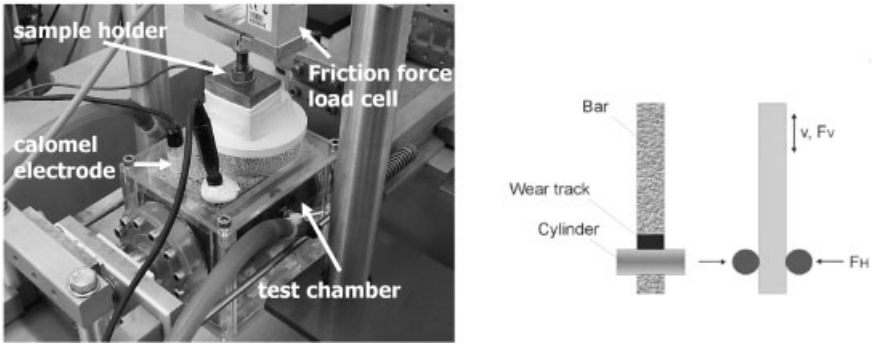


Figure 1: Reciprocating sliding wear test apparatus (l.) and schematic principal (r.) [7]

Table 1: Wear test operating variables

Operating Variables	
Normal force (F_H)	25 N
Nominal surface pressure (σ)	135 MPa
Frequency (f)	6 Hz
Amplitude (a)	3 mm
Temperature (T)	37 °C
Cycles	1000, 10000, 100000
Testing fluid	newborn calf serum + basic solution

2.3 Application of micro-topography

A micro-topography was applied to the metal bar surface by an etching process which has been previously described [6,8,9]. For tribological purposes it was first introduced by Büscher et al. [6]. Chromo-sulfuric acid at 70°C was used as the electrolyte. For the set-up the metal sample served as the anode and a platinized titanium electrode as the cathode. Prior to contact of the sample with the electrolyte an initial potential of 20V for the high nitrogen steel and 30V for the

Co-Cr-Mo was adjusted. After 30-45 seconds a full micro-topography was applied to the sample surface.

In order to characterize the micro-topographies on the bar's surface and to image wear appearances a confocal white light microscope (µSurf, Nanofocus, Oberhausen, Germany) and a field-emission scanning electron microscope (Gemini 1530, Leo, Oberkochen, Germany) with electro dispersive x-ray spectroscopy were used. The confocal white light microscope was also used for the determination of the potential contact area.

3 Results

The topographical appearance of the high nitrogen stainless steel (HNS) and the CoCrMo-alloy differed largely. The steel topography exhibited evenly distributed cones with a smooth surface. The maximum height of a cone was 24 µm and a diameter of 15 µm (fig. 2). The CoCrMo topography had a lower density of cones than the steel with large valleys in between them. The cones had a height of 24 µm and a diameter of 100-150 µm. The surface was much rougher than that observed on steel. Furthermore, dimples of former carbides covered the surface, which were torn off the surface during the electrochemical etching process (fig. 2).

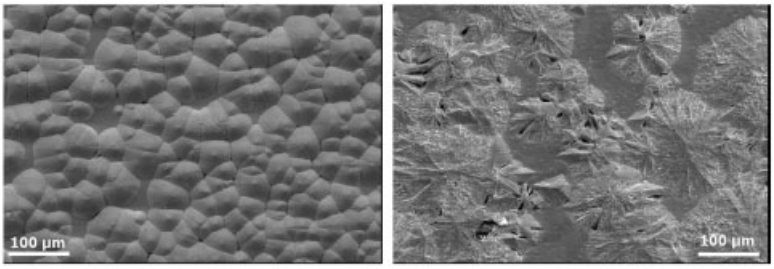


Figure 2: Topographies on high nitrogen steel (l.) and Co-Cr-Mo-alloy (r.)

The results of the confocal microscopy investigations (fig.3) exhibited the penetration of the topography of both materials during wear. With the increase of the potential bearing surface over cycles observed, it can be stated that both the HNS steel and the CoCrMo samples reached steady state after approximately 10^4 cycles. At this point the flattened tips of the asperities of the HNS steel reached a 1.5 times larger nominal contact area than the CoCrMo-alloy (fig.4).

After 10^5 cycles the volumetric wear of both textured samples was too small to be measured by means of weight loss. However, analysis of the 3D-data sets obtained with the confocal white light microscope, it was possible to calculate the volumetric material loss (fig.5). After 10^5 cycles the volumetric material loss of the CoCrMo bar was more than double the amount of the HNS steel bar.

The dissipated work of friction per cycle is plotted in fig. 6 versus the wear path. Nearly all specimens showed a similar tendency. The exception was the textured CoCrMo sample which exhibited less than half of the friction work compared to the other samples. However, it appeared that the polished samples reached steady state relatively early compared to textured samples which exhibited a slight increase.

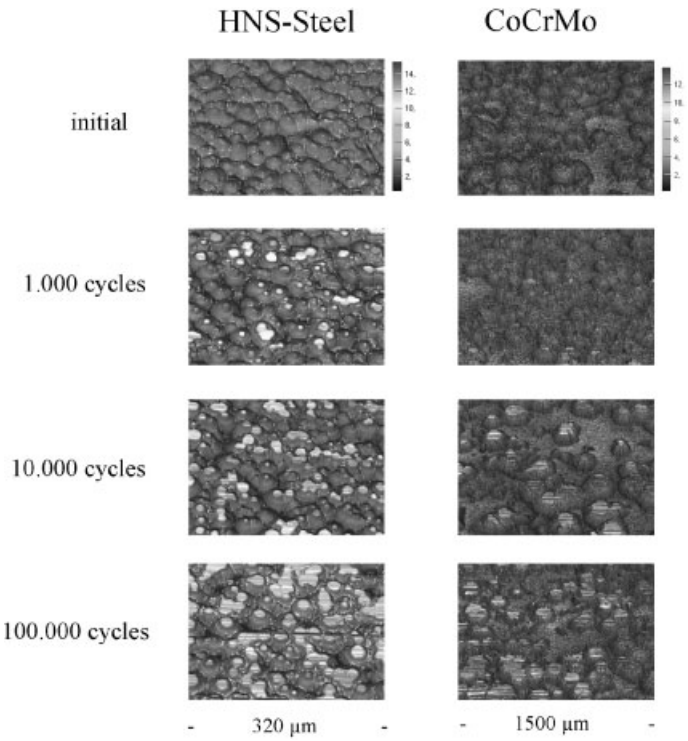


Figure 3: Wear appearances of the micro-topography on HNS steel and CoCrMo alloy

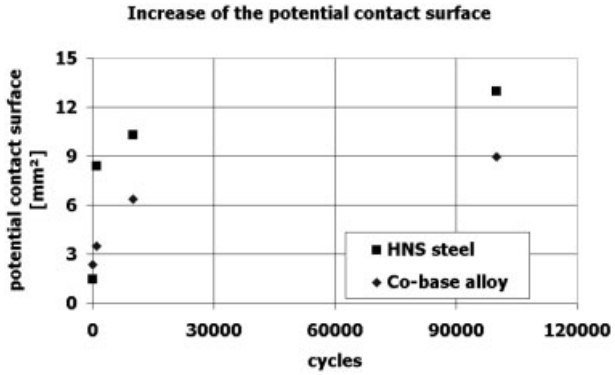


Figure 4: Increase of the potential contact surface during the run-in

The results of the SEM investigation clearly confirmed the assumption of wear debris entrapment in the depressions of the HNS steel sample. In figure 7 the top of the asperities are visible. The wear scars corresponded to the machining marks of the cylindrical counterpart. In between

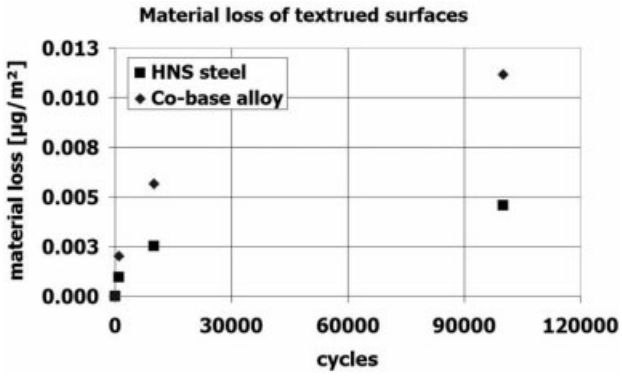


Figure 5: Volumetric wear of the samples with micro-topography during the run-in

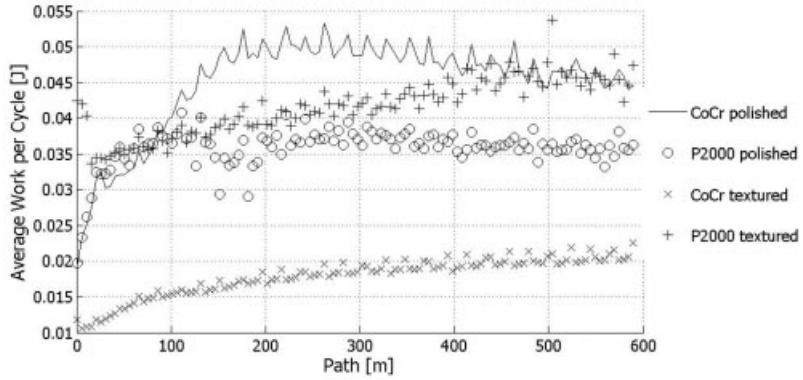


Figure 6: Friction loss over path for HNS steel and CoCrMo with polished and structured surface mode

the asperities, dried residue of the new born calf serum can be seen. The round bright particles have been identified by EDS as agglomerates of wear particles and residue of the testing fluid. No wear debris was found on the surface of the CoCrMo-alloy

The development of the open corrosion potential (OCP) during the wear tests differed between the polished and textured samples (fig.8). After the test start the value of the OCP dropped immediately by about 150–250 mV. However, during the test the OCP values for the polished samples increased slowly. The OCP value of the textured samples did not increase until test termination. After the end of the test the OCP rose up to the initial value.

4 Discussion

Regarding the quality of the micro-topography it should be noted that the etching process has to be modified for the CoCrMo-alloy. The cone density is lower than that on the HNS steel and the cone surface is rough and uneven. Even though a small amount of wear occurs during the

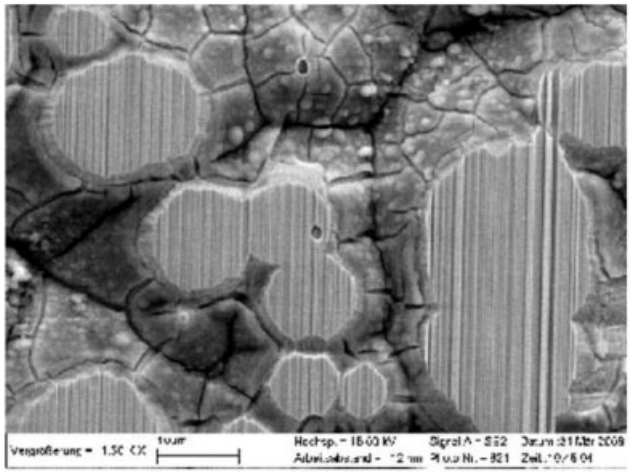


Figure 7: Entrapped agglomerates of wear particles in between the topography valleys. The cracks within the agglomerated layers are generated during drying before SEM investigation.

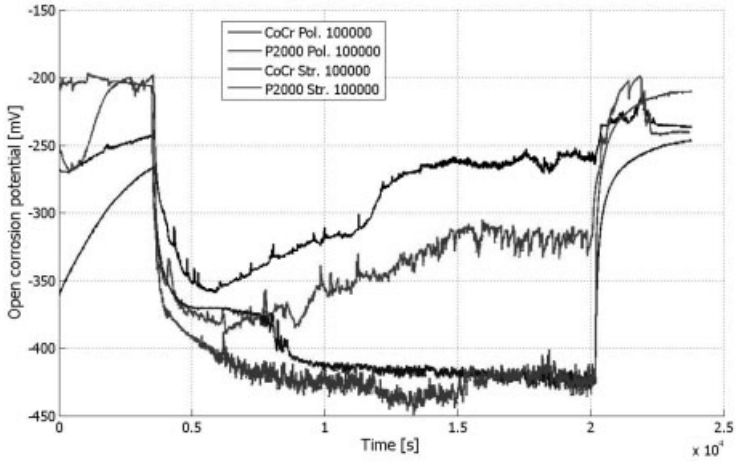


Figure 8: Development of the open corrosion potential during the wear test

first 10^5 cycles of the test, the CoCrMo sample exhibits a larger volumetric material loss than the HNS steel. This may be linked to the porous appearance of the cones. The term wear does not apply, since it is unknown which amount of the removed material left the tribosystem or got entrapped in between the surface asperities.

Both textured samples appear to have a similar run-in behavior as the polished samples. The low friction of the textured CoCrMo-alloy may be linked to the small contact area. The lubrication effect is unlikely since there are no isolated depressions in the surface. All depressions are corresponding allowing the lubricant to squeeze out of the surface and prohibiting the build

up of hydro-dynamic pressure as previously reported [3]. This is also the reason for the lack of wear debris found in-between the micro-topography of the CoCrMo-alloy. The lubricant flushed the wear debris from the interface, but did not entrap it in the surface. On the HNS steel the wear debris is clearly visible in the surface depressions. The emitted wear particles are sized in the nm-range (30–150 nm) [10]. The observed debris consists of agglomerates of such particles along with denatured protein. It can be stated that the surface modification of both materials succeeded to eliminate the wear debris from the tribological interface. The HNS steel topography also prevented the debris from entering the surrounding environment.

Regarding the results of the OCP measurements, the value drops after the test starts. At this point the passive layer on the metal surface is removed by the tribological load. The importance of this layer is well known [11]. However, the polished samples of both materials are able to recover during the test and build up a new passive layer within the contact zone, which is now stable enough to act as such under contact stresses. According to earlier findings this stable passive layer covers the entire contact surface and is a mixture of denatured proteins from the interfacial medium and metallic nanocrystals from the metal [7]. This is not observed for the textured samples. Here this stable layer cannot stand the acting tribological mechanism and is scratches away by abrasion. Still the sequence of mechanisms is not fully understood and will be investigated in the future.

5 Conclusions and Outlook

The goal of preventing wear particles from leaving the system has been achieved on the textured sample of the HNS steel. However, the electrochemical texturing process has to be modified for the CoCrMo alloy in order to apply this technique to the cup of an artificial hip joint. It appears that the entrapment of wear particles has a negative influence on the corrosion behavior of the alloy and that the passive film formation is inhibited. Thus, a potentio-dynamic approach has to be added to the wear test in order to judge the overall wear performance, both mechanically and corrosively. Furthermore, the wear performance of both materials and surface modifications (polished and textured) has to be tested further beyond the run-in period.

The testing fluid of all tests has been collected for metal content analysis and particle isolation. The shape, size, and chemical composition of all particles will be determined and compared.

Acknowledgements

The authors would like to thank the Zimmer Inc. for funding the present work and providing the CoCrMo material. We also thank Steffen Schweizer, Stefan Hingmann, Aykut Canpolat, and Christopher Knowlton for their valuable input.

References

[1] Pettersson, U., Jacobson, S.: Influence of surface texture on boundary lubricated sliding contacts, Tribology International **2003**, 36, 857-864

[2] Etsion, I.: State of the art in laser surface texturing, Journal of Tribology **2005**, 127, 248-253

[3] Wang, X., Kato K., Adachi K., Aizawa K.: Loads carrying capacity map for the surface texture design of SiC thrust bearing sliding in water, Tribology International **2003**, 36, 187–197

[4] Suh N.P., Mosleh M., Howard, P.S..: Control of friction, Wear **1994**, 175, 151–158

[5] Büscher, R., Fischer, A.: Sliding wear behaviour of an electrochemical modified austenitic high-nitrogen steel surface, WEAR **2003**, 254, 1318–1325

[6] Büscher, R., Fischer, A.: Tribological performance of austenitic high nitrogen steels for biomedical applications, Proc. Conf. HNS **2004**, 481–489

[7] Büscher, R.: Gefügeumwandlung und Partikelbildung in künstlichen Metall/Metall-Hüfgelenken, Fortschritt-Berichte VDI **2005**, Reihe 17, Nr. 256

[8] Jennissen H.P., Zumbrink T., Chatzinikolaidou M., Steppuhn J.: Biocoatings of implants with mediator molecules: surface enhancements of metals by pretreatment with chomosulfuric acid, Materialwissenschaft und Werkstofftechnik **1999**, 30, 838–845

[9] Büscher, R., Jennissen H.P., Chatzinikolaidou M., Fischer, A.: Characterization of wet-chemically nanostructured stainless steel surfaces, Proceedings of the Symposium on Material Research Society on Synthesis, Functional Properties and Applications of Nanostructures **2001**, 676, Y3.14

[10] Kurtz, S., Hodgson, A.W.E., Virtanen, S., Fervel, V., Mischler, S.: Corrosion characterisation of passive films on CoCrMo with electrocehmical techniques in saline and simulated biological solutions, European Cells and Materials **2002**, Vol. 3 Supp. 1, 26–27

[11] Catelas, I. et al.: Size, shape and composition of wear particles from metal-on-metal hip simulator testing: effects of alloy and number of loading cycles, Journal of biomedical materials research **2003**, 67A, 312–327

Tribology of Human Skin: Effect of Epidermal Hydration on Textile friction*

L.-C. Gerhardt[1,2], V. Strässle[1], N.D. Spencer[2], S. Derler[1]

[1] Laboratory for Protection and Physiology, EMPA, Swiss Federal Laboratories for Materials Testing and Research St. Gallen, Switzerland

[2] Laboratory for Surface Science and Technology, Department of Materials, ETH Zürich, Zürich, Switzerland

* This article is an abbreviated and modified version of a previously accepted paper, published in the Journal of the Royal Society Interface.

1 Introduction

In everyday life, human skin is in practically permanent contact with fabrics. Particularly in immobile or bedridden persons, friction and moisture at the skin-textile interface are often causes of mechanical skin irritations and wounds, such as *decubitus* (Figure 1). Therefore, friction and shear, as well as moisture and liquids are considered to be major clinical criteria for judging a person's risk of *decubitus* [1].

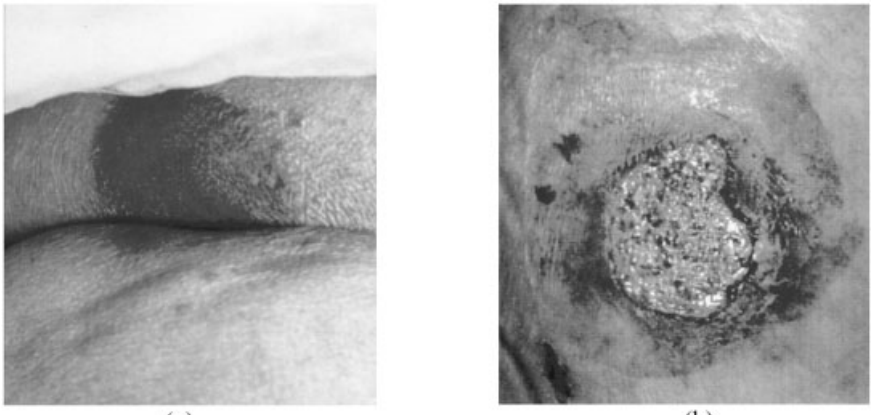


Figure 1: Two initial *decubitus* ulcers according to the European Pressure Ulcer Advisory Panel, (a) grade 1: non-blanchable erythema of intact skin (b) grade 2: partial thickness skin loss involving epidermis and/or dermis. The ulcer is superficial and presents clinically as an abrasion, blister or shallow crater (with permission and by courtesy of PAUL HARTMANN AG, Heidenheim, Germany).

Sivamani and Maibach have reviewed the current knowledge of skin tribology, derived from mainly dermatological studies concerning the effects of cosmetics [2]. Most of the *in vivo* skin friction studies were fundamental and performed with solids as rubbing partners. In the past, textile friction was primarily instrumentally determined without considering appropriate mechanical skin models [3]. A polyurethane-coated polyamide fleece with a surface structure similar to that of human skin has recently been shown to simulate human skin under dry sliding conditions [3].

In vivo skin-to-fabric friction was not yet studied in detail, and the role of textiles in the formation and prevention of *decubitus* is largely unexplored [4].

Moisture commonly increases the friction at the skin-textile interface, as can be experienced in sport or leisure activities. For skin friction, factors of 1.5 to 7 have been reported between wet and dry conditions [5-8]. So far, however, no systematic study on the functional relationship between skin moisture and textile friction has been presented. The goal of the present paper was to study in detail the influence of skin hydration on the friction against a hospital fabric. Skin moisture measurements were combined with friction experiments on a force plate to link the physiological skin condition to skin-textile friction.

2 Experimental

2.1 Test Subjects

Twenty-two Caucasians without any history of skin disease participated in the experiments. All persons (11 males, 11 pre-menopausal females, age: 31.7 ± 8.4 years, BMI: 23.3 ± 3.2 kg/m^2) signed informed consent to the study purpose.

2.2 Friction Experiments

Friction measurements were carried out using a quartz force plate (Model 9254, Kistler, Winterthur, Switzerland), as recently described in detail [3, 9]. The subjects were instructed to rub their dominant inner forearm in a reciprocating and uniform motion (≈ 20 cycles) against a cotton-polyester hospital textile on the force plate, using normal loads of 15 N. The average dynamic coefficient of friction (COF) obtained from at least 15 full friction cycles was calculated by the ratio of friction force and normal force. The friction process (frequency: 0.9 ± 0.2 Hz, estimated forearm stroke ≈ 80 mm) was carried out with a linear sliding velocity of about 140 mm/s. Prior to the friction experiments, the apparent contact area between the skin and the force plate was determined using a pressure-sensitive film, as reported in [9]. Average apparent contact areas varied between 36.3 and 56.6 cm^2, without any significant difference between both genders ($p = 0.52$). The applied normal loads and the person's underlying forearm geometry/anatomy resulted in average apparent contact pressures of 3.4 ± 0.5 kPa, which are clinically relevant contact conditions and close to maximum interface pressures in supine persons [10].

2.3 Skin Analysis

Skin hydration was measured at about 15 locations on the inner forearm using a Corneometer probe (CM 825, Courage&Khazaka, Köln, Germany), which measures the epidermal moisture content by penetrating the skin up to a depth of 10–20 μm[11]. The Corneometer method uses the high dielectric constant of water ($\varepsilon_r = 81$) for detecting water-related changes in the electrical capacitance of the skin. The corneometer has a high linearity with respect to water, demonstrated by experiments using a filter fleece soaked with different amounts of salt water [11]. Corneometer measurements are given in arbitrary units [a.u.] and were recently related to physiological skin types [12]. CM values below 30 characterise very dry, between 30 and 40 dry and greater than 40 normally moist skin. Measurements were conducted at 23 ± 1°C and 50 ± 2% relative humidity

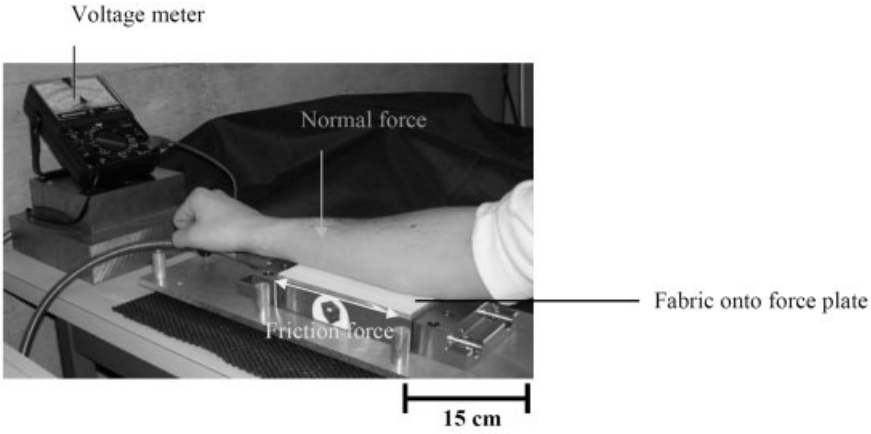


Figure 2: *In vivo* skin-fabric friction experiments on a force plate. Skin friction is determined by rubbing the volar forearm in a reciprocating motion against the textile on the force plate. Normal load is controlled by checking needle deflection of a voltage meter.

after an acclimatisation period of 15 minutes. For standardisation of the experimental procedure, the subjects were asked not to apply cosmetics on the test site for at least 2 days before the measurements, and not to shower 6 hours before skin testing. Excessive hair, if present at the forearm, was gently removed using scissors or razor blades about two days in advance.

2.4 Generation of Different Hydration States

Different skin hydration conditions of the skin were generated upon soaking into isotonic sodium chloride solution (0.9% w/v NaCl), using a water bath (35 ± 0.5°C, volume: 25 l). After the baseline measurements, i.e., skin analysis and friction experiment in the natural skin condition, the skin was iteratively soaked with NaCl solution for 5, 10, and 15 minutes. After each immersion period, visible excess water at the inner forearm was gently wiped away with a non-woven soft tissue. Subsequently, corneometer measurements were performed within 2 minutes, followed by the friction test on the force plate. In order to simulate extreme moisture/liquid accumulation on the skin surface, the fabric was completely soaked with NaCl solution ($\approx 10\ \mu l/cm^2$).

2.5 Statistics

Statistical analyses were performed using SPSS for Windows (Version 14.0.1, SPSS Inc., Chicago, IL, USA). Since data from all measurements showed neither normal distribution nor variance homogeneity even after transformations, distribution-free rank tests were chosen. For all analyses, statistical significance was considered at a probability value $p < 0.05$. All results are expressed as mean ± 1 s.d., or alternatively as a median, describing the typical value obtained from skewed experimental data. Depending on the person, maximum skin hydration (MSH) associated with maximum friction was achieved after the second or third soaking period. To assess gender-specific differences in moisture-related skin-fabric friction, the percentage change in

friction and moisture content at MSH in relation to the baseline were analysed using a two-tailed unpaired *U*-Test.

3 Results

A highly positive linear relationship between moisture and friction was found in all twenty-two persons, with coefficients of determination $R^2 > 0.72$, obtained from linear curve fitting (Figure 3, Table 1). Coefficients of determination found for quadratic or exponential functions were in the same order of magnitude. Figure 3 shows typical cases for 2 male and 2 female subjects. The baseline COFs of 0.41 ± 0.04 (men) and 0.42 ± 0.03 (women) increased to 0.56 ± 0.06 (men) and 0.66 ± 0.11 (women) as a consequence of the iterative soaking cycles.

At MSH, skin-fabric friction was typically 51% (median) higher in women and 37% (median) in men, while skin hydration increased by about 45% (median) compared to the baseline skin moisture. There was no significant difference in the increase in skin moisture between men and women ($p = 0.79$). However, the increase in friction was significantly higher ($p = 0.016$) for women. With a very similar increase ($\approx 45\%$) in skin moisture compared to the natural skin condition, female skin showed about 15% greater frictional resistance, i.e., the skin of women reacted more sensitively to moisture-induced changes.

By assigning all measured friction coefficients to physiological skin conditions [12], median COFs varied between 0.42 on very dry skin (men and women) and 0.53 (men) and 0.61 (women), respectively on normally moist skin. The COF increased typically by 26% in men and by 43% in women, indicating greater susceptibility of females to moisture-induced changes in skin-textile friction. A factor of more than two was found between the friction of skin in the natural condition and the measurement against the wetted fabric, with COFs of 0.88 ± 0.08 for men and 0.95 ± 0.04 for women being significantly different from each other ($p = 0.047$).

4 Discussion

We found a linear relationship between skin moisture and skin-fabric friction in each individual tested. Such a linear behavior was not expected because non-linear material behavior is typical for living tissues in general and soft tissues in particular [13]. Remarkably, the friction of female skin was more susceptible to moisture. Possible explanations can be gender-specific changes in the anisotropic mechanical properties of the *stratum corneum*, enhanced skin softening, or altered skin surface topography in women upon the soaking procedure. Smoother skin probably increases the real contact area (RCA) and adhesion to a fabric. Moisture uptake of the skin is believed to induce skin softening, smoothing and reduction of interfacial shear strength. Skin friction commonly increases upon moisture exposure, implying that increase in RCA dominates the interfacial shear strength reduction [5]. We attribute the large increase in friction to the plasticizing effect of water, leading to a greater RCA. We believe that fluid menisci (capillary bridges) formed by superficial water droplets play an unimportant role for the increase in RCA.

Until now, no significant gender differences have been reported for skin friction [7, 14, 15]. Recently, Ramalho *et al*. found particularly in women two skin-friction regimes [16]. They observed a transition from a low (COF = 0.27) to a high friction regime (COF = 0.83), when the index finger was rubbed against a glass surface and normal loads were varied up to 90 N,

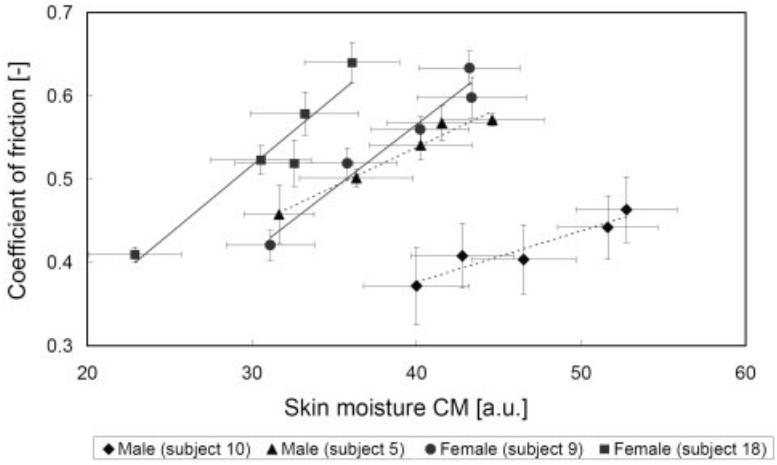


Figure 3: Influence of skin moisture on the friction of skin against a cotton-polyester medical textile. A high linear correlation between skin hydration and friction coefficient was observed for all subjects. The influence of moisture on the textile friction was more prominent in women, as indicated by greater slopes obtained from linear fits (see Table 1). For clarity, four typical cases of Table 1 are shown.

with an average transition normal load of ≈ 31 N. In the former studies [7, 14-16], other skin regions were investigated and different test methods were used, so that comparisons to our study are difficult.

We found that friction coefficients of skin against a hospital textile increased from very dry to normally moist skin by 33% (median of all 22 persons), which is in the range of literature data. Increases in friction between 20% for wool and 60% for polytetrafluoroethylene upon skin moisturization have been reported [6, 17]. The friction coefficients of skin against the completely wet fabric (COF = 0.91) exceeded those in the natural skin condition (COF = 0.42) by a factor of more than two, confirming results by Kenins [7]. Comaish and Bottoms measured on the back of the hand a dynamic COF of 0.40 for wool knitwear [6]. Zhang and Mak obtained dynamic COFs between 0.49 and 0.52, when rubbing cotton knitted fabrics against forearm skin [18]. Our baseline values were close to these values.

5 Conclusions

Skin analysis was combined with *in vivo* friction experiments on a force plate to study the effect of skin hydration on skin-textile friction. In a physiologically relevant range, friction increased linearly with skin hydration. Surprisingly, the influence of moisture on skin friction was more pronounced in women. From very dry to normal skin conditions, friction increased typically by 26% in men and by 43% in women. Measured against wet fabric, friction was more than two times higher than in the natural skin condition. Our results emphasize that friction and moisture reduction should have high priority in wound-prevention programs. The differences between men and women may offer implications for nursing interventions (e.g. turning and repositioning),

Table 1: Simple linear regression analysis. The results of all 22 subjects revealed a highly positive linear correlation between epidermal moisture and friction coefficient, measured on the volar forearm. The greater slopes in women indicate that the friction of female skin is more susceptible to hydration changes.

Person	Age	Gender	Slope	R^2	p value
1	25	male	0.008	0.818	0.035
2	30	male	0.010	0.883	0.018
3	44	male	0.009	0.950	0.005
4	22	female	0.028	0.821	0.034
5	36	male	0.009	0.964	0.003
6	28	male	0.007	0.917	0.010
7	28	female	0.018	0.821	0.034
8	29	female	0.012	0.943	0.006
9	39	female	0.015	0.956	0.004
10	44	male	0.006	0.901	0.014
11	19	male	0.011	0.776	0.048
12	42	male	0.008	0.766	0.052
13	38	male	0.011	0.906	0.013
14	27	female	0.011	0.848	0.026
15	31	female	0.027	0.815	0.036
16	46	male	0.010	0.814	0.036
17	32	female	0.009	0.943	0.006
18	17	female	0.016	0.920	0.010
19	26	female	0.008	0.721	0.069
20	40	male	0.010	0.914	0.011
21	21	female	0.009	0.802	0.040
22	37	female	0.017	0.989	0.001

especially if the skin becomes moist. This aspect may motivate future clinical studies to better understand if women really do form *decubitus* at a greater rate in comparison to men.

6 References

[1] B. Braden, N. Bergstrom, A conceptual schema for the study of the etiology of pressure sores. Rehabil. Nurs., 1987, 12, 8–12.

[2] R.K. Sivamani, H.I. Maibach, Tribology of skin. Proc. IMechE., Part J, 2006, 220, 729–737.

[3] S. Derler, U. Schrade, L.-C. Gerhardt, Tribology of human skin and mechanical skin equivalents in contact with textiles. Wear, 2007, 263, 1112–1116.

[4] W. Zhong, M.M.Q. Xing, N. Pan, H.I. Maibach, Textiles and human skin, microclimate, cutaneous reactions: an overview. Cutan. Ocul. Toxicol., 2006, 25, 23–39

[5] M.J. Adams, B.J. Briscoe, S.A. Johnson, Friction and lubrication of human skin. Tribol. Lett., 2007, 26, 239–253.

[6] S. Comaish, E. Bottoms, The skin and friction: deviations from Amontons' laws, and the effects of hydration and lubrication. Br. J. Dermatol., 1971, 84, 37–43.

[7] P. Kenins, Influence of fiber type and moisture on measured fabric-to-skin friction. Text. Res. J., 1994, 64, 722–728.

[8] L.J. Wolfram, Friction of skin. J. Soc. Cosmet. Chem., 1983, 34, 465–476.

[9] L.-C. Gerhardt, V. Strässle, A. Lenz, N.D. Spencer, S. Derler, Influence of epidermal hydration on the friction of human skin against textiles. J. R. Soc. Interface, In press/online available.

[10] L.-C. Gerhardt, N. Mattle, G.U. Schrade, N.D. Spencer, S. Derler, Study of skin-fabric interactions of relevance to *decubitus*: friction and contact-pressure measurements Skin Res. Technol., 2008, 14, 77–88.

[11] G. Khazaka, Assessment of stratum corneum hydration: corneometer CM 825. In Bioengineering of the skin: water and the *stratum corneum*, (Eds. J. Fluhr, P. Elsner, E. Berardesca, H.I. Maibach), CRC Press: Boca Raton, 2005, 249–261: Chapter 20.

[12] U. Heinrich, U. Koop, M.-C. Leneveu-Duchemin, K. Osterrieder, S. Bielfeldt, C. Chkarnat, J. Degwert, D. Häntschel, S. Jaspers, H.-P. Nissen, M. Rohr, G. Schneider, H. Tronnier, Multicentre comparison of skin hydration in terms of physical-, physiological- and product-dependent parameters by the capacitive method (Corneometer CM 825). Int. J. Cosmet. Sci., 2003, 25, 45–53.

[13] Y.C. Fung, Biomechanics: mechanical properties of living tissues. 2nd ed. Springer-Verlag. New York, USA, 1993. pages: 569.

[14] A.B. Cua, K.P. Wilhelm, H.I. Maibach, Skin surface lipid and skin friction: relation to age, sex and anatomical region. Skin Pharmacol., 1995, 8, 246–251.

[15] R.K. Sivamani, G.C. Wu, N.V. Gitis, H.I. Maibach, Tribological testing of skin products: gender, age, and ethnicity on the volar forearm. Skin Res. Technol., 2003, 9, 299–305.

[16] A. Ramalho, C.L. Silva, A.A.C.C. Pais, J.J.S. Sousa, *In vivo* friction study of human palmoplantar skin against glass. Tribologia Finnish J. Tribol., 2006, 25, 14–23.

[17] S. Nacht, J.-A. Close, D. Yeung, E.H. Gans, Skin friction coefficient: changes induced by skin hydration and emollient application and correlation with perceived skin feel J. Soc. Cosmet. Chem., 1981, 32, 55–65.

[18] M. Zhang, A.F. Mak, *In vivo* friction properties of human skin. Prosthet. Orthot. Int., 1999, 23, 135–141.

Introduction and Survey of the Research within the Collaborative Research Center 442 'Environmentally Friendly Tribosystems by Suitable Coatings and Fluids with Respect to the Machine Tool'

Hubertus Murrenhoff
RWTH Aachen University, Germany

Abstract

The introduction will point out the aim and methods of research and exemplary results of the Collaborative Research Center 442 'Environmentally Friendly Tribological Systems' (SFB 442) which is established at RWTH Aachen University.

The article will present the required structure of the research work carried out by different scientific disciplines and take a closer look at ongoing research work highlighting some achievements. The development of fluids is part of this description as well as the formulation of new and innovative composites by using PVD-coatings. It will be shown how these research results flow into different applications regarding a machine tool as an example. Bearings, gears, hydraulic components and -systems as well as cutting and cold forming machines are part of these research works.

Current research activities in the forth promoting phase of the SFB 442 focus on process chains to show interactions of the treated tribological systems. The results of the development of suitable coatings and fluids as well as the benchmark will be summarized in an expert system to ensure the use of this knowledge beyond the duration of the SFB 442.

1 Introduction

Tribological systems play a decisive role in the transmission of performance as well as in production processes. Besides their performance they cause a good ecological and economical balance of technical systems. This balance is shaped by a high ecotoxicological risk potential of the mineral oil-based and additive-alloyed intermediate substances. Due to leakage these intermediate substances attain to the environment and may cause damage. Furthermore inappropriate use of lubricants is causing a huge dissipation of resources [1–7].

The main idea of the SFB 442 consists in transferring the additive functions of fluids to the material surfaces of the tribological partners. Therefore, biologically fast degradable and non-toxic fluids are developed by using slightly dosed and environmentally friendly additives. In order to take over the missing lubrication and wear protection features by the material compounds of the tribological bodies basic research works has been done to determine suitable composite materials.

The basic course of action adopted within SFB 442 is described in **Figure 1.** The starting situation provides for the redesign of tribological systems on the basis of mineral oils and the aim is to achieve the effects of the surface-active additives by transferring the additive functions to the surfaces directly. This requires research into and development of new ester fluids based on

oleic acid methyl esters, as well as efficient coating systems, which are capable of performing the functions of the additives. Carbon coatings and coatings of hard material have been worked out as a function of the respective tribological system in this respect, which have been adapted to meet the specific requirements for the point or area of contact. A machine tool with both components and processes capable of running on environmentally compatible lubricants is envisaged as being the aim of the research project. At the same time, the concept must allow for the methodical approach of integrating environmental protection into the production process in accordance with the proposed new EU regulatory framework for Registration, Evaluation and Authorization of Chemicals (www.reach-info.de) which is discussed in greater detail below in chapter 3. At the end of the actual and concluding research phase, it will be possible to design the tribological systems with the help of a design and dimensioning method that incorporates the knowledge acquired from the test results stored in a database.

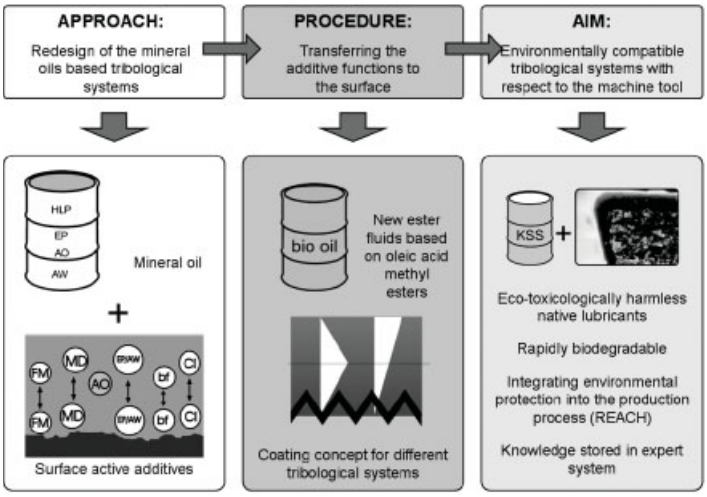


Figure 1: Course of action adopted by SFB 442 and the objective

2 Structure, Objectives and Proceeding

Scientists specializing in different fields have to work together very closely in order to achieve this objective. Activities have therefore been divided up into three project sections (PS).

- PS A: Substances and their characteristics
- PS B: Components, systems and processes
- PS C: Knowledge base and simulation

This grouping has proven to be very satisfactory and will therefore be maintained during the concluding of the research project.

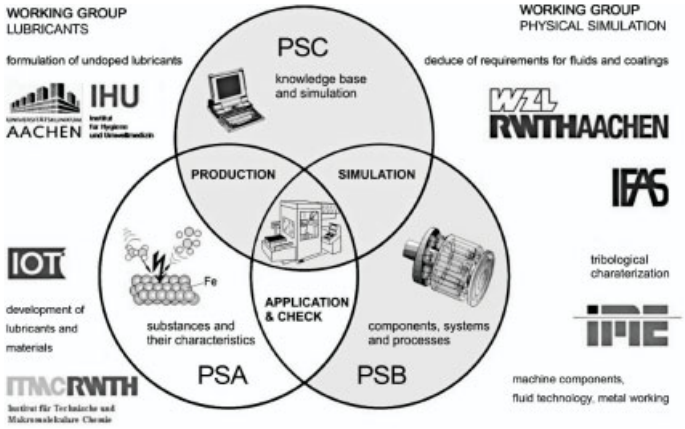


Figure 2: Structure of SFB 442

Activities in Project Section A 'Substances and their characteristics' are centred on developing the innovative intermediate substances and composite materials, as well as assessing their ecological and toxicological characteristics. The chemical and physical stability of the new intermediate substances is also investigated, allowing for their interaction with the composite material systems and the physical, chemical and mechanical characteristics of the composite materials. The new tribological systems are examined in various machine elements for the transmission of energy and power, such as gearboxes, linear guides, high-speed rolling bearings and screw drives, slow-speed rolling and sliding bearings and fluid power components in Project Section B 'Components, systems and processes'. The characteristics of the environmentally compatible tribological systems in forming and shaping processes are determined within cutting and forming technology. The data generated in these two project sections come together in Project Section C where the information is processed in a knowledge base so that it can be used for further development and to set up simulation models and correlation analyses.

The 'Physical simulation' working group serves to reinforce and focus the activities relating to the formulation of requirements to be met by the materials and lubricants involved in the tribological system.

Lubricants are of prime importance to the SFB, being the subject of research in all subprojects and this is the responsibility of the 'Lubricants' working group. The activities of this group include central coordination of work performed within the 'Lubricants' section, presupposing that the aim of realizing a fluid family is stringently pursued within the SFB, the number of fluid formulations to be produced remains within reasonable limits and that standard additives and associated fluid formulations are used. Central aspects of the working group are as follows:

- Specification and coordination of lubricants
- Support for the production of fluid formulations
- Examination of the interaction between lubricant additives and material surfaces

- Evaluation of the new lubricants and the way they change in use
- Correlation and establishment of lubricant production in the laboratory plant

The SFB 442 has so far been able to pursue its objectives during three completed phases of the project with the described structure and these working groups. The phases are shown in **Figure 3** whereby achievement of the objective – optimized environmentally compatible tribological systems - is to be demonstrated on a machine tool by way of example during the fourth concluding phase.

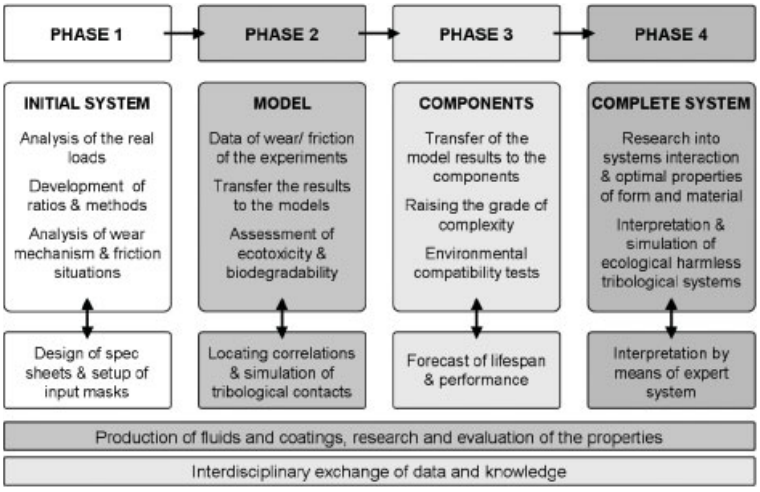


Figure 3: Procedure and structure of the research work within SFB 442

Phase 1:
This phase focussed on a review and evaluation of established parameters in order to describe the tribological, chemical and ecotoxicological properties of the fluids and coatings. These parameters were determined for marketable, rapidly biodegradable fluids and known composite materials, establishing points of reference for technical properties to which the development of the newly designed and ecologically optimized tribological systems was oriented. Model experiments were carried out to determine the tribological characteristics of these reference fluids and coatings, which were entered in the database and used to develop new intermediate substances and coatings that are in accordance with the SFB's central theme. Even at this early stage, the scientists were able to present successfully developed, future-oriented tribological system components, such as lubricants based on oleic acid methyl esters and such coating systems as HfC_g and TiHfN [8].

Phase 2:
The aim of this phase was to drive the development of environmentally compatible tribological systems forward. The studies carried out on the fluids and coatings were intensified and one example of the results achieved on the composite materials front was the successful development

of a graded carbon coating (ZrC_g). This is characterized by low wear accompanied by low coefficients of friction and provides impressive evidence of the ability to do without the surface-active additives used in the lubricants and transfer the fulfilment of complete requirements to the coatings, such as protection against corrosion and wear. New coating systems were also developed. Apart from the TiHfCrN-based systems for application in the cutting and forming sector, these included multilayer TiAlN + amorphous Al_2O_3 and CrAlN. Coatings and fluids that had been successfully studied in the tribometers were subjected to practice-oriented component tests, e.g. on displacement units in the case of the zirconium-based carbon layer. At the same time, enhanced tribometers were used to improve the performance of the coatings and fluids. Other promising results were obtained in the field of synthesizing new intermediate substances. Having synthesized several lubricants based on oleic acid methyl esters by adding acids and alcohols, and covering the spectrum of cooling lubricants and hydraulic fluids, it was possible to produce transmission fluids by epoxidizing glycerol trioleate and TMP oleate. This means that all of the fluid requirements for the entire machine tool can be met [9]. The various SFB 442 papers at the TAE convention 'Colloquium Tribology' go into this specific aspect in greater detail [10].

Phase 3:
The transition from models to complete components has been made during this phase of the project. It has been possible to carry the lubricant, which has been the subject of small-scale development and research with respect to its environmentally relevant characteristics and produced on a laboratory scale using a 25-liter reactor, over into a continuous production process so that the innovative new lubricant can now be supplied to complete test rigs. The composite materials have been further developed within the framework of low-temperature and high-temperature processes. The graded ZrC_g zirconium carbide coatings have produced very satisfactory results in systems with low surface pressure. The carbon and the alloying elements Ti and Si were able to reduce the frictional and wear behaviour considerably. As far as hard coatings are concerned, (Cr,Al)N was developed to meet extreme abrasion resistance requirements and was tested with successful results. The TiAlN coating system and the TiAlN+Al_2O_3 multilayer system were found to be ideal systems for coating tools used in high-temperature cutting processes. Successful results were also achieved with the nanolayer TiHfCrN for forming tribological systems. All of the layers were tested iteratively on such components as bearings, pistons, gears, cutting edges and forming tools. The use of pulsed technology in the plasma synthesis process has enabled the production of crystalline-Al_2O_3 and nanocomposite coating systems. The ecological research concepts were applied to the developed HISM and HIGTS fluids, leading to the optimization of the fluid synthesis process. The complete scope of SFB 442 was presented in two colloquia [10, 11] with reports on the results of the various individual projects.

Phase 4:
In this concluding phase the research concentrates on a holistic consideration of the components and systems used in the machine tool and to portray the holistic character of the newly developed tribological systems convincingly on the machine tool. When the SFB 442 project comes to an end, the research work conducted with reference to the expert system should have progressed to such an extent that it can be used to design and dimension environmentally compatible tribological systems. Development of this expert system began by analyzing the tribological systems

studied within SFB 442 and mapping them in a relational data model, which then serves as the basis for a tribological database. The results of all investigations are gathered together in the database, where they are stored in the form of qualitative and quantitative data, e.g. as wear parameters for new tribological systems in relation to a defined standard tribological system. During the second phase, initial correlations were found and these were incorporated into the development of the intermediate substances and composite materials. The parameters and correlation analyses were used for modelling in the third phase, enabling initial statements on safety, durability and failure probability. These activities were flanked by the continuation of lubricant synthesis, as well as the analysis of new fluids and the ways in which they change as a function of use. It is intended to portray the success of the research work with reference to process chains that are demonstrated on a Chiron machine tool and other systems, and to manufacturing techniques, these are described in greater detail in chapter 4.

3 Relevance of the Research

The search for environmentally compatible lubricants made from renewable resources has given rise to research projects all over the world in recent years. One of the most interesting approaches takes the form of a fundamental investigation into the coherences between composition, molecular structure, physical and chemical characteristics and ultimate suitability as a lubricant. The findings are then used to optimize the resulting lubricants by means of selective synthesis operations.

Numerous interesting studies have been carried out on the basis of the situation described in [12], [13] reports on pertinent analysis in the field of mineral-oil-based lubricants. As far as activities in the field of renewable raw materials are concerned, reference is made to the work of Hillion and Proriol [14] as one example. Sunflower oil with a high linoleic acid content was first isomerized, then codimerized with ethylene, catalytically saturated, purified by means of crystallization and finally transesterified with TMP (trimethylol propane). Saturation increases oxidation stability, branching improves the low-temperature characteristics (pour point) and transesterification enhances the hydrolytic stability.

Filley [15] combines methyl 9,10-dihydroxystearate (DHSM) with long chain aldehydes to form cyclic acetals and produces oils, which have a low pour point and good viscosity. This paper also correlates structural parameters (acetal instead of ketal, number of non-hydrogen atoms etc.) with macroscopic properties.

In recent years, it has been becoming increasingly evident that the effects of using environmentally hazardous substances are not only local, but global, which means that they are also putting people at risk. This is why the importance of environmental protection is growing to an ever increasing extent, particularly in the highly developed industrial countries. This is also made evident in the White Paper on a ‘Strategy for a future Chemicals Policy’ that was published by the European Commission in February 2001. With the overriding goal of sustainable development, this paper contains proposals for a single system to govern the handling of chemicals in order to protect human health and promote a non-toxic environment, which should also be implemented on a global scale in the long term. A new ruling was necessary because, although there were systematic regulations covering the testing and assessment of new chemicals, these proved to be inadequate for older substances which account for around 99 % of the total substances available

on the market. The new EU directive should supersede 40 existing legal acts, thereby creating a homogeneous system for all chemicals to ensure that both existing substances and new substances are subject to the same evaluation procedure in the future. The White Paper and the associated rulings are being implemented in the form of the REACH (**R**egistration, **E**valuation and **A**uthorization of Chemicals) Regulation, **Figure 4.** The idea behind REACH is to record the entire lifespan of a chemical substance, whereby manufacturers and importers are required to assess the hazard potential of each substance and mark it accordingly so that downstream users are able to take measures to minimize risks. The aim is to obtain more information about the handling and use of substances and to avoid or replace hazardous substances. The development of simple test and evaluation procedures that offer a means of testing chemicals while they are being developed plays a significant role in this respect (www.reach-info.de).

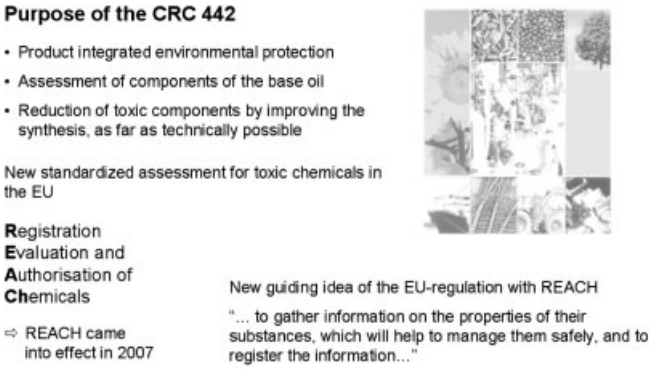


Figure 4: Research within the scope of REACH

The course of action adopted within SFB 442 is completely in accordance with the REACH requirements. Apart from using base oils obtained from renewable raw materials, the development of suitable coating systems should preclude the use of additives. The interdisciplinary cooperation enables recording and investigation of the entire lifespan of a lubricant, from its production via use, right through to disposal. This means that a contribution towards optimizing the substances can be made as early as in the development stage. **Figure 5** illustrates the fluid manufacturing cycle from development cycle that was established within SFB and as it will also be applied within the framework of interdisciplinary cooperation during the current phase of the project for the synthesis of new chemical substances or modification of existing substances.

As introduced in chapter 1 the research within SFB 442 includes all tribological contact surfaces being wetted or separated by those fluids. The industry has recognized the special potential of component and tool coatings in many sectors as described in the 2003 BMBF (Ministry of Science and Technology in Germany) report "Nanotechnologie als wirtschaftlicher Wachstumsmarkt" [16]. The importance of SFB 442 as a reflection of industrial developments can be illustrated by a few examples: the CrAlN coating system has been an integral element of research within SFB 442 as a low-temperature coating since 1998. This coating was launched onto the market as an industrial coating for cutting tools under the product designation BALINIT ® ALCRONA by Oerlikon Coating Services Balzers in 2003. The TiAlN/γ-Al_2O_3 coating system was presented within SFB 442 as a concept in the form of a multilayer coating system in 2003 and

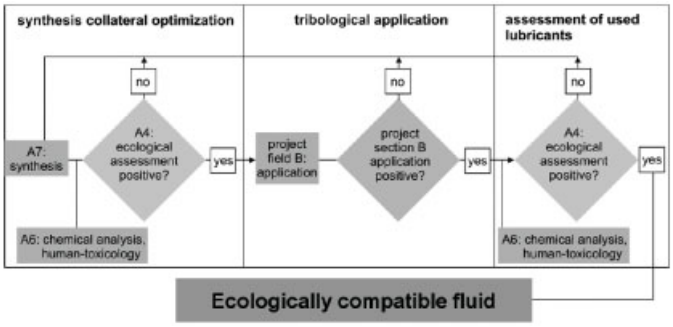


Figure 5: Fluid manufacturing cycle

the first technical realization was already available in 2004. Its industrial realization followed in 2005 under the name TIGERTEC® by Walter. Also very successfully used in cutting operations, the nanocomposite TiAlN was presented as a concept within SFB 442 in 2003 and successful realizations of this concept have been the subject of consistent further development.

Estimates of the market volume in the sector for automatic component coatings as displayed in **Figure 6** clearly show that a virtually explosive development is anticipated for the importance of coating technology on the free market in the future, which further accentuates the innovative position of SFB 442.

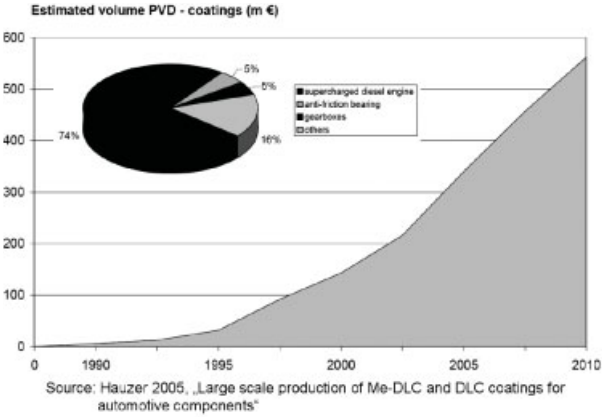


Figure 6: Market value of PVD coatings

4 Exemplary Results

Understanding how the research is conducted within the collaborative research centre is important before some examples are provided with regard to the development of fluids and composite

materials by means of PVD. **Figure 7** shows the typical cycles occurring in the various research projects. The left part depicts examples of components and processes while the loops can be seen on the right hand side.

Original investigations start with tribometer tests with results leading to analogies. Tests on real components follow when tribometer results are promising. Loads and wear mechanisms are fed back to establish specifications for fluids and material composites. All results and the knowledge gained is gathered in project section C where correlations are searched and simulations will lead to results building an expert system. Evaluating the data with respect to its relevance for the research objectives will establish priorities and an action list for the development and production of fluids and its variants. Those will be investigated and characterised closing the loop in the development cycle.

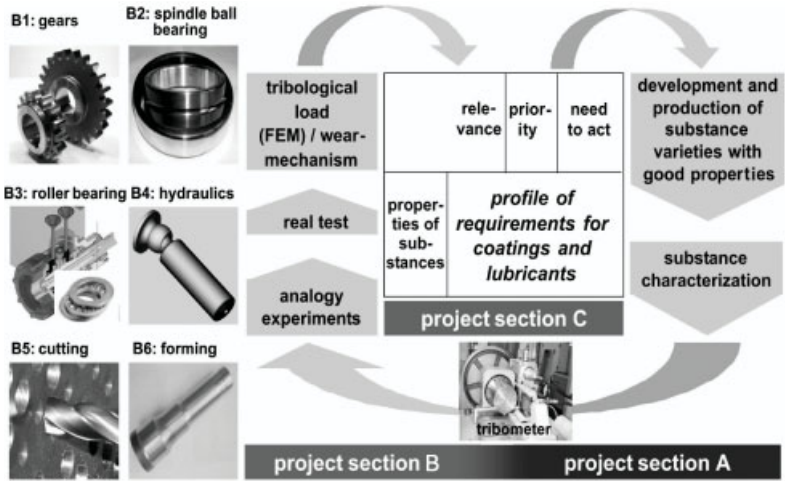


Figure 7: Cycles of research

Apart from providing the lubricating fluids for all sections of SFB 442, one of the main objectives of fluid development is to clarify the reaction and/or optimize the synthesis leading to the respective lubricants. In this respect, the synthesis process comprises two reaction stages. The first stage involves epoxidizing the double bond of the oleic acid methyl ester or glycerol trioleate by means of peracetic acid. The resulting epoxide is broken open during subsequent alcoholysis to produce the HISM or HIGTS lubricant, **Figure 8.** The HISM lubricant is customized to suit the pertinent application and unwanted by-products are reduced selectively by optimizing the synthesis process. The used educts consist of many methyl esters or trioleates, which means that the actual reaction is accompanied by numerous secondary reactions that exert a considerable influence on certain parts of the lubricating fluid synthesis process. In an effort to examine this extensive reaction system an analytical concept was established around gas chromatography as its core. This technique is capable of determining the composition and conversion level of the HISM lubricating fluid. The HIGTS is cracked by means of KOH/MeOH and carried over into a system similar to HISM, so that the composition and conversion level can also be determined here without the need for high-temperature GC. The typical characteristic values of lubricants,

such as acid number, iodine value or viscosity are also determined for a detailed characterization of the lubricating fluid. An in-line IR measuring technique that offers a means of monitoring the formation of precursors and products was developed in order to obtain more precise information concerning the progress of the reaction.

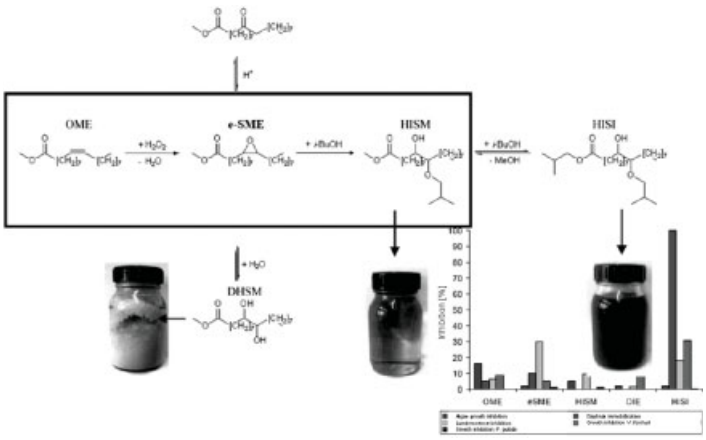


Figure 8: Development of HISM

Selective studies determine the effects of various influences and will be described in the project results belonging to the SFB 442 presentation.

For the development of PVD coatings two avenues were pursued. The first comprises component coating with low-temperature processes as shown in **Figure 9.** The graded zirconium carbide ZrCg (acc. to VDI 2840: a-C:H:Zr) coating system developed within the framework of SFB 442 belongs to the group of what are frequently referred to as Me-DLC coatings. Because of its low coefficient of friction, it is not only suitable for application to the components of Subprojects B1 (gear), B3 (rolling bearing) and B4 (hydraulic displacement unit), but also for such forming processes as the deep drawing of X5CrNi18-10 or backward cup extrusion of Al 99.5, as demonstrated by tests carried out within Subproject B6.

Chromium aluminium nitride (CrAlN) is another multilayer system (right part of **Figure 9**) that is suitable for a number of tribological components. The excellent adhesive strength, wear resistance capacity, resistance to alternating impacts, corrosion resistance and wettability of this system enable its use on such components as gears (SP B1), spindle bearings (SP B2) and rolling bearings (SP B3). Coating adhesion was improved considerably by using adhesion promoter layers during the second phase of the project. The scientists had not been able to lower the temperature to less than 200°C during the previous project phases, which was the reason why components tempered at high temperatures had to be used. In the course of the third project phase, pulsed power supplies made it possible to reduce the temperature to less than 200 °C in order to coat components tempered at low temperature and also offered a means of synthesizing a quasi-isotropic layer structure because of the high aluminium content.

The second path uses tool coating with high-temperature processes. Here Ti layers are build up which are mainly used in cold forming processes because of the required strength and wear

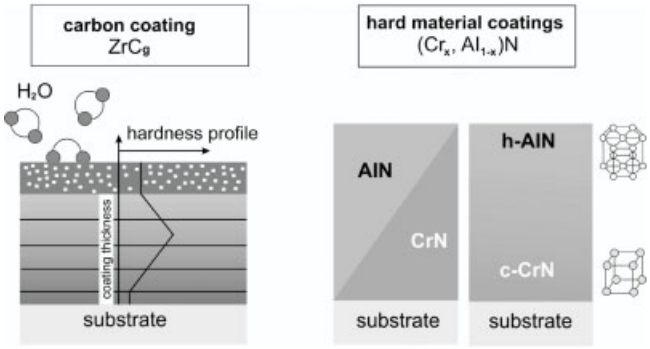


Figure 9: Low temperature coatings

resistance. In **Figure 10** three developed layers are depicted which are used in cold forming applications. Typical features are listed below each coating.

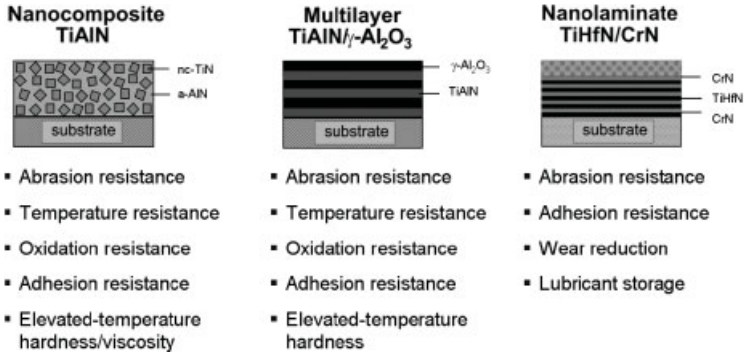


Figure 10: Ti - layers for high temperature processes

Main objective of the current project phase is to acquire a more detailed explanation of the coherence between the process parameters and the coating characteristics. The coating processes and the properties of the plasma in particular, undergo detailed analysis by means of process diagnostics within Subproject A2. The coating characteristics are then determined in Subproject A5 by means of highly precise techniques and the coherence between the process parameters and the coating characteristics is validated.

5 Highlights of the Current Research Phase

Detailed papers about results in the current research phase are provided by all subprojects and therefore do not need to be treated here. Developing the research phases as explained in chapter 2 and shown in **Figure 11** the first focus was directed towards models used in tribometer tests. The research then shifted to the components such as tools, pistons, gears and bearings.

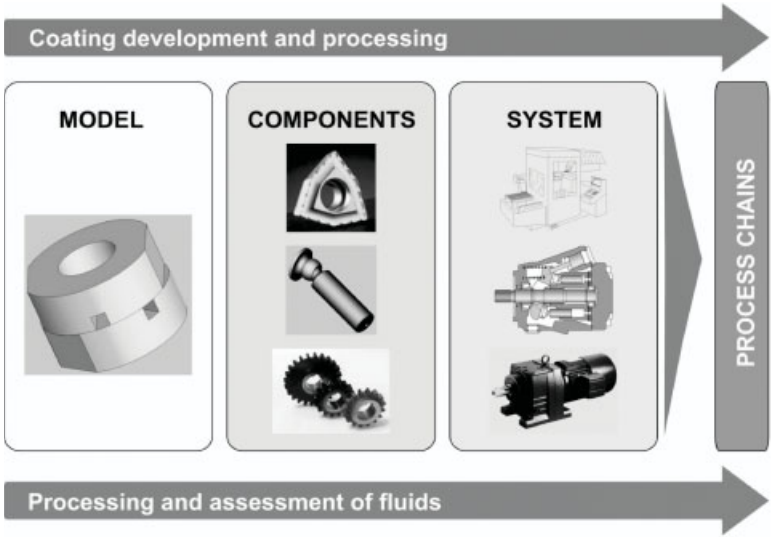


Figure 11: From model to system

Final research will concentrate on whole systems, e.g. machine tools in operation, piston units in hydraulic circuits and gear boxes. Development of PVD material coatings and fluids including its analysis will continue in phase. The validity of the SFB main idea will be verified in process chains.

An example can be seen in **Figure 12** where subproject results will be incorporated in a Chiron FZ22 machining centre.

This means that the performance of the developed tribological systems will be demonstrated in practical application by means of cutting materials with reference to real machining cycles and by means of the measurements and assessments made by the machining personnel. The work carried out within the individual subproject and the resulting SFB networking within the overall framework of the machine trials are outlined briefly below.

Implementation of the results of work performed within SP A2/A5 on the machine will take the form of coating the raceways of the spindle bearings with CrAiN and the bearing cages (PEEK) with ZrCg. Cutting tools will be optimized with multilayer TiAiN + g-Ai203 or nanocomposite TiAiN. Coating synthesis will be adapted to the changing requirements within Subproject A2. In this context, quality assurance for the coating processes implemented by Subproject A5 takes on major importance, particularly in the light of the growing number of components and tools to be coated. Focussing on the subject of synthesizing environmentally compatible lubricants and therefore providing the necessary lubricants for the machine and the cutting processes, SP A7's research work is directly connected to the work performed by SP A2/A5.

SP B2 will be equipping the main spindles and a feed shaft in the machine with the tribological systems that produced the best results on the test rig. Apart from coated spindle bearings, the traversing paths of the machine along the Z-axis are so short that ball screws and linear guides with PVD coatings from commercial suppliers will be used on this axis, as long as they demonstrate

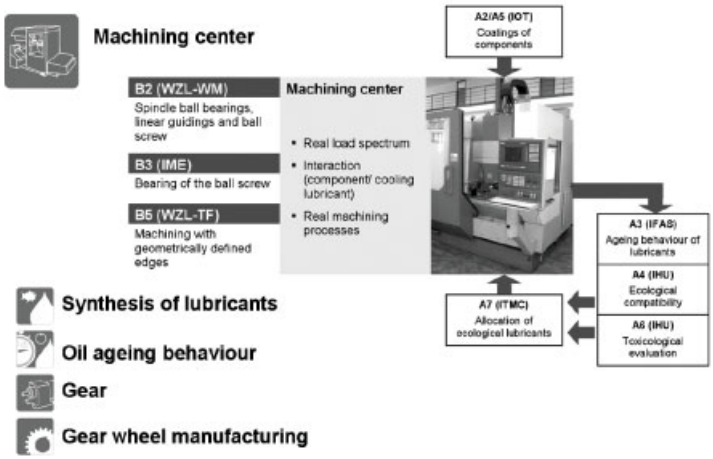


Figure 12: Integration of subprojects into a machine tool

sufficient potential during rig testing. Coated axial angular contact ball bearings from SP B3 will also be used in the machine's feed drive. These bearings often run through the mixed friction zone during the rapid starting and braking movements that characterize the operation of a cutting machine tool. Conventional rolling bearings therefore require lubricants with additives. These are substituted by the PVD coating in conjunction with environmentally compatible additive-free lubricants. The components will finally undergo practical trials in a real cutting process on an exemplified component made of tempering steel 42CrMo4+QT. The machining modes are milling and drilling, using tools that have been tested within SP B5 and have the high-performance coating systems (see above) developed within SP A2. Machining will be dry, with minimum quantity lubrication (HISM, SP A7).

Samples of the fluid will be taken continuously in the course of the manufacturing process on the machine and these samples will be examined with respect to their ecological compatibility and chemical composition within SP A4 and A6.

The outstanding wear characteristics and performance of the new tribological systems will therefore be verified under real machining conditions with the help of the demonstrator at the end of the project, proving that the SFB's objective of developing environmentally compatible tribological systems by means of suitable composite materials and has been achieved fully and completely and that the results of the work can be transferred into practical applications.

Further process chains that will be pursued in the concluding research phase are:

- gearbox process chain
- gear manufacturing process chain
- ageing test rig process chain
- lubricant synthesis process chain, ecological assessment, tribological appraise, use in the tribological system

As mentioned before the process chains are explained and discussed in detailed papers of the subproject and first results are introduced there.

6 Conclusion and Outlook

At the beginning of the concluding phase it was convincingly proven that the concept to locate functions of additives directly into the material surface is valid and carries a huge potential. A lot of new and highly innovative PVD coatings were developed as well as new processes to apply those on the base materials. Also the development of fluids and research into its analysis has made huge progress and the environmentally friendly esters are meanwhile used in components and systems.

The use of process chains to verify the results of the research within the framework of the collaborative research centre is actually intensively pursued and first feedbacks are promising.

For the outlook it is important to lay out how research results of 12.5 years are kept alive after the official ending of the funding period at the end of 2009.

The answer is explained with **Figure 13.** All results are fed into the expert system which will be updated and maintained by the interdisciplinary RWTH forums 'Material Sciences' and 'Environmental Sciences'. Most researchers and members of the SFB 442 are also members of these forums thus being able to carry the gained knowledge far into the future.

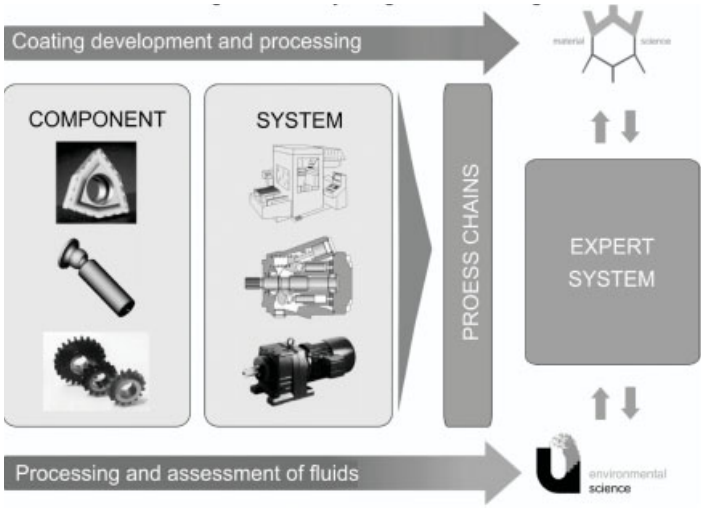


Figure 13: Outlook of the research work

7 Acknowledgments

The author gratefully acknowledges the financial support by the 'Deutsche Forschungsgemeinschaft' (DFG) within the collaborative research centre SFB 442: 'Development of Environmen-

tally Tribosystems by Suitable Coatings and fluids with respect to the Machine Tool' at RWTH Aachen University.

References

[1] Czichos H., Habig, K.-H., Tribologie Handbuch Reibung und Verschleiß, Vieweg, 2. Auflage 2003, ISBN 3-528-16354-2

[2] Gold, P.: Tribologie, Vorlesungsumdruck RWTH-Aachen, 2006

[3] Ostermeyer: Thesen zur Modellierung von Reibung und Verschleiß, Tribologie-Fachtagung "Reibung, Schmierung und Verschleiß", Göttingen, 2002

[4] Gesellschaft für Tribologie e.V.: Arbeitsblatt 7 Tribologie. Definitionen, Begriffe, Prüfung. Eigendruck der GfT e.V., Moers, 2002

[5] König, W., Klocke, F.: Fertigungsverfahren 1. Drehen, Fräsen, Bohren. 8. neubearb. Aufl., Springer, Berlin, 2006 (to be published in June)

[6] König, W., Klocke, F.: Fertigungsverfahren 4. Umformen. 5., revised edition, Springer, Berlin, März 2008, ISBN 978-3540234586

[7] Mang, T., Lubricants and Lubrication, WILEY-VCH,Weinheim, 2001

[8] Autorenkollektiv; Arbeits- und Ergebnisbericht zum SFB 442, RWTH Aachen, 2000

[9] Autorenkollektiv; Arbeits- und Ergebnisbericht zum SFB 442, RWTH Aachen, 2003

[10] General presentation of the SFB 442, 13th International Colloquium Tribology, Esslingen, 2002

[11] Autorenkollektiv; General presentation of the SFB 442, DGM - Tagung, 'Reibung und Verschleiß' 10.–12. März 2004, Fürth

[12] Autorenkollektiv; General presentation of the SFB 442, 15th International Colloquium Tribology, Esslingen, 2006

[13] Wagner Helena, Rolf Luther, Theo Mang, Lubricant base fluids based on renewable raw materials: Their catalytic manufacture and modification, Appl. Cat. A, 2001, 221, 429–442

[14] Stephen M. Hsu, Molecular basis of lubrication, Tribology International (2004), 37(7), 553–559.

[15] Gerard Hillion, David Proriol, Synthesis of a high-grade lubricant from sunflower oil methyl esters, Oleagineux, Corps Gras, Lipides (2003), 10 (5–6), 370–372

[16] Jonathan Filley, New lubricants from vegetable oil: cyclic acetals of methyl 9,10-dihydroxystearate, Bioresource Technology 96 (2005) 551–555

[17] Murrenhoff und SFB Mitglieder, Forschungsantrag zum SFB 442 (2007 - 2009, RWTH Aachen 2006

Epoxidation of Oleic Esters for the Synthesis of Environmentally Friendly Lubricants

M.J.S. Küppers, D.H. Müller, F. Pontzen, D. Herzog, M.A. Liauw, L. Greiner
RWTH Aachen University, Aachen

Abstract:
An environmentally friendly lubricant system was developed. The synthesis could be optimized by means of Reaction Calorimetry. First steps towards a continuous production in micro scale were accomplished.

1 Introduction

This work is part of the collaborative research center 442 (CRC 442). The aim of this CRC is to realize a tribosystem based on renewable resources without additivation. Therefore a route to synthesize an environmentally benign lubricant in a two-step-synthesis was established. This lubricant will be used in machine tools without or with less additivation. The problem of commercially available lubricants is the possible toxicological harm for the user who gets into contact with the oil and the ecological problems caused by loss lubrication. Therefore, the main idea of the CRC 442 is, to transfer the additives' task to the machine tool materials and their coatings.

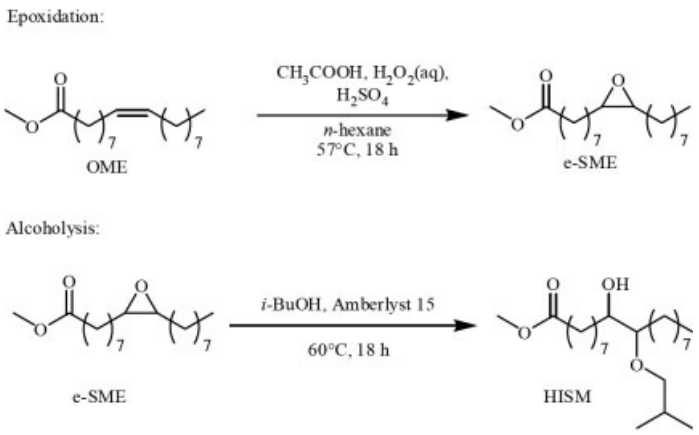


Figure 1: Reaction steps of the lubricant synthesis from OME via e-SME to HISM

As shown in Figure 1, the lubricant-synthesis consists of two steps: the epoxidation of oleic acid methyl ester (OME) to 9,10-epoxy stearic acid methyl ester (e-SME) and the subsequent alcoholysis of the e-SME to 9(10)-hydroxy 10(9)-isobutoxy stearic acid methyl ester (HISM). The first approach towards the synthesis and application for lubrication was performed by Hölderich *et al.* [1] in the first two periods (6 years) of this CRC. They chose the *in situ* generated peracetic acid as the epoxidizing agent. This peracetic acid is generated by acetic acid and a 35% aqueous

solution of hydrogen peroxide in the presence of a catalytic amount of sulphuric acid [2] which means that the first step proceeds in a biphasic system. Therefore, the system can be limited by mass transfer. The second step of the lubricant synthesis is the alcoholysis with *iso*-butanol. This step is catalyzed heterogeneously with the acidic ion-exchange-resin Amberlyst 15 (Rohm & Haas).

2 Established Procedure for the Lubricant Production

The starting material for this synthesis is technical grade OME which contains about 70% OME (C18:1, 18 carbon-chain with one double bond). It also contains the saturated esters C14:0, C16:0 and C18:0 as well as the unsaturated compounds linoleic (C18:2, 11%) and linolenic acid methyl ester (C18:3, 1–2%). These unsaturated compounds can react in the same way as the monounsaturated OME and the product of this reaction is a mixture of different compounds. The target product that should be produced most during the reaction is HISM.

The synthesized lubricant oils are characterized with the help of gas chromatography. Additionally the key data for the lubricants (saponification number, iodine number etc.) is determined in order to guarantee a consistent composition of the oils. Since the pour point is an important and characteristic number for lubricants, we investigated the correlation between the pour point and melting/crystallization point determined by differential scanning calorimetry (DSC). This tool offers the possibility to measure crystallization and melting points very precisely. We could show that the pour points match quite well the results determined by DSC (Table 2).

Composition, ecological and toxicological aspects of the produced oil batches are investigated at the institute for hygiene and environmental medicine (IHU). With this information the reaction can be further optimized. The aim of this CRC is an integrated process development including not only chemical aspects (selectivity, yield) but also environmental such as degradability and toxicity.

2.1 Synthesis

The lubricant synthesis was established by Hölderich *et al.* The reaction is performed in a 25 L batch-reactor. S. Eichholz optimized the reaction during his work at this institute. The reaction conditions he chose were a reaction time of 18 hours at 57°C and a stirring speed of 400 rpm [3]. At this time, a maximum of epoxide was formed with only a small amount of the consecutive hydrolysis reaction. After a phase separation, the aqueous layer is separated from the organic. The epoxide is washed with water for three times and the solvent *n*-hexane is distilled off. After that, the mixture of Amberlyst 15 (10 mass-%) and *iso*-butanol (5 eq.) is added to the epoxide. This mixture is stirred for another 18 hours at 60°C with 400 rpm. After completion of the reaction, Amberlyst 15 is filtered off the product mixture and the excess *iso*-butanol is distilled off. Eichholz *et al.* showed that sulphur-containing components leached from the catalyst which had to be separated from the product by steam stripping. This treatment hydrolyzed non-reacted epoxide as well. Three consecutive runs of steam stripping reduces both acid and epoxide value below the toxicologically significant threshold value (as verified by IHU). With this procedure performed in pilot-plant scale it is possible to run two batches per week, which is a total production of 25 L/w.

2.2 Properties of the Synthesized Lubricants

The synthesized lubricants are characterized concerning their properties such as viscosity and the key data of the lubricants. Figure 2 shows samples of the starting material, the intermediate product and the lubricant, respectively. The starting material is a light yellowish, the intermediate product a colourless and the lubricant a light brownish liquid.

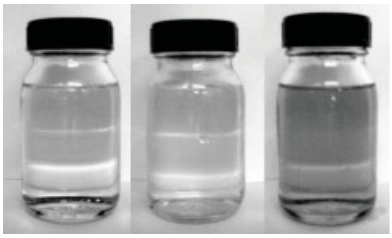


Figure 2: Samples of OME, e-SME and HISM (from left to right)

Table 1 shows the typical key data for the different compounds. The saponification number (correlated with the amount of esters) does not change during the synthesis because the ester group does not react in any way during the synthesis. The iodine number shows the degree of unsaturation. The starting material has the highest degree of unsaturation and the product the lowest, in the ideal case there should be no unsaturated position left in the product. The viscosity increases during the reaction from about 5 to 20 mm²/s due to the rising steric demand, molecular weight and polarity of the molecule.

Table 1: Typical key data for the starting material, the intermediate product and the lubricant

compound	saponification number [mg KOH/g]	iodine number [g Iodine/100 g]	viscosity at 40°C [mm²/s]
OME	58.4	88.5	4.7
e-SME	59.0	7.7	9.4
HISM	59.6	1.9	21.3

Table 2 shows the determined pour points and crystallization points determined by DSC. For the batches 157 and 159 pour point and crystallization temperature do not match as well as they do for the batches 161-165. A reason for this could be that the batches 161-165 were measured only a short time after their production while batches 157 and 159 were about 6 months old when the measurement was carried out.

Table 2: Crystallization temperatures and Pour Points of different lubricants

Lubricant	157.X.O.HISM	159.X.O.HISM	161.X.O.HISM	163.X.O.HISM	165.X.O.HISM
Crystallization temperature [°C]	–22.7	–22.1	–29.4	–26.9	–33.5
Pour Point [°C]	–9 ± 1.5	–9 ± 1.5	–33 ± 1.5	–18 ± 1.5	–33 ±1.5

3 Process Optimization of the Epoxidation of OME by means of Reaction Calorimetry

With the use of less or no solvent downstream processing is much simplified and waste is avoided. Since the results for solvent-free conditions were comparable or even better than for standard conditions, all following reactions were carried out without additional organic solvent.

Reaction Calorimetry (RC) is a useful tool for the direct investigation of kinetics as well as thermodynamics of chemical reactions [4]. The measured signal, the heat flow (QP), is directly proportional to the reaction rate ($QP \propto r_i$) with the molar reaction enthalpy ΔH_m as proportionality constant. QP therefore is a differential signal as opposed to concentrations or common spectroscopic signals, which are integral signals. By integration of the total heat flow the molar reaction enthalpy can be determined ($\Delta H_m \propto \int QP\, dt$).

Although QP incooperates all reactions occurring in the reaction volume at the same time, in many cases this signal gives very exact information about the reaction, which are necessary for a complete understanding of the process.

RC could be used for the investigation of the kinetics of the epoxidation of methyl oleate in a biphasic system containing OME and an aqueous solution of hydrogen peroxide, acetic and sulphuric acid. The aim of the investigations was to characterize the reaction kinetics as well as the influence of mass transfer. Due to the high viscosity of OME as well as limited solubility of the reactants in the substrate phase, the reaction was expected to be strongly influenced by mixing efficiency.

In order to prove this, a variation of temperature (50–90°C) and stirring speed (200–400 rpm) was done. In addition to the measurement of QP, GC analytics were used to investigate the chemical composition of the products. As measure for the reaction rate a 90% criterion (time until 90% conversion is reached), which was determined by a combination of RC and GC, was chosen.

The reaction is strongly exothermic with a mean adiabatic temperature rise of 99 ± 19K. The mean molar reaction enthalpy was 236 ± 25 kJ mol^{-1} with a good reproducibility.

3.1 Variation of Temperature

As shown in Figure 3 an increase in temperature leads to a decrease of the 90% criterion. Reaction times thus can be reduced 4 fold (18h at 60°C; 4h at 80°C).

Obviously the temperature dependence of the reaction kinetics cannot be described by a simple Arrhenius approach, which is mainly caused by the additional influence of mass transfer.

Surprisingly the selectivity of the epoxidation towards e-SME is nearly independent of the reaction temperature. A comparison shows that in all cases high conversions (95%) and good selectivities (85–86%) are obtained at 60°C standard conditions as well as at higher temperatures. This was found to be the case in 1 L as well as in 25 L scale.

3.2 Variation of Stirring Speed

As shown in Figure 3 the reaction rate is dependent on the stirring speed. Obviously the dependence is negligible for temperatures >80°C but significant for temperature <80°C. At 60°C an increase in stirring speed from 300 to 400 rpm leads to a 20% smaller 90% criterion.

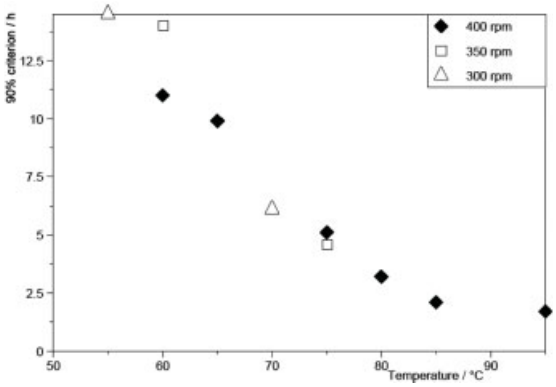


Figure 3: Dependence of 90% criterion on temperature and stirring speed.

For 85°C the decrease of 90% criterion is <5% when increasing stirring speed from 300 to 400 rpm. This can be explained by the fact that the viscosity of OME strongly decreases with increasing temperatures. This leads to an enhanced mass transfer by diffusion resulting in a weaker effect of stirring speed on reaction rate.

4 Continuous Epoxidation

The calorimetric measurements clearly indicated that higher reaction temperatures (>70°C) as well as more intense phase contact are beneficial for the productivity of the reaction. One possibility to improve both factors is the use of micro reaction technology [5]. Plug flow is favourable as the overall reaction rate and selectivity will be highest. A high surface to volume ratio is favourable in view of heat transfer to contain the exothermicity. Furthermore, good mass transfer can be obtained in the slug flow regimes in micro structured reactors.

In view of continuous reaction matching best conditions to the right reactor was carried out. As the above mentioned aims are best obtained in micro reactors the continuous reaction in a plug flow reactor was chosen. For good mixing a static micro mixer tee and as reaction way a coiled and thermostated FEP tube is used.

One example of an epoxidation reaction in the continuous reactor is show in Figure 4. At 60°C full conversion can be reached after a residence time of 10h. Here the flow rate was 2mL/h. Without optimization in this scale, the reaction is twice as fast as in the batch process [6]. By optimization of parameters like temperature or stoichiometry it is possible to shorten reaction time even further. At 90°C the reaction is almost complete within 0.5 h residence time, which was already indicated by RC investigations.

The results show the large potential of micro reaction technology for the present system leading to higher selectivities and productivities and a better control over the reaction conditions.

In order to obtain comparable amounts of lubricant compared to the batch process, the micro process has to be numbered up 4 fold approximately at best reaction conditions. Thus a fully automized process can be developed for the continuous production of the lubricant.

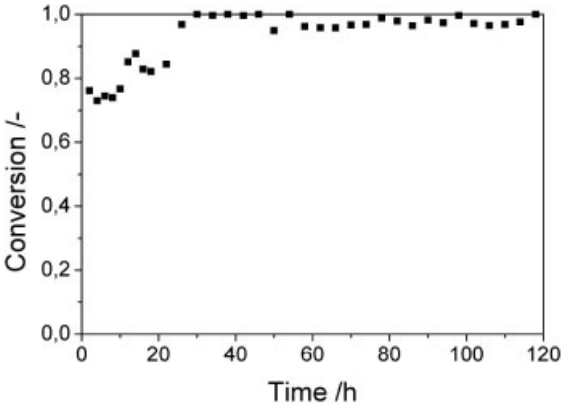


Figure 4: Example for a continuous epoxidation at 60°C, 10 h residence time

Acknowledgements:
We want to thank the company HiTec Zang for the reaction calorimeter and Mrs. I. Glowaki for the determination of the lubricants' key data. Financial support by the German research foundation (DFG) is gratefully acknowledged.

5 References

[1] L.A. Rios, P.Ph. Weckes, H. Schuster, H. Hausmann, W.F. Hoelderich, *Appl. Catal. A*, 253, 487–497, **2003**.

[2] F. P. Greenspan, R.J. Gall, *In situ epoxidation of organic esters with sulphuric acid and acetic acid*, USP 2,801,253 **1953**.

[3] S. Eichholz, *Dissertation*, RWTH Aachen University, Germany, **2007**.

[4] R. N. Landau, *Thermochim. Acta*, *289*, 101-126 **1996**.

[5] K. Jähnisch, V. Hessel, H. Löwe, M. Baerns, *Angew. Chem. Int. Ed.*, *43*(4), 406–466, **2004**.

[6] P. P. Weckes, *Dissertation*, RWTH Aachen, **2003**.

How Friction and Ageing Influence the Toxic and Ecotoxic Behaviour of Used, Bio-based Lubricants

J. Bressling[1], O.-C. Göhler[2], C. Bugiel[3], W. Dott[1], B. Erlenkämper[1/4*]
[1] Institute of Hygiene and Environmental Medicine, RWTH Aachen, Germany
[2] Fluidtronics GmbH, Krefeld, Germany
[3] Vestas Nacelles Deutschland GmbH, Dortmund, Germany
[4] EvonikDegussa GmbH, Hanau (Wolfgang), Germany
[*] Corresponding author (bibiane.erlenkaemper@ipw-rheinmain.de)

1 Introduction

Lubricants are used for reducing friction and wear in various technical applications like engines, hydraulic systems, gears or metal working processes. They consist of a base fluid and a variety of additives including anti-wear additives, antioxidants and corrosion inhibitors in order to enhance the technical performance and the lifetime of the lubricant by protecting it against oxidation and hydrolysis. More than 90% of the base fluids are mineral oils, a complex mixture containing varying portions of aliphatic, cycloaliphatic and aromatic hydrocarbons. Since the sensibility with respect to the environment has increased, nowadays lubricants have to fulfil ecological as well as technical requirements. Thus the development of lubricants based on renewable resources has gained more and more attention during the last years due to their low ecotoxicological impact.

The collaborative research centre "SFB 442" was established at the RWTH Aachen University in July 1997 to develop new environmentally friendly tribosystems and lubricants which facilitate the avoidance of additives by transferring their functions to suitable coatings of the tool. These ester based lubricants are a promising alternative to lubricants made of mineral oils for use in machine tools. In combination with specifically designed coatings for tools and components, the use of additives can be avoided. For optimizing the newly developed bio-based lubricants, named hydroxy isobutoxy glycerine tristearate (HIGTS) and hydroxy isobutoxy stearic acid methyl ester (HISM), their environmental characteristics have to be considered as well as the technical properties of the fluid before and during usage. The use may influence their composition and thereby ecotoxicity of the lubricants. Metals are transferred to the lubricants by abrasion and organic compounds are changed by high pressure and high temperatures.

In the following study the new lubricants were tested as a mixture in a tribological test bench with coated and uncoated gears and in an oxidation test bench without gears. It should be cleared if only the intake of metals has an influence on the ecotoxicological behaviour or ageing is another cause for the increasing toxicity after usage.

2 Materials and Methods

2.1 Samples

The lubricants hydroxy isobutoxy glycerine tristearate (HIGTS) and hydroxy isobutoxy stearid acid methyl ester (HISM) were mixed at a ratio of 65:35 v/v to achieve the technically required

kinematic viscosity of 100 mm^2/s. The lubricant mixture of "HIGTS/HISM" was tested in two different test benches.

2.2 Test Benches

2.2.1 Scoring test

The scoring test on a back-to-back test rig with uncoated and CrAlN coated gears according to DIN 51354 Part 1 was used to examine possibly developing scuffings [1]. Samples were taken at load stage (LS) 12 for the uncoated gears and at load stages 8 and 12 for the gears coated with CrAlN as described by Erlenkaemper et al. [2].

Table 1: Test conditions for the back-to-back test rig

	Scoring test
Lubrication	2 l splash lubrication
Load	Hertzian stress 147 to 1841 N/mm^2
Time	12 load stages (LS) à 15 min
T [°C]	90 ± 3

2.2.2 Oxidation Test

A modified Rotary Bomb test was used, to characterize the lubricant mixture HIGTS/HISM regarding their oxidative stability according to the procedure described by Goehler et al. [3]. The oil sample was put into a rotating and sealed container with an oxygen atmosphere of 6.25 bar and at 120 degrees. A metal coil catalyst can be added to the sample. As a result, this test provides the life time of the oil indicated by the time needed for a pressure drop of 1.75 bar from the pressure maximum. In order to focus on the oxidative stability and not on the hydrolysis of the ester, no water was added to each sample.

2.3 Preparation of Water Soluble Fractions (WSF)

Water extractions of the oil samples were performed according to the procedure described by Maxam et al. [4]. A mixture of oil fluid and Millipore™ water (ratio 100 g + 1 L) was agitated overhead for 24 h in dark DURAN™ glass bottles (Schott, Mainz, Germany). The aqueous extract was filtered with a glass fibre filter (pore size 1 µm, Gelman Sciences, Michigan, USA) after separation of phases over night. The pH-value and conductivity were measured electrochemically. The oily phase was ignored. Ecotoxicological testing was performed within 14 days with a dilution series of the WSF. The samples were stored at 4 °C in dark DURAN™ glass bottles in order to avoid photochemical reactions. For the 100 g/L water fractions effective loading rates (EL_{50}-values in % of the eluate) were calculated by means of probit transformation.

2.4 Chemical Characterisation of the Aqueous Extracts

Concentrations of the metals copper, zinc, iron, chromium and nickel were determined with inductively coupled plasma mass spectrometry (ICP-MS, Elan DRC II, Perlin Elmer SCIEX, Wellesley, USA).

2.5 Bioassays

Bacterial growth inhibition assays with *Vibrio fischeri* and *Pseudomonas putida* were performed using microplate photometers and incubators (IEMS-readers, Labsystems, Finland). The final test volume was 200 µl/well. The microplate photometers were placed in cabinets (Infors, Bottmingen, Switzerland) for cooling. The tests were performed at 20 °C (*V. fischeri*) and 21 °C (*P. putida*), according to standard test procedures [5, 6]. Each dilution of the water extract, the growth controls, and the blanks were tested in three replicates. For the acute luminescence inhibition assay with *V. fischeri* two replicates were tested [7]. Contrary to the standard test procedures cold-stored cultures of *V. fischeri* and *P. putida* cells were used for inoculation.

Algae growth inhibition tests with *Desmodesmus subspicatus* and immobilisation tests with *Daphnia magna* were performed according to standard procedures [8, 9]. The water extracts of the lubricant samples, the controls and the blanks were tested in three (algae) and four (daphnia) replicates respectively.

3 Results

3.1 Scoring Test

3.1.1 Aquatic toxicity of used lubricant mixtures

In addition to toxicity tests with newly synthesized lubricants the changes caused by application of lubricants in a tribological test bench were investigated. For the comparison of changes by usage the unused lubricants were also tested. The results for the 100 g/L aqueous extracts are presented in **Table 2** as already shown by Erlenkaemper et al. [2].

Table 2: EL_{50}-values [%] of 100 g/L eluates of used lubricants, lowest values are bold

sample	Algae growth inhibition	Daphnia immobilisation	Luminescence inhibition *V. fischeri*	Growth inhibition *V. fischeri*	Growth inhibition *P. putida*
HIGTS/HISM unused	**20.5**	24.1	10.4	26.5	> 50
HIGTS/HISM used LS 8 coated	35.5	33.1	7.5	23.3	30.4
HIGTS/HISM used LS 12 coated	47.6	32.9	6.7	34.2	**16.8**
HIGTS/HISM used LS 12 uncoated	24.4	**20.7**	**5.8**	**20.1**	17.3

All lubricants used in the scoring test on a back-to-back test rig showed a decrease in toxicity towards algae (**Table 2**). While HIGTS/HISM used with uncoated gears and taken at load stage 12 showed only a slight decrease, the two samples with coated gears showed a larger decrease in toxicity. The results for the toxicity test with daphnia showed a clear difference for the use of coated and uncoated gears. For HIGTS/HISM used with uncoated gears toxicity towards daphnia

increased slightly while both samples of HIGTS/HISM used with coated gears exerted less toxic effects on daphnia.

Values for the *V. fischeri* luminescence inhibition assay, as the most sensitive test in this context, were approximately equal (5.8 % to 7.5 %) and showed an increasing toxicity compared to the unused lubricant. For the *V. fischeri* growth inhibition assay the samples taken at load stage 12 (uncoated gears) and load stage 8 (coated gears) showed similar EL_{50}-values below the values of the unused lubricant. The lubricant taken at load stage 12 and used with coated gears was less toxic compared to the unused fluid. In contrast to the toxicity towards algae and daphnia, the *P. putida* growth inhibition assay whereas both samples taken at load stage 12 were more toxic than the sample taken at load stage 8. There were no toxic effects for the unused lubricant at maximum test concentration (EL_{50}-value > 50 %).

3.1.2 Metal Content of Used Lubricant Mixtures

Due to the fact that the lubricants were used in a tribological test system where they were exposed to different metallic materials the metal concentrations in the water extracts were analysed. These analyses might also support the toxicity identification. The metal concentrations in the aqueous extracts were determined with ICP-MS as described in 2.4. Results of this analysis are given in **Table 3** as already shown by Erlenkaemper et al. [2].

Table 3: Metal content of 100 g/L eluates [µg/L], highest concentrations are bold

sample	Cu	Zn	Fe	Cr	Ni
HIGTS/HISM unused	11.49	73.8	1.69	9.5	5.32
HIGTS/HISM used LS 8 coated	174.9	**275.8**	23.97	**15.38**	**9.26**
HIGTS/HISM used LS 12 coated	213.5	136.3	36.21	11.32	7.23
HIGTS/HISM used LS 12 uncoated	**263.4**	157.5	**53.62**	11.81	9.03

In all water extracts the content of metals increased after usage. The concentrations of copper, zinc and iron were significantly increased. Copper concentration was increased from 11.49 µg/L to a maximum of 263.4 µg/L and zinc from 73.8 µg/L to a maximum of 275.8 µg/L. The concentration of iron was significantly lower with maximum values of 53.62 µg/L for the used lubricants. The values of chromium and nickel were also lower with maximum concentrations of 15.38 µg/L chromium and 9.26 µg/L nickel in the used fluids at load stage 8. These values were not much different from the values of the unused fluid.

3.2 Aquatic Toxicity of Lubricant Mixture after Oxidation Test

Beside the intake of metals in the oil, changes of the lubricants itself may also lead to a change of the ecotoxicological behaviour. This so-called oil ageing is caused amongst others by oxidation processes. To examine this influence, the lubricant mixture of HIGTS/HISM was tested in the oxidation test. Results for the 100 g/L aqueous extracts are presented in **Figure 1**.

After the oxidation test with HIGTS/HISM a clear increase of the toxic effects was observed in all ecotoxicity tests because all EL_{50}-values were less than 10 %. Before the oxidation test HIGTS/HISM showed no toxic effect in the daphnia immobilisation assay as well as in both

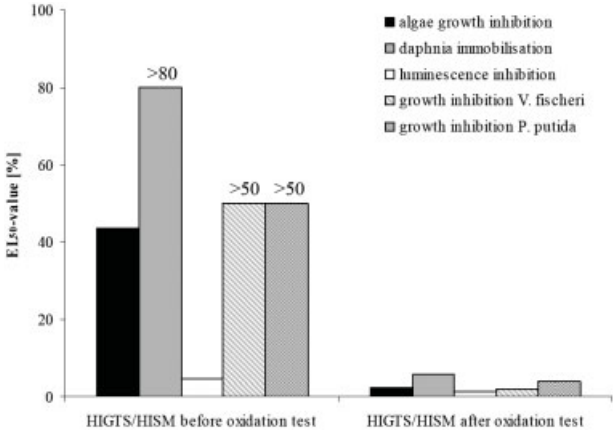


Figure 1: EL_{50}-values [%] of 100 g/L eluates before and after oxidation test

growth inhibition assays at maximum test concentrations. The most sensitive test was the luminescence inhibition assay whose toxic effect was still strengthened by usage.

4 Conclusion

Tests with used lubricants demonstrate that application in tribological systems not necessarily increases the measurable toxicity of a lubricant via bioassays (e.g. EL_{50}-values for algae growth inhibition assay and daphnia immobilisation assay, **Table 2**).

Furthermore the results clearly indicate that the abrasion of metallic particles during use leads to the intake of water soluble metal elements. These metals are available for uptake and accumulation in aquatic organisms. Nevertheless, there is no link up with lowest EL_{50}-values and highest metal concentrations in all used fluids taken at load stage 12. Moreover the artificially aged sample in the oxidation test clearly showed the influence of the oxidation on the ecotoxicological behaviour after usage. This emphasizes the statement of the metal investigations that they are not the only reason for toxic effects of used lubricants. Ageing of the lubricant itself and limited bioavailability of metals might be another explanation for negative changes in ecotoxicological behaviour.

These results underline the necessity for ecotoxicological tests in collaboration with chemical analysis of unused and used fluids since the ecotoxicological behaviour cannot be predicted by chemical analysis only.

5 Acknowledgements

This work is supported by the Deutsche Forschungsgemeinschaft (DFG): SFB 442 “Environmentally friendly tribosystems by suitable coatings and fluids with respect to the machine tool”, subproject A4 “Methods and strategies for the risk assessment of tribological systems referring to

ecology". The lubricants are synthesized and provided by the Institute for Technical and Macromolecular Chemistry (ITMC) of the RWTH Aachen. Lubricant mixtures are tested by the Laboratory for Machine Tools (WZL) and by the Institute for Fluid Power Drives and Controls (IFAS) of the RWTH Aachen. The authors want to thank Anne Rix and Sven Thoröe for their technical support.

6 References

[1] DIN 51354-1: Prüfung von Schmierstoffen; Prüfmaschine, **1990**, Deutsches Institut für Normung e.V., Beuth Verlag GmbH, Berlin.

[2] Erlenkaemper, B.; Dott, W.; Brinkmann, C.; Eisentraeger, A.: Consideration of toxicological aspects in the development of lubricants based on synthetic esters and their changes by usage: Proceeding of 15th International Colloquium Tribology, Automotive and Industrial Lubrication, January 17–19, **2006**, Stuttgart, Ostfildern.

[3] Goehler, O.-C.; Schmidt, M.; Murrenhoff, H.: Modelling the ageing behaviour of new environmentally friendly fluids using correlation analysis and neural networks: Proceeding of International Mechanical Engineering Congress and RD&D Expo (IMECE), November 13-19, **2004**, Anaheim, California.

[4] Maxam, G.; Hahn, S.; Dott, W.; Eisentraeger, A.: Assessment of the Influence of Use on Ecotoxicological Characteristics of Synthetic Ester Lubricants: Ecotoxicology, 11, **2002**, 349–355.

[5] DIN 38412 L37: Deutsche Einheitsverfahren zur Wasser-, Abwasser- und Schlammuntersuchung, Testverfahren mit Wasserorganismen (Gruppe L), Teil 37: Bestimmung der Hemmwirkung von Wasser auf das Wachstum von Bakterien (Photobacterium phosphoreum – Zellvermehrungs-Hemmtest), **1999**, Deutsches Institut für Normung e.V., Beuth Verlag GmbH, Berlin.

[6] ISO 10712: Water Quality - Pseudomonas putida growth inhibition test (Pseudomonas putida multiplication inhibition test), **1995**, International Organization for Standardization, Genf, Schweiz.

[7]]ISO 11348-1: Water Quality - Determination of the inhibitiory effect of water samples on the light emission of Vibrio fischeri (Luminescent bacteria test) – Part 1: Method using freshly prepared bacteria, **1998**, International Standard, Genf, Schweiz.

[8] DIN 38412 L33: Deutsche Einheitsverfahren zur Wasser-, Abwasser- und Schlammuntersuchung, Bestimmung der nicht giftigen Wirkung von Abwasser gegenüber Grünalgen (Scenedesmus-Chlorophyll-Fluoreszenztest) über Verdünnungsstufen, **1991**, Deutsches Institut für Normung e.V., Beuth Verlag GmbH, Berlin.

[9] ISO 6341: Water Quality - Determination of the inhibition of the mobility of Daphnia magna Straus (Cladocera, Crustacea) - Acute toxicity test, **1996**, International Organization for Standardisation, Genf, Schweiz.

Characterization of Substantial Changes of Different Native Ester-based Lubricants Before and After Tribological Application

S. Michael [1], K. Bobzin [2], A. Krämer [2], W. Dott [1], H. Maier [1]*
[1]Institute of Hygiene and Environmental Medicine, RWTH Aachen, Germany
[2]Institute of Surface Engineering, RWTH Aachen, Germany
*e-mail: heiko.maier@rwth-aachen.de

1 Introduction

Lubricants are widely used in industrial applications to minimize friction and wear in different technical systems, predominantly in combustion engines, hydraulic systems, gears, or metal forming processes. Traditionally lubricants consist of petrochemical products and various supplementary additives to improve their technical performance. Due to losses, e. g. loss lubrication or leakage, large amounts of lubricating oils reach in the environment. These entries occur in terrestrial and aquatic environmental systems. With respect to their ecotoxicity and restricted availability, petrochemicals constitute non-contemporary lubricants. Native or synthetic esters, derived from renewable resources, demonstrate an emerging alternative to established mineral oil products. The development of such lubricants with well biodegradable, non-genotoxic and excellent tribological properties are the main intention of the collaborative research centre “SFB 442”. Furthermore the avoidance of additives by transferring their function to suitable coatings of tools is an important part of the lubricant design. Thus the newly developed ester lubricants have to fulfill technical performance needs as well as environmental characteristics.

The aim of this study is comparing substantial changes of herbal and animal based lubricants with respect to their application. Therefore the influence of usage on the composition of ester-based lubricants was monitored from the synthesis to tribological application.

In a two step synthesis, analyzed lubricants were produced from herbal and animal oleic acid methyl ester (OME) to the low viscous lubricant hydroxy isobutoxy stearic acid methyl ester (HISM). Throughout their application mechanical, thermal and chemical effects are able to transform the ecological-toxicological properties of the oil. The usage of lubricants in machine tools causes an intake of metals due to abrasion from the surrounding components. In this study friction and wear are achieved in a pin-on-disc tribometer test, followed by the monitoring substantial changes of lubricant in analytical methods and biological screenings. The aim of this project is the development of sustainable lubricants [1].

2 Methods

2.1 Samples

All lubricants were produced and provided by the Institute for Technical and Macromolecular Chemistry (ITMC) of the RWTH Aachen. Lubricants were synthesized in a two step process from

herbal and animal oleic acid methyl ester (OME). In the first step, the double bond was epoxidized using hydrogen peroxide, sulphuric acid and acetic acid in hexane. Subsequently alcoholysis with *i*-butanol transformed the intermediate into hydroxy isobutoxy stearic acid methyl ester (HISM).

2.2 Pin-on-disc Test

The degree of the changes due to the usage of the lubricant was observed in pin-on-disc tests (CSM Instruments) described by Bobzin et al [2]. The test parameters were chosen as followed: surrounding atmosphere (23 ± 2 °C, 40 ± 5 % relative humidity) and lubricated running condition at a load of 15 N. 100Cr6 balls of 6 mm in diameter were used as counterparts for chromium aluminium nitride (CrAlN 2054) coated 100Cr6 discs. The test length was 1000 m at a track diameter of 5 mm. The test speed was set on 3 cm/s. About 63.500 overruns per point were reached. The lubricated wear tests were performed at room temperature (RT) and at 90 °C.

2.3 GC-Analysis

Identification of the several HISM components was realized on a Hewlett Packard 5890 series II gas chromatograph interfaced with a HP 5972 mass detector (GC-MS) with a mass range of m/z 45-450. The gas chromatograph was equipped with a unpolar column (Restek, Rxi-5ms, 30 m x 0,25 mm ID, 0,25 µm d_f). Quantitative analysis of the low viscous lubricant HISM was performed (GC-FID) on a Hewlett Packard 5890 series II gas chromatograph equipped with a flame ionisation detector (FID) and a Rxi-5ms column (Resteck, 60 m x 0,25 mm i.d., 0,25 µm d_f). The sample was diluted in methylene chloride and injected into a Hewlett Packard 7673 injector. Helium gas 5.0 was used as the carrier gas. The pre column pressure was constant at 195 kPa. The samples were introduced using the splitless mode. The injector temperature was set at 300 °C. The GC oven temperature was gradually increased from 30°C to 150 °C (both 0,01 min isotherm) and maintained at 300 °C for 4 min with a total runtime of 54 min. The flame ionisation detector was operated at 3000 °C throughout the analysis [1].

2.4 ICP-MS

The element-specific detection was performed with an ICP-MS System Elan DRC II (Perkin Elmer SCIEX, Wellesley, MA, USA) equipped with a quadrupole mass spectrometer. The detection parameters were the following: rf power 1100 kW, plasma gas flow 15 L min^{-1}, auxiliary flow 1.1 L min^{-1}, nebulizer gas flow 0.88 L min^{-1}. Metal concentrations were quantified using multi element calibration standards (Merck KgaA, Darmstadt).

2.5 *umu*-Genotoxicity test

The *umu* assay for measuring DNA damage by means of SOS induction was carried out according to the procedure described previously by Oda et al. and Reifferscheid et al [3, 4]. The test was performed with *Salmonella choleraesius subsp. chol.* TA1535/pSK100 in 96-wells mircoplates according to ISO 13829 [5]. Deviating from the ISO 13829 the samples were extracted in 100% DMSO and introduced as a 4% DMSO-extract in the test system. The extent of induction of the SOS-repair system, indicated by β-galactosidase units which result in the induction rate (IR). According to the standard (ISO 13829), a sample was supposed to be genotoxic if this induction

rate exceed 1.5. For the environmental samples, the first dilution with an induction rate below 1.5 and a growth factor exceeding 0.5 is presented (Lowest ineffective dilution: D_{LI}-value).

2.6 Biodegradability test

The combined biodegradability test system "O_2/CO_2 headspace test with GC-TCD" was performed according to standard procedures ISO 10708 (BODIS-test) and ISO 14593 (ISO CO_2 headspace test) with modifications [6, 7, 8]. The inoculum was a Lufa 2.2 (Landwirtschaftliche Untersuchungs- und Forschungsanstalt Speyer, Germany) soil. The assay based on the measurement of the ultimate aerobic mineralisation of test substances to carbon dioxide in water. Results are expressed as biological oxygen demand in relation to the theoretical oxygen demand (BOD/ThOD) and carbon dioxide production in respect to the theoretical carbon dioxide production (TIC/ThIC). Oxygen and carbon dioxide in headspace samples are measured with gaschromatography using a thermal conductivity detector (TCD, Perkin Elmer Autosystem) and a CTR 1 column (Alltech GmbH, Unterhaching, Germany). The test substance was evaluated as ready biodegradable, if degradation exceeds 60% within 28 days (OECD) [9].

3 Results

3.1 Chemical Analysis

3.1.1 GC-Analysis

Quantitative analysis of the ester based lubricant HISM was determined via GC-FID. The evaluation of usage-dependent changes was based on the HISM quantity. **Figure 1** represents the quantity changes of the HISM contents in the lubricants from two different reactants before and after usage at different temperatures. All lubricants except sample number 143 showed a usage-dependent decrease of HISM. For both animal reactants, this decrease did not depend on thermal effects. The decrement of HISM content varied between 13% (109) and 6% (121). Therefore sample 121 showed a higher resistance towards thermal and mechanical forces. Compared to the animal reactants, herbal reactants were characterized by lower initial values for HISM and diverging responses on both factors. Sample 143 showed equal values of HISM under all conditions. A decrease in HISM caused by usage and temperature effects was discovered only for sample 135.

In a direct comparison, animal lubricants are favourable due to higher concentration of HISM, although there is lower resistance against the tribological application compared to herbal reactants which are more resistant.

3.1.2 ICP-MS

In a tribological test system, mechanical interaction can contribute to the accumulation of metals. By this reason all tested lubricants were subjected to ICP-MS measurements. **Table 1** reflects the quantities of Fe, Zn, Al, Cr and Cu in used oils.

Before usage of lubricant the concentrations of metals is considered to be zero. As expected, usage in the test bench resulted in metal uptake. For copper, aluminium and zinc, this uptake

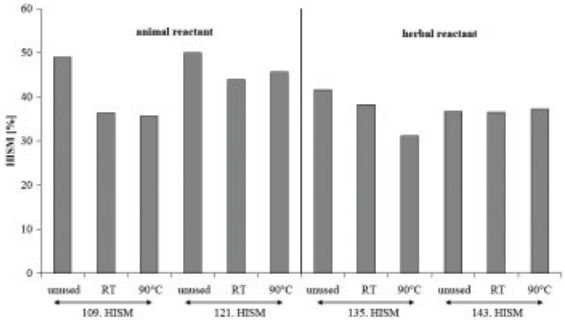


Figure 1: Percentage quantity of HISM before and after usage in the pin-on-disc tribometer

Table 1: Metal concentration of HISM after usage in the pin-on-disc tribometer

Sample	Al	Cr	Cu	Fe	Zn
			ng/g		
109. HISM RT	1361	-	155	35067	2433
109. HISM 90°	1140	949	555	20270	3305
121. HISM RT	1047	1193	-	3027	2678
121. HISM 90°	2175	13467	862	41878	3150
135. HISM RT	676	-	69	-	1819
135. HISM 90°	821	-	1856	-	2449
143. HISM RT	841	-	175	-	2525
143. HISM 90°	1509	4225	-	9761	2573

was observed as temperature-dependent. For iron no temperature-dependent behaviour could be detected **(Table 1)**.

3.1.3 Genotoxicity

All tested oil samples were subjected to the *umu*-test. D_{Li} values of the *umu* test demonstrated induction rates below 1.5 with growth factors larger than 0.5. No genotoxicity was observed for all tested lubricants and under any conditions of usage.

3.1.4 Biodegradability

Biodegradability depends on the composition of the lubricants. To verify this, the dismantling behaviour is determined for each sample. Relative values of biodegradability for used lubricants are shown in **Figure 2**.

As a reference substance, which fulfills the guidelines of the OECD, sodium benzoate is depicted in **Figure 2**. For herbal and animal based reactants, similar biodegradability after usage was detected. Sample 143, 135 (herbal) and 121 (animal) fulfill the guidelines of the OECD. No significant evidence for thermal influence could be observed. Composition of individual samples highly determined their biodegradability. The achieved data suggest a correlation between usage-dependent changes of lubricants and biodegradation.

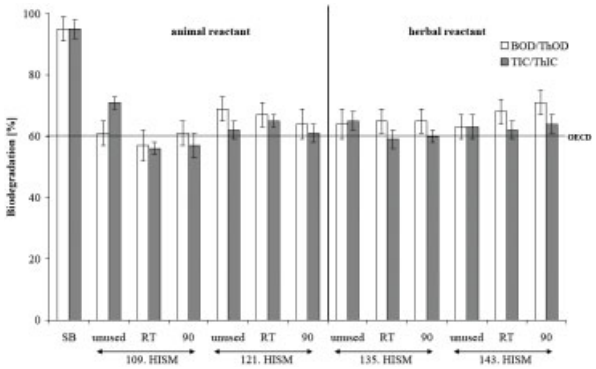


Figure 2: Aerobe biodegradation of different unused and used HISM samples; BOD/ThOD = biological oxygen demand/theoretical oxygen demand, TIC/ThIC = carbon dioxide production/theoretical carbon dioxide production, SB = sodium benzoate (first bar)

4 Conclusion

Chemical analysis revealed a direct correlation between the conditions in application and substantial properties of lubricants. As a result of abrasion the concentration of copper, aluminium and zinc increased with mechanical as well as thermal exposure. No genotoxic effects were detected for all tested samples. Two herbal and one animal originated lubricants fulfilled the guidelines of the OECD. Regarding technical performance, the results display higher initial HISM quantity for animal reactants. Herbal reactants are instead superior in mechanical and thermal stability. Mechanical and thermal effects simulated in tribological systems showed lower effects on environmentally relevant properties of the lubricants in this study.

This approach concerning environmental risk assessment of lubricants combines the application of chemical analysis and biological test systems. These results allow selection of contemporary lubricants at very early stage of product development and aims in monitoring high quality standards. The awareness of sustainable aspects for individual lubricants allows precise adjustment in synthesis according to contemporary needs. Practically the combined application of chemical analyzes and biological test systems allows constant quality assurance and environmental risk assessment.

5 Acknowledgements

This work is supported by Deutsche Forschungsgemeinschaft (DFG), SFB 442 “Environmentally friendly tribosystems by suitable coatings and fluids with respect to the machine tool”. The pin on disc test was kindly performed by the Institute for surface engineering of the RWTH Aachen. The authors want to thank N. Kuckelkorn and S. Thoröe for their excellent technical support.

6 References

[1] H. Maier, B. Erlenkämper, W. Dott, A. Eisenträger: Incorporating methods of ecotoxicity testing and chemical analysis for environmental risk assessment into the production of lubricants, W. J. Bartz (Editor), *16th International Colloquium Tribology-Lubricants, Materials and Lubrication Engineering, 15.-17.1.2008, Stuttgart/Ostfildern*, **2008**, page 205

[2] K. Bobzin, E. Lugscheider, R.Nickel, N. Bagcivan, A.Krämer: Wear behaviour of $Cr_{1-x}Al_xN$ PVD-coatings in dry running conditions, wear 263, **2007**, 1274–1280

[3] Oda Y., Nakamura S.-I., Oki I., Kato T., Shinagawa H., Evaluation of the new system (umu-test) for the detection of environmental mutagens and carcinogenes, Mutation Research, 147, **1985**, 219–229

[4] Reifferscheid G., Heil J., Oda Y., Zahn R.K.: A microplate version of the SOS/*umu*-test for rapid detection of genotoxins and genotoxic potentials of environmental samples. Mutation Research, **1991**, 253, 215–222

[5] ISO 13829, Water quality - Determination of the genotoxicity of water and waste water using the *umu*-test. International Standard, **2000**

[6] ISO 10708 , Water quality - Evaluation in an aqueous medium of the ultimate aerobic biodegradability of organic compounds – Method by determining the biochemical oxygen demand in a two-phase closed bottle test. International Standard, **1997**

[7] ISO 14593, Water quality - Evaluation of ultimate aerobic biodegradability of organic compounds in aqueous medium – Method by analysis of released inorganic carbon in sealed vessels (CO_2-Headspacetest). International Standard, **1999**

[8] Hahn S., Eisenträger A., Application of an "O_2/CO_2 headspace test with GC-TCD" for biodegradability testing of synthetic ester lubricants in water and soil. In: Burk A.R. (ed.): Water Pollution: New Research. Nova Science Publishers Inc., Hauppauge, USA, **2005**, 143–160

[9] OECD Guidelines for testing of chemicals: Summary of considerations in the report from the OECD expert group on degradation and accumulation. Organisation for Economic Co-operation and Development, Paris, **1992**

High Performance PVD Tool Coatings

K. Bobzin, N. Bagcivan, P. Immich, M. Ewering*, C. Warnke**
Surface Engineering Institute (IOT), RWTH Aachen University
*/** *corresponding authors*

1 Introduction

Tribological Systems belong to many technical applications. Within the Collaborative Research Centre SFB 442 “Environmentally friendly Tribosystems” at RWTH Aachen University, tribological functions are transferred from mineral oil based lubrication to surface coatings. Depending on the application area different PVD (Physical Vapour Deposition) thin films and deposition techniques are applied to enhance tool life, reduce or avoid lubrication and decrease costs. As an example, the present paper deals with two different coatings, which are designed for different tool applications: high performance metal forming and machining applications.

2 Nanolaminated (Ti,Hf)N/CrN for Metal Forming Tools**

After the first appearances in the mid 1990ies [1, 2, 3] specialized PVD coating architectures like multilayers and nanolaminates (superlattice) awaked increasing importance during the last years for several tool coating applications [4, 5, 6, 7]. It was shown that a (Ti,Hf)N/CrN coating [9] offers outstanding mechanical properties for several metal forming applications. Realized by the AIP PVD technique (Arc Ion Plating), the coating delivers a high adhesion to the tool substrate (critical scratch load of 90 N on carbide, 60 N on high speed steel HS-6-5-2) in hand with the required properties of high as possible hardness and low as possible Young’s modulus (see Figure 1). Also an outstanding wear resistance and oxidation stability was presented before [10].

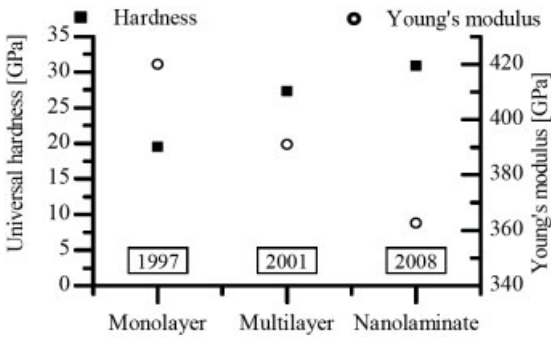


Figure 1: Development progress in coating hardness and Young’s modulus for different coating architectures in the material system Ti-Hf-Cr-N.

Different etching methods can be applied in the coating processes depending on different application demands. For all coating developments regarding a directed modification of material

properties the challenge always consists in achieving a high as possible coating to substrate adhesion. Coatings on round shaped functional surfaces like punch heads for cup backward extrusion processes (Figure 2 left) were deposited after a metal ion etching (MIE) process.

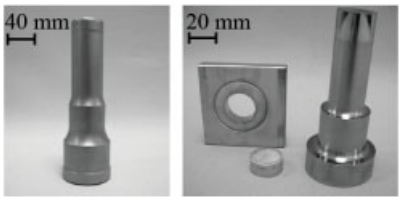


Figure 2: Typical metal forming tools: punch tool for cup backward extrusion (left), workpiece and cutting tool for fine blanking (right).

More demanding metal forming tools like fine blanking punches (Figure 2 right) require an adjustment especially in the etching stage. A customised high ionisation plasma etching was developed based on the AEGD technology (Arc enhanced glow discharge, [8]). The AEGD technology almost eliminates the deposition of macro particles during the etching stage whereby a higher coating to substrate adhesion is realized especially on sharp tool edges. Recently a new nanolaminated (Ti,Zr)N/CrN coating was developed based on former in-house research [9, 10]. It is shown that the recent development can as well deliver state-of-the-art material properties as even increase coating to substrate adhesion and reduce coating costs with regard to the industrial coating scale.

2.1 Experimental

A nanolaminated (Ti,Hf)N/CrN and a newly developed (Ti,Zr)N/CrN coating were deposited by Arc Ion Plating. Both coatings were deposited on carbide (WC/6%Co) samples using a Metaplas Ionon 20" AIP coating facility. For each deposition process cathode currents of 60 A, substrate bias voltages of -100 V and a total gas pressure of 1 Pa nitrogen were applied. The coating facility provides conventional MIE and also high ionisation plasma etching based on the AEGD Technology as described above. The adhesion tests were carried out by using an automatic scratch tester. In order to determine the critical load at which failure occurs several scratches with a length of 4 mm and a stepwise increase of 10 N were done and analyzed by light optical microscope. The load was kept constant during scratching. The scratches were performed with a velocity of 10 mm/min. Universal hardness was measured with a Nano Indenter XP® (MTS Systems Corp.) using a Berkovich diamond indenter. The indenter penetrated the coated surface perpendicular at a constant load of 10 mN. Calculations of the Young's modulus are based on Oliver and Pharr's equation and Poisson ratio was kept constant at $\nu = 0.25$ [11]. Indentation depth was less than 10 % of the coating thickness. The Rockwell adhesion test was performed with a conventional hardness tester. The indentation was analyzed according to VDI Guideline 3198. The tribological performance was examined using a CSM pin-on-disc (POD) tribometer, running the coated carbide specimens against carbide counter partners in non-lubricated experiments at different temperatures. The POD parameters were the following. Counter partner: carbide ball of 6 mm diameter, normal load 5 N, rotating speed 10 cm/s, wear track radius 2,5 cm, rel. humidity 40 %, ambient temperature 25, 200 and 400°C, running distance 500 m.

2.2 Results

Comparable to the preceding Hf-based coating version, the new (Ti,Zr)N/CrN coating also delivers adhesion class 1 in the Rockwell test. Regarding the critical scratch load actually a clear improvement from 80 to 100 N can be documented (see Figure 3).

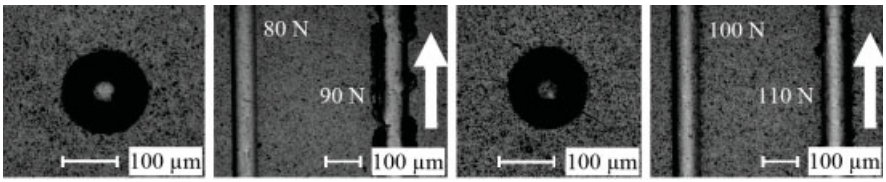


Figure 3: Results of Rockwell and scratch tests for the compared coatings (Ti,Hf)N/CrN (left) and the new (Ti,Zr)N/CrN (right) on coated carbide specimens. Both coatings were deposited with a film thickness of 3 µm ± 0.1 µm.

A comparison between the deposition rates showed an increased rate for the new Zr-based coating system of nearly 33 %, since the rate could be increased from 3 to 3.9 µm/h. This is due to the lower melting point of Zirconium compared to Hafnium and its lower specific evaporation enthalpy. By POD tests it was observed for both coatings that only adhesion wear on the counter partner appeared. Counter partner material was transfered to the coated specimen's surface. As an example the results of the measurement at 400 °C are shown in Figure 4.

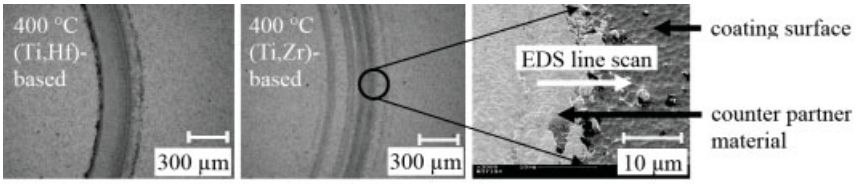


Figure 4: Wear tracks after dry POD sliding test on coated carbide specimens against carbide counter partners at 400 °C. a: LM picture, wear track on (Ti,Hf)N/CrN. b: LM picture, wear track on (Ti,Zr)N/CrN. c: SEM micrograph according to b

It was proven for all examination cases that only counter partner material was transfered to the coated specimen's surface (see Figure 4 c as example). Due to this result a wear rate of the coated specimens could not be detected. For the (Ti,Zr)N/CrN coating system it was shown that the counter partner's adhesive wear was reduced generally (compare Figure 4 a/b). The medial wear rate of the carbide counter partner was reduced by nearly 50 %. The results of nanoindentation on "as coated" specimens showed the same values of 32 ± 3 GPa as medial results of 15 measurements for both coatings. Corresponding to the results of nanoindentation calculations of the Young's modulus exhibited nearly the same result with 350 GPa for the new Zr-based nanolaminated coating.

3 TiAlN/γ-Al_2O_3 for High-Performance Machining*

Regarding cutting operations, difficult to machine materials like Inconel 718 are more often applied due to their high thermal stability. High thermal exposure on the cutting tool and high tool wear are the consequences. Therefore cutting tools with a high hot hardness, a low tendency to adhesion-related sticking, high oxidation resistance and high abrasion resistance are necessary. Tool coatings like TiAlN, TiN and TiCN are still state of the art [12]. Nevertheless these coatings are not applicable for demanding cutting operations, due to their low thermal stability. Within the second phase (2000–2003) of the SFB 442 a multilayer of TiAlN (DC-sputtered) and amorphous alumina (r.f.-sputtered) was developed offering a high thermal stability to fulfill these demands. But the generated coatings did not offer enough hardness. With the development of the pulse technology and the related higher ionization, crystalline γ-alumina was generated, resulting in a higher hardness (introduced by [13]). γ-Al_2O_3 offers good premises: it exhibits high hot hardness and high thermal and chemical stability at elevated temperatures [14, 15]. The major problem of the reactive sputtering of alumina is the so-called target poisoning. When a certain oxygen partial pressure is reached the target is totally poisoned and the deposition rate decreases, resulting in an amorphous film. On the other hand, a low oxygen partial pressure leads to the deposition of metallic films. Target poisoning strongly depends on the technological setup, particularly the ratio vacuum chamber volume to pumping speed as well as the target material. Compared to small laboratory coating units the deposition in industrial coating units is related to small process windows, in which crystalline alumina is formed. Another advantage of a laboratory is the application of higher possible target power densities. But for industrial application of alumina a further aim of the SFB 442 was the transfer of the process to an industrial coating unit. Further problems are the different bond types of the substrate, e.g. cemented carbide (metallic bond), and alumina (ionic and covalent bond). The adhesion of the coating is not sufficient. Additionally, the different gradient of residual stresses in coating and substrate degrades the adhesion. Therefore a bond coat like TiAlN is necessary. Another way to enhance adhesion is an improved etching process. In the following, a high-performance etching process by means of a hollow-cathode is compared to a standard etching process.

3.1 Experimental

For the etching and deposition processes an industrial coating unit CemeCon CC800 was used. As substrate WC-Co cutting inserts (THM 12, SNUN 120412 Kennametal Holding GmbH) were employed. As shown in table 1, three etching processes were investigated: A conventional m.f.-etching process (method A), an etching process, in which the gas is highly ionized by means of a hollow-cathode (method B), and a mixture of both (method C). After etching the samples were deposited without an optimized coating interface to provoke a bad adhesion and therefore clarify the effect of the etching process. The coatings were deposited using four cathodes in a two by two dual cathode arrangement. The cathodes were pulsed in a bipolar pulse mode using a rectangular pulse with a frequency of 18.51 kHz. The nanocomposite TiAlN coating was produced by co-sputtering of two TiAl-targets (6000 W) and two Al-targets (1000 W) at a total pressure of 500 mPa by reactive sputtering in a mixed atmosphere of argon and nitrogen. The deposition of the Al_2O_3 top layer was performed by two aluminum targets using the dual cathode arrangement (power 3500 W, pulse frequency 18.5 kHz). The process was voltage controlled:

the argon was kept at 200 sccm while the oxygen flow was varied. The oxygen partial pressure was set by adjusting a certain voltage at the cathodes.

Table 1: Parameters of different etching methods

	A (m. f.-etching)	B (hollow cathode-etching)	C (Mixture of A and B)
Etching time [min]	80	80	A: 40; B: 40
Argon flow [sccm]	120	150	120
Anode current [A]	–		20
Hollow cathode Voltage [V]	90	–	90
Table bias [V]	–650 (m.f, 350 kHz)	–200	A: –650 (m. f, 350 kHz), B: –200

Further process parameters are also described in [16]. The coatings were compared to a coating deposited in a laboratory sputtering device (Z400, Leybold-Heraeus) [17]. Hardness measurements, Rockwell adhesion test and the scratch test were performed as described above.

3.2 Results

Table 2 shows the results of the scratch test and the Rockwell test of TiAlN coatings with a thickness of 4 µm deposited with different etching pre-treatments. All coatings showed an adhesion class 1 in Rockwell test.

Table 2: Results of Rockwell and scratch test for different etching parameters

	Method A	Method B	Method C
Adhesion class (Rockwell test HRA)	1	1	1
Critical Scratch Load L_{C3} (N)	50	70	50

The best results for the scratch tests were achieved by using hollow cathode-etching. Here a critical scratch load of 70 N was achieved. Consequently, this etching process was used for further experiments. In comparison to the laboratory device Z400 the industrial unit CC800 shows some differences as shown in Table 3.

Table 3: Differences between the CC800 and the Z400 coating unit

	CC800	Z400
Pumping volume	1300 l/s	450 l/s
Chamber volume	0.64 m³	0.0305 m³
Possible aluminium target power density (limitation of the coating unit)	7.95 W/cm²	18.1 W/cm²

Due to the different chamber volume to pumping speed ratio the development of voltage and pressure as a function of oxygen flow differs enormously. Figure 5 shows the different results for the cathode voltage. In both diagrams the poisoning of the targets with increasing oxygen flow is obvious. As a result the cathode voltage decreases. Reason for this is the lower deposition rate and the lower yield of secondary electron emission at the target respectively. In comparison to the

laboratory unit (left diagram) the drop in cathode voltage of the industrial unit is much sharper (right diagram) than that of the laboratory unit. Therefore a precise process control is necessary to get crystalline alumina. This is realized by adjusting a certain voltage at the cathodes.

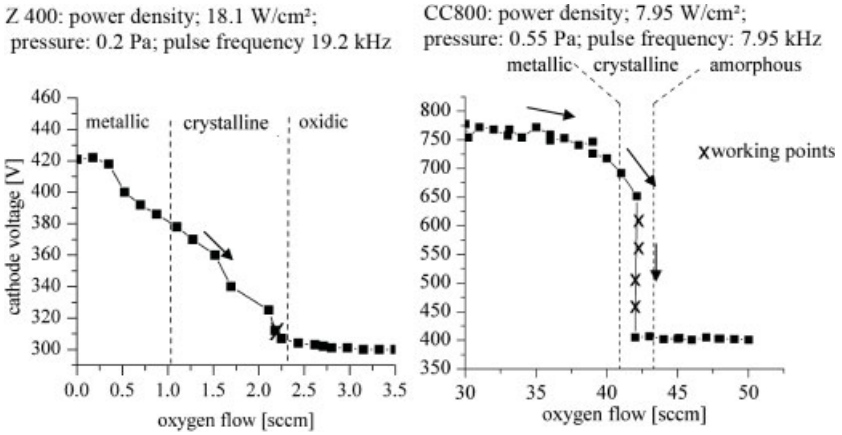


Figure 5: Cathode voltage as a function of oxygen flow for Z400 (left) and CC800 (right)

To find a suitable working point resulting in an appropriate coating, different working points within the hysteresis were investigated. Table 4 shows the examined working points and the hardness values.

Table 4: Working points and resulting hardness values

cathode voltage [V]	630	560	500	460
hardness [GPa]	4 ± 0.9	10 ± 1.2	19 ± 1.6	10 ± 0.8

The coating deposited at a cathode voltage of 500 V showed the highest hardness values. XRD analysis clarified, that this coating showed the highest intensity of the γ-alumina peaks. In Rockwell test the coating exhibited an adhesion class of 1, the critical scratch load was 90 N. In contrast to the coating deposited with the standard γ-Al_2O_3/TiAlN coating of the laboratory unit the hardness is lower (25 GPa vs. 19 GPa). A possible reason may be the lower target power density. Figure 6 shows cross sectional SEM pictures of the coatings deposited with a TiAlN interlayer on the industrial unit and the laboratory unit.

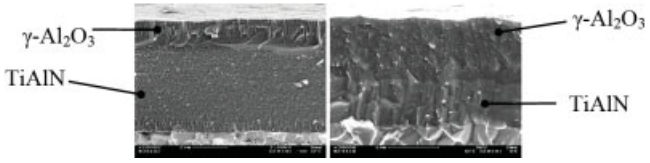


Figure 6: SEM Cross-section of TiAlN/γ-Al_2O_3 coatings deposited in the industrial unit (left) and the laboratory unit (right)

4 Conclusions

It was possible to generate a TiAlN/γ-Al_2O_3 thin film on an industrial coating unit. The coating is a promising candidate for its use in cutting operations. It exhibits an excellent crystallinity and strong adhesion.

The results of the development of a nanolaminated (Ti,Zr)N/CrN coating for metal forming tools were presented. The investigations show enhanced material system properties compared to former developments [9] together with a more economical coating process, since the same material properties were realized with a less expensive coating material. Due to the exchange of hafnium by zirconium, even the adhesive wear of carbide counter partners was reduced significantly.

5 Acknowledgement

The authors gratefully acknowledge the financial support of the German Research Foundation (DFG) within the collaborative research centre SFB 442 “Environmentally Friendly Tribosystems” at RWTH Aachen University. This publication is based on research results of the sub projects A2 and A5.

6 References

[1] L. A. Donohue, J. Cawley, J. S. Brooks and W. -D. Munz, Surf. and Coat. Techn. 1995, 74–75 , 123-134.

[2] H. Holleck, V. Schier, Surf. and Coat. Techn. 1995, 76–77, 328–336.

[3] L. A. Donohue, J. Cawley, J. S. Brooks,W. -D. Munz, Surf. and Coat. Techn. 1995, 74–75 , 123-134.

[4] Y. Kamata, T. Obikawa, Jour. of Materials Processing Techn. 2007, 192–193, 281–286

[5] P.Eh. Hovsepian, C. Reinhard and A.P. Ehiasarian, Surf. and Coat. Techn. 201 (2006), 4105–4110

[6] P.Eh. Hovsepian, Q. Luo, G. Robinson, M. Pittman, M. Howarth, D. Doerwald, R. Tietema, W.M. Sim, A. Deeming, T. Zeus, Surf.. and Coat Techn. 2006, 201, 265–272.

[7] Y.P. Purandare, M.M. Stack, P.Eh. Hovsepian, Surf. and Coat. Techn.2006, 201, 2006, 361–370.

[8] J. Vetter, W. Burgmer, A. J. Perry, Surf. and Coat. Techn.1993, 59, 152–155.

[9] E. Lugscheider, K. Bobzin, C. Pinero, F. Klocke, T. Massmann, Surf and Coat. Techn., 177-178, 616–622.

[10] K. Bobzin, E. Lugscheider, R. Nickel, P. Immich, C. Warnke, Conference Proceedings 2nd Vienna International Conference on Micro-and Nano-Technology, 295–300

[11] W.C. Oliver, G. M. Pharr, J. Mater. Res. 7 (1992) 1564–1583

[12] J. H. Wijngaard, A. Schütz, Vakuum in Forschung und Praxis (2003), 15/4,194

[13] O. Zywitzki, G. Hoetzsch, Surf. Coat. Techn. 1996. **86–87,** 640

[14] M. Åstrand, T. I. Selinder, F. Fietzke, H. Klostermann, Surf. Coat. Techn. 188–189 (2004) 186–192

[15] H. Schulz, J. Dörr, I. J. Rass, M. Schulz, T. Leyendecker, G. Erkens, Surf. Coat. Techn., 146-147 (2001) 480–485

[16] K.Bobzin, R. Nickel, P. Immich, M. Ewering, Proceedings, 6th International Conference The Coatings 2007, 197–187

[17] K. Bobzin, E. Lugscheider, M. Maes, C. Piñero, Thin Solid Films 2006, 494, 255–262

Manufacturing Tool-Coating-Compatible Stamping and Fine Blanking Tool Surfaces

F. Klocke, C. Zeppenfeld, P. Mattfeld, M. Zimmermann
Laboratory for Machine Tools and Production Engineering, RWTH Aachen University,
Steinbachstraße 19, D-52074 Aachen

1 Introduction

On account of high mechanical stresses and strains on forming dies the liability of tool coatings is decisive for their effect in use. Lacking layer liability leads to flaking or delamination, so that the coating cannot protect the tool surface any more. In some cases, unfavorable tool geometry and unfavorable loads on coating leads to chipping, even for tool coatings with good adhesive properties.

Special requirements for the tool coating are demanded for punches, used in stamping and fine blanking operations. These are usually manufactured sharp edged and sharpened in practice by surface grinding on the face, which leads to geometrically undefined burr-afflicted cutting edges, or the edges are finished manually.

In both cases the edge geometry leads to stress peaks on the tool surface during the stamping process, often leading to a layer separation. The tool coatings in raw cutting edges of the punch often show the first microscopic damages already after a few strokes. Starting from these areas the tools quickly start to wear out.

Hence, for the improvement of the tool edge life of stamping and fine blanking punches the cutting edges can be provided with a defined micro-rounding off. In this way on the one hand, edge-stability is raised in the process and on the other hand the layer liability is improved in these exposed tool areas.

This tool finishing can be realized with different manufacturing methods. One of these procedures is the brush-polishing process by means of plate brushes on which in the following is entered closer.

The results from basic investigations show the influence of different process parameters while brushing a cutting punch made of high speed steel and possible variations of edge rounding off.

2 Investigations of the Punch Cutting Edge of Stamping and Fine Blanking Punches

In many stamping and fine blanking companies, the edge contours of cutting punches are formed mostly intuitively. According to the operational know-how the punch edges are easily rounded off or sharply grinded and coated afterwards [1]. Stress minimization on coated punches for fine blanking processes was already investigated in 2001 in the SFB442 by Klocke et. al. [2]. By means of the Finite Element Analysis (FEA) different cutting edge geometries were simulated during the cutting process. As a result an optimum punch micro edge geometry was developed.

The simulation results showed that a chamfer on the front surface of the cutting punch with a small opening angle α leads to minimal stresses and strains in tool coating and substrate. In support of the results of Klocke et. al. it is the long-term purpose of the investigations introduced here to realize the determined micro–cutting edge economically and reproducibly by a brush-polishing process for stamping and fine blanking punches.

2.1 Experiment Set-Ups and Approach of the Brush-Polishing Machine

For the basic investigations introduced in this paper, simple test bodies from round material HSS BöhlerS390 are vacuum hardened to 63 HRC. Afterwards all samples are uniformly circular grinded to a diameter of 30 mm. The decisive creation of the cutting edge occurs in the final surface grinding on the face process. After the grinding process, the punch edge shows a very distinctive microscopic burr, which is only partially attached with the surrounding material. Coating this tool without edge-finishing would result in layer defects in the process after a few strokes.

For the cutting edge rounding off of the fine blanking punch a brush-polishing machine BP Smart by Gerber AG (Lyss-Switzerland) is used (Figure 1).

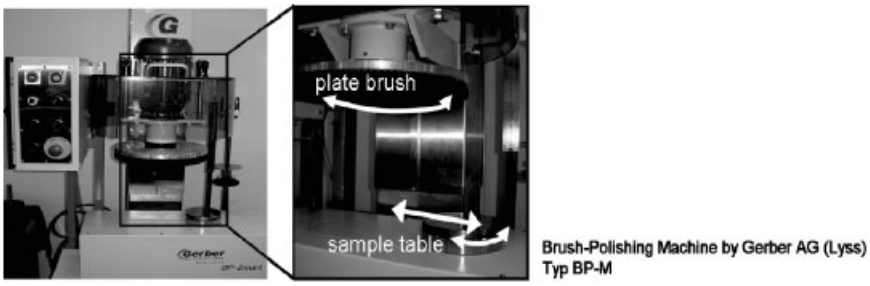


Figure 1: Brush-Polishing Machine by company Gerber AG (Lyss) for edge rounding off of cutting inserts

The machine was originally developed for rounding off cutting edges on hard metal-, cBN-and PKD-tools [3]. Nowadays, chipping tools made of hard metal are often already submitted to an edge finish [4]. The process parameters of the brush polishing machine are examined within the SFB442 for rounding off in punching and fine blanking tools and will be adapted to this process. Within the investigated rounding off method a plate brush takes over the function of the carrier for an abrasive medium in form of a diamond paste. By striking the bristles on the cutting edge of the punch material removal is accomplished. The sample to be rounded off is fixed on the oscillatory sample table of the brush-polishing machine and the plate brush is put parallel with the punch front surface. The machine construction allows different geometrical profile forms of the edge rounding off (see Figure 6). The influence taking machine-parameters are discussed in chapter 3.

2.2 Measuring the Cutting Punch Edges

The cutting edges before and after edge finishing are measured by means of a tactile 2D stylus instrument process.

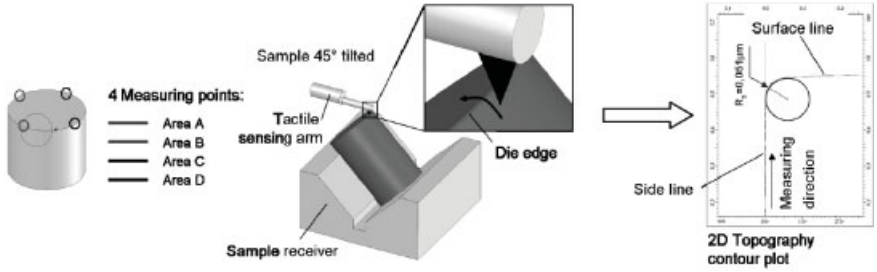


Figure 2: Characterization of the cutting punch edges by means of 2D contour plots

A round sample which is tilted 45° is measured before and after the rounding off process. To the investigation of the ability for reproduction of the edge rounding off about the sample radius four measurements were carried out on every sample (see Figure 2).

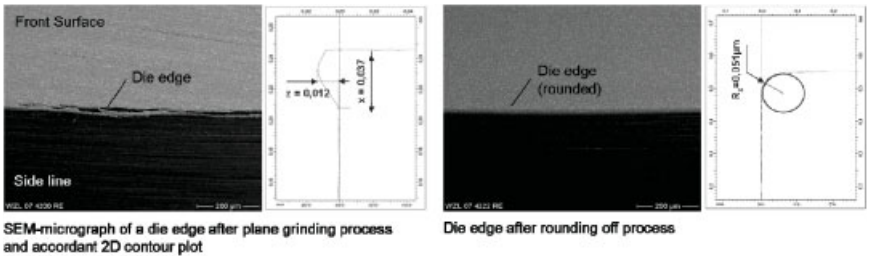


Figure 3: SEM-micrograph and according 2D contour plot

Scanning Electron Microscope (SEM) micrographs deliver, in addition, a qualitative verification of the results from the 2D topography measurements (see Figure 3).

2.3 Characterization of different Cutting Edges Rounding Off

The formative factor for rounding off cutting edge design is the working pressure p. The term "working pressure" describes the depth of immersion of the work piece in the bristles of the plate brush. The height of the edge rounding off h and therefore the dimension of the cutting edge is determined by it.

Different edge forms can be generated by specific choice of the parameters working pressure p and machining time t (see Figure 4), which are characterized by the profile classification number λ.

The adjustment between sample body and brush is critical. To produce a rounding off with $R_x < 20$ µm, the samples may only dip in 0.04–0.12 mms into the bristles of the plate brushes (p calculated by the manufacturer of the brushing machine given formula $p = 2....6 \cdot h$).

Nevertheless, the user cannot recognize, when the first contact takes place between punch and brush and therefore can only steer the working pressure p insufficiently. Edge rounding off thereby can hardly be compared with each other on account of strong form and position dispersion

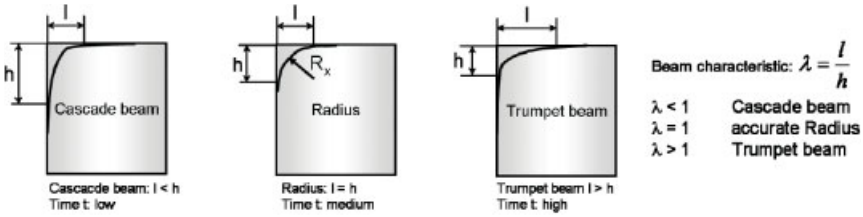


Figure 4: Profile shape with different treatment times

in different samples. In the introduced results some machining parameters were fixed: the number of revolutions U of the brushes correlates according to manufacturer's data with the wear of the bristles and is basically used for the balance of correction variations in the result. U was fixed with all attempts on the speed by 300 1/min. All edges preparations were carried out with a diamond paste of the grain size 2-4 µm.

3 Basic Investigations to the Factors of Influence on the Edge Rounding Off

The following factors of influence matter to edge rounding off:

- Machining time t [min]
- Brushing material
- Working pressure p [mm]
- Number of revolutions of brush U [1/min]
- Abrasive grain size d [µm]

3.1 Influence of the Machining Time on the Rounding Off Results

The influence of the machining time t on the cutting edge geometry of the sample is shown in Figure 5. All other parameters of influence on the rounding off process were fixed (test parameter see box, Figure 5).

At first the distinctive burr in the circumference of the sample is removed by the brushing process. A defined contour of the sample in form of a cascade profile appears after approximately 12 minutes. After 25 minutes machining time an exact radius appears on all samples. In spite of rising the brushing time on more than 40 minutes a distinctive trumpet profile could not be generated in any sample. The maximum achieved profile identification number is about λ =1.2.

3.2 Influence of the Brush Material on the Rounding Off

In the basic attempts three brush material types of different hardness grades from the company Gerber (horsehair (soft), Vitex (medium hard), Tampico (hard)) are investigated. With increasing

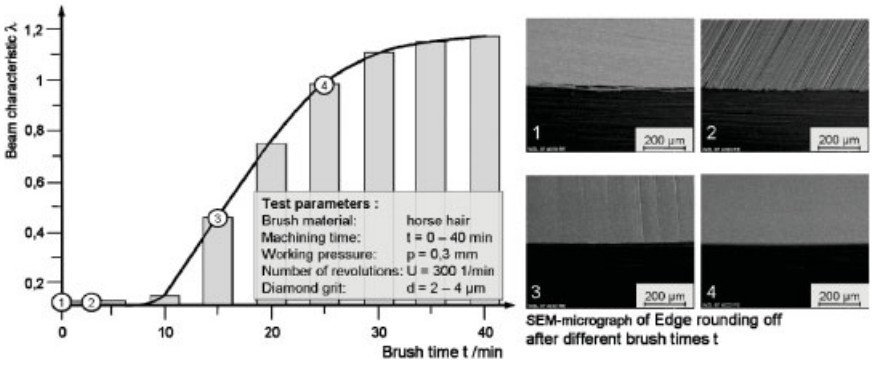


Figure 5: Influence of the machining time t on the rounding off process of the cutting edge

hardness of the bristles the ability for reproduction of the edge rounding off rises, i.e. the cutting edge geometry presented itself about the circumference of the whole test in the same geometrical stamping and dimension. Indeed, the range of the attainable geometry also economizes with rising brush hardness.

Within the series of experiments it is, in spite of high treatment times, not successful with the harder brush qualities Vitex and Tampico to generate a distinctive radius or trumpet profile on the sample bodies.

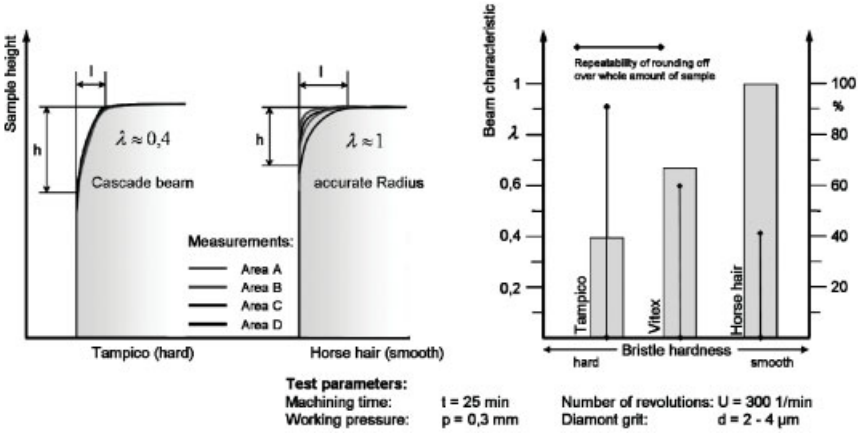


Figure 6: Rounding off results by use of plate brushes of different hardness grades with steady machine parameters

In addition, the edge geometry presents itself rather as a chamfer without distinctive rounding off. This refers probably to the fact that the bristle materials Vitex and Tampico are (originally developed for the edge treatment of hard metals) too hard for the treatment of HSS.

The application of soft horsehair brushes generates partly irregular and less reproducible edge rounding off with a wide dispersion of the geometrical dimensions about the sample circumference.

This is probably due to the fact that the untreated burr arrested in the cutting edge of the punch is differently strong tied with the remaining punch substrate and soft bristle material within the treatment duration cannot completely remove the different material volumes.

4 Summary and Preview

The wear behavior and therefore also the efficiency of coated stamping and fine blanking punches from high speed steel will be positively influenced by a specific rounding off of the cutting edges by brushing processes. The demanding process parameters of the introduced procedure complicate it to the user to achieve optimum cutting edge geometry by this technology. The results introduced here from basic investigations for brush-polishing of cutting punches, show the influence of different treatment parameters on the rounding off process in the area of the cutting edge. The present attempts have made clear that reproducible edge rounding off can be realized on cutting punches by the brush procedure. Nevertheless, the scales achieved in the preliminary investigations and edges profiles are not suitable optimally for the application in stamping and fine blanking punches.

To realize the optimum edge geometry ascertained by Klocke using a brushing process, optional process parameters should be examined in continuing series of experiments.

In addition a dumping/ tipping of the samples appeared in some preliminary investigations to the plate brush as a promising factor of influence on the rounding off results. In addition, the influence of complicated sample geometry (edges, narrow radii) for the rounding off results should be examined.

5 Acknowledgements

Parts of the work described in this paper were funded by the “Deutsche Forschungsgesellschaft” within the Collaborative Research Center 442 “Environmentally Improved Tribosystems”

6 References

[1] Herold, J.: Einfluss der Kantengestaltung von Schneidstempeln beim Scherschneiden auf die Stempelstanddzeit. UTF sience II (2003) 4

[2] Klocke, F., Sweeny, K., Raedt, H.-W.: Improved tool design for fine blanking through the application of numerical modeling techniques, Journal of Materials Processing Technology 115 (2001) 70–75

[3] Gerber, S.: Einsatzmöglichkeiten von Bürst-Poliermaschinen, IDR 31 (1997) Nr.2, S. 131–134

[4] Denkena, B., Friemuth, T., Spengler, C. Weinert, K., Schulte, M., Kötter, D.: Kantenpräparation an Hartmetall-Werkzeugen, VDI-Z Special Werkzeuge, März 2003, S. 51–54

PVD Coating Systems for Environmentally Friendly Machining

F. Klocke, K. Gerschwiler, S. Cordes, R. Fritsch
Laboratory for Machine Tools and Production Engineering, Chair of Manufacturing Technology, RWTH Aachen University, Aachen

1 Introduction

Environmentally friendly cutting technologies are rapidly gaining in importance in industrial production. Nano-structured PVD coatings are characterised by a high performance potential when drilling, turning and milling using a synthetic ester oil as the lubricoolant.

Native ester lubricants, free of additives and biologically degradable, possess the potential to replace water-based cutting fluids and mineral oil in machining operations. When drilling into the nickel-based alloy, Inconel 718, the use of an additive-free synthetic ester led to a significant improvement in tool life. In contrast to the emulsion used in the comparative tests, the number of holes produced was able to be doubled with the ester. The comparison between ester oils and mineral oils when turning the austenitic steel material, X5CrNi18-10 (AISI 304), reveals that the use of the ester oil in this machining operation leads to a considerable increase in performance.

New PVD-coating systems, such as nanolaminates, nanocomposites and crystalline γ-Al_2O_3, are characterised by a high performance potential under the given operating conditions. As the overall results show, synthetic esters in combination with adapted high-performance coating systems represent an efficient alternative to water-based lubricoolants and mineral oils, even in difficult machining operations. Their use as a lubricoolant in cutting processes thus not only contributes to environmental protection and to improving the working environment, but also to enhancing productivity. In a further part, the wear behaviour of tools coated with TiAlN/γ-Al_2O_3 during dry-cut milling operations is presented. As the tests demonstrate oxidic PVD coatings can contribute to a significant increase in cutting performance.

2 Tailored PVD Coatings

Machining of materials with a pronounced adhesive effect, such as austenitic steels or nickel-based alloys, requires tools that are optimally adapted to the particular demands of the machining task with respect to substrate, hard-material coating and the geometry of the cutting edges. Coating systems play a key role in this. Their proneness to adhesion should be minimal, and they should demonstrate a high degree of hardness at elevated temperatures, a great resistance to abrasive wear, a considerable level of resistance to high temperatures and oxidation, as well as good adhesion to the substrate. With new or enhanced PVD coating technologies, it is possible to generate innovative coating systems with highly sophisticated wear-relevant properties, such as hardness, toughness and resistance to oxidation, compared to those achieved with conventional hard-material coatings. Examples of such innovative coating systems are fine-crystalline coatings with an aluminium content of > 60 % [1,2], nanolaminates, nanocomposites [3,4] or crystalline γ-Al_2O_3 [5].

Nanolaminates represent a further development in multi-layer technology. The denomination nanolaminates refers to coating systems which consist of a multitude of extremely thin individual layers, the thickness of which only amounts to a few nanometers each [3]. The nanocomposites are among the most recent developments. These are nanocrystalline, isotropic multi-phase systems in which two phases that are not soluble in each other (e.g. Al, Ti, Si) are deposited on the surface of the tool during the coating process. Examples include the embedding of nanocrystalline cubic TiN in an amorphous AlN matrix (TiN/a-AlN), or of nanocrystalline TiAlN or AlCrN in an amorphous Si_3N_4 matrix [4]. Nanocomposites may be deposited as mono-layer or multi-layer coating systems. The layer boundaries and grain boundaries in nanolaminates and in nanocomposite coatings represent energy-consuming resistance for cracks. Crack formation and the crack propagation rate are thereby reduced. Nanolaminates and nanocomposite coatings are thus not only characterised by an extremely high hardness at elevated temperatures and thermal wear resistance, but also by good toughness properties.

The coating of tools with Al_2O_3 has thus up to now always been reserved for CVD technologies. Due to the outstanding wear protection and high performance potential of Al_2O_3 coatings, intensive research has been undertaken over the past few years into producing such coatings with the aid of the PVD process. By means of the pulsed magnetron sputtering process, it is nowadays possible to coat machining tools for turning, milling and drilling operations with crystalline γ-Al_2O_3 layers at substrate temperatures of between 500 °C and 650 °C. The γ-Al_2O_3 coating may be applied in such cases as a mono-layer or multi-layer coating in combination with nitride intermediate coatings.

3 Native Esters – an Environmentally Friendly Lubricoolant

Oils generate far lower costs when it comes to maintenance and disposal compared to emulsions. Their service life is practically unlimited. There are drawbacks, however. These include the higher costs associated with initial and subsequent filling processes, the proneness towards vapour and mist formation, and the high degree of adhesion of the oil on the workpieces, which necessitates washing of the components (Table 1). Oil vapour and oil mist may form a combustible mixture in the presence of air and can thus lead to deflagration.

Oils suitable for machining should, therefore, have a low viscosity, low emissions and a high flash point [6,7]. These prerequisites are met by native synthetic ester oils. Compared to mineral oils they are characterised by a low volatility, a high flash point, as well as better lubricating properties, skin tolerance and biodegradability [7]. In spite of the advantages which synthetic esters hold, mineral oils are still currently used in the majority of cases (approx. 90 %) where oils are employed as a lubricoolant in cutting processes. The reason for this has been the lower procurement costs of mineral oils to date. This advantage of mineral oils is, however, losing in significance due to the crude oil prices, which have seen a steep increase over the past few years.

Compared to emulsions, oils have a lower thermal capacity. They thus remove less heat from the machining site, leading to greater thermal load on the machining tool. On the positive side, oil has a superior lubricating effect that reduces friction and adhesion between tool, component and chips. The different cooling and lubricating properties of oils and emulsions have an effect on the wear mechanisms and on the progress of wear during the machining process.

Table 1: Differences between oil and emulsion.

	Oil	Emulsion
Percentage of consumption	10 %	90 %
Skin tolerance	good	problematic
Workplace contamination	high / low	low
Water hazard class	1–2	3–4
Media costs	high	low
Maintenance costs	low	high
Duration of use	unlimited	2–24 month
Disposal cost	low	high
Quantity of waste water	–	very high
Fire prevention cost	high	–
Time required for workpiece and toll cleaning	high	low

4 Test Results for Drilling Inconel 718 and Discussion

When drilling into the nickel-based alloy, Inconel 718, the question to what extent the replacement of an emulsion by an additive-free ester would affect the performance of coated carbide drilling tools was investigated. Due to their good cooling effect, emulsions are usually employed as a lubricoolant when drilling into high-temperature resistant nickel-based alloys.

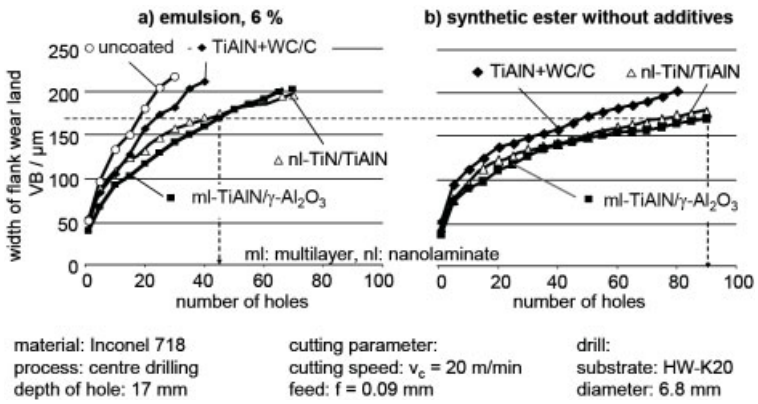


Figure 1: Effect of the lubricoolant and PVD coating system on tool wear when drilling Inconel 718.

The results shown in Figure 1, which are dependent on the coating system and lubricoolant used, reveal that the coating system has a considerable influence on tool wear when drilling using an emulsion. The tool life criterion was a wear land width of VB = 0.17 mm. The highest level of wear was measured on the uncoated tools. Significantly lower wear was observed on tools coated with the new coating systems nl-TiN/TiAlN and ml-TiAlN/γ-Al_2O_3.

When drilling using an emulsion, the cooling effect is dominant. Due to the low proportion of oil, which amounts to only 6 %, the lubricating effect is less prominent. Under these conditions, the coated tools wear at a significantly slower rate compared to the uncoated ones. This is due to the great hardness of the hard-material coating layers and to their high level of resistance to

abrasive wear. Although the synthetic ester has a poorer cooling effect compared to the emulsion, it does demonstrate a far better lubricating effect. The enhanced lubricating effects of the ester lead to better lubrication at the frictional contacts, and thus to a significant reduction in abrasive and adhesive wear processes on the tool flank. Subsequently, this results in a lower level of wear on all coated tools.

5 Effect of the Lubricoolants on Wear Formation when Turning Using PVD-coated Cemented Carbides

Mineral oils still represent the most commonly used oil-based lubricoolants during cutting processes. Before any switch from mineral oil to a synthetic ester may be made in a machining operation, the performance potential of the synthetic ester must be compared with that of the mineral oil for the tribological system of machining.

Appropriate tests were carried out during the turning (v_c = 200 m/min, f = 0:2 mm, a_p = 2 mm) of the austenitic steel, X5CrNi18-10 (AISI 304), using a synthetic ester (ν = 9.8 mm^2/s, flash point: 220°C) and a mineral oil (ν = 9.4 mm^2/s, flash point: 155°C) as lubricoolants. In order to eliminate the influence of additives on tool wear, pure base oil was used in each case. The tools were coated with TiAlN. The geometry of the indexable inserts (CNMG120408) and the cemented-carbide substrate (WC-6Co) was the same in the case of all inserts.

As the results in Figure 2 show, the mean tool life amounted to 20 min when using the cutting inserts with ester oil. This represents a 25% increase compared to that achieved when turning using mineral oil. The wear criterion determining tool life in the case of both fluids was the formation of crater wear. When using mineral oil, however, this crater wear developed at a significantly faster rate.

Compared to mineral oil, esters demonstrate a better lubricating effect due to their polar structure, and, as results from using hardening oil show, they also enable heat to be removed more efficiently and more evenly. Tests carried out when grinding high-speed steel using sintered corundum grinding wheels revealed that ester oils lead to a lower thermal impact on surface properties as compared to mineral oils [8]. Thus the higher level of crater wear evident when turning the austenitic steel material using mineral oil may be attributed to the greater friction and higher temperatures in the contact zone of the tool face compared to those arising with ester oils. Both effects promote wear formation on the tool face. Higher cutting temperatures, in particular, lead to rapid propagation of the crater wear in the cemented-carbide substrate as soon as the hard-material coating has been worn through.

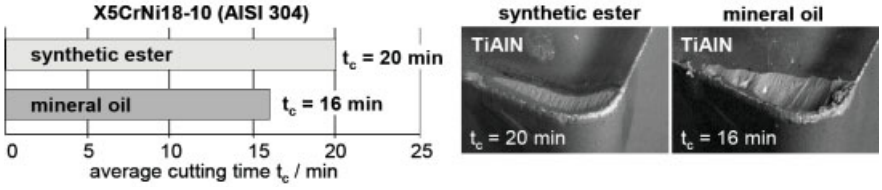


Figure 2: Influence of the lubricoolant on tool wear when turning X5CrNi18-10 (AISI 304).

6 Wear Behaviour when Dry Face Milling the Quenched and Tempered Steel SAE4140+QT

The high performance potential of oxidic PVD coating systems may be demonstrated effectively when dry-milling the quenched and tempered steel, SAE 4140+QT (42CrMo4+QT). Even after a milling path of 12 m, the inserts coated with the multi-layer coating system, ml-TiAlN/γ-Al_2O_3, did not reveal any comb cracks under a light microscope within the contact zone on the tool face, see Figure 3a. Only when carrying out analyses using a scanning electron microscope, very fine comb cracks could be discerned also in the cemented carbide coated with TiAlN/γ-Al_2O_3, see Figure 3c. By contrast, the reference inserts using the nitridic coating systems revealed initial comb-like cracks in the coating when examined under a light microscope after a milling path of only 4 m. These comb cracks then promoted either partial or even complete wear of the coating on the tool face and tool flank of these inserts. In the case of the milling inserts coated with crystalline γ-Al_2O_3, the contact zones remained completely coated until the end of the test (Figure 3c); on the tool flank, a considerably smaller wear zone formed, see Figure 3b.

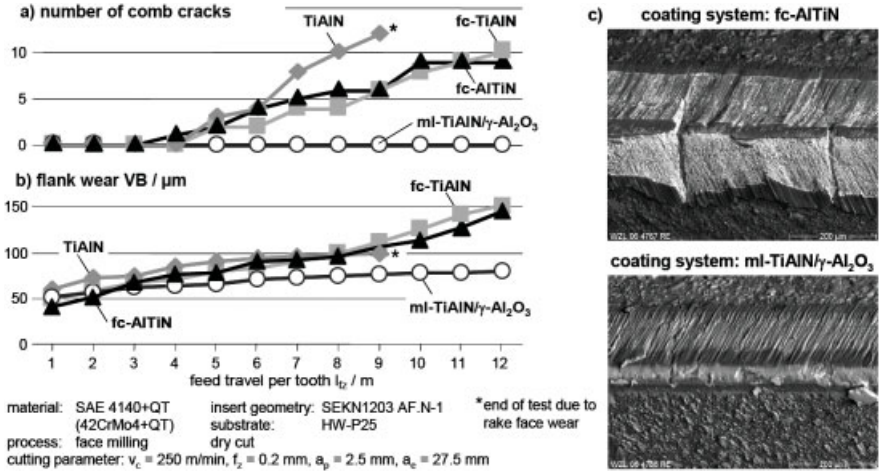


Figure 3: Effect of the coating system on the formation of comb-like cracks in the insert and on tool-flank wear.

Comb cracks are generated during milling operations due to the thermal alternating stress in the hard-material coating and the cemented-carbide substrate occurring as a result of the interrupted cut. The observation that no comb cracks formed in the cutting part of the inserts coated with TiAlN/γ-Al_2O_3 may be attributed not only to altered friction conditions in the contact zones but above all to the lower thermal conductivity of the oxidic coating system. As shown in Figure 3, this leads to more heat being led away via the chip, so that the substrate is subject to less thermal stress. As the graphics in Figure 3a, b and the scanning electron microscope images in Figure 8c effectively show, the performance potential of the inserts coated with TiAlN/γ-Al_2O_3 is by far not exhausted even after a milling path of 12 m.

7 Acknowledgments

The work presented in this paper has been supported within the framework of the Collaborative Research Centre (Sonderforschungsbereich – SFB 442) entitled “Environmentally Friendly Tribological Systems” of the German Research Foundation (Deutsche Forschungsgemeinschaft – DFG). The authors gratefully acknowledge the financial support of the German Research Foundation (DFG) within the project number KL 500/60-1.

8 References

[1] G. Erkens, Proceedings THE Coatings, Editions ZITI, Thessaloniki, 2005, p. 53.

[2] T. Leyendecker, O. Lemmer, R. Cremer, Pulvermetallurgie in Wissenschaft und Praxis, Band 20, ISL-Verlag, 2004, p. 229.

[3] T. Cselle, M. Morstein, et al., Werkzeug Technik, Nr. 77, März 2003.

[4] T. Cselle, Proceedings 3rd International Conference Coatings and Layers, Rosnow, CZ, 2004.

[5] K. Bobzin, E. Lugscheider, M. Maes, C. Piñero, Thin Solid Films, Elsevier, Vol. 494, 2005, p. 255–262.

[6] T. Mang, W. Dresel, Lubricants and Lubrication, Wiley-VCH, Weinheim, 2001.

[7] C. Freiler, Kontakt und Studium, Band 555, Expert Verlag, Renningen-Malmsheim, 2000, p. 249.

[8] E. Minke, Proceedings 3rd International Machining and Grinding Conference, Society of Manufacturing Engineers, Cincinnati, Ohio, 1999.

Wear Resistant PVD-Coatings for Components

K. Bobzin, N. Bagcivan, N. Goebbels, A. Krämer
Surface Engineering Institute, RWTH Aachen University, Aachen

Abstract

A substitution of toxic surface active additives in lubricants is the motivation of the collaborative research centre SFB 442 “Environmentally friendly tribosystems”. The aim is realized by a combination of a lubricating biodegradable synthetic ester and a wear resistant and friction reducing PVD-coating (PVD: Physical Vapor Deposition) which replaces the additivated lubricants. The challenge of PVD-coating design and development is the unique variety of applications which is covered by the research centre. First, the complex analysis of tribological and material scientific aspects considered with process technological options for each application led to a successful tribological system. The success of the “development on functional specifications” of the research centre has even aroused interest in industry.

At the Surface Engineering Institute (IOT, RWTH Aachen university) low-temperature component coatings like the carbon based graded Me-DLC (metal containing diamond like carbon) coating zirconium carbide (ZrC_g) and the hard coating chromium aluminum nitride (CrAlN) were developed within this project. Enhancements in process technology are considered hereby as well as novel material scientific insights. A lot of new knowledge was gained in the recent past. Mainly, the integration of process analytics led to further improvements and allowed a process transfer from a research unit upon an industrial facility. The advantage of this process transfer is a higher reproducibility of the coating process. The request of coating of all bearing components creates new challenges e.g. the coating of polymer substrates like bearing cages. Therefore, a plasma pretreatment process ensuring good coating adhesion was developed and evaluated. All developments in coating process and design are tested at the partner institutes of the research center to verify the successful approach. Furthermore, the co-action of synthetic ester and coating was investigated by pin-on-disc tests to check the achievement of the aim of the research center. The results showed that the realization is successful.

1 Introduction

With the aim to create an alternative for additivated lubricated tribological systems wear resistant and friction reducing PVD-coatings for components were developed considering the transfer of surface active functions of additives onto PVD-coatings. The development and characterization of these low temperature PVD-coatings were done within the sub-projects A2 and A5 within the collaborative research center SFB 442 “Environmentally friendly tribosystems” at the Surface Engineering Institute (IOT, RWTH Aachen). The coating development is mainly influenced by three aspects. First of all, the tribological complex of loads acting on the coated component should be considered. A second aspect is the component material and its properties and production

history. Last but not least the co-action with the biodegradable synthetic ester is a factor which has influence on hydrolysis stability, oxidation and catalyses.

Two types of coatings are investigated in the following: the graded Me-DLC (metal containing diamond like carbon) coating zirconium carbide (ZrC_g) and the hard coating chromium aluminum nitride (CrAlN). Both coatings are designed for components and are deposited in pulsed low temperature magnetron sputtering processes (<160 °C). Their suitability were shown in different applications in machine tools and for Me-DLC ZrC_g as well as for deep-drawing tools [1–7].

The Me-DLC coating ZrC_g is characterized by high wear resistance combined with good friction properties, a result of the graded coating design. Starting with a pure zirconium interlayer the gradation is achieved by a continuous increase of the partial pressure of the reactive gas acetylene during the magnetron sputtering process. The gradation results in a distribution of hardness along the coating thickness. The top layer consisting of a carbon-rich phase shows solid lubricant properties [4, 7].

A focus in the present research period was set on the analytical description of the deposition process of Me-DLC ZrC_g by plasma analytical methods and the correlation to coating characteristics. The results are used for an upscaling of the coating process. That means a transfer of the coating process from a research unit to an industrial facility. Another working point was to develop a pretreatment process for PEEK (poly ether ether ketone), a technically used thermoplastic. The aim was to evolve a coating process which ensures a good adhesion.

CrAlN is a hard coating of a metastable phase which provides a high wear resistance due to its high hardness and a good oxidation resistance because of its chemical stability. The coating is deposited in a reactive pulsed magnetron sputtering process. A good adhesion is achieved by a metallic interlayer while the tribological properties are gained in the nitride zone. Besides the nitrogen content the coating characteristics are dependent on the ratio Cr:Al [3, 5].

The aim was to improve the friction properties of CrAlN by adding a top-layer of hexagonal aluminum nitride. The hexagonal structure of the top-layer should lead to shearing planes comparable to graphite and improve the friction behavior. Another focus was set on the co-action of coating and biodegradable lubrication. For this, the alternative concept of coating and synthetic ester was tested in a pin-on-disk test against an unadditivated lubricant and coating respectively.

2 Experimental Details

For the plasma analytical investigation of ZrC_g the gradation was examined in discrete steps. After the deposition of the metallic interlayer a constant reactive gas flow was used for the deposition on hardened (HRC 63), polished (R_a: 0.03 µm) 100Cr6 (1.3505, SAE 52100) samples. Langmuir wire probe measurements (cylindrical tungsten tip, 40 µm in diameter, length 4 mm) were carried out to characterize the different phases of the deposition process. Floating potential, electron density and mean electron energy were determined. Next to plasma and process parameters (e.g. reactive gas flow) the mechanical, structural and chemical coating characteristics were ascertained by nanoindentation, x-ray diffraction, SEM (scanning electron microscopy), TEM (transmission electron microscopy) and glow discharge optical emission spectroscopy.

The development of a pretreament and coating process for PEEK bearing cages was carried out at the laboratrory unit PVT 550. Ultrafine grinded round blanks of PEEK (R_a: 0.76 µm) were precleaned in a multi-stage ultrasonic bath with alkaline solutions of different concentrations,

rinsed with deionised water and alcohol and dried. Afterwards, the samples were batched in the vacuum chamber which was subsequently evacuated. For the plasma pretreament, the influence of the etching gas (Ar, O_2, N_2) was investigated inter alia. After plasma pretreament the samples were immediately investigated by contact angle measurement to determine their surface energy and calculate the wetting behavior. Furthermore, PEEK samples were coated with ZrC_g after the pretreatment process. The coating adhesion was evaluated by tape and lattice cut test as well as by scratch test and Rockwell test.

The development of a friction reducing hexagonal AlN top-layer for CrAlN was carried out at the sputtering facility CC800 (CemeCon AG, Würselen). The deposition took place consequently after the CrAlN deposition as a pulsed reactive magnetron sputtering process. In magnetron sputtering process two aluminum targets (99.95 %) were used. The aim of the development was to deposit a hexagonal aluminum nitride layer with good adhesion. The coatings were characterized with regard to coating thickness, adhesion, morphology, structure and dry friction against 100Cr6.

For the investigation on the co-action of coating and lubricant hardened, polished and coated (ZrC_g, CrAlN) round blanks of 100Cr6 were tested in a pin-on-disk tribometer combined with a 100Cr6 ball of 6 mm in diameter and a lubricant (mineral oil based lubricant FVA2 (Deutsche BP, Landau), synthetic ester HISM109 (hydroxy isobutoxy stearic acid methyl ester) (Institute for Technical and Macromolecular Chemistry ITMC, RWTH Aachen). The testing parameters were chosen as followed: bath lubrication (12 ml) at a normal load of 15 N in an air-conditioned room (23 °C $\pm$ 2 °C, 40 % $\pm$ 5 % relative humidity). The test length was 1000 m at a track diameter of 5 mm. So, 63695 overruns per point were reached. The testing speed was varied from 1.5 cm/s, 2 cm/s, 3 cm/s, 5 cm/s up to 10 cm/s. Friction coefficients were noted automatically. Wear volumes and wear rates were calculated for sample and counterpart by the results of laser profilometry or light microscopy.

3 Results and Discussion

Within the plasma analytical investigation of the reactive deposition of discrete C-content containing ZrC coatings a dependence of the process and plasma parameters on target poisoning was ascertained. Target poisoning describes the effect of the formation of an isolating layer on the target surface, here a carbide layer. With increasing reactive gas share the cathode voltage at a constant target power increased due to the increasing target poisoning until the formation and sputtering of the isolating layer is balanced. By the reason that the target power is kept constant the cathode current dropped with the formation of the isolating layer. There is a dependence of the electron density and deposition rate on the cathode current. If the current drops the other will, too [8]. This effect was clearly seen. Further, it could be ascertained that the mean electron energy increased at the same time, caused by the increasing electric field related to the increasing cathode voltage. The opposed behavior of floating potential and mean electron energy was correlated to the electron repelling current which is earlier reached at higher electron energies. The characterization of coating showed no direct correlation to plasma parameters. The influence of the changing zirconium/carbon content and their phase formation was dominant in the investigation which is confirmed by GDOES measurements. Valued at the results of GDOES and nanoindentation measurements the stoichiometric ZrC phase was determined between a reactive gas share of 2–3 % (Figure 1). So, there is a very small zone of pure ZrC phase in the graded

coating which does not explain the good wear characteristics. The explanation is the formation of a broader nanocrystalline region between 3-6 % reactive gas share which could be detected by TEM and HRTEM investigations.

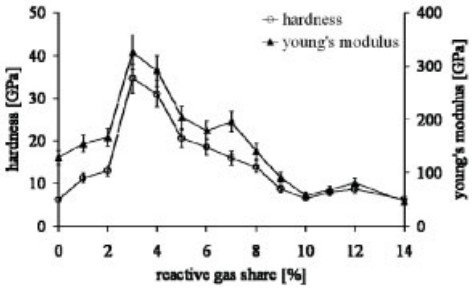
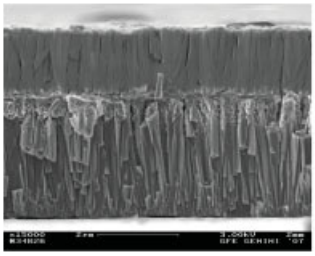


Figure 1: Mechanical properties of ZrC coatings and their dependence on the reactiv gas share

The different adhesion mechanisms between coating and metal or coating and polymer required that a new pretreament method had to be developed for the deposition of ZrC_g on the polymer PEEK as only metal substrates where coated within the research center yet. Plasma pretreaments of polymers had been proved as very effective to increase the adhesion between substrate and coating [9]. It was shown that polymers require different plasma pretreatments depending on their chemical com-pounds. In this case, the variations of the composition of etching gas showed that an etching process with a mixture of argon and oxygen (ratio 10:1) led to the best adhesion of the ZrC_g coating on PEEK substrates. The etching power variations showed that a power increase improved the coating adhesion with regard to the etching duration. Too long etching times at high etching powers destroyed the surface. Finally, with the developed pretreatment process the ZrC_g was successfully deposited on PEEK. Tape and lattice cut tests showed adhesion class of 0 and a critical load of 10 N in scratch tests after Olivier-Matthews which is quite high for a polymer/coating compound.

The aim of the development of the AlN top-layer was to deposit the hexagonal phase AlN on the cubic CrAlN phase. The connection between the different lattice structures was the challenge. By the change of lattice structure high intrinsic stress can originate which can lead to adhesion loss. But a good adhesion is a basic requirement for tribological applications. First the deposition of the hexagonal AlN was realized in a low temperature process. Via variations of target power and reactive gas flow hexagonal AlN was deposited (Figure 2 left). This was affirmed by x-ray diffraction measurements. Afterwards, the top-layer connection to the CrAlN layer was improved by variations of the interlayer structure. A direct connection from CrAlN to AlN could not be realized with sufficient adhesion. First a metallic interlayer of CrAl improved the adhesion. In Rockwell testing an adhesion class of 1 could be determined and a critical load of 70 N in scratch tests. The comparison of friction behavior of CrAlN and CrAlN with AlN toplayer showed that the top-layer improve friction behavior in dry running conditions (Figure 2 right).

The tribological investigation of the co-action of coating and lubricant showed that a broader distribution of friction coefficients is observed for lower rotation speed. CrAlN/FVA2 showed an improved friction behavior at increasing speed. CrAlN/ HISM109 showed opposed friction behavior. The results for ZrC_g showed that the level of friction coefficient for FVA2 reached a



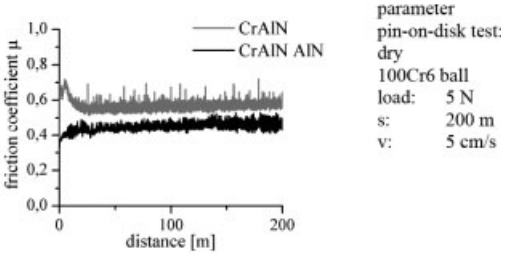


Figure 2: left) SEM micrograph of magnetron sputtered CrAlN-AlN; right) comparison of friction progression of CrAlN and CrAlN with AlN top-layer

static value up to a velocity of 5 cm/s. At a velocity of 10 cm/s a drop in friction coefficient was seen. ZrC_g/HISM109 showed a slight tendency to be dependent on the rotation velocity. A better friction behavior was achieved with increasing speed. The wear rates of samples indicated in all cases that the wear of both coatings is independent of the sliding velocity (Table 1). In contrast, the wear rates of the metallic counterparts showed trends depending on sliding velocity, coating and lubricant. These results can be interpreted that in dependence of the lubricant different areas of friction were reached. CrAlN/100Cr6 with FVA2 shows a friction behavior correlating to the mixed friction area, CrAlN/100Cr6 and HISM109 can be allocated in the transition area between mixed and fluid lubrication. The behavior of ZrC_g/100Cr6 can be related to the beginning of mixed friction area for both fluids where non-hydrodynamic characteristics prevail [10]. The different characteristics of lubricants and their wettability can lead to different levels of counterpart wear rates as well as coating roughness.

Table 1: Wear rates of samples and counterparts

	CrAlN	wear rate$_{sample}$ $\cdot 10^{-7}$ [mm³/Nm]	wear rate$_{counterpart}$ $\cdot 10^{-7}$ [mm³/Nm]	ZrC_g	wear rate$_{sample}$ $\cdot 10^{-7}$ [mm³/Nm]	wear rate$_{counterpart}$ $\cdot 10^{-7}$ [mm³/Nm]
FVA2	v1.5	3.26	16.70	v1.5	1.16	7.08
	v2	3.68	13.80	v2	1.33	6.97
	v3	3.92	12.80	v3	0.67	6.71
	v5	3.08	5.63	v5	0.85	7.46
	v10	4.11	3.53	v10	1.05	6.70
HISM 109	v1.5	5.04	4.44	v1.5	1.04	1.34
	v2	2.20	3.14	v2	1.68	0.86
	v3	3.66	5.29	v3	1.18	0.75
	v5	3.15	10.60	v5	0.75	0.61
	v10	3.17	7.92	v10	1.29	0.34

4 Conclusions and Outlook

Within the plasma diagnostical investigation a clear dependence on process parameters and plasma parameters were detected. A direct correlation between coating characteristics and plasma

parameters could not be seen yet. Further investigation is planned. It could be determined that the good wear resistance of ZrC_g is not only explained by the formation of the hard stoichiometric ZrC phase. Structural investigation showed that the structural change from a columnar to an amorphous structure contains a broad zone where a nanocrystalline coating is deposited. This has influence on the wear behavior. In future this aspect will be regarded.

A plasma pretreatment method was developed for the deposition of ZrC_g on PEEK substrates. The characterization of deposited coating showed good adhesion values (adhesion class of 0 in tape and lattice cut test, critical load in scratch test: 10 N). Current coated PEEK bearing cages are tested at partner institutes. The results of the investigations will be used for an iterative optimization process.

The change in lattice structure from the cubic CrAlN phase to the hexagonal AlN phase was the great challenge. First, a nm thick pure metallic CrAl layer between both phases led to a good adhesion, so that a critical load of 70 N in the scratch test was reached. In the tribological test a reduction of friction was observed. So, the concept of friction reducing top-layer was realized successfully. Future work will focus on inserting oxygen in the top-layer which should result in a further drop of friction coefficient.

The tribological investigation of CrAlN or ZrC_g coated samples with 100Cr6 balls showed that a lubrication with the developed synthetic ester HISM109 results in lower wear rates for samples and counterparts than the commercially available unadditivated mineral oil FVA2. This can be correlated to the different properties and wetting behavior of lubricants which results in different states of friction in use for the examined rotation velocities. Further investigations shall compare the developed alternative environmentally friendly lubricated tribosystem with a conventional tribosystem with additived lubricants.

Finally, it is to sum up that a lot of novel scientific insights have been gained. These results led and lead to further improvements of the coating designs. All gained knowledge is and will be documented in the expert system of the research center.

5 References

[1] K. Bobzin, E. Lugscheider, M. Maes, P.W. Gold, J. Loos, M. Kuhn, Surface and Coatings Technology, 2004, *188-189*, 649-654

[2] F. Klocke, T. Maßmann, K. Bobzin, E. Lugscheider, N. Bagcivan, Wear, 2006, *260-3*, 287–295

[3] C. Brecher, G. Spachtholz, K. Bobzin, E. Lugscheider, O. Knotek, M. Maes, Surface and Coatings Technology, 2005, *200*, 1783–1744

[4] K. Bobzin, M. Maes, N. Bagcivan, N. Goebbels, in *Proceedings TAE 15th International Colloquium Tribology, 17.–19.01.2006 Stuttgart/Ostfildern*

[5] K. Bobzin, E. Lugschneider, M. Maes, R. Cremer, T. Rasa, Tribologie und Schmierungstechnik, 2006, *53-1*, 15–19

[6] H. Murrenhoff. S. Scharf, International Journal of Fluid Power, 2006, *7-3*, 13–20

[7] K. Bobzin, E.Lugscheider, M. Maes, Materialwissenschaft und Werkstofftechnik, 2004, *35-10/11*, 843-850

[8] G. Franz, Niederdruckplasmen und Mikrostrukturtechniken, 3rd ed., Springer-Verlag, Berlin, 2004, chapter 9

[9] K. DeBruyn, M. Van Stappen, H. De Deurwaerder, L. Rouxhet, J.P.Celis, Surface and Coatings Technology, 2003, *163-164*, 422–428

[10] G. W. Stachowiak, A. W. Batchelor, Engineering Tribology, 2nd ed., Butterworth-Heinemann, Boston, 2001, chapter 3.6 + chapter 4.7

Numerical Calculation of Failure Stresses of PVD Coatings Based on Test Data

Univ.-Prof. Dr.-Ing. P. W. Gold, Dr.-Ing. J. Loos, Dipl.-Ing. H. Elgeti*
Institut für Maschinenelemente und Maschinengestaltung (IME), RWTH Aachen

1 Introduction

Reduction of friction and wear is a very important objective of the design process of modern tribological systems making PVD coatings become more and more popular. Especially carbon based coatings are characterised by very low friction coefficients corresponding with high wear resistances.

Whereas friction and wear properties of these coatings can be assessed directly in test rig investigations, the calculation of admissible stresses requires numerical simulations of representative tests. One of these tests is the so called “Scratch Test” in which a diamond cone moves laterally on a coated surface while the normal load increases continuously. The measured quantity in this experiment is the normal force at which the first damage of the coating occurs.

Numerical simulations with the Finite Elements Method of this test procedure make it possible not only to understand the microscopic damage processes but also to calculate the failure stresses corresponding with the failure load, which is necessary to identify the admissible loadings of coated components. These simulations have to consider nonlinear effects like plasticity, strain hardening and contact.

This document shows both the experimental tests and the corresponding simulations for an example coating, which is chrome aluminium nitride (CrAlN) with a thickness of 6.5 µm.

2 The Scratch Test

As shown in Figure 1 in the scratch test procedure, a Rockwell C cone scratches on a coated specimen, while the contact load increases continuously. This load leads to plastic deformation of both the substrate material and the coating, which has to be assessed. This kind of load causes complicated stress conditions in the coating, which can be characterized as bending stress in front of the indenter, frictional shear stress in the contact zone and remaining tension stress behind the indenter.

Depending on the typical failure mode of the assessed coating, damages may occur both due to the bending loading and in consequence of the high plastic strain in the transition of shear and tension zone. In most cases, the increasing normal force first causes small cracks, which may be detected analysing the acoustic emission or by microscopic investigation of the specimen. Higher loads will cause laminar flaking of the coating, which results in a significant rising of the lateral force [1].

The result of the scratch test procedure is the normal load, which corresponds to the first observed damages. For the CrAlN coating the scratch load arose to 80 N.

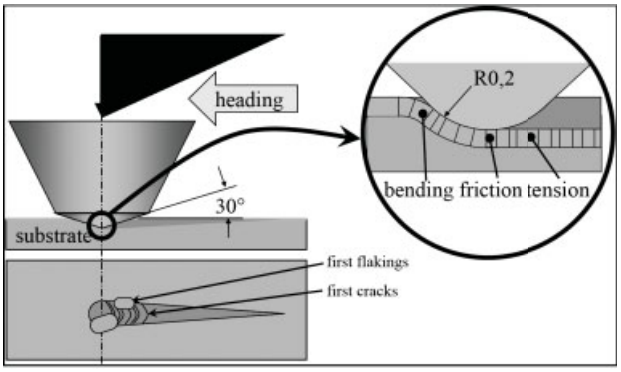


Figure 1: Functional principle of the scratch test

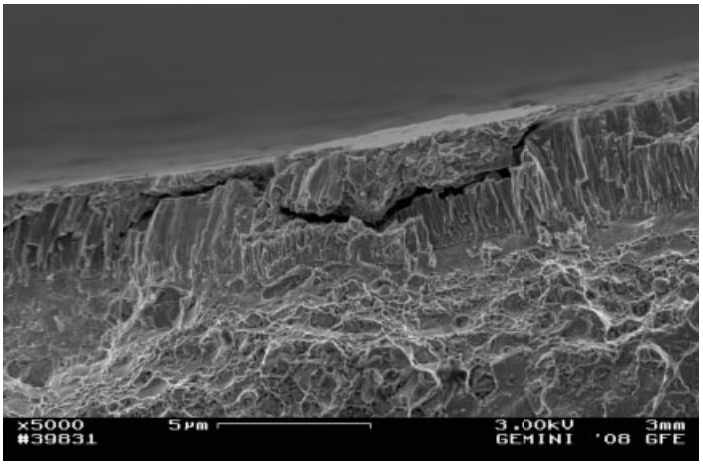


Figure 2: REM photography of a longitudinal grinding (by courtesy of IOT d. RWTH Aachen)

Figure 2 and Figure 3 show both a longitudinal and a transversal grinding of the damaged scratch trace of a CrAlN coating. It becomes apparent, that on one hand the cracks start at the edge of the trace, which is obviously the most stressed zone and one the other hand, that the columnar structure of the coating keeps its orientation and is just little textured. The latter issue indicates, that only very small plastic strains occur, which means that this material fails rather brittle.

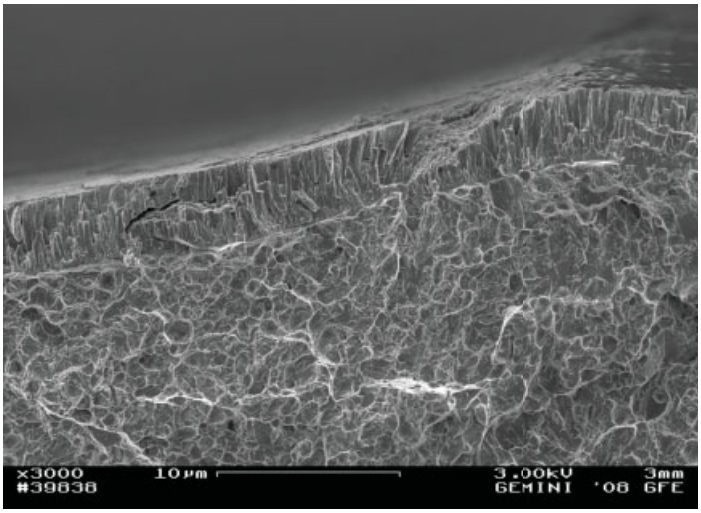


Figure 3: REM photography of a transversal grinding (by courtesy of IOT d. RWTH Aachen

3 Modeling

3.1 General

Figure 4 shows the Finite Elements Model of a coated specimen, which is investigated in the scratch test. The model contains a rigid body (blue) which represents the diamond cone with a tip radius of 0.2 mm and a tip angle of 120°, as it is specified for the Rockwell C indenter, and a continuous, deformable part with the properties of the steel substrate (green) and the coating (red).

In a first calculation step the contact load between both parts is applied whereas the friction coefficient is assumed to 0.1. This load already causes plastic strain in the substrate material. In a second calculation step the rigid body moves laterally by 100 µm. This value is sufficient to reach steady state conditions if the contact load stays constant.

3.2 Material Properties

In the first calculation, the material CrAlN is not assumed to be plastic, whereas its Young's modulus amounts to 305 GPa. In general, the plasticity properties of PVD coatings may be determined by nano indention investigations, since this coating is quite new, however, these investigations could not be done yet. To discuss possible effects of plasticity, the stress is limited by a yield point of 15 GPa in a second calculation.

The tested specimen is a coated disc of a axial roller bearing which consists of hardened 100Cr6. For this material the plastic behaviour of the near surface zone could be analyzed by simulating several ball on disc indentions with different loadings as Figure 5 shows.

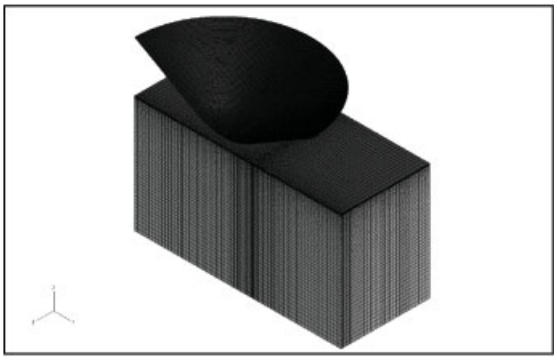


Figure 4: Finite Elements Model of the scratchtest

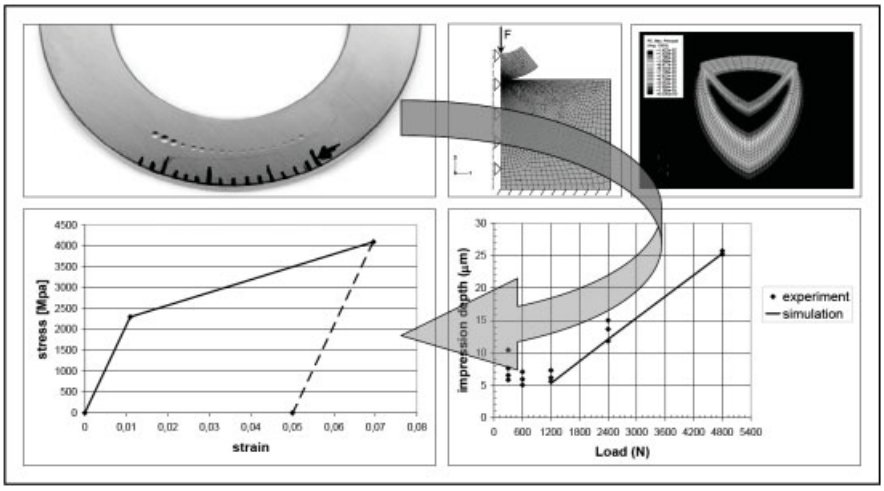


Figure 5: Analyzing the plastic properties of 100Cr6

4 Results

Figure 6 and Figure 7 show the stress distribution in the coating resulting when the assumption of total elastic behaviour is made. The maximum von Mises stress amounts to 47 GPa, which seems to be very high, so that a further investigation of the plastic property of this CrAlN coating is necessary. In Figure 7 it becomes apparent, that the maximum stress both for the bending and the tension zone is in the middle of the scratch trace which is in contradiction to the damages in Figure 3.This issue indicates a significant influence of plasticity. As Figure 8 shows, the maximum strain occurs in a shear zone at the edge of the scratch trace which corresponds perfectly to the observed damage.

Discussing these two calculations leads to the conclusion, that the calculated material strength is obviously an overestimation. Nevertheless, this way of modelling is helpful to understand the

damage mechanisms of the scratch test, which is absolutely necessary to compare test results of different specimen. Further, if the plastic behaviour of the coating will be investigated, this finite elements model will also be suitable to quantify the real material strength.

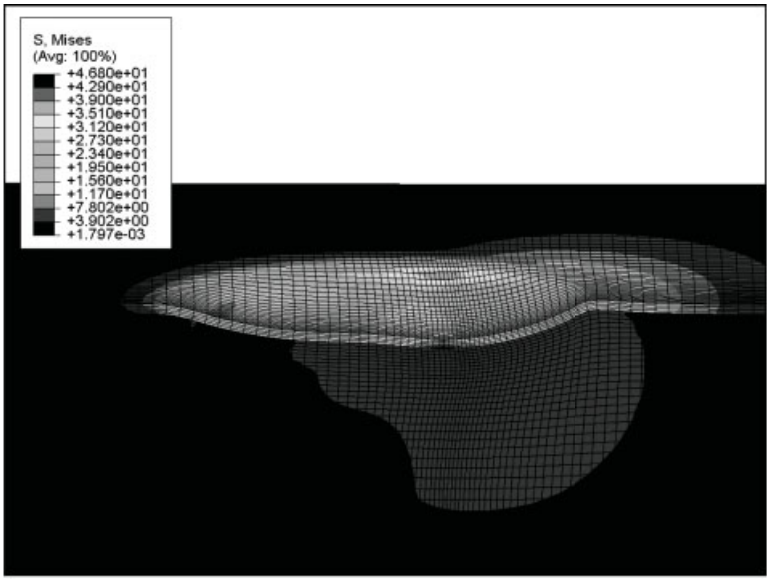


Figure 6: von Mises stress [GPa]

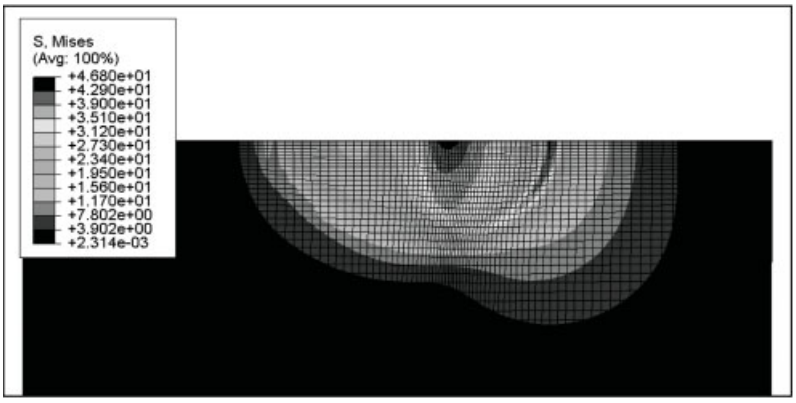


Figure 7: von Mises stress [GPa] underside the CrAlN coating

The authors gratefully acknowledge the support of the Deutsche Forschungsgesellschaft within the Collaborative Research Center SFB 442 “Environmentally Friendly Tribosystems”.

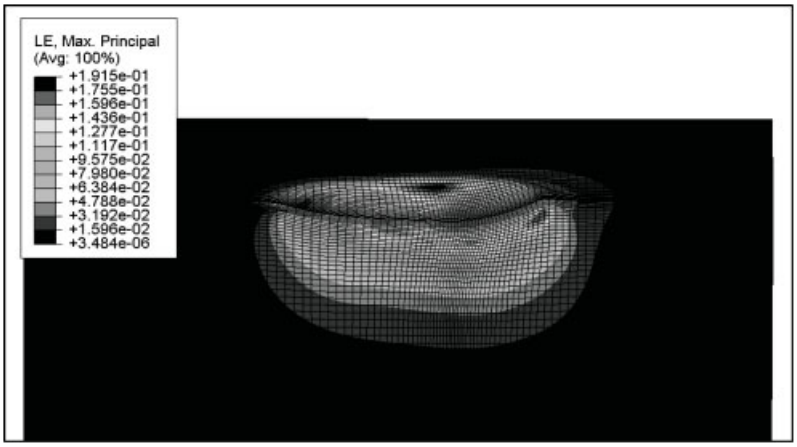


Figure 8: max. principal of the real strain for a assumed yield stress of 15 GPa

References

[1] Mittal (Hrsg.), Adhesion Measurement of Films and Coatings **1995,** VSP

Performance of DLC-coated Spindle Ball Bearings

Prof. Dr.-Ing. C. Brecher, Dipl.-Ing. G. Gerlach,
WZL Werkzeugmaschinenlabor, RWTH Aachen

1 Introduction

The main spindle systems of modern machine tools have to operate in higher performance ranges because of the required lower processing times. The requirements of spindle systems rise continuously with the increase of processing and cutting velocities. Furthermore the process cycle forces the bearing to work in mixed-film friction condition. The responding kinematic constraint results in higher loads of the tribological system. These operational demands have a strong influence on the resulting tribological system.

The Collaborative Research Centre (SFB 442) funded by the Deutsche Forschungsgemeinschaft (DFG) intends to develop "Environmentally compatible Tribological Systems". According to previous investigations different coatings and lubricants for high speed applications were tested. Thereby it turned out that low temperature coatings (Diamond Like Carbon-DLC) in combination with ceramic balls (Si_3N_4) are appropriate [1].

In this contribution test results of coated and uncoated spindle bearings in combination with additivated (synthetic ester) and unadditivated (environmentally compatible) lubricants are presented.

To improve the tribological system the coatings can be deposited onto the raceway of the bearings or onto the cages.

By means of test bench analysis the spindle bearings are checked under constant axial load for the application in a main spindle. In a first test run the bearings are exposed to higher load conditions and insufficient lubrication. In a second run the bearings are driven alternately by mixed-film friction from downtime to high speed range in order to determine the tribological characteristics in comparison of coated and uncoated bearing rings.

In a second step coated cages at standard and minimum lubrication and additionally at dry running condition were analysed in comparison to uncoated cages.

The decisive criteria for the qualification of the tribological systems are the resulting wear and temperature behaviour of the spindle bearing.

2 Spindle Ball Bearings and Coatings

For high speed application in main spindle systems a high reliability is required. In case of bearing failures the downtimes for demounting, repair, waiting time for spares and production downtimes due to a multiplication of the resulting loss. More than 80 % of the occurring failures causes of roller bearings are related to the lubrication condition. Even more than 50 % are caused by insufficient or inadequate lubrication [2].

One of the most frequent failures are broken cages, which can be caused by many different effects. Some of the steps who lead to that failure are the contact between cage and guide flange,

increasing friction, tarnishing of the cage, wear of cage material (guide flange and cage pocket), increasing temperature and effect reinforcement etc.

In order to understand the kinetic and kinematic conditions in the spindle ball bearing some important facts have to be mentioned.

2.1 Spindle Ball Bearings

Spindle ball bearings are precision angular contact ball bearings with a defined contact angle. In the composed bearing the radial clearance (e) is given. To initiate a defined axial overload (a) the preload class is manufactured. Afterwards the inner and outer rings have to be grinded onto the same width (Figure 1).

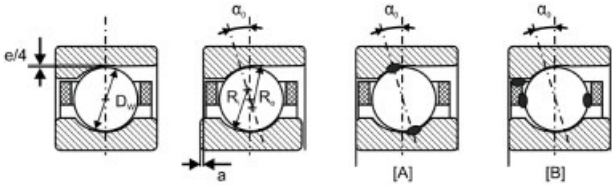


Figure 1: Basics of a spindle ball bearing

The tribological system in the ball bearing can be separated in two parts due to friction and wear. The first one is the rolling contact between the rolling element and the inner and outer rings [A]. The second tribological system exists between cage and (outer) ring and also between cage and rolling elements beeing defined as a slipping contact. An approach to reduce the occurring friction and wear is to protect the bearing by coating. Focus is on the reduction of the friction coefficient, the decrease of warming, wear protection, improvement of the characteristics at dry-running condition etc.

The basic demand for the coating process is the prevention of structural transformation of the substrate which can cause reduction of hard- and roundness. The typical substrate material is 100 Cr6 and should not be heated above 160 °C [3]. Form- and orientation tolerances have to be maintained and the coating may not have an influence onto the kinetic and kinematic attributes. A homogeneous coating-thickness on the raceway and on top of the cage has to be ensured. The coating itself has to possess a high roll-over protection at Hertzian stress more than 2000 MPa. The form and orientation tolerances of the cage are lower than the coating thickness which is negligible.

2.2 Coatings

The analysed coatings are amorphous hydrocarbon coatings. Both tribological systems of the bearing [A] and [B] are focused. For the analysis of the spindle ball bearings a metal-modified (a-C:H:W) and non-modified (DLC PECVD) coating have been selected. For the coating of the cage a metal-modified zirconium carbide (ZrC_g) and a non-modified coating (DLC PECVD) were chosen. The schedule for the experimental analysis is shown in Figure 2. Before the test run analysis the basic demands on the coatings have to be specified.

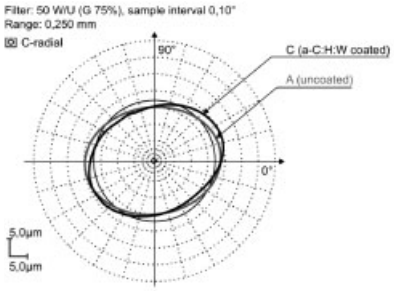
Row	Stage	Coating	Lubricant	Lubrication supply	Load [N]
1	1 Stage run	-	additivated	100 mm³/h	1000
		-	unadditivated	100 mm³/h	1000
		a-C:H:W	additivated	100 mm³/h	1000
		a-C:H:W	unadditivated	100 mm³/h	1000
	2 Alternating run	-	additivated	100 mm³/h	1000
		-	unadditivated	100 mm³/h	1000
		a-C:H:W	additivated	100 mm³/h	1000
		a-C:H:W	unadditivated	100 mm³/h	1000
	3 Minimum lubrication	-		0,001 g	1000
		a-C:H:W		0,001 g	1000
2	Stage run	-		5,0 g	800
		-		0,001 g	800
		-		-	800
		DLC PECVD		5,0 g	800
		DLC PECVD		0,001 g	800
		DLC PECVD		-	800

Row	Stage	Coating	Lubricant	Lubrication supply	Load [N]
3	1 Stage run	-	additivated	100 mm³/h	220
		ZrC_g	additivated	100 mm³/h	220
	2 Long-time test	-	additivated	100 mm³/h	220
		ZrC_g	additivated	100 mm³/h	220
	2 Dry-running condition	-	additivated	100 -> 0 mm³/h	220
		ZrC_g	additivated	100 -> 0 mm³/h	220
4	1 Stage run	-		5,0 g	800
		DLC PECVD		5,0 g	800
		ZrC_g		5,0 g	800
	2 Dry-running condition	-		-	800
		DLC PECVD		-	800
		ZrC_g		-	800

Figure 2: Schedule of experimental analysis of the spindle ball bearing (left) and the cage (right)

2.3 Qualification of the Coating

The results are shown in Figure 3 representing that the hardness of the inner and outer ring were not reduced by the coating process within the range of 59.0 HRC. Additionally the surface roughness in axial and radial direction and the roundness do not show a strong loss of precision through the coating process. The roundness failure of all analysed bearings is close to the maximum tolerance limit.



Bearing		A	B	C	D
Coating		-	-	a-C:H:W	a-C:H:W
Hardness [HRC]	OR	59,2	59,0	59,0	59,5
	IR	59,0	59,0	59,0	59,0
R_z [µm] axial	OR	0,33	0,45	0,70	1,09
	IR	0,24	0,26	0,31	0,19
R_a [µm] radial	OR	0,14	0,13	0,43	0,73
	IR	0,18	0,70	0,19	0,31
Roundness [µm]:[mm]	OR	4,73!	4,89!	6,30!	5,24!
	IR	1,00!	1,58!	0,98!	4,33!

Figure 3: Analysis of the spindle ball bearings

The different components are analysed in two different test benches. In the rotational tribometer the inner contact of the rolling element and the tribo disc leads to a higher hertzian stress. In the spindle ball bearing test bench realistic mounting arrangements and higher axial loads are realized [4]. The experimental analysis is separated in two setups. First the coated rings of the ball bearings are tested in two different rows on the spindle ball bearing test bench. Afterwards coated cages are analysed on the rotational tribometer and the spindle ball bearing test bench.

3 Experimental Analysis of the Spindle Ball Bearing

In Figure 2 the schedule of the test runs was already presented. The characteristics of temperature and friction torque of uncoated and a-C:H:W-coated bearings were compared with the application of additivated and unadditivated lubricant by oil-air-lubrication. The DLC PECVD coated were compared with uncoated bearings by use of additivated grease.

3.1 Ball Bearings with a-C:H:W-coating (Row 1)

The bearings were tested in three different stages. In stage 1 the bearings were driven for 3 h until the maximum speed of 24000 min^{-1}. The rotation speed was increased in steps of 2000 min^{-1} up to 10000 min^{-1} and then in 1000 min^{-1} increments.

In the second stage the bearings were driven alternately by mixed film friction from downtime to five different speeds (5000, 10000, 15000, 20000, 24000 min^{-1}) in order to determine the tribological characteristics. In a third stage run the lubrication was reduced onto a minimum of grease (0,001 g) to determine the characteristics of the coating, because spindle breakdowns are often caused by insufficient lubrication. The preload for the three test stages were in the upper-medium range of 1000 N.

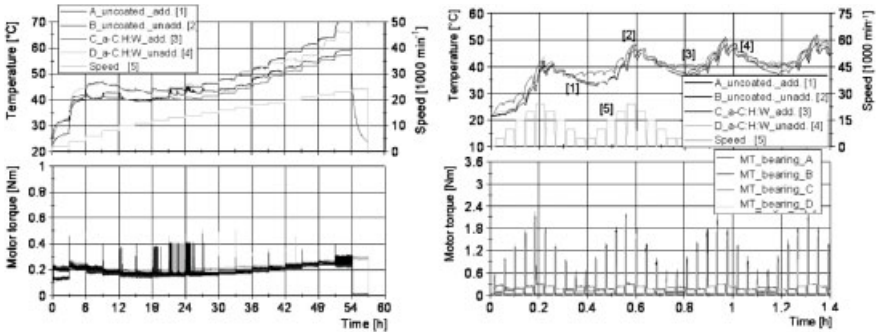


Figure 4: Results of the stage run (1) and the alternating run (2)

Results:
The yielding temperature and motor torque of stage 1 showed a uniform trend. Up to the maximum speed of 24000 min^{-1} the a-C:H:W-coating leads to a lower friction torque and temperature. In contrary the use of an unaddativated coating yields to higher friction torque and temperature. An uncoated bearing in combination with an additivated lubricant leads to a lower temperature than an a-C:H:W-coated bearing in combination with an unadditivated lubricant (Figure 4).

In the alternating run of stage 2 the similar have been achieved. With the additivated lubricant the friction torque and temperature of the uncoated and a-C:H:W-coated bearing are in the same range. In contrary to stage 1 the a-C:H:W-coated bearing in combination with an unadditivated lubricant runs on a lower level of temperature and motor friction. The analysed wear of the stages 1 and 2 is beyond the measurable quantity of the measuring system.

At minimum lubrication m_{min}=0.001 g (compared to standard: m_{stand}=5.0 g) in stage 3 the whole speed range of the a-C:H:W-coated spindle ball bearing showed a lower temperature. The

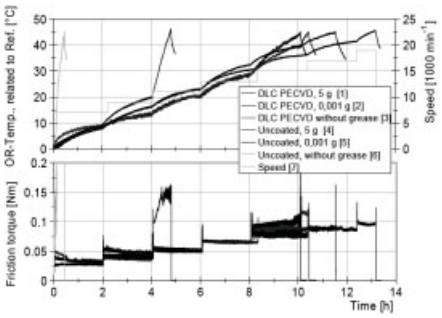
breakdown (maximum temperature of 70 °C) of the uncoated bearing occurred after 12.4 h at 19000 min^{-1} and of the a-C:H:W-coated bearing after 18.3 h at 22000 min^{-1}. This shows a strong postponement of the breakdown that could be reached by the applied coating.

3.2 Ball Bearings with DLC PECVD Coating (Row 2)

The DLC PECVD-coated bearing was compared with uncoated bearings with different amounts of grease lubricant: standard lubrication of 5.0 g, minimum lubrication of 0.001 g and dry-running condition without any grease. The stage run had a stage duration of t_{stage}=2 h and an initial speed of n_{start} = 7000 min^{-1} with an increasing speed of 2000 min^{-1} per step up to 20000 min^{-1}.

Results:

The DLC PECVD-coated bearings had a lower motor torque and temperature over the whole speed range until the temperature limit T_{limit} = 65 °C was reached. The difference at standard lubrication was about 4 °C at 17000 min^{-1} and a higher speed of 2000 min^{-1} could be realised. At minimum lubrication a strong postponement until T_{limit} could be realised and at dry-running condition the time until T_{limit} could be extended strongly (Figure 5).



Coating		Uncoated	DLC-PECVD	Uncoated	a-C:H:W
Preload [N]		800	800	1000	1000
Standard lubrication (5.0 g)	Time [h]	11.6	13.2		
	n [min^{-1}]	17000	19000		
Minimum lubrication (0.0001 g)	Time [h]	4.6	10.2	12.3	18.3
	n [min^{-1}]	11000	15000	19000	22000
Dry-running condition	Time [h]	0.5	10.6		
	n [min^{-1}]	7000	15000		

Figure 5: Comparison of the characteristics of DLC PECVD coated and uncoated bearings

4 Experimental Analysis of the Bearing Cage

In order to analyze the contact performance between the cage and the outer ring and the rolling elements the cage was coated by ZrC_g and DLC PECVD.

4.1 Cage Coated with ZrC_g Coating (Row 3)

The ZrC_g coated cages were analysed on the tribometer test bench. By reason of comparable test condition the same components (out of the cages) were used. To get a first impression of the characteristics the cages were driven in a stage run (stage 1) from 0..15000 min^{-1} for a duration of t_{st}=1 h and speed increments of 1000 min^{-1}.

At standard lubrication of 100 mm^3/h the friction torque and temperature curves showed a slight difference. All curves had the same characteristics. In the mixed-film friction condition the friction torque rises uniformly to the speed and the temperature of the bearing. The next range

is a reduction of the friction torque at steady temperature. Afterwards a range of sporadic non reproducible friction torque-peaks up to 8000 min^{-1} were measured (cage rattling) with a coeval increasing temperature. From 8000 up to 15000 min^{-1} the friction torque rises continuously with each stage (compare: Stribeck-curve).

Stage 2 was executed with a longer stage duration of t_{st}=8 h in the range of the cage rattling up to 8000 min^{-1}. In that case the sporadic peaks only occurred with uncoated cages. Cages coated with ZrC_g did not have occurring peaks of the friction torque and had a slightly lower temperature (Figure 6).

In the third stage the cages were oil-off tested at a constant speed of n=15000 min^{-1} in the spindle test bench. After a duration of 15 h the oil-air-lubrication was turned-off and the test went until the temperature-limit of t_{limit}=60°C. In the range of the constant lubrication the friction torque and the temperature had a steady-state condition. After the lubrication and air turn-off the temperature rose to a second steady-state level for a short time because of the missing cooling effect of the compressed air. When the lubrication is starting to be insufficient the friction torque and the temperature increased slowly until a peak overrun the temperature limit. The ZrC_g-coating could not extend the time until the breakdown. After the test friction marks could be found on the cages visually and a strong delamination of the cage side contacted to the guiding flange of the outer ring.

4.2 Cage Coated With DLC PECVD Coating (Row 4)

The DLC PECVD-coated cages were run in the spindle bearing test bench. The friction torque and temperature curve at standard lubrication in the test stage run just showed a slight difference. At dry-running condition and a speed of 7000 min^{-1} the uncoated cage showed an immediate increase of the friction torque until a peak causing a breakdown after 4.5 minutes. The DLC PECVD coating showed a nearly linear increasing friction torque and temperature until a peak causing the breakdown after 36 minutes (Figure 6).

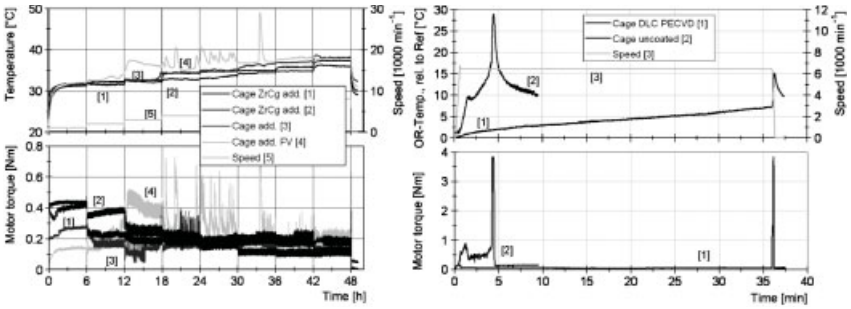


Figure 6: Results of the stage run (Row 3) and the oil-off test (Row 4)

5 Conclusion

The postponement of the breakdown was elongated by factor 8. At a visual control of the peak no indication of a beginning delamination could be found.

In this contribution different coated spindle ball bearings were tested at different loads and lubrication by the criterions of friction torque, temperature and wear.

- At standard lubrication a slight influence onto friction torque and temperature could be measured by a-C:H:W and DLC PECVD-coated inner and outer rings.
- At minimum lubrication a strong postponement of the breakdown have been achieved with both coatings.
- At dry-running condition a strong postponement of the breakdown by DLC PECVD coating have been shown.
- At standard lubrication no higher friction torque and temperature curves by application of the coated cages were measured (ZrC_g and DLC PECVD)
- At minimum lubrication and dry-running condition the DLC PECVD showed a strong postponement of the breakdown and no indication for a delamination of the coating.
- The influence of the unadditivated compared to the additivated lubricants in contrary to coatings is lower.
- A problem of the analysed coating systems for the application in bearing components is the low repeat accuracy of the coating quality.

6 Acknowledgement

The financial support of the German Research Association within the scope of the collaborative research program SFB442 “Environmentally-Compatible Tribological Systems” is gratefully acknowledged.

7 References

[1] Brecher, C.; Spachtholz, G., Advanced tribological properties of coated high precision spindle bearings, *in 15th International Colloquium Tribology – Automotive and Industrial Lubrication*, Technische Akademie Esslingen 28.01.2006, **2006**

[2] Martin, W., Moderne Diagnosestrategien – Basis für eine “Proaktive Instandhaltung”. In: Tagungsvortrag “Forum Vision Instandhaltung”. 25.–26.02.2005, Folie 22, **2005**

[3] Brecher, C.; Erkens, G.; Spachtholz, G., About the advantages of pulsed plasmas to apply advanced tribological coatings on bearing components. in *Proceedings The coatings, 5th International Conference and EUREKA Brokerage Event, Kallithea of Chalkidiki, Greece, 05-–07. October, **2005**, p.187–196*

[4] Brecher, C. et al, SFB442 – Umweltverträgliche Tribosysteme durch geeignete Werkstoffverbunde am Beispiel der Werkzeugmaschine, Final Report 2004, 2005, 2006, **2006**

[5] Brecher, C.; Spachtholz, G.; Gerlach, G., Einsatz von Hartstoffbeschichtungen bei Spindellagern *in Materialwissenschaften und Werkstofftechnik*, **2008**

Effects of PVD-coatings on Fatigue of Roller Bearings

Univ.-Prof. Dr.-Ing. P.W. Gold, Dipl.-Ing. T. Wolf, Dipl.-Ing. M. Plogmann*
Institute for Machine Elements and Machine Design (IME), RWTH Aachen University, Germany

1 Introduction

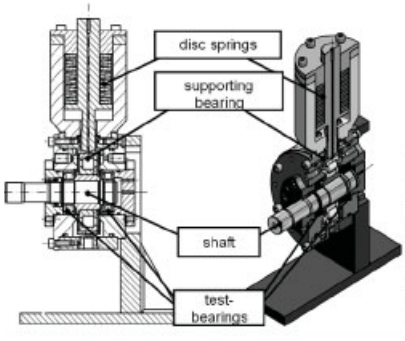
Today, rolling bearings are one of the most often used machine elements. Often AW- and EP-additives are helpful to improve their performance and to reduce wear when rolling bearings are driven under mixed friction conditions. Unfortunately, additives have some disadvantages. It was shown by several authors [1, 2] that they may lead to a reduction in rolling contact fatigue performance when they affect the surface of the rolling bearing. Another disadvantage is that they must be activated by high pressures and temperatures and may be inactive in a temperature-range as shown by [3].

Examinations of the IHU (Institute for environmental medicine) of the University Aachen show that most additives have an ecotoxic effect [4]. This is why the Collaborative Research Center SFB 442 wants to replace additives and use coatings for wear protection instead. Within this project the Institute for Machine Elements and Machine Design investigates, if PVD-coatings are able to protect the surface of rolling bearings. Therefore examinations are done with the help of a FE8-test-rig according to DIN 51819 [5]. The mass loss under boundary friction conditions is proven for several kinds of coatings. Because the bearing type (81212 axial cylindrical roller thrust bearing) used for these examinations has got regions of high slippage much wear is expected for improper lubricants. When using a PVD-coating the mass loss of the rollers was reduced from 1000 mg after 80 h testing time down to 4 mg after 400 h testing time [6]. Besides wear rolling contact fatigue lifetime of PVD-coated rolling bearings is of special interest when they shall be used in applications like gearboxes. Therefore the rolling contact fatigue properties of PVD-coatings are discussed in this paper.

2 Rolling Contact Fatigue Testing

For examinations concerning rolling contact fatigue lifetime of PVD-coatings the radial roller bearing fatigue test rig (RLP) of the Institute for Machine Elements and Machine design is used. Cylindrical Roller bearings NU206 were chosen for the examinations because this type of bearing is often applied. The complete bearing is tested because interactions between the components of the roller bearing together with the lubricant may take place. Figure 1 shows the test-rig used for the examinations and the chosen test conditions. The load is generated by disc-springs and transmitted into the supporting bearing, into the shaft and from there into the test-bearing. All bearing components are loaded periodically with every revolution of the shaft. The oscillation signal is controlled by a vibration-sensor.

When a pitting damage occurs, the vibration level increases and the sensor stops the test. The bearing lifetime is entered in the Weibull-diagram (figure 2). Because two bearings are tested at once, an interruption of the test is caused by the failure of one bearing while the other one is



test conditions	
test bearing	cylindrical roller bearing NU 206
basic dynamic load rating	39 kN/ 45kN
load	16 kN
rotational speed	2000 min^{-1}
lubricant	ester oil 32 cSt
method of lubrication	oil sump lubrication
viskosity rate κ	0,38

Figure 1: Radial roller bearing fatigue test rig (Radial-Lagerermüdungs-Prüfstand, RLP) and test conditions

still intact. Therefore it is necessary to use the sudden-death method for statistical evaluation. By its help it is possible to account the lifetime of the bearing with no failure. When it is applied the diagram for the tests with two bearings tested simultaneously is in accordance with the one for separately conducted bearing-tests. As can be taken from figure 1 the roller bearings run under mixed friction conditions. Because many roughness peaks will therefore be in contact, it is assumed that there will be an influence of the coating on fatigue lifetime.

2.1 Examined PVD-coatings

The examined coating systems originate from industry and the Surface Engineering Institute (IOT), RWTH Aachen University. A short description of the coatings can be taken from table 1, where several properties are listed. As shown in table 1, strong distinctions exist between the PVD-coatings examined. While the 2054.CrAlN-coating is carbon-free, the other coatings contain carbon (640.a-C:H) and metal in case of 1009.ZrC_g and 250.WC/C. Each coating has a different coating structure. Hardness as well as Young's modulus are different, too.

Table 1: Properties of different examined PVD-coatings

	2054.CrAlN	**1009.ZrC_g**	250.WC/C	640.a-C:H
coating structure	columnar	graded	multilayer	columnar + monolayer
coating thickness [µm]	3.6	2	approx. 3	3
hardness [GPa]	13.1	11.3	25	17 bzw. 25
Young's modulus [GPa]	305	155,5	120	275
adhesive strength HF	1	1	1	1
critical scratch load [N]	> 90	30	70	60N
deposition temperature	160°C	<200°C	180–200°C	approx. 210°C
source	IOT	IOT	industry	industry
further informations	[7]	[8], [9]	[10]	

IOT: Surface Engineering Institute, RWTH Aachen University

2.2 Test Results

The following figure 2 shows the Weibull-plot for the examinations conducted down to the present day. Rolling bearings which were partially coated with 1009.ZrC_g, 250.WC/C or 2054.CrAlN have a rolling contact fatigue lifetime that is nearly the same as for totally uncoated rolling bearings. Some coatings lead to a dramatically reduced bearing lifetime (640.a-C:H).

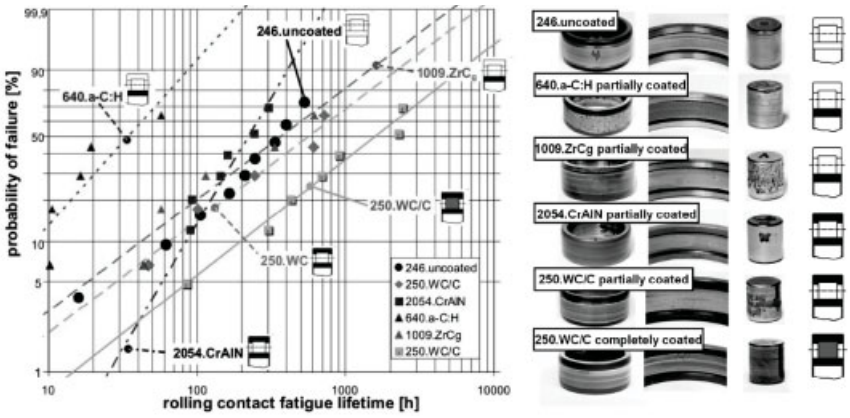


Figure 2: Weibull-diagram and tested roller bearings NU 206 (uncoated, partially coated, uncoated)

But taking a closer look at the tested bearing shows that the coated components most often stayed intact while in most instances the uncoated components failed (except for 640.a-C:H). This means that coatings are able to improve the lifetime of components under fatigue critical conditions. When the *whole bearing* was coated a life-enhancement of the whole bearing was observed under the chosen test-conditions. The lifetime for a probability of failure of 50 percent was 3 times higher compared to totally uncoated roller bearings. Further details concerning the fatigue lifetime of partially coated roller bearings can be taken from [11].

2.3 Interpretation of the Test Results

Based on the presented results the conclusion could be drawn that PVD-coatings may have a positive influence on rolling contact fatigue of roller bearings. The question comes up how this is possible. In the following potential factors are described concerning rolling contact fatigue of coated components. It should be mentioned that this list is not exhaustive.

It is well known that uncoated roller bearings can fail because of fatigue cracks initiated in the *subsurface region* and because of cracks initiated *nearby the surface*. Several authors have shown that surface initiated fatigue has become more important [12].

According to Ioannides [13] fatigue lifetime of uncoated rolling bearings is dominated by the time for crack initiation. Crack initiation in turn is strongly dependent on the appearing and the bearable stresses. Within the coating process, the material properties of the substrate in deeper regions shall not be affected. Therefore the bearable stresses of the substrate are supposed to be uninfluenced by the coating process. FEM-calculations made by the Institute for Machine Elements and Machine Design have shown that the appearing stresses in the subsurface region

will not be influenced by a PVD-coating (see figure 3). To show this a smooth contact between a roller and an inner ring of a cylindrical roller bearing NU206 was calculated without tangential forces and without significance of surface roughness. The result of this examination is that neither the magnitude of the maximum von-Mises stress nor its position is influenced by the coating. Therefore it is most probable that subsurface-initiated fatigue will not be affected by a PVD-coating.

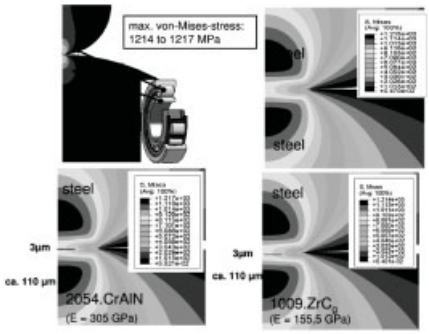


Figure 3: FEM-calculations for the contact between a roller and the inner ring of a cylindrical roller bearing NU 206, no tangential forces and no roughness peaks included in the calculation

The conducted bearing tests have shown that PVD-coatings may have a strong influence on rolling contact fatigue performance (see figure 2). If subsurface fatigue is not affected, it is obvious that surface initiated fatigue must be dominant. In the following figure 4 several factors are listed which may be influenced by PVD-coatings.

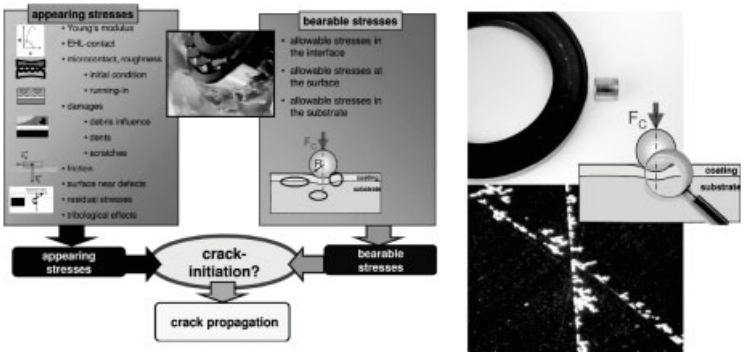


Figure 4: Factors concerning surface initiated fatigue influenced by PVD-coatings (left side); coating fatigue damage at the surface of ZrC_g-coated washers nearby roughness peaks after wear-critical test (right side)

a.) The appearing stress in the loaded near-surface region of every loaded body is most obviously influenced by the force transmitted between the contacting bodies and the Young's modulus. Young's modulus of the coating has got an influence on the strains in the substrate and the coating. A skipping concerning the stresses may occur in the interface region when Young's modulus of

the substrate and the coating are very different. Problems concerning the bonding of the coating may then occur [14].
b.) The roughness of the contacting surfaces is of special interest because it will lead to high pressure spikes as shown e.g. by [15]. While the stress in the subsurface region is more or less unaffected by surface roughness peaks, they have a strong influence on near-surface stresses. When testing coated rolling bearings in the FE8-test almost no wear was observed but surface near fatigue because of stress concentrations at roughness peaks occured (see figure 4) in case of ZrC_g. When testing completely 250.WC/C-coated roller bearings under fatigue critical conditions, some coating removal took place early in the test. A smoothening of the bearing surface appeared. In the opinion of several authors PVD-coating will prolong rolling contact fatigue lifetime by a smoothening of the counterpart [16].
c) Taking a look at the calculation method for bearing lifetime DIN ISO 281 [17], it becomes clear that debris has a strong influence. Because particle contamination can not be excluded and may be generated e.g. by gearings nearby the roller bearing, it is clear that the influence of debris concerning the lifetime of PVD-coated roller bearings must be examined in the future. Particles may have an abrasive-wear effect and an influence on rolling contact fatigue due to surface denting. Another aspect is that coatings shall not flake off when the surface is dented.
d.) Wear may play an important role concerning the pressure distribution in a rolling bearing [18]. Because PVD-coatings are able to reduce material loss in a considerable way, wear-induced fatigue damages will be prevented.
e) Coating a surface may lead to additional surface defects. For example droplets may occur on a coated rolling bearing. Most probable they will have a negative influence on rolling contact fatigue.
f) For uncoated rolling bearings it was shown by several authors that compressive residual stresses may have a positive influence on fatigue [19]. PVD-coatings imply compressive residual stresses while tensile stresses are generated within the near-surface substrate. If cracks are initiated within the coating, the compressive residual stresses may have a positive effect concerning rolling contact fatigue lifetime (time for crack initiation and crack propagation).
g) As a matter of course the bearable stresses in the coating, in the interface region and in the near-surface substrate will play an important role concerning rolling contact fatigue.
h) Besides crack initiation crack propagation may be significant concerning the lifetime of coated rolling bearings. Several authors have shown that crack propagation is influenced by the coating structure [20]. In case of 1009.ZrC_g and 250.WC/C it was observed that some kind of coating removal has taken place. Because under wear-critical conditions nearly no wear but fatigue cracks occurred (see figure 4) together with PVD-coated rolling bearings, it is strongly believed that fatigue is dominant in coated roller bearings under fatigue-critical conditions, too. When coating removal took place, cracks must be initiated within the coating. Because coating material is still on top of the substrate, cracks did not reach the substrate obviously. Therefore the coating structure will have an impact on crack propagation and rolling contact fatigue lifetime.

3 Summary and Outlook

When PVD-coated rolling bearings shall be used in industrial applications their rolling contact fatigue performance must be examined. Within the examinations made by the Institute for Machine

Elements and Machine Design it was found out that some PVD-coatings may have a negative influence while others have shown a positive effect on rolling contact fatigue under the chosen test conditions.

In this paper it was shown that it is very improbable that subsurface fatigue is affected by PVD-coatings. Instead surface initiated fatigue will be influenced very strong. Several possible explanations and influences were listed. Up to day it is not clear what is the major cause for the life-enhancement that can be reached by PVD-coatings. In the future the Institute for Machine Elements and Machine Design will conduct examinations concerning several aspects like testing coated components under debris contaminated conditions.

The authors gratefully acknowledge the financial support of the Deutsche Forschungsgemeinschaft (DFG) within the Collaborative Research Center (SFB) 442 “Environmentally Friendly Tribosystems by suitable coatings and fluids with respect to the machine tool”.

4 References

[1] Geheeb, N.: Einfluss von Additiven auf die Lebensdauer.; VDI-Berichte 1706: Gleit- und Wälzlagerungen; VDI-Verlag; Düsseldorf, ISBN 3 18 091706 7, **2002**, p. 97–102

[2] Wan, G. T. Y.; Amerongen, E.; Lankamp, H.: Effect of extreme-pressure additives on fatigue life of rolling bearings; Journal of Physics D: Applied Physics, Nr. 25, **1992**, S. 147–153

[3] Höhn, B.-R.; Michaelis, K.: Influence of oil temperature on gear failures; Tribology International, no. 37; 2004

[4] Deutsche Forschungsgemeinschaft, SFB 442, **2006**, Umweltverträgliche Tribosysteme durch geeignete Werkstoffverbunde und Zwischenstoffe am Beispiel der Werkzeugmaschine; SFB 442; Forschungsantrag

[5] DIN 51819, Prüfung von Schmierstoffen – Mechanisch-dynamische Prüfung auf dem Wälzlagerschmierstoff-Prüfgerät FE8; Beuth Verlag GmbH, 1999

[6] Gold, P.W.; Loos, J.; Kuhn, M.: **2004**, Umweltverträgliche Verschleißschutzkonzepte für Wälzlager im Mischreibungsgebiet, Materialwissenschaften und Werkstofftechnik, 35, No. 10/11, Wiley-VCH, Weinheim

[7] Bobzin, K.; Lugscheider, E.; Nickel, R.; Immich, P.: $(Cr_{1-x},Al_x)N$ ein Review über ein vielseitig einsetzbares Schichtsystem, Material und Werkstofftechnik, No. 10, 2006

[8] Gold, P.W.; Loos, J.; Kuhn, M.: TAE **2006** in Esslingen: The interaction of PVD-coated roller bearings, ester lubricants and additives; Vortrag

[9] Lugscheider, E.; Bobzin, K.; Bagcivan, N.: Gradiertes Zirkoniumkarbid – eine intelligente PVD-Schicht für tribologische Hochleistungsbauteile in der Antriebstechnik. Vortrag. März 2005 – EFDS/FVA-Workshop Hochleistungsbeschichtungen für die Antriebstechnik, Frankfurt (Germany)

[10] Michler, T.; Laakmann, M.: Verbesserung der tribologischen Eigenschaften von Verzahnungen durch WC/C-Schichten, Antriebstechnik 39, Nr.6, **1999**

[11] Gold, P.W.; Loos, J.; Plogmann, M.: Ermüdungslebensdauer PVD-beschichteter Wälzlager; GfT-Tagung **2007**; Göttingen

[12] Olver, A. V.: The mechanism of rolling contact fatigue: an update; Engineering Tribology; Vol. 219; **2005**

[13] Ioannides, E.; Bergling, G.; Gabelli, A.: An analytical formulation for the life of rolling bearings; Acta Polytechnica Scandinavica; ISBN 951-666-503-9, **1999**.

[14] Klaas, H.: Mechanische Charakterisierung dünner Schichten mit Hilfe von Indenterverfahren und elastisch-plastischer Modellierung; Dissertation RWTH Aachen; ISBN 3-86130-349-3; Verlag Mainz; **2007**

[15] Zhao, Y.; Maietta, D. M.; Chang, L.: An Asperity Microcontact Model Incorporating the Transition From Elastic Deformation to Fully Plastic Flow; Transactions of the ASME; vol. 122, **2000**

[16] Polonsky, I. A.; Chang, T. P.; Keer, L. M.; Sproul, W. D.: A study of rolling-contact fatigue of bearing steel coated with physical vapor deposition TiN films: Coating response to cyclic contact stress and physical mechanisms underlying coating effect on the fatigue life; Wear; vol. 215, Issues 1–2, , **1998**, pp. 191–204

[17] DIN ISO 281; Dynamische Tragzahlen und nominelle Lebensdauer - Lebensdauerbeiwert a_{DIN} und Berechnung der erweiterten modifizierten Lebensdauer; Beuth Verlag GmbH; Berlin; **2003**

[18] van de Sandt, N.: Gebrauchsdauer von axial belasteten Wälzlagern bei starker Mischreibung; ISBN 3-86130-125-3; Verlag Mainz; **2004**

[19] Cheng, X.: Experimental and Numerical Approaches for Improving Rolling Contact Fatigue of Bearing Steel through enhanced compressive residual stress, Ohio State University, Dissertation, **2007**

[20] Paskvale, S.: Properties of PVD hard coatings; University of Ljubljana; **2007**

Efficiency of Axial Piston Pumps With Coated Tribological Systems

C. Enekes, H. Murrenhoff
Institute for Fluid Power Drives and Controls of RWTH Aachen University, Aachen, Germany

1 Introduction

The Collaborative Research Center 442 “Environmentally Friendly Tribological Systems” (CRC 442) aims at the development of biologically fast degradable and environmentally friendly fluids in machine tools. Up to now, tribological systems are commonly realized with biologically questionable fluids based on mineral oils and additives. These additives cause a bad toxicological behaviour of those fluids. By using synthetical esters without additives, it is possible to improve the ecological toxicity, but with the disadvantage of loosing the good tribological features of the fluid. This necessitates the use of coated materials when using environmentally friendly fluids to improve the surface features compared to regular material combinations.

This paper describes results from different testing categories within the subproject B4 of the CRC 442. The subproject focuses on the tribological systems of an axial piston machine. Basic examinations to determine suitable coatings and fluids have been carried out by using tribometer tests. Based on these results, examinations of a single tribosystem piston-bushing were done. Finally, these results will be confirmed in a unit test. It will be shown, that newly designed tribosystems with coated components and bio-fluids facilitate lower values of wear and friction, so that these tribosystems are suitable to increase the efficiency of hydraulic pumps and to substitute common mineral oil based systems.

2 Use of Coated Test Specimen and its Effects on Friction and Wear

Examinations to determine wear and friction in hydraulic displacement units have been done, which convert mechanical energy in hydrostatic energy. Therefore an axial piston pump with a variable swivel angle had been selected. This unit consists of different tribosystems which are part of the rotary group, as shown in figure 1. Driven by the prime mover, the drive shaft rotates and causes a rotation of the cylinder. The pistons within the cylinder are taken along and are held against the sliding surface of the swashplate by the slipper pads. The pistons carry out a certain stroke, depending on the swivel angle and the position of the swashplate. A valve plate connects the turning bores of the cylinder to the high and low pressure port. Thereby, pressures up to 400 bar and volume flows up to 120 l/min are available with this particular unit. The flow is proportional to the input speed and the swashplate angle [1].

The tribosystems in figure 1 sustain different values and types of loads. Examinations showed a complex collective stress of the tribosystem piston / bushing, a detailed examination of the contact is required. A description of the losses of axial piston motors due to friction and leakage is shown in [2]. These examinations showed high losses of the piston / bushing contact, the highest of the rotary group. When using coated components it is important to understand the

load in the contact area to ensure that the allowable load of the coating is not exceeded. As a result of further investigations, it could be shown that the high contact load on the piston causes a failure of the coating. To reduce these high loads, which are caused by a line or point contact, it is helpful to enlarge the contact area by using contoured pistons. This is realised by optimising the cylindrical part of the piston by manufacturing a radius with a certain length in the contact points (1 and 2), as shown in figure 2. A contouring of the piston results in a lower friction coefficient as shown in [3]. This is valid, if the swashplate machine is running as a pump and as a motor. Other approaches like varying the gap between piston and bushing are difficult to manufacture and do not show an increase in efficiency. Another approach to reduce the friction between piston and bushing due to edge-scraping was the variation of the length of the piston, but this did not show a clear influence on efficiency [3].

To determine suitable geometries for piston and bushing, simulations can be used. Based on this test specimens are manufactured. The different levels of testing include basic tribometer tests, tests of the tribosystem piston / bushing and unit tests. All tests use environmentally friendly fluids and coatings as presented in [3, 5, 6].

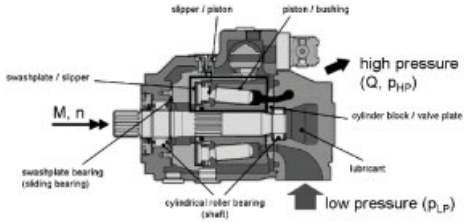


Figure 1: Sectional view of the tested axial piston pump with its tribological systems [4]

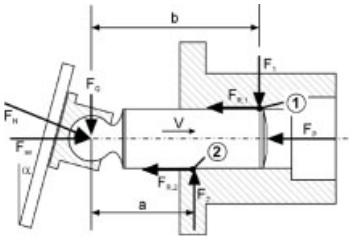


Figure 2: Forces and geometry of the tribosystem piston / bushing

2.1 Coatings

There has been a development of a variety of coatings for different applications. Coatings have been successfully tested in gears, guidings and bearings as well as for cold forming processes. Relevant coatings for hydraulic applications as tested in subproject B4 are the graded zirconium carbide ZrC_g and chromium aluminium nitride CrAlN. The ZrC_g-coating is a carbon-based coating (acc. to VDI 2840: a-C:H:Zr) and belongs to the group of Me-DLC coatings. Its advantages

are a low friction coefficient and its graded design with low values of hardness on the surface and a maximum hardness close to the middle of the coating. ZrC_g is commonly used as a coating for pistons and slipper pads. The CrAlN is a hard coating with a columnar structure and features an excellent adhesive strength, wear resistance capacity as well as resistance to alternating impacts, corrosion and wettability. CrAlN coatings are applied on valve plates [7].

2.2 Fluids

The basic idea of the CRC 442 is the development and examination of environmentally friendly fluids. This lead to the use of rapeseed as a reactant for the synthesis of suitable fluids. After getting the glycerine trioleate (GTO) from rapeseed and synthesizing oleic acid methyl ester (OME), a two-step synthesis takes place to get high (HIGTS) and low viscosity oil (HISM). By mixing both oils in varying ratios, it is possible to get the required viscosity for different applications. The two-step synthesis consists of an epoxidation and an alcoholysis either of GTO to HIGTS or OME to HISM. The high viscosity oil HIGTS or hydroxy isobutoxy glycerine tristearate is used in gears, guidings and for cold forming processes. The low-viscosity oil HISM or hydroxy isobutoxy stearid acid methyl ester is suitable for applications as bearings, chipping and hydraulics [7, 8, 9].

2.3 Tribometer tests

Model tests according to DIN 50322 allow a fast and cheap testing of specimens, which are simple to manufacture and coat. These tests can be used for parameter studies as well as for a preselection of suitable coatings and fluids.

To examine the general suitability of coatings and fluids basic tests have been carried out with a Siebel-Kehl tribometer, as shown in figure 3. The test rig consists of three main groups, the load module on top of the test rig, the test module and the drive module. The test module in the middle section consists of the two test specimens stator and rotor, as shown in the right part of figure 3.

The test specimens are discs under facial contact and are loaded by a normal force from the load module. The rotor is turned by a drive module. The contact is lubricated by oil, which is constantly cooled and filtered by a fluid circuit. Figure 4 shows a comparison of tribometer results. The results show a good running-in behaviour of the ZrC_g-coating while there are low friction coefficients in the galling test at higher contact forces. The good running-in behaviour is caused by the graded coating profile [5].

The comparison was done by using a Stribeck-test which means that the friction was measured while the speed was being reduced. It can be shown that another carbon-based and graded coating HfC_g showed the best running-in behaviour by having the lowest coefficient of friction at low speed, while ZrC_g shows the best compromise for all speeds. Furthermore, ZrC_g showed the lowest wear concerning the specimen surface on stator and rotor [7].

2.4 Tribological System Piston / Bushing

Based on the tribometer tests using model test specimens tests were carried out with a slow speed test rig to determine friction and wear. The test rig reproduces the tribosystem of a piston / bushing

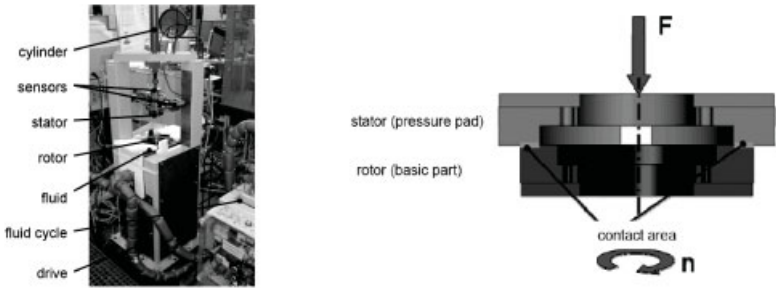


Figure 3: Siebel-Kehl tribometer and tested pairing

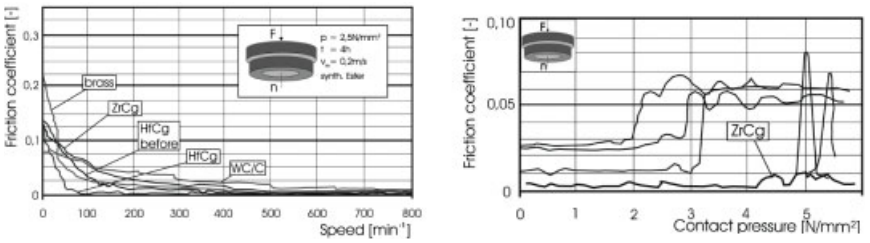


Figure 4: Comparison of different coatings and parameters in testing, Stribeck-Test (left) and galling test (right)

contact of a swashplate machine, as shown in figure 5. It is based on the test rig established by Renius [10].

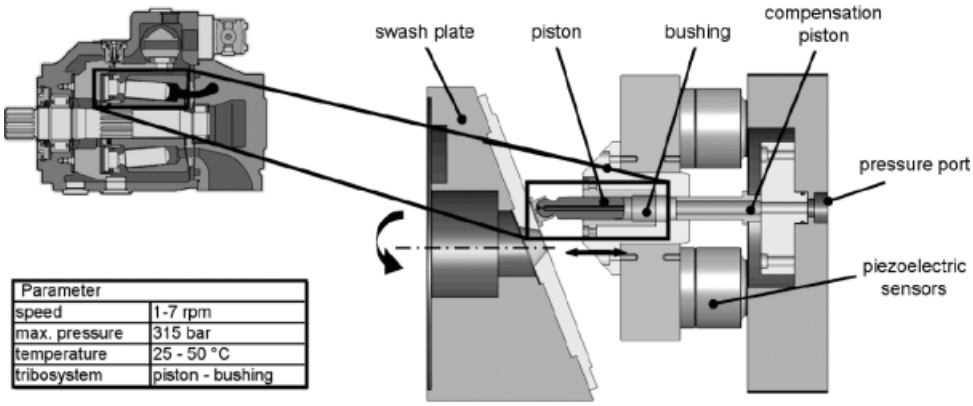


Figure 5: View of the slow speed test rig for the tribosystem piston-bushing

While the swashplate of the test rig is turning, it causes a movement of the piston relatively to the bushing. The speed of the swashplate ranges from 1 to 7 rpm to achieve high friction coefficients. Friction forces can be measured by piezoelectric sensors which connect the tested bushing

with the housing of the test rig. To separate the friction from the pressure force, a compensation piston between bushing and pressure port is used.

The reference pairing consists of a steel piston in a brass bushing. Examinations showed high values of friction which caused high wear of the brass bushing while the piston showed no significant wear [6, 11]. Figure 6 left shows a comparison of the reference pairing (KS3) and the influence of pre-treatment and contouring of the piston. A pre-treatment of the surface causes lower friction coefficients. Experiments with finished (F1), profile-grinded (IP3) and hard turned (H4) pistons have been done. All tests were carried out by using a reference oil 2.H.LP.ES.Ref.32 with a kinematic viscosity $\nu = 32\,\mathrm{mm^2 s}$.

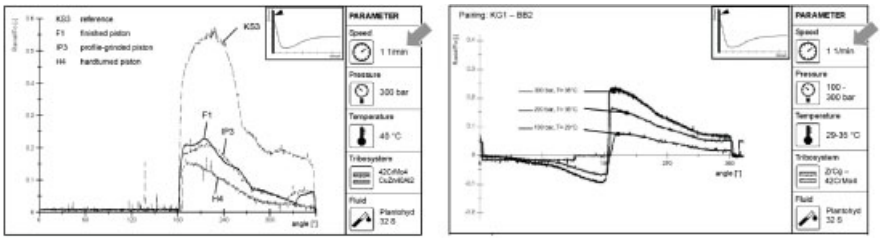


Figure 6: Relative friction depending on pre-treatment of pistons (left) and of a contoured and coated piston in an uncontoured bushing (right)

Contoured and pre-treated pistons show lower values of friction than the reference pairing, the relative friction is comparable to pre-treated pistons. These tests have been carried out by using CuZn40Al2 as bushing material. By using coated pistons the friction coefficient can easily be reduced due to better tribological properties of the coating. Using coated and contoured pistons in an uncontoured bushing (figure 6, right) reduces the relative friction as well as wear. Depending on the pressure in the contact, the friction reaches values comparable to pre-treated pistons [6].

The aim of minimizing the load on the coating by changing the geometry of both piston and bushing causes friction values which are a little higher than estimated. The used piston was tested twice in an uncontoured and later a contoured bushing, as seen in figure 7. The reason for the minimally increased friction may be the use of the piston in two tests and the increased temperature in the contact of 47 °C instead of 40 °C. Further research is necessary to determine the reason and explain the effects. The piston shows wear in the contact area to the bushing, especially in the area of the backward contact when high pressure is conducted, figure 7 (top). This position causes high wear of the bushing as well. It has to be shown, whether the increase of temperature caused this groove in the bushing.

For an improved geometry of the contact piston / bushing, it is important to avoid a small distance $b - a$ of the contact points, see figure 2. The momentum on the piston is constant. By reducing the distance between the points of contact, the contact force may increase and counteract the positive effect of the contouring.

2.5 Unit Tests with Coated Tribosystems

Further tests to determine the interactions between all tribological systems of the rotary group can be realized by using a contamination test bench and an ageing test bench. The contamination

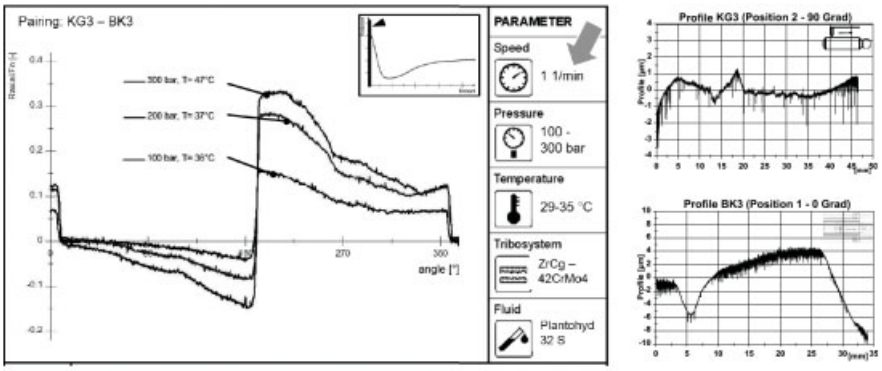


Figure 7: Relative friction of a contoured and coated piston in a contoured bushing (left) and surfaces of piston (above) and bushing (below) after the test

test rig can be used to determine the efficiency of a pump with clean or contaminated oil. The development of particles within the circuit will be detected permanently. The ageing behaviour of oil and its influence on the efficiency of a pump, running with coated components, can be examined with an ageing test bench. Tests with both benches are part of current examinations.

3 Conclusions

Examinations within the subproject B4 of the Collaborative Research Center 442 showed promising advantages by using coated components with environmentally friendly fluids. Tribometer tests showed the suitability of coatings for hydraulic applications. Different environmentally friendly fluids were tested as well. It could be shown that coatings are most suitable for optimised pistons of axial piston machines. The optimisation regards the piston's geometry and is required to reduce the contact load. Experiments with this contouring show a reduction of the relative friction in the contact, so that an increase of the efficiency can be expected. It should be taken into account that this increase concerns only the tribological system piston / bushing, because interactions between the tribosystems of the rotary group and the used fluid may have an influence, which have not been investigated up to now. A variation of the contouring parameters radius and length will show suitable geometries and pairings. The efficiency has to be shown in unit tests, which are currently in progress.

All presented results are part of the current examinations of the subproject B4 of the Collaborative Research Center 442 "Environmentally Friendly Fluids". This subproject has been carried out at the Institute for Fluid Power Drives and Controls of RWTH Aachen University, Germany and is funded by the German Research Foundation (DFG). The authors would like to thank the DFG for the financial contribution to these examinations.

4 References

[1] Ivantysyn, J. and M., *Hydrostatische Pumpen und Motoren*, Vogel Verlag, **1993**.

[2] Zhang, Y., *Verbesserung des Anlauf- und Langsamlaufverhaltens eines Axialkolbenmotors in Schrägscheibenbauweise durch konstruktive und materialtechnische Maßnahmen*, RWTH Aachen, Germany, **2000**.

[3] Breuer, D., *Reibung am Arbeitskolben von Schrägscheibenmaschinen im Langsamlauf* , RWTH Aachen, Germany, **2007**.

[4] Bosch Rexroth AG, www.bosch-rexroth.de, **2007**.

[5] van Bebber, D.-T., *PVD-Schichten in Verdrängereinheiten zur Verschleiß- und Reibungsminimierung bei Betrieb mit synthetischen Estern,* RWTH Aachen, Germany **2003**.

[6] Enekes, C., Murrenhoff, H., *Verwendung beschichteter Bauteile im tribologischen System Kolben-Buchse in Axialkolbenmaschinen,* 48. Tribologie-Fachtagung, **2007**.

[7] Autorenkollektiv, *Sonderforschungsbereich 442 – Umweltverträgliche Tribosysteme durch geeignete Werkstoffverbunde und Zwischenstoffe am Beispiel der Werkzeugmaschine*, Forschungsantrag 2006, RWTH Aachen, Germany, **2006**.

[8] Goehler, O.-C., *Alterungsuntersuchungen und Methoden zur Alterungsvorhersage für umweltverträgliche Schmierstoffe in neu gestalteten Tribosystemen*, RWTH Aachen, Germany, **2007**.

[9] Mang, T., Dresel, W., *Lubricants and Lubrication,* Wiley-VCH, **2001**.

[10] Renius, K.-T., *Untersuchung zur Reibung zwischen Kolben und Zylinder bei Schrägscheiben-Axialkolbenmaschinen,* VDI-Verlag, Duesseldorf, Germany, **1974**.

[11] Scharf, S., Murrenhoff, H., *Measurements of friction forces between piston and bushing of an axial piston displacement unit,* International Journal of Fluid Power, Volume 6, Number 1, **2005**.

Influence of Friction on Ageing of Lubricants

J. Schumacher, O.-C. Göhler, H. Murrenhoff
IFAS, RWTH Aachen

1 Introduction

Within the framework of the collaborative research centre CRC 442 at the RWTH Aachen University, environmentally friendly tribosystems are developed. The aim is to avoid noxious additives, which usually contain heavy metals. Two esters with different viscosities have been synthesized at the Institute for Technical and Macromolecular Chemistry (ITMC).

The ageing behavior of these lubricants is investigated in subproject A3. The results obtained are used to optimize the synthesis process. Up to now, the ageing behavior of lubricants is being examined with the hydrolysis test and the oxidation test [3]. With these tests the influence of water or oxygen can be determined separately. To expose the fluids to a more complex stress combination, a simple hydraulic circuit consisting of tank, pump, filter, cooler, some pipelines and pressure control valves is used as an ageing test bench. This enables an accelerated ageing under realistic conditions.

There is so far no way to examine the influence of a single tribosystem. Therefore the oxidation test is being supplemented with a tribometer.

2 Oxidation Test

The rotating vessel oxidation test (RVOT) has been standardized in ASTM D 2112. We use a modified test, called oxidation test. The copper spiral and water are not used, and the temperature is lowered to 120 °C. This way, the exclusive influence of oxygen on the ageing behaviour can be analysed. [1]

The typical test lifetime of the fluids developed in the CRC 442 is in the range of 10 to 30 min. This is considerably lower than commercial mineral oils, which have additives such as oxidation inhibitors.

3 Tribo Oxidation Test

In real applications the lubricant does not only contact metal materials but also has the task to separate component surfaces to assure a problem-free operation. To examine the ageing behaviour in presence of one single tribological system, a disk-disk-tribometer has been added into the pressure vessel. (figure 1)

The diameter of the discs is 43 mm. Different disc materials have been used. The stator was always made from 42CrMo4, a steel alloy which is used in many applications. The rotor was either made from 42CrMo4 or from brass alloy CuZn37Mn3Al2PbSi. Some steel rotors have been coated with ZrC_g applied in a PVD process. The carbon content of the coating is graded, assisting a running-in effect [6].

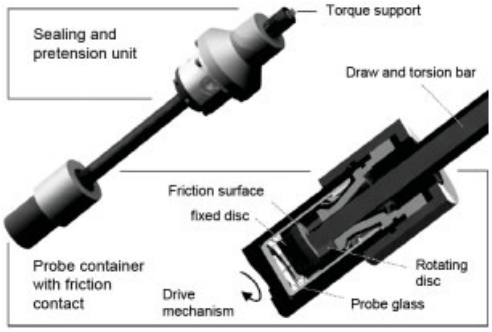


Figure 1: Assembly of the tribo oxidation test

The experiments can be performed with a gap or with variable surface pressure. Thereby the difference between the catalytic influence and the influence of friction can be distinguished. The surface pressure should be selected with care. In case of high temperature, the viscosity decreases, and a surface pressure of e. g. 7.5 N/mm², which is common for a piston-sleeve contact in an axial piston pump, stresses the tribological contact irregularly high. To obtain comparable results we use the Gümbel-number G (1), [5].

$$G = \frac{\eta \cdot \omega}{\sigma} \tag{1}$$

The load on the system depends on the ratio of viscosity to surface pressure and rotary frequency. The average of the ratios of the viscosities at 50°C and 120°C is about 7.5, so the surface pressure should be decreased by this ratio, as the load on the tribosystem at 120°C and 1 N/mm² is equivalent to the load at 50°C and 7.5 N/mm².

The experiments are executed with four oil-batches. Two feature low viscosity HISM and two high viscosity HIGTS.

Table 1: Experiments

Rotor	surface pressure N/mm²	lubricants			
42CrMo4	0	117+119.HISM	159.HISM	112.HIGTS	124.HIGTS
brass	0 and 1	117+119.HISM	159.HISM	112.HIGTS	124.HIGTS
ZrC_g	0 and 1	117+119.HISM		112.HIGTS	

4 Influence on Lifetime

The test lifetimes of the oils depend on the used materials and the surface pressures. Lifetimes of the tribo oxidation test cannot be compared with absolute lifetime results of the oxidation test. As a consequence of the higher mass, the test vessel heats up more slowly. Furthermore, the contact

area between oil and oxygen is smaller due to the inserted tribo system. But the ratio between the different batches of oil is identical to the oxidation test [1].

Each combination of discs is first tested with a gap between the discs. During this pass, there is only catalytic influence of the material on the ageing behavior. After this stage, the discs are cleaned and brightly polished. The second pass with the renewed discs shows the influence of friction on the ageing behavior. The lifetimes are shown in figure 2.

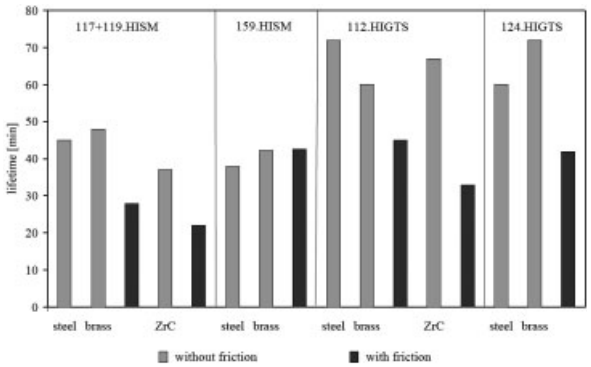


Figure 2: Lifetimes of the tribo oxidation test

The lifetimes of the friction passes are lower than the ones of the gap passes. This is attributed to different causes: higher temperature, higher shear rate, and a larger catalytic surface.

It can be assumed that there will be high flash temperatures in the friction area. These flash temperatures do not have a significant influence on the average temperature, but the oxidation reaction depends exponentially upon the local temperature. So oxidation is accelerated at these small points [3]. The resulting chemically changed molecules can afterwards initiate further ageing reactions and thus accelerate the deterioration of the fluid.

The tests are carried out in the domain of mixed friction. So there is a mechanical load on the oil in the lubrication gap. Even though the molecule size is smaller than the gap, the pressure in the gap is an additional load on the oil.

The friction area generates abrasion. These particles also accelerate the oxidation. The high surface to volume ratio provides an important reaction partner to the oil. In case of permanent wear, the blank metal surfaces in the gap stay in contact with the oil, and there are no oxidation layers or passivated layers on the disc surfaces.

As can be seen in figure 2, different materials have characteristic influences on the lifetime of different batches. HISM has the highest lifetime in presence of a steel and a brass disc. With ZrC, the lowest lifetimes are achieved.

The high viscosity HIGTS has higher lifetimes. Due to the higher viscosity, the oxygen can dissolve only slowly in the oil. The effects of friction and different disc materials are similar to those with HISM.

5 Change of Fluid Properties during the Tribo Oxidation Test

Chemical reactions occur between oil and oxygen during the tribo oxidation test. Fluid properties change as a consequence of these reactions. In the following, the changes of kinematic viscosity and acid number are discussed.

5.1 Kinematic Viscosity

The viscosity depends basically on the active groups and the structure of the molecules. The longer the molecular chain and the more branched the chain, the higher is the viscosity [4, 5].

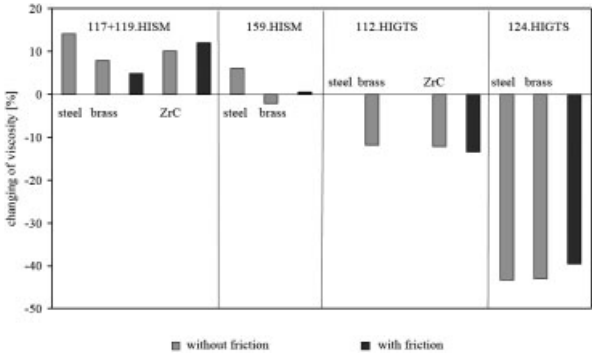


Figure 3: Change of the kinematic viscosities

The viscosity changes during the course of the tribo oxidation tests (figure 3). But different oils show different behaviours. The viscosity of HISM increases, while the viscosity of HIGTS drops.

There is no correlation between the change of viscosity and friction. There is evidence though that the change of viscosity mainly depends on the mass of oxygen that reacts with the oil. The variation of the viscosity changes can be explained by the different residence times of the oil in the pressure vessel after the test. When the test is finished, the pressure vessel has to be removed out of the heating bath. Then it has to be opened and the oil sample has to be decanted into a closed beaker. During the time needed for this procedure, the oil is still hot and can react with the oxygen in the pressure vessel or the ambient air.

5.2 Acid Number

The acid number of biological esters is an indicator for the balance of the hydrolysis reaction (2). The equilibrium can be shifted by adding one of the four components.

$$\text{ester} + \text{water} \rightleftharpoons \text{acid} + \text{alcohol} \tag{2}$$

The contained water reacts with the oil at high temperatures, increasing the acid number. There is no relation between disc materials and the change of the acid number. The change of the acid number depends mainly on the fluids initial properties.

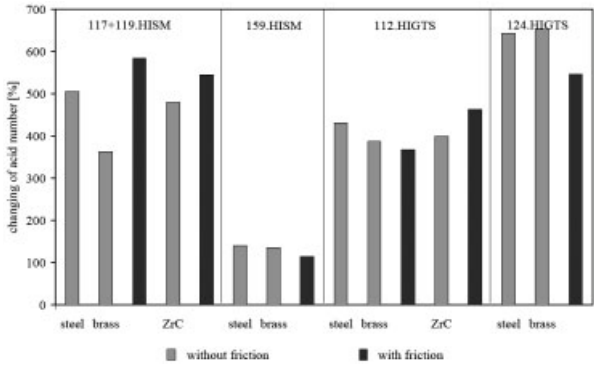


Figure 4: Change of acid number

5.3 Discolouration of Brass Disc

Coppery areas appeared on the brass discs. These discolorations are mainly on the backside of the disc, which is pressed against a steel adapter. It seems that the oil dissolves the zinc fraction. EDX analyses show that there is less zinc in the coppery areas than in the untouched areas. In figure 5 the coppery area is marked.

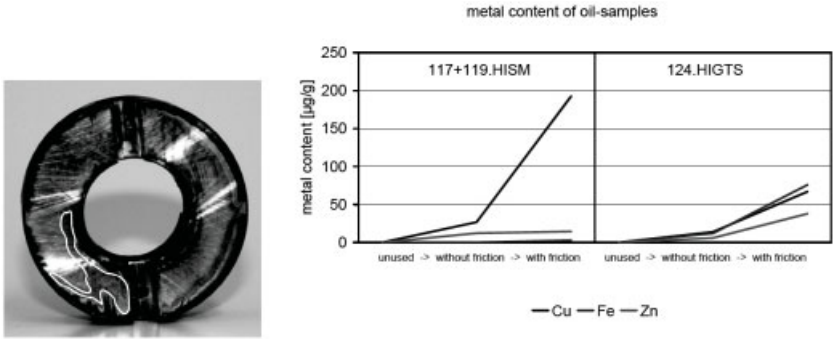


Figure 5: Coppery discoloured disc and metal content of the oil

In the oil-sample a high zinc-content could be found. Figure 5 shows the metal content of copper, zinc and iron of two samples. This confirms the hypothesis that the oil solves some fractions of the metal alloy.

6 Conclusions and Outlook

The tribo oxidation test enables the analysis of the influence of one single tribosystem. Thereby the gap between laboratory and test benches can be closed. The influence of friction is clearly visible. Discolourations on a brass disc and a high metal content in the oil after use suggest the

usage of coated components. Additionally preliminary tests have shown that the metal content downgrades the biodegradability.

More tests with different coatings will be carried out. Furthermore the chemical reactions of the ageing process with and without friction will be determined.

7 Acknowledgment

The work presented in this article is part of sub-project A3 of the research project concerning "environmentally compatible tribosystems by means of suitable composites and precursor materials, using the machine tool as an example" conducted by the collaborative research centre 442 at the Institute for Fluid Power Drives and Controls (IFAS) of RWTH Aachen University. This collaborative research centre is sponsored by the German Research Foundation (DFG), and the authors would like to thank the DFG for its financial support.

8 References

[1] Goehler, O.-C., Alterungsuntersuchungen und Methoden zur Alterungsvorhersage für umweltverträgliche Schmierstoffe in neu gestalteten Tribosystemen, Shaker Verlag, Aachen, **2008**

[2] Erlenkämper, B.; Dott, W.; Brinkmann, C.; Eisenträger, A.: Consideration of toxicological aspects in the development of lubricants based on synthetic esters and their changes by usage: Proceedings of the 15th International Colloquium Tribology, Automotive and Industrial Lubrication, January 17–19, Stuttgart, **2006**

[3] Schmidt, M.: Untersuchung und Ansätze zur modellhaften Beschreibung der Alterung auf Estern basierender Zwischenstoffe für den Einsatz in umweltverträglichen Tribosystemen, Shaker Verlag, Aachen, **2003**

[4] Mang, T.; Dresel, W.; Lubricants and Lubrication; Wiley-VCH, Weinheim, **2001**

[5] Gold, P. W.; Maschinenelemente Vorlesungsumdruck II, trans-aix-press, Aachen, **2003**

[6] Bobzin, K.; Nickel, R.; Bagcivan, N.; Goebbels, N.; Untersuchung des Einflusses unterschiedlicher Karbidbildner auf das tribologische Verhalten mittels reaktivem Magnetron-Sputter-Ion-Platting (MSIP) abgeschiedener Nanocomposite nc-MeC/a-C:H Beschichtungen; Proceedings of the 48. Tribologie-Fachtagung, September 24-26, **2007,** Göttingen

Improvement of the Efficiency of Parallel-Axis-Transmissions by Means of PVD-Coatings

C. Brecher, A. Bagh, C. Gorgels
RWTH Aachen University, Aachen

1 Introduction

The superior goal of the SFB 442 project is to use a machine tool as an example to modify different tribological systems in order to make them run by using a single biologically degradable fluid or at least biologically degradable fluids from one family of fluids. In order to achieve this goal coatings that take over the wear protecting functions of the toxic additives that are added to the current standard lubrications are applied on the components of the tribological systems. Beside this the increasing efficiency of power transmissions can be mentioned as another reason for the application of PVD-coatings on gears. In order to consider all positive effects of the application of PVD-coatings in power transmissions, coated parallel-axis gears have been studied in terms of their efficiency at WZL.

This study meets the fact that within the last few years there is an increasing demand in optimizing power transmissions in terms of efficiency in addition to conventional design criteria like load carrying capacity and noise emission. Especially in the automotive area, the economical use of energy is important for customers.

Energy losses are mainly generated within the engine. However, also in the power train of all kinds of vehicles, energy is wasted. One possibility to reduce these losses is to deposit PVD-coatings on the relevant machine elements of the power train. This is shown by studies described within this paper.

2 Test Rig and Test Gearings

The total power loss of a gear transmission P_L is composed of different parts:

$$P_L = P_{LG} + P_{LB} + P_{LS} + P_{LX} \tag{1}$$

P_{LG} stands for the power loss of the gears, P_{LB} for the power loss of the bearings, P_{LS} for the power loss of the seals and P_{LX} for the power loss of other components. The power loss of the gears effects a great part of the total power loss and depends on the gear geometry and the quality of the flank surface [1]. The efficiency factor of a power transmission is defined as the absolute value of the ratio of drive and output power:

$$\eta = \left| P_{out} / P_{in} \right| \tag{2}$$

There are two different methods to measure the efficiency factor of a power transmission. According to the first method the power loss and either the drive or the output power is measured. This method is used with a commuting suspension of the transmission, with a back-to-back test-rig or with a calorimetrical test. Using the second method the power differential of the transmissions drive and output is measured for example by torque and speed measurement shafts. In contrast to the measuring of the power loss the measurements precision of the second method only depends on the precision of the used measuring equipment and not on the current efficiency factor. [2]

In order to investigate the influence of a PVD-coating on the efficiency factor of one pair of gears the power differential of the gears was measured at WZL. In this test series two different gear geometries were tested.

2.1 The Test Rig

Figure 1 shows the test rig for the investigation of the efficiency factor.

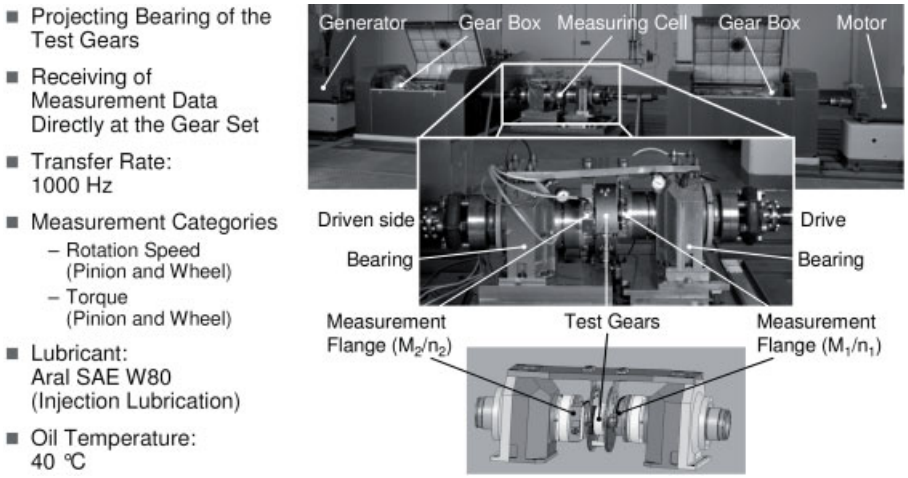


Figure 1: Test rig for the investigation of the efficiency factor

The test rig includes two identical electrical motors performing a maximum torque of M_{max} = 400 Nm up to a rotation speed of n = 3000 rpm. Since one of the engines is running in the generator mode, both of them are set up as an electrical back-to-back test rig for the test gears. Between the engines and the measuring unit two identical shift gear blocks are arranged to afford higher rotation speeds if necessary. Inside the measuring unit the intermating pair of gears is supported by projecting bearings. In order to measure the torque and the rotation speed, measurement shafts are used. The torsion caused by the torque is measured by resistance strain gauges, transferred into an electrical signal and transmitted optoelectrically to the evaluating processor unit. At the same time the rotation speed is measured by a magnetic speed measurement unit. The nominal torque of the measurement shafts is 2500 Nm, the nominal rotation speed 1200 rpm. In order to measure only the efficiency factor of the test

gears, the measurement shafts are assembled directly at the intermating pair of gears. In that way friction losses of the bearings and seals have no influence on the results. This means that the summands P_{LB}, P_{LS} and P_{LX} in equation (1) can be disregarded.

The power loss of the gears are given of load-dependent loss P_{LGD} and load-independent loss P_{LG0}:

$$P_{LG} = P_{LGD} + P_{LG0} \tag{3}$$

Using splash lubrication, the load-independent loss is caused by splashing, for injection lubrication the displacement of the oil in the contact zone of the teeth is the determining factor. Since the lubrication parameters are not changed within a test series the load-independent loss P_{VZ0} is neither supposed to change. The load-depending loss is defined by the following equation:

$$\left|P_{LGD}\right| = P_{in} \cdot \mu_{mZ} \cdot H_V \tag{4}$$

In this equation P_{in} stands for the drive power, μ_{mZ} stands for the medium friction factor and H_V for the geometry factor.

The test gears are lubricated by lubrication injection with a constant oil temperature of 40 °C. During one defined test period measured data for both the torque and the rotation speed are scanned. By means of this measured data it is possible to calculate the efficiency factor using the following equation [3]:

$$\eta = \left|\frac{P_{out}}{P_{in}}\right| = \left|\frac{M_{out} \cdot \omega_{out}}{M_{in} \cdot \omega_{in}}\right| = \left|\frac{M_{out} \cdot n_{out}}{M_{in} \cdot n_{in}}\right| \tag{5}$$

The current efficiency factor can be calculated for every single moment of the measuring time period.

In order to afford the comparability of the measurements the test rig was brought to working temperature and the measurement shafts were calibrated before starting a test series. The duration for warming-up of one single load case was defined to 10 minutes and the following measuring time was 30 seconds in a quasi-stable load case. The determination of one defined test result for each measurement period was conducted using the following equation:

$$\eta = \frac{1}{n} \cdot \sum_i \eta(t_i) \quad i = 1,2,...,n \tag{6}$$

2.2 Test Gear Geometries

The two tested gear geometries are a slightly modified machine tool gearing as reference on the one hand and a gearing that has been optimized in terms of the coating process within the SFB 442 project on the other hand. *Figure 2* shows the geometrical data of the test gearings as well as the developing of the specific sliding ζ along the path of contact.

The comparison of the gear geometries reveals that the optimized gearing has a significant smaller pressure angle than the reference. Additionally, this gearing has comparative short teeth as shown in the gear geometry drawings in *figure 2*. Both characteristics effect a nearly

constant allocation of the coating thickness and an economically optimized coating process. Beside this, the high pressure angle and the low profile height cause a reduction of the specific sliding along the path of contact.

The investigated PVD-coating is a commercially used carbon-based coating (a-C:H:W). All test series for both test gearings and each coating condition have been carried out with one pair of gears to avoid adulteration of the measurement data resulting from mounting. Furthermore the flank geometry of all tested gears was measured to exclude significant geometrical variations on the one hand, and all gears were prepared by a defined run in process on the other hand.

Reference Gearing	Gear Data Indices: 1-Pinion; 2-Wheel	Optimised Gear Geometry
2 mm	Module m_n	2 mm
35; 70	Number of Teeth $z_{1,2}$	35; 70
a-C:H:W (WC/C)	Coating	a-C:H:W (WC/C)
20°	Pressure Angle α_n	35°
79.292 mm; 153.741 mm	Tip Diameter $d_{a1,2}$	78.103 mm; 151.415 mm
+ 0.2; +0.1891	Addendum Modification Factor $x_{1,2}$	-0.8760; -2.5652
20 °	Helix Angle β	28.75 °
3.176	Total Contact Ratio ε_γ	3.001

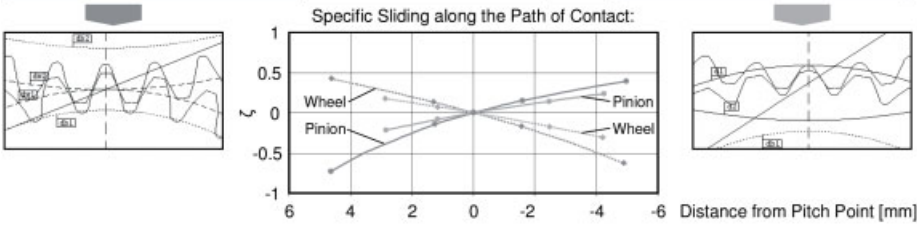


Figure 2: Test gear geometries and specific sliding along the path of contact

3 Test Results

In all test series the degree of efficiency of the intermating pair of gears was measured by increasing the torque from 135 Nm to 175 Nm in steps of 5 Nm with a constant rotation speed of 600 rpm. The results show the influence of the transmitted torque on the friction behaviour of the tested gears. For all pairs of gears the efficiency factor η was explicitly higher than 0.99 for all investigated loads. The projecting bearing allows only low torque ranges in order to avoid a radial distortion of the gears. The comparably low torque range leads to the high level of efficiency factors in the test results.

Figure 3 shows the test results for both test gear geometries without coating. For all load cases of the test series the efficiency factor of the coating-optimized gearing is approximately 0.003 higher than the efficiency factor of the reference gearing. The reason for this difference is given by the different geometry factors H_V of the test gears in *equation (4)*. As shown in *figure 3*, the optimized gearing has significant smaller amounts of specific sliding ζ along the path of contact. This causes lower load-dependent loss for the intermating pair of gears. In

both cases the range of dispersion shows a comparable negative gradient against the increasing torque. This result can be explained by an increase of the normal force on the tooth flanks that causes a growing friction factor μ_{mZ} [3]. Hence the test results correlate with the theoretical basics.

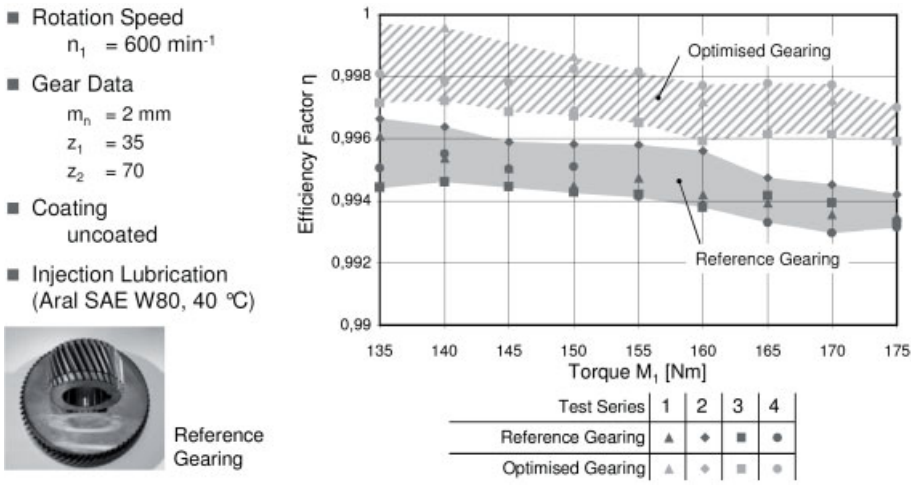


Figure 3: Variation of the torque (uncoated test gears)

Figure 4 shows both the range of dispersion of the a-C:H:W-coated and the uncoated gearing.

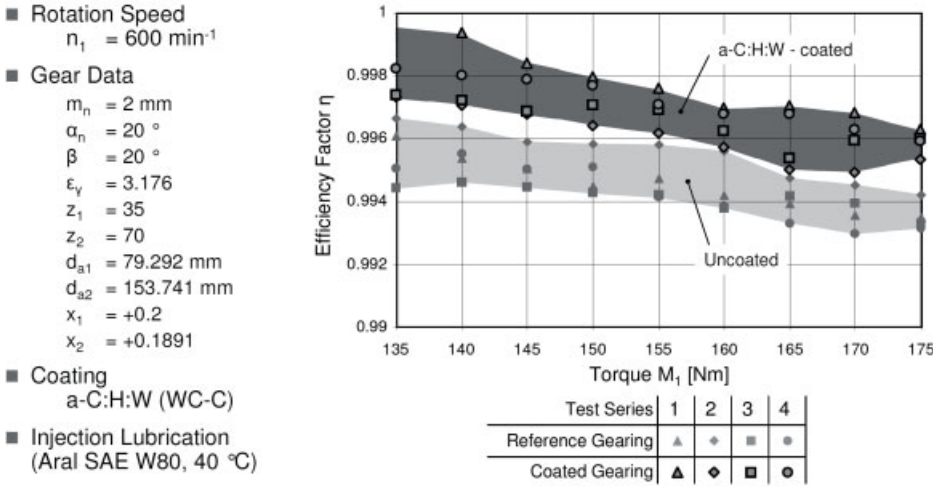


Figure 4: Variation of the torque (reference gearing)

The developing of the efficiency factor of the coated gearing overruns the efficiency factor of the reference gearing by $\Delta\eta = 0.003$ in average. Considering the high level efficiency of the tested gearings, the PVD coating effects a significant increase of the efficiency factor.
In *figure 5* the test results for the variation of torque for the uncoated and the coated optimized gearing are displayed. Both ranges of dispersion show the typical gradient developing. The range of the coated gearing is located slightly higher in the diagram than the range of the uncoated gearing. However, the difference between the two curves is negligibly small. This result shows that the application of the coating is not able to improve the efficiency factor of the optimized gearing as much as the reference gearing since the efficiency factor of the uncoated optimized gearing is already on a high level for the investigated load cases.

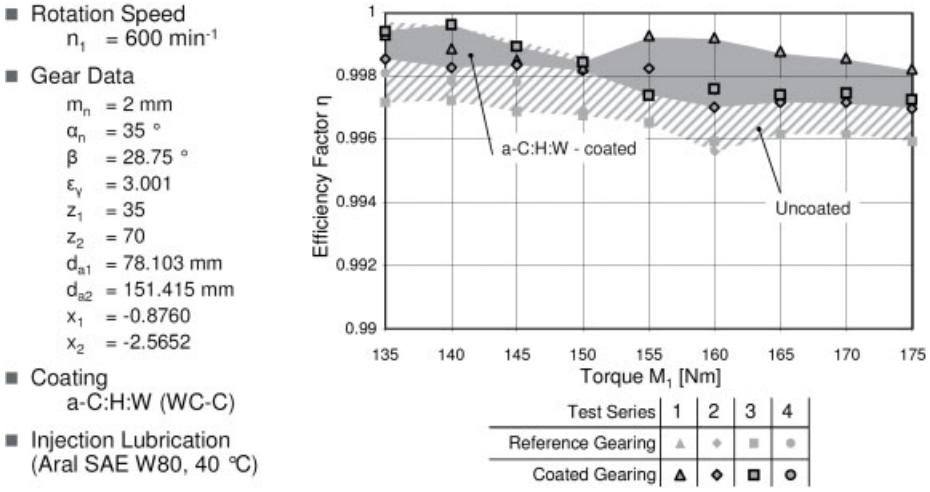


Figure 5: Variation of the torque (optimized gearing)

4 Summary and Outlook

This paper describes investigations of PVD-coated parallel-axis gears in terms of their efficiency performed at WZL of RWTH Aachen University.

Compared to conventional gears, PVD-coated gears showed a significantly reduced frictional behaviour, leading to an increased efficiency of the power transfer. This increase of efficiency was measured directly at the gear pair without measuring the loss of the bearings, seals and oil splashing. For the test series, a test set-up has been developed to measure torque and rotation speed directly at both sides of the pair of the intermating gears. With this method, the absolute efficiency of the gear set has been measured.

By means of this test set-up, two different gear designs were studied with coated and uncoated flank surfaces and the torque transfer efficiency was determined. In order to eliminate the influence of manufacturing deviations, the coating was deposited on the same gear pair

that was studied in the uncoated condition. The results for the reference gearing show clearly that the power loss of the gear pair can be reduced by the application of a PVD-coating. The comparison of the developing of the efficiency factors of the uncoated gearings also show that the efficiency of parallel-axes transmissions can be increased by an optimization of the gear design, as well.

Further research will determine the efficiency of complete power transmissions by varying coating condition of the components both gears and bearings in order to validate the presented results and to evaluate the interaction between coated and uncoated components.

5 Acknowledgement

The financial support of the German Research Association within the scope of the collaborative research program SFB442 “Environmentally-Compatible Tribological Systems” is gratefully acknowledged.

6 References

[1] Linke, H., Stirnradverzahnungen, Hanser, **1996**, *p. 95-96*.
[2] Imdahl, M., Hochgenaue Wirkungsgradbestimmung an Getrieben unter praxisnahen Betriebsbedingungen, Dissertation RWTH Aachen, **1998**, *p. 14*.
[3] Ohlendorf, H., Verlustleistung und Erwärmung von Stirnrädern, Dissertation TU München, **1958**, *p. 83-85*.

Part III
Poster

Influence of Solidification Microstructure on the Wear Resistance of Al-Si and Al-Sn Alloys Directionally Solidified under Unsteady State Conditions

K. Sabat, N. Cheung, J. E. Spinelli, L. C. Casteletti, A. Garcia
State University of Campinas – UNICAMP, Campinas –SP-Brazil and State University of São Paulo – USP – São Carlos – Brazil

1 Introduction

Al-Sn alloys are well known for having excellent tribological and mechanical properties making this kind of alloy system be suitable for engineering applications, particularly in combustion engine pistons and cylinder liners [1–3]. The Sn particles spread over a continuous Al-rich matrix function as solid lubricants. Al-Si alloys are also used in engineering components which are supposed to be exposed to critical wear conditions, such as engine parts, pistons, cylinder blocks and heads, water-cooled jackets, etc [4].

Dendrites are specific microstructures that arise in casting products. They are formed by branches that are like trees and constitute the solidification microstructure named dendritic. The constitutional undercooling is the phenomenon that is responsible for the dendritic structure formation. Such phenomenon is caused either by solute or solvent segregation at the solidification front, and induces instability at the solid/liquid interface, which is macroscopically planar in the beginning of the solidification process.

The dendritic structure can be analyzed both quantitatively and qualitatively. The qualitative analysis concerns both characterization of the microstructure morphology and chemical composition analysis of the dendritic array in order to determine the segregated material. The quantitative analysis of the dendritic structures is characterized by measurements of the spacing between two adjacent branches, which is the dendritic arm spacing (DAS). The measurable microstructural parameters are extremely important to the mechanical performance of the alloys. Previous studies have confirmed that dendritic arm spacings have a strong influence on the mechanical behavior of metallic alloys [5,6,7]. Furthermore, the dendritic structure also influences the corrosion resistance of metallic alloys exposed to corrosive environments [8]. Both tensile strength and corrosion resistance of metallic alloys are influenced by the size and the microscopic segregation of dendritic structures. Rao et al. [9] stated that strain hardening tendency of Al-Si alloys depends on the DAS and the size of the eutectic silicon, which ultimately govern the wear behavior of these alloys.

Al-Sn alloys typically present abnormal high solute concentration at the outer regions of the produced casting. In contrast, inner Sn-poor regions can be found within the same casting. This is known as inverse macrosegregation, which is reinforced in the case of Al-Sn alloys due to the large freezing range typical of such of alloys.

Therefore, this study is aimed to find evidences of the relationship between dendritic arm spacings and the wear resistance of Al-Sn and Al-Si alloys, which are widely used in tribological

applications. The wear resistance was evaluated by the calculation of the wear volume that was obtained by micro-abrasive wear tests.

2 Experimental Procedure

Upward unidirectional solidification experiments were carried out in unsteady state heat flow conditions in order to simulate solidification conditions typical of industrial foundry processes. The experimental setup is shown in Figure 1A. This apparatus consists of a water-cooled mold with heat being extracted from the bottom, promoting a vertical upward directional solidification. Additional details can be found in a recent study [10]. Experiments were carried out with Al-20wt%Sn and Al-3wt%Si alloys, being natural convection minimized since in the physical experimental configuration of vertical directional solidification, with melt on top and solid below, the melt is both thermally and solutally stable for both alloys.

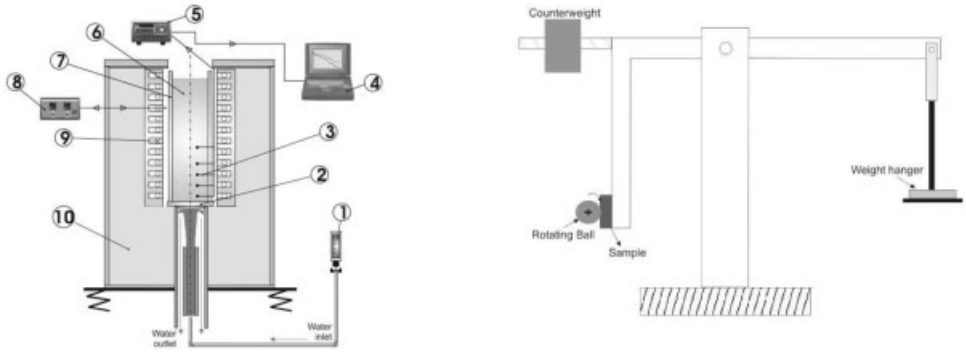
The microstructure characterization was carried out along the casting length (at 4, 10, 16, 21, 27, 32, 38 and 44 mm from the metal/mold interface, but, for Al-3wt%Si alloy, the positions 32 and 38 were excluded). From the bottom to the top of the ingot, the cooling rate decreases due to the increase in the thermal resistance during solidification. The reduction on the solidification kinetics causes the coarsening of the dendritic array making the dendritic arm spacings increase. Therefore, removing samples from different regions along the longitudinal section of the ingot is the best way of having different dendrite sizes. The operational sequence applied to obtain the samples from the ingots is shown in Figure 2. Such samples were polished and etched with a solution of 0.5 % HF in water. Image processing systems Neophot32 (Carl Zeiss, Esslingen, Germany) and Leica Quantimet 500 MC were used to measure the secondary dendritic arm spacings (λ_2) and to characterize the dendritic array. The λ_2 values were measured on the longitudinal section by averaging the distance between adjacent side branches.

Transversal samples were used in the micro-abrasive wear tests in order to analyze the effect of the secondary dendritic spacings on the wear volume. A sketch of the micro-abrasive wear tester used in this study is shown in Figure 1B. In the tests, a hard spherical ball was rotated against the sample, producing a wear crater. The used ball was made of bearing steel (AISI 52100), with diameter of 25.4 mm and hardness of 850 HV 0.050. The ball sliding speed was 0.33 m.s^{-1} (257 RPM) and the applied normal contact load was 0.6 N.

The tests were carried out under dry sliding conditions. For each sample, a set of three experiments were performed, corresponding to three sliding distances: 307 m (15 min), 410 m (20 min), 820 m (40 min). Four measurements of the craters diameter were determined; the average and standard deviation were calculated.

The aforementioned optical microscope was used to measure the diameter of the wear crater. The wear volume V was calculated according to Eq. (1), where d is the crater diameter, and R the ball radius [11,12].

$$V = \frac{\pi \cdot d^4}{64 \cdot R} \tag{1}$$



(A) (B)

Figure 1: Schematic representations of the (A) casting assembly used in the directional solidification experiments: 1) rotameter; 2) heat-extracting bottom; 3) thermocouples; 4) computer and data acquisition software; 5) data logger; 6) casting; 7) mold; 8) temperature controller; 9) electric heaters; 10) insulating ceramic shielding; and (B) Micro abrasive wear tester.

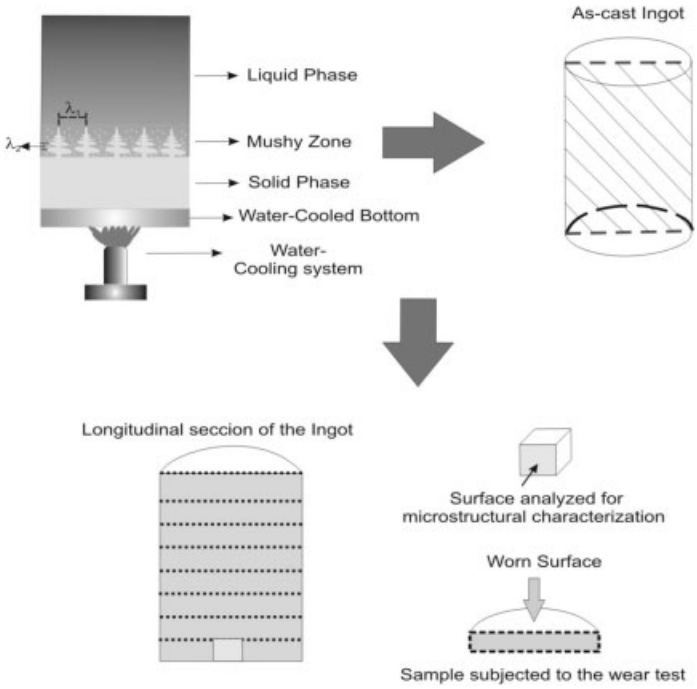
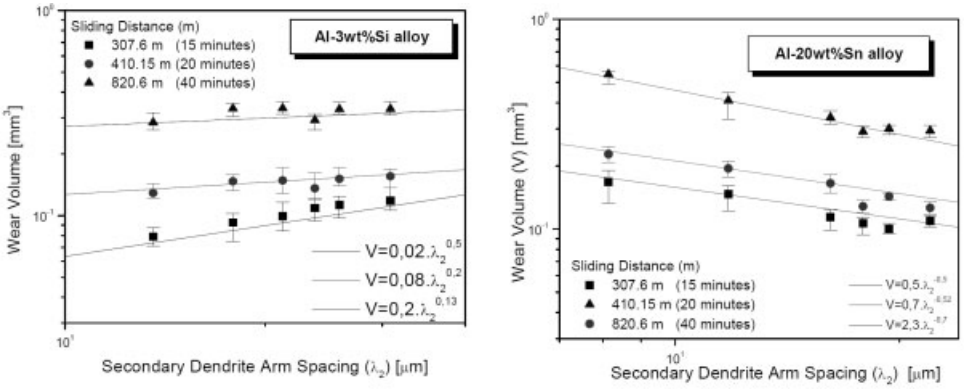


Figure 2: Sequence used to obtain the samples submitted to the microstructural characterization and micro abrasive wear test.

3 Results and Discussion

Figure 3 shows the wear volume as a function of the secondary dendrite arm spacing (λ_2) for Al-20wt%Sn and Al-3wt%Si alloys. Points are experimental results and lines represent an empirical fit of the experimental points, with the wear volume variation being expressed as a power function of secondary dendrite arm spacing. It can be seen that the relationship between λ_2 and the wear volume for the Al-20wt%Sn alloy is different from that for the Al-3wt%Si alloy. For the Al-20wt%Sn alloy, the wear volume decreases with increasing λ_2, while the behavior was the opposite for the Al-3wt%Si alloy.



(A) (B)

Figure 3: Wear volume as a function of secondary dendritic spacing for (A) Al-3wt%Si and (B) Al-20wt%Sn alloys.

Al-Sn is an immiscible binary alloy system, with an Al-rich dendritic matrix involved by a Sn-rich eutectic phase (Figure 04). Comparing the interdendritic regions of fine and coarse structures, the coarser one presents larger Sn-rich areas (larger interdendritic regions), despite its lower Sn concentration, which is a consequence of the inverse segregation phenomenon. The lower wear volume observed for coarse structures of the Al-20wt%Sn alloy seems to be associated with these larger Sn-rich regions. It seems that the lubrication effect of the soft Sn-rich areas is improved when such configuration is achieved. Concerning the Al-3wt%Si alloy, it can be seen that finer dendritic structures provide lower wear volumes than coarser ones. Al-Si hypoeutectic alloys are morphologically formed by a dendritic Al-rich α-phase and eutectic Si particles (Figure 05). The Si particles are coarse and characterized by an acicular or lamellar morphology. Finer dendritic structures provide a more homogeneous distribution of Si particles and this homogeneity seems to contribute for increasing the wear resistance. Kori and Chandrashekharaiah [**4**] observed that improved wear resistance in Al-Si hypoeutectic alloys can be achieved by the addition of grain refiner and/or modifier, which permits not only a reduction of Si particles but also a better distribution.

Power functions such as $V=C.(\lambda_2)^n$ seem to be the best functional relationship to generate the variation of the wear volume (V) with secondary dendritic spacing (λ_2) for both alloys. It can be seen that -0.5 power law characterizes the experimental variation of V with λ_2 for the

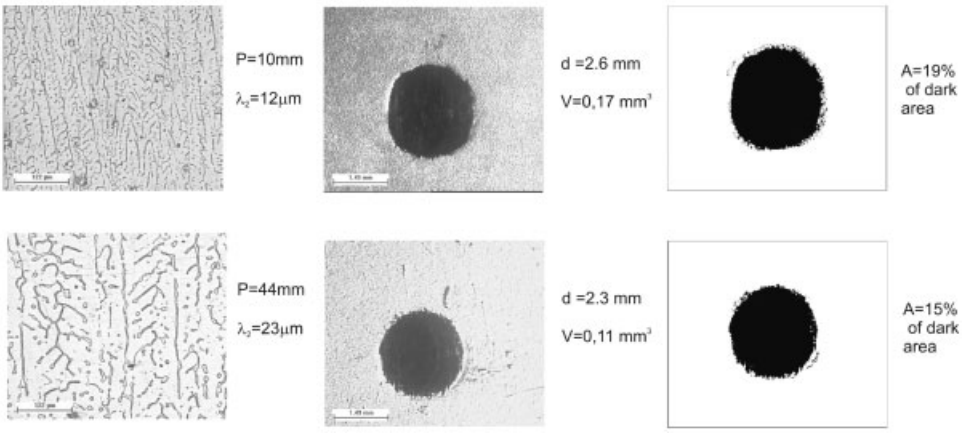


Figure 4: Correlation between dendritic network and the diameter of the crater for Al-20wt%Sn alloy for a sliding distance of 307.6 m: (A1) and (A2) Dendritic microstructure; (B1) and (B2) Craters in two positions (10 and 44mm) along the ingot length; (C1) and (C2) Crater areas for two different positions from the metal-mold interface. V-wear volume; P-position from the metal/mold interface; d- crater diameter.

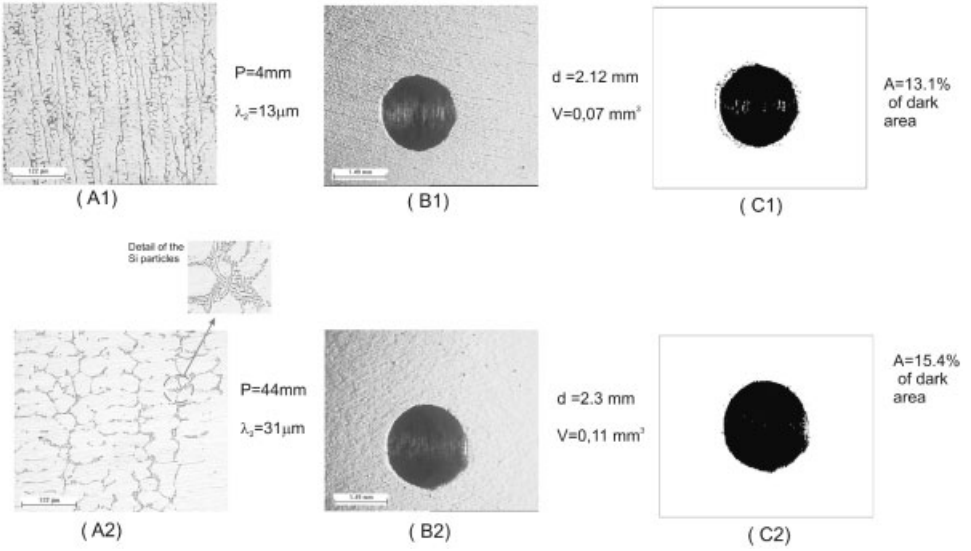


Figure 5: Correlation between dendritic network and the diameter of the crater for Al-3wt%Si alloy for a sliding distance of 307.6 m: (A1) and (A2) Dendritic microstructure; (B1) and (B2) Craters in two positions (4 and 44mm) along the ingot length ; (C1) and (C2) Crater areas for two different positions from the metal-mold interface. V-wear volume; P-position from the metal/mold interfae; d- crater diameter.

Al-20wt%Sn alloy, and the exponential factor “n” varies as a function of the sliding distance for the Al-3wt%Si alloy. This variation probably happens because the wear volume of the Al-

3wt%Si alloy tends to reach a constant regime as the sliding distance (SD) increases. Therefore, the diameters of the craters formed over Al-3wt%Si alloy samples for each positon from the metal-mold interface, for the SD = 820m, are not significantly different, indicating that the wear volume is essentially constant along the casting length. For the Al-20wt%Sn alloy, the constant regime seems not to be reached due to the lower values of hardness and mechanical resistance if compared to the corresponding figures of the Al-3wt%Si alloy.

Typical dendritic longitudinal microstructures and wear craters are shown in Figures 04 and 05 for Al-20wt%Sn and Al-3wt%Si alloys, respectively. The dendritic network becomes coarser with increasing distance from the metal/mold interface, and the diameter of the crater tends to change when the secondary dendritic spacing is increased.

4 Conclusions

The following conclusions are derived from this study:

1. The dendritic array seems to affect the wear resistance of the two alloys studied. For the Al-20wt%Sn alloy, the wear volume decreased with increasing secondary dendritic arm spacing (λ_2), while for the Al-3wt%Si alloy the wear resistance improved with decreasing λ_2.

2. The larger Sn-rich areas of the coarser Al-20wt%Sn alloy structures seem to improve the anti-friction properties of this alloy while the better-distributed Si needles near the bottom of the Al-3wt%Si alloy casting, due to the finer dendritic structure, guarantee lower volume wear. Probably, the larger Sn-rich areas make a more efficient solid-lubricant effect

3. Power functions such as $V=C.(\lambda_2)^n$ appear to be the best functional relationship to generate the variation of wear volume (V) with secondary dendritic spacing (λ_2) for both alloys, with lower "n values" found when higher sliding distances were performed for the Al-3wt%Si alloy.

5 References

[1] Yuan, G.C.; Li, Z.J; Lou, Y.X; Zhang, X.M; Mater. Sci. Eng. A, **2002,** v. 280, p.108-115.

[2] Forrester, P.G., Met. Rev., **1960,** p.507-512.

[3] Kaschnitz, E.; Romansky, M., High Temp. – High Press., **2002,** p.699-704.

[4] Kori, S. A.; Chandrashekharaiah, T. M; Wear, **2007**, v. 263, p.745-755.

[5] Osório, W.R. Goulart, P. R; Santos, G.A.; Moura Neto, C.; Garcia, A. Metallurgical and Materials Transactions A, **2006**, p. 2525-2538.

[6] Quaresma, J.M.V.; Santos, C.A.; Garcia, A., Metallurgical and Materials Transactions A, **2000**, v. 31A, p. 3167-3178.

[7] Goulart, P. R.; , Spinelli, J. E.; Osório, W. R.; Garcia,A., Materials Science and Engineering A, **2006**, v. 421, p.245-253.

[8] Osório, W.R.; Freire, C.M; Garcia, A., Journal of Alloys and Compounds, **2005,** v. 397**,** p**.** 179-191.

[9] Prasada Rao, A. K. ; Das, K. ; Murty, B. S.; Chakraborty, M., Wear, **2006**, v.261, p. 133-139

[10] Osório, W.R; Spinelli, J E ;Ferreira, I.L.; Garcia, A. , Electrochimica Acta, **2007,** v. 52, p. 3265-3273.

[11] Rutherford, K.L.; Hutchings, K. L.; I.M., Surf. Coat. Technol. **1996**; v.79, p.231-239.

[12] Gee, M.G.; Gant, A.; Hutchings, I. M.; Bethke, R.; Schiffman,K.; Van Acker, K., Poulat, S., Gachon, Y., Von Stebut, J., Wear, **2003,** v. 25**5,** p. 1-13.

Study of Different Aspects of a Novel Method for Surface Carburizing of CP-Ti

M. Aliofkhazraei[1,*], A. Sabour Rouhaghdam[1], H. Alimadadi[2]
1) Faculty of Engineering, Materials Engineering Department, Tarbiat Modares University, P.O.Box:14115-143, Tehran, Iran.
2) Department of Materials and Manufacturing Technology, Chalmers University of Technology, SE-412 96, Göteborg, Sweden.
*) Corresponding author, e-mail: maliofkh@gmail.com

1 Introduction

During the Pulsed bipolar nanocrystalline plasma electrolytic carburizing (PBNPEC) treatment the voltage reaches high values, above the dielectric breakdown voltage and the plasma envelop being formed. The temperature and plasma-chemical reactions occurring inside the surface give a fine crystalline hard layer which is called nanocrystalline carburized layer [1]. The inner part of the carburized area formed beneath the compound layer is called diffusion zone. Thus, the formed layers consist of various phases which varying according to the process conditions [2].

Despite the considerable effort that has been invested into understanding the wear and corrosion properties of different steels, it seems that little attention has been given to the role of PBNPEC in wear and corrosion procedure for commercially pure titanium (CP-Ti). In-depth understanding of the subject of wear and corrosion can not be achieved without a clear view of the role of morphological properties of the nanocrystalline layers. It is therefore the aim of this paper to further clarify the important role of nanocrystalline carburized layer formed by the means of PBNPEC treatment and its role on the wear of CP-Ti, using the abrasive wear test method following ASTM G105 guidelines. In present study, it is demonstrated that proper selection of experimental parameters can potentially provide beneficial surface modifications to the substrates by formation of compact nanocrystalline carburized layer.

2 Experimental

Disc samples made of CP-Ti with a diameter of 20 mm and thickness of 5 mm were grounded to different stages of metallographic polishing to obtain a near-mirror surface finish and then ultra-sonically cleaned in pure ethyl alcohol. PBNPEC treatment was performed in a cooling vessel to maintain temperature of electrolyte constant at 40 °C. The treatment electrolyte was a mixed organic solution of Gelycerol and chemically pure sodium carbonate (NaCO3). Sodium carbonate was added to provide a desirable electrical conductivity of electrolyte. Following our other works [3, 4], the workpieces were biased to pulsed current from a 20 KW power supply. Frequency and duty cycle of pulse current were maintained constant at 1000 Hz, 30 % (cathodic direction) and 60 % (anodic direction) respectively, during the coating process. Also peak voltage on anodic direction was maintained constant at 200 V and peak voltage on cathodic direction was changed in experiments. So the phrase „applied voltage“ will be use after this for peak voltage

in cathodic direction. An AISI 316 stainless steel cylinder of dimensions 15 cm dia $\times$ 22 cm formed the anode of the electrochemical system of coating process. An average current density of 0.5 A cm^{-2} was used during PBNPEC treatment. The surface temperature was approximately a linear function of the applied voltage in the PBNPEC treatment [5]. Therefore, the applied voltage could be selected according to the desirable surface temperature. Different experimental parameters applied in this work are summarized in samples codes. For example, sample with the code of 600-20 treated by 600 V of applied voltage at 20 minutes.

Morphologies and their quantitative analysis of the coatings were observed by the means of scanning electron microscopy (SEM). The studies were performed on a Philips XL-30 scanning electron microscope. In order to evaluate the cross sectional hardness of the treated samples Vickers micro hardness test was made with loads of 100 g having a maximum time of 15 seconds at the maximum load [6]. Nine microhardness measurements were made on each sample. The wear resistance of the samples was studied using the abrasive wear test. They were subjected to a normal force of 50 N against the wheel rotating at a constant speed of 200 rpm. After 1000 m of sliding distance, the weight loss of samples was determined by a digital balance with a resolution of 10^{-4} N.

To measure length to diameter ratio (L/D ratio) for nanocrystalline carbides, 5 SEM nanostructures with same magnification were analyzed trough commercial software for figure analysis called a4iDocu for each treated sample. Different measurements were interpolated to obtain average results. At least 40 measurments were done in each nanostructure for minimizing systematical errors. The distribution of nanocrystals was plotted and they have shown a Gaussian-shape. It is well known that for achieving better properties of nanocrystalline layers, it is better to have this Gaussian-shape curve narrower, which shows distribution of sizes of nanocrystals around a particular amount. So the ratio of height to width (in the middle of curve) (H/W ratio) of these Gaussian-shape curves were measured and plotted for different treated samples. They have been studied in order to maximize this ratio.

3 Results and Discussion

3.1 Layer Thickness and Microhardness

The hard layer thicknesses obtained on the specimen surfaces are shown in Fig. 1. The maximum layer thickness value was achieved in carburizing treatment (700 V, 30 minutes). The hardened layer thicknesses were between 6 μm and 38 μm for compound layer and between 15 μm and 98 μm for total influenced layer.

The thickness of the carburized layer depends on the treatment temperature and time. Previous studies have shown that treatment temperature (as a result of applied voltage) was much more effective on the layer thickness than the treating period. The layer thickness has increased parabolically with time [3]. The surfaces of the specimens for microhardness measurements were slightly polished and measurements made using a Vickers microhardness tester. The load was kept constant in all tests in order to compare their results. Surface hardness values are given in Fig. 2.

Microhardness values were found to be 1670 HV in specimens carburized for 30 minutes by 700 V. It can easily be seen that the microhardness values of carburized specimens are higher than those of untreated specimen ($\sim 250\,Hv_{0.1}$). The microhardness values increase with the

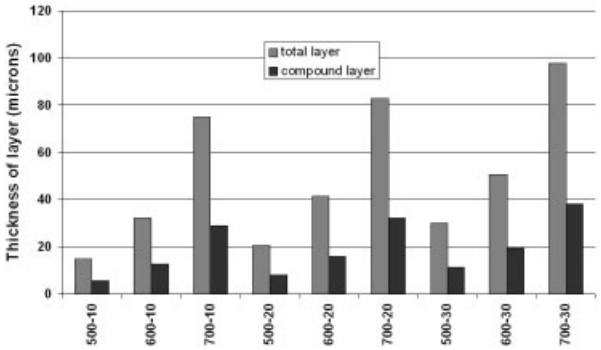


Figure 1: Thicknesses of compound layer and total influenced layer of treated samples.

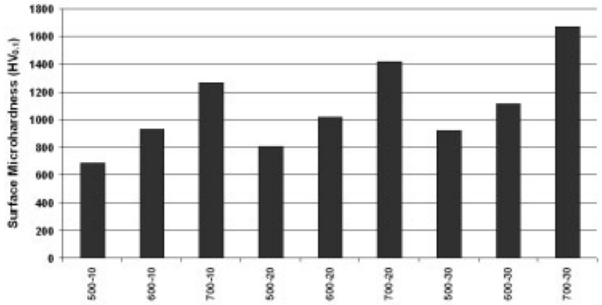


Figure 2: Surface Microhardness of treated samples.

carburizing period. The maximum hardness value was reached in specimens carburized for 30 minutes by 700 V.

3.2 Wear Test Results

Figure 3 shows the wear losses of different steels found through the wear tests performed after surface hardening treatment. From the wear tests performed under tribological conditions after 1 Km of sliding distance, the following results are obtained. The minimum wear losses were found to be 2.7 mg in 30 minutes carburizing by 700 V. The maximum values obtained for untreated samples (13.5 mg). Also it is seen that all of the specimens to which the carburizing treatment had been applied had higher wear strengths than raw material.

3.3 Average Size of Nanocrystals

Figure 4 shows the average sizes of nanocrystalline carbides of different treated samples found through the carburizing process. The minimum average size of nanocrystals was found to be 19.6 nm in 30 minutes carburizing by 700 V. As it can be seen the samples that have smaller average sizes of nanocrystals also have better wear resistances. From the above results, it can

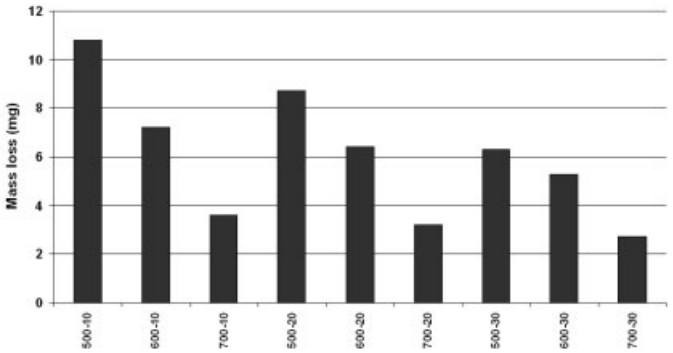


Figure 3: Wear mass loss of treated samples after 1 Km of sliding distance.

easily be said that lower average sizes of nanocrystalline carbides have been obtained with higher applied voltages and treatment times of carburizing process at constant frequency and duty cycles.

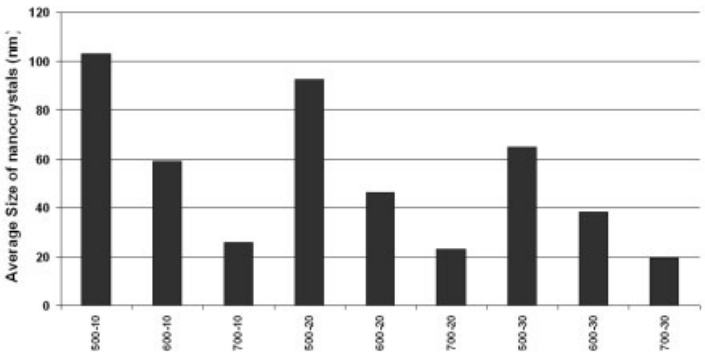


Figure 4: Average size of nancrystalline carbides for different treated samples.

3.4 L/D Ratio

Figure 5 shows the L/D ratio of nanocrystalline carbides found through the carburizing process. The minimum L/D ratio of nanocrystals was found to be 1.6. Smaller L/D ratios show that nanocrystals have shapes like spheres. As it can be seen the samples that have smaller L/D ratio of nanocrystals also have better wear resistances. In fact, in this process smaller nanocrystals have smaller L/D ratios which lead to higher wear resistances.

3.5 H/W Ratio

Figure 6 shows the height to width (H/W) ratio of distribution curves for nanocrystalline carbides of different steels found through the carburizing process. The maximum H/W ratio was

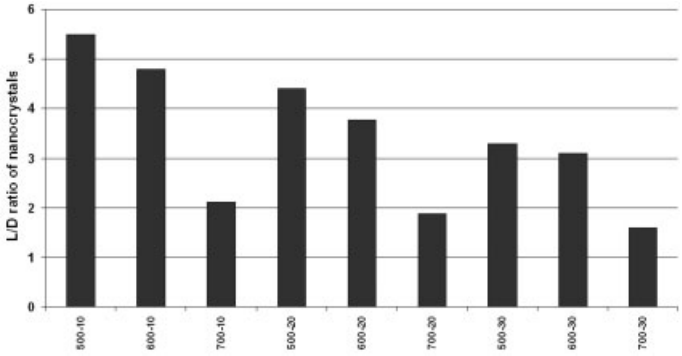


Figure 5: L/D ratio of nancrystalline carbides for different treated samples.

found to be 7.4 in 30 minutes carburizing by 700 V. Comparing with other obtained results, it can be seen that the samples with high H/W ratio have better wear resistances. High distribution of nanocrystals around a specific average value will lead to better wear resistances. Samples with lower amounts of this average value show better wear characteristics. This average value will decrease by higher applied frequencies and lower duty cycles [2], but in the case of constant values of frequency and duty cycle, such as this investigation, higher applied voltages and treatment times will affect this average value and H/W ratio. Also it can be seen that the contribution percentage of applied voltage is higher than contribution percentage of treatment time.

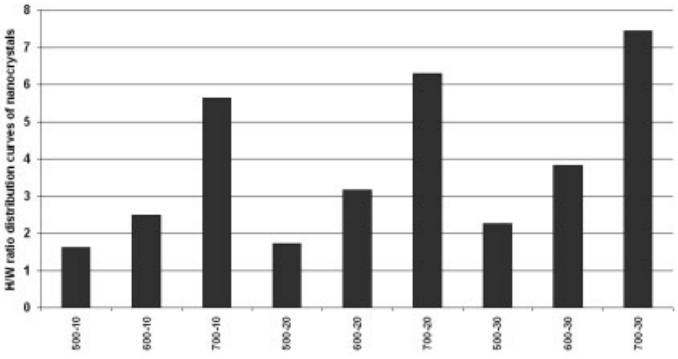


Figure 6: H/W ratio of nancrystalline carbides for different treated samples.

4 Conclusions

The conclusions drawn from the various tests explained in the previous sections are as follows:

1. In situations where abrasive wear is important, the best wear strengths were obtained in carburizing at 30 minutes by 700 V for CP-Ti substrates.

2. Hardness values results show that there is a linear relationship between hardness values and wear resistance for treated samples.

3. The microhardness values and wear strengths of carburized specimens were found to be higher than for untreated specimens.

4. Samples that have smaller L/D ratio of nanocrystals, have better wear resistances. In fact, in PBNPEC process smaller nanocrystals have smaller L/D ratios which lead to higher wear resistances.

5. In the case of constant values of frequency and duty cycle in PBNPEC process, higher applied voltages and treatment times will lead to higher H/W ratio. Also it can be seen that effect percentage of applied voltage is higher than treatment time.

5 Acknowledgement

The authors wish to express their thanks to Mr. P. Gupta (CAP international technologies, USA) for his useful guides during the experiments. This project is funded by Arvandan oil and gas production company (TMU 85-09-66) and national association of nanoscience and nanotechnology of Iran.

6 References

[1] Nie X., Tsotsos C., Wilson A., Yerokhin A.L., Leyland A., Matthews A., Surface and Coatings Technology **2001**, 139, 135–142.

[2] Aliofkhazraee M., Sabour Rouhaghdam A., Shahrabi T., Part 1, **2007**, Journal of Alloys and Compounds, in press.

[3] Aliofkhazraei M., Sabour Rouhaghdam A., Electrochemistry Communications **2007**, 9, 11, 2686–2691.

[4] Aliofkhazraei M., Sabour Rouhaghdam A., Sabouri M., **2008**, Journal of Materials Science, 43, 1624–1629.

[5] Aliofkhazraei M., Taheri P., Sabour A.R., Dehghanian C., **2007**, Materials Science, in press, will appear on No.6.

[6] ASTM E92-82, Standard Test Method for Vickers Hardness of Metallic Materials.

Study on Hardfaced Wear Resistant Bronze Alloy

Ionelia Voiculescu, Victor Geanta, Radu Stefanoiu
University "Politehnica" of Bucharest, Bucharest
Horia Binchiciu
SC SUDOTIM AS SRL, Timisoara
Ioan Vida Simiti, Nicolaie Jumate
Technical University of Cluj Napoca, Cluj-Napoca
Radu Vasiu
SC TEHNOMAG SA, Cluj-Napoca

1 Introduction

The copper and copper alloys have a very good electrical conductivity, but also good resistance at atmosphere corrosion. The particular physic-mechanical properties directly influence the weld ability of the copper alloys through the following aspects: the high thermal conductivity determines a fast heat dissipation in the metallic mass of the pieces to be welded; pre-heating and welding with extremely concentrated thermal sources are recommended; the considerable deformations due to the high linear dilatation coefficient can lead to cracks in the weld and the HAZ (Heat Affected Zone); crystallisation cracks and pores may appear due to the oxygen or hydrogen absorption during welding; the $Cu+Cu_2O$ formation, situated at the grains boundaries, with the melting temperature 1064 °C lower than the copper's melting temperature (1083 °C) can determine heat fragility [1, 2].

In the research paper the main objective was to elaborate and test special tubular electrodes in order to obtain wear resistant bi phase deposits made from bronze alloys with 10…12% tin. These alloys are used for pieces rehabilitation or bimetal components obtaining with different metallic inter-layers and special characteristics.

2 Experimental

More than 12…15% Sn content in the weld is important in order to assure the appropriate hardness, wear and corrosion resistance. This content is difficult to be used for the electrode wire, due to the low deformation capacity of the alloy. It is that why the original solutions proposed by the research team have focused on the obtaining of special electrodes as tubular wires, made in efficient economic and technological conditions. The solution proposed is the tubular copper wire with bronze powder composite core.

2.1 Electrodes

At the first stage of obtaining the new composite core, the CuSn7 powder was gravitationally cast in a copper tube of 350 mm length and 6 or 8 mm diameter, and then the two edges were closed through plastic deformation. After pre-sintering the copper rod at 780 ºC in a protective atmosphere, an infiltration with liquid Sn, in vacuum at 1.3 10^{-2} [at] pressure was applied. The final

sintering with the infiltrated liquid phase (Sn) was done at approximately 815 ºC for 35 minutes in a protective atmosphere (Endogas technique). The tubular electrode with bronze composite core, of 15 % Sn average percent, can furthermore be coated through coating extrusion, in order to be used for electric arc welding [3, 4].

2.2 Materials and Equipments

The basic materials used were copper, bronze, carbon steel and stainless steel plates. The different parent materials were selected to analyse the deposited metal's compatibility with various metallic networks (in order to study dilution, interface defects' appearance, wettability). Samples preparation for the metallographic analysis and micro-hardness used WC metallic carbides discs, which were then embedded in phenol resin through polymerisation at 170 °C, then polished with the automatic polisher machine. To obtain the polished surfaces for the electronic microscopic analysis, the following abrasive materials were used consecutively: 1200 granulation metallographic paper, 60 μm granulation alumina powders, 1650 cerium oxide with 6 μm granulation. The $FeCl_3$ reactive was used to highlight the phases and the metallographic components.

The samples' welding was performed through the TIG process (Tungsten Inert Gas), under continuous current, with reversed polarity. The control of the welding electric arc was performed through the inverter system of the welding source (COMBIWIG 3000DC), at constant wire introduction speed in the metallic bath.

2.3 Investigation Techniques

In order to evaluate the changes in the mechanical characteristics emerging in various joining areas, HV03 micro-hardness measurements were performed, using the Shimadzu HMV 2T microhardness equipment. For the structural analysis, the SEM electronic microscopy was used, with a HITACHI S2600 with energy dispersive analysis system (EDS) and FEI Inspect S electronic microscopes. The thermo graphic images of the welding deposits required for the thermal field dispersion analysis were taken with the IR ThermaCam PM350 Inframetrics.

2.4 Parameters

The welding regime parameters have a great influence on the deposit's geometrical and structural characteristics (Table 1).

Table 1: The regime parameters for the TIG process

Parameter	S1	S2	S3	S4
Welding current, Iw, A	130	115	133	138
Arc voltage, Uw, V	32	32	33	30
Gas flow, Dg, l/min	7.3	7.3	7.3	7.3

Analysing the bead shape for deposits width and crown weld they obviously depend on the material support. Thus, for copper plates, which allow massive three-dimensional heat dissipation, the deposit has a lower crown width (h, Table 2). The melted metal is overheated and the wettability towards the base material is higher, although the welding current had the lowest value. In

order to ensure a deposit with adequate Sn content values, knowing this element is highly volatile and melts rapidly in the electric arc, the heat input must be lower and the protective atmosphere must be inert, with a sufficient flow rate (6–8 l/min).

For the stainless steel and bronze plates, the deposits had highest widths (B) and highest crown weld (h) compared to the copper plates, resulting that the consumable melted area (F) is higher. The penetration was higher for copper and bronze plate, while for mild and stainless steel plate the penetration was minimal (Figure 1).

Table 2: The geometrical parameters of weld deposit

Shape parameter	S1	S2	S3	S4
Weld width, B, mm	10.85	15.90	13.20	12.90
Crown width, h, mm	3.20	2.50	3.60	4.40
Weld penetration, H, mm	2.30	2.50	0.01	1.10



Figure 1: Cross section of samples with weld deposit.

3 Results

3.1 The Welding Thermal Field

The thermograph analysis shows the uniform concentration in the weld area for the bronze samples (Figure 2), and the heterogeneous heat distribution of the deposit on the copper plate (Figure 3). The macro-graphic analysis pointed out a high unevenness of the deposited weld, an exaggerated width and a reduced over height.

The copper and bronze substrates favoured quick heat dissipation in the base material and its concentration in the weld's edges. Therefore, the areas exposed to high temperatures for a longer time risk having an altered chemical concentration and different structures compared to those cooled faster.

3.2 Microhardness

In order to evaluate the changes in the mechanical characteristics emerging in various joining areas, HV03 micro-hardness measurements were performed. The micro-hardness measured values are presented in Table 3. In the case of steel plates, the weld structure is composite like, with hard bi- or multi-phase islands surrounded by plastic metallic matrix (Figure 4).

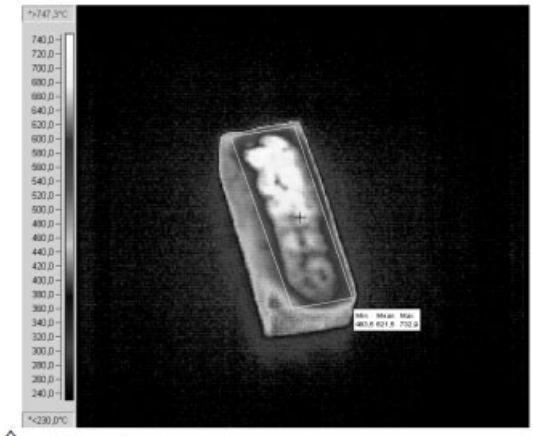


Figure 2: Bronze plate

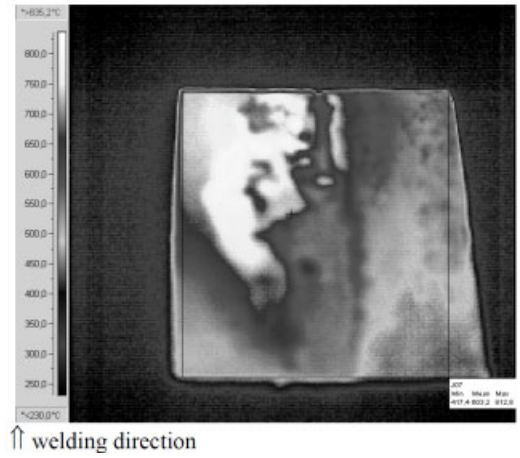


Figure 3: Copper plate.

Table 3: HV03 micro-hardness values (2.943N, 10 seconds)

Sample	S1	S2	S3	S4
Bronze alloy deposited	155	68	181 (401*)	152 (408*)
Heat affected zone	159	67	250	242
Base material	173	49	178	209

*Values measured on the hard phases

The increase of microhardness into the Heat Affected Zone (HAZ) for all samples can be justified by the diffusion of the Sn and Cu from the weld through fusion line. Moreover, in the

case of steel plates, the HAZ hardening is more effective because of the hard phases and multi-component precipitates presence.

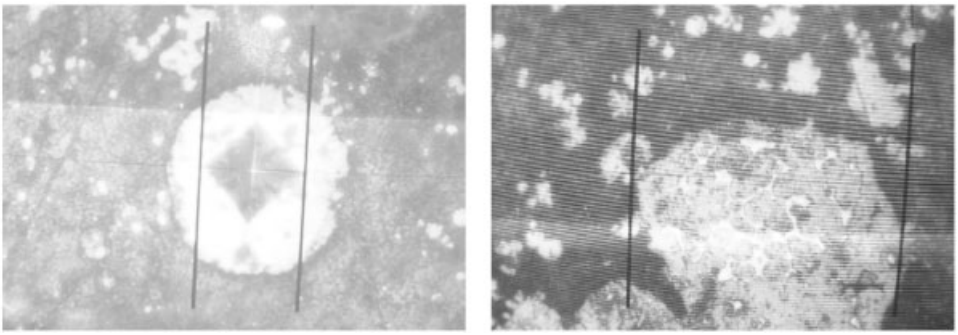


Figure 4: Hard multiphase (average diameter 57-120 μm) surrounded by plastic metallic matrix.

In the case of bronze and stainless steel support, the deposit has a lower microhardness compared to those of the base metal. The situation is different in the case of cooper and mild steel plate, were the microhardness increases in the weld deposit. However, the presence of hard multiphase compounds can increase the global hardness of the weld deposit.

3.3 Wear Tests

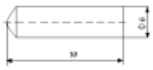
The wear tests have been carried out with different loads and sliding velocities, against hard steel disc (pin on disc method, Figure 5). The sample was cut from the centre of the welding zone and the welded edge was machined with 3 mm radius. For a set of 3 identical samples the normal force (F_n) was measured and friction force (F_f), was calculated using equation 1:

$$F_f = \frac{F_S \cdot R_S}{R} \tag{1}$$

were: F_s is reaction force of lamelar arch (N); R_s is distance up to catch pin (mm); R is wear disc radius D/2 (mm).

The wear test conditions were: loads successive values (12.8, 16, 18.2, 19.65 N), sliding velocity 350 rpm, sliding radius, R_s, 45 mm, temperature 25°C, relative humidity 40%. The values of the loads and calculated friction coefficient are presented in Table 4.

Table 4: Wear test values

Sample geometry, mm	F_n, N	F_s, N	F_f, N	μ_i
	12.8	2.28	2.05	0.16
	16	2.94	2.64	0.16
	18.2	3.59	3.23	0.17
	19.65	4.25	3.82	0.19

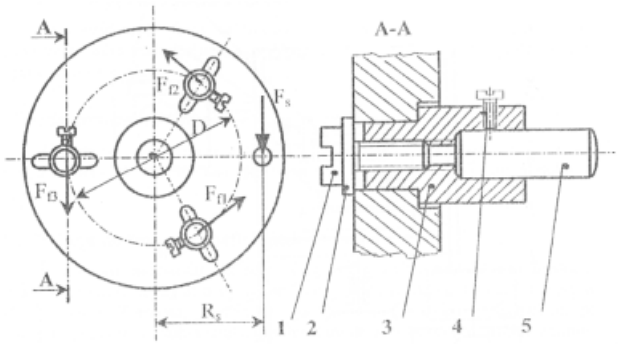


Figure 5: Tribometric system: 1 - screw; 2 - safety washer; 3 - stationary bushing; 4 - fixing screw; 5 - cilindrical sample

Analysing the results, we noticed that the different values of the friction coefficient appeared at the same sample due to the changes generated by the homogeneities of the composite metallic matrix, interaction between the two surfaces, surface heating in the contact zone and structural changes due to hot plastic deformation of the surfaces. The average values of friction coefficient are similar with those reported in the literature [1, 2].

3.4 Metallographic Analysis

The samples collected from different areas of the weld (base material, heat affected zone, weld deposit) were subjected to optical analysis, in order to identify the metallographic components (Figure 6). Based on the microscopy investigations, one can notice the columnar increasing of α and β crystals in the weld deposit and narrow fusion line with modified structure compared with those of base material (Figure 6.a). In the base material, apart from $\alpha - \beta$ phases one can also identify fine and very hard iron-rich particles, specific for the given chemical composition. No welding defects (discontinuities, inclusions) are visible. In the case of mild steel substrate, the fusion line is enriched with multi-phase precipitates (Figure 6.b).

The electronically examination of the weld deposit made on bronze substrate emphasises the higher agglomeration of α phase near the fusion line, on a depth of approximately 20 μm towards the base material, while in the weld deposit these phases do not appear (Figure 7a). The structure of weld deposit is more refined compared those of the base material (Figure 7b).

In the case of copper substrate, the type of transformation that occurs on cooling the β phase depends on the cooling rate. At slow to moderate cooling rates α precipitates on the grain boundary. Slow cooling favours transformation at small undercooling and the formation of equiaxed α richer in Cu than the parent β phases, and therefore the growth of α phase requires the long-range diffusion of Sn away from the advancing α/ β interfaces. This process is relatively slow, especially when Cu and Sn form substitutional solid solutions, and is favoured by the great heat input value during welding (Figure 8).

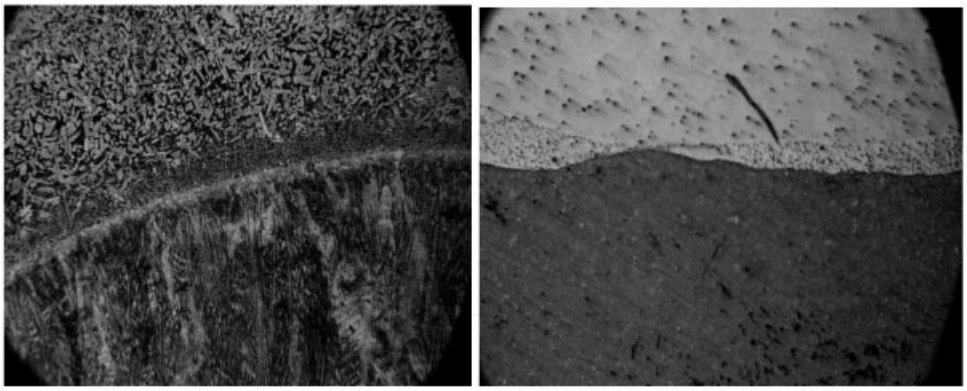


Figure 6: Optical microscopy of weld deposit: a) Cross-section through the CuSn alloy deposit on a bronze substrate, x50; b) Fusion line rich on multi-phase precipitates for mild steel substrate (x50).

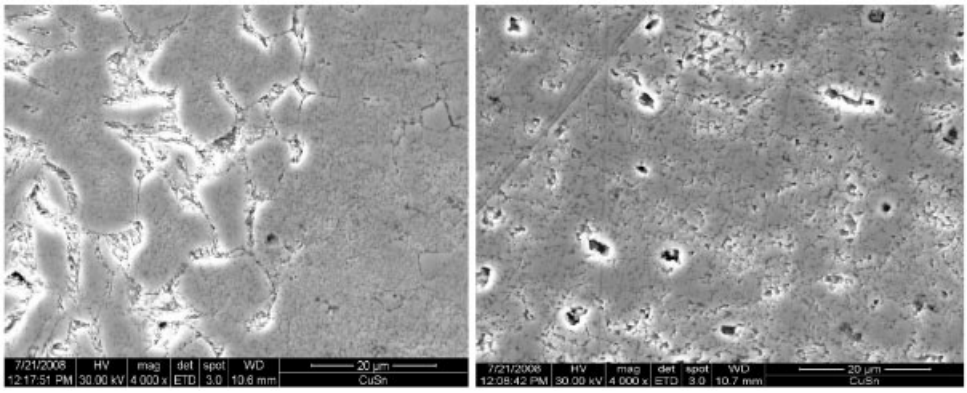


Figure 7: Electronically microscopy of CuSn weld deposit: a) Cross-section through the fusion line on bronze substrate (x4000); b) Weld deposit with refined structure (x4000).

4 Conclusions

The original solution proposed by the research team has focused on the obtaining of special tubular electrodes with bronze powder composite core, made in efficient economic and technological conditions.

The micro-hardness values were lower in the weld area and higher in the HAZ, especially for the bronze substrate sample; however, in the case of mild and stainless steel substrate hardening effects are based on the diffusion phenomenon through the fusion line. Thus, in the weld, the microhardness value depends on the presence of different hard phases (average values of 400 HV03) comparatively with the surrounding plastic metallic matrix (average values of 150-180 HV03).

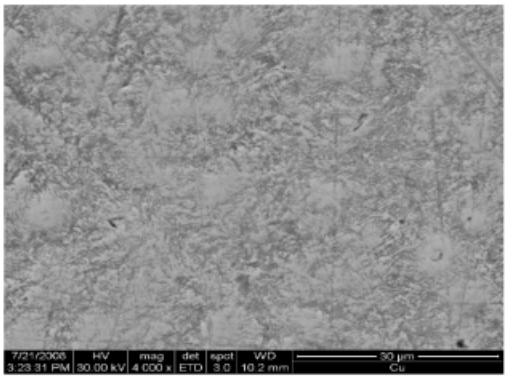


Figure 8: Electronically microscopy of CuSn weld deposit on copper plate (x4000).

The different values of the friction coefficient (0.16 – 0.19) appeared at the same sample can be explain by the changes generated by the homogeneities of the deposited composite metallic matrix.

References

[1] Rogers, M.N., ASM Handbook, *Vol. 6*, **1993**, USA, 752–771.

[2] Porter, D.A., Easterling K.E. Phase Transformations in Metals and Alloys, Alden Press, Oxford, **1981**, 525–538.

[3] Voiculescu, I., Geanta, V., Binchiciu, H., Vasiu, R., Proceedings European Congress on Advanced Materials and Processes, Euromat 2007, 10–13 September **2007**, Nurnberg, Germany, p. 69.

[4] Voiculescu, I., Geanta, V., Binchiciu, H., Vida-Simiti, I., Jumate, N., Vasiu, R., Proceedings 60th Annual Assembly and International "Welding and Materials – Technical, Economical and ecological Aspects", International Institute of Welding and Croatian Welding Society, 01 – 08 July **2007**, Dubrovnik & Cavtat, Croatia, p. 741–748.

[5] Voiculescu, I., Geanta, V., Binchiciu, H., Vida-Simiti, I., Jumate, N., Vasiu, R., Lungu, D., Proceedings Conference Excellence Research – A Way to ERA, Braşov, Romania, 24 – 26 October **2007**, L. 98.

Study of the Abrasive Wear Behaviour of Electrified Railway Wires

A. Garcia[1] (Sp), V. Lorenzo[2], A. Varela[1], C. Camba[1], V. Blazquez[2]
[1]Escuela Politécnica Superior (UDC), Mendizábal s/n, 15403 Ferrol, A Coruña (Spain)
[2]E.T.S.I.I. – U.P.M., José Gutiérrez Abascal,2, 28006 Madrid (Spain)

1 Introduction

Contact wires for railway applications are made by cold-drawing of high conductivity copper alloys [1, 2]. These alloys are selected because they allow to achieve an adequate mechanical strength while having a low electrical resistivity. The low resistivity is a requirement related to the necessity of assuring current transfer and the high strength is desirable for withstanding the constant tensile force that is applied under normal operating conditions. Contact wires were made of electrolytic tough-pitch copper, Cu-ETP, until two decades ago. Now, as a consequence of the more demanding exigencies of high running speeds, stronger copper alloys are used, mainly copper-silver and copper-magnesium in Europe.

Contact wires in overhead lines have to withstand not only static loads but other loads must be considered including dynamic loads and contact forces occurring between the wire and the current collector strip of the pantograph. The last of these effects is the main cause of the wear of the contact wire and, thus, the factor that limit the lifetime of this component. It has been reported that the wear of trolley can be obtained by the summation of mechanical and electrical contributions which relative importance depend on the operating conditions [3]. The observation of new experimental facts that cannot be explained by this simple model, like, for example, the minimum of the wear rate that has been found at high sliding speeds due to the current´s lubrication effect [2], requires a deeper understanding of the mechanisms that control the wear of the trolley wire.

In line of this, the aim of this paper is to present some preliminary results about the abrasive wear resistance of the copper alloys that are used for making the trolley wire.

2 Experimental

2.1 Materials

Three different copper alloys have been studied, a Cu-ETP, a copper-silver alloy, Cu-Ag0,1, and a copper-magnesium alloy, Cu-Mg0,5. The materials were received in form of contact wire for railway applications with sections that ranged from 107 to 150 mm^2. The chemical compositions of the samples were determined by optical emission spectrophotometry and the oxyigen contents of the three samples were calculated by methods of quantitative metallography. The results are summarized in Table 1.

In order to obtain a more detailed characterization of these materials, their mechanical and electrical properties were measured. The measured values for the tensile strength, Rm, the elongation at break, ε_B, and electrical conductivity, σ, are collected in Table 2.

Table 1: Chemical compositions of the analyzed copper alloys (concentrations are expressed in ppm)

	Ag	Ni	Pb	Mg	S	Sb	Sn	Zn	O
Cu-ETP	4	< 1	< 1	2	< 1	< 1	< 1	< 1	< 200
Cu-Ag0,1	808	< 1	15	1	< 1	<1	< 1	< 1	< 200
Cu-Mg0,5	14	< 1	< 1	4582	6	< 1	< 1	< 1	< 200

Table 2: Mechanical (tensile strength: Rm; elongation at break: ε_B) and electrical conductivity, σ, of the copper alloys that have been studied

	Rm (MPa)	ε_B (%)	σ (% IACS)
Cu-ETP	370	6	99,5
Cu-Ag0,1	375	5,5	98,7
Cu-Mg0,5	500	5	71,3

2.2 Methods

Microhardness, MH, was determined at room temperature (21±1 ºC) by using a Shimadzu model M microhardness tester that was equiped with a Vickers indenter. A contact time of 15 s and a 500 N load were employed. The reported values were obtained by averaging the results of six indentations and the intervals of confidence (95 % confidence level) for these measures were lower than ±2 % of the mean values.

The wear experiments were carried out by using a Microtest pin-on-disc high temperature tribometer that was provided with a 4 mm diameter hardened steel ball 52100. The hardness value for the ball was 60 HRC. The test were done over transversal sections of the wires that were previously polished for obtaining an average roughness (Ra) lower than 0.25 μm. A normal contact load of 5 N was applied on the surface of the specimens. A sliding speed of 0,075 m/s was selected for all the experiments and the test duration was 50 min and, consequently, the wear path that corresponds to these settings is 225 m. The samples were tested at different temperatures ranging from 20 to 350 °C.

The magnitude of the wear was determined by the difference between the weight of the samples before and after the test. The reported values are the average of several measurements and standard deviations range from 20 to 30 % of the average.

3 Results and Discussion

Figure 1 shows a micrograph of the wear track of the pin on disc tests. There are ruts on the surface generated by the microcutting process produced during abrasion step [4].

Figure 2 shows the relationship between the wear that was measured in room temperature pin-on-disc tests and Vickers microhardness. It can be seen that the losses of mass of the cold drawn copper alloys is a decreasing function of their hardness. These results are similar to those that have been previously reported for other materials, i.e., abrasive wear resistance becomes greater when hardness increases [5,6].

Figure 3 shows the dependence of the loss of mass that was experimented by the different samples as a function of the test temperature. It can be seen that the mass that is lost by the

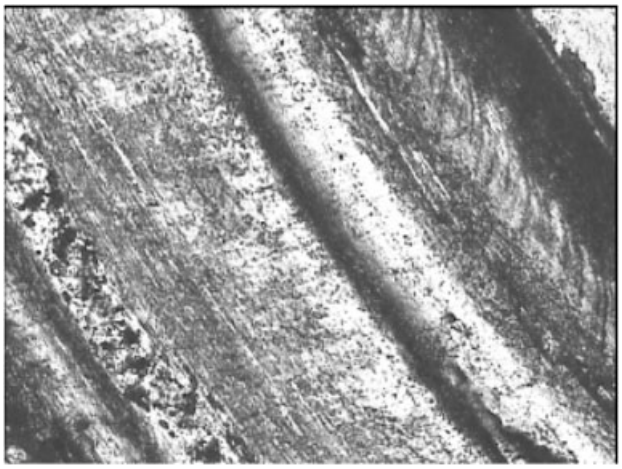


Figure 1: Micrograhp of the wear track of the pin on disc test

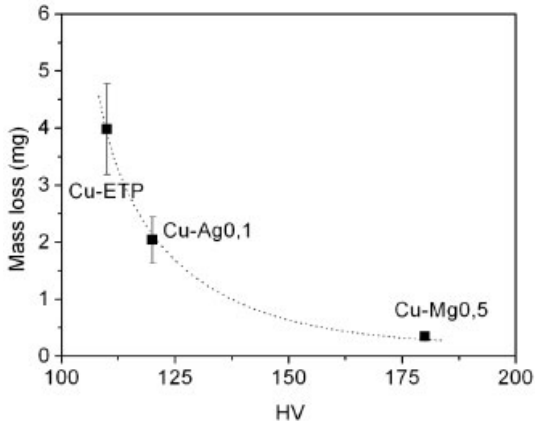


Figure 2: Relationship between the loss of mass at room temperature pin-on-disk experiments and Vickers micro-hardness, HV, of the different copper samples (the line is just a guide to the eye)

Cu-ETP are approximately the same for test temperatures that are lower than 175 °C and slightly decrease when temperature increases. The other alloys follow the same qualitative trend but the magnitude of the losses of mass of the Cu-Ag0,1 and Cu-Mg0,5 samples are about one-half and one-eighth, respectively, of those that experiment the Cu-ETP for this temperature range. However the behaviour of Cu-ETP is found to be different of those of the other materials for test temperatures that are higher than 225 °C. The loss of mass of Cu-ETP samples drops abruptly from values that are close to 4 mg to values lower than 1 mg whereas the abrasive wear resistance of Cu-Ag0,1 and Cu-Mg0,5 vary smoothly . As a consequence of the steep fall of the wear rate

of Cu-ETP, the high temperature mass decrements of this alloy are similar to that of Cu-Mg0,5 and lower than that of Cu-Ag0,1.

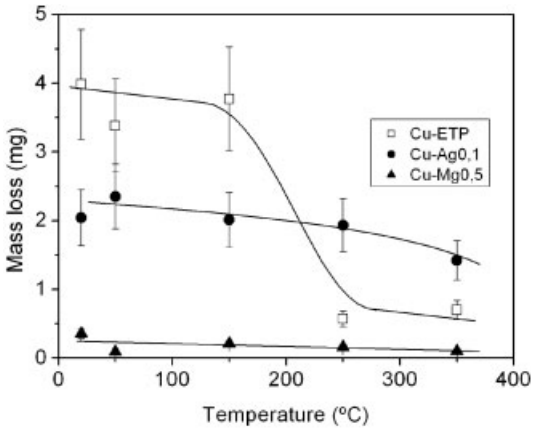


Figure 3: Losses of mass that are experimented by different copper alloys in pin-on-disk tests as a function of the temperature.

The sharp change of the abrasive wear resistance of the Cu-ETP samples seems to indicate that a structural transformation happens around 175 ºC. As Cu-ETP does not undergo any solid state phase transition, this behaviour can only be related to recrystallization. In fact, Cu-ETP for railway applications is drawn in order to balancing electrical and mechanical properties and it has been reported that this copper alloys recrystallizes in a temperature interval that ranges from 150 to 200 °C [2]. As a result of this transformation, room-temperature hardness of Cu-ETP falls abruptly to 55 HV. Even more, the extent of the recrystallization of copper is a monotonous increasing function of the annealing temperature and, consequently, the hardness of the samples that were tested at 350 °C is even lower than 55 HV.

According to this, the decrement of the loss of mass that is observed for the recrystallized Cu-ETP samples cannot be justified in terms of the variation of hardness. In order to explain these results, the changes of the mechanical behaviour of copper due to the recrystallization process must be considered. Hard drawn copper is a material with a relative high resistance and low ductility whereas strength of recrystallized copper is low and its elongation at break can be as high as 50%. As a consequence of the differences on the mechanical properties of hard drawn and recrystallized copper, the mechanism of the abrasive wear are distinct and the loss of mass that experiment these materials are different. The damage of the relatively brittle hard drawn copper is of particle formation type whereas that of the ductile recrystallized copper is of the deformation type [7].

The other alloys do not show the sharp change in the wear rate that is observed for Cu-ETP because their recrystallization temperatures are higher. It has been reported that the recrystallization temperature of Cu-Ag0,1 is close to 375 °C and that of Cu-Mg0,5 is greater than 500 °C [2]. Consequently, these materials do not recrystallize completely in the wear tests below 350 °C and only a slight change in the wear rate is observed.

Long term heating below recrystallization temperature due to the sliding of the current collector of the pantograph and due to current caption causes the recrystallization of the cold-drawn copper, process that is accompanied by an increment of plasticity and, consequently, by a modification of the wear mechanism. As the recrystallization temperature of Cu-ETP is lower than those of the other alloys, this change in behaviour appears for shorter service time than for the other copper alloys.

Because the importance of these preliminary results, new experiments involving other characterization techniques are in progress in order to get a deeper insight on the influence of the electrical and mechanical contributions of the wear of the trolley.

4 Conclusions

According to these results, the short term wear resistance of Cu-ETP at room temperature is similar and lower than those of Cu-Ag0,1 and Cu-Mg0,5.

It is possible to obtain information on the long term behaviour of trolley from the information provided by short time temperature dependent wear measurement.

At last, it has been proved that monitoring the loss of mass of metallic alloys in temperature dependent pin-on-disc experiments is an adequate tool for investigating the recrystallization of theese materials.

5 References

[1] Montesinos, J. and Carmona, M., "Tecnología de catenaria", Mantenimiento de Infraestructura de Renfe, Madrid, **2002**

[2] Kießling, F.; Puschmann, R. and Schmieder, A., "Contact Lines for Electrical Railways: Planning – Design – Implementation", Publicis Corporate Publishing, Munich Erlangen, **2001**

[3] Nagasawa, H. and Kato, K., Wear, **1998**, *216*, 179–183

[4] Zum Gahr, K., "Microstructure and wear of materials", Elsaevier, New York, **1987** (pp.80–131)

[5] Khruschov, M. M. , Wear, **1974**, *28*, 69–88

[6] Jeong, D. H.; Erb, U.; Aust, K. T. and Palumbo, G., Scr. Mater., **2003**, *48*, 1067–1072

[7] Bayer, R.G., "Mechanical Wear Prediction and Prevention", Marcel Dekker, Inc., New York, **1994**

Surface Alloying of CP-Ti Using Tungsten Inert Gas Process With Pre-Placed BN

R. Yazdi, F. Kashani Bozorg, L. Moazzemi and K. Hazeli
The university of Tehran, Tehran

1 Introduction

Titanium and titanium alloys have some excellent properties such as a good corrosion resistance and high strength to weight ratio. Its light weight and ability to resist extreme temperature make it suitable for aircraft applications. However a disadvantage of titanium is its high friction and poor wear resistance. It can be modified by surface modification which results a hard ceramic surface layer [1–3].

For this purpose, a number of surface modification techniques have been used to improve surface wear properties and these include conventional nitriding [4] , chemical/physical vapor phase coating processes [5,6], plasma source ion implantation [7], laser gas nitriding (LGN), tungsten inert gas and etc [8–10].

Furthermore, formation of Ti/TiN composite layer has been carried out by TIG surface melting in a pure nitrogen environment [11].

In present investigation, In order to improve surface properties, a non-consumable tungsten electrode was used to provide surface melting and then alloying with pre-placed BN. Changes in the surface wear characteristic were assessed using metallographic, microhardness and pin-on-disk wear techniques.

2 Experimental

TIG processing was done on CP-Ti alloy samples of size 100 mm × 25 mm × 7 mm. Fine boron nitride powder of size 10 μm and Ti powder of size 150μm were blended to make up a powder mixture containing 80 wt% Ti and 20 wt% BN.

Organic binder (polyvinyl alcohol) were used to pre-place the powder mixture onto the substrate surface so that the powder do not blow away during glazing action under a flow of inert gas which helps to product the melt from oxidation. The amount of binder was restricted within a limit in order to eliminate pore formation.

Finally, It was hand-brushed on the substrate surface to a thickness of about 0.8 mm. Prior to the coating, the titanium alloy samples were etched in a solution containing $HF+HNO_3+H_2O$ for about 5 min.

These powder-coated substrates were then dried in an oven to remove water and subsequently melted under the TIG torch.

Surface melting of the specimens was applied using the TIG torch. A tungsten electrode with a diameter of 2.4 mm was used to create an arc between the tip of the electrode and the specimen surface. The voltage (V) and current (I) to the electrode were maintained at 17 V and 60 A, respectively. The electrode height used was 2 mm. The specimens were held stationary under

the moving TIG torch while a shielding gas of pure argon was supplied with Gas flow rate 10 l min^{-1}. Tracks were produced along the width of the specimens at varying electrode-traversing speeds. The welding variables are given in Table 1.

Table 1: Calculated values of the arc energy density at different electrode-traversing speeds

E, (J mm^{-2})	Electrode-traversing, (mm min^{-1})	Voltage, (V)	Current, (I)
137	200	17	60
275	100	17	60
388	71	17	60

The alloyed samples were cut transversely to the traverse direction, polished by usual metallographic procedure and etched in a solution containing 5 ml concentrated HF, 15 ml concentrated HNO_3 and 80 ml H_2O for 10 s. Phases present inside the surface composite layer were analyzed by X-ray diffraction technique. The microstructures were observed by CAMSCAN scanning electron microscope. The hardness measurements were carried out with a MICROMET microhardness tester using a 200 g load on metallographically-polished and lightly-etched track sections.

The pin-on-disk tests were performed using a constant load of 20 N and a speed of 0.5 m s^{-1}. The specimens were ultrasonically cleaned before testing whilst immersed in methanol and blown dry with the air before placing them in the test machine. The tests performed against quench-temper steel discs with the hardness of 55 RC. Weight losses were obtained after certain sliding distances, by weighting the samples to an accuracy of 10^{-4}g using an electronic microbalance. All the specimens were cleaned with methanol before and after each measurement. Worn surfaces of materials were investigated using a scanning electron microscope.

3 Results and Discussion

3.1 XRD Pattern

The X-ray diffraction spectra taken from the surfaces are shown in Fig.1. Results of XRD analysis indicate that the main phases of the surface composite layers consist of TiN and TiB and Ti_3B_4. This is in broad agreement with the work of J. Senthil Selvan [12] who reported that the microstructure of Ti-6Al-4V resulted from laser alloying with BN pre-placed was identified by X-ray diffraction as TiN, TiB and Ti_3B_4.

The XRD patterns reveal that prominent peaks are present in the surface layer glazed at 388 J mm^{-2} arc energy density and weaker intensities are in the surface layers treated with 275 J mm^{-2} and 137 J mm^{-2}. As a result, the arc energy plays a significant role in the alloying process. Increasing the arc energy decreases the cooling rate and an adequate time will be available for alloying. So, It is reasonable to say that the lower of the alloying with decreasing of the arc energy density.

3.2 Microstructures

Fig. 2a shows the microstructure observed at different depth of the surface layer glazed at 137 J mm^{-2}. The microstructure shows the dendrites and needle phases. The population level

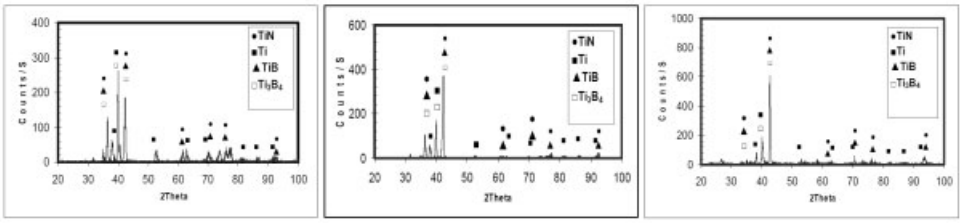


Figure 1: X-ray diffraction obtained for titanium surfaces alloyed with BN glazed at (a) $E = 137\,\mathrm{J\,mmm^{-2}}$, (b) $E = 275\,\mathrm{J\,mm^{-2}}$, (c) $E = 388\,\mathrm{J\,mm^{-2}}$

of dendrites and needle phases were found to be large by increasing the power density from 137 to $388\,\mathrm{J\,mm^{-2}}$ (Fig. 2). The dendrite and needle phases formed in the surface layers can be attributed to the hard nitrides and borides, respectively.

At The arc temperature, the surface layers containing BN melt, dissociate into B and N atoms and then is pushed to the melting pool by the pressure of argon gas. They make a reaction with molten titanium within the melting pool. Therefore, TiN, TiB and Ti_3B_4 nuclei are formed in the melting pool [12].

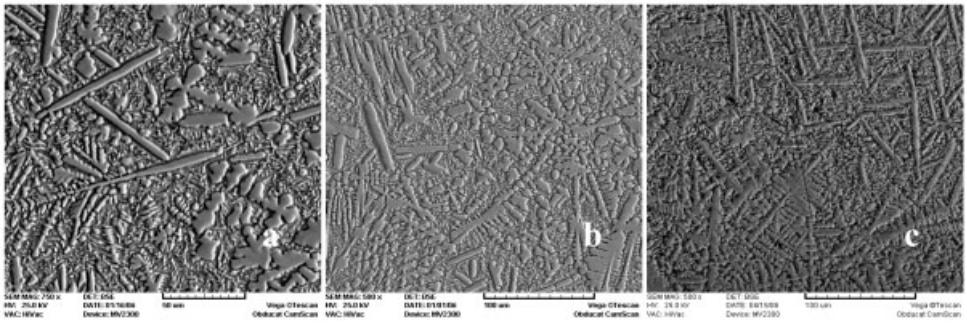


Figure 2: SEM images of surface composite layers glazed at (a) $E = 137\,\mathrm{J\,mm^{-2}}$, (b) $E = 275\,\mathrm{J\,mm^{-2}}$, (c) $E = 388\,\mathrm{J\,mm^{-2}}$, showing needle and dendritic phases within the martensitic structure

With regard to high cooling rate, the dendrite microstructure with a high level hardness can be related to titanium nitride [11]. The titanium borides, especially TiB, are reported [12] grown in a hexagonal pillar shape; so, the finely dispersed needlelike phase observed in the surface composite layers can be attributed to the formation of TiB.

On the other hand, the microstructures formed on the alloyed region were homogeneous. the random growth of dendrites and needle phases in the surface composite layers can be attributed to the stirring of the melt pool by convection and Marangoni forces. The concentration of gradient of diffused nitrogen and boron by this stirring action can result in homogeneous microstructure.

3.3 Hardness

Microhardness was measured from the surface down to substrate in the surface layers (Fig. 3). Maximum hardness of the layers glazed at 137, 275 and 388 J mm^{-2} are 680, 910 and 980 HV respectively; and they are four and five times higher than the hardness of pure titanium ($\sim$200 HV). As expected, the titanium boride and nitride increase the hardness. Thus it means that the hardness increases with increasing of volume fraction of these hard phases in the microstructures.

The hardness increase benefits from a combined action of (1) extreme hardness of TiN, TiB and Ti_3B_4 second phases formed, (2) probable effect of lattice deformation or coherent hardening in the surface composite layers, and (3) hardness of the dendritic base metal caused by high cooling rate.

The TiB needle precipitates may also act as a fiber reinforcing force. Therefore, the combination of high level hardness and fiber reinforcing force created in the alloyed zone might yield adequate ductility and fracture toughness [12].

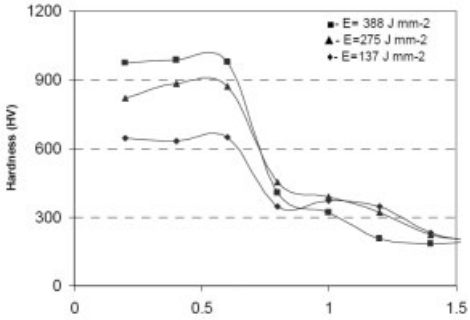


Figure 3: Hardness profiles for samples glazed at $E = 137, 275$ and $388\,\mathrm{J\,mm^{-2}}$

3.4 Wear Assessment

Fig. 4 shows the mass loss of the titanium sample and the alloyed samples. Specimens treated with BN pre-placed have the somewhat mass loss, compared to the unalloyed sample. It means that the coating improved the wear resistance of titanium by formation of the hard phases in the microstructure.

Archard [13] predicted that the wear resistance of a material is proportional to the hardness. Therefore, these results are consistent with the microhardness values, showing that the greater concentration of hard phases formed in the surface improve the surface wear properties of the titanium.

It is reported that titanium alloys have sever wear behavior over a wide range of sliding speed [7]. The results in this study also show that the untreated titanium surface suffers high wear. Severe wear of pure titanium is attributed to its weak hardness and also to its chemical activity. In addition, the transferred titanium associated with the adhesion became work-hardend after multiple contacts in the wear couple, which in turn resulted in severe abrasive wear damage on the Ti surface. This confirmed by the deep abrasive grooves.

Likewise, the sample glazed at 388 J mm^{-2} had a better wear resistance than the specimen processed at lower arc energy density (275 J mm^{-2}) which is attributed to the higher hardness of coating and to the excellent metallurgical bonding between the hard phases and Ti matrix. When the wear debris increased, they accumulated among the hard phases, which resulted in a faster wear rate through the formation of pits.

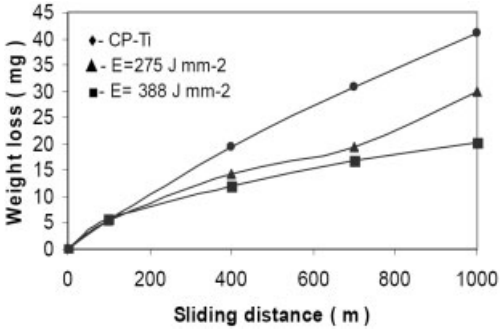


Figure 4: Weight loss of the CP-Ti alloy and alloyed samples processed at $E = 275$ and 388 J mm^{-2}

On the other hand, the wear behavior of the surface composite layers and unalloyed sample investigated with SEM are shown in Fig. 5. Extensive and deep plastic ploughing and cutting is seen on the worn surface of pure titanium, compared to the shallower grooves of the treated samples after 1000 m.

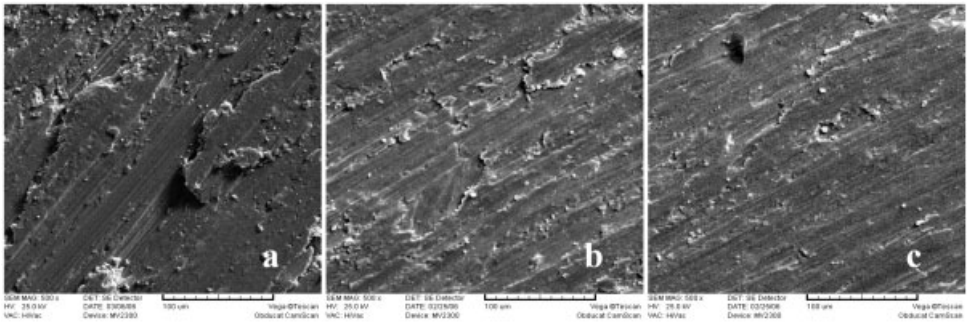


Figure 5: SEM images of worn surface of: (a) the untreated CP-Ti alloy, (b) the alloyed layer processed at 275 J mm^{-2}, (c) the alloyed layer processed at 388 J mm^{-2} after 1000 m sliding.

Fig. 5b and Fig 5c show a distinct change in surface wear mechanism. When the surface had been treated with BN, severe adhesive wear was absent, and smooth regions appear to have worn far less than other surface areas. The wear debris from the coated samples had fine particles, while for the untreated sample the particles were large (Fig. 5a).

4 Conclusion

The surface composites were fabricated by different arc energy densities, and their microstructures, hardness and wear resistance were investigated with following conclusion.

1. Microstructural studies and X-ray diffraction of surface composite layers have shown that the melt zones consisted of TiN dendrites, TiB and Ti_3B_4 structures. The X-ray diffraction patterns also disclosed that the hard phases increased within surface layers with increasing the arc energy density and decreasing the cooling rate.
2. A large amount of hard phases such as TiB and TiN improved the hardness of the surface composite layer up to five times greater than that of the substrate. In particular, the surface composite fabricated with the arc energy density of 388 J mm^{-2} had a highest volume fraction of hard phases homogeneously distributed in the martensitic matrix, and thus showed the best hardness.
3. The wear resistance property of the surface layers are about 1.5–2 times that of untreated titanium alloy.

5 References

[1] Metal Handbook,Non-Ferrous Alloys, 1988, ASM,Ohio,Vol2,9th ed,.pp. 588–591

[2] J. Polmear, 1987, Light Alloys and Metallurgy of Light Alloys, 1st ed, Edvard Arnolds, London, pp. 225–232

[3] Y.Massiani, A Medjahad, P. Crousier ,1992, Thin Solid Films, 217, 31-37

[4] S. Thongtem, P. Jentrakul and T. Thongtem, 2005, Material Pross., 212–218

[5] Metal Handbook, Non-Ferrous Alloys, 1988, ASM,Ohio,Vol18, 9th ed, pp.779–781

[6] Gokul Lakshmi , D. Arivuoli, 2006, Tribology International, 39, 548–55

[7] H. Ji, L. Xia, X.Ma, Y.Sun, 2000, Wear, l246, 40–45

[8] E. gyorgy, A. Perez del Pino, P. Serra, J.L. Morenza, 2003, Surface Coatings Tech., 73, 265–270

[9] S. Mridha, T.N baker, 1998, Material pross. 77, 115–121

[10] I. Garcia, J. De la Fuente, J.J. de Damborenea, 2002, Material Letters, 53, 44–51

[11] S. Mridha, 2005, Material pross. , 168, 471–477

[12] J. Senthil Selvan, K. Subramanian, A. K. Nath, H. Kumar, 1999, Material Science & Engineering A, A260, 178–187

[13] Hyman, M. E. McCullough, J. J. Valencia, C. G. Levi, R. Mehrabian, 1989, Metal Trans. A 20A, 1847–1859

[14] J. F. Archard, ibid. 24 (1953) 981.

Influence of Surface Condition on Wear and Demoulding Behaviour of Mould Inserts for Micro Powder Injection Moulding

J. Schneider[1], K.-H. Zum Gahr[1], A. Kienzler[2], V. Schulze[2]

[1] Institute of Materials Science and Engineering II, University of Karlsruhe (TH) andInstitute for Materials Research I, Forschungszentrum Karlsruhe

[2] Institute of Materials Science and Engineering I, University of Karlsruhe (TH)

1 Introduction

Success of micro technology, which is regarded as a key technology for the 21st century strongly depends on the utilization of a broad range of materials as well as the utilization of cost effective process technology [1]. Micro injection moulding is considered to be a promising technology for the large scale production of micro components and has already reached high precision standards for polymeric micro components [2, 3]. The processing of abrasive ceramic and metallic feedstocks requires mould inserts with increased wear resistance compared to those used in micro injection moulding of polymers [4]. Cemented carbides as well as established tool steels are promising materials for these challenging demands. Machining processes such as micro milling, electrical discharge machining (EDM) or laser ablation [5–8] are available to fabricate micro mould inserts from these materials.

The aim of this research work, which is carried out within the scope of the Deutsche Forschungsgemeinschaft (DFG) Collaborative Research Centre 499 [9], is to characterize the influence of surface condition and feedstock composition on wear and demoulding behaviour of mould inserts made from tool steels and ultra fine WC-Co cemented carbide in micro powder injection moulding (μPIM) with ceramic feedstock. Specimens machined by micro milling and EDM were investigated as well as specimens finished by abrasive micro peening [10] or ultrasonic wet peening [11] after machining. Experiments were carried out using a laboratory tribotester simulating powder injection moulding and a specially adapted static friction tester. Tribological testing was accompanied by analysis of the machined and worn surfaces using scanning electron microscopy.

2 Materials and Experimental Methods

2.1 Materials

Tests were carried out with specimens made from low-alloyed tool steel 30CrMo6 (Toolox 44, SSAB Oxelösund, Sweden; 0.3 % C, 1.35 % Cr), high-alloyed PM-steel X175VCrMo9-5 (CPM9V, Crucible, USA; 1.75 % C, 9 %V, 5 % Cr) and ultra fine cemented carbide WC-12Co (TSF44, Ceratizit, Austria, 12 wt% Co, d_{WC} = 0.2 – 0.5 μm). The microstructure of tool steel 30CrMo6, which was hardened and tempered at 590 °C by the manufacturer to a hardness of 454 HV30, was characterized by a matrix of tempered martensite with homogeneously distributed carbides (Fig. 1a). PM-steel X175VCrMo9-5 was austenitized in vacuum at 1120 °C for 60 min, oil quenched and tempered at 560 °C (2 × 60 min). This martensitic steel with about 20 vol%

fine, homogeneously distributed carbides had a hardness of 719 HV30 (Fig. 1b). The highest hardness of 1825 HV30 was measured for the ultra fine cemented carbide (Fig. 1c).

The machining and structuring of the specimens for the tribological tests was done at the Institute of Production Science, University of Karlsruhe (TH), by micro milling of the two steels and electro discharge machining (EDM) of the PM-steel and cemented carbide. A detailed description of the experimental technology is given in [6, 7].

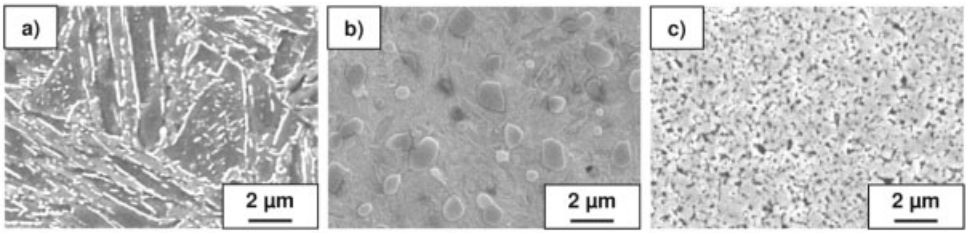


Figure 1: SEM micrographs of the microstructures of (a) steel 30CrMo6, (b) PM-steel X175VCrMo9-5 and (c) cemented carbide WC-12Co.

2.2 Surface Finishing and Surface Characterization

A blasting machine of the type IEPCO Peenmatic 770 equipped with an additional peening device Micropeen 200 was used for the surface finishing of the machined specimens [12]. A mixture of Al_2O_3, SiC and glass beads with a diameter between 10 and 20 µm is used as blasting agent. This peening process guarantees that burrs and sharp profile peaks at the surface can be removed. Further peening parameters were adopted: peening pressure 2 bar, nozzle diameter 1.2 mm, nozzle-workpiece distance 10 mm, nozzle-workpiece angle 90°, nozzle velocity 2 mm/s.

The topographical characterization of the machined micro moulds was carried out with a confocal white light microscope of the type "Nanofocus µSurf" and the hardness of the surfaces was measured using a depth sensing ultra micro hardness tester (Fischerscope H100).

The residual stress states in the samples were determined for the parallel and transverse directions with respect to the axes along which the mechanical surface treatments were performed. These two directions defined by the azimuthal angles $\varphi = 0°$ and 90° on the instrumental coordinate system, refer to the two principal in-plane residual stresses σ_{11} and σ_{22}. The $\sin^2\psi$ method [13] was used to evaluate the residual stresses from the measured X-ray diffraction strain data. More experimental details can be found in [14].

2.3 Tribological Testing

Wear tests were done using a laboratory tribometer simulating micro injection moulding [15]. A piston with two pairs of micro machined specimens was moved up and down with a velocity of 2 mm/s within a cylinder filled with 14 ± 1 cm^3 of feedstock (Fig. 2a). Thereby molten feedstock was pushed through a square slot (1.5×1.5 mm^2) at an average flow velocity of 245 mm/s. Depending on the binder system of the tested feedstock, the complete tribometer was heated up to 150 °C (polyolefine/wax, polyethylene/wax, polyethylene glycol/polymethyl methacrylate) or 170 °C (polyoxymethylene) before starting the tests. After the tests with 1400 or 2800 simulated

injections gravimetric wear was measured and volumetric wear was calculated from the mass loss W_m according to $W_V = W_m/\varrho$. A detailed description of the test procedure is given in [15]. One POM based feedstock with 58 vol% Al_2O_3 (d = 0.4 – 0.6 µm) was used for the tests as well as zirconia feedstocks based on the four different binder systems PO/wax, PE/wax, PEG/PMMA and POM. The volume of zirconia particles (d = 0.3 – 0.4 µm) within the feedstocks was varied between 47 and 53 vol%.

Laboratory demoulding tests were carried out with a specially adapted static friction tester (Fig. 2b). Green bodies made from the PO/wax feedstock with 50 vol% ZrO_2 were pressed against steel plates with a normal load of 50 N, heated up to 150 °C and held at this temperature for 5 min to simulate the filling of a mould cavity. After cooling down to a demoulding temperature of 60 °C the plate specimen was pulled in the tangential direction with the loading rate of 1.16 N/s. The normal load (F_N) and tangential force (F_T) were measured using a biaxial force sensor. After the transition from static to kinetic friction, relative sliding generally occurred with the velocity of 8.3 µm/s. Tribological testing was accompanied by analysis of the worn surfaces using scanning electron microscopy.

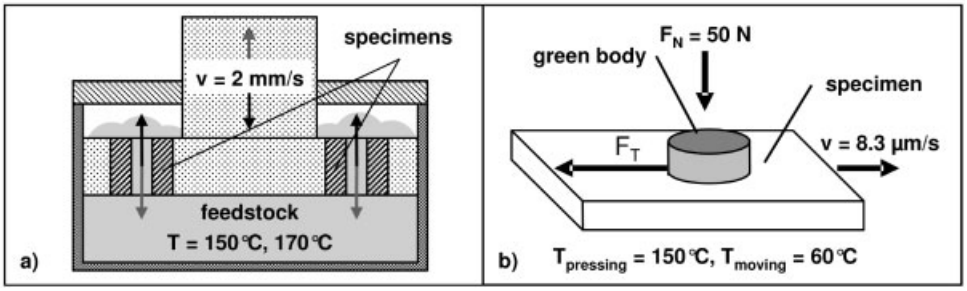


Figure 2: Schematic description of the tribosystems simulating (a) powder injection moulding and (b) demoulding.

3 Results

3.1 Surface Condition

Fig. 3 shows machined surfaces of steel 30CrMo6 after different manufacturing processes. Feed marks caused by the tool movement could be observed on the micro milled surface (Fig. 3a). Due to the abrasive micro peening process feed marks resulting from the previous micro milling were abolished and a homogeneous surface topography was created (Fig. 3c). The disadvantage of the abrasive micro peening process was the increase of roughness from R_z = 1.15 µm after micro milling to R_z = 1.59 µm after abrasive micro peening. The surface resulting from EDM was characterized by a molten and resolidified layer ("recast layer") with typical discharge craters (Fig. 3b). Microcracks were present within this layer due to the rapid solidification and shrinkage of the molten material. These conditions decrease the quality of the micro mould and may induce defects in the demoulded micro parts. For cemented carbide WC-12Co the thermally damaged recast layer generated by EDM showed a reduced surface hardness of 1400 ± 208 HV_{100} compared to the bulk material. Abrasive micro peening was able to remove this surface layer and

resulted in a surface hardness of 1800 ± 210 HV_{100} similar to the initial value. Another benefit of the finishing process for WC-12Co was the reduction of the surface roughness from about R_z = 0.9 µm to R_z = 0.62 µm.

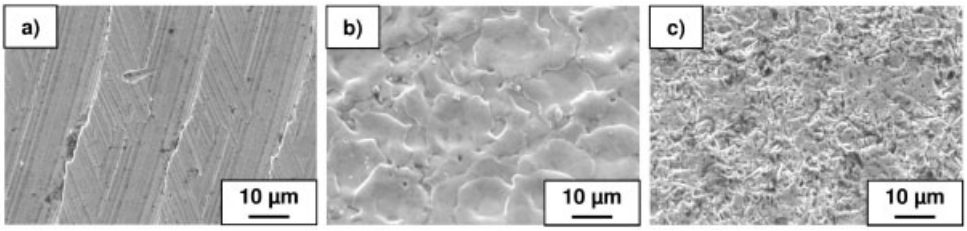


Figure 3: SEM images of steel 30CrMo6 machined by (a) micro milling, (b) EDM and (c) micro milling with subsequent abrasive micro peening.

3.2 Residual Stresses

The residual stress depth profiles for the steel 30CrMo6 measured after the machining by micro milling and EDM using synchrotron X-rays are shown in Fig. 4a. The residual stress profiles for the micro milling process indicate compressive stresses in the whole depth range covered by the measurements. The values of σ_{11} and σ_{22} at the surface, about -300 MPa and -600 MPa, respectively, are quite different whereas at a depth of z ˜ 4.5 µm almost equal values in the range of about -700 MPa are observed. Similar to micro milling, a non-equiaxed biaxial stress state up to a depth of z ˜ 4 µm can be seen after EDM. While the value of σ_{11} is constant at about 300 MPa, σ_{22} changes from compressive stresses to tensile stresses at z ˜ 2.5 µm and then attains a value of about 300 MPa, creating an equi-biaxial stress state in the sample at z ˜ 4.5 µm. The reason for the absence of rotational symmetry at the surfaces is the movement of the tool over the workpiece area. Fig. 4b shows that after abrasive micro peening high compressive residual stresses in the range of -800 to -1000 MPa are induced in the samples. The residual stress states after abrasive micro peening are equi-biaxial in nature as is evidenced by the similar courses for φ = 0° and 90°. Similar profiles of the residual stress states after abrasive micro peening indicate that they are not influenced by the previous machining processes.

3.3 Tribological Properties

Volumetric wear of differently machined specimens after 1400 simulated injections with alumina feedstock (POM binder) is shown in Fig. 5a. The highest wear of about 0.29 mm^3 was measured for low alloyed steel 30CrMo6 in the micro milled condition. Further tests with other surface conditions revealed that there was no significant influence of the machinig process on the wear resistance of 30CrMo6. In contrast to this the machining clearly influenced the wear resistance of PM-steel X15VCrMo9-5 and cemented carbide WC-12Co. For these two materials wear resistance was lowest when tested with the EDM surface condition. With abrasive micro peening the wear resistance increased by a factor of about 3. The abrasive micro peened cemented carbide showed a wear of 0.01 mm^3 which was the lowest value of all tested specimens. After 1400 simulated injections with alumina feedstock the recast layer on the surface of the electro discharge

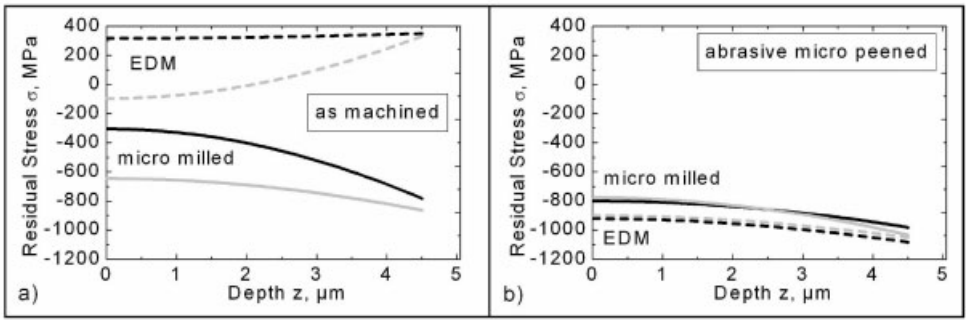


Figure 4: Residual stress depth profiles (a) after micro milling and EDM, (b) after micro milling and EDM with subsequent abrasive micro peening (each at two rotational angles $\varphi = 0°$, black and $\varphi = 90°$, grey).

machined PM-steel X175VCrMo9-5 was worn off in large parts (Fig. 5b) and the surface was characterized by the selective washout of the soft steel matrix around the hard carbide particles similar to that of the micro milled specimen (Fig. 5c).

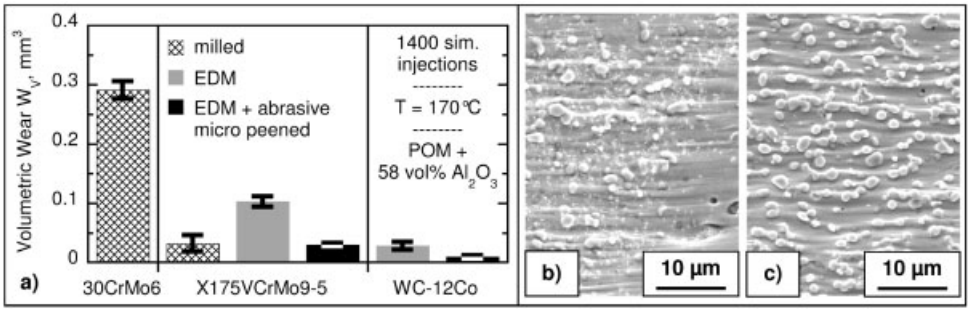


Figure 5: (a) Influence of surface condition on volumetric wear of steel 30CrMo6, X175VCrMo9-5 and cemented carbide WC-12Co (Al_2O_3-POM feedstock, T = 170°C) and (b, c) scanning electron micrographs of originally (b) electro discharge machined and (c) micro milled surfaces of X175VCrMo9-5 worn by Al_2O_3-POM feedstock (1400 simulated injections, T = 170°C).

Fig. 6 illustrates the influence of the amount of zirconia hard particles and the binder system on wear of 30CrMo6 steel. In tests with a zirconia content of 50 vol% the highest wear was measured for the POM based feedstock with about 0.175 mm^3 after 2800 simulated injections. Wear was about a factor of 3 higher compared to tests with feedstocks based on PEG/PMMA and PO/wax binders. The lowest wear of about 0.016 mm^3 was detected after the tests with the PE/wax based feedstock. An increase in the amount of zirconia particles from 47 to 53 vol% the volumetric wear after 2800 simulated injections in tests with PO/wax based feedstock doubled from 0.36 mm^3 to more than 0.72 mm^3.

The experimental results point out that materials of both a high microstructural homogeneity and a sufficient hardness, e.g. due to a high amount of reinforcing hard particles, are needed for the utilization of wear resistant µPIM mould inserts. This is in particular required due to the erosive action of the fine ceramic particles within the feedstocks during micro injection moulding.

In the same way one has to keep in mind a proper machining or finishing of the tribologically loaded surfaces. Electro discharge machined surfaces led to a reduced wear resistance compared to micro milled or abrasive micro peened surfaces, which was attributed to the process-related recast layer. A negative influence of such recast layers with reduced hardness and tensile residual stresses, was also observed in fatigue tests and tribological sliding tests with cemented carbide [16, 17]. Another possibility for wear reduction arises from the feedstock development. Feedstocks based on polymer/wax combinations lead to dramatically reduced wear of steel 30CrMo6 and moreover allowed to reduce injection temperature by 20 °C compared to an established commercially available POM based feedstock. However green bodies made from these low viscosity feedstocks often show a relatively low mechanical strength and therefore can result in problems during demoulding or handling of the moulded micro parts.

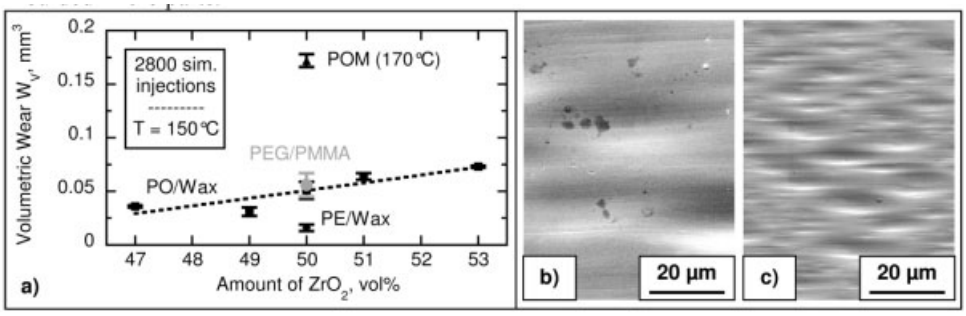


Figure 6: (a) Influence of binder and amount of zirconia particles on volumetric wear of steel 30CrMo6 after 2800 simulated injections and (b, c) scanning electron micrographs of worn surfaces after 2800 simulated injections with feedstocks based on (b) PE/wax binder and (c) PEG/PMMA binder (both with 50 vol% ZrO_2).

Fig. 7a summarizes results of laboratory demoulding tests with the low alloyed tool steel 30CrMo6 and green bodies from the PO/wax feedstock with 50 vol% zirconia. The tangential force necessary to overcome the stiction during the experiments increased with increasing surface roughness from about 30 N for the specimens with micro milled surface to values of about 45 N for the surfaces, which were electro discharge machined or finished by abrasive micro peening. Worn surfaces of the specimens were characterized by a transfer of feedstock after the demoulding tests, which was more pronounced for the rougher electro discharge machined surface than for the micro milled surface (Fig. 7b, c).

4 Conclusion

The influence of the surface condition and feedstock composition on wear and demoulding behaviour was analyzed using specimens made from tool steels 30CrMo6 and X175VCrMo9-5 as well as from ultra fine cemented carbide WC-12Co. Results showed that a high wear resistance in micro powder injection moulding of highly abrasive ceramic feedstocks could only be achieved with mould insert materials of high homogeneity and hardness combined with a suitable machining and finishing process. Recast layers due to EDM, which dramatically reduced wear resistance, were successfully removed by a newly developed abrasive micro peening process. The

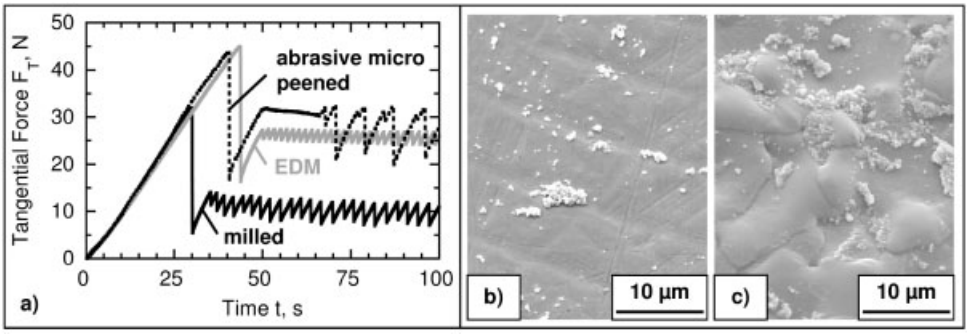


Figure 7: (a) Effect of surface condition of steel 30CrMo6 on the transition from static to kinetic friction in demoulding tests mated with green bodies from ZrO_2-PO/wax feedstock and scanning electron micrographs of (b) micro milled and (c) electro discharge machined steel surface after the demoulding tests.

remarkable potential of wear reduction due to the development of low viscosity feedstocks was pointed out by laboratory tests with low alloyed steel 30CrMo6 and various zirconia feedstocks.

5 Acknowledgements

The authors would like to thank the German Research Foundation (DFG) for financial support within the frame of the Collaborative Research Centre 499 (SFB 499).

6 References

[1] J. Hesselbach, A. Raatz, J. Wrege, H. Herrmann, H. Weule, C. Buchholz, H. Tritschler, M. Knoll, J. Elsner, F. Klocke, M. Weck, J. von Bodenhausen, A. von Klitzing, wt werkstattstechnik online 2003, 93, 119–128.

[2] R. Heldele, M. Schulz, D. Kauzlaric, J. Korvink, J. Hausselt, Microsys. Techn. 2006, 12, 941–946.

[3] J. Giboz, T. Copponnex, P. Mele, J. of Micromechanics and Microengineering 2007, 17, R96-R109.

[4] A. Bonsen, R. Beenders, Kunststoffe 2003, 93, 48–53.

[5] B. Denkena, et al., Microsys. Techn. 2006, 12, 659–664.

[6] J. Fleischer, D. Löhe, J. Kotschenreuther, V. Schulze, M. Deuchert, G. Halvadjiysky, S. Haupt, A. Kienzler, wt werkstattstechnik online 2007, 97, 847–851.

[7] J. Fleischer, J. Kotschenreuther, Intern. J. of Advanced Manufacturing Techn. 2007, 33, 75–85.

[8] W. Pfleging, W. Bernauer, T. Hanemann, M. Torge, Microsys. Techn. 2002, 8, 67–74.

[9] O. Kraft, J. Haußelt, R. Ruprecht, B. Emmerich in Kolloquium Mikroproduktion (Eds.: O. Kraft, B. Emmerich), 2007, 7–11.

[10] A. Kienzler, C. Horsch, V. Schulze, D. Löhe, in Proc. 7th Euspen International Conference, Bremen, Germany, 2007, Vol. II, 372–375.

[11] C. Horsch, V. Schulze, D. Löhe, Microsystems Techn. 2006, 12, 691–696

[12] C. Horsch, V. Schulze, D. Löhe in Advanced micro and nanosystems (Eds.: D. Löhe, J. Haußelt), Vol. III: Micro-engineering in metals and ceramics, Wiley-VCH, Weinheim, 2005, 221–249.

[13] E. Macherauch, P. Müller, Z. f. Angew. Phys. 1961, 13, 305–312.

[14] A. Kienzler, B. Okolo, V. Schulze, A. Wanner, D. Löhe, Advanced Engineering Materials 2008, accepted.

[15] J. Schneider, H. Iwanek, K.-H. Zum Gahr, Mat. Sci. and Eng. Techn. 2004, 35, 729–735

[16] L. Llanes, E. Idanez, E. Martinez, B. Casas, J. Esteve, Intern. J. Refractory Metals & Hard Materials 2001, 19, 35–40.

[17] B. Casas, Y. Torres, L. Llanes, J. Refractory Metals & Hard Materials 2006, 24, 162–167.

Study of Pulsed Bipolar Nanocrystalline Plasma Electrolytic Carburizing on Nanostructure and Friction Coefficient of Compound Layer

M. Aliofkhazraei[1,*], A. Sabour Rouhaghdam[1], H. Alimadadi[2]

[1]Faculty of Engineering, Materials Engineering Department, Tarbiat Modares University, P.O.Box:14115-143, Tehran, Iran

[2]Department of Materials and Manufacturing Technology, Chalmers University of Technology, SE-412 96, Göteborg, Sweden

*Corresponding author, e-mail: maliofkh@gmail.com

1 Introduction

Carburizing is a thermochemical process that diffuses carbon into the surface of ferrous materials at certain elevated temperatures. The diffusion region brings about an improvement of fatigue strength when compared to an untreated material. In this region, carbon atoms are dissolved interstitially in the ferritic lattice, and form the carbide precipitates [1–4]. Carburizing can be applied in solid, liquid and plasma atmospheres. The plasma carburizing is more economical, friend with environment and produces faster carbon diffusion, lower gas consumption compared to other carburizing techniques. It is applied widely with various materials such as carbon steels, alloy steels, tool steels, stainless steels, cast irons and sintered materials [1, 5–7]. The treatment media may determine the composition and thickness of a compound layer, as well as the depth of the diffusion zone due to the difference in the diffusion rates of carbon atoms. Liquid state techniques use a salt bath (e.g. NaCN) and generate good quality compound layers but they are often toxic. The plasma process offers excellent control of the gas mixture and processing conditions. Along with reduced processing times, energy consumption and treatment gas consumption, there is also the advantage of no toxic waste or fumes, and no risk of explosion.

Plasma electrolytic saturation (PES) techniques [8, 9], such as plasma electrolytic carburizing (PEC), are a relative new group of atmospheric plasma techniques which have been used to successfully diffusion-treat low-alloy ferrous materials, such as mild steel. Because of the similar equipment configuration to classical bath electroplating, and the rapidity of treatment, these processes are potentially very suitable for mass production of complex-shaped components, due to the uniform plasma envelope created around the workpiece. In this study, this method was used for applying penetrative coatings on a AISI 4140 steel substrates. Pulsed current was used in order to achieve nanocrystalline compound layer with better properties [10]. Nanostructure of carbide nanocrystallites and their friction coefficient were studied. Then statistical method of "Taguchi" has been effectively applied to optimize these properties of coatings [11, 12]. The Taguchi method uses a special design of orthogonal arrays to study all the designed factors with a minimum of experiments at a relatively low cost. Orthogonality means that factors can be evaluated independently of one another; the effect of one factor does not interfere with the estimation of the influence of another factor [12]. The design of experiments took into account the influencing extent of individual process parameters. This consideration led to the selection of four

influential factors, i.e. frequency, duty cycles for positive and negative directions and treatment time with three different levels (1–3). Pin-on-disc wear tests were conducted to determine the friction coefficient of coated and uncoated samples. The results of the factor response analysis were used to derive the optimal levels combinations. Confirmation experiments were conducted to verify the obtained results. The percentage contribution of each factor was determined by an analysis of variance.

2 Experimental

Cylinder shape samples (20mm (dia) × 5mm) of AISI 4140 steel (C 0.41 wt.%, Cr 1.01 wt.%, Mn 0.85 wt.%, Mo 0.24 wt.%, Ni 0.12 wt.%, Si 0.2 wt.%, P 0.024 wt.%, S 0.031 wt.%) were used as substrates in this study. All samples were prepared from a bar by usual machining. After polishing to about *R*a 2 μm using Al_2O_3 slurry, the samples were first cleaned with acetone and then ultrasonically cleaned in ethanol. Electrolytes were prepared from solutions of Gelycerol in distilled water with an addition of Sodium carbonate (Na_2CO_3) for changing electrical conductivity of electrolyte. During carburizing, the samples to be coated as cathode of the system and a stainless steel bath used as an anode were connected to a 20 KW (3 phase) variable power source (590Volts, 34 Ampers(Max) after DC conversion). The details of the pulser rig setup used in this study can be found in Ref [13]. Bipolar current was used to achieve better properties of compound layer with higher peak voltages in cathodic direction than anodic direction. The "quality characteristics" of concern are the average friction coefficient (μ) and average sizes of nanocrystalline carbides (ASN). The wear experiments were performed using a pin-on-disc machine measuring the friction of a loaded test specimen sliding against a hard ball (2.5 N normal load and 250 m sliding distance with a 10-mm diameter WC-Co ball counter face). The nanostructure morphology and hardness profile of PBNPEC films were examined by XL-30 (PHILIPS) scanning electron microscope (SEM) and Buhler Micromet1 micro hardness tester. To measure ASN, 5 SEM nanostructures with same magnification were analyzed trough commercial software for figure analysis called a4iDocu for each treated sample. Different measurements were interpolated to obtain average results. At least 40 measurements were done in each nanostructure for minimizing systematical errors.

3 Results and Discussion

Figure 1 shows the relation among μ of different coated samples with their ASN. As it can be seen, for all treated and examined samples, μ will decrease with decreasing ASN. Also it was observed that samples with lower ASN have nanocrystallites with the shapes near to spheres.

Four factors (frequency, duty cycle of cathodic direction, duty cycle of anodic direction and duration of process) with three levels were selected shown in Table 1. The factors and levels were used to design an orthogonal array L_9 (3^4) for experimentation. The nine Taguchi experiments were conducted twice to ensure the reliability of experimental data for a signal-to-noise analysis. Equations related to Taguchi method were described elsewhere [14] and will not repeat here again. To minimize the influence of ASN variation on the analysis of experimental data, the signal-to-noise (S/N) ratio was employed, which converts the trial result data into a value for the response to evaluate coating quality in the optimum setting analysis.

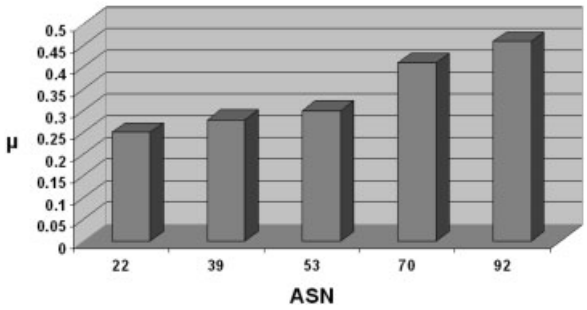


Figure 1: Average friction coefficient versus average size of carbide nanocrystallites.

Table 1: Design factors and levels

Level	Factor			
	Frequency (kHz) (A)	Duty cycle of cathodic direction (%) (B)	Duty cycle of anodic direction (%) (C)	Time (min) (D)
1	5	20	60	10
2	10	30	70	20
3	15	40	80	30

The results of the ASN tests for the different coatings on 4140 steel are given in Table 2. High frequency, low cathodic duty cycle, high anodic duty cycle and extended treatment as demonstrated in Experiment 7 produces a high quality coating, which significantly decreases the ASN as well as average friction coefficient of treated sample.

Table 2: The S/N ratios

Experiment	Frequency (kHz) (A)	Duty cycle of cathodic direction (%) (B)	Duty cycle of anodic direction (%) (C)	Time (min) (D)	ASN (nm) (A_i)		S/N ratio
					Test1	Test2	
1	5	20	60	10	55.0	56.1	34.894
2	5	30	70	20	72.5	75.5	37.386
3	5	40	80	30	91.7	96.7	39.484
4	10	20	70	30	47.5	51.0	33.854
5	10	30	80	10	51.7	54.2	34.48
6	10	40	60	20	75.0	79.5	37.762
7	15	20	80	20	36.7	39.3	31.601
8	15	30	60	30	60.0	64.7	35.903
9	15	40	70	10	62.5	66.2	36.175

Based on specific equation [14], two sample's ASN measurements for each experiment were converted into one S/N ratio. The response of each factor to its individual level was calculated by averaging the S/N ratios of all experiments at each level for each factor. The determined factor responses are summarized in Table 3. Figs. 2-5 show the effect of the four selected factors on the mean S/N ratios, respectively.

Table 3: The factor response

Level	Factor			
	Frequency (kHz) (A)	Duty cycle of cathodic direction (%) (B)	Duty cycle of anodic direction (%) (C)	Time (min) (D)
1	37.255	33.450	36.186	35.183
2	35.365	35.923	35.805	35.583
3	34.560	37.807	35.188	36.414

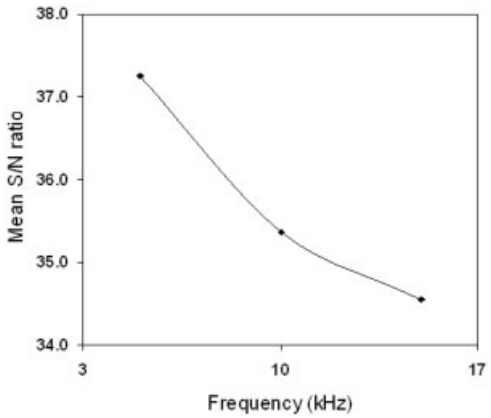


Figure 2: Effect of frequency on mean S/N ratio.

The response of the S/N ratio to the selected factors needs to be further investigated. By selecting the lowest value of mean S/N ratio for each factor, the optimal level can be determined. On this basis, the optimum combination of levels in terms of minimizing the ASN of the treated 4140 steel is A3B1C3D2; i.e. 15 kHz for frequency, 20 % for duty cycle of cathodic direction, 80 % for duty cycle of anodic direction and 20 minutes for treatment time.

The contribution of each factor to the ASN of coatings can be determined by performing analysis of variance. The results of analysis of variance (ANOVA) are summarized in Table 4. The data given in Table 4 shows that the contribution of the four factors, i.e. frequency, duty cycle of cathodic direction, duty cycle of anodic direction and treatment time is 26.08 %, 65.09 %, 3.46 % and 5.37 %, respectively. The contribution of duty cycle of cathodic direction (65.09 %) is more than the sum (34.91 %) of the contributions of all the other three factors. It is evident that, among the selected factors, duty cycle of cathodic direction has the major influence on the formation of carbide nanocrystallites on coatings. It can be seen that the frequency is second important factor that affects on ASN of the coatings. Furthermore, it can be assumed that duty cycle of anodic

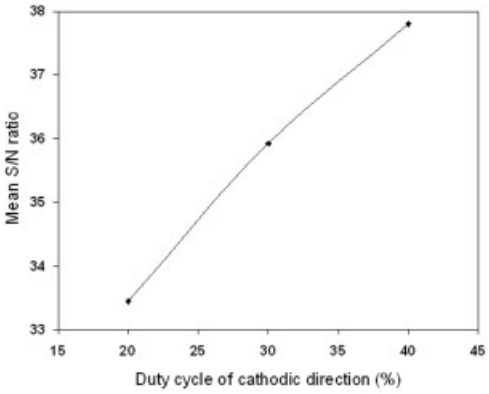


Figure 3: Effect of duty cycle of cathodic direction on mean S/N ratio.

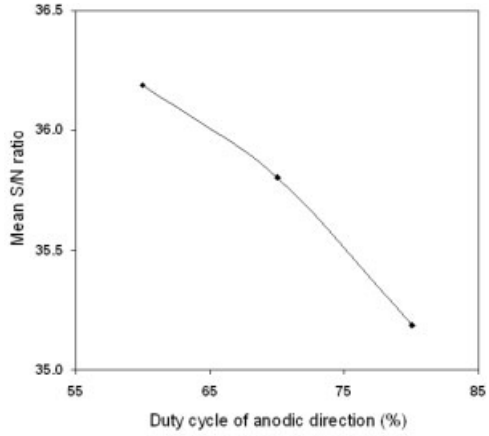


Figure 4: Effect of duty cycle of anodic direction on mean S/N ratio.

direction and treatment time have almost the same effect on ASN and thus average friction coefficient of coatings because of the minor difference in the contribution percentages among these two factors. It is evident from Table 4 that ANOVA analysis not only specifies how important a factor is to the ASN of coatings by numbers but also shows their relative effect. By ranking their relative contributions, the sequence of the four factors affecting the ASN and thus average friction coefficient is duty cycle of cathodic direction, frequency, duty cycle of anodic direction and treatment time. It is also worth mentioning that, in the ANOVA analysis, if the percentage error (*P*e) contribution to the total variance is lower than 15 %, no important factor is missing in the experimental design. In contrast, if the percent contribution of the error exceeds 50 %, certain significant factors have been overlooked and the experiments must be re-designed [12]. As shown in Table 5, the percentage error (*P*e) is 0 %. This indicates that no significant factors are missing in the experimental design.

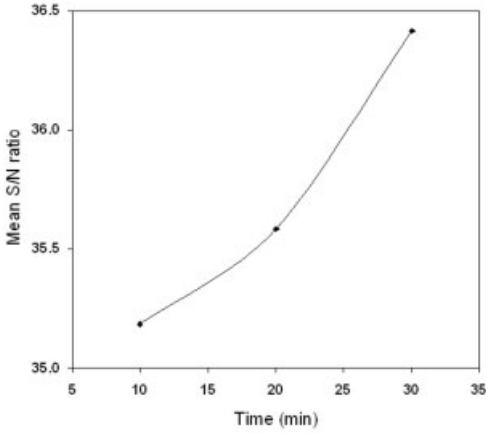


Figure 5: Effect of treatment time on mean S/N ratio.

Table 4: Results of the ANOVA for ASN

Symbol	Factors	Degree of freedom (D)	Sum of squares (SS)	Variance (V)	Corrected sum of squares (SS´)	Contribution (P, %)	Rank
A	frequency	2	11.4817	5.74085	11.4817	26.08	2
B	duty cycle of cathodic direction	2	28.6532	14.326	28.6532	65.09	1
C	duty cycle of anodic direction	2	1.5217	0.76085	1.5217	3.46	4
D	Treatment time	2	2.3645	1.182275	2.3645	5.37	3
Error		9	0	0		0	
Total		17	44.0211			100	

The confirmation experiment is the final step in verifying the conclusions from the previous round of experimentation. If the results of the confirmation runs are not consistent with the expected conclusions, a new Taguchi method design is required. The confirmation experiment was performed by setting the experimental condition of the four factors as: 15 kHz for frequency, 20 % for duty cycle of cathodic direction, 80 % for duty cycle of anodic direction and 20 minutes for treatment time. Table 5 shows the results of the coated sample from the confirmation run. The ASN of the optimized coating is the lowest value among other coatings obtained in the present study. Thus the average friction coefficient of the optimized coating is lower than other coatings. The nanograph and hardness profile of the optimal coated sample can be seen in Fig. 6 and Fig. 7.

Table 5: Results of ASN for confirmation run

Samples	A_i (nm)
Optimized coating	35.2

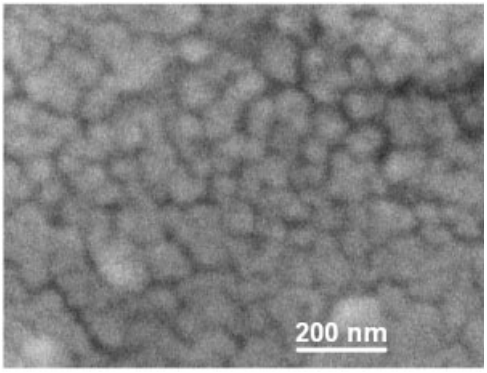


Figure 6: Nanostructure of optimized coating.

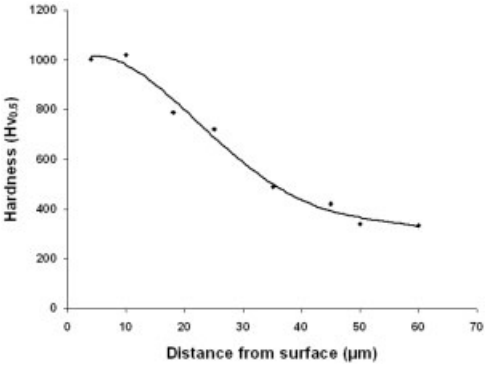


Figure 7: Nanostructure of optimized coating.

4 Conclusions

It has been revealed that average friction coefficient of treated samples has a direct relation with average size of nanocrystalline carbides. Statistical method for the design of experiment has been used for optimizing coating process parameters for the production of compound coating with lower average size of nanocrystalline carbides and thus lower average friction coefficient for AISI 4140 steel. The frequency during coating process is found to be the major factor affecting the ASN of the coating. Also the duty cycle of cathodic direction is found to be the second important factor affecting the ASN of the coating while duty cycle of anodic direction and treatment time have a similar and smaller effect on the ASN of the coatings. The percentage contributions of

the frequency, duty cycle of cathodic direction, duty cycle of anodic direction and treatment time is 26.08 %, 65.09 %, 3.46 % and 5.37 %, respectively. The optimized processing parameters are 15 kHz for frequency, 20 % for duty cycle of cathodic direction, 80 % for duty cycle of anodic direction and 20 minutes for treatment time. The ASN of the optimized coating is 35.2 nm.

5 Acknowledgement

The authors would like to express their thanks to Arvandan Oil & Gas Production Company (TMU 85-09-66) for financially support this project. This research was also financially supported by the Iranian nano science and technology research organization.

6 References

[1] T. Bell, ASM handbook, vol. 4, Heat treating **1997**, 425–436.

[2] Malinova T., Malinov S., Pantev N., Surface and Coatings Technology **2001**, 135, 258–267.

[3] Qiang Y.H., Ge S.R., Xue Q.J., Journal of Materials Processing Technology **2000**, 101, 180–185.

[4] Al-Rubaie K.S., Steinmeier F., Pohl M., Wear **2000**, 243, 112–121.

[5] Rembges W., Oppel W., Surface and Coatings Technology, **1993**, 59, 129–134.

[6] Krishnaraj N., Iyer K.J.L., Sundaresan S., Srinivasan P.B., Wear **1998**, 215, 123–130.

[7] Bell T., Sun Y., Suhadi A., Vacuum **2000**, 59, 14–23.

[8] Gupta P., Tenhundfeld G., Daigle E.O., Ryabkov D., Surface and Coatings Technology **2007**, 201, 21, 8746–8760.

[9] Aliofkhazraei M., Sabour Rouhaghdam A., Electrochemistry Communications **2007**, 9, 11 2686–2691.

[10] Aliofkhazraee M., Sabour Rouhaghdam A., Shahrabi T., **2007**, Part 1, Journal of Alloys and Compounds, in press

[11] Ross P.J., McGraw-Hill Int. Editions, **1988** USA.

[12] Phadke M.S., AT&T Bell Laboratory, **1989** NJ, USA.

[13] Aliofkhazraei M., Mofidi S.H.H., Sabour Rouhaghdam A., Mohsenian E., Journal of Thermal Spray Technology, ASM International **2008**, in press

[14] Aliofkhazraee M., Sabour Rouhaghdam A., **2007**, Part 2, Journal of Alloys and Compounds, in press

Abrasive Wear Resistance of AISI 420 Stainless Steel After Laser Surface Treatment

M. A. Larosa[1], M. A. Pinto[2], M. C. F. Ierardi[3]
[1,3] State University of Campinas, Campinas, [2] Federal University of Ouro Preto, Ouro Preto

Abstract

The present work is concerned with the laser surface melting of AISI 420 stainless steel samples in order to evaluate the effects of the treatment on the resulting microstructure. The structural characterization of the treated surface was performed by scanning electron microscopy, X-rays diffraction and Vickers microhardness test. The abrasive wear resistance was analyzed using micro-scale abrasive wear tests.

1 Introduction

In the last few decades, metals and alloys laser treatments became a new technique for surface modification, making possible to harden the surface of these materials with or without melting. The processing parameters affect the microstructure and, consequently, the properties of treated material, mainly in the case of stainless steel [1, 2]. In processes of rapid solidification of ferrous alloys, the primary solidification phase can be austenite or ferrite-δ. In laser surface treatments, the growth of austenite is kinetically favored by laser beam scanning speed and because of the thermal gradient in the melted pool is positive [3, 4]. These treatments can be a good alternative for improvement in mechanical and metallurgical properties and wear or corrosion resistance [5–8].

The tribological characterization of materials by traditional techniques such as pin-on-disc or reciprocating sliding wear tests or the dry sand rubber wheel test have been used successfully [9, 10], but, particularly for thin hard surface, there can be considerable difficulties in performing tests [11] due to the very small mass changes associated with removal of thin surface layer [12]. Thus for successful measurements of the surface wear, only small amounts of wear can be tolerated. Traditional measurement methods such as mass loss become ineffective and even profilometry techniques often cannot be used for components with normal engineering finishes as the depth of the wear damage is within the uncertainty of measurement caused by the original roughness of the surface [11].

Because of these situations, a considerable incentive for develop new methods for abrasion and erosion tests and much progress have been made in this area over the past two decades [12]. A relatively recent evaluation technique for coatings and surface engineered materials wear resistance is the micro-scale abrasive wear test. This technique allows testing very small samples, its applicable to plane or cylindrical specimens and can determine the treated surface layers properties, independently of their thickness and adhesive strength [13, 14].

In the micro-scale abrasion test, a steel sphere is rotated against a sample in the presence of slurry of fine abrasive particles, which produces wear scar. The geometry of the wear scar

is assumed to reproduce the spherical geometry of the ball, and the wear volume may then be calculated by crater diameter. The wear volume may be deduced as a relative sliding distance function and the wear coefficient K calculated from the Equation 1, where b is the diameter of the wear crater, R is the radius of the sphere, S is the total distance slid by the sphere relative to the specimen surface and N is the normal force between sphere and sample [15–19].

$$K = \frac{\pi b^4}{64R} \cdot \frac{1}{SN} \,[\mathrm{m}^3/\mathrm{Nm}] \tag{1}$$

In this test, which employs free abrasive particles, two distinct wear modes have been identified. The dominant process is controlled by the nature of the abrasive particle motion in the contact region between the ball and the specimen. If the particles do not move in relation to the ball surface, but act as fixed indenters moving across the specimen, a series of fine parallel grooves is produced on the specimen surface. This leads to so-called grooving wear or two-body abrasion. If on the other hand, the abrasive particles roll between the two surfaces, multiple indentations with no evident directionality are produced in a process known as rolling abrasion or three-body abrasion [14]. The dominant wear modes in the micro-scale abrasion test have been reported to be influenced by applied load, volume fraction of abrasive in the slurry, abrasive material, materials of both ball and specimen, and the surface condition of the ball [17–22]. According Zum Gahr [23], a more general model was developed which describes abrasive wear by distinguishing four types of interactions between abrasive particles and a wearing material namely microploughing, microcutting, microfatigue and microcracking.

Since wear is a system response and is not a material property, the wear resistance of a material can vary over a wide range if different wear mechanisms are induced by different test conditions [24]. For repeatable and reproducible wear resistance measurements in a standard wear test, the test conditions must be carefully controlled so that the wear mechanism is predictable and reproducible [14].

The present work concerned with the laser surface melting of AISI 420 stainless steel samples in order to evaluate the effects of the treatment on the resulting microstructure and the wear resistance. The abrasive wear rate was evaluated using micro-scale abrasive wear tests and the results were compared with those of AISI 420 stainless steel quenched and tempered by traditional heat treatment.

Among the main AISI 420 applications are surgical instruments, high-speed components for use in marine environments, cutlery, pumps, steam turbine parts and the specific interest in this work are surgical instruments such as nippers and scissors

2 Experimental Procedure

The steel used in the present study was AISI 420 martensitic stainless steel, whose chemical composition is shown in Table 1. Surface melting treatment was carried out with a 1 kW CW CO_2 laser using power densitiy of 318 W/mm^2 and scan rate of 700 mm/min. Samples were subjected to multiple scan passes laser, with the tracks overlapped 50 %, in order to produce a modified surface layer. Surface oxidation was prevented using argon gas.

The microstructure of the material was analysed by scanning electron microscopy (SEM), Vickers microhardness (80gf) and X-ray diffraction. The proportion of retained austenite was

Table 1: Chemical composition of the stainless steel used.

Element	Weight (%)
C	0,30
Cr	12,34
Ni	0,28
P	0,035
Mn	0,40
S	0,011
Si	0,20
Fe	balance

estimated by the relative intensity of the peaks in the X-ray diffractograms, using the method proposed by Jatczak et al. [25].

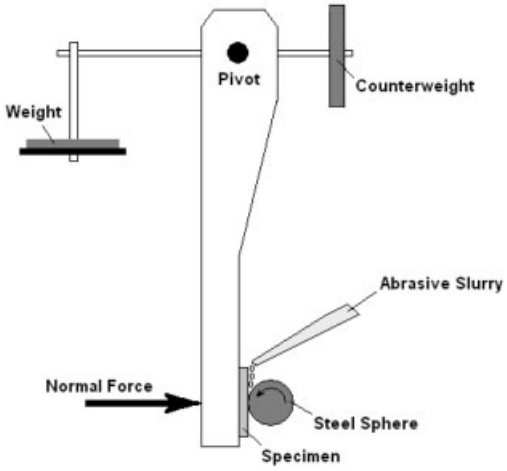


Figure 1: Schematic diagram of the micro-scale abrasive ball-cratering wear test machine.

Figure 1 shows a schematic diagram of the micro-scale abrasive ball-cratering wear test machine used in this work. The ball is driven positively by a shaft. The polished surface of the sample is mounted vertically on the pivoted L-shaped arm and is loaded against the ball by a weight hanging from the horizontal lever. The slurry of 6μm silica particles in distilled water was fed drop by drop into the contact area. The specification of the apparatus and experimental details are shown in Table 2. Five tests were performed on each sample. Steel sphere was treated before use to produce fine surface pitting. This modification is necessary because the pits aid in the entrainment of the abrasive into the contact area [17,18].

The worn surfaces of the laser melted and quenched and tempered samples were observed by scanning electron microscopy to identify the dominant wear mechanism and the wear coefficient was calculated using Equation (1).

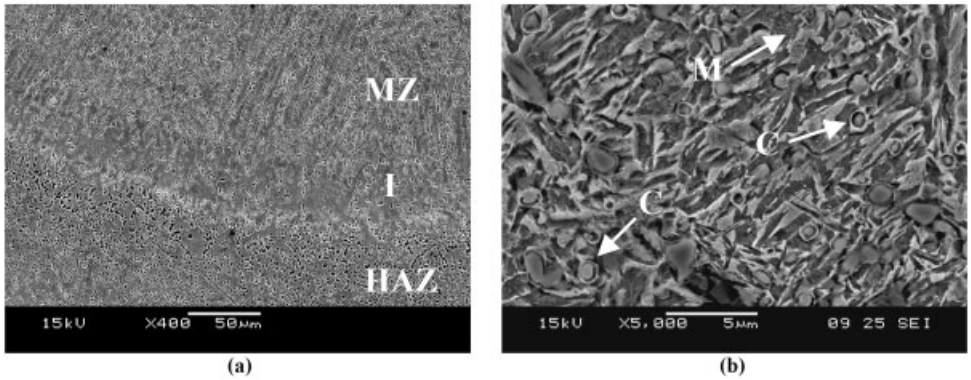
Table 2: Specification of the micro-abrasion apparatus.

Load	1 N
Ball material	AISI 52100
Ball diameter	25 mm
Ball speed	100 rpm
Slurry	6 μm silica particles in distilled water
Slurry concentration	200 g/l
Sliding distance	180 m

3 Results and Discussion

3.1 Microstructural Characterization

Laser melting treatment resulted in the formation of two zones in material, a melted zone (MZ) and a heat-affected zone (HAZ), beyond a interface (I) between these zones (Figure 2a). Figure 2b shows that heat-affected zone is constituted of refined martensite (M) and carbides (C). Figure 3a shows a refined microstructure in melted zone and the dendritic growing direction change. The melted microstructure is consisted of austenite dendrites (γ) partially transformed to martensite, during cooling, and carbides (Figure 3b). Retained austenite is shown in Figure 3c. The mean primary dendritic arm spacing (λ_1) measured was 3 μm. No ferrite-δ has been observed after laser treatment.



(a) (b)

Figure 2: Zones obtained after treatment (a) and heat-affected zone (b).

Figure 4 shows the X-ray diffractograms of AISI 420 stainless steel as received and after laser treatment. The microstructure of steel as received is consisted of martensite and Cr_7C_3 type carbide. The microstructure of the melted layer is consisted of martensite, retained austenite and Cr_7C_3 and $Cr_{23}C_6$ type carbides. The retained austenite proportion was 37 % in laser treatment. The microhardness profile shows that the hardness increased 112,5 % in melted zone and 69,5 % in HAZ (Figure 5).

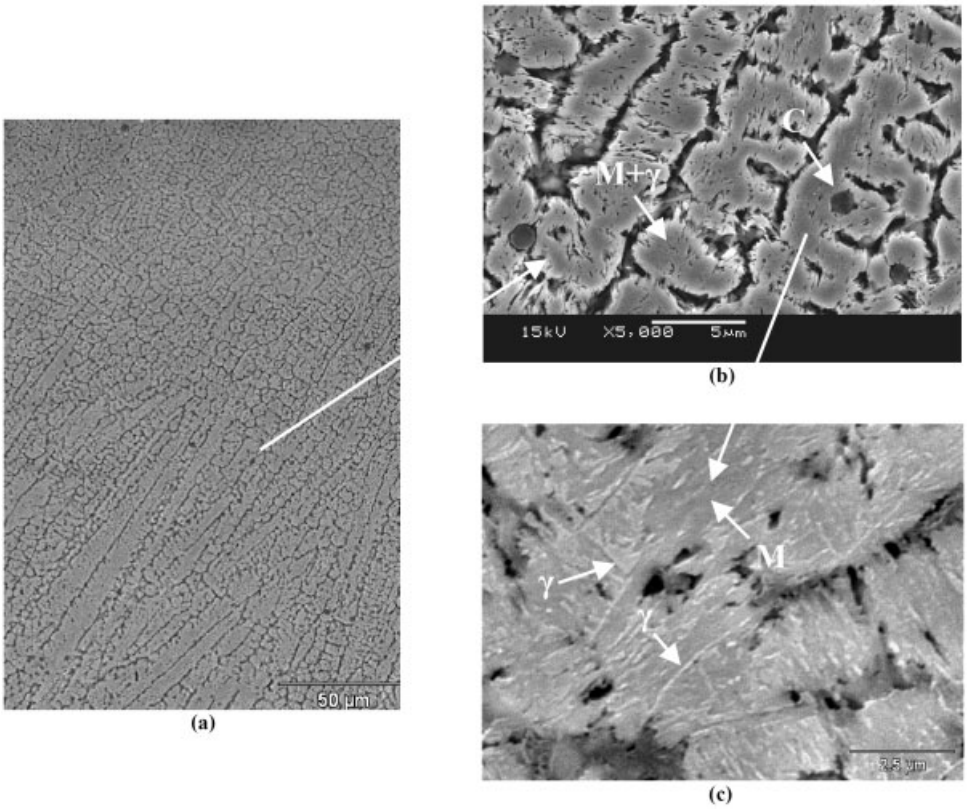


Figure 3: Melted zone of AISI 420 steel: dendritic growing direction change (a), austenite dendrites partially transformed to martensite and carbides (b) and retained austenite (c).

3.2 Wear Resistance

The non-treated laser samples presented the best abrasive wear resistance in comparison with laser melted steel. The wear rate resulting of the micro-scale abrasive wear tests of the samples treated and non-treated by laser were $9{,}07 \times 10^{-13} m^3/Nm$ and $8{,}15 \times 10^{-14} m^3/Nm$, respectively.

Scanning electron microscopy analysis of the quenched and tempered steel sample by traditional heat treatment revealed that the wear craters present a series of fine parallel grooves and multiply indented with no evidence surface directionality, as shown in Figure 6. This behavior was termed “mixed-mode” and involved two mechanisms: microcutting and microploughing.

The laser melted samples presented a wear rate higher than those quenched and tempered samples by traditional heat treatment. The laser melted sample presented the wear surface formed by grooves parallel to the direction of sliding, characteristic of the microcutting wear mechanism (Figure 7).

Besides the parallel scratches, it can be observed that the smaller carbides, present in the structure, were easily removed from the matrix increasing the wear volume (indicated by the arrows

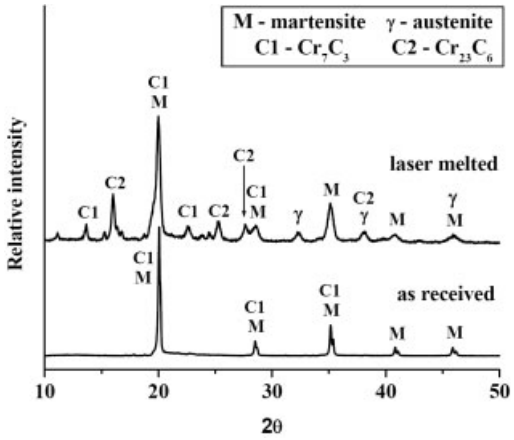


Figure 4: X-ray diffractograms of steel before and after laser treatment.

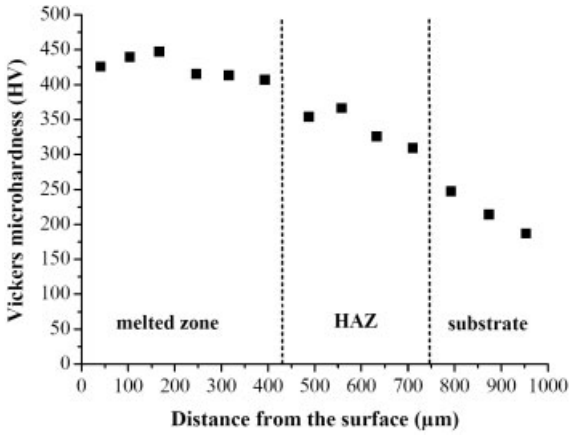


Figure 5: Vickers microhardness profile of steel after laser melting.

in the Figure 7). The presence of retained austenite high volume fraction may be decreased the capacity of the matrix to resist the action of abrasive particles allowing the carbide removing, which is in agreement with studies of Colaço et al. [8,26], where the abrasive wear resistance of laser surface melted stainless steel decreases with increasing retained austenite proportion.

4 Conclusions

After laser melting, the resultant phases in material were martensite, retained austenite and Cr_7C_3 and $Cr_{23}C_6$ type carbides. Significant increase on hardness has been observed, in spite of the retained austenite high volume fraction, due to the refined microstructure and precipitated

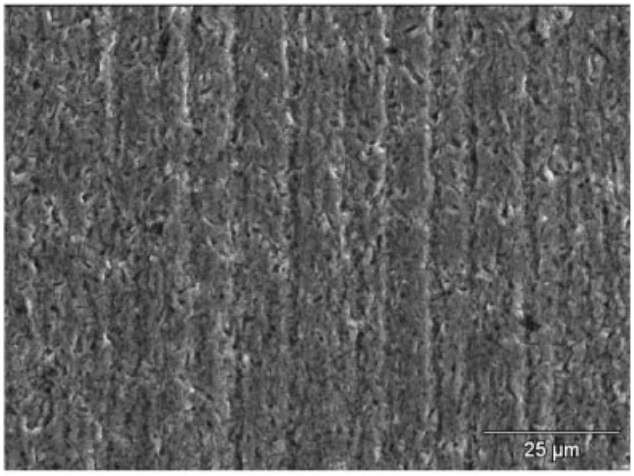


Figure 6: SEM image of the quenched and tempered AISI 420 stainless steel worn surface.

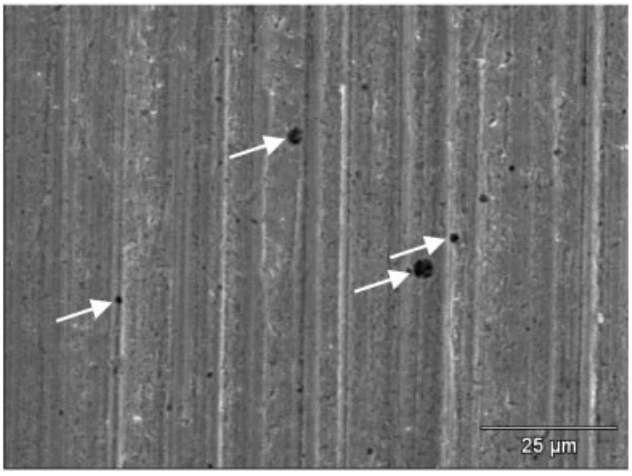


Figure 7: SEM image of the laser melted AISI 420 stainless steel worn surface.

carbides promoted by laser treatment. The laser melted samples presented a wear rate higher than those quenched and tempered samples by traditional heat treatment. The presence of retained austenite high volume fraction in the laser melted samples may have contributed to increasing of the wear rate. Is important to optimize the laser parameter in order to reduce the retained austenite formation.

Acknowledgements

The authors acknowledge financial support provided by FAPESP (The State of São Paulo Research Foundation, Brazil) and CAPES (Brazilian Government Agency). The authors also thank Brazilian Synchrotron Light Laboratory for permitting the use of laboratory facilities and Mr. Eli Wenzel de Siqueira for processing the samples in the laser machine.

References

[1] Wollenweber, J., Advanced Materials & Processes 1996, 150, 225–226.

[2] Ierardi, M.C.F.; Garcia, A.; Costa, A.R.; Vilar, R., Lasers in Engineering 1999, 9, 47–56.

[3] Colaço, R.; Vilar, R., Scripta Materialia 1997, 36, 199–205.

[4] Colaço, R.; Vilar, R., Journal of Materials Science Letters 1998, 17, 563–567.

[5] Olaineck, C.; Ruge, J., Metallurgia 1996, 63, 87-89.

[6] Steen, W.M., Laser Material Processing, 3nd ed., Springer, London, 2003.

[7] Colaço, R.; Vilar, R., Materials Science and Engineering A 2004, 385, 123–127.

[8] Colaço, R.; Pina, C.; Vilar, R., Scripta Materialia 1999, 41, 715–721.

[9] Santner, E.; Klaffke, D.; Meier zu Kocker, G., Wear 1995, 190, 204–211.

[10] Ronkainen, H.; Holmberg, K.; Fancey, K.; Mattews, A.; Mathes, B.; Broszeit, E., Surface and Coatings Technology 1990, 43–44, 888–897.

[11] Gee, M.G; Gant, A.; Hutchings, I.M.; Bethke, R.; Schiffman, K.; Van Acker, K.; Poulat, S.; Gachon, Y.; Von Stebut, J., Wear 2003, 255, 1–13.

[12] Hutchings, I.M., Tribology International 1998, 31, 5–15.

[13] Rutherford, K.L.; Hutchings, I.M., Journal of Testing and Evaluation 1997, 25, 250–260.

[14] Adachi, K.; Hutchings, I.M., Wear 2003, 255, 23–29.

[15] Rutherford, K.L.; Hutchings, I.M., Surface and Coatings Technology 1996, 79, 231–239.

[16] Gee, M.G., Wear 2005, 259, 1448–1452.

[17] Trezona, R.I.; Allsopp, D.N.; Hutchings, I.M., Wear 1999, 225–229, 205–214.

[18] Allsopp, D.N.; Trezona, R.I.; Hutchings, I.M., Tribology Letters 1998, 5, 259–264.

[19] Kassman, A.; Jacobson, S.; Erickson, L.; Hedenqvist, P.; Olsson, M., Surface and Coatings Technology 1991, 50, 75–84.

[20] Trezona, R.I.; Hutchings, I.M., Wear 1999, 233-235, 209–221.

[21] Staia, M.H.; Enriquez, C.; Puchi, E.S.; Lewis, D.B.; Jeandin, M., Surface Engineering 1998, 14, 49–54.

[22] Stack, M.M.; Mathew, M., Wear 2003, 255, 14-22.

[23] Zum Gahr, K.H., Tribology International 1998, 31, 587–596.

[24] Adachi, K.; Kato, K.; Chen, N., Wear 1997, 203–204, 291–301.

[25] Jatczak, C.F.; Larson, J.A.; Shin, S.W., Society Automotive Engineers, 1980.

[26] Colaço, R.; Vilar, R., Wear 2005, 258, 225–231.

Enhanced Wear Resistance of Precipitation Hardening Steels by Laser Solution Annealing and Subsequent Aging Treatment

Jörg Kaspar, Berndt Brenner, Arnhold Luft, Frank Tietz, Jörg Bretschneider
Fraunhofer Institut für Werkstoff- und Strahltechnik, Dresden

1 Introduction

Precipitation hardening martensitic stainless steels are used for structural components in aircraft, chemical, naval, nuclear and power generation industries because they offer a good combination of strength, ductility and toughness, good fabrication characteristics and corrosion resistance. Unlike quenched and tempered steels which gain their strength by the formation of martensite, in precipitation hardening martensitic stainless steels small precipitations considerably contribute to strength. Hence these steels contain precipitation-forming elements like copper, aluminum, titanium or niobium [1]. The conventional way to achieve the precipitation hardened state consists of a solution annealing treatment to obtain a homogenized austenite, the transformation to martensite upon cooling to room temperature and an aging treatment to form small precipitates within the martensite.

For many applications precipitation hardening martensitic stainless steels must guarantee high ductility and toughness as well as low susceptibility to stress corrosion cracking. For this reason these steels are normally used in an overaged but not in the peak aged condition. However in an overaged condition the steels do not exhibit the maximum strength, hardness and wear resistance which would be desirable for some applications.

To overcome this drawback an effective surface modification technique has been developed at Fraunhofer IWS Dresden, which allows the selective generation of wear resistant surface regions up to several millimeters in depth without altering the mechanical properties in the bulk of the material [2]. The present work evaluates the capability of this novel surface hardening technique, which is based on a laser solution annealing and subsequent aging treatment, improving the hardness and the resistance to cavitation erosion of the steel X5CrNiCuNb16-4 (16-4 PH). Furthermore, the microstructure within the laser treated surface region was studied in detail by metallographic methods and transmission electron microscopy (TEM).

2 Experimental

2.1 Specimens and Laser Treatment

The experiments were carried out on the precipitation hardening martensitic stainless steel 16-4 PH of the following chemical composition (wt%): Cr: 15.65, Ni: 4.30, Cu: 3.05, Mn: 0.45, Nb: 0.30, Si: 0.27, C: 0.038, P: 0.018, S: 0.001, Fe: balance. This steel is strengthened by the precipitation of small Cu particles within lath martensite structure [3]. The as delivered condition of this steel is characterized by the conventional solution annealing and aging treatment specified in table 1.

In order to increase surface hardness and wear resistance the as delivered samples were subjected to an additional heat treatment cycle which is called *"Surface age hardening"* and consists of a short time solution annealing of the surface by laser treatment followed by rapid self-quenching and a subsequent aging treatment of the whole sample at temperatures below 560 °C (table 1).

The laser solution annealing was performed with a 6 kW CO_2-laser and a 4 kW diode laser, respectively. In order to ensure a fast and exact local temperature control a fast pyrometer or a camera based temperature measuring system *E-MAqS* [4] and the laser power control unit *LompocPro* [5] were integrated in the laser surface annealing process. A beam shape device based on approved galvanometer scanner technology and developed for the conventional laser hardening [6] has been applied to generate variable tracks up to 40 mm in width. The laser surface annealing was conducted at a constant surface temperature of about 1350 °C and at different dwell times (0.75 s to 10 s) by varying laser power and transverse speed. The aging of the laser solution annealed samples was done at temperatures between 480 °C and 550 °C, i.e. below the conventional aging temperature of 560 °C, to modify the precipitation structure within the laser annealed surface region but leave the structure in the bulk of the material unchanged.

Table 1: Parameters of the conventional heat treatment and the surface age hardening process

Cycle	Heat treatment	Temperature	Dwell time	cooling
I: Conventional heat treatment	Ia: Solution annealing	1050 °C	0.5 h	air
	Ib: aging	560 °C	3 h	air
II: Surface age hardening	IIa: Laser surface annealing	1350 °C	0.75 – 10 s	self quenching
	IIb: aging	440 – 550 °C	3 - 8 h	air

2.2 Characterisation Methods

Metallographic cross sections of the surface age hardened samples were prepared by a sequence of cutting, grinding, polishing and etching and analyzed by optical microscopy. The hardness of the samples was measured at the cross sections by means of a Vickers microhardness tester using a 50 g load.

Furthermore TEM was used to investigate in detail the microstructures of the steel in the as delivered condition and after the laser solution annealing and subsequent aging treatment. The specimens were cut at a depth of about 0.1 mm underneath the surface and thinned by a sequence of grinding, twin-jet electro-polishing and ion beam bombardment. The TEM examinations were done utilizing a JEOL JEM 2010 microscope equipped with a double-tilt stage operating at 200 kV.

An ultrasonic device was used to carry out the cavitation erosion tests in deionized water at 25 °C (ASTM G32-92). The specimens were set opposite to a vibrating tip of Ti-6Al-4V. Cavitation was induced by longitudinal oscillation of the tip at 20 kHz using an amplitude of 40 µm and a distance between tip and sample of 0.50 mm. The samples to be tested had dimensions of 20 mm by 15 mm. Their surface was carefully ground. The mass loss was determined with an accuracy of 0.1 mg at certain time intervals during a total testing period of 20 h.

3 The New *Surface Age Hardening* Technology

Existing and well established surface hardening techniques, e.g. cladding, case hardening or high temperature nitriding, providing sufficient wear protection are not applicable to the 16-4 PH steel because they destroy the well balanced precipitation structure in the surface region and hence degrade the overall mechanical performance. Generally, only insufficient technical solutions for wear protection of such steels are available, if the wear type requires thick protection layers (e. g. cavitation and droplet erosion) and the components are heavily fatigue loaded. However, low pressure turbine blades made of 16-4 PH have to withstand such severe conditions. In order to significantly improve the resistance to cavitation and water droplet erosion without essentially degrading the outstanding overall mechanical and environmental behavior (e.g. toughness, ductility, corrosion, stress corrosion cracking) of 16-4 PH the *Surface age hardening* technique was proposed and developed [1]. This approach assumes that the different demands on surface and bulk properties can be achieved by specifically adapted heat treatment cycles (cp. table 1):
I) *Conventional heat treatment:* Solution annealing and precipitation hardening of the whole component at relatively high temperatures (overaging) to obtain the required bulk properties optimized for the demands of strength, HFC fatigue and toughness by establishing a relatively coarse Cu precipitation structure in the lath martensite (size: 10–50 nm).
IIa) *Laser solution annealing:* Selective short-time surface solution annealing (austenitization) at unusual high temperatures to completely dissolve the Cu precipitations in the near surface region and maintain the solid solution upon rapid self-quenching and transformation to lath martensite.
IIb) *Surface precipitation hardening:* Aging of the whole component at relatively low temperatures to optimal strengthen the solution annealed surface regions by very small Cu rich precipitations (size 1–5 nm).

4 Results

Applying the novel laser based *Surface age hardening* technique the hardness of the steel 16-4 PH can be considerably increased. Depending on transverse speed and hence dwell time the depth of the surface hardened zone can be adjusted from about 1 mm to about 4 mm (Fig. 1a). Generally, the hardness of the surface age hardened surface region can be significantly increased with respect to the as delivered state by choosing the appropriate laser and aging treatment (Fig. 1b). The maximum surface hardness of about 480 HV0.05 is achieved, by an aging treatment at 480 °C for 8 h. However, even considerably overaging at 550 °C for 3 h led to a maximum hardness of about 420 HV0.05 in the laser solution annealed surface region, i.e. an increase in hardness of about 100 HV0.05 if compared to the as delivered state.

It is supposed that the higher hardness in the surface age hardened region can be mainly attributed to the denser arrangement of smaller Cu precipitates, which is present in these samples compared to the conventional heat treated samples although other micro-structural processes may be involved, too. In order to prove this assumption, the microstructure of the as delivered state and a surface age hardened state were comparatively analyzed by TEM.

TEM analysis of the as delivered samples disclosed the following features (Figs. 2a and b): i) lath martensite exhibiting high dislocation density; ii) small amounts of reverted austenite along the boundaries of lath martensite; iii) Cu precipitates varying in size between 10–50 nm; iv) a random distribution of NbC particles 50–200 nm in size.

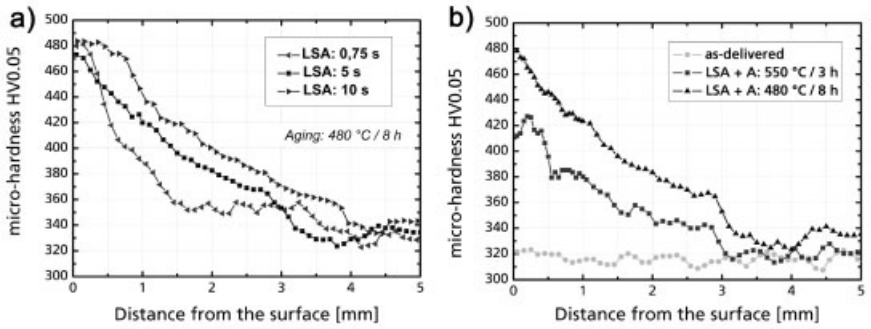


Figure 1: Micro-hardness depth profiles measured on the cross section of surface age hardened samples (laser surface annealed and subsequently aged = LSA +A)
a) Variation of dwell time during laser solution annealing. b) Comparison of as delivered state and surface age hardened samples.

Figure 3 reveals that in the surface age hardened region the size of the Cu precipitates is much smaller, however, the precipitation density is much higher than in samples of the as delivered condition. Peak-aging at 480 °C for 8 h predominately led to the formation of a very high amount of Cu-rich particles only about 1–3 nm in size and homogenously formed within the laths of the martensite. Overaging at 550 °C for 3 h resulted in a precipitation structure that is characterized by a dense arrangement of fcc ε-phase Cu-rich particles about 20 nm in size. Consequently, in the surface aged hardened regions the precipitation density is significantly higher whereas the size of the Cu particles is much smaller than in samples of the as delivered state. This even applies, if the aging conditions of conventional heat treatment and *Surface age hardening* are comparable (550 °C / 3 h versus 560 °C / 3 h).

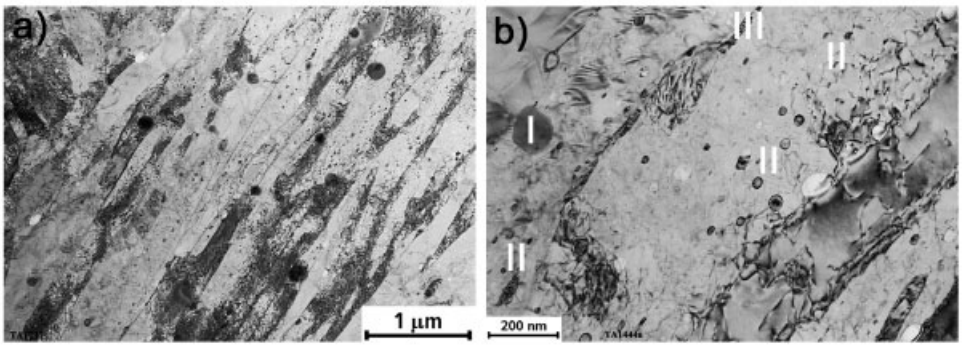


Figure 2: Microstructure of the steel 16-4 PH in the as delivered state.
a) TEM micrograph (overview): Typical lath martensite morphology.
b) Detail of b): I NbC particles; II fine Cu precipitates of different sizes; III reverted austenite along the boundaries of the lath martensite.

In Figure 4 it is shown that the novel *Surface age hardening* technology enables a substantial improvement of the cavitation erosion resistance. Compared to the as delivered state the resis-

tance against cavitation erosion of the steel 16-4 PH can be increased approximately by a factor of three. Because of this encouraging result the novel surface age hardening technique was adjusted and successfully applied for the wear protection of low pressure turbine blades made of the steel 16-4 PH [7].

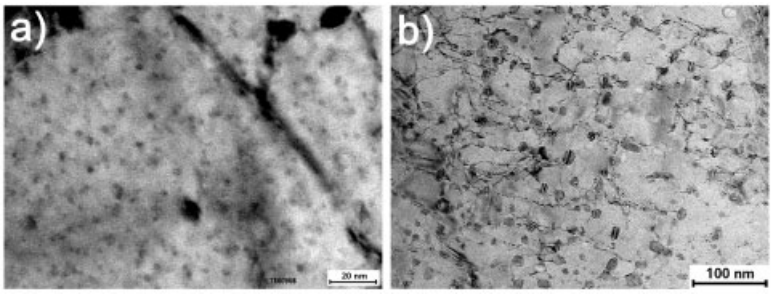


Figure 3: Microstructure of the steel 16-4 PH in the surface age hardened state using different aging treatments.
a) Aging 480 °C / 8 h: Very small Cu-rich precipitates (1–3 nm)
b) Aging 550 °C / 3 h: Cu-rich precipitates (fcc ε-phase) about 20 nm in size.

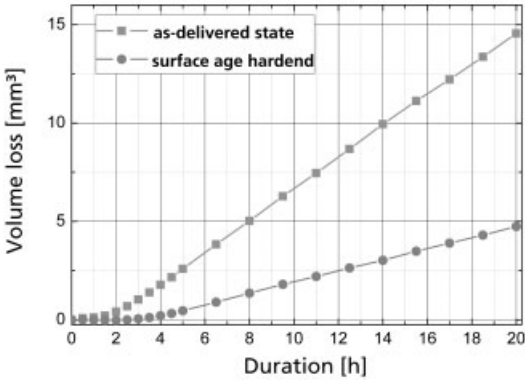


Figure 4: Cumulative volume loss during a cavitation erosion test. Comparison of a sample in the as delivered state and a sample afterlaser solution annealing and subsequent aging treatment (Aging: 480 °C / 8 h).

5 Conclusions

In the present work the innovative *Surface age hardening* technique which is based on laser solution annealing and subsequent aging treatment was introduced and successfully applied to improve the surface hardness and cavitation erosion resistance of the precipitation hardening steel 16-4 PH. In order to evaluate the capability of this technique the hardness, microstructure and wear resistance of the as delivered state and of surface aged hardened samples were comparatively investigated. Based on the results the following conclusions are drawn:

1. By applying the *Surface age hardening* technique the hardness of the steel 16-4 PH can be increased by about 50 % and the resistance to cavitation erosion by about 300 %.

2. By altering the parameters of the laser and aging treatments the required hardness and depth of the surface age hardened zone can be easily adjusted.

3. In the surface age hardened region a more homogenous and finer arrangement of small Cu-rich precipitates is formed than in the conventionally heat treated samples of the as delivered state.

6 References

[1] E. Hornbogen in Physical Metallurgy Physical Part II: Metallurgy of steels (Ed. R. W. Cahn, P. Haasen), North Holland Physics Publishing, Amsterdam, 1983, p. 1075.

[2] B. Brenner, F. Tietz, German Patent DE10030433C2, 2002

[3] K. C. Antony, Journal of metals 1963, 15, 922–927

[4] S. Bonß, M. Seifert, J. Hannweber, U. Karsunke, E. Beyer, in Proc. of the ICALEO, Vol. 98, LIA, 2005, 851–855

[5] S. Bonß, M. Seifert, B. Brenner, E. Beyer, in Proc. of the ICALEO, Vol 90, LIA, 2000, 19–27

[6] S. Bonß, J. Hannweber, U. Karsunke, M. Seifert, B. Brenner, E. Beyer, Proc. of the LAMP, Japan Laser Processing Society, 2006

[7] Anonymous, Stahl und Eisen 2006, 126, 38–39

Smart Pastes for Improvement of Wear Resistance of Metals

N. Dahl, D. C. Lou, O. M. Akselsen, M. I. Onsøien
SINTEF Materials and Chemistry, 7465 Trondheim, Norway

1 Introduction

Wear and corrosion are major causes of materials wastage and unfavourable friction conditions are a principal origin of energy dissipation [1, 2] in many industrial processes. To protect equipment, tools, dies and machinery from wear, corrosion and oxidation, different coating techniques have been established. These include diffusion processes, thermal spraying, hardfacing, laser cladding and deposition processes (physical vapour deposition, PVD, chemical vapour deposition, CVD), etc. Boronising is a well known and effective diffusion coating process with respect to improvement of surface hardness [3]. Conventional boronising is most often carried out by pack-cementation [4] which can easily be applied to work pieces having different shapes and size. However, the powder technique requires very high working temperatures and a great deal of manual work, which prevents boronising becoming a widespread surface modification technique [5].

In this work, the use of smart boronising pastes as an alternative method for surface modification of metals will be demonstrated. The pastes are recently developed at SINTEF [6] and have shown promising results with respect to improvement of metal surface properties. Smart paste surface modification is based on diffusion of active elements from the paste into a substrate forming desired surface layers. The pastes are self-protective which mean that they can be used in any heating furnace, including microwave heating, without protective aid or atmosphere. Further, the pastes have low-cost and easy handling characteristics, and are well suited for partial surface treatment of work pieces and components with complex geometries. In addition, by the use of different pastes with specific active elements, different kinds of surface modification can be carried out on different parts of a component in one heating process. This is difficult to execute by conventional surface technology.

2 Characterizations of the Pastes

2.1 Working Principle of the Pastes

The smart paste agents consist of compounds that release elements giving full protection against oxidation, species that release the diffusing elements, diffusion aid (if necessary), fill substances and a binder solution. The pastes can contain sources for single or multiple active elements (such as B, Si, C, N) dependent on the required properties of the final coating/diffusion layer. For boronising, one or more boron-compounds are the boron supplying source. Desired amounts of the different dry powders are mixed together and a sticky solution is added to the powder mixture in order to make a paste consistency.

The principle of self-protective paste treatment is presented in Figure 1. The surface to be modified is covered by a 3–5 mm thick layer of the smart paste, followed by drying at room tem-

perature or at a temperature less than 100 °C. Afterwards, the coated specimens are heated to a specified temperature and held for a certain soaking time, depending on the required thickness of the boronised/diffusion layer and on the type of substrate material. After the treatment, the diffusion coated material is cooled in air, followed by removal of paste residue. The final coatings or diffusion layers are typically from 20 μm up to 1mm thick, depending on the treatment parameters. Figure 2 shows a typical temperature versus time cycle for smart paste treatment. The actual diffusion process is carried out at temperatures from 650 °C to 1100 °C, depending on the paste composition. Specific low temperature pastes are developed for treatment of temperature sensitive components, in order to avoid thermal distortions etc. The pastes can also be tailored to fit into the thermo mechanical treatment cycle of the component in question in order to avoid adding an extra heat treatment operation.

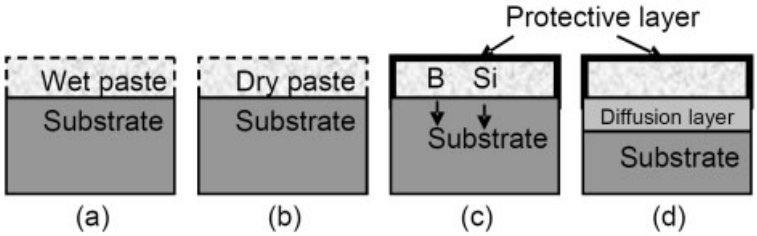


Figure 1: Principle of self-protective paste treatment. (a) Application of paste, (b) Drying of paste, (c) At specified temperature and soaking time: formation of protective layer at the paste surface and diffusion of active species into the substrate, (d) Diffusion layer is formed and paste residue can be removed.

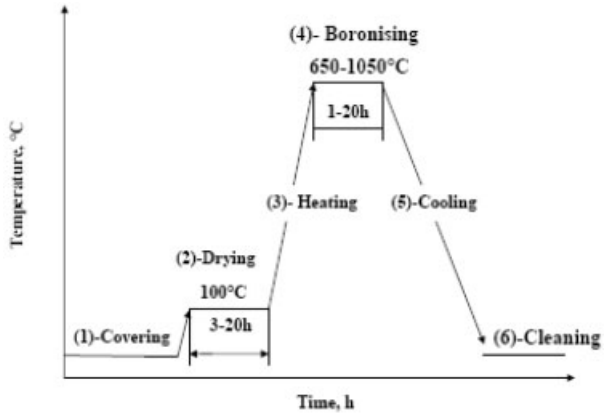


Figure 2: Temperature versus time in a typical paste treatment cycle where boron is the active diffusing element.

2.2 Applied Materials and Geometries

The pastes have been tested for various metal substrates, such as low, medium and high carbon steels, stainless steels, cast irons, nickel alloys and cobalt. Examples are given in Table 1 where

the tested substrate materials are presented together with results from hardness testing before and after paste treatment. As the table shows, a remarkable increase in hardness is observed after paste treatment.

The easy handling characteristics of the pastes makes them well suited for treatment of complicated shapes with various geometries such as cutters, screws, gears, slits cavities, inside of pipes and tubes, etc. Examples are given in Figure 3. In addition, by applying different pastes, on different regions of a component, various kinds of surface modification may be carried out in one heating process.

Table 1: Examples of substrates selected as testing materials and hardness before and after treatment with two variants of self-protective pastes.

Testing materials	Self-protective paste I Before treatment	After treatment	Self-protective paste II After treatment
Nimonic 90	300-400HV	1000-1400HV	2200-2500HV
Inconel 625	300-400HV	1000-1400HV	2200-2500HV
Hard alloy(WC/Co)	1100-1300HV	1700HV	
Steel H13	500-550HV	1400-1800HV	
Steel QRO90	500-550HV	1400-1800HV	
DSS(Duplex stainless steel)	300-330HV	1600-2000HV	
A240-stainless steel	200-250HV	1600-2000HV	
316L stainless steel	200-250HV	1600-2000HV	
AISI 1040	100-250HV	1400-1800HV	
Cast iron	200HV	1400-2000HV	

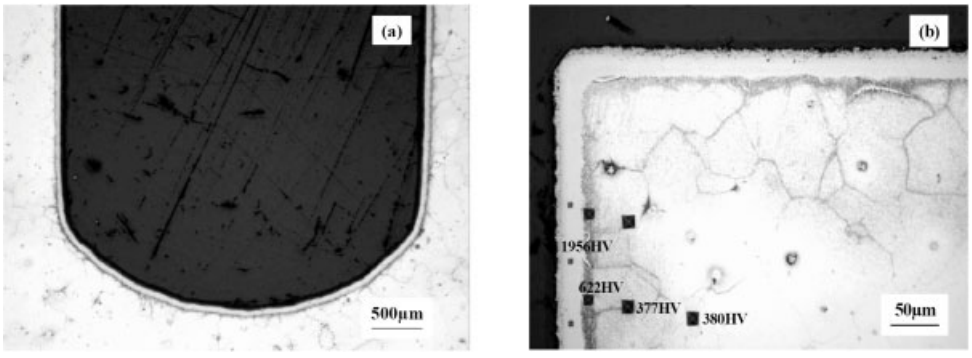


Figure 3: Surface modification of Nimonic 90 with different geometries: (a) U-shaped pipe, (b) Sharp edge/corner of cubic sample.

3 Diffusion Layer Structures

Typical microstructures of the various diffusion layers are presented as follows: Figure 4 shows the diffusion layers of hot work tool steels H13 and QRO90. The layers consist of FeB+Fe_2B

(Figure 4a) or Fe_2B (Figure 4b), depending on the substrate, paste composition and treatment parameters. The layers are usually 50–100 μm.

In Figure 5, diffusion layers, multiple layers (a) and composite layer (b) of stainless steels as substrate are shown. Multiple layers on stainless steels form at certain temperatures and with certain composition of the paste. The formation of composite diffusion layers requires high temperature soaking. The micrograph in Figure 5b shows that the composite layer consists of $(Fe,Cr)_2B$ and alloy matrix.

Figure 6 shows the diffusion microstructures of nickel alloys (Nimonic 90 and Inconel 625) which consist of large amount of needles in the layers. The average microhardness of the diffusion layers is about 2200-2500HV. The needles consist of high amounts of CrB which is believed to be most governing with respect to the hardness [7].

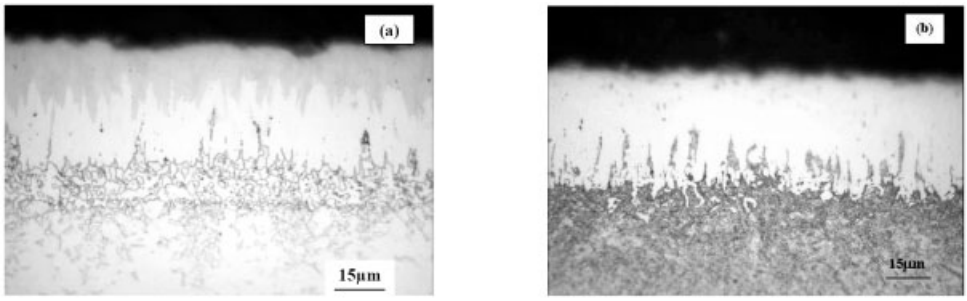


Figure 4: Boronised diffusion layers of hot work tool steels: (a)-H13 and (b)-QRO90.

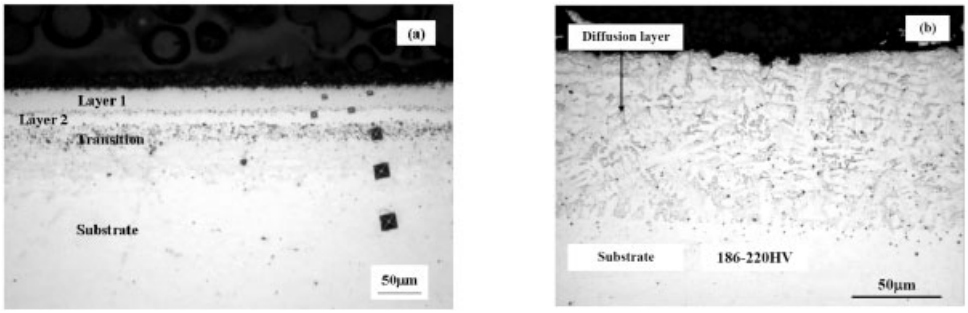


Figure 5: Boronised diffusion layers on stainless steels: a) Multilayer coating on 22Cr-5Ni Duplex Stainless Steel (DSS) treated at 950ºC for 5hrs, b) Composite layer on stainless steel A240 boronised at 1100 °C for 1 h.

4 Wear Resistance and Hardness

Measurements of micro hardness were carried out for the different boronised metal substrates. The micro hardness was measured by a Vickers pyramid hardness intender at 25g loads ($HV_{0.025}$). Typical hardness profiles from the surface, trough the diffusion layer and into the bulk substrate

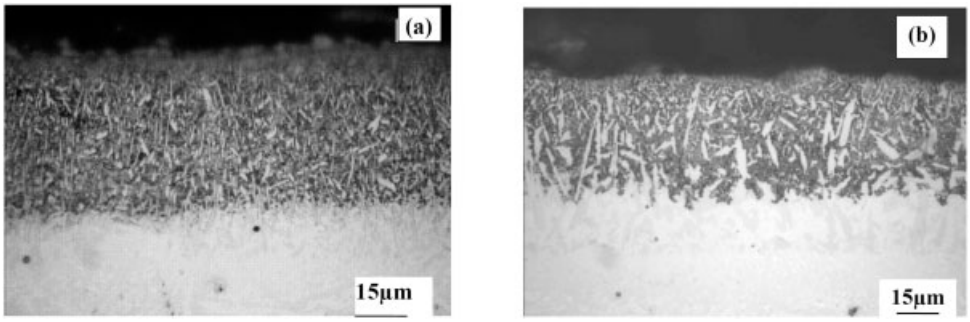


Figure 6: Microstructure of boronised diffusion layers of nickel alloys: a) Nimonic 90, b) Inconel 625.

for smart paste boronised H13 steel and Ni-alloy Nimonic 90 are plotted in Figure 7a. In the figure, corresponding hardness measurements of a standard nitrided tool steel are also presented. In Figure 7b, hardness as function of treatment time and temperature for the Ni-alloy Nimonic 90 are presented. The results clearly demonstrate the positive effect of the paste surface modification, causing a remarkable increase in microhardness from about 400 up to 2500 for the treated Nimonic 90 alloy, while the tool steel surface hardness was raised from about 500 to almost 1700. Note also the significant improvement as compared to the nitrided tool steel. The hardness profiles show that the hardness is relatively stable from the surface and approximately 30 µm into the diffusion layer. Further into the diffusion layer and closer to the transition between the diffusion layer and the pure substrate, the hardness decreases. An increase in boronising temperature or time will increase not only the total diffusion layer thickness, but also the distance with extra high hardness (Figure 7b).

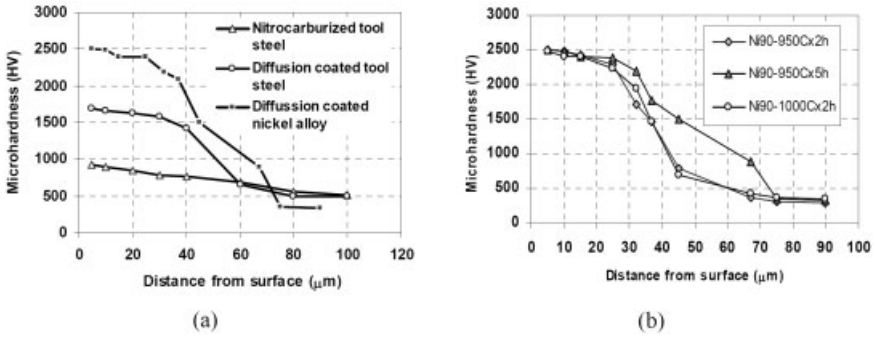


Figure 7: Hardness profiles of boronised metal alloys: (a) Comparison of nitriding and paste treatment of H13 steel and nickel alloys, (b) Hardness profiles of Nimonic 90 alloy at varying paste treatment time and temperature.

Abrasive wear measurements of some smart paste treated substrate metals are carried out on a Struers microwear tester. Results from testing of boronised and corresponding not boronised hot work H13 steel, duplex stainless steel (DSS) and cast iron are presented in Figure 8a. The wear resistance of boron-siliconised Ni-alloy Nimonic 90 was also investigated (Figure 8b). When

boron-siliconising, the paste is modified and a Si compound is added [7]. The results show that volume loss of the substrates during wear was reduced by a factor of 3-5 after surface treatment. I.e. the abrasive wear resistance is significantly improved by the paste treatment.

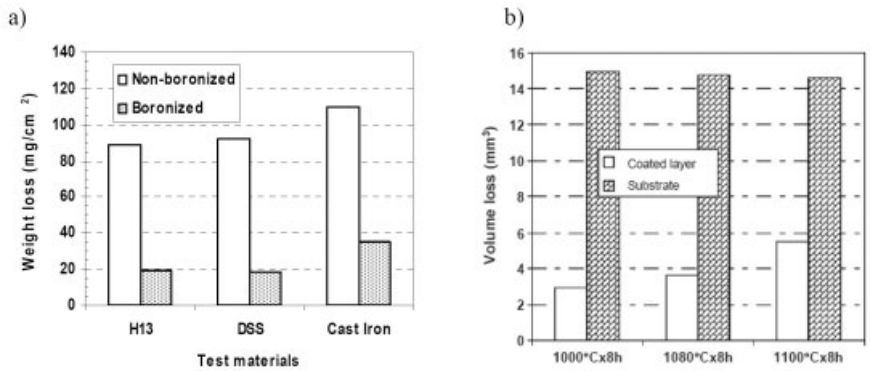


Figure 8: Results from testing of abrasive wear resistance before and after boronising of (a) steels and cast irons, and (b) Nimonic 90 alloy (boron-siliconising).

5 Conclusions

- Self-protective smart pastes that can be used for surface modification of metals in any heating furnace have been developed and demonstrated on several substrates.
- The smart paste self-protective treatment give hardness increase of 100–200 % and the abrasive wear resistance of treated metal substrates increase by a factor of 3–5.
- The pastes required no need for protective or reductive furnace atmosphere and the paste has low-cost and easy handling characteristics.
- The treatment method is suitable for partial surface treatment of work pieces and components with various geometries such as screws, gears, slits cavities, inside of pipes and tubes, etc.
- By the use of different pastes, various kinds of surface modification may be carried out on different surface-parts of a component in one heating process.

6 References

[1] Jin H.W., Park C.G., Kim M.C.; Current Applied Physics 2001, *1*, 473–477.

[2] Wood R.J.K; Wear 2006, *261*(9), 1012–1023.

[3] P. Gopalakrishan & Al; Met. And Mats. Trans. 33A (2002), 1475–1485.

[4] Zhang T.C., Li D.Y.; Mater. Sci. Eng. A 2000, *277*, 18–24.

[5] Kuper A., Qiao X., Stock H.R., Mayr P.; Surf. Coat. Technol. 2000**,** *130*, 87–94.

[6] Lou, D. No. Patent Application N2007 0885, 2007.

[7] Lou D., Akselsen O. M., Solberg J.K., Onsoien M.I., Berget J., Dahl N.; Surf. Coat. Technol. 2006, *200*, 3582–3589.

Tribological Properties of 316 LVM Austenitic Stainless Steel Processed by Mechanical Pulse Treatment and Hydrostatic Extrusion

J. Budniak, O. Kyryliv, M. Lewandowska, K.J. Kurzydlowski
Warsaw University of Technology, Faculty of Materials Science and Engineering, Woloska 141, 02-507 Warsaw

1 Introduction

Austenitic stainless steels are widely used in various fields of engineering and in biomedical applications. From this point of view, the improvement of their properties is of great importance. One of the efficient ways to achieve higher mechanical properties is grain size refinement down to nanometer scale. This refinement may be induced either in a bulk or surface zone. The surface refinement is, in particular, recommended for elements subjected to wear.

The aim of this work was to determine tribological properties of the nanostructured 316 LVM austenitic stainless steel. In order to refine the structure in the surface zone, 316 LVM steel was subjected to mechanical pulse treatment (MPT) which is an emerging method of surface engineering by high-speed friction [1–2]. Carbonizing environments (mineral oil with addition of low-polymeric fraction polyethylene) can be employed and the grain size refinement might be accompanied by modifications of chemical composition. Samples of 316 LVM were also studied with nanostructure in the entire volume. These samples were obtained via hydrostatic extrusion (HE), which is one of the efficient SPD methods of grain refinement [3–5].

2 Experimental

The material used in this study was 316 LVM with the chemical composition given in Table 1. The supplied material was in the form of rods ϕ 10 and of a 6 mm thick sheet.

Table 1: Chemical composition of 316 LVM (wt %)

316 LVM	C	Si	Mn	P	S	Cr	Ni	Mo	Cu	N
	0.025	0.6	1.7	0.025	0.003	17.5	13.5	2.8	0.1	<0.1

The rods subjected to seven passes of HE to the final diameter 4 mm. This corresponds to a cumulated true strain of 1.84. The microstructure of the 316 LVM steel before and after HE are shown in Fig. 1–2. The microstructure in the as-received state is typical of a low stacking fault energy material after cold deformation and contains numerous deformation twins. HE brings about structure refinement and the resulting microstructure consists of nano-twins.

MPT was performed on coupons of 6 mm 316 LVM sheet annealed at temperature of 1050 ºC and furnace cooled. The microstructure of the steel after MPT is shown in Fig. 3 and Fig. 4. Uniaxal grains with twin-boundaries, typical of annealed austenitic stainless steel appear in the core, whereas the sample surface is strongly deformed.

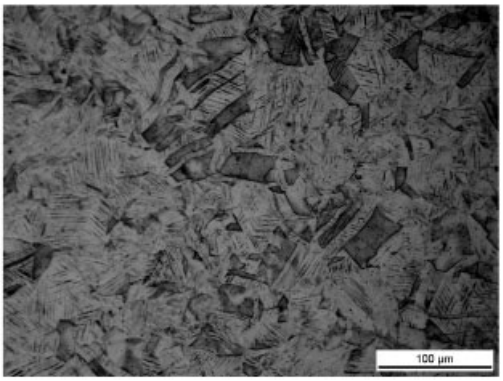


Figure 1: SEM image of the microstructure of 316 LVM steel in as-received state

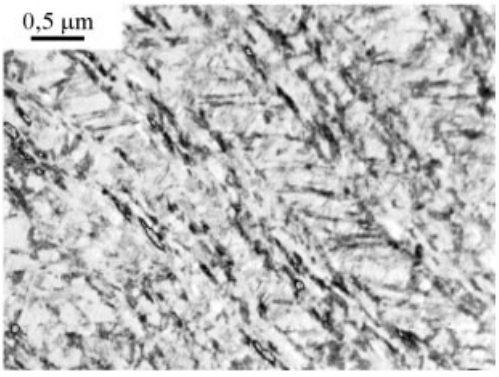


Figure 2: TEM image of the microstructure of 316 LVM steel after hydrostatic extrusion

The mechanical properties were assessed by microhardness $HV_{0,2}$ measurements. Wear properties were investigated using pin-on-disc tribometer. Pin samples of 4 mm diameter were made of the material in initial states, as well after HE and MPT. During the tests, pins were pressed against the hardened steel X17CrNi16-2 or ultra-high molecular weight polyethylene (UHMWPE) disc moving at a speed of 0.01 m/s. The applied loads at the interface were 1, 3.5 and 6 MPa. The test duration was 60 minutes. All tests were conducted under lubricated conditions in normal saline solution (0.9%NaCl). The surface roughness before and after the tribological tests was measured using a WYKO NT9800/9300 Profiler. The weight loss was measured using an analytical balance. Surface morphologies of the wear scarf were investigated using a scanning electron microscope.

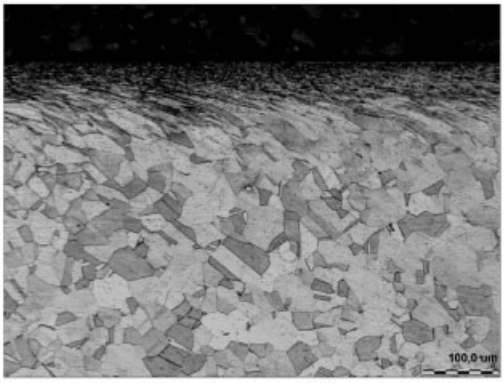


Figure 3: Microstructure of 316 LVM steel sheet after MPT. Light microscope

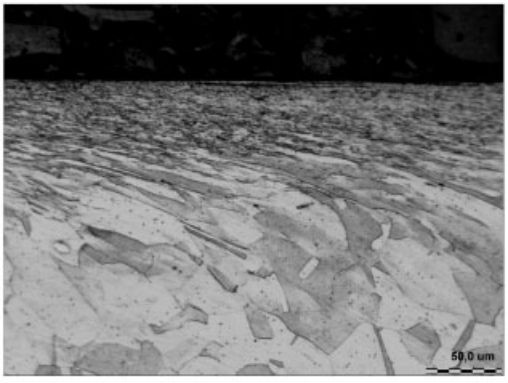


Figure 4: Microstructure of 316 LVM steel sheet after MPT. Light microscope

3 Results and Discussion

The microhardness of 316LVM steel in the as-received state and after HE is given in Table 2. It can be seen that as a result of HE processing, microhardness increases from 354 to 416 $HV_{0,2}$.

Table 2: Microhardness parameters for 316LVM steel in the as-received state and after HE

Sample	Mean Value $HV_{0,2}$	Standard deviation	Variation coefficient
as-received state	354	15.44	0.04
after HE	416	16.17	0.04

For MPT processed samples, the microhardness profile from surface to the core is presented in Figure 5. The microhardness at the top MPT sample is about 277 $HV_{0,2}$ and decreases gradually

to about 160 $HV_{0,2}$ in the core. Figure 6 shows the microhardness along strengthened layer. It indicates that the microhardness is in fairly homogeneous.

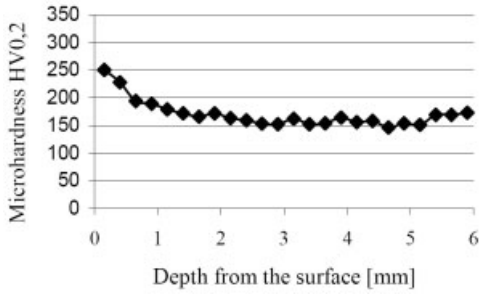


Figure 5: Changes of microhardness from surface to substrat

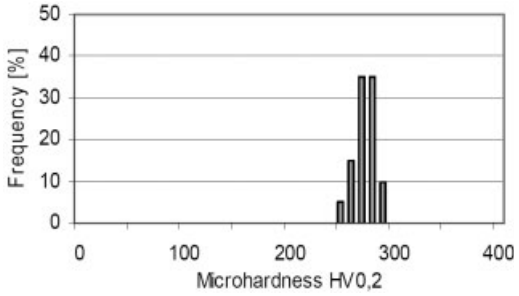


Figure 6: Histogram of microhardness at MPT processed the surface

The results of wear test of 316 LVM pins in the as-received state and after HE during sliding against X17CrNi16-2 steel are presented in Table 3. The value of load, average steady-state friction coefficient, weight loss and surface roughness are also given.

Table 3: Results of tribological tests during sliding against steel disc

Sample	Load [MPa]	Friction coefficient μ	Weight loss [g]	Surface roughness Ra [μm]	
				before test	after test
as-received	1	0.53	0.0098	0.12	1.65
	3.5	0.38	0.0162		2.91
	6	0.47	0.2026		8.20
after HE	1	0.50	0.0098	0.10	1.12
	3.5	0.38	0.0083		2.13
	6	0.48	0.1916		2.34

No significant difference in friction coefficients and weight loss is found between samples in the as-received state and after HE at a load of 1 MPa. For the normal load of 3.5 MPa, the friction coefficients for samples in both states decreased to the value of 0.38. On the other hand the wear

weight loss of the HE sample is lower than that of in the as-received state. It can be attributed to stability of friction coefficient as a function of time. At a test load of 6 MPa for the as-received state and after HE did not significantly differ except the surface roughness. The lower surface roughness for HE samples were registered for all tribological tests.

The results of tribological tests performed with low-polymeric fraction polyethylene as a counterspecimen are shown in Table 4.

Table 4: Results of tribological tests during sliding against UHMWPE

Sample	Load [MPa]	Friction coefficient μ	Surface roughness Ra [μm] before test	after test
as-received	1	0.11	0.12	0.49
	3.5	0.10		0.57
	6	–		0.45
after HE	1	0.13	0.10	0.41
	3.5	0.14		0.33
	6	0.12		0.51

In the case of UHMWPE counterface, the friction coefficients were lower then for the steel. In addition, these coefficients are only slightly higher for the samples after HE compared to as-received ones. The tests resulted in a non measurable weight loss of pins. The surface roughness after friction test was similar for the samples in the as-received state and after HE. It should be noted that surface roughness is much smaller in this case than of steel disc in the case of counterpart.

The results of wear test for sample before and after MPT are presented in Table 5. In such friction conditions the influence of surface strengthening on the wear resistance was negligible. The friction coefficient and surface roughness have similar values for as-received and MPT samples.

Table 5: Results of tribological tests during sliding against steel disc under a load of 3.5 MPa

Sample	Friction coefficient μ	Weight loss [g]	Surface roughness Ra [μ] before test	after test
as-received	0.40	0.0038	0.50	2.30
after MPT	0.42	0.0030	0.40	2.14

The worn surfaces were examined using a scanning electron microscopy. Typical morphologies are shown in Figure 7–10.

The surface observations of samples in the as-received state, after HE and after MPT sliding against a steel showed the combination of adhesion, plastic deformation and abrasion. No significant difference were noticed, except of sliding under 3.5 MPa load, where sample in the as-received state revealed more intensive wear damage (Figure 7,8). The combined wear mechanism causes the similar results of weight loss. The surface morphology of pin in the as-received state and HE after friction with UHMWPE are similar. The surface roughness after friction increased (Table 4 and Figure 9).

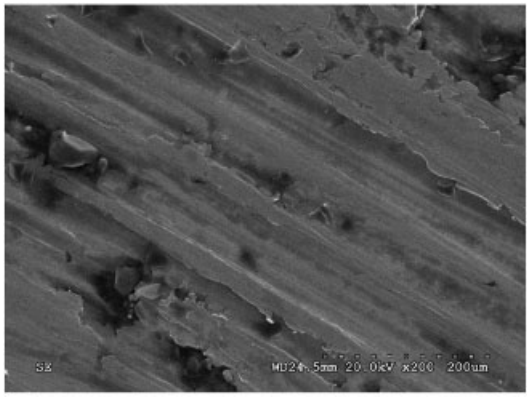


Figure 7: SEM images of the worn 316LVM pin in the as-received state after sliding against steel counterface at a load of 3.5MPa

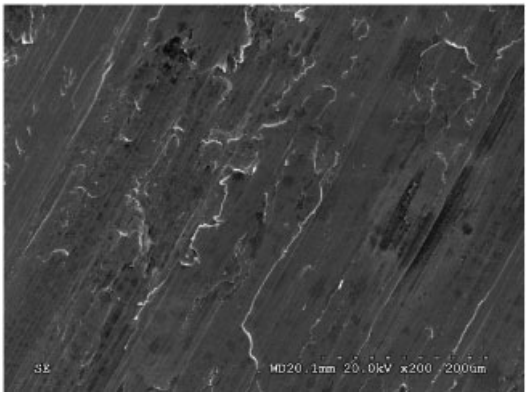


Figure 8: SEM image of the worn 316LVM HE pin after sliding against steel counterface at a load of 3.5MPa

4 Conclusions

The results obtained in this work lead to the following conclusions:

- hydrostatic extrusion and mechanical pulse treatment lead significantly increase microhardness of 316 LVM austenitic stainless steel;
- the higher microhardness of materials after the treatments does not influence on their wear resistance;
- during wear against X17CrNi16-2 steel a combined mechanism of adhesion, plastic deformation and abrasion was observed whereas in the case of UHMWPE as a counterpart specimen no measurable changes/ wear can be observed.

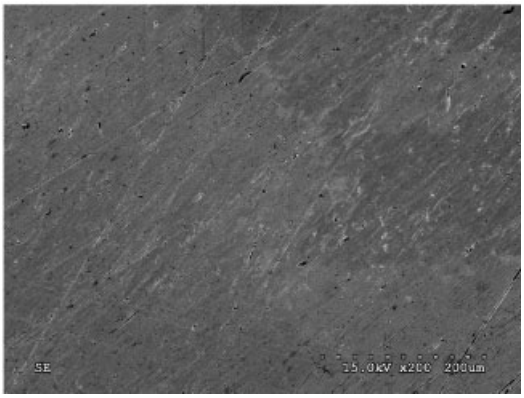


Figure 9: SEM image of the worn 316LVM HE pin after sliding against UHMWPE counterface at a load of 3.5MPa

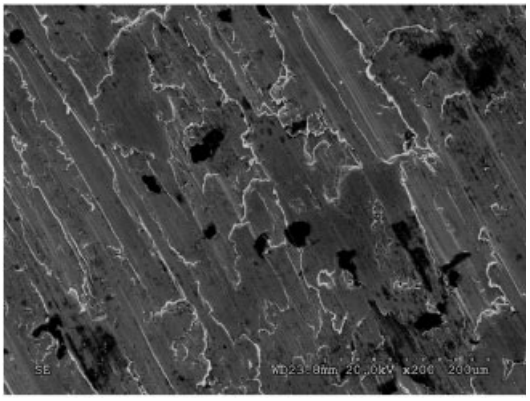


Figure 10: SEM pictures of the worn 316LVM MPT pin after sliding against steel counterface at a load of 3.5MPa

5 References

[1] V.I. Kyryliv: Materials Science, Vol. 34, No. 3, 1998, p. 416–419

[2] H.M.Nykyforchyn, V.I. Kyryliv, Dz.V. Slobodjan, Ju.M.Koval: Surface and Coating technology 100–101, 1998, p. 125–127

[3] H. Garbacz, M. Lewandowska, W. Pachla, K.J.Kurzydlowski: Journal of Microscopy 223, 2006, p. 272–274

[4] M. Lewandowska, H. Garbacz, W. Pachla, A. Mazur, K.J. Kurzydlowski: Solid State Phenomena, 101, 2005, p. 65

[5] K.J. Kurzydlowski: Mat. Sci. Forum 503–504, 2006, p. 341–348

Trybological Properties of the Surface Layers, Rich in Nitrogen, Produced on Stainless Steel 316LVM

R. Slesinski, K. J. Kurzydlowski
Technical University of Warsaw, Faculty of Materials Science, Warsaw, Poland

1 Introduction

Nowadays one of the popular materials in biomedical applications is 316LVM stainless steel. This steel has a good corrosion-resistance and advantageous mechanical properties. It is relatively inexpensive and easy to process. On the other hand, 316LVM shows low hardness and poor wear resistance. This rationalizes the development of tribological technologies intended to improve its properties. The paper presents the results of investigations of the tribological properties of the surface layers produced on 316LVM stainless steel by new technological processes such as oxidation and plasma nitriding.

The surface layers obtained were characterized in terms of their microhardness, roughness and wear-resistance in physiological saline. The layers were examined using light/electron microscopes. The results reveal an appreciable improvement of hardness and wear resistance.

2 Experimental Details

The material used in this study was Sandvik Bioline 316 LVM with the chemical composition given in Table 1 and the mechanical properties listed in Table 2. Figure 1 shows the microstructure in the as-received state. The microstructure with numerous deformation twins is typical of this steel after cold deformation.

Table 1: Chemical composition of Sandvik Bioline 316 LVM steel according to the ISO standard (wt %)

316 LVM	C	Si	Mn	S	P	Cr	Mo	Ni	N	Cu
ISO 5832 1 1997	0.018	0.54	1.69	0.001	0.015	17.48	2.75	14.34	0.058	0.069

Table 2: Mechanical properties of 316LVM steel

Tensile strength Rm [Mpa]	Yield point $Re_{0.2}$ [Mpa]	Elongation A_5 [%]	Hardness [HB]
1167	862	15	320

The material was delivered in the form of cold-worked cylindrical rods, 12 and 16 mm in diameter. The rods were sliced to cylindrical samples sized at ø16x3 mm and, counter-specimens sized at ø12x5. All the samples (discs and rings) were divided into 3 groups. The samples of the first group, which were intended to be the reference samples, were subjected to grinding with abrasive papers and then electropolished. The samples of the second group were oxidized.

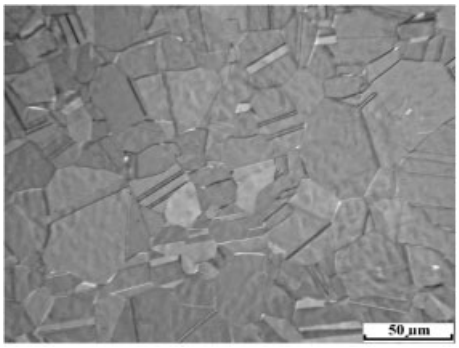


Figure 1: Microstructure of 316LVM stainless steel in the as-received state; light microscope – polarised light

The samples of the last group [1] after grinding and electropolishing, were subjected to plasma nitriding processes.

In order to study the behaviour of the surface layers after wear tests, they were examined using a scanning electron microscope (Hitachi S 3000N). The values of the surface roughness parameters Ra and Rz were measured using a Taylor-Hobson Talysurf 10 device. The microhardness was analyzed in a Neophot 21. The basic tribological properties were investigated by the disc-on-ring method using a "Trybometer" device (Fig. 2).

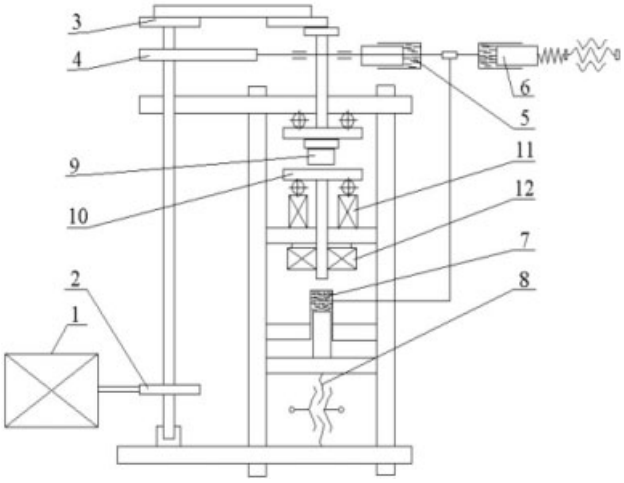


Figure 2: Schematic representation of the "Tribometer": electric engine (l), gear (2), crank mechanism (3), cam (4), hydraulic pump (5), controller of the pressure (6), hydraulic servo-motor (7) helical lift (8), sample (9), countersample (10)

This device enables investigating the processes that proceed in a pair in friction, and measuring trybological properties. The specimen and counter-specimen are set in a rotary motion. They are mounted in an annular holder, designed, for continuous lubrication. During the test, the

pressure and the friction couple were recorded in a continuous way, and the recorded values were used for calculating the friction coefficient. The test was conducted at a load of 8 MPa; lubrication was effected using a 0.9 % NaCl water solution at room temperature. The results obtained (2000 measurements) were plotted in the form of diagrams of the friction force and the friction coefficient as a function of the applied load.

The mechanical properties of the material in the as-received state and after the surface modification were evaluated using the microhardness as the criterion. The measurements were carried out by the Vickers method under a load of 0.1 kg. The microhardness was examined on a sample cross-section along its diameter. The sample surface was prepared for the test by grinding with abrasive papers of increasing grades, and then by polishing with an oxide alumina suspension.

In order to examine more precisely the hardness of the surface layer itself, the nanohardness was examined using MST CSEMEX hardness-meter. During the test, the load, displacement and side force on a length of 2 mm were measured. Three series of measurements were made for each of the three kinds of surface finishing. The individual measurement series differed in the final diameter of the indentation (with the electro-polished and passivated layers, these diameters were: 50, 100 and 200 nm, whereas with the nitrided layers they were 50, 100, and 360 nm).

3 Results and Discussion

The results of the roughness measurements are shown in Table 3. It can be seen that in the oxidized and nitrided samples the parameter R_a is only slightly higher (0.075 and 0.076, respectlively) than that obtained in the reference samples (0.066). The parameter R_z, also undergoes only small changes. It increases from $R_z = 0.34$ in the sample subjected to electropolishing, to $R_z = 0.47$ in the oxidized and to $R_z = 0.53$ in the nitrided samples. These results have been confirmed by microscopic observations of the sample surfaces. Images of the surface topography are shown in Fig. 3. In the topography of the electro-polished samples are can see well-marked boundaries of grains and twins. Samples subjected to nitriding show a strong heterogeneity of the surface (Fig. 4) which was results for the new phases being formed in the surface layer during the nitriding under plasma conditions. The microphotograph of the oxidized samples shows no observable heterogeneity of the surface.

Table 3: Values of the roughness parameter R_a and R_z measured in the surface modified samples

Samples	R_a	R_z
electropolished	0.066	0.34
oxidized	0.075	0.47
nitrided	0.076	0.53

Table 4: Surface microhardness (HV0,1)

Samples	Mean value	Standard deviation
Electropolished	367	18.7
Oxidized	382	21.9
Plasma nitrided	1525	218

The results of HV0,1 microhardness measurements are shown in Table 4. As can be seen, the values of HV0.1 obtained for the electro-polished and passivated surfaces, which range from 333 to 446, are markedly smaller than those obtained for the nitrided surfaces and the results reveal a small scatter. In the nitrided sample, the values of the microhardness are about 3.5 times higher but their scatter is highly: the microhardness values range from 1050 to 1850 HV. It therefore appears that the surface modification effected by glow discharge assisted nitriding increases significantly the microhardness compared to electro-polishing and chemical passivation, but it results in a significant heterogeneity of the surface layer.

The measured values of the nano-hardness are given in Table 5.

Table 5: Values of the nano-hardness measured in the surface modified samples

	Sample surface								
	Electropolished			passivated chemically			glow discharge nitrided		
Maximum indentation depth [nm]	50	100	200	50	100	200	50	100	360
Mean HV value	97	290	429	229	347	432	513	622	687
Mean E value [GPa]	130	164	204	165	191	200	169	145	165

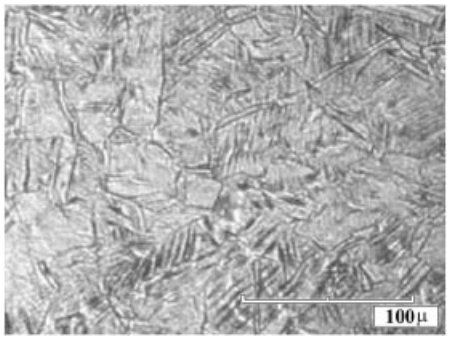


Figure 3: Topography of the reference sample

As can be seen in Table 5, at an indentation depth of 200 nm, the nano-hardness and the Young modulus of the electro-polished and passivated samples are comparable. When the indentation depth was decreased to 50nm, the nanohardness of the passivated surface was doubled and became similar to that measured in the electro-polished one at a depth of 100 nm. The Young modulus of these samples behaves in a similar manner. In the sample with the glow discharge nitrided surface, the nanohardness was considerably higher than that in the other samples, whereas the Young modulus remained at the same level of about 160 GPa. It is worth noting that, in the nitrided sample, the results are widely spread. This can be explained in terms of the heterogeneity of the surface layer.

The effect of the surface modifications on the tribological properties of steel was examined by observing the behaviour of the samples in friction. The friction tests were conducted at various unit loads including extreme loading conditions.

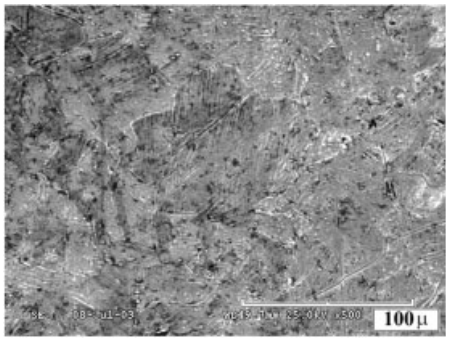


Figure 4: Topography of the nitrided samples

The results of the friction tests were used for calculating the friction coefficients (µ) at the maximum magnitudes of the friction forces, i.e. when the operational conditions are most disadvantageous for the pair in friction. Typical variation curves of µ as a function of time are plotted in Figs. 5, 6 and 7. Figs. 8, 9, and 10 show the wear traces visible on the sample surfaces after the friction test.

As can be seen in these figures, the diagrams obtained for the sample surfaces modified by various methods differ considerably from one another. Nevertheless certain general relationships can be indicated. In the electro-polished samples, the friction coefficient remains almost unchanged during the entire test: it ranges from 0.5 to 0.7 (Fig. 5). It is a high value at which the working conditions of the frictional pair are difficult. This was confirmed by observations of the sample surface after subjecting it to friction (Fig. 8). An analysis of the friction traces suggests that the wear has the adhesive character.

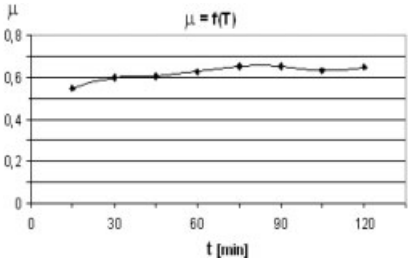


Figure 5: Variation of the friction coefficient µ as a function of time measured on the electro-polished surfaces

The oxide layer formed on the steel surface alters the frictional conditions (Fig. 6). The friction coefficient increases from the value $\mu = 0.45$ at the beginning of the test to $\mu = 0.7$ at its end. The value of μ initially lower than that measured on the electro-polished surface may by taken to be evidence of an advantageous effect of the oxide layer. The increase of μ with increasing friction time may be attributed to the destruction of the thin oxide layer. The slight irregularities of the friction coefficient visible in the diagram may be explained in terms of the alternate formation and destruction of the successive oxide films during the test. The appearance of the surface of

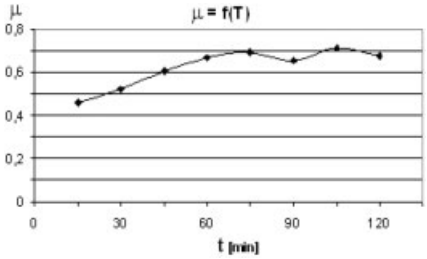


Figure 6: Variation of the friction coefficient μ versus time measured on the passivated surfaces

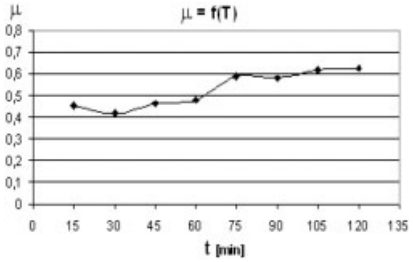


Figure 7: Variation of the friction coefficient μ measured on the nitrided surfaces

the passivated sample after the friction test suggests a significant of loubrication adhesive wear. At a large magnifications, are can also see the traces of frictional wear which occurred as a result of displacements of hard particles of the friction products (Fig. 9).

In the case of the samples subjected to glow discharge assisted nitriding (Fig. 8), the values of the friction coefficient were low at the beginning of the test and increased only after the test lasted for 1 hour. This may suggest that the nitrided layer improves the tribological properties of 316LVM steel. One can see from the images of the friction traces (Fig. 10) that the protective surface layer remains cohesive.

The nitrided samples show decidedly less wear than the electro-polished and passivated samples. After the friction test, the nitrided surfaces were smoothed, and only few traces of frictional wear could be seen on them. We can therefore conclude that the glow discharge assisted nitriding of 316LVM steel improves the friction conditions and increases the frictional wear resistance of the steel.

4 Summary and Conclusions

Our experiments indicate that the samples subjected to glow discharge assisted nitriding have good tribological properties. Taking into account the results of the microscopic observations jointly with the results of the measurements of nano- and micro-hardness, the electro-polished surface seems to be least resistant to a concentrated load. It is however the smoothest (less developed) compared to the surfaces modified by the other methods.

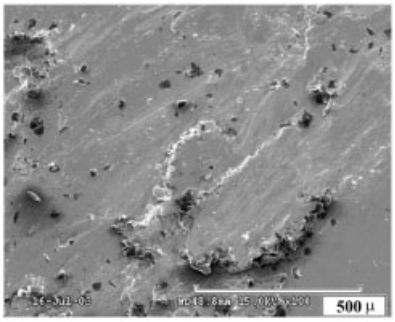


Figure 8: Microphotographs of the friction traces left on the electro-polished sample surface

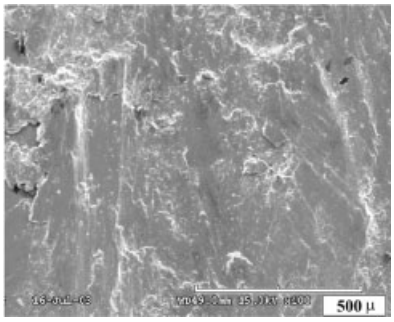


Figure 9: Microphotographs of the frictional wear visible on the passivated sample surface

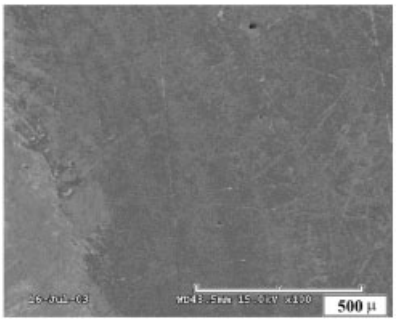


Figure 10: Microphotographs of the frictional wear visible on the nitrided sample surface

The surface modification using glow discharge assisted nitriding improves significantly the tribological properties of the 316LVM steel, by decreasing its friction coefficient and reducing its wear. It should be noted that in all the layers, the scatter of the properties on the surface was significant.

The results obtained in the present study permit believing that it is possible to improve further the properties of the layers produced on the steel medical engineering applications. In particular the properties of the glow discharge nitrided layers are of interest which may be used for the fabrication of short-term implants.

5 Acknowledgements

This work was supported by grants from the Polish Ministry of Science and Higher Education (134/E-365/SPB/COST/KG/DWM68/2005-2008) within the COST 533 Action.

6 References

[1] Wierzchon T., unpubished results, Faculty of Materials Science and Engineering, Warsaw University of Technology

[2] Bedzinski R.; “Biomechanical engineering”, Publishing house of the Wroclaw of technology, 1997

[3] Burakowski T., Wierzchon T.; “Engineering of surface layer”, WNT, Warsaw 1995

[4] Wierzchon T., Michalski J.; Journal of Materials Science, 27, 1992, s. 771–776

[5] Wierzchon T., Ulbin-Pokorska I., Sikorski K., Trojanowski J.; Vacuum 53 (1999), s. 473–479

[6] Büscher R., Gleising B., Dudzinski W., Fischer A.; Wear 257 (2004) 284–291

Tribological Testing on the Steel Hardening with Laser

G. Demian, M. Demian, L. Grecu, V. Grecu
University of Craiova, Craiova

1 Introduction

Using high power laser with continuous emission give the possibility to use some heat treatment technology and the results is the improvement of the mechanical and anticorrosive properties of metallic materials. The attitude of the carbon steel at wear and friction is influenced by the structure and chemical composition. The wear is smaller when the steel has a martensitic structure. After the experimental researches, the martensitic structure of the hardened steels by quenching has a high wear resistance [1], [2].

2 Materials and Methods

The samples are a cylinder (figure 1) and a block with the dimension $17 \times 15 \times 12$ mm. The cylinder sample (2C50 – EURONORM 10083-1) is superficial hardened with high power CO_2 laser in continuous wave. Table 1 shows the chemical composition and the hardness of the cylinder–block samples and figure 2 illustrates the microstructure of the hardened layer.

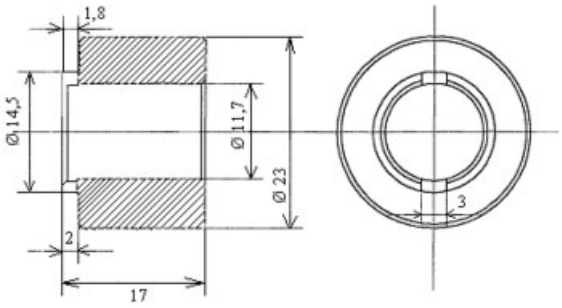


Figure 1: Cylinder sample

Superficial heat treatment with laser was made using a displacement of the sample in the field of the laser radiation.

The results are surface in ring or spiral form with a width approximately equal with diameter of the laser beam 2,4 mm [3], [4].

To obtain a hardened zone in ring form the sample was rotate with 5 mm/s linear speed or 10 mm/s. to obtain a hardened zone in helical form, the sample must make a roto-translation movement.

The sample expose to the laser hardening proceedings was analyzed from microstructural point of view in the initial phase and after the heat treatment with laser beam.

Table 1: Chemical composition and the hardness of the cylinder – block samples

Chemical composition %	C	S	Co	Cr	Cu	Mn	Mo	Ni	P	Si	Sn	hard-ness (HV)
cylinder sample (2C50 EU-RONORM 10083-1)	0,49	-	0,12	0,159	0,223	0,67	0,24	0,16	0,013	0,217	0,015	224
block sample	0,584	0,0304	-	0,069	0,223	1.07	0,011	0,074	0,0203	0,320	0,015	244

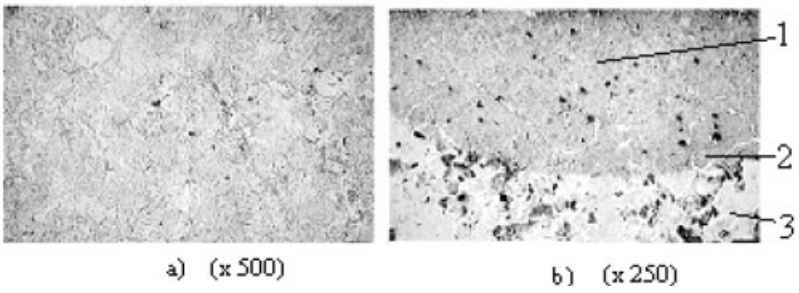


Figure 2: Hardened layer microstructure

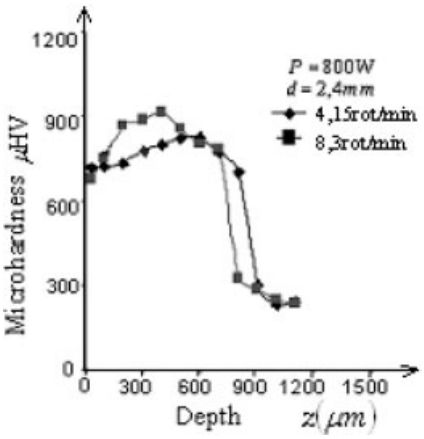


Figure 3: Hardened layer microhardness

In the initial phase the material has a ferrite-pearlite structure and after the heat treatment it is possible to distinguish three zone from the surface to the interior sample: in zone 1 there is a martensitic structural transformation; in the zone 2 it is a ferrite-bainite transformation; in zone 3, beyond the laser radiation depth penetration the structure is untreated and is a ferrite-pearlite

structure. After the laser radiation action, the heating of the superficial layer from the surface of treated material is quickly. The heat energy in the superficial layer is quickly dissipated by conduction in the sample after laser heat treatment. The cooling of the heated zone takes as effect the quenching of material from the treated zone.

The experiment shows that the hardened zone dimension is modified with the speed displacement of the sample in front of the laser beam, power and laser beam diameter.

To determine the microhardness it been used Vickers method on the Leco microhardness and the measurements was made from 100 μm to 100 μm with a 50 g charge and the time penetration was 10 seconds. Microhardeness of the hardened layer, figure 3, it is relative constant on all his depth (approximately 800 μHV), the jump to core are made abruptly.

Table 2: Process parameters

Cylinder Sample (C)	Trace	Translation velocity	frequency	Diameter laser beam	power
C_A	helical	0.57 mm/s	4.15 rot/min	2.4 mm	800 W
C_B	helical	0.72 mm/s	8.3 rot/min	2.4 mm	800 W
C_C	ring		8.3 rot/min	2.4 mm	800 W
C_D	ring		4.15 rot/min	2.4 mm	800 W
C_E			untreated		
C_F			untreated		

3 Friction and Wear Tests

The tribological experiments refer to the qualitative interpretation of cylinder sample hardened with beam laser, samples which were tested for friction and wearing under dry friction [5], [6].

Tribological evaluation was made using as appreciation criteria the friction coefficients and gravimetric wear of each couple element block-cylinder and the wear for each couple block-cylinder (Table 3).

Table 3: Used sample

Nr. Crt.	Block sample (B)	Cylinder sample (C)	treatment	Observations
1	B_1	C_E	untreated	All the surfaces have been rectified at $R_a = 0.4$ μm
2	B_2	C_F	untreated	
3	B_3	C_C	Laser hardening	
4	B_4	C_A	Laser hardening	
5	B_5	C_B	Laser hardening	
6	B_6	C_D	Laser hardening	

A conventional tribometer (Timken) was used for tribological test under dry condition and it allows the determination wear and the friction coefficient for the different couples of materials.

The equipment is shown in fig. 5 and it is consists of the following elements: (1) electrical engine, which transmits the motion to the intermediary shaft (3) through the reducer (2). Through the elastic clutch with a helical spring (5) that is set in the glass-shaped elements (4) and (6), the shaft (3) involves the axle (7) on whose inferior end is the roll (8) attached. The shoe (9), fitted

in a holder (10) witch isn't described in the diagram leans upon the roll (8). The whole system may be introduced into a bath with the tested lubricant inside the thermostat receptacle (11). The charging/loading is done using a level system (12).

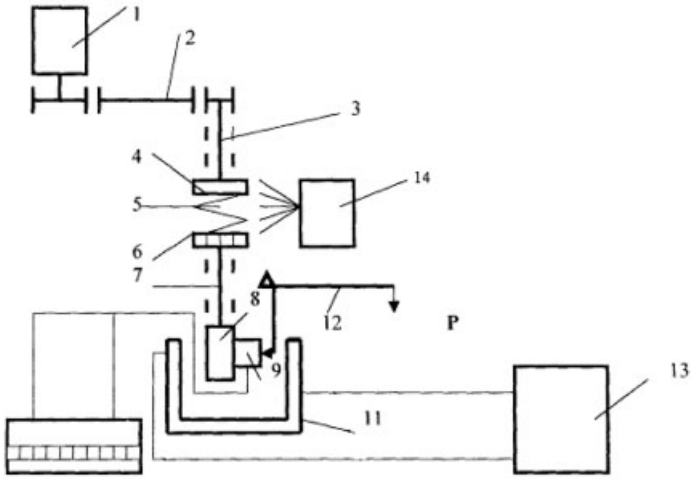


Figure 4: Timken tribometer

The functional parameters: speed of rotation: 1450 rot/min (V=1,65 m/s); dry friction.

All the cylinder and block samples had been cleaned in petrol, dried and weighted with analytic balance with four decimal before the experiments. The tribological tests were accomplished in two stages.

At the firs stage, each couple cylinder- block was set on the installation, it was run in for 5 minutes, and then it functioned for 15 minutes at the loading of 4daN, and the unitary load varying from 220-25 daN to 5 daN.

The cylinders and the blocks were weighed at the end of the test. Its important to know that in the case of the couple cylinder- block (hertzian contact) the unitary load is not constant during the test, the wearing indentation on the block becoming larger and, consequently, the unitary load getting smaller.

The second stage consisted in the running of each friction couple for still three rounds of 15 minutes, so that the whole working time for each couple cylinder- block was an hour.

After each stage of 15 minute the sample were weighed to determine the gravimetric wear

Both at the first stage and at the second one (three 15 minutes resumptions) the working times was one minute, followed by a cooling brake of 5–10 minutes, so that the temperature of the surfaces mustn't exceed 50 °C; the working speed was $\sim$ 1.65 m/sec (1450 rot/min).

4 The Experimental Results

The results of the tests are presented in table 4 which shows that the gravimetric wear corresponding to the first stage of the working friction couples and the average friction factors. Figures 5–10 show the diagrams concerning the progressive wears of each friction couple.

Table 4: The gravimetric wears and the average friction factors after 15 minutes

Nr. Crt.	Materials couple	block wear (g)	cylinder wear, (g)	Friction factor
1	B_1/C_E - untreated	0,0086	0,010	0,55
2	B_2/C_F - untreated	0,0100	0,0181	0,511
3	B_3/C_C-treated	0,0044	0,0081	0,44
4	B_4/C_A-treated	0,0139	0,0020	0,685
5	B_5/C_B - treated	0,0088	0,0071	0,511
6	B_6/C_D-treated	0,0022	0,0071	0,44

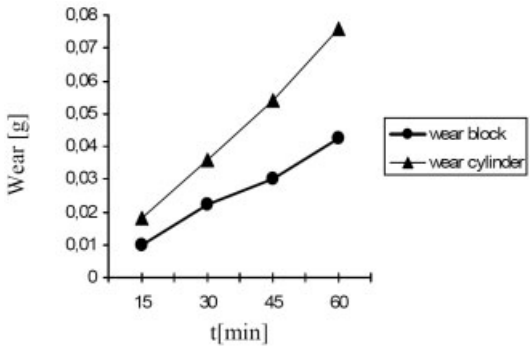


Figure 5: Progressive wear of couple shoe-roll B_1/C_E

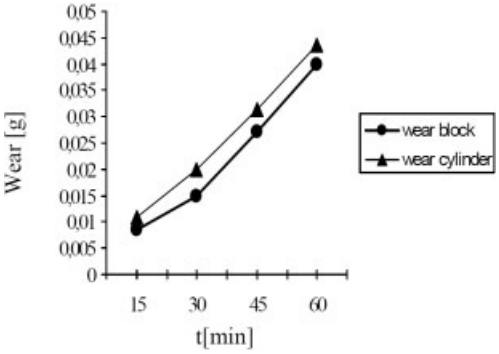


Figure 6: Progressive wear of couple shoe-roll B_2/C_F

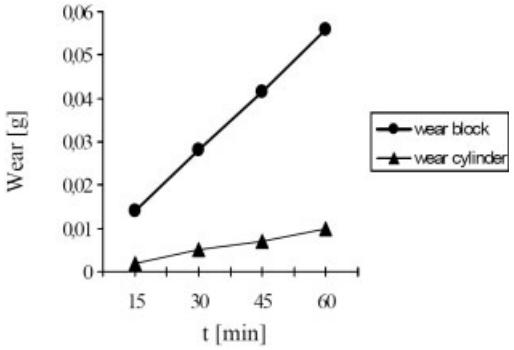


Figure 7: Progressive wear of couple shoe-roll B_3/C_C

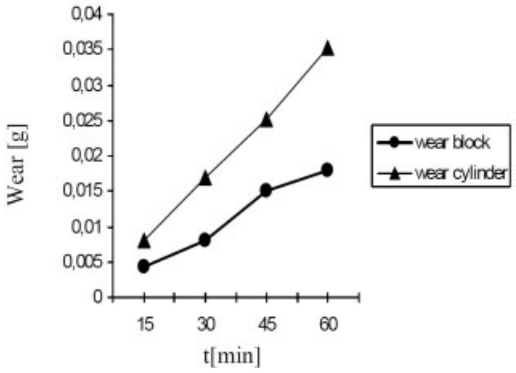


Figure 8: Progressive wear of couple shoe-roll B_4/C_A

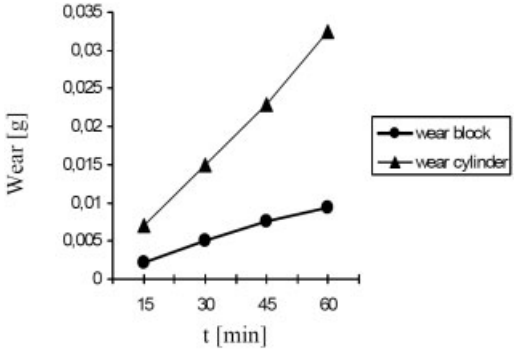


Figure 9: Progressive wear of couple shoe-roll B_5/C_B

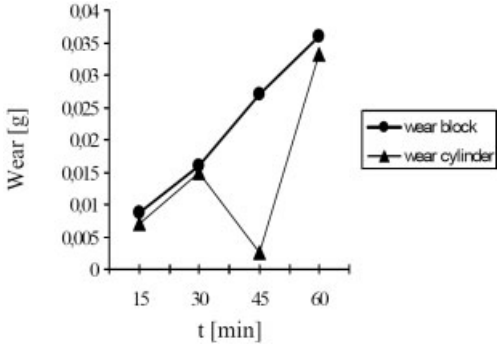


Figure 10: Progressive wear of couple shoe-roll B_6/C_D

From the figure 5 to 10 can be observed that the wear of the cylinder is bigger then block wear in all the cases.

The wear size increase almost linear but the descents are different for block and cylinder.

Materials for the friction couple used at the heat treatment with laser had a wear smaller with 20 %–30 % that the untreated materials.

5 Conclusions

The principal goal of laser surface treatments is to create a hard, strong and wear resistant surface.

Corroborating the data concerning the wear of the tested friction couples and those concerning the friction factors, we can draw up the fallowing conclusions:

- Heat treatment with laser in ring form assure a high wear resistance that the heat treatment in helical form;
- The couples of materials in which the rolls were thermal treated had a tribologic behaviour superior to that of the couples in which the rolls were not treated except couple B_4/C_A (experiment 4) with which the roll wear was very low and the wear of the mating shoe was bigger than in all the other situations;
- Regarding the couples in which the rolls were treated thermal we noticed close wears of the couple B_6/C_D (experiment 6) and of the couple B_3/C_C (experiment 3) as well as equal and constant friction factors along the testing time (0,44);
- If we made a qualitative hierarchy from a tribologic point of view we should situate the couple B_6/C_D (experiment 6) on the first place, fallowed by the couple B_3/C_C (experiment 3), then the couple B_5/C_B (experiment 5) having a bit higher wears and friction factors.

6 References

[1] Steen, W.M. Laser Material processing, Springer-Verlag, 266p, **1991**.

[2] H.W. Bergmann, K. Schutte, E. Schubert and A. Emmel Laser-surface processing of metals and ceramics for industrial applications**,** Applied Surface Science, Volume 86*,* Issues 1–4, February **1995**, p 259–265.

[3] Gabriela Demian, Mihai Demian, Theoretical and experimental study of the heat treatment of steel surface using CO_2 laser, U.P.B. Scientific. Bulletin. Series A, Vol 16, Nr 76–82, **2002**, p. 73–80.

[4] Bach J, Damascheck R, Geissler E, Bergmann H.W. Laser transformation hardening of different steels. In: Bergmann HW and Kupfer R, editors. *Proceedings of the 3*rd *European Conference on Laser Treatment of Materials (ECLAT'90)*; 1990 Sep 17–19; Coburg, Germany: Sprechsaal Publising Group.; **1990**. p. 265–282.

[5] Makarov, A.; Korshunov, L.; Malygina, I.; Osintseva, A. Effect of laser quenching and subsequent heat treatment on the structure and wear resistance of a cemented steel 20KhN3A, The Physics of Metals and Metallography, Volume 103, Number 5, May **2007**, p. 507–518.

[6] Makarov, A.; Korshunov, L.; Malygina, I.; Osintseva, A. Effect of laser quenching and subsequent heat treatment on the structure and wear resistance of a cemented steel 20KhN3A, The Physics of Metals and Metallography, MAIK Nauka/Interperiodica Volume 103, Number 5, May **2007** , p. 507–518.

Hot Direct Extrusion of Abrasion Resistant Fe-base Metal Matrix Composites – Interface Characterization and Mechanical Properties of Co-Extruded Layered Structures

P.A. Silva[1], S. Weber[1], M. Karlsohn[2], A. Röttger[2], W. Theisen[2], W. Reimers[3], A.R. Pyzalla[1]

[1] Max-Planck-Institut für Eisenforschung GmbH, Max-Planck-Str.1, 40237 Düsseldorf, Germany

[2] Institut für Werkstoffe, Ruhr-Universität Bochum, Universitätsstrasse, 44780 Bochum, Germany

[3] Institute of Material Sciences and Technologies, Sekr. BH18, TU Berlin, Ernst-Reuter-Platz 1, 10587 Berlin, Germany

Keywords: hot extrusion, MMC, tool steel, wear resistance, interface microstructure, diffusion

1 Introduction

Materials with high resistance against abrasive wear are of strong interest for many tool applications e.g. in the mining industry. For many purposes the wear resistant material is not necessary or even useful for the whole tool, but only in the near-surface region. Such a layered structure necessitates the cladding of the wear resistant material onto a dissimilar substrate.

A high resistance against abrasive wear has been achieved by the development of metal matrix composites with coarse carbide hard phases [1, 2]. These hard phase reinforced steel composites so far could only be clad onto a steel substrate by hot isostatic pressing [3]. Compared to hot isostatic pressing hot extrusion of the mixture of steel powder and hard phase powder onto a steel substrate appears beneficial with respect to production costs, product size, and versatility. Therefore a novel manufacturing route via direct hot extrusion of bulk steel bars and pre-sintered tool steel powders, partly mixed with hard particles, was developed [4, 5].

The extrusion trials were performed at the Extrusion Research & Development Center of TU Berlin and cylindrical rods consisting of claddings of either steel MMCs with hard phases or tool steel on lower alloyed steel substrates were produced successfully [2].

The aim of this work is a characterization of the microstructures at the interface between the steel substrate cores and the wear resistant coatings using optical and scanning electron microscopy with energy dispersive X-ray analyses and electron backscatter diffraction tools. The results of the investigations reveal that carbon diffusion against the concentration gradient influences the microstructure and mechanical properties, such as hardness and fracture toughness, at the interface region of three different combinations of wear resistant coatings co-extruded with the same steel substrate.

2 Materials and Experiments

A gas-atomized cold work tool steel powder X220CrVMo13-4 (1.2380) and a gas-atomized hot work steel powder X40CrMoV5-1 (1.2344) were selected as metal matrices for the coatings because of their good hardenability and high wear resistance. A hot work steel bar 55NiCrMoV7 (1.2714) with a diameter of 30mm was chosen as the substrate core also due to the good harden-

ability, strength and toughness. The chemical compositions of the metal matrix of the coatings and of the substrate are shown in Table 1.

Table 1: Chemical composition of the coating steel powders and substrate core

Designation		Composition [wt.-%]								
		C	Cr	Mo	V	Mn	Si	Cu	Ni	Fe
1.2380 (*C*)	Coating	2,39	12,56	1,10	3,69	0,37	0,55	-	-	Bal.
1.2344 (*H*)		0,40	5,04	1,34	0,97	0,30	0,19	-	-	
1.2714	Substrate	0,56	1,15	0,46	0,08	0,75	0,29	0,11	1,74	

The three materials combinations investigated are:

- *C+1.2714* where cold work tool steel powder 1.2380, here denominated *C*, is hot extruded on the steel 1.2714 as substrate.
- *HW1+1.2714* stands for the hot work steel 1.2344, H as hot, as coating on the same substrate. *W1* means the addition of 10 vol.% of WC/W_2C (fused tungsten carbides, FTC) particles to the coating.
- *CW1+1.2714*, also extruded with 10 vol. % of WC/W_2C (FTC), is analysed.

The extrusion process and the process parameters of the investigated specimens were described previously [5]. Microstructure examination was carried out using optical microscopy (OM), scanning electron microscopy (SEM) and electron backscatter diffraction (EBSD). The samples were cut parallel to extrusion direction by electro discharge machining (EDM) in order to minimize the influence of cutting on the microstructure. All specimens were ground and polished down to 1µm grade. For OM and SEM the specimens were etched with Nital 4%. For EBSD a final polishing step using colloidal silicon oxide was necessary.

The extruded bar HW1+1.2714 was austenitized at 1050 °C for thirty minutes, quenched in oil to room temperature and afterwards tempered at 570 °C two times for two hours being cooled in air between each step. Specimens C+1.2714 and CW1+1.2714 were austenitized at 1070 °C for thirty minutes, quenched in air to room temperature and afterwards tempered at 520 °C three times for two hours being cooled in air between each step. In order to investigate the effect of the heat treatment (HT) on the diffusion mechanisms, a second austenitizing treatment of eight hours at 1150 °C was carried out on the *C+1.2714* specimen in the as-extruded state. Considering the first two hours of pre-heating before the extrusion process and not considering the annealing time, the heat treatment in this case has 10 hours in total [5]. After the prolonged high temperature heat treatment of C+1.2714, it was hardened and tempered in the same way as described above for the same specimen.

In order to evaluate the bond strength between the substrate and the wear resistant coating, tensile tests with miniaturized specimens were performed at room temperature using a Zwick/Roell Z100 testing machine and a cross-head speed of 0.5 mm/min. For characterizing the mechanical properties at the interface, micro hardness measurements were performed using the Fischerscope H100 equipment with a load of 0.1 N for 20 s. An area of 260 x 130 µm in size, symmetric with respect to the interface region between substrate and coating of the extrudates, was defined and micro hardness was measured with a point distance of 10µm. Due to the small load used in

the measurement, any influence of work hardening was detected with respect to the small point distance used for the indentations. Additionally, Vickers hardness profiles with a load of 0,3 kg (ASTM E 384-99) were determined.

3 Results and Discussion

3.1 Microstructure (LOM/SEM + EBSD)

An overview of an extruded bar is depicted in Fig.1a. The coating thickness is approximately 8mm for all extrudates. Full densification of the steel powders of the coating both with and without hard particles occurred [2, 4]. Microscopy showed that even the FTC hard particles do not seem to harm the densification and the bonding between 1.2380 coating steel and the 1.2714 substrate, even if a WC/W_2C particle is located exactly at the interface region. Further, the interface region between coating and substrate is free of defects, which is a necessity for good bonding between MMC cladding and steel substrate. The steel matrix of the coating *HW1* is almost carbide free (Fig. 1b). Both the matrices of the cold work steel *C* (Fig. 1c) and *CW1* with FTC (Fig. 1d) consist of tempered martensite with embedded globular chromium carbides (M_7C_3) and vanadium carbides (MC). The interface region appears as a band between coating and substrate with an average width of 15–20 µm. Phase boundaries can be recognized and, even at higher magnifications, a defect free interface region could be found.

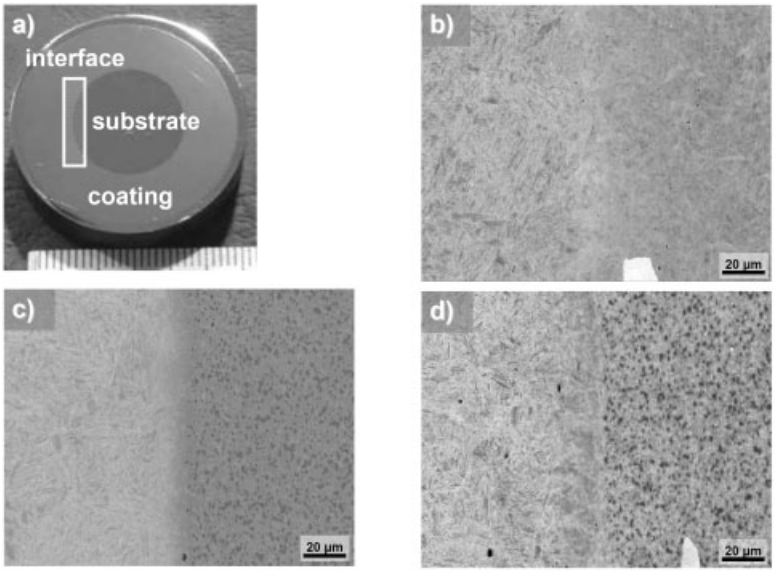


Figure 1: a) macro view of a cross section showing substrate, coating (~ 8 mm thickness) and external capsule. SEM images of the interface region between the substrate steel 1.2714 on the left hand side and the coating steel powders on the right hand side: b) *HW1*, c) *C* and d) *CW1*. The extrusion direction is parallel to the interface region.

In the EBSD image of the combination CW1+1.2714 (Fig. 2) Cr_7C_3 carbides with an average size of 2–2.5 µm can be detected in the metal matrix of the coating. The shape of these Cr_7C_3 carbides varies between ellipsoid and globular. Ellipsoidal Cr_7C_3 appear aligned with respect to the extrusion direction. Beside the Cr_7C_3 carbides a small amount of VC with an average size of 0.8–1.2 µm is dispersed within the martensitic matrix of the coating.

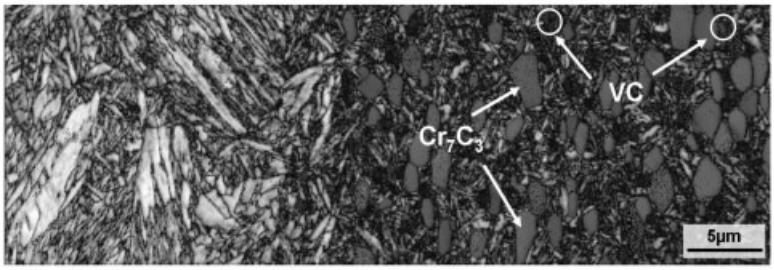


Figure 2: EBSD scan of *CW1+1.2714* showing the α-martensite of the substrate (left hand side) and the matrix of the coating. The coating contains Cr_7C_3 carbide particles (grey) and vanadium carbides as the small and dispersed particles (dark grey). The extrusion direction is parallel to the interface region.

3.2 Mechanical Properties

Yield strength and ultimate tensile strength (UTS) values (Tab. 2) for the three extrudates in the hardened and tempered condition (hot extruded after 2 h at 1150 °C + annealing afterwards) were determined as average values of at least five specimens each. A typical stress versus strain curve of each substrate/coating combination and a sketch of the micro tensile test specimen are shown in Figure 3.

Analyses of the tensile curves (Fig. 3a) reveal that plastic deformation occurs in the substrates of the specimens *C+1.2714* and *CW1+1.2714*. In case of the hot work tool steel coating on *HW1+1.2714* the specimens do not show plastic deformation.

Table 2: Results of the tensile tests (values are an average of five micro tensile tests)

Combination	Yield Strength [MPa]	Ultimate Tensile Strength (UTS) [MPa]	Plastic Strain [%]
HW1+1.2714	—	715 ± 100	—
C+1.2714	810 ± 140	1300 ± 150	3.5
CW1+1.2714	245 ± 5	415 ± 30	˜8

Fracture occurs on the coating side of the specimens close to the interface region in all specimens (Fig. 4). Parts of the coating material remain on the substrate indicating that fracture occurs within the coating in a distance of about 50µm and not right at the interface. This confirms the good bonding between coating and substrate that was indicated by microscopy images of the interface region. The low yield strength and UTS values for CW1+1.2714 cannot be explained yet.

Micro hardness profiles (Fig. 5a) and micro hardness maps (Fig. 5b, 5c) show a decrease of hardness of the substrate in the region near the interface. In contrast to the hardness decrease of

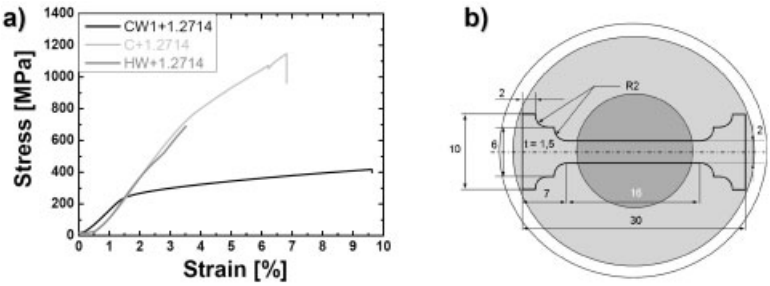


Figure 3: a) Micro tensile test curves and b) sketch of the miniaturized specimens used for the tensile tests.

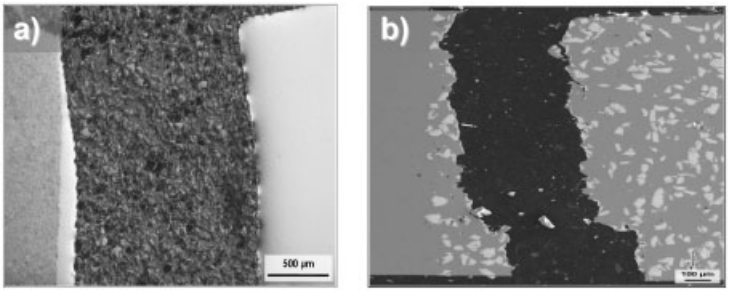


Figure 4: EM image of fractured surface: a) *C+1.2714* and b) *CW1+1.2714*. The coating is located on the right hand side.

the substrate a pronounced increase in hardness appears close to the interface region in the coating in all three different co-extruded material combinations. This peak hardness of the coatings is located between about 25µm and 50µm distance to the interface region. This distance to the interface region corresponds to the area where fracture occurred in the tensile tests.

The micro hardness profile and the micro hardness maps further reveal a softening of the substrate in case of *C+1.2714* and *HW1+1.2714*, but not for *CW1+1.2714*. A carburization of the coating and a decarburization of the substrate are expected due to a difference in the carbon activity for the combination *C+1.2714* [5].

4 Summary and Conclusions

- Wear resistant coatings on steel substrates were manufactured by co-extruding massive tool steel bars and a mixture between tool steel powders and coarse hard particle powders, e.g. fused tungsten carbides;
- Microstructure investigations reveal a macroscopically defect-free interface between tool steel substrates and coating indicating a good bonding between them;

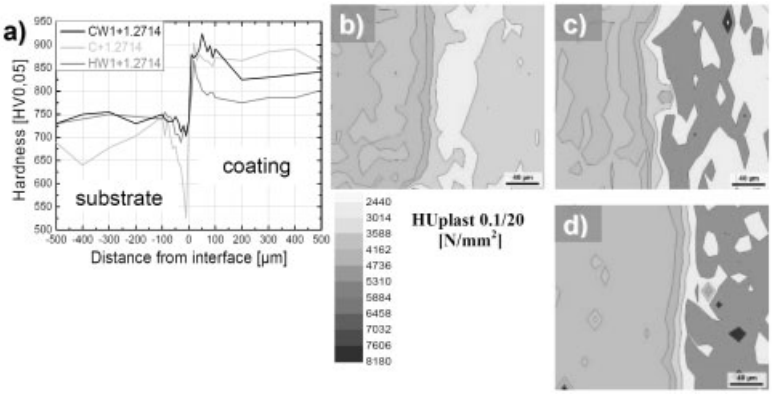


Figure 5: a) Micro hardness profile of the three combinations. Micro hardness maps: b) *HW1+1.2714*, c) *C+1.2714* and d) *CW1+1.2714*. The coating is located on the right hand side.

- While the difference in carbon activity results in softening of the substrate near the interface region the hardness of the coating metal matrix increases near the substrate / coating interface, due to carbon diffusion;
- The mechanical properties of the interface region of the specimens were tested using micro tensile tests. Fracture of the specimens occurred within the hardened region of the coatings.

5 References

[1] W. Theisen, Mat.-Wiss. u. Werkstofftech 2005, 36, 360–364 (in German).

[2] H. Berns, Wear 2003, 254, 47–54.

[3] W. Theisen, Wear 2001, 250, 54–58.

[4] W. Theisen, M. Karlsohn, Wear 2007, 263, 896–904.

[5] P.A. Silva, S. Weber, M. Karlsohn, S. Müller, W. Theisen, W. Reimers, A.R. Pyzalla, Steel Research International 2008 [accepted for publication].

The Role of Admixed Solid Lubricants in Sintered Steels

A. Liersch, H. Danninger, R. Ratzi*
University of Technology Vienna, Institute Of Chemical Technologies and Analytics, A-1060 Vienna, Austria
*MIBA Sinter Austria GmbH, A-4655 Vorchdorf, Austria

1 Introduction

The modern market economy requires materials as innovative products with specific properties such as long life cycle, environmental compatibility, saving of energy and resources. Wear reduction becomes more and more important. Through powder metallurgy, it is possible to combine the different metallic and non-metallic structural materials with lubricating or otherwise wear-lowering materials in order to obtain a technically effective compound [1].

Addition of solid lubricants is a common measure in various types of materials to improve the sliding behaviour, e.g. in case of insufficient hydrodynamic lubrication. Through the PM routes it is easy to manufacture component parts with solid lubricants in the matrix. A large variety of different components (e.g. graphite, hBN, MoS_2, PbS and MnS) can be added to the starting powder mix if these components themselves are available as powders, and due to the very low tendency to segregation, quite even distribution of the additives can be attained [2, 3]. The addition of these compounds has been described in the literature; it showed that most of the sulfides are not stable in a ferrous matrix during sintering, reacting with the matrix, and after cooling a eutectic structure of iron sulfide at the interparticle boundaries remains [4, 5]. This agrees well with literature data for the respective ternary systems [6]. The exception is MnS which remains stable during sintering. Graphite and hBN are chemical compounds with similar structure but BN is chemically more stable [7], in particular in atmospheres containing nitrogen [8]. Also CaF_2 has high stability and does not react with the matrix during sintering; although it is not classical solid lubricant.

Further interesting effects of solid lubricants in sintered steels could be observed during machining of these materials. The additives offered in part considerably improved machinability. Usually, pressed and sintered components are more difficult to machine than their cast and wrought counterparts, but machining is inevitable in many cases. The favourable effect of MnS has been used in practice for a long time, but a positive effect has been reported for hBN as well [9, 10]. Machinability tests are usually carried out by drilling.

The effect of various solid lubricants as e.g. fine and coarse hexagonal BN, MnS, MoS_2 or graphite has been studied and published by the authors in the last years [3, 8, and 11]. In this work the results were compared with addition of CaF_2 which also shows a layered lattice structure. The influence on machinability of PM steels was studied in turning, the quality of the machined surface being used as the criterion.

2 Experimental Procedures

Standard water atomized iron powder ASC 100.29 (Höganäs AB, Sweden) and different amounts (0 – 2 wt%) of fine solid lubricant CaF_2 (<1 µm) and, in parallel, other additives like MnS and MoS_2 for comparison were dry mixed for 60 min in a tumbling mixer. There were no segregation problems except with very coarse hBN and graphite grades (natural MFL, 200 µm/artificial KS75, 200–700 µm/ KS150, >700 µm). 0.5 mass% ethylene bisstearoylamide (Microwax C) was added as pressing lubricant. In part 0.8 wt% natural graphite UF4 (Kropfmühl) was added to study the influence of carbon on these systems.

Compacting was done in a tool with floating die for standard impact test bars with cavity dimension of 55 x 10 mm (ISO 5754) at a pressure of uniformly 600 MPa. The compacts were sintered for 60 minutes in an electrically heated pusher furnace with Mo heating elements (Degussa type "Baby") in flowing hydrogen atmosphere. The carbon-free specimens were embedded in Al_2O_3 granulate; getter boats with Al_2O_3-5 % graphite getter were used for the carbon containing steels to avoid decarburization. All specimens were investigated and tested in the as-sintered state. The samples were characterized by measurements of green and sintered density. Of course a mix with 2.0 % BN or CaF_2 must be regarded to be unsuitable for industrial use but it is well suited as a model material for studying the effects of these solid lubricants. Characterization of the specimens included impact testing, metallographic and fractographic studies. The microstructures were studied on metallographic sections by LOM (light optical microscopy). Dry sliding tests were performed on a pin-on-disc testbed depicted in Figure 1. The counter material was bearing steel 100Cr6 (AISI 52100), heat treated to 62–64 HRC, with freshly ground surface (R_a = 0.2 µm). All tests were done in laboratory air. From these results friction and wear coefficients could be determined. Machining tests were done by finish turning of cylindrical surfaces to 6 mm diameter (feed rate 0.15 mm.rev^{-1}, cut depth 0.1 mm, dry cut, cutting speed about 15 m.min^{-1}). The very low cutting speed was chosen since it had been found that under these unfavourable conditions the effect of machining aids on the surface finish stands out more clearly [11]. The surface roughness – characterized by R_z and R_a values after machining –- was examined by a roughness depth analyzer, and the surface quality was evaluated and described by LOM.

3 Mechanical Properties and Wear Behaviour

The specimen properties are given in Table 1 for the sintered plain Fe based materials and in Table 2 for the materials based on Fe-0.8 % C.

In iron the additives tend to cause shrinkage during sintering except hBN (Table 1). The influence of solid lubricants on impact energy is more significant: the higher the amount the lower the impact energy especially in the case of hBN.

When 0.8 % C is added to these systems (Fe-CaF_2 and Fe-BN) the dimensional changes are decreased compared to carbon free specimens (Table 2). Coarse graphite particles tend to cause swelling (Table 2). Generally with higher carbon the impact energy decreases. This sintering behaviour and the influence on impact energy can be explained by the microstructure. Generally, materials with CaF_2 show higher impact energy than ferrous materials with BN.

Metallographic studies [5] did not show marked effects of CaF_2 and MnS on the microstructure of the Fe- and Fe-C-systems, and the dissolution of graphite in the ferrous matrix is not inhibited. A very homogeneous microstructure was observed after sintering of Fe-CaF_2/MnS and Fe-C-

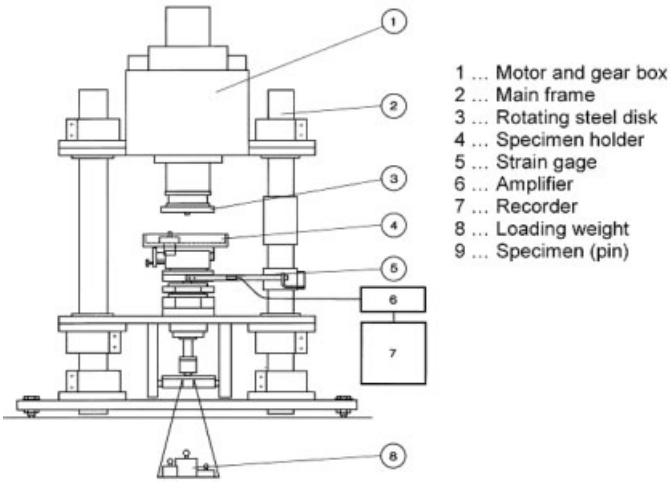


Figure 1: Pin-on-disc wear test bed used in dry run.

Table 1: Properties of PM plain Fe containing different additives. Compacted 600 MPa, sintered for 60 min

Matrix	Additive Content [wt%]	T_{sint} [°C]	Atmosphere	Green Density [$g \cdot cm^{-3}$]	Sintered density [$g \cdot cm^{-3}$]	Dim. Change [%lin]	Impact energy [$J \cdot cm^{-2}$]
Fe	0,0	1120	H_2	7,12	7,26	-0,24	>31,4
Fe-CaF_2	0,5	1120	H_2	7,13	7,17	-0,13	25,5
	2,0	1120	H_2	6,89	6,99	–0,18	11,8
Fe-BN	0,5	1120	H_2	7,07	7,04	0,10	9,2
	2,0	1120	H_2	6,84	6,85	0,06	2,0
Fe-MnS	0,5	1120	H_2	7,16	7,21	–0,12	>26,8
	2,0	1120	H_2	7,07	7,11	–0,17	11,6
Fe-MoS_2	2,0	1120	H_2	7,03	7,06	–0,11	18,3

CaF_2/MnS at 1120°C, consisting of ferrite or pearlite and the solid lubricant particles, which can be found at the grain boundaries. hBN in contrast inhibits the formation of stable metallic bridges and also the dissolution of graphite in the ferrous matrix during sintering [8]; MoS_2 decomposes during sintering, and a Fe-S eutectic is formed and Mo is dissolved in the matrix. When coarse graphite (MFL or KS) is used as lubricant in an Fe-C-system sintered at 1070°C, it is only dissolved at the iron graphite particle interface and here, a huge amount of Fe_3C is formed.

The remaining carbon is apparently still contained as graphite – in a pearlitic matrix – that, if present in the pressing contacts, further lowers the interparticle strength, as also does hBN [11].

Based on the results of the metallographic studies, wear tests have been done on various sintered steel specimens with admixed CaF_2 and compared with the results of Fe-BN, -MoS_2 and -Graphite (Figure 2). Since it had been shown that MoS_2 decomposes during sintering and thus

Table 2: Properties of PM Fe-0.8%C containing different additives. Compacted 600 MPa, sintered for 60 min

Matrix	Additive Content [wt%]	T_{sint} [°C]	Atmosphere	Green Density [$g \cdot cm^{-3}$]	Sintered density [$g \cdot cm^{-3}$]	Dim. Change [%lin]	Impact energy [$J \cdot cm^{-2}$]
Fe-C	0,0	1120	H_2	7,05	7,03	–0,10	11,7
Fe-C-CaF_2	0,5	1120	H_2	7,09	7,10	–0,09	8,5
	2,0	1120	H_2	6,78	6,85	–0,07	3,8
Fe-C-BN	0,5	1120	H_2	6,95	7,01	–0,05	6,1
	2,0	1120	H_2	6,73	6,70	0,23	1,8
Fe-C-MFL*	0,5	1070	H_2	7,15	7,02	0,09	6,2
	2,0	1070	H_2	6,89	6,77	0,23	4,7
Fe-C-KS150*	0,5	1070	H_2	7,04	6,93	0,23	3,1
	2,0	1070	H_2	6,74	6,42	0,79	1,9
Fe-C-KS75*	0,5	1070	H_2	7,10	6,97	0,2	3,9
	2,0	1070	H_2	6,86	6,69	0,57	1,0

*From graphite, both natural MFL and artificial KS grades were tested. MFL and KS75 are much finer than KS150

cannot be regarded as lubricating additive any more, the wear and friction behaviour is nearly the same as that of plain iron. Wear tests were thus concentrated on the more stable additives such as graphite and CaF_2. The friction and wear coefficients are given in Figure 2. 2.0 % CaF_2 improves wear and friction in plain Fe slightly, but not in the Fe-0.8 % C material. Additives of MFL and KS have no influence on the wear behaviour of Fe-0.8 % C except KS75, which decreases K_c and μ. hBN shows the highest wear and friction coefficient, i.e. the wear behaviour is deteriorated.

In summary, none of the additives caused significant improvement of the wear behaviour.

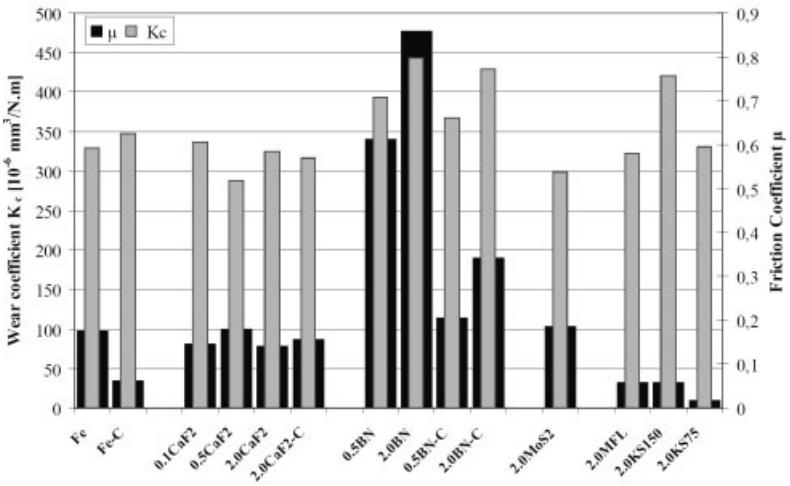


Figure 2: Wear and friction coefficients for Fe-x%solid lubricants-(0,8%C), sintered 60 min at 1120 °C (containing MFL,KS150 and 75 at 1070 °C) in H_2, pin-on-disk test against 100Cr6, 60 N, 0.5 m/s

4 Machinability

The investigated solid lubricants in sintered steels are apparently unfavourable for the wear resistance, but the machinability can be improved strongly. A special case was the addition of MnS powder into PM steel components that are to be machined after sintering [12]. Here, the machinability tests were done for MnS, graphite and CaF_2 (Figure 3 and 4). It can be shown that the roughness R_a of the machined surfaces was significantly lowered by addition of MnS and also by CaF_2. MnS yields low roughness values and is quite effective. CaF_2 also strongly improves the machinability of sintered steels. Above all the Fe-C-steels showed lower roughness values than Fe based grades and higher CaF_2 content gave an additional improvement of surface quality. The sintered Fe materials containing 0,5 % CaF_2 yield similar results as MnS, as given in Figure 3; but it cannot be stated definitely if it is caused through the tool lubricating effect (cutting effect) or chip breaking effect.

Summarising, a very homogeneous microstructure and distribution of the CaF_2 lubricant in the Fe and Fe-C matrix has a strongly positive influence on the machinability.

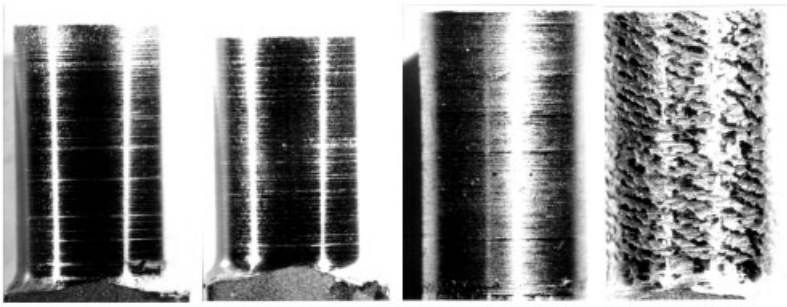


Figure 3: Machined surfaces of sintered Fe containing admixed solid lubricants, sintered 60 min at 1120 °C in H_2. Finish turning, hardmetal insert P20, $v_c = 15$ m/min, 0.15 mm/rev

5 Conclusions

Compared to other admixed solid lubricants such as many sulfides, fine CaF_2 only marginally affects the sintering responses, being thermodynamically stable during sintering under standard conditions. The adverse effect on the mechanical properties is much lower than e.g. with hBN. Wear and friction coefficients are not very different compared to plain Fe or Fe-C, i.e. CaF_2 is not a true "solid lubricant". However, it significantly improves the machinability of PM iron and steels in turning, resulting in significantly better surface finish, even superior to that obtained with the common machining aid MnS.

The experiments with admixed CaF_2 have shown that CaF_2 in PM steels is more evenly distributed in the matrix than the hygroscopic MnS, and already the machined surface is smoother at lower CaF_2 concentrations and therefore the machining behaviour is improved.

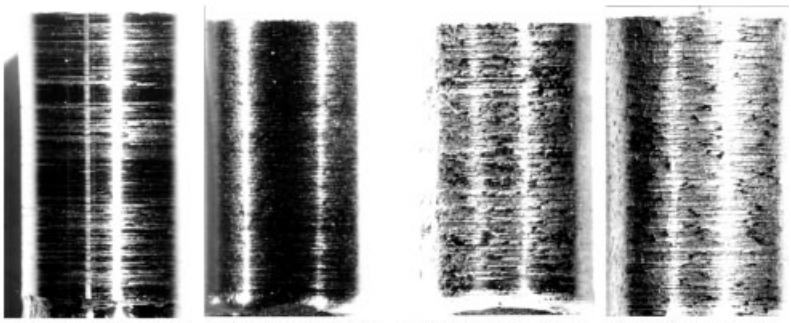


Figure 4: Machined surfaces of sintered Fe-0.8%C-x%solid lubricants, sintered 60 min at 1120 °C (containing MFL at 1070 °C) in H_2. Finish turning, hardmetal insert P20, $v_c = 15$ m/min, 0.15 mm/rev

6 Acknowledgement

The authors wish to thank BBU Chemie, now Chemetall GmbH, Arnoldstein, Austria, for supplying part of the solid lubricants used, and Dr. A. Šalak and Dr. M. Selecká, Košice, for helpful discussions.

7 References

[1] W.J. Huppmann, Ing.-Werkstoffe, 1989, 5-6, 38–42.

[2] ASM Handbook, Powder Metal Technologies & Applications, ASM, Materials Park OH, 1998, 7.

[3] H. Danninger, A. Liersch, R. Ratzi, Proceedings of 2000 Powder Metallurgy World Congress, Kyoto. Part 2.Eds. K. Kosuge, H. Nagai. The Japan Soc. Of Powder and Powder Metall., 2001, p. 1108.

[4] S. Strobl, Diploma Thesis, TU Wien, 1992.

[5] A. Liersch, Doctoral Thesis, TU Vienna, 1994.

[6] V. Raghavan, V.; in: Phase Diagrams of Iron Ternary Alloys, Part II, The Indian Inst. Of Metals, Calcutta, 1988.

[7] Handbook of Chemistry and Physics, 67th Ed., CRC Press, Boca Raton, 1987.

[8] A. Liersch, H. Danninger, C. Gierl, R. Ratzi, Powder Metall. Progress, 2007, 7, Part1.

[9] M. Gagne, Adv. Powder Metall. 1989; Gasbarre TG, Jandeska WF eds., MPIF, Princeton NJ, 1989, 1, p. 365.

[10] M. Gagne, M. Gaumont, G. Olschewski, Materials and Processing Trends for PM Components in Transportation, Proc. EuroPM2000 Munich, EPMA, Shrewsbury, 2000, 25.

[11] A. Liersch, H. Danninger, R. Ratzi, Powder Metall. Progress 4, 2004, 4, p. 192.

[12] U. Engström, Powder Metall., 1983, 26, p.137.

Investigations of Wear Mechanisms in Diamond Tools with Fe-Based Matrices Reinforced with WC-Co Particles

J. Garcia[1], S. Weber[1], A. Kostka[1], A. Pyzalla[1], L.F. Garcia[2], A. Lammer[2]
[1] Max-Planck-Institut für Eisenforschung GmbH, Düsseldorf , 40237, Germany
[2] Hilti Corporation, Schaan, 9494, Liechtenstein

1 Introduction

Diamond segments have widely been used in the construction industry for drilling and sawing in concrete and reinforced concrete, enabling to do the job fast, accurate and at relative low costs [1]. The standard production technology consists in mixing diamond particles and metallic powders and to consolidate the cutting elements in a hot-pressing system. The diamond is the cutting element which destructs and removes the work piece material, its grain size and wear rate has to be adjusted to the cutting rate of the cutting system. The matrix is the supporting material which holds the diamonds in place. It consists of various metals and its wear rate has to be adjusted to the cutting rate of the cutting system. Different combinations of elements in the Fe-Cu-Co system are been used to adjust the desired wear resistance depending mainly on the tool power, diamond concentration and concrete base-material [2].

Commercial and environmental reasons have driven the partial substitution of Co by Fe and other elements. Difficulties arise since Fe-rich matrices exhibit lower wear resistance in this application [3]. The objective of this research was to establish a wear test configuration that enables a direct comparison with the wear of the diamond segments during drilling. Another main purpose of this work was to characterize the wear and the physical and structural properties of a Fe/Cu-based bonding system reinforced with granules of cemented WC-Co. A good correlation of the wear tests and core drilling performance in a C35 strength limestone-quartz mixed aggregate concrete was observed.

2 Experimental

2.1 Specimens Preparation

Diamond-free samples were prepared from metallic powders and consolidated in a hot-press using conventional sintering parameters. Standard Fe, Co and Cu powders were used. The reinforcement particles were 88WC-12Co produced by H.C. Starck with an average grain size of 45 μm ± 15 μm. Samples with the base composition around 47Fe-47Cu-6Co and with additions of 2.5, 5, 10 and 20 vol% of the WC-Co reinforcement particles were prepared. Additionally, pure Co specimens were consolidated as reference. All samples had dimensions of $30 \times 15 \times 4.5$ mm.

2.2 Wear Tests

A three-body abrasive wheel test apparatus as of Figure 1 was used for determining the wear rate of samples. As abrasive SiO_2 particles from EUROQUARZ GmbH of different grain-size were

used (5, 29, 41, 47 and 114 microns of average particle size). A water-slurry with 25vol% SiO_2 was used for the tests. This abrasive concentration and the particle size were selected according to measurements of core bits perforating reinforced concrete of class C35 strength. The average removed particle size of a C35 class concrete was around 10 microns. The wear resistance was defined and calculated according to [2] using the equation (1). The normal force between sample and wheel was controlled and kept constant at 50 N. The samples were placed in the apparatus and tested a fixed amount of time in order to cover a sliding distance of around 2000 m.

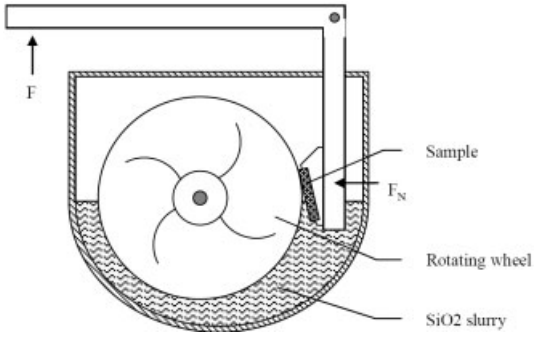


Figure 1: Schematic representation of the three-body-abrasive-wheel-test apparatus

2.3 Microstructure Characterization

The microstructure of the sintered segments was investigated by SEM using a Jeol SEM JSM-6490. Micro-hardness tests were carried out with a load of 50 gr. The matrix-diamond interface and the worn matrix were investigated by TEM. The sample preparation for TEM analysis was carried out with Focus Ion Beam (FIB JEM-9320FIB).

3 Results

By using the arrangement described in section 2.2, the specific-wear-resistance in J/mm3 was determined and used as a comparison index.

3.1 Effect of WC-Co Concentration and Abrasive SiO_2 Acting Particles

In Figure 2 the results for the specific wear resistance of samples containing 2.5, 5, 10 and 20vol% WC-Co to the base 46Fe-46Cu-6Co for the different SiO_2 particle diameters are presented. The wear resistance increases with the WC-Co reinforcement for all SiO_2 grain-sizes. A second observation of Figure 2 is that for increased vol% of WC-Co particles, the slope of the lines describing the relation increases. This means that by increasing the WC-Co amount the alloys become more sensitive to the grain size of the acting SiO_2 particles on the system. The implication in field operations of these results is that core-bits with diamond segments which have high WC-Co additions would tend to be less-universal as base compositions without reinforcement.

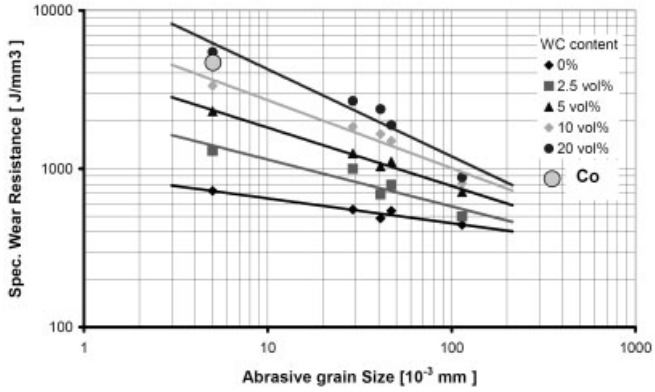


Figure 2: The specific wear resistance of a 46Fe-46Cu-6Co matrix with different WC-Co additions [3].

3.2 Correlation with Drilling Operations

Drilling tests were performed in C35-strength concrete with a 2.6 kW drilling tool. The core-bits used were of diameter 202 mm with 16 segments and diamonds with a US mesh 40/50. The specific tool-life, defined as the drilled metres per mm of segment worn-down is shown in Figure 3. The specific tool life for the 46Fe-46Cu-6Co composition and the same composition reinforced with 5vol%WC is summarised. A factor of 2 in specific life-time can be observed which correlates with a factor of 2 in specific wear-resistance for SiO_2 particles of 10 microns grain-size (see Figure 2).

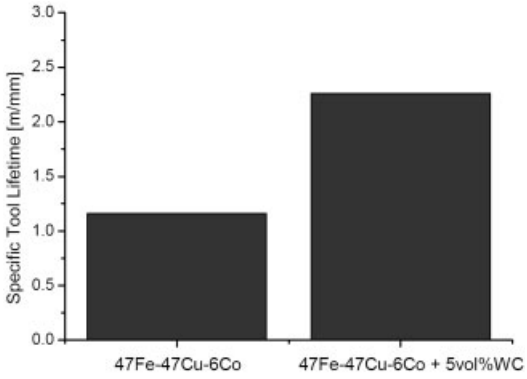


Figure 3: The specific tool life time of a 47Fe-47Cu-6Co matrix with and without reinforcement. Results are average for 5 core-bits for each composition.

3.3 Microstructure Characterization

In Figure 4 an overview of the TEM lamella interface between the diamond and the metallic matrix is shown. The TEM investigation revealed a good interface bonding between the Fe-Cu-Co matrix and the diamond particles; free of pores and without the presence of intermediate layers. Small steps on the diamond part are visible (arrows). The TEM image of the metal matrix (Figure 5) presents a bad bright-field contrast due to an extremely high density of dislocations.The diffraction pattern shows a distortion of the diffraction reflections, confirming also a high density of defects. This may be associated with a strain hardening effect.

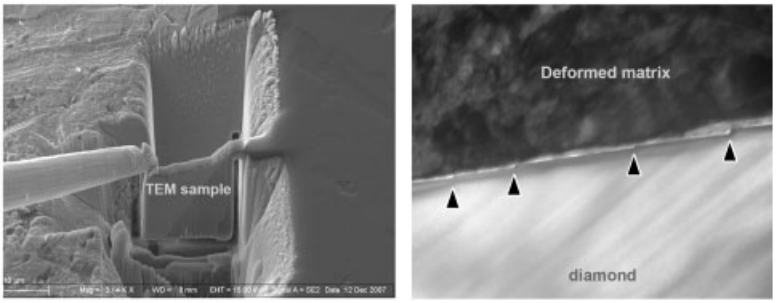


Figure 4: Details of TEM sample preparation with FIB method (left) and interface matrix-diamond (right).

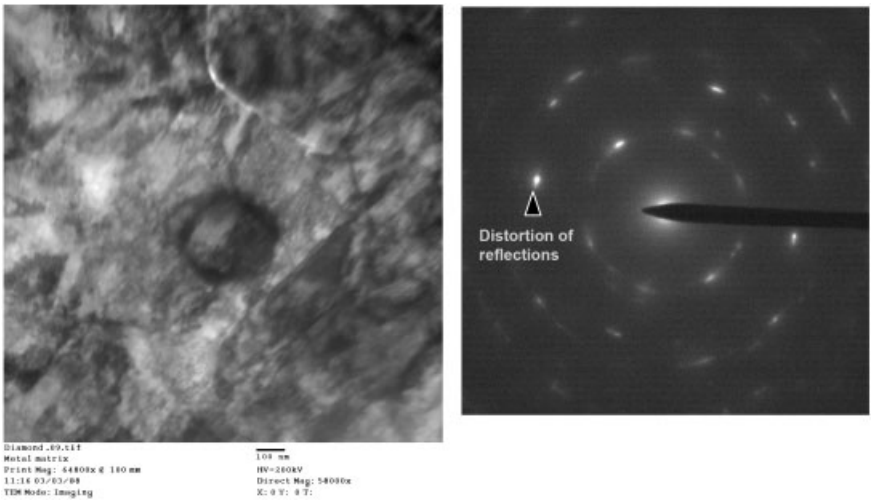


Figure 5: TEM image of the Fe-Cu-Co matrix (left) and diffraction pattern (right) showing a high density of dislocations and hence a high deformation of the matrix.

4 Conclusions

The index-value of J/mm3 of the three-body abrasive wheel test can be used for indexing different matrix systems. Different concentrations of the slurry and particle diameters (corresponding to the drilled concrete) can simulate real world drilling conditions. A good correlation between wear and application testing has been established.

By using a 46Fe-46Cu-6Co base alloy with additions of WC particles, it is possible to achieve the same wear resistance as for pure cobalt in this application. The wear resistance of the hard metal reinforced metal matrix depended strongly on the SiO_2 particle size. The higher abrasion resistance is accompanied by less application universality in terms of SiO_2 particle size.

TEM investigations of the matrix-diamond boundary revealed a good interface free of pores or intermediate layers. The metal matrix is very deformed presenting a high density of defects, as revealed by the TEM image and the associated diffraction pattern.

5 References

[1] Konstanty J., Powder Metallurgy Diamond Tools, **2005** Elsevier, ISBN 1-85617-440-9

[2] Fleischer G.; Bosse H., “Berechnung der Reibung auf energetischer Grundlage”. In: Wissenschaftliche Zeitung der TU Magdeburg 26, **1982**, Nr. 6, S. 17–27

[3] Garcia L.F.; Garcia J.; Kostka A.; Weber S.; Lammer A., Wear behaviour of Cu-Fe-Co diamond tool bonding matrices reinforced with hardmetal granules, Int. Conference on the Science of Hard Mat., Montego Bay, Jamaica, **2008**, 10–14th March.

Tribocorrosion Study of 316L Stainless Steel and TA6V4 Alloy in Various Electrolytes

P. Henry, J. Takadoum, P. Berçot
MINAMAS-MN2S-Institut FEMTO-ST-ENSMM.
26,Chemin de l'épitaphe, 25030 Besançon cedex, France.

Abstract

Tribocorrosion phenomena involve mechanical and chemical/electrochemical interactions between surfaces in relative motion in the presence of a corrosive environment. The objective of this work is to study the tribocorrosion phenomena of stainless steel 316L and titanium alloy TA6V4 when sliding against a polycrystalline alumina ball in two different corrosive electrolytes: sulphuric acid 0.5 $mol \cdot L^{-1}$ and 0.9 % sodium chloride aqueous solution. These alloys naturally form a thin passive film which prevents from the corrosion process. Nevertheless, this film can be destroyed by the action of a counter-part rubbing on it. Thus, a competition between repassivation kinetics and the sliding speed takes place and control the material removal rate. The specimens have been studied under cathodic, free and anodic electrochemical applied potentials. Friction coefficient, wear rate and the current density were measured and the obtained results were correlated to passivation kinetics.
Keywords: Tribocorrosion; Electrochemistry; Repassivation kinetics; Wear rate; Stainless steel; Titanium alloy.

1 Introduction

Tribocorrosion is the deterioration of a tribological contact resulting from simultaneous metal removal by mechanical wear and by the action of chemical or electrochemical oxidation. The different mechanisms of tribocorrosion are not entirely understood yet, as they involve properties of contacting material surfaces, mechanics of the contact and corrosion conditions. Tribocorrosion causes a greater material loss than the addition the mechanical and the chemical damages when the two processes act independently. During tribocorrosion tests, on one hand, corrosion is accelerated by the rubbing, and on the other hand, wear can also be accelerated by the corrosion effect. This synergistic effect of the two contributions is responsible of the major part of the final wear, but is still approximately quantified.

Tribocorrosion phenomena can be found in various technological domains where they cause important damage to systems. On the other hand, tribocorrosion can be put to good use, like in chemo-mechanical polishing.

In the present work, tribocorrosion phenomena of 316L stainless steel and titanium alloy TA6V4 sliding against an alumina ball in two different corrosive environments (sulphuric acid H_2SO_4 0.5 mol.L-1 or 0.9%wt NaCl aqueous solution) have been investigated by measuring the coefficients of friction, the electrochemical responses and the total metal losses. The general idea was first to simulate the tribological behaviour of the two materials used in a hip prothesis, held in

a physiologic liquid such as Ringer's solution. The concentration of NaCl was chosen as it is used in Ringer's solution. The tribocorrosion study was then enlarged to a study of the tribological behaviour of these materials immersed in sulphuric acid, another conducting solution.

Results have been discussed taking into account the influence of the electrochemical applied potential and the depassivation/repassivation kinetics of materials.

2 Experimental Procedure

2.1 Materials

Tribocorrosion tests have been carried out using two different alloys:

- Austenitic stainless steel 316L.
- Titanium alloy TA6V4.

Two corrosive solutions have been used:

- Sulfuric acid H_2SO_4 of 0.5mol.L^{-1} concentration
- NaCl 0.9%wt aqueous solution, a concentration close to the one in Ringer's solution.

Samples are disks of 25 mm in diameter and 5 mm thick. They are polished thanks to grinding paper from grade 120 down to grade 1000, then diamond solution from 15 µm down to 1 µm. In order to limit the active surface area face to the reactive solution, an adhesive film is applied to the sample surface so that only a surface of 0.4 cm² is in contact with the corrosive environment.

A polycrystalline alumina ball of 5 mm diameter is loaded on the sample surface under a weight of 5 N. Thus, maximum Hertz pressures of 1466 Mpa for 316L and 1109 Mpa for TA6V4 are obtained.

These values of Hertz pressures are well correlated to values found in literature like those employed by Favero[1], Spriano[2] and Berradja[3].

2.2 Equipment and Procedure

2.2.1 Specific Tribometer

Tribocorrosion experiments have been carried out at room temperature using a specific alternative ball on disk tribometer coupled to an electrochemical cell presented in [4]. The tank and the ball holder are made of PTFE so that no electrochemical interference may happen during the tests. The electrochemical cell is composed of three different electrodes, a work electrode, the sample, a platinum counter-electrode and a reference electrode, saturated mercury sulphate (MSE, +658 mV vs. SHE) when tests in H_2SO_4, and saturated calomel (SCE, +241 mV vs. SHE) when tests in NaCl.

Friction tests have been run with a reciprocating motion at three different frequencies: 1.2 Hz, 0.6 Hz or 0.9 Hz. The effective rubbing duration is 100 minutes. Before and after rubbing, a phase of 10 minutes without any friction is applied to measure the current evolution. Tangential force is recorded in order to determine the coefficient of friction. Electrochemical potentials are controlled thanks to a PGP201 potentiostat and Voltamaster software.

2.2.2 Experimentation

In order to identify the different electrochemical domains related to the used alloys, potentiodynamic polarisations at a rate of 1 mV/sec from –1300 mV to 2000 mV versus the appropriate reference electrode have been carried out. Three electrochemical potentials, cathodic potential, free potential and anodic potential have then been applied in order to quantify the influence of a specific electrochemical potential on the coefficient of friction and the total wear generated.

During the whole duration of the test, the coefficient of friction is recorded. Two kinds of test are possible. In the cathodic or anodic domain, the specific electrochemical potential is applied, and the corresponding current density is recorded. The other one is related to the evolution of the free potential with rubbing. No potential is then applied, only the evolution of the open-circuit potential is recorded.

The used protocol is described as follows:

- The sample is immersed in the corrosive solution during a few minutes until the stabilization of the free potential.
- An electrochemical potential is applied and the current density starts to be recorded (10 min).
- Sliding motion is initiated and the coefficient of friction is recorded (100 min).
- Rubbing is stopped, as the current density is still recorded (10 min).

3 Results and Discussion

3.1 Influence of Mechanical Parameters on the Current Evolution

The most significant change in the current density during tribocorrosion tests occurs when an anodic potential is applied. The main mechanical criterion in tribocorrosion tests is the applied load. Its influence will then be seen by the destruction of the passive film formed on the sample's surface. Several tests, as can be seen on figure 1, under loads from 0 N to 5 N show a difference in the jump of current as the ball starts running over the sample surface. Table 1 gathers the different applied loads and the corresponding maximum Hertz pressures related to the used materials. For the smaller loads, the current density remains quite stable and low during the test, as it is much higher and continuously increases with time for a higher load (5 N).

Table 1: Maximum Hertz pressure values in MPa for both materials under different applied loads.

	0.5 N	1 N	5 N
316L	680	857	1466
TA6V4	515	648	1109

It is understood as the passive film covering the surface is only partly destroyed so the current is less important in order to rebuild the passive film. Under a 5 N load, the current density raises with time, which shows that the entire passive film is removed and the wear track surface increases due to long period of rubbing.

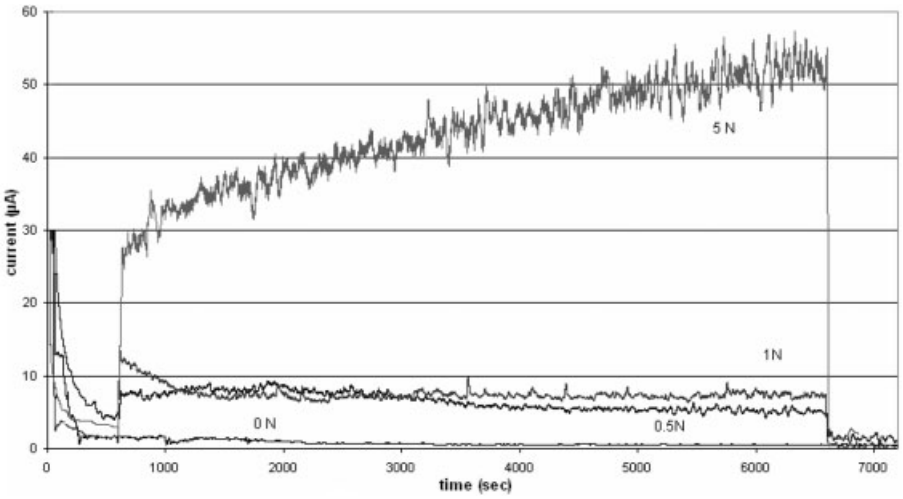


Figure 1: Current densities of 316L with the applied load in the passive domain, in H_2SO_4 0.5M solution, with 1.2 Hz frequency of rubbing.

From this result, tribocorrosion tests will be performed under a 5 N load, in order to provide an entire passive film breakdown.

Another influent mechanical factor is the frequency of rubbing of the alumina ball in contact with the alloys. In order to investigate the material's repassivation kinetic during friction, the three different frequencies of rubbing have been compared. As it can be seen on figure 2, the current density of the tribocorrosion tests increases with the frequency of rubbing which shows that for lower frequencies, the alloy surface has the sufficient time to repassivate between two successive strokes of the ball. We also note that the lower the frequency of rubbing, the lower the average current on the whole track surface.

3.2 Influence of Friction on the Electrochemical Behaviour

During tribocorrosion tests, the samples were first held for 10 minutes in the cathodic, free or anodic potential and then submitted to friction. The rubbing duration was 100 minutes followed by a 10 minute phase, where samples were held again at the same potential.

3.2.1 Cathodic Potential

In H_2SO_4 solution, the evolution of the current density suffers no change with the starting of rubbing for both materials. On the contrary, in NaCl media, alloy's behaviour changes. Thus, 316L and TA6V4 will show a current density drop, which could prove the presence of a film on the alloy surface, which is destroyed as rubbing starts. Therefore, current density tends to recover its original value once rubbing stops, as it can be seen on figures 3-a and 3-b.

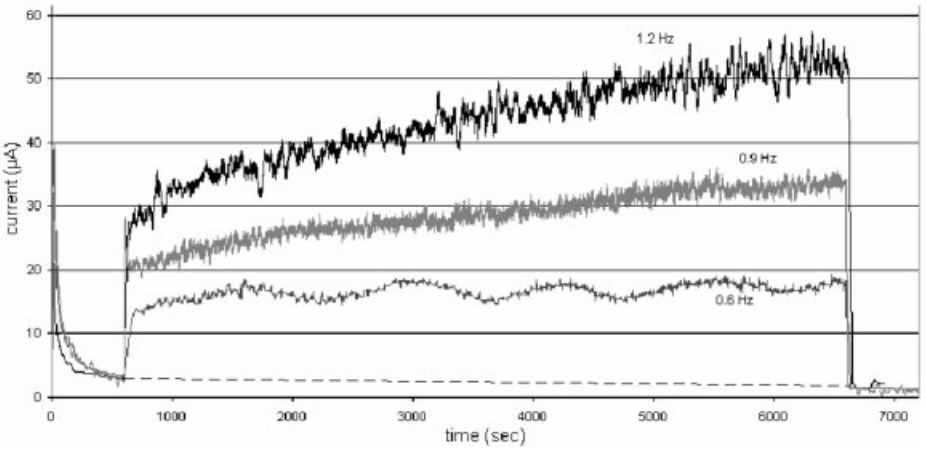


Figure 2: Current densities of 316L steel with the frequencies of rubbing in passive domain, in H_2SO_4 0.5M solution, 5 N load.

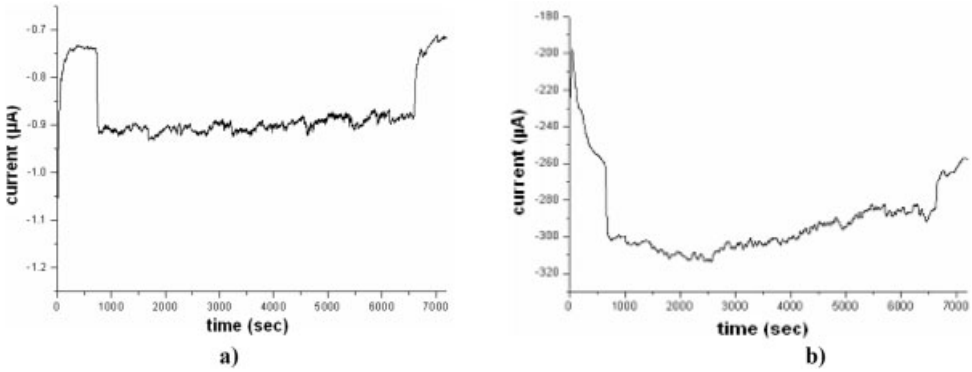


Figure 3: Current densities of a) 316L, b) TA6V4 in cathodic domain at –1300 mV/SCE, in NaCl 0.9% wt solution, with 1.2 Hz frequency of rubbing, 5 N load.

3.2.2 Free Potential

Behaviours of 316L and TA6V4 are really close for both solutions. They show a cathodic drop due to the film breakdown, as can be seen on figures 4-a and 4-b, which causes the presence of a galvanic couple as described by Berradja [5], Kok [6] and Benea [7]. It can be explained with an electrochemical point of view as did Favero [1]. Free potential results from a galvanic current between depassivated surface and the surface staying at a passive state. Even though the current value I equals 0, there is an exchange of current between the depassivated surface (oxidation current, I_t anode) and the passive surface (reduction current I_p cathode) with $I_t + I_p = I$. On the bare metal surface, several anodic and cathodic reactions take place:

- An anodic oxidation of steel, iron and chromium, which causes a kind of parallel challenge between alloy dissolution and passive film restoration.
- A cathodic reduction of dissolved oxygen and reduction of hydrogen, which will be able to diffuse into the superficial layers of the alloy and then cause a surface embrittlement.

  The passive films which form on the alloys' surfaces, Cr_2O_3 for 316L stainless steel and TiO_2 for TA6V4 are more noble than the bare metal, that is why a cathodic drop occurs when the sample is submitted to friction. The alloys tend to recover the original value once friction is stopped, which can be understood as a film reformation.

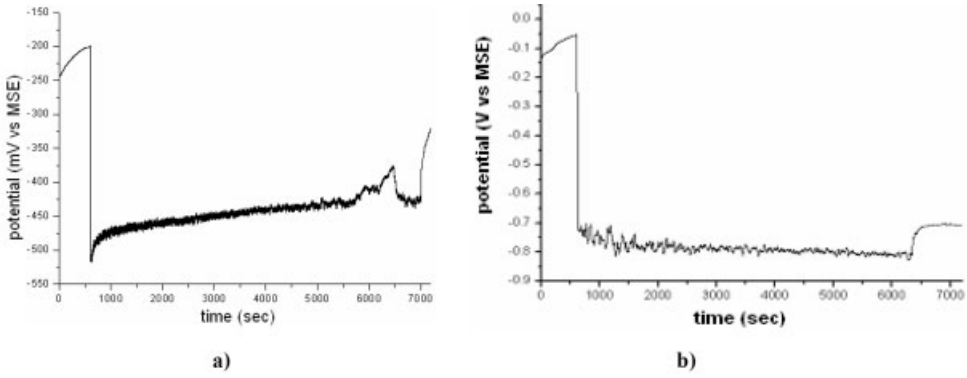


Figure 4: Free potential evolution of a) 316L, b) TA6V4, in H_2SO_4 0.5M solution, with 1.2 Hz rubbing frequency, 5 N load.

3.2.3 Anodic Potential

A material's behaviour said as passive in an anodic range, without friction, naturally forms a protective film on its surface, thus avoiding any electron transfer. During tribocorrosion tests, this protective layer is broken by the action of the ball, and then we can observe a sudden raise in the current density, which causes an increase in the corrosion action on the bare material. At the end of friction, the current density decreases again to the value recorded before rubbing. We can deduce an alloy repassivation with the restoration of the passive film inducing a current density of a few µA/cm². Nevertheless, the current density during friction rises slightly with time. This is linked to a change in the active/passive surface ratio due to wear. Another influence will be the presence of pits at the metal surface, especially in NaCl media, due to a Cl^- ion attack. Then, the current density will be higher than the one before rubbing, as it can be seen on figure 5 a) with 316L in NaCl. Figure 5 b) shows the tribocorrosion behaviour of 316L in H_2SO_4 media under an anodic polarization. The current density at the end of rubbing reaches the value measured before friction, even though the current density rises during rubbing. It then emphases the damage caused by Cl^- ions on the passive film.

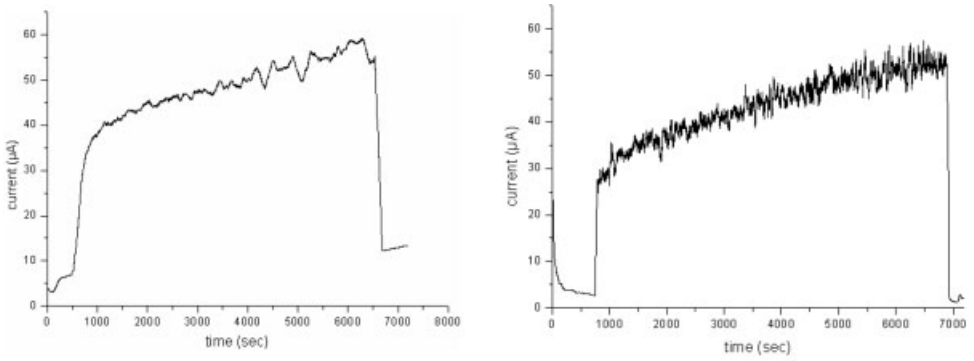


Figure 5: Current density of 316L in the passive range, in a) NaCl 0.9%wt solution, b) H_2SO_4 0.5M solution, with 1.2 Hz rubbing frequency, 5 N load.

3.2.4 Repassivation Kinetics

When the current density evolution at the end of rubbing is analysed, time between the end of friction and the recovery of the current's original value indicates the kinetic of repassivation of the material in the corrosive environment. Olsonn [8], through the study of two types of contact, has established a model which determines the thickness change of the passive film created on the surface of stainless steel 304L.

Equation (1) describes the passive film growth with time:

$$\xi = \frac{1}{\frac{\alpha^+ nF}{RT} \cdot E_0} \ln\left(1 + \frac{\alpha^+ nF}{RT} \cdot E_0 \cdot k_{\text{film}} \cdot i^0_{\text{growth}} \cdot e^{\frac{\alpha^+ nF}{RT} U} t\right) \tag{1}$$

where ξ is the film thickness in nm, n is the number of electrons exchanged in the reaction, for instance when 316L stainless is tested:

$$2\text{Cr} + 3\text{H}_2\text{O} \rightarrow \text{Cr}_2\text{O}_3 + 6\ \text{H}^+ + 6\ \text{e}^-$$

F is the Faraday constant, R the Boltzmann constant, T the temperature in K.

α^+ is the apparent charge transfer coefficient, it is calculated from the coefficient βa identified thanks to Tafel's lines.

i^0_{growth} is the mean current density needed for the film growth (A/cm²).

E_0 is the electric field in the film (V/nm), k_{film} is the film growth constant set as:

$$k_{\text{film}} = \frac{V_{\text{ox}}}{n \cdot F} \tag{2}$$

With V_{ox} the specific oxide volume in cm³/mol. For instance, k_{film} for an oxide film Cr_2O_3, which growths on a stainless steel surface equals 504 nm·cm²/A·s.

We then obtain curves characterizing the passive film growth with time for the two alloys when placed in presence of the two corrosive medias, H_2SO_4 0.5M and NaCl 0.9% wt, as shown on figure 6.

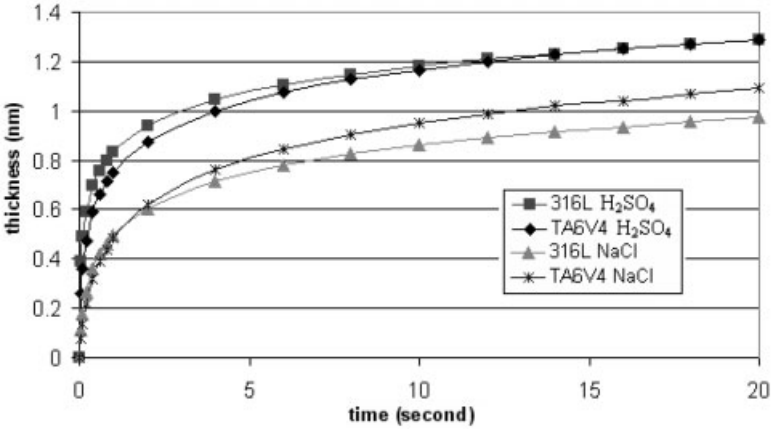


Figure 6: Passive film growth of 316L and TA6V4 in H_2SO_4 0.5M and NaCl 0.9%wt solutions.

Values of passive film thicknesses calculated with this model are close to those found in literature, measured by XPS or ellipsometry [9] [10]. The interest of the repassivation kinetic is to know if, between two successive strokes of the ball, the alloy has enough time to reform a protective layer. Thus, rubbing frequency plays an important role on the amount of metal loss. Some XPS and profilometry measurements are currently carried out to validate this model.

3.3 Influence of an Applied Potential on Tribological Properties

3.3.1 Role of the Passive Film

During tribocorrosion tests, friction has an important influence on free potential or current density evolution. But the application of a specific potential causes an influence on the coefficient of friction, as this one depends whether the material is covered by a passive film or not. Furthermore, unless an entire film breakdown, the coefficient of friction will not be the same according to the electrochemical applied potential.

For a tribocorrosion test in the anodic range, a passive film on the sample surface causes a coefficient of friction higher than on bare metal. As shown by Landolt [11], every decline of the current density is linked to a raise in the coefficient of friction, as the passive film on 316L is composed mainly of chromium oxides, which in contact with an alumina ball, causes a stronger coefficient of friction. During our tests, the applied load, 5 N, is enough to break the entire passive film, and the frequency of rubbing, 1.2 Hz, does not enable the alloy to repassivate. The coefficient of friction remains constant, as the current density rises with time. This is due to an increase in the wear track surface, as the rubbing goes. Thus, the alumina ball rides continuously on the bare metal, as shown on figure 7.

We finally obtain different coefficients of friction for the different electrochemical applied potentials as shown in table 2. Coefficients of friction are similar for every electrochemical applied potential, as the alumina ball is in contact with the bare material, and no influence of a film covering the surface can be noticed.

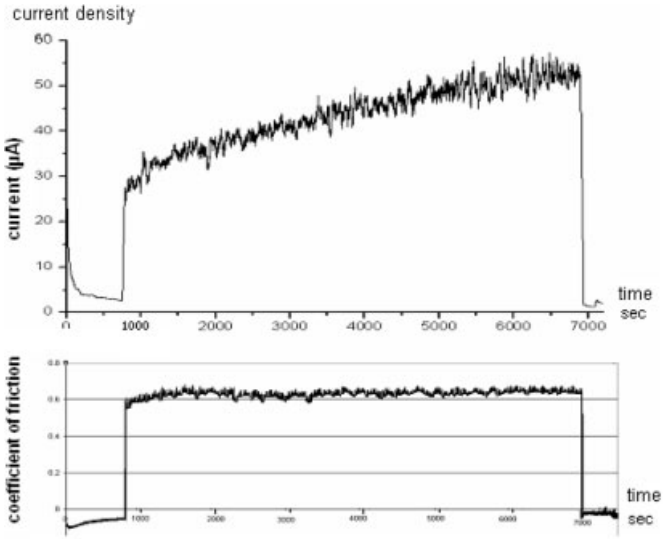


Figure 7: Current density and coefficient of friction of 316L in the passive range, in H_2SO_4 0.5M solution, with 1.2 Hz rubbing frequency, 5 N load.

Table 2: Coefficients of friction of 316L and TA6V4 with the applied potentials in H_2SO_4 and NaCl for tests under 5 N load.

	Cathodic domain	Free potential	Passive domain
316L H_2SO_4	0.62	0.60	0.63
TA6V4 H_2SO_4	0.60	0.60	0.63
316L NaCl	0.75	0.4	0.75
TA6V4 NaCl	0.6	0.59	0.61

Tribocorrosion tests under loads of 0.5 N or 1 N, as seen on figure 1, do not cause an entire passive film breakdown. The friction coefficient measurements shows a higher value, 0.75 compared to 0.63 on bare metal, in the case of 316L stainless steel in H_2SO_4 0.5M. This difference in the values of friction coefficients is in accordance with the results presented by Landolt [11].

3.3.2 Wear Rate

Wear volumes are measured using 3D profilometry. The wear rate is expressed with the factor K from equation (3):

$$K = \frac{V}{F \cdot L} \tag{3}$$

where F is the applied load in N, L is the total sliding distance of the ball in m, and V is the wear volume in mm^3.

Figure 8 shows the results obtained for the two materials when tested in the two different solutions under different electrochemical applied potentials.

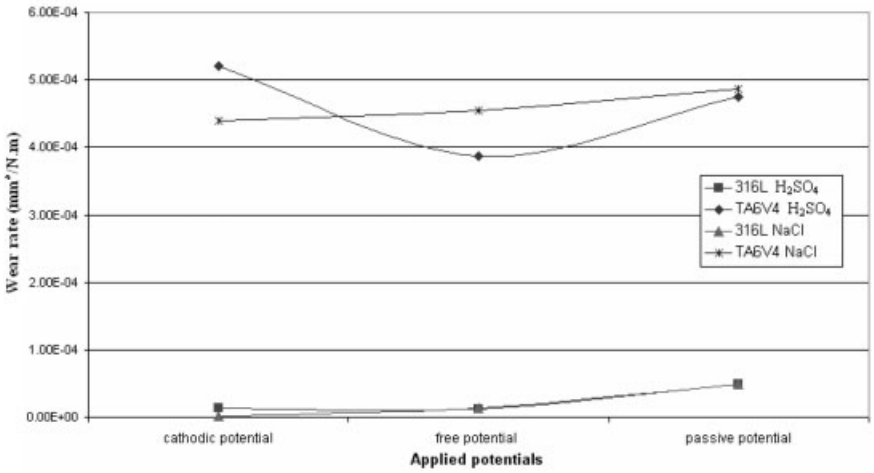


Figure 8: Wear rates according to the applied potentials in H_2SO_4 and NaCl medias, with 1.2 Hz rubbing frequency, 5 N load.

When the materials are held in the cathodic region (cathodic protection), the absence of corrosion leads to a reduction in the material loss due to friction. In the case of TA6V4 in H_2SO_4 solution, the high value of wear rate obtained may be explained by the formation of a titanium hydride film which is a very brittle material when sliding, the latter leading to enhanced total volume of material loss.

Frequency of rubbing also has an important influence on the quantity of wear. Three different frequencies were applied, 0.6 Hz, 0.9 Hz and 1.2 Hz, all at the same passive potential, in the two different corrosive solutions, as it can be seen on figure 9. A significant difference between the wear rates exists, and the evolution in 3 of the 4 cases is linear with the frequency of friction. These results may be correlated to the repassivation kinetics of the materials. If the time between two successive strokes of the ball is lower than the time for the material to repassivate, then the sample is continuously submitted to dissolution and rubbing and consequently, the wear rate increases.

4 Conclusions

Tribocorrosion behaviour of materials 316L and TA6V4 in corrosive solutions H_2SO_4 and NaCl change with the electrochemical applied potential. The consequences are found on the coefficient of friction, the current density resulting of the alumina ball action, the wear rate (wear volume), and the kinetic of repassivation at the end of rubbing. We can generally see an increase of the wear rate with the electrochemical applied potential and the frequency of rubbing. This can be correlated to the speed of repassivation so that there is a challenge between the speed of the ball ride and the time for the material to repassivate.

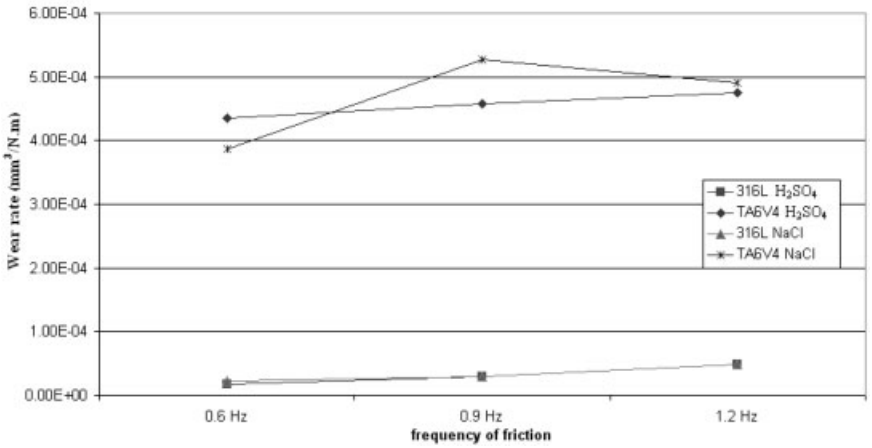


Figure 9: Wear rates according to the frequency of rubbing in H_2SO_4 and NaCl medias, with 5 N load.

5 References

[1] M. Favero, P. Stadelmann, S. Mischler, J.Phys.D: Appl. Phys. **2006**, 39, p. 3175–3183.

[2] S. Spriano, E. Verne, M.G. Faga, Wear **2005**, 259, p. 919–925.

[3] A. Berradja, F. Bratu, L. Benea, G. Willems, J.-P. Celis, Wear **2006**, 261, p. 987–993.

[4] J. Takadoum, Corrosion Science **1996**, 38, p. 643–654.

[5] A. Berradja, D. Deforge, P. Ponthiaux, F. Wenger, J.-P. Celis, J. Phys. D: Appl. Phys. **2006**, 39, p. 3184–3192.

[6] Y.N. Kok, R. Akid, P.E. Hovsepian Wear **2005**, 259, p. 1472–1481.

[7] L. Benea, P. Ponthiaux, F. Wenger, J. Galland, D. Hertz, J.Y. Malo, Wear **2004**, 256, p. 948–953.

[8] C.-O.A. Olsson, M. Stemp, Electrochimica Acta **2004**, 492, p. 145–2154.

[9] Liang, Journal of Chemical Society **1994**, 90, p. 1271–1278.

[10] Krisnamurthy, Electrochimica Acta **2001**, 46, p. 3387–3396.

[11] D. Landolt, J. Phys. D: Appl. Phys. **2006**, 39, p. 3121–3127.

Wear Characteristics of Diamond Grain-Types in Steel-Ceramic-Compound Grinding

B. Denkena, N. Kramer
Institute of Production Engineering and Machine Tools (IFW)Leibniz Universität HannoverHannover, Germany

1 Introduction

An ever-increasing demand for low wear, high performance parts calls for locally adapted material properties. This is achieved by joining several materials in one part featuring common functional surfaces which have to be machined afterwards in one single process. Different materials cause different material removal mechanisms which influence tool wear, cutting forces and surface properties [1, 2]. In this paper, the problem of grinding ceramic-steel-compounds, like they are used in forging dies, is addressed [3].

In initial investigations grinding performance of different abrasive types and bonding systems was evaluated. Vitrified bonded diamond grinding wheels were found to be most suitable. General tool wear described by the radial wear of the grinding wheel was investigated and the corresponding grinding forces were recorded. Radial tool wear of the grinding wheel corresponds mostly to the wheel loading with chips during steel grinding. Chips sticking to the grinding wheel surface are likely to provoke increasing adhesions with each grinding wheel revolution, filling the pores of the grinding wheel. This imposes an increasing pressure onto the ceramic bond bridges between the grinding grains, which will finally break, leading to a loss of grinding grain clusters. In comparison, tool wear during grinding of ceramic was considerably smaller. In steel grinding, wear increases with increasing chip thickness and thus decreases with higher cutting speeds. Although higher cutting speeds will increase cutting temperature in the contact zone, there is no indication that thermal overloading of the diamond appeared. Thermal wear of the diamond will provoke a dull wheel, resulting in significantly higher grinding forces. This was not observed [4, 5].

Whenever the material compound is machined perpendicular to its transition, changes in wheel wear and grinding force will cause a geometry error. This error – measured as a remaining step in height directly at the material transition – is due to the process imposing mechanical and thermal loads onto the workpiece during grinding. Process forces will cause elastic deformations of the machined workpiece and the machine tool while thermal loads cause a shrinking workpiece after it is machined. Due to the different material properties of the compound, process forces and workpiece behavior is different for each material, provoking the above named geometry error. In order to eliminate such an error, adapted process parameters in combination with an in-process material identification and a model predicting this error can be applied [6, 7].

Process stability, part quality, and reliability of predictive process models used to determine locally changing, material adapted cutting parameters, are all depending on stable, controlled grinding wheel behavior. In previous investigations, two types of diamond crystal wheels were used to grind ceramic-steel compounds. Grinding forces and wear behavior was, though generally low, crystal type specific [8]. This is due to different fracture toughness and crystal morphology of the used diamonds [9, 10]. Nevertheless, state of the art methods to evaluate grinding wheel wear

are unsuited to investigate the causes of a crystal specific wear behavior. Negative profiles like graphite or sheet imprints give reliable information on radial wheel wear but loose all information on topography changes. A comparison of material ratios before and after grinding may distort the impression, since contradicting effects like wheel loading and grain loss, which usually happen simultaneously at different areas of the observed grinding wheel surface, compensate each other's influence on the material ratio.

In order to further investigate the crystal specific wear behavior of the grinding wheel, detailed surface topography maps are measured of the newly dressed and used grinding wheels. Three different crystal types of identical grain diameter are used to grind steel and ceramic intermittently. By comparing the topography maps of identical areas of the grinding wheel surface before and after grinding, a diamond crystal specific wear behavior is observed and further information on the geometrical changes of the grinding wheel due to thermal and mechanical loads is gained.

2 Experimental Procedure

2.1 Grinding of Material Compounds

All grinding experiments are performed on a surface grinder using vitrified bonded grinding wheels with a diameter of d_s = 80 mm, width of b_s = 15 mm and a grain size of d_g = 91 µm. The cutting parameters are kept constant as follows: cutting speed v_c = 30 m/s, depth of cut a_e = 25 µm, width of cut a_p = 10 mm and tangential feed speed v_{ft} = 1200 mm/min.

Prior to each experiment, the grinding wheels are dressed. A form dresser with hand-set polycrystalline diamond plates is used in a point crushing operation, i. e. no relative speed between grinding wheel and dressing wheel is applied. Dressing speed is v_{cd} = 30 m/s, dressing feed per stroke a_{ed} = 1 µm, overlap rate U_d = 3 and speed ratio consequently q_d = 1.

With each of the three grinding wheels, specified by the diamond crystal types MBG 600 (sharp, angular with excellent friability), MBG 620 (well formed facets, increased bulk strength) and RVG (irregular shaped, medium toughness and friability) but otherwise unchanged bonding specification, grain size, and diamond concentration, two compounds are ground. Both samples have a length of l_c = 100 mm and a width of b_c = 10 mm. Although both samples feature a ceramic steel portion of 50:50 %, the average distance between the transitions is Δ_{sc} = 10 mm in one sample, Δ_{sc} = 50 mm in the other. Thus, the number of transitions and the lengths of each material are significantly different for both samples.

In each experiment, a specific volume of $V'_w = 250\,\text{mm}^3/\text{mm}$ is removed, resembling 100 grinding strokes. The cutting direction is kept constant, resulting in a down-grinding process. Mineral oil is used as a coolant, supplied by a tangential nozzle providing an almost laminar coolant jet at a coolant speed v_l = 30 m/s and a specific coolant flow of $Q'_l = 3.6\,\text{l}/(\text{min mm})$.

2.2 Grinding Wheel Topography Evaluation

The grinding wheel surface is measured by a scanning confocal laser microscope with a lateral resolution of 10 µm. An identical area, identified by a marker on the wheel's face, of 15 mm in circumferential direction by 17 mm in axial direction is measured before and after grinding. The same area is found at the center of the photographs shown in Figure 1.

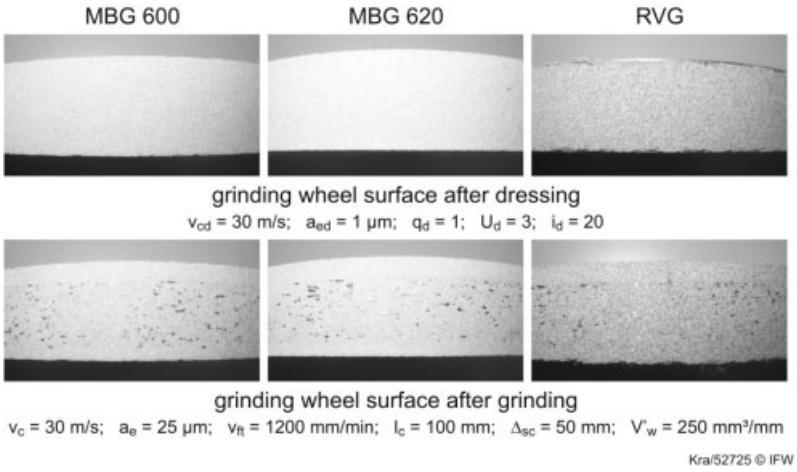


Figure 1: Grinding wheel surface after dressing and grinding

Conventionally, the 3D-data gained by the confocal laser microscope is used to determine an Abbott-Firestone curve of the grinding wheel topography. A linewise Gaussian filter according to ISO 11562 with a cut-off length of l_{co} = 2500 µm is used to separate the long- and shortwave profile. By subtracting the longwave profile from the original data, the grinding wheel's curvature is removed and the shortwave profile remains as a local deviation from the mean level. Although the material ratio is suited to compare surfaces of different roughness, it is not well suited to describe changing surfaces because different type of wear compensate each other in their effects on the Abbott-Firestone curve. Thus, no detailed information on the underlying effects can be gained. For example the loss of grains vs. the retreat of the bond material or loading of pores vs. flattening of the diamond grains cannot be distinguished.

To overcome these limitations, a novel approach to visualize changes of the grinding wheel topography is developed. The measured 3D-data of identical wheel surface areas in different states of wear is directly compared. The aim is to match two data sets in the best possible way and evaluate the resulting differences. By this procedure, curvature is discarded making any additional data filtering obsolete. As a benefit, all profile information in axial direction of the grinding wheel is maintained. This is not the case if linewise filtering is applied. Both approaches, the conventional as well as the novel one, are shown in Figure 2.

As described above, the measurements are all taken at nearly the same area of the grinding wheel. Due to the fixture in the microscope, a small shift in axial position and a rotation in circumferential position occur, while a skewness along the grinding wheel's axis is suppressed. To evaluate these shifts and rotations, image processing procedures are applied.

Because of the experimental procedure, the unused areas of the grinding wheel surface are located at identical section of the surface for each wheel and run. Profile information from these areas is used to match the two consecutive profiles. First, the extracted surface data is transformed into binary images. Secondly, the lateral shift of these two images is identified by an auto correlation. Then, the lateral shift is used to calculate the axial shift and the circumferential

rotation. Next, one of the 3D-data sets is accordingly manipulated. Finally, the now matching data sets are subtracted from each other. Here, the data of the grinding wheel surface after grinding is subtracted from the grinding wheel surface after dressing. Thus loading of pores and adhering chips will appear as a positive deviation while loss or wear of grains will be resembled by a negative deviation.

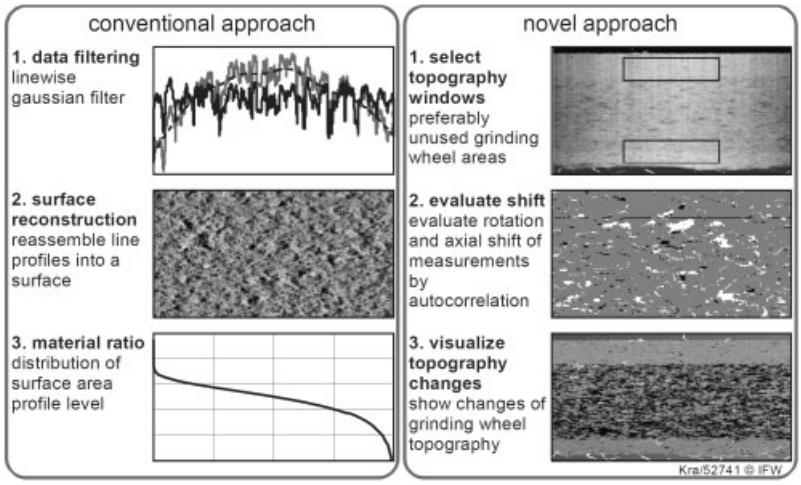


Figure 2: Conventional and novel approach to evaluate wear induced surface changes

3 Experimental Results and Conclusion

3.1 Material Ratio of the Grinding Wheel Surface

The material ratio determined by the conventional approach after dressing is crystal type specific. The RVG diamond, which is much easier to fracture, results in a planer surface after dressing. Both MBG crystal types, which are much tougher and thus less likely to fracture, account for more bond breakage leading to a loss of whole grains instead of grain fractures. Nevertheless, due to the irregular, somewhat longish shape of the RVG crystal, more or larger pores are present.

As the photographs in Figure 1 show, loading is a major problem. Still, a material ratio calculated from the surface data before or after grinding gives almost identical results for the newly dressed and the worn surface. Thus, crystal specific wheel differences are observed while no wear effects are identified by comparing the Abbott-Firestone curves before and after grinding.

3.2 Visualization of Changes of the Grinding Wheel Surface

Exemplary results for the MBG 600 grinding wheel gained by the novel approach are shown in Figure 3 and Figure 4. While Figure 3 visualizes the change of the grinding wheel surface for grinding a compound with a transition distance of Δ_{sc} = 10 mm, Figure 4 displays how grinding the compound with a transition distance of Δ_{sc} = 50 m changes the grinding wheel.

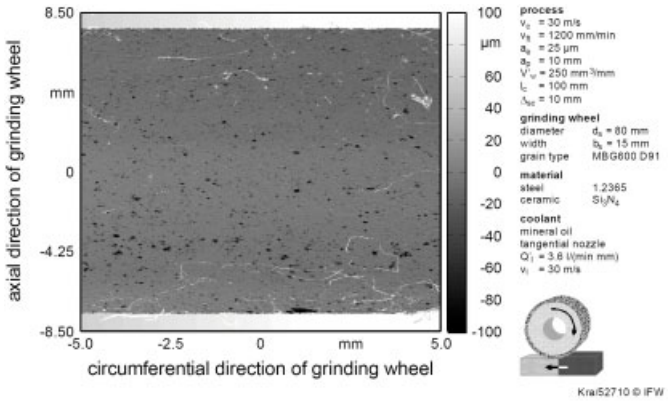


Figure 3: Difference of matched grinding wheel surface before and after grinding Δ_{sc} = 10 mm

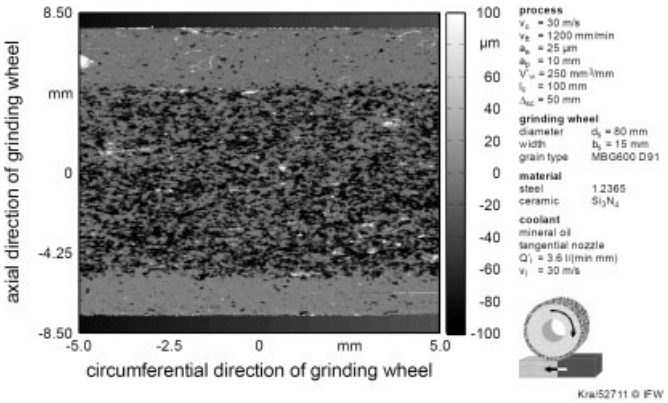


Figure 4: Difference of matched grinding wheel surface before and after grinding Δ_{sc} = 50 mm

Grinding the rapidly intermitting material compound does not significantly change the grinding wheel surface. The small dark patches seen in Figure 3 resemble a negative deviation, indicating some single grain losses. Nevertheless, no loading, which would be indicated by light areas, resembling a positive deviation, can be observed.

As indicated by the visual impression, grinding long distances of steel severely increases wheel loading. In Figure 4 large patches of elevations can be found, which are consistent with the loaded areas seen on the photograph in Figure 1. Nevertheless, large areas of the grinding wheel surface suffer from a significant loss of grains or whole grain clusters.

The crystal specific wear behavior of the grinding wheels can be clearly distinguished if a material ratio is calculated from the data set differences presented above. Only the used area of the grinding wheel surface is considered and the resulting material ratio curves represent the areas protruding respectively retreating from the original surface. Thus, not the crystal or pore

morphology is described but the wear induced changes of the grinding wheel surface. If no changes had occurred, the material ratio would result in a flat, horizontal line.

In Figure 5 the different material ratio progression for all six experiments is shown. Both, crystal specific differences as well as the influence of the transition distance Δ_{sc} can be seen. As the visual impression and the grinding forces observed in previous investigations [8] indicate, the RVG crystal – compared to the MBG crystal types – provokes loading the surface with steel chips. For both transition distances a plateau like progression for up to 30 % of the material ratio indicates severely loaded areas. Grain loss is increased with the distance of the material transitions. Especially the MBG crystals wear much slower if the material transition distance is reduced.

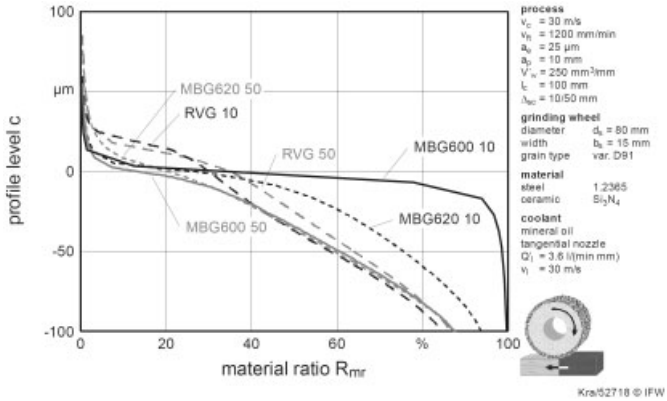


Figure 5: Material ratio of radial matched grinding wheel surface difference

4 Summary and Outlook

The presented new approach to visualize and characterize wear induced changes of a grinding wheel topography improves the possibility to evaluate crystal specific wheel performance. The gained surface differences identify both, the wear progress and its causes on the grain level as well as the radial profile decrease.

A material ratio taken from the radial matched grinding wheel surface difference will maintain all information to compare different grinding conditions or tools. By this, the amount of data is significantly reduced and comparing different grinding wheel specifications becomes possible.

As the results indicate, loading is the major wear mechanism when grinding ceramic steel compounds. Here, regular, well formed facets are less likely to cause adhering steel chips. Grinding of ceramic creates abrasives particles removing the steel adhesions. Thus smaller transition distances reduce wear progression due to loaded pores and loss of grain clusters.

To understand the process of initial chip adhesion, continuous loading, increasing pressure bearing onto the bond causing the pull-out of whole grains or grain clusters in more detail, selected experiments will be repeated and the wheel surface will be periodically measured to document the progress.

Due to the lateral resolution and the significant time consumption for each measurement of the used scanning confocal laser microscope, it was not possible to distinguish wear induced changes of single grains. Therefore, the presented methods will be applied on stereo-microscopic SEM pictures of single grains. To do so, MBG 600, MBG 620, and RVG crystals are brazed onto small tips. These tools will be used for single grain scratching test on the compound material. Pictures before and after scratching will be compared to gain detailed information on grain fracture or thermally induced wear.

5 References

[1] D. Boehnke, Qualitätsorientierte Zerspanung von Parallelverbunden im kontinuierlichen Schnitt, PZH, Garbsen, 2007.

[2] H. B. Dyer, Industrial Diamond Review. 1968, 28/326, 6–13.

[3] B.-A. Behrens, L. Barnert, A. Huskic, Production Engineering (WGP), 2005, XII/2, 131–136.

[4] B. Denkena, T. Friemuth, M. Stahl, wt Werkstattstechnik online, 2002, 92 11/12, 577–580

[5] B. Denkena, J.C. Becker, A. Karyazin, Production Engineering (WGP), 2005, XII/1, 41-44.

[6] N. Kramer, CIRP Annals, 2007, 56/I, 331–334

[7] B. Denkena, N. Kramer, Proceedings of the International Conference on Advances in Abrasive Technology, 2008, XI.

[8] B. Denkena, Fr.-W. Bach, B.-A. Behrens, N. Kramer, K. Möhwald, T.-A. Deißer, M. Bistron, 4th International Conference and Exhibition on Design and Production of Machines and Dies/Molds, 2007.

[9] Diamond Innovations, RVG Diamond Products, www.abrasivesnet.com, 2008.

[10] Diamond Innovations, MBG Diamond Products, www.abrasivesnet.com, 2008.

The Correlation of Thermo-Mechanical Stresses on Cutting Tool Wear

D. Biermann, J. F. Felderhoff, M. Heilmann
Institute of Machining Technology, Technische Universität Dortmund, Dortmund

1 Introduction

Machining processes are limited by tool wear caused by high thermo-mechanical stresses. These stresses are caused by the resistance between the workpiece material and the movement of the tool. Because of that the stresses occurring in machining processes are significantly dependent on the physical properties of the workpiece material. The knowledge of loads in cutting operations is important for a process design adapted to the machining task. In this research three examples of the correlation between thermo-mechanical stresses and tool wear will be presented. These examples are cylindrical turning, short hole drilling with indexable inserts and single-lip deep hole drilling.

The workpiece materials used were stainless steels. These materials possess specific usage properties. Especially stainless steels with an austenitic or austenitic-ferritic microstructure have good properties because of their favorable combination of high chemical resistance and good mechanical properties. However, these usage properties cause problems in the machining process, in particular high tool wear [1, 2]. The steels used differ in their alloying elements and, because of that, in their microstructure. The steel X2CrNiMo17-12-2 has an austenitic microstructure. This steel has a very high corrosion resistance with improved mechanical properties and good formability in comparison to other austenitic stainless steels. The other material used is the steel X2CrNiMoN22-5-3. It has a very high content of the alloying elements nickel, chromium, molybdenum. In addition, nitrogen is added. Because of this chemical composition, this steel exhibits very good corrosion resistance, strength and durability. These characteristics are due to its microstructural austentitic and ferritic phases. The main properties of the workpiece materials used are presented in table 1.

Table 1: Properties of workpieces materials

	X2CrNiMoN22-5-3	X2CrNiMO17-12-2
Microstructure:	Austenitic-ferritic	AusteniticTensile
strength R_m:	790 N/mm²	621 N/mm²
Elastic limit $R_{p0.2}$:	606 N/mm²	375 N/mm²
Elongation at fracture A_5:	36.7 %	46.5 %
Heat conductivity λ:	15 W/m · K	15 W/m · K
Specific heat capacity c_p:	500 J/kg · K	500 J/kg · K

2 Turning of a Stainless Steel Workpiece with Austenitic-Ferritic Microstructure

The process characteristics of turning make this the ideal this cutting process for experimental investigations. This process is very suitable for wear analysis because of high flexibility, simple process kinematics, good chip removal and a long cutting time without interruptions. Here, the influence of different cooling lubricant concepts on the thermo-mechanical loads and on the tool wear is presented using the material with the austenitic-ferritic microstructure X2CrNiMoN22-5-3. To avoid the influence of these factors all the other process parameters were kept constant. To measure the mechanical loads, a dynamometer was used. For the measurement of thermal loads holes with a diameter of $d = 0.5$ mm were produced by Electrical Discharge Machining (EDM) at a predefined position in the cutting inserts. Thermocouples were mounted in these holes. To calculate temperatures directly at the rake face surface in the contact zone between chip and tool, a calibration using chip roots was done. The influence of the cooling lubrication concepts on tool wear is presented in figure 2.

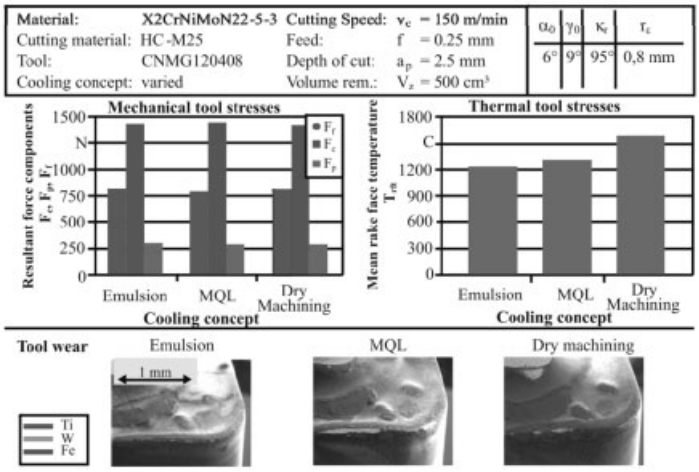


Figure 1: Influence of the cooling lubrication concept on thermo-mechanical loads in turning

To analyze the influence of cooling lubrication concepts, the following concepts were applied: A flood lubrication with emulsion, minimum quantity lubrication with esther oil and dry machining. The cooling lubrication concept shows only minor influences on the mechanical tool stresses. The resultant force components measured are not significantly different. An influence of the thermal stresses on tool wear can be seen. The rake face temperatures increase from the temperature $T_{rft} = 1220$ °C, occurring in the process using the emulsion, to $T_{rft} = 1580$ °C in the process under dry conditions. When using MQL the resulting rake face temperature lies between the two temperatures mentioned above. The emulsion has a high cooling effect because of the high specific heat capacity of water. The lowest thermal stresses in this comparison, that is those occurring when emulsion is used, can be explained by the high cooling effect based on the composition of the coolant as well as the high volume flow. In comparison to that, the slightly higher

rake face temperatures using MQL can be explained by the lack of an effective cooling. Using MQL with esther oil the cooling effect is achieved only by evaporation of the oil and convection of the aerosol. Here, the lubricating effect dominates. The combination of a lower cooling effect compared to these effects when using flood lubrication with emulsion leads to higher rake face temperatures and because of that, to higher thermal tool stresses. With respect to tool wear, a significant effect of thermal loads resulting from the use of different cooling lubrication concepts is occurred. The defining wear mechanism in machining this workpiece material is adhesive wear. Workpiece material was detected, in particular, at the rake face. In addition, the coating at the cutting edge peeled off in experiments when MQL and dry machining were used. The increase in thermal stresses seen in the comparison of rake face temperatures for the three lubrication concepts used leads to an increase in adhesive wear.

3 Short Hole Drilling of a Stainless Steel Workpiece with Austenitic Microstructure

With respect to the continuous cut and single point tool design, short hole drilling is comparable to turning. The main differences between these two processes are the dependence of the tool radius on the local cutting speed and the more difficult chip removal out of the bore hole when drilling. The problems that arise are the high thermo-mechanical loads. Therefore, here the influence of cutting speed on thermo-mechanical loads and tool wear is analyzed. The factors feed, cutting material, coating and insert design were kept constant. The cooling lubrication concept applied was an MQL with inner supply. The experimental set-up used is comparable to the set-up used in turning experiments. The mechanical loads were measured by a dynamometer and the thermal stresses with thermocouples embedded in the prepared inserts. Channels for thermocouples were brought into the inserts by EDM and by micro milling in the tool body. To analyze the influence of decreasing cutting speed in the direction of the center of the tool, the rake face temperature was measured near the cutting edge corner and near the tool center. The influence of cutting speed on thermo-mechanical stresses and the correlated tool wear in short hole drilling of stainless steel with austenitic microstructure is presented in figure 2.

Drilling of the austenitic steel leads to high thermo-mechanical tool loads. The feed force and torque decrease slightly with increasing cutting speed. This effect can be explained by referring to the results of the temperature measurement at the inserts. In the area of the cutting edge corner the rake face temperature increases linearly with increasing cutting speed. Here, very high rake face temperatures were detected. At the inner insert in the area of the tool center another effect of cutting speed and temperature occurred. A low cutting speed leads to very high temperatures at the tool center. The temperature measured near the tool center is comparable to the temperature at the cutting edge corner. The high temperature at the tool center can be explained by the creation of built-up edges. Material adhered at the tool rake face and flank face because of high compressive stresses this resulted a hardening of this material at low local cutting speeds. In addition, an increase in the mechanical tool load in this area occurred and this resulted in high thermal stresses. Besides high thermal stresses, high compressive stresses at the inner cutting edge when using the lowest cutting speed caused tool breakage. At the outer cutting edge material adhesion occurred. A significant tool wear at the flank face and the rake face is not visible. Increasing the cutting speed to v_c = 200 m/min caused a uniform wear behavior to

occur. At both inserts adhesive wear appeared but a significant defect is not noticeable. This cutting speed leads to a homogeneous distribution of thermo-mechanical loads and, because of that, to low tool wear. A further increase in cutting speed is reflected in the wear behavior at the outer cutting edge. The high thermal stresses lead to a plastical deformation of the cutting edge and massive adhesive wear. Although there are higher thermal stresses at the cutting edge corner, tool breakage occurred at the inner cutting edge. This breakage is caused by an overload of mechanical stresses [3].

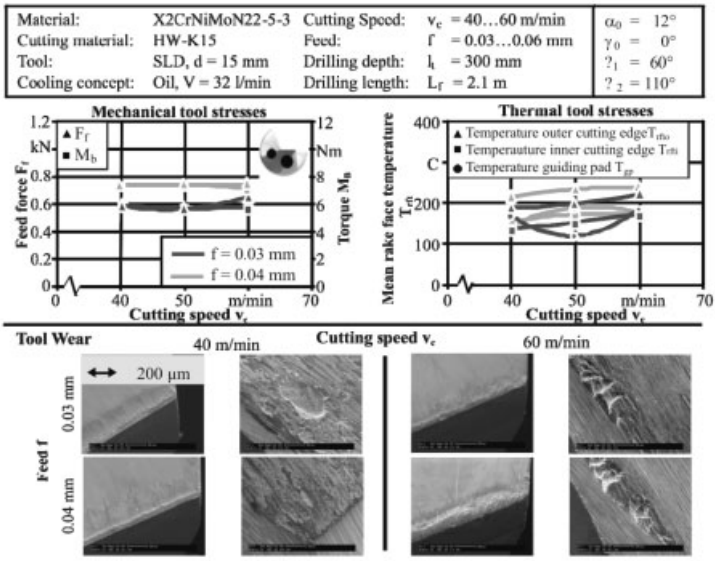


Figure 2: Influence of cutting data on thermo-mechanical loads and tool wear in short hole drilling

4 Single-lip Deep Hole Drilling of a Stainless Steel Workpiece with Austenitic-ferritic Microstructure

The conventional deep hole drilling tools are distinguished by their tool design. These tools have an asymmetrical single point design. The guiding pads reduce the effect of the resultant radial force in causing the drilling tool to move to the side. Thereby there is a self-guidance of the tool and high drill hole quality. In deep-hole drilling, not only the main cutting edge, but also the guiding pads, are confronted with high thermo-mechanical loads caused by friction. Because of that the rake face temperatures near the cutting edge corner and near the tool center ,as well as the temperature at the guiding pad, were measured. The set-up used allows the measurement of the thermo-mechanical loads in a rotating system. The tool preparation is comparable to the preparation of the tool in short hole drilling. Starting at the cooling channel exits, holes were made by EDM up to the measuring points at the cutting edge and guiding pad. In these channels thermocouples were mounted. Because of the loads that occur the rake face temperatures near the

cutting edge corner and near the tool center, as well as the temperatures at the guiding pad, were measured. For the wireless signal transmission a telemetrical system was used. The mechanical loads on the side of the workpiece were measured using a dynamometer [4]. In these experiments the workpiece material was the same material as that used in turning, the steel X2CrNiMoN22-5-3. Here, the influence of cutting data in single-lip deep hole drilling was investigated. Their influence on thermo-mechanical loads and tool wear is presented in figure 3.

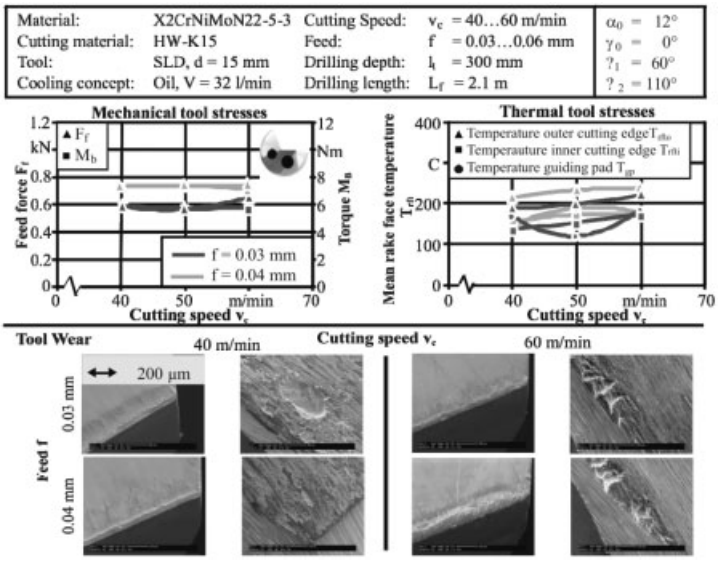


Figure 3: Influence of cutting data on thermo-mechanical loads and tool wear in single-lip deep hole drilling

The cutting speed influences the thermal stresses, especially at the rake face. With increasing cutting speed a higher cutting power is brought into the process. Because of this more heat is generated. With respect to the thermal stresses in the area of the guiding pad higher temperatures were measured due to the friction occurring at increased cutting speeds. The mechanical loads show no dependence on the cutting speed. The observed values for feed force and torque remain nearly constant when cutting speed is varied. The resultant temperatures are not high enough to cause a thermal softening of the material. Feed has a significant influence on thermo-mechanical loads. When the feed is increased, the cross-section of undeformed chips increases as a result. Here, a higher amount of energy is necessary for material separation and deformation during the chip formation, which leads to higher thermo-mechanical loads. In the process with the lower feed and the lowest cutting speed, crater wear occurred after a drilling length of $L_f = 2.1$ m. This is caused by a long contact time of chip and rake face of $t_h = 82.5$ min. An increase in feed reduces the contact time. Because of that the crater wear occurred is reduced in the experiment using increased feed. Here, the contact time is $t_h = 70.4$ min. At the guiding pad surface defects occurred in the experiment using the lower feed because of disruptions in the lubrication supply. When using the higher feed adhesion is the dominant wear mechanism. An increase in cutting speed leads to a reduction in crater wear when the contact time is further shortened at the feed

f = 0.03 mm. At the guiding pad surface defects occurred. In comparison to the wear at the guiding pads in experiments with the cutting speed v_c = 40 m/min the wear is lower using the higher cutting speed. An increase of feed at higher cutting speed leads to adhesive wear at the rake face founded in higher compressive stresses. The guiding pad wear is comparable for both feeds at the higher cutting speed [5].

5 Conclusion

Tool wear in machining stainless steels is influenced by the resulting thermo-mechanical loads. These loads can be influenced by the process variables and minimized by an adapted process design. In turning, the cooling lubrication concept influences the thermal tool loads. In addition, the adhesive wear increases with increasing rake face temperatures. In short hole drilling, compressive stresses at the tool center are produced by built-up edges and can lead to tool breakage caused by high thermo-mechanical loads. Here, the cutting speed must be high enough to avoid high compressive stresses and a hardening of the material. In single-lip deep hole drilling only the thermal stresses are dependent on the cutting speed. An increase in feed leads to higher thermo-mechanical loads. At higher cutting speeds and feed, tool breakage occurs. In conclusion, when machining stainless steels the thermal stresses are the determining factor in tool wear.

6 References

[1] Agrawal, S.; Chakrabarti, A. ; Chattopadhyay, K. A. B., Journal of Materials Processing Technology **1995**, 52, 610–620

[2] Schoß, V., Martensitische Umwandlung und Ermüdung austenitischer Edelstähle – Gefügeveränderungen und Möglichkeiten der Früherkennung von Ermüdungsschäden Dissertation Technische Universität Bergakademie Freiberg, **2001**

[3] Hesterberg, S., Trockenbearbeitung nichtrostender Stähle – Prozessgestaltung für das Drehen und Bohren mit Wendeschneidplatten, Dissertation Universität Dortmund, **2006**

[4] Weinert, K., Heilmann, M., Wittkop, S., VDI-Z, Integrierte Produktion, **2007**, 1/2, 54–57

[5] Wittkop, S., Einlippentiefbohren nichtrostender Stähle, Dissertation Universität Dortmund, **2007**

Influence of Microstructure and Coating on the Abrasive Edge Wear of WC-Co

P. Krakhmalev
Karlstad University, Karlstad, Sweden

1 Introduction

Application of hard coatings in casting, machining, forming operations and for improvement of tribological performance of sliding parts of mechanical components is a common practice during last decades. Commercial TiN and CrN coatings may efficiently improve tools performance die to their high mechanical and tribological characteristics.

Recent progress in improvement of properties and performance of coatings involves fabrication of advanced multilayer, interlayer and quaternary or ternary coatings like TiAlN, CrTiN and CrAlN [1, 2].

Tribological performance of CrAlN coatings has been extensively investigated last decades for different applications. For example, it has been shown that CrAlN coatings demonstrate better resistance to adhesive wear comparing to binary CrN [3]. Scheerer at al. demonstrated promising results for application of CrAlN for dry machining operations [4]. Sliding wear resistance of CrAlN coating have been investigated in [5] and it has been shown that CrAlN coating showed better resistance against a combination of abrasive and oxidative wear. Besides, quaternary alloying has been found very promising for improvements of tribological properties of CrAlN coating tested by laboratory pin-on-disc test facilities and, for example, for machining of stainless steel [6–8].

In the present article, authors investigated abrasive wear of WC-Co polished edge coated by CrAlN against SiC abrasive paper under two-body dry abrasion conditions with edge-on-disc test arrangements. The specimens had an edge angle of 90 degrees and were abraded in a direction perpendicular to the edge line. Abrasive wear is commonly investigated using flat specimens, which can not simulate a situation when edge of the sliding component meets abrasive particles (debris, undesirable dust or particles, etc.). Influence of hard coating is discussed in relation to observed wear mechanisms and wear rates.

2 Materials and Method

WC-Co hardmetals of different WC grain size PVD coated by CrAlN hard coating were investigated. Following the supplier specification, the coarse grade (4.5 µm mean WC grain size) and the ultrafine grade (0.3–0.5 µm WC grain size) were selected as substrates for the coating. The specimens were ground and polished at two sides forming the 90 degrees edge with 3 µm diamond finishing paste and then coated. The coatings were deposited by PVD arc evaporation technique, at 480–500 ºC temperature in the industrial BAI 1200 coating system.

Composition of the coating measured by means of EDS SEM corresponded to $Cr_{0.24}Al_{0.35}N_{0.41}$. Thickness of the coating can be estimated of about 3 µm mean, as seen

in an example of the cross-section. The cross-section of the coating and polished and coated edge illustrations are given in Fig. 1.

The polished specimens were mounted on the vertically movable holder, then loaded with a static weight of 200 g onto the table coated with STRUERS P800 SiC abrasive paper and then slid. The P800 grit (21.8 μm average grain size) SiC abrasive papers were utilized in the experiments. Specimens always slid over new abrasive surface in a direction perpendicular to the edge line. The specimens slid without lubrication with a sliding speed of 0.5 m/min.

Sliding was interrupted for SEM observations and then further continued until the final sliding distance achieved. Worn specimens were examined with a GEMINI LEO 1530 scanning electron microscope (SEM) to measure the widths of the worn surface and observe the worn surfaces morphology. Since approximately one third of the SiC grain protruded from the resin [8], the effective size of abrasive particles causing the abrasive damage was estimated to be comparable to the WC grain size in the investigated coarse WC-Co grades. The results of the measurements were drawn in a form of a width of the worn surface vs. sliding distance diagram.

3 Results and Discussion

Cross section of the coating is illustrated in Fig. 1 a. It is seen that coating is well adhered to the substrate and possesses a typical columnar microstructure. Columns are of submicron size range and re-nucleation sites are quite well distinguishable. Usually, sharp edges are avoided in design of components for PVD coatings due to residual stresses in the coating that may cause peeling the coating off. Nevertheless, it is seen that edge has no defects, cracks or peeled off regions. Some observed porosity and uneven surface morphology close to the very edge is caused by edge effect on deposition process.

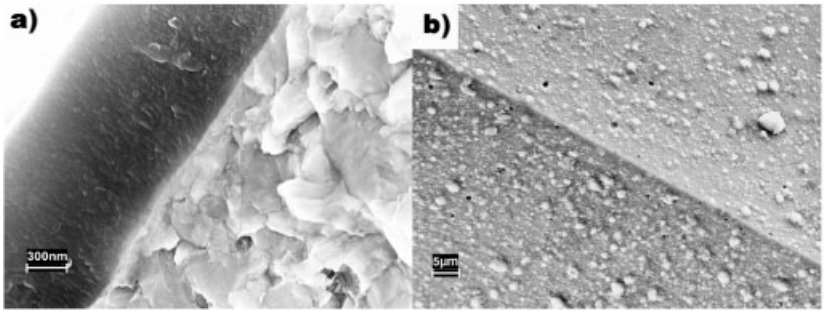


Figure 1: Cross-section of the CrAlN coating (a), and sharpness of the coated edge (b).

Morphologies of worn surfaces of coated and uncoated specimens are illustrated in Fig. 2. It has previously been shown [9] that uncoated coarse and ultrafine WC-Co grades behave differently. Fine and ultrafine WC-Co grades demonstrated rather homogeneous tribological behaviour (ploughing), while heterogeneous microstructure response was observed for coarse grades (fragmentation and pullout of WC grains). Such behaviour has been attributed to different response of microstructure and strain localization in binder phase in the case of coarse grades [10].

Comparison of surface morphologies of coated and uncoated specimens shows similar response of the substrate. In all the cases, ultrafine grade demonstrated homogeneous behaviour, but coarse grades demonstrated fragmentation and pull out of WC grades.

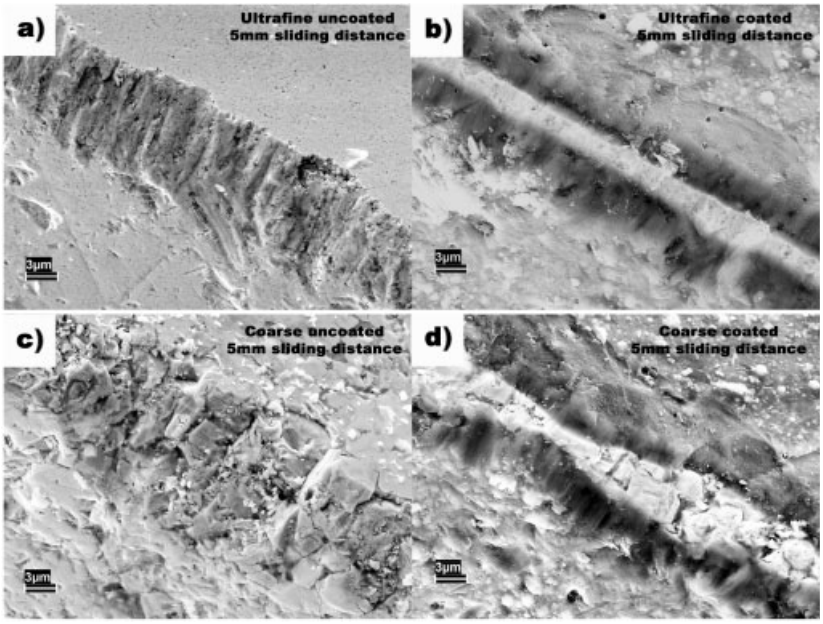


Figure 2: Surface morphologies after 5mm sliding distance. Ultrafine uncoated (a), ultrafine coated (b), coarse uncoated (c) and coarse coated (d) grades. Sliding direction if from bottom left to top right corner at all the images.

Remarkable difference is that roughness of worn WC-Co substrate is lower for coated specimens. This may be explained by analysis of the interaction zone, i.e. actual size of SiC asperity interacting with the edge and hardness of substrate, coating and asperity. Fig. 3 a, illustrates SEM image of the abrasive paper after contact to the edge. It is seen that, actual size of contact is smaller than the nominal size of SiC grit and is about 20–50 % of the nominal grist size (21.8μm average grain size) protrude from the resin and worn due to abrasive contact with the tested specimen.

Hardness of interacting phases is decreased in order CrAlN (∼3000–3200 HV) – SiC (2200–2600 HV (bulk)) – ultrafine WC-Co (2050 HV) – coarse WC-Co (1290 HV), and, therefore, coating is an efficient protection at the first contact with abrasive particle, providing lower wear of the substrate, which is softer than the coating and abrasive asperity.

Comparison of widths of worn surfaces also shows differences between coated and uncoated specimens, Fig. 3 b. It is seen that coating improves edge wear resistance as for coarse and ultrafine WC-Co substrate. Nevertheless, comparison of measured mean values of worn widths reveals that coating is more efficient in the case of ultrafine substrate. This also may be related to hardness of the substrate, but also has to be associated to acting wear mechanisms.

It is seen in Fig. 4 that contact of abrasive particles with the edge leads to rounding of coating on the forward side of the edge. Then, substrate is in the contact and wear mechanisms depend

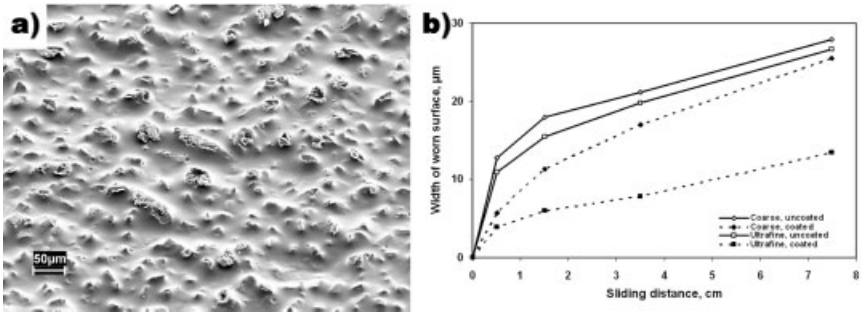


Figure 3: Surface of the abrasive P800 paper after contact (a) and width of worn surface vs. sliding distance (b).

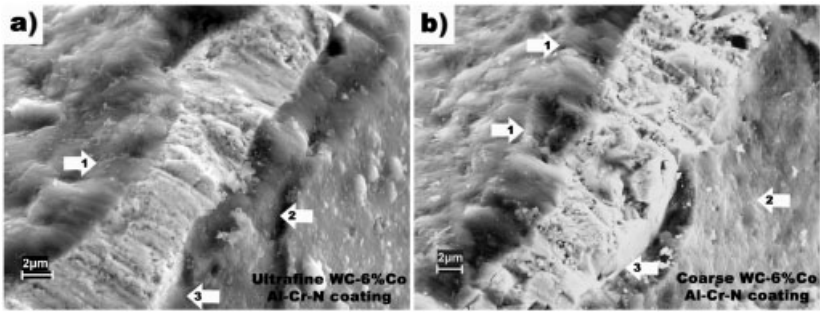


Figure 4: Close view of coated ultrafine (a) and coarse (b) WC-Co edges after 15 mm sliding distance. Arrows show observed wear mechanisms, (1) rounding of the forward side, (2) chipping (flaking) on the back side, and (3) micro-scale peeling off and flaking on the back side of the edge.

on WC grain size as it was mentioned for uncoated specimens [9]. In the case of ultrafine grade, main wear mechanism of substrate is ploughing. Coarse grade demonstrated fragmentation of WC grains, which deteriorate influence of coating. Fractured fragments of substrate are removed together with coating that result in peeling off and flaking of the coating on the back side of the edge. In the case of ultrafine grade, homogeneous character of the substrate wear does not cause severe flaking of the coating.

As it seen in Fig. 3 b lowest wear rates observed for the coated ultrafine WC-Co cemented carbides. Discussion above demonstrated that even though hardness of coating is higher than hardness of abrasive particles, substrate also influence substantially on the observed wear resistance. Observed edge wear mechanisms, which are basically similar to the ones investigated for the uncoated edges [9], may influence tribological performance of the coated edge and, deteriorate wear resistance as it was observed for the coarse WC-Co grades in the present research.

4 Conclusions

Ultrafine and coarse WC-Co cemented carbides uncoated and coated with CrAlN hard coating were tested under dry two-body abrasion conditions in order to examine influence of coating on the edge wear behaviour. Following results may be concluded.

- Coating improves edge wear resistance especially at the very beginning stages. Roughness of worn surface of coated specimens is remarkably lower comparing with the uncoated ultrafine and coarse grades.
- Positive influence of coating is more pronounced for ultrafine substrate grade. Such behaviour attributed to the substrate tribological response. Removal of fragments of WC phase observed for coarse grades leads to initiation of peeling off and flaking of the coating that deteriorate influence of coating.
- Rounding of the coating from the forward side of the edge and micro peeling of the coating from substrate and chipping (flaking) of the coating from the back side of the edge were the main observed wear mechanisms.

5 Acknowledgments

Author would like to thank Sandvik Hard Materials, Coventry, UK for materials supply and fruitful discussion.

6 References

[1] S. PalDey, S.C.Deevi, Mat. Sci. Eng. A. 2003, 342, 58–79.

[2] X.-Z. Ding, X.T. Zeng, Surf. Coat. Tech. 2005, **200**, 1372–1376.

[3] M. Brizuela, A. Garcia-Luis, I. Braceras, J.I. Oñate, J.C. Sánchez-López, D. Martínez-Martínez, C. López-Cartes, A. Fernández, Surf. Coat. Tech. 2005, **200**, 192–197.

[4] H. Scheerer, H. Hoche, E. Broszeit, B. Schramm, E. Abele, C. Berger, Surf. Coat. Tech. 2005, **200**, 203–207.

[5] J.L. Mo, M.H. Zhu, B. Lei, Y.X. Leng, N. Huang, Wear. 2007, 263, 1423–1429.

[6] J.L. Endrino, G.S. Fox-Rabinovich, C. Gey, Surf. Coat. Tech. 2005, **200**, 6840–6845.

[7] P.L. Tam, Z.F. Zhou, P.W. K.Y. Shum, Li, Thin Solid Films. in press, 2007, doi:10.1016/j.tsf.2007.07.127

[8] J.B.J.W. Hegeman, J.Th.M. De Hosson, G.de With, Wear. 2001, 248, 187–196.

[9] P.V. Krakhmalev, T. Adeva Rodil, J. Bergström, Wear. 2007, 263, 40–245.

[10] P.V. Krakhmalev, J. Sukumaran, A. Gåård, Int. J. Ref. Met. Hard Mat. 2007, 25, 171–178.

Chromium Based PVD Coatings for Injection Moulding Tools

K. Bobzin[a], W. Michaeli[b], N. Bagcivan[a], P. Immich[a], F. Klaiber[b], S. Theiß[a]*

[a] Surface Engineering Institute, RWTH Aachen University, Aachen

[b] Institute of Plastics Processing, RWTH Aachen University, Aachen

* Corresponding author

Abstract

Moulding of nano- and microstructures by injection moulding leads to special requirements for the tools, e.g. wear resistance and as low as possible release forces of the moulded components. On the other hand it is not allowed to affect the replication precision. Physical Vapour Deposition (PVD) is one of the promising technologies for applying coatings with adapted properties like high hardness, low roughness, low Young's modulus and less adhesion to the plastic melt. Using the Arc Ion Plating (AIP) technology, tool steel (1.2083) was coated with different chromium based coatings. Compared to other coating materials the chromium based coatings offer a wide range of advantages, like high corrosion resistance and low adhesion affinity to most commonly used plastics. This paper deals with further development of different tool coatings; chromium-nitride (CrN), chromium-aluminum-nitride (Cr_{1-x},Al_xN) and chromium-aluminum-oxynitride (Cr_{1-x},Al_x)ON for plastic processing. After deposition, the coatings were analyzed by common thin film techniques regarding hardness, Young's modulus and adhesion. Additionally, application oriented tests were carried out, to determine the contact angle depending on the used plastics. Especially (Cr,Al)ON coatings show an increase of the contact angles for polycarbonate plastics in wetting experiments.

Keywords: CrAlON, AIP-PVD, wear protection, plastics, injection mould

1 Introduction

Nowadays, the plastics industry requires high durability tools with low adhesion of the plastic melt and easy ejection for small sized structures. The moulding of nano- and microstructures in a near net-shape process requires the reduction of releasing forces for moulded parts. To fulfill these requirements important process parameters like injection speed and holding pressure have to be reduced in order to enable a demoulding without damage. This results in incomplete replication of the nano- and microstructures and the reduction of surface functionality. The key for success is to modify tool surfaces by using modern surface engineering. Especially, the thin film process technology Physical Vapour Deposition (PVD) promises good properties for tool protection of plastic moulds. Due to the high mechanical loads during the die filling a high wear resistance of the coating is recommended. For the production of optical products a chemical inert and wear resistant die surface is needed to reduce the contamination of the produced optical products. Chromium (Cr) containing coatings offer a high potential as protective coatings. First chromium-nitride films were deposited in the 1980s [1, 2]. Though hardness of titanium-nitride

(TiN) could not be reached [3], increased corrosion resistance of many mediums was observed [4, 5]. Furthermore the addition of aluminum (Al) results in an increase of hardness [6, 7, 8, 9] and influences the film microstructure [10]. Also a high potential as wear protective coating is observed [11, 12].

2 Experimental Setup

2.1 Coating Deposition

For deposition Arc Ion Plating (AIP) PVD was used. The deposition unit Metaplas Ionon MultiArc PVD 20" was equipped with random arc sources. Advantages of this coating technology are strong film adhesion and high deposition rate. The used samples (1.2083, cold working steel) were polished with a 6 µm diamond suspension to a roughness of 0.02 µm Ra. For the deposition of CrN a one cathode setup was used. For the deposition of (Cr,Al)N and (Cr,Al)ON a two cathode setup was used. The purity of the targets was 99.7% for chromium and 99.5% for aluminum. As reactive gases N_2 and O_2 both with a purity of 99.999% were used. For the deposition of (Cr,Al)ON coating a graded oxygen structure was generated by varying the reactive gas composition. After five minutes coating with pure nitrogen, oxygen was added stepwise until a maximum oxygen share of 25% of the O_2/N_2 gas mixture was reached. Prior to deposition, the substrates were cleaned in alkaline solutions of different concentrations and finally rinsed. After batching, the samples were etched for 20 minutes in argon glow discharge plasma (GD) at -1000 V bias. Then the chromium target was switched on maintaining -1000 V bias to bombard the samples for five minutes by ejected chromium ions (Metal Ion Etching, MIE). The parameters of these processes are shown in table 1. Afterwards a 60 minutes deposition process was started with a reduced bias voltage (cp. table 2). The rotating speed of the substrate table was 3 min^{-1} during all processes.

Table 1: Process parameters of glow discharge and metal ion etching processes

Process	Process time [min]	Pressure [Pa]	Bias [V]	Ar gas flow [sccm]	Target current [A]
GD	20	2	–1000	60	–
MIE	5	$5 \cdot 10^{-3}$	–1000	–	50

Table 2: Parameters of the deposition processes

Coating	Deposition Time [min]	Pressure [Pa]	Bias [V]	O_2 gas flow [sccm]	N_2 gas flow [sccm]	Cr/Al target current [A]
CrN	60	2	–50	–	75	60/–
(Cr,Al)N	60	1	–50	–	80	45/50
(Cr,Al)ON	60	1	–100	18	70	45/50

2.2 Analysis of Adhesion and Mechanical Properties of the Coating

The film thickness was determined by using the calo test (DIN EN 1071-2, CemeCon AG Kalottchen/L). The coating adhesion was analyzed by Rockwell indentation (VDI 3198). The roughness of the coating was measured before and after deposition with a Hommel-Etamic T2000 profilometer. Nanoindentation (Equipment: MTS Nanoindentation XP) was performed with a Berkovic indenter. The indenter penetrated the surface perpendicular with a maximum indentation depth of 200 nm. Calculations of hardness and Young's modulus are based on Oliver and Pharr's equations and Poisson ratio was kept constant at $\nu = 0.25$ [13]. The morphology of the coatings was examined by Scanning Electron Microscopy (SEM, Zeiss DSM 982 Gemini). Furthermore the atomic Cr:Al concentration was measured by energy dispersive X-ray spectroscopy (EDS). To obtain the nanolaminate structure of the (Cr,Al)ON coating high resolution transmission electron microscopy (HRTEM) was carried out using a scanning transmission microscope (STEM, FEI Tecnai F20). The phases of the deposited thin films were analyzed using grazing incidence X-Ray Diffraction (XRD) Seifert 3000 HT X-Ray Diffraction System (GE Inspection Technologies) scanning the range of 20 °–80 ° at an constant angle of incidence at 3° using CuK_{α} (40 kV, 40 mA) radiation and a step size of 0.05 °. For analysis of the XRD patterns the JCPDS-cards 11-65 for cubic CrN and 25-1495 for cubic AlN were used.

2.3 Application Oriented Measurements: Contact Angle Measurements

To investigate the adhesion of plastics melt on the coated tool and consequently, the release force, the contact angles of melted plastic resin on the coatings were measured. For these measurements a contact angle measuring device (Krüss DSA 10) was used. To melt the plastics granulate a coated specimen with a single plastics grain on it was placed in a closed device with windows at the sides and high-performance heaters on bottom and top. The temperature was observed by two separate thermocouples. For the investigations two different thermoplastics are selected, the polymethyl methacrylate (PMMA 6N) from the company Röhm, Germany and polycarbonate (Makrolon LQ2647) from the company Bayer Material Science AG, Germany. Before the measurements were carried out, the plastic grains were dried at least for two hours at 85 °C (cp. processing details). Afterwards the grains were put on the preheated specimen. Temperature was increased stepwise until the processing temperature was reached. After two hours an asymptotic value of the contact angle was reached and 60 measurements were done in order to obtain a mean value. In order to realize low release forces a high contact angle of the molten plastics grain is required.

3 Results and Discussion

Table 3 shows the basic properties of these coatings and the uncoated substrate material.

Due to the addition of aluminum to CrN an increase of hardness is achieved. On the one hand hardness and the Young's modulus decrease with the formation of ionic bonds by adding oxygen to (Cr,Al)N [14]. On the other hand this formation for Cr_xO_y is supposed to reduce adhesion of the plastic melt. Moreover the addition of oxygen leads to a decrease of roughness compared to CrN and (Cr,Al)N coatings [15]. With the high temperature contact angle method three coatings

Table 3: Basic characterization of the coatings and the substrate material

Coating	Thickness [µm]	Hardness [GPa]	Young's modulus [GPa]	Roughness Ra [µm]
uncoated	–	5.4 ± 0.5	184.0 ± 12.0	0.02
CrN	3.5	19.8 ± 2.6	329.8 ± 30.8	0.15
(Cr,Al)N	3.4	30.2±2.8	372.2 ± 26.4	0.16
(Cr,Al)ON	3.7	24.8 ± 3.6	278.2 ± 28.9	0.13

as well as the substrate material were studied regarding the contact angle of PMMA 6N and Makrolon LQ2647 melt. Figure 1 shows the results of these measurements.

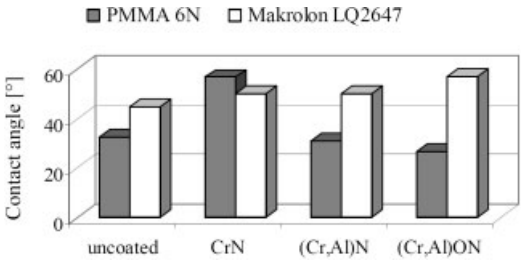


Figure 1: Comparison of contact angle from different coating/plastics combinations

The CrN coated samples show increased contact angles for both plastics compared to the uncoated samples. A further increase of the LQ2647 contact angle can be observed by using the (Cr,Al)ON coating system. (Cr,Al)N coatings show no further enhancements. In order to analyze the coatings morphology SEM pictures were taken of CrN and (Cr,Al)ON cross sections (see Figure 2).

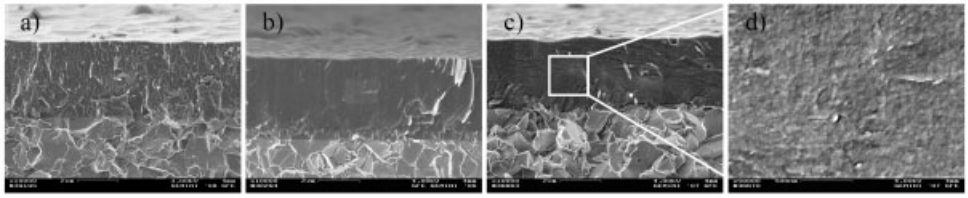


Figure 2: Cross section fracture surface morphology of the coatings on cemented carbide specimens; a) CrN; b) (Cr,Al)N; c) (Cr,Al)ON; d) enlarged section of the (Cr,Al)ON coating with nanolaminate structure

Figure 2a) shows a SEM cross section of the crystalline CrN coating. The second pattern shows the cross section of (Cr,Al)N. The cross section of (Cr,Al)ON, shown in Figure 2c), exhibits a fine crystalline structure. In Figure 2d) a picture with higher magnification of (Cr,Al)ON is shown. A nanolaminate structure caused by the substrate rotation can be seen. Further investigations were done to determine the composition of (Cr,Al)N and (Cr,Al)ON. The atomic Cr:Al concentrations determined by EDS result in $(Cr_{0.51},Al_{0.49})N$ and $(Cr_{0.51},Al_{0.49})ON$, respectively. These measurements show that adding oxygen to the N_2 atmosphere does not result in target

poisoning. The XRD investigations (cp. figure 3) show, that all deposited coatings forming a cubic–fcc structure.

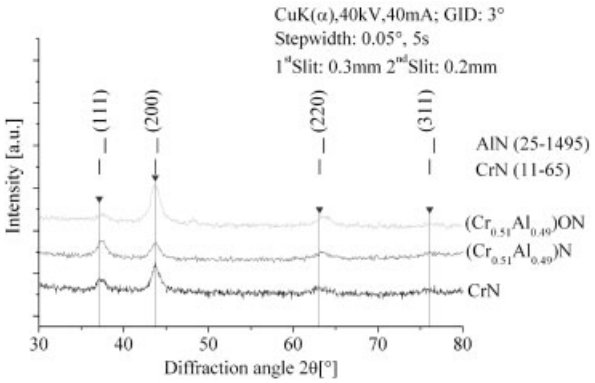


Figure 3: XRD patterns of CrN, (Cr,Al)N and (Cr,Al)ON films

The coatings also show a preferred (200) orientation, which increases by adding oxygen to the CrAl solid solution crystal. For the (Cr,Al)ON coating a peak broadening was observed, resulting in a decrease of the domain size of the crystallites. For a more precise analyses of the nanolamited (Cr,Al)ON STEM measurements were done.

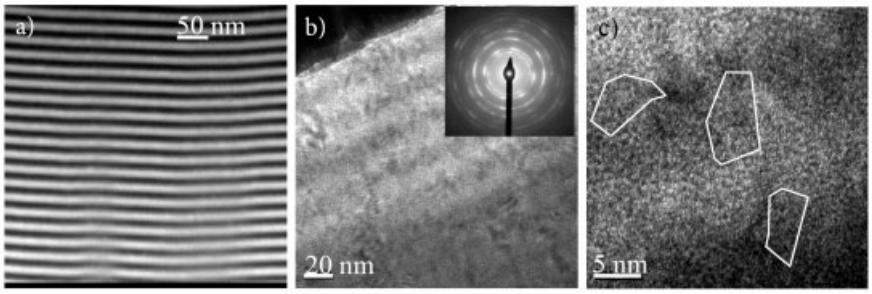


Figure 4: a) HAADF STEM of (Cr,Al)ON nanolaminate; b) bright field and diffraction pattern of (Cr,Al)ON nanolaminate; c) HRTEM of (Cr,Al)ON nanolaminate

Figure 4a) shows the High Angle Annular Dark Field (HAADF) of the nanolaminate structure. The bright parts of the picture relate to chromium and the dark ones to aluminum. The thicknesses of the nanolaminate are 11 nm (Cr) and 9 nm (Al), respectively. The bright field and the diffraction pattern of the HRTEM are shown in Figure 4b). Figure 4c) shows a HRTEM picture. Here the face-centred solid solution structure can be found. The crystal sizes in this picture are about 6 nm. The crystal structure is obtained for fcc-$Cr_{1-x}Al_xN$ solid solution crystal with incorporated oxygen near the surface. Possible traces of Cr_xO_y are detected. In fact of the lower resolution for this formation, this can not be seen in the XRD measurements. The formed structure can be a possible spinel type $Cr_{1-x}Al_xO_yN$. Further investigations need to be done to understand the correct crystallographic structure.

4 Conclusions

With the addition of oxygen to the $(Cr_{0.51},Al_{0.49})N$ coating a film composition is generated, which combines the advantages of CrN and (Cr,Al)N to realize low adhesion of the high performance plastic Makrolon LQ2647 and a high wear protection for injection moulding tools. The implantation of few oxygen atoms enables the generation of ionic bindings, which provide low adhesion of certain plastics. The oxide containing $(Cr_{0,51},Al_{0.49})ON$ coating in this configuration can not achieve the hardness of (Cr,Al)N neither the all-round qualities against the adhesion for both plastics of CrN, but it is a good compromise with best adhesion values for Makrolon LQ2647. The applicability of finishing treatments has to be investigated to reduce the roughness of the coatings. Further variations have to show how the amount of oxygen affects the adhesion of plastics melt and how other plastics react with these coatings. A next step is the application of a $(Cr_{0,51},Al_{0.49})ON$ coating on a micro structured injection moulding tool to determine the practical feasibility.

Acknowledgements

The authors gratefully acknowledge the financial support of the German Research Foundation (DFG) within the Clusters of Excellence (CoE) “Integrative Production Technology for High-Wage Countries” at RWTH Aachen University. This publication is based on actual research results of the CoE sub project C-3.2 “Functional Surfaces via Micro- and Nano-Scaled Structures”.

References

[1] H. Holleck, *Gebr. Bornträger*, ISBN 3-44323-007-5, 1984

[2] O. Knotek, W. Bosch, M. Atzor, W.-D. Münz, D. Hoffmann, J. Goebel, High Temperature – High Pressures, 1986, 18, 435

[3] C. Friedrich, G. Berg, E. Broszeit, C. Berger, *Materialwissenschaften und Werkstofftechnik,* 1997, Volume 28, No. 59

[4] A. Schrey, Dissertation RWTH Aachen, *Mainz-Verlag* ISBN 3-93008-545-3, 1993

[5] K. Reiche, Dissertation Universität Dortmund, *VDI-Verlag* ISBN 3-18144-605-X, 1991

[6] M. Atzor, Dissertation RWTH Aachen, *VDI-Verlag* ISBN 3-18145-605-5, 1989

[7] H.-J. Scholl, Dissertation RWTH Aachen, *VDI-Verlag* ISBN 3-93008-507-0, 1993

[8] S. Guerreiro, Dissertation RWTH Aachen, *VDI-Verlag* ISBN 3-18353-305-7, 1998

[9] T. Hornig, Dissertation RWTH Aachen, *Mainz-Verlag* ISBN 3-89653-935-3, 2002

[10] S.H. Lee, J.J. Lee, Am. *Vac. Soc.* A 13 (4), 1995, Page 2030.

[11] Yueh-Jaw Lin, Ashutosh Agrawal and Yunmei Fang, *Wear* Volume 264, Issues 3–4, 4 February 2008, Pages 226–234.

[12] J.L. Mo, M.H. Zhu, B. Lei, Y.X. Leng and N. Huang, *Wear* Volume 263, Issues 7–12, 10 September 2007, Pages 1423–1429.

[13] W.C. Oliver, G.M. Pharr, *Journal of Materials Research* Volume 7, No. 6, 1992, Pages 1564–1583

[14] H. Holleck and V. Schier, *Surface and Coatings Technology* Volumes 76–77, Part 1, November 1995, Pages 328–336.

[15] M. Maes, Dissertation RWTH Aachen, *Shaker-Verlag* ISBN 3-83226-570-8, 2007

Contact Stress Analysis of a Spherical Wear Particle between Seal and Steel Surface

Tae-Jo Park and Hyun-Dong Cho
School of mechanical and Aerospace Engineering, ReCAPT
Gyeongsang National University, Jinju, 660-701, Korea

Abstract

In many dynamic seals such as lip seal and compression packings, it is well known that wear occur at the surface of heat treated steel shaft as results of the intervened wear particle. It is widely understood that the dominant wear mechanism related in dynamic sealing surfaces is abrasive wear. However, little analytical and experimental studies about this problems have been done until now. In this paper, a contact analysis is carried out using MARC to investigate the wear mechanism in contact seal applications considering elastomeric seal, a elastic micro-spherical particle and steel surface. Deformed seal shapes, contact and von-Mises stress distributions for various particle sizes and interference are showed. The maximum von-Mises stress within steel shaft was exceeded its yield strength and plastic deformation occurred. Therefore, the sealing surface can be also worn by sub-surface fatigue due to wear particles together with well known abrasive wear. The numerical methods and models used in this paper can be applied in design of dynamic sealing systems, and further intensive studies are required.

1 Introduction

In order to avoid leakage of lubricants or high pressured system fluids, various types of seals such as gaskets, O-rings, rubber lip seals and rotary mechanical seals are used in machinery. And the subsequent important function of seal is prevention of foreign particle ingression into the sealing system [1]. Most of dynamic seals adopted in the clearance between relatively sliding machine parts are made from elastomers and should always be maintained in compressed state. Because the sealing surfaces are continuously rubbed with the steel shaft etc. during operation, the seals are gradually deteriorated and then finally failed. Therefore, the worn or failed seals should be replaced with new ones to maintain its sealing performances after a certain period.

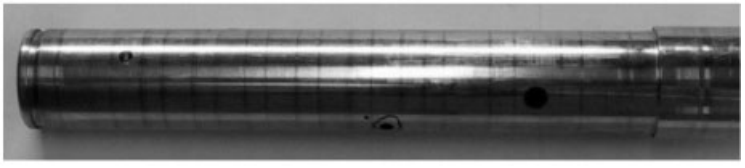


Figure 1: Wear marks of steel shaft surface sealed with lip seal.

In practical applications, a large number of very small hard particles are contained in the sealing fluid. It is generally acknowledged that the wear or foreign particles can play following adverse effects on sealing [2]. That is, the entrapped particles between sealing surfaces were embedded within the seals, and then rubbed with sliding metal components during operation. This resulted in abrasion on the counterpart of seal. Figure 1 shows the worn steel shaft surface which is sealed with PTFE lip seal for rotary union. However, it is not enough to explain the detailed wear mechanism at the sealing surface of steel shaft. So, further studies are required about the complicated contact problem related with relatively soft rubber seal, elastic particle and elastic steel shaft.

However, in spite of a great number of researches on the contact problems, relatively little studies were done on the three body contact problem [3]. Sun et al. [4] analyzed the contact problem between a rigid ball and TiN coated substrate using a finite element package. Conveney & Menger [5] studied the behavior of a rigid abrasive particle between elastomer and steel surfaces. Mirghany and Jin [6] showed the effects of an abrasive particle within the articulation between a cobalt chromium alloy femoral component and ultra-high molecular weight polyethylene (UHMWPE) cup of artificial joints. They have analyzed successfully the three elastic body contact problem.

In this paper, a three body contact model is developed to simulate the entrapment of a micro-spherical elastic wear particle between elastomeric seal and steel surfaces. The contact problems are analyzed using MARC, and the results are showed to investigate the detail wear mechanism of sealing surfaces.

2 The Finite Element Model

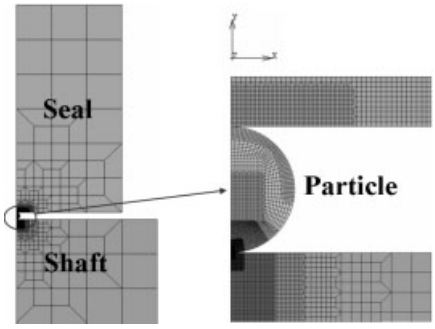


Figure 2: Seal contact model used in analysis.

In order to prevent fluid leakage, proper amount of interferences are required to make the seal and shaft were tightly contact with each other. Figure 2 shows a two-dimensional axisymmetric finite element contact model adopted in this paper to investigate the wear mechanism in a sealed shaft. Where a micro-spherical wear particle was entrapped between seal and steel shaft. The material properties of seal, wear particle and shaft used are given in Table 1. Only spherical shaped relatively harder particle made from tungsten carbide(WC) were considered in this paper.

The steel shaft and wear particle were modeled as linear elastic-perfect plastic materials, where the seal was modeled as isotropic elastic-plastic material. The contact conditions between all surfaces were assumed as frictionless. It was necessary to use a refinement of the mesh in order to predict accurate stress distribution in highly stressed region near contact area. The size variation of the elements from contact region to the outer sides on x and y directions was constructed as shown in Figure 2 to reduce the number of elements and the total amount computation time.

Because of the load symmetry and axisymmetric geometry, only half of the media was considered. The nodes of the bottom line were fixed, so the displacements at the bottom plane were assumed to be zero in the vertical and horizontal directions. The seal interferences were simulated by imposing small incremental displacements to the nodes on the upper line of the seal. The general purpose, non-linear finite element code MARC[7] was used to analyzed the seal contact model.

Table 1: Mechanical properties of contacting materials

	Young's modulus, GPa	Poisson's ratio	Yield strength, GPa
Seal(PTFE)	0.46	0.46	–
Particle(WC)	520	0.24	4.16
Steel shaft	200	0.30	1.619

3 Results and Discussions

Where the results shown in Figure 3–Figure 5, the spherical wear particle diameter is fixed at 10 μm.

Figure 3 illustrates the deformed seal shapes and von-Mises stress distributions for different interferences. As the amount of interference increase, the relatively harder wear particle became fully embedded within PTFE seal, and the seal was in direct contact with steel shaft [6]. In practice, the embedded wear particle and sliding motion at the sealing surface can generate repeated abrasion on the steel shaft. Based on these results, it can be explained that the main reason of sealing surface failure as shown in Figure 1 is abrasive wear due to the embedded wear and/or foreign hard particles. Moreover, it is also noted that a very small interference result in the von-Mises stress reaching yield strength and plastic deformations are occurred on steel shaft by presence of wear particle. These results suggest that the steel shaft can be worn by sub-surface fatigue due to hard wear particles.

Figure 4 shows the displacements and maximum contact stress distribution along the steel shaft surface when the interference is 5 μm (See Figure 3(a)). At contact regions, very high compressive stress has reached its yield strength, and then the steel surface can be permanently deformed.

Figure 5 and Figure 6 show the von-Mises stress distributions in the steel shaft for different particle sizes and interferences. These results show that the depth where the maximum von-Mises stress occur are increased with particle size and interference, and easily reached yielded state. Therefore, as discussed in Figure 3, the fatigue can be initiated at the sub-surface region of steel shaft.

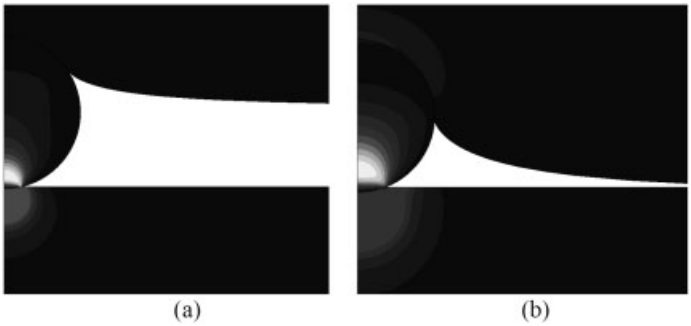


Figure 3: Deformed seal shape and von-Mises stress distribution for different interferences. (a) 5 μm, (b) 50 μm

Figure 7 shows the effect of particle size and interferences on the maximum contact and von-Mises stresses of the steel shaft surface. These results suggest that very small wear particle embedded in elastomeric seal can make the sealing surface to yield more easily, and fatigue wear due to wear and/or foreign particle can be occurred.

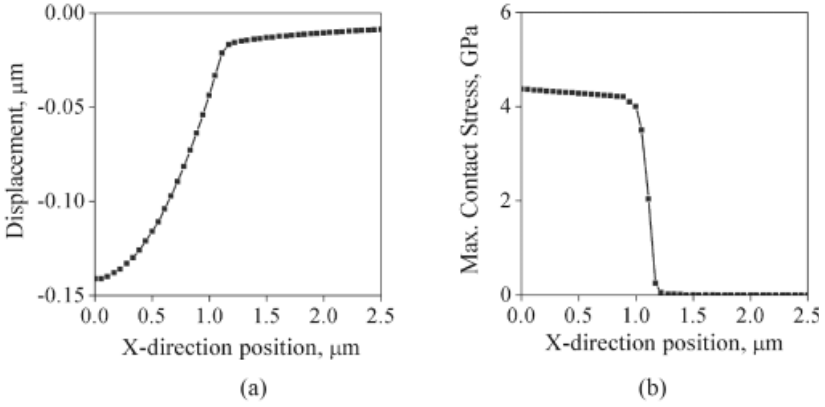


Figure 4: Path plot along steel shaft surface. (a) displacement, (b) contact stress

4 Conclusions

In this paper, a simple contact problem was analyzed and discussed to investigate the wear mechanism of steel shaft which is in contact with elastomeric seal. A simple axisymmetric finite element contact model was developed to simulate the entrapment of a micro-spherical WC wear particle between PTFE seal and steel shaft surfaces, and solved using MARC. The deformed seal shapes, contact stress and von-Mises stress distributions in the steel shaft for various particle sizes and seal interferences are showed. The small entrapped wear particle between seal and steel shaft can produce very high contact and von-Mises stresses. The maximum von-Mises stress within

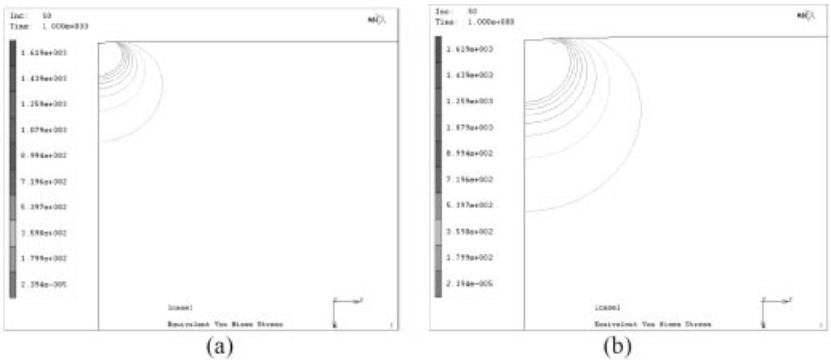


Figure 5: von-Mises stress distribution in MPa. Particle size is 10 μm, interference : (a) 1 μm, (b) 2 μm

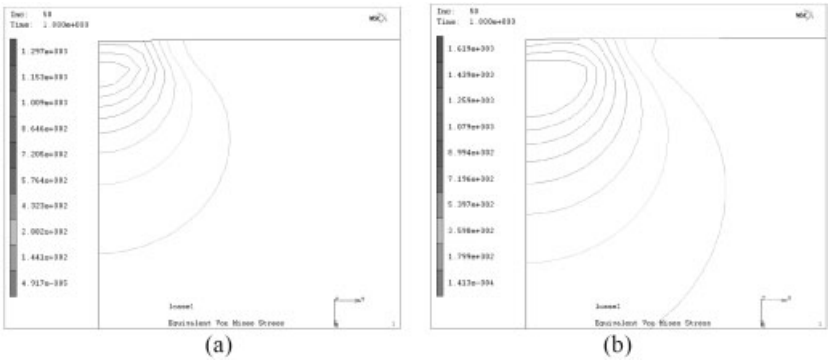


Figure 6: von-Mises stress distribution in MPa. Particle size is 100 [339B?], interference : (a) 1 μm, (b) 2 μm

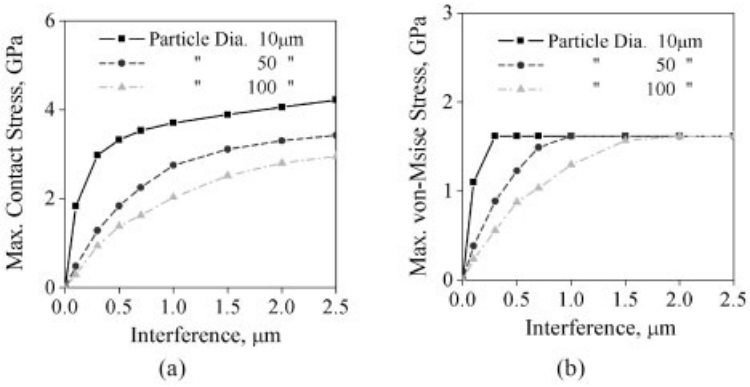


Figure 7: Variation of max. stresses with interference. (a) contact stress, (b) von-Mises stress

steel shaft was exceeded its yield strength and plastic deformation occurred regardless of particle sizes and interferences. Therefore, the sealing surface of sliding metal shaft can be also worn by surface fatigue due to wear particles together with previous well known abrasive wear. The three elastic body contact models and numerical methods adopted in this paper can be applied in design and performance improvement of various sealing systems, and further intensive studies are required.

5 Acknowledgements

This research was supported by the Second Stage BK 21 Project, New University for Regional Innovation (NURI) of Gyeongsang National University and by grant No. RTI04-01-03 from the Ministry of Education, Science Technology (MEST) and Korea Industrial Technology Foundation (KOTEF) through the Human Resource Training Project for Regional Technology Innovation.

6 References

[1] H. K. Müller and B. S. Nau, Fluid Sealing Technology – Principles and Applications, **1998**, Marcel Dekker.

[2] B. Bhushan, Principles and Applications of Tribology, **1999**, John Wiley & Sons.

[3] K. L. Johnson, Contact Mechanics, **1985**, Cambridge Univ. Press.

[4] Y. Sun, A. Bloyce and T. Bell, "Finite Element Analysis of Plastic Deformation of Various TiN Coating/Substrate Systems under Normal Contact with Rigid Sphere", *Thin Solid Films*, **1995**, Vol.271, pp.122–131.

[5] V. A. Coveney and C. Menger, "Behaviour of Model Abrasive Particles between a Sliding Elastomer Surface and a Steel Counterface", *Wear*, **2000**, Vol.240, pp.72–79.

[6] M. Mirghany and Z. M. Jin, "Prediction of Scratch Resistance of Cobalt Chromium Alloy Bearing Surface, Articulating against Ultra-high Molecular Weight Polyethylene, Due to Third-body Wear Particles", *Proc. of IMEchE, J. of Engineering in Medicine*, **2004**, Vol.218, pp.41–50.

[7] MSC, MSC. MARC/MENTAT 2005r2 User's Guide, **2005**, Vol.A-E.

Research Regarding Hot Wear Resistance of MARAGING Steels

D. F. Tarata, D.D. Cealicu, G. Vaduvoiu
University of Craiova, Romania

1 Introduction

Many mechanical failures are caused by manufacturing defects: material, forging, casting, welding, heat treatment [1]. In the field of metal deformation, to know the way wear occurs and develops in moulds is important, as this mostly affects the mould life.Wear is the main reason of mould damage in plastic deformation, besides spontaneous damage due to fatigue induced fracture, mainly in extrusion with a high extrusion factor, as stress concentration in the interface is critical. So, there are two main reasons of the mould failure: fatigue and wear.

The main factors influencing failure are: *(i)* the mould geometry, *(ii)* the material and *(iii)* thermal state. These define three possible ways to increase mould reliability [2,3]. The use of MARAGING steels both in intensively used machine components [4] and in moulds [5], increases reliability and wear resistance.

This work aimes to compare the wear behavior of MARAGING 200 steels (0,03%C, 0,1%Mn, 18%Ni, 4,48%Mo, 8,99%Co, 0,69%Ti, 0,03%Al.) in comparison with allied tool steels of type 55VMoCrNi16 (0,6%C, 0,6%Mn, 0,3%Si, 0,8%Cr, 1,7%Ni, 0,1%V, 0,3% Mo).

2 Method

The study of the mould behavior was done in three stages: *(i)* finite-element analysis for both materials, using DEFORM and SolidWorks software packages; *(ii)* measurements on a real mould (Figure 1 shows the drawing of the forged component), before use and wear; *(iii)* measurements on a real mould after real 400 cycles of real use and wear in industrial conditions, to produce naval components.

2.1 Finite Element Analysis of the Mould

Forging was done on a friction press (140 kN) – the mould temperature 300 °C, the forged semiproduct (carbon steel OLC 35 with the chimical composition: 0,35 %C, 0,8 %Mn, 0,3 %Si, 0,04 %P, 0,015 %S) temperature 1200 °C, forging velocity 250 mm/s. Starting with these parameters the material flow checking was performed and then the determination of tensions, deformations and wear occuring in the mould during the process of upsetting. In the beginning, the influence of the semiproduct type was checked (form and size) for flow and filling of the mould. In Figure 2, incomplete filling of the mould nest can be seen. In consequence of such incomplete filling of marginal sections, a preliminary forging was necessary, to be able to use a semiproduct with a shape close to the final geometry (Figure 3). The finite element analysis [6] proceeded in more steps: *(i)* tridimensional modeling of the component parts and their positioning; *(ii)* domains discretization; *(iii)* defining technological parameters; *(iv)* program run; *(v)* result analysis.

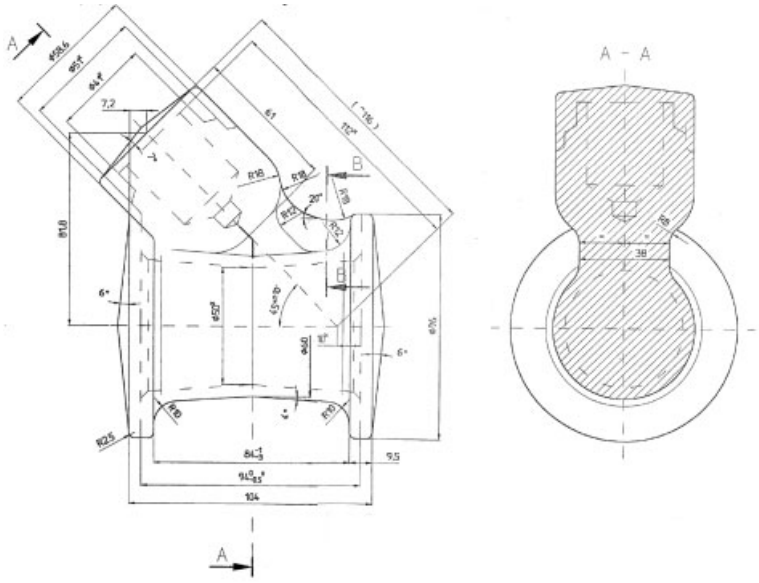


Figure 1: Drawing of the forged part

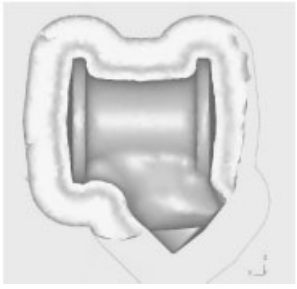


Figure 2: Incomplete filling of the mould nest

To insure a reasonable discretization, 45000 elements were generated for each component. Physical properties of the materials, required as input, were taken from the literature for the 55VMoCrNi16 and MARAGING 200 steels and are shown in Table 1. The temperatures of the semiproduct (1200 ºC) and moulds (300 ºC) were taken into consideration, as well as the areas of heat exchange between objects and with environment (20 ºC).

The movement parameters of the punch were defined as a constant velocity of the mould (250 mm/s) and a friction coefficient of 0,3 was specified between the semiproduct and the mould. The simulation of the hot deformation was performed in 72 steps (each step of 1 mm).

The temperature distribution for the upper mould, corresponding to the final deformation for the two steels is shown in Figure 4.

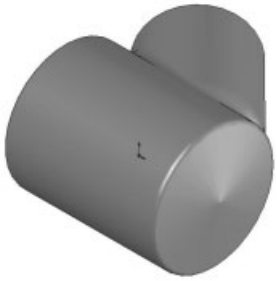


Figure 3: Initial shape of the semiproduct.

Table 1: Material properties for the two moulds

Material	55VMoCrNi16	MARAGING 200
Young modulus E [N/m^2]	1.9×10^{11}	1.95×10^{11}
Poisson coefficient ν	0.3	0.3
Thermal expansion coefficient [/°C]	1.1×10^{-5}	1.2×10^{-5}
Thermal conductibility [W/m °C]	24.5	30
Thermal capacity [N/mm^2 °C]	4.5	5.5
Emisivity	0.7	0.7
Density [g/cm^3]	7.8	8
Hardness [HRC]	47	46



Figure 4: Comparative distribution of the temperatures in the upper mould for the 55VMoCrNi16 steel (left, upper scale 506 ºC) and MARAGING 200 (right, upper scale 453 ºC)

As can be seen, the temperature in MARAGING 200 is lower (upper scale 453 ºC) than in 55VMoCrNi16 (upper scale 506 ºC).

The experimental studies on the moulds from 55VMoCrNi16 steel shows that the temperature increases from the preliminary stage (300°C) up to 500°C. This temperature increase it's almost constant until the end of the batch work (400 parts) because of loosing of the heat with the atmosphere, other metalical parts in contact and lubricant.

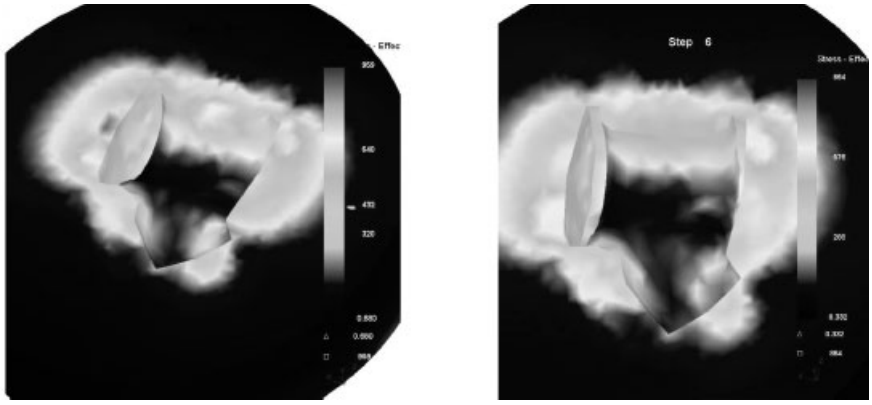


Figure 5: Comparative distribution of tensions in the lower mould in 55VMoCrNi16 (left) and MARAGING 200 (right) steels

It has been also noticed that both the upper and lower moulds reach higher temperatures than the initial temperatures because of the heat transfer and of the friction with the semiproduct in a plastic state.The analysis of the tensions (Figure 5) and deformations (Figure 6) within the punch and mould shows maximal tensions in the separation plane area (practically they are lower due to the joining rays) and in corner areas (where actually cracks occur during use), as well as in the cross area between the two spindles (Figure 5). It can be seen that maximal displacement is lower in MARAGING 200 steel, 25 % less than in 55VMoCrNi16 steel.

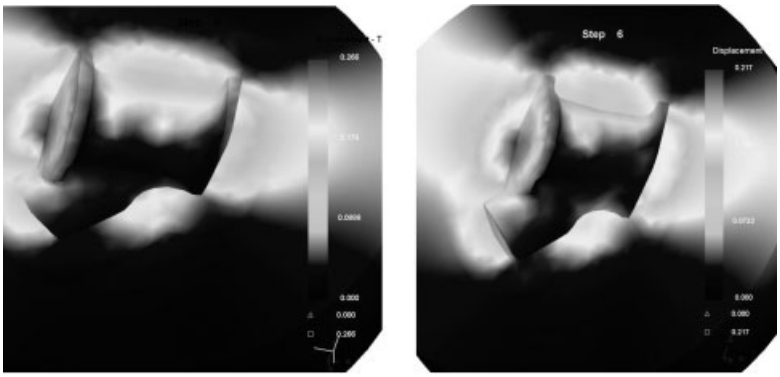


Figure 6: Comparative distribution of deformations in the upper mould in 55VMoCrNi16 (left) and MARAGING 200 (right) steels

In our analysis, the Archard wear model was used (abrazive) suitable to cold and hot plastic deformation [3]:

$$Z_{AB} = \int K \frac{p^a v^b}{H^c} dt \tag{1}$$

Z_{AB} = depth of abrazive wear; p = interface pressure; v = slipping velocity; H = tool material hardness (constant or a function of temperature); dt = time increment; a, b, c, K = experimentally calibrated coefficients (usually $a, b = 1$ and $c = 2$ for steel tools); $K = 0.002$. The other analysis parameters are the same (forging velocity 250 mm/s, 72 steps).

The place where wear occurs are especially interesting in this stage, more than its exact value. Figure 7 shows the total wear distribution at the end of step 72 (final step, when wear is maximal) for the upper mould.

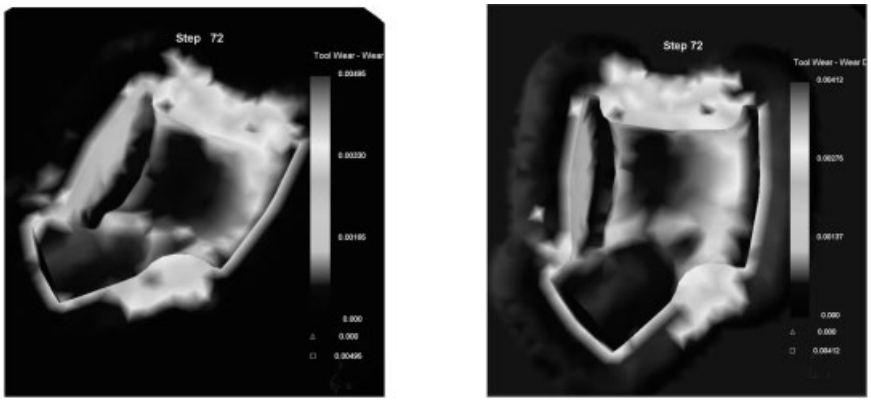


Figure 7: Comparative distribution of wear in the upper mould for type 55VMoCrNi16 (left) şi MARAGING 200 (right) steels

Decreasing of the hot hardness in the mould because of increasing of the temperature up to 500°C is according to Archard's law. This hot hardness decrease has a negative influence of the wear, but not very important especially for Maraging steel in comparison with 55VMoCrNi16 steel.

After the execution of 400 parts the maximum wear becomes 1.64 mm for the upper mould for MARAGING 200 and 1.98 for 55VMoCrNi16 steels, results which are also comparable with the experimental data.

Comparing wear in allied steel moulds for hot processing and MARAGING 200 moulds the study shows that wear is 15-20% lower for MARAGING 200, suggesting that the life of these moulds will be this percentage longer when using this steel. This result, together with lower tension and displacement when using MARAGING 200 compared with 55VMoCrNi16 steel, in similar working conditions, advocates the use of MARAGING 200 steel in such applications.

2.2 Experimental Studies

Measurements were done to determine the values of wear for the upper and lower moulds, made by allied tool steel 55VMoCrNi16, after 400 cycles of use under industrial conditions. To this purpose, a tridimensional coordonate measuring machine (CAM 2 Gage Plus, FARO, Italy) was used, which allows online dimension measurement using a mobile arm and Power Gage software package. Through determining initial and final dimensions, total wear can be assessed.

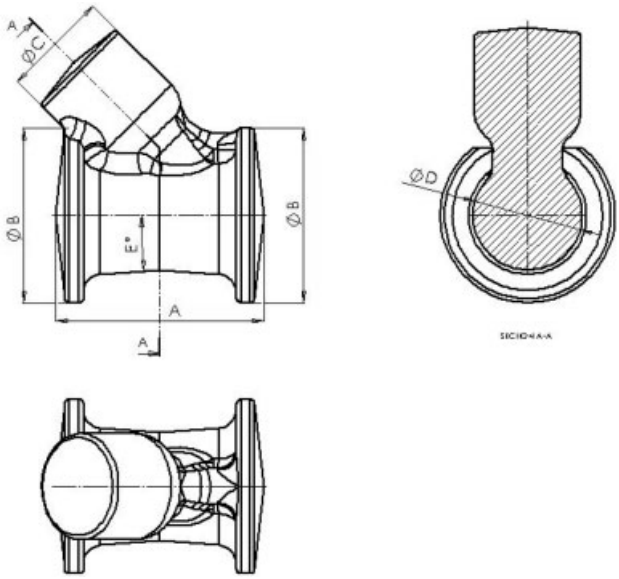


Figure 8: Measure diagram-mould dimension

Table 2: Inferior mould dimensions 55VMoCrNi16

Dimensions	A[mm]	ØB [mm]	ØC [mm]	ØD [mm]
Before wear	115,45 (+1.8/-1.0)	97,15 (+1.8/-1.0)	59,3 (+1.7/-0.8)	60,72 (+1.7/-0.8)
After real wear	119,11 (±0.0025)	98,71 (±0.0025)	61,19 (±0.0025)	63,74 (±0.0025)
After EF simulated wear	118,9	99,1	62,1	63,3

The instrument is operated by Power Gage software package via a PC and the measurements are automatically saved to generate final reports. At first the models were measured, then lower and upper moulds. The measurement diagram is shown in Figure 8. The main measured dimensions were the ØB, ØC, ØD diameters, dimension A. The average values of the relevant dimensions of the mould, figure 8, within the three steps are shown in table 2 (measurement tolerance was 0.005 mm).

3 Conclusions

The Maraging steels are recommended for casting mould of Al-alloys, hot deform moulds, special railway parts, parts for aeronautic industry according to the target prices of these products.

The main modalities of improving reliability and durability of moulds have to take into account mould geometry, the material used and thermal conditions.

The results of this study confirm a better wear resistance of MARAGING 200 steel in comparison with 55VMoCrNi16 type allied tool steel used for hot processing.

The simulation study for tensions, deformations and wear performed with the DEFORM package are close to the experimentally determined measurements (±1.5%).

For the MARAGING 200 steel lower distributions of tensions, displacement and wear resulted after simulation, comparing to the 55VMoCrNi16 type (Von Mises equivalent stress are with 8–11 % lower, maximal displacement is 25 % lower, wear is 15–20% lower). This means the mould life duration is 15–20% higher.

The future experimental results with Maraging steels will give us all the data necessary to recommend each type of steel related with the production costs.

4 Acknowledgements

This work was done under contract “Cercetări privind mecanismul durificării şi stabilitatea la cald a oţelurilor tip MARAGING – MeDur“, CEEX Nr. 297/2006, ANCS Bucharest, Romania.

5 References

[1] M. Pepil, Journal of Failure and Prevention , 2002, Nr.1, Vol.2, p.43–49.

[2] L.H. Van Vlack in The Addison- Wesley Publishing Company, Inc., Michigan, USA, 1989, Chapter 9.

[3] G.-A. Lee, Y.-T. Im – Journal of Materials Processing Tehnology 1999, p. 123–127.

[4] Y.Ohuea, K. Matsumotob, Wear, 2007, 1-6, Vol.263, p.782–789.

[5] R.S.Lee, J.L.Jou, Journal of Materials Processing Technology, 2003, Vol.140, p.43–48.

[6] N. Faur- Elemente Finite - Fundamente, Editura Politehnica, Timisoara, Romania, 2002, Chapter 1.

Author Index

A
Akselsen, O. M. 110, 660
Albers, A. 453, 467
Alimadadi, H. 604, 637
Aliofkhazraei, M. 604, 637
Al-Khalil, J. A. 33
Amann, T. 409
Andersson, S. 3
Arrieta, V. 314
Atkins, A. G. 207

B
Bagcivan, N. 240, 527, 547, 737
Bagh, A. 588
Baltruschat, H. 178
Bartel, D. 473
Bay, N. 439
Beauvais, S. 467
Becker, M. 314
Behrendt, M. 453
Beiss, P. 104
Berçot, P. 708
Berger, L.-M. 423
Berkes Maros, M. 393
Berlet, P. 446
Bertling, J. 339
Bielek, J. 67
Biermann, D. 726
Binchiciu, H. 610
Blazquez, V. 618
Blömer, J. 339
Bobzin, K. 130, 240, 521, 527, 547, 737
Bode, K. 301
Bonß, S. 74
Bosse, H. 52
Bouvet, D. 185
Bouvier, V. 256
Brecher, C. 560, 588
Brenner, B. 74, 654
Bressling, J. 515
Bretschneider, J. 74, 654
Broda, M. 124
Bsul, J. 467
Budniak, J. 667
Bugiel, C. 515
Bulia, B. 159
Burger, W. 467

C
Camba, C. 618
Casellas, D. 327
Casteletti, L. C. 597
Cealicu, D.D. 750
Cetin, A. 81
Chen, C. 52
Cheung, N. 597
Cho, H.-D. 744
Cordes, S. 541
Cruz, M. R. 327

D
Dahl, N. 110, 660
Danninger, H. 696
Declercq, M. 185
Delaunois, F. 264
de Leon, L. 227
Demian
– G. 682
– M. 682
Denkena, B. 227, 719
Derler, S. 487
Deters, L. 52, 473
Dietrich, A. 93
Dott, W. 515, 521
Drygalov, M. 104
Dudzinski, W. 140
Durst, K. 171
Dzigrashvili, T. 159

E
Eichlseder, W. 45
Elgeti, H. 554
Emmer, Å . 67
Enekes, C. 575

Erhard, Ph. 446
Erlenkämper, B. 515
Ernst, F. 130
Ewering, M. 527

F
Fafoutis, V. 473
Fandrey, J. 247
Fehsenfeld
– C. 446
– P. 446
Feinle, P. 93, 290
Felderhoff, J. F. 726
Finnerud, L. O. 110
Fischer, A. 140, 271, 278, 479
Friedrich, K. 20, 417
Fritsch, R. 541
Fünfschilling, S. 383

G
Gachot, C. 59
Garcia
– A. 597, 618
– J. 703
– L.F. 703
Gathen, M. 234
Geanta, V. 610
Gerhardt, L.-C. 487
Gerlach, G. 560
Gerschwiler, K. 541
Gleising, B. 140
Gleß, M. 473
Gnyusov, S.F. 402
Gódor, I. 45
Goebbels, N. 240, 547
Goedecke, A. 307
Göhler, O.-C. 515, 582
Göken, M. 171
Gold, P. W. 554, 568
Gorgels, C. 588
Gräber, H.G. 216
Grebe, M. 290
Grecu
– L. 682
– V. 682
Greiner, L. 509
Grosse, S. 256
Großmann, U. 339
Grün, F. 45
Gventsadze, D. 159
Gyurova, L. A. 417

H
Hahn, M. 140
Hassan, A. M. 33
Hausen, F. 178
Hazeli, K. 623
Hegadekatte, V. 256, 347
Heilmann, M. 726
Henry, P. 708
Hernández, R. 327
Herzog, D. 509
Hollstein, T. 191
Huber, N. 256, 347
Hunsicker, W. 290

I
Ierardi, M. C. F. 645
Immich, P. 527, 737

J
Janietz, D. 409
Jiang, Z. 417
Jumate, N. 610

K
Kailer, A. 191, 198, 383, 409
Kalkanli, A. 81
Karlsohn, M. 152, 690
Kashani Bozorg, F. 623
Kaspar, J. 74, 654
Kellermann, K. 247
Kern, A. 93
Khader, I. 383
Kienzler, A. 629
Kirma, T. 81
Klaiber, F. 737
Kleinrahm, A. 446
Klocke, F. 535, 541
Koncsik, Z. 393
Konrath, G. 409
Kostka, A. 703

Kovácik, J. 67
Kraft, O. 347
Krakhmalev, P. 732
Krämer, A. 521, 547
Kramer, N. 719
Krummhauer, O. 191, 198
Kulkov, S.N. 402
Küppers, M.J.S. 509
Kurzenhäuser, S. 376
Kurzydlowski, K. J. 667, 674
Kutelia, E. 159
Kuzsella, L. 393
Kyryliv, O. 667

L
Lammer, A. 703
Lancaster, J. K. 207
Larosa, M. A. 645
Larsson, P.-L. 321
Leibenguth, P. 59
Lewandowska, M. 667
Lewis, R. 124
Liauw, M.A. 509
Liersch, A. 696
Löffler, F. 460
Loos, J. 554
Lorenzo, V. 618
Lou, D. C. 110, 660
Luft, A. 654

M
Maier, H. 521
Mashal, Y. A-H. 207
Mattfeld, P. 535
Meeß, R. 460
Menezes, L.F. 165
Michael, S. 521
Michaeli, W. 737
Mikadze
– G. 159
– O. 159
Mischler, S. 185
Moazzemi, L. 623
Mock, R. 307
Momeni, S. 234
Moral, A. 227
Mücklich, F. 59
Müller, D.H. 509
Münch, A. 431
Murrenhoff, H. 494, 575, 582

N
Ndlovu, S. N. 171
Nickel, K. G. 191, 198
Nielinger, M. 178
Nilsson, D. 314

O
Oberacker, R. 383
Oliveira, M.C. 165
Olsson, D. D. 439
Onsøien, M. I. 660
Ostermeyer, G.-P. 301
Ott, S. 453

P
Park, T.-J. 744
Picas, I. 327
Pinto, M. A. 645
Plogmann, M. 568
Podghainiy, N. 178
Pontzen, F. 509
Pourzal, R. 479
Presser, V. 191, 198
Provatidis, C. G. 473
Pyzalla, A. R. 152, 690, 703

R
Ramalho, A. 165
Ratzi, R. 696
Rechberger, M. 339
Reimers, W. 152, 690
Repphun, G. 473
Richardt, K. 130
Riera, M.D. 327
Rosiwal, S. M. 247
Röttger, A. 152, 690

S
Saaro, S. 423
Sabat, K. 597
Sabour Rouhaghdam, A. 604, 637

Samerski, I. 278
Sandberg, O. 333
Savchenko, N.L. 402
Sawade, H. 409
Schipper, D. J. 278
Schläfer, T. 130
Schlarb, A. K. 417
Schneider, J. 369, 376, 629
Schöfer, J. 278
Schriever, U. 93
Schulz, K. 431
Schulze, V. 629
Schumacher, J. 582
Selcuk, E. 81
Senk, D. 431
Silva, P.A. 152, 690
Simiti, I. V. 610
Singer, R. F. 247
Slatter, T. 124
Slesinski, R. 674
Solberg, J. K. 110
Spencer, N.D. 487
Spinelli, J. E. 597
Stahr, C. C. 423
Stefanoiu, R. 610
Steiner, L. 256
Stojadinovic, J. 185
Strässle, V. 487

T
Takadoum, J. 708
Tarata, D. F. 750
Tashtoush, G. M. 33
Theisen, W. 152, 690
Theiß, S. 737
Theissmann, R. 140
Thiele, S. 423
Thuvander, A. 333
Tietz, F. 654
Tillmann, W. 234
Treutler, C.P.O. 256
Tsurtsumia, O. 159

V
Vaduvoiu, G. 750
van der Meer, M. 227
Varela, A. 618
Vasiu, R. 610
Verpoort, C. 130
Vitry, V. 264
Vogli, E. 234
Voiculescu, I. 610

W
Wackers, P. 314
Wahl, R. 355
Wallstabe, R. 369
Warnke, C. 527
Wäsche, R. 216
Wassenberg, R. B. 104
Wauthier, K. 355
Weber, S. 152, 690, 703
Weisheit, A. 117
Werner, A. 314
Winderlich, B. 74
Wirth, R. 198
Wissenbach, K. 117
Wolf, T. 568
Wöppermann, M. 362
Woydt, M. 423
Wredenberg, F. 321

Y
Yazdi, R. 623
Yilmaz, K. 240

Z
Zeppenfeld, C. 535
Zhang, Z. 417
Zietsch, Ch. 271
Zimmermann, M. 535
Zum Gahr, K.-H. 355, 362, 369, 376, 629

Subject Index

A

abrasion resistant Fe-base metal matrix composites, hot direct extrusion 690
admixed solid lubricants, role for sintered steels 696
ageing, lubricants 582
aging treatment, precipitation hardening steels 654
AISI 420 stainless steel, laser surface treatment 645
Al-4wt% Mg alloys, hardness and wear resistance 33
Al-Si and Al-Sn alloys, directionally solidified 597
alumina mated against steel, dry friction performance 369
aluminum based sliding materials, with soft phases 45
anti-galling, tool steel 333
aqueous media lubricated sliding 191
asperities, creep behavior 307
asperity dry contacts, comparison of experiments and analytical computer simulation 271
atomic force microscopy, nanotribology at electrodes 178
austenitic high nitrogen stainless steel, reciprocating sliding wear 479
axial piston pumps, with coated tribological systems 575

B

bearings, rolling friction apparatus 460
Bi-metal casting, production of coal crushing hammer heads 81
bio-based lubricants, toxic and ecotoxic behaviour 515
BN, tungsten inert gas process 623
brake systems, dynamic friction phenomena 301
bronze alloy, hardfaced wear resistant 610

C

car engines, thermally sprayed nanocrystalline cylinder running surfaces 130
carbon fiber TiO_2, wear and friction 417
carburizing, pulsed bipolar nanocrystalline plasma electrolytic 637
casting, steel 431
cavitation erosion resistance, improvement by laser nitriding 74
cemented carbide, microtribological characterization 376
ceramic/ceramic pairs, surface textured 362
ceramic materials, for dental restorations 216
– tribological characterization 207
ceramic/steel friction pairs, oil lubricated 355
chelating agents, influence on tribocorrosion mechanisms 185
chromium based PVD coatings, for injection moulding tools 737
CMC, high-speed dry sliding on steel 402
co-extruded layered structures, mechanical properties 690
coal crushing hammer heads, production by Bi-metal casting 81
coated tribological systems, axial piston pumps 575
coatings
– compatible stamping 535
– DLC *see* DLC coatings
– PVD *see* PVD coatings
– thermal spray 140, 423
– WC-Co 732
CoCrMo-alloy, reciprocating sliding wear 479
collaborative research center 442, environmentally friendly tribosystems 494
compacted graphite iron, influence of induction hardening 124

composites
– Cu-graphite 67
– Fe base metal matrix 152, 690
– particle reinforced steel matrix 110
– polymer 20
– wear-resistant 159
compound layer, pulsed bipolar nanocrystalline plasma electrolytic carburizing 637
contact stress analysis, seal and steel surface 744
contacts
– fully plastic 307
– highly loaded mixed lubrication 453
– multiple asperity dry 271
copper wire, hot rolling 383
CP-Ti
– surface alloying 623
– surface carburizing 604
Cu-graphite composites, friction coefficient 67
cutting processes, wearing effects 339
cutting tool wear, and thermo-mechanical stresses 726
CVD-diamond coating, wear protection for standard heat-treatable steel 247
cylinder bores, thermally sprayed coatings 140

D
dental materials, ceramic 216
diamond grain-types, steel-ceramic-compound grinding 719
diamond tools, wear mechanisms 703
die loads, computation of 333
die material, effect on friction 104
DLC-coated spindle ball bearings, performance 560
DLC coatings
– wear modeling 256
– wettability 240
DLC layers, influence on unhardened steel moulds 234
dry contacts, multiple asperity 271
dry friction performance, alumina mated against steel 369
dry sliding
– on steel 402
– thermal spray coatings 423

E
elastic-plastic thin films, scratching on elastic substrates 321
elastic substrates, scratching of elastic-plastic thin films 321
electrified railway wires, abrasive wear behaviour 618
electrode potential, influence on tribocorrosion mechanisms 185
electroless nickel-boron deposits, mechanical and tribological properties 264
electrolytes, tribocorrosion studies 708
engineering ceramics
– microtribological characterization 376
– tribological characterization 207
environmentally friendly lubricants, epoxidation of oleic esters 509
environmentally friendly machining, PVD coating systems 541
environmentally friendly tribosystems, collaborative research center 442 494
epidermal hydration, effect on textile friction 487
ester, wettability of DLC coatings 240
ester-based lubricants, characterization of changes 521
extrusion, abrasion resistant Fe-base metal matrix composites 152

F
failure stresses, numerical calculation 554
false-brinelling effect 290
fatigue life, rolling contacts 473
Fe-base metal matrix composites
– abrasion resistant 152, 690
Fe-based matrices, reinforced with WC-Co particles 703
Fe-Cr-Al alloys, heat-resistant 159
fine blanking tool surfaces, manufacturing 535
finite element modelling (FEM), forming tool performance 327

forming tool performance, finite element modelling (FEM) 327
fretting wear prediction, energy based 314
friction
– effected by die material 104
– influence on ageing of lubricants 582
friction coefficient, Cu-graphite composites 67
friction forces, influence of adsorbates and potential 178
friction phenomena, brake systems 301
fully plastic contact, creep behavior of asperities 307

G
graded layers, for wear and corrosion protection 117
graphite addition, effect on hardness and wear resistance 33
graphite iron, influence of induction hardening 124
grinding, steel-ceramic-compound 719

H
hard ore material, comminution 439
hardmetals, WC-Co 171
hardness, effect of graphite and silicon carbide addition 33
heat-resistant Fe-Cr-Al alloys, wear-resistant composites 159
heat-treatable steel, CVD-diamond coating 247
high and low wear regimes, influence of surface topography 278
high performance PVD tool coatings 527
high-speed dry sliding, on steel 402
highly loaded mixed lubrication contacts 453
highly loaded tribological contacts 467
highly wear-resistant special structural steels, wear behavior 93
hot direct extrusion
– abrasion resistant Fe-base metal matrix composites 152, 690
human skin, tribology 487
hydrostatic extrusion, stainless steel 316LVM 667

I
implant materials, scratch tests 227
induction hardening, compacted graphite iron 124
injection moulding tools, PVD coatings 737
intermittent surface pressure, highly loaded mixed lubrication contacts 453
iron powder compaction, effect of die material 104
isooctane, sliding of steel/ceramic and ceramic/ceramic pairs 362

L
laser cladding, graded layers 117
laser hardening, of steels 682
laser interference induced microstructural architectures, in metallic systems 59
laser nitriding, improvement of cavitation erosion resistance 74
laser solution annealing, precipitation hardening steels 654
laser surface treatment, AISI 420 stainless steel 645
liquid crystalline fluids, lubricant for reciprocating systems 409
low frequency loading, fretting wear 314
lubricants
– admixed solid 696
– bio-based 515
– environmentally friendly 509
– ester-based 521
– friction and ageing 515
– influence of friction on ageing 582
– liquid crystalline fluids 409
lubricated sliding conditions, magnesium alloy AZ91D 52
lubricated systems, advanced 446
lubrication, continuous casting of steel 431
lubrication contacts, highly loaded mixed 453

M
machine tools, suitable coatings and fluids 494
machining, environmentally friendly 541
magnesium alloy AZ91D, friction and wear behavior 52
MARAGING steels, hot wear resistance 750
mechanical pulse treatment, stainless steel 316LVM 667
metal matrix composites, Fe-base 152
metallic systems, laser interference induced microstructural architectures 59
metals, improvement of wear resistance 660
micro linear bearings, rolling friction apparatus 460
micro-machines, modelling and simulation of wear 347
micro powder injection moulding, mould inserts 629
microstructural architectures in metallic systems, tribological properties 59
microstructure, WC-Co 732
microtribology, engineering ceramics 376
MMC, high-speed dry sliding on steel 402
model bench, highly loaded mixed lubrication contacts 453
modeling
– unlubricated oscillating sliding wear 256
– wear in micro-machines 347
motor tests, thermally sprayed coatings in cylinder bores 140
mould inserts, influence of surface condition 629

N
nano-TiO_2, wear and friction 417
nanocrystalline cylinder running surfaces, thermally sprayed 130
nanocrystalline plasma electrolytic carburizing, pulsed bipolar 637
nanotribology, at electrodes 178
natural nacre, scratch tests 227
nickel-boron deposits, mechanical and tribological properties 264
nitrogen-rich surface layers, stainless steel 316LVM 674

O
oil lubricated ceramic/steel friction pairs, at high sliding speeds 355
oleic esters, epoxidation 509
online wear measurements, lubricated systems 446

P
parallel-axis-transmissions, PVD coatings 588
particle reinforced steel matrix composites, adhesion resistance 110
passenger car engines, thermally sprayed nanocrystalline cylinder running surfaces 130
polyalphaolefin, wettability of DLC coatings 240
polymer composites, in tribology 20
pre-placed BN, tungsten inert gas process 623
precipitation hardening steels, laser solution annealing 654
pulsed bipolar nanocrystalline plasma electrolytic carburizing 637
PVD coating systems, for environmentally friendly machining 541
PVD coatings
– chromium based 737
– effects on fatigue of roller bearings 568
– efficiency of parallel-axis-transmissions 588
– numerical calculation of failure stresses 554
– wear resistant 547
PVD tool coatings, high performance 527

R
railway wires, abrasive wear behaviour 618
reciprocating sliding wear, stainless steel 479
reciprocating systems, ultralow friction and wear 409

roller bearings, effects of PVD coatings 568
rolling
– copper wire 383
– engineering ceramic, cemented carbide and steel 376
rolling and sliding contacts, wear simulation 3
rolling contacts, fatigue life 473
rolling friction apparatus, for micro linear bearings 460
rough surfaces, rolling contacts 473

S
scratch testing, WC-Co hardmetals 171
scratch tests, on natural nacre 227
scratching, of elastic-plastic thin films 321
seal surface, contact stress analysis 744
sheet forming, dies of tool steel with improved anti-galling properties 333
short carbon fiber TiO_2, wear and friction 417
Si_3N_4 composites, tribological investigation 393
silicon carbide, corrosion behavior 191
silicon carbide addition, effect on hardness and wear resistance 33
silicon carbide tribo-corrosion, P-T conditions 198
silicon nitride tool, hot rolling copper wire 383
simulation
– multiple asperity dry contacts 271
– wear in micro-machines 347
simulation approach, cutting processes 339
simulative wear testing, tool materials 439
sintered steels, role of admixed solid lubricants 696
sliding
– aqueous media lubricated 191
– steel/ceramic and ceramic/ceramic pairs 362
sliding conditions, lubricated 52
sliding directions, superposed on highly loaded mixed lubrication contacts 453
sliding friction, global versus local analysis 165
sliding materials, aluminum based 45
solid lubricants, role for sintered steels 696
solidification microstructure, Al-Si and Al-Sn alloys 597
spindle ball bearings, DLC-coated 560
spray coatings, thermal 423
stainless steel
– laser surface treatment 645
– surface modified austenitic high nitrogen 479
stainless steel 316L, in electrolytes 708
stainless steel 316LVM
– mechanical pulse treatment and hydrostatic extrusion 667
– surface layers 674
stamping, tool-coating-compatible 535
standstill marks, influence factors 290
steel-ceramic-compound grinding, diamond grain-types 719
steel/ceramic pairs
– oil lubricated 355
– surface textured 362
steel hardening, with lasers 682
steel matrix composites, particle reinforced 110
steel moulds, unhardened 234
steel surface, contact stress analysis 744
steels
– continuous casting 431
– heat-treatable 247
– high-speed dry sliding 402
– highly wear-resistant 93
– laser solution annealing 654
– laser surface treatment 645
– lubrication experiments 431
– MARAGING 750
– microtribological characterization 376
– sintered 696
– stainless *see* stainless steel
– tool 333
stress analysis, seal and steel surface 744
structural steels, highly wear-resistant 93
suitable coatings and fluids, with respect to machine tool 494

surface alloying, CP-Ti 623
surface carburizing, of CP-Ti 604
surface layers, stainless steel 316LVM 674
surface modified austenitic high nitrogen stainless steel, reciprocating sliding wear 479
surface pressure, highly loaded mixed lubrication contacts 453
surface texture, ceramic/ceramic pairs 362
surface topography, influence on wear regimes 278

T
TA6V4 alloy, in electrolytes 708
temperature measurements, thin film layer sensors 467
textile friction, effect of epidermal hydration 487
thermal spray coatings, dry sliding wear properties 423
thermally sprayed coatings, wear mechanisms and microstructural changes 140
thermally sprayed nanocrystalline cylinder running surfaces, car engines 130
thermo-mechanical stresses, and cutting tool wear 726
thin film layer sensors, for temperature measurements 467
TiO_2
– short carbon fiber and/or nano- 417
– thermal spray coatings 423
titanium alloys, laser nitriding 74
tool-coating-compatible stamping, manufacturing 535
tool materials, simulative wear testing 439
tool steel, with improved anti-galling properties 333
tool surfaces, fine blanking 535
toxicity, bio-based lubricants 515
tribocorrosion
– 316L stainless steel 708
– TA6V4 alloy 708
tribocorrosion mechanisms, tungsten 185
tribological contacts, thin film layer sensors 467
tribological systems, coated 575
tribology
– ceramic materials 207
– forming tool performance 327
– of human skin 487
– polymer composites in 20
– Si_3N_4 composites 393
– stainless steel 316LVM 667, 674
– steel hardening with lasers 682
tungsten, tribocorrosion mechanisms 185
tungsten inert gas process, surface alloying of CP-Ti 623

U
ultralow friction and wear, reciprocating systems 409
unhardened steel moulds, influence of DLC layer 234
unlubricated oscillating sliding wear, modeling and simulation 256
unsteady state conditions, Al-Si and Al-Sn alloys 597

W
WC-Co, abrasive edge wear 732
WC-Co hardmetals, scratch testing 171
WC-Co particles, for reinforcement of Fe-based matrices 703
wear particle, between seal and steel surface 744
wear prediction 314
wear regimes, transition between high and low 278
wear resistance, effect of graphite and silicon carbide addition 33
wear simulation, rolling and sliding contacts 3